CHEMICAL ENGINEERING RESEARCH & DESIGN

Transactions of The Institution of Chemical Engineers

Editor
Brian Gay

Editorial Board
C. Hanson
P. J. Heggs
C. N. Kenney
J. C. Middleton
J. F. Pillow
B. Yates

Associate Editors
J. R. Bourne (*Continental Europe*)
R. B. Keey (*New Zealand*)
R. G. H. Prince (*Australia*)
M. M. Sharma (*India*)
J. M. Smith (*Continental Europe*)
J. O. Wilkes (*USA*)

Contents

1 Editorial.
2 Notes for Authors.
3 Measurement of Bubble Size Distribution in Turbulent Gas—Liquid Dispersions.
M. Greaves and K. A. H. Kobbacy.
13 Effective Interfacial Area and Liquid Side Mass Transfer Coefficients in Absorption Columns Packed with Hydrophilised and Untreated Plastic Packings.
V. Linek, P. Petricek, P. Benes and R. Braun.
22 Isothermal Two-phase Flow of Air and Aqueous Polymer Solutions in a Smooth Horizontal Pipe.
R. P. Chhabra, S. I. Farooqi and J. F. Richardson.
33 Influence of Phase Ratio on Electrostatic Coalescence of Water-in-oil Dispersions.
P. J. Bailes and S. K. L. Larkai.
39 Flow Regimes on Sieve Trays: The Significance of the Emulsion Flow Regime.
F. J. Zuiderweg, P. A. M. Hofhuis and J. Kuzniar.
48 Drop Coalescence in Liquid—Liquid Dispersions by Flow through Glass Fibre Beds.
V. Grilc, J. Golob and R. Modic.
Shorter Communications.
53 Liquid Dispersion and Efficiency on a Sieve Tray with Inch Diameter Perforations.
O. Ogboja.
57 Decomposition of Trichlorofluoromethane (R11) under Static and Flow Conditions.
P. Srinivasan, S. Devotta and F. A. Watson.
60 Correspondence.
63 Doctorates in Chemical Engineering 1982/83.
Book Reviews: pages 32, 52.

VOL
62
198



Vol 62 No 1 January 1984

ISSN 0263–8762

Published by The Institution of Chemical Engineers

CHEMICAL ENGINEERING RESEARCH & DESIGN

Transactions of The Institution of Chemical Engineers

Editor
Brian Gay

Editorial Board
C. Hanson
P. J. Heggs
C. N. Kenney
J. C. Middleton
J. F. Pillow
B. Yates

Associate Editors
J. R. Bourne (*Continental Europe*)
R. B. Keey (*New Zealand*)
R. G. H. Prince (*Australia*)
M. M. Sharma (*India*)
J. M. Smith (*Continental Europe*)
J. O. Wilkes (*USA*)

Contents

1 Editorial.
2 Notes for Authors.
3 Measurement of Bubble Size Distribution in Turbulent Gas—Liquid Dispersions.
M. Greaves and K. A. H. Kobbacy.
13 Effective Interfacial Area and Liquid Side Mass Transfer Coefficients in Absorption Columns Packed with Hydrophilised and Untreated Plastic Packings.
V. Linek, P. Petricek, P. Benes and R. Braun.
22 Isothermal Two-phase Flow of Air and Aqueous Polymer Solutions in a Smooth Horizontal Pipe.
R. P. Chhabra, S. I. Farooqi and J. F. Richardson.
33 Influence of Phase Ratio on Electrostatic Coalescence of Water-in-oil Dispersions.
P. J. Bailes and S. K. L. Larkai.
39 Flow Regimes on Sieve Trays: The Significance of the Emulsion Flow Regime.
F. J. Zuiderweg, P. A. M. Hofhuis and J. Kuzniar.
48 Drop Coalescence in Liquid—Liquid Dispersions by Flow through Glass Fibre Beds.
V. Grilc, J. Golob and R. Modic.
Shorter Communications.
53 Liquid Dispersion and Efficiency on a Sieve Tray with Inch Diameter Perforations.
O. Ogboja.
57 Decomposition of Trichlorofluoromethane (R11) under Static and Flow Conditions.
P. Srinivasan, S. Devotta and F. A. Watson.
60 Correspondence.
63 Doctorates in Chemical Engineering 1982/83.
Book Reviews: pages 32, 52.

VOL
62
198



Vol 62 No 1 January 1984

ISSN 0263–8762

Published by The Institution of Chemical Engineers

CHEMICAL ENGINEERING RESEARCH & DESIGN

Transactions of The Institution of Chemical Engineers

OL.
62
984

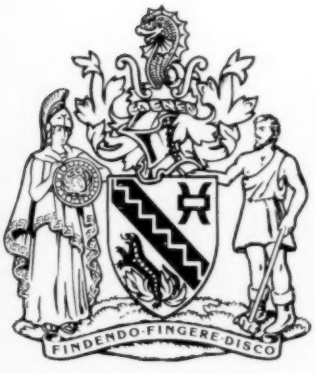
Editor
Brian Gay

Editorial Board
P. Eisenklam
C. Hanson
P. J. Heggs
J. C. Middleton
J. F. Pillow
B. Yates

Associate Editors
J. R. Bourne (*Continental Europe*)
R. B. Keey (*New Zealand*)
R. G. H. Prince (*Australia*)
M. M. Sharma (*India*)
J. M. Smith (*Continental Europe*)
J. O. Wilkes (*USA*)

Contents

65 Editorial.
66 Notes for Authors.
67 Review Paper.
Development and Potential of Power Fluidics for process Flow Control.
G. H. Priestman and J. R. Tippetts.
81 Kinetic Analysis of the Catalytic Dehydration of Alcohols over Zeolites.
P. L. Yue and O. Olaofe.
92 Studies of Fluid Displacement by Foam in Porous Media.
R. W. Burley, C. W. Nutt and M. Gh. Bayat.
101 Fault Tree Synthesis Based on Control Loop Structure.
A. Shafaghi, P. K. Andow and F. P. Lees.
111 Liquid Passage on Sieve Trays Operating in the Spray Regime.
J. A. Raper, W. V. Pinczewski and C. J. D. Fell.
117 Laboratory Evaluation of Lin's Model of Continuous Sterilisation of Micro-organisms.
K. R. Davey and D. G. Wood.
123 Power Consumption in the Mixing of Boger Fluids.
D. R. Oliver, A. W. Nienow, R. J. Mitson and K. Terry.
128 Heat Transfer and Pressure Drop Characteristics of Alternate Rotation Swirl-Flow Inducers in a Circular Duct.
D. Burfoot and P. Rice.
133 Shorter Communication.
Biomass Hold-up Correlations for a Fluidised Bed Biofilm Reactor.
W. K. Shieh and C. Y. Chen.
Book Reviews: pages 100, 122, 136.



Vol 62 No 2 March 1984

ISSN 0263–8762

Published by The Institution of Chemical Engineers

CHEMICAL ENGINEERING RESEARCH & DESIGN

Transactions of The Institution of Chemical Engineers

VOL.
62
198

Editor
Brian Gay

Editorial Board
P. Eisenklam
C. Hanson
P. J. Heggs
J. C. Middleton
J. F. Pillow
B. Yates

Associate Editors
J. R. Bourne (*Continental Europe*)
R. B. Keey (*New Zealand*)
R. G. H. Prince (*Australia*)
M. M. Sharma (*India*)
J. M. Smith (*Continental Europe*)
J. O. Wilkes (*USA*)

Contents

137 Editorial.
138 Notes for Authors.
139 Vertical Co-Current Flow of Air and Shear Thinning Suspensions of Kaolin.
Z. Khatib and J. F. Richardson.
155 Biomass Hold-ups and Overall Rates of Substrate (Glucose) Uptake of Support Particles Containing a Mixed Microbial Culture.
B. Atkinson, J. D. Cunningham and A. Pinches.

165 Book Reviews (continued on page 172).

167 Molecular Sieving Effects of Zeolites in the Dehydration of Alcohols.
P. L. Yue and O. Olaofe.
173 Bubble Size Measurements and Correlation in a Fluidised Bed at High Temperatures.
J. F. Stubington, D. Barrett and G. Lowry.
179 Effect of Scale-up on Secondary Nucleation Kinetics for the Sodium Chloride-Water System.
P. A. M. Grootscholten, L. D. M. v. d. Brekel and E. J. de Jong.

190 Correspondence.

Shorter Communications.
191 Scaling-up Distillation Tray Efficiency under Conditions of Weeping or Entrainment when Liquid Channelling also Occurs.
T. Plaka, I. S. Ahmed and M. J. Lockett.
194 Effect of Flow Ratio on the Performance of an Experimental Absorption Cooling System.
P. Kumar, S. Devotta and F. A. Holland.
197 Role of Cavity Formation in Stirred Gas-Liquid-Solid Reactors.
M. M. C. G. Warmoeskerken, M. C. van Houwelingen, J. J. Frijlink and J. M. Smith.

200 Corrections.
Please note the important correction to the authors' names on page 128 in the March issue.

Vol 62 No 3 May 1984

ISSN 0263–8762

Published by The Institution of Chemical Engineers

CHEMICAL ENGINEERING RESEARCH & DESIGN

Transactions of The Institution of Chemical Engineers

Editor
Brian Gay

Editorial Board
P. Eisenklam
C. Hanson
P. J. Heggs
J. C. Middleton
J. F. Pillow
B. Yates

Associate Editors
J. R. Bourne (*Continental Europe*)
R. B. Keey (*New Zealand*)
R. G. H. Prince (*Australia*)
M. M. Sharma (*India*)
J. M. Smith (*Continental Europe*)
J. O. Wilkes (*USA*)

Contents

201 Editorial.
202 Notes for Authors.
203 Review Paper.
Developments in Anaerobic Treatment of High Strength Industrial Waste Waters.
M. A. Bull, R. M. Sterritt and J. N. Lester.
214 Mixing of Particles in Liquid Fluidised Beds.
A. P. van der Meer, C. M. R. J. P. Blanchard and J. A. Wesselingh.
223 Effect of Pressure on Combustion of Char in Fluidised Beds.
E. Turnbull, E. R. Kossakowski, J. F. Davidson, R. B. Hopes, H. W. Blackshaw and P. T. Y. Goodyer.
235 Mass Transfer Processes During the Adsorption of Solutes in Aqueous Solutions in Batch and Fixed Bed Adsorbers.
G. McKay.
247 Solid-Liquid Mass Transfer Coefficient in Mechanically Agitated Contactors.
V. K. Patil, J. B. Joshi and M. M. Sharma.
255 Gas Hold-up and Interfacial Area in Aerated Suspensions of Small Particles.
E. Capuder and T. Koloini.
261 Enhanced Collection Efficiency for Cyclone Dust Separators.
M. Biffin, N. Syred and P. Sage.
266 Shorter Communication.
Thermal Decomposition of Trichlorotrifluoroethane (R113) Under Static and Flow Conditions.
P. Srinivasan, V. R. Patwardhan, S. Devotta and F. A. Watson.
269 Correspondence.
Book Reviews: pages 222, 234

Vol 62 No 4 July 1984

ISSN 0263-8762

Published by The Institution of Chemical Engineers

CHEMICAL ENGINEERING RESEARCH & DESIGN

Transactions of The Institution of Chemical Engineers

VOL
62
198

Editor
Brian Gay

Editorial Board
P. Eisenklam
C. Hanson
P. J. Heggs
J. C. Middleton
J. F. Pillow
B. Yates

Associate Editors
J. R. Bourne (*Continental Europe*)
R. B. Keey (*New Zealand*)
R. G. H. Prince (*Australia*)
M. M. Sharma (*India*)
J. M. Smith (*Continental Europe*)
J. O. Wilkes (*USA*)

Contents

273 Editorial.
274 Notes for Authors.
275 Review Paper.
Particle Deposition Behaviour from Turbulent Flows.
P. G. Papavergos and A. B. Hedley.
296 Comparison between Indirect and Direct Contact Cooling Methods for the Crystallisation of Potassium Sulphate.
J. W. Mullin and J. R. Williams.
303 Absorption during Gas Injection through a Submerged Nozzle.
Part I: Gas Side and Liquid Side Transfer Coefficients.
F. A. N. Rocha and J. R. F. Guedes de Carvalho.
315 Fixed Bed Sorption with Recycle.
Part I: Mathematical Model and Single Reversible Reactions.
J. T. Casey and A. I. Liapis.
321 Clear Liquid Height on Sieve and Valve Trays.
H. Dhulesia.
327 Electrostatic Hazards Associated with Marine Chemical Tanker Operations. Criteria of Incendivity in Tank Cleaning Operations.
M. R. O. Jones and J. Bond.
334 Shorter Communication.
Measurement of bubble sizes and velocities in gas—liquid dispersions.
D. A. Lewis, R. S. Nicol and J. W. Thompson
Book Reviews: pages 302, 314, 320.



Vol 62 No 5 September 1984

ISSN 0263-8762

Published by The Institution of Chemical Engineers

CHEMICAL ENGINEERING RESEARCH & DESIGN

Transactions of The Institution of Chemical Engineers

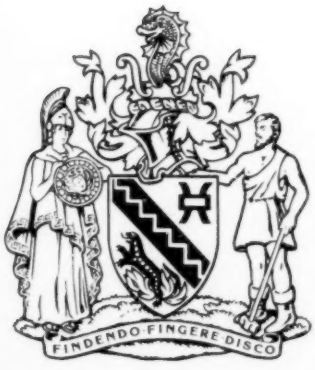
Editor
Brian Gay

Editorial Board
P. Eisenklam
C. Hanson
P. J. Heggs
J. C. Middleton
J. F. Pillow
B. Yates

Associate Editors
J. R. Bourne (*Continental Europe*)
R. B. Keey (*New Zealand*)
R. G. H. Prince (*Australia*)
M. M. Sharma (*India*)
J. M. Smith (*Continental Europe*)
J. O. Wilkes (*USA*)

Contents

337 Editorial.
338 Notes for Authors.
339 Metal deposition in residuum hydrodesulphurisation catalysts.
L. O. Oyekunle and R. Hughes.
344 Fixed bed sorption with recycle.
Part II: Parallel Reversible Reactions.
J. T. Casey and A. I. Liapis.
351 Gas explosions in compartmented vessels: pressure piling.
J. Singh.
367 Forced convection heat transfer of power law fluid at low Peclet number flow
V. D. Dang
373 Alternative model for ultrafiltration.
M. S. Le and J. A. Howell
381 Use of frequency-consequence curves to examine the conclusions of published risk analyses and to define broad criteria for major hazard installations.
D. O. Hagon.
387 Model of isothermal transport line (riser) and moving-bed catalytic reactor.
A. A. Shaikh and J. J. Carberry.
391 Application of modelling and computer simulation to pharmaceutical processes: the Williamson synthesis.
A. R. Wright.
398 Correspondence.
400 List of Referees 1984
401 11th Annual Research Meeting.
Heat transfer, catalysis and catalytic reactors.
P. J. Heggs and A. Gilmore.
406 Index to Volume 62.
Book Reviews: pages 343, 350.



Vol 62 No 6 November 1984

ISSN 0263-8762

Published by The Institution of Chemical Engineers

INDEX TO VOLUME 62, 1984

AUTHORS AND PAPERS

Ahmed, I. S., see Plaka, T.
Andow, P. K., see Shafaghi, A.
Atkinson, B., Cunningham, J. D. and Pinches, A., Biomass hold-ups and overall rates of substrate (glucose) uptake of support particles containing a mixed microbial culture 155

Bailes, P. J. and Larkai, S. K. L., Influence of phase ratio on electrostatic coalescence of water-in-oil dispersions 33
Barrett, D., see Stubington, J. F.
Bayat, M.Gh., see Burley, R. W.
Benes, P., see Linek, V.
Biffin, M., Syred, N. and Sage, P., Enhanced collection efficiency for cyclone dust separators 261
Blackshaw, H. W., see Turnbull, E.
Blanchard, C. M. R. J. P., see van der Meer, A. P.
Bond, J., see Jones, M. R. O.
Braun, R., see Linek, V.
Bull, M. A., Sterritt, R. M. and Lester, J. N., Developments in anaerobic treatment of high strength industrial waste waters 203
Burfoot, D. and Rice, P., Heat transfer and pressure drop characteristics of alternate rotation swirl-flow inducers in a circular duct 128
Burley, R. W., Nutt, C. W. and Bayat, M.Gh., Studies of fluid displacement by foam in porous media 92

Capuder, E. and Koloini, T., Gas hold-up and interfacial area in aerated suspensions of small particles 255
Carberry, J. J., see Shaikh, A. A.
Casey, J. T. and Liapis, A. I., Fixed bed sorption with recycle. Part I: Mathematical model and single reversible reactions 315
Casey, J. T. and Liapis, A. I., Fixed bed sorption with recycle. Part II: Parallel reversible reactions 344
Chen, C. Y., see Shieh, W. K.
Chhabra, R. P., Farooqi, S. I. and Richardson, J. F., Isothermal two-phase flow of air and aqueous polymer solutions in a smooth horizontal pipe 22
Cunningham, J. D., see Atkinson, B.

Dang, V. D., Forced convection heat transfer of power law fluid at low Peclet number flow 367
Davey, K. R. and Wood, D. G., Laboratory evaluation of Lin's model of continuous sterilisation of micro-organisms 117
Davidson, J. F., see Turnbill, E.
de Jong, E. J., see Grootscholten, P. A. M.
Devotta, S., see Kumar, P. and Srinivasan, P.
Dhulesia, H., Clear liquid height on sieve and valve trays 321

Farooqi, S. I., see Chhabra, R. P.
Fell, C. J. D., see Raper, J. A.
Frijlink, J. J., see Warmoeskerken, M. M. C. G.

Gilmore, A., see Heggs, P. J.
Golob, J., see Grilc, V.
Goodyer, P. T. Y., see Turnbull, E.
Greaves, M. and Kobbacy, K. A. H., Measurement of bubble size distribution in turbulent gas-liquid dispersions 3
Grilc, V., Golob, J. and Modic, R., Drop coalescence in liquid-liquid dispersions by flow through glass fibre beds 48
Grootscholten, P. A. M., v.d. Brekel, L. D. M. and de Jong, E. J., Effect of scale-up on secondary nucleation kinetics for the sodium chloride-water system 179
Guedes de Carvalho, J. R. F., see Rocha, F. A. N.

Hagon, D. O., Use of frequency-consequence curves to examine the conclusions of published risk analyses and to define broad criteria for major hazard installations 381
Hedley, A. B., see Papavergos, P. G.
Heggs, P. J., and Gilmore, A., 11th Annual Research Meeting: Heat transfer, catalysis and catalytic reactors 401
Hofhuis, P. A. M., see Zuiderweg, F. J.
Holland, F. A., see Kumar, P.
Hopes, R. B., see Turnbull, E.
Howell, J. A., see Le, M. S.
Hughes, R., see Oyekunle, L. O.

Jones, M. R. O., and Bond, J., Electrostatic hazards associated with marine chemical tanker operations: criteria of incendivity in tank cleaning operations 327
Joshi, J. B., see Patil, V. K.

Khatib, Z., and Richardson, J. F., Vertical co-current flow of air and shear thinning suspensions of kaolin 139
Kobbacy, K. A. H., see Greaves, M.
Koloini, T., see Capuder, E.
Kossakowski, E. R., see Turnbull, E.
Kumar, P., Devotta, S. and Holland, F. A., Effect of flow ratio on the performance of an experimental absorption cooling system 194
Kuzniar, J., see Zuiderweg, F. J.

Larkai, S. K. L., see Bailes, P. J.
Le, M. S. and Howell, J. A., Alternative model for ultrafiltration 373
Lees, F. P., see Shafaghi, A.
Lester, J. N., see Bull, M. A.
Lewis, D. A., Nicol, R. S. and Thompson, J. W., Measurement of bubble sizes and velocities in gas-liquid dispersions 334
Liapis, A. I., see Casey, J. T.
Linek, V., Petricek, P., Benes, P. and Braun, R., Effective interfacial area and liquid side mass transfer coefficients in absorption columns packed with hydrophilised and untreated plastic packings 13
Lockett, M. J., see Plaka, T.
Lowry, G., see Stubington, J. F.

McKay, G., Mass transfer processes during the adsorption of solutes in aqueous solutions in batch and fixed bed adsorbers 235
Mitson, R. J., see Oliver, D. R.
Modic, R., see Grilc, V.
Mullin, J. W. and Williams, J. R., Comparison between indirect and direct contact cooling methods for the crystallisation of potassium sulphate 296

Nicol, R. S., see Lewis, D. A.
Nienow, A. W., see Oliver, D. R.
Nutt, C. W., see Burley, R. W.

Ogboja, O., Liquid dispersion and efficiency on a sieve tray with inch diameter perforations 53
Olaofe, O., see Yue. P. L.
Oliver, D. R., Nienow, A. W., Mitson, R. J. and Terry, K., Power consumption in the mixing of Boger fluids 123
Oyekunle, L. O. and Hughes, R., Metal deposition in residuum hydrodesulphurisation catalysts 339

Papavergos, P. G., and Hedley, A. B., Particle deposition behaviour from turbulent flows 275
Patil, V. K., Joshi, J. B. and Sharma, M. M., Solid-liquid mass transfer coefficient in mechanically agitated contactors 247
Patwardhan, V. R., see Srinivasan, P.
Petricek, P., see Linek, V.
Pinches, A., see Atkinson, B.
Pinczewski, W. V., see Raper, J. A.
Plaka, T., Ahmed, I. S. and Lockett, M. J., Scaling-up distillation tray efficiency under conditions of weeping or entrainment when liquid channelling also occurs 191
Priestman, G. H. and Tippetts, J. R., Development and potential of power fluidics for process flow control 67

Raper, J. A., Pinczewski, W. V. and Fell, C. J. D., Liquid passage on sieve trays operating in the spray regime 111

VOL. 62 1984

Rice, P. and Burfoot, D., Heat transfer and pressure drop characteristics of alternate rotation swirl-flow inducers in a circular duct 128
Richardson, J. F., see Chhabra, R. P. and Khatib, Z.
Rocha, F. A. N. and Guedes de Carvalho, J. R. F., Absorption during gas injection through a submerged nozzle. Part I: Gas side and liquid side transfer coefficients 303

Sage, P., see Biffin, M.
Shafaghi, A., Andow, P. K. and Lees, F. P., Fault tree synthesis based on control loop structure 101
Shaikh, A. A. and Carberry, J. J., Model of an isothermal transport line (riser) and moving-bed catalytic reactor 387
Sharma, M. M., see Patil, V. K.
Shieh, W. K. and Chen, C. Y., Biomass hold-up correlations for a fluidised bed bio-film reactor 133
Singh, J., Gas explosions in compartmented vessels: pressure piling 351
Smith, J. M., see Warmoeskerken, M. M. C. G.
Srinivasan, P., Devotta, S. and Watson, F. A., Decomposition of trichlorofluoromethane (R11) under static flow conditions 57
Srinivasan, P., Patwardhan, V. R., Devotta, S., and Watson, F. A., Thermal decomposition of trichlorotrifluoroethane (R11) under static and flow conditions 266
Sterritt, R. M., see Bull, M. A.
Stubington, J. F., Barrett, D. and Lowry, G., Bubble size measurements and correlation in a fluidised bed at high temperatures 173
Syred, N., see Biffin, M.

Terry, K., see Oliver, D. R.
Thompson, J. W., see Lewis, D. A.
Tippetts, J. R., see Priestman, G. H.
Turnbull, E., Kossakowski, E. R., Davidson, J. F., Hopes, R. B., Blackshaw, H. W. and Goodyer, P. T. Y., Effect of pressure on combustion of char in fluidised beds. 223

v.d. Brekel, L. D. M., see Grootscholten, P. A. M.
van der Meer, A. P., Blanchard, C. M. R. J. P. and Wesselingh, J. A., Mixing of particles in liquid fluidised beds 214
van Houwelingen, M. C., see Warmoeskerken, M. M. C. G.

Warmoeskerken, M. M. C. G., van Houwelingen, M. C., Frijlink, J. J. and Smith, J. M., Role of cavity formation in stirred gas-liquid-solid reactors 197
Watson, F. A., see Srinivasan, P.
Wesselingh, J. A., see van der Meer, A. P.
Williams, J. R., see Mullin, J. W.
Wood, D. G., see Davey, K. R.
Wright, A. R., Application of modelling and computer simulation to pharmaceutical processes: the Williamson synthesis 391

Yue, P. L. and Olaofe, O., Kinetic analysis of the catalytic dehydration of alcohols over zeolites 81
Yue, P. L. and Olaofe, O., Molecular sieving effects of zeolites in the dehydration of alcohols 167

Zuiderweg, F. J., Hufhuis, P. A. M. and Kuzniar, J., Flow regimes on sieve trays: the significance of the emulsion flow regime 39

TITLES OF PAPERS

Absorption during gas injection through a submerged nozzle. Part I: Gas side and liquid side transfer coefficients. F. A. N. Rocha and J. R. F. Guedes de Carvalho 303
Alternative model for ultrafiltration. M. S. Le and J. A. Howell 373
Application of modelling and computer simulation to pharmaceutical processes: the Williamson synthesis. A. R. Wright 383

Biomass hold-up correlations for a fluidised bed biofilm reactor. W. K. Shieh and C. Y. Chen 133
Biomass hold-ups and overall rates of substrate (glucose) uptake of support particles containing a mixed microbial culture. B. Atkinson, J. D. Cunningham and A. Pinches 155
Bubble size measurements and correlation in a fluidised bed at high temperatures. J. F. Stubington, D. Barrett and G. Lowry 173

Clear liquid height on sieve and valve trays. H. Dhulesia. 321
Comparison between indirect and direct contact cooling methods for the crystallisation of potassium sulphate. J. W. Mullin and J. R. Williams 296
Corrections 200

Decomposition of trichlorofluoromethane (R11) under static and flow conditions. P. Srinivasan, S. Devotta and F. A. Watson 57
Development and potential of power fluidics for process flow control. G. H. Priestman and J. R. Tippetts 67
Developments in anaerobic treatment of high strength industrial waste waters. M. A. Bull, R. M. Sterritt and J. N. Lester 203
Doctorates in chemical engineering 1982/83 63
Drop coalescence in liquid–liquid dispersions by flow through glass fibre beds. V. Grilc, J. Golob and R. Modic 48

Effective interfacial area and liquid side mass transfer coefficients in absorption columns packed with hydrophilised and untreated plastic packings. V. Linek, P. Petricek, P. Benes and R. Braun 13
Effect of flow ratio on the performance of an experimental absorption cooling system. P. Kumar, S. Devotta and F. A. Holland 194
Effect of pressure on combustion of char in fluidised beds. E. Turnbull, E. R. Kossakowski, J. F. Davidson, R. B. Hopes, H. W. Blackshaw and P. T. Y. Goodyer 223
Effect of scale-up on secondary nucleation kinetics for the sodium chloride-water system. P. A. M. Grootscholten, L. D. M. v.d. Brekel and E. J. de Jong 179
Electrostatic hazards associated with marine chemical tanker operations; Criteria of incendivity in tank cleaning operations. M. R. O. Jones and J. Bond 327
Eleventh Annual Research Meeting; Heat transfer, catalysis and catalytic reactors. P. J. Heggs and A. Gilmore 393
Enhanced collection efficiency for cyclone dust separators. M. Biffin, N. Syred and P. Sage 261

Fault tree synthesis based on control loop structure. A. Shafaghi, P. K. Andow and F. P. Lees 101
Fixed bed sorption with recycle. Part I: Mathematical model and single reversible reactions. J. T. Casey and A. I. Liapis 315
Fixed bed sorption with recycle. Part II: Parallel reversible reactions. J. T. Casey and A. I. Liapis 344
Flow regimes on sieve trays; The significance of the emulsion flow regime. F. J. Zuiderweg, P. A. M. Hofhuis and J. Kuzniar 39
Forced convection heat transfer of power law fluid at low Peclet number flow. V. D. Dang 367

Gas explosions in compartmented vessels: pressure piling. J. Singh 351
Gas hold-up and interfacial area in aerated suspensions of small particles. E. Capuder and T. Koloini 255

Heat transfer and pressure drop characteristics of alternate rotation swirl-flow inducers in a circular duct. D. Burfoot and P. Rice 128

Influence of phase ratio on electrostatic coalescence of water-in-oil dispersions. P. J. Bailes and S. K. L. Larkai 33
Isothermal two-phase flow of air and aqueous polymer solutions in a smooth horizontal pipe. R. P. Chhabra, S. I. Farooqi and J. F. Richardson 22

Kinetic analysis of the catalytic dehydration of alcohols over zeolites. P. L. Yue and O. Olaofe 81

Laboratory evaluation of Lin's model of continuous sterilisation of micro-organisms. K. R. Davey and D. G. Wood 117
List of Referees 400
Liquid dispersion and efficiency on a sieve tray with inch diameter perforations. O. Ogboja 53
Liquid passage on sieve trays operating in the spray regime. J. A. Raper, W. V. Pinczweski and C. J. D. Fell 111

Mass transfer processes during the adsorption of solutes in aqueous solutions in batch and fixed bed adsorbers. G. McKay 235
Measurement of bubble size distribution in turbulent gas-liquid dispersions. M. Greaves and K. A. H. Kobbacy 3

Measurement of bubble sizes and velocities in gas-liquid dispersions. D. A. Lewis, R. S. Nicol and J. W. Thompson 334
Metal deposition in residuum hydrodesulphurisation catalysts. L. O. Oyekunle and R. Hughes 339
Mixing of particles in liquid fluidised beds. A. P. van der Meer, C. M. R. J. P. Blanchard and J. A. Wesselingh 214
Model of isothermal transport line (riser) and moving-bed catalytic reactor. A. A. Shaikh and J. J. Carberry 379
Molecular sieving effects of zeolites in the dehydration of alcohols. P. L. Yue and O. Olaofe 167

Particle deposition behaviour from turbulent flows. P. G. Papavergos and A. B. Hedley 275
Power consumption in the mixing of Boger fluids. D. R. Oliver, A. W. Nienow, R. J. Mitson and K. Terry 123

Role of cavity formation in stirred gas-liquid-solid reactors. M. M. C. G. Warmoeskerken, M. C. van Houwelingen, J. J. Frijlink and J. M. Smith 197

Scaling-up distillation tray efficiency under conditions of weeping or entrainment when liquid channelling also occurs. T. Plaka, I. S. Ahmed and M. J. Lockett 191
Solid-liquid mass transfer coefficient in mechanically agitated contactors. V. K. Patil, J. B. Joshi and M. M. Sharma 247
Studies of fluid displacement by foam in porous media. R. W. Burley, C. W. Nutt and M. Gh. Bayat 92

Thermal decomposition of trichlorotrifluoroethane (R113) under static and flow conditions. P. Srinivasan, V. R. Patwardhan, S. Devotta and F. A. Watson 266

Use of frequency-consequence curves to examine the conclusions of published risk analyses and to define broad criteria for major hazard installations. D. O. Hagon 373

Vertical co-current flow of air and shear thinning suspensions of kaolin. Z. Khatib and J. F. Richardson 139

REGULAR FEATURES

Doctorates in Chemical Engineering 63
List of Referees 400
Annual Research Meeting Report 401

REVIEW PAPERS

Developments and potential of power fluidics for process flow control. G. H. Priestman and J. R. Tippetts 67
Developments in anaerobic treatment of high strength industrial waste waters. M. A. Bull, R. M. Sterritt and J. N. Lester 203
Particle deposition behaviour from turbulent flows. P. G. Papavergos and A. B. Hedley 275

BOOKS REVIEWED

Chemical Process Dynamics. R. Mohilla and B. Ferencz. (Elsevier). Reviewed by P. Norman 32
Dense Gas Dispersion. R. E. Britter and R. F. Griffiths. (Elsevier). Reviewed by D. J. Gunn 52
Chemical Reaction Equilibrium Analysis. W. R. Smith and R. W. Missen. (Wiley). Reviewed by P. F. Tiley 100
Adhesion of Dust and Powder. Second Edition. A. D. Zimon (Plenum). Reviewed by T. Allen 122
Biotechnology. Volume 3. Fermentation. H. Dellweg (Verlag Chemie). Reviewed by M. A. Winkler 136
Heat Exchanger Design Handbook. Five Volumes. E. U. Schlunder (Hemisphere). Reviewers as follows:
1. Heat Exchanger Theory. P. J. Heggs 165
2. Fluid Mechanics and Heat Transfer. C. J. Norman 165
3. Thermal and Hydraulic Design of Heat Exchangers. G. H. Walter 166
4. Mechanical Design of Heat Exchangers. D. J. Wilson 166
5. Physical Properties. B. Edmonds 172
Handbook of Solvent Extraction. C. Lo Teh, M. G. Baird and C. Hanson (Wiley). Reviewed by G. V. Jeffreys 222
Fundamentals of Fluidized-bed Chemical Processes. J. G. Yates (Butterworth). Reviewed by D. Harrison 234
Industrial Enzymology. T. Godfrey and J. Reichelt (Macmillan). Reviewed by J. F. Kennedy and C. A. White 302
Industrial Crystallisation. The State of the Art. Second Edition. J. Nyvlt (Verlag Chemie). Reviewed by A. Scrutton 302
Mixing in Continuous Flow Systems. E. B. Nauman and B. A. Buffham (Wiley). Reviewed by J. C. Lee 314
Foundations of Boundary Layer Theory for Momentum, Heat and Mass Transfer. J. E. Schetz (Prentice Hall). Reviewed by R. M. Nedderman 320
Unified Analysis and Solutions of Heat and Mass Diffusion. M. D. Mikhailov and M. N. Ozisik (Wiley). Reviewed by G. V. Jeffreys 343
Chemical Reactor Design and Operation. K. R. Westerterp, W. P. M. van Swaaij and A. A. C. M. Beenackers (Wiley). Reviewed by S. P. Waldram 350

CORRESPONDENCE

From V. S. Guru Rajan and Dr A. Datta 60
From Dr M. J. Slater 61
From Professor P. N. Rowe 190 and 398
From Dr J. J. J. Chen 269 and 398
From Dr J. H. Hills 271
From Dr J. B. Joshi 271

VOL. 62 1984

DL.
62
984

VOL.
62
1984

CHEMICAL ENGINEERING RESEARCH & DESIGN

Transactions of The Institution of Chemical Engineers

EDITORIAL

The central importance of behaviour between phases and phase dispersion/coalescence to chemical engineering is again well illustrated by this issue.

M. Greaves and K. A. H. Kobbacy discuss 'Measurement of bubble size distribution in turbulent gas–liquid dispersions.' They describe a photoelectric capillary probe for the measurement of the local size distribution of bubbles in such dispersions. Conditions for choosing the correct sampling rate are discussed. Data obtained for homogeneous gas dispersions indicate that the new method gives good results. It also exploits an on-line microcomputer for data acquisition and processing. The developments described in this paper should be of great interest to workers in this field.

V. Linek, P. Petricek, P. Benes and R. Braun report on 'Effective interfacial area and liquid side mass transfer coefficients in absorption columns packed with hydrophilised and untreated plastic packings'. The authors find that plastic packings (Pall rings) rendered hydrophilic chemically have volumetric mass transfer coefficients (k_La) and interfacial areas (a) comparable to those for ceramic and metallic packings of good wetting properties. Correlations for k_La and a for both hydrophilic and untreated packings are given and the information in this paper should be of value to the designer.

In 'Isothermal two-phase flow of air and aqueous polymer solutions in a smooth horizontal pipe', R. P. Chhabra, S. I. Farooqi and J. F. Richardson report on average liquid holdup and two-phase pressure drop for three different polymers. They demonstrate that for inelastic fluids in laminar and turbulent flow and viscoelastic fluids in turbulent flow, the average liquid holdup agrees with a previous correlation for shear-thinning and Newtonian fluids. For laminar viscoelastic fluids however it was necessary to introduce a correction factor based on the Deborah number. Injection of air into the polymer solution in laminar flow showed reduction of the two-phase pressure drop with a minimum in agreement with that found for shear-thinning suspensions. No reduction was found for solutions in turbulent flow.

Continuing previous work, P. J. Bailes and S. K. L. Larkai discuss the 'Influence of phase ratio on electrostatic coalescence of water-in-oil dispersions'. Using a pulsed d.c. field and insulated electrodes, coalescence of the dispersion was measured. The coalescence efficiency was found to vary with dispersed phase holdup and to be a maximum at 25% holdup. The authors also present a correlation of coalescence efficiency as a function of a collision frequency developed in a previous paper. In due course it would be very interesting to see an economic assessment of this technique.

In 'Flow regimes on sieve trays: the significance of the emulsion flow regime', F. J. Zuiderweg, P. A. M. Hofhuis and J. Kuzniar identify the flow regimes existing on distillation trays. In particular they report an experimental study of density profiles on sieve trays. At high liquid rates and low vapour flows a 'bubbly' or emulsion flow develops. The paper discusses flow over the weir, transition to emulsion flow, capacity (downcomer performance) and efficiency. It should prove valuable to designers and experimentalists concerned with distillation equipment.

V. Grilc, J. Golob and R. Modic report experimental data in 'Drop coalescence in liquid/liquid dispersions by flow through glass fibre beds'. Their system consisted of polydispersions of water in organic solvents and in an oil containing a surfactant. A correlation of these data is presented which contains different numerical constants for each group of liquid systems. The authors point out that this correlation can be used to design a glass fibre bed for a given capacity and a required degree of separation.

A Shorter Communication by O. Ogboja presents data on liquid dispersion and tray efficiency on a rectangular sieve tray with large holes. The dispersion coefficient is compared with previous data and is correlated with liquid and gas flow rates. The tray efficiency data are correlated with a modified Peclet number.

P. Srinivasan, S. Devotta and F. A. Watson report on the decomposition of trichlorofluoromethane in a Shorter Communication. New data under flow conditions were found to be consistent with previously reported data for static conditions. The significance of the data is that they should enable the calculation of the working life of trichlorofluoromethane when used as the working fluid in a heat pump.

The issue is completed by book reviews, correspondence and the list of doctorates in chemical engineering for 1982–3.

Brian Gay
Hon. Editor

Notes for Authors

Editorial Policy and Standards

1. Papers published in the Journal will be original contributions to chemical engineering knowledge, not previously published. In particular, the Editorial Board encourages the submission of papers which show how the results of research may be used in chemical engineering design. Such implications for design should be brought out clearly in the paper and its summary.

Accounts of research work of an experimental or theoretical nature which throw new light on established principles, which identify problems not yet solved, or indicate practical areas to which research effort may usefully be applied are also invited. Reports from industry and from research establishments are particularly welcome.

Papers may also deal with new developments of plant or processes if these developments are related to underlying principles and can be given quantitative expression.

2. Authors need not be members of the Institution. Papers must be in English and should normally be of 2500 to 5000 words, including Appendices. Figures should also be included in this count, each being estimated as equivalent to 250 words.

3. The Editorial Board will, however, also welcome Shorter Communications (less than 2500 words) for consideration for publication; these would describe, for example, novel research techniques, new analyses of previous work, or interesting aspects of work still in progress. A faster refereeing procedure has been arranged for such short Papers.

4. The Journal also publishes a limited number of longer Review Papers, which are critical assessments of previously published work in a selected area of chemical engineering. In conformity with editorial policy, Reviews should show how the results of research can be used in the design of plant and equipment.

Most Reviews are specially commissioned by the Editorial Board, but authors are also invited to offer Reviews for consideration for publication. In view of the substantial effort required, authors are advised to communicate with the Editor before embarking on a Review.

5. It is the policy of The Institution to publish only papers of the highest quality. To help maintain these standards all papers submitted are sent to referees familiar with the branch of chemical engineering covered. They advise as to whether the paper is acceptable or not and, in addition, indicate to the author possible ways in which, in their opinion, the paper might be improved. The final decision on publication is taken by the Editor in light of this advice.

Manuscript Requirements

1. The text should be typewritten, using one side of the paper only, double-spaced and with adequate margins to allow for revision and copy preparation marks. A summary, preceding the text, should briefly describe the essential original contents of the paper.

2. Mathematical expressions can sometimes be more easily interpreted by the printer if carefully written by hand. Where many equations appear, a list of symbols used should be inserted at the end of the paper, before the references. SI units should *always* be used; the negative index notation is preferred to the oblique stroke.

3. References are listed in the order in which they are first cited in the text, where they are indicated by superscript numbers. They should give in order: Authors' surnames and initials, Year, Title of book or journal, Volume, Issue, Page numbers , followed by name and town of publisher in the case of a book.

4. Tables, drawings and photographs should be on separate sheets at the end of the manuscript and not interspersed in the text. Tabulated data should not duplicate values detailed in the text or on graphs. Drawings submitted should be clear and complete and preferably in a form suitable for direct reproduction. Photographs should be restricted to the minimum necessary.

5. Where limitations of space preclude publication of detailed results, mathematical derivations, etc, authors are invited to include in their paper a statement that this information is available from them on application. Authors may make an appropriate charge for supplying items requested in this way. Such material should be supplied with the paper when submitted to the Editor.

Submission of Papers

1. Three copies of the paper should be sent to:

The Editor, Chemical Engineering Research and Design,
Institution of Chemical Engineers,
George E. Davis Building,
165–171 Railway Terrace,
Rugby CV21 3HQ, England.

or to an Associate Editor as follows:

Australia:
Prof R. G. H. Prince,
Department of Chemical Engineering,
University of Sydney,
Sydney 2006, New South Wales, Australia.

Continental Europe:
Prof Dr J. R. Bourne,
Technisch-Chemisches Laboratorium,
ETH-Zentrum,
CH-8092 Zürich, Switzerland.

Continental Europe:
Prof J. M. Smith,
Laboratorium voor Fysische Technologie,
Technische Hogeschool Delft,
Prins Bernhardlaan 6,
2628 BW Delft, Holland.

India:
Prof M. M. Sharma,
Department of Chemical Technology,
University of Bombay,
Matunga Road,
Bombay 400 019, India.

New Zealand:
Prof R. B. Keey,
School of Engineering,
University of Canterbury,
Christchurch 1, New Zealand.

USA:
Prof J. O. Wilkes,
Department of Chemical Engineering,
University of Michigan,
Ann Arbor,
Michigan 48109, USA.

2. A full address to which readers may send correspondence should be specified, including the post code. The address at which the work was carried out, if different, should also be indicated. Where there are several authors, one should be nominated to check proofs and to receive all correspondence.

3. A proof will be sent to the nominated author, to be checked for possible typographical errors. Other alterations cannot be incorporated at this late stage without incurring higher printing costs, and extensive alterations would necessitate postponement of publication of the paper to a later issue.

4. Following publication the nominated author will receive 50 off-prints of the paper (or 25 where there is just one author). Any further off-prints required should be ordered at proof stage. Reprints, ordered after publication, are more expensive.

VOL.
62
1984

MEASUREMENT OF BUBBLE SIZE DISTRIBUTION IN TURBULENT GAS–LIQUID DISPERSIONS

By M. GREAVES (MEMBER) and K. A. H. KOBBACY

School of Chemical Engineering, University of Bath, England

The local size distribution of bubbles in a turbulent gas–liquid dispersion has been measured by means of a photoelectric capillary probe. A high speed microcomputer was used to process the measurement signal on-line. Sampling from a stirred vessel was achieved using a near-to-optimum gas flowrate (of bubbles) to ensure that only those bubbles with trajectories passing very close to the probe tip were withdrawn. An investigation of two-phase flow inside the capillary tube was made to determine the effect of coalescence, bubble breakage and flow interaction on measurement accuracy. Excellent reproducibility of results was obtained over the size range 0.4×10^{-3} to 5×10^{-3} m.

INTRODUCTION

Two-phase dispersed flows occur in many types of equipment, such as bubble columns, stirred tank reactors, condensers, distillation columns, coolant circuits of nuclear reactors and thermo-syphon reboilers. Knowledge of the size distribution of a dispersed phase flow is therefore important for the prediction of mass transfer, heat transfer and chemical reaction. It also underlies any attempt at improving understanding and design of such systems. The application in this paper is concerned with the measurement of bubble size in turbulent gas–liquid dispersions produced in a stirred tank reactor.

In agitated dispersions, the bubble size can be determined by direct or indirect methods, ranging from photographic, to highly sophisticated electrical probe techniques. The widely used interfacial area method[1-4] requires the overall gas holdup to be measured in order to determine the Sauter mean bubble diameter from the relationship:

$$d_{32} = 6h/a$$

However, it does not provide any information on the mean bubble size or its distribution, nor is it suitable for high values of gas holdup[5,6]. Alternatively, chemical methods can be employed, though it has been suggested that the mass transfer effective interfacial area is smaller than the total specific interfacial area[7]. Direct photography, despite the tedious effort involved, usually does not provide very high accuracy. Figueiredo's application[8] of the electro-resistivity probe technique, which was developed by Burgess and Calderbank[9], showed that, in practice, a successful bubble encounter with the probe was a relatively rare event. There is also some doubt surrounding the sampling method, vis à vis attraction of certain classes of bubble size.

The eminently simple principle of elongation of a bubble (or droplet) inside a fine glass capillary has been known for some time. However, with the exception of Wisdom's capacitance suction probe[10], useful applications have been mainly restricted to static or equilibrium measurements of bubble size. Very recently though, Weiland et al.[11] have developed a photoelectric capillary probe device for the measurement of bubble size distribution in fermentation media in a stirred tank and loop reactor. This measurement technique is similar to the one which is described in this paper, except that their signal condition was designed to respond to the level of light absorption, rather than the intensity of light transmission. The method was less successful at high gas holdup values and did not allow the local gas holdup to be measured. In other respects, their approach in using the capillary method was over-simplified. No account was taken of the complex pattern of two-phase flow inside the capillary tube.

This paper describes a micro-computer-based capillary probe system which has been developed for measuring bubble size and gas holdup in a stirred gas–liquid reactor. The complex pattern of two-phase slug flow occurring in capillaries is investigated and a semi-empirical relationship developed for the bubble slug volume.

BUBBLE SLUG FLOW IN CAPILLARIES

The nature of the two-phase slug flow occurring inside a capillary tube is complex. Practically all of the previous investigations in this area have assumed a simple flow pattern model, i.e., a uniform cylindrical slug of gas traversing through a thin film of surrounding liquid. This isolated bubble, steady-state viewpoint, ignores the complexities arising when multi-bubble sequences are flowing, as is the case when sampling from a gas–liquid dispersion. In the refrigeration equipment area also, where capillaries are widely employed as restrictors, Mikol[12] and Whitesel[13] have observed a pulsating mode of flow, with the bubbles enlarging as they move downstream. Nevertheless, the elongation of a gas bubble into a cylindrical slug inside a capillary tube, is the principal basis on which the bubble size measurement technique is based.

Starting with a simple steady-state model. If the bubbles and liquid slugs are flowing with steady speeds

© Institution of Chemical Engineers

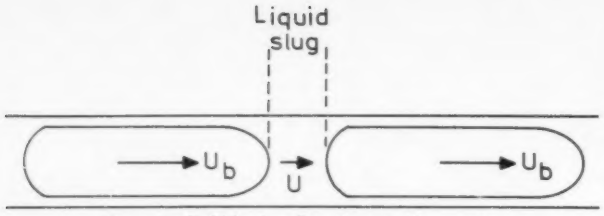


Figure 1. Bubble-slug flow in a capillary tube.

of U_b and U, respectively (see Figure 1), it can be shown that, if the viscosity ratio μ_L/μ_G is very large, then the liquid film surrounding the bubble does not move[14]. The fraction of the tube cross-section occupied by the liquid film is then given by

$$m = \frac{U_b - U}{U_b} \tag{1}$$

From measurements of U and U_b, Fairbrother and Stubbs[15] developed the following empirical relationship for low bubble speeds

$$m = \left(\frac{\mu_L U_b}{\sigma}\right)^{1/2} \tag{2}$$

where σ is the surface tension. Taylor[16] showed this to be a good approximation in the range $0 < \mu_L U_b/\sigma < 0.09$. From photographic observations Suo and Griffiths[14] found that at higher flow velocities, where inertial effects are significant, there was only a 1% deviation of their experimental values from equation (2). A later study by Suo[17], measuring simultaneously the pressure drop and bubble velocity, showed that, if $\rho_G \ll \rho_L$ and $\mu_G \ll \mu_L$, then each bubble slug is essentially a region of constant pressure. The pressure drop per slug was correlated by:

$$\Delta P_S = \left(\frac{8U}{\pi r^2}\right)\left(\frac{\mu_L U_b}{r}\right) + 4\frac{\mu_L U_b}{r} \quad \text{for} \quad Re_b < 270 \tag{3}$$

$$\Delta P_S = \left(\frac{8}{\pi r^2}\right)\left(\frac{\mu_L U_b}{r}\right) + 0.163\rho U_b^2 \quad \text{for} \quad 270 < Re_b < 630 \tag{4}$$

where Re_b is the Reynolds number based on bubble velocity, liquid viscosity and tube radius. The first term in these two equations represents the pressure drop as if the flow were fully developed laminar flow and the second term accounts for the nose and tail effect of the bubble slug.

Observation of Flow using Photo-electric Switches

A photo-electric switch, incorporating an emitter and detector, and having a switching time of a few hundred microseconds, is a useful device for studying capillary slug flow. Two optical switches were used to observe the motion of a bubble slug over a certain length of capillary tube. In its final form, the measuring system only employed one switch—the details of the measuring system are described later. When the narrow collimated light beam from the optical switch is directed through the glass wall of the capillary tube, the maximum light transmission occurs when passing through a liquid slug.

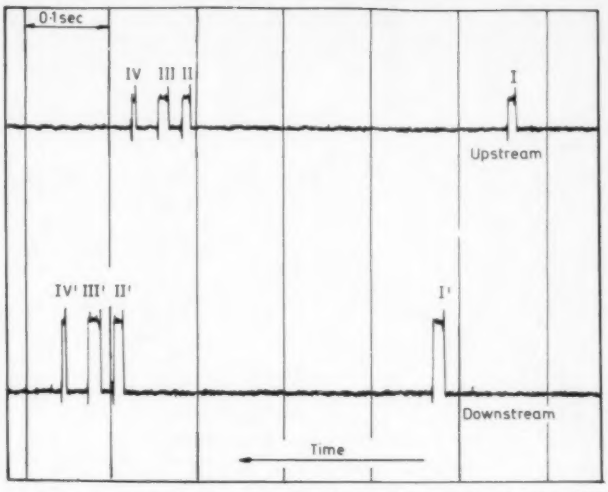


Figure 2. Output signals of two optical switches recorded by UV recorder. Upstream detection position 0.08 m from probe tip. Downstream detection position 0.3 m from probe tip. (Air–water system; capillary diameter = 0.61×10^{-3} m; capillary length = 0.35 m.)

The intensity of the light beam is reduced by the passage of a gas slug. Figures 2 and 3 show typical output signals from the optical switches recorded by a UV recorder (the signal voltage is inverted by the optical switch). Pulses I, II, III and IV represent the time taken by bubbles to pass the detection point (i.e. collimated light beam) near to the entrance tip of the capillary tube (upstream position). I′, II′, III′ and IV′ are the corresponding pulses recorded for the same bubbles at the second detector position, located 0.3 m downstream from the tip. If the time duration of a pulse is t_b, then

$$t_b = L/U_b \tag{5}$$

where L and U_b are the length and average speed of a bubble, respectively. This is defined by the condition when the nose, or leading interface of the bubble-slug is just at the detection point.

The bubble identified by pulse I (Figures 2 and 3) can be considered to be free of axial interaction since there are no other bubbles close to it. It is also evident, that

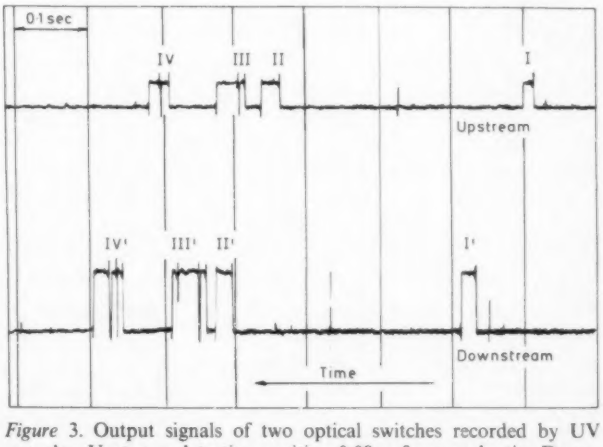


Figure 3. Output signals of two optical switches recorded by UV recorder. Upstream detection position 0.08 m from probe tip. Downstream detection position 0.3 m from probe tip. (Air–water system; capillary diameter = 0.61×10^{-3} m; capillary length = 0.35 m).

VOL. 62 1984

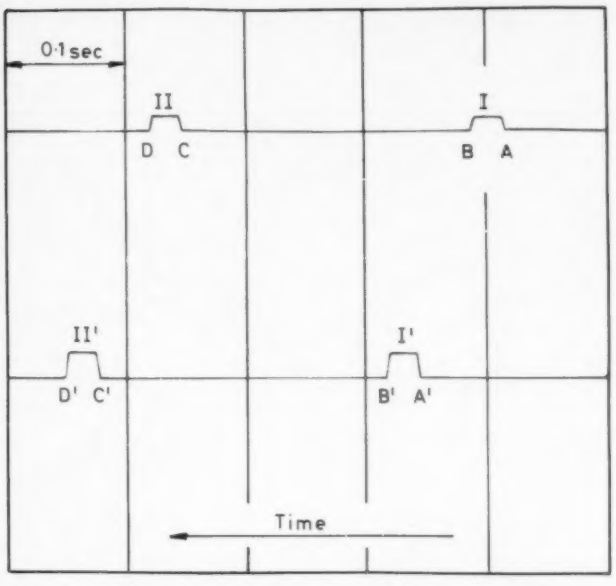


Figure 4. Method of measuring the average bubble velocity in capillary tube using two optical switches. The time elapsed between the detection of the ends of the two bubbles is the same for both optical switches, i.e. BD = B′D′ and C′D′ > CD. Therefore, bubble expansion occurs in the direction of flow. Based on this conclusion, $U_b = l/t$, where U_b = average bubble velocity, l = distance between the two optical switches and t = time elapsed.

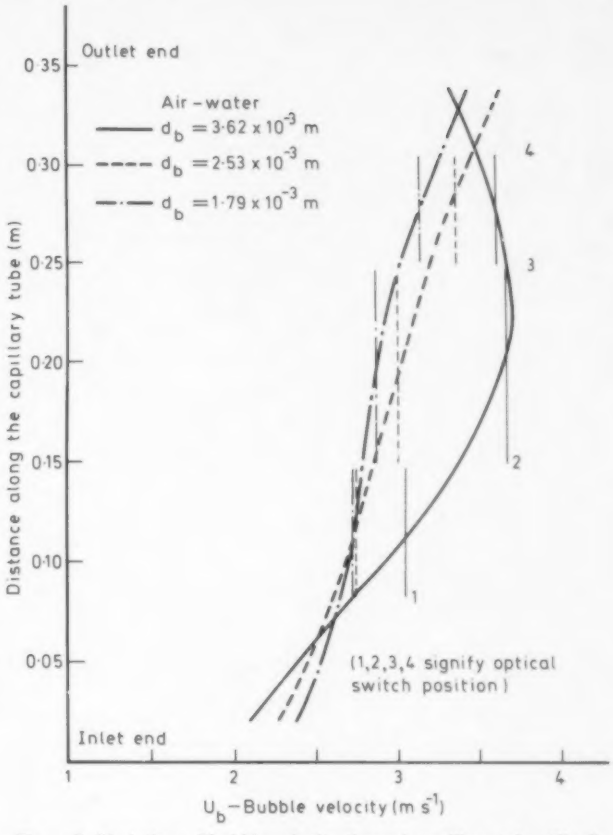


Figure 5. Variation of bubble velocity through capillary tube. (Capillary diameter = 0.61×10^{-3} m.)

the width of pulse I′ (downstream) is greater than that of pulse I (upstream). At first sight, the bubble length has either increased or else its velocity has decreased. Figure 4 shows the method of determining the average bubble velocity using two optical switches. It is clear from this, that expansion of the bubble occurs in the direction of flow. The variation of bubble velocity was investigated by making additional measurements along the capillary tube, as shown in Figure 5. Arising from the expansion effect, the resulting bubble velocity is therefore higher at downstream locations, with the exception of the largest bubble ($d_b = 3.62 \times 10^{-3}$ m). This shows a reduction near to the outlet of the capillary.

There are two different classes of axial interaction effect between bubbles. The first class is represented by pulses II, III and IV in Figure 2. For this group, the average bubble diameter is less than twice the capillary tube diameter. In this case, the change in bubble speed due to axial interaction never exceeded by more than 10% that of a bubble of the same size which was free from axial interaction effects. This effect would lead to under-estimation of the expected pulse width at the observation point (upstream) and, consequently, the measured bubble volume, as will be shown later. Pulses II, III and IV in Figure 3 represent the second category of axial interaction effect where one, or more, of the bubbles is larger than the rest in the group and has a diameter over three times the capillary tube diameter. The largest effect occurs when a bubble is trailed by a larger one (pulses II and III in Figure 3). The acceleration of the leading bubble, due to the relatively large expansion of the trailing one, becomes quite considerable and can lead to underestimation of the expected pulse width (upstream) by up to 30%. However, the error in estimating the size of the trailing bubble remains in the region of 10%. The acceleration of the leading bubble, Pulse II, is very significant, to the extent that Pulse II′ becomes shorter, obscuring the opposite effect of bubble elongation. The bubbles identified by pulses III and IV in Figure 3 also exhibit another effect. There is a discontinuity in the signals due to break-up of the bubbles inside the capillary. The effect of bubble break-up and coalescence is discussed later in the section concerned with measurement accuracy.

Estimation of Bubble Slug Volume

As mentioned previously, it is possible to measure the bubble velocity U_b and the time t_b required for it to pass a given location in the capillary. To estimate from these quantities the true bubble volume V_b, at the point of sampling, the expansion of the bubble in the capillary and the thickness of the surrounding film have to be considered. In the following analysis, a relation between V_b and the measured quantities U_b and t_b is derived. It assumes that there is only a single bubble flowing in the capillary, i.e. axial interaction between bubbles is neglected.

Consider that V_b is the true volume of a bubble at the entrance to the capillary. After travelling a certain distance inside the capillary, the bubble-slug expands so that its volume is now V_b^* and its length L^*. This condition corresponds to the situation when the leading end (nose) of the bubble is just at the point of obser-

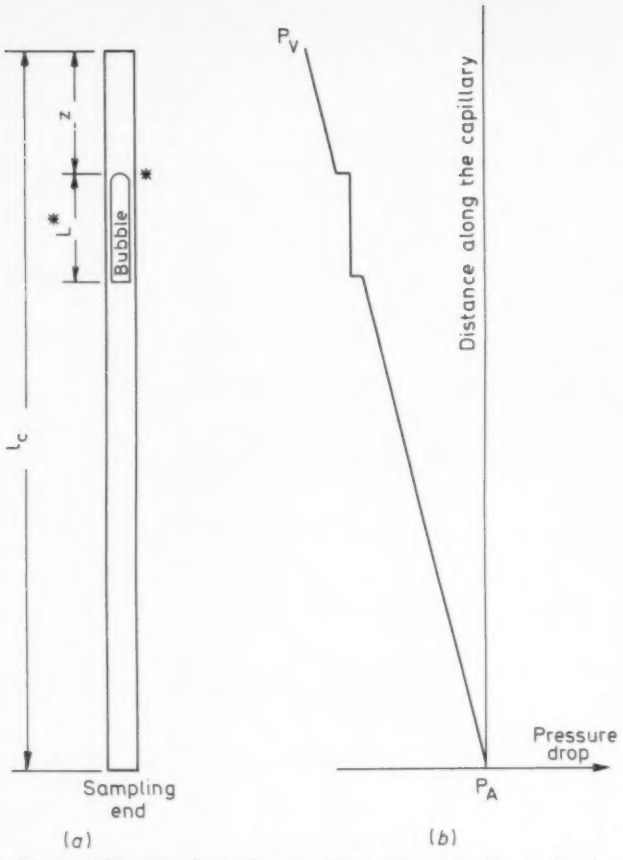


Figure 6. Pressure drop along capillary tube. Asterisk marks the detection point (position of optical switch). See also list of symbols used.

vation; see Figure 6(*a*). Therefore:

$$V_b^* = K^*(V)V_b \tag{6}$$

and

$$V_b^* = L^*(1-m^*)A \tag{7}$$

where $K^*(V)$ is an expansion factor which depends on the bubble volume, A is the capillary tube cross section area and m^* is the corresponding fraction of the tube cross section occupied by the liquid film.

From equations (6) and (7)

$$L^* = \frac{K^*(V)V_b}{(1-m^*)A} \tag{8}$$

and by substituting for m from equation (2):

$$L^* = K^*(V)V_b \Big/ \left[1-\left(\frac{\mu U_b}{\sigma}\right)^{1/2}\right]A \tag{9}$$

Using equations (5) and (9) we obtain:

$$V_b = \frac{t_b^* U_b^*}{K^*(V)}\left[1-\left(\frac{\mu U_b^*}{\sigma}\right)^{1/2}\right]A \tag{10}$$

To estimate the expansion factor $K^*(V)$ in equation (10), the simple pressure drop model shown in Figure 6(*b*) is used. Assuming that the bubble expands according to ideal gas law behaviour, then from equation (6):

$$K^*(V) = \frac{V_b^*}{V_b} = \frac{P_A}{P^*} \tag{11}$$

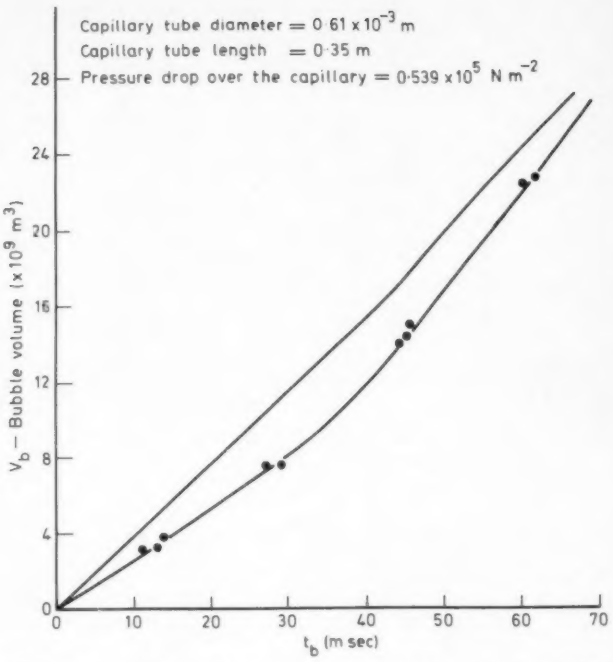


Figure 7. Comparison of bubble volume calculated from equation (15) with micro-syringe measurement.

where P_A is the pressure at the sampling point. The pressure drop due to the end effect of the bubble is:

$$\Delta P_b = 0.163\rho U_b^2 \tag{12}$$

Using equation (12), in conjunction with Figure 6, it can be shown that

$$P^* = P_A - \frac{z}{l_C - L^*}(P_A - P_V - 0.163\rho U_b^{*2}) \tag{13}$$

By substituting (13) into (11),

$$K^*(V) = P_A \Big/ \left[P_A - \frac{z}{l_C - L^*}(P_A - P_V - 0.163\rho U_b^{*2})\right] \tag{14}$$

Substitution of L^* from (9) into (14), and then into (10), the final result is

$$V_b = \frac{t_b^* U_b^* A}{P_A}\left[1-\left(\frac{\mu U_b^*}{\sigma}\right)^{1/2}\right] \times \left[P_A - \frac{z}{l_C - t_b^* U_b^*}(P_A - P_V - 0.163\rho U_b^{*2})\right] \tag{15}$$

For calculation purposes, the hydrostatic head of dispersion above the sampling point was neglected and P_A taken equal to the atmospheric pressure. A calibration of the true bubble volume V_b was obtained by injecting bubbles of accurately known size by means of an 'Alga' micro-syringe. It is clear from Figure 7 that equation (15) overestimates the bubble volume by up to 37%. The average overall error is approximately 30% or, in terms of equivalent spherical diameter, about 9%. This is attributed mainly to the error incurred in using equations (2) and (4), and also the assumptions concerning the expansion factor $K(V)$, together with any possible inaccuracy in the measurement of U_b.

VOL. 62 1984

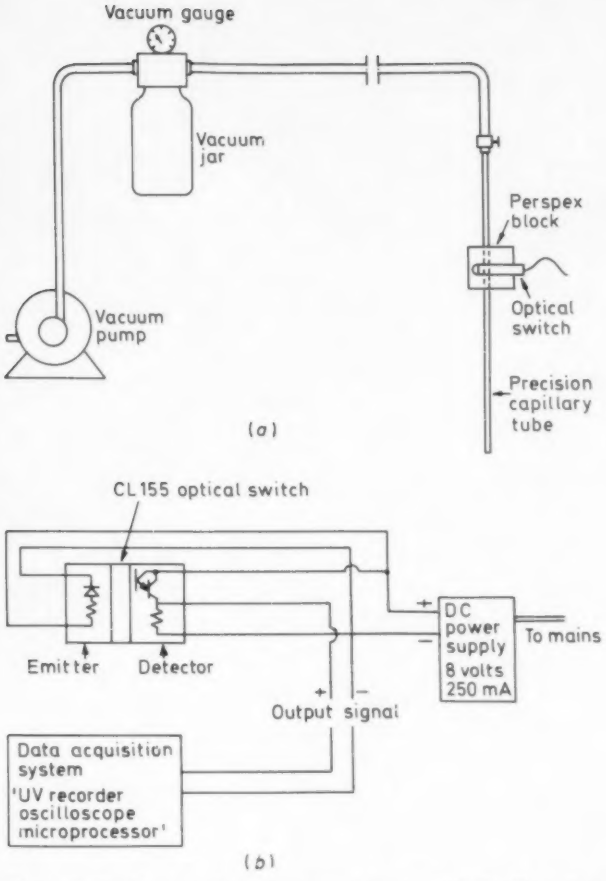


Figure 8. Capillary probe measurement system. (a) Capillary flow arrangement. (b) Measurement and data acquisition circuits.

CAPILLARY PROBE MEASUREMENT SYSTEM

The measurement system is shown in Figure 8. The detection part of the equipment includes a precision glass capillary on which is mounted a single photo-electric switch. This was a type C155 switch supplied by Clairex Electronics. It incorporates an IR emitter and photo-darlington detector having a fall or rise time between switching of 300 μs. With unobstructed light transmission, the switch provides a signal output of approximately 50 mA d.c. The amplitude of the signal, under measurement conditions, was increased by covering the detection area of the capillary tube by a short section of black tape. A pair of 'windows', approximately 1 mm square, was cut into the tape to allow passage of the collimated light beam. The optical switch was positioned accurately at one end of the capillary tube by means of the perspex block holder. The remaining section of the capillary, about 0.3 m, was then used as a probe for sampling the dispersion inside a 0.2 m diameter stirred tank reactor.

The capillary tube, which had a funnel-shaped entrance with a cone angle of approximately 60°, was immersed at the sampling point by vertically traversing through the cover plate on top of the agitated vessel. A continuous sample of dispersion was withdrawn through the capillary by the vacuum pump. The output signal from the optical switch (Figure 9) shows that it is similar

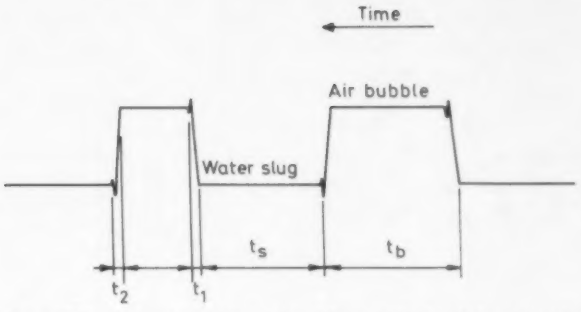


Figure 9. Typical output voltage signal from optical switch as recorded by UV recorder. $t_1 = t_2 = 0.3 \times 10^{-3}$ s.

to a binary type pulse. The high level voltage represents the passing of a gas bubble and the low level voltage represents a water slug. An Analog Devices Macsym II data acquisition system was used to sample and process this signal at high speed. The sampling rates were 1000 s^{-1} on air-tap water and 2000 s^{-1} using 'non-coalescent' air–0.11 M K_2SO_4 solution.

Bubble Size

The accuracy afforded by equation (15) was considered to be insufficient for measurement purposes though, in practice, it would have been more convenient to implement on the microcomputer. Instead, the direct calibration procedure already referred to, was adopted. The calibration procedure was repeated for each size of capillary tube used for various pressure drops over the total length of the capillary. Three such calibrations are shown in Figure 10. Increasing the pressure drop for a given tube size shifts the curves relatively to the left. In practice, the calibration curve was fitted to a third order polynomial, so that, the bubble volume is then determined by:

$$V_b = xt_b + yt_b^2 + zt_b^3 \qquad (16)$$

where x, y and z are constants depending on tube size and pressure drop.

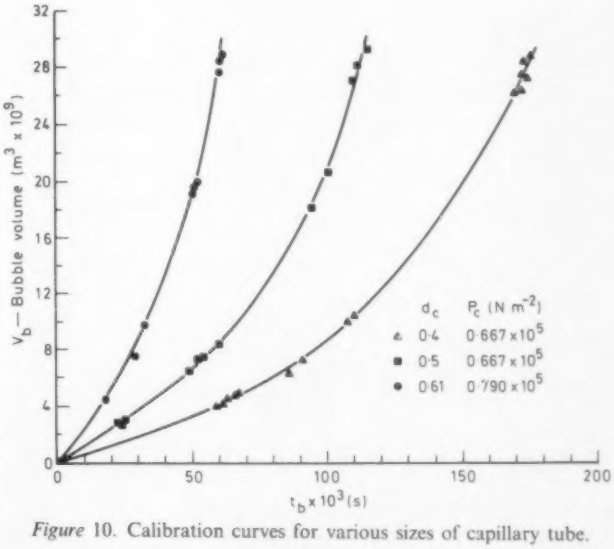


Figure 10. Calibration curves for various sizes of capillary tube.

The method of determining bubble size depends, of course, on being able to sample the dispersion correctly and, as will be discussed next, there is a need to sample at different rates in order to estimate the true point gas holdup. Therefore, each of the coefficients of the polynomial was fitted to a second order polynomial as a function of pressure drop. The general form of the calibration equation is:

$$V_b = \sum_{i=1}^{3} (a_i + b_i P_C + c_i P_C^2) t_b^i \quad (17)$$

where P_C is the pressure drop over the capillary.

The procedure for taking bubble size measurements is then a relatively simple process. The sample rate of dispersion is set by adjusting the pressure drop over the capillary by means of the vacuum pressure control regulator. Following this, the sequence of data acquisition, i.e. sampling the output signal from the optical switch, was handled automatically by the microcomputer system. This was achieved by means of a computer programme which is listed elsewhere[18]. The equivalent spherical diameter of each bubble in the sample was calculated and the bubbles classified according to size. These results, together with the mean bubble diameter (d_{10}) and the Sauter mean diameter (d_{32}), were then printed out on a teletype.

Gas Holdup

Determination of the gas holdup at the point of sampling in the dispersion forms an integral part of the process of bubble size measurement. Figure 11 shows the output signal from the optical switch over a total sampling period t_t. The signal represents 3 bubbles and 4 liquid slugs. The time taken by the water slugs to flow across the detection point is:

$$t_s = \sum_i t_{si} = t_t - \sum t_b \quad (18)$$

The average liquid flowrate (q_L) can be estimated from the total volume of liquid collected in the vacuum jar. Hence, the point gas holdup is given by:

$$h_p = \frac{\Sigma V_b}{\Sigma V_b + t_t q_L} \quad (19)$$

Determination of h_p in this way (estimating q_L for each run) is very time consuming and would give poor results if the sampling period were too short. Therefore, an approximate value of the point gas holdup was first

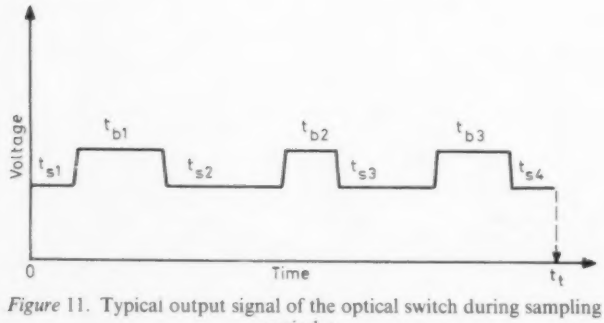


Figure 11. Typical output signal of the optical switch during sampling period t_t.

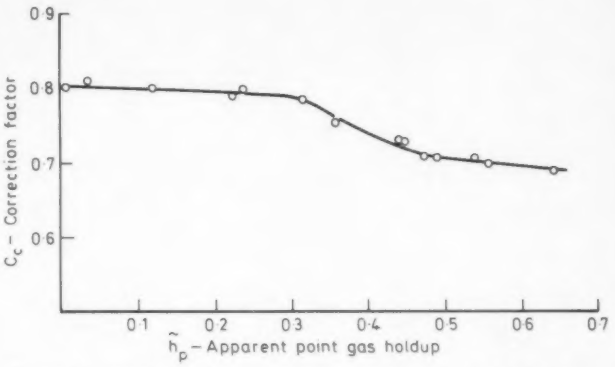


Figure 12. Correction factor for estimating point gas hold-up for air –0.11 *M* K_2SO_4.

calculated as follows. Let this first approximation be:

$$\tilde{h}_p = \frac{\Sigma V_b}{\Sigma V_b + t_s q'_L} \quad (20)$$

where q'_L is the flow rate of water only, at the same sampling condition. On this basis, it was found that:

$$q'_L = x' p^{y'} \quad (21)$$

$y' = 1.3$ for the three sizes of capillary used (bore diameters of 0.4, 0.5 and 0.61 $\times 10^{-3}$ m). The coefficient x' increases sharply with increasing capillary diameter. By taking a number of samples, and calculating the values of h_p and $\tilde{h}_p$ for each case, a correction factor can be determined, so that, $C_c = h_p/\tilde{h}_p$. The variation of this quantity against $\tilde{h}_p$ is shown in Figure 12. In the tap water case, C_c was found to be close to 1. The lower values obtained for air-electrolyte may, in part, be attributed to the much greater number of bubbles present at correspondingly higher gas holdups.

Sampling Rate

Nienow et al[19] have pointed to the difficulties in achieving isokinetic sampling from dispersions in stirred tanks. To study the sampling rate effect, very small bubbles were generated near to the capillary probe tip; first without agitation. The capture zone at the entrance was found to extend almost half-a-sphere from the periphery of the funnel tip. Bubbles failed to enter the capillary tube if their trajectories did not cross this capture zone. This is in accord with Wisdom's observation[10], that preferential attraction of bubbles at high sample flow rates is not significant.

Under actual agitation conditions, when the total pressure drop over the capillary is increased, the point gas holdup calculated from equation (20), varies in the manner shown in Figure 13. Therefore, as the sample flow rate is increased, the apparent gas holdup increases up to a maximum value and then begins to fall. This effect can be interpreted schematically, as shown in Figure 14. As the sample flow rate, q_G, of gas (bubbles) increases, depending on P_c, it continues to increase up to a critical point (1), after which it remains constant. At the critical sampling rate, every bubble passing by the 'attraction zone' is drawn in. Any further increase in the sampling rate leads to an increase of the water flow

VOL. 62 1984

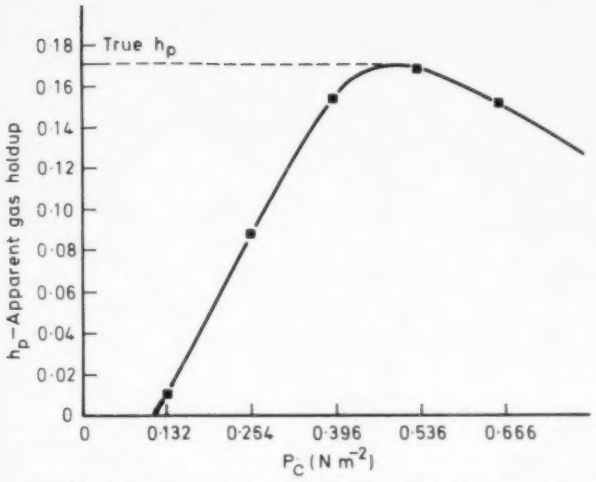


Figure 13. Apparent point gas hold-up in agitated vessel against pressure drop over capillary tube.

through the tube, without further increase in the rate at which gas bubbles are sampled. This explains the drop in the apparent gas holdup after the maximum is reached (point 2).

The sampling rate which would correspond to the true point gas holdup, should be when every bubble reaching the tip of the probe is drawn in, i.e. when the bubble sampling rate is just equal to the rate at which they arrive. In the strictest sense, this can only be satisfied by sampling isokinetically and co-linearly in the direction of the mean flow. This view is consistent with the type of directed-mean flow likely to be established when using a probe of quite large dimensions. A tube, for example, could have a cross-sectional area for flow many hundred times greater than a capillary, and would, consequently, exhibit a very significant disturbing effect on the immediate flow field. In contrast to this, the 'zone of attraction' at the entrance of capillary is very weak. Accordingly, this is a very desirable feature for sampling turbulent gas–liquid dispersions, because the capillary

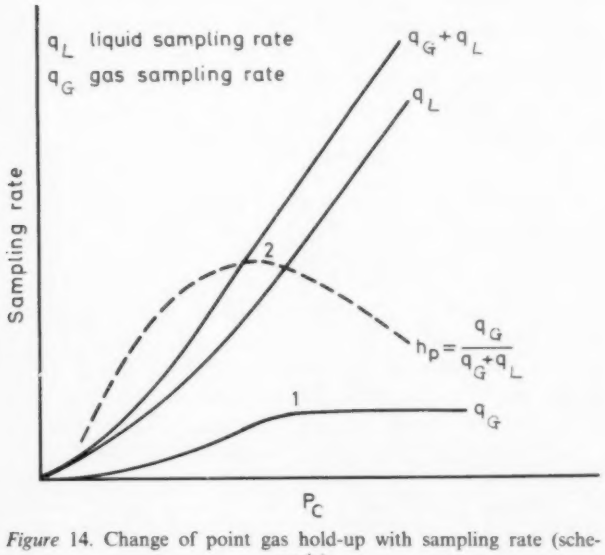


Figure 14. Change of point gas hold-up with sampling rate (schematic).

probe only responds to the flow condition at the 'point' entrance zone.

The fluctuating velocity components in a three-dimensional turbulent flow are, of course, point properties and any suitable sampling device must be capable of responding to these. As mentioned previously, only bubbles which cross the small 'attraction zone' at the entrance of the capillary, in the course of their normal motion, are drawn in. The orientation of the capillary probe is, therefore, much less critical, certainly as far as sampling bubbles is concerned, than would be the case if strict isokinetic sampling were required. Now, as the sampling rate through the capillary is increased, the 'zone of attraction' will also increase slightly. There is the possibility then, that bubbles just outside, or on the edge of this zone, will disengage from the liquid sample flow. However, the 'optimum' sampling condition will have been exceeded. Point (1) on the q_G curve in Figure 14 is the only point which satisfies the 'optimum' sampling requirement. The maximum exhibited by the apparent gas holdup curve (point 2) is close to point (1), but the two do not necessarily coincide. On this basis, it was concluded that the maximum gas holdup condition should provide a good estimate of the true gas holdup prevailing at the sampling point in the vessel. Accordingly, all of the bubble size measurements were made using a sample flow rate determined in this way. Any test of the accuracy of measured local holdup values, which attempts to compare them with the total gas holdup in the vessel must, ultimately, depend on how wel! the measurement sampling grid defines the point-to-point variations in the mixing space. It is tempting to consider that the h_p values could be integrated by assuming that they apply to a certain volume surrounding the probe. However, this volume is not really known. Instead, we have relied on calculating average estimates.

To illustrate the situation for air–water, the 14 point values shown in Figure 15 have been averaged using: (i) the unweighted values and (ii) values weighted according to radial position. These estimates of $\bar{h}_p$ are compared with the total holdup obtained from the change in liquid level, as shown in Table 1.

(i) unweighted:

$$\bar{h}_p = \sum_0^n h_p \Big/ n$$

(ii) weighted:

$$\bar{h}_p = \sum_0^n V(r) h_p \Big/ n$$

where n = number of sampling points, and $V(r)$ = weighting fraction based on radial position of sampling point. In the main, both estimates of $\bar{h}_p$ are significantly higher than h although, at the highest impeller speed, $\bar{h}_p$ is less than h using the second method.

Evidently, the number of sampling points in the measurement grid is not sufficient to enable an accurate result to be obtained. Significantly, the region below the impeller is not included and neither are there any measurements close to the vessel wall. The volume section closest to the wall has the highest weighting effect on h_p which, combined with the lower holdup there, could significantly improve the second estimates in Table

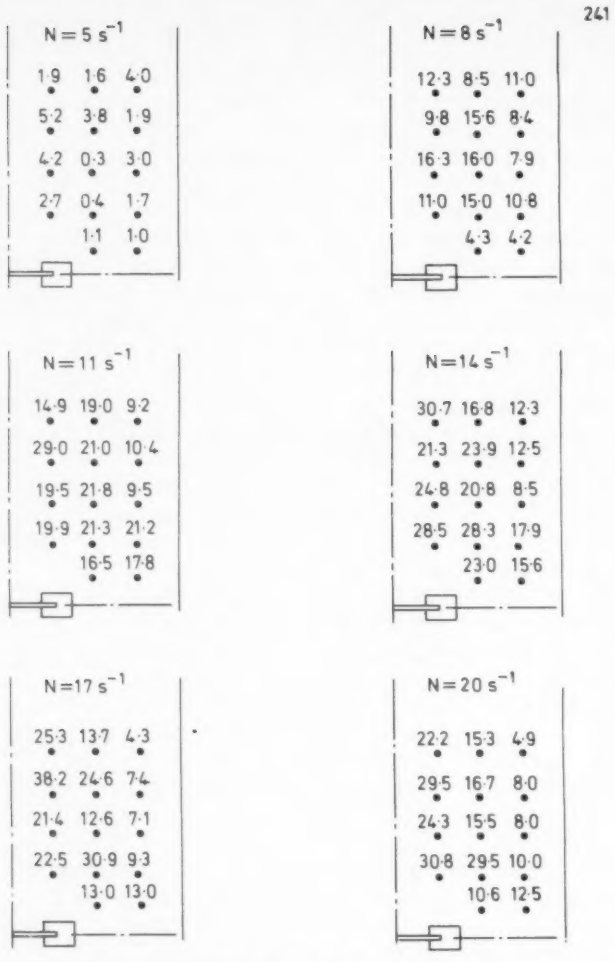


Figure 15. Point gas hold-up (%) for air–water. Dots mark sampling positions. $D = 0.0762$ m, $Q = 3.77 \times 10^{-4}$ m^3 s^{-1} (3.4 vvm), $N_{FI} = 9.95$ s^{-1}, $N_{RI} = 18$ s^{-1}.

Figure 16. Point specific interfacial area (m^{-1}) for air–0.11 *M* K_2SO_4 solution. Dots mark sampling positions. $D = 0.0762$ m, $Q = 3.77 \times 10^{-4}$ m^3 s^{-1} (3.4 vvm).

1. The results do not indicate any significant bubble disengagement effect since, if this were the case, $\bar{h}_p$ should underestimate h. At the lowest speed ($N = 5$ s^{-1}), even though there is virtually no gas below the impeller, the main reason for the low estimate is the lack of resolution in the measurement grid, i.e. too few sampling points.

It should be possible to obtain a more definitive test of point gas holdup values (even using a simple average method), when the dispersion of gas in the vessel is fairly homogeneous. 'Non-coalescing' systems tend to produce much smaller bubble size, so that it is easier to achieve more uniform gas dispersion. Figure 16 shows specific interfacial area values for 'non-coalescing' air –0.11 M K_2SO_4 solution, at 6 points in the vessel. For each impeller speed, the averaged point value is compared with the total specific interfacial area (obtained from independent measurements of the total gas holdup), where:

$$\bar{a}_p = \frac{\Sigma 6h_p/d_{32}}{n} \quad \text{and} \quad a = \frac{6h}{d_{32}}$$

and n = number of sampling positions. At the highest impeller speeds ($N = 14, 17, 20$), where there is generally good dispersion of gas, excellent agreement is obtained between a and $\bar{a}_p$ (or h and $\bar{h}_p$). There is a worsening difference, however, at lower speeds. From Nienow's visual observations[19], it is clear that, at $N < N_{FI} \sim 5$ s^{-1}, there is virtually no gas below the impeller. This is probably the main reason for the high value of $\bar{a}_p$ in this case. At $N = 8$ and 11 s^{-1}, the dispersion does not achieve the same degree of homogeneity compared with higher speeds. Again though, it is the relative coarseness of the measurement grid, i.e., too few sampling points, which is responsible for the inaccuracy of the averaging process.

Table 1. Total gas holdup compared with estimates from point values of Figure 15 for air–water

N (s^{-1})	h	$\bar{h}_p$ unweighted	$\bar{h}_p$ weighted
5	0.066	0.023	0.022
8	0.079	0.108	0.098
11	0.011	0.179	0.169
14	0.117	0.204	0.186
17	0.138	0.175	0.151
20	0.158	0.170	0.146

VOL. 62 1984

Accuracy and Reproducibility

There are a number of points arising concerning use of the capillary probe technique for sampling and measurement of bubbles from a turbulent dispersion:

(i) dynamical pressure gradients
(ii) axial interaction between bubbles
(iii) breakage and coalescence
(iv) speed of data sampling

It has already been demonstrated in Figure 7, that there is reasonable agreement between the semi-theoretical relationship for V_b and directly calibrated values. The calibration procedure used did not take into account the effect of dynamical pressure gradients likely to be present in a stirred vessel environment. Comparing the sample flow rate of liquid under agitated and non-agitated conditions however, did not reveal any significant difference. On the other hand, any effect on the sampling of gas bubbles is automatically accounted for by taking measurements at the 'optimal' sampling rate (Figure 14). In general, the optimal rate of sampling of dispersion from a stirred vessel depends on the impeller speed, gas flow rate, the location of sampling and the direction of flow relative to the probe.

The complicating effect of axial interaction between bubbles flowing inside the capillary tube can be summarised as follows. From extensive measurements, more than 80% of the bubbles in a sample behaved as though only a single bubble were flowing inside the tube. So, for this class, axial interaction could be ignored. For the remainder, the trailing bubble accelerates due to the wake-effect of the leading bubble, while the leading bubble accelerates due to the expansion of the trailing one. This effect was proportional to the size of the bubbles. The measurement error was less than 10% (under-estimation) of the total gas volume in the sample. Also, the measured bubble size distribution is expected to be slightly skewed to the right.

During the wide range of experiments conducted, coalescence of bubbles inside the capillary tube was never observed. However, frequent breakage of bubbles occurred if the size of the bubble exceeded a critical volume. This volume depended both on the capillary tube diameter and the sampling rate. On breakup, the smaller bubbles produced continued to travel close together. The distance separating successive pairs of secondary bubbles was always very small compared with that between the original bubbles (see pulses III and IV in Figure 3). Based on this observation, a simple solution to the bubble breakage problem was found. In processing the output signal from the optical switch, the computer program was designed to measure the time between every successive pair of bubbles in the sample. If that time was less than a certain value (9×10^{-3} s) the pair was considered to be the result of breakage of a larger bubble. Subsequently, the width of the pulses associated with these bubbles was added together and processed as one pulse, representing one bubble.

For the air–water and air–electrolyte dispersions, the range of bubble size measured by the capillary probe was 0.4×10^{-3} to 5.0×10^{-3} m equivalent spherical diameter. An important factor determining the accuracy of measurement is the speed of sampling of the 'binary' pulse signal from the optical switch by the data acquisition system. The main limitation here was the size of the micro-computer's operating memory (RAM). Of the 32 k memory, approximately 15 k was available for data storage after the 'Macbasic' compiler had been installed. Two 16 bit words are needed on this machine to encode a piece of data. Thus, data acquisition time for the air–water system, using a sampling rate of 1000 s^{-1}, was limited to approximately 7 s. It was correspondingly less for the air–electrolyte system using a sampling rate of 2000 s^{-1}. In the case of air–water, the number of bubbles found in a sampling period of 5 s was typically about 30. Processing of the data on the microcomputer required about 3 min. Therefore, a sample of 200 bubbles needed about 20 min to complete the cycle from data acquisition to print out. This is about 10 times faster than the electroresistivity probe technique used by de Figueiredo[8]. Although a 'start-stop' sequence is needed to process samples of this size, the sampling rates compare favourably with those achieved on a pipe flow dispersion using a laser beam and Ronchi gratings technique[20]. Theoretically, the capillary probe system is capable of very high bubble sampling rates, up to 100 s^{-1}, or more. In practice, the rate will be dictated by such factors as the availability of bubbles in the dispersion, their size, and the size of computer memory.

An important measure of the accuracy of any measurement technique is the reproducibility of the results obtained. Figure 17 demonstrates the bubble size distribution for two successive samples of the air–electrolyte dispersion. There is clearly good agreement between the distributions. For the air–water system, larger deviations were generally observed. Figure 18 compares two samples which were obtained under identical conditions, but taken three days apart. The differences can be attributed partly to the sensitivity of bubble coalescence in 'pure' liquids to impurities and also the relatively small sample size.

CONCLUDING REMARKS

The detection of gas slugs flowing through a fine glass capillary by means of a high speed photoelectric switch, has provided an efficient method for measuring bubble size distributions. The problem of sampling the tur-

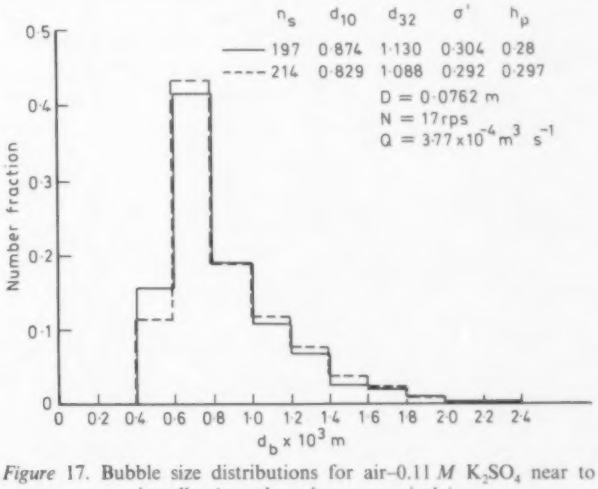


Figure 17. Bubble size distributions for air–0.11 *M* K_2SO_4 near to impeller (samples taken successively).

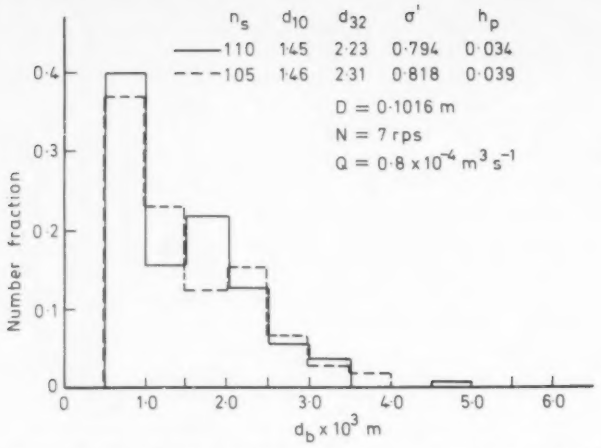


Figure 18. Bubble size distributions for air–tap water near to liquid surface (samples taken 3 days apart).

bulent gas–liquid dispersion in a stirred vessel was resolved, principally, by selecting a gas flow rate (of bubbles) that was near-to-optimum, so that only bubbles arriving at the probe tip were withdrawn. A good approximation to this condition was achieved by detecting the relatively sharp maxima in the associated local gas holdup profile. Excellent confirmation of the accuracy of local point holdup values was obtained when the dispersion of gas throughout the whole vessel was fairly homogeneous. However, for less homogeneous dispersion conditions, the process of integrating point values depends very heavily on there being a sufficient number of sampling points available.

The relative acceleration-expansion between bubbles flowing inside the capillary was found to have only a small effect on measurement accuracy. Although breakage of bubbles was frequently observed, there was no evidence of coalescence taking place. A semi-empirical equation developed for the bubble volume showed reasonable agreement when compared with directly calibrated values.

High measurement rates were achieved by interfacing the output signal from the photoelectric switch to a microcomputer data acquisition system. Measurements made on air–water, and especially air–electrolyte solution, showed good reproducibility of the bubble size distributions over the size range 0.4×10^{-3} to 5×10^{-3} m. With certain modifications, the measurement technique could be applied to a variety of plant-scale equipment in which turbulent gas–liquid (and liquid–liquid) processes are operated.

SYMBOLS USED

a	interfacial area per unit volume of dispersion	(m^{-1})
$\bar{a}_p$	average point specific interfacial area	(m^{-1})
A	internal cross-section area of capillary tube	(m^2)
C_c	correction factor for point gas holdup	
d_{10}	equivalent mean spherical bubble diameter	(m)
d_{32}	Sauter mean bubble diameter	(m)
d_C	capillary tube inner diameter	(mm)
D	impeller diameter	(m)
h	overall gas holdup of dispersion	
h_p	point gas holdup of dispersion	
l_C	capillary tube length	(m)
L	bubble slug length at detection point	(m)
m	fraction of capillary tube cross-section occupied by liquid film	
n_s	bubble sample size	
N	impeller rotational speed	(s^{-1})
P_A	pressure at sampling point	($N\,m^{-2}$)
P_C	pressure drop over capillary tube	($N\,m^{-2}$)
P_S	liquid slug pressure drop	($N\,m^{-2}$)
P_V	pressure at capillary tube outlet	($N\,m^{-2}$)
q_G	sample flowrate of bubble phase	($m^3\,s^{-1}$)
q_L	sample flowrate of liquid phase	($m^3\,s^{-1}$)
r	internal radius of capillary tube	(m)
Re_b	bubble Reynolds number	
U	liquid slug velocity	($m\,s^{-1}$)
U_b	bubble slug velocity	($m\,s^{-1}$)
t_1, t_2	rise and fall time, respectively, of optical switch signal (Figure 9)	(s)
t_b	time for bubble slug to pass detection point on capillary tube	(s)
t_s	time for liquid slug to pass detection point on capillary tube	(s)
t_t	total sampling time defined by equation (18)	(s)
V_b	bubble volume	(m^3)
z	distance between point of observation and outlet of capillary tube	(m)
μ	dynamic viscosity	($Ns\,m^{-3}$)
ρ	fluid density	($kg\,m^{-3}$)
σ	surface tension	($N\,m^{-1}$)

Affixes

L	liquid phase
G	gas phase
*	detection point on capillary tube

REFERENCES

1. Sridar, T. and Potter, O. E., 1980, *Ind Eng Chem Funda.*, 19(1): 21.
2. Lee, J. C. and Meyrick, D. L., 1970, *Trans I Chem E*, 48: 37.
3. Calderbank, P. H., 1958, *Trans I Chem E*, 36: 443.
4. Vermeulen, T., Williams, G. M. and Langloss, G. E., 1955, *Chem Eng Prog*, 51(2): 85.
5. Robinson, C. W. and Wilke, C. R., 1974, *AIChE J*, 20(2): 285.
6. Nienow, A. W. and Miles, D., 1971, *Ind Eng Chem, Proc Des Dev*, 10(1): 41.
7. Hassan, I. T. M. and Robinson, C. W., 1980, *Chem Eng Sci*, 35: 1277.
8. de Figueiredo, M. M. L., 1978, *PhD Thesis* (University of Edinburgh).
9. Burgess, J. M. and Calderbank, P. H., 1975, *Chem Eng Sci*, 30: 743; 1107, 1511.
10. Wisdom, D. J., 1974, *PhD Thesis* (University of London).
11. Weiland, P., Brentrup, L. and Onken, U., 1980, *Ger Chem Eng*, 3: 296.
12. Mikol, E. P., 1963, *Proc. Ashrae Semiannual Meeting, New York*, 69: 213.
13. Whitesel, H. A., 1957, *Refrig Eng*, 75: 42.
14. Suo, M. and Griffith, P., 1964, *J Basic Eng. Trans ASME*, Series D, 86: 576.
15. Fairbrother, F. and Stubbs, A. E. J., 1935, *J Chem Soc*, 1: 527.
16. Taylor, G. I., 1961, *J Fluid Mech*, 10(2): 161.
17. Suo, M., 1968, *J Basic Eng, Trans ASME*, Series D: 140.
18. Kobbacy, K. A. H., 1981, *PhD Thesis* (University of Bath).
19. Nienow, A. W., Wisdom, D. J. and Middleton, J. C., 1977, *Proc. 2nd Euro Conf Mixing* (BHRA, Cranfield).
20. Semiat, R. and Dukler, A. E., 1981, *AIChE J*, 27(1): 148.

ACKNOWLEDGEMENTS

The authors gratefully acknowledge the financial support of the Science and Engineering Research Council, and the University of Bath for equipment. One of us (K.A.H.K.) wishes to thank the University of Bath for the award of a research studentship during the tenure of this project.

ADDRESSES

Correspondence about this paper should be sent to Dr M. Greaves, School of Chemical Engineering, University of Bath, Claverton Down, Bath, BA2 7AY. Dr K. A. H. Kobbacy is now with the Kuwait Oil Company, Reservoir Department, Ahmadi, Kuwait.

The manuscript was received 9 June 1982 and accepted for publication after revision 16 June 1983.

VOL. 62 1984

EFFECTIVE INTERFACIAL AREA AND LIQUID SIDE MASS TRANSFER COEFFICIENTS IN ABSORPTION COLUMNS PACKED WITH HYDROPHILISED AND UNTREATED PLASTIC PACKINGS

By V. LINEK, P. PETŘÍČEK, P. BENEŠ and R. BRAUN

Institute of Chemical Technology, Czechoslovakia and Raschig GmbH, W. Germany

Data are given on the liquid side volumetric mass transfer coefficient, k_La, and interfacial area, a, for Pall rings of nominal sizes 15, 25, 35, and 50 mm made of polypropylene and polyvinylidenflouride. Surface of the plastic packings was either untreated or was rendered hydrophilic chemically. The k_La values were obtained by physical desorption of oxygen from water into pure nitrogen stream and the a values were calculated from carbon dioxide absorption into sodium hydroxide solution with fast chemical reaction. The k_La and a values for hydrophilic plastic packings are higher by about 60% and by 90 to 130% than the respective values for untreated packings, and thus are comparable to those for ceramic and metallic packings of good wetting properties. Correlations of k_La and a values with contact angle, packing size, and liquid flow rate were derived.

INTRODUCTION

In recent years, ceramic tower packing is tending to lose ground to packings made of steel or plastics. Apart from their application in water treatment, sea-water desalting etc., plastics (especially high-stabilised PP) also prevail in the chemical field (e.g., in modern CO_2 removal units in methanol and ammonia synthesis). High-grade plastics such as PVDF will be of more significance in the future.

However, literature is scarce as to data on the interfacial areas and the volumetric mass transfer coefficients for plastic packings of various shapes. Danckwerts and Rizvi[1] report areas for PP 38.1 mm (1.5 in) Pall rings and 50.8 mm (2 in) Intalox saddles, Sahay and Sharma[2] give areas and k_La values for PP 25.4 mm (1 in) Pall rings and Intalox saddles, and Billet and Mackowiak[3] indicate k_La for Pall rings and 25 mm Tellerets. For a given packing size, Pall rings give the highest interfacial area[4]. For a given packing shape, plastics very often give the smallest interfacial area—smaller than that of ceramic, carbon, or metallic packing[1,2,4]. This is due to poor wetting of the plastic packing by water and aqueous solutions.

Wettability of plastic packings can however be improved very considerably, thus attaining areas comparable to those of ceramic packings of identical shapes[5-7]. Certain treatments by which plastic packings can be rendered hydrophilic on a commercial scale have been patented[8] and are based on chemical bonding of hydrophilic groups onto the packing surface by reactions which proceed in either the gaseous or the liquid phase, at normal temperature and pressure.

Correlations proposed in literature[9,10] for interfacial area calculations from the wettability of packings either are unsuitable for non-hydrophilised polypropylene Pall rings due to disregarding the occurrence of small droplets on the packing, whereby the interfacial area obtained can be lower by up to 50%[4] (the correlation by Onda *et al*[9]), or underestimate the effect of wetting whereby they overestimate by up to 100% the contact area on non-wettable PP packing[6,7] (the correlation by Puranik *et al.*[10]). Some difference exist between effective interfacial areas depending upon whether or not chemical reaction occurs in the absorption process and upon the reaction rate[11]. Values of interfacial area determined by absorption accompanied by nth order reaction should not be used for design of physical ansorbers[4]. The k_La data are well suited for this purpose.

This paper presents the values of effective interfacial area for absorption with fast chemical reaction involving pseudo nth order reaction as well as the values of the volumetric mass transfer coefficient for physical absorption as measured on Pall rings of various size made of PP or PVDF. Untreated packings and packings rendered hydrophilic by chemical treatment described in a Czechoslovak patent[8] were used.

EXPERIMENTAL

Procedure of k_La Determination

A schematic diagram of the experimental set-up is shown in Figure 1. The column was constructed of a perspex tube of 0.29 m inner diameter provided with an eleven-armed liquid distributor[12] (having 63 openings of 9 mm diameter) and a cap-type gas distributor[13] (having 16 openings of 20 mm inner diameter for gas and 3 openings of 40 mm inner diameter for liquid at regular spacing all over the column foot cross-section). The column was packed to the height of 1 m. The characteristics of the packing employed are listed in Table 1.

The set-up permitted the measurement of either the absorption of atmospheric oxygen into oxygen-free water or the desorption of oxygen dissolved in water into

© Institution of Chemical Engineers

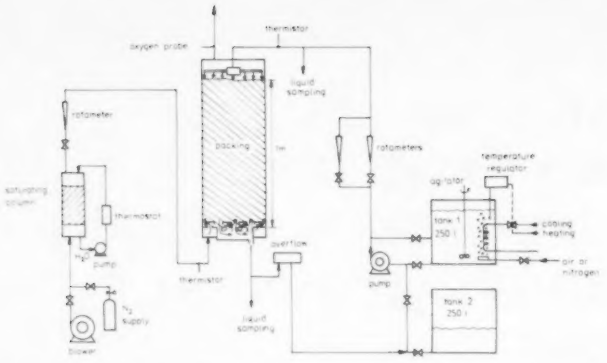


Figure 1. Apparatus for physical absorption or desorption experiments.

a pure nitrogen stream. Most experiments were performed in the counter-current desorption mode. Nitrogen was led into the column at constant superficial velocity of $0.0253\ m\ s^{-1}$. At 20° C liquid superficial velocities from 2.02×10^{-3} up to $0.0252\ m\ s^{-1}$ were used. A polarographic oxygen probe was used to monitor the oxygen concentration in the outlet gas and in the inlet and outlet liquid streams.

The k_La values were calculated from the steady state oxygen concentrations in the column inlet, c_{LA1}, and outlet, c_{LA2}, liquid streams using the relationships

$$k_La = \frac{v_L}{H} \ln (c_{LA1}/c_{LA2}) \quad (1)$$

for desorption experiments and

$$k_La = \frac{v_L}{H} \ln [(c^+_{LA} - c_{LA1})/(c^+_{LA} - c_{LA2})] \quad (2)$$

for absorption experiments. Here c^+_{LA} is the oxygen concentration in air-saturated water under the given experimental conditions.

In deriving the relationships (1) and (2) it has been assumed (i) that the oxygen concentration in the gas phase is constant along the column and equals its concentration in the incoming gas stream and (ii) that the liquid phase conforms to plug flow.

The first assumption was met safely inasmuch as the oxygen concentration changes in the gas phase never exceeded 0.2 vol% in the experiments, due to low oxygen solubility in water. Such negligible concentration changes also are a guarantee of negligible influence of axial dispersion in the gas phase.

Table 1. Characteristics of hydrophilic and untreated packings stated by manufacturer†

Type of packing	Material	d_p (mm)	Number/m^3	a_t (m^{-1})
Pall ring	PP	15	215,000	350
Pall ring	PP	25	51,000	220
Pall ring	PVDF	25	51,000	220
Pall ring	PP	35	19,000	160
Pall ring	PP	50	6700	110

†Packings manufactured by the Raschig GMBH, D-6700 Ludwigshafen/Rhein (W. Germany) and Hydrophilised according to the Czechoslovak Patent No. 210.175 by the firm.

The effect of the axial dispersion of liquid phase on k_La and thus the validity of the second assumption may be estimated by a procedure given, e.g., in Sherwood *et al.*[30]. The data[30b] suggest that the maximum axial dispersion occurs at low superficial liquid velocity on 50.8 mm Raschig rings where the particle Peclet number P_p (notation identical to Sherwood *et al.*[30]) varies about 0.2 so that the column Peclet number P_{eL} for 1 m column height equals 4. For the case of 90% absorption obtained in our experiments with 50 mm Pall rings at the lowest liquid flow rate, i.e., for $N_{oLp} = 2.3$, we may extract from the data [30a] the information that the k_La value calculated on the assumption of plug flow is lower by 30% than that calculated with axial dispersion. Hence, the axial dispersion of the liquid phase is significant and ought to be taken into consideration whenever the k_La values are to be evaluated.

Unfortunately, the literature gives rather discrepant data on liquid phase Peclet numbers. It has even been ascertained[13] that the Peclet dependence on liquid flow rate is dependent on the way in which the tracer is introduced into the liquid: Peclet numbers established by conductivity measurements (where tracer is introduced into bulk liquid) increase with flow rate, whereas those based on a technique where tracer is being absorbed across the gas-liquid interface fade off with increasing flow rate.

A predominant share of papers[2,3,6,7,19,20,22,23] dealing with comparisons of the transport properties of packings issue from the plug flow model which has become conventional. Data processing by means of this model yields lower k_La values and, hence, safe design height of absorption columns. The k_La values thus obtained can however be easily converted to true values as long as reliable data on axial mixing of the liquid phase is available.

VOL. 62 1984

Procedure of K_Ga Determination

The schematic diagram of apparatus used is given in Figure 2. The column and column top were the same as those used in the previous k_La determination. The arrangement of the column foot is apparent from the schematic drawing. Dilute carbon dioxide (1 vol% mixture with air) was absorbed in 1 *M* sodium hydroxide solution. Temperature of both inlet streams was maintained at 20 ± 0.3°C. No appreciable temperature rise was noted during absorption. The solution was renewed when the conversion of NaOH to carbonate reached about 50%.

Carbon dioxide concentration in gas phase in the column was monitored by means of an infra-red analyser simultaneously at three levels of the packed section (level spacings indicated in Figure 2) by three gas samplers distributed regularly along the column diameter. The measurements were carried out at liquid superficial velocities in the range from 2.02×10^{-3} up to $0.028\ m\ s^{-1}$. Gas superficial velocity was constant at $0.382\ m\ s^{-1}$.

The over-all volumetric mass transfer coefficient of carbon dioxide, K_Ga, was calculated from CO_2 concen-

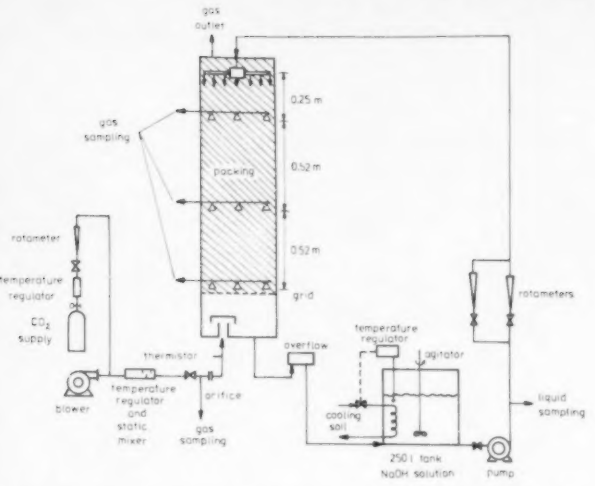


Figure 2. Apparatus for carbon dioxide absorption into NaOH solution.

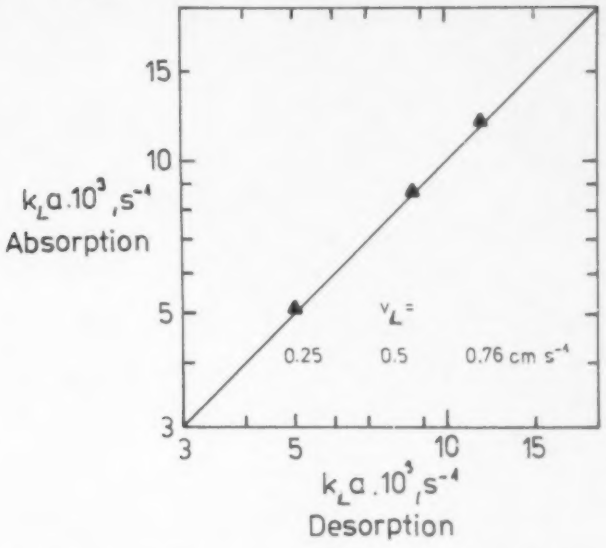


Figure 3. Comparison of K_La values determined from absorption and desorption experiments for untreated PP Pall rings 25 mm.

trations in gas phase at the foot, x_{GB1}, and at the top, x_{GB2}, of the packing from the relationship

$$K_Ga = \frac{v_G}{H} \ln (x_{GB1}/x_{GB2}) \quad (3)$$

This relation assumes plug flow of gas phase in the column. Axial dispersion of the liquid phase has no effect on CO_2 chemisorption (absorption with fast chemical reaction) since the liquid phase composition remains practically unchanged along the column. The effect of axial dispersion of the gas phase on the K_Ga values can be assessed again by the procedure given in Sherwood *et al.*[30].

Literature data on the Peclet numbers for the gas phase are in much better agreement than those for the liquid phase[13]. The data [30b]indicate that, at the gas flow rate used ($v_G = 0.028$ m s^{-1}), the intensity of axial dispersion is highest at the maximum superficial liquid velocity $v_L = 0.028$ m s^{-1} for 25.4 mm Raschig rings where the particle Peclet number amounts to $P_p = 0.3$, and for $H = 1$ m the corresponding column Peclet number is $P_{eG} = 12$. For the absorption efficiency of 72%, i.e., $N_{oGp} = 1.27$, we may deduce [30a]that the difference between the true value of K_Ga and the value calculated from (3) assuming plug flow is 9%. Considering that P_p values are higher for Pall rings than for Raschig rings of the same size, the value given above represents in fact an overestimate of the maximum possible K_Ga difference due to neglecting the axial dispersion of the gas phase.

EXPERIMENTAL RESULTS

Physical Absorption of Oxygen

Comparison of absorption and desorption; effect of gas flow rate. The values of k_La derived from oxygen absorption and desorption are identical within the margin of experimental error, as can be seen clearly in Figure 3. All the k_La values given below were obtained by desorption experiments which were the simpler of the two to carry out. It has been confirmed (cf. Figure 4) that the experiments were run in a region where the transport coefficients are gas flow independent.

Effect of hydrophilic packing The treatment by which the packings were made hydrophilic had a marked influence on the k_La values for all sizes of packing over the entire range of superficial velocities used, as is clear from Figure 5 to 9. The hydrophilic packings gave values which as a rule, were higher by 60% than those obtained with untreated packings. The smallest increase observed was 45% for 25 mm PVDF Pall rings. The upgrading was highest with 50 mm Pall rings made of PP (75%).

Comparison with published data Our results for untreated Pp packings obtained at packed height $H = 1$ m agree well enough with data for 25 mm Pall rings ($H = 2$ m) by Billet and Mackowiak[3] as well as with data for 25.4 mm Pall rings ($H = 0.87$ m) by Sahay and Sharma[2] (see Figure 6), and also agree with our earlier data[7] for both hydrophilic and untreated 33 mm Pall

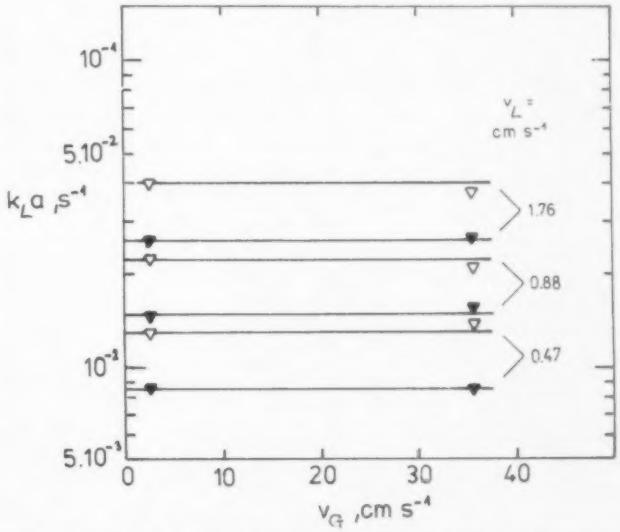


Figure 4. Effect of gas flow rate on k_La values for PP Pall rings 15 mm. (Open points correspond to hydrophilic packing.)

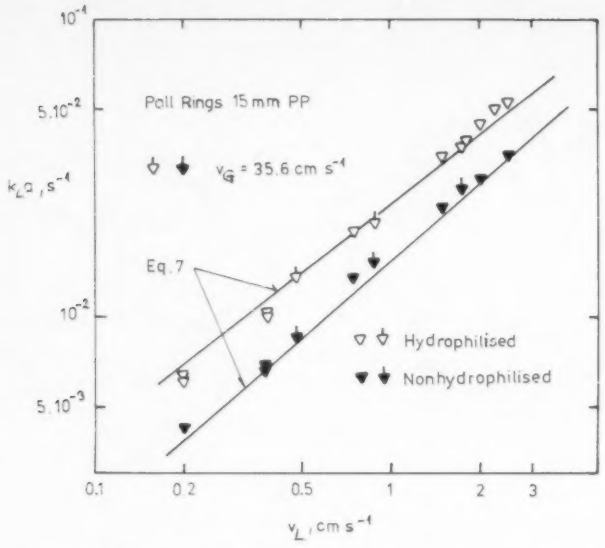


Figure 5. Effect of liquid flow rate and of packing hydrophilisation upon k_La values for PP Pall rings 15 mm.

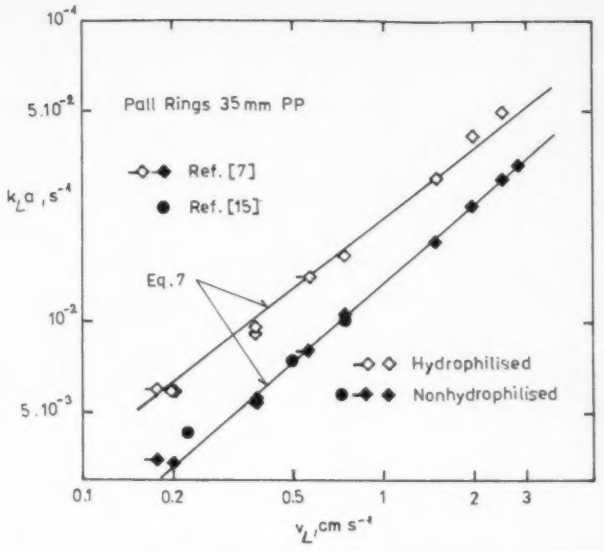


Figure 7. Effect of liquid flow rate and of packing hydrophilisation upon k_La values for PP Pall rings 35 mm.

rings ($H = 0.69$ m), Figure 7. Very good agreement has also been reached with other values obtained by us[15], see Figure 6, 7, and 8.

Our data for hydrophilic PP and PVDF Pall rings 25 mm also agree very well with the correlation by Sahay and Sharma[2] for 25.4 mm stainless steel Pall rings:

$$k_La = 6.16 \times 10^{-4} v_L^{0.806} \tag{4}$$

and with Norman's correlation[19] for ceramic Raschig rings and Berle saddles.

$$\frac{k_La}{D} = 27.2\left(\frac{\rho v_L}{\mu}\right)^{0.75} Sc^{-0.5} \tag{5}$$

A comparison plot is given in Figure 10. It follows that hydrophilic PP and PVDF packing rank abreast with ceramic or metallic packings considered to have the best wetting properties.

The effect of the wetting properties of the various types of packing on the k_La values is estimated using the following correlation of the mass transfer coefficient k_L by Onda *et al.*[9].

$$k_L\left(\frac{\rho}{\mu g}\right)^{1/3} = 0.0051\left(\frac{v_L\rho}{a\mu}\right)^{2/3} Sc^{-1/2}(a_t d_p)^{0.4} \tag{6}$$

in combination with Onda's[17] correlation (13) of the wetted surface area a of the packing.

To establish the effect of wettability the critical surface tension σ_c was used. The following values of σ_c were used for individual materials in the calculations: For untreated PP and PVDF packings, $\sigma_c = 0.02$ kg s^{-2} as indicated in [24] for polypropylene, polyethylene, and

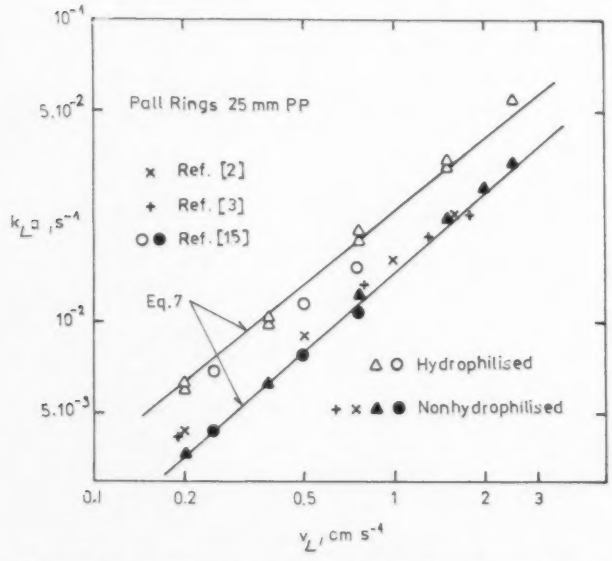


Figure 6. Effect of liquid flow rate and of packing hydrophilisation upon k_La values for PP Pall rings 25 mm.

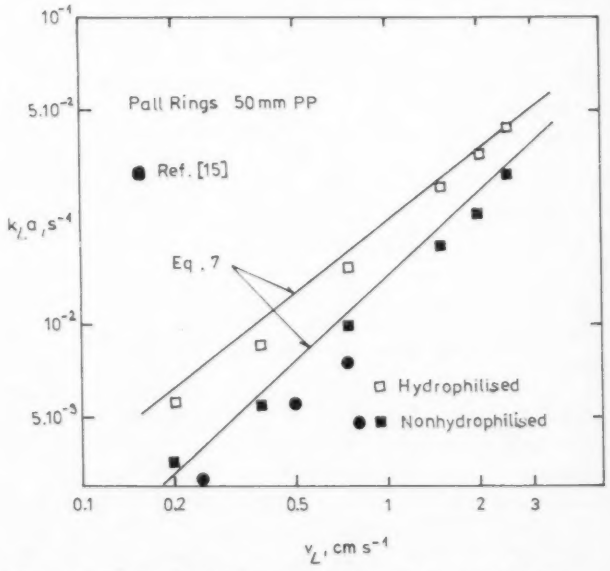


Figure 8. Effect of liquid flow rate and of packing hydrophilisation upon k_La values for PP Pall rings 50 mm.

VOL. 62 1984

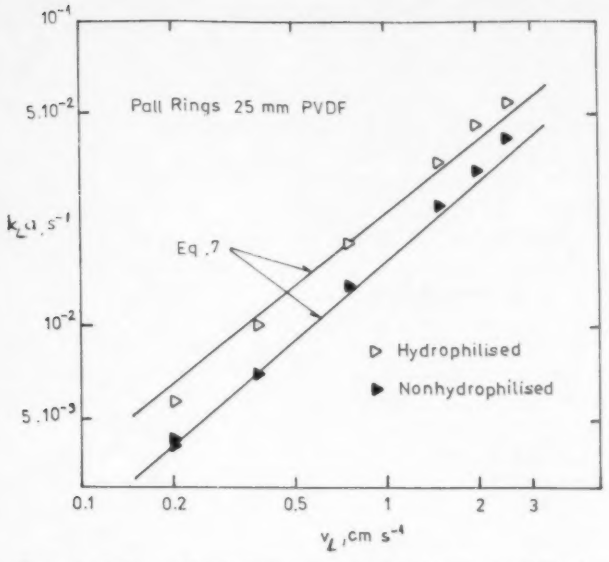


Figure 9. Effect of liquid flow rate and of packing hydrophilisation upon $k_L a$ values for PVDF Pall rings 25 mm.

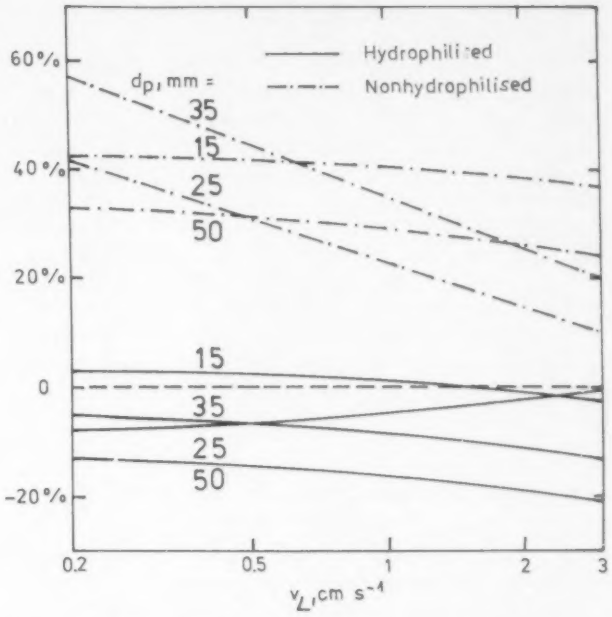


Figure 11. Relative deviations between $k_L a$ values calculated from Onda's correlations (6) and (13) and the experimental values as a function of superficial liquid velocity.

teflon. For hydrophilic PP and PVDF packings, $\sigma_c = 0.071\ \mathrm{kg\,s^{-2}}$ as a value recommended[29] for metal packings to which our data for the hydrophilic packing can well be compared.

Figure 11 gives the realtive deviations between $k_L a$ values calculated from Onda's correlations (6) and (13) and the experimental values, as a function of superficial liquid velocity for all the packings tested. To make the drawing easy to the eye, the experimental points are not plotted, however, their scatter about the lines shown is small, not exceeding about $\pm 5\%$.

Onda's correlation give a fairly true picture of the $k_L a$ values obtained on hydrophilic packings but tend to considerably overestimate the values for untreated packings (by up to 60%). As a consequence to this, these correlations predict a lower increase (about 25%) in the $k_L a$ values due to surface treatment than is actually the case (about 60%). This holds true even for packings of other shapes, as follows from our earlier work[7] giving data for Super Torus saddles.

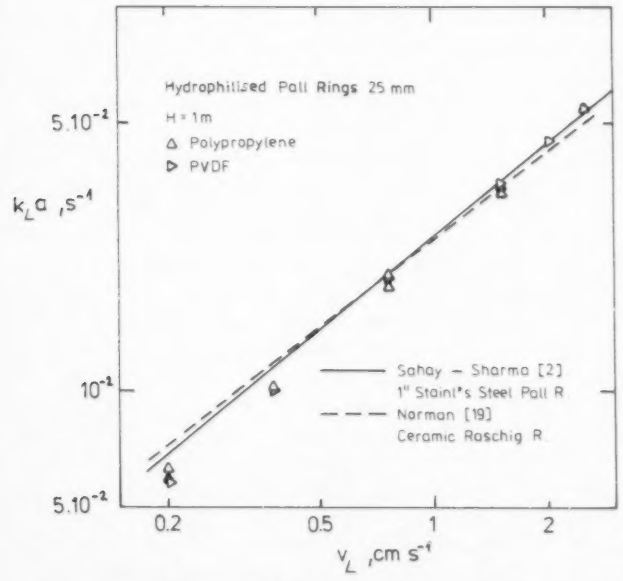


Figure 10. Comparison of hydrophilic PP and PVDF packings with ceramic and metallic packings.

Although a large number of researchers have published correlations for $k_L a$ in packed columns[2,3,19-23], the correlations are not suitable for a range of systems, operating conditions, and packing materials. The equations presented are generally empirical in nature and usually are related to just a single material, type, and size of packing[2,3,19,20,22].

An exception is the correlation derived by Davidson[21] from a notion that the packing is composed of a great number of planar, randomly tilted surfaces of random lengths up to the maximum length of each packing element, d_p. The liquid was assumed to run down the surface by gravity in laminar flow, being fully mixed at each packing junction.

Ponter[23] has expanded the Davidson model[21] to cover such cases as where the packing is not completely wetted, the liquid is not completely mixed at the junctions of the packing surfaces, and different ring sizes are involved. The model yields the correlation:

$$k_L a = \frac{v_L}{A d_p \alpha}\left(\frac{d_p}{d}\right)^{0.5} Sc^{-0.5}\, Re^{m}\, Gr^{1/6} \tag{7}$$

$$\alpha = 3.46 \times 10^2 \left[(1-\cos\theta)^{0.6}\, Ka^{0.2}\right]^{0.728} \tag{8}$$

$$\frac{d}{d} = \lambda\left(10^3 \frac{v_L \rho}{\mu}\right)^{\eta} \tag{9}$$

$$\eta = 2\left[(1-\cos\theta)^{0.6}\, Ka^{0.2}\right]^{-0.126} \tag{10}$$

$$\lambda = 0.155\, Ka^{-0.171} \tag{11}$$

with $A = 0.05974$ and $m = 0.61$ for Raschig rings from 1.27 to 5.06 cm.

The captive bubble method[24] applied to samples of materials from which the packings used in our work were made gave the following values of the contact angle θ used henceforward in our calculations: $66.6 \pm 2.5°$ for untreated PP packings, $54.5 \pm 2.5°$ for untreated PVDF packings, and $22.5 \pm 2.5°$ for all the treated, i.e., hydrophilic packings (both PP and PVDF). The agreement of our data with this correlation is not good, with an average deviation of 38%. The following values were obtained for the constants by regression on our data: $A = 0.02357$ and $m = 0.438$. The agreement is good for all sizes and types of packing with average deviation of 9% (see lines calculated from equation (7) given in Figures 5 to 9).

Absorption of Carbon Dioxide with Fast Chemical Reaction.

The relationship for the over-all mass transfer coefficient of dilute carbon dioxide absorption into sodium hydroxide solution assumes the form[16-18]

$$K_G = He_B (D_B k_2 c_C)^{0.5} \qquad (12)$$

where c_C is the concentration of OH^- ions within the liquid phase, The value of the exponent, $n = 0.5$, established experimentally for the relation $K_G a \sim (c_C)^n$ agrees with the value predicted by the formula (12), see Figure 12.

The over-all mass transfer coefficient K_G was determined experimentally from the absorption rate of CO_2 mixed with air in concentrations of 0.3, 0.8, and 1 vol% into a mechanically stirred solution of 1 kmol NaOH m^{-3} across a quiet and undisturbed surface of known interfacial area at 20°C. The experimental value of $K_G = (2.24 \pm 0.08) \times 10^{-3}$ m s^{-1} related to $c_C = 1$ kmol m^{-3} is in excellent agreement with the value

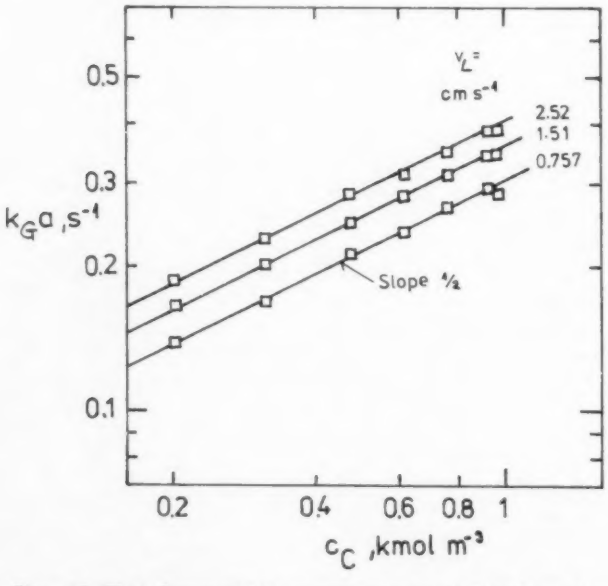


Figure 12. The influence of OH^- concentration (as the NaOH solution is being converted to carbonate during absorption experiments) upon $K_G a$ values.

calculated by the relationship (12) from literature data on the kinetics of the accompanying reaction ($k_2 = 9078$ kmol^{-1} m^3 s^{-1}, Pinset *et al.*[25]), CO_2 diffusivity ($D_B = 1.2 \times 10^{-9}$ m^2 s^{-1}, Aiba[26]), and CO_2 distribution coefficient ($He_B = 0.6675$ derived from CO_2 solubility in water, Danckwerts and Sharma[28], and from the correlation by Danckwerts[27] for the salting-out effect of NaOH) as $K_G = 2.2 \times 10^{-3}$ m s^{-1}.

Effective interfacial areas were calculated from $K_G a$ values obtained by formula (3), from experimental K_G, and from appropriate OH^- concentrations in the absorptive solution, c_C, which were determined by titration. The results obtained with two packing heights were processed to plots of the (a/a_t) ratio against liquid flow rate and are shown in Figures 13 to 17 for both hydrophilic and untreated packings.

There is no significant difference between values of area determined at 0.52 and 1.04 m packed heights. The differences fluctuate about 7% at low liquid flow rates and are quite indiscernible at higher flow rates. Hydrophilic 15 mm Pall rings are an exception: at 0.52 m packed height the areas obtained at liquid flow rates below 0.015 m s^{-1} were lower by 30% than those at 1.04 m height, whereas at high liquid flow rates the differences were within the bounds of experimental scatter even for this kind of packing. The coincidence of areas established with different packed heights appears to be a consequence of the experimental arrangement used: the gas sampling point was located inside the packing and at a sufficient distance from the liquid distributor, so that the result does not account for absorption in the end devices of the absorption column.

Effect of hydrophilic packing: The effective interfacial area is significantly higher on packings whose surface has been treated to obtain hydrophilic properties. On the average, the hydrophilic packings give areas higher by 90 to 130% than the original, untreated packings at liquid flow rates v_L below 0.015 m s^{-1} (see Figures 13 to 17). At higher flow rates, $v_L > 0.015$ m s^{-1}, the untreated packing is subject to an increase in interfacial area due to the occurrence of small droplets on the packing, and the resultant effect of the hydrophilic surface is mitigated: with 50 mm Pall rings where droplet formation is most pronounced the increase in area due to hydrophilic packing surface is about 40% at the highest liquid flow rate tested. With smaller-size packing elements less susceptible to droplet formation the increase in area due to hydrophilic packing surface is at least 70% even at maximum liquid flow rate (Pall rings 15 mm).

The a-values obtained after the treatment are 90 to 130% higher, while the $k_L a$ increase by only 45 to 75%. This may be explained in two ways:

(i) It is obvious that some differences exist between the effective interfacial areas for absorption with and without a chemical reaction. In pure physical absorption, the semi-stagnant liquid pockets and very thin liquid films tend to become saturated in a very short time, and hence their surfaces become ineffective for mass transfer[4,7].

(ii) Hydrophilisation of the surface may lower the mass transfer coefficient k_L, since an enlargement of the wetted surface area results in a decrease in the liquid flow rate in the film.

VOL. 62 1984

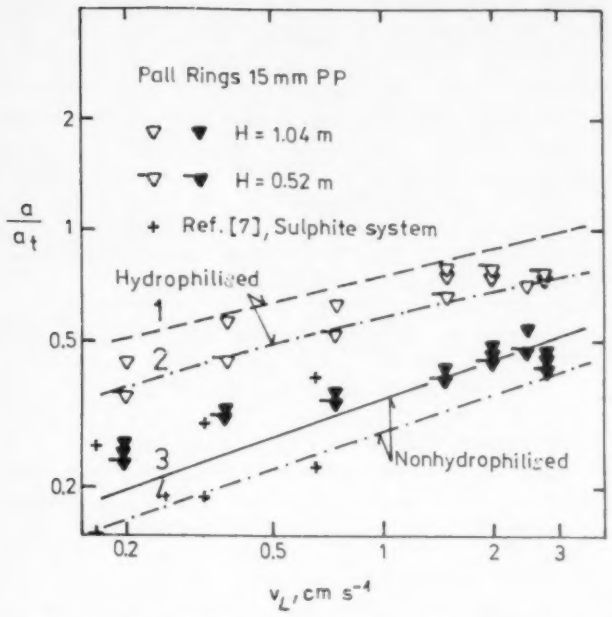


Figure 13. Effect of packing height, of packing hydrophilisation and of liquid flow rate upon effective interfacial area for PP Pall rings 15 mm. Lines: 1. equation (15) for hydrophilic packing; 2. equation (13) for hydrophilic packing; 3. equation (15) for untreated packing; 4. equation (13) for untreated packing.

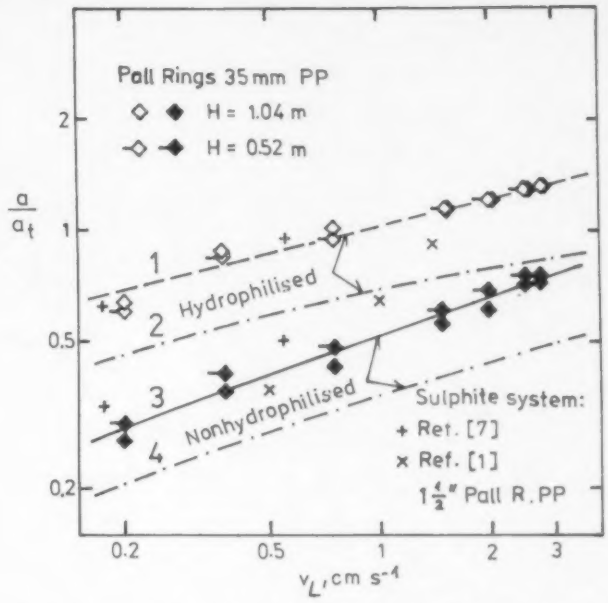


Figure 15. Effect of packing height, of packing hydrophilisation and of liquid flow rate upon effective interfacial area for PP Pall rings 35 mm. Lines see Figure 13.

According to Onda's correlation, equation (6), the relative decrease in k_L due to the hydrophilisation of the surface is equal to the ratio of the wetted surface area of hydrophilised to non-hydrophilised packing raised to a power of 2/3. Correlation (6) predicts that, for example, an enlargement of the surface area by 100% will produce a decrease in k_L by 40%. However, the extent to which factors (i) and (ii) affect the results cannot be determined with confidence from our measurements.

Comparison with published data: Good agreement was found between our measurements on untreated 35 mm Pall rings and the results by Danckwerts and Rizvi[1] on 38.1 mm PP Pall rings in spite of a different absorption system used (see Figure 15). Our previous measurements[7] of the surface area of hydrophilised and non-hydrophilised Pall rings of 33 and 50 mm in di-

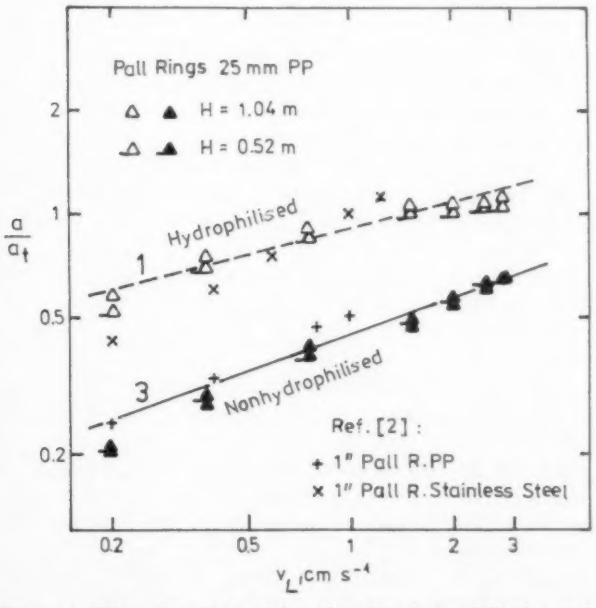


Figure 14. Effect of packing height, of packing hydrophilisation and of liquid flow rate upon effective interfacial area for PP Pall rings 25 mm. Lines see Figure 13.

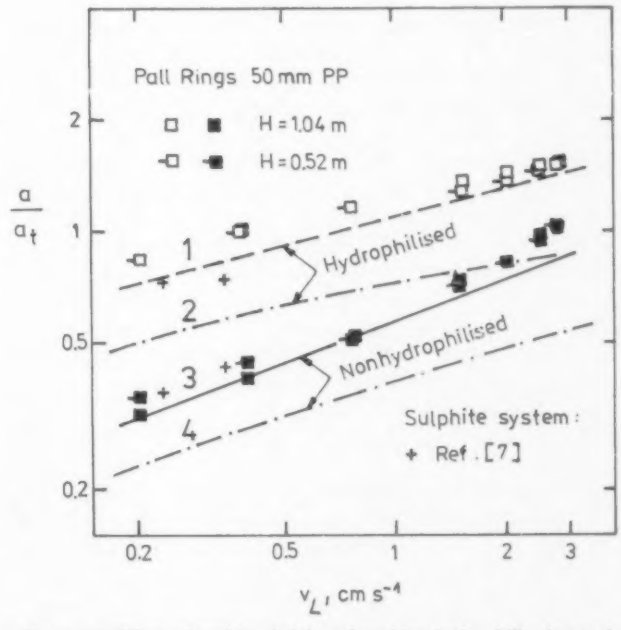


Figure 16. Effect of packing height, of packing hydrophilisation and of liquid flow rate upon effective interfacial area for PP Pall rings 50 mm. Lines see Figure 13.

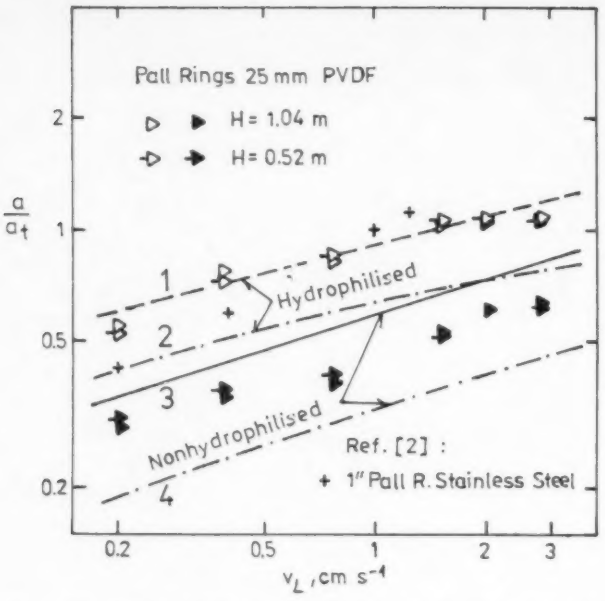


Figure 17. Effect of packing height, of packing hydrophilisation and of liquid flow rate upon effective interfacial area for PVDF Pall rings 25 mm. Lines see Figure 13.

ameter, carried out by use of the sulphite system, are also in good agreement with the present data (see Figures 15 and 16).

For 15 mm Pall rings, however, the present data (Figure 13) are by about 70% higher than those measured previously[7]. This is presumably due to some kind of systematic error in our previous measurements[7] on 15 mm Pall rings, since again the previously obtained values for the relative increases in the wetted surface area after hydrophilisation (between 55 and 75%) are in good agreement with those obtained in this work (around 70%).

Similarly, our results are in good agreement with those of Sahay and Sharma[2] obtained on 25.4 mm PP Pall rings (Figure 14). Even their areas[2] for 25.4 mm stainless steel Pall rings agree with out data for hydrophilic Pall rings 25 mm of PP and PVDF (Figure 16).

Hence, the hydrophilic PP and PBDF packings are in no way inferior to metallic or ceramic packings of satisfactory wetting properties, as far as the effective interfacial area is concerned. This is also confirmed by results of our previous studies[6,7] in which the surface areas of the ceramic and hydrophilised 15 mm PP Raschig rings were found to agree.

The correlation proposed by Onda *et al*[9] for the calculation of effective interfacial area,

$$\frac{a}{a_t} = 1 - \exp\left\{-1.45(\sigma_c/\sigma)^{0.75}\, Re^{0.1}\, Fr^{-0.05}\, We^{0.2}\right\} \qquad (13)$$

on packings of different wetting properties would not work well in correlating our results (see lines 2 and 4 in Figures 13 to 17). Correlation (13), which was originally derived[9] from data measured on Raschig rings, Berl saddles, spheres and Rods, underestimates consistently, by 40 to 70%, the surface areas for both the non-hydrophilised and hydrophilised Pall rings. At the same time, however, it gives a good description of the relative enlargement of the wetted surface area of plastic packings as a result of the hydrophilisation treatment (see Figures 13 to 17, and Figure 2 of ref. 7). However, correlation (13) predicts that the maximum possible value of the ratio (a/a_t) equals 1 but experimental values higher than that are frequently encountered at higher liquid flow rates on well wetted larger size packing elements (e.g., see Danckwerts and Rizvi[1], data for 38.1 mm ceramic Raschig rings: $a/a_t = 1.12$ at $v_L = 0.022$ m s^{-1}; and Sahay and Sharma[2], data for 25.4 mm stainless steel Pall rings: $a/a_t = 1.15$ at $v_L = 0.013$ m s^{-1}).

Not even the correlation by Puranik and Vogelpohl[10]

$$\frac{a}{a_t} = 1.045\, Re^{0.041}\, We^{0.133}\, (\sigma/\sigma_c)^{-0.182} \qquad (14)$$

give an adequate fit to our experimental data. The mean deviation of experimental values of area for the 1.04 m packing from values calculated by the above correlation (14) constitutes 40%. In calculating the empirical constants of their correlation (14) the authors[10] made use just of that part of published data which gives $(a/a_t) < 1$. For instance, of the data by Danckwerts and Gillham[14] for 38.1 mm ceramic Raschig rings which embrace values up to $a/a_t = 1.08$ they only used those up to about 0.9, as is clear from the Figure 1 of their paper[10]. In fact, the inadequacy of their correlation for our data follows clearly enough from a comparison of experimental and correlated values of the ratio of interfacial areas for hydrophilic and untreated packings. The experimental ratios range from 1.4 to 2.3, whereas the correlation predicts a constant ratio equal to 1.26 and independent of the liquid flow rate.

Therefore other shapes were examined and various criteria adopted for correlation of the surface areas of Pall rings. The best fit was obtained using the empirical correlation

$$\frac{a}{a_t} = 0.0277\, W^{3.477}\, (a_t d_p)^{1.585}\, Re^{0.641 - 0.407\, W} \qquad (15)$$

which describes the effect of the packing wettability in terms of the ratio of the work of adhesion between the liquid phase and the packing material to the work of cohesion of the liquid; this ratio is given[24] as $W = (1 + \cos\theta)/2$. The goodness of fit may be judged with reference to Figures 13 to 17, where lines 1 and 3 have been calculated from correlation (15) for hydrophilic and non-hydrophilic packings, respectively. The scatter of the experimental data about the calculated lines amounts to 10%.

CONCLUSIONS

Volumetric mass transfer coefficients, $k_L a$, are higher by 45 to 75% for hydrophilic PP and PVDF packings than for untreated (non-hydrophilic) packings and are comparable to those for ceramic or metallic packings of good wetting properties. Correlation by equation (7) is well suited for $K_L a$ calculations involving both hydrophilic and untreated packings. With constants $A = 0.02357$ and $m = 0.438$, the correlation estimates of $k_L a$ value are accurate to 9% over a range of Re from 5 to 240.

VOL. 62 1984

Effective interfacial areas of hydrophilic packings are higher by 40 to 130% than those of untreated packings. Interfacial area enhancement is greater with larger-size packing elements and at lower liquid flow rates. The areas attained with hydrophilic packings agree with areas published for well wetted metallic or ceramic packings of the same size. Equation (15) can be used to calculate interfacial areas of both hydrophilic and untreated packings to 10% accuracy at *Re* from 7 to 213.

SYMBOLS USED

a	effective interfacial area per unit volume of packing (m^{-1})
a_t	geometrical surface area per unit volume of packing (m^{-1})
A	dimensionless empirical constant in equation (7)
c	concentration (kmol m^{-3})
d	effective length of packing element, equation (9) (m)
d_p	nominal size of packing (m)
D	diffusivity ($m^2 s^{-1}$)
g	gravitational constant ($m s^{-2}$)
H	packing height (m)
k_2	second-order reaction rate constant (kmol^{-1} $m^3 s^{-1}$)
k_L	liquid side mass transfer coefficient ($m s^{-1}$)
K_G	over-all mass transfer coefficient ($m s^{-1}$)
m	empirical exponent of Reynolds number, equation (7)
v	superficial velocity ($m s^{-1}$)
W	$= (1 + \cos\theta)/2$
x	molar fraction

Dimensionless numbers

$Fr = a_t v_L^2/g$; $Gr = \rho^2 g d_p^3/\mu^2$; $Ka = \rho\sigma^3/(\mu^4 g)$; $Re = v_L \rho/(a_t \mu)$; $Sc = \mu/(\rho D)$; $We = v_L^2 \rho/(\sigma a_t)$

Greek symbols

α	mixing factor, equation (8)
η	dimensionless quantity defined by equation (10)
θ	contact angle (°)
λ	quantity defined by equation (11) ($cm^{-\eta}$)
μ	dynamic viscosity of liquid (kg $m^{-1} s^{-1}$)
ρ	density of liquid (kg m^{-3})
σ	surface tension of liquid (kg s^{-2})
σ_c	critical surface tension of packing material (kg s^{-2})

Substripts

1	inlet stream
2	outlet stream
L	Liquid phase
G	gas phase
A	oxygen
B	carbon dioxide
C	OH^- ion

Abbreviations

PP	polypropylene
PVDF	polyvinylidenfluoride

REFERENCES

1. Danckwerts, P. V. and Rizvi, S. F., 1971, *Trans IChemE*, 49: 124.
2. Sahay, B. N. and Sharma, M. M., 1973. *Chem Eng Sci*, 28: 41.
3. Billet, R. and Mackowiak, J., 1980, *Chem Tech*, 5: 219.
4. Charpentier, J. C., 1976, *Chem Eng J*, 11: 161.
5. Linek, V., Stoy, V. and Křivský, Z., 1974, *Chem Eng Sci*, 29: 1955.
6. Linek, V., Křivský, Z. and Hudec, P., 1977, *Chem Eng Sci*, 32: 323.
7. Linek, V., Petříček, P., Beneš, P. and Křivský, Z., 1980, *Verfahrenstechinik*, 14: 733.
8. Czechoslovak Patent, 1981, No 210.175
9. Onda, K., Takeuchi, H. and Okumoto, Y., 1968, *J. Chem. Eng Japan*, 1: 56.
10. Puranik, S. S. and Vogelpohl, A., 1974, *Chem Eng Sci*, 29: 501,
11. Joosten, G. E. H. and Danckwerts, P. V., 1973, *Chem Eng Sci*, 28: 453.
12. Shulman, H. L., Savini, C. G. and Edwin, R. V., 1963, *AIChE J*, 9: 479.
13. Linek, V., Beneš, P., Sinkule, J. and Křivský, Z., 1978, *Ind Eng Chem Fundl*, 17: 298.
14. Danckwerts, P. V. and Gillham, A. J., 1966, *Trans IChemE*, 44: 42.
15. Linek, V., Špirko, K., Petříček, P. and Beneš, P., *Sci Papers Prague Inst Chem Technol*, (in press).
16. Yoshida, F. and Miura, Y., 1963, *AIChE J*, 9: 331.
17. Onda, K., Sada, E. and Takeuchi, H., 1968, *J. Chem Eng Japan*, 1: 62.
18. Sharma, M. M. and Danckwerts, P. V., 1970, *Brit Chem Eng*, 15: 522.
19. Norman, W. S., 1961, *Distillation, Absorption and Cooling Towers*, (Longmans Green, London).
20. Sherwood, T. K. and Hollway, R. P., 1940, *TransAIChE*, 36: 39.
21. Davidson J. F., 1959, *Trans ichemE*, 37: 131.
22. Mangers, R. J. and Ponter, A. B., 1980, *Ind Eng Chem, Proc Des Dev*, 19: 530.
23. Ponter, A. B. and Au-Yeung, P. H., 1982, *Canad J Chem Eng*, 60: 94.
24. Adamson, A. W., 1967, *Physical Chemistry of Surfaces*, 2nd edn (Intersci Publ, John Wiley, New York).
25. Pinset, B. R., Pearson, L. and Roughton, F. J. W., 1956, *Trans Faraday Soc*, 52: 1512.
26. Aiba, K., 1981, *Ind Eng Chem Fundl*, 20: 89.
27. Danckwerts, P. V., 1970, *Gas-Liquid Reactions* (Mcgraw-Hill, New York).
28. Danckwerts, P. V. and Sharma, M. M., 1966, *The Chemical Engineer* CE244.
29. Onda, K., Takeuchi, H. and Koyama, Y., 1967, *Kag Kog*, 31: 126.
30. Sharwood, T. K., Pigford, R. L. and Wilke, C. R., 1975, *Mass Transfer* (McGraw-Hill, New York), *a* Fig. 11.9, *b* Fig. 11.10

ADDRESSES

Correspondence on this paper should be addressed to Dr. V. Linek, Department of chemical Engineering, Institute of Chemical Technology, 166 28 Prague 6, Czechoslovakia. Dr. R. Brown is with Füllkörper-Abteilung, Raschig GmbH, D-6700 Ludnigshafen/Rhein, West Germany.

The manuscript was received 14 *February* 1983 *and was communicated by Professor J. R. Bourne, Associate Editor for Continental Europe*

ISOTHERMAL TWO-PHASE FLOW OF AIR AND AQUEOUS POLYMER SOLUTIONS IN A SMOOTH HORIZONTAL PIPE

R. P. CHHABRA (GRADUATE), S. I. FAROOQI (GRADUATE) and J. F. RICHARDSON (FELLOW)
Department of Chemical Engineering, University College of Swansea

Experiments have been carried out on two-phase flow of air and aqueous polymer solutions (both inelastic and viscoelastic) in a 42 mm internal diameter pipe under isothermal conditions. Average liquid holdup and two-phase pressure drop have been measured for a wide range of combinations of input rates of air and polymer solutions. It is demonstrated that the average liquid holdups for inelastic liquids in both laminar and turbulent flow and for viscoelastic liquids in turbulent flow are in conformity with values obtained for shear-thinning suspensions. However, for viscoelastic liquids in laminar flow the elasticity gives rise to an increased holdup. Elasticity appears to have little effect on two-phase pressure drop. For laminar flow of liquid, minimum drag ratios are consistent with figures obtained for shear-thinning suspensions; and for turbulent flow, the Lockhart–Martinelli correlation is applicable.

INTRODUCTION

The simultaneous two-phase flow of gases and liquids is encountered in many chemical processing industries. Over the past three decades, much progress has been made in the understanding of two-phase flow in horizontal tubes when the liquid phase exhibits a constant Newtonian viscosity, and the resultant voluminous literature has been summarised in several books, e.g. Govier and Aziz[1]. Many of the materials handled in the chemical and process industries, including petroleum products, drilling muds, plastics and food-stuffs exhibit complex rheological behaviour. Despite the great industrial importance of these materials, very little work has been reported on two-phase co-current flow in horizontal tubes, especially when the liquid phase exhibits viscoelastic behaviour.

The two most important hydrodynamic characteristics of two phase gas–liquid systems are pressure drop and holdup. Considerable efforts have in the past been devoted to the development of methods to estimate these two quantities as a function of the input rates and physical properties of the gas and liquid. Several different flow patterns exist in two-phase systems and the transition from one to another often occurs over a fairly wide range of conditions, and thus the distinction between any two flow patterns is not always well defined. The existence of these different flow patterns has hindered the development of generalised correlations. However, Lockhart and Martinelli[2] in 1949 proposed an empirical approach to correlate two-phase pressure drop and holdup by means of a dimensionless ratio, subsequently termed the Lockhart–Martinelli parameter. Their correlation has gained wide acceptance for the two-phase flow of gases and Newtonian liquids. Though the values of the empirical constants in their correlation have been a matter of some disagreement amongst several workers[3,4,5] the basic functional relation has been used almost unaltered.

It is now generally agreed[6–8] that the correlation overpredicts the value of average liquid holdup under laminar conditions for the liquid. Recently, Farooqi and Richardson[8] have presented an analytical form of the correlation to represent most of the liquid holdup data available on air/water and air/water–glycerol mixtures for the slug flow regime. Several other empirical correlations which predict the value of average liquid holdup for all flow regimes have been reviewed by Govier and Aziz[1]. Another method of interpreting results for both Newtonian and non-Newtonian flow is based on the drift flux model of Zuber and Findlay[9]. The average velocity of the gas is shown to be a linear function of the mixture velocity with the slope and intercept dependent on the flow regime and on the physical properties of the two phases.

Similarly several correlations for estimating two-phase pressure drop have been reported in the literature and most of these have been reviewed by Govier and Aziz[1]. Dukler et al[10] and Heywood[4] concluded that, overall, the correlation of Lockhart and Martinelli[2] which predicts the two-phase pressure drop with a maximum error of $\pm 30\%$ is the best available for estimating two-phase pressure drop in all flow regimes.

Thus for the two-phase flow of gases and Newtonian liquids, the values of both average liquid holdup and of two-phase pressure drop can be predicted with a reasonable level of accuracy.

In contrast to this, very little work has been reported on the horizontal two-phase flow of gases and non-Newtonian liquids. From recent experimental work with polymer solutions[7,11,12] and shear-thinning pseudo-homogeneous suspensions of china clay and anthracite[8,13], it is concluded that for liquid initially in laminar flow the average liquid holdup in the case of non-Newtonian shear-thinning liquids is lower than that for Newtonian liquids at constant Lockhart–Martinelli parameter. Recently Farooqi and Richardson[8] have presented a modification of the Lockhart–Martinelli correlation to include the effects of shear-thinning behaviour. However, when the liquid is in turbulent flow the same correlation applies to both Newtonian and

VOL. 62 1984

© Institution of Chemical Engineers

non-Newtonian liquids. Their correlation, however, remains yet to be tested for the flow of air and polymer solutions which show not only shear-thinning effects but also viscoelasticity.

Several investigations[7,8,13-17] of two-phase pressure drop for the horizontal flow of gases and non-Newtonian materials have been carried out and these have been adequately reviewed in recent publications[8,18,19]. It is now well established that the injection of air into shear-thinning materials in the laminar flow regime may result in a reduction in the two-phase pressure drop. This observation has been reported for air/polymer solutions[7,11] and for the flow of air and particulate suspensions in small as well as large diameter pipes[8,13,15,16]. In fact, at constant liquid flow rate, the two-phase pressure drop generally passes through a minimun value as the gas flow rate is increased and eventually exceeds the value for the flow of liquid alone. Recently Farooqi and Richardson[8] have proposed a mechanism whereby drag reduction occurs, and have identified the conditions necessary to achieve the maximum drag reduction for a liquid of given rheological properties and specified operating conditions. Indeed, their approach has reconciled most of the data available in the literature, especially for particulate suspensions and pastes. However, the applicability of their approach to polymer solutions (both inelastic and viscoelastic) has not yet been established.

In this communication, the results of an experimental investigation dealing with the horizontal two-phase flow of air and aqueous polymer solutions (inelastic and viscoelastic) are presented. The applicability of the correlations referred to above which are based on data for shear-thinning particulate suspensions is examined, and Zuber and Findlay's approach[9] is also used.

EXPERIMENTAL APPARATUS AND MATERIALS

A schematic diagram of the experimental apparatus is shown in Figure 1. It consists of 41.7 mm internal diameter unplasticised PVC pipe in the form of two parallel arms joined by a U-bend, giving an approximately 18 m long horizontal pipeline. The test liquids were prepared in a small mixing tank and transferred to a 0.9 m^3 capacity holding tank. An open impeller Vacseal grit centrifugal pump was used to circulate the liquids through the flow loop. Liquid flow rate was controlled by manipulating diaphragm valves A and B as indicated in Figure 1 and was measured using an electromagnetic flowmeter. The heat imparted to the liquid by the pump during circulation was removed by circulating water through a 3/8″ nominal size copper coil immersed in the liquid in the holding tank, and thus temperature was maintained at a constant value during the course of each experiment.

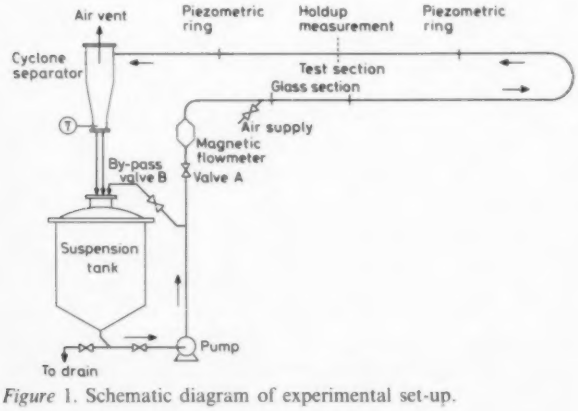


Figure 1. Schematic diagram of experimental set-up.

Pressure drop measurements are known to be difficult due to the inherent variable nature of two-phase flow. In this work pressure drop was recorded over a 4.57 m long straight test section, using simple U-tube manometers containing either carbon tetrachloride, diiodomethane or mercury beneath water. At times, especially at high air input rates, it was necessary to constrict the manometer lines to reduce the fluctuations; manometer leads were frequently flushed with water to remove polymer solution or air that had entered.

Average liquid holdup at the midpoint in the test section was measured using a gamma-ray absorption technique, described in detail elsewhere[4,6]. The test section was continuously scanned for six separate periods of 20 s to obtain an average value of the liquid holdup.

Air was taken from the laboratory mains at a pressure of 0.6 MPa above atmospheric and reduced to 0.28 MPa before introducing into the pipeline through a simple 45° T-piece. The injection point was situated at a sufficient distance upstream from the first piezometric point for calming to occur before the mixture entered the test section. The air flow rate was measured by one of three rotameters connected to a common manifold. More detailed descriptions of the experimental set up are available elsewhere[6,8].

Three different types of polymer, namely, carboxymethyl cellulose (7H grade, a product of Hercules Chemicals), hydroxymethyl cellulose (Natrosol 250L, a product of Hercules Chemicals), and polyacrylamide (Separan AP-30, marketed by Gold Crest Chemicals, UK) were used. Thus a wide variety of chemically different polymers was available. Test liquids were prepared by dissolving the required amount of polymer in tap water, and stirring until a homogeneous solution was obtained. Biological degradation was prevented by adding trace amounts of Formalin, as recommended by the suppliers of the polymers.

EXPERIMENTAL PROCEDURE

The relevant flow properties, namely shear stress and primary normal stress difference, were measured for all the polymer solutions using an R-17 Weissenberg Rheogoniometer. The instrument was used in the steady rotational mode, using a 50 mm diameter cone and plate geometry. Measurements of the torque on the upper plate, and the total normal thrust on the lower cone enabled calculations of shear stress and primary normal stress difference as a function of shear rate. The procedure for data analysis is well documented by Walters[20]. The effect of solvent evaporation on normal stress difference measurements was minimised by the application of a film of inert silicone oil, of comparable viscosity to that of test fluid, around the circumference of the gap between the cone and plate[21]. Normal force mea-

surements at higher shear rates were corrected for inertial effects[20]. All the rheogoniometric measurements were carried out at a constant temperature (to within ± 0.25 K), and this was the same as in the pipeline experiments (within ± 0.5 K). The specific gravity of each test fluid was measured with a relative density bottle and none was found to be significantly different from unity.

On the flow rig, initial experiments were carried out with each of the test fluids on its own and pressure drop was measured as a function of flow rate: in effect the test section was used as a pipe viscometer. This set of experiments provided an independent check on the accuracy of rheogoniometric measurements (shear stress–shear rate relationship only, however). After evaluating the laminar flow properties of polymer solutions, experiments were performed on co-current flow with air. At the end of each run, pressure drop was again measured for liquid alone as a function of flow rate, and within the limits of experimental accuracy, this was unaltered. Hence no significant degradation could have occurred in the case of polymer solutions.

Experiments were conducted at constant superficial liquid velocities, in the range of 0.25 to 2 ms^{-1}, and the superficial air velocity was increased in stages from 0 to 7 ms^{-1}. Two-phase pressure drop and average liquid holdup were measured for each combination of gas and liquid velocity. Under these conditions the flow pattern appeared to correspond to bubble, plug or slug flow, predominantly the last-mentioned.

To assess the accuracy and reliability of the measuring techniques, experiments were carried out on the co-current flow of air and water, and the results so obtained compared with the well accepted correlations in the literature.

RESULTS AND DISCUSSION

Rheological Properties of Test Liquids

All the test fluids exhibited shear thinning behaviour under steady shear. Rheograms for three of the liquids, shown in Figure 2, are typical of all the test fluids. In the lower half of this figure, typical data for 0.75% and 1% Separan AP-30, and 1.25% carboxymethyl cellulose are plotted on logartihmic coordinates as wall shear stress $\frac{1}{4}D(-\Delta P_L/L)$ versus nominal wall shear rate $(8V_L/D)$. Evidently over this limited range of shear rates, a power law equation of the type

$$\frac{D}{4}\left(-\frac{\Delta P_L}{L}\right) = K'\left(\frac{8V_L}{D}\right)^{n'}$$

can be fitted for each of these fluids. These parameters n' and K' are related to the true power law parameters as

$$n = n' \quad \text{and} \quad K = K'\left(\frac{4n'}{1+3n'}\right)^{n'} \tag{1}$$

The values of n' and K' obtained from the pipeline viscometry are summarised in Table 1 and the corresponding values of n and K (using equation (1)) are also included.

For all the liquids, the shear stress–shear rate relations were also obtained from the Weissenberg rheogoniometer and the typical results for 0.75 and 1% Separan AP-30 and 1.25% carboxymethyl cellulose are plotted as points in the upper half of Figure 2 as shear stress against true shear rate. The solid lines correspond to the values of n and K obtained from the pipeline viscometer. An excellent agreement between the two independent sets of measurement is evident. Similar results were obtained for all the liquids, except in the case of 1.5% Separan AP-30 solution in which case the two slopes were the same but the value of K obtained from the pipeline viscometer was about 12% lower than that obtained from the rheogoniometric measurements. In view of the fact that even a small temperature variation can lead to a discrepancy of this magnitude, the agreement between the two independent measurements is considered to be satisfactory and acceptable. Results obtained using the Weissenberg rheogoniometer are also presented in Table 1.

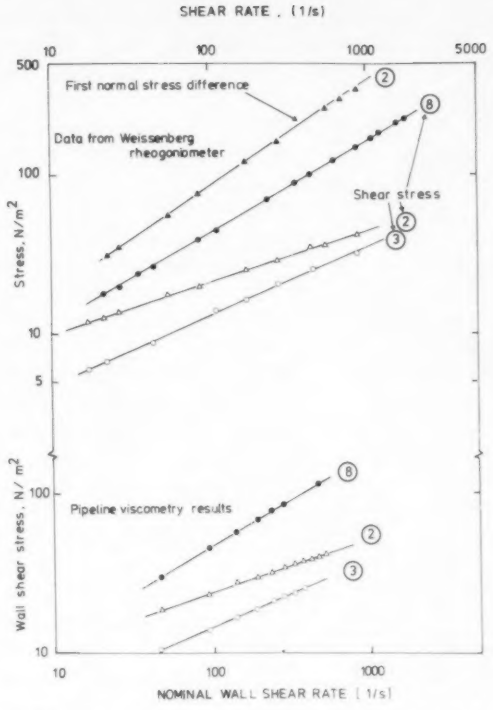


Figure 2. Rheograms for three polymer solutions. Numbers refer to liquids (See Table 1).

In addition to shear-thinning characteristics, aqueous solutions of polyacrylamide (Separan AP-30) exhibited finite normal stress differences in steady shearing conditions. Typical data for one of the test fluids are shown in Figure 2. Admittedly the most dilute solution (0.10% Separan AP-30) exhibited very small normal stress differences which were not measurable on the existing rheogoniometer, but Park[22] has reported such measurements for an identical solution. None of the other test fluids (i.e. solutions of carboxymethyl cellulose and Natrosol) exhibited detectable normal stress differences. In view of this fact therefore the latter test fluids are considered to be purely shear-thinning (visco-inelastic) whereas the Separan solutions are treated as viscoelastic liquids.

VOL. 62 1984

Table 1. Rheological and physical properties of test fluids.

Type of polymer	conc. % w/w	Test fluid identification number	Temp. (K)	From pipeline viscometry			From Weissenberg Rheogoniometer				
				$n = n'$	K' (N m^{-2} s^{n})	K (N m^{-2} s^{n})	n	K (N m^{-2} s^{n})	m (N m^{-2} s^{p})	p	θ (s)
Separan AP 30	1.50	1	298	0.28	10.00	8.70	0.28	9.70	23.05	0.46	2.20
	1.00	2	301	0.33	5.15	4.50	0.33	4.45	4.50	0.66	0.081
	0.75	3	300	0.42	2.10	1.85	0.42	1.90	0.37	0.96	0.011
	0.30	4	298	0.58	0.33	0.30	0.58	0.30	0.07	1.15	0.020
	0.10	5	298	0.70	0.10	0.093	0.70	0.098	0.004	1.65	0.016
Natrosol 250L	2.00	6	298	0.79	0.15	0.14	0.79	0.145	—	—	—
	1.50	7	298	0.89	0.039	0.038	0.89	0.040	—	—	—
CMC	1.25	8	298	0.58	3.20	2.90	0.58	3.00	—	—	—
	1.00	9	298	0.72	0.56	0.52	0.72	0.51	—	—	—
	0.75	10	299	0.92	0.064	0.063	0.92	0.064	—	—	—

Usually the viscoelasticity of the fluid is characterised in terms of a 'fluid characteristic time', and the viscoelastic effects in a flow situation are accounted for by defining a Deborah number which is merely a ratio of the fluid characteristic time to the time scale of the flow process. There are several ways of defining a fluid characteristic time; perhaps one of the simplest definitions is based upon a combination of the power law constants for shear stress (n', K') and for primary normal stress difference (m, p). That is, the normal stress difference–shear rate data are approximately represented as

$$N_1 = m(\dot{\gamma})^p$$

over the limited shear rate range. Values of m and p for the Separan solutions are included in Table 1. Note that the values of m and p for the most dilute solution are based on the data presented by Park[22]. A characteristic time for these liquids may be defined as

$$\theta = \left(\frac{m}{2K'}\right)^{1/(p-n)} \tag{2}$$

The factor of 2 in equation (2) is quite arbitrary but is retained here to be consistent with the form of presentation used by others[23,24]. The time scale of the process is defined as D/V_M where D is the diameter of the pipe and V_M is the mixture velocity of the system. Thus a Deborah number, defined as

$$De = \frac{\theta V_M}{D} \tag{3}$$

will be used in analysing the two phase flow of air and viscoelastic liquids. The values of θ calculated using equation (2) are given in Table 1.

The adequacy of the power law model to give an approximation to the shear stress–shear rate relationship is further demonstrated by plotting the Fanning friction factor as a function of Metzner–Reed Reynolds defined as

$$Re_{MR} = \frac{\rho_L V_L^{2-n} D^n}{8^{n-1} K'} \tag{4}$$

Under laminar flow conditions, the Fanning friction factor is related to Re_{MR} by the same equation as for the Newtonian liquids i.e.

$$f = \frac{16}{Re_{MR}} \tag{5}$$

The present results are plotted in this form in Figure 3. The good agreement between these results and equation (5) for both viscoelastic and visco-inelastic liquids is obvious. Therefore it can be concluded that the power law model indeed provides an adequate representation over the limited shear-rate range of interest.

Holdup Results

Time averaged values of liquid holdup were first analysed by the equation proposed by Zuber and Findlay[9], in which average linear velocity of air ($\bar{V}_g = V_g/\alpha_g$) is plotted against no slip (or mixture) velocity ($V_M = V_L + V_g$) viz:

$$\bar{V}_g = \frac{V_g}{\alpha_g} = C_0 V_M + V_{dv} \tag{6}$$

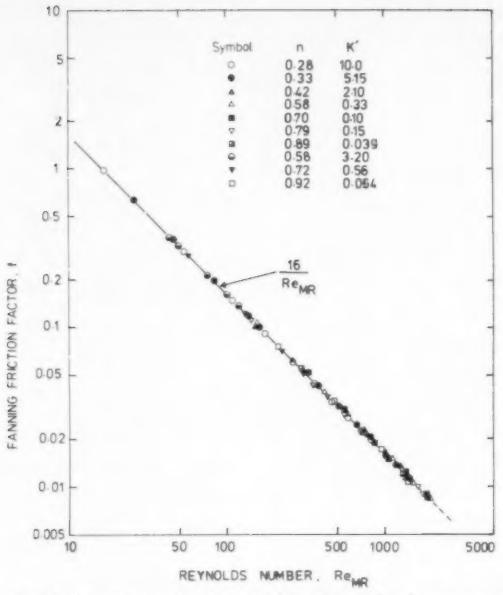


Figure 3. Friction factor data for laminar flow of polymer solutions.

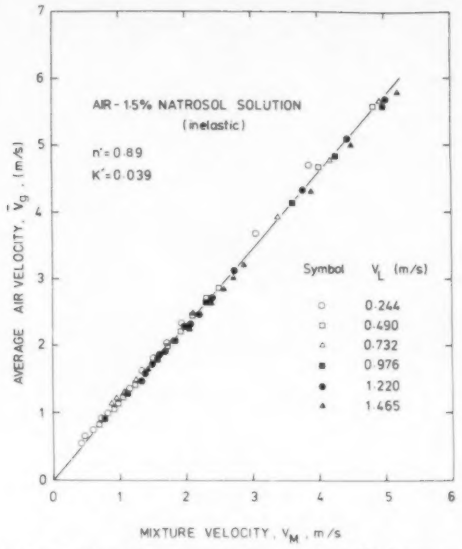


Figure 5. Correlation of holdup for flow of air–1.5% Natrosol solution (inelastic).

where C_0 is a distribution constant and V_{dv} is referred to as the drift velocity. In the case of vertical two phase slug flow, V_{dv} corresponds to the velocity of ascending slugs in a stationary column of liquid. Weber[25] has recently advanced similar arguments for horizontal two-phase flow, but the available experimental results[6–8] do not seem to confirm his hypothesis. For the flow of air–water mixtures, the results for the slug flow regime ($V_g > 1$ ms^{-1}) are plotted in Figure 4. Clearly, equation (6) is seen to be followed with C_0 having a value of 1.16 and V_{dv} zero, values which are consistent with those reported in the literature by other investigators[6,8]. Figures 5 and 6 which show similar results for the flow of mixtures of air and two polymer solutions are typical of the results obtained with all the test liquids. An examination of these two Figures (5 and 6) reveals that there is no discernible trend with respect to superficial liquid velocity. In Table 2 are recorded the values of C_0 and V_{dv} for the various systems and it will be noted that while the drift velocity varies over a wide range (0.02–0.33 ms^{-1}), the distribution constant C_0 varies from 1.10 to 1.36; it will be seen that similar values are reported in the literature[4,8,12]. It is interesting to note that even though in some cases the values of C_0 are close to that for air–water mixtures, the drift velocity always has a non-zero value. Thus, although the Zuber–Findlay approach is applicable to viscoelastic and visco-inelastic polymer solutions, the method does not provide a predictive means for calculating values of the average liquid holdup because it is not possible, at this stage, to express the

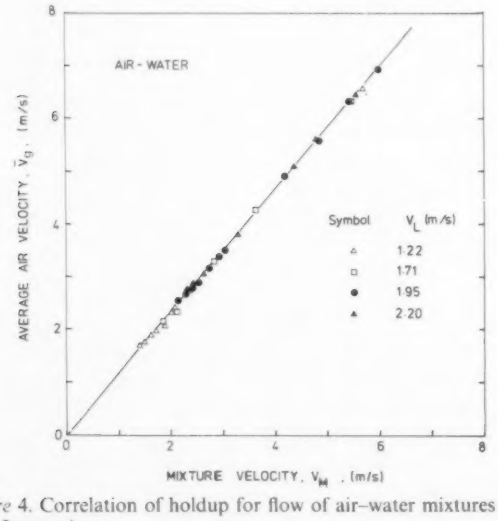


Figure 4. Correlation of holdup for flow of air–water mixtures in the slug flow regime.

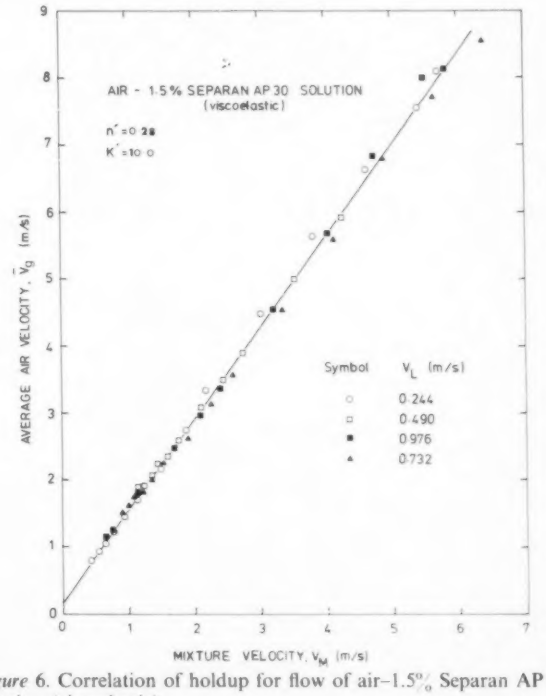


Figure 6. Correlation of holdup for flow of air–1.5% Separan AP 30 solution (viscoelastic).

VOL. 62 1984

Table 2. Values of Zuber–Findlay parameters

Investigator	System	C_o	V_{dv} (ms^{-1})
Present work	air–water	1.16	0.00
	air–1.5% Separan AP 30	1.36	0.20
	air–1.0% Separan AP 30	1.36	0.18
	air–0.75% Separan AP 30	1.26	0.30
	air–0.3% Separan AP 30	1.19	0.18
	air–0.10% Separan AP 30	1.10	0.20
	air–1.25% CMC	1.24	0.17
	air–1.00% CMC	1.16	0.12
	air–0.75% CMC	1.23	0.33
	air–2.0% Natrosol	1.14	0.15
	air–1.5% Natrosol	1.14	0.02
Rosehart et al. {30}†	air–CMC/Carbopol/Polyhall	1.34–1.57	0.25–0.56
Heywood {4}†	air–aqueous kaolin suspensions	1–1.43	−0.027–0.90
Farooqi et al. {13}†	air–aqueous anthracite suspensions	1.21–1.31	0–0.52

†ranges of values of C_0 and V_{dv} are shown.

parameters (C_0 and V_{dv}) in terms of the rheological behaviour of the liquid.

Farooqi and Richardson[8] recently extended the applicability of the Lockhart–Martinelli correlation to the two-phase horizontal flow of air and shear-thinning china clay suspensions, by including a correction factor when liquid is flowing in laminar conditions prior to the injection of air. In turbulent conditions, the original correlation of Lockhart–Martinelli was reported to be satisfactory. Their modification is as follows:

$$\chi' = \chi \left(\frac{V_L}{V_{LC}} \right)^{1-n'} \tag{7}$$

where χ is the original Lockhart–Martinelli parameter, defined as the ratio of the pressure drops for the liquid and gas when flowing alone at the same flowrates. V_L is the superficial liquid velocity and V_{LC} is its value at the laminar–turbulent transition point (taken for the purposes of calculation as when the Metzner–Reed Reynolds number $Re_{MR} = 2000$).

Although equation (7) has no sound theoretical justification, it does reduce to the appropriate form for Newtonian behaviour ($n' = 1.0$) and the correction becomes increasingly important as the deviation from Newtonian behaviour becomes greater and as the liquid velocity is reduced below its critical value (V_{LC}). Experimental results for liquid holdup α_L for the two-phase flow of air and china clay suspensions in horizontal[8] as well as in vertical pipelines[19] have been correlated by the following equation

$$\begin{aligned} \alpha_L &= 0.186 + 0.0191\,X & 1 < X < 5 \\ \alpha_L &= 0.1432\,X^{0.42} & 5 < X < 50 \\ \alpha_L &= (0.97 + 19/X)^{-1} & 50 < X < 500 \end{aligned} \tag{8}$$

For turbulent flow $X = \chi$ and for laminar flow $X = \chi'$.

Most of the present results relate to conditions where the liquid flow is laminar prior to the injection of air, though a few refer to the turbulent regime.

Two different types of liquids, namely visco-inelastic (carboxymethyl cellulose and Natrosol solutions) and viscoelastic (Separan AP-30 solutions) were used and the present results are segregated into these two categories in order to assess the role of liquid viscoelasticity.

Laminar Visco-inelastic Flow

Average values of liquid holdup for the two-phase flow of air and visco-inelastic polymer solutions are compared with equation (8) in Figure 7. The experimental results embrace the following ranges of operating conditions: $0.15 < V_g < 7\,\text{ms}^{-1}$; $0.25 < V_L < 2\,\text{ms}^{-1}$ and

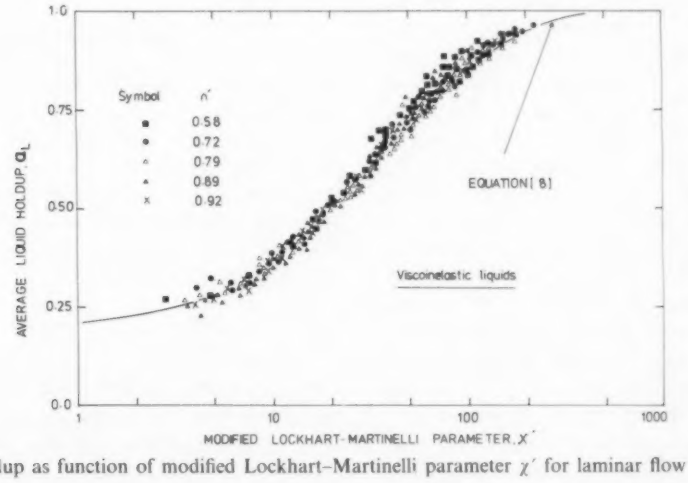


Figure 7. Average liquid holdup as function of modified Lockhart–Martinelli parameter χ' for laminar flow of visco-inelastic liquids.

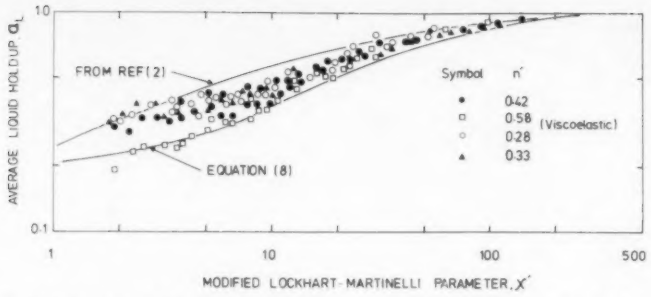


Figure 8. Average liquid holdup as function of modified Lockhart–Martinelli parameter χ' for laminar flow of viscoelastic liquids.

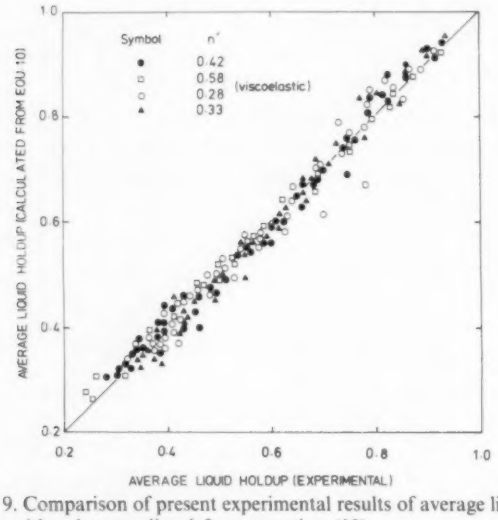


Figure 9. Comparison of present experimental results of average liquid holdup with values predicted from equation (10).

rheological characteristics: $0.58 < n' < 0.92$ and $0.039 < K' < 2.9\ \mathrm{N\,m^{-2}\,s^{n'}}$. The solid line which corresponds to equation (8) (with $X = \chi'$) and the experimental points are in excellent agreement and there appears to be no trend with superficial liquid velocity V_L. Thus it can be concluded that the same correlation can be used for cocurrent flow of air with Newtonian liquids, with shear-thinning suspensions and with inelastic shear thinning polymer solutions.

Laminar Viscoelastic Flow

The experimental results for viscoelastic liquids are shown in a similar way in Figure 8 which extends over two decades of value of χ' and the range of rheological properties is given in Table 1. Included in the same figure are lines corresponding to the original Lockhart–Martinelli correlation[2] and its modified form (equation 8). In this case, the experimental results all lie in between these two curves. Since equation (8) has been shown to be applicable to all the purely shear-thinning liquids studied, the deviations in Figure 8 must be due to the viscoelasticity of the test liquids. The results deviate increasingly from the correlation as the value of χ' is decreased i.e. for increasing superficial air velocity at a constant superficial liquid velocity.

It is not easy to explain the effect of viscoelasticity. However, it was observed that the liquid tended to move backwards following the passage of a gas slug, thus increasing its holdup. On the assumption that the effect of elasticity can be expressed as a function of χ' and Deborah number, De (equation 3), the following empirical form of the relation between the liquid holdup for inelastic and viscoelastic liquids, α_{LV} and α_{Li} respectively, was tried:

$$\frac{\alpha_{LV}}{\alpha_L} = 1 + a\chi'^{b} De^{c} \tag{9}$$

The constants a, b, c were estimated using a nonlinear regression approach to give

$$\frac{\alpha_{LV}}{\alpha_L} = 1 + 0.56\,\chi'^{-0.5}\,De^{0.05} \quad 0.3 < De < 340 \tag{10}$$

In Figure 9, the experimental values of α_{LV} (about 200 in number) are shown plotted against the values calculated from equations (8) and (10) and the correlation is seen to be satisfactory, with an average deviation of about 5.4%.

Turbulent Flow of Viscoelastic and Visco-inelastic Liquids

The results for average liquid holdup for turbulent flow ($V_L > V_{LC}$) are plotted in Figure 10 against the Lockhart and Martinelli parameter χ for both viscoelastic and visco-inelastic polymer solutions and for water. The solid line is the plot of equation (8) previously obtained for Newtonian liquids and for suspensions. It is thus seen that the single correlation is applicable to the turbulent regime for all the liquids studied (Newtonian, shear-thinning suspensions and viscoelastic and visco-inelastic polymer solutions).

Two-Phase Pressure Drop

Flow or Air–Water Mixtures

Preliminary experiments were carried out using air–water mixtures; all the data relate to turbulent flow conditions. Two phase pressure drop was expressed in the form of a dimensionless drag ratio ϕ_L^2 which is defined as the ratio of the two-phase pressure drop to the pressure drop for liquid flowing on its own at the same volumetric rate. Thus

$$\phi_L^2 = \frac{-\Delta P_{TP}/L}{-\Delta P_L/L} \tag{11}$$

The present results are compared with the widely used Lockhart–Martinelli correlation[2] in Figure 11, where the drag ratio is plotted against the Lockhart–Martinelli parameter χ. The agreement is seen to be good consid-

VOL. 62 1984

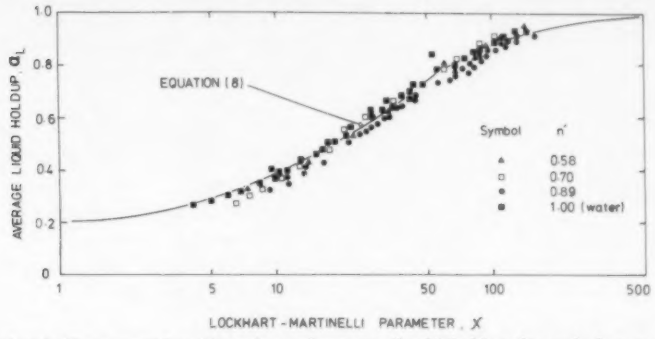


Figure 10. Experimental and predicted (from equation (8)) values of average liquid holdup for turbulent conditions.

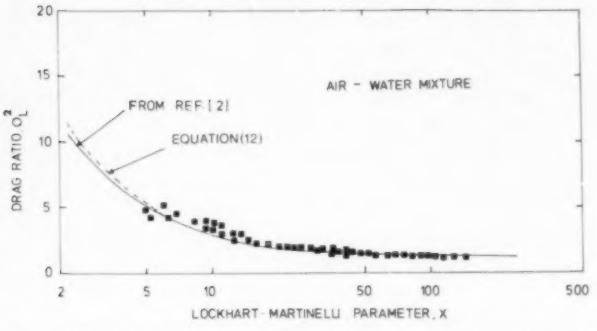


Figure 11. Comparison of drag ratios for air–water flow with Lockhart–Martinelli correlation.

ering that the correlation has an error band of $\pm 30\%$. The relationship due to Chisholm[26] is also shown in Figure 11:

$$\phi_L^2 = 1 + \frac{C}{X} + \frac{1}{X^2} \tag{12}$$

where C depends upon flow conditions and the physical properties of the fluids[27]; it has a value of 21 for the air/water system in the turbulent regime. It can be seen that there is very little difference between the correlation of Lockhart and Martinelli and equation (12).

Flow of Air–Polymer Solutions Mixtures

Most of the experimental results for the flow of air and polymer solutions correspond to the liquid in laminar flow (prior to the air injection) i.e. $Re_{MR} < 2000$. However, it should be emphasised that the liquid flow will become turbulent above a certain air flow rate; but this flow condition is still labelled as 'laminar flow' for the liquid and thus this classification scheme is somewhat superficial. The experimental results have been segregated into two classes: laminar and turbulent conditions for the liquid.

Two-phase pressure drop data for these systems are also analysed in the form of drag ratio, ϕ_L^2 as defined in equation (11).

Laminar flow

Drag ratios for one visco-inelastic and for one viscoelastic liquid are plotted against superficial air velocity in Figures 12 and 13 respectively. Similar results were obtained for all other liquids. Evidently, as a result of the introduction of air, the drag ratio falls below unity, passes through a minimum and then rises again as the air rate is increased. This behaviour is consistent with that observed previously for shear-thinning suspensions[8,13,16].

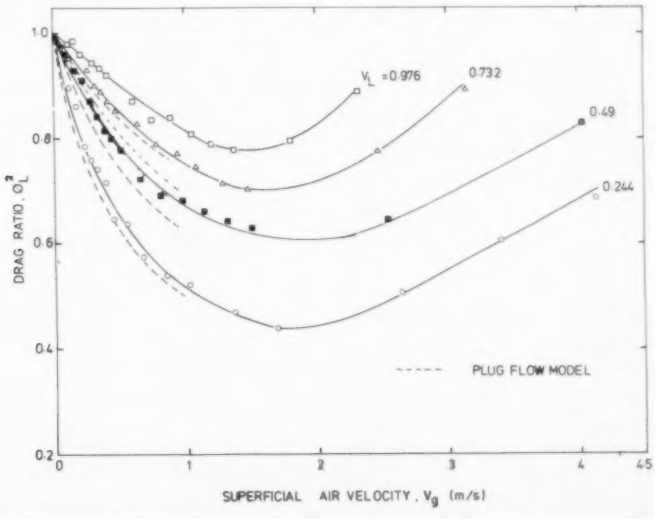


Figure 12. Drag ratio as a function of superficial air velocity for the flow of air and 1.25% carboxymethyl cellulose solution (visco-inelastic) in laminar flow. Predictions from the idealised plug flow model are included as dotted lines for conditions $V_g < 1\ ms^{-1}$ and $Re_{MR} \leq 500$.

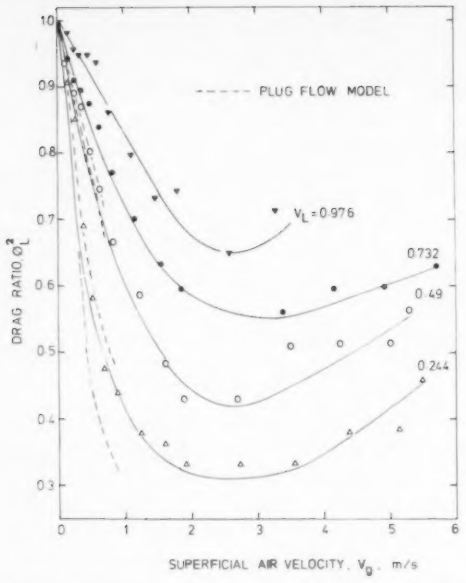


Figure 13. Drag ratio as a function of superficial air velocity for the flow of air and 1.5% Separan AP 30 solution (viscoelastic) in laminar flow. Predictions from the idealised plug flow model are included as the dotted lines for conditions $V_g < 1\ \text{ms}^{-1}$ and $Re'_{MR} \leqslant 500$.

A plug flow model, originally proposed by Carleton et al.[29] and subsequently developed by Richardson and co-workers[8,16,28] postulates:

(1) that the air and liquid form discrete flat-ended plugs each filling the entire cross-section of the pipe and there is no slip between the liquid and gas phase,
(2) that the pressure drop across a gas plug is negligible and
(3) that the pressure gradient along a liquid plug is determined by the mixture velocity, $V_M (= V_L + V_g)$.

Under these simplifications it can be shown that the drag ratio is given as

$$\phi_L^2 = \frac{1}{\lambda_L} \frac{f_{TP}}{f_L} \tag{13}$$

where f_{TP} and f_L are Fanning friction factors for two phase flow and for liquid flow alone, respectively, and λ_L is input liquid fraction. When the liquid plug is in laminar flow, both before and after the air injection, equation (13) reduces to

$$\phi_L^2 = (\lambda_L)^{1-n'} \tag{14}$$

Although the idealised plug model is likely to underestimate the magnitude of two-phase pressure drop, Heywood and Richardson[28], Farooqi et al.[8] and others[16] have concluded that it gives reasonable estimates of drag ratios provided $V_g < 1\ \text{ms}^{-1}$ and Re_{MR} (based on mixture velocity) is less than 500. The values of drag ratio, calculated from the plug flow model, are shown as dotted lines in Figures 12 and 13. As the liquid velocity is increased, deviations from the model become progressively greater. The model does not predict a minimum, but as soon as the flow of liquid becomes turbulent, equation (14) no longer applies and the drag ratio increases with air rate. Furthermore, secondary flow patterns will develop at high air flow rates which will invalidate the assumptions involved in the model. With suspensions of high apparent viscosity, the minimum drag ratio occurs when the value of the Metzner–Reed Reynolds number (based on mixture velocity) is in the region of 1000–2000, i.e. it is close to the value for the laminar–turbulent flow transition. With the dilute polymer solutions, the presence of the air bubbles in these liquids of relatively low apparent viscosity induces turbulent eddies (secondary flow) which become stabilised even at Reynolds number less than the usual transitional value—streamline to turbulent flow. Hence the minimum drag ratio occurs at a somewhat lower value of Re_{MR}. For example, for a 1.5% Natrosol solution which has an apparent viscosity of $22\ \text{mNsm}^{-2}$ at a shear rate of $100\ \text{s}^{-1}$, the minimum drag ratio occurs at a value of Re_{MR} as low as 250.

Farooqi and Richardson[8] have given an empirical relationship between the minimum drag ratio and a dimensionless factor λ_c denoted here by J. Their equation is:

$$\begin{aligned} (\phi_L^2)_{min} &= J^{0.205} && 0.6 \leqslant J \leqslant 1.0 \\ (\phi_L^2)_{min} &= 1.0 - 0.0315\, J^{-2.25} && 0.35 \leqslant J \leqslant 0.6 \\ (\phi_L^2)_{min} &= 1.9\, J && 0.05 \leqslant J \leqslant 0.35 \end{aligned} \tag{15}$$

where $J = (V_L/V_{LC})^{1-n'}$. This dimensionless parameter J, deduced purely from considerations of the shear-thinning behaviour, implicitly includes the effects of rheological properties (n', K') and pipe diameter (D). In Figure 14, experimental points for the minimum drag ratio as a function of $(V_L/V_{LC})^{1-n'}$ are shown in conjunction with the plot of equation (15) which is reproduced as a solid line. It is apparent that equation (15), based on results for inelastic shear-thinning suspensions, is

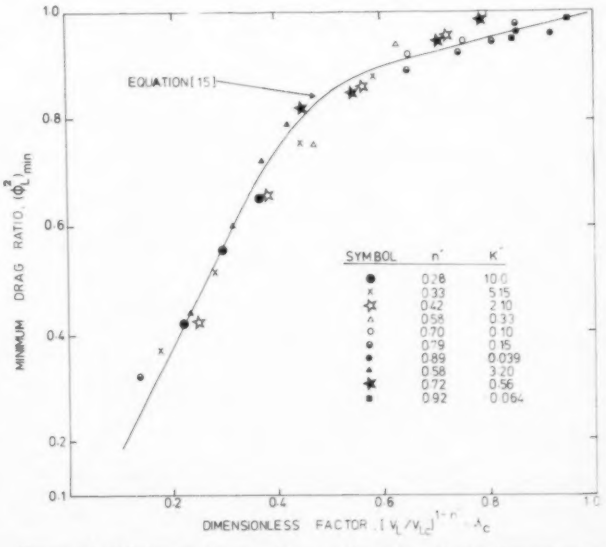


Figure 14. Minimum drag ratio as a function of the dimensionless ratio, J; solid line corresponds to Equation (15).

VOL. 62 1984

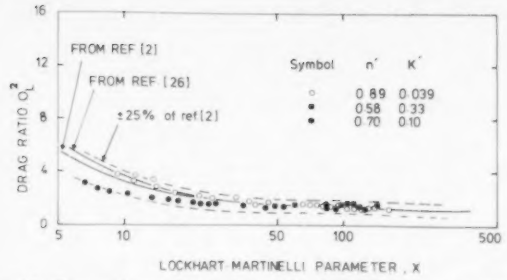


Figure 15. Comparison of experimental values of drag ratio obtained under turbulent conditions with the correlation of Lockhart–Martinelli[2] and its modification[26].

applicable to both elastic and inelastic polymer solutions. It is somewhat surprising that elastic effects do not influence the value of minimum drag ratio, particularly in view of their significant effect on holdup.

Turbulent flow

When air was introduced into any of the liquids flowing initially under turbulent conditions ($Re_{MR} > 2000$), the pressure drop always increased, and thus the drag ratios were greater than unity. In Figure 15, drag ratio is shown as a function of the Lockhart–Martinelli parameter χ and it is seen that the experimental points tend to be somewhat lower than those from the Lockhart–Martinelli correlation, though deviations do not exceed 25% which is the limit of reproducibility of data in this field of work. It should be reiterated that the analysis of the turbulent flow data is based on flow properties of the fluids obtained under laminar conditions.

Similar results have previoulsy been reported by Rosehart et al.[30] for polyacrylamide solutions, by Otten and Fayed[31] for dilute solutions of Carbopol 941 and by others[8] for pseudohomogeneous suspensions.

CONCLUSIONS

Average liquid holdup and two-phase pressure drop have been measured for the two-phase flow of air and aqueous solutions of three different polymers in a smooth horizontal pipe. Rheological properties, namely shear-thinning characteristics and fluid elasticity (primary normal stress difference), were measured using a Weissenberg Rheogoniometer.

It has been established that the equation developed by Farooqi and Richardson[8] for calculating liquid holdup during laminar flow of china clay suspensions which show shear-thinning behaviour is also applicable to polymer solutions which are inelastic. However, when the liquid exhibits viscoelastic characteristics, it is necessary to introduce a correction factor which incorporates a Deborah number. For both elastic and inelastic liquids flowing in turbulent conditions, the holdup values are satisfactorily represented by the correlation available for Newtonian liquids.

The injection of air into polymer solutions in laminar flow can give rise to a substantial reduction in two-phase pressure drop. As noted by earlier workers, as the air flow rate is increased the two-phase pressure drop passes through a minimum value. These minimum values are in excellent agreement with values calculated from the equation given by Farooqi and Richardson[8] for shear-thinning suspensions. On the other hand, if the polymer solution is initially in turbulent flow, the pressure drop is always increased by the injection of air regardless of the rheological behaviour of liquid and may be calculated using the correlation of Lockhart and Martinelli[2].

The present work has been confined to a small diameter pipe and it would be desirable in future work to ascertain whether the results are applicable to pipelines of large diameters. It has already been shown[16] that for suspensions similar results are obtained in pipes of diameters 42 and 208 mm.

SYMBOLS USED

C	constant in equation (12) (–)
C_0	distribution coefficient in equation (6) (–)
D	diameter of pipe (m)
De	Deborah number (–)
f	Fanning friction factor (–)
J	parameter $(V_L/V_{LC})^{1-n'}$
K	flow consistency in true power law model ($Nm^{-2}\ s^n$)
K'	flow consistency in apparent power law model ($Nm^{-2}\ s^{n'}$)
L	pipe test section length (m)
m,p	power law constants for primary normal stress difference ($Nm^{-2}\ s^p$), (–)
$n\ (=n')$	flow behaviour index for a true power law fluid (–)
N_1	primary normal stress difference (Nm^{-2})
$-\Delta P$	pressure drop (Nm^{-2})
Re_{MR}	generalised Reynolds number of Metzner and Reed (–)
Re'_{MR}	generalised Reynolds number of Metzner and Reed based on mixture velocity (–)
V	superficial velocity (ms^{-1})
$\bar{V}$	average linear velocity (ms^{-1})
V_{ds}	drift velocity (ms^{-1})
X	parameter equal either to χ or to χ' (–)

Greek letters

α	average holdup (fraction of pipe volume occupied by particular fluid) (–)
$\dot{\gamma}$	shear rate (s^{-1})
θ	fluid characteristic time (s)
λ	input volume fraction of particular fluid (–)
ρ	density (kgm^{-3})
χ	the Lockhart–Martinelli parameter $= \left(-\frac{\Delta P_L}{L} \Big/ -\frac{\Delta P_g}{L}\right)^{1/2}$, (–)
χ'	the generalised parameter of Farooqi and Richardson $= \chi\left(\frac{V_L}{V_{LC}}\right)^{1-n'}$, (–)

Subscripts

c	critical
g	gas or air
L	liquid
M	mixture
MR	Metzner and Reed
TP	two phase
v	viscoelastic

REFERENCES

1. Govier, G. W. and Aziz, K., 1972, *The Flow of Complex Mixtures in Pipes*, (Van Nostrand Reinhold Co., NY).
2. Lockhart, R. W. and Martinelli, R. C., 1949, *Chem Eng Prog*, 45: 39.
3. Chisholm, D. and Laird, A. D. K., 1958, *J Heat Transfer, Trans ASME, Ser C*, 80: 276.
4. Heywood, N. I., 1976, *PhD Thesis* (University of Wales).

5. Baker, O., 1953, *Oil and Gas J*, 53: 185.
6. Heywood, N. I. and Richardson, J. F., 1979, *Chem Eng Sci*, 34: 17.
7. Oliver, D. R. and Young-Hoon, A., 1968, *Trans IChemE*, 46, T106.
8. Farooqi, S. I. and Richardson, J. F., 1982, *Trans IChemE*, 60: 292 and 323.
9. Zuber, N. and Findlay, J. A., 1965, *J Heat Transfer, Trans ASME, Ser C*, 87: 453.
10. Dukler, A. E., Wicks, M. and Cleveland, R. G., 1964, *AIChEJ*, 10: 38.
11. Srivastava, R. P. S. and Narasimhamurthy, G. S. R., 1973, *Chem Eng Sci*, 28: 553.
12. Rosehart, R. G., Rhodes, E. and Scott, D. S., 1975, *Chem. Eng J*, 10: 57.
13. Farooqi, S. I., Heywood, N. I. and Richardson, J. F., 1980, *Trans IChemE*, 58: 16.
14. Mahalingam, R. and Valle, M. A., 1972, *Ind Eng Chem Fundam*, 11: 470.
15. Ward, H. C. and Dallavale, J. M., 1954, *Chem Eng Prog Symp Ser*, 10: 1.
16. Chhabra, R. P., Farooqi, S. I., Richardson, J. F. and Wardle, A. P., 1983, *Chem Eng Res Des*, 61: 56.
17. Eisenberg, F. G. and Weinberger, C. B., 1979, *AIChEJ*, 25: 240.
18. Mahalingam, R., 1980, *Adv Trans Proc* 1: 58.
19. Chhabra, R. P., Farooqi, S. I., Khatib, Z. and Richardson, J. F., 1982, *J Pipelines*, 2: 165.
20. Walters, K., 1975, *Rheometry*, (Chapman and Hall, London).
21. Boger, D. V. and Ramamurthy, A. V., 1969, *Trans Soc Rheo*, 13: 405.
22. Park, H. C., 1972, *PhD Thesis*, (Michigan State University, USA).
23. Grimm, R. J., 1978, *AIChEJ* 24: 427.
24. Chhabra, R. P., Tiu, C. and Uhlherr, P. H. T., 1981, *Can J Chem Eng* 59: 771.
25. Weber, M. E., 1981, *Can J Chem Eng*, 59: 398.
26. Chisholm, D., 1967, *Int J Heat Mass Transfer*, 10: 1767.
27. Chisholm, D. and Sutherland, L. A., 1969–70, *Proc IMechE* 184 (Pt. 3C): 24.
28. Heywood, N. I. and Richardson, J. F., 1978, Paper C1, *Hydrotransports, Hanover* (B.H.R.A., Fluid Engineering, Cranfield).
29. Carleton, A. J., Cheng, D. C-H. and French, R. J., 1973, Paper F2, *Pneumo Transport* 2, (B.H.R.A. Fluid Engineering, Cranfield).
30. Rosehart, R. G., Scott, D. S. and Rhodes, E. 1972, *AIChEJ*, 18: 744.
31. Otten, L. and Fayed, A. S., 1976, *Can J Chem Eng*, 54: 111.

ACKNOWLEDGEMENTS

The financial support from the Science and Engineering Research Council (UK) in the form of a research grant is gratefully acknowledged. Our thanks are also due to the Hercules Chemical Co. and the Goldcrest Chemicals Co. (UK) who kindly supplied the polymers used in this work.

ADDRESS

Correspondence on this paper should be addressed to Professor J. F. Richardson, Department of Chemical Engineering, University College of Swansea, Singleton Park, Swansea SA2 8PP. Dr S. I. Farooqi is now with National Refineries Corporation, Karachi, Pakistan.

The manuscript was received 8 November 1982 and accepted for publication 7 February 1983.

VOL.
62
1984

BOOK REVIEWS

Chemical Process Dynamics
R. Mohilla and B. Ferencz
Elsevier Scientific Publishing Co, 1982
pp 300, US$69.75

This book is an enlarged English version of the Hungarian original. The authors claim to help process and control engineers understand each other by the use of a common language to describe control systems and process dynamics. To some extent they do this by the clarity of their presentation, and this is to be welcomed, but there is nothing particularly novel.

This, then, is a text which follows a traditional pattern. The emphasis is on controlling processes by a knowledge of their dynamic behaviour and that of practical control schemes. This is presented in terms of Laplace transformation of linearised equations, applied to small disturbances. There is, however, increasingly a need to understand process dynamics in isolation from control systems and in situations where the conventional mathematical analysis may not be suitable. Examples include the effect of sudden let-down of pressure, explosion, and so on. Such gross preturbations are not dealt with. Multivariable and stochastic processes are also explicitly omitted.

The authors begin with fundamentals, which include mathematical description of unit operations and basic concepts of process control. Conservation equations are derived in rigorous mathematical form, using vector notation which forms the basis for further development. The mathematical manipulations are interspersed with good verbal descriptions and this makes the development of arguments easy to follow.

The next two sections deal with, respectively, lumped and distributed parameter models. Some examples are of operations which are not often described in other texts. These include transport of solids and the dynamics of drying.

The body of the text finishes with some applications of multi-loop control systems.

A glance at the bibliography shows there is a good selection of international references, although inevitably some are Hungarian publications to which, through the difficulty of translation, only the most persistent will have access. Unfortunately, most of the specific references are at least 10 years old. This really characterises the book. There is very little reference to recent developments in the theory and practice of process control and dynamics apart from some additional reading matter quoted in the bibliography.

In summary, this book is a very readable presentation of traditional process dynamics. I would not recommend it for anyone seeking the latest developments in the area or as a practical quide to implementing process simulation. It is, however a good account for those who would like to be acquainted with process dynamics in more detail than that normally encountered in a chemical engineering degree course.

Peter Norman

Book Reviews continue on p 52

INFLUENCE OF PHASE RATIO ON ELECTROSTATIC COALESCENCE OF WATER-IN-OIL DISPERSIONS

By P. J. BAILES (MEMBER) S. K. L. LARKAI
Schools of Chemical Engineering, University of Bradford

The effect of dispersed phase hold-up on the separation of a liquid–liquid dispersion in pulsed d.c. fields has been studied. Experimental results have shown that there exists a high hold-up plateau region where best coalescence is obtained. An existing correlating model has been modified to account for the influence of hold-up in this region. The optimum pulsation frequency of the applied electric field is not affected by hold-up.

INTRODUCTION

Dispersions and emulsions of water drops in oil, or liquids which have essentially the same character as water and oil, can be separated into two bulk phases by the action of electrical forces. At present, the only large-scale application of this method occurs in the oil industry where high voltage a.c. fields and, less commonly, high voltage d.c. fields are used to promote the separation of water drops from crude oil. The effect of the electric field is to cause interdroplet coalescence, although the manner in which this comes about is not clearly understood. Efforts to apply this technology directly to other liquid phase separations have been hampered by the need to avoid bridging of the electrodes by the conducting aqueous phase. This limitation is sufficient to exclude systems such as those found in solvent extraction where the proportion of polar phase is usually higher than the 10% or thereabouts favoured in the oil industry. However, it has been shown[1] in recent work with dispersions typical of those generated in solvent extraction that electric fields can be extremely effective in accelerating phase separation in such systems. The essential elements of this breakthrough are that pulsed d.c. fields when used in conjunction with insulated electrodes will coalesce dispersed phase even though this represents 50% by volume of the dispersion. Field strength and pulse frequency have been found to be the key factors governing performance and the correct combination, for example, 80 V cm^{-1} and 8 Hz gives an excellent result with very low power consumption[2].

The application of this new approach to the coalescence of systems in which the dispersed phase hold-up is less than 50% is of considerable practical importance since such systems are commonly encountered in solvent extraction and in water-washing of vegetable and mineral oils. For example, in the Petroleum Industry where it is necessary to 'desalt' many crude oils by contacting them with water[3], the procedure is to mix as intimately as possible the minimum quantity of water into the oil consistent with the requirement for salt removal. In practice, it is usual to create a water-in-oil emulsion containing less than 5% water and rarely to exceed 10%. The use of more wash water than this entails additional production costs but more importantly it is difficult with the traditional electrical separators to avoid overstressing the electrical equipment because of the development of a direct and efficient conductive path between the electrodes. Collapse of the field, of course, removes the coalescing force. If it were not for this electrical limitation there is, in theory, at least one advantage in using more water, that is, the same interfacial area per unit volume for mass transfer can be achieved with less subdivision of the aqueous phase. In other words, on average the drops of water would be larger and therefore growth by coalescence to a size which allows them to settle out would be more easily achieved. High phase separation rates are particularly desirable on offshore locations where space and weight are at a premium.

The use of pulsed a.c. fields[4] also half-wave rectified a.c.[5-8] has been considered in connection with typical crude oil emulsions. The present technique of using insulated electrodes and d.c. field pulsed at other than mains frequency is substantially different from these methods. So far, the experiments on tailored frequency pulsed d.c. have been restricted to dispersions in which the phase ratio is unity. However, it is clear for the reasons already mentioned that there is a need to establish whether the technique is as successful with more dilute dispersions. The experimental investigation reported here is concerned with the effect of dispersed phase fractional volumetric hold-up on coalescence of dispersions in pulsed d.c. fields. The data have been used to improve an earlier model[1] for the calculation of a derived droplet collision frequency: this frequency is known to correlate with coalescence performance.

EXPERIMENTAL

The study employed a convenient procedure for examining the influence of various experimental parameters on coalescence performance with pulsed d.c. fields which has been described previously by the authors[9]. The method uses a turbine agitated mixer box to generate the desired water-in-oil dispersion on a continuous basis. The dispersion then flows through the electrical test section into a simple gravity settler. Coalescence caused by the electric field influences the depth of dispersion

© Institution of Chemical Engineers

band in the gravity settler and, at steady state, the depth registered in the gravity settler provides a measurement of electrostatic coalescence performance.

The laboratory equipment was the same as that used before, in particular the internal dimensions of the perspex electrical test section were maintained at 178 mm by 178 mm by 25.4 mm deep. The thickness of the perspex chosen to separate the high voltage electrode from the dispersion was 3 mm. This 'flat box' electrostatic coalescer geometry is very suitable for experimental purposes but it is important to appreciate that coated electrodes when used with pulsed d.c. fields are extremely effective in many other geometries.

The investigation was conducted on dispersions of dilute sulphuric acid in an organic phase made up of 20% LIX 64N^{R} in kerosene (Escaid 100^{R}). The phases were presaturated with one another and transferring solutes were absent; details of their physical properties are given elsewhere[9]. The combined total flow rate to the mixer was maintained at 1.0 litre min^{-1} at a temperature of 28 ± 0.5°C. This is very much less than the maximum throughput which the electrostatic coalescer can treat but adequate for present purposes. Organic and aqueous flows were varied within the prescribed total flow to give phase ratios (O:A) between 1:1 and 19:1. Mixing with a constant turbine impeller speed of 900 rpm was sufficiently uniform to ensure that these flow ratios gave dispersed phase hold-ups of between 50 and 5% respectively. The applied voltage was in the range of 0.2 to 10 kV and frequency was between 0.5 and 60 Hz for square pulse form.

RESULTS AND DISCUSSION

The effectiveness of the electric field in separating dispersions of differing hold-ups was estimated in terms of a coalescence parameter P. This was calculated as the percentage reduction of the dispersion band depth in the gravity settler from its value under zero-field conditions.

The dimensions of the gravity settling area in the measuring settler were maintained constant throughout at 64 mm long by 165 mm wide. This area could have been varied to give greater depths of dispersion in the settling zone, particularly for low hold-up dispersions, but such a change in scale would have caused an alteration in the wall effect. Table 1 shows the variation of dispersion band depth in the settling zone with hold-up. The results are for the zero field datum condition in the electrostatic coalescer, that is, ΔH_0. Depth of dispersion was read from a scale to within an accuracy of 1 mm but nevertheless it is clear from Table 1 that the percentage error in ΔH_0 measurements becomes appreciable for dispersions with a low volumetric fraction of dispersed phase. The percentage error in subsequent measurements of dispersion band depth upon application of an electric field varies according to the dispersion band depth. Below 10% hold-up these errors cannot be ignored and they illustrate a deficiency in the experimental technique which is currently the subject of further study.

It was observed during the experiments that, under zero field conditions, as hold-up was reduced entrainment of aqueous drops in the effluent organic phase

Table 1. Dispersion band depth under zero field conditions for various values of hold-up

x	ΔH_0 (cm)	| Error | (%)
0.5	25.5	0.39
0.33	20.0	0.50
0.25	12.5	0.80
0.20	9.0	1.11
0.167	3.0	3.33
0.125	2.275	4.40
0.10	2.05	4.88
0.083	0.90	11.11
0.05	0.50	20.00

increased. This is to be expected since the mixer was operated at a constant impeller speed and so the power input per unit volume of dispersed phase increased as dispersed phase hold-up decreased, causing a reduction in drop size[10]. However, with the field applied to the electrostatic coalescer, the level of entrainment of fine aqueous drops decreased as the applied voltage was increased. This was true for all values of hold-up. Above 6 kV no entrainment could be detected visually. It appears that, in the presence of an electric field, the fine drops causing entrainment coalesce with each other and with other drops to sizes big enough to enable them to gravitate from the continuous organic phase. Drops removed in this way were not accounted for in the measurement of the dispersion band depth in the absence of an electric field and, therefore, this entrainment affects the coalescence parameter, especially at lower values of hold-up of dispersed phase where original entrainment levels were much higher. This reduction in entrainment levels in the presence of electric fields is very important from a practical point of view, however, since minimising entrainment is one of the problems facing designers and users of liquid–liquid contacting equipment.

Figure 1 shows the effect of pulse frequency on the coalescence parameter of three dispersions of different aqueous phase hold-up at an applied voltage of 400 V. The curves all show an optimum frequency between 4.0 and 5.5 Hz. Outside this range the coalescence parameter drops sharply. It is believed that the aqueous drops polarise in the electric field creating interdroplet forces which cause them to accelerate towards/away from one another resulting in random collisions and coalescence. At the optimum frequency the field is on long enough to enable the intervening dielectric system to experience its full polarisation state at the peak electric field strength. This in turn allows the aqueous drops to attain their full induced polarisation charges by virtue of the polarised intervening dielectric system. The interdroplet forces are at a maximum under these electrical conditions resulting in the maximum number of collisions and hence coalescence is at its best possible value. It should be noted that the aqueous drops have a relaxation time of 10^{-11} s thus enabling them to quickly polarise in response to the prevailing electrical conditions to which they are exposed. At frequencies lower than the optimum frequency, even though the intervening dielectric system has enough time to polarise, the rate at which it attains the full polarisation state dictated by the peak electric

VOL. 62 1984

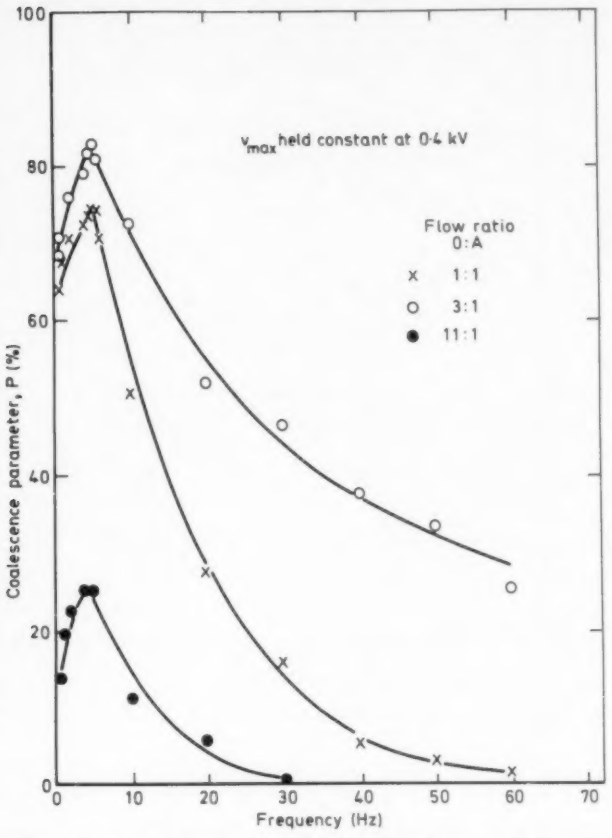


Figure 1. Effect of aqueous phase holdup on coalescence performance under constant applied voltage over the range of pulsation frequency.

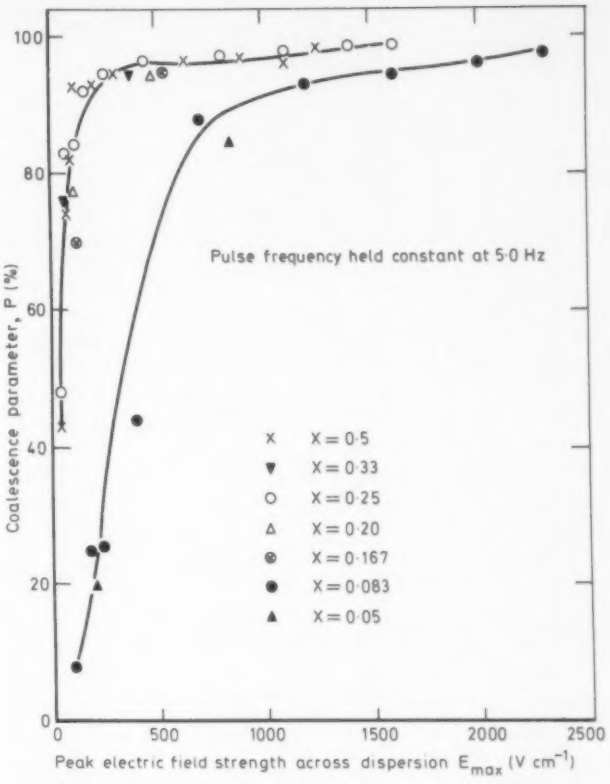


Figure 2. Dependence of coalescence parameter on peak electric field strength and holdup for one pulse frequency.

field strength is slower because the field itself is not changing quickly enough. Hence the aqueous drops also do not experience the full polarisation charges that can be induced on them quickly enough resulting in less rapid collisions and poorer coalescence than at the optimum frequency. On the other hand, at frequencies higher than the optimum frequency the intervening dielectric system does not have enough time to reach its full polarisation state and of course the drops only charge up to the extent that the intervening dielectric system does. This once again results in less rapid collisions and hence coalescence is poorer than at the optimum frequency. At a higher peak electric field strength, the level of polarisation of both the intervening dielectric system and the aqueous drops would be higher resulting in larger interdroplet forces and hence more collisions and better coalescence. This does not, however, alter the optimum frequency even though it can reduce the effect of frequency.

The intervening dielectric system is that which separates the drops from the high voltage electrode, that is, the settled continuous phase liquid in the coalescer and the electrode coating material. The polarisation/relaxation characteristic of this heterogeneous dielectric system is described by the interfacial relaxation time, the average effect of the individual dielectric relaxation times[11]. The optimum frequency for the intervening dielectric system can be calculated on this basis from equations given previously[1]. In the present case the predicted optimum frequency is 5.5 Hz which is in very good agreement with the practical result.

It is clear from the foregoing discussion that changing the hold-up should not affect the polarisation/relaxation characteristics of the intervening dielectric system, which alone determines the optimum frequency. The interfacial relaxation time depends on the thicknesses and electrical properties of the electrode coating and the continuous phase only. However, since hold-up affects the size and number of drops in the dispersion, it will also affect the polarisation charge that can be induced on each drop for a given applied field and frequency. Hence hold-up has an effect on the collision rate of the drops and the coalescence parameter.

Figure 1 indicates that a hold-up exists at which best coalescence performance of the electrostatic coalescer is obtained (this may be seen more clearly in Figure 3). Furthermore, it is interesting to note from Figure 1 that, for a hold-up of 8.3% the coalescence parameter is zero for frequencies above 30 Hz at an applied voltage of 400 V. As discussed earlier, for such a low hold-up, there is a significant proportion of very fine aqueous drops in the dispersion to be treated, which is greatly reduced upon application of an electric field. Therefore, drops previously unaccounted for in the measurement of ΔH_0 are incorporated in the value recorded for ΔH, thus it is likely that for this low hold-up some coalescence takes place at 30 Hz and above but this cannot be distinguished by the present measuring system. Indeed, this

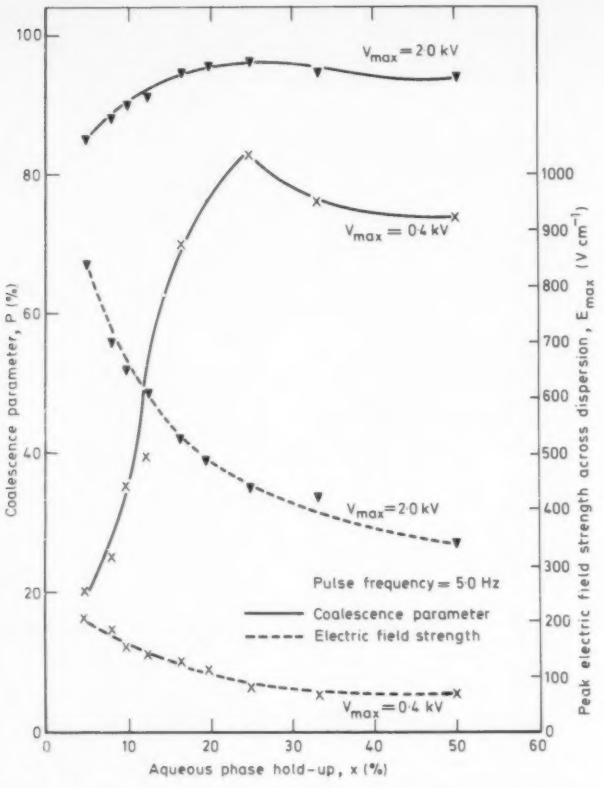


Figure 3. Effect of holdup on coalescence performance and peak electric field strength across the dispersion at different applied voltages but constant frequency.

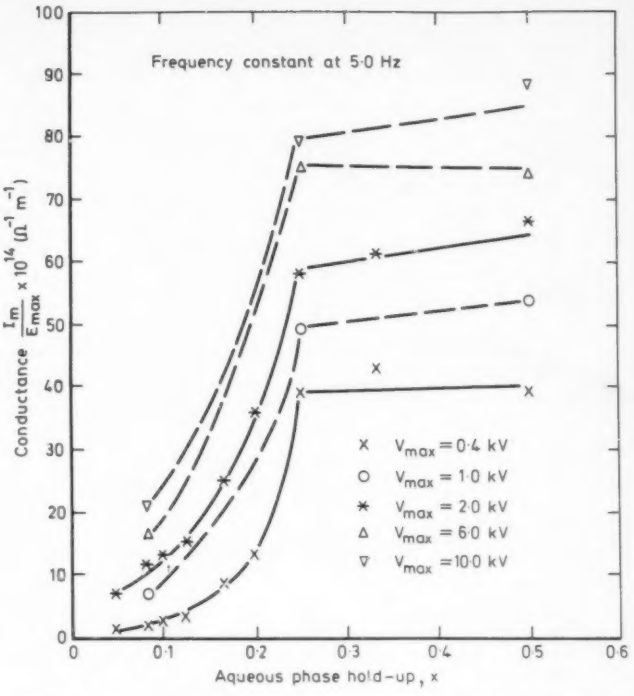


Figure 4. Conductance as a function of holdup at different applied voltages.

problem affects the coalescence parameter over the whole frequency and voltage range for all values of hold-up but the effect is more pronounced at lower values of hold-up where zero field entrainment levels are much higher.

The trend in coalescence parameter with peak electric field strength across the dispersion is shown in Figure 2 for a pulse frequency of 5.0 Hz. In view of the reservations already expressed concerning the accuracy of the experiment to determine the coalescence parameter at low hold-up, it is sufficient to note that the relationship is of the expected form, although the absolute magnitude of the coalescence parameter at low hold-up is suspect.

Figure 3 shows coalescence parameter and peak electric field strength across the dispersion as a function of hold-up for a frequency of 5.0 Hz and for applied voltages of 400 V and 2.0 kV. It is evident that for a given applied voltage the electric field strength decreases rapidly as the hold-up increases. This is in agreement with the observations of Hendricks and Sadek[12], and Prestridge[13]. The reason is the higher conductivity of the dispersion at higher values of hold-up as a result of large numbers of chains of drops forming conducting paths, thus making it more difficult to maintain a high electric field strength. The coalescence data in Figure 3 show a threshold value of hold-up at 25% above which best coalescence performance is achieved. The results for an applied voltage of 400 V show a sharp decrease in the coalescence parameter with hold-up for values of hold-up below the threshold. Comparison with the way the electric field strength behaves shows an opposite trend. Coalescence performance must, therefore, depend on factors other than simply field strength.

It would seem that when the hold-up is reduced the drops are far apart and smaller and it takes much longer to effect collision and coalescence of the drops to a size big enough to cause them to sediment out of the dispersion. This reasoning leads to the conclusion that a good balance must exist between electric field strength, drop size, number of drops and drop separation for maximum electrostatic coalescence with minimum energy input. In this connection it is worth noting that at an applied voltage of 2.0 kV the differences in coalescence parameter for the various values of hold-up are much less than at 400 V, though 25% is still an optimum hold-up. Consequently, it appears that, despite the effects of several factors on the performance of the electrostatic coalescer, at this scale, the electric field strength is one of the most important. At a sufficiently high field strength, the effects of the other factors are masked.

The influence of the spatial distribution of the drops on coalescence can be deduced in some detail once it is appreciated that the hold-up and hence the size and proximity of the drops to each other affects the conductance of the system. Thus, high hold-up dispersions have a high conductance due to the presence of more chains of drops than low hold-up dispersions. In this work a conductance was calculated from measured values of the mean conduction current and the corresponding maximum field strength across the dispersion. It is evident from Figure 4 that a graph of conductance versus

VOL. 62 1984

hold-up can be divided into two regions and that this approach clarifies the situation considerably. The two regions may be considered as follows:

Region 1: $x < 0.25$

The conductance (I_m/E_{max}) increases markedly over the hold-up range 5–25%. In this region phase separation improves as the hold-up increases, particularly at low values of applied voltage.

Region 2: $0.25 < x < 0.50$

The conductance is substantially constant over the hold-up range for a given applied voltage. Coalescence performance in this region is also reasonably constant (see Figure 3).

One practical point which emerges is that there seems to be a threshold value of hold-up beyond which electrically augmented coalescence is at its most efficient for a given applied voltage. In principle there could be some advantage in deliberately recycling quantities of dispersed phase around an electrostatic coalescer in order to take advantage of this effect.

The use of conductance to gauge the relative extent of chain formation and coalescence requires electrical data only; this means that the measurements can be made at low hold-up with much greater precision than is possible with the coalescence parameter. The absolute magnitude of the conductance depends on the design of the experimental equipment and various geometrical factors. These, coupled with the non-Ohmic character of the liquid system and the unsteady nature of the applied field, mean that little significance can be attached to the numerical value of the conductance.

CORRELATION OF RESULTS

The above deductions are based on the reasonable assumption that the conductance of the dispersion is proportional to the total rate N_T at which drops are colliding in the system since it is this that governs that spatial distribution of the drops, thus:

$$I_m/E_{max} \propto N_T \tag{1}$$

In a previous paper[1], a model based on a random collision/coalescence mechanism was derived for data correlation using an energy balance between the electrical energy consumption and the mechanical work done within the coalescer during coalescence. This model allowed the derivation of a mean drop collision frequency N, which was found to correlate very well with the coalescence parameter of a 50% hold-up dispersion of dilute sulphuric acid in 20% LIX 64N in Escaid 100. The model equation for the collision frequency was:

$$N = \frac{I_m d}{2.89\,\varepsilon\varepsilon_0\,V_c\,E_{max}x\,[(\phi/x)^{1/3} - 1]} \tag{2}$$

The spatial distribution of the drops, in the monodispersion which is assumed, is measured by the packing term ϕ/x. In the derivation it was considered that the concentration of drops would cause them to distribute so that their imaginary spheres of influence would close pack into a rhombohedral configuration with a constant packing factor of 0.74. This assumption is quite tenable at a drop hold-up of 50% but it is likely that as the hold-up is reduced the packing factor will alter. To build this variation into the model is not possible without values of N which have been directly determined.

Some progress can be made in the case of Region 2, however, when it is recalled that the conductance is reasonably constant above 25% hold-up, thus:

$$I_m/E_{max} = \text{const.} \tag{3}$$

and since

$$N \propto N_T/x \tag{4}$$

it follows that

$$N \propto I_m/xE_{max} \tag{5}$$

$$= R/x \tag{5a}$$

where R is a suitable constant of proportionality. This relationship implies that for hold-ups in the range 25–50% the term (ϕ/x) in equation (2) must remain constant. Retaining the initial assumption of a rhombohedral configuration for $x = 0.5$ gives the equation:

$$\phi = 1.48x \tag{6}$$

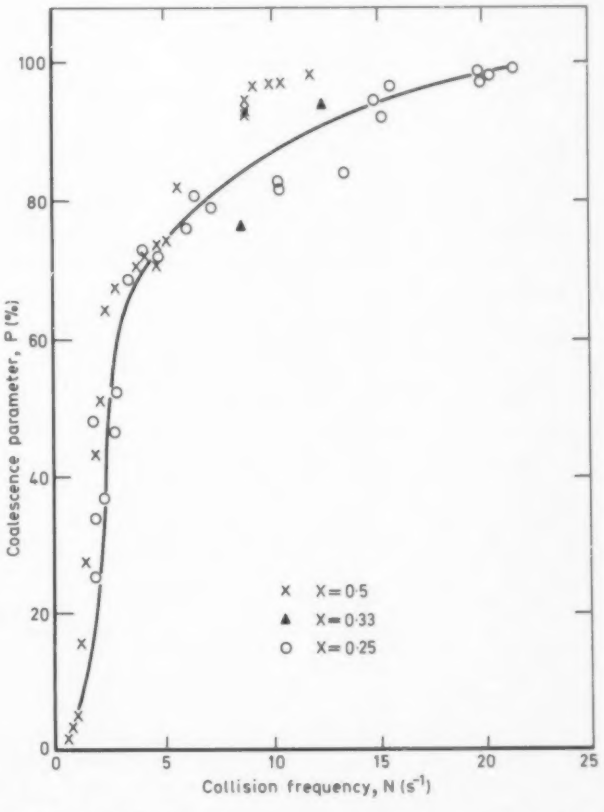


Figure 5. Coalescence parameter versus calculated mean collision frequency.

Substituting this into equation (2) and noting that the area of high voltage electrode in contact with the dispersion is A gives:

$$N = \frac{2.48}{\varepsilon\varepsilon_0 A}\frac{I_m}{xE_{max}} \quad (7)$$

Figure 5 shows the experimentally determined coalescence parameters plotted as a function of mean drop collision frequency for 25, 33 and 50% dispersed phase hold-up used in this study. The mean collision frequency is calculated from experimental values of I_m and E_{max}. The data plotted in Figure 5 cover a range of frequencies from 0.5 Hz to 60 Hz and applied voltages from 0.2 kV to 10 kV. The collision model therefore appears to offer some promise as a means of unifying the treatment of electrostatic coalescence data at higher hold-up.

The concept of regular droplet interaction is difficult to sustain at low hold-up and so the model as postulated at present tends to lose its meaning. Empirically, a power law relationship appears to exist between conductance and hold-up in Region 1. Indeed, further examination of this idea, coupled with the knowledge that the transition point between regions occurs at $x = 0.25$, does result in an identical expression for the collision frequency as that already deduced for Region 2. This may not help with modelling the coalescence process in the low hold-up region. However, it probably explains the somewhat surprising fact that when the low hold-up results are also plotted on Figure 5 they fit within the data obtained at high hold-up.

CONCLUSIONS

An investigation into the effect of dispersed phase hold-up on electrostatic coalescence has been made experimentally. The study has revealed that a threshold value of hold-up exists beyond which best coalescence performance is obtained. Visual observation of the electrostatic coalescer used in the tests has shown it to be capable of reducing the level of aqueous entrainment in the organic effluent.

An existing correlating model has been modified to account for the effect of hold-up.

NOMENCLATURE

A	electrode area (m^2)
d	distance between electrodes in coalescer (m)
E_{max}	peak electric field strength ($V\,m^{-1}$)
ΔH	dispersion band depth in gravity settler (cm)
ΔH_0	dispersion band depth in gravity settler under zero field conditions (cm)
I_m	mean conduction current (A)
N	mean drop collision frequency (s^{-1})
N_T	total collision rate (s^{-1})
P	coalescence parameter = 100 $(1 - \Delta H/\Delta H_0)$ %
R	proportionality constant
V_c	effective volume of coalescer (m^3)
x	fractional volumetric hold-up of dispersed phase
Greek symbols	
ε	relative permittivity or dielectric constant of continuous phase
ε_0	permittivity of free space ($F\,m^{-1}$)
ϕ	Packing factor

REFERENCES

1. Bailes, P. J. and Larkai, S. K. L., 1982, *Trans I Chem E*, 60 (2): 115.
2. Bailes, P. J. and Larkai, S. K. L., British Patent Application Nos. 8035196 and 8123653.
3. Waterman, L. C., 1965, *Chem Eng Prog*, 61 (10): 51.
4. Wolfe, K. M., 1944, U.S. Patent No. 2 364 118.
5. Stenzel, R. W., Oct. 1958, U.S. Patent No. 2 855 356.
6. Winslow, J. D., Sept. 1977, U.S. Patent No. 4 049 535.
7. Hodgson, R. A., Nov. 1977, U.S. Patent No. 4 056 451.
8. Martin, R. B., Oct. 1980, U.S. Patent No. 4 226 690.
9. Bailes, P. J. and Larkai, S. K. L., 1981 *Trans I Chem E*, 59 (4): 229.
10. Godfrey, J. C. and Grilc, V., 1977, *Second European Conference on Mixing*: Paper C1.
11. Birks, J. B. (Ed), 1967, *Progress in Dielectrics*, 7: 71.
12. Hendricks, C. D. and Sadek, S., 1977, *IEEE Trans Ind Appl*, IA-13 (5): 489.
13. Prestridge, F. L., Nov. 1983, US Patent No. 3 772 180.

ACKNOWLEDGEMENTS

The authors wish to thank the Science and Engineering Research Council for their financial support during the course of this work.

ADDRESSES

Correspondence concerning this paper should be addressed to: Dr P. J. Bailes, Schools of Chemical Engineering, University of Bradford, Bradford, West Yorkshire, BD7 1DP.

The manuscript was received 7 December 1982, and accepted for publication after revision 8 June 1983.

VOL. 62 1984

FLOW REGIMES ON SIEVE TRAYS: THE SIGNIFICANCE OF THE EMULSION FLOW REGIME

By F. J. ZUIDERWEG (FELLOW), P. A. M. HOFHUIS and J. KUZNIAR

Delft University of Technology, The Netherlands

In the discussion of flow regimes on distillation trays, interest has been focussed mainly on the spray regime, which is dominant at low liquid rates and at high vapour velocities. More recently it has been found that an inverse regime exists at high liquid velocities and at comparatively low vapour rates; this regime has been called emulsion flow. This paper discusses the transition into this regime on sieve trays and its significance for tray performance characteristics, such as capacity (e.g. foam formation) and efficiency (e.g. vapour back mixing).

INTRODUCTION

In the classical text books on the Unit Operations of Chemical Engineering the flow of vapour on a distillation tray is usually assumed as bubbling freely through a coherent layer of liquid which flows horizontally over the tray floor. When after World War II the study of distillation devices expanded from laboratory work into pilot plant and even commercial scale investigations, it was soon found out that in reality the vapour/liquid contacting occurred predominantly by way of liquid droplets, moving about in a continuous upflow of vapour. Apparently, bubble rise velocities, at maximum about 0.3 m s^{-1}, cannot cope with the large vapour rates (above 1 m s^{-1}) as usually applied in commercial columns. Therefore the vapour finds its way by jetting through the liquid, at the same time dispersing the liquid into small droplets.

The two phase system in which droplets are dispersed into a continuous flow of vapour has been the subject of many investigations during the last decades. In particular the conditions at which the extreme situation develops of a complete dispersion of the liquid—the so called 'spray regime'—has been studied quite extensively. For a summary see e.g. Lockett[5]. As a result of the vapour rates at which the spray regime develops can now be reasonably well predicted.

With so much interest centred on the spray regime, little effort has been devoted as yet to the possibility of the existence and the significance of the 'old fashioned' bubbly flow of vapour through a continuous layer of liquid. In a recent study by Hofhuis[3,4] an attempt has been made to find an answer concerning this problem. In this work two phase flow regimes have been investigated, covering a range of vapour and liquid rates, representative for the commercial application of the contacting device selected, i.e. sieve trays.

DENSITY PROFILES

The experimental study concerned mainly the gamma ray measurement of density profiles on sieve trays with a bubbling area of 0.8 m^2. The experimental equipment and methods have been described elsewhere[4]. A typical example of the vertical profiles at about mid-position on such sieve trays is given in Figure 1. From the profiles the following information can be directly determined:

(i) the bed height
(ii) the hold up—total and over and below the weir
(iii) the average density

Further, by application of a trajectory model[4] estimates can be made of the vertical liquid velocities and their variance.

FLOW OVER THE WEIR

The outlet weir on a distillation tray serves to retain sufficient liquid on the tray area for adequate vapour/liquid contacting. In general, the liquid hold up on a tray is considered to consist of a static part below the weir and a dynamic part equivalent to the liquid head required for the weir flow. Therefore, many relationships for the calculation of the liquid hold up are based on the classical Francis weir flow equation. For a homogeneous, coherent gas in liquid dispersion we have:

$$h_{ow} = 0.48 \left(\frac{u_L}{b} \right)^{2/3} \varepsilon_{L,ow}^{1/3} \qquad (1)$$

This equation can be checked using the experimental h_{ow} values derived from the density profiles. It has then been found that at low liquid loads h_{ow} is much higher than predicted by equation (1). The data can reasonably be reconciled[4] by correlating $h_{ow,exp}/h_{ow,Francis}$ with the flow over the weir, divided by the vapour load factor, see Figure 2. It is concluded that the mechanism of the flow over the weir must be quite different at low and high liquid loads. This is also confirmed by visual observation. At low liquid rates, the liquid is sprayed or jetted over the weir, whereas at high loads some sort of continuous gas in liquid emulsified flow over the weir develops, see Figure 3.

An attempt has been made to relate the flow at low liquid rates with the initial vertical liquid velocities,

© Institution of Chemical Engineers

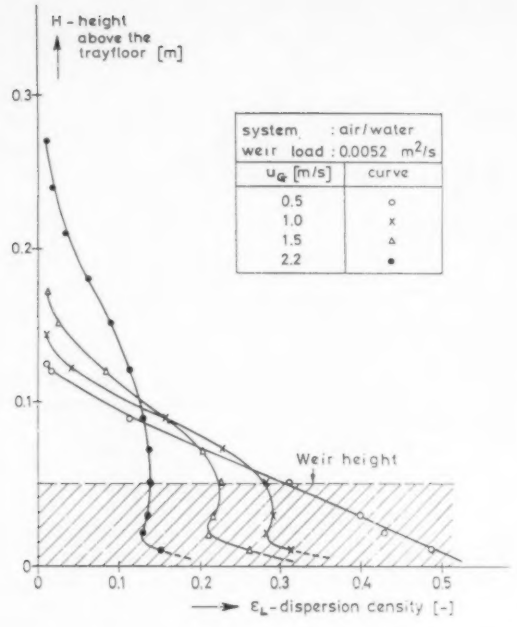


Figure 1. Effect of the gas velocity on the liquid profile. (tray open area 7%, 7 mm holes).

derived from the two phase bed density plots by employing a liquid trajectory model. The vertical initial velocities (v_0) can be described by a dominant velocity and its variance. The dominant velocity is fairly close to:

$$v_{dom} = \frac{u_{G,hole}}{C_D}\left(\frac{\rho_G}{\rho_L}\right)^{0.5} \qquad (2)$$

as can been seen in Figure 4; its relative variance has been found to be about 0.25.

It can be attempted to employ this velocity to describe the flow over the weir by splashing and spraying as observed at low liquid loads. This can be achieved by introducing a horizontal velocity component v_x next to the vertical initial velocity v_0 of the liquid drops. In that case the liquid also describes trajectories in the horizontal directions; this is confirmed by visual observation. Figure 5 illustrates that the horizontal trajectories into the direction of the weir accomplish the flow over the weir. The total amount of liquid being transported over the weir will depend on the initial velocity components [and therefore on the hole gas velocity, equation (2)], the distance to the weir from where the drops are launched and the total number of drops (the hold up).

Drops that are launched in the direction opposite to the weir will travel only very short distances because the horizontal displacement will be hindered by collision and coalescence with surrounding drops. The same will hold for drops with a horizontal velocity into the direction of the weir but launched at some distance from the weir. Therefore it is evident that only the drops generated and launched at holes close to the weir can contribute to the transport over the weir.

This mechanism has been used by Hofhuis[3] to calculate the total amount of liquid drops (hold up) in order to establish the required flow over the weir; it was assumed that $v_x = (1/3)v_o$. Figure 6 shows the results for a typical case (tray open area 7%, 10 mm holes, 25 mm weir). In order to enable comparison with the experimental data and with the hold up required by the Francis calculation the hold up's are plotted against the flow parameter divided by the specific weir length, FP/b.

It is seen that in the very low liquid load region, corresponding to the spray regime, experimental hold up is very close to the values predicted by the splashing model. Increasing the liquid load, the actual hold up diverges more and more from the spray model values;

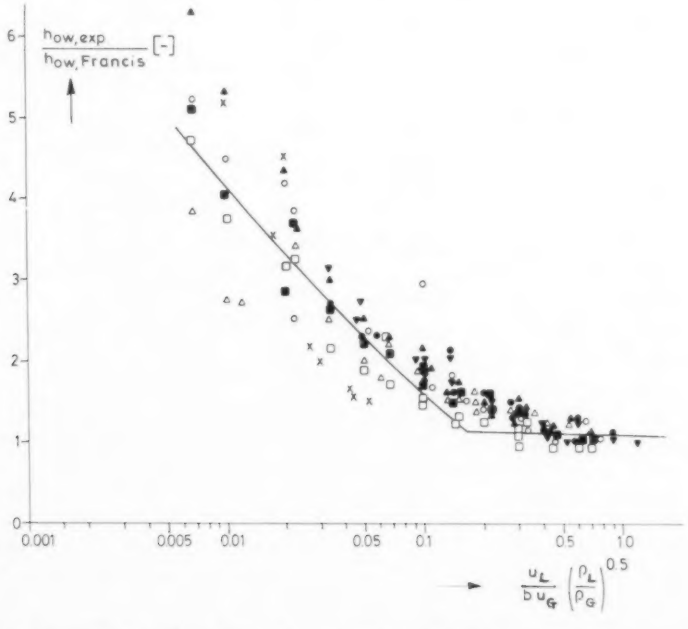


Figure 2. Correlation of hold-up above the weir. (Data obtained with 8 different tray designs).

VOL. 62 1984

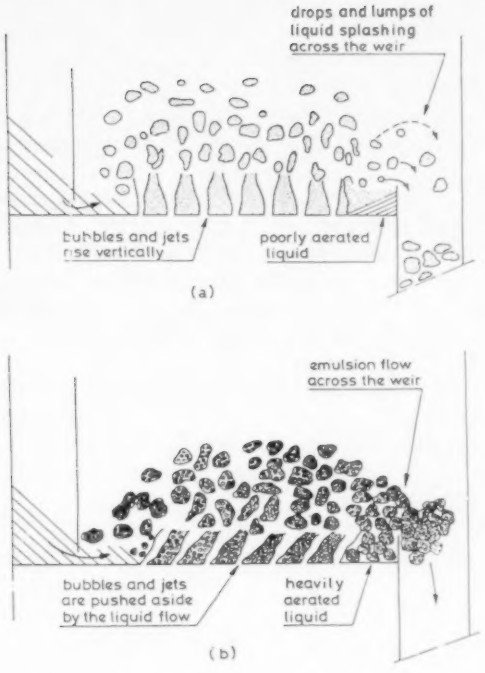


Figure 3. Flow over the weir by (*a*) splashing and (*b*) continuous phase flow.

apparently a higher hold up entirely consisting of suspended droplets becomes unstable under these conditions. By coalescence of droplets more and more continuous liquid phase is formed. This causes a gradual transition into Francis weir flow, which requires a much lower hold up to maintain the flow over the weir.

Though the mechanism of the flow over the weir and therefore also the formation of the hold up is different for high and low liquid loads, Hofhuis[4] found that the total hold up over the full range of liquid flows could be correlated with a single equation:

$$h_L = 0.6\, H_w^{0.5}\, p^{0.25}\, (FP/b)^{0.25} \qquad (3)$$

with the restriction that 25 mm $< H_w <$ 100 mm.

Since at the highest liquid rates the hold up becomes equal to the values predicted by the Francis model, it is concluded that at these conditions the liquid is predominantly flowing as a continuous phase. This is confirmed by visual observation of the flow over the weir. Another characteristic is that under these conditions the vapour jets emerging from the tray orifices are bent over by the liquid flow causing—at least in part—dispersion ('emulsification') of the jets into small bubbles. It has therefore been proposed to call this flow regime 'emulsified flow'[4]. This regime resembles the classical text book pictures on flow on distillation plates; one might say therefore that 'history repeats itself'. However, there is a difference since in 'emulsion flow' the bubbles are not freely rising and their size is very much controlled by the dispersive action of the horizontal liquid flow.

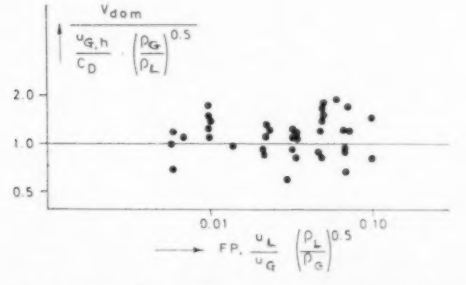


Figure 4. Ratio of dominant initial vertical liquid velocity and hole vapour velocity ($C_D = 0.7$).

THE TRANSITION INTO 'EMULSION' FLOW

A flow regime in which vapour is the predominantly dispersed phase might be expected to have some major influence on tray performance aspects, such as two phase density, liquid mixing, vapour/liquid separation, mass transfer, etc. It is therefore important to be able to predict the conditions at which this flow regime becomes dominant. It has been suggested[3] that the transition into emulsion flow occurs when the horizontal momentum flux of the liquid exceeds the vertical momentum flux of the vapour emerging from the holes in the sieve plate:

$$\frac{\hat{u}_L}{u_{G,h}}\left(\frac{\rho_L}{\rho_G}\right)^{0.5} > 1$$

or

$$\frac{u_L F}{b h_L u_G}\left(\frac{\rho_L}{\rho_G}\right)^{0.5} > 1 \qquad (4)$$

Although the transition into emulsion flow cannot be determined very accurately by experiments, relation (4) is roughly confirmed by analysis of the data plotted in Figure 2, i.e. at the point where the ordinate values become approximately equal to unity. It is found that at transition:

$$\frac{u_L}{b h_L u_G}\left(\frac{\rho_L}{\rho_G}\right)^{0.5} = \frac{FP}{b.h_L} \simeq 3 \qquad (5)$$

where FP is the flow parameter. The data are too inaccurate to confirm the effect of the open area, suggested by (4); it is therefore omitted from equation (5).

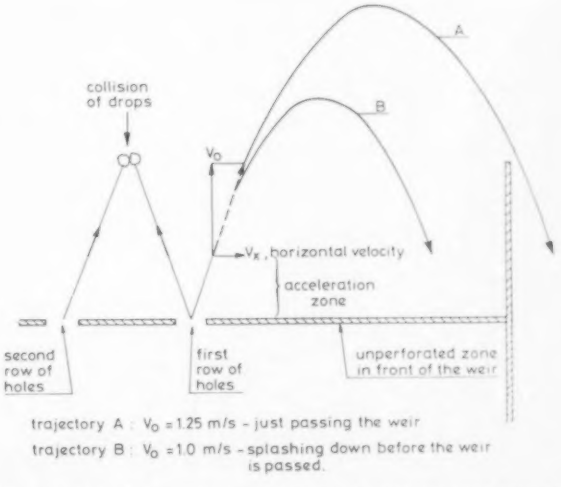


Figure 5. Model for transport over the weir by splashing and spraying.

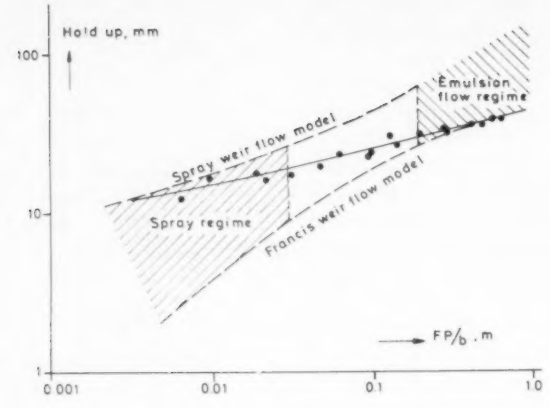


Figure 6. Comparison of experimental hold-up and calculated hold-up for spray weir flow and Francis weir flow. (tray open area 7%, 10 mm holes, 25 mm weir).

The transition into emulsion flow is not identical with the transition into the spray regime[5]. Depending on the tray layout, there is a smaller or larger transition range between the spray regime and the emulsion flow regime. It has been proposed to call the transition range the 'mixed regime'[4]. Equation (5) implies that the transition into emulsion flow is significantly influenced by the ratio of the densities of liquid and vapour and it would therefore follow that the liquid/vapour ratio at transition is sensitive to pressure.

Since equation (5) is solely based upon air/water experiments, additional work has been done to find confirmation of the effect of the ratio of phase densities. In this latter study use has been made of the already mentioned observation that at the transition the vapour jets were bent over by the liquid flow. This bending and distortion of the jets was studied in separate experiments in which a single gas jet was exposed to a horizontal liquid flow. The apparatus consisted of a perspex rectangular channel in the bottom of which different sizes of orifices could be mounted. Photographs of the gas jets emerging from the orifice were taken; the angle of inclination, α, of the jets was determined from these pictures, see for example Figure 7. It was observed that when $\tan\alpha \simeq 0.3$ the jet became almost completely dispersed.

Experiments with orifices of different diameters, ranging between 3 and 10 mm, showed that the angle of inclination of the jets was uniquely determined by the hole gas velocity and that it was independent of the orifice size. Also the influence of the liquid hold up was negligible in the range of $10 < h_L/d < 15$ investigated.

The effect of the gas density and the liquid velocity is shown in Figure 8 in which $\tan\alpha$ is plotted against $(u_{G,h}/\tilde{u}_L)(\rho_G/\rho_L)^{0.5}$, with the horizontal liquid velocity as parameter.

For a given liquid velocity the effect of the gas density is apparently well covered by the introduction of the square root of the density ratio in the abcissa variable of Figure 8. On the other hand the ratio of velocities of gas and liquid seems to be inadequate to describe the inclination of the jet. However, by extrapolation of the liquid velocity lines in the direction of the origin, they converge to $\tan\alpha = 0.3$ at $(u_{G,h}/\tilde{u}_L)(\rho_G/\rho_L)^{0.5} = 1$. This is the condition where the gas becomes completely dispersed.

Comparative experiments with kerosine/air (surface tension 26.10^{-3} N m^{-1}) at a constant value of $(u_{G,h}/\tilde{u}_L)(\rho_G/\rho_L)^{0.5}$ but varying liquid velocities also implied convergence for the two systems at low angles of inclination (Figure 9).

These studies lend support to the use of group $(u_L/u_G b h_L)(\rho_L/\rho_G)^{0.5}$ to describe the transition into emulsion flow.

SIGNIFICANCE OF EMULSION FLOW REGIME

Capacity

In emulsion flow the vapour containing liquid flows into the downcomer where it is expected to separate. With insufficient separation, hold up in the downcomer

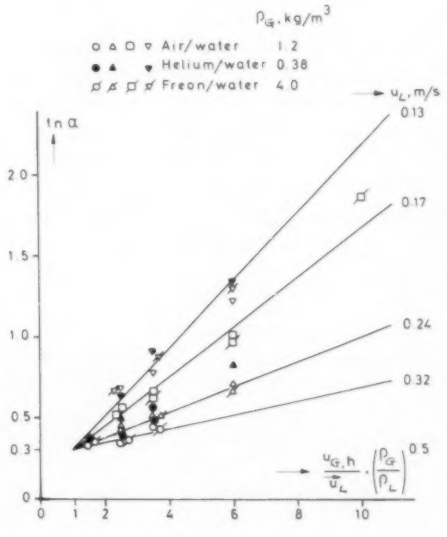


Figure 8. Influence of gas density and horizontal liquid velocity on angle of inclination of the gas jet. (orifice diameter 7 mm, liquid height in channel 70 mm).

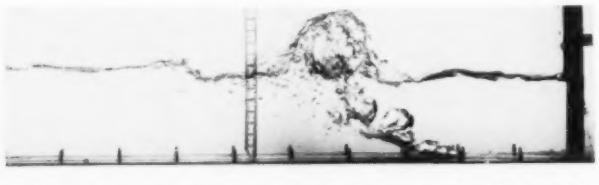


Figure 7. Inclining gas jet under influence of a horizontal liquid flow. (7 mm orifice, $u_{G,h}g^{0.5} = 15.4$ m s^{-1} (kg m^{-3})$^{0.5}$, $u_L = 0.29$ m s^{-1}).

VOL. 62 1984

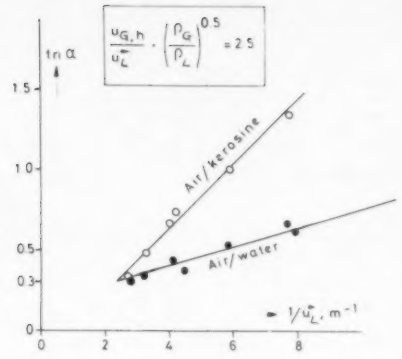


Figure 9. Influence of liquid properties on inclination of gas jet (7 mm orifice, liquid height 70 mm).

increases. Ultimately this will lead to tray flooding. Flooding data in the emulsion flow regime were recently published by FRI (Fractionation Research Inc)[7,8] for two commercial sieve tray designs. These data are plotted on a capacity factor (CF) versus flow parameter (FP) diagram in Figure 10. The results show that the capacity in the emulsion flow regime is very much system (i.e. pressure) dependent. In particular the total reflux (TR) data are of interest. For this condition, the flow parameter equals the vapour/liquid density ratio:

$$FP_{TR} = \frac{u_L}{u_G}\left(\frac{\rho_L}{\rho_G}\right)^{0.5} = \frac{L}{V}\left(\frac{P_G}{\rho_L}\right) = \left(\frac{\rho_G}{\rho_L}\right)^{0.5} \tag{6}$$

This means that at $FP = 1$, ($\rho_L = \rho_G$) critical conditions are reached at which flow is no longer possible ($CF = 0$). Figure 10 confirms that the total reflux capacities extrapolate to zero at $FP = 1$. It is therefore concluded that the capacity decrease is caused by the changing physical properties, i.e. the decreasing surface tension and decreasing density difference between vapour and liquid. These changes prevent a rapid phase separation in the downcomer. FRI confirm in their paper that the downcomer flooding limits the capacity at high pressures.

The data provided by FRI can be used to calculate the fraction liquid, $\varepsilon_{L,d}$, in the downcomer at 'incipient' flooding. Incipient flooding is defined as the condition at which the downcomer is just filled completely with foam; the incipient flooding point can be identified from the reported pressure drop and bed height data. For an example see Figure 11. It is found that the incipient flood point, $CF_{inc} \simeq 0.9\, CF_m$. Using this value for all the FRI capacity data in the emulsion flow regime, $\varepsilon_{L,d}$ can be calculated by the method described elsewhere[2]:

$$\varepsilon_{L,d} = \frac{\Delta H}{H_T + H_W} \tag{7}$$

in which

$$\Delta H = h_L + \frac{\Delta P}{g\Delta\rho} + \frac{(1-\beta^4)u_m^2\rho_m}{2C_{D,1}^2 g\Delta\rho} \tag{8}$$

with

$$u_m = u_{L,s}/\varepsilon_{L,s} \tag{9}$$

$$\rho_m = \varepsilon_{L,s}\rho_L + (1-\varepsilon_{L,s})\rho_G \tag{10}$$

For $C_{D,1}$ an average value is proposed ($C_{D,1} = 0.8$, data by Hofhuis[3]) and for the hold up the Hofhuis correlation [equation (3)] is applied. Further

$$\Delta P = gh_L\rho_L + \tfrac{1}{2}\frac{\rho_G u_{G,h}^2}{C_{D,2}^2} \tag{11}$$

with $C_{D,2} = 0.67$. The liquid fraction in the mixture flowing through the downcomer slot opening has been taken in accordance with the observations by Lockett and Gharani[6] that at the prevailing high velocities the underflow vapour content is approximately 0.8–0.9 times the average vapour content in the downcomer.

The vapour and liquid velocities in the above equations were derived from the incipient flooding rate, i.e. corresponding to 90% of the reported flooding points. The resulting ε_L and $\varepsilon_{L,s}$ values are shown in Figure 12 as a function of the superficial downcomer velocity. Surprisingly, about the same values are found for the different systems, the average (about 30–40% liquid content or 60–70% vapour content) is however very

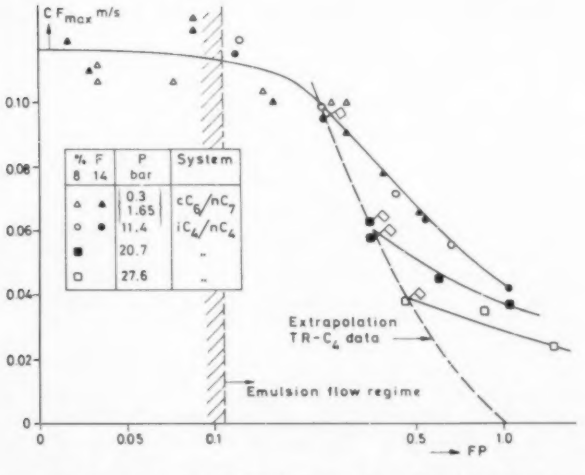


Figure 10. Capacity plot of FRI sieve tray data. Flagged points: total reflux data.

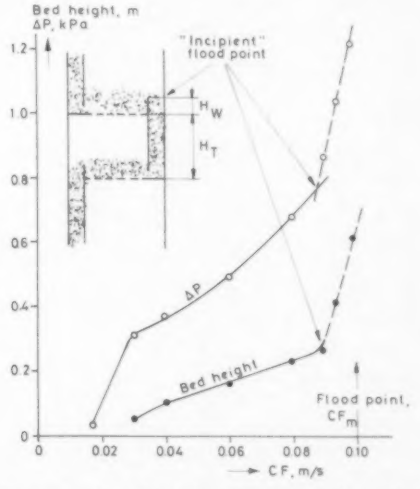


Figure 11. Determination of incipient flood point. (example: FRI sieve tray, 8% open area, C_4 system at 11.4 bar).

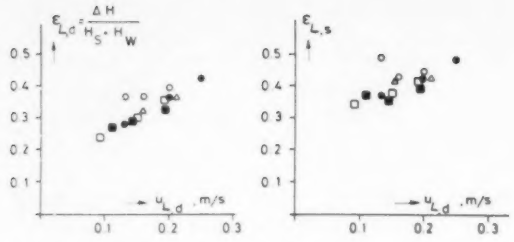


Figure 12. Calculated fraction liquid in downcomer (ε_L) and in the downcomer underflow ($\varepsilon_{L,s}$). For symbols see Figure 10.

much different than generally assumed. The high vapour content of the downcomer liquid results from the high vapour to liquid ratio of the dispersion on the tray which enters the downcomer. The vapour content on the tray can be calculated by equation (12), derived from Hofhuis density measurements in the mixed regime and in the emulsion flow regime[10]:

$$\frac{\varepsilon_G}{1-\varepsilon_G} = 40\left[\frac{u_G}{(gh_L)^{0.5}}\left(\frac{\rho_G}{\rho_L}\right)^{0.5}\right]^{0.8} \qquad (12)$$

In Figure 13 the vapour content on the tray is compared with the downcomer vapour content. It is concluded that both values tend to become equal only at the highest vapour densities. Visual observation establishes that with low vapour densities even in the emulsion flow regime part of the vapour bypasses the vapour/liquid dispersion. Apparently the volume of vapour that can be transported by the bubbles is too small at low pressures; the bubble transport capacity is adequate only at high pressures where the volumetric vapour flow becomes small.

From the above it follows that the classical downcomer hold-up calculation explains the observed flooding relations reasonably well on the basis of the high vapour content in the downcomer.

The flow pattern of the liquid and the vapour in the downcomer has been studied by Lockett and Gharani[6] with the air/water system. A representative example of their measurements is given in Figure 14. The downcomer was 102 mm wide and an average water velocity of 0.3 m s^{-1} was applied. The location of the measurements was at 115 mm above the downcomer bottom. The flow profiles show a high downward velocity for both liquid and gas at the column wall; at the side of the overflow weir the gas flow shows a small upward velocity. The slip velocity between the two phases is in the order of 0.1–0.2 m s^{-1}.

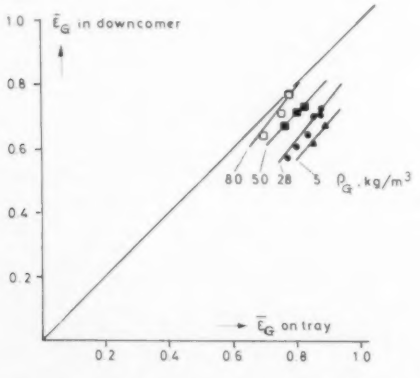


Figure 13. Comparison of the average vapour content in downcomer with the average vapour content of the two phase mixture on the trays.

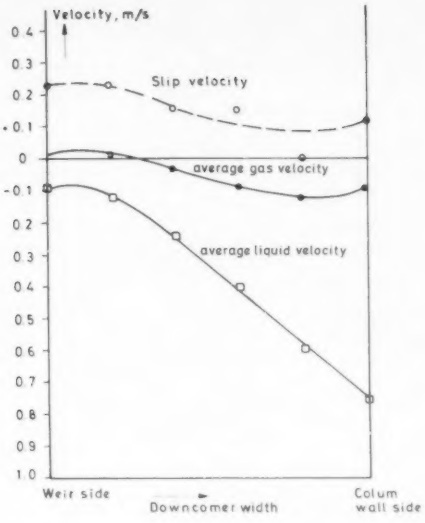


Figure 14. Superficial liquid velocity and gas velocity profiles and the slip velocity profile in a downcomer (Lockett and Gharani[6]).

It is reported that at least 90% of the gas entering the downcomer is entrained with the underflow. The average bubble content at the location of measurement was about 20 vol%; higher up in the downcomer the gas content increased. The measured flow profiles suggest a bubble circulation in the downcomer as shown in Figure 15. For the (partial) separation of the vapour bubbles high up in the downcomer, they move countercurrently with the down-flowing liquid.

The upflow of vapour can possibly restrict the net liquid flow into or within the downcomer. Such a flow restriction was actually observed by Lockett and Gharani; they report pressure drop plots similar to the diagram in Figure 11, from which incipient flooding points can be identified. At a constant vapour load

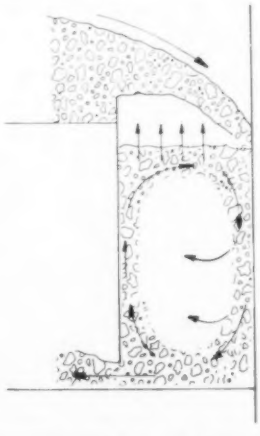


Figure 15. Flow of vapour bubbles in a downcomer close to flooding.

VOL. 62 1984

$CF = 0{,}05\ \mathrm{m\,s^{-1}}$ the maximum liquid velocity in the downcomer varies between 0.3 and 0.4 $\mathrm{m\,s^{-1}}$, depending on the size of the downcomer.

It is quite possible that the liquid downflow capacity in the downcomer is influenced by the ease by which the liquid/vapour mixture entering the downcomer will be able to separate. In order to find an expression for this separation ability, we will simulate the separation by the upflow of a packed bed of bubbles in a continuous liquid phase; the cross section of the 'packed bed' will be taken equal to the cross section of the downcomer entrance. Since at high liquid velocities at least 90% of the vapour is entrained with the liquid, the slip velocity between the bubbles and the liquid is small enough to use the laminar flow expression for the relative liquid velocity:

$$u_{L,d} \propto \frac{g\Delta\rho\varepsilon_L^2}{(1-\varepsilon_L)a^2\eta} \tag{13}$$

with

$$u_{L,d} = \frac{u_L A_b}{A_d} \tag{14}$$

The bubble area, a, is taken as proportional to the mass transfer interfacial area, a_{mt}, as derived from the reported tray efficiency data[9]:

$$a_{mt} \propto \left(\frac{h_L u_G \rho_G^{0.5} u_L \rho_L^{0.5}}{\sigma}\right)^{0.5} F^{-0.3} \tag{15}$$

Assuming that ε_L of the dispersion entering the downcomer entrance is equal ε_L in equation (13) it is found that:

$$a \propto \frac{a_{mt}\varepsilon_L}{h_L(1-\varepsilon_L)}$$

The combination of equations (13) to (16) will result in a relation between the vapour velocity in the bubbling area and the liquid velocity at the downcomer entrance. By substitution, using equation (3) for h_L and rearranging in order to arrive at a relation between CF and the flow ratio group FP/bh_L, the following is obtained:

$$CF \propto g^{1/3}\left(\frac{A_d F^{0.6}}{A_b b^{7/4} H_w^{1.2} p^{1/4}}\right)^{1/3} \times \left(\frac{\rho}{\eta}\right)^{1/3}\left(\frac{\rho_L}{\Delta\rho}\right)^{1/6}\left(\frac{bh_L}{FP}\right)^{2/3}\left(\frac{1-\varepsilon_L}{FP^{1/4}}\right)^{1/3} \tag{17}$$

Since the variation of the term $[(1-\varepsilon_L)/FP^{1/4}]^{1/3}$ is small and further that in the FRI experiments $A_d A_b$, H_w, p and b were not varied, equation (17) suggests a plot of:

$$\frac{CF_{max}}{F^{0.2}}\left(\frac{\Delta\rho}{\rho_L}\right)^{1/6}\left(\frac{\eta}{\sigma}\right)^{1/3}\left(\frac{\eta}{\sigma}\right)^{1/3} \text{ against } \frac{FP}{bh_L}$$

Figure 16 shows that the data correlated in this way show satisfactory agreement. Air/water data, taken in a column of about the same size as the FRI column also agree with the correlation. (Data on air/water were obtained on the column described by Hofhuis[3]. Corrections were made according to equation (17) for the slightly different b and A_d/A_b values as compared with the FRI trays.) Further, the results show that the correlation line intersects with the line, representing the flooding level in the non-emulsion regime (mixed regime), at a value of $FP/bh_L \simeq 3$ to 4, i.e. in the transition point.

The data plot in Figure 16 is little more than an empirical correlation of flooding points for a single tray layout. It is of some interest however to check the influence of the important variable A_d/A_b as suggested in equation (17), using the incipient flooding data that can be derived from Lockett and Gharani's downcomer study. Substituting h_L for H_w and p by using equation (3) and further noting that in the FRI experiments $CF_{inc} = \text{abt } 0.9\, CF_{max}$, it is found on the basis of Figure 16:

$$CF_{inc} = 0.035\left[g^{1/3}\left(\frac{A_d}{A_b}\right)^{1/3} F^{1/5}\right] \times \left[\frac{h_L^{1/3}}{(FP)^{7/12}}\right]\left(\frac{\rho_L}{\Delta\rho}\right)^{1/6}\left(\frac{\rho}{\eta}\right)^{1/3} \tag{18}$$

The following table summarises the calculations of CF_{inc} for the Lockett and Gharani experiments (plate size 0.127 m × 0.46 m, $F = 0.08$, $H_w = 0.076$ m, $p = 0.014$ m).

A_d/A_b	0.055	0.083	0.111	0.139	0.166	0.220
q_w† (m^3/ms)	1.0	1.65	1.9	2.35	2.65	2.85
FP	0.44	0.72	0.83	1.01	1.16	1.25
CF_{inc} (m/s)	0.039	0.035	0.036	0.035	0.035	0.036

†From the pressure drop inflection points (ref. 6, Fig. 14).

It is found that CF_{inc} is approximately constant which is in agreement with the experimental condition of constant air rate in all experiments. The applied rate, $CF = 0.05$, however, is markedly higher than the average calculated value $CF_{inc} = 0.036$. From the experimental pressure drop data it is estimated that in Lockett and Gharani's small column the hold-up is about twice the values calculated by using equation (3). Using this information, the calculated value would increase to about $CF_{inc} = 0.045$, which is fairly close to the gas rate applied.

The basis of the above correlation, i.e. the speculation that the flow into the downcomer itself is the cause of flooding, implies that the capacity at incipient flooding should be independent of such factors as tray spacing or downcomer length. However, with variations in tray spacing the space between the next higher tray and the bed level at incipient flooding will also vary. This will

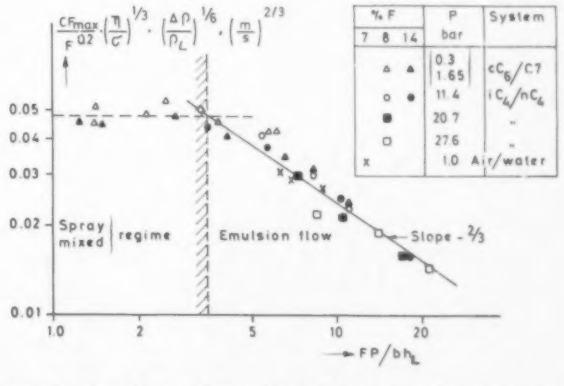


Figure 16. Correlation of capacity data in the emulsion flow regime.

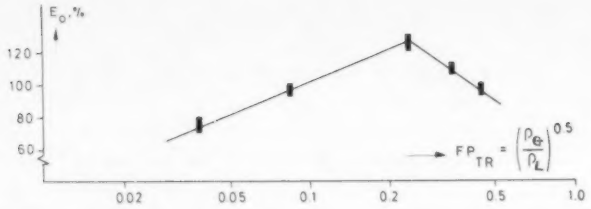


Figure 17. FRI total reflux overall plate efficiencies as function of the flow parameter. Data represent average E_o's for the systems (left to right): C_6/C_7 0.3 bar, C_6/C_7 1.65 bar, iC_4/nC_4 11.4 bar, iC_4/nC_4 20.7 bar and iC_4/nC_4 27.6 bar.

allow various degrees of accumulation of liquid in the loading range beyond incipient flooding. Therefore the difference of about 10% between incipient flooding and tray flooding for a tray spacing of 0.6 m will increase for higher tray spacings and decrease for lower distances between the trays. Thus, even with a constant value of the incipient flooding point, the total tray capacity can be expected to increase with tray spacing.

Efficiency

In addition to pressure drop and capacity, FRI has also made available efficiency data over a wide range of pressures. At the highest pressure, at which the emulsion flow regime still dominates, efficiency decreases after an initial rise with pressure at lower levels (in the spray and mixed regimes). This is demonstrated in the plot of E_0 against $(\rho_G/\rho_L)^{0.5}$ ($=FP$ at total reflux) in Figure 17. This decrease in efficiency is surprising, since one would expect a steady increase because of the continuously improving mass transfer properties of the systems with pressure. One might even speculate that the point efficiency would go to 100% when the critical pressure is approached. Some recently published data on point efficiency at high pressures by Haselden and Saleh[1] seem to confirm this speculation. Figure 18 shows some of their data on a similar plot as in Figure 17. For both systems, pentane/heptane and benzene/heptane, the data seem to extrapolate to 100% point efficiency at $\rho_G/\rho_L = 1$. The benzene/heptane system is very much 'Marangoni negative', which explains its comparatively low level of efficiency.

The overall efficiencies reported by FRI can be converted into 'apparent' point efficiencies by using the well known equations:

$$E_o = \frac{\log 1 + E_{m,oG}(S-1)}{\log S} \tag{19}$$

and

$$E_{m,oG} = \frac{1}{S}\left(e^S E_{p,oG} - 1\right) \tag{20}$$

with $S = KV/L$, stripping factor.

Equation (20) assumes that the liquid is flowing in plug flow over the plates; axial mixing correlations[9] confirm this to be true for the FRI runs under consideration. In Figure 19 the apparent $E_{p,oG}$'s are compared with the Haselden–Saleh point efficiencies. The results indicate that the trend with pressure for the apparent

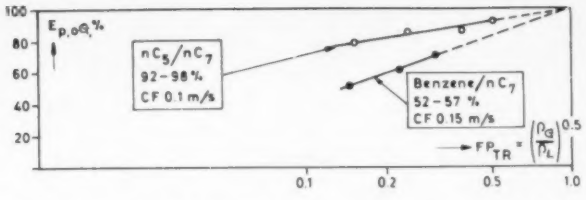


Figure 18. Point efficiencies, determined by Haselden and Saleh[1].

FRI efficiencies is the same as that implied by the data of Saleh. The apparent efficiencies start to deviate at high pressures however. Since deterioration of the basic mass transfer properties seems very unlikely, the cause of this deviation most probably is some non-ideality in flow around the FRI plates. In particular, the large volume of vapour recycling with the liquid through the downcomers is suspected. At the highest pressures, because of the high vapour densities, the high volumetric flow results also in a high molal flow rate. Based on underflow vapour contents of about 90% (with segregation, see previous paragraph) and 100% (no segregation) of the average downcomer vapour content, the molal vapour to liquid underflow ratios, plotted in Figure 20, were calculated.

Hoek[2] developed a model to predict the effect of vapour recycle on overall tray efficiency. This model assumes plugflow of the liquid on the plates and a continuous flow of 'emulsified' vapour with the liquid over the plates and through the downcomers. Figure 20 also shows the range of overall efficiencies, calculated with this model, using the 'ideal' (i.e. the extrapolated) point efficiencies and the vapour recycle ratios as estimated in the previous paragraph. The trend predicted by the model is apparently similar to that observed for the experimental FRI data. It is therefore concluded that the loss of tray efficiency at very high pressures is most likely caused by vapour 'back mixing'.

Finally, it is of some interest to speculate on the extrapolation of the overall efficiency towards the critical condition. Since, at total reflux, the identical flow rates of the two phases are approaching zero, the mixture in the downcomer will approach a composition of about 50% vapour and 50% liquid, i.e. $L/V' = 1$. Further at zero flow the phases become totally mixed. This would mean that with a recycle ratio of unity, overall plate efficiency is half the 'ideal' point efficiency[6], i.e. 50%. For the same reason the 'apparent' point efficiency becomes equal to the overall plate efficiency, i.e. also 50%. Figure 21 shows that these extrapolations agree with the trend of the experimental FRI data.

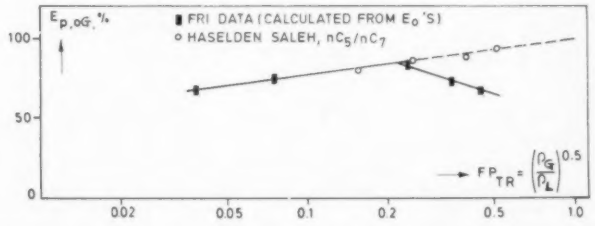


Figure 19. 'Apparent' FRI point efficiencies, compared with the Haselden and Saleh data.

VOL. 62 1984

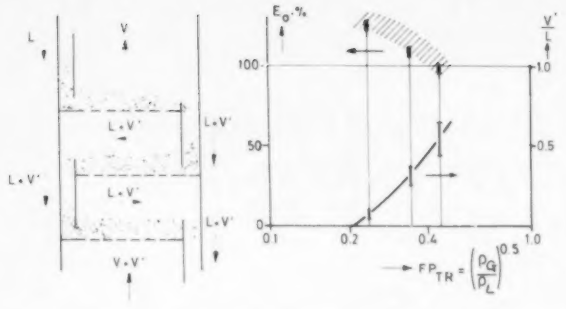


Figure 20. Vapour entrainment/efficiency model, calculated vapour/liquid entrainment ratio's and comparison of model calculations (hatched area) with FRI experimental E_0's.

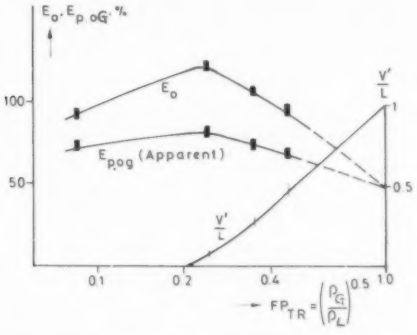


Figure 21. Speculation on the extrapolation towards the critical pressure of the entrainment ratio, E_0, and the apparent point efficiency.

CONCLUSION

The identification of flow regimes on distillation trays, in particular the extremes of the spray regime and the emulsion flow regime, improves our understanding of tray performance, such as the liquid flow over the weir, downcomer performance and the loss of tray efficiency at very high pressure. The latter, caused by the entrainment of vapour, is in analogy with the loss of tray efficiency in the spray regime as result of liquid entrainment in that regime.

Symbols used

A_b	Bubbling area (m^2)
A_d	Downcomer area (m^2)
a	Bubble area per unit volume of bubbles (m^{-1})
a_{mt}	Mass transfer area per unit bubbling area
b	Specific weir length, per unit bubbling area (m^{-1})
$C_{D,1}$	Discharge coefficient for downcomer underflow
$C_{D,2}$	Discharge coefficient for dry tray pressure drop
CF_{inc}	Capacity factor at incipient floodings ($m\,s^{-1}$)
CF_m	Maximum capacity factor at tray flooding ($m\,s^{-1}$)
d	Hole size(m)
E_{moG}	Murphree plate efficiency, vapour side
E_0	Overall plate efficiency
$E_{p,oG}$	Point efficiency, vapour side
F	Fraction plate open area on bubbling area
FP	Flow parameter
g	Acceleration by gravity ($m\,s^{-2}$)
ΔH	Total liquid back up in downcomer (m)
H_t	Tray spacing (m)
H_w	Weir height (m)
h_L	Liquid hold-up (m)
h_{ow}	Liquid hold-up above weir (m)
K	Molal distribution coefficient
L	Liquid load ($Mol\,s^{-1}$)
ΔP	Pressure drop ($N\,m^{-2}$)
p	Pitch of holes on sieve tray (m)
q_w	Liquid flow over weir ($m^3\,m^{-1}\,s^{-1}$)
S	Stripping factor
u_G	Vapour velocity, on bubbling area ($m\,s^{-1}$)
$u_{G,h}$	Vapour velocity in sieve tray holes ($m\,s^{-1}$)
u_L	Liquid velocity, on bubbling area ($m\,s^{-1}$)
$u_{L,d}$	Liquid velocity on downcomer cross-section ($m\,s^{-1}$)
$\bar{u}_L$	Average horizontal liquid velocity, Figs 8 and 9 ($m\,s^{-1}$)
$u_{L,s}$	Liquid velocity in downcomer slot opening ($m\,s^{-1}$)
u_m	Vapour/Liquid mixture velocity in downcomer slot ($m\,s^{-1}$)
V	Vapour load ($Mol\,s^{-1}$)
V'	Vapour, entrained with liquid ($Mol\,s^{-1}$)
v_{dom}	Dominant initial vertical liquid velocity ($m\,s^{-1}$)
v_0	Initial vertical liquid velocity ($m\,s^{-1}$)
v_x	Horizontal liquid velocity component ($m\,s^{-1}$)
α	Angle of inclination to the horizontal of vapour jet ($m\,s^{-1}$)
β^2	Square root of the ratio of downcomer slot opening to downcomer cross-sectional area
ε_G	Vapour fraction in two phase mixture on the tray
ε_L	Liquid fraction in two phase mixture
$\varepsilon_{L,d}$	Liquid fraction in two phase mixture in downcomer
$\varepsilon_{L,ow}$	Liquid fraction in flow over weir
$\varepsilon_{L,s}$	Liquid fraction in downcomer underflow
η	Liquid viscosity ($Ns\,m^{-2}$)
ρ_G	Vapour density ($kg\,m^{-3}$)
ρ_L	Liquid density ($kg\,m^{-3}$)
σ	Surface tension ($N\,m^{-1}$)

REFERENCES

1. Haselden, G. G. and Saleh, A., 1981, *Proc 3rd World Congress of Chem Eng* Vol. IV, page 479, Montreal.
2. Hoek, P. J. and Zuiderweg, F. J., 1982, *AIChE J* 28: 535.
3. Hofhuis, P. A. M., 1980, *Thesis* (T.U. Delft).
4. Hofhuis, P. A. M. and Zuiderweg, F. J., 1979, *Distillation* (IChemE, Symp Series 56), p. 2.2/1.
5. Lockett, M. J., 1981, *Trans IChemE* 59: 26.
6. Lockett, M. J. and Gharani, A. A. W., 1979, *Distillation* (IChemE, Symp Series 56), p. 2.3/43.
7. Sakata, M. and Yanagi, T., 1979, *Distillation* (IChemE, Symp Series 56), p. 3.2/21.
8. Yanagi, T. and Sakata, M., 1981, *9th Nat AIChE Meeting*, Symp 44, Houston.
9. Zuiderweg, F. J., 1981, *Proc 3rd World Congress of Chem Eng* Vol. IV, page 268, Montreal.
10. Zuiderweg, F. J., 1982, *Chem Eng Sci* 37: 1441.

ADDRESSES

Correspondence on this paper should be addressed to Professor F. J. Zuiderweg, Laboratory for Process Equipment, Delft University of Technology, Delft, The Netherlands. Dr P. A. M. Hofhuis is with Gist-Brocader NV, Delft, The Netherlands. Dr J. Kuzniar is at the Institute of Chemical Engineering and Heating Equipment, Wroclaw Technical University, Wroclaw, Poland.

This paper was received 6 April 1983 and was communicated by Professor J. M. Smith, Associate Editor for Continental Europe.

DROP COALESCENCE IN LIQUID/LIQUID DISPERSIONS BY FLOW THROUGH GLASS FIBRE BEDS

By V. GRILC†, J. GOLOB‡ and R. MODIC‡

†*Boris Kidrič Chemical Institute and* ‡*Edvard Kardelj University, Ljubljana, Yugoslavia*

The separation of fine dispersions of water in pure organic solvents, and of water in Shell Sol K with a surfactant added, by passage through glass fibre beds was examined. Dispersions were generated in a stirred tank and the Sauter mean diameter of the water droplets was between 10 and 50 μm. Interfacial tensions as well as viscosities varied over a wide range. It was shown that the experimental results could be correlated by a modified form of the Spielman and Goren equation, with only the numerical constants being different for each group of dispersions.

INTRODUCTION

The present paper deals with the coalescence and separation of fine liquid/liquid dispersions in glass fibre beds. The dispersions were generated in a stirred tank and were always continuous organic ones with dispersed aqueous droplets, mainly in the mean diameter range from 10 to 50 μm, this being a type of dispersion that often occurs in industrial processes after primary phase separation, or where the dispersion from the mixing process is such that it would not separate readily. The aim was to establish a correlation between the critical separation velocity, defined as the superficial velocity of the dispersion through a fibrous bed at which the outlet concentration of the dispersed phase exceeds a fixed value, and the relevant physical properties of the system. We consider this work worthwhile because there is no such information at hand that could be applied for the design of fibrous bed coalescers using more common physical and operating data.

PREVIOUS PUBLICATIONS

The most important applications and relevant literature in the field of coalescence of secondary dispersions through a fibrous bed have been summarised by Sareen *et al.*[1] and by Spielman and Goren[2].

There is a significant feature that characterises published papers, some of them[1–7] considering organic liquids dispersed in water and others water in organic liquids[8,9]. They are, namely, more concerned with the mechanism of separation[2,3,5,7,8] and less with its practical aspects than may be important for the design of coalescers. Nevertheless, great progress in understanding the mechanism of coalescence in fibrous beds has been achieved, a considerable number of qualitative conclusions of practical importance made, and three quantitative correlations for the separation efficiency proposed[4,6,7].

As a measure of separation efficiency, the filter coefficient, defined by:

$$\lambda = -\ln\left(\frac{n_L/n_0}{L}\right) \tag{1}$$

was introduced (see list of Symbols Used), and its dependence on the relevant system variables in the form of a quantitative relationship presented. The correlations, however, can hardly be used for the design of fibrous bed coalescers or for the prediction of their performance, because there would scarcely be enough information at hand to solve the equations.

The most interesting of the correlations from the theoretical and practical point of view seems to be that obtained by Spielman and Goren[3,4]. These authors developed a general mathematical description of porous coalescer performance. For porous media of similar geometry and wettability, when the capture of droplets in the fibrous bed is due to convection and van der Waals attraction, i.e. for droplets much smaller than the fibre diameter, they proposed a correlation for the dimensionless filter coefficient as a function of the dimensionless adhesion number:

$$\frac{\lambda\, d_f^3}{d_p^2} = C\left(\frac{A\, d_f^2}{\mu_c\, U\, d_p^4}\right)^a \tag{2}$$

The results of their experimental work generally supported the theory and the numerical coefficients in equation (2) were obtained for oil-in-water dispersions, both for preferentially oil-wetted and oil-nonwetted fibres.

While the filter coefficient in equation (2) refers to monodisperse systems, there is no term to account for the interfacial tension which is known to affect strongly the separation efficiency[1,8,9]. Instead, the Hamaker constant characterising the attraction energy is applied. It was, however, kept constant in the experiments as well as the interfacial tension.

Adaptation of the Spielman and Goren equation

The experiments of the present work were carried out with polydisperse systems, with Sauter mean droplet

© Institution of Chemical Engineers

VOL. 62 1984

diameters of the order of magnitude of the fibre diameter. In such cases the effect of van der Waals forces in the capture of the droplets would be less dominant and it seemed appropriate to replace the Hamaker constant with another physical property, which relates to interfacial energy such as the product of the interfacial area (proportional to d_p^2) and the interfacial tension. This assumption is not quite correct since for some systems, for instance those with a surfactant added, the interfacial tension is not a property which adequately characterises the interfacial forces. Nevertheless, it has proved to be useful in correlation of experimental data.

It will be pointed out later that the distribution function for the volume fraction in dilute dispersions generated in a stirred tank is normal and depends only upon the average droplet size d_{ps}. The standard deviation of the distribution curve is independent of geometry and of the physical properties of the systems[13]. Therefore it seemed appropriate to replace the diameter of the droplets in monodisperse systems in equation (2) with the Sauter mean droplet diameter d_{ps} for the polydisperse systems used.

The ratio of the number of droplets leaving the bed to the number entering it in a unit volume of dispersion n_L/n_0 in equation (1) has accordingly been substituted by the corresponding ratio of the outgoing to incoming volume of the dispersed phase in the same volume of dispersion, x_L/x_0.

We also assumed that at critical separation velocities, defined as the superficial velocities of the dispersion through the fibrous bed at which the outlet volume concentration of the dispersed phase exceeds a fixed value above the solubility limit, these concentrations will be approximately equal to $x_L \sim 0.002$ vol% and dependent mainly upon the analytical accuracy. While in all our experiments the inlet concentration of the dispersed phase was kept constant, $x_0 = 1.0$ vol%, the filter coefficient, based on volume concentrations, λ_x, was inversely proportional to the fibrous bed depth:

$$\lambda_x = k/L \tag{3}$$

The constant $k = -\ln(x_L/x_0)$ was approximately 6.2 in our cases and can be calculated for other inlet (and outlet) volume concentrations.

Considering these alterations and the fact that U in equation (2) refers now to the critical separation velocity, U_{cr}, a modified Spielman and Goren equation of the following form:

$$\frac{d_f^3}{d_{ps}^2 L} = K\left(\frac{\gamma\, d_f^2}{\mu_c U_{cr} d_{ps}^2}\right)^b \tag{4}$$

is obtained, which correlates the critical separation velocity as a measure of fibrous bed coalescer efficiency to variables which are known to exert significant effects on coalescer performance.

It will be shown that this form of the equation satisfactorily correlates the results of experiments performed with pure liquid/liquid systems, as well as those made with systems containing a surface active agent. Since all the variables that enter the equation can easily be determined, it offers the possibility of calculating the dimensions of a glass fibre bed for a given capacity and the required quality of separation.

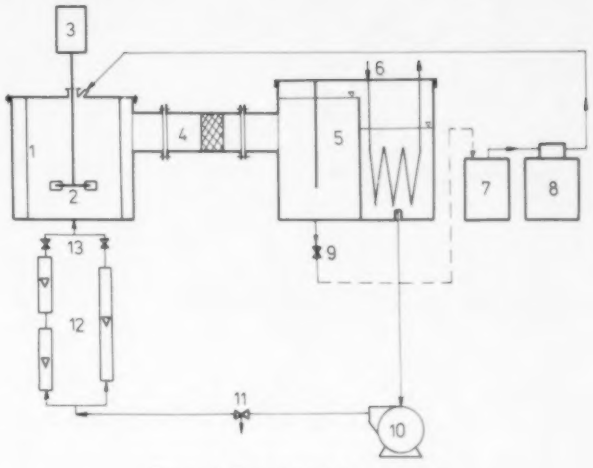


Figure 1. Experimental equipment.
1 mixing vessel; 2 turbine stirrer; 3 drive; 4 coalescer tube with fibrous bed; 5 settler; 6 cooling coil; 7 dispersed phase reservoir; 8 peristaltic pump; 9 coalesced liquid outlet; 10 centrifugal pump; 11 drainage; 12 flowmeters; 13 control valves.

Experimental

Experiments were carried out on the rig shown in Figure 1. It consisted of a covered square cross-section mixing vessel in the form of a 15 cm cube, baffled with two wall baffles of 1.5 cm width opposite each other. The vessel was stirred with a standard six-blade turbine 5 cm in diameter, centrally located 5 cm above the bottom. Inlets for the continuous and dispersed phase were arranged centrally through the bottom and the top plate, respectively. An outlet for the dispersion formed during agitation was provided in the unbaffled side wall through a hole and tube of 5 cm diameter in the upper part of the tank. The outlet tube was connected to a coalescer unit shown schematically in Figure 2, by means of flanges. The coalescer tube was made of stainless steel.

A bed of the required depth was formed *in situ* by loading thin layers of pre-wetted glass fibres simultaneously across the cross-section of the coalescer tube, and then compressed by a perforated plate to the required thickness. Thus a bed of relatively constant porosity can be obtained provided its thickness is not too small, i.e. less than 3 mm. No problems regarding the reproducibility of the experimental results were noted.

Samples of outlet liquid were withdrawn by means of a radially mounted 5 mm tube in the central line of the coalescer, 1 cm away from the outlet screen.

Occasional air entrainment was removed by means of a thin tube. After passing the coalescer, the phases were allowed to disengage in a covered box settler of 5 litres volume. Due to the heat effects of pump and stirrer, a cooling coil was provided in the settler. Clear phases were recycled back to the mixing tank by the use of pumps. Flow rates were controlled by calibrated rotameters (continuous phase) and with a calibrated peristaltic pump (dispersed phase). Mixer and settler were made of stainless steel and the recycling tubing of teflon.

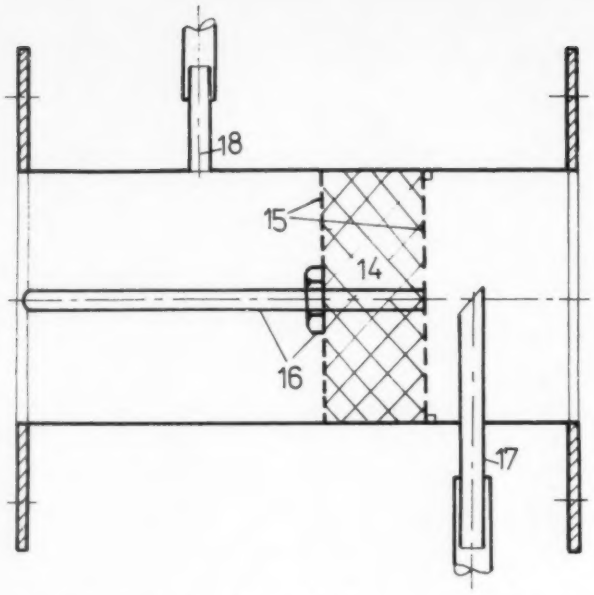


Figure 2. The fibre bed embedded in the coalescer tube. 14 fibrous bed; 15 perforated plates; 16 screw; 17 sampling tube; 18 deaeration tube.

Both liquids, with or without an additive, were agitated approximately one hour in a storage tank to assure mutual saturation and were then left to clarify overnight. The carefully formed glass fibre bed was pre-soaked in water before being used. Experiments started with a fixed bed of smallest depth and lowest flow rate, which was subsequently increased and the water content in the effluent liquid determined. Tests revealed that thirty minutes of operation were sufficient to obtain steady-state conditions. When breakthrough of the dispersion was established analytically and visually, the experiment was carried out at higher values of flow rate and then terminated. The procedure was repeated with a thicker fibrous bed. Dispersions at an aqueous-organic phase ratio of 1:100 were generated in the mixing tank at various stirrer speeds. The exact phase ratio was established by means of accurate inlet flow measurement of the liquids.

The mean droplet size in the dispersion resulting from the agitation of immiscible liquids was calculated using the correlation for the Sauter mean droplet diameter:

$$d_{ps} = 0.053\, D\, We^{-0.6} \qquad (5)$$

which was proposed for the range of conditions used in this work[13,14]. It is known that the distribution function for the volume fraction is normal in such dispersions, and that it depends only[13] upon d_{ps}.

The dispersion flowing out of the mixing vessel proved quite stable with no larger drops that would separate readily in the dispersed phase reservoir at the inlet side of the coalescer tube.

The concentration of the dispersed aqueous phase in the continuous organic phase was determined by the Karl Fischer titration method[12]. Samples of about 20 cm^3, withdrawn from the coalescer, were left for one minute in order to allow bigger drops to separate, after which appropriate amounts of the sample were used for analysis.

The fibrous bed was made of glass fibres approximately 15 mm long and with diameters ranging from 12 to 35 μm. With the smallest fibre diameter of 12 μm the porosity ε was always 0.94. This porosity, however, could not be obtained with thicker fibres. Here the corresponding bed depths are not regarded as having their actual value, but rather with an equivalent bed depth, i.e. with that bed depth of 12 μm fibres having the same total fibre surface at $\varepsilon = 0.94$. Thus the porosity of 20 μm fibre beds was 0.93 and of 35 μm fibre beds 0.92. Such a consideration seems to be correct, since it is known[2] and confirmed in our own experiments that in the range of normal porosities of about $\varepsilon = 0.88$ to 0.94 the effectiveness of coalescence depends far more upon total fibre surface than on surface area per unit volume, which is inversely proportional to porosity.

All experiments were carried out at room temperature of about 293 K.

RESULTS AND DISCUSSION

Some typical results of experiments carried out with the specified system are presented in Figure 3 (results taken from Table 2). As can be seen, the water content in the effluent liquid is a function of flow rate and bed depth, if all other relevant variables are kept constant. The transition from effective performance at lower flow rates to ineffective operation at higher flow rates is not instantaneous but smooth, and usually indistinct, so that it spreads over a wider interval. For each particular case the critical velocity was therefore determined by means of graphical interpolation. Good agreement with visual observation was found in most cases.

The water content in the sample liquid coming out from the bed represents dispersed and soluble water. As can be seen from Figure 3, the amount of soluble water for this system is about 0.07 kg/m^3. Concentrations above this value represent dispersed water remaining in the continuous phase and indicate poor coalescer performance.

Two groups of liquid/liquid systems were investigated. The first one consisted of water dispersed in pure organic

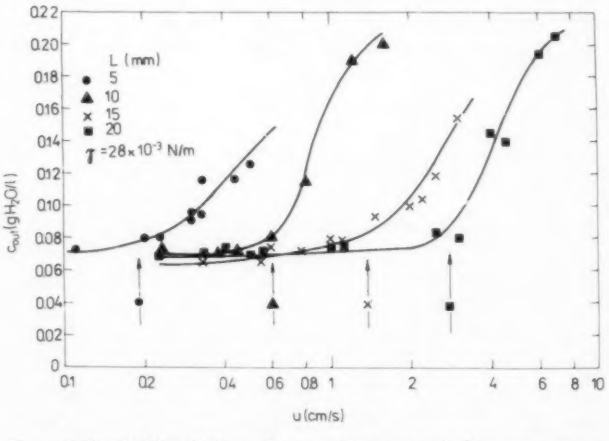


Figure 3. Typical break-through curves for a water-in-kerosene system with the surfactant added.

VOL. 62 1984

Table 1. Dispersions of water in pure organic liquids

Organic liquid	Interfacial tension γ (mN m^{-1})	Continuous phase viscosity μ_c (mPa s)	Continuous phase density ρ_c (kg m^{-3})	Fibre diameter d_f (μm)	Impeller speed N (min^{-1})	Mean droplet diameter d_{ps} (μm)	Bed depth L (cm)	Critical separation velocity U_{cr} (cm s^{-1})
Paraffin oil	43.7	29.3	840.0	12	1200	42	1.0	0.1
							2.0	0.3
					1600	30	2.0	0.25
Paraffin oil and kerosene (3 + 1)	34.2	12.3	825.3	12	1200	36	0.5	0.65
							1.0	0.45
Paraffin oil and kerosene (1 + 1)	32.7	6.0	809.7	12	1200	36	0.5	1.2
							1.0	1.8
Kerosene	28.3	1.6	778.4	20	1200	33	1.0	3.0
				35	1200	33	0.5	0.4
							1.0	2.5
Shell Sol K	40.0	1.5	794.0	12	1200	42	0.25	1.52
							0.5	2.36
							0.75	3.40
							1.0	5.50
					1700	28	1.0	5.0
Ethylacetate	6.5	0.49	901.3	12	1200	13	0.5	0.29
							1.0	0.47
							1.5	0.48
Butylacetate	12.9	0.74	882.4	12	1200	19	0.25	0.29
							1.0	1.35
					500	56	1.0	1.45
					1700	13	1.0	0.8
							2.0	2.2
				20	1200	19	0.6	0.1
					700	37	0.6	0.35
					500	56	1.2	0.85

liquids and the second one of water in Shell Sol K, with small amounts of an oil soluble surfactant, Sarcosyl O, added, in order to vary the interfacial tension between 7 mN m^{-1} and 35 mN m^{-1}. The results of experiments with both groups of systems, given as critical separation velocities U_{cr} at various bed depths L and at various relevant system variables, are given in Table 1 and Table 2. The experiments of Table 2 were conducted at constant density, 794 kg m^{-3}, and viscosity, 1.5 mPa s, of the continuous phase, and within the interfacial tension range between 7.6 and 35 mN m^{-1}, the stirrer speed being 20 s^{-1} and the glass fibre diameter 12 μm.

Table 2. Dispersions of water in Shell Sol K with Sarcosyl O added

Interfacial tension (mN m^{-1})	Mean droplet diameter d_{ps} (μm)	Bed depth L (cm)	Critical separation velocity U_{cr} (cm s^{-1})
7.6	15	0.5	0.04
12.4	21	0.5	0.04
22.8	30	0.5	0.09
23.6	30	0.5	0.11
28.0	33	0.5	0.17
15.9	24	1.0	0.09
22.8	30	1.0	0.34
22.8	30	1.0	0.26
28.0	33	1.0	0.64
35.0	38	1.0	1.02
28.0	33	1.25	1.27
16.9	25	1.5	0.26
22.8	30	1.5	0.59
28.0	33	1.5	1.53
31.0	36	1.5	2.33
12.3	20	2.0	0.09
19.6	27	2.0	0.51
23.6	30	2.0	1.27
29.1	34	2.0	2.55
10.9	19	3.0	0.08
12.3	20	3.0	0.13
19.6	27	3.0	0.59
23.7	30	3.0	2.29

Having in mind the simplifications and assumptions mentioned, the results from both tables could be surprisingly well correlated with the same form of equation (4). The constants K and b in this equation were calculated by linear regression analysis. Using the experimental data from Table 1, values of $K = 1.55 \times 10^{-5}$ and $b = 0.592$ were obtained. The regression coefficient was 0.8404 and the standard error 0.301. Using the experimental data from Table 2, the values were $K = 8.35 \times 10^{-6}$ and $b = 0.463$, with the regression coefficient 0.8437 and the standard error 0.183. As already mentioned, the constant K is valid only for the inlet and outlet concentrations of the dispersed phase observed and must be corrected for other values.

The difference in numerical constants is probably due to different conditions at the interface. When a surfactant is present, a barrier, mechanical or electrical in nature, will probably appear at the interface with an adverse effect on coalescence efficiency, and the interfacial tension is no longer a sufficient property to characterise the interfacial forces. With pure liquids, however, the hindrances to the coalescence of dispersed droplets are much weaker. It is evident that the correlations given above are useful for the design of fibre bed coalescers, since they are based on variables which can easily be evaluated for a given dispersion.

ACKNOWLEDGEMENT

The authors are indebted to the Research Council of Slovenia for financial support.

SYMBOLS USED

A	Hamaker's constant
a	exponent defined by equation (2)
b	exponent defined by equation (4)
C	correlation constant of equation (2)
D	impeller diameter
d_f	fibre diameter
d_p	droplet diameter
d_{ps}	Sauter mean droplet diameter
k	correlation constant of equation (3)
K	correlation constant of equation (4)
L	fibrous bed depth
N	impeller speed
n_L	outgoing number of droplets per unit volume of dispersion
n_0	incoming number of droplets per unit volume of dispersion
U	separation velocity
U_{cr}	critical separation velocity
We	Weber number
x_L	outgoing volume of droplets per unit volume of dispersion
x_0	incoming volume of droplets per unit volume of dispersion

Greek Letters

γ	interfacial tension
ε	porosity
λ	filter coefficient
μ_c	viscosity of the continuous phase
ρ_c	density of the continuous phase

REFERENCES

1. Sareen, S. S., Rose, P. M., Gudesen, R. C. and Kintner, R. C., 1966, *AIChE J*, 12: 1045
2. Spielman, L. A. and Goren, S. L., 1970, *Ind Eng Chem*, 62: 10
3. Spielman, L. A. and Goren, S. L., 1972, *Ind Eng Chem, Funda*, 11: 66
4. Spielman, L. A. and Goren, S. L., 1972, *Ind Eng Chem, Funda*, 11: 73
5. Sherony, D. F. and Kintner, R. C., 1971, *Can J Chem Eng*, 49: 314
6. Sherony, D. F. and Kintner, R. C., 1971, *Can J Chem Eng*, 49: 321
7. Rosenfeld, J. J. and Wasan, D. I., 1974, *Can J Chem Eng*, 52: 3
8. Hazlett, R. N., 1969, *Ind Eng Chem, Funda*, 8: 625
9. Hazlett, R. N., 1969, *Ind Eng Chem, Funda*, 8: 633
10. Spielman, L. A. and Yeang-Po Su, 1977, *Ind Eng Chem, Funda*, 16: 272
11. Hamaker, H. C., 1937, *Physica, s'Gravenhage*, 4: 1058
12. Michell, J. and Smith, D. M., 1977, *Aquametry*, 2nd edn. (J. Wiley)
13. Chen, H. T. and Middleman, S., 1967, *AIChE J*, 13: 989
14. Guanasundaram, S., Degaleesan, T. E. and Laddha, G. S., 1979, *Can J Chem Eng*, 57: 141

ADDRESSES

Correspondence on this paper should be addressed to J. Golob and R. Modic, Department of Chemistry and Chemical Technology, Edvard Kardelj University, Murnikova 6, P.O. Box 537, Ljublijana 61001, Yugoslavia. V. Grilc is at the Boris Kidrič Chemical Institute, Ljubljana.

The paper was communicated 9 August 1983 by Professor J. M. Smith, Associate Editor for the Journal in Continental Europe.

Book Reviews continued from p 32

Dense Gas Dispersion
Edited by R. E. Britter and R. F. Griffiths
Elsevier Scientific Pub. Co. 1982
pp 247 US$74.50

The present importance of dense gas dispersion has its origin in the analysis of accidents such as that at Flixborough in 1974, in which it was found that the link in the chain of events leading to the explosion and starting with rupture of a pipe, was dispersion of the dense gas from the point of emission to a position in the plant where the gas mixture was ignited. There was a substantial loss of life at Flixborough, and also at the sites of a number of other accidents around the world in which dense gases played a part. Public, professional and private concern has been shown in the conception and execution of several large scale trials in which mixtures of dense gases were injected into the natural environment, and the dilution and extension of the gas cloud was followed by fixed arrays of gas sensors. The most recent of such trials is the set of experiments into the dispersion of nitrogen–freon mixtures at Thorney Island, commissioned by the Health and Safety Executive with international sponsorship, of which the first phase has been completed by the National Maritime Institute.

Dense Gas Dispersion is a collection of eleven articles, first published as a special issue of the *Journal of Hazardous Materials*, Vol. 6, Issues 1 and 2. The Thorney Island trials are too recent to receive more than a passing reference, but some of the preliminary results of the Shell trials at Maplin Sands, and a more extended discussion of the trials at China Lake, California are included as separate papers.

Of the eleven papers, one is devoted to some preliminary results of the Maplin experiments on spillage of liquefied propane and LNG, while experiments on the spillage of 40 m^3 of LNG at China Lake are described in a second paper. The same Burro series of experiments at China Lake is compared with model simulations in a third paper, while earlier series of experiments carried out by Esso, and by the HSE at Porton Down are compared with simulations of several models. Two further papers are devoted to mathematical models of dispersion, one a catalogue of the broad characteristics of a large number of models, and the second a description of the SIGMET LNG vapour dispersion model. A paper on wind tunnel experiments on dense gas dispersion describes some of the problems of experimentation at small scale. The four remaining papers broadly describe hazard assessment, review the history of ammonia releases, and consider future directions of research. The penultimate paper of the collection is on the use of statistics in dispersion, and makes the important point that probability density functions of concentration should be considered in models since fluctuations about the mean are not small; small time fluctuations are ignored in other models considered in the book.

Although expensive, the book provides a panoramic view of contempory theoretical and experimental work in dense gas dispersion that should be useful to the research worker and the research administrator with particular interests in this field. Research workers less familiar with the field, however, are likely to find the book confusing since the fundamental characteristics of the various models are not made apparent, and the prologue and epilogue are separated and not integrated with the main body of papers.

D. J. Gunn

VOL. 62 1984

SHORTER COMMUNICATION

LIQUID DISPERSION AND EFFICIENCY ON A SIEVE TRAY WITH INCH DIAMETER PERFORATIONS

By O. OGBOJA (MEMBER)

Department of Chemical Engineering, University of Lagos, Nigeria

Liquid dispersion has been studied on a 0.9144 m × 0.3048 m rectangular sieve tray containing 25.4 mm (one inch) diameter holes. Air and water were employed as the system fluids. The results obtained are correlated. The tray efficiency data obtained on the same tray using air-CO_2/water and air-CO_2/Na solution were correlated with the mixing data. The tray efficiency was found to increase with increase in the degree of liquid mixing. For the various liquid and gas flow rates employed, all the mixing and efficiency data are correlated.

INTRODUCTION

The tray efficiency models available in the literature relate tray efficiency to the degree of liquid mixing or dispersion coefficient on the tray. In order to use the models, a knowledge of the dispersion coefficient on the tray in consideration is therefore required. As has been observed by Sterbacek,[1] the models do not accurately agree among themselves even for similar conditions on the tray. This can be attributed to the fact that most sieve tray data have been correlated against liquid flow rate, gas flow rate, and weir height only, ignoring the influence of such geometrical parameters as tray size and hole size. The effect of the ignored parameters may be significant. For example, Thomas[2] has reported that small columns tend to support higher froth heights than large columns, and Ogboja[3] has observed that froth oscillation on large trays is almost nil.

Most of the availabe data have been reported mainly on perforation diameters in the range 1.5875 to 9.525 mm. The need to avoid weeping has kept researchers working within this range for quite a long time. However, in operations where dirt or solids can cause hole blockage, large holes are to be preferred. Lemieux and Scotti[4] and Thomas and Ogboja[5] have successfully operated trays perforated with 25.4 mm holes over a wide range of liquid and gas flow rates without weeping. It can be shown that hole size is a significant parameter by comparing the work reported by Thomas and Haq[6] and Thomas and Ogboja[5] on 9.525 and 25.4 mm holes in the same column. Hence, data on small holes should be used with caution in designing large hole trays. The present work was carried out to obtain mixing data on a sieve tray having 25.4 mm holes arranged on 76.2 mm triangular pitch.

THEORY

Mass transfer on the sieve tray with convection in the x-direction can be represented as

$$\frac{\partial C}{\partial t} + u_x \frac{\partial C}{\partial x} = D_E \frac{\partial^2 C}{\partial x^2} \tag{1}$$

where

C = concentration of transferring component or tracer.
u_x = velocity of liquid at distance x from tray inlet
t = time measured from the instant of tracer injection
D_E = axial dispersion coefficient

If u_x is replaced by the mean liquid velocity on the tray, u_m, and equation (1) is rendered dimensionless by defining, $\theta = t/t_m$, $u = u_x/u_m$ and $\eta = x/z$ we have

$$\frac{\partial C_\theta}{\partial \theta} + \frac{\partial C_\theta}{\partial \eta} = D \frac{\partial^2 C_\theta}{\partial \eta^2} \tag{2}$$

where

$D = D_E/u_m z$ and z is the length of the tray.

The initial and boundary conditions for the solution of equation (2) are:

$$C_\theta(\eta, 0) = 0 \tag{3}$$

$$C_\theta(0, \theta) = f_i(\theta) \tag{4}$$

$$C_\theta(1, \theta) = f_e(\theta) \tag{5}$$

In the present work, $f_i(\theta)$ was correlated in the form:

$$f_i(\theta) = \beta \theta^\gamma \exp(-\alpha\theta) \tag{6}$$

where α, β and γ are constants.

Consequently, by using Laplace Transform and noting that C_θ must approach zero as θ approaches infinity for impulse tracer injection, the solution of equation (2) is:

$$C_\theta = \frac{2\beta}{\sqrt{\pi}} \exp\left(\frac{n}{2D} - \alpha\theta\right) \int_{k/2\sqrt{\theta}}^{\infty} \left[\theta - \left(\frac{k}{2p}\right)^2\right] \exp\left[-p^2 + \left(\frac{k}{2p}\right)^2 (a^2 - \alpha)\right] dp \tag{7}$$

For predicting tracer concentration at the tray exit, 1 should be substituted for η in equation (7).

The solution of equation (7) should closely match the

© Institution of Chemical Engineers

experimental data, $f_e(\theta)$, in values and trend and thereby satisfy the following conditions:

$$\int_0^\infty C_\theta \, d\theta = 1 \tag{8}$$

$$\int_0^\infty \theta C_\theta \, d\theta = 1 \tag{9}$$

$$\int_0^\infty \theta^2 C_\theta \, d\theta - 1 = \sigma_e^2 \tag{10}$$

The conditions are used as checks in solving equation (7) for D by trial and error from a knowledge of α, β, and γ.

EXPERIMENTAL

Apparatus and Procedure

The description of the geometry of the experimental tray is given in Table 1. Air and water were used as the gas and liquid, respectively. The tracer was nigrosine, a dye that does not alter the physical properties of water when dissolved in it. A special dye concentration measuring instrument was built and connected with a circuit which gave a continuous digital record of dye concentration against time on paper tape. The instrument and the circuit have been described in detail by Thomas and Ogboja[5].

The dye was injected into the liquid stream at the downcomer side of the inlet weir while concentration measurements were taken simultaneously at the tray side of the inlet weir and on the exit weir. This was done for various values of liquid and gas flow rates.

Results and Discussion

The normalised tracer concentration distribution function at inlet, $f_i(\theta)$, and at exit, $f_e(\theta)$, were obtained as outlined by Danckwerts[7] from the experimental measurements. The mean liquid residence time, the mean liquid velocity and the dispersion coefficient were calculated using equations (11), (12) and (13) respectively.

$$t_m = \sum_{t=0}^{\infty} t \, g_e(t) \, \Delta t \Big/ \sum_{t=0}^{\infty} g_e(t) \, \Delta t \tag{11}$$

$$u_m = z/t_m \tag{12}$$

$$D_E = D u_m z \tag{13}$$

Figure 1 shows the variation of D_E with liquid flow rate

Table 1. Description of experimental tray.

Length of tray	0.9144 m
Width of tray	0.3048 m
Thickness of tray	3.175 mm
Diameter of perforations	25.4 mm
Pitch of perforations	76.2 mm
Percentage of tray area perforated	12.2
Length of inlet calming section	0.13 m
Length of exit calming section	0.19 m
Length of weir	0.3048 m
Height of weir	76.2 mm
Tray spacing	1.8288 m

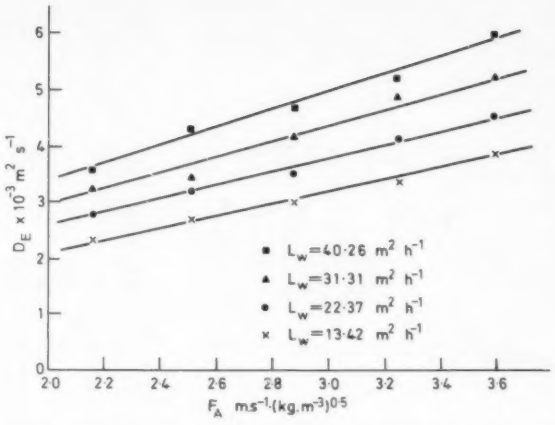


Figure 1. Variation of dispersion coefficient with liquid and gas flow rates.

per meter of weir length, L_w, and gas kinetic energy factor, F_A, defined as

$$F_A = u_G \rho_G^{0.5} \tag{14}$$

All the experimental results have been correlated as shown in equation (15)

$$10^3 D_E = 1.104 \, L_w^{0.418} + 1.264 \, F_A - 3.979 \tag{15}$$

The experimental D_E values are plotted against those calculated from equation (15) in Figure 2. A measure of the deviation of the calculated values from the experimental values is defined by

$$N\sigma_D^2 = \{100 \, [(D_E)_{cal} - (D_E)_{exp}]/(D_E)_{exp}\}^2 \tag{16}$$

where N is the total number of experimental points.

The value of σ_D was found to be 5.2%. Hence, equation (15) is a reasonably good fit of the experimental data.

Figure 1 shows that D_E values increased with increase in L_w or F_A. This is in order since increasing L_w or F_A should result in greater gas–liquid interaction. The form of equation (15) is not significant, rather, it is a con-

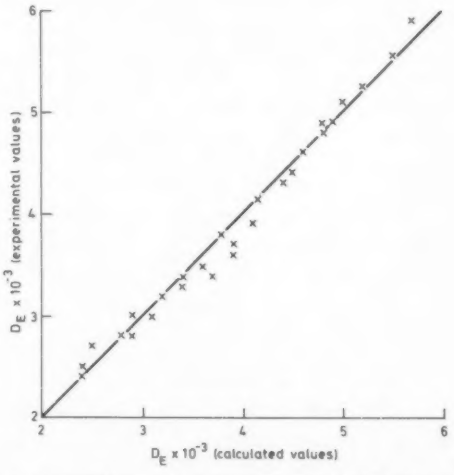


Figure 2. Comparison of measured and calculated dispersion coefficient values.

VOL. 62 1984

Table 2. Comparison of experimental systems.

	This Work	Sterbacek[1]	Sohlo and Kinnunen[9]	Barker and Self[8]
Plate dimensions	0.9144 m × 0.3048 m (rect)	0.6 m × 0.6 m (rect.)	0.5 m (dia)	1.74 m × 0.46 m (rect.)
%Free area	12	5–15	10	5
Perforation diameter	25.4 mm	5 mm	5 mm	4.76 mm
Liquid type	Water	Water	Water	Water
Gas type	Air	Air	Air	Air
Weir height	76.2 mm	0–60 mm	20–50 mm	50.8, 76.2 mm
Gas flow	0.5–1.0 m s^{-1} (superficial vel.)	7.5–17.5 m s^{-1} (hole velocity)	0.4–1.2 m s^{-1} (superficial vel.)	0.3–1.2 m s^{-1} (superficial vel.)
Liquid flow	5–45 m^2 h^{-1}	3–80 m h^{-1}	2.8–8.5 m^2 h^{-1}	5–45 m^2 h^{-1}

venient way of correlating all the experimental data with one equation. A comparison of the present work with some of the literature data is shown in Figure 3 from which equation (17) has been deduced.

$$\frac{2D_E}{u_m^3 Z_c} = 0.0079\left(\frac{Z_c u_m}{Z_f}\right)^{-2.682} \quad (17)$$

This is the form in which most of the literature data have been presented. Some more work still has to be done on the coefficient and the exponent of $Z_c u_m/Z_f$ before a generalised form of equation (17) can be produced.

Figure 3 shows that the present work compares with the literature data very well in trend. However, while the results of Barker and Self[8] and Sohlo and Kinnunen[9] are in the ranges 0.001 to 0.023 and 0.001 to 0.008 m^2 s^{-1} respectively, for the present work the result is in the range 0.002 to 0.006 m^2 s^{-1}. The differences in these results may be attributed to the differences in the experimental set-ups as shown in Table 2.

A good basis for comparing experimental results should reflect the peculiarities of the experimental set-ups. Hence, Peclet number[10], $P_E = u_m Z/D_E$, is preferrable in comparing mixing data from different sources. The values of the dispersion coefficients reported by Barker and Self[8] are higher than those obtained in this work, but while their P_E values are in the range 15 to 30, the range in this work is 9 to 21. Thus, in terms of Peclet number, the present system produced more mixing than the system of Barker and Self[8]. The P_E values in this work have been correlated against L_W and F_A as shown in equation (18).

$$P_E = 3.781 L_w^{0.461} - 2.972 F_A + 7.123 \quad (18)$$

The tray efficiency data which has been reported earlier on the same column by Thomas and Ogboja[5] has been correlated with the mixing data. The variation of the tray efficiency with the degree of liquid mixing is shown in Figure 4. All the efficiency and the mixing data have been correlated with a single straight line by plotting E_{ML} against $P_E = u_G/u_m$ in Figure 5. The plot

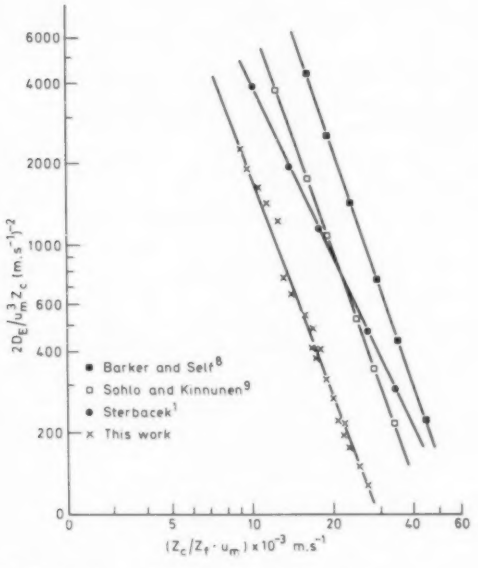


Figure 3. Comparison of results with the literature.

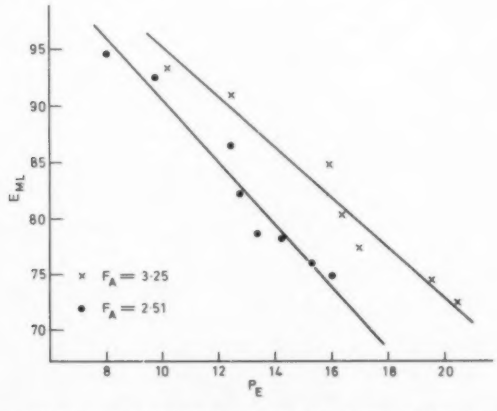


Figure 4. Variation of tray efficiency with the degree of liquid mixing.

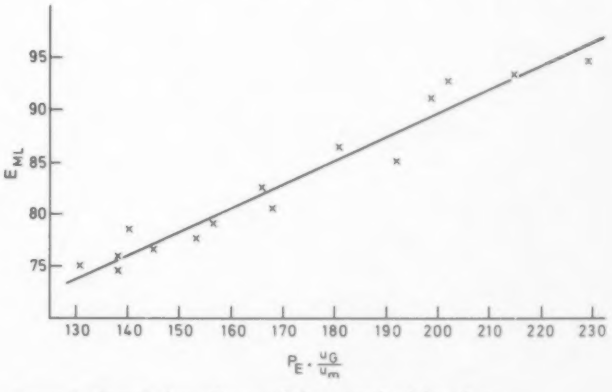


Figure 5. Correlation of tray efficiency and mixing data.

is well represented by the equation

$$E_{ML} = 0.223 P_E \left(\frac{u_G}{u_m}\right) + 44.866 \quad (19)$$

CONCLUSION

The results of the present work are well correlated by equations (15), (18) and (19). The equations are applicable over the following ranges of variables:

$L_w = 5\text{–}45\ \text{m}^2\,\text{h}^{-1}$

$F_A = 2.0\text{–}4.0\ \text{m s}^{-1}\,(\text{kg m}^{-3})^{0.5}$

$u_m = 0.03\text{–}0.09\ \text{m s}^{-1}$

$u_G = 0.5\text{–}1.0\ \text{m s}^{-1}$

ACKNOWLEDGEMENTS

The author wishes to express his thanks to Professor S. R. Tailby and Dr W. J. Thomas for providing the facilities for carrying out the experimental aspect of this work at the Department of Chemical Engineering, University of Surrey, Guildford, England.

SYMBOLS USED

A,B	Constants in equation (8).
C	Calculated tracer concentration (arbitrary units)
C_θ	Calculated dimensionless tracer concentration.
D	Dimensionless dispersion coefficient.
D_E	Dispersion coefficient ($\text{m}^2\,\text{s}^{-1}$).
E_{ML}	Murphree tray efficiency (%)
F_A	Gas kinetic energy factor ($\text{m s}^{-1}\,(\text{kg m}^{-3})^{0.5}$).
F	Dimensionless tracer distribution function measured at dimensionless distance η from tray inlet
f_e	Dimensionless tracer distribution function measured at tray exit.
f_i	Dimensionless tracer distribution function measured at tray inlet.
g_e	Tracer concentration measured at tray exit (arbitrary units).
L_w	Liquid flow rate per metre weir ($\text{m}^2\,\text{h}^{-1}$).
P_E	Peclet number (reciprocal of D).
t	Time measured from the instant of tracer injection (s).
t_m	Mean liquid residence time (s).
u_G	Gas superficial velocity (m s^{-1}).
u_m	Mean liquid velocity (m s^{-1}).
u_x	Point liquid velocity (m s^{-1}).
x	Distance from tray inlet (m).
z	Tray length (m).
Z_c	Clear liquid height on tray (m).
Z_f	Froth height on tray (m).
α,β,γ	Constants in equation (6).
η	Dimensionless distance along the tray.
θ	Dimensionless time.
ρ_G	Gas density (kg m^{-3}).
σ_e^2	Dimensionless variance of residence time distribution at exit.
σ_D	Measure of deviation between experimental and calculated D_E values.

REFERENCES

1. Sterbacek, Z. 1968, *Trans IChemE* 46: T167.
2. Thomas, W. J. 1964, *ABCM Distillation Symposium* (London).
3. Ogboja, O. 1975, *PhD Thesis* (University of Surrey).
4. Lemieux, E. J. and Scotti, L. J. 1969, *Chem Eng Prog* 65(3): 52.
5. Thomas, W. J. and Ogboja, O. 1982, *Ind Eng Chem, Proc Des Dev* 21: 217.
6. Thomas, W. J. and Haq, A. M. 1976, *Ind Eng Chem, Proc Des Dev*, 15: 509.
7. Danckwerts, P. V. 1953, *Chem Eng Sci*, 2: 1.
8. Barker, P. E. and Self, M. F. 1962, *Chem Eng Sci*, 17: 541.
9. Sohlo, J. and Kinnunen, S. 1977, *Trans IChemE*, 55: 71.
10. AIChE, 1958, *Bubble Tray Design Manual* (New York) p. 46.

ADDRESS

Correspondence on this paper should be addressed to Dr. O. Ogboja, Department of Chemical Engineering, University of Lagos, Akoka, Lagos, Nigeria.

The manuscript was received 5 *August* 1982 *and accepted for publication after revision* 16 *May* 1983

VOL. 62 1984

SHORTER COMMUNICATION

DECOMPOSITION OF TRICHLOROFLUOROMETHANE (R11) UNDER STATIC AND FLOW CONDITIONS

By P. SRINIVASAN, S. DEVOTTA and F. A. WATSON (FELLOW)

Department of Chemical Engineering, University of Salford

Decomposition rates of trichloroflouoromethane (R11), as determined under flow conditions at temperatures between 360°C and 450°C, are reported. These results have been analysed and decomposition rate constants have been determined assuming that the overall decomposition reaction is second order with respect to R11. A similar analysis has been carried out on decomposition data obtained under static conditions which have previously been reported. The combined results are consistent with the assumptions made and suggest that the same mechanism applies over the temperature range 180–450°C and probably at lower temperatures. The combined results suggest a relationship for the rate constant of the form: $\ln k = -1.7414 - 3594/T$ This equation should allow the expected working life of R11 to be estimated when used as a heat pump working fluid over a wide range of temperatures of industrial importance.

INTRODUCTION

A major limitation to the development of high temperature vapour compression heat pumps is the long term stability of the working fluids used in the systems. Some fluorocarbons and fluorocarbon mixtures have proved to be stable for many years under the operating conditions usual in low temperature application such as air-conditioning or refrigeration systems. The upper working temperature is limited to the critical temperature of the fluorocarbon since latent heat cannot be transferred at higher temperatures. Coefficients of performance and other thermodynamic parameters have been evaluated for a range of potentially useful heat pump working fluids by Holland *et al.*[1] for the ideal Rankine cycle at various condensing temperatures and operating temperature ranges. The criteria for the chemical and thermal stability of working fluids under the temperature cycling encountered in practical heat pump systems have not yet been well established. If it proves possible to predict the on-stream life of a charge of working fluid as a function of temperature then it should be possible, in conjunction with prices and thermodynamic data, to assess the economic viability of heat pump systems for specific duties.

Stability tests for the working fluids used for refrigeration purposes have traditionally been carried out using static methods. In earlier publications[2,3] the authors have described in detail the equipment and experimental procedure for static tests and have also described a novel dynamic equipment which enables the working fluid to be heated to high temperatures and cooled cyclically in a manner similar to that encountered in vapour compression heat pump systems. The latter equipment enables results to be obtained much more rapidly than is possible with a static system and is useful as a screening test for the elimination of unsuitable working fluids relatively quickly and cheaply.

The decomposition of R11 (trichlorofluoromethane, CCl_3F) has been the subject of several investigations[4-9]. There are considerable discrepancies in the reported rates of decomposition of R11. Partly, this is due to different criteria being used to assess the extent of decomposition. Some investigators have proposed possible mechanisms for the decomposition, but these reactions are complex and the proposed mechanisms have not been confirmed. The present paper presents the results of an investigation of the stability of R11 by the flow method which is described below and compares the results so obtained with those obtained by the static method.

EXPERIMENTAL

In the flow method of testing, the working fluid was heated to about 130°C by passing it through an electrically heated steel tube and was allowed to impinge on a copper target plate which was maintained at a temperature in the range 360–450°C. This target was used to simulate the hot spots encountered in the compressor of a vapour compression heat pump system. The working fluid was then cooled to about 90°C before entering a compressor which was used to circulate the working fluid under conditions similar to those encountered in a heat pump system. Because of the elevated temperatures used at the target, the duration of a typical run was only about 25 h. During this time samples were taken at regular intervals. The samples were analysed by means of a Pye Unicam 204 Gas Chromatograph and the results used to estimate the extent of the decomposition of R11. Details of the equipment and of the analytical techniques used have been reported elsewhere[2,3].

The flow equipment has been provided with the facility to circulate working fluid alone, lubricating oil alone or preset mixtures of the two. In the present study no lubricating oil was deliberately circulated with the working fluid. However, under certain conditions some oil, used in the compressor for lubrication, was carried over by the working fluid to the target. In these cases a black deposit was formed on the target. The results from such runs were discarded.

DISCUSSION OF RESULTS

The results obtained from experiments on R11 cycling between temperatures of 90 and 130°C for 5 target

© Institution of Chemical Engineers

temperatures are presented in Figure 1 which shows the effect of target temperature on the extent of decomposition with time. The high target temperatures used enable a reasonable amount of decomposition to take place in a relatively short time. This technique is, therefore, useful as a rapid screening test to eliminate unsuitable working fluids or working fluid/lubricant combinations. The results obtained from the flow method can be used to estimate the rate constants for the decomposition if the type of reaction and the order of reaction are known.

For the decomposition of R11 in the presence of univalent metal, Church and Mayer[6] and Eiseman[10] have proposed the mechanism of equation (1):

$$2CCl_3F + M \rightarrow MCl_2 + FCl_2C - CCl_2F \qquad (1)$$

The present experiments do not confirm this model. Chernyuk[5], Lyapin[11], Lisov *et al.*[12] and Okazaki[13] all detected R12 (CCl_2F_2) and carbon tetrachloride (CCl_4) in the decomposition products of R11. The proposed reaction is presented as equation (2):

$$2CCl_3F \rightleftharpoons CCl_4 + CF_2Cl_2 \qquad (2)$$

Lisov *et al*[12] showed that this reaction was not complicated in the presence of nickel or of the special alloy ZI-437B whereas the products and the rate varied widely in the presence of other metals and alloys. However, in the presence of iron or of copper, one of the basic products was found to be R12. The latter result was confirmed by the present experiments although no special attempt was made to identify all the decomposition products. However, the CCl_4 peak was found in the chromatograms although not in the stoichiometric proportions required by equation (2). Nevertheless, the rate constant at each target temperature was estimated by assuming that the rate controlling step in the decomposition was second order with respect to R11.

In order to test this assumption the values of $1/C_{Ao} - 1/C_A$ were plotted against reaction time, t. Straight lines were fitted to these points by the method of least squares. The slopes of such lines are the required rate constants. Although the maximum number of points so fitted at a given target temperature was only eight, the correlation coefficients of all lines lay in the range 0.96–0.99. This is considered to be a justification of the accuracy of the data obtained and of the adequacy of the assumption of second order decomposition for the purpose of extrapolating to lower target temperatures.

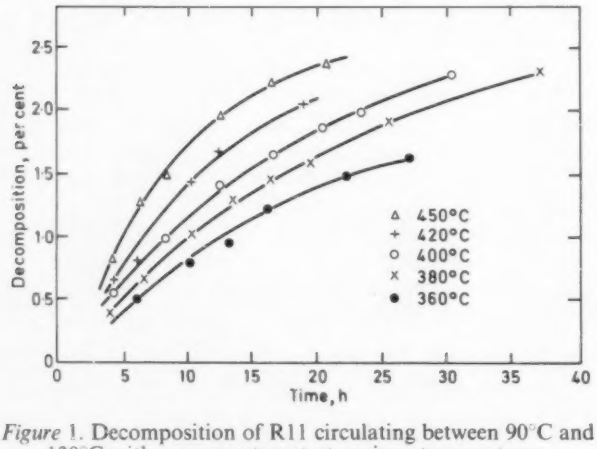


Figure 1. Decomposition of R11 circulating between 90°C and 130°C with a copper target at various temperatures.

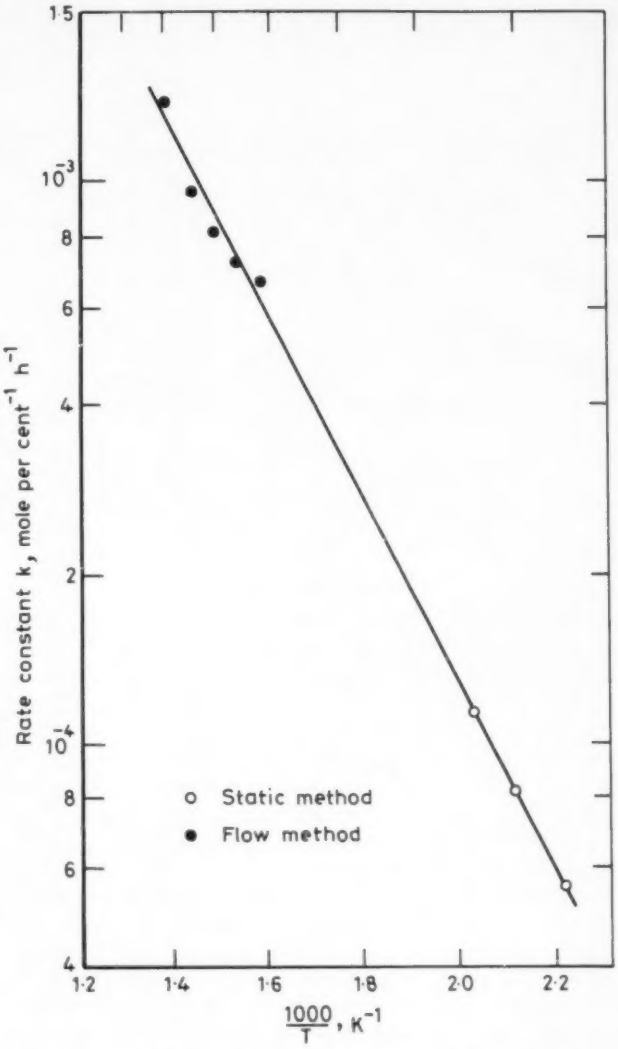


Figure 2. Combined Arrhenius plot for the decomposition of R11.

For comparison, a similar procedure was used to estimate the rate constants from results obtained from decomposition tests on R11 under static conditions at temperatures of 180, and 220°C. The results of both sets of experiments are presented in Figure 2 in the form of an Arrhenius plot. It is clear that the reaction mechanism of the decomposition of R11 in the presence of copper and of iron may be considered to be independent of the highest temperature in the system in the range 180–450°C. The combined data provide eight experimental values which have been fitted by the method of least squares to give equation (3)

$$\ln k = -1.7414 - 3594/T \qquad (3)$$

with a correlation coefficient of 0.99.

Since the mechanism of decomposition does not appear to change and because the fit of the data is so good,

VOL. 62 1984

equation (3) may reasonably be used to estimate the expected rates of decomposition of R11 when used as the working fluid in a vapour compression heat pump using an unlubricated compressor. Typical values of the time required to reach a given percentage decomposition of R11 at temperatures of 100, 125 and 150°C are presented in Table 1. These temperatures are currently of interest for industrial applications of heat pumps but values for other temperatures can readily be calculated from equation (3).

Table 1. Extrapolated time (days) required for decomposition of R11

Temperature (°C)	Decomposition 1%	2%	5%	10%
100	31	69	187	400
125	17	38	101	217
150	10	22	60	128

In an actual heat pump it is usual to use a lubricated compressor. The effect of the choice of lubricant on the mechanism and the rate of decomposition of some fluorocarbons, including R11, have previously been reported by the authors[2,3,14] and also by Borchardt[4]. Further work should elucidate the relationships between the type and quantity of the lubricating oil carried by the gas stream. However, it is considered that equation (3) should be of immediate value to those contemplating the use of unlubricated compressors and that any system not economic when evaluated using equation (3) will be less attractive when lubricant is present.

NOMENCLATURE

C_A concentration of R11 at any time t (mol%)
C_{Ao} initial concentration of R11 (mole%)
k rate constant (mole%$^{-1}$ h^{-1})
t reaction time (h)
T reaction or target temperature (K or °C)

REFERENCES

1. Holland, F. A., Watson, F. A. and Devotta, S., 1982, *Thermodynamic Design Data for Heat Pump Systems* (Pergamon Press, Oxford, UK)
2. Abbas, S. P., Srinivasan, P., Devotta, S. and Watson, F. A., 1981, IChemE North West Branch, Symposium Papers, No. 3, Salford, 7.1–7.13.
3. Watson, F. A., Abbas, S. P., Srinivasan, P. and Devotta, S., 1982, *Proc Int Conf Ind Appl Heat Pumps*, (BHRA, Cranfield).
4. Borchardt, H. J., 15 Sept., 1979, *Revue Pratique du Froid et du Conditionnement d'Air*, 59–62.
5. Chernyuk, G. P., 1981, *Z Prik Khim* 54 (6): 1384–1388.
6. *Church, J. M. and Mayer, J. H.*, 1961, *J Chem Eng Data*, 6(3): 449–453.
7. Parmelee, H. M., 1965, *ASHRAE Trans* 71 (1): 154–161.
8. Scholten, W., 1962, *DKV Tagungsbericht*, 4: 249–277.
9. Walker, W. O., Rosen, S. and Levy, S. L., *ASHRAE J* 4 (8): 59–72.
10. Eiseman, B. J., 1971 *Progress in Refrigeration Science and Technology* (Proceedings of the International Congress on refrigeration 2) 648–653.
11. Lyapin, A. P., 1976, *Russian Journal of Physical Chemistry*, 50(1): 169.
12. Lisov, V. N., Lyapin, A. P., Karchishin, A. D. and Serkova, L. P., 1974, *Ukrainskiz Khim Z*, 40(12): 1264–1268.
13. Okazaki, S., 1968, *Shokubai* 10(4): 242–251.
14. Srinivasan, P., Abbas, S. P., Ghosh, S., Devotta, S. and Watson, F. A., 1982, *Trans I Chem E* 60: 380–382.

ACKNOWLEDGEMENTS

The authors wish to thank the Science and Engineering Research Council, UK, for their financial support. Thanks are also due to Professor F. A. Holland, Chairman of the Department of Chemical Engineering, University of Salford, UK, for his active involvement and continued interest and support of this work.

ADDRESS

Correspondence on this paper should be addressed to Dr. S. Devotta, Department of Chemical Engineering, University of Salford M5 4WT.

The manuscript was received 6 April 1983 and accepted for publication 20 May 1983.

CORRESPONDENCE

From
V. S. Guru Rajan and Dr. A. Datta
R & D Division Engineers India Limited,
4, Sansad Marg, New Delhi, India-10058

We wish to make the following comments on the derivation of the collection efficiency equation, the equation for Sauter-mean diameter and the comparison of results reported by L. P. Bayvel[1] in "The effect of polydispersity of drops on the efficiency of a Venturi scrubber"

(i) In the droplet continuity equation (equation 4 in the article) the terms N_d and N_{dt} represent droplet concentration (i.e. number of droplets of radius r_d per unit volume) at any position in the venturi scrubber and at the throat respectively. However, the author has substituted for N_{dt} an expression (equation 7 in the article) which defines N_{dt} as droplet loading per unit volume of gas (i.e. number of droplets of radius r_d injected at the throat per unit volume of gas). As a result, his subsequent expressions leading to collection efficiency are erroneous. Moreover, the droplet concentration term N_d is missing from the equation for number of collisions (equation 2 in the article).

It is easy to express N_d in terms of gas and droplet velocities and liquid loading as shown below:

According to droplet continuity equation,

$N_d V_d S$ = total number of droplets of radius r_d injected per unit time.

$$= \frac{3\,Q_L\,g(r_d)dr_d}{4\,\pi r_d^3}$$

$$= \frac{3q\,Q_g\,g(r_d)dr_d}{4\,\pi r_d^3}$$

$$= \frac{3q\,S\,V_g\,g(r_d)dr_d}{4\,\pi r_d^3}$$

Hence

$$N_d = \frac{3q\,V_g\,g(r_d)\,dr_d}{4\pi r_d^3\,V_d}$$

whereas N_d has been incorrectly expressed as

$$N_d = \frac{3q\,g(r_d)\,V_{dt}\,V_g\,dr_d}{4\,\pi r_d^3\,V_d\,V_{gt}}$$

(equation 8 in the article). Substituting the corrected expression for N_d into equation (3) in the article we get,

$$dn_i = -\pi r_d^2\,n_i\,|V_g - V_d|\,\frac{3q\,V_g\,g(r_d)\,dr_d\,\eta_t\,dt}{4\pi r_d^3\,V_d}$$

Therefore

$$\frac{dn_i}{n_i} = -\frac{3q}{4}\,\frac{\eta_t\,g(r_d)\,|V_g - V_d|\;V_g\,dt\,dr_d}{r_d\,V_d}$$

Replacing $V_g\;dt = dl$, the expression for collection efficiency becomes

$$\eta_i = 1 - \exp\left[-\frac{3q}{4}\int_o^L\int_o^{R_d}\frac{\eta_t\,g(r_d)\,|V_g - V_d|}{r_d\,V_d}\,dr_d\,dl\right]$$

It is seen that the correct expression for collection efficiency taking into account polydispersity of droplets, is different from equation (12) in the article. Moreover, it is noted that for monodisperse droplets, our expression for collection efficiency matches exactly with that reported by Boll[2] whereas equation (12) in the article does not match.

(ii) The second constant term of 6×10^{-3} in the Nukiyama–Tanasawa equation (N–T equation) reported by the author (equation 14 in the article) differs considerably from the widely reported value of 0.458 (for the same set of units as employed by author) by Ekman and Johnstone[3] David Leith and Douglas Cooper[4], William Licht[5] and Roberts[6]. Moreover, it is surprising to note that the Sauter-mean radius reported in Figure 2 of the article (curves 1, 2, 4 and 5) is not in conformity with equation (14) in the article. For example, for a throat velocity of 80 m s^{-1}, equation (14) predicts a Sauter-mean radius ranging from 31.25 μm to 31.38 μm as the liquid loading is increased from 0.1 to 0.8 lm^{-3} while in figure (2) the Sauter-mean radius is shown to vary from about 30 μm to 44 μm.

(iii) The author has stated that he has compared the collection efficiency taking into account polydispersity of droplets with that for monodisperse droplets proposed by Ekman and Johnstone[3]:

$$\eta_1 = 1 - \exp(-kq\sqrt{K})$$

Table 1. Estimation of Constant k from Figure 4 in the article. System: Air containing dibutyl phthalate and water. Operating pressure = 1 ata. Operating temperature = 30°C. Aerosol particle radius = 0.5 μm. Aerosol particle density[8] = 1045 kg/m^3.

Gas velocity at throat ms^{-1}	Liquid loading q lm^{-3}	Sauter-mean radius from eqn (14) in the article μm	Stokes number K	Collection efficiency from Fig. 4 η	k
70	0.1	35.72	3.37	0.35	2.35
70	0.2	35.73	3.36	0.57	2.30
70	0.4	35.76	3.36	0.81	2.26
70	0.6	35.80	3.36	0.92	2.30
90	0.1	27.78	5.56	0.43	2.38
90	0.4	27.82	5.55	0.88	2.25
110	0.1	22.73	8.31	0.48	2.27
110	0.4	22.77	8.29	0.92	2.19
130	0.1	19.24	11.61	0.55	2.34
130	0.4	19.28	11.58	0.95	2.20
150	0.1	16.67	15.45	0.60	2.33
150	0.4	16.71	15.41	0.97	2.23

VOL. 62 1984

Table 2. Estimation of Constant k from Ekman and Johnstone's data

Gas velocity at throat ms^{-1}	Liquid loading lm^{-3}	Saute-mean diameter eqn (1) μm	Stokes Number K	$q\sqrt{K}$ (X)	η	$\ln\left[\frac{1}{1-\eta}\right]$ (Y)
		Radial Outward Injection				
88.41	0.049	56.86	5.34	0.113	0.104	0.110
114.33	0.545	55.24	7.11	1.453	0.636	1.011
90.85	0.236	58.31	5.35	0.546	0.221	0.250
79.57	0.674	78.66	3.48	1.256	0.476	0.646
74.69	0.862	89.83	2.86	1.457	0.634	1.005
68.90	1.112	106.10	2.23	1.660	0.707	1.227
106.10	0.198	49.64	7.34	0.536	0.231	0.263
103.96	0.368	54.48	6.55	0.942	0.407	0.522
99.69	0.513	60.66	5.64	1.220	0.492	0.677
148.17	0.120	34.93	14.57	0.458	0.295	0.349
97.86	0.663	66.53	5.05	1.490	0.619	0.965
130.18	0.297	43.04	10.39	0.957	0.353	0.435
107.62	0.176	48.57	7.61	0.486	0.190	0.211
93.90	0.737	71.33	4.52	1.566	0.681	1.142
140.56	0.265	39.47	12.23	0.927	0.442	0.583
		Radial Inward Injection				
75.91	0.662	81.26	3.21	1.186	0.432	0.565
79.88	0.452	71.28	3.85	0.887	0.319	0.384
81.71	0.262	65.03	4.31	0.544	0.207	0.232
82.32	0.180	62.93	4.49	0.381	0.161	0.175
99.08	0.529	61.48	5.53	1.244	0.616	0.957
105.79	0.210	50.01	7.26	0.566	0.323	0.390
106.71	0.205	49.50	7.40	0.558	0.289	0.341
111.28	0.174	47.00	8.13	0.496	0.256	0.296
135.06	0.167	38.97	11.90	0.576	0.440	0.580

$k = \Sigma XY/\Sigma X^2 = 0.63$

However he has not reported the value of the constant k. From Figure (4) of the article, we calculated the value of k for several gas velocities and liquid loadings based on equation (14) of the article. It appears, as is evident from Table 1, that the author has used a value of about 2.30 for k. We analysed the data of Ekman and Johnstone[3] for both radial inward and outward injections and obtained a value of 0.63 by least square technique for the constant k as shown in Table 2. In this calculation the widely reported N–T. equation,

$$D_{32} = \frac{5000}{V_{gt}} + 28.6\,(q)^{1.5} \qquad (1)$$

is used for the Sauter-mean diameter. This value of k also agrees with slope of the plot of $\ln(1-\eta)$ against $q\sqrt{K}$ reported by Johnstone[7]. Therefore, not only the collection efficiency for polydisperse droplets but also the collection efficiency for mono-disperse droplets has been incorrectly calculated and reported by the author.

Symbols used

Q_l = liquid flow rate ($m^3\,s^{-1}$)
Q_g = gas flow rate ($m^3\,s^{-1}$)
R_d = maximum droplet radius (μm) or (m)

The rest of the symbols have the same meaning as reported by the author.

REFERENCES

1. Bayvel, L. P., 1982, *Trans IChemE* 60 (1): 31.
2. Boll, R. H., 1972, *Ind Eng Chem Fund*, 12 (1): 40.
3. Ekman, F. O. and Johnstone, H. F., 1951, *Ind Eng Chem*, 43, (6): 1358.
4. Leith D. and Cooper D. W., 1980, *Atmosph Envir*, 14: 657.
5. Licht, W. 1980, *Air Pollution Control Engineering* (Marcel Dekker Inc., New York) 353.
6. Roberts D. and Hill J. C., 1981, *Chem Eng Commun*, 12: 33.
7. Johnstone H. F., Field R. B. and Tassler M. C., 1954, *Ind Eng Chem*, 46: 1601.
8. Perry R. H. and Chilton C. H. (Ed) 1973, *Chemical Engineers Hand Book*, 5th Edition (McGraw-Hill Kogakusha Ltd.) 3.32.

From
Dr M. J. Slater
Schools of Chemical Engineering
University of Bradford
Bradford, West Yorkshire
BD7 1DP

The use of SI units in *Chemical Engineering Research & Design* (and other journals) has become more common, which is to be welcomed. The SI is described in various sources[1-6] but some practical points seem to require emphasis, judging from my own experience in checking manuscripts for publication. Improvements are required, I believe, in presenting scientific data to aid understanding and to avoid inconsistencies and misinterpretation (the aims of the SI). Authors, reviewers and editors all have responsibility for setting the highest possible standards: one learns a lot by example and journals should demonstrate an intelligent use of SI units. Casual use of the system can lead to absurdities in conversion, to difficulties in absorbing information and to possible confusion.

My further comments fall into three categories–common errors or poor practice, labelling of graphs, and my own guidelines.

Common errors include Kw and KW (for kW) and mole (should be mol or kmol in units). The letter p (per) should not be used. The abbreviations ppm, rpm, gpm, tpy are not SI units. For ppm use $g\,m^{-3}$, $ml\,m^{-3}$, $mg\,l^{-1}$, $mg\,kg^{-1}$ as appropriate; for rotational speed use s^{-1}, min^{-1} or h^{-1} and for periodic frequency use Hz. Poor practice includes cc (for ml) or cu metre (for m^3) and the mixing of unit names and symbols. I think it is pedantic for an engineer to use dm^3 instead of l: the rule to avoid using prefixes in the denominator (except for kg) would not allow dm^3 as a denominator (i.e. use $g\,l^{-1}$ or $kg\,m^{-3}$ not $g\,dm^{-3}$). Prefixes should be used in place of powers of 10 except in calculations (use the base units) or perhaps when a very wide numerical range of the variable is experienced. For viscosity 1 mPa s is better than 1×1^{-3} $kg\,m^{-1}$ or $1\,g\,m^{-1}s$.

It seems to me bad practice to use factors of power of 10 associated with units on graph axes. There is often room for doubt whether the factor is associated with the units or the numerical values. Appropriate prefixes should be used in expressing the units or the scale of numbers should be labelled with powers of 10 in difficult cases. One should try to use numbers in a limited range and absorb factors of 10 into prefixes. Awkward cases have been noted such as $g^2\,cm^{-4}$ s with a scale of 10^{-11} to 10^{-7}; $kg^2s\,m^{-4}$, scale 10^{-5} to 10^{-9}, is surely better, using base units when combinations of units with little physical meaning of size are used. Further improvement is difficult with such wide ranging numerical values. However, 10^{-3} $kmol\,s^{-1}$, 10^{-3} m^3 s^{-1}, 10^{-4} $N\,m^{-2}$, 10^4 $W\,m^{-2}\,K^{-1}$, on axes can be improved to mol s^{-1}, $l\,s^{-1}$, $mN\,m^{-2}$, $kW\,m^{-2}\,K^{-1}$. There seems to be a misguided notion that only base units can be used and that powers of 10 are better than prefixes.

My own guidelines include the following:

1. Use units in common use to help sense of size, i.e. mm rather than dm, l (or L) rather than dm^3, t (tonne) rather than Mg.

2. Do not change prefix for a series of comparable measurements quoted in text or tables. Strict use of prefixes to get numbers between 0.1 and 1000 is not always helpful. Do not mix cm and mm (use mm as in general engineering use). Prefer prefixes n, μ, m, k, M (varying by 10^3) to intermediate prefixes. For volumes prefer l to dm^3, ml to cm^3 but μl or mm^3 to suit text.

3. Avoid prefixes on denominator. Prefer $kg\,m^{-3}$ to $g\,ml^{-1}$, $g\,m^{-2}$ to $mg\,cm^{-2}$.

4. Temperature: use °C for temperatures measured as such in experimental work and not subject to further calculations. Use K in context of thermodynamics or reaction kinetics. In Arrhenius plots use T^{-1}, K^{-1} with scale 0.003 etc. (accepting numbers less than 0.1).

5. Do not mix unit symbols and unit names, i.e. use $g\,l^{-1}$ or gramme per litre not g per litre.

6. Measurements in non-SI units are often best quoted with SI equivalents in parenthesis, if the item is constructed according to British units for example. Silly numbers and spurious accuracy are to be avoided. Quote no more than one extra significant digit in conversions (35 ft gives 10.7 m not 10.668 m).

For exercise try to improve 10^6 Ag (mol), Cu $mol\,cm^{-2}$ $s^{-1} \times 10^9$, Rate $(mol\,cm^{-2}\,s^{-1} \times 10^7)$, k $(cm\,s^{-1}) \times 10^2$, log (Cu) $(mg\,l^{-1})$, 4.9 million hectares.

I am not the first nor will I be the last to consider how best to use SI units. I hope my own experiences which have led to writing this note might be helpful to others.

VOL. 62 1984

REFERENCES

1. BSI PD 5686, 1972.
2. IEEE 268–1975.
3. ASTM E 380-76.
4. McGlashan, M. L., *Physico-Chemical Quantities and Units*, 2nd edn., Royal Society of Chemistry, Monographs for Teachers, No. 15, 1971.
5. IUPAC, *Manual of Symbols and Terminology for Physico-Chemical Quantities and Units*, Pure and Applied Chemistry, Vol. 15, 3rd edn., (Pergamon, Oxford) 1979.
6. Dasher, J., *Using the Modern Metric System*, Mining Engineering, (Feb.) 1981, p. 147–148.

1982–83 DOCTORATES IN CHEMICAL ENGINEERING IN THE UNITED KINGDOM AND IRELAND

The following is a list of authors and titles of PhD theses (with names of research supervisors) in chemical engineering accepted in British and Irish Universities and Polytechnics during the academic year 1982–83. The list is as complete as possible, but we regret any omissions. Some information about earlier years is available in "Index to Theses..." obtainable from ASLIB, 3 Belgrave Square, London SW1 in printed form, or on magnetic tape from Learned Information Ltd, Besselsleigh Road, Abingdon, Oxfordshire. Many theses are held by the British Library, Boston Spa, Yorkshire and can be made available to registered users of this library.

University of Aston in Birmingham

Dr E. K. E. Abusabah. *Chromatographic separation of carbohydrates.* (Prof. P. E. Barker).
Dr M. Altiokka. *Study of sulphation of alpha olefins.* (Prof. G. V. Jeffreys).
Dr S. Baez-Poleo. *Coalescence of secondary dispersions in packed beds.* (Prof. G. V. Jeffreys).
Dr H. W. Cheong. *Drying of small drops of particulate slurries.* (Prof. G. V. Jeffreys).
Dr J. A. Clark. *Recovery of valuable vapour phase solvents using activated charcoal cloth.* (Dr R. G. Temple).
Dr F. A. Dawodu. *Mechanisms of liquid extraction in a pilot plant sieve plate column.* (Dr C. J. Mumford).
Dr A. B. A. Hamid. *Modification of solvents for liquid-liquid extraction processes.* (Prof. G. V. Jeffreys).
Dr A. M. Karim. *Gaseous heat transfer in cross-flow.* (Dr J. K. Maund).
Dr J. Krska. *Kinetic and hydraulic studies in high-rate biological filters.* (Dr E. L. Smith).
Dr A. Kumar. *Velocity distributions in a plate heat exchanger channel.* (Mr A. F. Price).
Dr K. R. Onifade. *Studies of droplet behaviour in spray drying towers.* (Prof. G. V. Jeffreys).
Dr A. F. B. Shafii. *Use of microprocessors in the control of chemical plant with special reference to the use of distributed processors.* (Dr B. Gay).
Dr S. Thawait. *Separation of fructose from carbohydrate mixtures by chromatographic techniques.* (Prof. P. E. Barker).
Dr M. Tsiaparis. *Production of phenol-formaldehyde resin composites.* (Mr A. F. Price).

University of Bath

Dr R. E. Hayes. *Kinetics and carbon deposition studies in methanation.* (Prof. W. J. Thomas).
Dr J. Hernandez. *Catalytic activity and kinetic studies for the hydrodesulphurisation of thiophene.* (Prof. W. J. Thomas).
Dr F. Khan. *Photo-assisted production of hydrogen and ammonia* (Dr P. L. Yue).
Dr V. Y. Loh. *Three-phase mixing in a stirred vessel.* (Dr M. Greaves).

The Queen's University of Belfast

Dr J. Aga. *Colour removal from aqueous solutions using adsorption techniques.* (Dr G. McKay).
Dr M. J. Bino. *Mass transfer processes in the adsorption of industrial pollutants onto activated carbon.* (Dr G. McKay).

University of Birmingham

Dr A. Bahia. *Behaviour of some palladium-rare earth intermetallic catalysis in the vapour-phase hydrogenation of buta-1,3-diene.* (Dr J. M. Winterbottom).
Dr Y. R. Patel. *Effects of variations in growth conditions on strengths and sizes of continuously cultivated microbial cells.* (Dr D. A. J. Wase).
Dr A. K. Vaid. *Cellulase production by a specially isolated and matured Aspergillus fumigatus strain.* (Dr D. A. J. Wase).
Dr B. K. V. Yeo. *Studies of particulate deposition in a finned tube heat exchanger model.* (Dr T. R. Bott).
Dr K. R. Yüregir. *Temperature effects on fluidised bed behaviour.* (Dr J. S. M. Botterill).

correction to last year's list:

Dr C. I. Hussain. *Particulate magnetite fouling from flowing suspensions in simulated heat exchanger tubes.* (Dr T. R. Bott).

University of Bradford

Dr M. Ahmadi-Khalili. *Isotropy of packed powder beds.* (Dr T. Allen).
Dr D. S. Al-Salman. *Stresses generated by particulate solids in a vertical cylinder.* (Dr J. C. Williams).
Dr J. M. R. Carvalho. *Solvent extraction of copper in pulsed sieve-plate columns.* (Dr M. J. Slater).
Dr S. Georghiades. *Heat transfer in polymer processing.* (Prof. M. F. Edwards).
Dr A. A. Jaafari-Asl. *Shuttle heat transfer.* (Dr J. B. Harness).
Dr Y. S. Soo. *Injection moulding of thermoplastic polymers.* (Prof. M. F. Edwards).

University of Cambridge

Dr D. J. Graziano. *Shear induced optical textures in liquid crystalline polymers.* (Dr M. R. Mackley).
Dr H. R. N. Jones. *Mass spectrometry of ions in flames* (Dr A. N. Hayhurst).
Dr K. Hidajat. *Fixed bed adsorption of methyl iodide.* (Dr C. N. Kenney).
Dr J. Lindsay. *Radiative heat transfer in fluidised beds.* (Dr W. Morton).
Dr S. T. Pemberton. *Entrainment from fluidised beds.* (Prof. J. F. Davidson).
Dr M. S. Powell. *Bacterial motility and adhesion and their relevance to contamination mechanisms.* (Dr N. K. H. Slater).
Dr Y. M. Rojas de Puga. *Catalysis of the oxidation of hydrogen chloride.* (Dr C. N. Kenney).

University College, Dublin

Dr J. M. D. MacElroy. *Diffusion of gases in microporous solids.* (Dr J. J. Kelly).

University of Exeter

Dr M. K. Jackson. *Two-phase characteristics of turbulent water jets.* (Dr T. W. Davies).
Dr P. Sobhani. *Theoretical and experimental study of miscible displacement in porous media.* (Drs R. B. Shearn and R. J. Wakeman).

Heriot-Watt University, Edinburgh

Dr J. K. Ali. *Foam in enhanced oil recovery.* (Prof. C. W. Nutt).
Dr G. R. Assar. *Selectivity of bismuth-molybdate catalysts for the oxidation of methane.* (Prof. C. W. Nutt).
Dr J. Clark. *Microencapsulated diets for marine fish larvae.* (Mr K. R. Murray).

Dr A. Klapsis. *Design of self-cleaning aeration tanks for biological application.* (Dr R. Burley).
Dr T. G. P. McHugh. *Fundamental aspects of spouted bed granulation.* (Dr B. Waldie)
Dr T. W. A. Rampling. *Kinetics of coal gasification at high pressure.* (Dr B. Waldie)

University of Leeds

Dr N. Abdullah. *Experimental investigation of a regenerative catalytic reactor.* (Dr P. J. Heggs).
Dr J. S. Abughazaleh. *Study of the autothermal pyrolysis of methane and ethane in a regenerative reactor.* (Dr D. Handley).
Dr E. Amooie-Foumeny. *Heat transfer in cyclic regenerators.* (Dr P. J. Heggs).
Dr J. A. A. de M. e Castro. *Aspects of modelling chemical processes for adaptive control.* (Prof. C. McGreavy).
Dr C. Y. Chan. *Modelling of the oil-free single screw compressor.* (Prof. G. G. Haselden).
Dr K. E. Connelly. *Development of a baffled distillation tray system.* (Prof. G. G. Haselden).
Dr G. H. Tan. *Influence of capacitances on distillation column dynamics.* (Prof. C. McGreavy).
Dr K. S. Teo. *Optimisation of baffle tray design.* (Prof. G. G. Haselden).

University College, London

Dr F. J. V. Alonso. *Influence of dissolved oxygen tension on the synthesis of catechol-1,2-dioxygenase in Pseudomonas putida.* (Prof. M. D. Lilly).
Dr R. A. Wisdom. *The interesterification of triglycerides by immobilised microbial lipases.* (Dr P. Dunnill).

University of Technology, Loughborough

Dr E. E. A. H. Baddar. *Emulsion polymerisation in a continuous flow stirred reactor.* (Dr B. W. Brooks).
Dr D. Burfoot. *Turbulent single phase forced convection heat transfer and pressure drop characteristics of circular ducts containing swirl flow inducers on pull rings.* (Dr P. Rice).
Dr A. A. Caldwell. *Propagation of a mechanical impulse in a granular medium.* (Mr B. Scarlett).
Dr M. A. Jasim. *Functional plastein from fish waste.* (Prof. J. Mann).
Dr R. Sibbett. *Effect of particle size on electrostatic powder coating.* (Mr. P. J. Lloyd).

University of Manchester Institute of Science and Technology (UMIST)

(Including doctorates awarded 1981–82).

Dr M. Abdel-Ghani. *Coalescence and flow of secondary dispersions in fibre beds.* (Dr G. A. Davies).
Dr M. S. Ali. *Experimental studies of convective mass transfer in an electrochemical reactor with particular reference to the effects of gas agitation.* (Dr D. J. Pickett).
Dr R. Al-Husseini. *Estimation of mass transfer model parameters from concentration profile measurements in a liquid-liquid extraction column.* (Dr W. J. Korchinsky).
Dr T. D. Boardman. *Conversion of piggery waste to microbial protein.* (Dr D. E. Brown).
Dr A. G. R. Jeganathan. *Mass transfer studies in a pilot plant distillation column.* (Dr R. Bragg).
Dr A. K. Shah. *Condensation of vapours on a horizonatal tube bank.* (Dr D. R. Webb).
Dr F. Sweis. *Dust explosion studies.* (Dr C. G. Sinclair).

University of Newcastle upon Tyne

Dr J. O. Bello. *Liquid-liquid extraction of metal ions in electric fields.* (Prof. J. D. Thornton).
Dr S. G. E. Denis. *Control of a fluidised bed electrochemical reactor.* (Prof. F. Goodridge).
Dr K. J. Forster. *Development of a combined backwash and extraction unit for metal extraction.* (Prof. J. D. Thornton).
Dr G. Vassallo. *Holdup, droplet size and backmixing in a pulsed perforated-plate column.* (Prof. J. D. Thornton).

University of Nottingham

Dr N. J. A. Edmonds. *General model for cooler-condensers in nitric acid plants.* (Dr J. A. Wilson).

University of Salford

Dr S. S. Adefila. *Studies on high temperature heat pump systems.* (Prof. F. A. Holland).
Dr R. C. Marrow. *Use of gas in low energy dwellings of high thermal capacity.* (Dr R. Pritchard).
Dr C. Moraes. *Oscillatory behaviour in the catalytic oxidation of carbon monoxide.* (Dr R. Hughes).
Dr M. I. Pathan. *Study of heat transfer in liquid-solid and three-phase fluidised beds.* (Dr J. B. Stepanek).
Dr B. E. Siddig-Mohammed. *Performance studies on a reversed absorption heat pump.* (Prof. F. A. Holland and Mr F. A. Watson).
Dr P. C. P. Wong. *Measurement and analysis of thermal protection in diving.* (Dr R. Hughes).

University of Sheffield

Dr S. Babajan. *Energy integration of distillation trains.* (Dr G. L. Wells).
Dr M. Brikci-Nigassa. *Pilot scale study of monosized coal combustion in a fluidised bed combustor.* (Dr A. B. Hedley).
Dr P. R. Ereaut. *Simultaneous size and velocity measurements of droplets in fuel sprays, using laser doppler anemometry.* (Dr N. A. Chigier and Prof. J. Swithenbank).
Dr M. R. Gibbons. *Study of the kinetics of the decomposition of methyl chloride and the formation of pyrolytic carbon.* (Dr K. Littlewood).
Dr H. S. I. Naji. *Cavitation in directed jet devices.* (Prof. J. Swithenbank).
Dr D. O. Onwu. *Kinetics of coal devolatilisation and gasification in a fast fluidised bed.* (Dr N. A. Chigier and Dr K. Littlewood).
Dr M. P. Subzwari. *Atmospheric and pressurised rotating fluidised bed combustion.* (Prof. J. Swithenbank).

University of Strathclyde

Dr S. D. Cave. *Effect of growth rate and carbon dioxide on the growth, physiology and intracellular biochemistry of the filamentous mould Aspergillus nidulans.* (Dr J. R. Todd and Prof. J. E. Smith).

University of Surrey

Dr K. Morris. *Vibratory cleaning of flat geometry dust filters.* (Dr C. A. Millington).
Dr M. S. Chauhdry. *Excess volumes of mixing of some binary aqueous mixtures at pressures up to 2.2 kbar.* (Dr J. A. Lamb).
Dr N. J. Warren. *Mathematical model of simultaneous heat and mass transfer in a rigid porous material during the falling rate period of drying.* (Dr R. J. Litchfield).

University College of Swansea

Dr M. Ahmed. *Bubble coalescence in gas-liquid reactors: a study of coalescence between the bubbles growing from adjacent orifices.* (Dr J. C. Lee).
Dr S. F. Azevedo. *Modelling and operation of a tubular fixed-bed catalytic reactor.* (Dr A. P. Wardle).
Dr K. M. Hamilton. *Continuous lactic acid fermentation in a hollow fibre reactor.* (Dr J. A. Howell).
Dr A. L. Herrera-Zeppelin. *Production and kinetics of Trichoderma Reesei Cellulase.* (Dr J. A. Howell).
Dr M. S. Le. *Membrane ultrafiltration fouling and treatment.* (Dr J. A. Howell).
Dr K. Nezhati. *Heat transfer and power consumption in an agitated vessel.* (Mr R. K. Sinnott).
Dr K. Rashid. *Finite element analysis, non-Newtonian flow and heat transfer: some engineering applications.* (Dr J. F. T. Pittman).

Teeside Polytechnic

Dr A. Ahmed. *Studies in the solvent extraction of metals.* (Dr M. M. Anwar and Dr D. W. Pritchard).
Dr R. Chowdhury. *Some studies of the differential vapour absorption process.* (Prof. C. Hanson, University of Bradford, Dr M. M. Anwar and Dr D. W. Pritchard).
Dr J. M. Tuffnell. *Studies on amino acid assays using E. coli.* (Dr J. W. Payne, University of Durham).

Polytechnic of Wales

Dr D. P. Jenkins. *Investigation into the suitability of coal/oil and other slurries on blast furnace tuyere injectants.* (Dr C. Davies).

VOL. 62 1984

CHEMICAL ENGINEERING RESEARCH & DESIGN

Transactions of The Institution of Chemical Engineers

EDITORIAL

The Editorial Board would like to express its gratitude to the Yorkshire Branch of the Institution whose generous financial support has made it possible to publish extra pages in this issue. The Branch's support will also make it possible to publish extra pages in future issues of the journal.

The Review Paper "Development and potential of power fluidics for process flow control" by G. H. Priestman and J. R. Tippetts covers a topic which may be less than familiar to many chemical engineers. Developed mainly for applications in the nuclear industry where maintenance-free reliability is very important, power fluidics may nevertheless find application by designers in other process industries.

"Kinetic analysis of the catalytic dehydration of alcohols over zeolites" by P. L. Yue and O. Olaofe reports a study of the dehydration of ethanol, isopropanol and n-butanol over three commercial zeolites. In almost all cases both olefin and ether were formed. Simple power-law rate models satisfactorily represent the kinetics of olefin formation and most cases of ether formation. Olefin kinetics can also be modelled by the Hougen–Watson type of rate expression and ether formation by the Langmuir–Hinshelwood and Rideal–Eley mechanisms.

R. W. Burley, C. W. Nutt and M. Gh. Bayat report on "Studies of fluid displacement by foam in porous media". Comparison of the displacement efficiencies of water and oil by gas-drive from beds of sand with and without the presence of a surfactant showed that the surfactant enhanced the displacement efficiency of both fluids. The paper contains many interesting data which are of course pertinent to the problems of enhanced recovery from oil fields.

In "Fault tree synthesis based on control loop structure" A. Shafaghi, P. K. Andow and F. P. Lees consider fault tree synthesis by modelling the control loop structure of a plant rather than by modelling the plant units. An example of the manual development of a fault tree by this method is given. The authors state however that the technique can also be applied in a computer-based synthesis. The method has the advantage of producing fault trees with a clearer structure.

In "Liquid passage on sieve trays operating in the spray regime" J. A. Raper, W. V. Pinczewski and C. J. D. Fell report residence time distributions on sieve trays operating in the spray regime. The authors conclude that a pool of liquid builds up near the exit weir and flows back along the tray floor. Consequently residence time distributions should be measured by tracer injection at the inlet weir and tracer monitoring at the outlet weir. Implications for the design of industrial trays are considered.

K. R. Davey and D. G. Wood report on "Laboratory evaluation of Lin's model of continuous sterilisation of micro-organisms". Solutions of carbapol containing the organism *E. coli* were sterilised continuously by steam injection. Results are compared with Lin's model obtained from heating similar solutions in such small diameter tubes. The authors conclude that Lin's simple flow model based on kinetic data from capillary tubes is not applicable to sterilisation by steam injection.

"Power consumption in the mixing of Boger fluids" is considered by D. R. Oliver, A. W. Nienow, R. J. Mitson and K. Terry. Boger fluids are highly elastic fluids with a constant shear viscosity. The higher-viscosity Boger fluids gave significantly reduced power numbers in the laminar region but an abrupt transition to higher power numbers at moderate Reynolds numbers. It is suggested that centripetal forces due to elasticity oppose centrifugal effects at low speeds and reduce power consumption. At the transition point elastic forces suddenly become dominant. For less viscous Boger fluids the transition is not clearly defined.

D. Burfoot and P. Rice report on "Heat transfer and pressure drop characteristics of alternate rotation swirl-flow inducers in a circular duct". Data for a range of insert spacings and arrangements are presented and compared with those of other workers. Results are correlated in terms of a friction factor ratio and a heat transfer factor ratio. Of particular interest is that alignment of the leading edges of the inserts reduced the pressure drop significantly with a lesser reduction in heat transfer.

In a Shorter Communication, W. K. Shieh and C. Y. Chen report on the fluidisation behaviour of particles consisting of a support medium carrying a film of biologically active material (bioparticles). They conclude that the Richardson–Zaki correlation provides a good description of the fluidisation behaviour and that the settling velocity and expansion index are functions of the Galileo number.

Brian Gay
Honorary Editor

Notes for Authors

Editorial Policy and Standards

1. Papers published in the Journal will be original contributions to chemical engineering knowledge, not previously published. In particular, the Editorial Board encourages the submission of papers which show how the results of research may be used in chemical engineering design. Such implications for design should be brought out clearly in the paper and its summary.

Accounts of research work of an experimental or theoretical nature which throw new light on established principles, which identify problems not yet solved, or indicate practical areas to which research effort may usefully be applied are also invited. Reports from industry and from research establishments are particularly welcome.

Papers may also deal with new developments of plant or processes if these developments are related to underlying principles and can be given quantitative expression.

2. Authors need not be members of the Institution. Papers must be in English and should normally be of 2500 to 5000 words, including Appendices. Figures should also be included in this count, each being estimated as equivalent to 250 words.

3. The Editorial Board will, however, also welcome Shorter Communications (less than 2500 words) for consideration for publication; these would describe, for example, novel research techniques, new analyses of previous work, or interesting aspects of work still in progress. A faster refereeing procedure has been arranged for such short Papers.

4. The Journal also publishes a limited number of longer Review Papers, which are critical assessments of previously published work in a selected area of chemical engineering. In conformity with editorial policy, Reviews should show how the results of research can be used in the design of plant and equipment.

Most Reviews are specially commissioned by the Editorial Board, but authors are also invited to offer Reviews for consideration for publication. In view of the substantial effort required, authors are advised to communicate with the Editor before embarking on a Review.

5. It is the policy of The Institution to publish only papers of the highest quality. To help maintain these standards all papers submitted are sent to referees familiar with the branch of chemical engineering covered. They advise as to whether the paper is acceptable or not and, in addition, indicate to the author possible ways in which, in their opinion, the paper might be improved. The final decision on publication is taken by the Editor in light of this advice.

Manuscript Requirements

1. The text should be typewritten, using one side of the paper only, double-spaced and with adequate margins to allow for revision and copy preparation marks. A summary, preceding the text, should briefly describe the essential original contents of the paper.

2. Mathematical expressions can sometimes be more easily interpreted by the printer if carefully written by hand. Where many equations appear, a list of symbols used should be inserted at the end of the paper, before the references. SI units should *always* be used; the negative index notation is preferred to the oblique stroke.

3. References are listed in the order in which they are first cited in the text, where they are indicated by superscript numbers. They should give in order: Authors' surnames and initials, Year, Title of book or journal, Volume, Issue, Page numbers , followed by name and town of publisher in the case of a book.

4. Tables, drawings and photographs should be on separate sheets at the end of the manuscript and not interspersed in the text. Tabulated data should not duplicate values detailed in the text or on graphs. Drawings submitted should be clear and complete and preferably in a form suitable for direct reproduction. Photographs should be restricted to the minimum necessary.

5. Where limitations of space preclude publication of detailed results, mathematical derivations, etc, authors are invited to include in their paper a statement that this information is available from them on application. Authors may make an appropriate charge for supplying items requested in this way. Such material should be supplied with the paper when submitted to the Editor.

Submission of Papers

1. Three copies of the paper should be sent to:

The Editor, Chemical Engineering Research and Design,
Institution of Chemical Engineers,
George E. Davis Building,
165–171 Railway Terrace,
Rugby CV21 3HQ, England.

or to an Associate Editor as follows:

Australia:
Prof R. G. H. Prince,
Department of Chemical Engineering,
University of Sydney,
Sydney 2006, New South Wales, Australia.

Continental Europe:
Prof Dr J. R. Bourne,
Technisch-Chemisches Laboratorium,
ETH-Zentrum,
CH-8092 Zürich, Switzerland.

Continental Europe:
Prof J. M. Smith,
Laboratorium voor Fysische Technologie,
Technische Hogeschool Delft,
Prins Bernhardlaan 6,
2628 BW Delft, Holland.

India:
Prof M. M. Sharma,
Department of Chemical Technology,
University of Bombay,
Matunga Road,
Bombay 400 019, India.

New Zealand:
Prof R. B. Keey,
School of Engineering,
University of Canterbury,
Christchurch 1, New Zealand.

USA:
Prof J. O. Wilkes,
Department of Chemical Engineering,
University of Michigan,
Ann Arbor,
Michigan 48109, USA.

2. A full address to which readers may send correspondence should be specified, including the post code. The address at which the work was carried out, if different, should also be indicated. Where there are several authors, one should be nominated to check proofs and to receive all correspondence.

3. A proof will be sent to the nominated author, to be checked for possible typographical errors. Other alterations cannot be incorporated at this late stage without incurring higher printing costs, and extensive alterations would necessitate postponement of publication of the paper to a later issue.

4. Following publication the nominated author will receive 50 off-prints of the paper (or 25 where there is just one author). Any further off-prints required should be ordered at proof stage. Reprints, ordered after publication, are more expensive.

VOL.
62
1984

REVIEW PAPER

DEVELOPMENT AND POTENTIAL OF POWER FLUIDICS FOR PROCESS FLOW CONTROL

By G. H. PRIESTMAN (GRADUATE) and J. R. TIPPETTS
Department of Chemical Engineering and Fuel Technology, Sheffield University

Power fluidics uses no moving parts and relies for its effectiveness upon fluid dynamic phenomena. This paper is an overall review and unification of the wide variety of power fluidic components and systems which have been developed, in particular during the last decade. The current major applications are indicated as are performance capabilities and limitations. An objective is to demonstrate the potential of no-moving-part power fluidics for process flow control and to promote its wider use.

INTRODUCTION

Power fluidics is the engineering of no-moving-part components and systems in which fluid dynamic effects are used to manipulate a fluid important for its energy or chemical content. This distinguishes it from signal fluidics in which the fluid is important solely for its information content.

Without moving parts, fluidics must rely for its effectiveness upon the use of fluid energy, either that inherent in the fluid being handled or that specifically introduced by, for example a control fluid. A wide range of fluid dynamic phenomena can be employed to utilise this energy, the fluid vortex, the directed jet, the Coanda effect and flow diffusion being common examples.

To date a major part of the work in power fluidics has been in component development, maximising the effects to be gained from the fluid dynamics and combining those effects to form more sophisticated components. Although there is certainly still scope for improvement and innovation in component design, an increasingly important development area is in the evolution and design of multicomponent power fluidic systems, such as fluidic pumping and ventilation systems. In fluidic system design not only is it important to know component characteristics and the limitations imposed by cavitation or compressibility effects, but also how the component effects interact, with overall system stability being of prime importance.

When deciding whether or not to apply power fluidics, in many instances the advice must be don't. In these cases the advatages often associated with conventional moving part fluid handling of total effectiveness, stability and relatively high efficiency, outweigh the susceptibility to mechanical wear or failure, and the sometimes slow system response. In other cases the application of fluidics is not viable. There are, however a significant number of cases in which the advantages offered by power fluidics outweigh other considerations. Many such instances have already been identified, but the potential for much wider application can only be fully exploited through a much wider knowledge and understanding of the possibilities offered by power fluidics.

Probably the first application of power fluidics was by the Romans[1]. They used the simplest fluidic component, the resistance, in the form of pieces of bronze pipe of specified length and diameter. These were installed at set positions on main supply tanks and aqueducts to regulate individual water supplies in Rome. There is strong indication that they also inadvertently took advantage of the Venturi effect to increase the flowrate by placing divergent pipe sections immediately downstream of the resistance.

The advantages associated with power fluidics first became apparent in the mid-nineteenth century with the advent of Giffard's water injector[2]. This was used 'to feed steam boilers by a self-acting apparatus, without the intervention of machinery and free from the liability to wear and tear incidental to machinery in motion'. The steam ejector proved so successful that it was widely adopted for locomotive boilers and some years later was reported[3] to have almost universally replaced conventional feed pumps on most boiler systems. The ejector or jet pump is now a commonly used power fluidic component although it is normally not classed as such. There are available many other power fluidic components which could prove to be equally useful.

Design criteria and performance capabilities of fluidic components and systems are presented in this paper together with their current applications and advantages. Clearly it is not possible to present all the available information, but an attempt is made to include the major details.

THE DIFFUSER

Although generally widely understood a brief outline of diffusing elements is included here because they often

© Institution of Chemical Engineers

form an integral part of more complex fluidic components. It also serves as a useful introduction to parameters often used to describe fluidic devices and to indicate the importance of cavitation and compressibility effects.

Diffuser performance can be simply described by a flow Euler number, *Eu*, based upon the liquid velocity at the throat, v:

$$Eu = \Delta P / 0.5\ \rho v^2 \tag{1}$$

The efficiency of pressure recovery in conical diffusers depends mainly upon the angle of cone divergence and the fluid inlet velocity profile and boundary layer thickness. The latter factors result in a variation of efficiency with Reynolds Number, *Re*. Gibson[4,5] found the most efficient total cone angle to be about 6 to 8°. Moller[6] and Ackeret[7] reported the effect of *Re*. For a straight 8° diffuser with favourable inlet conditions and non-cavitating incompressible flow, *Eu* rises slowly from about 0.1 at $Re \simeq 3 \times 10^5$ to about 0.2 at $Re \simeq 3 \times 10^4$, with more rapid increase at lower *Re*.

The radial diffuser, in which diffusion occurs between two parallel discs, can achieve performance almost comparable to that of a conical diffuser with a similar dependence[6] upon inlet conditions and *Re*.

For liquid flow, diffuser performance is limited by cavitation, which occurs when the static pressure at the throat falls to the liquid vapour pressure. This limits the throat velocity to a value, v_m, dependent upon the upstream absolute pressure and liquid vapour pressure, and independent of the downstream pressure:

$$v_m^2 = 2\, e_v / \rho\, Eu_c \tag{2}$$

The cavitating Euler number, Eu_c, accounts for any departure from the ideal represented by Bernoulli's Theorem, and is normally just greater than 1.

For compressible flow, performance is limited by the transition to sonic flow at the throat, which is induced prematurely by the static pressure gradient in the diffuser. The sonic mass flowrate is independent of downstream conditions in an analogous manner to the cavitation flow limit.

When a diffuser is used for flow in the reverse direction the throat acts as a sudden expansion, with *Eu* about 0.8 for a diameter ratio of 3. The diffuser can therefore be used as a fluid diode. Fluid 'diodicity', D, is normally defined as the ratio of forward to reverse flow at the same pressure drop:

$$D = \frac{Q_f}{Q_r} = \left(\frac{Eu_r}{Eu_f}\right)^{0.5} \tag{3}$$

When *Eu* varies with *Re* this differs from diodicity based upon the square root of pressure ratio at a given flow. From equation (3) it follows that a diffuser has a maximum diodicity of almost 3. Despite this performance limitation the simplicity of the diffuser can sometimes still make it an attractive diode. For example, Petermann and Kosyna[8] developed a 2-diode pump using conical diffusers to pump molten steel.

HIGH 'RESISTANCE' AND THE FLUID DIODE

The use of a sufficiently small restriction to provide a large pressure drop is sometimes excluded by the possibility of fouling or blockage, or by the need to have a low pressure drop when the flow is in the opposite direction. For such elements a good measure of performance in relation to susceptibility to blockage, is *Eu* based upon fluid velocity at the minimum flow area, which for a simple orifice restriction is about 1.0. Diodicity is also important for bi-directional flows.

Fluidic Throttles

The most effective fluidic flow retardant is that based upon the pressure drop across a vortex, a concept first developed in early pioneering work by Thoma[9], Heim[10] and Zobel[11]. Consider a simple vortex chamber of diameter d_c with a tangential port of diameter d_t and a single axial port of diameter d_a, as shown in Figure 1(*a*). For a frictionless incompressible vortex, the tangential velocity at the chamber periphery, v_1, is related to that at the axial port, v_2, by:

$$v_1 d_c = v_2 d_a \tag{4}$$

Applying the ideal Bernoulli equation across the chamber therefore gives an Euler number, Eu_v, based upon the tangential port throat fluid velocity, v_t, of:

$$Eu_v = (d_c/d_a)^2 - 1 \tag{5}$$

In practice Eu_v is limited both by a velocity recovery factor, α, between v_t and v_1, and by a circulation factor, τ, due to chamber friction losses. This gives:

$$Eu_v = (\alpha\tau\, d_c/d_a)^2 + 1 - 2\,\alpha^2 \tag{6}$$

Work by Bichara and Orner[12] and Wormley[13] enables α and τ to be related to chamber geometry, friction coefficients, *Re*, and empirically to a modified boundary layer coefficient.

For a simple design similar to that shown in Figure 1(*a*), with chamber height $h \simeq d_t \simeq d_a$, the maximum value of Eu_v for non-cavitating, incompressible flow has been found[14] to be about 40. This performance is very good, giving a minimum hole size about 2.5 times the orifice size required to give the same presure drop. A vortex throttle of this very basic type of design has been developed successfully in North America and Canada for sewer flood control[15]. Brombach[16–18] has developed a sophisticated range of vortex throttles. One of these is the bistable vortex throttle[16,17], developed for flood control in combined waste and sewerage systems and shown schematically in Figure 1(*b*). At low flows no vortex is formed and the device acts as a normal elbow with relatively low resistance. The inclined cone design prevents any solids accumulation in this state. At a critical flow a vortex is formed and the resistance increases accordingly. The device is therefore a crude form of constant flow controller. Special advantages in this



Figure 1. Vortex throttles and Diodes (*a*) Basic throttle (*b*) Brombach throttle (*c*) Zobel diode.

VOL. 62 1984

application are the peak low head flow which helps to flush the system and the mixing and aeration provided in the vortex state which increases oxygenation, aiding subsequent treatment processes.

Another use of vortex throttles is in sampling, where bleeding a small flow from a high pressure main stream can present blockage problems. Basic vortex throttles with their relatively large minimum hole size have been successfully applied in this field. The throttles can be used singly or in series.

The high *Eu* of vortex devices makes them a useful component in developing fluidic circuits. The increase in *Eu* with *Re* is a particularly useful property. Over a certain *Re* range an increase in viscosity can result in a decrease in flow resistance[11], offering scope for detecting temperature changes for example, or if suitably combined with a normal resistance, the formation of viscosity-independent flow controllers.

Of course the most common use of a vortex-based fluidic device is the standard cyclone separator, although the vortex pressure drop is often not specifically exploited in this application.

Fluidic Diodes

For certain applications the size of the throttling device is determined not so much by blockage considerations, but by the requirement to offer a low resistance to flow in the opposite direction, thus requiring a component with good diodicity.

Early work by Zobel[11] did much to optimise vortex diodes and his optimum design is still often regarded as the best available compromise between good performance and ease of manufacture. Figure 1(*c*) indicates the Zobel type of design. The chamber peripheral edge is rounded and vanes placed in the axial port to increase vortex flow pressure drop, normally termed 'reverse flow'. To decrease the resistance to the opposite 'forward flow', conical diffusers are introduced at the axial and tangential ports and the tangential port entry region is rounded. The vortex chamber is relatively 'thick', $h \simeq d_t$, so no significant radial diffusion occurs. The axial port normally represents the minimum area, $d_a \simeq 0.8\, d_t$, so the forward and reverse Euler numbers are based upon the axial port fluid velocity.

The variation of Eu_f and Eu_r with *Re* for Zobel's optimum design is shown in Figure 2. Although Eu_r is lower than for a basic vortex throttle, the low value of Eu_f gives a much improved diodicity of almost 11, compared with about 3.5 for a vortex throttle and only 3 for a conical diffuser.

For liquid flow, cavitation reduces vortex diode performance, as indicated in Figure 2 using the Thoma cavitation parameter σ. Reverse flow cavitation produces a vapour core at the centre of the vortex which extends down the axial port. The resulting degradation of performance has not yet been successfully correlated. Its relative effect, however, is much less significant than that of cavitation on forward flow performance. Both cavitating and non-cavitating forward flow performance have been correlated[19,20], based largely upon analysis of the diffuser flow.

Other types of vortex diode have been developed by Syred *et al*[21–23]. One design, referred to as a catherine wheel diode, has multiple tangential ports, a thin radially diffusing chamber and either one or two axial ports. For certain flow conditions it is claimed to have performance superior to that of the Zobel diode, although, for the same pressure drop it has been shown[24] to have very similar diodicity. Thin chamber diodes are generally more difficult to manufacture and more prone to blockage.

Zobel[11] tested diodes with steam and found the performance to be similar to that with water. George *et al.*[25] also tested vortex diodes with compressible flow and again reported relatively good performance. Some work on the transient response of vortex diodes has been done by Jacobs and Baker[26].

Besides vortex diodes and the diffuser, other types of fluidic diode have been developed. These include the scroll diode[27], the cascade diode[28] and the momentum flueric diode[29]. None of these devices, however, can match the overall performance of the vortex diode[30,31], and they can be difficult to manufacture.

The fluidic diode was first developed as a form of non-return valve[11], and there is much scope for application in this role. Grant *et al.*[32,33] introduced its use for plant protection. A fluidic diode on the inlet to a pressure vessel for example greatly reduces leakage in the event of a pipe failure. Grant[34] describes the main advantages of fluidic protection systems; high reliability, no power requirement and fast response with no associated shock, and indicates how effectiveness can be further improved by combining the diode with con-

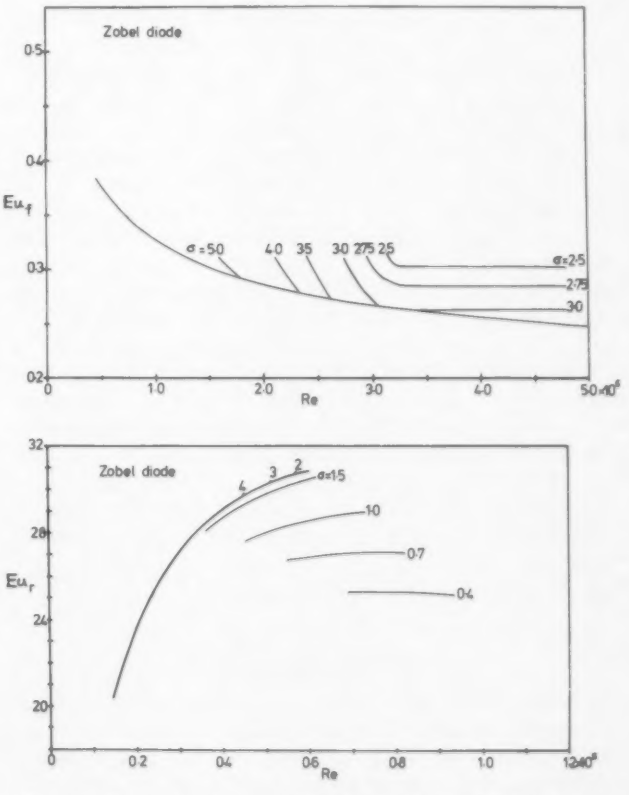


Figure 2. Forward and reverse flow characteristics of Zobel diode.

ventional valves or fluidic diverters, or by upgrading it to a vortex amplifier. Diodes have been applied to AGR protection following work by George *et al.*[25] Mori and Premoli[35] tested diodes for PWR protection.

The vortex diode has been used in hydro-electric plant, as described by Gspan[36]. The diodes, up to 8 m in diameter, dissipate fluid energy associated with surge oscillation.

A major application of fluidic diodes is as a replacement for conventional non-return valves in displacement pumping systems, as investigated by McGuigan and Boucher[37]. Although not as effective as moving part valves, their maintenance-free reliability makes them attractive for many pumping applications. Fluid rectifiers based both upon fluidic diodes and upon other specifically designed fluidic components, are described in the discussion of fluidic pumping systems. The fluidic diode is also a useful component for other fluidic circuit systems, particularly for cavitation suppression.

THE FLUID AMPLIFIER

Although we can trace various fluidic devices such as diodes and jet pumps back into a 'pre-fluidic' era it was only when 'fluid amplifiers' were invented, *circa* 1959, that fluidics could evolve as a distinct technology. The inventions which initiated fluidics occurred in the Harry Diamond Labs as described by Kirshner[38,39] in response to a need by the US military for very reliable control systems. The significance of 'fluid amplification' was emphasised by Billy M. Horton, at that time the leader of the HDL group: without devices which could amplify fluid signals, only the most trivial systems could be made, but with fluid amplifiers a whole new field analogous to electronics could be contemplated.

Various physical effects can provide the amplification so there are many types of fluid amplifier which embody these effects in differing ways. These devices now tend to be referred to by more specific names: vortex amplifiers, wall-attachment amplifiers, directed-jet elements, etc. In the early 1960's their signal-amplifying properties commanded great attention especially from the control engineering fraternity, but the significance of amplification may not be very apparent to those wishing to handle process fluids. In fact amplification is just as essential in the fluids handling field (or 'power fluidics') as in signal processing, but other attributes which are sometimes harder to get are needed also. For example, in a fluidic wall-attachment amplifier used as a flow diverter its amplifying ability means that only a very small brief signal is needed to control it, but this is fairly easily achieved. The more demanding task is to design the diverter to match the system that it connects to, so that the fluid goes where it is supposed to go without incurring excessive pressure losses.

Vortex Amplifiers

The vortex amplifier or 'VA' can be regarded as being derived from the vortex diode in that a vortex is used to impede fluid flow. Figure 3 shows the basis of VA design. Flow into the control port forms a vortex which increases the resistance to the main radial flow from the supply port to the outlet port. Sufficient control pressure can stop or reverse the main supply flow.

The characteristics of a typical VA are often given in the form shown in Figure 3 where the supply flow and the control flow are functions of the control pressure. The supply pressure is constant and the outlet is the datum for the pressures. The control pressure is normalised with respect to the supply pressure and the flows are expressed as fractions of the maximum supply flow.

A measure of performance or flow amplification is the 'turndown ratio' T given by

$$T = \frac{\text{supply flow (with } q_c = 0)}{\text{control flow (with } q_s = 0)} \left.\begin{matrix}\\\\\end{matrix}\right\} \begin{matrix}\text{for the same supply–}\\\text{outlet pressure drop}\end{matrix} \qquad (7)$$

Values of T up to 25 are possible but it is unlikely that very much higher values could be obtained, so generally the gain of the VA is not as great as for electronic devices such as transistors.

An important feature of the VA is the fact that control flow must be forced into it from a pressure higher than that at the supply port. This is in strong contrast to transistors (over most of their operating range) and means that VA circuits have to be designed to accommodate this limitation.

The type of flow regime influences the design and performance of VAs. If incompressible non-cavitating conditions prevail then a conical diffuser can be used in

VOL. 62 1984

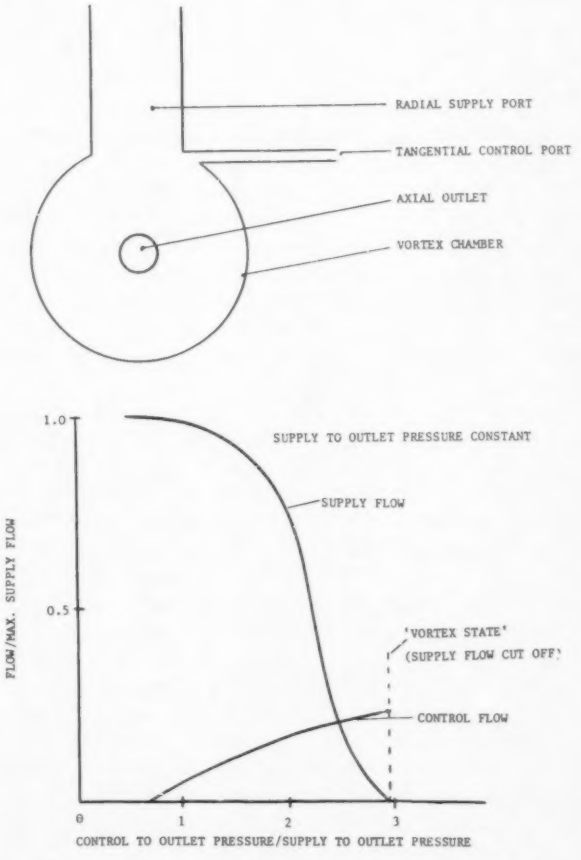


Figure 3. Basic vortex amplifier design and characteristics.

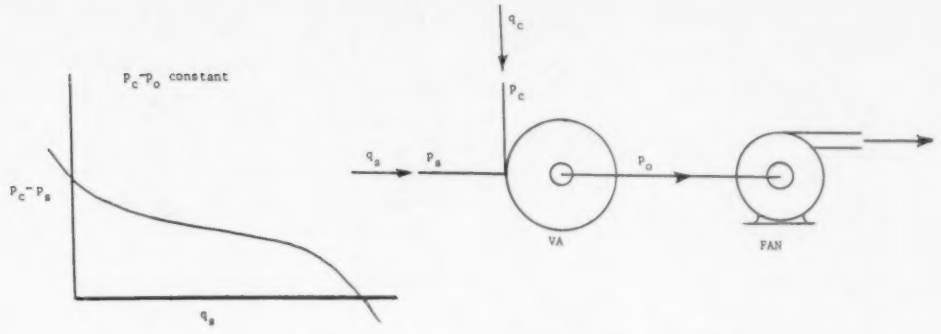


Figure 4. Vortex amplifier characteristics, constant control-to-outlet pressure.

the outlet from the vortex chamber. This greatly improves performance because its resistance to flow is smaller than an equivalent orifice for non-swirling flow. For vortex flow the resistance is only slightly less than that of an orifice so diffusers enable VAs to have T values of near to 20. The onset of cavitation or sonic choking in these outlet diffusers greatly reduces performance (by a factor of 2 or more). Effective operation under highly compressible conditions is however perfectly possible and the Bendix Corporation developed many VA power control systems[40-42] using gas at high pressures and in some cases high temperatures. In one system for missile thrust vectoring a multistage VA circuit controlled the flow from a solid fuel rocket motor. The main VA was made of silver-infiltrated tungsten to withstand what is probably the most aggressive 'fluid' likely to be encountered in power systems.

The response time of a VA is approximately that needed to replace the flow field in the vortex chamber. This usually means that the response is very fast by comparison with moving part devices, but, of course, in common with any other controller, the overall system response depends on the other circuit components also.

Fundamental information about VAs and VA circuits, mainly for pneumatic power control, is described by Taplin and Mayer[40-42] of the Bendix Corporation. Other sources of detailed design and performance data on VAs are Wormley[43], Syred[44] and Saunders[45].

The practical design of the VA can vary considerably depending on the type of application. Small VAs (about 30 mm diam.) controlling pneumatic power may consist essentially of a straight-walled cylindrical chamber with one or two inlets and control ports, this being easy to form from machined solid or laminate. For large airflows, as used in ventilation systems, the VA may be fabricated from welded steel sheet, the objective being to minimise machined components; curvilinear contours, however, are fairly easily incorporated. VAs of this latter type[46], are made in sizes up to 1.2 m across for handling low pressure air flows up to 140 $m^3\ min^{-1}$.

Consideration of the VA in ventilation systems shows up a common requirement in fluidic technology: the need to represent the operation of a device in the most appropriate way for the application. It is therefore very useful to put the characteristics of the VA in the alternative form shown in Figure 4. Here the pressure drop between the control port and the supply port is given as a function of supply flow while the control-to-outlet pressure is constant. This closely represents the result of drawing air through a VA with a fan thereby converting the suction characteristic of the fan to a new characteristic at the supply port of the VA having the form given in Figure 4. In a typical extract ventilation system suction is 'distributed' from a single centralised fan complex to various regions such as glove boxes, reaction vessels or rooms. Each region is connected through a VA which acts as a 'pressure' regulator for maintaining specific small values of vacuum (e.g. – 0.3 kPa gauge) despite changes in the extracted flow. This mode of control is being used in UK nuclear fuel reprocessing plants and within this specialised but important and demanding field the VA has advantages of cost, speed-of-response and above all reliability.

The VA is usually regarded as being a flow amplifier and to some extent its amplification can be chosen by appropriately specifying the size of the control jets. Small jets require less control flow and give high flow gain but a law of diminishing returns eventually sets in so that the maximum possible flow gain is of the order of 25. The penalty is very greatly increased control pressure. The scope for increased flow gain is greatly improved, however, by using a jet pump[46] to supply the control flow to the VA as shown in the two alternative circuits in Figure 5. In both circuits the jet pump entrains flow from within the circuit so there are still only three pipe connections to it overall, but the entrainment can be either from upstream or downstream of the VA. The main effect is a greatly increased flow gain (circa 200 in one application) but the two circuits have distinctive characteristics which suit them to particular applications. Thus the upstream entrainment connection has been used as a pressure relief valve in ventilation systems by supplying the jet pump with a fixed flow of compressed air. This maintains a vortex in the VA and establishes a fairly distinct pressure drop below which the through-flow resistance is very high. At higher pressure-drops the resistance is very low so the circuit provides the desired function of a relief valve.

The downstream entrainment connection can be used again with a constant jet pump supply flow but in this case as a pressure regulator. This is because the pressure-drop produced by the VA is more constant over a wide range of through-flow than in the relief valve circuit. The mode of operation is similar, however.

Both types of circuit have been developed for use in ventilation systems which typically enable 30 L min^{-1} of

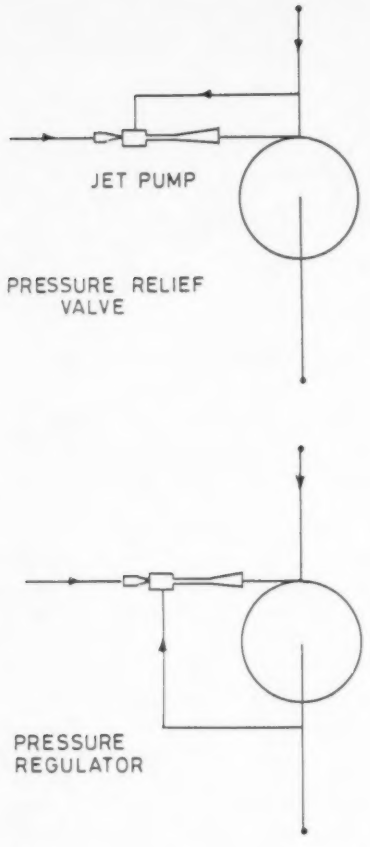


Figure 5. Control valves using jet pump and vortex amplifier.

compressed air to control air flows of the order of 6 m^3 min^{-1}.

Another configuration for the VA produces a more compact device by having a primarily axial flow path. The flow passes around a centre-body upstream of a converging-diverging section, control flow being introduced just upstream of the convergence. These 'axial VAs' were investigated in detail by Al Shamma[47,48] who obtained reasonably good performance (T up to 13) with very compact pipe-like devices. Their operation, however depends strongly on the recovery of pressure by the diverging diffuser-like section of the VA.

Other forms of the VA suitable for controlling the outflow of water from flood retention basins have been developed by Brombach[49,50]. The size of these VAs is measured in metres and in some cases are made of heavy gauge steel sheet backed up by concrete. The objective is to maintain a reasonably constant outflow from the reservoir regardless of the water level in it. Normally the flow from a simple outlet orifice would increase in square-root fashion with the height of water but by using the vortex valve as an outlet, control flow can be used to increase its resistance as the water level rises. This is done by feeding the control flow to the VA from various points up the reservoir wall so that below these off-take points there is no control flow and the valve's resistance is low while at progressively higher levels more off-takes are submerged and the valve's resistance increased. The overall effect is to make better use of the storage capacity of the reservoir.

The applications potential of VA systems is indicated by papers describing the following topics: aircraft fuel systems taking advantage of the VA in unusual operating modes[51], oil hydraulic power control[52], hot combustion gas clean-up[53], and a thrust vectoring system developed by the Martin–Marietta Corp[54]. Consideration of these shows that there is scope for the use of VAs in a wide variety of applications but the problems of fully engineering practical systems are considerable.

Turn-up Vortex Amplifier

Further variants on the design of the VA convert it into a variety of devices with different control functions. One such device on which Mayer[55] has a patent is the so-called 'turn-up vortex amplifier' shown in Figure 6 in which the main flow enters the vortex chamber tangentially and control flow is fed in opposition so that it reduces the resistance of the VA by cancelling the vortex produced by the main flow. The effect is therefore to turn up the main flow rather than to turn it down as in the case of the standard VA. One characteristic of the turn-up VA is that it has a 'negative resistance' for certain ranges of input flow and pressure. This can be used to make oscillator circuits or for cancelling unwanted positive resistance. Examples of this compensating action are the filter-blockage compensator[56] and the feedback compensated jet pump[57,58]. In the first of these circuits a turn-up VA gradually decreases its resistance to compensate for the gradual increase of resistance of a filter element as it accumulates debris. The overall resistance of the turn-up VA plus filter therefore remains constant over a useful range.

In the turn-up VA-compensated jet pump, the entrainment rate is held constant irrespective of back pressure by feeding back control flow to a turn-up VA on the entrainment port of the jet pump. Possible, but as yet untried, applications are for maintaining stoichiometric flow ratios over a reasonable turn-down range or proportioning chemical feeds.

Diverter Switched Vortex Valve

A unique bistable vortex valve[59] is formed as shown in Figure 7 by connecting a wall-attachment diverter to a vortex amplifier. The diverter can thus switch flow

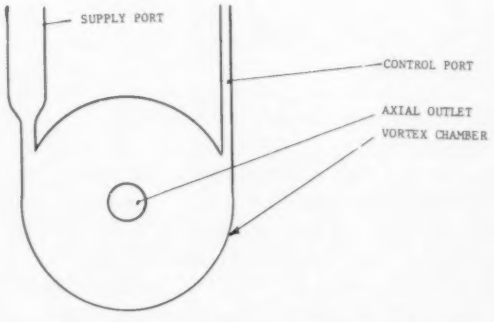


Figure 6. Basic turn-up vortex amplifier design.

VOL. 62 1984

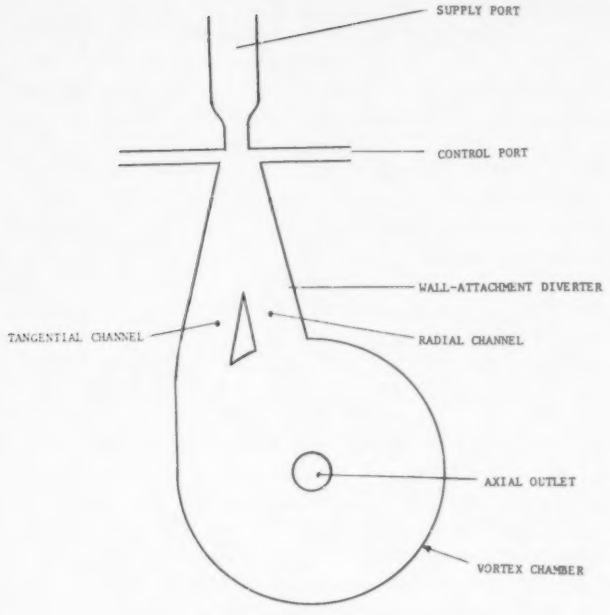


Figure 7. Diverter switched vortex valve.

radially or tangentially into the vortex chamber so that the device has a high or low resistance depending on whether or not a vortex forms. A measure of effectiveness is the ratio of flows in the two states for a fixed pressure-drop across the device. This ratio can be about five if a diffusing outlet can be used on the vortex chamber[60]. A very large switched vortex valve for possible use in ventilation control was made by Tesar[61] with a 1.14 m diameter vortex chamber.

Potentially there are many uses for a device such as the switched vortex valve with its high or low resistance states but in practice a lot depends on its performance and ability to be built into a circuit. Obviously its low flow ratio, usually less than five, and its rather awkward shape limit its uses. One rather interesting application is in a no-moving-part hydraulic ram[62]. The switched valve is made to oscillate continuously by joining its control ports and it is supplied by a long ram pipe in which liquid is alternately accelerated and retarded by the oscillatory valve. Large pressure pulses are therefore produced upstream of the valve.

THE WALL-ATTACHMENT AMPLIFIER AND FLOW DIVERSION

The bistable wall-attachment amplifier shown in Figure 8 is probably one of the most distinctive inventions of the HDL researchers. Their original intention was to make a momentum-controlled proportional amplifier in which transverse control jets would deflect a main jet, using a design conceived very much like that shown in Figure 8. Surprisingly the resulting device was a bistable switch implying a strongly hysteretic mode of operation. Proportional action is only obtained when the sidewalls confining the jet are set very well back from the main jet. The digital action is the basis of a range of well-established fluid logic devices, but also it provides the basis for hydraulic or pneumatic fluid power switching. Design and performance of general bistable amplifiers (i.e. not specifically for logic or flow control) are described by several workers[63–65].

Regarded as a flow switch or diverter, the action is as follows: Supply flow from the main nozzle attaches to one or other of the sidewalls and is thus diverted to the adjacent outlet. Brief pulses of control flow injected or extracted at the control ports switch the jet from one side to the other. The propensity of a fluid jet to attach itself to a 'wall' or other surface is called the 'Coanda effect' and is due to the entrainment of the previously stagnant fluid between the jet and the wall. The special feature of the wall attachment amplifier is that, despite the symmetry of the diverging interaction region, the flow field is bistable. Thus the effects of the two walls do not cancel each other out and a centre-stable flow is not usually possible (unless there are excessive flows from both control ports).

For use as a logic device or in some types of power amplifier, vents are placed just downstream of the splitter to dump excess flow and to de-couple the two outputs. Thus, in an appropriately designed vented amplifier, the active output can be blocked or unblocked without affecting the inactive output or the state of the control ports. By contrast, if the objective is to control flow, then vents cannot be used and any interaction of the outputs with the downstream load must be anticipated and accommodated in the overall circuit design.

The wall attachment and bistability of the jet are strong effects in turbulent, non-cavitating flow at moderate Mach numbers (say up to two but this depends on the design). Typically the pressure difference across the jet as it emerges from the main nozzle and is deflected to the wall is 0.2 times its dynamic pressure. Most of this pressure difference is negative with respect to the inactive

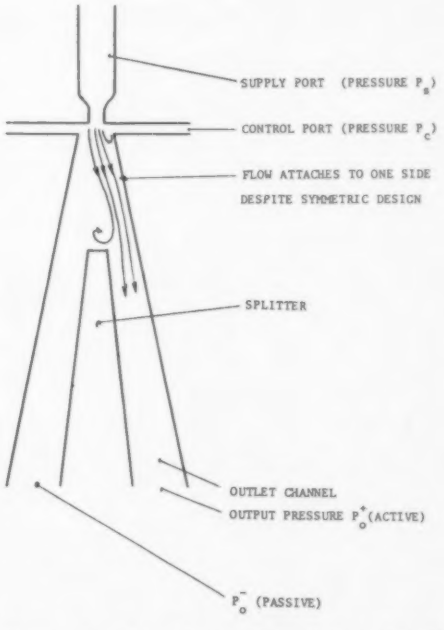


Figure 8. Unvented wall-attachment flow diverter (bistable fluid amplifier) all cross-sections rectangular.

outlet so if, for example, the diverter was discharging to atmosphere, the control port on the active side would be at a sub-atmospheric pressure and would tend to suck in control flow. This has an obvious significance for whatever system supplies the control flow but it also implies certain cavitation or compressibility-induced limits on the operation of the amplifier. If the negative pressure falls near to the vapour pressure in liquids or to a small fraction of the absolute upstream pressure in gases, the necessary pressure difference across the jet cannot be maintained and the device malfunctions. Thus, as with other fluid dynamic devices, its operation is confined by cavitation and Mach number limits. Within these limits there is no constraint on size, so large fluidic diverters can be made with just as much reason as large turbomachines.

When a wall-attachment amplifier is used to divert a flow stream entirely from one output to another the pressure available at the outputs is only a proportion of the supply pressure. This proportion is defined as the efficiency and it is typically of the order of 50% so we understand immediately that a considerable pressure loss penalty has to be paid for using the no-moving-part diverter.

This efficiency parameter corresponds to just one point on the characteristics of the amplifier as shown in Figure 9. Here the output pressure P_o and the control pressure P_c are plotted as function of the outflow q_o with the supply flow held constant. (The pressure at the inactive output is the datum for these pressures.) Since the diverter is unvented and the control flows are zero, only at one point on the characteristic is all of the supply flow directed out of one output. At other points flow is either entrained or leaked at the other 'inactive' port. Usually the desired operating point is the no-leakage-or-entrainment point but achieving this is a matter of matching the load pressure-drop to the characteristics of the diverter. If the pressure-drop is solely due to pipework resistance then this might be represented by a curve

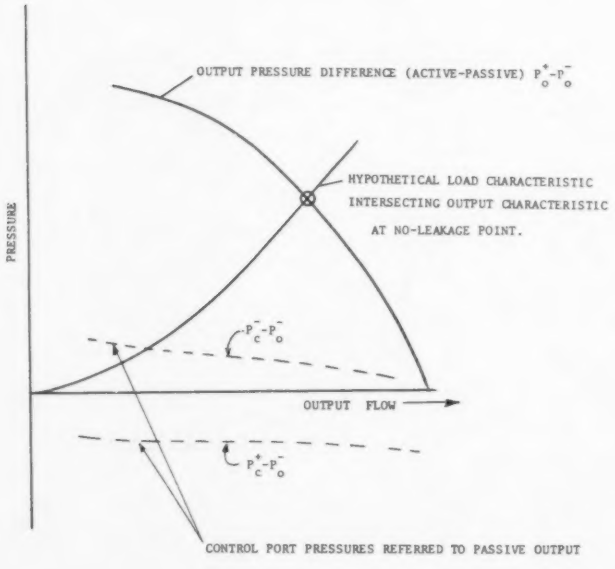


Figure 9. Characteristics of flow diverter.

emanating from the origin and intersecting the no-leakage point for a perfect match as shown in Figure 9. If there were a hydrostatic component in the output pressure then a suitable constant offset would appear in the graphical representation. The intersection of the diverter's output characteristics and these 'load characteristics' form the basis for rational circuit design procedures similar to those for fan and ductwork systems. The design and performance of flow or fluid power handling diverters are described in various sources[61,66–70].

Fluidic diverters were used early in the 1960's for thrust vectoring of rockets[71]. The main jet was the efflux from a small rocket and control was from atmospheric air aspirated through several pilot amplifiers. (Other closely related military applications have been described[72–75].) In addition to this rather spectacular demonstration of power fluidic control many industrial liquid flow diverters have been (and still are being) installed as described by Adams[67]. These are usually as individual flow diverters controlled by air drawn in from atmosphere. Thus small brief air flows control liquid flows. In some cases the liquid is heavily loaded with particulate or fibrous material and then the fluidic device has an obvious advantage over conventional valves. In other cases even with benign fluids the fluidic device is cheap and convenient.

In general, favourable applications are where the output loading is well defined and constant and where the necessary pressure-loss is unimportant. Frequent switching and high temperature debris-laden flows also favour the choice of a fluidic diverter.

In another type of application[76] the speed of switching of the diverter is used to advantage in controlling the reactants to a chemical gas dynamic laser.

The bistable amplifier can be made to oscillate either by connecting its two control ports together or by feeding back a signal from each output to each control port. These can be applied as flowmeters in which the oscillation frequency is a measure of volume flow or as indicators of other attributes[77–80]. For example, if the pipe connecting the two control ports is suitably designed in relation to the rest of the device, the frequency becomes determined by the speed of sound in gas (gas only is considered). This in turn can be used as a measure of temperature or of gas composition.

Multistage bistable amplifier systems involving oscillators, vented and unvented amplifiers can be used to control pneumatic power in fluidic pump drive units[81]. In these, attributes of both signal and power fluidic elements are utilised. In general these units provide, in embryonic form at least, the interface between small-signal fluidic logic and 'heavy-current' power handling fluidics.

FLUIDIC PUMPING SYSTEMS

Various fluidic pumping systems have been developed based upon the principle of liquid displacement and rectification. The extent to which fluidic components are used in the system can vary depending upon the demands of the application, from simply the use of fluidic non-return valves in an otherwise conventional mechanically driven positive displacement pump, to having an

VOL. 62 1984

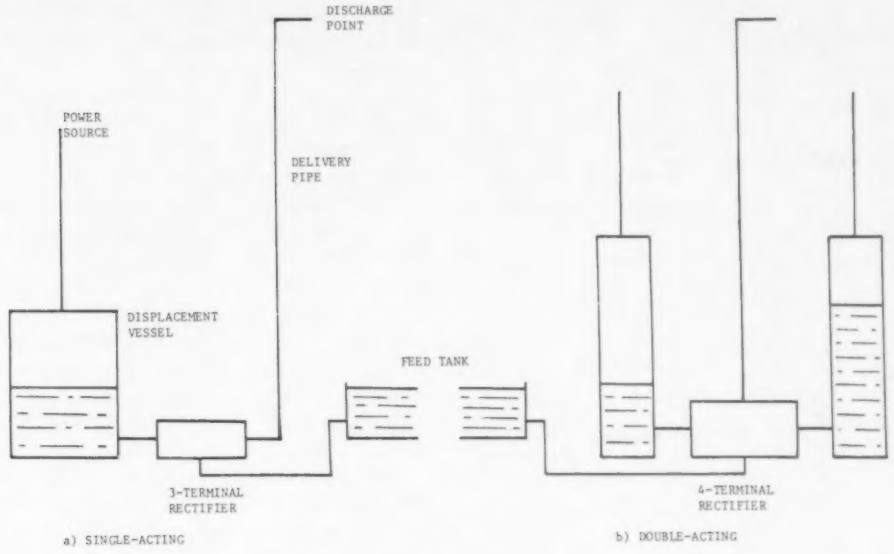


Figure 10. Basic fluidic pump designs (*a*) Single acting (*b*) Double acting.

entire no-moving-part fluidic system with a pneumatic power input and a pumped liquid output[81].

Two main categories of fluidic pump have been developed, single-acting and double-acting. Single-acting pumps, as shown in Figure 10(*a*), use a single displacement vessel or cylinder with a three-terminal half-wave rectifier to give an intermittent liquid output. Double-acting pumps, Figure 10(*b*), use two displacement vessels with a four terminal full-wave rectifier to give a continuous liquid output. Various components can be used in either category of pump. Component selection and pump system design for a given application is dictated largely by consideration of the restrictions imposed by cavitation on the rectifier performance and the requirement to maintain stability and maximise efficiency of the overall pump system.

Pump Rectifiers

The most obvious pump rectifiers are those which use fluidic diodes in conventional rectifier circuits. Previous mention has been made of the use of two simple conical diffuser diodes for pumping molten steel[8]. However, the better performance of the vortex diode enables greater rectification efficiency to be achieved. Various displacement pumping arrangements based upon both two and four fluidic diode rectifiers are proposed in the patent of Golder and Grant[83]. However this is predated by the proposal by Horn and Hughes[84] for a two vortex-diode pumping system for molten potassium sulphate slag at 1300°C. Further development of the four diode bridge rectifier is reported by McGuigan and Boucher[37,85] and Grant and Strong[86].

A completely different concept is the directed jet rectifier. This exploits the rectifying property of the uni-directional nature of a fluid jet, with useful static pump head being obtained by flow diffusion in the jet receiver. The jet pump is an obvious example of this type of device. Although the jet pump is useful for low output head applications, the requirement for greater output heads with less significance being placed upon jet entrainment, has led to the recent development of more suitable directed jet rectifiers. Walkden *et al.*[82,87], Tebbs and Markland[88] and Tesar[89] have proposed various directed jet rectifiers, however perhaps the most useful elements are those based upon the reverse flow diverter (RFD) as developed by Tippetts *et al.*[90–95]. Figure 11 shows the basic design and drive characteristics of an RFD. For single-acting pumps the RFD can be used alone[81–95], in which case the rectifying action can be supplemented by the behaviour of a delivery pipe with an unsubmerged discharge point, or in conjunction with a diode[95] to retard delivery pipe fallback. For double-acting pumps a four terminal rectifier can be formed by combining an RFD with either another RFD[95], a specially designed flow junction[94], or two diodes[93,96]. Figure 12 shows the basic design of the various fluidic pump rectifiers.

Fluidic rectifier efficiency is a strong function of the operating pressure ratio E_h and the possible effects of

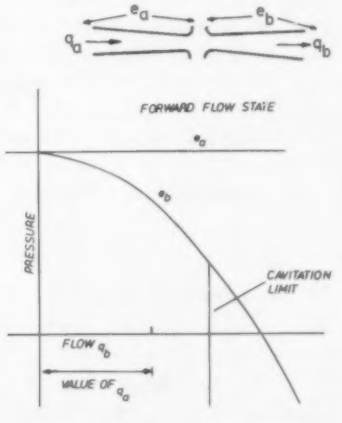


Figure 11. Basic design and characteristics of reverse flow diverter.

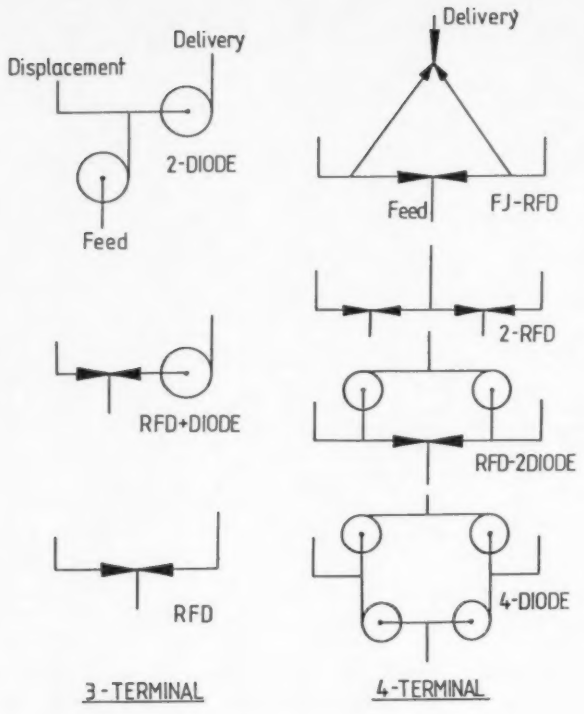


Figure 12. Fluidic rectifiers.

cavitation. The different response of the various possible rectifiers to these pressures and cavitation is one factor influencing rectifier selection. In a comparative analysis of single-acting pump non-cavitating steady state recifier efficiency[97], the RFD and the 2-vortex diode rectifier are shown to have similar efficiencies in the range 40 to 50%, with the RFD-Diode rectifier being just less than 30%. The RFD is shown to be best operated at $E_h \simeq 0.6$ to 0.7, with the 2-Diode at a lower drive pressure corresponding to $E_h \simeq 0.8$ to 0.95. Double-acting pump rectifier efficiencies have been evaluated by Tippetts *et al.* For a 4-Diode bridge[92] a peak efficiency of about 40% can be expected and for an FJ-RFD[98] a peak of about 27%. The diode bridge requires some negative pressures to be applied during the cycle, whereas the FJ-RFD does not. Thus, the fluidic rectification efficiency typically lies in the range 30 to 50%. The effect of cavitation on Diode rectifiers has been studied by Priestman and Tippetts[19], and Naji[99] has studied cavitation in RFD based rectifiers. The main general effects of cavitation are to limit the rate at which liquid can be refilled into the pump displacement vessel(s), and to degrade the rectifier output above a certain output pressure. Further significant differences between the various rectifiers become apparent when considering the pump system as a whole.

Pump Liquid Displacement

The liquid displacement required for pumping can be achieved by a normal mechanical piston and cylinder arrangement[100], in which case the piston frequency is limited by cavitation, with a rectangular wave piston motion being preferable to a sinusoidal one[19]. Much of the development to date on fluidic pumps has been directed towards handling radioactive and hazardous liquids for the nuclear industry. As a consequence the use of potentially unreliable mechanical pistons has been precluded and liquid displacement has been achieved by gas pressure. The liquid, contained in a displacement vessel consisting typically of a squat vertical pipe section, is driven down by high pressure gas with a quiescent gas–liquid interface, then allowed to rise either due to the liquid head in the pump feed tank or under suction. A period of gas expansive working, or blowdown, of the high pressure drive gas can be incorporated into the pump cycle to improve system efficiency. The behaviour of the gas during a pumping cycle has been successfully modelled[101] by considering the system as a variable volume gas container which is either charging or discharging in the presence of heat transfer.

The simplest method of controlling the gas mass flow into and out of the displacement vessel is to use solenoid valves and timers. Nuclear applications however, require that any possibly contaminated air does not contact moving part solenoid valves. Thus an intermediate fluidic secondary controller must be used between the valves and the vessel. This must provide the necessary gas flows whilst isolating any moving parts from the gas venting from the vessel. Various secondary controller designs have been developed[95-100] using both directed jet and vortex based elements. In certain cases, where solenoid valves cannot be tolerated, a complete fluidic free-running oscillator and secondary controller can be used[81]. If containment of the possibly contaminated vessel gas is required a barrier liquid system can be used. The concept of a heat generated pump pressure cycle was proposed by Grant and Golder[83].

The efficiency of the pump controller can vary widely from about 10 to 80% depending upon the control system used and the pump pressure requirements. Typically a controller consisting of solenoid valves with a well designed twin-jet pump secondary controller, giving pressures equivalent to lifts in the range 5 m to 20 m of water, would have an efficiency of between 30 and 15%.

Pump System Performance, Stability and Control

It is important to define, as within the pumping system, all the elements affecting the pump behaviour. Consider for example perhaps the simplest and to date most widely applied pumping system, the single-acting RFD pump. An integral part of this pump is the delivery pipe, the statics and dynamics of which strongly influence the pump performance and stability. Indeed the first step in the design of these pumps can be the sizing of the delivery pipe.

The stability and control of pumping systems depends largely upon their dynamics. The main failure mode in gas driven systems is the departure of the gas liquid interface from the displacement vessel, either flooding the controller or blowing gas into the rectifier. The most efficient mode of operation for the single-acting RFD pump is the 'kinematic mode'[102], in which the liquid in the delivery pipe falls back to its steady state level during vessel refill. Thus there is a level 'reference point' at the end of vessel refill, with static liquid levels on all three

VOL. 62 1984

rectifier terminals. This makes the system very stable and enables either fixed cycle time or fixed level operation. When this pump is operated in the 'dynamic mode'[102], or for RFD-Diode or 2-Diode rectifiers, the delivery pipe only partially drains and there is no static level reference point in the cycle, although hydrostatic forces do tend to stabilise the cycle. In these cases it is more reliable to use either vessel level detection or displacement by a fixed, e.g. mechanical, means.

In double-acting pumps the delivery pipe remains full and its dynamics are less important. Gas driven double-acting pumps can operate over a range of feed tank levels and cycle times with hydrostatic stabilisation[97,104]. However, they do not have a fixed reference point and the use of level detection or fixed displacement can therefore improve stability and extend operating flexibility.

Both single-acting and double-acting pumps can have very good turndown ratios. Up to 100% turndown has been demonstrated for an FJ-RFD pump using cycle frequency modulation. The kinematic single-acting RFD pump can have similar turndown, with no loss of efficiency, simply by introducing increasing dead time at the static reference point.

In theory any delivery rate can be achieved by simply scaling pump components. For vortex based elements *Re* effects make it beneficial to use large diodes.

Overall system efficiency generally tends to decrease with increasing pump head, due to both the effect of cavitation in the rectifier and gas compression losses. Vortex diode based rectifiers and the RFD can continue pumping up to quite high heads. A single-acting RFD pump has been successfully operated at 30 m of water, and in theory higher heads can be achieved given the necessary input pressures. The lower drive pressure ratio, E_h, required for diode rectifiers gives them some advantage for high lifts. It has been shown[19] that output diode cavitation need not occur for heads up to 35 m of water, with pumping still being possible above this head.

The FJ-RFD and 2-RFD rectifiers rely upon jet entrainment for their pumping action, and cavitation limits their operating range to up to about 12 m of cold water, and lower heads for hot water. An FJ-RFD pump has successfully operated to 6 m with nearly boiling water[104].

A disadvantage of fluidic pumps is their relatively low overall efficiency. The special requirements of pumps for the nuclear industry of being gas driven with no gas venting through moving parts, produces overall efficiencies as low as about 3% for a double-acting pump with an all fluidic oscillator, to about 12% for a single-acting pump with an electromechanical oscillator. Fluidic rectification efficiency can range from 40 to 50% so, for applications in which the pump liquid displacement can be by more conventional and efficient means, overall system efficiencies of the order of 25 to 35% should be possible.

An advantage of fluidic pumps is their ability to handle suspended solids. The action of the pump cycle can actually inhibit solids build-up and blockage. Solids degradation can also be low. Component design can be very simple, enabling fabrication from exotic, resistant materials. Simple design also facilitates system sterilisation. The possibility of liquor contamination from lubricants is removed and the use of barrier or buffer systems can enable the correct chemical environment to be maintained. The pump systems described do not aerate or dilute the pumped liquor, as occurs in more conventional fluidic steam ejector or air lift pumps.

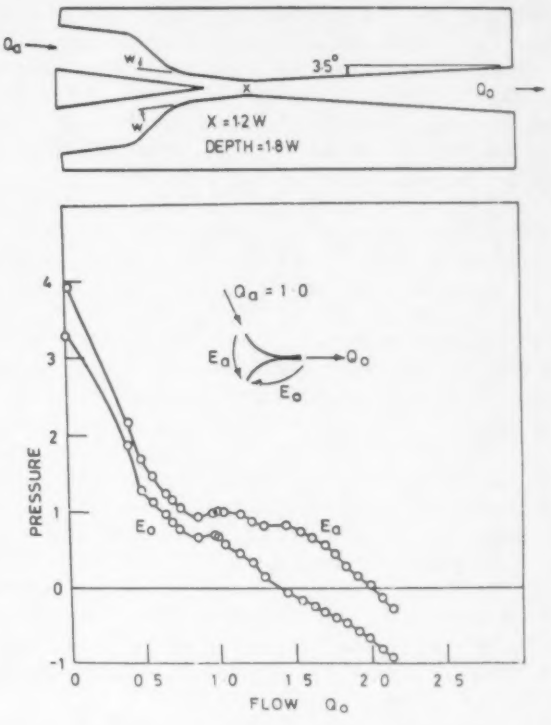


Figure 13. Flow junction design and characteristics.

To date various fluidic pumping systems have been installed and operated successfully within the nuclear industry[96]. Oruh *et al.*[105] describe one important application in which a kinematic single-acting RFD pump handles hot highly active waste liquor containing up to 50% v/v suspended solids. It is to be expected that this successful application of fluidic pumping systems within the nuclear industry will be followed by much wider usage in other process industries.

OTHER COMPONENTS AND APPLICATIONS

There are many simple-looking devices which nevertheless are very important either as single components or when they are part of a fluidic circuit. The 'flow junction' shown in Figure 13 is a good example[94], it is a specially designed Y-joint which transmits flow from either one of the inlets ('arms' of the Y) to the outlet (the 'leg') with the least possible pressure loss but also minimising the back flow out of the other inlet. It is used in double-acting fluidic pumps in combination with diodes or RFDs, or it can be used alone for combining flows into one outlet. For example, two fans can be connected by a flow junction so that if one fan fails, the flow from the other fan still supplies the load without bypassing it by flowing backwards through the failed fan.

In this fan application a compromise must be made between the degree of protection needed (against

backflow) and the running cost under normal conditions. The flow junction incurs an inevitable added pressure loss which increases running cots but it provides simple and reliable non-return valve type action when one fan fails. Assessing the costs and benefits of this depends on many factors quite unrelated to fluidics but this is a frequently encountered situation.

The flow junction like the RFD depends on the momentum of jets which are directed in a particular way to obtain a useful function. Many other so-called 'directed-jet devices' can be made which depend on similar principles. Several of these use the head-on impact of opposing jets sometimes accompanied by the recovery of the impacted flow in a radial (disc-shaped) diffuser[106]. A device embodying this effect is the so-called 'tee-junction modulator'[107] which can be regarded as being derived from a tee-joint by arranging three diffusers so that flow decelerates from the centre of the tee to any outlet. It has a large range of negative resistance in its characteristics, which can be used to cancel unwanted positive resistance elsewhere in a circuit, or it can be used as an oscillator. Another use for the tee-junction modulator is in combination with another type of Y-joint (not a flow junction) to form a 4-terminal fluidic valve[108] somewhat analogous to the double acting pump[108].

Closely related to the tee-junction modulator are a series of devices called opposed jet controllers[94,106,109,110]. The simplest of these uses a single control jet to change the resistance to a much larger main flow. The overall effect is like that of the vortex amplifier but the gain is less than that of a VA under its optimum working conditions.

A similar controlling effect is provided by an annular control jet in the 'radial pinch amplifier' described by King and Syred[111].

Other forms of opposed jet device can be used to provide the back-and-forth reciprocating air flow needed to drive fluidic pumps[102]. The main benefit from using these opposed jet devices is achieved when they are supplied by other fluidic elements such as diverters because they reduce the adverse effects of compressibility which would occur with more obvious elements such as jet pumps.

The motivation for developing many of the directed-jet devices has come from processes needed in nuclear plant. One requirement is to sample one flow from many possible sources. This has promoted the development of multiple inlet flow junctions and networks of flow junctions to combine flow from many inlets. Grant *et al.*[32,112] describe two methods of monitoring reactor fuel elements. One method is based upon multiple Coanda divertors. The other, potentially more useful, method[112] is the 'monitoring tree system' formed simply from a lattice work of interconnected pipes. The application of monitoring theory to the carefully designed lattice enables a large number of inputs to be continuously monitored by a small number of detectors.

Other circuits have been made to drive liquid jet mixer settlers[96,106] using opposed jet devices and fluidic oscillators. Similar systems are under development for driving pulse columns.

Directed jet elements similar to the RFD described earlier can be combined in various ways to make circuits which could handle combustion gases in regenerative heat exchange circuits[90,92,110]. Although the basic circuits have been proven, further development is needed to apply them in practice. Now that coal has again become an important fuel there is considerable interest in cleaning the waste gases. This is particularly necessary if coal firing is considered for a gas turbine power plant. With this as the overall objective Syred and Owen[53] have been developing a vortex-amplifier-switched filtration circuit for handling the very hot gases straight from a coal combustor. This enables one filter to be back-flushed while another is filtering. The control flows for the VAs are produced by jet pumps which enable very small but high pressure cold gas flows to switch the much larger hot gas flows. An important objective is to minimise the dilution of the hot gas stream.

A steady stream of papers describing ingenious fluidic developments has come from Tesar at the Technical University of Prague (CVUT). These include carefully optimised designs for wall-attachment diverters[61,69], ventilation pressure controllers[113], heat meters[114], greater-than-square law pressure-flow resistors and associated circuits[115], carburation systems, and pneumatically controlled looms. Anyone following up the large volume of Tesar's work will have no doubt as to the wide scope of fluidics technology.

VOL. 62 1984

CONCLUSIONS

It has been shown that there is currently a significant number of power fluidic components and systems which have useful potential for wider application to process flow control. The flow diffuser is perhaps the simplest true power fluidic component which, in addition to forming an integral part of more complex components, has also found usage in its own right as a simple diode. The fluid vortex is the basis of a variety of components. The simplest is the vortex throttle which can offer a high flow resistance, with a minimum hole size about 2.5 times the orifice of equivalent resistance. The vortex throttle can be modified, mainly by introducing flow diffusers, to form a high performance fluid diode. Introducing a control flow into the vortex chamber creates another device, the vortex amplifier. A different type of fluid amplifier is the wall-attachment amplifier which is based upon the Coanda effect, and which is particularly well suited to flow diversion. Another genus of fluidic elements are those based upon the directed jet, such as the Reverse Flow Diverter pump rectifier, the flow junction and the tee-junction modulator. These typical fluidic components illustrate the various fluid dynamic phenomena utilised by fluidics and indicates the wide range of functions which can be achieved.

In order to indicate the scope and potential of power fluidics for process flow control details have been given of the major current successful applications as well as the performance capabilities of the various components and systems, with an indication of the limits imposed by liquid cavitation and gas compressibility.

To date a significant proportion of power fluidic applications have been within the British Nuclear Industry where the high premium placed upon maintenance

free reliability enables even very poor efficiency system to be cost-effective. Outside the Nuclear Industry equipment maintenance is more acceptable and can be equated to capital and running costs. The often lower efficiencies and greater pressure losses of fluidic components when compared to their moving part equivalents tends to exclude their use for many applications. Several areas, however, can be identified in which power fluidics may have potential for cost-effective application. Low efficiency is of reduced importance when running costs are either insignificant because of the small scale of the process, or are outweighed by other factors such as the risk of fire or explosion or of fluid contamination or damage. Maintenance can become a dominant factor, the fluid may be particularly abrasive, toxic or chemically aggressive. The internal flow pattern in fluidic components can reduce abrasive wear and the often simple design lends itself to manufacture from exotic or difficult materials. In certain applications fluidics can provide a unique or much simplified solution to a flow control problem, as exemplified by the vortex amplifier control of glove box depression or the compensated jet-pump control of flow ratio.

The future application and development of power fluidics is to some extent reliant upon a broader appreciation of its capabilities. For although fluidic components and systems can and have been developed to satisfy standard well defined functions such as pumping or throttling, the development of less standard applications sometimes needs the stimulus of user demand. Fluidic systems or even components may have to be engineered to satisfy the sometimes unique demands of specific flow handling problems. The need for a more 'fluid systems engineering' approach, analogous to that used in electrical circuit analysis, is a factor which can tend to inhibit the application of fluidics, although static and dynamic analysis of fluid flow systems is slowly becoming both more sophisticated and more widely used.

NOMENCLATURE

d_a axial port throat diameter of vortex throttle or diode (m).
d_c chamber diameter of vortex throttle or diode (m).
d_t tangential port throat diameter of vortex throttle or diode (m).
D component diodicity (−).
e_a pump drive pressure relative to feed tank pressure (Nm^{-2}).
e_b pump load pressure relative to feed tank pressure (Nm^{-2}).
e_v absolute pressure upstream of device minus liquid vapour pressure (Nm^{-2}).
E_h e_b/e_a (−).
Eu Euler Number (−).
Eu_c diffuser cavitating flow Euler Number (−).
Eu_f vortex diode forward flow Euler No. based on axial port throat liquid velocity (−).
Eu_r vortex diode reverse flow Euler No. based on axial port throat liquid velocity (−).
Eu_v vortex throttle high resistance flow Euler No. based on tangential port throat liquid velocity (−).
h vortex chamber height or thickness (m).
P_c^+ diverter active control port pressure; $^-$passive port (Nm^{-2}).
P_o^+ diverter active output channel pressure; $^-$passive (Nm^{-2}).
P_s diverter supply port pressure (Nm^{-2}).
ΔP pressure drop across component (Nm^{-2}).
q_c vortex amplifier control port flowrate ($kg\,s^{-1}$).
q_s vortex amplifier supply port flowrate ($kg\,s^{-1}$).
Q_f flowrate through vortex diode or throttle in forward or low resistance direction ($kg\,s^{-1}$).
Q_r flowrate through vortex diode or throttle in revese or high resistance direction ($kg\,s^{-1}$).
Re Reynolds number (−).
T vortex amplifier turndown ratio (−).
v diffuser throat liquid velocity ($m\,s^{-1}$).
v_1 tangential fluid velocity at vortex chamber periphery ($m\,s^{-1}$).
v_2 tangential fluid velocity at vortex chamber axial outlet ($m\,s^{-1}$).
v_m cavitation limit of diffuser throat liquid velocity ($m\,s^{-1}$).
v_t tangential port throat liquid velocity ($m\,s^{-1}$).
α v_1/v_t(−).
ρ fluid density ($kg\,m^{-3}$)
σ Thoma cavitation number; total absolute downstream pressure minus liquid vapour pressure all divided by ΔP (−).
τ $v_2 d_a/v_1 d_t$ (−).

REFERENCES

1. Herschel, C., 1899, *The Two Books on Water Supply of the City of Rome of Sextus Julius Frontinus* (Boston).
2. Robinson, J., 1860, *Proc I Mech E.*, 39.
3. Savill, A. S., 1884, *Proc I Mech E.*, 167.
4. Gibson, A. H., 1910, *Proc R Soc L.*, 83A: 366.
5. Gibson, A. H., 1913, *Trans R Soc Edinburgh*, 49: 97.
6. Moller, P. S., 1966, *J Basic Eng, ASME*, March: 155.
7. Ackeret, J., 1965, *Proc Symp Fluid Mechanics of Internal Flow*, ed. Sovran, G. (General Motors Res Labs, Michigan).
8. Petermann, H. and Kosyna, G., 1973, *Proc Pumpentagung* (Univ. Karlsruhe).
9. Thoma, D., 1930, *VDI-Zeitschrift*, 74: 1098.
10. Heim, R., 1929, *Trans Hydr Inst Munich*, 3, (ASME Translation by M. P. O'Brien, 1935).
11. Zobel, R., 1936, *Mitt Hydr Inst Munich*, 8, (UKAEA Risley Translation No. 439).
12. Bichara, R. T. and Orner, P. A., 1969, *J Basic Eng, ASME*, 755.
13. Wormley, D. N., 1969, *J Basic Eng, ASME*, June: 264.
14. Brombach, H. and Elalfy, Y., 1976, *Korrespondenz Abwasser*, 23: 295.
15. *New Civil Engineer*, 1980, Sept: 24.
16. Brombach, H., 1980. *IFAC Symp Pneumatic and Hydraulic Components and Instruments in Aut Control* (Warsaw): 109.
17. Brombach, H., 1982, *Wasserwirtschaft*, (2): 1.
18. Brombach, H., 1982, *Schweizer Ingenieur und Architekt*, 72, (33–34): 670.
19. Priestman, G. H. and Tippetts, J. R., 1982, *J Mech Eng Sci*, 24(4): 191.
20. Tippetts, J. R. and Priestman, G. H., 1983. *J Fluids Eng, ASME*, Sept, 105: 350.
21. Syred, N. and Roberts, P. J., 1979, *ASME*, 79-HT-9.
22. Roberts, P. J. and Syred, N., 1978, *Fluidics Q.*, 10, 49.
23. Sidhu, B. S., Syred, N. and Styles, A. C., 1980, *ASME, WAM, Vortex Flows*, 113.
24. Boucher, R. and Tippetts, J. R., 1982, *Investigation into the Advantages of Fluidics in Fluid Processing*, Part 2 (Aer Res Inst Sweden, Stockholm).
25. George, P. T., Ward, J. R. and Mitchell, F. M., 1975, *Process Control by Power Fluidics Symp* (Inst Meas Control, London) paper 23.
26. Jacobs, B. E. A. and Baker, P. J., 1972, *5th Fluidics Conf*, (BHRA, Cranfield) paper E2.
27. Linderoth, E. T., 1955, *U.S. Patent* 2, 727, 535.
28. Jacobs, B. E. A. and Baker, P. J., 1968, *3rd Fluidics Conf*, (BHRA, Cranfield) paper K5.
29. Paul, F. W., 1968, *IFAC Symp. Fluidics, London*, paper A1.
30. Jacobs, B. E. A., 1973, *Power Fluidics for Process Control Symp., Surrey*, (Inst Meas Control, London) 11.
31. Baker, P. J., 1967, *2nd Fluidics Conf.*, (BHRA, Cranfield) paper D6.
32. Grant, J. and Wright, J., 1967, *2nd Fluidics Conf* (BHRA, Cranfield) paper K2.
33. Grant, J. and Marshall, V. C., 1975, *Process Control by Power Fluidics Symp., Sheffield* (Inst Meas Control, London) paper 21.
34. Grant, J., 1977, *Critical Reviews in Environmental Control* (CRC Press) Nov., 353.
35. Mori, G. and Premoli, A., 1973, *European Two-Phase Flow Meeting, Brussels*, paper A5.
36. Gspan, J., 1979, *Wasserwirtschaft*, 69(12): 376.

37. McGuigan, J. A. K. and Boucher, R. F., 1973, *Power Fluidics for Process Control Symp., Surrey* (Inst Meas Control, London) 97.
38. Kirshner, J. M. and Katz, S., 1975, *Design Theory of Fluidic Components*, (Academic Press).
39. Kirshner, J. M. and Horton, B. M. 1970, *Fluidics at the Harry Diamond Laboratories; Fluidics Feedback*, September 225.
40. Taplin, L. B. and McFall, R. H., 1969, *Bendix Tech. J.*, pp. 33–41.
41. Mayer, E. A., 1967, *Advances in Fluidics*, ed. Brown, F. T. (ASME).
42. Taplin, L. B., 1968, *AGARDograph*, 118, ed. S. Y. Lee (AGARD).
43. Wormley, D. N., 1976, *AGARDograph*, 215, ed. J. M. Kirshner (AGARD) Jan.
44. Syred, N., 1975, *Proc Symp Process Control by Power Fluidics* (Inst Meas Control. London) Sept.
45. Saunders, D. H., 1973, *Proc Symp Power Fluidics for Process Control*, (Inst Meas Control, London).
46. Tippetts, J. R., Rimmer, E., Higginson, J. and McGuigan, J. A. K., 1978, *Fluidics Q*, 10 (3): 67.
47. Al Shamma, K. A., 1971, *PhD Thesis* (Dept Mech Eng, Univ Sheffield).
48. Al Shamma, K. A., Royle, J. K., Boucher, R. F. and Asquith, R. W., 1972, *Proc 5th Fluidics Conf* (BHRA, Cranfield) paper B2.
49. Brombach, H., 1975, *Proc Symp Process Control by Power Fluidics* (Inst Meas Control, London).
50. Brombach, H., 1981, *J. Dyn Syst Meas. Control ASME*. 103: 338.
51. Taylor, A. F., 1970, *4th Fluidics Conf* (BHRA, Cranfield) paper B2.
52. McCloy, D. and Stevenson, I. J., 1972, *Proc 5th Fluidics Conf.*, (BHRA, Cranfield) paper D6.
53. Owen, I. and Syred, N., 1980, *Proc Symp 20th Anniv Fluidics, ASME*, 187.
54. Brodersen, R. K. and Papadopoulos, J., 1981, *IEEE Trans Aut Control*, AC-26 (3): 625.
55. Mayer, E. A., 1973, *British Patent* 1339642, London.
56. Oruh, S. N. and Tippetts, J. R., 1978, *Proc 3rd Colloq Pneumatics-Hydraulics*, pp. 225–238 (Sci Soc Mech Eng, Hungary) Sept.
57. Tippetts, J. R., 1981, *British Patent* 1595452.
58. Oruh, S. N. and Tippetts, J. R., 1983, *WAM, ASME*, 83-WA/DSC-5.
59. Adams, R. B. and Morre, C. B., 1966, *US Pat ext* 3267946.
60. Tippetts, J. R., 1969, *PhD Thesis* (Dept Mech Eng, Univ Sheffield).
61. Tesar, V., 1975, *Proc Symp Process Control by Power Fluidics* (Inst Meas Control, London) Sept.
62. Tippetts, J. R., 1974, *Fluidics Q*, 6 (2): pp. 45–53.
63. Warren, R. W., 1962, *Symp Fluid Jet Control Devices, ASME*, p. 75.
64. *British Patent* 1053021, Dec, 1966.
65. Sarpkaya, T., 1969, *J Basic Eng, ASME*.
66. Fisher, M. and Thompson, A., 1968, *Proc 3rd Fluidics Conf*, (BHRA, Cranfield) paper B4.
67. Adams, R. B., 1974, *Proc Fluidic State-of-the-Art Symp*, Vol. 5, paper 62. (Harry Diamond Labs, Washington DC) Oct.
68. Tippetts, J. R. and Royle, J. K., 1971, *Fluidics Q*, 3 (4) 1.
69. Tesar, V., 1983, *Messen Steuern Regeln, Berlin*, 26 (4): 189.
70 Carbonaro, M., 1974, *6th Fluidics Conf* (BHRA, Cranfield) paper J2.
71. Campagnuolo, C. J. and Holmes, A. B., 1967, paper K3, *Proc 2nd Fluidics Conf* (BHRA, Cranfield)
72. Dunaway, J. C., 1974, *Proc Fluidic State-of-the-Art Symp*, Vol. 5, paper 72 (Harry Diamond Labs., Washington DC).
73. Byrd, J. L., 1974, *Ibid*, paper 73.
74. Gottron, R. N. and Fox, L. S., 1974, *Ibid*, paper 70.
75. Eastman, N., 1968, *3rd Fluidics Conf* (BHRA, Cranfield) paper C3.
76. Limpaecher, R. and Woodroffe, J., 1977, *Proc 15th AIAA Aerospace Sci Mtg*, 61.
77. Campagnuolo, C. J. and Lee, H. C., 1969, *Proc Winter Annual Meeting, ASME*, paper 69-WA/Flcs-8.
78. Tippetts, J. R., Ng, H. K. and Royle, J. K., 1973, *Automatica*, 9: 35.
79. Boucher, R. F. *et al.*, 1975, *7th Fluidics Conf* (BHRA, Cranfield) paper C4.
80. *Product Information*, 1982 (AIResearch, Garrett Co., Phoenix, Arizona).
81. Tippetts, J. R., 1978, *Proc 5th Int Fluid Power Symp* (BHRA, Cranfield) paper C2.
82. Walkden, A. J. and Barley, R. L., 1972, *Symp Jet Pumps and Ejectors, London* (BHRA, Cranfield) paper E4.
83. Golder, J. A. and Grant, J., 1972, *British Patent* 1300401, Filed Jan. 1969.
84. Horn, G. and Hughes, E. M., 1967, *Trans I Chem E*, 45, T182.
85. McGuigan, J. A. K. and Boucher, R. F., 1972, *5th Fluidics Conf*, (BHRA, Cranfield) paper X10.
86. Grant, J. and Strong, R. E., 1973, *Power Fluidics for Process Control Symp, Surrey* (Inst Meas Control, London).
87. Walkden, A. J. and Kell, R. C., 1967, *GEC Journal*, 34: 9.
88. Tebbs, M. J. and Markland, E., 1973, *Power Fluidics for Process Control Symp., Surrey* (Inst Meas. Control, London).
89. Tesar, V., 1981, *Proc. Pneu-Hidro '81; 4th Colloq Pneumatics and Hydraulics, Györ, Hungary*, Sept. 57.
90. Holmes, B. A., Swithenbank, J. and Tippetts, J. R., 1972, *Proc 5th Fluidics Conf* (BHRA, Cranfield) paper B6.
91. Tippetts, J. R., 1973, *Power Fluidics for Process Control Symp, Surrey*, (Inst Meas Control, London).
92. Tippetts, J. R. and Swithenbank, J., 1973, *Power Fluidics for Process Control Symp, Surrey* (Inst Meas Control, London).
93. Tippetts, J. R., Syred, N., Grant, J. and Strong, R. E., 1976, *AGARDograph, Fluidics Technology, 215* ed. Kirshner, 537.
94. Tippetts, J. R., 1975, *Process Control by Power Fluidics Symp, Sheffield*, (Inst Meas Control, London) paper 9.
95. Tippetts, J. R., 1975, *Process Control by Power Fluidics Symp, Sheffield*, (Inst Meas Control. London) paper 10.
96. Tippetts, J. R., Priestman, G. H. and Thompson D., 1981, *J Dyn Syst Meas Control, Trans ASME*, 103, 342.
97. Tippetts, J. R. and Priestman, G. H., 1981, *Proc 7th Tech Conf BPMA*, (BHRA, Cranfield) paper 6.
98. Tippetts, J. R., 1974, *Proc 6th Fluidics Conf* (BHRA, Cranfield) paper F3.
99. Naji, H. S. I., 1981, *PhD Thesis* (University of Sheffield).
100. Owen, I. and Syred, N., 1981, *Proc 7th Tech. Conf BPMA*, (BHRA, Cranfield).
101. Priestman, G. H. and Tippetts, J. R., 1982, Paper 82-WA/DSC-1, *Proc ASME Winter Annual Meeting*, November.
102. Tippetts, J. R., 1979, *Proc 6th Tech Conf BPMA* (BHRA, Cranfield) paper B1.
103. Syred, N., 1975, *Process Control by Power Fluidics Symp, Sheffield*, (Inst Meas Control, London) paper 1.
104. Priestman, G. H. and Tippetts, J. R., 1983, *WAM, ASME*, 83-WA/DSC-2.
105. Oruh, S. N., Bowe, M. J. and Dobson, A. J., 1983, *Proc. Symp. Heat and Fluid Flow in Nuclear and Process Plant Safety* (I Mech E) paper 19.
106. Tippetts, J. R., 1982, *UK Patent* 2016739B.
107. Oruh, S. N. and Tippetts, J. R., 1979, *Fluidics Q*, 11 (1): 41.
108. Oruh, S. N. and Tippetts, J. R., 1979, Paper WA/FE-19, *Proc ASME Winter Annual Meeting*, December.
109. Tippetts, J. R., 1976, *AGARDograph, Fluidics Technology*, 215 ed. Kirshner, 567.
110. Tippetts, J. R., 1974, *Fluidics State-of-the-Art Symp* Vol. 3, (Harry Diamond Labs, Washington, DC) 94.
111. King, C. F. and Syred, N., 1980, *Proc 20th Anniv Fluidics Symp, ASME*, 201.
112. Grant, J., 1980, *Proc 20th Anniv Fluidics Symp, ASME*, 209.
113. Tesar, V., 1979, *Fluidics Q, 11(3):* 43.
114. Tesar, V., 1982, *Czechoslovak Patent Application*, PV 3057-82.
115. Tesar, V., 1980, *IFAC Symp. on Pneumatic and Hydraulic Components and Instruments in Aut Control*, May.

ACKNOWLEDGEMENTS

The authors are supported in work on power fluidics by UKAEA (Risley) and British Nuclear Fuels Ltd.

ADDRESSES

Correspondence on this paper should be addressed to Dr G. H. Priestman, Department of Chemical Engineering and Fuel Technology, Sheffield University, Mappin Street, Sheffield, S1 3JD.

The manuscript was recieved 26 July 1983 and accepted for publication after revision 31 October 1983.

VOL. 62 1984

KINETIC ANALYSIS OF THE CATALYTIC DEHYDRATION OF ALCOHOLS OVER ZEOLITES

By P. L. YUE and O. OLAOFE

School of Chemical Engineering, University of Bath

The catalytic dehydration of ethanol, isopropanol and n-butanol has been studied over three types of zeolites: Laporte 13X, 4A and Norton Zeolon ZNa. Reaction rate data, covering the temperature range 200 to 350°C and alcohol partial pressure up to 0.6 bar, were obtained from a stirred gas-solid reactor. In almost all cases both olefin and ether were formed. Power law and Houghen–Watson type of rate expressions have been used to model the dehydration kinetics. The former gives satisfactory non-isothermal correlation of the data except in the case of dibutyl ether formation over ZNa, while the latter is suitable in representing the rate of formation of both products. Reaction orders vary between zero and one with respect to alcohol. Other kinetic and adsorption parameters have been evaluated. Reaction activation energies indicate that ether production over ZNa modernite is affected by pore diffusion.

INTRODUCTION

Zeolite catalysis and its interpretation have made much exciting progress in the past decade. Synthetic faujasites are now widely used as commercial fluid cracking catalysts. Enhanced conversion, product selectivity and much improved coke selectivity have all contributed to the ever increasing popularity of zeolites. Not only has zeolite catalysis introduced new catalytic processes to the chemical industries, the science of catalysis and surface chemistry too has been greatly enriched by such research.

The present study is concerned with the catalytic dehydration of alcohols over zeolites. The analysis of rate data and modelling of reaction kinetics are presented in this paper. A subsequent paper will deal with the catalytic selectivity and activity of the zeolites and the reactivity of the alcohols. Ethanol, isopropanol and n-butanol have been chosen for this study. These form a combination of two primary alcohols and one secondary alcohol. Three commercial zeolites: Laporte 13X and 4A zeolites and Norton zeolon ZNa (modernite) have been used. They cover a varied range of cage structures, pore sizes and acidity. The dehydration of ethanol over 13X has been performed using different experimental equipment and will be considered in a separate paper[1], where the reaction will be examined in detail in relation to the effect of intra-crystalline diffusion and catalyst deactivation.

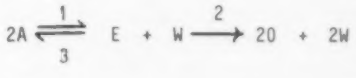
LITERATURE REVIEW

Most studies on alcohol dehydration have been conducted over alumina. Only in a few cases were zeolites used as catalyst. Table 1 gives a summary of relevant work[2-23] reported to date. Alcohols have been found to dehydrate primarily to form ethers and/or olefins, depending on the conditions under which the reactions are performed. Values of activation energies deduced from data in literature vary quite widely. The majority of experimental work reported covers only a range of fairly low partial pressures of alcohols. From the kinetic modelling point of view, it would be useful to extend the study of the reactions to higher alcohol concentrations.

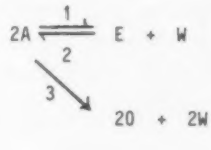
There is no general agreement in the literature as to what pathway the reactions follow. Principally, three schemes have been proposed: (i) consecutive, (ii) parallel and (iii) combinations of (i) and (ii). These can be represented as in Figure 1.

The consecutive reaction scheme was chosen on the basis of a maximum in ether concentration observed both in reaction progress curves and plots of product concentrations as a function of temperature[24]. However, the same behaviour can occur with a parallel reaction

(i) Consecutive reactions:



(ii) Parallel reactions:



(iii) Consecutive and parallel reactions:

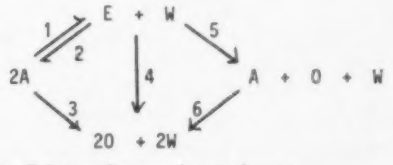


Figure 1. Schemes for reaction pathways.

© Institution of Chemical Engineers

Table 1. Catalytic dehydration of alcohols in the literature

Alcohol	Catalyst	Product	T range (°C)	P_A range (atom)	Model	Reaction Order	E_A/E_E (kJ g mol^{-1})	Ref.
n-butanol	Zeolites: X	O	228	low	PL	1	126	2
	Y	O	256	low	PL	1	113	2
	γ-Alumina	O, E	348–428	0.6	PL	0	129	3
	Silica beads	O	205–307	1.0–7.8	HW	—	68	4
	Alumina	O	400	1.0–500	HW	—	—	5
	Alumina	O	350, 410	—	—	—	—	6
Isopropanol	Linde 13X powder	O	240–270	0–0.013	PL	1	119	7
	Linde 13X unexchanged	O	210–277	0–0.1	PL	0	139	8
	Linde 13X exchanged	O	110–157	0–0.1	PL	0	120	8
		E	110–157	0–0.1	PL	0	110	8
	Zeolites Y and X exchanged	O	140–200	pulse technique	PL	1	80	9
	Zeolites NaX and NaY	O	112–190	pulse technique	PL	1	92, 88	10, 11
	γ-Alumina	O	246	0–0.004	HW	—	—	12
	Resin	O, E	90–110	0–1.0	HW	0	120, 100	13
	Alumina	O, E	285	0–1.0	—	—	—	14
	Oxides	O, E	160–22	0.01–0.03	PL	<1	109–143	15
	Zeolites X and Y exchanged	O, E	100–200	0.008–0.04	HW	—	—	16
Ethanol	Alumina	O, E	307	0.013–0.14	HW	0–2	—	17
	Exchanged resin	O, E	105–125	0–1.0	HW	—	129	18
	Alumina	O, E	138–220	0–0.04	HW	$\frac{1}{2}$–0	117–126	19
	Alumina	O, E	205–307	0–0.2	HW	—	108(O), 42(E)	20
	Linde 10X, 13X, and 5A	O	300–375		PL	1	79, 75, 88	21
	Linde 10X	O			HW	—	88	21
	Zeolites 3A, 4A, 5A and 13X	O, E	200–250	low	—	—	—	22
	Linde 13X	O, E	270	0.6	PL	0	134, 84	23
	Linde 4A	O, E	350	0.6	PL	0	130, 63	23
	Norton ZNa	O		0.6	PL	0	109, 96	23
	Alumina	O		0.6	PL	0	138, 113	23

VOL. 62 1984

mechanism if the dehydration reaction to form ether is reversible. The drop in ether formation could be due to the rapid hydration of ether to revert back to alcohol[25]. The reverse reaction is further enhanced by the co-prodution of water from reactions 1 and 3 under scheme (ii). Indeed, this effect offers an explanation for the existence of a fairly pronounced maximum in ether concentration reported in the literature better than scheme (i). Rate data have been more satisfactorily correlated according to parallel reaction routes than consecutive routes. The addition of ether to the alcohol feed[26] has also been found to have less effect on the formation of olefin than would be expected from scheme (i). Furthermore, the olefin concentration curves obtained by different researchers exhibit no inflection at short residence times. Such an inflection period, however, is usually characteristic of consecutive reactions. Thus there is more evidence supporting the parallel reaction scheme than the consecutive one.

Allied to these discussions on the pros and cons of different reaction pathways is the consideration of reaction mechanism. Although fundamental mechanistic studies are outside the scope of the present paper, it should be noted that, in general, surface intermediates are usually invoked to elucidate reaction mechanisms. Brey and Krieger[25] suggested an intermediate carbenium ion, formed from an alcohol molecule, may convert to olefin, ether, or back to alcohol. Topchieva and Yun-Pin[26] named an 'aluminium alcholate' intermediate and claimed that their scheme offered a better explanation to the product distribution curves than simple parallel or consecutive paths. The discrimination between different surface mechanisms may, however, not be possible by kinetic data analysis alone.

The most elaborate reaction network, shown here as scheme (iii), has been proposed by Knözinger and co-workers[27]. Reactions 5 and 6 are not significant at temperatures above 300°C when ethanol is dehydrated. The hydration of ether, i.e. reaction 2, is, however, important at high temperatures. Reactions 4 and 5 are dependent on the concentration of ether. In most studies on alcohol dehydration, and certainly in the present case, ether concentration is low. Thus this complex scheme really reduces to scheme (ii), which is adopted for the anlaysis of the present rate data.

Both simple power-law (PL) and Hougen–Watson (HW) type of rate models have been used in literature to represent kinetic data, see Table 1. When the power-law rate expression was used, the order of reactions for both the formation of olefin and ether varied between zero and one. Typically, at low alcohol concentrations, the reaction order tends to one and falls to zero as the concentration is raised. Authors who used the HW type of rate equations have mostly assumed that surface reaction is the rate-controlling step. In a few cases, dissociative adsorption of alcohol was considered to be rate-limiting. These, however, applied only to low temperatures. In one study, after more extensive investigation the authors[28] rejected their earlier support for dissociative-adsorption control.

Dehydration rate expressions based on single-site and dual-site mechanisms have been proposed and tested by

Table 2. Physical and chemical properties of zeolites

Properties	13X	4A	ZNa
Chemical formula or structure	$Na_{41}Al_{41}Si_{106}O_{294}264H_2O$	$Na_{12}Al_{12}Si_{24}O_{48}27H_2O$	$Na_8Al_8Si_{40}O_{96}24H_2O$
SiO_2/Al_2O_3	2.6	2.0	10.0
Nominal aperture size (A)	10.0	4.2	5.7 by 7.0
BET surface area ($m^2\ g^{-1}$)	359	10	103
Bulk density ($kg\ m^{-3}$)	670	740	680
Particle size (mm)	1.0–2.0	1.0–2.0	1.588 by 3.5
Binder	natural clay	natural clay	self binding
Percentage of binder	15–20	15–20	—
Crystalline structure	body centre cubic	simple cubic	elliptical/cylindrical
Physical form	spherical beads	spherical beads	1.588 mm extrudates

some authors[17–19]. The exponent for the adsorption terms in the denominator of the rate equations will either be one or two, depending on which mechanism is adopted. Data in the literature appear to support both mechanisms equally well. Pines and Manassen[29] suggested that both acidic and basic sites are involved in the dehydration reactions. The poisoning and titration studies by Bakshi and Gavalas[30] gave evidence that the formation of olefin and ether occurred at different sets of acidic–basic sites. It should also be noted that the adsorption coefficients obtained for the olefin and ether rate expressions do not necessarily have the same values. de-Boer et al[17], and Kabel and Johanson[18] have tested the di-ethyl ether formation reaction independently with rate expressions for bimolecular reactions based on Langmuir–Hinshelwood and Rideal–Eley mechanisms. The correlation of their data was found to be satisfactory.

EXPERIMENTAL

The Norton Zeolon is in the cylindrical extrudate form, while the Laporte zeolites are spherical beads. Their physical and chemical properties are given in Table 2. The location of catalytic sites are mainly within the pore structure, although the external surface can also contribute to the reaction[31].

The dehydration reactions were performed in a continuous stirred gas–solid reactor, similar to that discussed by Brisk et al[32]. The stirring was achieved by spinning the catalyst which was housed in a circular basket. The basket was connected to a magnetic coupling system which was driven by a motor. The coupling eliminated the leakage of materials from the reactor. The merits of such a reactor have already been fully discussed in the literature[32]. An improvement over the design of Brisk et al is the addition of a small purge line along the rotating shaft. Thus materials are prevented from condensing or depositing on the shaft. The rotating speed of the shaft was measured by a reed switch counting the number of times a magnet on the shaft passed by. The reactor was heated in an oven fitted with a circulating fan and a temperature controller. The reactor chamber temperature was measured by a Chromel/Alumel thermocouple. Heat transfer calculations gave an estimate of less than 1°C difference between chamber and catalyst temperatures. Reactor pressure was kept at 1 bar gauge, thus minimising ignition hazards which could be caused by the ingress of air if there were leakages.

A schematic diagram of the experimental equipment is shown in Figure 2. High purity nitrogen was used as a reactant diluent. It was passed through a column containing 13X zeolite to remove any moisture present. Gas chromatographic analysis of the nitrogen feed showed no detectable impurities. Alcohol of purity higher than 99.5% was delivered by a metering pump to an evaporation unit where it was mixed with the nitrogen diluent. The mixed feed was brought to nearly the chosen reaction temperature in this electrically heated furnace. Connecting tubings were kept at high enough

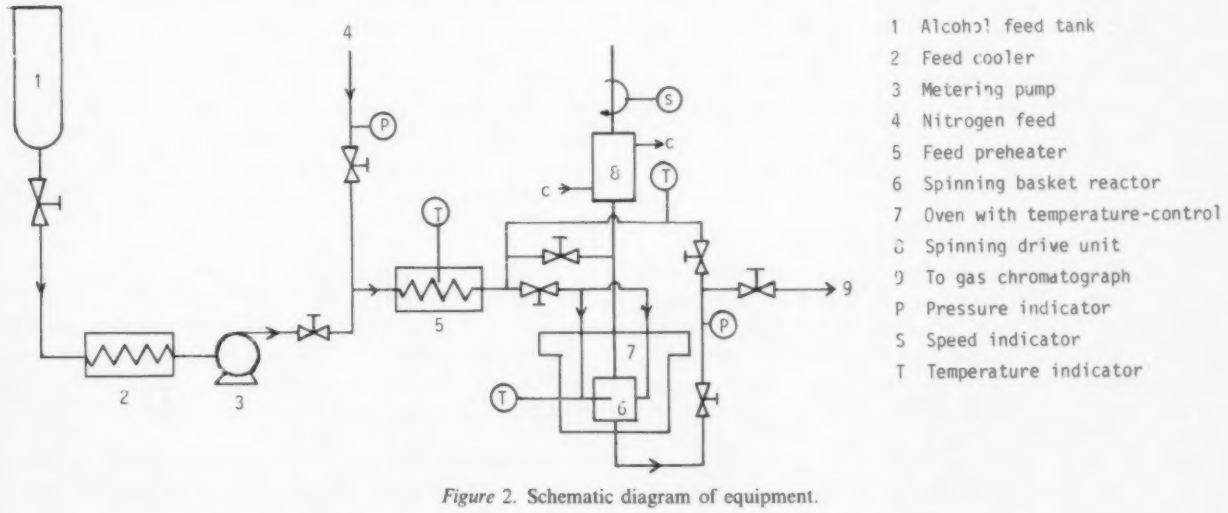


Figure 2. Schematic diagram of equipment.

temperatures by heating tapes to avoid the condensation of materials. The following ranges of reaction temperature were chosen for the various alcohols: (*a*) ethanol 270–350°C, (*b*) isopropanol 200–300°C and (*c*) n-butanol 200–300°C. The alcohol feed rate was varied to achieve a wide range of alcohol partial pressures at constant total pressure. At least five partial pressures of alcohol were used for a given reaction temperature and zeolite.

Reactor effluent was analysed by a gas chromatograph. The packing materials, column temperatures, column dimensions, carrier gas flow rates and detector temperatures varied, depending on the alcohol used. Full details of the analyses can be found in a thesis[33]. Calibration curves for the different components were prepared. Mean values of the measurements were obtained from three or more reproducible analyses. Error analysis gave a deviation of no more than 4% from the mean for each component. Alcohol flow rate was measured by a burette attached to the feed tank. The nitrogen supply was regulated by a mass flow control valve. Its flow rate was measured by a bubble flow meter downstream of the reactor after the removal of the condensable materials.

True surface reaction rates can be obtained only if the experiments have been performed under conditions which are not limited by diffusional processes. At high gas velocities, external, i.e. interphase mass transfer, will not be rate-limiting. The spinning speed was therefore varied to establish the conditions when the rates were not controlled by interphase diffusion.

The effect of pore diffusion was more difficult to assess. Zeolites have unique pore structures, possessing well defined cages and channels. The pores offer a very high surface area for reaction, but obviously contribute significant resistance to mass transfer. The study of diffusional processes within the zeolite crystals has been and continues to be an interesting subject for research[34]. These intra-crystalline migrations are not fully understood as yet. Unlike conventional porous catalysts, the absence of pore diffusion effects in zeolites cannot be ensured by performing the reactions with varying particle size. Experiments with different particle sizes can determine the influence of molecular and Knudsen diffusion, but not configurational diffusion in the pores. The reactor used in the present study does not permit the use of fine catalyst particles. Intra-crystalline transport was therefore examined using another piece of equipment and will be reported elsewhere[1]. In the following discussion, possible influence of pore diffusion on the present results will be noted wherever appropriate.

RESULTS AND DISCUSSION

Product analysis showed that small quantities of side products were sometimes produced. Aldehydes were formed from the primary alcohols and ketone from the secondary alcohol. These were products of the dehydrogenation of the alcohols which were catalysed by copper and nickel[4]. Experiments without zeolites in the reactor confirmed the formation of aldehydes catalysed by the copper and nickel present in the tubings and reactor wall. The dehydration reactions, however, are not affected by these metals. The rates of formation of olefin and ether were calculated based on material balances which had taken the side products into account.

Since the zeolites were found to deactivate with time, their activity was measured regularly. It was found that when fresh catalysts were used, catalytic activity always dropped rapidly in the initial stage of the experiments and then levelled off for a considerable time. The present kinetic data were obtained in the period of constant activity and the results were reproducible to within $\pm 10\%$. The problem of catalyst deactivation and regeneration was studied separately by extensive experimentation over a much longer period of time. Discussion on the study of the variation of catalyst activity with time is not relevant here and will be presented elsewhere[1].

Reaction rates determined at different reactor spinning speeds were compared to establish the minimum speed required to eliminate the influence of external mass transfer. This critical point varies slightly with gas flow rate. In general, above 2000 rev/min, reaction rates are unaffected by external mass transfer, which agrees with the conclusions of others[35,36]. The rate data have been gathered at reactor spinning speeds above this value.

All the rate data have been modelled according to both power-law kinetics and Hougen–Watson type of kinetic expressions. The latter approach is based on the classical Langmuir–Hinshelwood mechanism, with surface reaction or adsorption–desorption of reactants and/or products assumed to be rate controlling. Preliminary discrimination of all plausible rate expressions was conducted to eliminate some of the less probable models. For example, the adsorption–desorption equilibrium constants of ether and olefin have been found to be very small, hence the desorption of these two species cannot be rate limiting. The partial pressures of ether, olefin and water in the present experiments were very low compared with that of alcohol, thus the products $K_E p_E$, $K_O p_O$, $K_W p_W$ were much smaller than $K_A p_A$. The adsorption of nitrogen on zeolites is not appreciable[37] above 244 K. Thus $K_A p_A$ is the major contribution to the adsorption term in the Hougen–Watson model. The equilibrium constant of the olefin formation reaction is high and the reaction can be considered irreversible.

Parameters in the remaining models were estimated according to the methods proposed by Kittrell[38]. Both multi-linear and non-linear regression analyses were applied to the experimental data. Results from linear regression were used as first estimates for non-linear regression. The theoretical aspects of parameter estimation and regression techniques are well established[39,40] and details of the computer programs have been given by Dixon and Brown[41].

FORMATION OF OLEFINS

Some typical rate data are presented in Figures 3–5. The rates of formation of propene and butene are almost independent of the partial pressure of alcohol, indicating that the reactions tend towards zero order in alcohol in terms of power-law kinetics. For the formation of ethene, the reaction order is higher, but is still short of first order in alcohol. Of all the power-law rate expres-

VOL. 62 1984

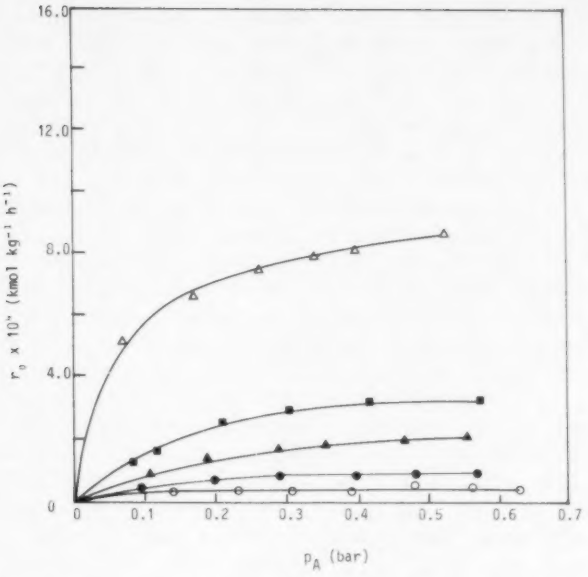


Figure 3. Rate of butene formation over zeolite 13X as a function of alcohol partial pressure —○— 228° C, —●— 241° C, —▲— 252° C, —■— 258° C, —△— 272° C.

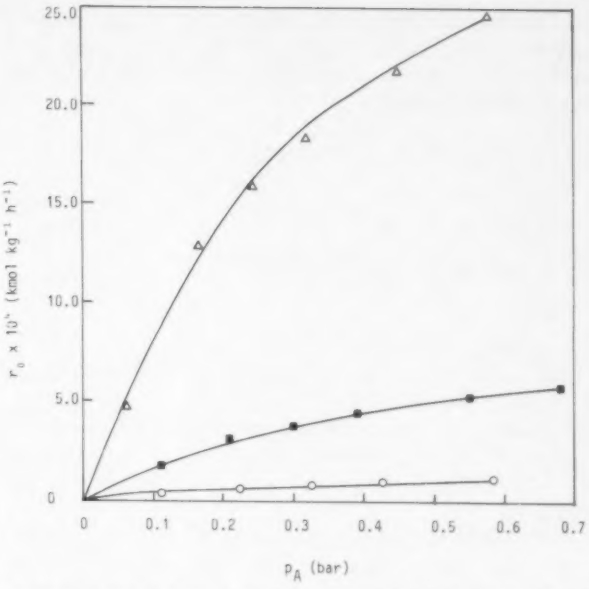


Figure 5. Rate of ethene formation over zeolite 4A as a function of alcohol partial pressure —○— 279°C, —■— 313°C, —△— 349°C.

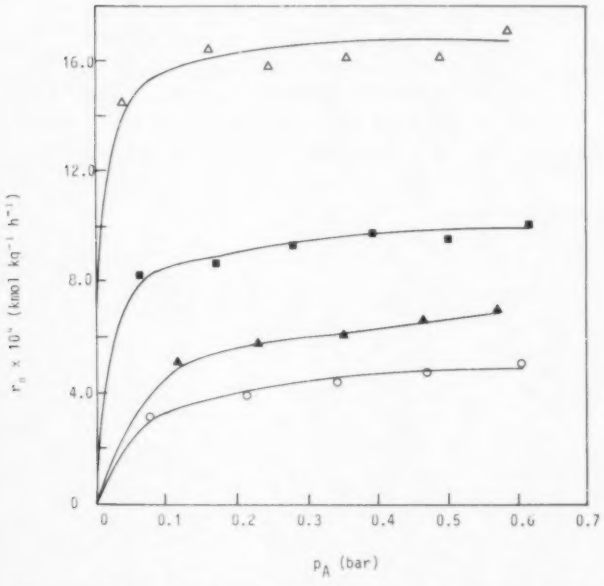


Figure 4. Rate of propene formation over zeolite ZNa as function of alcohol partial pressure —○— 228° C, —▲— 238° C, —■— 254° C, —△— 274° C.

sions tested, the most successful one was

$$r_O = A_O \exp(-E_O/RT) p_A^n \quad (1)$$

Table 3 gives the best estimates of the constants for equation (1), together with the statistical properties: t-ratio, F-ratio and R-squared coefficient. A high t-ratio means small standard deviation, hence a higher confidence level. The calculated F-ratio gives an indication of the significance of the regression; while the last column shows the observed F-ratio at 95% confidence level. If the observed F-ratio exceeds the critical F-ratio at 95% confidence level by a factor of four, statistically significant regression is said to have been attained[42]. The R-squared coefficients give a measure of how well the regression expression fits the experimental data. Results in Table 3 show that regression of the rate data for olefin formation according to power-law kinetics are statistically satisfactory over all the zeolites. Propene and butene formation are close to zero order and ethene formation is just over half order with respect to alcohol partial pressure. These conclusions are in general agreement with those in the literature, see Table 1. The low reaction orders suggest that the active sites of the catalyst are nearly saturated with alcohol and also implies the absence of external mass transfer effect.

Table 3. Kinetic Parameters for Power Law Model: Olefin Formation

Alcohol	Zeolite	A_O (kmol kg^{-1} h^{-1} bar^{-n})	E_O (kJ gmol^{-1})	n	t-ratio	R^2	F-ratio (critical)	F-ratio (observed)
n-butanol	13X	1.4×10^{12}	159	0.28	8.0	99	20	1200
	4A	5.6×10^{10}	151	0.12	4.1	99	20	770
	ZNa	8.0×10^{5}	105	0.17	4.9	99	20	3000
Isopropanol	13X	1.1×10^{8}	109	0.29	14	99	20	660
	4A	8.5×10^{5}	96	0.38	12	99	20	200
	ZNa	2.8×10^{3}	67	0.14	6.6	99	20	690
Ethanol	4A	7.5×10^{7}	126	0.67	19	100	20	150
	ZNa	3.0×10^{4}	92	0.79	12	93	20	83

The two rate expressions derived for the formation of olefin, based on the assumption that surface reaction is rate-limiting, are the so-called dual-site and single-site mechanism models[43].

Dual-site mechanism (SR1)

$$r_O = \frac{k_O K_A p_A}{(1 + K_A p_A)^2} \quad (2)$$

Single-site mechanism (SR2)

$$r_O = \frac{k_O K_A p_A}{(1 + K_A p_A)} \quad (3)$$

Effects of the weakly adsorbed species and those present in relatively small concentrations have been neglected. Equation (2) predicts a reaction order between 1 and -1 in alcohol while equation (3) allows for an order of less than 1. Both equations indicate a rate inhibition by alcohol.

High R-squared coefficients were obtained from linear regression at all reaction temperatures and over all the zeolites. However, a negative adsorption coefficient was found in the case of butene formation over ZNa zeolite at 235°C according to model SR1. Non-linear regression confirmed that the single site model was not appropriate for this set of data because an unlikely high adsorption equilibrium constant was obtained. In the non-linear analysis, a small value of the sum of squares of residuals (SSR) means that satisfactory correlation is achieved. For the sake of brevity, only the non-linear regression results are shown in Tables 4(*a*), (*b*), (*c*); and a comparison of the linear and non-linear methods is illustrated in Table 5. There is excellent agreement between the parameters obtained from both techniques which suggests that the kinetic data are good. Both surface reaction models (SR2 and SR1) represent the data well, yielding very small residuals; the latter model, however, fails to correlate the butene data over the modernite.

The temperature dependence of the kinetic and adsorption parameters is illustrated in Figure 6. The kinetic parameters were found to follow the Arrhenius equation and yielded good straight line plots, indicating that the kinetic data were obtained in the surface reaction rate-controlling regime and no significant catalyst deactivation occurred. Temperature variation of the adsorption–desorption equilibrium constants was in accordance with the van't Hoff type of equation. Except for the adsorption of n-butanol on zeolite ZNa and possibly also on 4A, the adsorption plots have negative slopes, showing that the alcohol adsorption process is endothermic and dissociative. Estimates of the pre-exponential factors (for the HW kinetic parameters), activation energies and enthalpies of adsorption of isopropanol, obtained by linear regression, are shown in Table 6. The results of activation energies from the Hougen–Watson type models agree quite well with those from the power-law model, which suggests that the adsorption process has no significant effect on the apparent activation energies of the dehydration reactions, probably because of low reaction orders. The heats of adsorption for both 13X and ZNa, obtained from the SR1 model, are probably too high. Except in the case of ZNa, the results show no discernible effects of either external or pore diffusion. It should, however,

VOL. 62 1984

Table 4. Parameters for Hougen–Watson models

(*a*) *Butene formation*

Zeolite	Model	T (°C)	$k_O \times 10^4$ (kmol kg^{-1} h^{-1})	SD ($\times 10^4$)	K_A (bar^{-1})	SD	SSR ($\times 10^{10}$)
13X	SR2	228	1.9	0.28	1.3	0.62	1.0
		241	4.0	0.16	2.2	0.34	1.0
		252	8.0	0.43	2.0	0.39	3.0
		258	13	0.32	1.6	0.12	1.0
		272	33	1.4	2.7	0.48	52
13X	SR1	228	0.59	0.15	6.3	5.2	1.0
		241	1.2	0.04	12	2.0	<0.5
		252	2.4	0.15	11	2.6	1.0
		258	4.4	0.37	6.3	1.7	3.0
		272	9.4	0.30	17	2.7	8.0
4A	SR2	232	0.55	0.03	3.3	0.72	<0.5
		250	2.0	0.07	3.1	0.47	<0.5
		271	9.0	0.55	2.7	0.65	9.0
		278	11	0.40	2.7	0.42	5.0
		297	32	1.8	2.7	0.61	104
4A	SR1	232	0.14	0.01	46	25	<0.5
		250	0.49	0.01	44	13	<0.5
		271	2.4	0.01	28	11	2.0
		278	2.9	0.07	24	4.0	<0.5
		297	8.4	0.47	29	13	29
ZNa	SR2	235	0.80	0.03	4.5	0.49	<0.5
		255	1.9	0.12	3.0	0.66	<0.5
		275	4.7	0.15	2.9	0.37	1.0
		300	13	0.56	2.5	0.38	6.0
ZNa	SR1	235	0.18	0.01	17×10^2	0	<0.5
		255	0.52	0.02	23	5.0	<0.5
		275	1.2	0.04	30	8.3	<0.5
		300	3.6	0.20	14	3.4	2.0

Table 4. (continued) Parameters for Hougen–Watson models

(*b*) *Propene formation*

Zeolite	Model	T (°C)	$k_O \times 10^4$ (kmol kg^{-1} h^{-1})	SD ($\times 10^4$)	K_A (bar^{-1})	SD	SSR ($\times 10^8$)
13X	SR2	231	36	1.7	1.5	0.24	0.25
		240	52	2.0	2.0	0.32	0.88
		255	103	5.8	2.4	0.59	8.7
		286	320	29	9.9	2.5	150
13X	SR1	231	11	0.66	6.9	1.4	0.10
		240	15	0.61	12	2.5	0.22
		255	29	2.3	16	7.1	3.8
		286	75	1.4	140	16	3.5
4A	SR2	200	1.0	—	0.97	—	—
		229	4.7	0.20	1.1	0.12	0.00
		252	14	2.6	1.1	0.46	0.22
		275	27	5.1	1.3	0.71	1.6
		301	68	7.1	1.2	0.31	2.1
4A	SR1	200	0.38	—	2.9	—	—
		229	1.6	0.08	3.7	0.50	0.00
		252	4.1	0.95	4.7	2.7	0.17
		275	7.4	1.3	11	7.8	1.1
		301	22	2.8	5.0	1.6	1.4
ZNa	SR2	228	20	1.3	2.4	0.59	0.35
		238	27	1.4	2.5	0.52	0.44
		254	42	2.7	3.9	0.84	2.1
		274	77	7.6	5.9	1.6	11
ZNa	SR1	228	5.5	0.31	17	4.8	0.08
		238	7.4	0.40	19	6.1	0.11
		254	10	0.24	74	24	0.13
		274	17	0.31	220	97	0.33

Table 4. (continued) Parameters for Hougen–Watson models

(*c*) *Ethene formation*

Zeolite	Model	T (°C)	$k_O \times 10^4$ (kmol kg^{-1} h^{-1})	SD ($\times 10^4$)	K_A (bar^{-1})	SD	SSR ($\times 10^8$)
4A	SR1	349	4.2	0.29	2.6	0.35	0.39
		313	0.95	0.050	2.4	0.25	0.01
		279	0.24	0.016	1.9	0.23	0.00
4A	SR2	349	11	0.53	0.90	0.09	0.39
		313	2.6	0.10	0.80	0.07	0.20
		279	0.60	0.040	0.71	0.08	0.00
ZNa	SR1	349	2.4	0.91	0.46	0.21	0.02
		312	0.44	0.066	1.9	0.54	0.02
		285	0.20	0.019	0.80	0.10	0.00
ZNa	SR2	349	5.3	1.9	0.21	0.09	0.02
		312	1.2	0.04	0.65	0.15	0.02
		285	0.46	0.042	0.34	0.04	0.00

be cautioned that diffusion limitations might manifest at higher reaction temperatures[1].

FORMATION OF ETHERS

Some typical rate data are shown in Figure 7. The power-law model is, in most cases, satisfactory in representing the kinetics of ether formation. In the dehydration of n-butanol to dibutyl ether, the rate expression

$$r_E = A_E \exp(-E_E/RT) p_A^m \qquad (4)$$

is adequate for 13X and 4A zeolites, but not for the modernite ZNa. The same equation works reasonably well with isopropanol dehydration over all three zeolites. No ether was found when ethanol was dehydrated over ZNa. Values of the kinetic parameters in equation (4), together with the R-squared coefficients and F-ratios are given in Table 7.

The reaction orders for ether formation are higher than those for olefin formation for all the alcohols. The ether formation reaction is, of course, bimolecular rather than monomolecular, thus reaction order could arguably be higher. The ethanol and isopropanol dehydration reactions tend towards first order with respect to alcohol, while n-butanol dehydration is between zero and half order. The results are in general agreement with literature values, see Table 1. The activation energies for the formation of ether are shown in Table 7. Comparing these results with those reported in the literature shows that in most cases the rates have been affected by pore diffusion. Internal diffusion limitations are doubtlessly reflected in the data on modernite ZNa, both in the

Table 5. Comparison between linear and non-linear regression: n-butanol over ZNa zeolite

Model	SR2				SR1			
Regression method	Linear		Non-linear		Linear		Non-linear	
Parameter	$k_O \times 10^4$ (kmol kg^{-1} h^{-1})	K_A (bar^{-1})	$k_O \times 10^4$ (kmol kg^{-1} h^{-1})	K_A (bar^{-1})	$k_O \times 10^4$ (kmol kg^{-1} h^{-1})	K_A (bar^{-1})	$k_O \times 10^4$ (kmol kg^{-1} h^{-1})	K_A (bar^{-1})
(°C)								
235	0.81	4.9	0.80	4.6	0.15	−19	0.18	1100
255	2.0	3.0	1.9	3.0	0.55	16	0.52	23
275	4.8	2.7	4.7	2.9	1.3	26	1.2	30
300	13	2.4	13	2.5	3.6	14	3.6	14

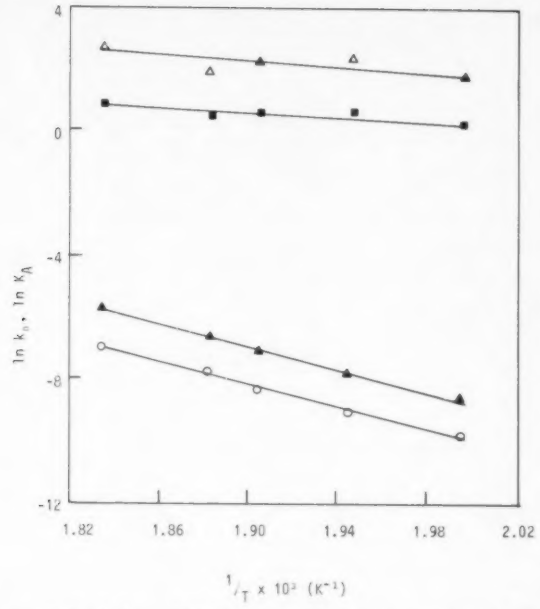


Figure 6. Variation of kinetic parameter and adsorption-desorption equilibrium constant with temperature: butene formation over 13X —○— ln k_O (SR1), —▲— ln k_O (SR2), —■— ln k_A (SR1), —△— ln k_A (SR2).

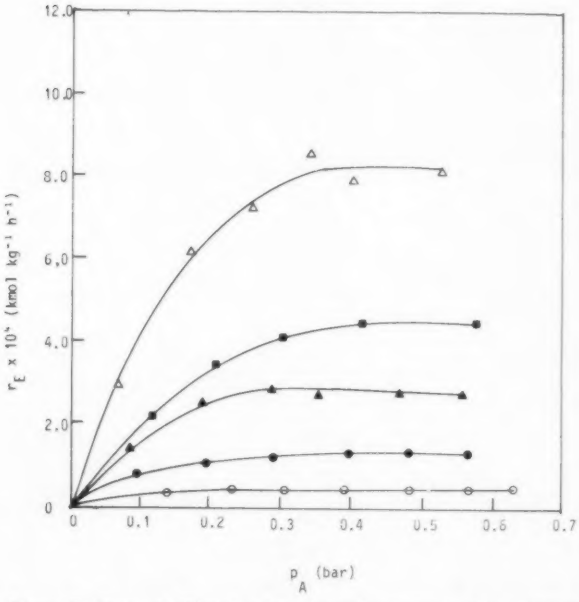


Figure 7. Rate of dibutyl ether formation over zeolite 13X as a function of alcohol partial pressure —○— 228° C, —●— 241° C, —▲— 252° C, —■— 258° C, —△— 272° C.

Table 6. Kinetic and adsorption parameters for Hougen–Watson models: dehydration of isopropanol

Zeolite	Model	A'_O (kmol kg^{-1} h^{-1})	E_O (kJ kmol^{-1})	ΔH_A (kJ kmol^{-1})
13X	SR2	2.2×10^7	96	80
	SR1	3.8×10^5	84	125
4A	SR2	2.4×10^5	88	20
	SR1	2.2×10^4	92	6.3
ZNa	SR2	2.0×10^4	67	50
	SR1	2.3×10^2	54	138

VOL. 62 1984

Table 7. Kinetic parameters for power-law model: ether formation

Alcohol	Zeolite	A_E (kmol kg^{-1} h^{-1} bar^{-n})	E_E (kJ gmol^{-1})	m	t-ratio	R^2	F-ratio (critical)	F-ratio (observed)
n-butanol	13X	4.1×10^{10}	142	0.38	5.8	95	20	280
	4A	1.7×10^{3}	84	0.29	5.7	95	19	88
	ZNa	4.7	54	0.56	4.8	79	19	17
Isopropanol	13X	1.6×10^{2}	59	0.96	9.7	88	20	54
	4A	1.4×10^{6}	117	1.30	10	94	20	102
	ZNa	1.1	42	0.89	16	95	20	170
Ethanol	4A	1.6×10^{3}	67	0.70	15	98	20	300

dehydration of n-butanol and isopropanol. With 13X zeolite, which has the largest pore aperture (10 Å), the results suggest that pore diffusion has influenced ether formation from isopropanol, but not n-butanol. However, it must be stressed again that the latter inference is applicable only in the temperature range considered. The effect of internal diffusion is also manifested in ether formation over 4A zeolite, except in the case of isopropanol. Gottifredi et al[13], obtained an apparent activation energy of 120 kJ g mol^{-1} for the formation of di-isopropyl ether over a non-porous cation exchange resin, which compares well with the present value of 117 kJ g mol^{-1}. It could well be that the size and shape of di-isopropyl ether molecules are such that they could only be formed at the external surface of this zeolite, and the ether molecules could not leave the crystals. Molecular size and shape selectivities will be discussed in greater detail in a subsequent paper.

The rate data on ether formation have also been correlated with Hougen–Watson type of kinetic expressions. Many rate expressions can be derived, but only three models, which assume that the bimolecular surface catalysed reaction is the rate controlling step, will be discussed here. The models are based on the following reaction mechanisms[43].

(*a*) *LHM model* assumes that the surface reaction takes place according to the Langmuir–Hinshelwood mechanism in which two adjacently chemisorbed alcohol molecules react to form the chemisorbed products. The rate of formation of ether is given by

$$r_E = \frac{k_E K_A^2 (p_A^2 - p_W p_E / K^*)}{(1 + K_A p_A)^2} \tag{5}$$

(*b*) *REM1 model* assumes that the surface reaction follows the Rideal–Eley mechanism in which one alcohol molecule in the gas phase reacts directly with another chemisorbed alcohol molecule, in the presence of a vacant site adjacent to the chemisorbed products. The rate is represented by

$$r_E = \frac{r_E K_A (p_A^2 - p_W p_E / K^*)}{(1 + K_A p_A)^2} \tag{6}$$

(*c*) *REM2 model* assumes that the surface reaction occurs according to the Rideal–Eley mechanism as in (*b*), but not in the presence of an adjacently vacant site, and that only the product water is chemisorbed, while the product ether goes directly into the gaseous phase. The rate of ether formation is

$$r_E = \frac{k_E K_A (p_A^2 - p_W p_E / K^*)}{(1 + K_A p_A)} \tag{7}$$

Qualitatively, models (*a*) and (*b*) predict an order of reaction between 0 and 2, while model (*c*) allows for a reaction order between 1 and 2. All three expressions predict the depressive behaviour of alcohol on the rate of formation of ether, but the influence is stronger with the first two equations. The models have also included the effect of the reverse reaction.

Again, both linear and non-linear regression analyses were performed. In all cases, results obtained from the former method were confirmed by the latter. Values of the kinetic and adsorption parameters evaluated by linear regression for all three cases are presented in Tables 8(*a*), (*b*), and (*c*). The correlations show very high R-squared coefficients, but the adsorption–desorption equilibrium constants were often found to be either very high or negative with the REM2 model. Although it has been argued that a negative adsorption coefficient is due to 'enhanced adsorption', the concept has not been widely accepted, thus the last model is rejected. Both the LHM and the REM1 model give equally good representation of data.

The variation of kinetic and adsorption–desorption equilibrium constants with temperature has also been examined. The temperature dependence again follows the Arrhenius and van't Hoff equations respectively. The estimated pre-exponential factors, apparent activation energies and heats of adsorption are presented in Table 9. The activation energies from the LHM and REM1 models compare well with those obtained from the power-law model. Rate limitation by pore diffusion can again be seen in the value of E_E for ethanol over 4A zeolite.

It is not appropriate to distinguish between LHM and REM1 models by the regression of kinetic data. Mathematically the two models have the same form and only differ in the parameter k_E. The apparent activation energies obtained from the two models should be related to each other by the heat of adsorption, i.e.,

$$E_E(\text{LHM}) = E_E(\text{REM1}) + \Delta H_A \tag{8}$$

The present results clearly support this relationship. For example, in the dehydration of n-butanol, E_E(LHM) has the value of 151 kJ g mol^{-1}, which is practically equal to the sum of E_E(REM1), 121 kJ g mol^{-1}, and ΔH_A which is -29 kJ g mol^{-1}.

Finally, it should be pointed out that the values of the adsorption equilibrium constants for ether formation are higher than those for olefin formation under the same reaction conditions. This behaviour suggests that alcohol dehydrates to form ether and olefin via different active sites. Furthermore, it indicates that the saturation

Table 8. Parameters for Hougen–Watson models

(*a*) *Dibutyl ether formation*

Zeolite	Model	T (°C)	$k_E \times 10^4$ (kmol kg^{-1} h^{-1})	SD ($\times 10^4$)	K_A (bar^{-1})	SD	SSR ($\times 10^{10}$)
13X	LHM	228	0.63	0.03	28	6.0	<0.5
		241	1.6	0.04	31	3.0	<0.5
		252	3.4	0.21	30	8.0	4.0
		258	5.9	0.43	15	3.1	6.0
		272	11	0.77	18	4.0	29
13X	REM1	228	17	3.0	28	0.0	<0.5
		241	48	3.9	31	3.0	<0.5
		252	99	22	30	8.0	4.0
		258	90	12	15	3.0	6.0
		272	200	30	18	4.0	29
13X	REM2	228	1.1	0.15	60×10^2	0	3.0
		241	3.2	0.46	35×10^3	0	18
		252	6.9	1.1	26×10^3	0	95
		258	10	1.5	76×10^2	0	150
		272	21	2.7	49×10^2	0	460

Table 8. (continued) Parameters for Hougen–Watson models:

(*b*) *Di-isopropyl ether formation*

Zeolite	Model	T (°C)	$k_E \times 10^4$ (kmol kg^{-1} h^{-1})	SD ($\times 10^4$)	K_A (bar^{-1})	SSR ($\times 10^{10}$)
13X	LHM	231	1.5	0.06	6.9	<0.5
		240	2.2	0.07	6.7	<0.5
		255	10	2.27	1.8	<0.5
13X	REM1	231	10	0.36	6.9	<0.5
		240	15	0.45	6.7	<0.5
		255	18	0.59	1.8	1.0
13X	REM2	231	1.8	0.11	8.1×10^3	1.0
		240	2.6	0.16	4.1×10^3	3.0
		255	5.4	0.44	9.7	<0.5

Table 8. (continued) Parameters for Hougen–Watson models:

(*c*) *Di-ethyl ether formation*

Zeolite	Model	T (°C)	$k_E \times 10^3$ (kmol kg^{-1} h^{-1})	SD ($\times 10^3$)	K_A (bar^{-1})	SD	SSR ($\times 10^8$)
4A	LHM	349	3.8	0.47	4.2	0.69	0.71
		313	2.0	0.18	5.1	0.75	0.28
		279	1.1	0.13	7.4	1.6	0.18
4A	REM1	349	16	0.82	4.2	0.69	0.71
		313	10	0.65	5.1	0.75	0.28
		279	8.0	0.88	7.4	1.6	0.18

partial pressure of alcohol is higher for ether formation than for olefin formation. This is also evident in the difference in the reaction orders, as has been discussed previously.

CONCLUSIONS

Both olefin and ether were formed when ethanol, isopropanol and n-butanol were dehydrated over Laporte zeolites 13X and 4A and Norton modernite ZNa, except in the case of ethanol dehydration over the modernite. Simple power-law rate models can satisfactorily represent the kinetics of olefin formation and most cases of ether formation, except for dibutyl ether formation over the modernite. The olefin formation reactions vary between zero and half order with respect to the partial pressure of alcohol. Ether formation from

Table 9. Kinetic and adsorption parameters for Hougen–Watson models

Alcohol	Zeolite	Model	$k_E \times 10^4$ (kmol kg^{-1} h^{-1})	E_E (kJ kmol^{-1})	ΔH_A (kJ kmol^{-1})
n-butanol	13X	LHM	2.6×10^{11}	151	−29
		REM1	8.3×10^9	121	
Isopropanol	13X	LHM	1.6×10^{15}	184	−134
		REM1	1.9×10^8	50	
Ethanol	4A	LHM	71	50	−23
		REM1	3.2	28	

VOL. 62 1984

ethanol and isopropanol tends towards first order, while the dehydration of n-butanol to dibutyl ether is approximately half order.

The Hougen–Watson type of rate expressions based on dual-site mechanism are successful in modelling the olefin kinetics, but single-site mechanism fails in some cases. For the bimolecular reaction of ether formation, models based on Langmuir–Hinshelwood and Rideal–Eley mechanisms, including the effect of the reverse reaction, can correlate the rate data well.

Activation energies for the formation of olefins obtained from the power-law model show no discernible effect of pore diffusion in the temperature range studied. However, the influence of pore diffusion can be seen in the results of ether formation over 4A zeolite. The production of di-isopropyl ether over 4A is probably only confined to the external surface of the catalyst. Adsorption–desorption equilibrium constants obtained from the Hougen–Watson models follow van't Hoff type of equation.

The dehydration of the three alcohols to olefin and ether can be considered as parallel surface reactions, but the ether reaction is reversible. The alcohols probably dehydrate to form olefin and ether via different active sites. In most cases, the rate controlling step is that of surface reaction. It should, however, be noted that the conclusions are only valid when the effect of water on the reactions is negligible.

SYMBOLS USED

A_j	pre-exponential factor for the formation of j in power-law models (kmol kg^{-1} h^{-1} bar^{-n})
A'_j	pre-exponential factor for the formation of j in Hougen–Watson models (kmol kg^{-1} h^{-1})
E_j	activation energy for the formation of j (KJ $gmol^{-1}$)
ΔH_A	heat of adsorption (KJ $gmol^{-1}$)
k_j	kinetic parameter in HW models for the formation of j (kmol kg^{-1} h^{-1})
K_j	adsorption–desorption equilibrium constant for j (bar^{-1})
K^*	chemical equilibrium constant for the reversible ether formation reaction (–)
m,n	reaction order in equations (4) and (1) respectively
p_j	partial pressure of j (bar)
r_j	rate of formation of j (kmol kg^{-1} h^{-1})
T	absolute temperature (K)
Subscripts or in reaction schemes	
A	alcohol
E	ether
O	olefin
W	water
Abbreviations	
HW	Hougen–Watson type of rate expression
LHM	Langmuir–Hinshelwood mechanism
PL	power law
REM1	Rideal–Eley mechanism based on dual site
REM2	Rideal–Eley mechanism based on single site
SR1	surface reaction mechanism based on dual site
SR2	surface reaction mechanism based on single site
SSR	sum of squares of residuals
SD	standard deviation

REFERENCES

1. Birk, R. H., Yue, P. L. and Thomas, W. J., paper to be published.
2. Gryaznova, Z. V., Ermilova, M. N., Tsitsishvili, G. V., Androwiashvilli, T. G. and Krupennikova, Yu. A., 1969, *Kinetics and Catalysis, USSR*, 10: 1099.
3. Stauffer, J. E. and Kranich, W. L., 1962, *Ind Eng Chem Fund*, 1(2): 107.
4. Miller, D. N. and Kirk, R. S., 1962, *AIChE J*, 8(2): 183.
5. Maurer, J. F. and Sliepcevich, C. M., 1952, *AIChE Symp Ser*, 48(4): 31.
6. Pines, H. and Haag, W. D., 1960, *J Amer Chem Soc* 82: 2471.
7. Butler, J. D., Poles, T. C. and Wood, B. T., 1970, *J Catal* 16: 239.
8. Gentry, S. J. and Rudham, R., 1970, *J Chem Soc Trans Faraday*, I(70): 1685.
9. Stone, F. S. and Agudo, A. L., 1969, *Z Phys Chem*, Frankfurt, 64: 161.
10. Topchieva, K. V. and Tkhoang, H. S., 1973, *Kinetics and Catalysis, USSR*, 14: 398.
11. Topchieva, K. V. and Tkhoang, H. S., 1973, *Kinetics and Catalysis, USSR*, 14: 1491.
12. Leaute, R. and Lana, I. G. D., 1979, *J Catal*, 60: 460.
13. Gottifredi, J. C., Yeraman, A. A. and Cunningham, R. E., 1968, *J Catal*, 12: 245.
14. Jain, J. R. and Pillai, C. N., 1970, *J Catal*, 9: 322.
15. de-Mourgues, L., Peyron, F., Trambouze, Y. and Pettre, M. J., 1967, *J Catal*, 7: 117.
16. Jacobs, P. A. and Uytterhoeven, J. B., 1977, *J Catal*, 50: 98.
17. de-Boer, J. H., Fahim, R. B., Linsen, B. G., Visseren, W. J. and de-Vleesschauwer, W. F. N. M., 1967, *J Catal*, 7: 163.
18. Kabel, R. L. and Johanson, L. N., 1962, *AIChE J*, 8: 621.
19. Figueras, F., Nohl, A., de-Mourgues, L. and Trambouze, Y., 1971, *Trans Faraday Soc*, 67: 1155.
20. Butt, J. B., Bliss, H., and Walker, C. A., 1962, *AIChE J*, 8: 42.
21. Krishnaprasad, T. N. and Ravindram, M., 1977, *Hungarian J Ind Chem*, 5: 13.
22. Ralek, M. and Gruber, O., 1964, *Proc. 3rd Int Cong Catalysis* (Elsevier, Amsterdam, Holland) 2: 1302.
23. Bryant, D. E. and Kranich, W. L., 1967, *J Catal*, 8: 8.
24. Alvarado, M., 1928, *J Amer Chem Soc*, 50: 790.
25. Brey, W. S. and Krieger, K. A., 1949, *J Amer Chem Soc*, 71: 6637.
26. Topchieva, K. V. and Yun-Pin, K., 1955, *Zh Fiz Khim*, 29(10): 1854.
27. Knözinger, H., Ress, E. and Buhl, H., 1968, *J Catal*, 12: 121.
28. Knözinger, H., Kochloefl, K. and Meye, W., 1973, *J Catal*, 28: 69.
29. Pines, H. and Manassen, J., 1966, *Adv Catal*, 16: 49.
30. Bakshi, K. R. and Gavalas, G. R., 1975, *AIChE J*, 21(3): 494.
31. Csicsery, S. M., 1976, *Zeolite Chemistry and Catalysis*, Rabo, J. A. (ed.), (American Chemical Society, Washington, D.C.), p. 680.
32. Brisk, M. L., Day, R. L., Jones, M. and Warren M. A., 1968, *Trans I Chem E*, 46: T3.
33. Olaofe, O., 1982, *PhD Thesis* (Univ. Bath).
34. Ruthven, D. M., Derrah, R. I. and Loughlin, K. F., 1973, *Can J Chem Eng*, 51(21): 3514.
35. Ford, F. E. and Perlmutter, D. D., 1964, *Chem Eng Sci*, 19: 371.
36. Santacesaria, E., Morbidelli, M. and Carra, S., 1981, *Chem Eng Sci*, 36: 909.
37. Hersh, C. K., 1961, *Molecular Sieves* (Reinhold Publ Corp., New York), p. 79.
38. Kittrell, J. R., 1970, *Adv Chem Eng*, 8: 97.
39. Kittrell, J. R., Mezaki, R. and Watson, C. C., 1965, *Ind Eng Chem*. 57(12): 18.
40. Lapidus, L. and Peterson, T. I., 1965, *AIChE J*, 11: 891.
41. Dixon, W. J. and Brown, M. B., 1979, *Biomedical Computer Programs*, (Univ Calif Press).
42. Draper, N. R. and Smith, H., 1966, *Applied Regression Analysis*, (John Wiley and Sons, New York).
43. Hougen, O. A. and Watson, K. M., 1947, *Chemical Process Principles*, Part 3 (John Wiley and Sons, New York).

ACKNOWLEDGEMENTS

The research would not have been possible without the generous gift of zeolite samples given by Laporte Industries Ltd and Norton Chemicals Ltd. Helpful discussion with Mr R. H. Birk is also much appreciated. One of the authors (O.O.) was supported by a Commonwealth scholarship.

The manuscript was received 2 June 1983 and accepted for publication 4 October 1983.

STUDIES OF FLUID DISPLACEMENT BY FOAM IN POROUS MEDIA

By R. W. BURLEY (MEMBER), C. W. NUTT (FELLOW) and M. Gh. BAYAT
Department of Chemical and Process Engineering, Heriot-Watt University

Studies of the displacement of water and oil by foam from well-characterised sand-packs, under controlled conditions of pressure and flow have been carried out. Gamma-ray scanning equipment was used to monitor (continuously) changes on in-situ fluid saturation during gas-drive or foam flood recovery experiments. In order to demonstrate the nature of the flow of foam through graded sand-packs, a subsidiary apparatus was also designed so that the modification of the displacing front by foam would be demonstrated visually. Comparison of the displacement efficiencies of water and oil by gas-drive with and without the presence of surfactant solution and subsequent foam formation, showed that foam formation enhanced the displacement efficiency of both fluids. The study has confirmed that the differential flow impeding characteristics of foam increase the gas-drive recovery of residual fluids from porous media and that it is important to select a compatible surfactant capable of producing and maintaining stable interfaces in a given porous media. Foam enhanced gas-drives were found to modify the overall flow pattern, stop channelling, prevent early gas breakthrough, reduce the rate of gas production and enhance the fluid displacement process. The potential for wider application of foam as a mobility control agent in other operations is underlined.

INTRODUCTION

The present interest in the use of foam as a mobility control agent in enhanced oil recovery for a variety of gas and steam drive processes[1-3] has generated a large interest and research effort into the effectiveness of foam as an enhanced oil recovery technique. The potential for the use of foam lies in its unusual rheological characteristics[4] which give rise to a higher apparent viscosity in larger pores. This effectively blocks the larger pores relative to the smaller pores where residual oil may be trapped after primary or secondary recovery has occurred, so that differential flows are minimised and residual fluids may be mobilised. The mobility control of foam may also be used to advantage where large horizontal differences in the porosity in the ranges of oil bearing strata occur; here the long-term stability of foam is important, whilst gravity override can be reduced by the potential of the selective blocking mechanism, due to the prevention of natural drainage.

Principles of Foam Drive Enhanced Oil Recovery

Bond and Holbrook[5] were the first to describe the use of foam to improve oil recovery in a patent of 1958. In their method, a water-soluble surface-active agent with the required foam characteristics was injected into an underground formation as an aqueous slug. The slug was followed by gas to generate a foam bank within the rock matrix.

Fried[6] observed that oil saturation in porous media was reduced through the application of foam and that foam displaced oil normally irrecoverable by conventional water floods or gas drives. Bernard[7] showed, under laboratory conditions, that the displacement efficiency of a gas-drive could be increased by the generation of foam *in situ*. He observed that a foam-drive was much more efficient than the normal gas-drive in displacing oil, recovering up to three times as much oil at gas break-through. Minssieux[8] concluded that the application of foam enhanced the recovery of gas-drives more than water flooding.

Comprehensive reviews of the literature on the use of foam in the petroleum recovery industry have been presented elsewhere, for example, by Marsden *et al*[11] with particular reference to steam injection processes.

Foam has, over the years, been used in many other applications in petroleum recovery, for example as a drilling fluid, or as a fluid to plug natural or artificial rock fissures, and as a fluid to remove particulate and other material during air drilling. Bayat[9,11] has also previously reviewed the literature on applications of foam in enhanced oil recovery techniques, identifying three main areas of interest. These included the restriction of the flow of undesired gas or liquid; the improvement of areal sweep efficiency of fluid injection processes and improvement of gas-drive efficiency by promotion of an even distribution of the injection front.

Foam in Porous Media

Foam introduces large numbers of tenacious and resilient interfaces into a formation. It should be noted that while foam is a useful term in this context, it is unlikely that it exists within porous media as observed in an unconfined state, i.e. in a pore the interfaces of the lamellae will be of the same order of thickness as the pore radius. The multiplicity of these mobile interfaces develops the combination of forces required to dislodge immobilised oil globules. Other factors which favour the use of foam as an enhanced oil recovery agent include the improved sweep efficiency and the fact that high gas saturation can be achieved without producing a high gas-liquid ratio.

© Institution of Chemical Engineers

VOL. 62 1984

A foam bank which is generated in a formation first penetrates into the largest pore-channels, for example, those which have already been flushed of their oil content by a primary drive. The resistance to flow increases due to the high effective viscosity of the foam in the larger pores, and at the higher injection pressures so developed, the foam is forced into the smaller and unflushed channels.

Foam Rheology

A number of investigators have studied the rheology of foam. It may be considered[1,2] to be a non-Newtonian fluid which possesses many of the characteristics of a Bingham plastic, having a definite yield stress with a linear relationship between the shear stress and shear rate at low flow rates. Foams exhibit viscosities markedly greater than the sum of the separate viscosities of their constituents. The bulk viscosity of foam increases with quality at any single value of shear rate where quality is defined as the gas volume to total fluid volume. The viscosity of foam is independent of shear rate in the foam quality range of zero to 54%[4]. For foams of qualities greater than 54% the viscosity becomes dependent on both foam quality and shear rate. In this range the viscosity increased linearly with quality for any single shear rate up to a value of 0.92 and at greater qualities an abrupt rise in viscosity occurs[8]. Figure 1 summarises a schematic foam viscosity–quality relationship[4]. The relationship between quality and effective viscosity is further complicated by its dependence on pore size[4] so that the material can exhibit different properties under different pore size distributions simultaneously. Marsden and Khan[13] have shown that as the foam quality increases the mobility of the foam decreases, a point central to its application in improved oil recovery techniques.

Foam Flow Mechanisms in Porous Media

Various types of microscopic observations have shown that when two immiscible phases (e.g. gas and water) flow concurrently through a porous medium each phase occupies a certain number of channels according to its proportion; each phase flows in its own channel and the effective permeability to that phase is a single-valued function of its saturation. However, this is not the case for foam flow through the same type of porous media. Different mechanisms have been postulated to explain how foam propagates through porous media.

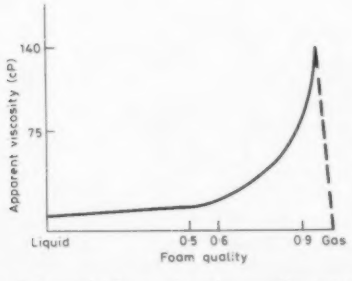


Figure 1. Schematic foam viscosity–quality relationship.

Some mechanisms proposed are as follows:

(i) The foam structure moves as a body; the rate of gas flow is the same as the rate of liquid flow[6,13].

(ii) Gas flows as a discontinuous phase by breaking and reforming films. The liquid flows as a free phase[4].

(iii) A large portion of the gas is trapped in the porous medium and a small fraction flows as free gas, following Darcy's law[15].

Fried[6] described the flow of foam through porous media as 'plug-type', non-Newtonian. By comparison, Bernard and Holm[16] treated foam as a mixture of gas and liquid which does not move through the porous medium as a composite body. In particular, Holm[17] using separate tracers for gas and liquid has suggested that foam does not flow homogeneously through the porous medium even when injected as foam. Liquid moved through the porous media via the network of interfaces, whilst gas, being the discontinuous phase, flowed through the media as lamellae broke and reformed. The flowrate of liquid and gas depended upon the number and strength of the films in the porous medium. It can therefore be concluded that surfactant concentration, stability of the lamellae, and wettability of formation will play an important role in the flow of foam in a porous medium as they will both affect the interface stability.

When oil is present, it has been shown[18] that foam stability always decreases, but this foam degradation in the presence of oil can be alleviated[8] with stabilising agents, capable of increasing the viscosity of the aqueous phase.

The steady-state flow of foam through porous media, once established, has been found[5,8,18] to occur under uniform pressure gradient, whilst in-situ water saturation measurements at steady-state foam flow conditions have also revealed uniform fluid distribution throughout the medium, regardless of the foam quality or the pressure level.

The gas blocking tendency of in-situ foam has been reported by several investigators[18–20] for many surfactant systems, and it has been demonstrated that this foam effect could persist for as long as two months[18]. This long term stability is of vital importance in blocking relatively porous strata.

Experimental Objectives

From the foregoing brief review of an extremely wide-ranging and developing field of knowledge, it can be seen that the potential applications of foam drive in enhanced oil recovery will depend on the intrinsic process efficiency and its economic viability. In turn, the economic aspects depend on adsorption data under dynamic conditions, which have been studied and reported on previously[22].

The experimental work reported here had as its main objective the investigation of the improvement of displacement efficiencies of gas-drive processes either by foam injection or in-situ generation. Several other objectives included:

(1) The evaluation of the effect of surfactant in reducing gas production and gas-liquid ratio in a gas-drive process.

Table 1. Classification of fluid-displacement experiments by gas and foam-drive.

Series No.	Experiments	Variables
1	Air, P_i → Water saturated → Air; Water	Columns A and B P_i = 2·1–6·2 psig
2	Air, P_i → SAA, Water → Air; Water	Column A P_i = 5·0–5·2 psig SAA = 0·1 ; 1·0 PV SAA Conc. = 1000 ppm
3	Air; Water or SAA → Water → Air; Water	Column A P_i = 5·0 psig Slug flow rates = 20–80 cm³ h⁻¹ SAA Conc. = 500; 1000 ppm
4	Foam → Water → Air; Water	Columns A and B P_i = 5·0–9·0 psig
5	Air; SAA → γ-counter, Water, γ-source → Air; Water	Column C P_i = 5·0–20·0 psig SAA Slug = 0·05 PV SAA Conc. = 5000 ppm
6	Air; Water or SAA → Water or SAA	Qualitative observations
7	Air; Water or SAA → Water + oil + air → Air; Liquid	Columns A and B Oil = 'n-Decane'; 'Isopar L'

(2) A study of the effect of surfactant solution on gas injectivity into a sand-packed column.

(3) A study of the saturation distribution of water during gas and foam-drives.

(4) The determination of the flow restriction due to the presence of foam in a stratified formation.

Details of the experiments carried out[10] and referred to in the text are summarised in Table 1, which outlines the range of work of this basic study. The surfactant employed was Triton X-100® (Rohm and Haas Ltd) a polyoxyethylene condensate of octyl-phenol, containing up to ten ethylene oxide molecules, with a molecular weight of 647. It is a 100% active nonionic, biodegradable anhydrous surfactant, with a cloud point of 62°C.

Table 2. Sand-packed column specifications

	Column A	Column B	Column C
Length (cm)	46	91.5	100
C.S.A. (cm²)	5.087	11.847	11.240
Total volume (cm³)	232	1,082	1,124
Sand weight (g)	332.5	1,697	1,694
Sand volume (cm³)	1255	640.5	622.5
Pore volume (cm³)	106.5	441.5	501.5
Permeability (darcy)	1.75	11	7.0
Porosity	0.459	0.408	0.446
Sand size (BS)	100–170	70–100	120–150 150–240†
$\frac{\text{inlet dia.}}{\text{column dia.}} = \frac{d}{D}$	$\frac{1}{4}$	$\frac{1}{6}$	$\frac{1}{6}$
$\frac{\text{column dia.}}{\text{column length}} = \frac{D}{L}$	$\frac{1}{18}$	$\frac{1}{24}$	$\frac{1}{26}$

†Ratio 4.8.

Fluid Displacement Studies

Figure 2 outlines the main apparatus used to carry out fluid displacement studies. It was designed to operate up to 500 psig pressure and temperature up to 95°C (although all displacement studies were carried out at ambient temperatures). It consisted of the following parts:

Injection System. Provision was made to inject either water, surfactant solution, gas or foam under controlled conditions into the sand-pack, as outlined in Table 1.

Sand-Pack. Two types of sand-packed columns were made for this work. The first type consisted of a sand-pack contained in a glass tube for low pressure and ambient temperature studies. The sand-pack details are given in Table 2. For high pressure work, a water jacketted stainless steel column was employed, so that the effect of temperature could be investigated.

Effluent Concentration. As shown in Figure 2, the effluent from the sand-pack flowed into a gas–liquid separator,

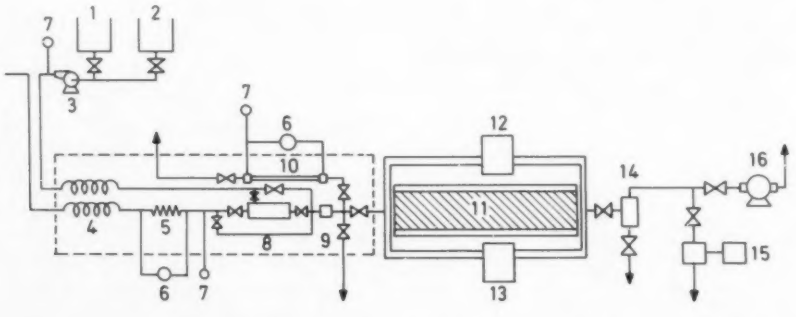


Figure 2. Schematic diagram of apparatus for fluid displacement studies. 1,2. Surfactant and water reservoirs. 3. Positive displacement pump. 4. Heat Exchangers. 5. Capillary tube for metering of gas. 6. Differential pressure gauge. 7. Pressure gauge. 8. Sand-pack foam generator. 9. Foam observation cell. 10. Capillary tube for foam viscosity measurements. 11. Sand-pack column and its water jacket. 12. Radio-active source holder. 13. Scintillation counter holder. 14. Gas-liquid separator. 15. Vacuum pump. 16. Gas wet test meter.

VOL. 62 1984

item 14, from which the gas flowed to the wet test meter and the liquid drained into a graduated cylinder for measurement. A vacuum pump, item 15, was used in certain experiments to ensure removal of air and permit 100% initial liquid saturation of the sand-packs.

Gamma Adsorption Measurements. Using data derived from previous tests[10], an apparatus was designed for the measurement of the fluid saturations of sand-packs in-situ. In this apparatus a radio-active source and scintillation counter in lead holders were moved along the sand-pack under controlled drive. The system automatically stepped the position of the assembly along the sand-pack, when the gamma absorbtiometer automatically logged saturation data for pre-set periods of time.

Apparatus for the Demonstration of Foam Mobility. A second piece of equipment shown in Figure 3 was also constructed to observe the flow of foam through sand-packs of different sand size ranges and permeabilities. Five parallel tubular holes (12 mm dia, 145 mm long) were drilled in a solid piece of perspex and subsequently packed with sand of different size ranges. At the top of each water saturated sand-pack a long empty column permitted observation of the amount of liquid production; or a shorter column which formed a gas–liquid separator could be mounted. Displacement of the water by foam was carried out at 20 $cm^3 h^{-1}$ through a common inlet manifold.

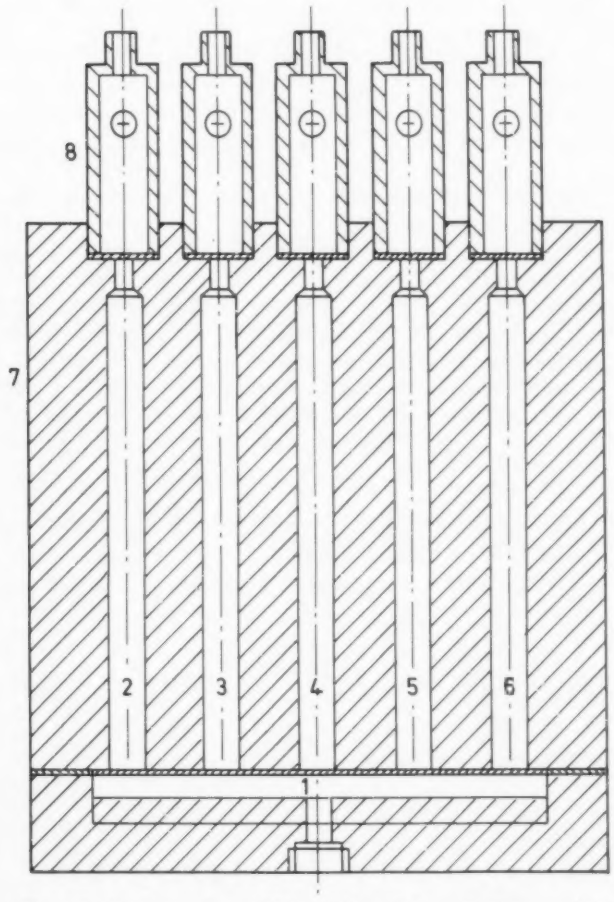


Figure 3. Apparatus for mobility studies of foam. 1. Common inlet manifold. 2–6. Sand-packed columns of 12 mm dia., 145 mm length, packed with sand of the following BS sizes respectively: 2. (22–30) BS, $k = 100$ darcy. 3. (52–60) BS, $k = 40$ darcy. 4. (72–85) BS, $k = 23$ darcy. 5. (100–120) BS, $k = 9$ darcy. 6. (120–170) BS $k = 5$ darcy. 7. Solid perspex material. 8. Gas-liquid separators.

RESULTS AND DISCUSSION OF EXPERIMENTS

The experiments are described in comparative order and referred to in Table 1 in detail.

Qualitative Foam Studies

From the sixth series of experiments observation of the accumulation of displaced water from the columns of the equipment shown in Figure 2(b) showed that the presence of the surfactant, Triton X-100®, greatly improved the efficiency of the gas-drive. For columns up to 100 Darcys permeability, the advance of the foam front through the rest of the columns was greatly reduced as indicated by the rate of observed colour change in each of the columns.

Initially foam (lamellae) flowed into and moved up the more permeable column of sand. After some minutes this process slowed, as the effective permeability decreased and foam entered the next column. The process continued so that the relative velocity of the displacing fronts tended to a common value in all columns. These observations showed clearly that the blocking mechanism of foam in the larger pores led to an equilibration of pressure drop over the sand-packed columns of different permeability. Thus the apparent non-Newtonian flow characteristics of foam can be utilised to equilibrate the advance of a displacing front through a stratified formation by generating gas–liquid interfaces in-situ.

Water Production by Gas-drive

Figure 4 shows the results for gas injection pressure, water production at gas breakthrough and the break-

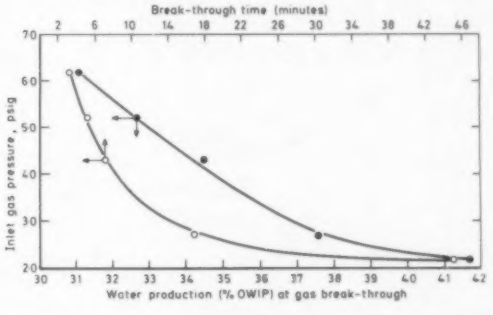


Figure 4. Inlet gas pressure, breakthrough time, water production relationship (from experiments 1.1–1.5, see Table 1).

Drive pressure at RT (psig)	BT time (min)	Water production at BT (cm^3)	Exp. no.
2.1	45	41.7	1.1
2.7	17	37.6	1.2
4.3	6:40	34.5	1.3
5.2	5:20	32.7	1.4
6.2	3:30	31.10	1.5

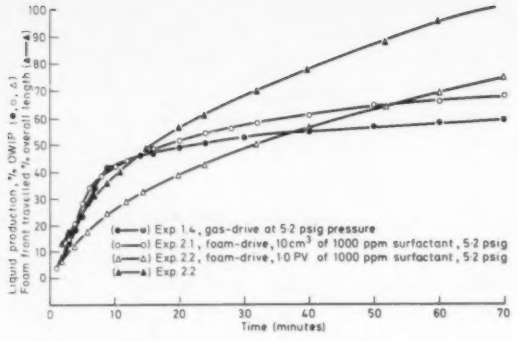


Figure 5. The effect of surfactant on water production by gas-drive process.

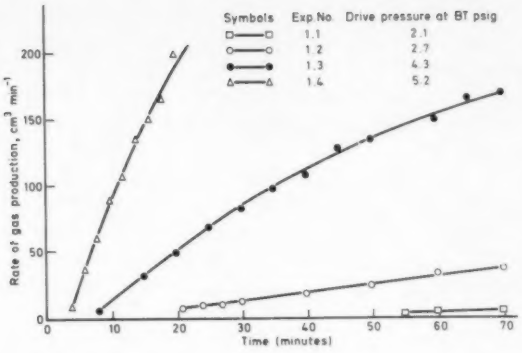


Figure 7. Rate of gas production versus time by gas-drive.

through time for gas-drive experiments. The higher gas injection pressure leads to lower water production before gas breakthrough. The production of water showed a sharp rate change at gas breakthrough, this change being smaller for higher pressure conditions, i.e. the production of water after gas breakthrough continued at a reduced rate, but according to injection pressures. After long elapsed times, it can be seen that more water was produced in the case of higher injection pressures. Also, it was found that at higher pressures more water was produced for similar amounts of gas production.

Effect of Surfactant on Water Production

Figure 5, compares water production with and without surfactant and demonstrates that the presence of surfactant markedly increases the efficiency of gas-drive. Similar observations were made in experiments of series 5 as presented in Figure 6, where, due to the larger amount of water in-place, the production per unit volume of gas was more pronounced.

In experiments 2.1 and 5.4 (see Table 1) a single slug of surfactant solution had been introduced to the sand-pack, whereas in experiment 2.2, the whole sand-pack had been initially saturated with the solution. It can be seen from Figure 5 that in the case of experiment 2.2, the efficiency of the gas-drive exceeded that of the experiment 2.1 and it may be concluded that the gas phase in this case was moving as a dispersed phase which produced a more uniform flow profile.

Gas Production by Gas-drive

Gas production in the gas-drive experiments, shown in Figure 7, increased quickly after gas breakthrough. As water production continued, the rate of gas production increased. Eventually the rate of gas production approached an asymptotic value.

The gas–water ratio produced in the gas-drive processes shown in Figure 8 increased in an exponential manner over the range investigated (after the gas breakthrough), the rate of water production dropped, whereas the rate of gas production increased substantially. The gas/liquid ratio would therefore continue to increase as production continued.

The rate of gas production and the gas/liquid ratios shown in Figures 7 and 8 show a sharp rise at increased drive pressures. In an oil reservoir these two features impose limits on the amount of oil which can be recovered economically. Gas/liquid ratios of 50 and 100, as two typical economical limits, are marked on the production lines as Figure 9, which shows the effect of increasing pressure gradients on water production.

Effect of Surfactant on Gas Production by Gas-drive

The data of Figures 10 and 6, show that in gas-drive surfactant processes, the flow of gas was restricted by

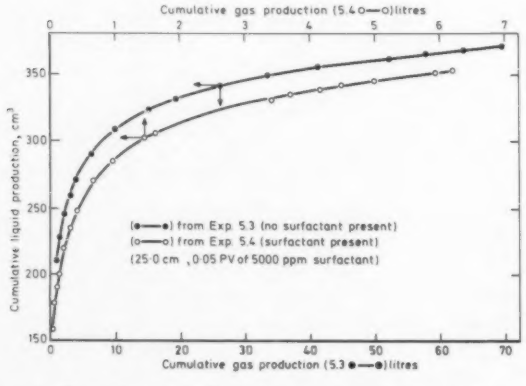


Figure 6. The effect of surfactant on gas production versus liquid production in a gas-drive process.

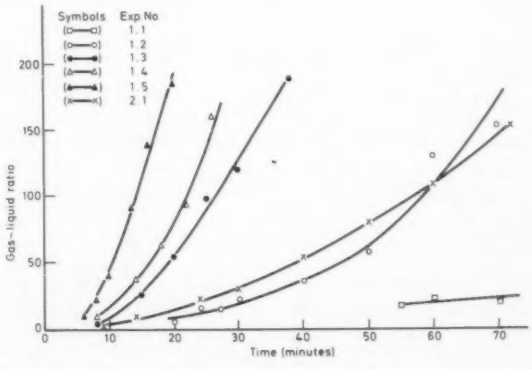


Figure 8. Gas/water ratio versus time by gas-drive.

VOL. 62 1984

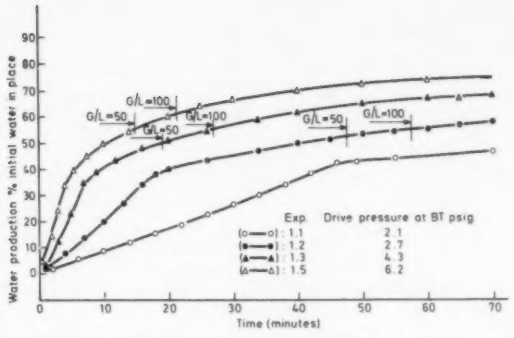


Figure 9. Water production versus time by gas-drive.

interface formation and its displacement efficiency exceeded that of a straight gas-drive process.

Figure 11 compares the rate of gas production versus water production from series 5 experiments, with and without surfactant, from which the advantage of surfactant can be seen. This effect of surfactant in gas-drive is highlighted by comparing the data shown in Figure 12 where it can be seen that the rate of gas production in the presence of surfactant remained considerably lower than in its absence. Figure 12 also shows that the gas/liquid ratio in the presence of surfactant increases at a much lower rate, and as the rate of gas production remained relatively unchanged, this increase was largely due to the reduction in the rate of liquid production.

The rate of gas production, shown in Figure 11, in the presence of surfactant remained relatively unchanged with water production. Under these conditions this system exhibited a restricted two-phase flow, and did not

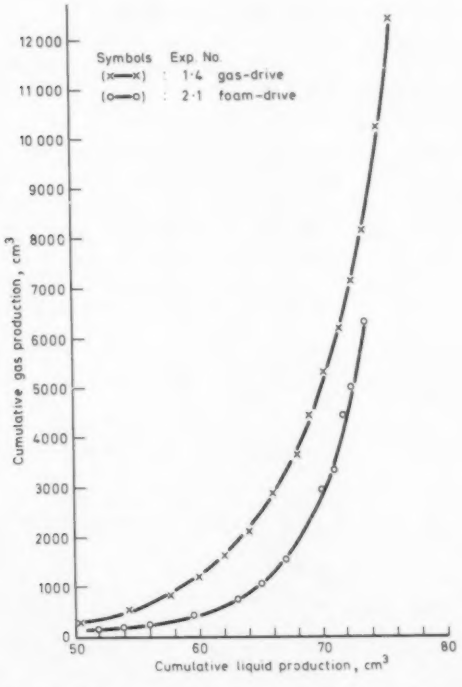


Figure 10. The effect of surfactant on the efficiency of a gas-drive process.

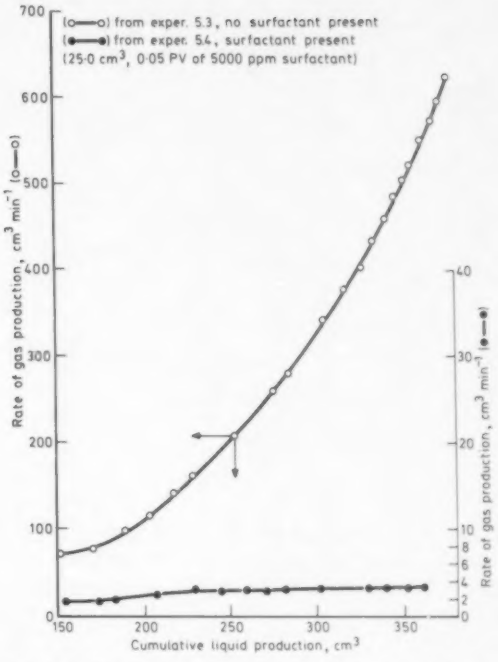


Figure 11. The effect of surfactant on the rate of gas production versus water production in a gas-drive process.

obey the simple saturation-permeability relationship expected from a normal two-phase flow system. Experiments reported in series 3 and 4.3 were designed to take advantage of this foam property to restrict the flow of gas phase.

The comparative effect of the presence of surfactant in restricting the rate of gas production is shown in Figure 13. The Figure also shows that had the surfactant injection been carried out at an earlier stage, it could have been more effective, in reducing the gas production rate.

Water Distribution During Gas-drive

It was shown in Figure 11 that the rate of gas production in the presence of surfactant remained rela-

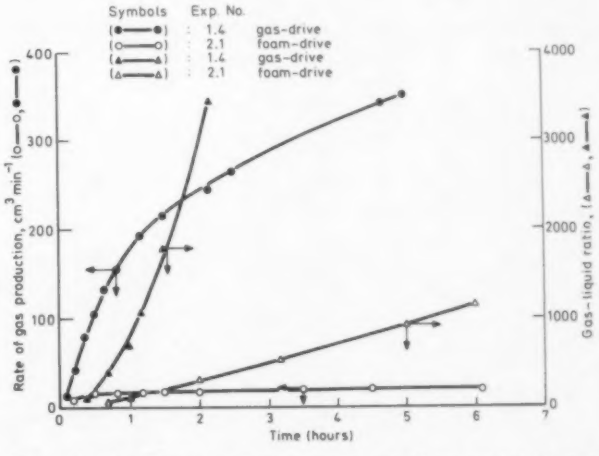


Figure 12. The effect of surfactant on the rate of gas production and gas/water ratio at a gas-drive process.

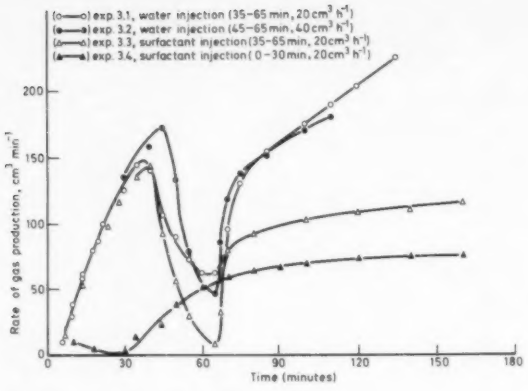


Figure 13. The effect of surfactant on the gas injectivity and gas production of a sand-packed column.

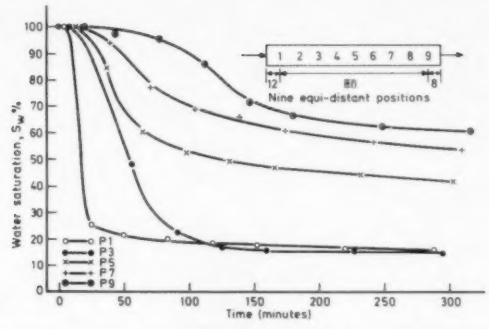


Figure 15. The effect of surfactant on the distribution of water along a sand-pack during a gas-drive process (from exp. 5.4, 25 cm³; 0.05 pv of 5000 ppm surfactant present).

tively unaffected by the water production, giving rise to an increase in the gas saturation. It was shown in Figure 6 that gas-drive in the presence of surfactant had a substantially higher efficiency in producing water from a sand-pack. These two observations show the change in distribution of water along the sand-pack column during a gas-drive in the presence of surfactant.

The saturation distribution data for water, measured by the gamma ray adsorption technique outlined earlier, along the sand-pack are presented in Figure 14. Over the first half-hour and hour respectively, water saturation dropped to 0.40–0.60, and 0.30–0.45. From this point onwards saturation dropped at a relatively constant rate, producing saturation differences of less than 0.10 between the first to the last fixed positions.

By constrast, Figure 15 shows that saturation distribution in the presence of surfactant was quite different. In the first half-hour, saturation at the first point dropped below 0.25, while saturation for the rest of the tappings remained between 0.80–1.00. Over the first hour, position three dropped to a saturation of 0.40 and within an hour and a half, reached the limiting saturation of 0.2, whereas elsewhere the saturation ranged from 0.55 to 0.95. Thus, apart from positions one and two, the rest of the saturation changes tended to be extremely slow. It must be pointed out that the data of Figures 14 and 15 cannot be directly compared, but within Figure 14 it can be seen that up to the second position in the column, there had been a much more efficient piston-like displacement of water due to foam formation in situ, and the subsequent pore blocking described in the qualitative measurements.

Oil Recovery Improvement

The results of the seventh series of experiments (see Table 1 for details) are given in Figure 16 where enhanced oil recovery was achieved by direct injection of foam in a sand-pack of high oil saturation.

The oil did not form a continuous phase along the column at an initial saturation of 0.58. The data shows that injection of foam initially resulted in water production, after which oil production started and water production fell. Water production then remained insignificant until some 150 cm³ of oil, 67% of original-oil-in-place (OOIP) had been produced. From this stage, water production started and continued at a rate of 40 cm³ h⁻¹, equivalent to the rate of injection of surfactant solution. This implied that water had initially been produced up to its connate saturation, oil production then continued to some 73% of the OOIP, in 4 h and subsequently remained insignificant. Foam breakthrough finally occurred after 10 h.

The total amount of surfactant injected during this experiment was 400 cm³ at 1000 ppm which was less than 0.90 pore volume (PV). The sand-pack consisted of

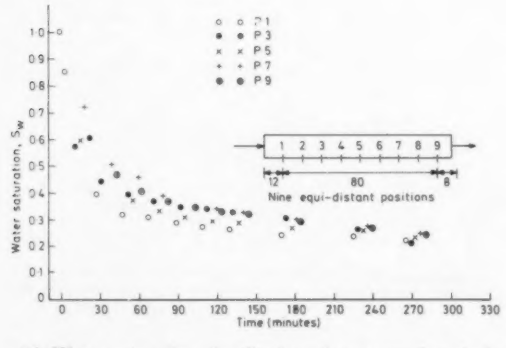


Figure 14. Water saturation distribution along a sand-pack during a gas-drive process (from exp. 5.3, no surfactant present).

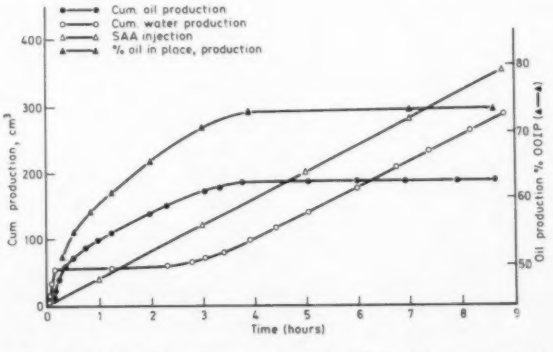


Figure 16. Enhanced recovery of oil by foam-drive process (from exp. 7.1).

VOL. 62 1984

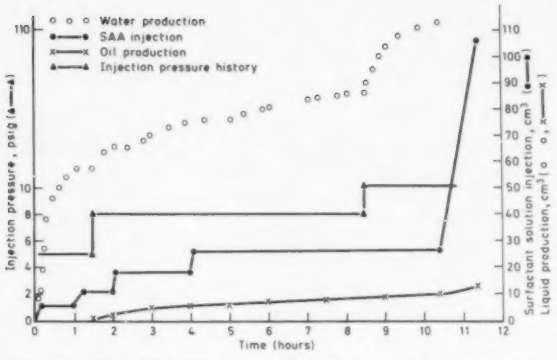


Figure 17. Enhanced recovery of oil by foam-drive process (from exp. 7.2).

1690 g of sand of 70×10^{-6} (g of surfactant per g of sand) adsorption capacity[22]. Gas break-through and gas production were substantially controlled. Some oil emulsion was produced just before the foam break-through occurred, indicating the development of an oil-displacing front. Although the foam injected continued for a further 4 h, no more emulsion or oil was produced.

The second experiment in the seventh series applied the foam drive at a later stage when water-flooding had been terminated and oil saturation had been reduced substantially from an initial $S_0 = 0.74$ to $S_0 = 0.18$. Then the foam was generated in-situ by injection of slugs of surfactant at certain intervals and a continuous injection of gas. Finally, the injection pressure was raised in steps.

As shown in Figure 17, the production of oil by the foam-drive process started one and a half hours after the beginning of the process. Oil production continued gradually at a relatively constant rate, and after ten hours, the oil saturation, S_0 had dropped to 0.06, with indication that further increase in the gas injection pressure would have resulted in further oil production. A total of 26.0 cm^3 of 5000 ppm surfactant solution, some 0.25 total pore-volume was used in this case. The sand-pack consisted of 332.5 g of sand which had an adsorptive capacity of 120×10^{-6} (g of Triton X-100® per g weight). The pressure was increased to 10 psig after 505 min and was sufficient to mobilise some of the interfaces, as can be seen from the sharp rise of the water production curve in Figure 17. The foam breakthrough followed shortly afterwards at 515 min.

Total oil production after 625 min was 10 cm^3, and injection of a further 80.0 cm^3 of 5000 ppm surfactant solution resulted in a small amount of emulsion. Initially 79 cm^3 of oil was contained in the sand-pack which was reduced to 19.5 ($S_0 = 0.18$) after water-flooding. The final oil saturation was 0.06. The 12% reduction in oil saturation represents a significant improvement in recovery from the watered-out sand-pack.

SUMMARY AND CONCLUSIONS

The relationship of injection pressure, water production and gas break-through has been investigated for water-filled sand-packs using gas-drive. It was found that under similar pressure conditions, the presence of surfactant significantly improved the efficiency of water recovery by the gas-drive process due to foam formation by surfactant solution or gas mixing in the sand-pack. Further, the gas/water ratio produced from a gas-drive increased significantly in the region of interest and the higher the injection pressure, the higher the gas/liquid ratio at corresponding depletions. It was also found that the amount of water produced at gas-break-through in a gas-drive was greater the lower the gas-injection pressure. On the other hand, foam retarded the advance of the water displacement front within a permeability range of 5 to 40 darcy for the sand-packs studied.

With respect to gas production it was found that the rate of gas production was always significantly reduced by the presence of surfactant and subsequent foam formation, whilst the injection of surfactant solution slugs reduced the rate of gas production of a gas-drive process to a greater extent when compared with a surfactant-free process.

Surfactant solution slugs injected in the early stages of a gas-drive operation have a more pronounced effect on its efficiency. They also restrict the rate of gas production to a more significant extent. The measurements made in the course of all gas-drive experiments showed almost uniform fall of water saturation distribution after gas break-through in the homogeneous sand-packs used. The presence of surfactant similarly increased the efficiency of displacement in the parts of the sand-pack being affected, and developed a piston-like displacement of water.

The presence of surfactant always delayed the gas break-through time for the gas-drive processes, due to the formation of interfaces or lamellae. The passage of gas is thus retarded as its rate of passage will depend on the rate at which the interfaces are formed and reformed.

Tests with foam injection into oil saturated columns produced up to 73% of the original-oil-in-place before break-through using less than 0.9 pore volume of 1000 ppm solution of Triton X-100®. The generation of foam in-situ to recover oil from a water flooded sand-pack reduced the residual oil saturation on average from 0.18 to 0.06.

The study has accumulated data which together with sorption data[22] may be used to determine optimum conditions for foam drive processes. It is clear that foam will have a potentially important role to play in improving oil recovery under specified conditions. Economic viability will depend on adsorption and stability of foam in porous media, together with the level of pressure drive necessary to use the foam at an appropriate quality for mobilising residual oil.

A continuing programme of research aimed at identifying suitable surfactants for foam drives, together with studies of the effect of quality and other process variables on the improvement of oil recovery from sand-packs is currently underway, so that optimum conditions of generation and application can be determined and an understanding of the basics of the flow of foam lamellae can be gained. The programme is also aimed at identifying surfactants which will give stable interfaces under reservoir conditions and are not significantly adsorbed by the surrounding strata.

REFERENCES

1. Chiang, J. C. and Sawgal, S. K. et al, 1980, *50th Ann Calif Reg Mtg, SPE-AIME, Los Angeles*, SPE 8912.

2. Doscher, T. and Hammerschaib, E. C., 1981, *2nd Joint Symp EOR, Tulsa, Oklahoma*, SPE/DOE 977.
3. Doscher, T. and Kunskra, V. A., 1982, *Oil and Gas J.* (Feb) p. 99.
4. Mitchell B. J., 1969, *PhD Dissertation* (Graduate College, Univ Oklahoma).
5. Bond, D. C. and Holbrook, I. C., 1958, *US Potent* 2866507.
6. Field A. N., 1961, *USBM Report*, R1 5866.
7. Bernard, G. G., 1963, *Producers Monthly* (Jan.).
8. Minnsieux, L., 1974, *J Pet Tech* (Jan.).
9. Bayat, M.Gh., Nutt, C. W. and Burley, R., 1978, *Euro Symp E.O.R.* (Heriot-Watt Univ, Edinburgh).
10. Bayat, M. Gh., 1977, *PhD Thesis* (Heriot-Watt Univ, Edinburgh).
11. Marsden, S. S. et al, 1977 (Dec). *SUPRI-Tech Report* 3. (Stanford University, Petroleum Research Institute).
12. Bickerman, J. J., 1973, *Foam: Theory and Industrial Applications* (Reinhold, New York).
13. Marsden, S. S. and Khan, S. A., 1966, *SPEJ* (March).
14. Bernard, G. G., Holm, L. W. and Jacobs, W. A., 1965 (Dec.). *SPEJ* (Dec.) p. 295.
15. Kolb, G. C., 1963, *MS Thesis* (Pennsylvania State University).
16. Bernard, G. G. and Holm, L. W., 1964, *SPEJ* Sept. 1964. p. 267.
17. Holm, L. W., 1968, *SPEJ* 1968 (Dec.).
18. Raza, S. H., 1970, *SPEJ* 1970 (Dec.).
19. Altrecht R. A. and Marsden G.G., 1970, *SPEJ* March 1970.
20. Bernard, G. G. and Holm, L. W., 1970, *SPEJ* March, 1970.
21. Raza, S. H. and Marsden, S. S., 1967, *SPEJ* 1967. p. 359.
22. Nutt, C. W., Bayat, M. Gh. and Burley, R., 1980, *Chem Eng Sci*, 36: 609–619.

The manuscript was originally received 25 October 1982 and was accepted for publication after revision 7 September 1983.

BOOK REVIEWS

Chemical Reaction Equilibrium Analysis
W. R. Smith and R. W. Missen
John Wiley and Sons Ltd, 1982
pp 364, £35.50

This is an ambitious book. In about 200 pages of text, the authors attempt to explain and review the current state of the art of computing reaction equilibrium composition for ideal and non-ideal systems involving, if necessary, solutions of non-electrolytes and electrolytes, in addition to gases and single-species phases. The text is supplemented by 80 pages of program listings, 25 pages of examples and 10 pages of references up to 1981.

Ambitious it may be, but amibition is not always a grievous fault, and whilst the authors have over-reacted themselves in trying to deal with non-ideality in only 16 pages, at least they provide some up-to-date well chosen references. Also, the first 150 pages provide an excellent account of the formulation of the problem of reaction equilibrium in mathematical terms, of the numerical methods available for its solution, and of the construction therefrom of various algorithms.

The old dichotomy between the classical equilibrium-constant approach and the direct free-energy minimisation method is shown to have no real mathematical basis. Instead, the authors prefer a classification based on a 'stoichiometric formulation' in which the closed system constraint is treated by a set of stoichiometric equations, and a 'non-stoichiometric formulation' in which this constraint is included by the use of Lagrange multipliers. The two major program listings illustrate this, the Villars–Cruse–Smith program based on the former, and the Brinkley–NASA–RAND program on the latter formulation. Both these Fortran programs are claimed to deal with up to 150 species, 15 chemical elements and 2 multispecies phases.

Finally, what of the sceptic who clings to the age-old comment on computing–'garbage in, garbage out'? The answer is provided by the chapter (brief, alas!) on sensitivity analysis, a topic which is surely now an essential feature of all computing courses for engineers and scientists. In simple terms, sensitivity analysis will show quantitatively how the reliability of the results is related to the estimated errors of the input data, particularly free-energy data.

This book can be recommended unreservedly to the researcher or designer who has a problem involving equilibrium considerations (as distinct from rate processes). The quality of production is excellent, and the clarity of exposition is such that it should be readily comprehended by anyone who has a grounding in chemical thermodynamics and also in numerical methods and computing.

P. F. Tiley

VOL. 62 1984

Book Reviews continue on page 122

FAULT TREE SYNTHESIS BASED ON CONTROL LOOP STRUCTURE

By A. SHAFAGHI, P. K. ANDOW (MEMBER) and F. P. LEES (FELLOW)
Department of Chemical Engineering, Loughborough University of Technology

Fault tree analysis is widely used for the identification and assessment of hazards. Although the construction of fault trees is normally a manual process, there is increasing interest in systematic, computer-based methods of fault tree synthesis. Typically these methods are based on decomposition of the plant into a set of units and creation of the corresponding unit models. A weakness of this approach is that it does not bring out clearly the structure of the fault propagation in the plant and that in consequence the fault trees derived tend to be opaque. A method of fault tree synthesis is outlined which overcomes this defect. It is based on the modelling of the control loop structure of the plant. The method itself is described and an illustrative example is given. The application of the method to event tree synthesis is also outlined. In its present form the method is a manual one, but it is considered to be applicable also to computer-based synthesis.

INTRODUCTION

In recent years the chemical industry has faced severe problems of plant safety and reliability. It has responded to these in a number of ways, one of which has been the development of improved methods of hazard identification and assessment.

A technique of particular importance both for hazard identification and for hazard assessment is the fault tree method. The construction, or synthesis, of the fault tree is normally a manual process, but for the analysis of the tree there are available a number of systematic methods embodied in computer codes.

It is attractive, however, to develop more systematic methods of fault tree synthesis also. In a previous paper[1] an account was given of a systematic method of representing the fault data structure of process plants which can be used at the design stage for fault tree synthesis and at the operations stage for process computer alarm analysis. In this method information is provided in the form of the plant configuration and of a set of unit models which describe the fault propagation structure of the units. Thereafter the synthesis of the fault tree is completely systematic. The two main steps involved are the creation for each unit model of a set of mini-fault trees and the combination of these minitrees to construct the overall fault tree.

Based on this work an interactive computer facility for the representation of the fault propagation structure of process plants has been developed. Information is entered on the plant configuration and on the unit models; the latter are drawn from a unit model library or alternatively are created by the user. The fault propagation structure can then be interrogated in various ways. One application is fault tree synthesis. Fault trees can be plotted using a graph plotting facility and the usual information derivable from a fault tree can be obtained. Another application is alarm analysis. The fault propagation structure can be held in a process computer and interrogated as alarms occur in real time to provide alarm diagnosis. Other applications are currently under investigation. One is the use of the fault propagation structure for hazard identification, producing information akin to that obtained in a hazard and operability study. Another is the use of the structure for instrument system design, improving the degree of discrimination between faults.

In addition to the description of the basic fault propagation method and its applications to fault tree synthesis and alarm analysis[1], accounts have been given[5] of the generic features of the fault propagation problem and of the philosophy underlying the fault propagation facility just described[2] and of the modelling method used and in particular of the basic fault information required[3].

A deficiency of the fault trees produced by the method just described and, apparently, by other methods described in the literature is that they tend to lack a clear structure and are therefore rather opaque to the user. It is with this problem that the present paper is primarily concerned. A method of fault tree synthesis is described which is based on the control loop structure of the plant. The fault tree so derived consists of branches representing control loop failures which constitute the skeleton of the tree and of other branches representing failures of protection by instrument protective systems and by the process operator.

At present this method is a manual one and constitutes an approach separate from the computer-based method. There appears to be no fundamental difficulty in replacing the manual features by a systematic approach, although this has not yet been done.

SYSTEM DECOMPOSITION

The first stage in fault tree synthesis for process plants is system decomposition. The way in which this is done is critical, since it determines the whole approach taken thereafter, but its significance appears often to be underrated.

In the decomposition of process plant systems there are two choices. The plant may be decomposed into a set of units or into a set of structures. Most previous work, including that of Martin-Solis, Andow and Lees, has

© Institution of Chemical Engineers

been based on decomposition into units. The present work by contrast involves decomposition into structures, in this case control loop structures.

PREVIOUS WORK ON FAULT TREE SYNTHESIS

Work on fault tree synthesis was reviewed recently[1] and a full review is therefore not given again here. It is convenient, however, to summarise the methods of fault tree synthesis which have been described in the literature. These methods are shown in Table 1.

Table 1. Methods of fault tree synthesis

Modelling Method	Workers
Input–output models/digraphs	Lapp and Powers[4]
Decision tables	Salem, Apostolakis and Okrent[5,6] Berenblut and Whitehouse[7]
Mini-fault trees	Fussell[8]
Functional models/mini-fault trees	Martin-Solis, Andow and Lees[1]
Transition tables	Taylor[9]

UNIT MODELS AND MODELLING

The methods of fault tree synthesis just mentioned have the common feature that they are all based on the representation of the plant as a set of items of equipment, or units. The units are characterised by a set of unit models, the modelling method used being different in each case.

The various methods may be illustrated by reference to the control valve shown in Figure 1. For convenience of exposition consideration is limited to the three input and two output variables shown, the pipe input pressure P1 and flow Q1 and the signal input pressure P3 and the pipe output pressure P2 and flow Q2.

In the Lapp and Powers method[4] the basic unit model is the input–output model. Such a model for the control valve is shown in Table 2. This table applies to the pipe outlet flow Q2. From the input–output model it is possible to derive the corresponding directed graph (digraph) as shown in Figure 2 and from a set of such models to derive the digraph for the whole plant. Feedforward and feedback loops, including control loops, are then identified from the plant digraph.

The method of Salem et al[5,6] uses a decision table model. Such a model for the control valve is shown in Table 3. This table applies to the pipe outlet pressure P2 and flow Q2. Decision table models are also used by Berenblut and Whitehouse[7].

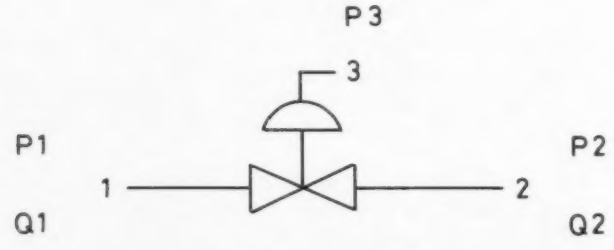


Figure 1. A control valve.

Table 2. Input–output model for control valve (after Lapp and Powers)

Output Q2		
Input		
Q1	+1	Fault-free
P3	+1	states
Fails OPEN	+10	
Fails CLOSED	−10	Faults
Fails STUCK	0†	

1 normal effect (LO, HI)
10 intense effect (V HI, V LO)
\+ output same sign as input
− output opposite sign to input
† gain change between P3 and Q2

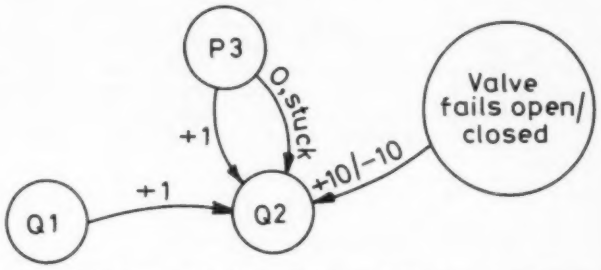


Figure 2. Digraph model for control valve (after Lapp and Powers).

Mini-fault tree models are used in the methods of Fussell[8] and of Martin-Solis et al[1]. In the former method the minitree is the basic model, while in the latter it is derived from a basic model consisting of a set of functional equations.

In the Martin-Solis et al method the starting point is a set of functional equations. Such equations for the control valve are shown in Table 4. A functional equation shows for the left hand side, or output, variable which input, or right hand side, variables affect it and in which directions. The corresponding minitree model can be derived, in part, from the functional equation. Figure 3 shows a minitree for the deviation of pipe outlet flow Q2 LO. The three left hand inputs are derived directly from equation (2) of Table 4. In order to complete the minitree, however, information on faults occurring in the unit is also required. This is provided by the event/fault information, which is also given in Table 4.

Table 3. Decision table model for control valve (after Salem, Apostolakis and Okrent)

	Inputs			Internal	Outputs	
	Q1	P3	P2	states	P1	Q2
1	1	−1	−1	−1	1	1
2	2	3	−1	−1	2	2
3	−1	1	−1	−1	2	1
4	−1	2	−1	−1	1	2
5	−1	−1	2	−1	2	1
6	−1	3	1	−1	1	2
7	−1	−1	−1	101	1	2
8	−1	−1	−1	102	2	1
9	2	−1	−1	103	2	2
10	−1	−1	1	103	1	2

1 = LO
2 = HI
3 = unchanged
−1 = don't care
101 = fails OPEN
102 = fails CLOSED
103 = fails STUCK

VOL. 62 1984

Table 4. Functional equation model and event/fault information for control valve (after Martin-Solis, Andow and Lees)

Functional Equations
$dP1/dt = f(Q1, -Q2)$ (1)
$Q2 = f(P1, -P2, P3)$ (2)
Event/Fault Information
BLOCKAGE: Q2 LO
LK-LP-ENV: Q2 LO
DUMMY: Q2 LO
(DUMMY is the top event of a separate minitree which has inputs P1 LO and VALVE STUCK)

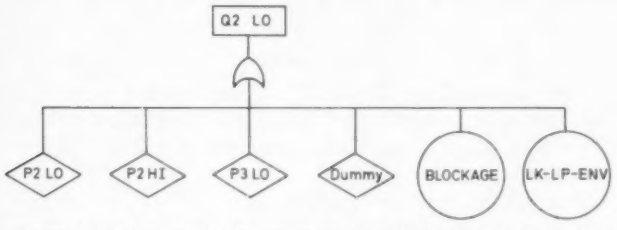


Figure 3. Minitree model for control valve (after Martin-Solis, Andow and Lees).

In Taylor's method[9] the starting point is again a set of equations not unlike the functional equations just described which is formulated as an equation digraph. From this digraph there is derived by a number of intermediate steps a transition table model. Such a model for the control valve is shown in Table 5.

CONTROL LOOP STRUCTURE MODELLING

In contrast to the unit modelling methods just described the approach taken in the method outlined in this paper is based on structure modelling.

In structure modelling the plant system is decomposed into a set of functional subsystems which consist generally of a number of units. In the method described here the subsystems considered are the control loops. It is shown that the fault propagation structure of the plant can be represented in terms of the control loop structure.

The elements of a control loop as treated here include the individual instruments in the loop such as the measuring instrument, or sensor, the controller and the control valve, but also other items of equipment such as vessels, heat exchangers and pumps which are sources of loop disturbances.

Loop Analysis

Control Loop Function, Elements and Variables

The control loop is a subsystem which has the function of maintaining the controlled variable at its desired value, or setpoint. Failure of the control loop is defined as deviation of the controlled variable outside the defined limits.

The control loop has the following elements:

(i) Control		Sensor
		Controller
		Control valve
(ii) Process	say	Vessel
		Heat exchanger
		Pump
		etc.

In terms of the quantity controlled the control loop has a single output, the controlled variable, and a number of inputs which can perturb that variable. In addition, however, there are other inputs which pass through the loop uninfluenced. For example, an input temperature deviation passes through a flow control loop uninfluenced as an output temperature deviation.

Control Loop Interconnections, Boundaries and Environment

The control loop is a subsystem which is connected to the other subsystems. The inputs to the loop are either inputs across the plant system boundary or outputs from other loops and the output from the loop is either an output across the plant boundary or an input to another loop.

The control loop consists of the control elements and of certain process elements. The criterion for allocating the latter to that particular loop is that failure in these elements affects the loop by causing a deviation of the controlled variable.

The control loop is exposed to an environment the influence of which can cause a deviation of the controlled variable. The environmental influences include particularly utility failures and heat and cold. Interventions of the process operator may also be classed under this head.

Table 5. Transition table model for control valve (after Taylor)

		Conditions					
Events		V ZERO	V LO	V D LO	V NORMAL	V D HI	V HI
P1	ZERO	—	ZERO	ZERO	ZERO	ZERO	ZERO
P1	LO	—	LO or D LO	LO or D LO	LO or D LO	LO or D LO	LO
P1	D LO	—	D LO	D LO	D LO	D LO	D LO
P1	D HI	—	D HI	D HI	D HI	D HI	D HI
P1	HI	—	HI or D HI	HI or D HI	HI or D HI	HI or D HI	HI
P1	V HI	—	V HI	V HI	V HI	V HI	V HI

D HI Disturbed high: high but controllable by control loop and/or trip loop
HI High: high and uncontrollable by control loop but controllable by trip loop
V HI Very high: high and uncontrollable by control or trip loop

Control Loops and Protective Systems

A protective system is handled in two different ways. If the protective system acts to prevent the deviation of a variable which is not controlled by a control loop, it is treated as a trip loop. If the variable is controlled by a control loop, however, the protective system is treated as part of that control loop.

Control Loop Classification

For present purposes control loops may be classified into the following types:

(i) Single loop	Feedback
	Feedforward
(ii) Multiple loop	Feedback/feedforward
	Cascade
(iii) Manual control	
(iv) Self-regulating devices	Pressure relief valves

Disturbances

A deviation of the controlled variable occurs as the result of a disturbance. The disturbances may be external or internal to the control loop.

The external disturbances which cause deviation of the controlled variable may be classed into three types. The first is a disturbance of a process variable which saturates the control action available so that although the valve is fully open or fully shut there is still a controlled variable deviation. The second is a disturbance of a process variable which lies within the range of potential correction of the loop but which causes a controlled variable deviation because an element in the loop has failed in a fixed position, i.e. failed stuck. The third is a disturbance which induces failure of a susceptible element in the loop. These external disturbances are shown in Section A of Table 6.

The internal disturbances which cause controlled variable deviations may be classed into two types. The first is the case where the element has an inherent weakness and fails spontaneously. The second is that where the element has a susceptibility to failure and fails due to an external failure-inducing disturbance. These internal disturbances are shown in Section B of Table 6.

It is also necessary to consider failures of protective systems. A protective device may fail to protect on demand. Such a protection disturbance is shown in Section C of Table 6. Whether a complementary condition applies in this case depends on whether or not the variable is also acted on by a control loop.

Table 7. Control loop failure modes

1. Uncontrollable disturbance UD
2. Controllable disturbance CD AND Element invariant failure SK
3. Failure-inducing disturbance FD AND Element susceptibility ES
4. Element or process equipment failure EF
5. Process equipment controllable failure CF AND Element invariant failure SK

Loop Failure

The various disturbances just described can give rise, severally or in combination, to control loop failures. The different modes of loop failure are shown in Table 7 and in Figure 4.

Where there is a combination of a control loop and a trip loop acting on the same variable, the modes of loop failure are as shown in Figure 5.

Where a variable is acted on by a trip but not by a control loop, the structure is still treated as a loop, namely a trip loop, and there is a single failure mode, which is that of the trip.

OUTLINE OF FAULT TREE SYNTHESIS METHOD

The object of the fault tree synthesis method which is described here is the creation of fault trees in which the functional relations are more explicit and transparent. At present the method is a manual one.

The information supplied consists of the plant control loop structure and the loop failure structure tables. The control loop structure information comprises the list of controlled variables, the set of control loops with defined boundaries and loop digraphs, and the plant digraph showing the interconnections between the loops. The loop failure structure tables list the disturbances which can cause a deviation of the controlled variable.

From the plant digraph there is derived a connection table. This is an $n \times m$ matrix, where n is the number of control loops and m is the maximum number of inputs to a loop. Thus each row of the table represents a control loop and the elements in the row the inputs to that loop. As an illustration consider the plant digraph given in Figure 6. The corresponding connection table is shown in Table 8.

Table 6. Control loop disturbances

Disturbance		Complementary Condition
A. *External disturbance*		
Uncontrollable disturbance	UD	—
Controllable disturbance	CD	Element invariant failure SK
Failure-inducing disturbance	FD	Element susceptibility ES
B. *Internal disturbance*		
Element or process equipment failure	EF	—
Element invariant failure	SK	Controllable disturbance CD Process equipment controllable failure CF
Process equipment controllable failure	CF	Element invariant failure SK
Element susceptibility	ES	Failure-inducing disturbance FD
C. *Protection disturbance*		
Protective device failure	PF	Control loop failure or None

VOL. 62 1984

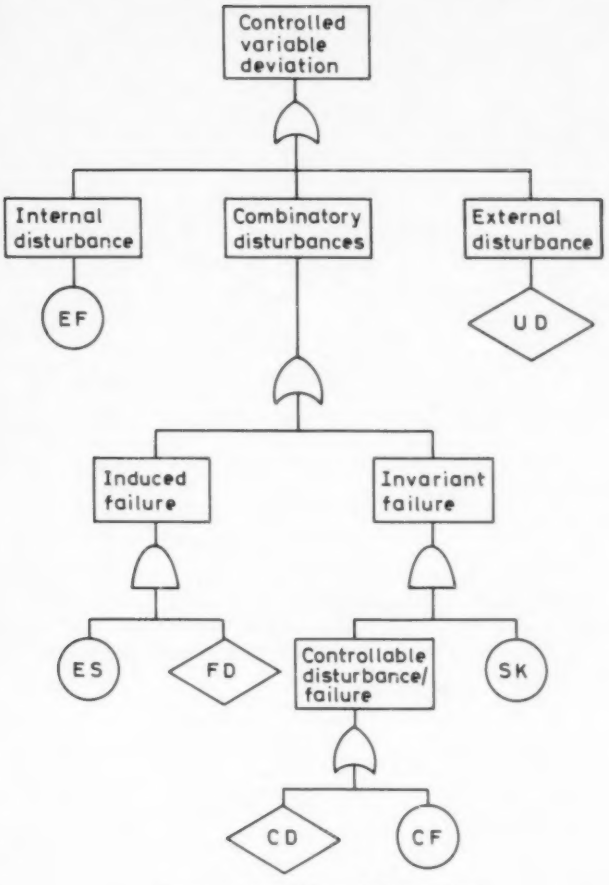


Figure 4. Control loop failure modes.

The connection table is then used to derive the generalised fault tree. The top event of the fault tree is selected. This top event is a deviation of the controlled variable of a particular control loop and is placed at Level 0, or top, of the tree. The connection table is then entered at the row corresponding to the control loop number. The elements of the row are placed at Level 1 of the tree. In turn each element of Level 1 yields a new row number which is itself developed. The generalised fault tree for the plant digraph shown in Figure 6 derived from the connection table given in Table 8 is shown in Figure 7.

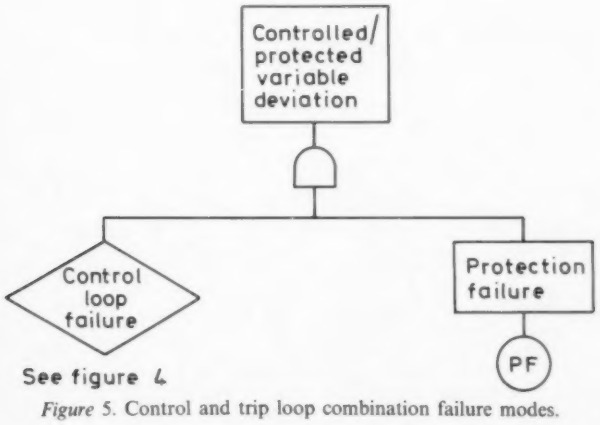


Figure 5. Control and trip loop combination failure modes.

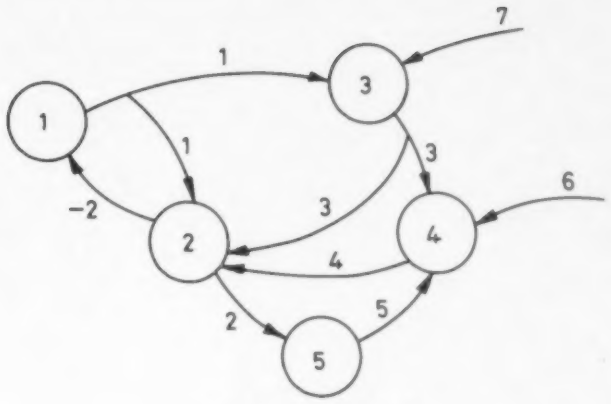


Figure 6. A plant digraph.

Table 8. Connection table for plant digraph shown in Figure 6

−2	—	—
1	3	4
1	7	—
3	5	6
2	—	—

There are several points of detail in the construction of the generalised fault tree which should be noted. Each level of the tree must be completed before the next level is started. The appearance of a number at one level does not exclude its occurrence at a lower, and higher-valued, level, where the loop variable may have a different deviation or may be combined in a different logic. A number greater than n implies a disturbance coming not from another loop but across the plant system boundary. A negative element implies a disturbance which is uninfluenced by the control loop such as a temperature deviation passing through a flow control loop.

The specific fault tree is obtained from the generalised fault tree by replacing each circle in the latter containing a positive number up to and including n by the appropriate loop failure structure. The circles containing positive numbers greater than n or negative numbers are replaced by the disturbances which they represent.

In this method there is a limitation on the range of top events which can be selected for investigation. Only deviations of those variables which are acted on by control and/or trip loops can be chosen as top events. However, this limitation is not as restrictive as it at first appears, since critical variables are nearly always subject to control and/or trip action. In this connection it should be noted that a variable which is critical but which is not controlled or protected automatically may still be subject to manual control or protection, in which case the method can still handle it.

Moreover, it is expected that the limitation would not apply if the method is used as envisaged to give structure to fault trees generated by a systematic computer-based method.

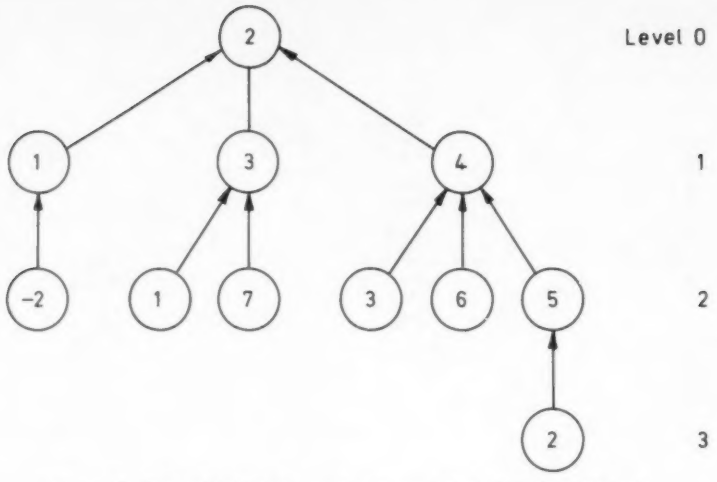


Figure 7. Generalised fault tree for Loop 2 fault for plant digraph shown in Figure 6.

ILLUSTRATIVE EXAMPLE OF FAULT TREE SYNTHESIS

The method of synthesising the fault tree is illustrated by an example. The plant considered is that given in the flow diagram in Figure 8.

In this plant, which is a section of an ethylene oxide plant, ethylene and oxygen are mixed together and then pass as feed to a reactor. The flow of oxygen is controlled by a flow control loop. The corresponding flow controls for the ethylene are not shown. The oxygen concentration of the mixed gas feed is measured by a single oxygen analyser which shuts a trip valve in the oxygen line if the oxygen concentration rises too close to the lower flammability limit. The temperature of the gaseous product from the reactor is measured by three thermocouples connected in a 2-out-of-3 majority voting logic which also shuts the trip valve if the outlet temperature rises above a defined limit.

There are three controlled variables on this plant: the oxygen flow, the feed oxygen concentration and the product temperature. The plant can therefore be decomposed into three control/trip loops.

These three loops are analysed in turn. For each loop the analysis involves the definition of the loop boundaries, the identification of the loop inputs and outputs and construction of the loop digraph, and the identification of the external and internal disturbances and of the failure structures. The boundaries and digraphs of the three loops are shown in Figures 9–11 and the loop analyses in Tables 9–11, respectively.

From the digraphs of the individual loops the plant digraph is obtained as shown in Figure 12. The links 1–3 correspond to the outputs of the three loops and the links 4 and 5 to the two inputs A and B across the system boundaries, respectively.

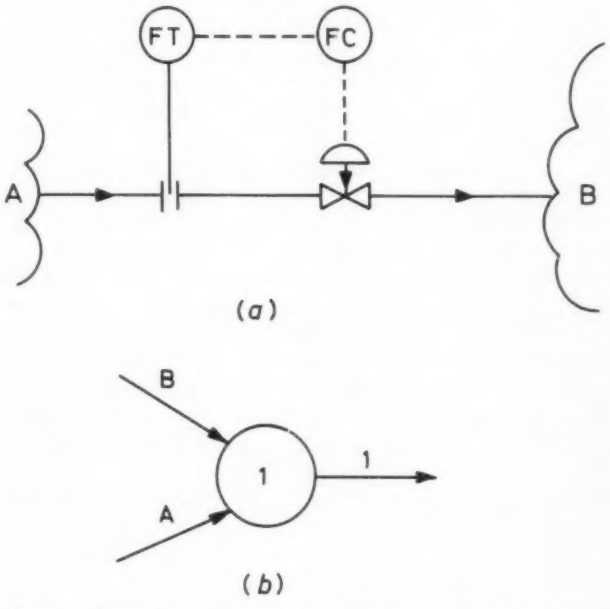


Figure 9. Control Loop 1 in ethylene oxide plant system (a) Control loop (b) Digraph of loop.

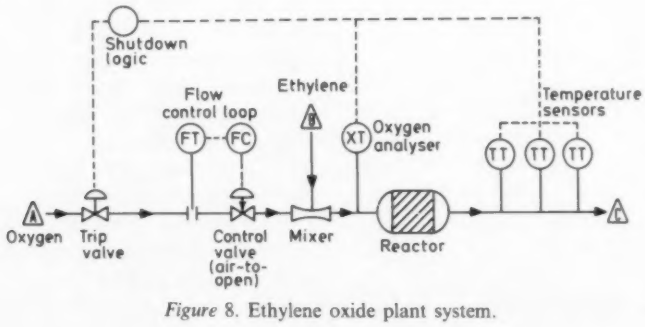


Figure 8. Ethylene oxide plant system.

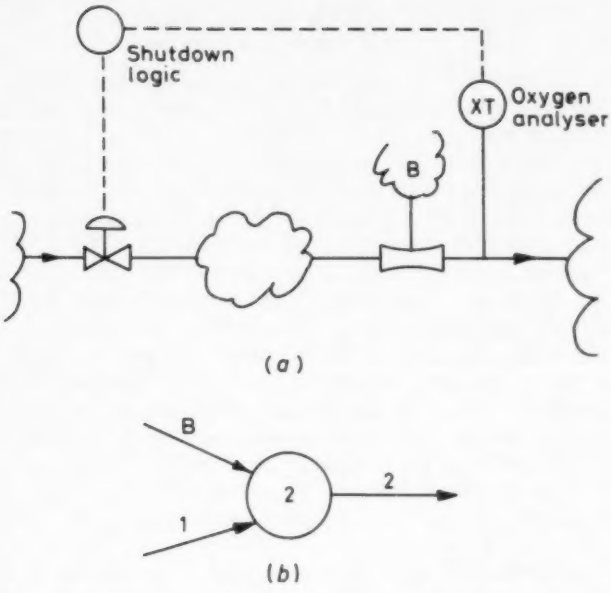


Figure 10. Trip Loop 2 in ethylene oxide plant system (a) Trip loop (b) Digraph of loop.

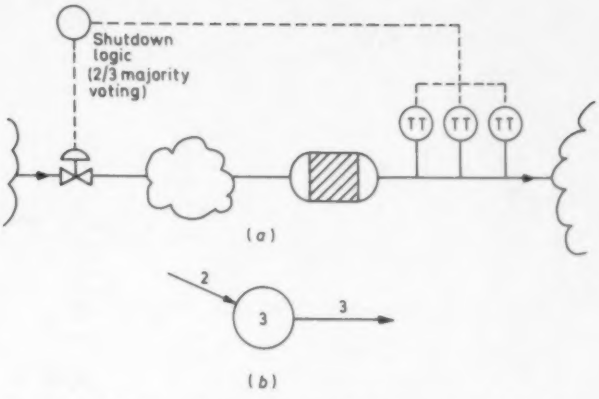


Figure 11. Trip Loop 3 in ethylene oxide plant system (a) Trip loop (b) Digraph of loop.

The connection table is derived from the plant digraph and is shown in Table 12.

The fault tree is synthesised from the connection table and the failure structure. The top event considered is the event T3 HI. This is a deviation of the output from Loop 3. The generalised fault tree is therefore headed by Loop 3 and is as shown in Figure 13. The specific fault tree is obtained from the generalised fault tree by replacing

Table 9. Loop analysis for Control Loop 1 in ethylene oxide plant system

Loop Elements		
Instruments	Sensor 1; controller 1; control valve 1 (air-to-open)	
Process equipment	—	
Protective devices	—	
External Disturbances		
Disturbance	Complementary condition	Controlled variable deviation
PA HI CD	IN1 SK	Q1 HI
PA LO UD	—	Q1 LO
PB HI UD	—	Q1 LO
PB LO CD	IN1 SK	Q1 HI
SP HI UD	—	Q1 HI
SP LO UD	—	Q1 LO
IN1 = Sensor 1 OR Controller 1 OR Control valve 1		
Internal Disturbances		
Disturbance	Complementary condition	Controlled variable deviation
Sensor 1 F HI	EF —	Q1 LO
Sensor 1 F LO	EF —	Q1 HI
Controller 1 F HI	EF —	Q1 HI
Controller 1 F LO	EF —	Q1 LO
Controller 1 F LO†	ES Instrument air pressure LO	Q1 LO
Control valve 1 F OPEN	EF —	Q1 HI
Control valve 1 F CLOSED	EF —	Q1 LO
Failure Structure Q1 HI		
PA HI AND IN1 SK		
PB LO AND IN1 SK		
Sensor 1 F LO		
Controller 1 F HI		
Control valve 1 F OPEN		
SP HI		
Failure Structure Q1 LO		
PA LO		
PB HI		
Sensor 1 F HI		
Controller 1 F LO		
Controller I F LO† AND Instrument air pressure LO		
Control valve 1 F CLOSED		
SP LO		

†Controller failure conditional on instrument air failure

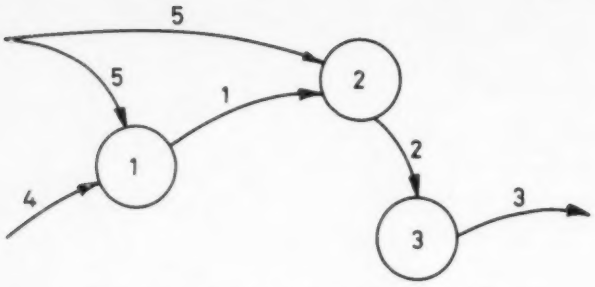


Figure 12. Plant digraph for ethylene oxide plant system.

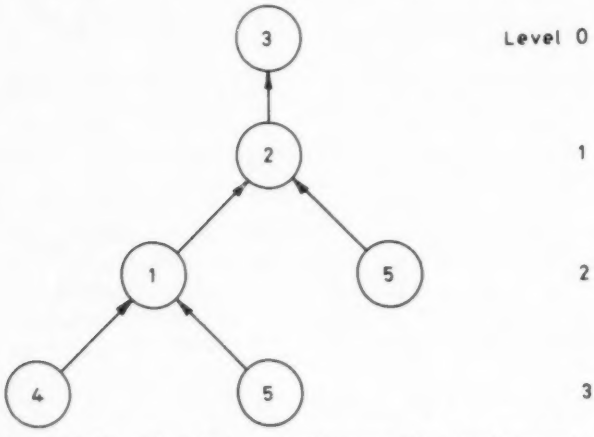


Figure 13. Generalised fault tree for Trip Loop 3 fault in ethylene oxide plant system.

each circle by its equivalent fault structure table and is shown in Figure 14.

A more substantial illustrative example of fault tree synthesis using the method here described has been given elsewhere[10,11].

APPLICATION OF METHOD TO EVENT TREE SYNTHESIS

The method just described has been developed with fault tree synthesis in mind, but it can also be applied to event tree synthesis.

In this application the procedure is the same as that outlined for fault tree synthesis up to the point where the connection table is obtained. The connection table is then used to derive the generalised event tree. The start event of the event tree is then selected. This start event is a deviation of the controlled variable of a particular control loop and is placed at Section 0, or left hand side, of the tree. The connection table is entered and the rows in which the loop number occurs as an element are identified. These row numbers are placed at Section 1 of the tree. In turn each loop number of Section 1 yields further rows which are themselves developed. The generalised event tree for the plant digraph shown in Figure 6 derived from the connection table given in Table 5 is shown in Figure 15.

It should be noted that each section of the tree must be completed before the next section is started. The appearance of a number in one section does not exclude its occurrence at a later, and higher-valued, section, where the loop variable may have a different deviation or may have different causes. Positive numbers greater than n and negative numbers do not occur.

The start event of the event tree is not strictly a cause event, since it is itself the effect of a failure of that loop.

In contrast to the circles of the generalised fault tree, those in the generalised event tree do not represent control loop failure structures. They represent rather the conditions which allow faults to propagate through the plant.

The specific event tree is obtained from the generalised event tree by replacing each circle in the latter by a

Table 10. Loop analysis for Trip Loop 2 in ethylene oxide plant system

Loop Elements		
Instruments	Sensor 2; shutdown logic 2; trip valve 2	
Process equipment	Mixer	
For simplicity shutdown logic failure is not considered.		
External Disturbance		
Disturbance	Complementary condition	Controlled variable deviation
Q1 HI CD	IN2 SK	X2 HI
Q1 LO UD	—	X2 LO
PB HI UD	—	X2 LO
PB LO CD	IN2 SK	X2 HI
IN2 = Sensor 2 OR Trip valve 2		
Internal Disturbances		
Disturbance	Complementary condition	Controlled variable deviation
Sensor 2 F HI	EF —	X2 LO
Sensor 2 F LO	EF —	X2 HI
Control valve 2 F CLOSED	EF —	X2 LO
Failure Structure X2 HI		
Q1 HI AND IN2 SK		
PB LO AND IN2 SK		
Sensor 2 F LO		
Failure Structure X2 LO		
Q1 LO		
PB HI		
Sensor 2 F HI		
Trip valve 2 F CLOSED		

VOL. 62 1984

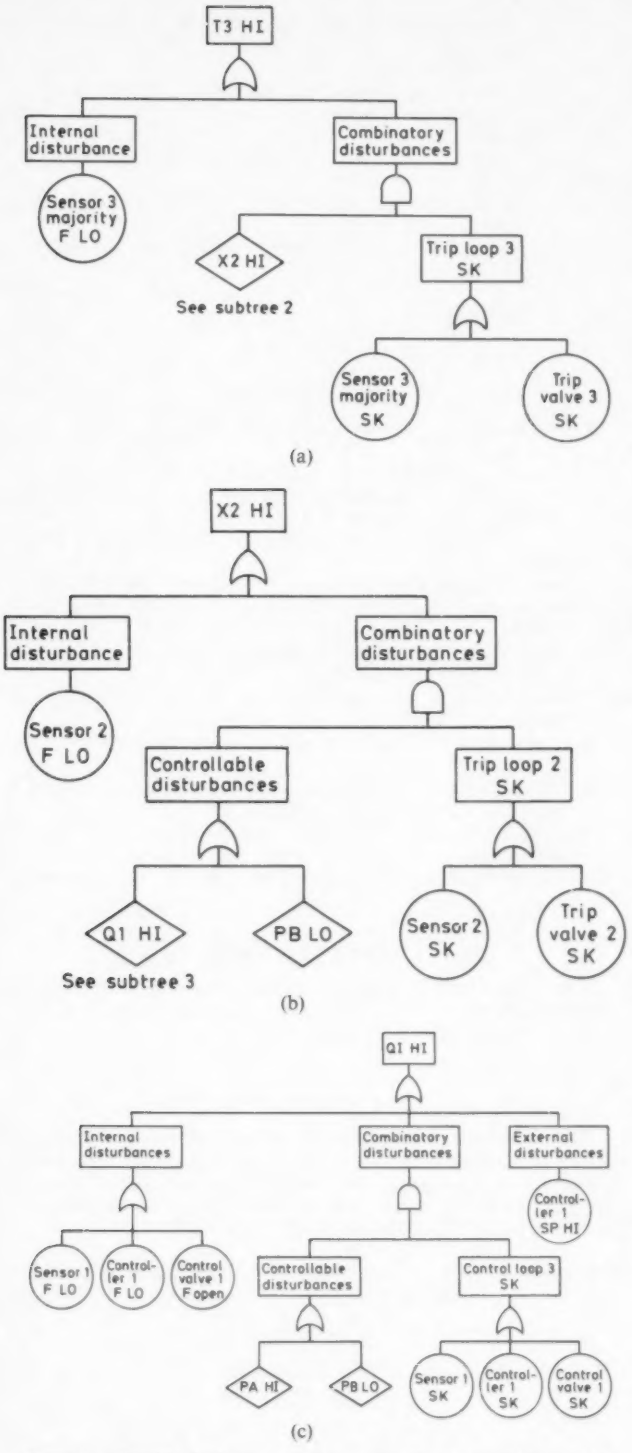


Figure 14. Specific fault tree for top event T3 HI in ethylene oxide plant system (a) Subtree 1 for T3 HI (b) Subtree 2 for X2 HI (c) Subtree 3 for Q1 HI.

condition obtained from the appropriate loop failure structure.

DISCUSSION

The method of fault tree synthesis just outlined is based on structure modelling rather than unit modelling and in consequence it yields fault trees which have a more clearly defined structure and are therefore more transparent.

In its present form the method is a largely manual one. The exception is the derivation of the generalised fault and event trees from the connection table, which is systematic and for which a computer program has been written.

The main effort required in the application of the method is the specification of the loop failure structure data. In the example described these failure data have been kept fairly simple, but in practical examples they tend to be more extensive. As already mentioned, a more substantial illustrative example has been given elsewhere.

Table 11. Loop analysis for Trip Loop 3 in ethylene oxide plant system

Loop Elements

Instruments	Sensor 3/1, sensor 3/2, sensor 3/3; shutdown logic 3; trip valve 3
Process equipment	Reactor

The 2-out-of-3 majority state of sensors 3/1–3/3 is referred to as the Sensor 3 majority. For simplicity shutdown logic failure is not considered.

External Disturbances

Disturbance	Complementary condition	Controlled variable deviation
X2 HI CD	IN3 SK	T3 HI
X2 LO UD	—	T3 LO

IN3 = Sensor 3 majority OR Trip valve 3

Internal Disturbances

Disturbance	Complementary condition	Controlled variable deviation
Sensor 3 majority F HI	EF —	T3 LO
Sensor 3 majority F LO	EF —	T3 HI
Trip valve 3 F CLOSED	EF —	T3 LO

Failure Structure T3 HI
X2 HI AND IN3 SK
Sensor 3 majority F LO
Failure Structure T3 LO
X2 LO
Sensor 3 majority F HI
Trip valve 3 F CLOSED

Table 12. Connection table for plant digraph in ethylene oxide plant system

$$\begin{bmatrix} 4 & 5 \\ 1 & 5 \\ 2 & — \end{bmatrix}$$

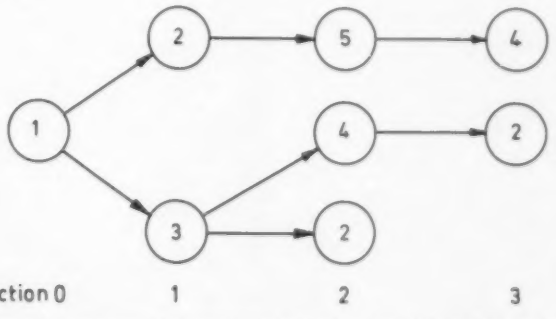


Figure 15. Event tree for Loop 1 deviation for plant digraph shown in Figure 6.

There appears, however, to be no difficulty of principle in combining the method described here, which is based on structure modelling, with the fault propagation facility described earlier, which is based on unit modelling. In this case the failure structure data required could be obtained automatically from the extensive failure information in the unit models for which there is a unit model library.

In describing the method attention has been confined to automatic control and trip loops, but there is no difficulty in handling manual control and trip loops. The manual loop is defined with an appropriate sensor and hand valve or other manipulated device and is then treated in a manner analogous to that for an automatic loop.

CONCLUSIONS

A method of fault tree synthesis for process plants has been described, which, in contrast to other methods, is based on modelling of structure rather than of units. It has the advantage that the fault trees which are produced have a clearer structure and are thus more transparent to the user.

The method in its present form is a largely manual one, but no difficulty of principle is foreseen in incorporating it in the systematic, computer-based fault propagation facility which has been developed for fault tree synthesis and other applications.

It should be emphasised, however, that fault tree synthesis of the kind described here is seen not as a replacement but as a supplement to manual fault tree synthesis.

SYMBOLS USED

Physical Variables

P	pressure
Q	flow
T	temperature
V	valve stem position
X	composition

Disturbances/Faults

CD	potentially controllable disturbance
CF	process equipment controllable failure
EF	control loop element or process equipment spontaneous failure
ES	control loop element susceptibility to failure-inducing disturbance
FD	disturbance with potential to induce failure in control loop element
PF	protective device failure
SK	control loop element invariant failure (failure stuck)
UD	uncontrollable disturbance

Abbreviations

F	failure
HI	high
IN	loop instrument: sensor OR controller OR control/trip valve
LK-LP-ENV	leak to low pressure environment (e.g. atmosphere)
LO	low
SP	setpoint

REFERENCES

1. Martin-Solis, G. A., Andow, P. K. and Lees, F. P. 1982, *Trans IChemE*, 60: 14.
2. Andow, P. K., Lees, F. P. and Murphy, C. P., 1980, *Chemical Process Hazards with Special Reference to Plant Design*, 7: 225 (IChemE Symp Series 49).
3. Lees, F. P., Andow, P. K. and Murphy, C. P., 1980, *Reliab Eng*, 1: 149.
4. Lapp, S. A. and Powers, G. J., 1977, *IEEE Trans Reliab*, R-26: 2.
5. Salem, S. L., Apostolakis, G. E. and Okrent, D., 1975, *Trans ANS*, 22: 475.
6. Apostolakis, G. E., Salem, S. L. and Wu, J. S., 1978, EPRI-705, (Electric Power Res Inst, Palo Alto, Calif).
7. Berenblut, B. J. and Whitehouse, H. B., 1977, *The Chemical Engineer* 318: 175.
8. Fussell, J. B., 1973, ANCR-1098 (Aerojet Nuclear Co., Idaho Falls, Idaho).
9. Taylor, J. R., 1979, *A Background to Risk Analysis*, Vols 1–4 (Riso Nat Lab, Riso, Denmark).
10. Shafaghi, A., 1982, *PhD Thesis* (Loughborough University of Technology).
11. Shafaghi, A., Lees, F. P. and Andow, P. K., *Reliab Eng*, in press.

VOL. 62 1984

ACKNOWLEDGEMENTS

The authors wish to acknowledge the support received by two of them (P.K.A., F.P.L.) on grants on related projects from the Science and Engineering Research Council.

ADDRESSES

Correspondence about this paper should be addressed to Professor F. P. Lees, Department of Chemical Engineering, Loughborough University of Technology, Loughborough, Leicestershire LE11 3TU, England. Dr P. K. Andow is at the same address. Dr. A. Shafaghi is at the Battelle Institute, Columbus, Ohio 43221, USA.

The manuscript was received 8 July 1982 and accepted for publication after revision 14 March 1983.

LIQUID PASSAGE ON SIEVE TRAYS OPERATING IN THE SPRAY REGIME

By J. A. RAPER (MEMBER), W. V. PINCZEWSKI (MEMBER) and C. J. D. FELL (FELLOW)

School of Chemical Engineering and Industrial Chemistry
University of New South Wales, Australia

Measurements of residence time distributions of liquid on sieve trays operating in the spray regime indicate that except for a limited region close to the exit weir where the retention of liquid in a pool at the tray floor leads to substantial localised backmixing, the liquid crosses the tray with considerably lower levels of backmixing than expected. Contrary to earlier reports, backmixing decreases as gas loading increases. The existence of relatively high levels of backmixing in the region close to the exit weir means that liquid residence time distributions on trays operating in the spray regime are most appropriately determined by an unsteady-state downstream monitoring of a tracer injected at the tray inlet, rather than by the alternative approach of upstream monitoring of a tracer injected close to the exit weir.

INTRODUCTION

Interest in the mode of liquid passage across sieve trays used for distillation or gas absorption stems from a desire to determine whether tray mass transfer is likely to be enhanced by the development of a longitudinal concentration profile in the liquid as a result of limited backmixing on the tray. Higher levels of backmixing result in a lowering of the range of possible enhancement of overall tray efficiency over point efficiency.

The most effective means of characterising liquid passage across a tray is the measurement of liquid residence time distribution. Two methods have been used for this. The first[1-3] involves the injection of a tracer (usually a pulse) at the tray inlet and subsequent monitoring of the concentration of the tracer at the tray exit (unsteady-state method). The second[4,5] involves the steady injection of the tracer near to the exit weir, and monitoring of tracer concentration *upstream* at locations along the tray floor (steady-state method).

Bell[6] has pointed out that the information from the above two methods can be quite different if retrograde flow of liquid occurs on the tray. Here, counterflow mixing pools are set up near to the tray walls. However, by choosing a rectangular geometry for experimental purposes, it is possible to eliminate the effects of retrograde flow and to simulate the flow conditions likely to apply in the centre section of an industrial tray.

The interpretation of the experimentally determined concentrations from the two different tracer techniques is usually based on the assumptions that the dispersion on the tray is uniform and that liquid mixing is superimposed on a bulk flow of liquid in the direction of the exit weir.

A comparison of the mixing results from the two methods for trays of rectangular geometry operating in the *froth* (liquid continuous) regime may be made by comparing the eddy diffusivities as reported by Shore and Haselden[2] and Barker and Self[5] for equivalent loadings. It is apparent that the two methods give the same results in the froth regime of tray operation. This suggests that the simple 'bulk flow with backmixing' model provides an adequate description of the manner in which liquid crosses the tray in the froth regime.

In the spray regime of tray operation where the liquid is the discontinuous phase, the liquid flow pattern may be expected to be different from that in the froth (liquid continuous) regime and simple 'bulk flow with backmixing' models may no longer be appropriate. Two mechanisms have been proposed for liquid passage across a tray operating in the spray regime. Porter and co-workers[4] regard the dispersion on the tray as a highly backmixed fluidised bed of droplets with liquid passage occurring as a consequence of a droplet concentration gradient. Others[7] claim that the liquid is successively atomised in a series of backmixed zones along the tray with the droplets in the last zone effectively jumping the exit weir. Since the extent of backmixing is different in each case, it becomes necessary to determine which of the mechanisms applies in the spray regime in order to provide realistic predictions of overall tray efficiency.

In their study of liquid flow in the spray regime, Porter and co-workers[4] have used the Barker and Self[5] method of upstream monitoring of a steady tracer concentration with tracer being continuously injected near to the exit weir (steady-state method). Although they postulate that liquid crosses the tray by successive random motions, they proceed to interpret their experimentally measured tracer concentrations according to the 'bulk flow plus backmixing' model outlined by Barker and Self[5]. Their inferred eddy diffusivities are similar to those reported by Barker and Self[5] and show that eddy diffusivity increases rapidly with gas superficial velocity in the spray regime.

No measurements of liquid residence time distributions, based on the unsteady state tracer method, are currently available for trays operating in the spray regime. However, Barker and Self[5] report the results of mixing experiments on trays with no crossflow of liquid using an unsteady state tracer method. It is significant

© Institution of Chemical Engineers

that in these experiments, for conditions consistent with operation in the spray regime, the calculated eddy diffusivities decrease rapidly with increasing gas velocity. This behaviour is contrary to that observed for steady-state experiments. Barker and Self[5] have attempted to explain this difference in terms of the lateral oscillations that occur in the dispersion on the tray at high gas velocities. However, Biddulph[8] has demonstrated that oscillations in the dispersions produced on sieve trays, at gas loadings consistent with operation in the spray regime, do not significantly affect the degree of backmixing on the tray.

It is therefore not clear whether the steady-state and unsteady-state tracer methods yield the same information for liquid mixing on trays operating in the spray regime. Further, it is not clear whether the eddy diffusivities reported by Porter and co-workers[4] are indicative of an increased level of backmixing with increasing gas loading in the spray regime or if their method of determining these diffusivities is not appropriate to the characterisation of liquid flow on trays operating in the spray regime.

The purpose of the present work is to compare the results obtained for the steady-state and unsteady-state methods of monitoring of an input of tracer on a sieve tray operating in the spray regime, both to see if the two methods yield compatible results in this regime and to use the information obtained to determine how liquid crosses the tray. The experimental system used is air–water but the results obtained are expected to apply also to industrial systems.

EXPERIMENTAL

The sieve tray simulator used in the experimental program has been earlier described[9]. It had an active area of 0.305 m by 0.610 m, and could be fitted with trays having hole diameters of 6 to 19 mm and hole areas from 5 to 15%. Air was supplied to the underside of the tray through a false flow equilibration tray and water was supplied from a downcomer having clearance of 25 mm. Water left the tray over an adjustable exit weir which was set at 25 mm.

Two modifications (Figure 1) were made to the simulator for the unsteady-state method of measuring liquid residence times. These were the provision of a three-ported injection manifold immediately before the downcomer clearance for tracer injection, and the installation of an angled exit liquid trap into which liquid leaving the weir passed before entry into the downcomer proper.

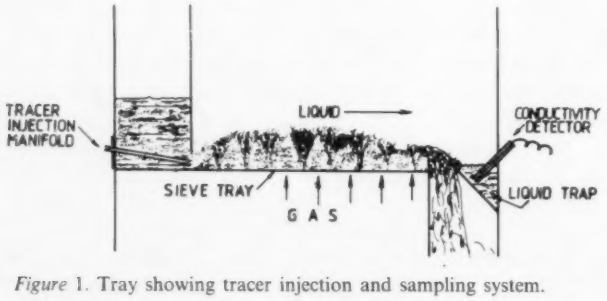


Figure 1. Tray showing tracer injection and sampling system.

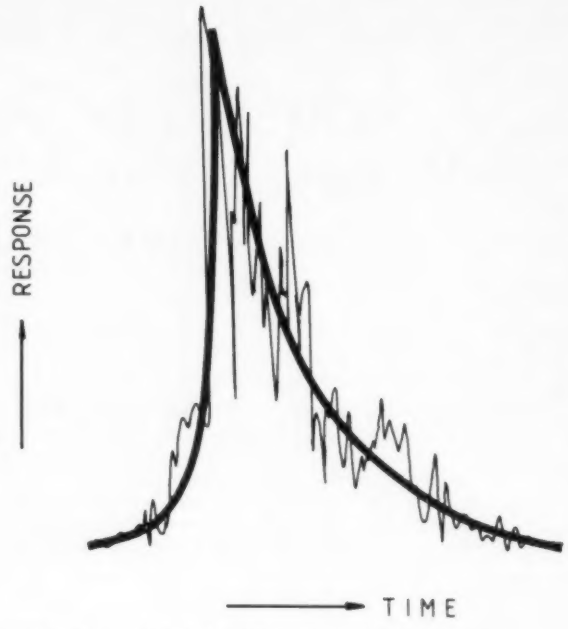


Figure 2. Shape of typical residence time distribution curve.

The residence time of liquid in the trap was small (< 400 ms).

To carry out a residence time experiment, a 20 ml pulse of 100 g l^{-1} KCl solution was injected simultaneously (injection time approximately 300 ms) into the three injection ports, and the conductivity of the liquid leaving the tray was monitored by a Phillips PW 9510 conductivity cell placed in the trap and connected to a Wayne Kerr Autobalance Universal Bridge. Output from the bridge was fed to a Linear Instruments Corporation strip chart recorder having a chart speed of approximately 0.5 m min^{-1}. Concentrations in the tray exit liquid stream could be read to ±2% and times to ±100 ms.

Gas loadings used in the experimental program were set to be compatible with those in an earlier study[10] in which tray liquid holdups were determined by gamma-ray densitometry. All corresponded[9] to fully developed spray regime operation of the tray. For all runs the liquid loading was kept at 10 m^3 h^{-1}—m weir.

For the steady-state method of measuring liquid residence times, a continuous stream of 50 g l^{-1} of KCl solution was fed to the tray floor immediately in front of the exit weir by a three-ported injector. The progress of the tracer was monitored by sampling both the dispersion and the liquid on the tray floor at various upsteam locations. To allow comparison with the results of Porter et al[4] a similar tray geometry and identical gas and liquid loadings to those employed by these workers were used. Samples taken from the tray were analysed conductiometrically.

Interpretation of Output from Unsteady-State Experiments

Experimental residence time distribution curves took the form shown in Figure 2 and were smoothed to

VOL. 62 1984

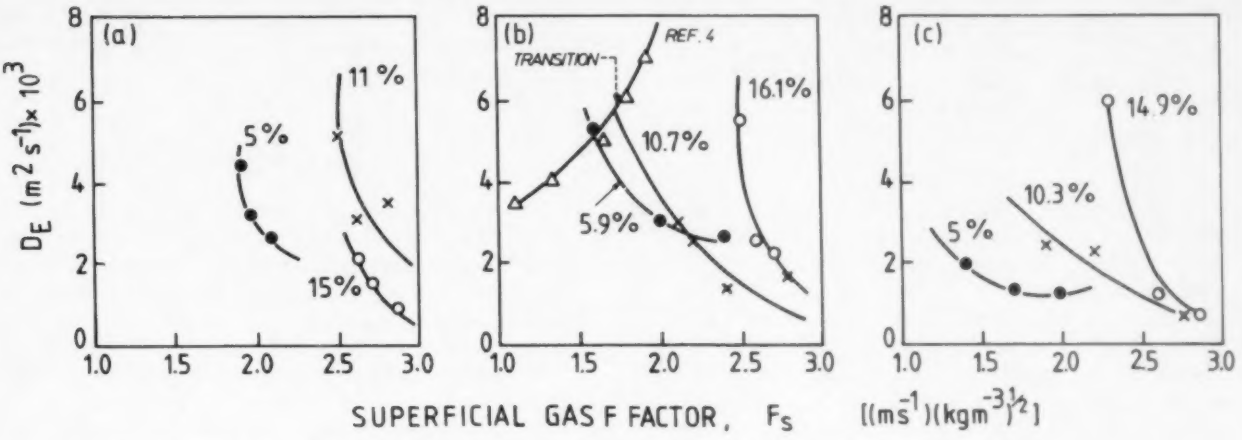


Figure 3. Experimental eddy diffusivities (D_E) (*a*) $d_h = 6.4$ mm (*b*) $d_h = 12.7$ mm (*c*) $d_h = 19.1$ mm.

remove high frequency fluctuations before analysis. The characteristic shape of the tracer residence time distribution curve suggests a limited degree of backmixing which makes it possible to apply the approximate analysis of Levenspiel[11] and Shore and Haselden[2]. Here the extent of backmixedness of the flow is characterised by an eddy diffusivity (D_E) defined by equation (1):

$$\frac{\partial c}{\partial \theta} = \frac{D_E}{uL}\frac{\partial^2 c}{\partial z^2} - \frac{dc}{\partial z} \tag{1}$$

and D_E is related to the first ($\bar{t}$) and second (σ) moments of the tracer residence time distribution by the following equations:

$$2\left(\frac{D_E}{uL}\right) - 2\left(\frac{D_E}{uL}\right)^2\left[1 - \exp\left(-\frac{uL}{D_E}\right)\right] = \frac{\sigma^2}{\bar{t}^2} \tag{2}$$

$$\bar{t} = \frac{\Sigma ct}{\Sigma c}$$

$$\sigma^2 = \frac{\Sigma ct^2}{\Sigma c} \tag{3}$$

Values of eddy diffusivity (D_E) are plotted against gas loading on Figure 3(a)–(c). Spray regime eddy diffusivities obtained in the present program are considerably less (0.4 times less) than those reported by Porter et al[4] (see Figure 3(*b*) and tend to *decrease* with gas loading rather than to increase as Porter has suggested. There is also a dependence of D_E on tray geometry with, for the same gas loading, large free area, large hole diameter trays giving (in general) lower eddy diffusivity.

Interpretation of Output from Steady-State Experiments

Barker and Self[5] have shown that for eddy diffusivity (D_E) defined by equation (1), D_E may be calculated from the concentration gradient on the tray by plotting ln $[(x - x_f)]/(x_g - x_f)]$ versus $(1 - z)$ according to the relationship:

$$\frac{x - x_f}{x_g - x_f} = \exp\left[-Pe\,(1 - z)\right] \tag{4}$$

where

$$Pe = uL/D_E \tag{5}$$

Upstream concentrations have been plotted in this way in Figure 4 for continuous weir injection of salt solution. The gas loadings used were $F_s = 1.74$ and $F_s = 2.3$ respectively.

It is apparent that the straight line relationship reported by Barker and Self[5] for the froth regime no longer applies in the spray regime as $(1 - z)$ increases.

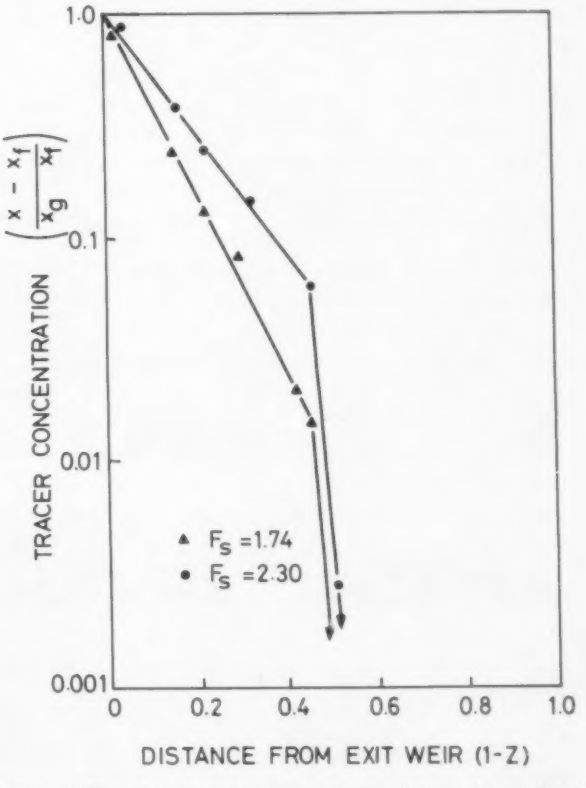


Figure 4. Plot of tracer concentration versus distance from exit weir according to steady state backward monitoring technique.

Table 1. D_E values for region near to exit weir

F_S	D_E (This Work)	D_E (Porter et al[4])
1.74	0.006 $m^2 s^{-1}$	0.006 $m^2 s^{-1}$
2.30	0.010 $m^2 s^{-1}$	0.011 $m^2 s^{-1}$

Indeed, the linear relationship is restricted to a small portion of the tray immediately adjacent to the exit weir. By considering the first section of each curve it is possible to calculate D_E values for the region near to the exit weir. The computed values agree well with those of Porter et al[4] for a similar tray (Table 1):

However it is apparent from the data plotted in Figure 4 that D_E declines rapidly as the distance from the exit weir increases and the degree of backmixing on the tray as a whole is much less than that determined in the exit zone by this particular experimental method.

Cine Film

To aid in identifying the mode of liquid passage across the tray in the spray regime, a cine film (64 frame s^{-1}) was taken of the progress of a dye tracer injected into the inlet downcomer. A frame-by-frame tracing was made, and selected frame traces have been reproduced in Figure 5. The conditions used are $F_S = 2.4$ on a 12.7 mm hole diameter, 10.7% hole area tray. It should be noted that to obtain the necessary colour intensity in the film it was necessary to continue injecting dye for a period of 3 to 5 s. The start and finish of the injection sequence corresponded respectively to a step increase and step decrease in dye concentration. Interpretation of the frame traces should therefore be based on initial and final movement of the dye front.

At the start of the injection sequence the dye front moves across the tray with limited backmixing. Some of the dye progresses across the tray in the liquid pool on the tray floor (typically depth 2 to 5 mm), but the bulk of the dye appears in the dispersion proper. There appears to be a rapid interchange between liquid on the tray floor and that in the dispersion.

When injection of dye ceases, dye persists on the tray for a considerable time (a further 8 s). This dye is trapped in a backmixed pool near to the exit weir and is successively atomised until it eventually finds its way out over the exit weir.

DISCUSSION

It is apparent from the experimental study that the unsteady state and steady state methods for monitoring liquid residence time distributions do not give equivalent results on sieve trays operating in the spray regime. The unsteady state method gives a liquid residence time characteristic of the tray as a whole, whilst the steady state method monitors behaviour in the back-mixed region close to the exit weir.

In an earlier publication[7] we have argued from characteristic droplet size and extent of mass transfer on the tray that the liquid is atomised a number of times in its passage across the tray. Liquid flowing onto the tray spreads as a pool along the tray floor for some distance before it is atomised by entrainment at the tray orifices. The droplet population undergoes a trajectory in the intertray space before returning to the tray floor for re-atomisation. In this region of the tray the liquid is only partially backmixed.

Close to the exit weir, however, it would appear that liquid which has not been successful in crossing the exit weir as droplets builds up in the form of a clear pool of liquid and is fed back along the tray floor to the orifices immediately before the weir for atomisation. This backflow of liquid results in a high level of localised backmixing in the region close to the exit weir and may therefore have an adverse effect on the overall mass transfer performance of the tray.

Based on the above description we can, to a first approximation, model the liquid passage across a sieve tray operating in the spray regimes by dividing the dispersion on the tray into two idealised regions. In the first region, which would be expected to account for the bulk of the dispersion volume on an industrial scale tray, plug flow of liquid is assumed. In the second region where the liquid flow pattern is dominated by the presence of the exit weir, backmixed flow is assumed. A two region model of this type is shown in Figure 6(*a*)

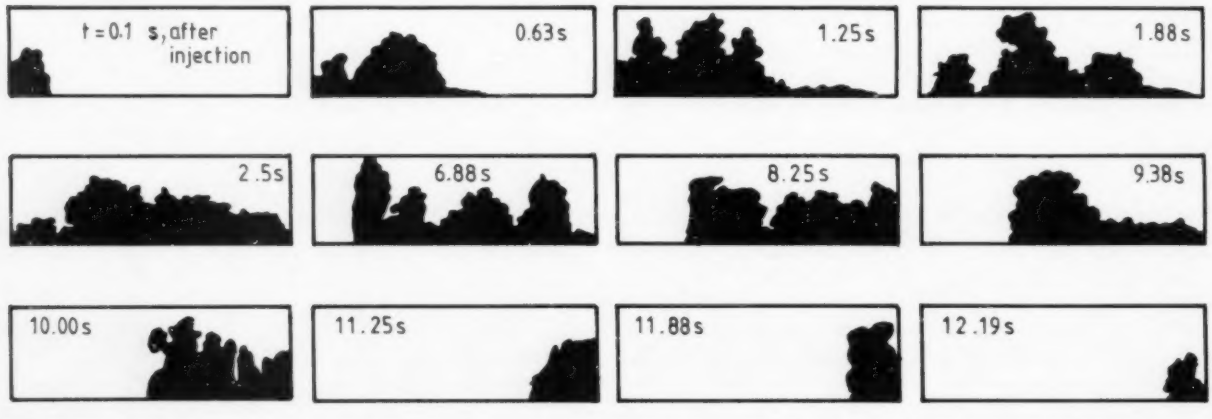


Figure 5. Tracings of cine film showing dye progression across tray. Note that tracings for the period 2.5 to 6.9 s are not included as injection of tracer was prolonged.

VOL. 62 1984

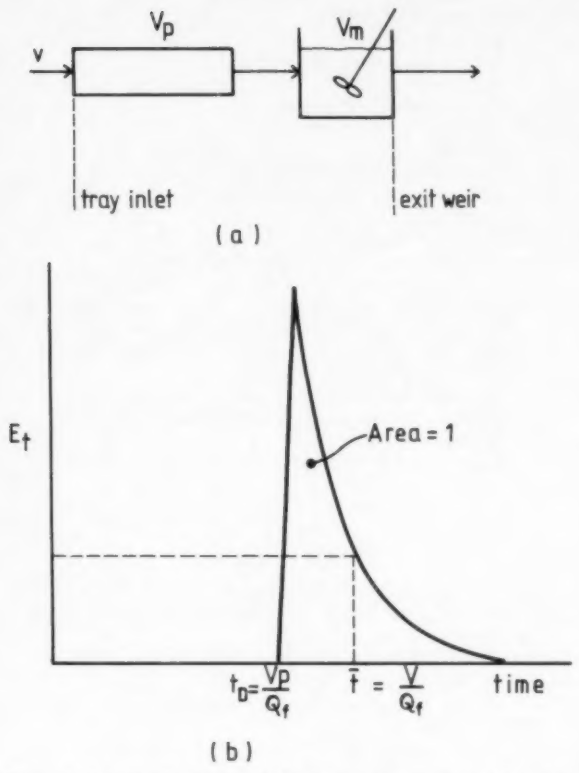


Figure 6. (*a*) Idealised model for interpretation of residence time distribution. (*b*) Typical response from idealised model. Fraction plug flow $= V_p/v = t_D/\bar{t}$.

and the corresponding idealised tracer response curve for an unsteady-state tracer test is shown in Figure 6(*b*). The idealised response is clearly similar to the experimentally measured curve shown in Figure 2. Using the experimentally measured time for the tracer pulse to first appear at the exit weir, t_D $(= V_p/Q_f)$, and the mean residence time $\bar{t}$ $(= V/Q_f)$ as calculated from the tracer response using equation (3) it is possible to estimate the fraction of the total dispersion volume which is in plug flow $(= t_D/\bar{t})$. The results of this calculation are shown in Table 2.

Table 2. Fraction of dispersion in plug flow from idealised model of tray

Orifice Diameter (mm)	Free Area (%)	F_s [m s^{-1} (kg m^{-3})$^{1/2}$]	Fraction in Plug Flow
6.4	5.0	1.80	0.37
		2.15	0.61
6.4	11.0	2.50	0.33
		2.83	0.41
6.4	15.0	2.60	0.55
		2.84	0.58
12.7	5.9	1.60	0.25
		2.40	0.58
12.7	10.7	2.10	0.49
		2.40	0.68
12.7	16.1	2.50	0.63
		2.60	0.82
19.1	5.0	1.40	0.58
		2.00	0.69
19.1	10.3	2.20	0.55
		2.82	0.56
19.1	14.9	2.30	0.50
		2.82	0.67

For the experimental trays employed the fraction of the dispersion which was in plug flow varied from approximately 0.25 to 0.75. This shows that for the relatively short liquid flow path trays used in the study (0.6 m) the effect of the exit weir on liquid mixing was considerable. More significantly, however, the results show that the fraction of the tray which is in plug flow *increases* with increasing gas loading and this is consistent with the observation that the effective eddy diffusivity *decreases* with increasing gas velocity. Clearly, the observations of Porter et al[4], that eddy diffusivity *increases* with increasing gas velocity mirrors only the behaviour of the backmixed pool at the exit weir. Since with increased gas velocity the ability of droplets to clear the exit weir is enhanced, the extent of the backmixed pool at the exit weir is expected to decrease, as the experimental results suggest.

The dependence of the eddy diffusivity in Figure 3 on tray design parameters (free area, hole diameter) can be explained in terms of the liquid entrainment capacity of individual orifices. At constant gas loading, large free areas or large orifice diameters both promote liquid atomisation[7], leading to a smaller backmixed weir zone. Hence both could potentially be used to minimise tray backmixing. There is, however, the constraint of tray hydrodynamics, which prevents a unilateral adjustment of each of these parameters.

The present experimental results provide no support for the model of liquid passage proposed by Porter et al[4]. As indicated earlier, these authors treat the dispersion as a fluidised bed of droplets with the driving force of liquid transfer across the tray being the droplet concentration at the tray inlet. For such a model to be appropriate there would have to be a gradient in droplet density across the tray. Previously measured dispersion density profiles[10] do not suggest this. In addition, the dispersion as a whole would have to be substantially backmixed, which it clearly is not.

Implications for Design of Industrial Trays

The present study indicates that sieve trays operating in the spray regime are probably less backmixed than previously considered, and that much of the backmixing experienced can be ascribed to the effect of the exit weir.

For experimental trays it has been documented[12] that tray efficiency increases with gas loading in the spray regime, and this effect is possibly due to reduced backmixing on the tray as loading increases. For heavily loaded industrial sieve trays the improvements in efficiency to be expected when long flow paths are used are not realised in practice. Based on the present work, we would interpret this to be a result of imperfect liquid flow paths (retrograde flow) rather than backmixing within the dispersion and there may be a case for using directional slots as described by Weiler et al[3] to improve flow direction.

The present experimental results suggest that there may be some advantage in using high free area, large hole diameter trays to minimise backmixing, but the advantages must be weighed against criteria for tray

hydrodynamic performance. There would, however, appear to be a strong case for spray regime trays to keep the exit calming zone down to an absolute minimum as the provision of orifices close to the outlet weir would increase the ease with which liquid leaves the tray, and minimise the backmixed pool at the exit weir.

CONCLUSIONS

The following conclusions can be drawn about the gross liquid motion in industrial sieve tray spray regime dispersions:

1. The passage of liquid across the sieve tray in the spray regime is by successive atomisation of the liquid at the tray orifices. There is a pool of liquid at the tray floor close to the exit weir in which backflow of liquid occurs. Within the bulk of the dispersion away from the exit weir the liquid is only lightly backmixed.

2. Calculated eddy diffusivities from experimental residence time distributions determined by tracer injection at the inlet weir and monitoring liquid concentration at the tray outlet do not agree with previously reported values determined by injecting tracer at the exit weir and measuring upstream concentrations. It would appear that the latter method of measurement cannot be applied to the spray regime because of the existence of a liquid pool on the tray floor which is deeper at the exit weir and in which tracer injected behind the weir becomes excessively concentrated. Rows of holes back from the exit weir are fed from this liquid pool and concentration measurements near the exit weir result in apparent eddy diffusivities which are higher than those appropriate to the tray as a whole.

3. Experimentally measured eddy diffusivities in the spray regime are of the order of those measured experimentally in the froth regime but decrease with increasing gas rate. They are also found to decrease with increasing hole area and hole diameter.

4. It would appear that industrial sieve tray spray regime efficiencies may be more influenced by imperfect (retrograde) liquid flow on the tray than by intrinsic backmixing in the spray dispersion.

SYMBOLS USED

c	concentration of tracer (mol m^{-3})
D_E	eddy diffusivity on tray (m^2 s^{-1})
E_t	response, Figure 6(b) ($-$)
F_s	gas loading (kg$^{1/2}$ m$^{-1/2}$ s^{-1})
h_L	clear liquid holdup on tray (m)
L	length of tray (m)
Pe	Peclet number $= uL/D_E$ ($-$)
Q_f	volumetric liquid flowrate (m^3 s^{-1})
t	time (s)
t_D	time for tracer pulse to first appear at exit weir (s)
$\bar{t}$	mean residence time of liquid on tray from residence time distribution (s)
u	velocity of liquid on tray ($Q_f/h_L w$) (m s^{-1})
x	concentration of tracer (mole fraction)
x_f	concentration of tracer in feed (mole fraction)
x_g	concentration of tracer at place of injection (mole fraction)
V_p	holdup in plug flow section of tray (Figure 6) (m^3)
V_m	holdup in back-mixed section of tray (Figure 6) (m^3)
V	total holdup on tray (m^3)
w	tray width (m)
z	dimensionless distance from inlet weir $= z'/L$ ($-$)
θ	dimensionless time $= t/\bar{t}$ ($-$)
σ	second moment of tracer residence time distribution (s)

REFERENCES

1. Foss, A. S., Gerster, J. A. and Pigford, R. L., 1958, *AIChEJ* 4: 231.
2. Shore, D. and Haselden, G. G., 1969, *Distillation '69, IChem E Symp Series* 32: 2/54.
3. Weiler, D. W., Delnicki, W. V. and England, B. L., 1973, *Chem. Eng Prog*, 69 (10): 67.
4. Porter, K. E., Safekourdi, A. and Lockett, M. J., 1977, *Trans. IChemE* 65: 190.
5. Barker, P. E. and Self, M. F., 1962, *Chem. Eng Sci*, 17: 541.
6. Bell, R. L., 1972, *AIChEJ*, 18: 491.
7. Raper, J. A., Hai, N. T., Pinczewski, W. V. and Fell, C. J. D., 1979, *Distillation '79, IChemE Symp. Series* 56: 2.2/57.
8. Biddulph, M. W., 1975, *AIChEJ*, 21: 41.
9. Pinczewski, W. V. and Fell, C. J. D., 1972, *Trans IChem E*, 50: 102.
10. Pinczewski, W. V. and Fell, C. J. D., 1974, *Trans IChem E*, 52: 3.
11. Levenspiel, O., 1962, *Chemical Reaction Engineering* (Wiley, New York)
12. Hai, N. T., Burgess, J. M., Pinczewski, W. V. and Fell, C. J. D., 1977, *2nd Aust Heat Mass Transf Conf Sydney*, 377.

ADDRESSES

Correspondence about this paper should be addressed to Professor Chris Fell, School of Chemical Engineering and Industrial Chemistry, University of New South Wales, Kensington, N.S.W. 2033, Australia. Dr Val Pinczewski is at the same address and Dr Judy Raper is at the Department of Chemical Engineering, University of Newcastle, N.S.W. 2306, Australia.

The manuscript was received 2 May 1983 and accepted for publication after revision 7 September 1983.

VOL. 62 1984

LABORATORY EVALUATION OF LIN'S MODEL OF CONTINUOUS STERILISATION OF MICRO-ORGANISMS

By K. R. DAVEY (GRADUATE) and D. G. WOOD (MEMBER)
CSIRO Division of Food Research and University of Melbourne, Australia

Present models for the simulation of the continuous sterilisation of liquid food are limited in that no comprehensive experimental testing has been previously undertaken. The predictions of the model of Lin, based on kinetic data determined from heating samples of *E. coli* (ATCC 25922) in a 2 kg m^{-3} Carbopol 934 solution of pH 7 in tubes of small diameter, have been compared with results obtained in a laboratory scale steriliser with steam injection heating. Many more bacteria were inactivated than predicted at temperatures between 53.5 and 59°C, especially as the holding time increased from about 8 to 37.5 s. It was concluded that model predictions were inapplicable to these data because the inactivation kinetics differed significantly depending on whether samples were heated in tubes of small diameter or by steam injection heating in a flow system. This difference in inactivation kinetics is thought to be the result of a protective matrix which is influenced by different rates of heating. The pseudoplastic index of the Carbopol and the shear conditions used closely simulate conditions used in the commercial heat sterilisation of many liquid foods.

INTRODUCTION

The adequate sterilisation of various bulk liquid media is an essential procedure in the food and fermentation industries. Because of economy and reliability, thermal sterilisation is widely used either as a continuous or batch process. The advantages of a continuous process stem from operation at steady state where greater control of the process temperature and exposure time is possible than with the more conventional batch process. These advantages include[2] an improved product quality due to a lower nutrient denaturation, a higher production rate with simplified quality control and aseptic handling. Generally, reduced production costs are also predicted[3].

The principles used in the design of a continuous steriliser are those that apply to the design of a continuous flow reactor in which the relevant reaction is the thermal inactivation of micro-organisms. The two main parameters to be determined are the sterilisation temperature and the holding time. The design is therefore influenced by what is known of the thermal behaviour of the contaminating micro-organism and by both the rheological and heat transfer characteristics of the medium. A continuous steriliser usually consists of three main sections: a heating section, a holding section and a cooling section. The holding section, normally of circular cross-section, is made long enough to ensure that the liquid is allowed sufficient residence time at a given temperature for microbial inactivation. The design criterion is expressed in terms of a reduction in the number of viable micro-organisms from an initial population to some selected final value; the micro-organism considered is the most heat resistant. Thermal damage to nutrients is known from experiment to be minimised by high-temperature/short-time (HTST) sterilisation.

For a large number of liquids, operating conditions have evolved empirically and often result in over-treatment. This is wasteful in processing costs and damages nutrients and has led to the development of several mathematical analyses of the process. Deindoerfer and Humphrey[4], perhaps the earliest analysis, assumed turbulent flow, and hence a flat velocity profile. Simpson and Williams[5] however have noted that laminar flow is the only economical regime for processing liquid foods because of the prohibitive pumping costs associated with turbulent flow. Charm[6] demonstrated the concept of integrating parameters describing thermal inactivation kinetics with the effect of laminar velocity profile. His analysis is applicable to the isothermal flow of liquid with instantaneous heating and cooling. Ruyter and Brunet[7] and Manson and Cullen[8] discussed the basic considerations and theory necessary for sterilising liquid containing discrete particulate matter where the controlling step is the slow conduction through the food fragments. Lin[9] investigated the thermal sterilisation of a liquid where the effective dispersion of micro-organisms was considered and allowed for variation with temperature whereas earlier models had not. Lin[1] proposed an instantaneous heating and isothermal holding model similar to that of Charm[6]. Both instantaneous and non-instantaneous cooling were considered. The model is applicable to the isothermal HTST sterilisation of liquid in laminar flow. Lin[1] and earlier Simpson and Williams[5], also included a first order reaction for the thermal denaturation of vitamins. There is, however, a lack of published experimental data for comparison with theoretical predictions. Previous studies have been fragmented, in that predictions have been based on unrelated values of physical properties selected from the range of values given in the literature. Clearly, with this approach, predictions may not be applicable to real situations. Against this background an experimental study of the continuous sterilisation of liquid was undertaken and the results are presented in this paper.

© Institution of Chemical Engineers

THE LIN MODEL

The present authors considered the instantaneous heating and cooling model as the most simple and feasible experimentally and chose the equations of Lin[1] because they are the most appropriate, being based on chemical reactor principles. The model is given by:

$$\frac{\langle C \rangle}{C_0} = 2\int_0^1 \exp\left(\frac{-kL}{u}\right)\frac{u}{\langle u \rangle} R\, dR \quad (1)$$

$$\frac{u}{\langle u \rangle} = \frac{3n+1}{n+1}(1 - R^{(n+1)/n}) \quad (2)$$

$$k = A \exp\left(\frac{-\Delta E}{R_g T}\right) \quad (3)$$

where the symbols used are defined at the end of this paper.

The assumptions implied in the analysis are:

1. The flow in the holding tube is laminar.
2. Incompressible flow.
3. The flow is steady-state.
4. There is no slip at the tube wall, i.e. the velocity of the liquid at the tube wall is equal to the velocity of the wall surface which is zero.
5. Isothermal conditions occur at every point in the tube.
6. End effects are negligible.
7. The liquid is non-Newtonian and can be described by the power law equation.
8. Bacteria are uniformly distributed in the liquid.
9. There is no slip between the bacteria and the liquid, i.e. the bacteria travel on the velocity streamlines.
10. The kinetics for the inactivation of the bacteria are first order.
11. The bulk temperature of the liquid containing the bacteria rises instantaneously to the holding temperature.
12. The temperature of the liquid is instantaneously reduced to a non-lethal temperature.

Deviations from laminar flow will alter the residence time distribution. An increase in the residence time will decrease the fraction of viable micro-organisms that remain at the end of the steriliser. Assumptions 2, 3 and 4 are usual in such analyses and are realistic for a liquid in laminar flow in a tube[10]. The practical implementation of assumptions 5 and 6 might not be easily realised and they are therefore particularly relevant to the experimental determination of data for testing the model. It is difficult to assess the validity of assumptions 7, 8 and 9. If bacteria are uniformly dispersed, the 'no slip' assumption, assumption 9, is reasonable. With the power law assumption, 7, the pseudoplastic index (n) is assumed independent of temperature. The pseudoplstic index is normally empirically determined from data obtained at isothermal conditions. Further, assumption 7 implies that the liquid is time-independent and therefore the shear stress in the liquid is a unique function of the applied shear rate. The power law equation as applied to liquid food is discussed by Holdsworth[11]. The equation is valid only for the range of shear measurements from which the constants are determined. It does not predict the correct limiting viscosities as the shear rate approaches 0 or ∞.

MATERIALS AND METHODS

Test Liquid

A water solution of 2 kg m^{-3} Carbopol® 934 resin, neutralised to pH 7 with sodium hydroxide solution, was selected as the test liquid because the pseudoplastic index (and energy of activation for flow) was found to be within the range for many liquid foods. Other liquids, e.g. tomato puree, condensed milk and orange juice were considered but were not used because of considerations such as short shelf life, cost in quantity, irreproducible liquid uniformity, impractability for dye-trace studies and because of their ability to support microbial growth. The Carbopol solution exhibits a number of characteristics advantageous to this study, it is resistant to attack by micro-organisms, does not support the growth of micro-organisms and is non-toxic, does not have the aging effects associated with solutions such as carboxy methylcellulose[12], is transparent and therefore suitable for dye-trace studies, has good shelf stability, and with the exception of viscosity, has the same thermal properties as water[13].

Sterile water for dissolving both the Carbopol and sodium hydroxide was obtained with a 0.45 μm filter. The solutions had excellent product uniformity and reproducibility. A Rheomat 15, Cone and Plate viscometer[14], with a vapour shield to prevent evaporation of water from solution, was used to determine the value of the pseudoplastic index (n) over an applied shear range of 11.2 to 706 s^{-1} and a temperature range 25 to 90°C. The rheological characteristics were not sidnificantly affected by the presence of dispersed test micro-organisms.

Test Micro-organism

Escherichia coli was selected as the test micro-organism, the particular strain was the 'Seattle' strain, American Type Culture Collection (ATCC) number 25922 (from the Microbiological Diagnostic Unit, University of Melbourne). This micro-organism satisfied the essential requirements of significant sensitivity to temperature (55 to 65°C), simple growth requirements and an easy dispersion as individual cells. The bacterium is non-spore forming, and is a component of the normal intestinal flora and appears as a colourless rod about 1 μm by 2 to 3 μm in liquid media examined microscopically. Because most of the information about genetic organisation of procaryotic cells is derived from studies with *E. coli* it is particularly well documented. Kinetic data for inactivation were determined from heating samples of Carbopol liquid containing the bacteria in thin-walled glass capillary tubes of small (1.1 mm i.d.) diameter.

The advantage of this method is the rapid heating and cooling of samples. Bacterial counts were made on heated and control (unheated) samples according to standard microbiological practice[15]. Samples were plated on nutrient agar and colony growth observed followed incubation at 37°C for 24 h.

VOL. 62 1984

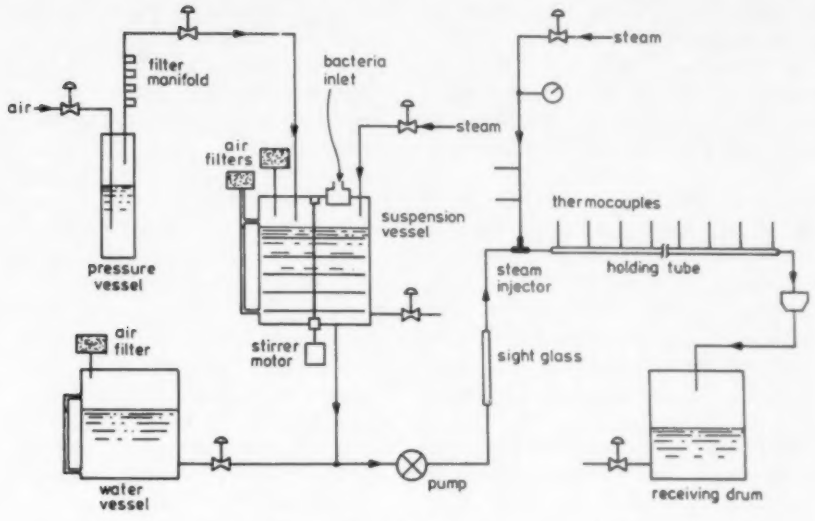


Figure 1. Flow diagram of the experimental steriliser.

Continuous Steriliser

Figure 1 is the flow diagram of the main apparatus. Direct steam injection heating was used for the practical realisation of the model. The advantages of this method of heating include a high rate of heat transfer and the elimination of indirect heat exchanger equipment in the heating section which might be subject to fouling.

The Carbopol containing the bacteria was pumped from the continuously stirred suspension vessel through the steam injector and into the insulated holding tube of 9.53 mm i.d. The holding tube consisted of cold drawn, type 316 stainless steel tubing in a number of sections connected together with Swagelok® fittings to give the required length. As well as enabling the lengths and steam injector to be easily connected, this fitting produced an aseptic seal and avoided gaps between matching tube ends. The insulation was asbestos rope. The injector is shown as Figure 2. The dimensions were fixed using equations derived from an energy balance around the injection point[16]. Dilution of the Carbopol by steam condensate was predicted at $7 \pm 0.5\%$ over the range of flow and temperature conditions used and was assumed constant at 7%. Steam pressure was indicated by a stainless steel Bourdon gauge.

Total liquid flow—Carbopol solution and condensed steam—was controlled to give bulk velocities within the range 0.05 to 0.15 ms^{-1} in the holding tube. This range corresponds to flow velocities used in commercial sterilisation[3]. Corresponding volumetric flow rates are in the range 3.57 to 10.7 $cm^3 s^{-1}$. The flow could be set at the required rate by a variable speed, magnetically coupled, stainless steel gear pump; the total liquid flow rate was determined by weighing. A section of glass tubing in the pump delivery line was used to check for the presence of air bubbles. Liquid was collected in a receiving drum that contained phenolic disinfectant. Temperatures were measured with copper–constantan thermocouples placed at intervals along the holding tube. The thermocouples were embedded in the wall of the tube and, to minimise heat conduction along the sheath, were bent so that 0.05 m of the couple was parallel with the holding tube. Thermocouples were also placed in the steam line. Water was pumped from the water storage to flush the system at the conclusion of an experimental run. Steam inlets were arranged to allow the whole apparatus to be steam-sterilised *in situ*. All flow connections to the pump inlet were made with autoclavable silicone rubber tubing.

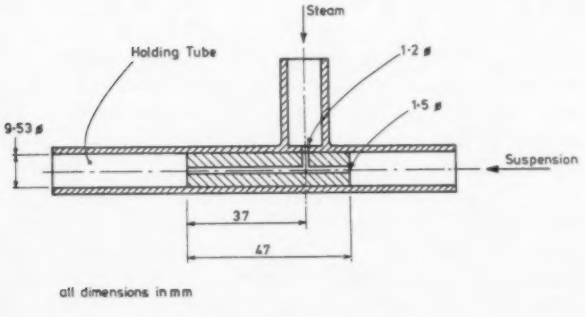


Figure 2. The steam injector.

Experimental Procedure

The suspension vessel was steam-sterilised *in situ* and allowed to cool. Distilled water was sterilised by passing through a 0.45 μm filter and transferred aseptically to the vessel. A manifold of four filters was used for the filtration and approximately 25 to 30 litre was transferred from the pressure vessel using compressed air. Air filters were fitted to ensure sterility of vessels. Sufficient Carbopol powder was introduced to give a 2.14 $kg\,m^{-3}$ concentration when the volume of both the sodium hydroxide solution used for neutralisation and 400 cm^3 of bacterial suspension (see below) were taken into account.

Dilution with condensed steam during passage through the steam injector gave the specified 2 $kg\,m^{-3}$

Carbopol concentration in the holding tube. After the Carbopol powder was mixed continuously for 6 h, sodium hydroxide was added aseptically and the mixing continued for a further 15 to 30 min. Samples were taken and a sterility check made by plating and observing for colony growth. The liquid was allowed to stand overnight.

Half an hour prior to an experimental run, 400 cm^3 of bacterial suspension of between 10^8 and 10^{10} bacteria cm^{-3} of sterile water, was added and dispersed with continuous stirring. During this time the pump, pump lines and holding tube were steam-sterilised. The steam pressure to the steam injector and the flow rate of liquid were set to the required levels. Temperatures were continuously recorded and the steam pressure noted at regular intervals.

Sample volumes to 28 cm^3 of the heated Carbopol were rapidly cooled by release into an equal volume of sterile, chilled (approximately 4°C) Ringer's solution. Bacterial counts were made on control (unheated) and heated samples in an identical mannet to the capillary tube samples of the kinetic studies.

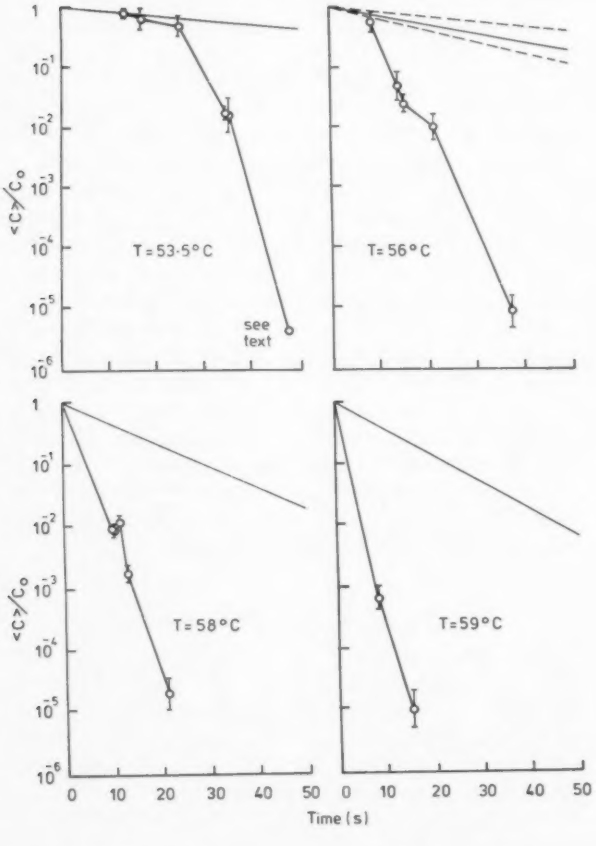


Figure 3. Comparison of the predictions of the Lin[1] model (continuous line) with experimental data for temperatures of 53.5, 56, 58 and 59°C where $\langle C \rangle$ = bulk concentration of bacteria and C_0 = initial concentration of bacteria. Broken lines are error curves which result from experimental error in the data used for prediction. The vertical bars indicate 95% confidence limits for experimental data, based on three replicate samples.

RESULTS AND DISCUSSION

The values obtained for the physical properties (n, A, ΔE) for prediction with the model are listed with the Symbols Used. The experimental procedures used in their determination have been described more fully elsewhere[16]. Figure 3 compares the predictions of the model with survivor data obtained in the continuous steriliser at different temperatures. The data are presented as the logarithm of the fraction of bacteria ($\langle C \rangle / C_0$) which remained viable after heating versus the bulk holding time, $t = L/\langle u \rangle$. Error bars show the 95% confidence limits on three replicate samples. Holding tube lengths of 1.015, 1.470, 2.015 and 2.284 m gave a range of holding times of 8.1 to 37.5 s. Temperatures were controlled to within $\pm 1\%$ of absolute values and bulk liquid velocities ranged from 0.0384 to 0.1251 m s^{-1}. The initial concentrations of bacteria (C_0) range from 1.99×10^6 to 1.0×10^7 cm^{-3}. Typical error curves resulting from experimental errors in the value of the physical properties used for prediction are shown for a temperature of 56°C as dashed lines.

Figure 3 shows that at each temperature many more bacteria are inactivated than predicted; especially as the holding time increases. At holding times greater than 37.5 s and less than 50 s, insufficient numbers of the bacterial population remained for accurate counting, i.e. there were less than 30 colonies per plate following incubation. At holding times greater than 50.0 s no colonies were observed on plating samples of the heated liquid. The additional data point at a temperature of 53.5°C, while consistent with the trend, must be regarded as unreliable because it is based on one determination using a small number of colonies (three or four). No reliable data were determined for temperatures greater than 59°C since there were too few survivors.

From Figure 3, the survivor curves for 53.5 and 56°C appear non-linear with respect to the logarithmic coordinate. This may suggest that thermal inactivation is a result of several first order reactions; a concept that has been recognised by others[17].

To test that the data were obtained at conditions satisfying the major assumptions of the model (assumptions 1, 5, 6, 11 and 12) flow conditions inside the holding tube were examined.

Photographs taken from a film of dye-trace studies of the steam injector during operation with a glass holding tube[16] showed that laminar flow, assumption 1, was attained in a short distance from the injector outlet and that the entrance length was quite short. At the combination of highest bulk velocity and shortest holding time ($\langle u \rangle = 0.1251$ m s^{-1} and $L = 1.015$ m), the entrance length accounted for about 15.7% of the holding tube. Rapid mixing and condensation of steam in the injector was evident from the absence of vapour bubbles. Because the longitudinal variation in temperature of the holding tube wall during any one run was less than 0.5°C, it can be assumed that there was no heat transferred from the tube wall to the surroundings and, therefore, there was no radial temperature profile, i.e. the liquid flow was isothermal in the holding tube. Thus assumptions 5, 6 and 11 were implemented. The procedure for sampling of the heated liquid from the

VOL. 62 1984

steriliser ensured that samples rapidly cooled to sub-lethal temperatures (less than 40°C) and that sterilisation during cooling was minimised. Assumption 12 was thus implemented. The data therefore, were obtained at conditions satisfying the assumptions of the model.

The experimental error in the data of Figure 3 will have arisen largely from the error in viable count and to a lesser extent from a combination of errors in flow, temperature and sample volume measurement. The error in flow measurement was small at about 1.7% as flows were determined by weighing samples of 0.202 to 0.536 kg collected over a period of 60 s. The error in the sample volume was found to be less than 2%. This was determined by comparing the weights of 14 sampled volumes with those of 14 randomly selected and accurately dispensed, control samples.

Electron micrographs of the bacterium in samples of liquid sampled after heating in the steriliser showed the bacterial cell appendages[2], the flagellum and pili, intact, indicating that the shear forces associated with steam injection were not sufficient to sever these. Importantly, wall shear conditions inside the injector and holding tube corresponded to the shear range from which the pseudoplastic index (n) was obtained[16].

As noted earlier, design methods for continuous sterilisers have been based on the design of continuous flow reactors in which the relevant reaction is the thermal inactivation of micro-organisms. The design data for continuous flow reactors are usually obtained from batch reactors. This approach is well established and usually provides very satisfactory results in non-biological systems[18]. The batch reactor is used because it is simple, needs little supporting equipment, and is therefore ideal for experimental studies on reaction kinetics. The results of this investigation however emphasise that the thermal inactivation of living cells is not completely analogous to the study of chemical reactions in non-biological systems as the predictions based on batch sterilisation (capillary tube) data do not agree satisfactorily with data obtained in the continuous steriliser. The thermal inactivation of micro-organisms is obviously more complex than depicted in the models.

For the most part, studies involving microbial inactivation kinetics have been concerned with representing the gross behaviour of cells. whilst this may give a good description of experimental events, it gives no insight into the actual events that occur at the micro- or molecular level. The thermal inactivation of a bacterial cell implies a loss of ability to grow and not a destruction in the physical sense. This loss in viability is not well understood. Inactivation is thought to be a result of either denaturation of an enzymatic protective mechanism[19], denaturation of a number of 'heat-induced' and 'heat-labile' reproductive initiators[20], or the inactivation of a number of 'sensitive volumes' in the cell[21]. That is, the bacterial cell is thought to contain a discrete number of thermally sensitive sites. Cerf and Metro[19], and Humphrey and Nickerson[20] specifically postulate that the denaturation of certain enzymes leads to inactivation. Loss of viability is thought to occur when a number of these sites are inactivated. Humphrey and Nickerson have extrapolated survivor curves back to zero time and found that the intercept was usually greater than zero. the intercept gave a zero-time concentration of 4 to 10 times the initial concentration of bacteria. From this, they suggested that there are 4 to 10 initiators in each cell.

With the steam injection heating in the steriliser, the heat-up time of the liquid was between 0.0239 and 0.0073 s (based on the average residence time of the liquid in the injector). These times are not precise, as a degree of back-mixing will occur in the injector, but they are useful for comparison with the slower heat-up time of the capillary tube samples of a maximum of one second[16]. The rate at which the bacteria were heated in the injector is therefore 42 to 137 times faster than that in the capillary tubes. The two possibilities consistent with the data are that the slower heating of samples in the capillary tubes produces some sort of protective matrix which is not produced during the more rapid heating of the liquid in the steriliser, or that an initial protective matrix is formed on the addition of the bacteria to the Carbopol, which is unaffected by the slower heating of the capillary tubes, but which is ruptured under rapid heating in the steriliser.

The pattern of survivor kinetics obtained in this investigation may be the result of a chance combination of micro-organism and test liquid, but the findings show clearly that the thermal behaviour in the capillary tubes differs significantly from that in the continuous steriliser. Caution is therefore necessary in extrapolating from thermal inactivation data obtained with batch sterilisers to the design of continuous sterilisers. Present models based on simple flow analogies do not take into account all conditions applicable to the behaviour of micro-organisms during heating. In particular, these are the effect of the rate of heating and the possibility of interaction between micro-organism and liquid.

CONCLUSION

The thermal inactivation kinetics of *E. coli* ATCC 25922 in 2 kg m^{-3} Carbopol liquid differ significantly depending on whether samples are heated in glass capillary tubes of small diameter or in a continuous steriliser heated by steam injection; inactivation in the flow system is much greater. Predictions from Lin's simple flow model based on kinetic data determined from capillary experiments are therefore not applicable to sterilisation by steam injection.

SYMBOLS USED

A	frequency factor for microbial inactivation (1.22×10^{47} s^{-1})
C_0	initial concentration of microorganisms (number cm^{-3})
$\langle C \rangle$	bulk concentration of microorganisms (number cm^{-3})
ΔE	activation energy for microbial inactivation (3.05×10^5 J mol^{-1})
k	rate coefficient for microorganism inactivation (s^{-1})
L	holding tube length (m)
n	pseudoplastic index (0.37, dimensionless)
R	dimensionless radial coordinate
R_g	gas constant
u	local velocity (m s^{-1})
$\langle u \rangle$	bulk velocity (m s^{-1})
t	bulk residence time ($L/\langle u \rangle$, s)
T	liquid temperature (K)

REFERENCES

1. Lin, S. H., 1976, *Chem Eng Sci* 31: 77.
2. Aiba, S., Humphrey, A. E. and Millis, N. F., 1973, *Biochemical Engineering*, 2nd edn. (Univ. of Tokyo, Tokyo).
3. Pfeifer, V. F. and Vojnovich, C., 1952, *Ind Eng Chem* 44(8): 1940.
4. Deindoefer, F. H. and Humphrey, A. E., 1959, *Appl Microbiol* 7: 264.
5. Simpson, S. G. and Williams, M. C., 1974, *J Food Sci.* 39: 1047.
6. Charm, S. E., 1966, *Food Technol* 20 (May): 97.
7. Ruyter, P. W. de, and Brunet, R., 1973, *Food Technol* 27 (July): 44.
8. Manson, J. E. and Cullen, J. F., 1974, *J Food Sci* 39: 1084.
9. Lin, S. H., 1975, *J Ferment Technol* 53(2): 92.
10. Bird, R. B., Stewart, W. E. and Lightfoot, E. N., 1960, *Transport Phenomena* (Wiley, New York).
11. Holdsworth, S. D., 1971, *J Texture Studies* 2: 393.
12. Naik, S. C., Lee, J. C., and Richardson, J. F., 1977, *Can J Chem Eng* 55: 90.
13. Christiansen, E. B. and Craig, S. E., 1962, *AIChEJ*, 8(2): 154.
14. Sherman, P., 1970, *Industrial Rheology—with particular reference to food, pharmaceuticals and cosmetics* (Academic Press, London).
15. Meynell, G. G. and Meynell, E., 1970, *Theory and Practice in Experimental Bacteriology* (Univ Press, Cambridge).
16. Davey, K. R., 1980, *PhD Thesis* (University of Melbourne).
17. Cerf, O., 1977, *J Appl Bacteriol* 42: 1.
18. Levenspiel, O., 1972, *Chemical Reaction Engineering*, 2nd edn. (Wiley and Sons, New York).
19. Cerf, O. and Metro, F., 1977, *J Appl Bacteriol* 42: 405.
20. Humphrey, A. E. and Nickerson, J. T. R., 1961, *J Appl Microbiol* 9: 282.
21. Charm, S. E., 1958, *Food Technol* 12 (Jan): 4.

ACKNOWLEDGEMENTS

The financial support of a University of Melbourne Postgraduate Research Award to K. R. Davey is gratefully acknowledged. The authors wish to thank The Microbiological Diagnostic Unit and Dr N. F. Millis for their assistance and guidance with the microbiological aspects of the work and Dr S. H. Lin for his assistance during the initial stages of the study.

ADDRESSES

Correspondence in connection with this paper should be addressed to Dr K. R. Davey, CSIRO Division of Food Research, Meat Research Laboratory, Cannon Hill, Queensland, 4170, Australia.

Dr D. G. Wood is a senior lecturere in the Department of Chemical Engineering, University of Melbourne, Victoria, 3052, Australia.

The manuscript was received 19 July 1983 and was communicated by Professor R. G. H. Prince, Associate editor of the journal for Australia.

VOL. 62 1984

Book Reviews continued from page 100

Adhesion of Dust and Powder: 2nd Edition
A. D. Zimon
Plenum Publishing Corp, 1982
pp 438, US$55.00

The first edition of this book was published in 1967 and translated in 1969. This edition updates the work to 1973. The author deserves congratulations for his lucid treatment of the subject, to be shared by Robert K. Johnston for his excellent translation. A number of topics covered in the first edition have been omitted here due to space limitations. 'Wetting of Powders' for example has acquired such importance that a separate monograph has been devoted to it.

The book reflects the author's interest in the analysis of adhesive interaction when roughness and other surface properties are taken into account; the characterisation of adhesion of irregularly shaped particles; the relationship between the structure of the boundary layer and the conditions for particle detachement by an air stream.

The first chapter deals with the fundamental concepts of particle adhesion for both monosize and log-normal distributions of particle size. The efiects of surface roughness are discussed in Chapter 2 and the third chapter deals with methods for determining adhesive forces. Sources of adhesion in a gaseous medium and the effects of particle shape are discussed in the next two chapters and adhesion in liquid media in Chapter 6. Chapter 7 deals with particle detachment by application of an electric field and Chapter 8 with the adhesion of particles to paint and varnish coatings. Adhesion and detachment of particles in an air stream and a water stream are covered next and the book concludes with discussion of features of adhesion processes under industrial and agricultural conditions.

The range of industrial processes in which adhesion is of importance is very wide. One can list filtration, gas cleaning, electrophotography, powder storage, treatment of plants with pesticide; and there must be many others. Dust deposition is also of importance to the environmentalist as a health and nuisance hazard, and dust detachment leads to soil erosion. The breadth of potential readership is therefore great and this is increased since the book forms a most interesting introduction to the subject and also has much to commend it for the more informed reader.

T. Allen

Book Reviews continue on page 136

POWER CONSUMPTION IN THE MIXING OF BOGER FLUIDS

By D. R. OLIVER, A. W. NIENOW (FELLOW), R. J. MITSON (STUDENT) and K. TERRY

Department of Chemical Engineering, University of Birmingham

The power absorbed by a six-bladed Rushton turbine when mixing Newtonian and Boger fluids is compared. Boger fluids are glucose syrups to which small amounts of polyacrylamide have been added, giving highly elastic liquids with near-constant viscosity. Data obtained with Newtonian fluids give approximate agreement with the expected power number/Reynolds number curve. The higher-viscosity Boger fluids give significantly reduced power numbers in the laminar régime, but there is an abrupt transition at moderate Reynolds numbers when the power increases by about 50%. At the same time, the Weissenberg rod-climbing effect appears around the drive shaft. It is suggested that centripetal forces due to fluid elasticity oppose centrifugal effects at low speeds and reduce power consumption. At the transition point, the elastic forces suddenly become dominant and an inward flow with a strong central vortex develops. For less viscous Boger fluids, the transition is not clearly defined and the power number curve has a wavy shape. Flow visualisation work is also described and some of the photographs taken are reproduced.

INTRODUCTION

The existence of highly elastic, transparent fluids with a *constant* shear viscosity was first reported in 1977 by Boger[1]. The advantage of using such fluids in experimental work have recently been summarised[2]. Most elastic liquids are shear-thinning in character, and this causes difficulty in the interpretation of experimental results in which effects due to fluid inertia, fluid elasticity and changing viscosity combine to affect the observed flow behaviour. This often makes it difficult to perform experiments in which the effects of fluid elasticity alone are investigated.

Boger fluids are corn syrup solutions to which small amounts of polyacrylamide have been added[1,2]. The viscosity is normally in the range 10–100 Pa s and the first normal stress difference shows a quadratic dependence on shear rate at very low values of shear rate. However, at shear rates in excess of unity, this dependence slowly changes so that the normal stress is lower than that predicted on the basis of the quadratic relationship. Also, when small additional quantities of water are present in the fluid, some shear thinning may occur[2].

High elasticity and constant viscosity make Boger fluids interesting from the point of view of mixing studies. The Reynolds number ($D^2 N\rho/\mu$) may readily be specified and elastic effects should be large enough to affect the power consumption, assuming that such changes are measurable. Being transparent, flow patterns may be observed in the fluids.

Several authors have suggested that fluid elasticity has no effect on agitator power consumption[3–6]. However, most of this work was carried out in the laminar flow régime ($Re < 10$) and the fluids were less elastic than those used in the present work. Rieger and Novak[4] did note a tendency for viscoelastic liquids to give lower power consumption than inelastic liquids in the laminar flow régime, but the magnitude of the reduction was of the same order as the experimental error. Conversely, Nienow *et al*[7] have measured up to 60% *enhancement* of power number for viscoelastic liquids in the laminar flow régime but a significant *reduction* of power number, compared with inelastic liquids, in the turbulent flow régime. There is clearly scope for further work in this field, with Boger fluids as practical 'model liquids'. The work is of considerable industrial importance, since many polymerisation reactors, polymer mixers and fermentation systems are nowadays involved with liquids of high elasticity.

APPARATUS

The Perspex vessel is of 218 mm internal diameter and 286 mm in height, with four vertical baffles of cross-section 20 mm × 5 mm. The vessel is contained in a cubic, transparent box of side 300 mm, which is fed with water at 22.0°C. Possible variation of the bulk fluid temperature from this value is discussed later.

The impellers used are of the six-bladed Rushton type, placed centrally 70 mm from the base of the vessel. The impeller of diameter 100 mm has blades of size 24 × 19 mm whilst that of diameter 110 mm has blades of size 25 × 23 mm. The impeller is driven at speeds between 0 and 600 rpm by a 1.5 hp d.c. motor; torque is measured by means of a transducer operated by a steel arm attached to the tank, which floats on an air bearing. The torque meter (reading in millivolts) is calibrated by using a pulley and weights. Accuracy is better than 4% for high values of torque, but this cannot be achieved at low torques.

For flow visualisation purposes, the tank was illuminated from a vertical slit, directing light across the tank just in front of the impeller shaft. Glass beads of diameter 2 mm were used to indicate flow patterns but the tank also contained air bubbles. The camera was a 35 mm Nikon; photographs were taken at various impeller speeds and exposure times in order to get suitable streak photographs.

© Institution of Chemical Engineers

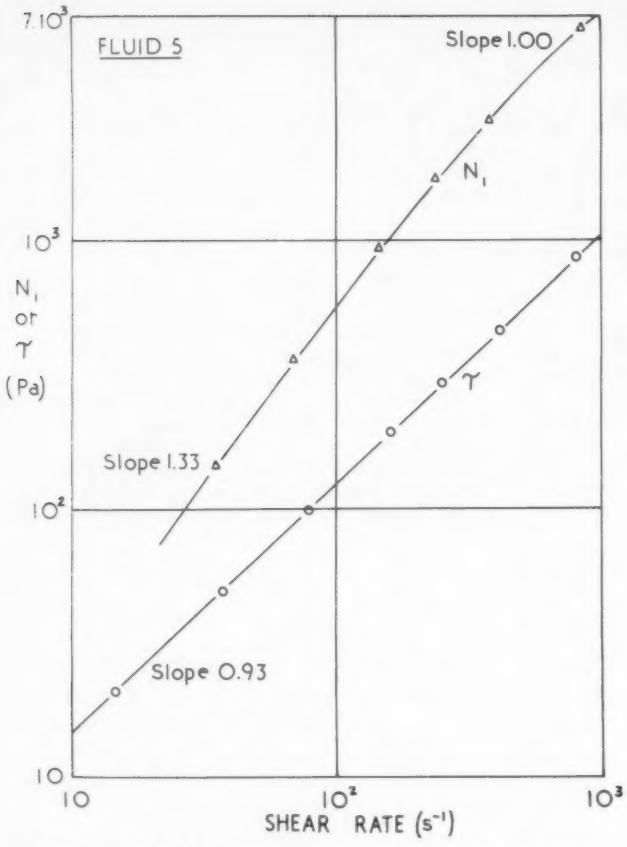


Figure 1. Relationship between first normal stress difference (N_1) or shear stress (τ) and shear rate for Boger fluid 5.

FLUIDS USED

Three Newtonian and three Boger fluids were used, all based on the same glucose syrup (glucose G 140, supplied by Tunnel Refineries, Tunnel Avenue, London SE10, UK). The viscosities were varied by adding different amounts of water to the syrup, together with a small quantity of benzoic acid to prevent bacterial growth. Each of the Boger fluids contained 500 ppm of the anionic polyacrylamide Magnafloc LT25 of molecular weight 2×10^7 (Allied Colloids, Bradford, West Yorks, UK). Shear stress and normal stress data for fluids 4, 5 and 6 were obtained by using a Weissenberg rheogoniometer. Problems were experienced due to evaporation of water and hence skin formation at the rim of the plates, but these were overcome by coating the fluid with a thin layer of silicone liquid of the same viscosity. The results for fluid 5, which are typical data for these fluids, are shown in Figure 1. The shear rates are higher than those previously used for the more viscous Boger fluids[2]; the addition of water may have been responsible for the gradient of the 'shear stress' line falling below unity. The values of first normal stress difference N_1 for fluids 4, 5 and 6 are respectively 2.8×10^3, 5.6×10^2 and 3×10^2 Pa at a shear rate of $10^2\ s^{-1}$. The physical properties of the fluids are listed in Table 1.

RESULTS

Figure 2 shows some of the results obtained when mixing Newtonian liquids. These are compared with curve 6 from Figure 15 of the classic Rushton[8] paper, which relates to a turbine of similar type to that now being used.

The power (P) used to drive the turbine is $2\pi TN$ watts, where T is the torque in Nm and N is the speed in rps. This is used in calculating the Power Number, $P/D^5N^3\rho$, which is then plotted against the Reynolds number, $D^2N\rho/\mu$. When Boger fluids are used, the viscosity μ varies slightly and the value taken[9] is that appropriate to a shear rate of $13N\ s^{-1}$.

Power number versus Reynolds number data for Boger fluids are shown in Figures 3–6.

The photographs in Figures 7 and 8 show typical flow patterns for Newtonian and Boger fluids respectively; these are sketched in the line drawings alongside the photographs. The Weissenberg (rod climbing) effect which occurs at the higher rotational speeds in Boger fluids is shown in the photograph in Figure 9.

DISCUSSION OF RESULTS

The Boger fluids used in the present work have properties similar to those originally described[2]. The main physical differences are the use of a very high molecular weight polyacrylamide having remarkable effects in aqueous solutions[e.g. 10] and the presence of water in the solutions. This permits the shear rate to be raised to the high values shown in Figure 1 and is probably responsible for the slight shear-thinning properties of the fluids[2]. Boger's original fluids gave graphs of first normal stress difference (N_1) against shear rate which had gradients of 2.0 at shear rates below unity, but at higher shear rates this gradient became approximately 1.0. The present fluids give gradients of about 1.5 in the lower

Table 1. Physical properties of fluids (22.0°C).

Fluid No.	Density ($kg\ m^{-3}$)	Weight % Water	Weight % Magnafloc	Viscosity (Pa s)	Weissenberg Number ($N_1\tau^{-1}$)
1	1.31×10^3	19.5	0	0.53	0
2	1.33×10^3	15.0	0	0.97	0
3	1.35×10^3	10.5	0	2.68	0
4	1.34×10^3	12.6	0.05	3.70(4.50)†	7.55†
5	1.34×10^3	17.0	0.05	1.27(1.45)†	4.41†
6	1.31×10^3	21.4	0.05	0.58(0.68)†	5.18†

† At shear rate $100\ s^{-1}$. Figures in brackets refer to shear rate at $10\ s^{-1}$.

VOL. 62 1984

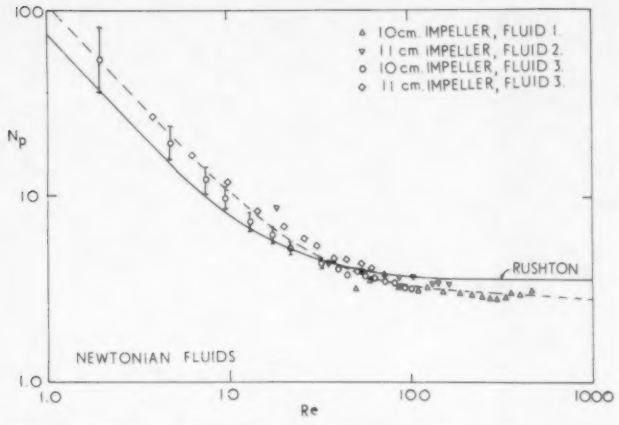


Figure 2. Power number/Reynolds number relationship for Newtonian fluids.

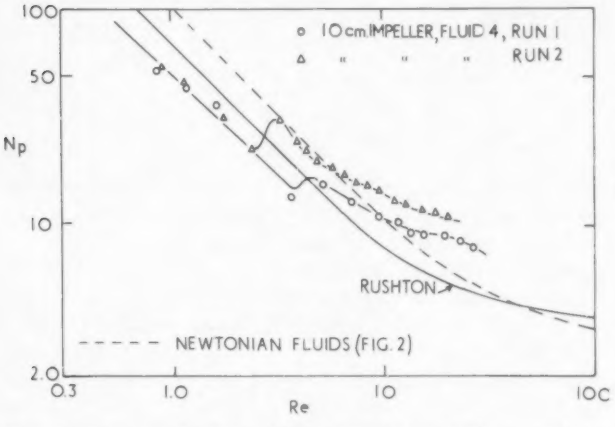


Figure 3. Power number/Reynolds number relationship for Boger fluid 4, using impeller of diameter 100 mm.

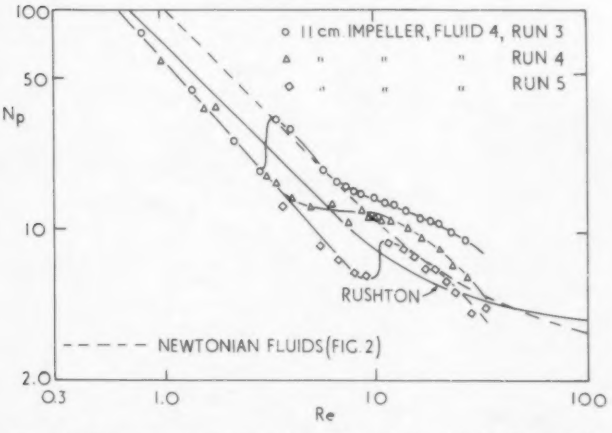


Figure 4. Power number/Reynolds number relationship for Boger fluid 4, using impeller of diameter 110 mm.

range of shear rates (20–80 s^{-1}) but approach 1.0 at high shear rates. The first normal stress difference exceeds the shear stress by a factor of about 7, which is broadly comparable with that achieved in the original fluids.

During the initial phase of mixing dilute Magnafloc solutions with glucose syrup, some quite exceptional

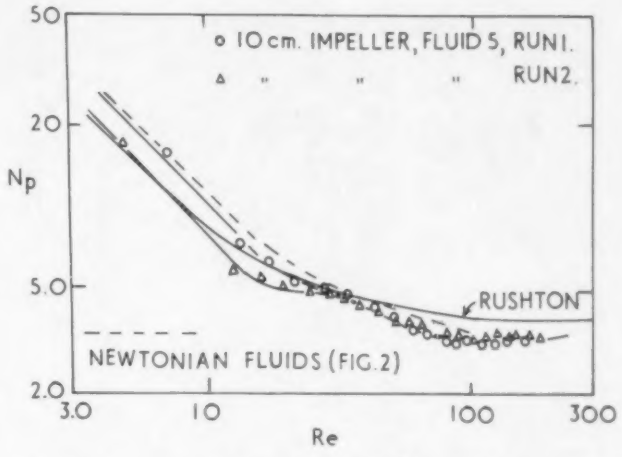


Figure 5. Power number/Reynolds number relationship for Boger fluid 5, using impeller of diameter 100 mm.

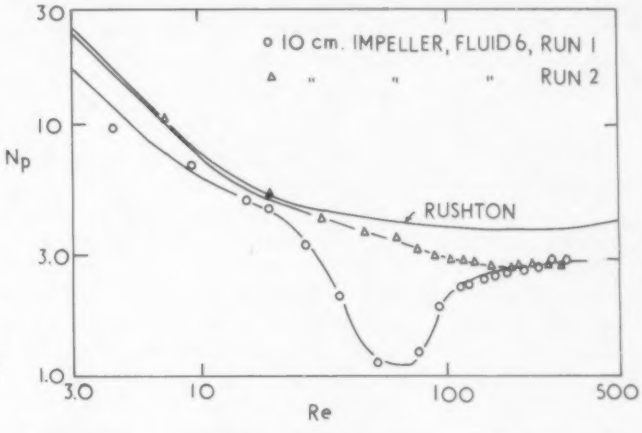
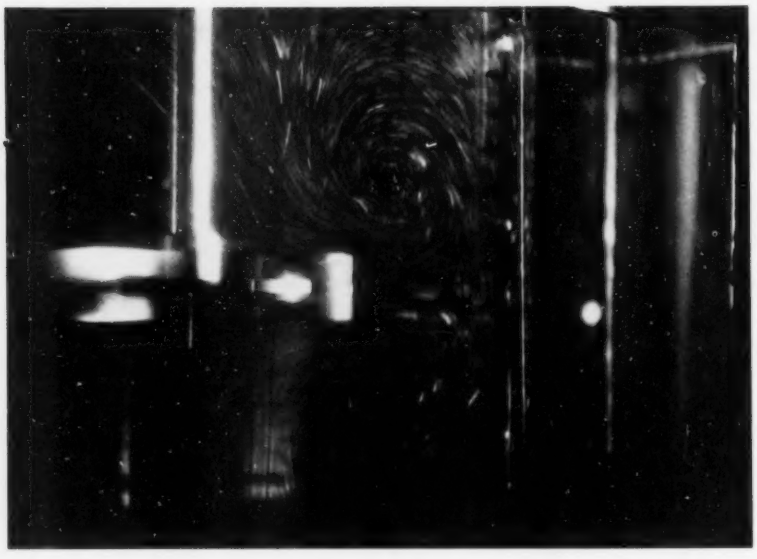


Figure 6. Power number/Reynolds number relationship for Boger fluid 6, using impeller of diameter 100 mm.

rod-climbing effects were observed, nearly half the fluid being raised as an irregular, rotating mass over 30 cm above the normal fluid level. After some 1–2 hours of mixing, the more traditional effect shown in Figure 9 was obtained and subsequently the effect changed only very slowly. The highly elastic behaviour of fresh, partially mixed polyacrylamide solutions has been noted before[10], but remains something of a mystery.

The power requirements for mixing Newtonian fluids were in approximate agreement with the Rushton line (Figure 2) but had a tendency to be high in the laminar region and slightly low in the turbulent region. The error in torque measurement increases greatly at low stirrer speeds (see error bars) and another possible source of discrepancy is local temperature variation brought about by viscous heating of the fluid being mixed. However, this has been calculated to be about 2°C for the duration of a typical experiment and should predominate at high mixer speed. Since fluid viscosity has little effect on power consumption in this region is is not thought that local heating is a major source of error. It may also be observed that the variations of power number which occur as a result of changing the impeller diameter are



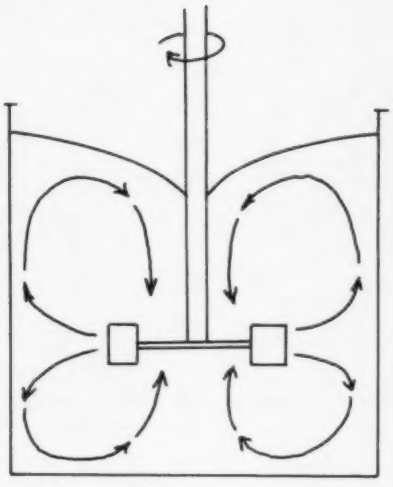
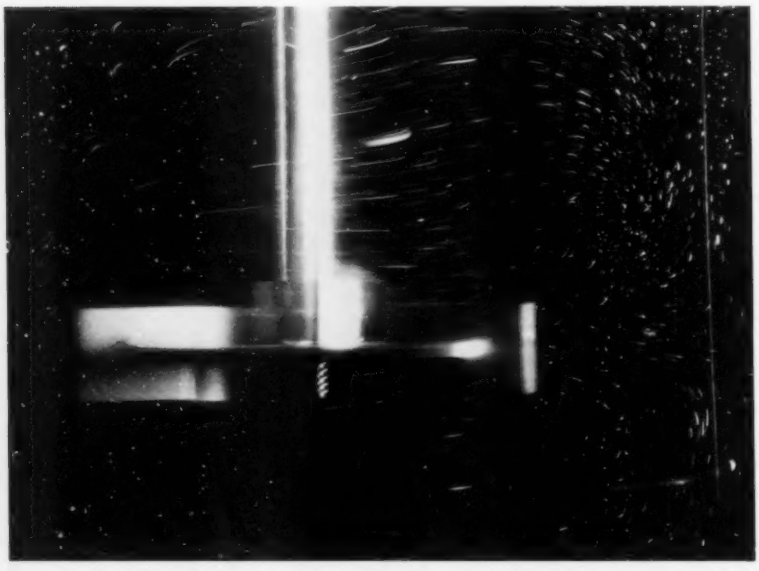


Figure 7. Typical flow pattern in Newtonian fluid.

comparable with those which occur from run to run or those which are caused by a change in fluid viscosity.

A marked change in the power number–Reynolds number curve occurs when Boger fluids are mixed (Figure 3: fluid 4). Relatively low power numbers are obtained in the low speed region, which may be caused by the inhibition of the centrifugal flow pattern by elastic forces, most of the fluid motion occurring near the impeller. However, an abrupt rise in the power requirement occurs at moderate Reynolds number. This coincides with the *onset* of the rod-climbing phenomenon, suggesting that at this point the centripetal forces due to fluid elasticity suddenly begin to dominate the flow pattern. As shown in Figure 8, this is quite different from the usual centrifugal pattern (caused by forces due to fluid inertia) and produces inward flow towards an extremely rapid, energy consuming, vortex near the drive shaft. This should improve the quality of mixing in this region, but towards the corners of the vessel the movement is slow and it is doubtful whether the overall rate of mixing is improved. The rapid rotation of the core is caused by the conservation of angular momentum as the rotating fluid is forced inwards by elastic forces, but the only source of energy is the turbine and this must provide the extra power required. The value of Reynolds number at which the power suddenly rises depends on

VOL. 62 1984



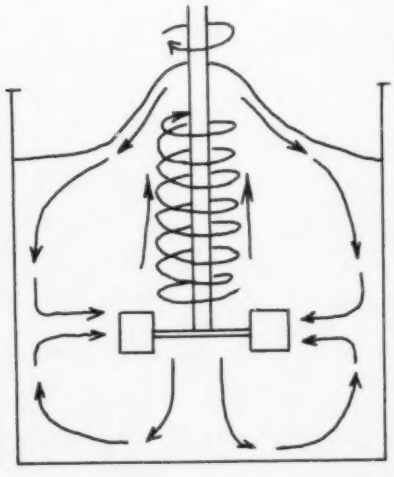


Figure 8. Typical flow pattern in Boger fluid.

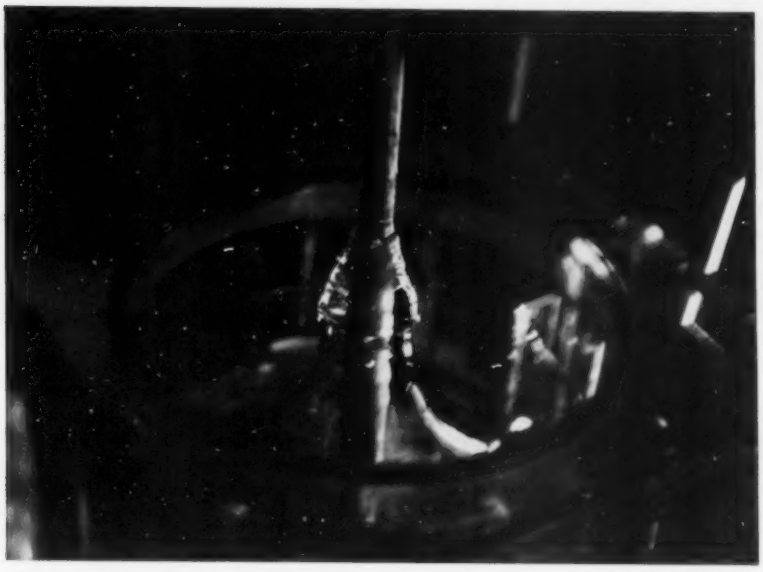


Figure 9. The Weissenberg or rod climbing effect at the agitator shaft.

the degree of mixing and on the degradation of the solutions. The value varies from run to run and is rather unpredictable in character (see also Figure 4).

As the turbine speed increases further, the data points continue to rise above the line appropriate to Newtonian fluids (Figure 3), but in later examples the rise in power number is followed by a fall, thus at high Reynolds numbers, on Figure 4, all three curves are falling quite steeply. The middle curve shows a more gradual form of transition, in the middle range of Reynolds numbers, which gives the line a 'wavy' appearance. This is for the fluid of highest viscosity (fluid 4), but the trend becomes more noticeable when a lower viscosity Boger fluid is used (Figure 5, fluid 5). There is little doubt that the characteristic wavy shape of these curves is related to the elastic character of the liquids, but once the 'centripetal' mixing pattern had become established there was no visible evidence of the cause of the undulations in the power curve.

Figure 6 illustrates an unusual phenomenon obtained when using the Boger fluid of lowest viscosity (fluid 6). A large drop in power requirement has been reported by Nienow *et al*[7] when mixing various viscoelastic solutions under *aerated* conditions, and it is possible that large bubbles were temporarily induced behind the turbine blades. These may have been ejected via the central core in the high-speed centripetal flow period of operation.

The present results highlight the problems of studying power requirements when mixing viscoelastic liquids. The main advantage of using Boger-type fluids stems from their high elasticity, which causes effects which may be difficult to explain but at least are clearly defined. It should be mentioned that the effects may be greatly affected by the scale of the system as well as the age of the solutions. Further work planned includes a study of the rate of mixing in Boger fluids.

NOTATION

D	diameter of impeller
N	speed of impeller (rps)
N_1	first normal stress difference
N_p	$= P/D^5N^3\rho$ power number
P	power consumed by impeller
Re	$= D^2N\rho/\mu$ Reynolds number of impeller
T	torque applied to impeller
ρ	density of liquid
τ	shear stress in liquid
μ	viscosity of liquid

REFERENCES

1. Boger, D. V., 1977, *J Non-Newtonian Fl Mech* 3: 87.
2. Boger, D. V., 1980, *Rheology*, Vol. 1, ed G. Astarita, G. Marucci, L. Nicolais. (Plenum Press) 195.
3. Chavan, V. V. and Ulbrecht, J. 1973, *Trans IChemE* 51: 349.
4. Rieger, F. and Novak, V., 1974, *Trans IChemE* 52: 285.
5. Ulbrecht, J., 1974, *The Chemical Engineer*, 286: 347.
6. Kelkar, J. V., Mashelkar, R. A. and Ulbrecht, J., 1972, *Trans IChemE*, 50: 343.
7. Nienow, A. W. et al. 1983, *Chem Eng Comm*, 19: 273.
8. Rushton, J. H., Costich, E. W. and Everett, H. J., 1950, *Chem Eng Prog*, 46: 395, 467.
9. Metzner, A. B. and Otto, R. E., 1957, *AIChEJ*, 3: 3.
10. Oliver, D. R. and Bakhtiyarov, S. I., 1983, *J Non-Newtonian Fl Mech*, 12: 113.

ACKNOWLEDGEMENT

The authors wish to thank Mr R. Badham for his help in making fluid property measurements.

ADDRESS

Correspondence on this paper should be addressed to Dr D. R. Oliver, Department of Chemical Engineering, University of Birmingham, P.O. Box 363, Edgbaston, Birmingham B15 2TT.

The manuscript was received 24 May 1983 and accepted for publication 6 September 1983.

HEAT TRANSFER AND PRESSURE DROP CHARACTERISTICS OF ALTERNATE ROTATION SWIRL-FLOW INDUCERS IN A CIRCULAR DUCT

By D. BURFOOT (STUDENT) and P. RICE

Department of Chemical Engineering, University of Technology, Loughborough

The reported experimental investigations show the pressure drop and heat transfer characteristics of tubes containing pairs of Kenics mixer inserts with various equidistant spacings. A single curve, with logarithmic coordinates of friction factor ratio and heat transfer factor ratio, represents the data well. Correlations are presented which adequately represent the present data and that of the manufacturers for the conventional Kenics system pressure drop. The alignment of the leading edges of consecutive elements is shown to significantly reduce the pressure drop, with a lesser reduction in the heat transfer, compared to the Kenics system. Reynolds numbers in the range 11000 to 104000 were used in the tests.

INTRODUCTION

Previous work by the authors[1] investigated the heat transfer enhancement that is obtained by using swirl flow inducing inserts of identical twist direction in a circular duct. As a further part of that study the enhancement obtained by using helices of alternate twist direction was also investigated. The results that were obtained are presented in this paper.

One of the insert configurations that was used is known as a Kenics static mixer, see Figure 1. This device consists of a number of helices each of which possesses a twist of 180° either in a clockwise or anticlockwise direction. The elements are positioned inside circular ducts so that consecutive elements have alternate twist direction and their leading edges are perpendicular. The turbulent flow pressure drop characteristics of the Kenics static mixer system have been reported previously[2-8]. Chen[9] indicates that the heat transfer coefficient increase, compared to an empty tube, is approximately a factor of three in the turbulent flow regime. Azer et al[10] used pairs of Kenics elements, a counterclockwise and clockwise rotation element with perpendicular leading edges, with spacings between the pairs; they found that the heat transfer coefficient increase can be as large as a factor of nine. However, this data was obtained in the Reynolds number range of 890 to 5500. In the laminar flow regime in empty tubes the heat transfer coefficients are low. The insertion of a Kenics mixer disrupts the flow and increases the heat transfer coefficients above the values obtained with a laminar flow at the same nominal Reynolds number. Furthermore, as shown by Chen[9], see above, the Kenics mixer also increases the heat transfer coefficient in the turbulent flow regime. On the basis of this discussion the large increases in the heat transfer coefficient found by Azer et al[10] are to be expected since they operated in the Reynolds number range which, for an empty tube, produces a laminar flow.

The present study, performed in the Reynolds number range of 11000 to 104000, examined the effects on the heat transfer and pressure drop characteristics of interspacing of the Kenics elements and the alignment of the leading edge of successive elements.

VOL. 62 1984

EXPERIMENTAL EQUIPMENT AND METHOD

The experimental equipment and the operating procedure have been described previously[1]. A brief description is now given for the reason of completeness.

A double pipe heat exchanger was used in the tests. The heated tube length of 1067 mm was preceded by a 965 mm long calming section. Water was passed through the inner copper tube (20 mm i.d.) of the exchanger; hot water was passed through the annulus. The average temperatures of the tube side and annulus side fluids along the heated section were 35°C and 80°C. Pressure drops were measured using four manometers each of which was approximately 2 m long. One manometer contained carbon tetrachloride the remaining three, which could be connected in series, contained mercury.

Six steel helices with 180° twists were obtained from the Kenics Corporation. Three of these inserts possessed an anticlockwise twist, the remainder had clockwise twists. Further inserts were produced by moulding using solder alloy (Grade J). The dimensions of the inserts were the same as those used previously[1] i.e. diameter = 20 mm; length = 40.5 mm; and thickness = 3.175 mm (steel inserts), 2.8 mm (solder inserts). The

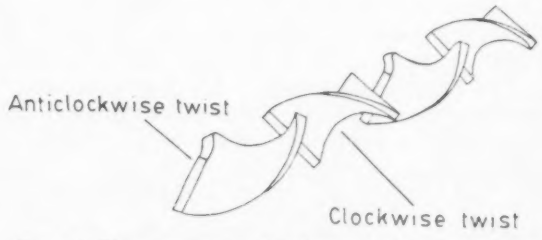


Figure 1. The arrangement of helices to form a Kenics mixer.

© Institution of Chemical Engineers

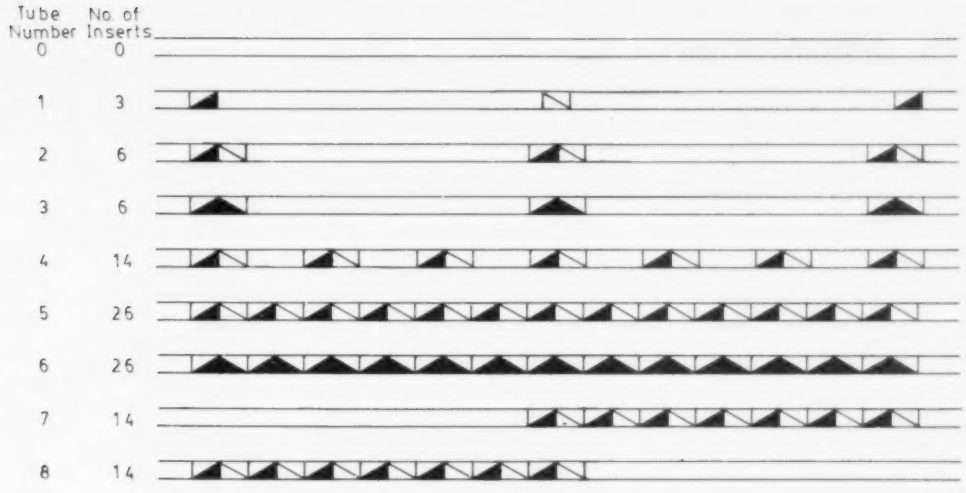


Figure 2. Details of insert configurations.

inserts fitted tightly within the tube but the high fluid pressures and the significant forces on the elements led to the use of the fixing method adopted previously[11]. Figure 2 shows the insert configurations that were studied.

CALCULATION PROCEDURES

The pressure drop characteristics were correlated in the form used previously[1] i.e.

$$\ln[\phi] = \ln\left[\frac{\Delta\rho d}{4\rho u^2 l}\right] = \ln[A] + B\ln[Re] \qquad (1)$$

The heat transfer data was converted into dimensionless form using an adaptation of the Wilson plot method[11]. The equation used was

$$\ln\left[\frac{d_T}{[(1/U) - C]k\ Pr^{0.4}}\right] = \ln[Nu/Pr^{0.4}] = \ln[F] + E\ln[Re] \qquad (2)$$

The heat transfer resistance, C, that was due to the scale, tube wall, and annulus fluid film, was determined from empty tube tests as described before[1].

EXPERIMENTAL RESULTS

Pressure loss data was obtained under heating conditions over the Reynolds number range 15500 to 104000, under isothermal conditions at room temperature (16°C to 24°C) over the range $Re = 11000$ to 78000, and for some configurations under isothermal conditions with an average fluid temperature of 35°C over the range $Re = 15500$ to 104000. Average friction factors, based on the values at $Re = 15500$ and 78000, show that the results obtained under isothermal and heating conditions agreed to within 3.1%. Two exceptions to the latter were noted; for the empty tube and configuration 1S the isothermal friction factors are greater than the heating values by approximately 11% and 8%, respectively. The reason that large reductions are produced by the heating conditions, when using the latter two configurations, has been discussed[1]. However, at the present time, no reason can be offered as to why the results obtained using three solder inserts, configuration 1, do not exhibit the same trend.

To reduce the amount of data, only the results obtained under heating conditions will be further considered in the present work. The friction factor data is presented in Table 1.

In the previous work[1] it was necessary to vary the heat transfer through the tube wall as the tubeside Reynolds number was varied and the annulus side flowrate was held constant. In the present work the minimum and maximum heat flowrates required were 6.1 kW and 17.1 kW. The heat transfer results are presented as Table 2.

Table 1. Friction factor data obtained under heating conditions. (S refers to stainless steel inserts).

Tube	A	$-B$	No.	A.A.D.	R.A.D.	M.A.D.	R^2	CON
0	0.0304	0.234	405	1.26	1.60	5.11	0.987	0.003
1	0.159	0.239	27	0.98	1.13	1.92	0.994	0.008
2	0.256	0.198	27	1.39	1.59	2.83	0.982	0.011
3	0.250	0.207	27	1.26	1.51	3.27	0.985	0.011
4	0.664	0.222	27	1.58	1.81	3.19	0.981	0.013
5	1.08	0.167	54	1.27	1.66	3.99	0.972	0.008
6	1.21	0.276	27	2.66	3.14	5.62	0.964	0.022
7	0.577	0.172	27	1.20	1.45	2.84	0.980	0.010
8	0.656	0.183	27	1.68	1.89	3.39	0.969	0.015
1S	0.124	0.199	27	1.16	1.33	2.52	0.987	0.009
2S	0.294	0.208	27	1.78	2.11	3.84	0.965	0.017

Table 2. Heat transfer data obtained under heating conditions. (S refers to stainless steel inserts).

Tube	F	E	No.	A.A.D.	R.A.D.	M.A.D.	R^2	CON
0	0.0253	0.800	432	3.21	4.16	15.33		
1	0.0362	0.794	27	0.86	1.26	3.49	0.999	0.009
2	0.0555	0.771	27	4.98	5.85	14.08	0.984	0.041
3	0.0480	0.783	27	2.18	2.54	4.87	0.997	0.018
4	0.0442	0.818	27	4.68	5.08	7.64	0.989	0.036
5	0.0648	0.808	54	4.37	5.80	21.27	0.984	0.029
6	0.0872	0.772	27	3.16	3.75	8.08	0.993	0.026
7	0.0399	0.808	27	2.96	3.79	8.89	0.994	0.026
8	0.0487	0.794	24	4.20	4.72	8.92	0.989	0.036
1S	0.0415	0.790	27	3.13	4.00	9.14	0.993	0.028
2S	0.0424	0.801	27	3.52	4.68	11.28	0.988	0.039

Table 3. Typical values of the friction factor ratio for the Kenics static mixer. The K values are based on $\phi_0 = 0.0396\ Re^{-0.25}$. The average K is the mean of the results evaluated at the limits of the Reynolds number range for each of the reference studies. Due to the low Reynolds numbers used in the tests, Chakrabarti's data has been evaluated at $Re = 2800$.

Reference	Conditions	Twist ratio	δ/d	Re range	Average K value
Bor[6]	Unknown	Unknown	Unknown	Turbulent	60 to 80
Grace[7]	Unknown	1.5	Unknown	5×10^3 to 10^7	230
Smith[8]	Isothermal	1.5	0.074	3×10^2 to 10^5	85
Chakrabarti[12]	Isothermal	1.43	0.1	1.6 to 2.8×10^3	77
Morris and Benyon[5]	Mass transfer	2.5	0.079	6×10^3 to 3×10^4	13
Proctor[4]	Mass transfer	2.0	0.079	1.1×10^4 to 3×10^4	15
Proctor[4]	Mass transfer	1.5	0.079	1.1×10^4 to 2.2×10^4	22
Proctor[4]	Heat transfer	1.5	0.079	6×10^3 to 2×10^4	36

DISCUSSION

Table 3 shows typical values of the friction factor ratio, reported in the literature, for lengths of unspaced Kenics elements. However, by far the most extensive amount of data is that of Chen[2] and Kenics Corp[3]. The latter references use the following notation: K = ratio of the friction factors, based on the inside diameter of the tube, for the mixer and the empty tube at the same nominal Reynolds number, and:

$$K = Z\,K_{OT} \tag{3}$$

Chen[2] shows that Z is a parameter which is dependent on the Reynolds number only. It appears that a good approximation to the data of Chen is:

$$Z = 0.62\ Re^{0.104} \tag{4}$$

Values of K_{OT}, for various pipe diameters, are given by Chakrabarti[12] and Grace[7]. The data is correlated here using terms involving either the twist ratio y, or $y/(y-1)$; the latter factor was proposed by Date[13] for the correlation of twisted tape data. Regression analyses of the data of Chen[2] show that

$$\text{either } K = 72.0\ D^{-0.190}\ y^{-2.24}\ Re^{0.104} \tag{5}$$

$$\text{M.A.D.} = 6.2,\ \text{A.A.D.} = 1.1$$

$$\text{or } K = 5.24\ D^{-0.196}\ [y/(y-1)]^{1.61}\ Re^{0.104} \tag{6}$$

$$\text{M.A.D.} = 6.6,\ \text{A.A.D.} = 1.2$$

Regression analyses of the data of Kenics Corp[3] show that

$$\text{either } K = 75.8\ D^{-0.207}\ y^{-2.46}\ Re^{0.104} \tag{7}$$

$$\text{M.A.D.} = 5.9,\ \text{A.A.D.} = 0.81$$

$$\text{or } K = 5.08\ D^{-0.211}\ [y/(y-1)]^{1.57}\ Re^{0.104} \tag{8}$$

$$\text{M.A.D.} = 6.5,\ \text{A.A.D.} = 0.83$$

The data of Chen[2] for a tube inside diameter of 20.8 mm was not used in the above analyses since the value of K_{OT} for that pipe diameter was a misprint[14].

Cathie[15] suggests that for $d < 38$ mm the thickness of commercial Kenics mixers is reasonably approximated by using $\delta/d = 0.1$. Using this information and the empty tube correlations that were used by the reference authors it is possible to convert equations (5) to (8) to an equivalent diameter basis. The results of these calculations, after conversion back to a nominal diameter basis, are presented in Table 4. Reasonable agreement is obtained between the isothermal results of this work and the predictions even though the extrapolation of the manufacturers data from twist ratios of 1.8 to 2.03, and the assumption that δ/d is 0.1 for the Kenics inserts, are tentative. It is also interesting to note the good agreement concerning the effect of flowrate on the friction factor ratio: the sources cited[2,3] indicate that K depends on $Re^{0.104}$ while the present work shows a dependency on $Re^{0.111}$ under isothermal conditions.

It is difficult to compare the results of the present heat transfer investigations with those obtained by previous workers. Chen[9] and Proctor[4] indicate that in the turbulent flow regime the heat transfer coefficient may be increased by a factor of approximately three by inserting a continuous full length Kenics mixer into an empty tube. Grace[7] suggests that the increase may be 3.26. These results were obtained using inserts with a twist ratio of 1.5 and with relative thicknesses, δ/d, equal to 0.1, approximately, or 0.079. The continuous mixer used in the present work had inserts with a twist ratio of 2.03 and a relative thickness of 0.14, such a device produced 2.8 fold increases of the heat transfer coefficient.

Friction factor ratios and heat transfer factor, $Nu/Pr^{0.4}$, ratios have been determined by comparing the regression equations applying to the packed and empty

VOL. 62 1984

Table 4. Comparison of the friction factors calculated using the equivalent flow concept with equations (5) to (8). ϕ_P = calculated friction factor, ϕ_R = friction factor determined from the reference study, $\% = (\phi_P - \phi_R) \times 100/\phi_R$, MT = Mass transfer. The results of the present work at Reynolds number of 11000 and 78000 were obtained under isothermal conditions. The results at 15500 and 104000 were obtained under heating conditions.

Reference	Reynolds Number	ϕ_R	equation (5) ϕ_P	%	equation (6) ϕ_P	%	equation (7) ϕ_P	%	equation (8) ϕ_P	%
Present work	11000	0.226	0.194	−14	0.205	−9	0.168	−26	0.194	−14
	78000	0.156	0.132	−15	0.140	−10	0.114	−27	0.132	−15
	15500	0.215	0.159	−26	0.168	−22	0.138	−36	0.159	−26
	104000	0.157	0.124	−21	0.131	−16	0.107	−31	0.124	−21
Smith[8]	300	0.471	0.476	1	0.505	7	0.441	−6	0.468	−1
	100000	0.235	0.204	−13	0.216	−8	0.189	−20	0.200	−15
Chakrabarti[12]	2800	0.420	0.418	0	0.470	12	0.391	−7	0.434	3
Morris and Benyon[5]	6000	0.0528	0.108	105	0.140	164	0.0897	70	0.134	153
	30000	0.0442	0.0854	93	0.110	149	0.0709	60	0.106	139
Proctor[4] (MT, $y = 2.0$)	11000	0.0530	0.163	207	0.171	223	0.142	169	0.163	207
	30000	0.0515	0.141	173	0.148	187	0.123	139	0.141	173
Proctor[4] (MT, $y = 1.5$)	11000	0.0789	0.310	293	0.329	317	0.289	266	0.307	289
	22000	0.0784	0.280	257	0.298	280	0.261	233	0.278	254
Proctor[4] ($y = 1.5$)	6000	0.138	0.339	145	0.360	161	0.316	129	0.336	143
	20000	0.135	0.284	111	0.302	124	0.265	97	0.282	109

tubes at Reynolds numbers of 15500 and 104000. For each configuration the average values of the two ratios so determined are shown in Figure 3. This graph does not distinguish the results of configurations 7 and 8; it was found that the results for these two configurations showed deviations of 0.57% and 2.37% from the mean values of the friction factor and heat transfer factor ratios, respectively.

Figure 3 does not include the results obtained with the thicker stainless steel inserts. For configuration 1 the use of the thicker inserts increased the friction factor and heat transfer factor ratios by 19.3% and 10.2%, respectively; for configuration 2 the corresponding increases were 4.6% and 5.3% when compared to the results obtained using the solder alloy inserts.

Figure 3 shows the following interesting features:

(1) A single curve adequately represents the data obtained using inserts positioned with perpendicular edges. The effect of Reynolds number on this curve is not particularly significant.
(2) The use of seven pairs of inserts with equidistant spacings, configuration 4, clearly provides a greater heat transfer enhancement than does seven unspaced pairs, configurations 7 and 8. The advantage of using intermittent inserts has also been noted in previous work[1].
(3) The full length perpendicular edge arrangement, configuration 5, produces a considerably larger pressure loss than the aligned edge arrangement, configuration 6, although a relatively small increase in the heat transfer coefficient is obtained.

The last feature agrees with the heat/momentum analogy. The form drag that is produced by the perpendicular edges does not greatly increase the shear stress at the tube wall and therefore the heat transfer coefficient increase is small compared to the increase of the pressure loss.

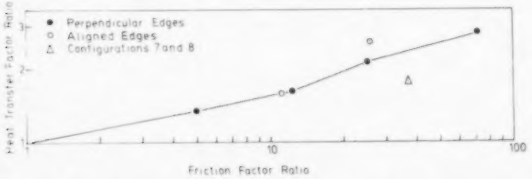


Figure 3. Comparison of heat transfer and friction factor increases relative to an empty tube.

It is interesting to compare the pressure losses that occurred across the continuous full length arrangements used in this work with those reported previously. Over the same flow range as that used in this work, it was found[1] that the friction factor ratio, K, is 11 for a twisted tape, while the K value for a continuous length of identically twisted 180° helices with perpendicular edges is 21. The continuous lengths of alternately twisted helices used in this work produce K values of 26 (aligned edges) and 73 (perpendicular edges). These results show that the larger pressure loss encountered with the Kenics mixer, compared with the twisted tape, is due to the combined effects of the alternate rotation and perpendicular edges and the difference is not simply dominated by one of these effects.

The large pressure losses encountered with the Kenics mixer in the turbulent flow region may prevent the use of this device. Although configuration 6 does not produce flow division, the production of radial flow channel mixing may make this device useful for the mixing of low viscosity fluids in the turbulent flow regime. The Kenics device is useful for mixing viscous fluids in laminar flow.

The constant power basis used by Lopina and Bergles[16] is a measure of the heat transfer improvement relative to the same length of empty pipe requiring the same pumping power; on this basis configuration 6 is the most beneficial layout. Lopina and Bergles used the following equations to represent the empty tube characteristics:–

$$\phi_0 = 0.023\ Re^{-0.2} \tag{9}$$

and

$$Nu_0/Pr^{0.4} = 0.023\ Re^{0.8} \tag{10}$$

Using these equations the Nusselt number ratio at a constant power is 1.14 for configuration 6. However, using the experimental empty tube data of the present work, the Nusselt number ratio for configuration 6 is found to be 1, approximately; this value is a better representation of the effectiveness of the inserts.

SYMBOLS USED

A	a parameter in equation (1)
B	Reynolds number exponent in equation (1)
C	tube wall and outside film resistance to heat transfer
d	tube inside diameter
d_T	tube outside diameter
D	tube inside diameter, inches
E	Reynolds number exponent in equation (2)
F	a parameter in equation (2)
k_T	tube wall thermal conductivity
K	friction factor ratio
K_{OT}	a parameter which is dependent on the tube size and twist ratio of the inserts
l	packed length of tube (including spacings)
N	number of inserts
Nu	Nusselt number based on the tube inside diameter
Pr	Prandtl number
R^2	correlation coefficient
Re	Reynolds number $= du\rho/\mu$
u	fluid velocity, based on the tube i.d.
U	overall heat transfer coefficient
y	twist ratio = number of pipe diameters per 180° of insert rotation
Z	a parameter which is dependent on the Reynolds number as shown by equation (6)
Greek letters	
δ	insert thickness
μ	fluid viscosity
ρ	fluid density
ϕ	friction factor
Subscript	
0	empty tube value
Abbreviations	
A.A.D.	average absolute percentage deviation from the least squares line
CON.	95% confidence interval, on the slope of the least squares line, obtained using Students t-distribution
M.A.D.	maximum absolute percentage deviation from the least squares line
No.	number of experimental data points used to obtain the least squares line
R.A.D.	root mean square absolute percentage deviation from the least squares line

REFERENCES

1. Burfoot, D., Rice, P., 1982, Chem. Eng. Res. Des., 16, No. 4, 253–258.
2. Chen, S. J., 1972, Kenics Corporation Bulletin KTEK-2.
3. Kenics Corporation, 1977, Bulletin KMOD-10.
4. Proctor, R., 1977, An investigation into convective heat and mass transfer in the Kenics static mixer, M.Phil. thesis, Univ. of Sussex.
5. Morris W. D., and Benyon, J., 1976. Ind. Eng. Chem. Proc. Des. Dev. 15, 338–342.
6. Bor, T., 1972, The Kenics static mixer and it's applications in the chemical process industries, Paper presented at 4th Int. Cong. of Chem. Eng. Equip. Design, Prague.
7. Grace, C. D., 1971, Chem. Proc. Eng. 52, 57–59.
8. Smith, J. M., 1978, Chem. Engnr., 827–830.
9. Chen, S. J., 1979, Kenics Corporation Bulletin KTEK-3.
10. Azer, N. A., Lin, S. T., Fan, L. T. 1980, Ind. Eng. Chem. Proc. Des. Dev., 19, 246–250.
11. Wilson, E. E., 1915, Trans. ASME 37, 47–71.
12. Chakrabarti, A., 1979, Mixing of liquids in a static in-line mixer, Ph.D. thesis, Univ. of Bradford.
13. Date, A. W., 1972, Prediction of friction and heat transfer characteristics of flow in tubes containing twisted tapes, Ph.D. thesis, Univ. of London.
14. Stanbury, R. G., Kenics Europe (Belgium), 1980, personal communication.
15. Cathie, N. M., Kenics Europe (Belgium), 1980, personal communication.
16. Lopina R. F., and Bergles, A. E., J. Heat Trans., 434–442.

ACKNOWLEDGEMENTS

One of us (D.B.) wishes to express his thanks to the Science and Engineering Research Council for the grant received throughout the duration of this work. Also thanks are due to Mr. H. Peters for his invaluable assistance throughout the experimental study.

ADDRESSES

Correspondence in connection with this paper should be addressed to D. Burfoot, Engineering and Development Division, Meat Research Institute, Langford, Bristol BS18 7DY.

VOL. 62 1984

SHORTER COMMUNICATION

BIOMASS HOLD-UP CORRELATIONS FOR A FLUIDISED BED BIOFILM REACTOR

By W. K. SHIEH and C.-Y. CHEN

Department of Environmental Engineering National Chung Hsing University, Taiwan

Fluidisation mechanics in a fluidised-bed biofilm reactor (FBBR) are defined in terms of a bioparticle terminal settling velocity U_t and an expansion index n. Experimental data demonstrate that the Richardson–Zaki correlation provides a good description of FBBR fluidisation mechanics. Both U_t and n are functions of the Galileo number N_{Ga}, which characterises biofilm, medium, and liquid. Their biomass holdup predicted from correlations developed herein compares favourably with that experimentally measured.

INTRODUCTION

A fluidised-bed biofilm reactor (FBBR) is a novel biological process in which small, fluidised particles are used to immobilise biomass within the reactor. Immobilisation of biomass in a FBBR results in a high biomass holdup, enabling the reactor to be operated at significantly higher liquid throughputs with practical absence of biomass wash-out. This is a significant breakthrough in biochemical engineering, especially in biological wastewater treatment[1-3].

Mulcahy, Shieh, and LaMotta[3,4] have demonstrated that an accurate prediction of biomass holdup is essential to process design and control of a FBBR. A logical and convenient way of predicting biomass holdup in a FBBR is to define fluidisation mechanics in terms of some measurable parameters. The resulting correlations would give the number and size of bioparticle (medium + biofilm) per unit fluidised volume and hence predict the biomass holdup.

BIOMASS HOLDUP IN FBBR

Numerous solid liquid fluidisation correlations linking particle concentration in a fluidised state to the physical characteristics of a fluidised-bed system have been developed in past decades[5-8]. Among them, the Richardson–Zaki correlation is widely used (see list of symbols used):

$$U/U_t = \varepsilon^n \tag{1}$$

Figure 1 presents a schematic of a spherical bioparticle. It has been demonstrated by dimensional analysis that[9]:

$$U_t = f(\rho,\rho_l,\mu,\delta,\rho_m,d_m) \tag{2}$$

$$n = g(U_t) \tag{3}$$

The number of variables in equations (2) and (3) can be reduced by incorporating them into a dimensionless parameter (the Galileo number) characterising biofilm, medium, and liquid:

$$N_{Ga} = d_p^3\rho_l(\rho_p - \rho_l)g\mu^2 \tag{4}$$

Thus

$$U_t = f(N_{Ga}) \tag{5}$$

and

$$n = g(N_{Ga}) \tag{6}$$

The bioparticle density is:

$$\rho_p = \rho_m(d_m/d_p)^3 + \rho[1 - (d_m/d_p)^3]/(1 - P) \tag{7}$$

where P is the biofilm moisture content.

Once the functional relationships shown in equations (5) and (6) are quantitatively defined, the bed porosity can be evaluated by equation (1) and the biomass holdup X in a FBBR by:

$$X = \rho(1 - \varepsilon)[1 - (d_m/d_p)^3] \tag{8}$$

EXPERIMENTAL RESULTS

Experimental data reported by Mulcahy and LaMotta[9] in their FBBR denitrification study are used

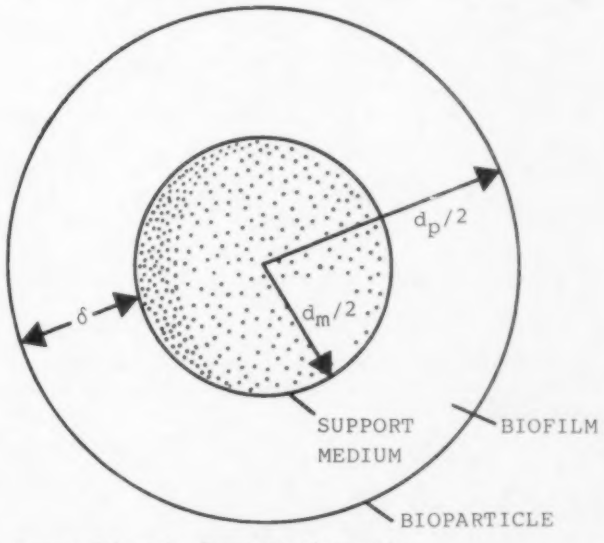


Figure 1. Schematic of a spherical bioparticle.

© Institution of Chemical Engineers

to define the functional relationships in equations (5) and (6). A brief description of their experimental methodology is presented here.

Experimental Denitrification FBBR

The denitrification FBBR was fed with the clarified effluent from an extended aeration unit at the University of Massachusetts Wastewater Pilot Plant and was operated at a temperature of $20 \pm 2°C$ and a pH of 7.0 ± 0.2. The reactor was 150 cm high and 4 cm in diameter. Several sampling ports were installed on the reactor wall to remove liquid and solid samples. The degree of bed expansion and thus the biofilm thickness were controlled at given values with a mixer, which removed the biofilm from the medium by vigorous agitation. Spherical glass beads with a density of $2.42\ g\ cm^{-3}$ were used as the medium.

Determination of Relevant Variables

Wastewater density and viscosity.

The wastewater density determined with a pycnometer was found to be the same as that for clear water. Thus, the reported values of ρ_l and μ were used.

Medium diameter and biofilm thickness.

A microscope equipped with a micrometer was used to determine d_m and d_p. At least one hundred measurements were made for each determination. A surface-averaged, or Sauter, mean diameter was then calculated as[10]:

$$d_S = \Sigma m_i d_i^3 / \Sigma m_i d_i^2 \tag{9}$$

The biofilm thickness is:

$$\delta = (d_{p,S} - d_{m,S})/2 \tag{10}$$

Biomass concentration.

Samples withdrawn directly from the reactor were used to determine the biomass concentrations. The amount of biomass was expressed in terms of total volatile solids in the sample.

Bed porosity.

At a given superficial velocity, a small portion of bed materials was withdrawn from the reactor and the change in the expanded bed height (Δh) was noted. The number of bioparticles in the sample (ΔN) was calculated as:

$$\Delta N = \frac{\text{weight of glass beads in the sample}}{\rho_m \pi\, d_{m,S}^3/\sigma} \tag{11}$$

Then, the bed porosity is calculated as:

$$\varepsilon = 1 - (\pi d_{p,S}^3\, \Delta N / 6 \Delta h A) \tag{12}$$

Table 1 summarises values of the relevant variables to be used to define the functional relationships in equations (5) and (6).

Table 1. Values of relevant variables to be used to define the functional relationships in equations (5) and (6)

Variable	Value
ρ_l	$0.998\ g\ cm^{-3}$
μ	$0.009548\ g\ cm^{-1}\ s^{-1}$
δ	$40–1200\ \mu m$
ρ	$40–65\ mg\ cm^{-3}$
ρ_m	$2.42\ g\ cm^{-3}$
U	$0.56–1.8\ cm\ s^{-1}$
$d_{m,S}$	0.0682 cm
P	0.925

Biofilm dry density, ρ, and biofilm moisture content, P, are calculated using the procedures recommended by Shieh *et al.*[11]. The required inputs include the biomass concentration, biofilm thickness, wastewater density and viscosity, medium diameter, and medium density.

DISCUSSION

Twenty sets of experimental data obtained over wide ranges of biofilm thicknesses are used to prepare plots of $\ln(\varepsilon)$ versus $\ln(U)$ to determine whether the Richardson–Zaki correlation is applicable for describing the FBBR fluidisation mechanics, and, if so, the values of U_t and n. The linearity of the $\ln(\varepsilon) - \ln(U)$ relation is determined via linear regressional analysis. For nineteen of the twenty sets of data, correlation coefficients in excess of 0.99 are obtained. Figure 2 presents typical examples on $\ln(\varepsilon)$–$\ln(U)$ plots. Thus, the Richardson–Zaki correlation, as shown in equation (1), provides a good description of the fluidisation mechanics in a FBBR.

Values for n and U_t are evaluated from the slope and the U value at $\varepsilon = 1.0$ of the $\ln(\varepsilon)$–$\ln 1U)$ plot, respectively, by linear regressional analysis. They are then plotted against the Galileo number for each set of experimental data, as shown in Figure 3. It is seen that:

$$U_t = 5753.71 N_{Ga}^{-0.8222} \tag{13}$$

$$n = 47.36 N_{Ga}^{-0.2576} \tag{14}$$

The relatively high correlation coefficients obtained indicate that U_t and n depend mainly on the physical characteristics of the biofilm, medium, and liquid.

To verify the validity of equations (13) and (14) in describing the fluidisation mechanics of a FBBR, the biomass holdup in a FBBR is calculated by substituting equations (13) and (14) into equations (1) and (8) and comparing with those experimentally measured by Mul-

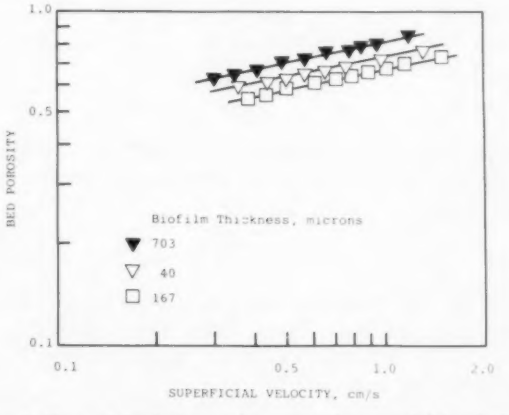


Figure 2. Plots of the bed porosity versus the superficial velocity.

VOL. 62 1984

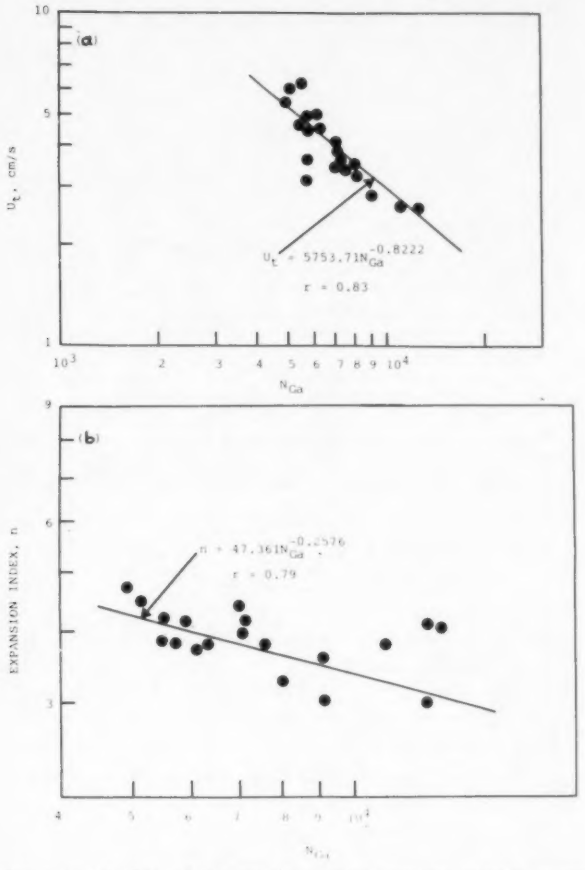


Figure 3. (*a*) Plot of bioparticle terminal settling velocity versus Galileo number, and (*b*) plot of expansion index versus Galileo number.

cahy and LaMotta[9]. Figure 4 presents the comparison between predicted and measured biomass holdup values in a FBBR. Also included in Figure 4 is a set of experimental data obtained by Shieh, Sutton and Kos[11]

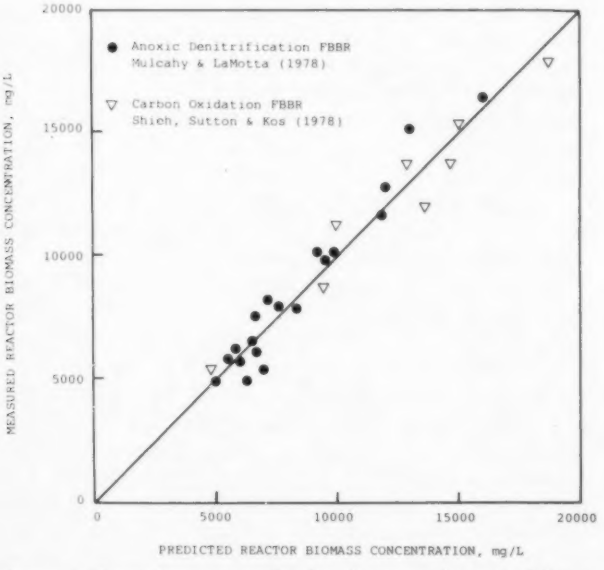


Figure 4. Comparison of predicted and measured reactor biomass concentration in a FBBR.

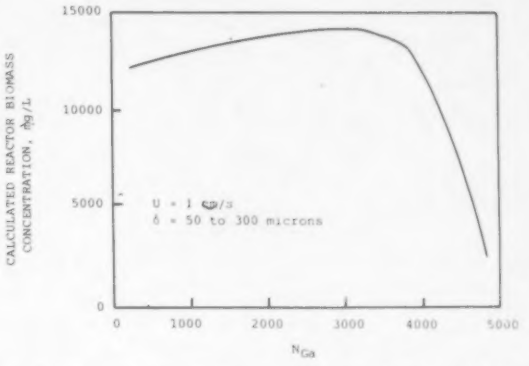


Figure 5. Effect of the Galileo number on the reactor biomass concentration.

from a pilot-scale aerobic FBBR treating the municipal wastewater.

The close agreement between predicted and measured biomass hold-up values indicates that the fluidisation correlations developed herein are adequate. These correlations are simple and can be directly applied to predict fluidisation mechanics and biomass hold-up of a FBBR, provided that the physical characteristics of the biofilm, medium, and liquid are specified. However, it is worthwhile mentioning that equations (13) and (14) are defined on the basis of experimental data obtained over a relatively narrow N_{Ga} range (5000 to 15000). But they are adequate for the N_{Ga} values ranging from 1000 to 15000 because the data reported by Shieh, Sutton, and Kos[11] were obtained over a N_{Ga} range of 1000 to 3500. Further refinement of these correlations with experimental data over wider N_{Ga} ranges is recommended.

Figure 5 presents a sensitivity analysis on the effect of N_{Ga} on the reactor biomass concentration. It is seen that, under a given set of operating conditions, there is a narrow N_{Ga} range within which the reactor biomass concentration is maintained near a maximum value. It is also seen that the stability of a FBBR is much less when the biofilm thickness becomes thicker (i.e., high N_{Ga}). On the other hand, when the biofilm is thin, a FBBR is more stable as can be seen by the flat slope of the left portion of the curve.

CONCLUSIONS

1. The Richardson–Zaki correlation provides a good description of the fluidisation mechanics in a FBBR.
2. The bioparticle terminal settling velocity U_t and the expansion index n are functions of the Galileo number N_{Ga}, which characterises the biofilm, medium, and liquid.
3. The empirical correlations developed herein provide a good prediction of biomass holdup in a FBBR over a N_{Ga} range of 1000 to 15000.
4. Further refinement of the empirical correlations developed herein is recommended.

SYMBOLS USED

A cross-sectional area of the reactor (L^2)
d_m diameter of support medium (L)

d_p $= d_m + 2\delta$ bioparticle diameter (L)
d_s Sauter mean diameter (L)
h expanded bed height (L)
m_i number of particles of diameter d_i (—)
n expansion index (—)
N number of bioparticles (—)
N_{Ga} Galileo number (—)
P biofilm moisture content (—)
U superficial velocity ($L T^{-1}$)
U_t bioparticle terminal settling velocity ($L T^{-1}$)
X biomass holdup in a FBBR ($M L^{-3}$)
δ biofilm thickness (L)
ε bed porosity (—)
μ liquid viscosity ($M L^{-1} T^{-1}$)
ρ biofilm dry density ($M L^{-3}$)
ρ_l liquid density ($M L^{-3}$)
ρ_m medium density ($M L^{-3}$)
ρ_p bioparticle density ($M L^{-3}$)

REFERENCES

1. Atkinson, B. and Knight, A. J., 1975. *Biotech Bioeng*, 17: 1245.
2. Cooper, P. F., 1981, *The Chemical Engineer*, 373.
3. Mulcahy, L. T., Shieh, W. K. and LaMotta, E. J., 1980, *Prog. Wat. Tech.*, 12: 143.
4. Mulcahy, L. T., Shieh, W. K. and LaMotta, E. J., 1980 *73rd Annual AIChE Meeting*.
5. Richardson, J. F., and Zaki, W. N., 1954, *Trans I Chem E*, 32: 35.
6. Lewis, E. W. and Bowerman, E. W., 1952, *Chem Eng Prog*, 48: 603.
7. Wen, C. Y. and Yu, Y. H., 1966, *Chem Eng Prog Symp Ser* 62: 100.
8. Vasalos, I. A., Rundell, D. N., Megiris, K. E. and Tjatjopoulos, G. T., 1982, *AIChE J*, 28: 346.
9. Mulcahy, L. T., and LaMotta, E. J., 1978, *Env Eng Prog Report* No. Env. E. 59-78-2 (Dept Civil Eng, Univ Massachusetts).
10. Bailey, J. E. and Ollis, D. F., 1977, *Biochemical Engineering Fundamentals* (McGraw-Hill, New York).
11. Shieh, W. K., Sutton, P. M. and Kos, P., 1979, *Biomass Holdup in a Fluidized Bed Biofilm Reactor (FBBR)* (Internal Report, Dorr-Oliver, Inc).

ADDRESS

Correspondence on this paper should be addressed to Professor Chiu-Yang Chen, Department of Environmental Engineering, National Chung Hsing University, Taichung, Taiwan, Republic of China.

The manuscript was received 3 October 1983 and was communicated by Professor J. O. Wilkes, Associate Editor of the journal in the U.S.A.

Book Reviews continued from p 122

Biotechnology, Vol. 3 Fermentation
Edited by H. Dellweg
Verlag Chemie, 1983
pp. 642, DM495

Volume 3 of this 8-volume treatise is in fact the second volume to appear (Vol 1 was reviewed in July 1983, p 252), and deals mainly with primary products of fermentation—microbial cultures and biomass, ethanol and organic acids.

Each fermentation process is reviewed in a self-contained section of length varying between 6 and 150 pages covering, in most cases, the microbiology and biochemistry of each process, its ancillary upstream and downstream processes, economics and process plant. The balance of attention given to these different aspects varies somewhat from one section to another. The depth of treatment given to each process in the longer sections is similar to that in other series of process reviews such as "Economic Microbiology" or "Advances in Biochemical Engineering", and indeed, a similar selection of processes is covered.

The book falls into two more or less equal parts, the first on biomass production and the second on the production of ethanol and other primary metabolites. The part on biomass covers much the same ground as volume 4 of "Economic Microbiology"—even to a section on mushroom growing—with concise, well-balanced accounts of algal biomass and biomass from hydrocarbons. There are interesting accounts of starter-cultures and microbial cultures for special uses, including microbial insecticides, but the section on biomass from carbohydrates concentrates on baker's yeast production, with a disappointingly brief consideration of whey and starch utilisation. These may however be dealt with in the forthcoming volume on "Food and Feed Production".

The second part includes a good detailed account of ethanol production, which, combined with the timely chapter on energy from renewable resources, would make an excellent separate monograph on this currently intensely investigated topic. The section on amino-acids gives a detailed account of the microbiology and biochemistry but lacks detail of the actual industrial processes. The sections on other key organic acids—principally acetic, lactic, citric and gluconic acids—are concise, well-balanced accounts, as are those on microbial polysaccharides, emulsifiers and de-emulsifiers.

The major proportion of this volume is written by authors who are not native English speakers, but the standard of English is good, with few actual ambiguities. The style, however, does at times tend towards the convolutions of Eurospeak, with the arcane usage of the word "technical" characteristic of German-speaking authors. This volume would benefit from sub-editing by someone whose mother-tongue is English. The index is adequate, but information retrieval would be considerably simplified had page-numbers been included in the contents-lists at the head of each chapter.

Overall, this volume has much in common with that other well-known biomass product, the curate's egg. Parts of it are excellent, most of it gives competent, concise and well-balanced accounts of the detailed background needed for an understanding of key processes of industrial microbiology, and parts of it are disappointing. More of the authors should have given attention to the treatment, disposal and utilisation of process wastes, as fermentation processes in general produce highly polluting effluents.

On its own, this volume does not add a great deal to the material already available in the appropriate sections of existing series, such as "Economic Microbiology", apart from being a few years more recent. As part of the complete 8-volume treatise, however, there is no doubt that it will contribute to providing a useful work of reference for undergraduate and postgraduate students as well as a valuable introduction to engineers and researchers starting work in an unfamiliar area of biotechnology. Unfortunately, the cost of this volume (DM495, about £130) will put it beyond the reach of smaller institutions.

M. A. Winkler

VOL. 62 1984

CHEMICAL ENGINEERING RESEARCH & DESIGN

Transactions of The Institution of Chemical Engineers

EDITORIAL

In "Vertical co-current flow of air and shear thinning suspensions of kaolin", Z. Khatib and J. F. Richardson report experimental measurements of average slug hold-ups and pressure drop for two-phase co-current flow of air and flocculated kaolin slurries in a vertical pipeline. A gamma-ray absorption method together with a conductivity probe were used to estimate the probability density functions of void fractions from which flow patterns and other parameters are obtained. Average liquid hold-up is correlated in terms of modified Lockhart-Martinelli parameters. A model for predicting the total pressure drop during slug flow of a two-phase mixture is proposed. Both models show agreement (generally within 20%) between the predictions and the experimental results.

B. Atkinson, J. D. Cunningham and A. Pinches report on "Biomass hold-ups and overall rates of substrate (glucose) uptake of support particles containing a mixed microbial culture". Biomass support particles, such as the spheres formed from wire used in this investigation, offer a number of advantages for biological process engineering. Experimental data from a fluidised bed reactor are reported and interpreted to take account of both diffusional limitations and the presence of biomass other than within the support particles. Particle biomass hold-up followed a hyperbolic relationship with substrate concentration. The overall rate of substrate uptake was found to vary as the square root of substrate concentration.

In "Molecular sieving effects of zeolites in the dehydration of alcohols", P. L. Yue and O. Olaofe report on the dehydration of ethanol, isopropanol and n-butanol over three zeolites. The patterns of activity and product selectivity of the zeolites are examined in light of geometrical and molecular selectivity and the effect of reaction temperature. A mechanism for the dehydration of alcohol to olefin is proposed.

J. F. Stubington, D. Barrett and G. Lowry describe a study of "Bubble size measurements and correlation in a fluidised bed at high temperatures". The bed material used was electrode carbon of 250 to 300 μm particle size and the bed temperature ranged from 26 to 1006°C. Bubble size was found to decrease by 5 to 15% as the temperature increased to about 300°C and thereafter remained constant (for constant excess fluidising gas velocity and height above the distributor). Above 300°C a correlation similar to that of Darton et al predicted bubble size. The authors suggest that the difference between their correlation parameters and those of Darton et al may be due to differences in distributor design.

In "Effect of scale-up on secondary nucleation kinetics for the sodium chloride–water system", P. A. M. Grootscholten, L. D. M. v.d. Brekel and E. J. de Jong report laboratory and pilot-scale studies of crystallisation with a scale-up ratio of 1:5000. Nucleation kinetics are correlated with agitator speed, the solids residence time and the magma concentration. The effect of scale-up on the nucleation rate constant can be accounted for by the dimensionless impeller number and the impeller diameter.

In a Shorter Communication, T. Plaka, I. S. Ahmed and M. J. Lockett discuss the effect of weeping and entrainment of the efficiency of a distillation tray. The trays in question have no provision for liquid residence control and liquid channeling occurs. The authors conclude that the effect of weeping depends on tray diameter and that large diameter trays may be relatively insensitive to weeping. On the other hand entrainment causes a reduction in efficiency at all diameters.

P. Kumar, S. Devotta and F. A. Holland report in a Shorter Communication on further experiments on an absorption cooling system. Heat losses from the system were reduced and high flow rates were used. This resulted in a lower generator temperature for a given evaporator temperature. The authors conclude that this broadens the scope for relatively low temperature heat sources to be used in absorption cooling systems. They further suggest that it is feasible to operate such a system using air cooling.

The Shorter Communication by M. M. C. G. Warmoeskerken, M. C. van Houwelingen, J. J. Frijlink and J. M. Smith reports experiments on three-phase behaviour in a stirred vessel. The authors found that in a three-phase system suspension is at first more easily maintained than in a liquid solid system. Only when gas loading leads to the formation of large gas cavities behind the impeller does sedimentation occur. It is concluded that the suspension of solids is greatly affected by the two-phase hydrodynamics of the impeller.

Brian Gay
Honorary Editor

Notes for Authors

Editorial Policy and Standards

1. Papers published in the Journal will be original contributions to chemical engineering knowledge, not previously published. In particular, the Editorial Board encourages the submission of papers which show how the results of research may be used in chemical engineering design. Such implications for design should be brought out clearly in the paper and its summary.

Accounts of research work of an experimental or theoretical nature which throw new light on established principles, which identify problems not yet solved, or indicate practical areas to which research effort may usefully be applied are also invited. Reports from industry and from research establishments are particularly welcome.

Papers may also deal with new developments of plant or processes if these developments are related to underlying principles and can be given quantitative expression.

2. Authors need not be members of the Institution. Papers must be in English and should normally be of 2500 to 5000 words, including Appendices. Figures should also be included in this count, each being estimated as equivalent to 250 words.

3. The Editorial Board will, however, also welcome Shorter Communications (less than 2500 words) for consideration for publication; these would describe, for example, novel research techniques, new analyses of previous work, or interesting aspects of work still in progress. A faster refereeing procedure has been arranged for such short Papers.

4. The Journal also publishes a limited number of longer Review Papers, which are critical assessments of previously published work in a selected area of chemical engineering. In conformity with editorial policy, Reviews should show how the results of research can be used in the design of plant and equipment.

Most Reviews are specially commissioned by the Editorial Board, but authors are also invited to offer Reviews for consideration for publication. In view of the substantial effort required, authors are advised to communicate with the Editor before embarking on a Review.

5. It is the policy of The Institution to publish only papers of the highest quality. To help maintain these standards all papers submitted are sent to referees familiar with the branch of chemical engineering covered. They advise as to whether the paper is acceptable or not and, in addition, indicate to the author possible ways in which, in their opinion, the paper might be improved. The final decision on publication is taken by the Editor in light of this advice.

Manuscript Requirements

1. The text should be typewritten, using one side of the paper only, double-spaced and with adequate margins to allow for revision and copy preparation marks. A summary, preceding the text, should briefly describe the essential original contents of the paper.

2. Mathematical expressions can sometimes be more easily interpreted by the printer if carefully written by hand. Where many equations appear, a list of symbols used should be inserted at the end of the paper, before the references. SI units should *always* be used; the negative index notation is preferred to the oblique stroke.

3. References are listed in the order in which they are first cited in the text, where they are indicated by superscript numbers. They should give in order: Authors' surnames and initials, Year, Title of book or journal, Volume, Issue, Page numbers , followed by name and town of publisher in the case of a book.

4. Tables, drawings and photographs should be on separate sheets at the end of the manuscript and not interspersed in the text. Tabulated data should not duplicate values detailed in the text or on graphs. Drawings submitted should be clear and complete and preferably in a form suitable for direct reproduction. Photographs should be restricted to the minimum necessary.

5. Where limitations of space preclude publication of detailed results, mathematical derivations, etc, authors are invited to include in their paper a statement that this information is available from them on application. Authors may make an appropriate charge for supplying items requested in this way. Such material should be supplied with the paper when submitted to the Editor.

Submission of Papers

1. Three copies of the paper should be sent to:

The Editor, Chemical Engineering Research and Design,
Institution of Chemical Engineers,
George E. Davis Building,
165–171 Railway Terrace,
Rugby CV21 3HQ, England.

or to an Associate Editor as follows:

Australia:
Prof R. G. H. Prince,
Department of Chemical Engineering,
University of Sydney,
Sydney 2006, New South Wales, Australia.

Continental Europe:
Prof Dr J. R. Bourne,
Technisch-Chemisches Laboratorium,
ETH-Zentrum,
CH-8092 Zürich, Switzerland.

Continental Europe:
Prof J. M. Smith,
Laboratorium voor Fysische Technologie,
Technische Hogeschool Delft,
Prins Bernhardlaan 6,
2628 BW Delft, Holland.

India:
Prof M. M. Sharma,
Department of Chemical Technology,
University of Bombay,
Matunga Road,
Bombay 400 019, India.

New Zealand:
Prof R. B. Keey,
School of Engineering,
University of Canterbury,
Christchurch 1, New Zealand.

USA:
Prof J. O. Wilkes,
Department of Chemical Engineering,
University of Michigan,
Ann Arbor,
Michigan 48109, USA.

2. A full address to which readers may send correspondence should be specified, including the post code. The address at which the work was carried out, if different, should also be indicated. Where there are several authors, one should be nominated to check proofs and to receive all correspondence.

3. A proof will be sent to the nominated author, to be checked for possible typographical errors. Other alterations cannot be incorporated at this late stage without incurring higher printing costs, and extensive alterations would necessitate postponement of publication of the paper to a later issue.

4. Following publication the nominated author will receive 50 off-prints of the paper (or 25 where there is just one author). Any further off-prints required should be ordered at proof stage. Reprints, ordered after publication, are more expensive.

VOL.
62
1984

VERTICAL CO-CURRENT FLOW OF AIR AND SHEAR THINNING SUSPENSIONS OF KAOLIN

by Z. KHATIB and J. F. RICHARDSON (FELLOW)

Department of Chemical Engineering, University College, Swansea

Experimental measurements of flow pattern, average holdup and pressure drop are reported for two-phase cocurrent flow of air and flocculated kaolin slurries in a 38.8 mm bore vertical pipeline. Instantaneous values of holdup, estimated by rapid scanning of a horizontal cross-section of the pipe, were used to give Probability Density Functions (PDFs) from which values of average film and slug holdup, average slug length and average slug frequency were obtained. Average liquid holdup was correlated in terms of a method previously developed for horizontal flow. A model for slug flow of air/Newtonian and air/non-Newtonian mixtures has been developed and the values of film and slug holdup have been used to calculate the various components of the total pressure drop along the vertical pipeline.

INTRODUCTION

There are many examples of the flow of gas–liquid mixtures in the chemical, petroleum and mineral industries. In two-phase flow, momentum, heat and mass transfer, and back mixing are all highly dependent on the flow pattern prevailing in the pipeline.

In vertical flow, several flow patterns are observed and these may be classified as follows, in order of increasing gas content: bubble, slug, churn and annular flow. The occurrence of any particular flow pattern depends on the flow rates and properties of the two fluids as well as on the pipe size (diameter and length). Although many investigators have stated that the flow pattern has a major influence on most two-phase (gas–liquid) transport phenomena, most of the published correlations are based on data obtained over a wide range of flow rates often covering several flow regimes. For slug flow, several models for holdup have been developed and these are based on considerations of spherical-nosed gas bubbles in a liquid[2,6,14]. For pressure drop, one of the most recent correlations is that developed by Dukler and Hubbard[4] as the result of visual observations of air–water mixtures in slug flow in a horizontal pipe. They assumed that a liquid slug extending over the full cross-sectional area of the pipe picked up liquid from a film surrounding the gas bubble and shed it from its wake, giving rise to acceleration as well as frictional losses.

The purpose of the present paper is to present results of experiments carried out on the co-current flow of air with water and with flocculated suspensions of kaolin in water under both laminar and turbulent conditions.

For the slug flow regime preliminary information was obtained on the relevant parameters (film and slug holdups, slug frequency, film and bubble velocity, etc.) using instantaneous measurements of liquid holdup. The probability density functions (PDF's) of void fractions, as originally developed by Jones and Zuber[10] and later applied by Heywood and Richardson[8] have been used in conjunction with conductivity probe measurements to give a qualitative flow pattern discriminator for the three dominant regimes studied in this work, namely: bubble, slug and churn flow. Film thickness, slug and film holdup, and slug and bubble lengths were also readily obtainable from the PDF data.

A further extension of the concepts of Dukler and Hubbard led to the development of a slug flow model to predict two-phase pressure drop in vertical pipelines.

THEORETICAL BASIS OF THE SLUG FLOW MODEL

In slug flow, the gas flows predominantly in the form of slugs which span the whole of the cross-section of the pipe, with the exception of the region very close to the wall where a liquid film will be in either upward or downward flow, according to the flow conditions. The remaining small proportion of the gas will be in the form of small bubbles entrained within the liquid slugs which separate consecutive gas slugs. The model which is proposed for slug flow is based on the following assumptions:

(*a*) That a fast moving liquid slug overruns a slow moving liquid film, accelerating the liquid in the film to the slug velocity: this occurs in the mixing region located at the front of the liquid slug.

(*b*) That the film once established is neither accelerating nor decelerating, and, therefore, the gravitational force acting on it must be entirely balanced by the combined effect of the shear forces at the wall and at the gas–liquid interface.

(*c*) That the pressure gradient along an individual gas slug is negligible and, therefore, the entire pressure drop is attributable to the liquid slugs in the remainder of the pipe, (see Figure 1).

On this basis, the total pressure drop, $(-\Delta P_s)_{TP}$, across a slug unit has been attributed to the following two components.

(i) The static pressure gradient due to the gravitational force acting on the liquid in the slug. This pressure gradient, expressed per unit total length of pipe, is directly proportional to the average liquid holdup, β_s, in

© Institution of Chemical Engineers

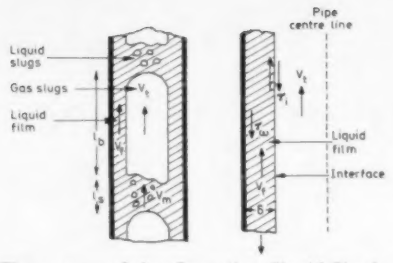


Figure 1. The process of slug formation (liquid film in down flow).

the liquid slug and to the slug length ratio (l_s/l_t);

$$\left(-\frac{\Delta P_s}{l_t}\right)_{Gr} = \rho_L \beta_s g \frac{l_s}{l_t} \tag{1}$$

where ρ_L is the density of the liquid; l_s is the average length of a liquid slug, and; l_t is the average length of a unit composed of one liquid and one gas slug.

(ii) The pressure gradient $(-\Delta P_s/l_t)_{Fr}$, necessary to overcome the wall shear stress and to accelerate the liquid in the slow moving film to the slug velocity, is given by

$$\left(-\frac{\Delta P_s}{l_t}\right)_{Fr} = \left(-\frac{\Delta P_s}{l_t}\right)_{Acc} + \left(-\frac{\Delta P_s}{l_t}\right)_{Fs} \tag{2}$$

where the frictional component:

$$\left(-\frac{\Delta P_s}{l_t}\right)_{Fs} = \frac{2 f_m V_m^2}{D} \beta_s \rho_L \frac{l_s}{l_t} \tag{3}$$

and the accelerational component

$$\left(-\frac{\Delta P_s}{l_t}\right)_{Acc} = \rho_L \frac{\beta_f}{l_t} (V_t - V_f)(V_m - V_f) \tag{4}$$

The derivation of equation (4) is given in the Appendix. f_m is the Fanning friction factor based on the mean velocity V_m of the liquid slugs and $\beta_s \rho_L$ is the mean density of the liquid together with the entrained air bubbles.

For co-current flow of air and Newtonian liquid, f_m is as a first approximation given in terms of the slug Reynolds number $V_m \rho_L \beta_s D/\mu$ by the normal pipe friction chart. For liquid with non-Newtonian characteristics, the rheology of the liquid will be important. If the Power Law model may be used over the range of shear rates encountered in the experimental work, the friction factor will be related to the modified Metzner and Reed Reynolds No:

$$Re_{MR} = \frac{D^n V_m^{2-n} \rho_L \beta_s}{\gamma} \tag{5}$$

with

$$\gamma = K 8^{n-1} \left(\frac{1+3n}{4n}\right)^n$$

where n and K are the power law index and consistency respectively.

For laminar flow

$$f_m = \frac{16}{Re_{MR}} \tag{6}$$

In turbulent flow, the method of Heywood and Richardson[9] and of Kemblowski and Kolodziejski[11] may be used to estimate f_m. In this treatment, the liquid in the slug is considered as being a homogeneous fluid with a density equal to that of the mixture and a viscosity equal to the apparent viscosity of the liquid or slurry.

Therefore, for the flow of an air–liquid mixture in the slug flow regime, the total predicted pressure gradient is the sum of three components, viz.

$$\left(-\frac{\Delta P_s}{l_t}\right)_{TP} = \rho_L \beta_s g \frac{l_s}{l_t} + \rho_L \frac{\beta_f}{l_t}(V_t - V_f)(V_m - V_f) + \frac{2 f_m V_m^2 \beta_s \rho_L}{D} \frac{l_s}{l_t} \tag{7}$$

EXPERIMENTAL APPARATUS AND PROCEDURE

The apparatus used for the study of flow of both air–water and air–slurry mixtures consisted basically of an air supply system, a main holding tank (1.5 m^3 capacity), the test section, and the control systems.

Water or slurry was circulated from the feed tank by a centrifugal pump to a straight vertical test section, constructed from 38.8 mm i.d. ABS plastic pipe, from which it discharged at atmospheric pressure and returned through a 150 mm i.d. uPVC plastic pipe (not running full) to the feed tank, as shown schematically in Figure 2. Diaphragm valves 1 and 3 controlled the water or slurry rate, which was metered by an electro-magnetic flow meter. Diaphragm valve 2 was used to control the by-pass flow which was introduced horizontally in order to maintain the slurry in suspension. Using differential 'U' tube manometers, pressure drops in the test section

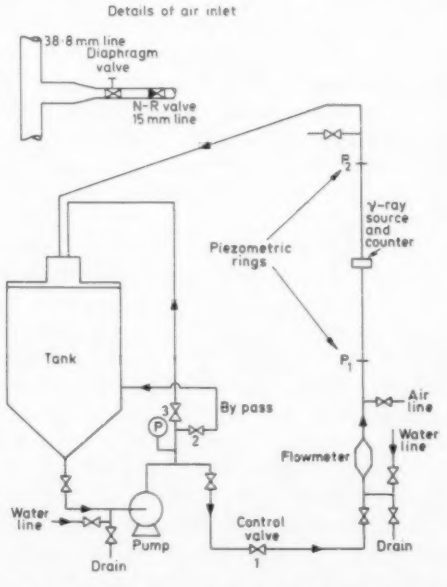


Figure 2. Schematic diagram of the experimental flow loop.

VOL. 62 1984

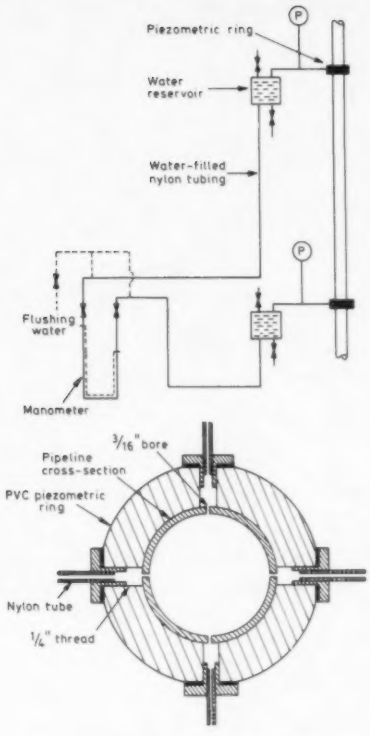


Figure 3. Pressure drop measurement.

(6.03 m long) were measured by means of two uPVC piezometric rings glued to the pipe at each end of the test section (Figure 3). Mercury, diiodomethane and carbon tetrachloride were used as manometer liquids, with water above and in the manometer lines which were purged regularly of any air bubbles. The upstream pressure tapping, P_1, was located at about 40 pipe diameters downstream from the air inlet. Air was introduced into the pipeline through a simple T-piece and was metered by one of three rotameters of different ratings connected in parallel. The pressure at the upstream end of the test section, and the pressure of air at the rotameters were measured with Bourdon tube gauges.

Void fractions were measured mid-way between the two pressure tappings in the test section by a gamma-ray absorption method which could be used to give either average values of void fractions or 'instantaneous' values by rapid scanning of the horizontal cross-section of the pipe. An Americium-241 line source (100 mc) with an active length of 30 mm and diameter 2.35 mm was selected. The gamma radiation was collimated by a slit 1.8 mm wide and 20 mm long. The gamma-radiation, which was emitted horizontally, scanned one half of the pipe cross-section; symmetry of flow about a vertical axis was assumed. The intensity of the emerging radiation was measured by a scintillation counter. The technique for scanning, as described by Heywood and Richardson[8], was adopted; similar operating conditions and scanning times were used. For average holdup measurements a scanning time of 30 s was used: for the separate estimation of slug and film holdup a succession of 0.1 s scanning times was used. The time for the passage of a slug unit was fairly constant at about 1 s.

The average frequency of passage of gas slugs in the test section was estimated using an electrical conductivity technique. Double electrode units were placed on diametrically opposite sides of the pipeline; one electrode was inserted so that its tip coincided with the centre of the pipe cross-section, the other was mounted flush with the surface of the tube wall; the electrical connections to the electrodes were insulated. The electrical circuit was so designed that when both electrodes were in contact with liquid, a voltage of about 9 V was recorded on a chart recorder. When a gas slug passed, the circuit was opened, and there was an immediate drop in voltage.

Experiments were carried out for a number of combinations of superficial air (0.1–7.5 m s^{-1}) and liquid (0.244–2.74 m s^{-1}) velocities for water and for kaolin suspensions of concentrations (7.6, 8.9, 13.7, 18.9, 21.9, 23.1% by volume). The results of a preliminary series of experiments for turbulent flow of water alone showed that the frictional pressure gradient was given by the Blasius equation and therefore the wall of the pipe could be regarded as hydrodynamically smooth.

The kaolin was supplied by English Clays Lovering Pochin & Co. Ltd. The specific gravity was 2.64; 95% by weight of the particles were less than 10 μm and 40% less than 1 μm; at a pH of 5.5–6.0 the material was self-flocculating in water.

The operating conditions were specified at the bottom pressure tapping of the test section; the pressure ranged from 0.15–0.25 MPa and the temperature of the air and water from 15° to 25°C. Isothermal expansion of the air was assumed.

For each operating condition, (slurry concentration, liquid rate and air rate), visual observations were made of the nature of the flow in the inspection tube (in the test section) and measurements were made of

(*a*) Average holdup
(*b*) Instantaneous holdup
(*c*) Slug frequency
(*d*) Pressure drop across the test section
(*e*) Pressure and temperature at the bottom pressure tapping.

By virtue of the fluctuating nature of two-phase flow, readings were necessarily average values and for the measurement of pressure drop it was necessary to damp the oscillations of the manometers by constricting the lines between the manometers and the piezometric rings.

RESULTS AND DISCUSSION

The Rheological Behaviour of the Flocculated Kaolin Suspensions

Wall shear stress ($-\Delta P_s D/4L$) nominal shear rate ($8V_{sl}/D$) data have been obtained for seven different flocculated kaolin suspensions flowing in the pipe line. The rheograms of these suspensions, plotted in Figure 4, represented typical flow curves for pseudoplastic behaviour. At low nominal shear rates corresponding to laminar flow, the average pressure gradient rose very slowly as the slurry velocity was increased, passed a distinct transition point and then increased at an appreciably greater rate under turbulent conditions. The transition from streamline to turbulent flow is shown by

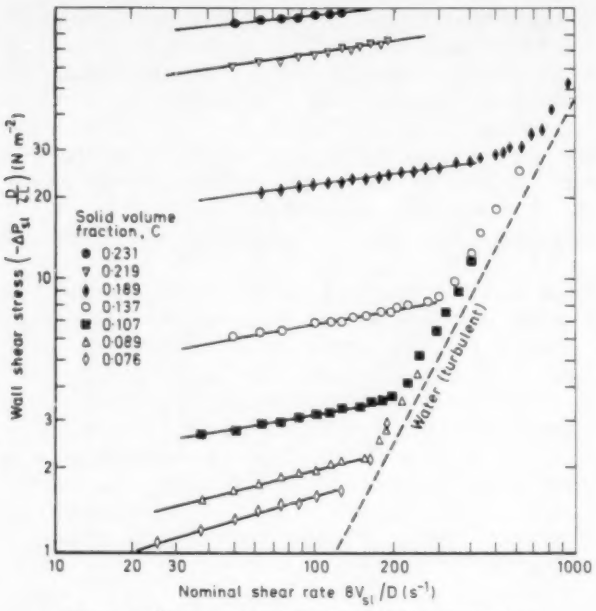


Figure 4. Rheograms for flocculated kaolin suspensions.

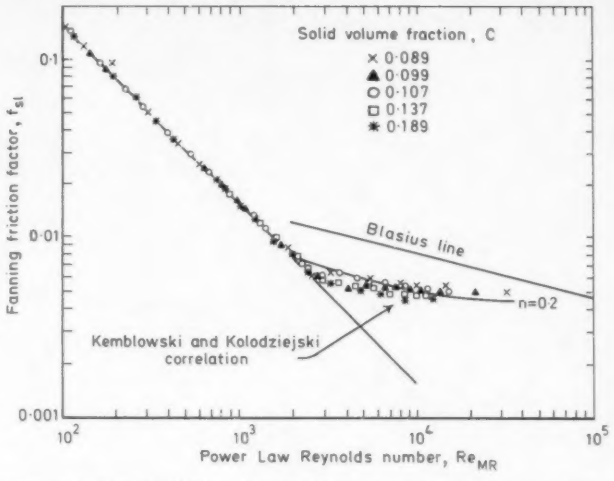


Figure 5. Typical friction factors for flocculated kaolin suspensions.

a sharp transition in the slope of the lines. The rheograms showed that for a given flow rate the pressure gradient in the laminar region increased significantly as the slurry concentration was increased, whereas under turbulent conditions the pressure gradient was almost independent of slurry concentration and lay a little above the line for water. Furthermore, the suspension velocity at which the transition between laminar and turbulent occurred, increased with the kaolin concentration.

Since over the range of shear rates 30–1300 s^{-1}, for which the flow was laminar, the curves were linear when a log–log scale was used, the power law model was appropriate for describing the rheological behaviour of these materials over the range of shear rates of interest. The flow behaviour index n, was given by the slope of the lines and the consistency, K, was obtained from the intercept on the shear stress axis at nominal shear rate of unity.

$$\tau_w = K\left(\frac{8V_{sl}}{D}\right)^n\left(\frac{1+3n}{4n}\right)^n \tag{8}$$

i.e.

$$\log\tau_w = n\log\left(\frac{8V_{sl}}{D}\right) + \log K\left(\frac{1+3n}{4n}\right)^n \tag{9}$$

The resulting rheological parameters n and k are listed in Table 1. The Fanning friction factors, f_{sl} defined by

$$-\frac{\Delta P_{sl}}{L} = \frac{2f_{sl}\rho_{sl}V_{sl}^2}{D} \tag{10}$$

were plotted as a function of the generalised Reynolds No.

$$Re_{MR} = \frac{D^n V_{sl}^{2-n}\rho_{sl}}{\gamma} \tag{11}$$

where

$$\gamma = K\left(\frac{3n+1}{4n}\right)^n 8^{n-1} \tag{12}$$

in Figure 5. For values of Re_{MR} less than 2100, the data are well represented by the line $f_{sl} = 16/Re_{MR}$ which is the theoretical relationship for the laminar region.

For turbulent flow, the wall shear stress is almost independent of rheological properties over the range studied with the suspensions.

Heywood and Richardson[9] have shown that flocculated aqueous suspensions may exhibit Bingham-plastic behaviour in the higher shear rate range of 2000–11,000 s^{-1}. Therefore erroneous values for the friction factor would be obtained if n were assumed constant instead of being evaluated at the appropriate wall shear rate. However, since the actual wall shear rate is not known, it is generally useful to obtain f_{sl} from

Table 1. Estimated values of n and K for each suspension (and water) (25°C)

Solid volume fractions, C	Flow behaviour index, n	Consistency K (N s^n m^{-2})	Apparent viscosity at a shear rate of 100 s^{-1} (N s m^{-2})	Density kg m^{-3}
0	1	0.001	0.001	1000
0.076	0.240	0.44	0.013	1120
0.089	0.227	0.62	0.018	1140
0.107	0.210	1.11	0.029	1180
0.137	0.178	2.67	0.061	1230
0.189	0.167	11.2	0.242	1320
0.219	0.155	29.6	0.604	1360
0.231	0.135	46.5	0.866	1380

VOL. 62 1984

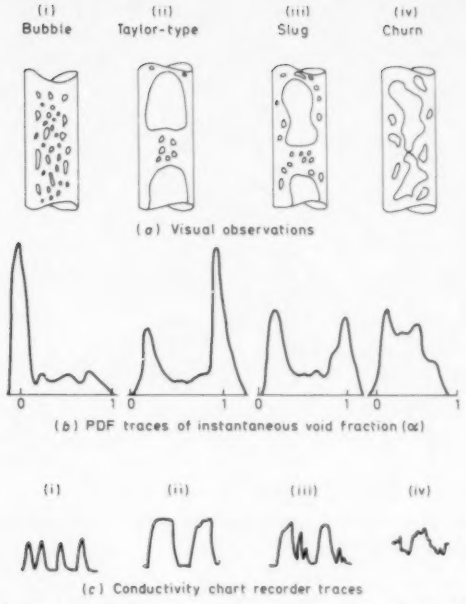


Figure 6. Flow patterns for cocurrent vertical flow of air–liquid mixtures.

Figure 5 for the turbulent flow regime; and the pressure gradient due to friction would then be obtained from equation (10). Only one curve ($n = 0.2$) is shown in Figure 5.

FLOW PATTERN IN TWO-PHASE FLOW

Flow patterns for the two-phase flow of air with water and with flocculated kaolin suspensions were categorised and coded on the basis of visual observations, of conductivity probe readings, and of void measurements from the gamma-ray system. Measurements were all made at distances greater than 100 pipe diameters from the point of air injection.

For a given flow rate of any of the liquids, the bubble, slug and churn flow regimes were all observed as the air flow rate was progressively increased; see Figure 6. In slug flow, gas slugs were observed to be cylindrical with spherical leading ends, but the shape tended to become distorted with progressive increase in the air flow rate. At the rear of the gas slugs considerable mixing in the liquid was observed. The shape of the forward face of the gas slugs has been predicted for Newtonian liquids by Taylor[18] from considerations of energy. Oliver and Young Hoon[15] have also observed this behaviour.

The probability density function (PDF) traces of the void fraction fluctuations were characterised, as suggested by Jones and Zuber[10], by a single-peaked PDF at low void fraction for bubble flow, a twin-peaked PDF at intermediate void fraction for slug flow and a single peaked PDF at high void fractions for annular flow. Figure 6(*b*) demonstrates how an increase in the superficial air velocity at constant liquid flow rate affects the shape of the PDF trace. The average time for which a liquid slug remained within the collimated beam of gamma-ray became less as the gas flow rate was increased. In a typical trace (trace (ii)) it was seen that the height of the peak corresponding to the low voidage region decreased, and that for the high voidage region increased. At somewhat higher air flow rates, the liquid slug became too short to form a stable bridge between consecutive gas bubbles and, as a consequence, the falling film around the bubble penetrated deeply into the liquid slug creating a highly agitated aerated mixture. This behaviour was characterised by three PDF peaks (trace (iii)); the first referred to the liquid slug void fraction, the second (small) peak referred to the mixing region, and the third peak to the bubble void fraction. As still more air was introduced, the highly agitated aerated mixture extended to incorporate the whole of the liquid and gas slugs, in which an oscillatory behaviour developed, with a wide-peaked PDF trace (trace (iv)) indicating the existence of froth flow. The traces obtained by the conductivity chart recorder show similar patterns for the various flow regimes. Values of void fraction α of greater than unity appear as a result of fitting a continuous function to a histogram and as a result of the random nature of the gamma-radiation.

Generally, similar flow patterns were observed for air–water and air–slurry mixtures. However, the transition point for bubble flow to slug flow was found to be a function of the slurry properties. The air rate required to initiate slug flow became higher as the concentration of the kaolin suspension was increased. This may be largely attributed to the greater resistance to air movement offered by the suspension of high viscosity; the coalescence of bubbles to form slugs appears to be impeded.

Figures 7 and 8 present typical experimental data for air–water and air–slurry ($C = 0.189$) mixtures superimposed on the Taitel et al[17] flow pattern map.

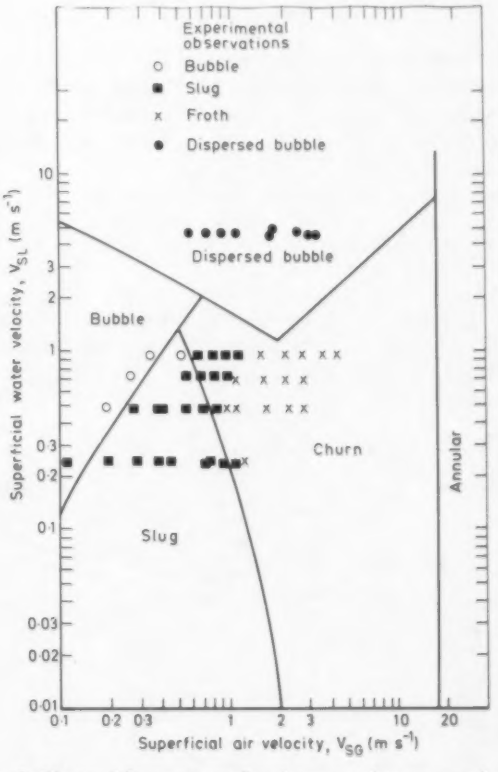


Figure 7. Observed flow patterns for air–water mixtures superimposed on Taitel et al flow pattern map.

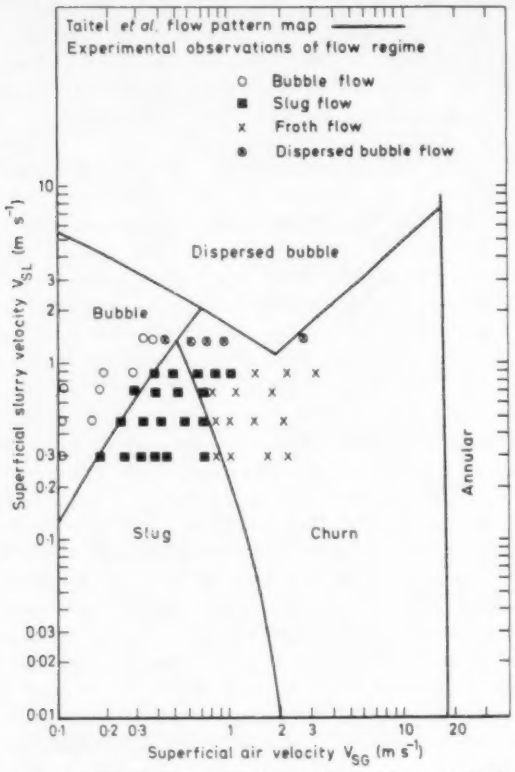


Figure 8. Observed flow patterns for air–slurry ($C = 0.189$) mixtures superimposed on Taitel et al flow pattern map.

HOLDUP IN TWO-PHASE FLOW

(i) General Holdup Data

The gamma-ray equipment was first checked for linearity; then average void fractions, and hence average slurry holdup, were calculated from time-averaged values of gamma-ray counts obtained over 30 s scanning periods.

The average air holdup $(1-\alpha)$ as given by

$$\alpha = \left(\frac{\ln I/I_1}{\ln I_2/I_1}\right) \tag{13}$$

where I_1 is the emerged radiation intensity when the pipe is full of liquid, I_2 is the intensity when the pipe is full of air, and I is the intensity when a two-phase mixture is present.

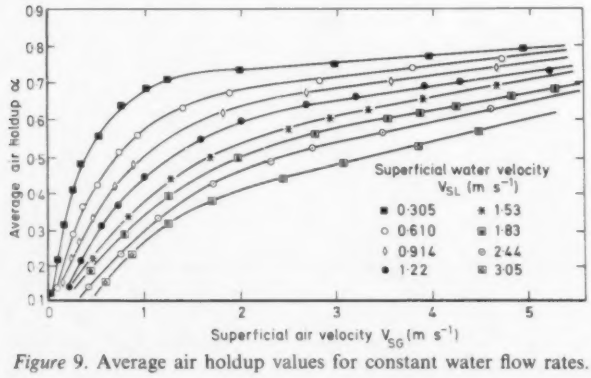


Figure 9. Average air holdup values for constant water flow rates.

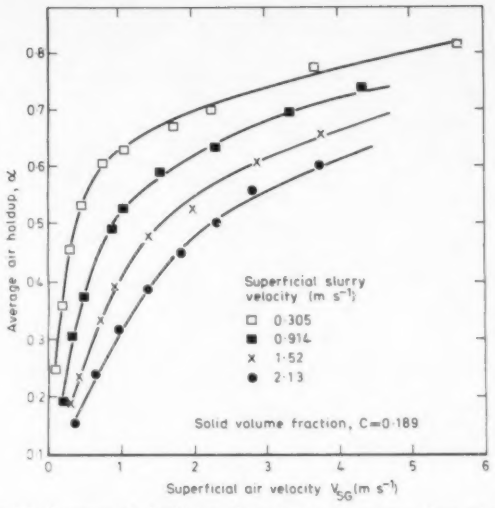


Figure 10. Average air-holdup values for the cocurrent flow of air and flocculated kaolin suspension.

The inherent inaccuracies of the method and the selection of scanning time have been discussed elsewhere[8].

For a given liquid (water or slurry), the experimentally measured values of air holdup (void fraction) were generally found to become greater as the air flow rate was increased and as the liquid flow rate was decreased. (See Figure 9 which refers to water, Figure 10 which refers to slurry of solid volume fraction 0.189 and Figure 11 which refers to slurry of solid volume fraction 0.231). For slurries of solid volume fractions up to 0.189, the average air holdup has been found to be largely independent of slurry concentration, and hence of slurry rheology, particularly under turbulent conditions. However, at higher solid volume fractions, the properties of the slurry appear to play an important role in influencing the flow pattern and thus the holdup values. Figure 12 shows results for slurries of a range of concentrations from 0 to 0.231, all at a constant superficial liquid velocity of 0.305 m s^{-1}. At the two highest slurry concentrations, the air holdup is markedly lower; the rather different behaviour of the slurries of high concentration is discussed later.

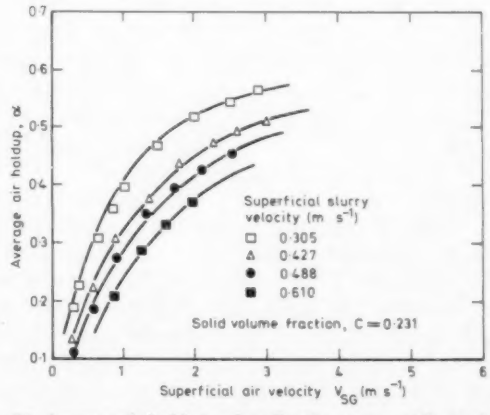


Figure 11. Average air holdup values for the cocurrent flow of air and flocculated kaolin suspensions.

VOL. 62 1984

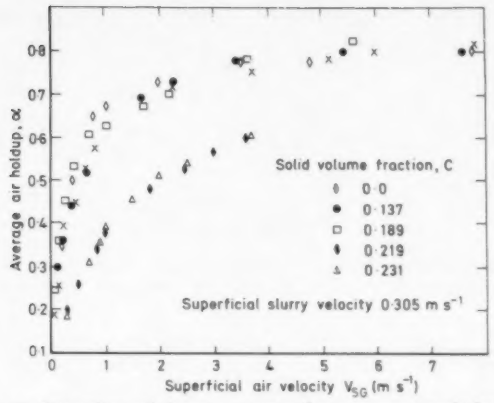


Figure 12. The effect of slurry concentration on average air holdup.

(ii) Jones and Zuber Model

The superficial velocities of the liquid and gas, V_{SL} and V_{SG} respectively are defined as being equal to the volumetric rates of flow of the phases in question per unit cross-sectional area of the pipe. The superficial mixture velocity V_m, is then taken to be equal to $V_{SL} + V_{SG}$. If there were no relative velocity between the phases V_m would then be equal to the mean linear velocity of each of the two phases; it is therefore referred to as the 'no-slip' velocity. The average linear velocity of a phase is equal to its superficial velocity divided by its holdup, and thus the average value of the slip velocity is given by

$$V_{SP} = V_G - V_L = \frac{V_{SG}}{\alpha} - \frac{V_{SL}}{1-\alpha} \tag{14}$$

where α and $1-\alpha$ are the average holdup values for gas and liquid respectively.

Jones and Zuber[10] have suggested that, as a first approximation, V_G might be expected to be a linear function of the no-slip velocity V_m, i.e.

$$V_G = C_o V_m + V_o \tag{15}$$

In this expression V_o is the rise velocity of a gas slug in a stationary liquid in a tube of the same diameter and C_o is a factor which allows for the distribution of liquid velocity over the cross-section of the pipe; the bubble rise velocity is determined more by conditions at the centre line of the slug than by the average velocity. Thus values of C_o would be expected to approximate to the ratio of the centre line to the average velocity over the cross-section. On this basis:

For laminar flow (Newtonian flow behaviour of liquid)

$$C_o \approx 2$$

For laminar flow (Power flow behaviour of liquid)

$$C_o \approx \frac{1+3n}{1+n}$$

For turbulent flow (Rheological properties not critical)

$$C_o \approx 1.2$$

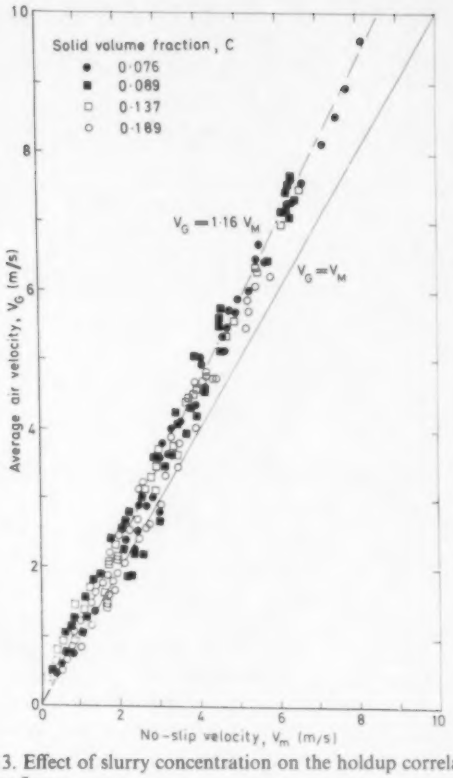


Figure 13. Effect of slurry concentration on the holdup correlation for turbulent flow.

From Davis and Taylor's work[3], for a spherical capped bubble in an inviscid liquid

$$V_o = 0.35\sqrt{(gD)} \tag{16}$$

In Figure 13 air velocity, V_G, is plotted against no-slip velocity V_m for slurries of concentrations up to 0.189 under turbulent conditions; i.e. when the slug Reynolds No. $V_{sl}^{2-n} D^n \rho_{sl}/\gamma > 2000$. It should be noted that for slurry transport $\beta_{sl} \rightarrow 1$ and has therefore been omitted. For these materials, the constant C_o was equal to about 1.16, which is close to the predicted value of 1.2. However, for slug Reynolds numbers less than 2000, C_o is seen from Figure 14 to be dependent on slurry concentration; C_o ranges from 1.18 to 1.39.

The value of the slug rising velocity V_o as calculated from equation (16) is 0.21 m s^{-1}. However, in both Figures 13 and 14, the experimental data are better correlated by lines through the origin than by lines with intercepts of 0.21 m s^{-1}.

(iii) Lockhart–Martinelli Correlation

Holdup data may also be expressed in the form used by Lockhart and Martinelli[12] and modified by Farooqi and Richardson[15] for the co-current flow of air and shear thinning liquids in horizontal pipes.

In Figure 15 average liquid holdup obtained for the flow of a kaolin suspension ($C = 0.137$) is plotted against Lockhart–Martinelli parameter

$$\chi = \left[\left(-\frac{\Delta P_f}{L}\right)_L \Big/ \left(-\frac{\Delta P_f}{L}\right)_G\right]^{1/2} \tag{17}$$

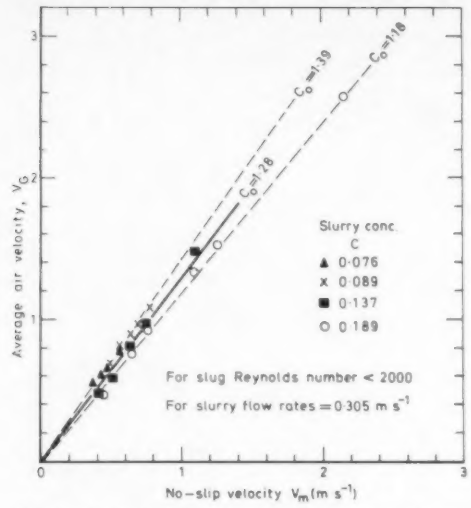


Figure 14. No slip velocity as function of average air velocity for laminar flow conditions.

where $[-(\Delta P_f/L)]_L$, $[-(\Delta P_f/L)]_G$ are respectively the pressure gradients for the liquid and the gas when flowing alone at the same rates. It will be noted that holdup is dependent on liquid flow rate, but that the dependence becomes progressively less marked as liquid flow rate increases and turbulent conditions are approached.

The experimental results for all the systems were then separated according to whether the liquid was in laminar or turbulent flow before air injection. Figure 16 shows that the data for turbulent flow of water and three of the kaolin suspensions ($C = 0.076$, $C = 0.089$, $C = 0.137$) all fall on the same curve and that neither liquid flow rate nor liquid properties has any significant influence.

For laminar flow, the modified parameter χ', introduced by Farooqi and Richardson[5] and defined as

$$\chi' = \chi \left(\frac{V_{sl}}{(V_{sl})_c} \right)^{1-n} \tag{17a}$$

was used in place of χ. Here, V_{sl} is the superficial velocity of the slurry and $(V_{sl})_c$ is the value of V_{sl} corresponding to a Metzner and Reed Reynolds number of 2000, the transition point between laminar and turbulent flow.

For one particular kaolin suspension ($C = 0.137$), liquid holdup is plotted against χ for turbulent flow ($V_{sl} > 1.52$ m s^{-1}) and χ' for laminar flow ($V_{sl} < 0.91$ m s^{-1}) in Figure 17, and the data can be represented by a single curve with an error not exceeding

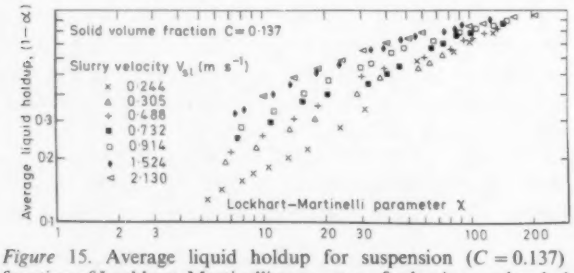


Figure 15. Average liquid holdup for suspension ($C = 0.137$) as function of Lockhart–Martinelli parameter χ for laminar and turbulent conditions.

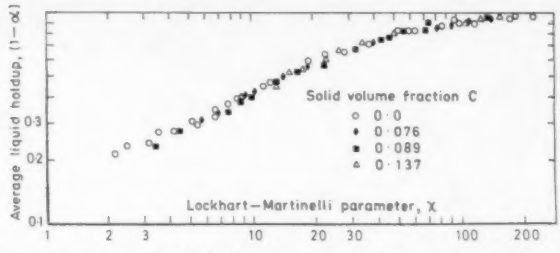


Figure 16. Average liquid holdup for water and suspensions as function of Lockhart–Martinelli parameter χ for turbulent conditions only.

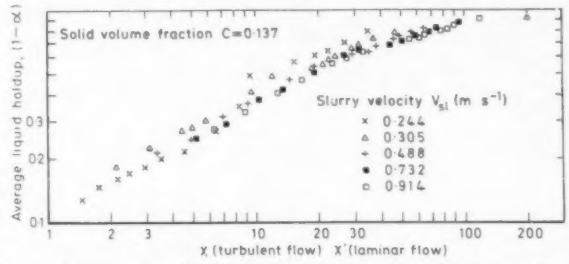


Figure 17. Average liquid holdup for suspension ($C = 0.137$) as function of modified parameter χ' for laminar flow and χ for turbulent flow.

$\pm 20\%$. In Figure 18 the data for laminar flow of kaolin suspensions ($C = 0.089$–0.231) are compared with the correlations given by Farooqi and Richardson[5] [F–R] for flow in a horizontal pipe of 38 mm diameter and that of Lockhart–Martinelli[12] [L–M].

For suspensions of concentrations C up to 0.189, Farooqi's correlation for horizontal flow is moderately satisfactory though it underpredicts liquid holdup for χ' values between about 0.2 and 0.5. For very low values of χ', slug flow is no longer encountered and the correlation is unsuccessful.

As previously mentioned, suspensions of high kaolin concentrations ($C = 0.219$ and 0.231) exhibit anomalous behaviour presumably because of major differences in flow pattern.

TWO-PHASE PRESSURE DROP

The total pressure gradient was first examined as a function of the flow rates of the two phases and subsequently an estimate was made of the various components for slug flow.

For the cocurrent flow of air with any of the liquids studied (water and flocculated suspensions of kaolin of several concentrations), the total pressure drop was observed to decrease upon injection of air. In Figures

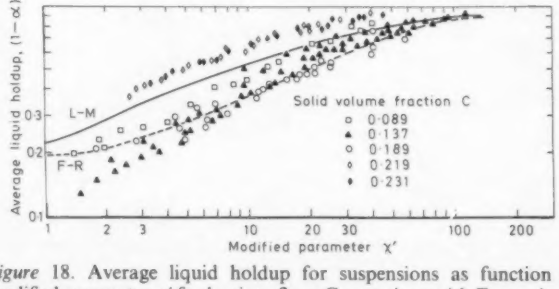


Figure 18. Average liquid holdup for suspensions as function of modified parameter χ' for laminar flow. Comparison with Farooqi and Richardson and with Lockhart and Martinelli.

VOL. 62 1984

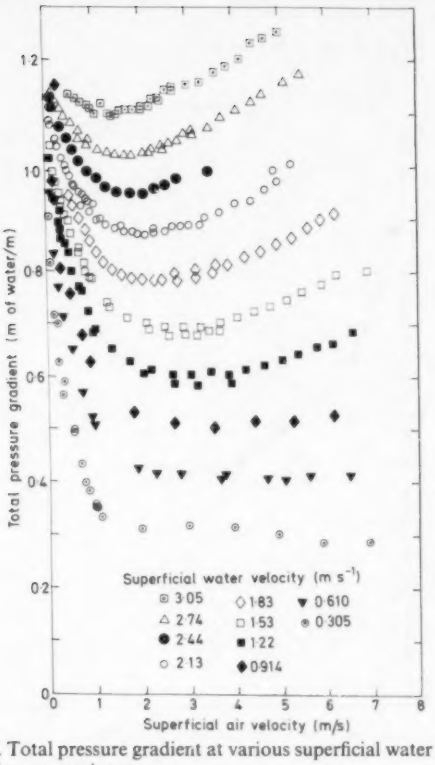


Figure 19. Total pressure gradient at various superficial water velocities for the air–water mixtures.

19–23, ($C = 0.00, 0.089, 0.137, 0.189, 0.231$ respectively), pressure drop is plotted against superficial air velocity with superficial liquid velocity as parameter. This reduction is attributable mainly to the reduced hydrostatic pressure arising from the smaller holdup of the liquid. As

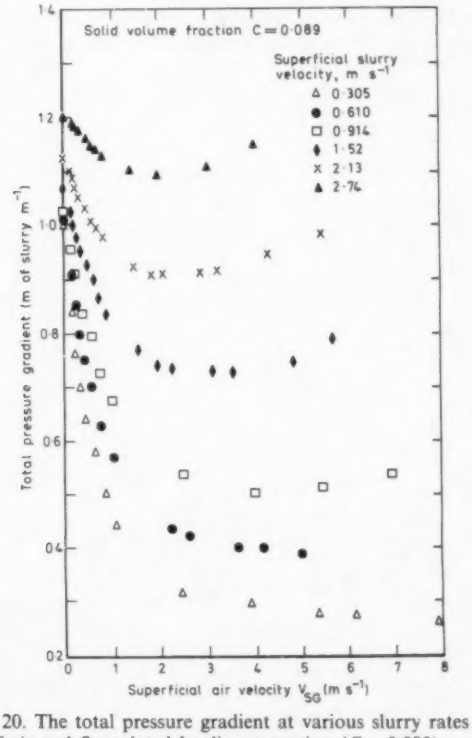


Figure 20. The total pressure gradient at various slurry rates for the flow of air and flocculated kaolin suspension ($C = 0.089$).

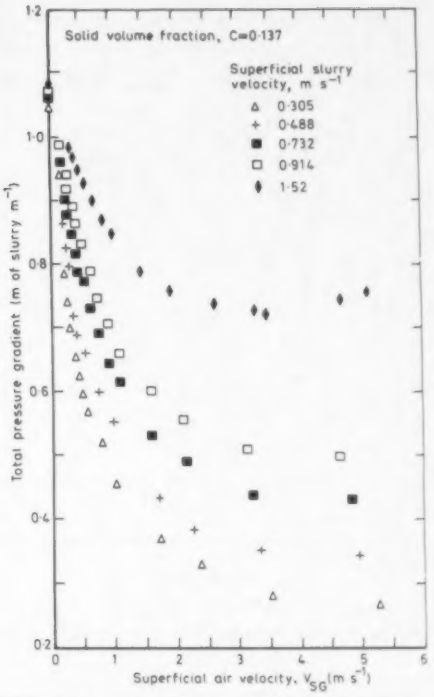


Figure 21. Total pressure gradient at various slurry rates for the flow of air and flocculated kaolin suspension ($C = 0.137$).

the flow rate of air is progressively raised, the frictional pressure drop increases and the total pressure gradient passes through a minimum and then increases again. For water and for kaolin suspensions of concentrations up to 0.189, the minimum pressure gradient always occurs at a mixture velocity of between about 4 and 5 m s^{-1}. However, for the two highest concentrations ($C = 0.219$ and 0.231), the minimum always occurred at mixture (or no-slip velocity) of about 2–2.5 m s^{-1}; thus quite different results were obtained for both holdup and pressure gradient with these highly concentrated sus-

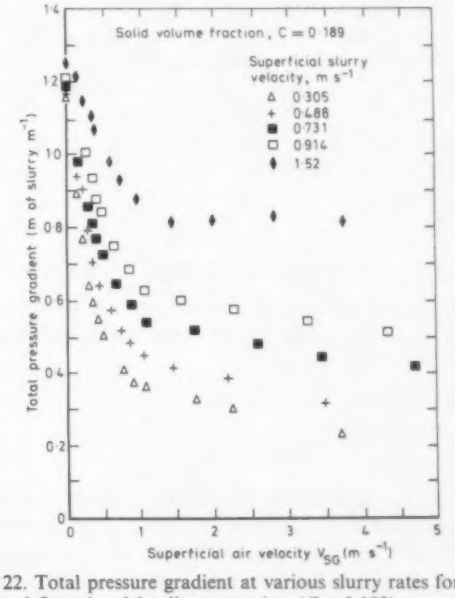


Figure 22. Total pressure gradient at various slurry rates for the flow of air and flocculated kaolin suspension ($C = 0.189$).

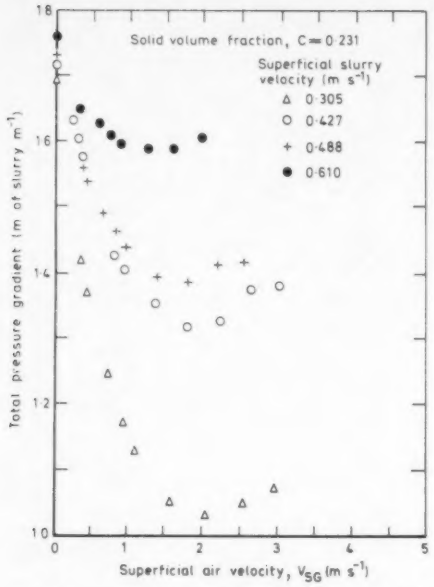


Figure 23. Total pressure gradient at various slurry rates for the flow of air and flocculated kaolin suspension ($C = 0.231$).

pensions. For laminar flow of shear thinning suspensions in horizontal pipelines[5], the minimum pressure gradient for a given liquid also occurs at a constant mixture velocity. In this case it corresponds to a slug Reynolds number Re_{MR} of about 2000; in vertical flow the minimum occurs at values of Re_{MR} ranging from 100–10,000.

Values of the drag ratio (pressure drop multiplier), ϕ_T^2, defined as the ratio of total pressure gradient, $-\Delta P_m/L)_{TP}$ for two-phase slurry flow to that for slurry alone flowing at the same rate, were compared with those recently published by Heywood and Charles[7]; see Figure 24.

For given superficial slurry and air velocities, it was observed that for each of the lower slurry concentrations ($C = 0.0$, 0.076, 0.089, 0.137, 0.189) there was no significant change in the total pressure gradient as the concentration was varied. For example, Figure 25 gives results obtained at a constant superficial liquid velocity of $0.305\ m\ s^{-1}$. However, for the slurries of higher concentration ($C = 0.219$ and 0.231), the total pressure gradient at that same flow rate was up to three times greater; this unusual behaviour has been commented upon earlier.

FRICTIONAL PRESSURE DROP

As indicated earlier, the total pressure drop may be considered to be made up of three components, attributable respectively to:

(*a*) Gravity (hydrostatic)
(*b*) Fluid friction
(*c*) Acceleration effects

Because the accelerational effects are largely inseparable from those due to friction, even though it is theoretically possible to account for the energy required to accelerate the liquid in the film, it is convenient to lump components (*b*) and (*c*) together as the effective frictional loss. This combined term is calculated by subtracting the hydrostatic component from the total pressure drop.

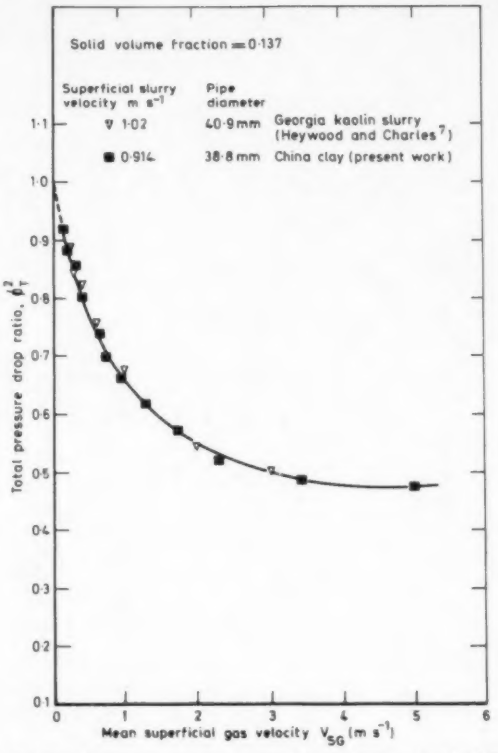


Figure 24. Total pressure drop ratio for the cocurrent vertical flow of air and kaolin slurries.

There are two ways of calculating the hydrostatic pressure gradient. The first is to regard the whole of the liquid in the vertical section of pipeline as making a contribution. Then, if the measured value of the average

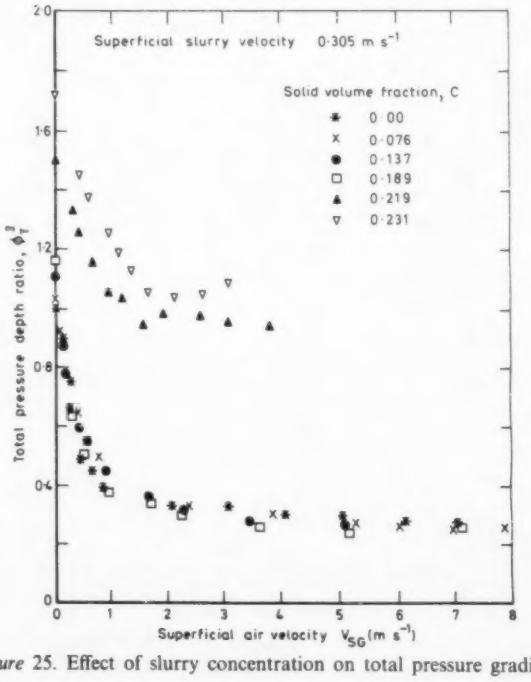


Figure 25. Effect of slurry concentration on total pressure gradient.

VOL. 62 1984

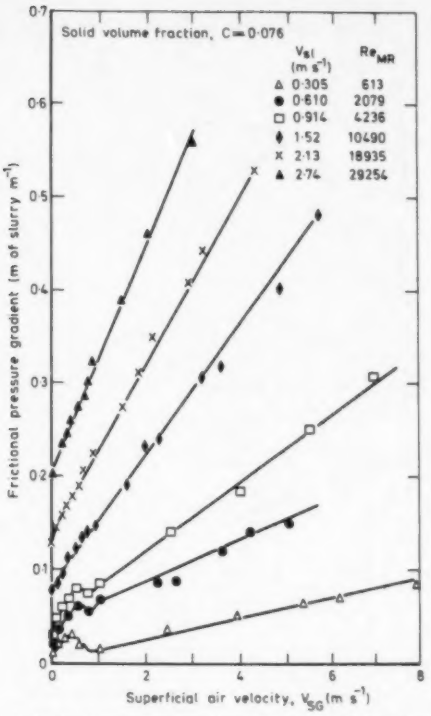


Figure 26. Frictional pressure gradient for air and flocculated kaolin suspensions at various superficial slurry velocities.

liquid holdup is β;

$$\left(-\frac{\Delta P}{L}\right)_{Gr} = \beta \rho_L g \tag{18}$$

In Figure 26 frictional pressure gradient, calculated in this way and expressed as m slurry/m pipeline, is plotted against superficial air velocity with liquid velocity (or Metzner and Reed's Reynolds number Re_{MR}) as a parameter for the flow of a kaolin suspension ($C = 0.076$). Graphs for $C = 0.137$, $C = 0.189$ and $C = 0.231$ are shown in Figures 27, 28 and 29 respectively. Similar results were obtained for concentrations of 0.089 and 0.219. The curves show the following general characteristics:

(*a*) For high values of Re_{MR}, corresponding to very

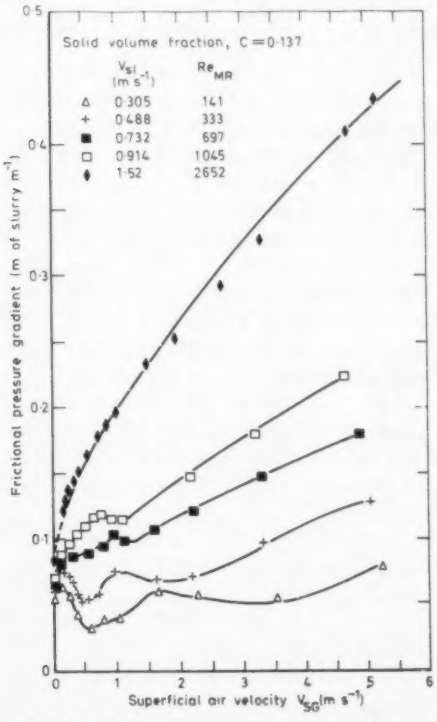


Figure 27. Frictional pressure gradient for air and flocculated kaolin suspensions at various superficial slurry velocities ($C = 0.137$).

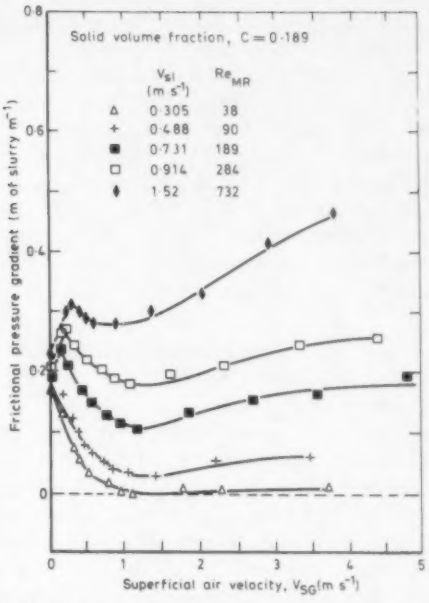


Figure 28. Frictional pressure gradient for air and flocculated kaolin suspensions at various superficial slurry velocities ($C = 0.189$).

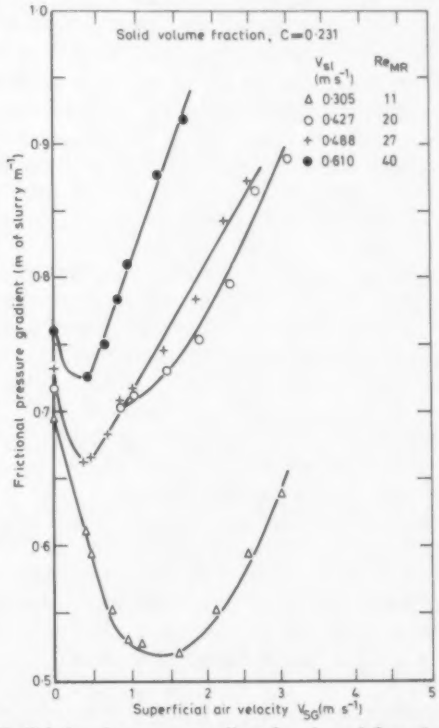


Figure 29. Frictional pressure gradient for air and flocculated kaolin suspensions at various superficial slurry velocities ($C = 0.231$).

turbulent flow, frictional pressure gradient increases rapidly with air flow rate.

(*b*) For intermediate values of Re_{MR} ($100 < Re_{MR} < 1000$), as the air rate is increased, the frictional pressure gradient initially passes through a maximum, then falls again to a minimum and finally shows a steady rise.

(*c*) For low values of Re_{MR} ($Re_{MR} < 100$), the initial rise does not occur. The frictional pressure drop falls to a minimum and then slowly rises as air rate is increased.

It will be noted that in some cases, the frictional pressure drop falls to about zero. This indicates that the hydrostatic pressure gradient calculated in this way can equal and even exceed the total pressure gradient. This phenomenon, which has been reported previously[14,16] is attributable to the fact that in slug flow the liquid which is present as a film surrounding the gas slugs will not, in general, be contributing to the hydrostatic component because its weight is supported by the shear force of the wall of the tube as it runs down the surface.

It was difficult to determine the conditions for the minimum in the frictional pressure drop at any combination of air and slurry flow rates because its value was obtained from the difference of two quantities, each of which is subject to experimental error. However, for any slurry concentration, the air flow rates required to achieve the minimum were usually in the range of 0.7–1.5 m s^{-1}.

The initial increase in the frictional pressure gradient (for example, as shown in Figure 27) was in the bubble flow regime and may be attributed to energy losses due to air–liquid interaction. In this region, the bubbles can give rise to considerable circulation of the liquid. Similar results were observed for horizontal flow by Oliver and Young Hoon[15] and Mahalingam and Valle[13]. In the slug flow regime, however, the liquid film surrounding each of the gas slugs is supported by the forces due to shear stresses at the wall and at the gas–liquid interface. Therefore, if the interfacial shear stresses are negligible, the pressure gradient over the gas slugs may be disregarded. Thus the total measured pressure gradient will result from the hydrostatic and frictional effects of the liquid slugs. However, the rapid increase of the frictional pressure gradient occurring at the onset of the churn flow regime arises from the higher degree of interaction then occurring between the two phases, as air impinges on the surface of the liquid film, giving rise to surface waves and bubble entrainment. Because these surface waves present a rough surface to the passage of air, there is considerable energy dissipation as rapid liquid circulation and drop entrainment occur.

By using the instantaneous values of holdup for slug flow and expressing them as probability density functions, it is possible to identify the proportion of the liquid attributable to holdup in the film and the slug, as detailed in the Appendix. The hydrostatic pressure gradient attributable to the liquid slugs is then given by equation (1).

Frictiona! pressure gradients have been calculated on this basis and plotted in Figure 30 for two slurries ($C = 0.137$ and $C = 0.189$). The results are inconclusive since there are considerable errors in subtracting two nearly equal pressure gradients, each of which is subject to a large experimental error.

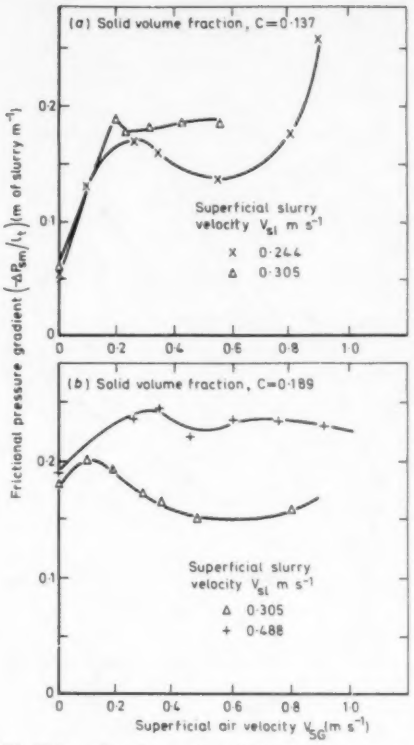


Figure 30. Values for the predicted frictional pressure gradients.

APPLICATION OF THE SLUG FLOW MODEL

From a knowledge of slug and film holdup, average holdup, slug frequency and slug length, the total predicted pressure gradient was calculated from equation (7). For both air–water and air–slurry mixtures, the calculated values of total pressure drop were up to 20% lower than the measured values. Typical data are included in Tables 2 and 3 for the slurries of concentrations $C = 0.137$ and 0.189. The discrepancy is no greater than would normally be expected in measurements of two-phase flow. Thus the total pressure gradient may be predicted well when the flow pattern does not deviate greatly from that assumed in the slug flow model; the principal assumptions in that model are that the film is neither accelerating nor decelerating ($V_f = \text{const}$), that the pressure gradient across the gas-slug is negligible, and that there are no bubbles entrained in the liquid slug.

The friction factor, f_m, for the flow of the liquid slug has been taken as equal to that for a liquid flowing alone at the same Reynolds number, even though the flow pattern of the liquid in the slug differs considerably from that of a simple fluid.

It is possible to evaluate a modified friction factor f_m^*, for the frictional pressure gradient along the liquid slug $(-\Delta P_{sm}/l_t)^*$ obtained by subtracting the hydrostatic component from the total measured two-phase pressure

VOL. 62 1984

Table 2. Typical data for the cocurrent flow of air and flocculated kaolin suspension in a vertical pipe.
$C = 0.137$; $n = 0.178$; $K = 2.67\ \mathrm{N\,s^n\,m^{-2}}$

Run	V_{SL} ($m\,s^{-1}$) (1)	V_{SG} ($m\,s^{-1}$) (2)	β (3)	β_s (4)	β_f (5)	υ_s (s^{-1}) (6)	δ (m) (7)	V_t ($m\,s^{-1}$) (8)	V_f ($m\,s^{-1}$) (9)	V_m ($m\,s^{-1}$) (10)	Re_{MR} (11)	$\left(-\frac{\Delta P_s}{l_t}\right)_{Gr}$ (12)	$\left(-\frac{\Delta P_s}{l_t}\right)_{Fs}$ (13)	$\left(-\frac{\Delta P_s}{l_t}\right)_{Acc}$ (14)	$\left(-\frac{\Delta P_s}{l_t}\right)_{TP}$ (15)	$\left(-\frac{\Delta P}{L}\right)_{TP}$ (16)	f_m (17)	f_m^* (18)
D1	0.244	0.104	0.799	0.949	0.471	1.29	0.0053	0.669	0.014	0.348	181	7833	464	275	8548	9431	0.088	0.265
D2	0.244	0.262	0.644	0.830	0.401	0.78	0.0044	0.875	0.045	0.506	358	5650	339	222	6211	7748	0.045	0.247
D3	0.244	0.347	0.617	0.810	0.390	0.78	0.0042	0.986	0.026	0.591	476	5261	325	236	5822	7232	0.034	0.180
D4	0.244	0.804	0.495	0.660	0.341	1.20	0.0036	1.58	0.014	1.05	1351	3841	263	512	4617	5923	0.012	0.070
D5	0.244	0.902	0.346	0.486	0.240	1.70	0.0025	1.71	0.635	1.15	1590	2516	175	1221	3912	5610	0.010	0.108
E1	0.305	0.194	0.668	1.0	0.251	1.14	0.0026	0.866	0.596	0.499	349	6691	401	648	7739	8911	0.046	0.181
E2	0.305	0.224	0.640	1.0	0.245	1.17	0.0025	0.905	0.629	0.529	360	6287	381	690	7357	8409	0.041	0.155
E3	0.305	0.325	0.601	0.981	0.245	0.95	0.0025	1.04	0.622	0.630	534	5704	353	571	6632	7884	0.030	0.135
E4	0.305	0.385	0.578	0.980	0.245	0.85	0.0025	1.11	0.618	0.690	631	5336	339	519	6193	7521	0.025	0.125
E5	0.305	0.433	0.557	0.990	0.251	0.90	0.0026	1.18	0.579	0.738	713	4936	317	652	5794	7188	0.022	0.121
E6	0.305	0.544	0.534	0.981	0.250	1.05	0.0026	1.32	0.569	0.849	920	4582	302	652	5535	6837	0.017	0.092
F1	0.488	0.191	0.753	1.0	0.265	1.42	0.0028	1.10	0.489	0.679	613	7979	505	778	9262	9916	0.026	0.060
F2	0.488	0.217	0.727	1.0	0.256	1.42	0.0027	1.13	0.542	0.705	656	7608	485	821	8913	9546	0.024	0.056
F3	0.488	0.313	0.664	1.0	0.262	1.30	0.0027	1.26	0.489	0.801	828	6546	427	748	7720	8634	0.019	0.061
F4	0.488	0.371	0.631	1.0	0.262	1.32	0.0027	1.33	0.481	0.859	940	6009	396	772	7177	8276	0.017	0.064
F5	0.488	0.418	0.604	1.0	0.267	1.25	0.0028	1.40	0.439	0.906	1036	5525	368	723	6616	7895	0.015	0.069

Column No.
1 Superficial slurry velocity.
2 Superficial air velocity.
3 Average slurry holdup.
4 Average slug holdup.
5 Average film holdup.
6 Average slug frequency.
7 Film thickness obtained from Appendix.
8 Rising velocity of the bubble obtained from Appendix.
9 Film velocity obtained from Appendix.
10 Mixture velocity = column 1 + column 2.
11 Slug Reynolds number obtained using equation (4).
12 Hydrostatic pressure gradient due to the liquid slug obtained using equation (1).
13 The frictional pressure gradient due to the liquid slug obtained using equation (3).
14 The accelerational pressure gradient in slug flow obtained using equation (4).
15 The total predicted pressure gradient across liquid slugs = columns (12 + 13 + 14).
16 The total experimentally measured gradient.
17 Fanning friction factor obtained using equation (6).
18 Fanning friction factor obtained using equation (19).

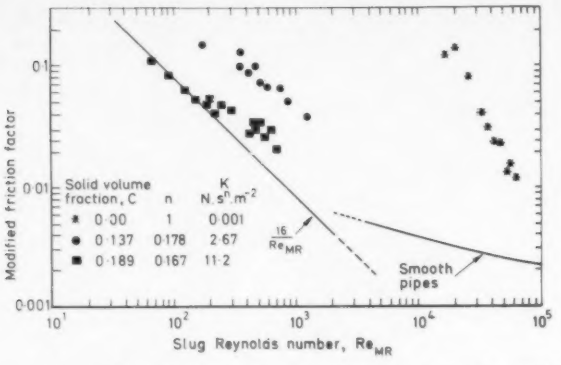


Figure 31. Modified friction factor as predicted by slug flow model.

gradient. Then f_m^* will be given by

$$\left(-\frac{\Delta P_{sm}}{l_t}\right)^* = \frac{2f_m^* V_m^2}{D}\beta_s \rho_{sl}\frac{l_s}{l_t} \tag{19}$$

The values of f_m^* are plotted in Figure 31 as a function of the slug Reynolds number, Re_{MR} for the air–slurry mixtures of the various kaolin concentrations ($C = 0.00$, $C = 0.137$, $C = 0.189$). The results show that the friction factor is a function both of slurry concentration and of slug Reynolds number which is in turn a function of air rate. At high slurry concentrations and low air rates (approaching ideal slug flow pattern), the pressure gradient along the liquid slugs may be calculated in the same way as for a single phase fluid. However, as both the slurry concentration decreases and the air rate increases (churn flow prevails), there is an increased dissipation of energy caused by the circulation currents induced by the dispersed small bubbles in the liquid slug. Thus the effect of the bubbles on the friction factor may be regarded as qualitatively similar to that of the surface irregularities in rough pipes.

CONCLUSIONS

Measurements of two-phase pressure drop and average slurry holdup were obtained for air–water and air–slurry flow under both turbulent and laminar conditions.

The total pressure drop for any system was found to decrease sharply as the superficial air velocity was increased to reach a minimum and then to increase again. In all cases, air holdup increased monotonically as the air flow rate was increased at constant liquid rate.

Average liquid holdup was correlated in terms of modified Lockhart–Martinelli parameters. A model has been proposed from which total pressure drop during slug flow of two-phase mixtures may be calculated. Instantaneous measurements of void fractions have been used so as to distinguish between the liquid holdup in the liquid slug and in the film surrounding the gas slug.

In both models, agreement (generally within 20%) between the predictions of either model and the experimental results was considered satisfactory in view of the assumptions made and of the accuracy with which measurement can be made in two-phase flow.

APPENDIX

Measurement of Slug and Film Holdup

For each combination of input air and water fluxes, the midpoint of the test section was scanned repeatedly for 0.1 s periods during a total time scan of 120 s. The test section was also scanned when the pipe was full of water (slurry) and when it was empty. The corresponding void fraction for each count was calculated according to equation (13), using the mean of the water (slurry) counts to be equivalent to zero void fraction and the mean of the air counts to be equivalent to a voidage of unity.

A probability density function (PDF)[1,10] of each trace was evaluated, and a histogram of the values of the void fraction was constructed for each operating condition of input air and water (slurry) flow rates. A smoothing of the PDF histogram was effected by using a smooth continuous histospline function which transformed the histogram into a density curve[8]. Since the system noise was found to be Gaussian, the two maxima in the histospline PDF (see Figure 32) correspond to the most probable values of the slug and film holdup.

Calculation of Slug Flow Parameters

(a) Film Velocity, V_f, and Gas Slug Velocity.

By consideration of overall continuity over the slug unit (liquid plus gas slug) and by assuming that both

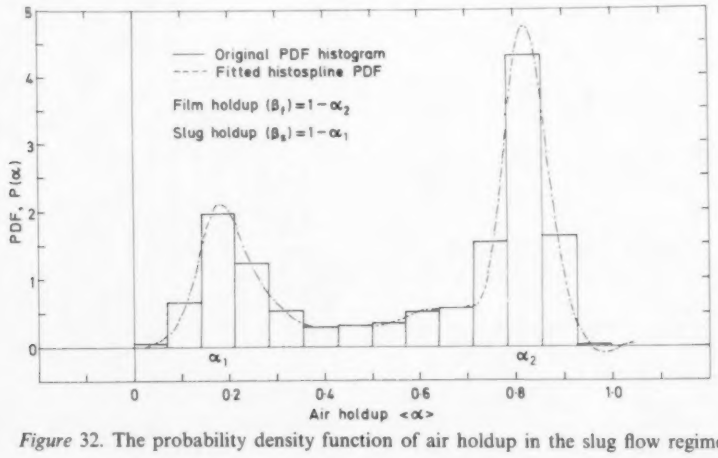


Figure 32. The probability density function of air holdup in the slug flow regime.

VOL. 62 1984

fluids are incompressible, the following relation is obtained between the gas slug velocity, V_t, film velocity, V_f, and the liquid slug velocity, V_m; all taken as positive vertically upwards.

$$V_m A = V_t A_t + V_f A_f \tag{A1}$$

This equation applies provided that the liquid slug contains no entrained bubbles ($\beta_s = 1$). If β_s is significantly less than 1, equation (A1) becomes:

$$V_m A \beta_s = V_t(\beta_s A - A_f) + V_f A_f \tag{A1a}$$

If δ is the film thickness and D is the pipe diameter, one may write:

$$A = \frac{\pi D^2}{4}, \quad A_t = \frac{\pi}{4}(D - 2\delta)^2, \quad \text{and}$$

$$A_f = \frac{\pi D^2}{4} - \frac{\pi}{4}(D - 2\delta)^2$$

Substituting in equation (A1) and rearranging for the film velocity gives

$$V_f = \left[V_t\left(1 - \frac{2\delta}{D}\right)^2 - V_m \right] \Big/ \left(\frac{4\delta}{D} - \frac{4\delta^2}{D^2}\right) \tag{A2}$$

where

$$V_m = V_{SG} + V_{SL} \tag{A3}$$

and as given by Nicklin et al[14]

$$V_t = C_1 V_m + V_o \tag{A4}$$

(b) Film Thickness in Terms of Film Holdup

If it is assumed that there is no gas entrainment in the film, the film thickness δ may be obtained from the film holdup β_f. The film holdup is expressed as

$$\beta_f = \frac{\pi R^2 - \pi(r - \delta)^2}{\pi R^2} \tag{A5}$$

Rearranging for the film thickness, δ, gives:

$$\delta = R[1 - \sqrt{(1 - \beta_f)}]$$

(c) The Slug Length Ratio, l_s/l_t

A mass balance over a length of pipe L, $= Nl_t$ containing N liquid slugs and N gas slugs yields:

$$Nl_t\beta = N\rho_f l_b + N\beta_s l_s \tag{A7}$$

where

β is the average liquid holdup
l_t is the length of a slug unit $= l_s + l_b = L/N$

Rearranging eq. (A7) gives

$$\frac{l_s}{l_t} = \frac{\beta - \beta_f}{\beta_s - \beta_f} \tag{A8}$$

(d) The Length of the Slug, l_s

Assume that the volume of the small bubbles within the liquid slug is negligible and consider a plane normal to the flow at some position downstream when fully developed slug flow exists. The time taken for the liquid slug to pass, T_s, is l_s/V_t and the time taken for the bubble to pass, T_b, is l_b/V_t. Then the time for the slug unit to pass the reference plane is

$$T_t = \frac{l_s + l_b}{V_t} = \frac{1}{v_s} \tag{A9}$$

where v_s is the average slug frequency obtained from the conductivity probe measurement. Rearranging equation (A9) for the average slug length and substituting the values of l_b and V_t gives

$$l_s = \frac{C_1 V_m + V_o}{v_s}\left(\frac{\beta - \beta_f}{\beta_s - \beta_f}\right) \tag{A10}$$

The above analysis applies to any two-phase system in slug flow and may, therefore, be used in connection with the flow of air and slurries. However, the velocity profile in a fluid showing non-Newtonian behaviour will, in general, be different and therefore constants such as C_1 will be expected to have different values as discussed in the paper.

(e) Acceleration contribution

A slug that has stabilised in length can be considered as receiving and losing mass at equal rates. The velocity of the liquid in the film just before pickup V_f is lower than that in the slug V_m and a force is therefore necessary to accelerate this liquid to the liquid slug velocity.

Dukler and Hubbard[4] have given the pressure drop, $(-\Delta P_s)_{Acc}$, attributable to this force as:

$$(-\Delta P_s)_{Acc} = (Y/A)(V_m - V_f) \tag{A11}$$

where Y is the mass rate at which the liquid slug picks up liquid from the film ahead of it.

The mass rate of pickup is

$$Y = \rho_L A \beta_f (V_t - V_f) \tag{A12}$$

where β_f = average film holdup. V_t is greater than V_m because of the additional velocity attributable to the extra mass of liquid picked up by the liquid slug as it overtakes the film. The relation between V_t, V_f and V_m is given by (A1) and (A1a).

Substituting (A12) into (A11) one may express the accelerational pressure drop per unit slug length, l_s, by

$$\left(-\frac{\Delta P_s}{l_s}\right)_{Acc} = \rho_L \frac{\beta_f}{l_s}(V_t - V_f)(V_m - V_f) \tag{A13}$$

V_t, V_f and V_m are taken as positive in the upwards direction.

SYMBOLS USED

A	cross-sectional area of the pipe. (m^2)
A_f	cross-sectional area of the liquid film. (m^2)
A_t	cross-sectional area of the gas slug. (m^2)
C	solid volume fraction in the slurry. ($-$)
C_o	distribution coefficient in the drift flux model. ($-$)
C_1	coefficient which takes into account the effect of non-uniform flow including velocity profile. ($-$)
D	pipe inside diameter. (m)
f	Fanning friction factor. ($-$)
g	acceleration due to gravity. ($m\,s^{-2}$)
I	radiation intensity. (Photons $m^{-2}s^{-1}$)

K consistency index in Power Law model. ($N\,s^n\,m^{-2}$)
L length of the test section. (m)
l_b average bubble length. (m)
l_s average slug length. (m)
l_t average slug unit length ($=l_s+l_b$). (m)
N number of gas or liquid slugs. (−)
n flow behaviour index in Power Law Model. (−)
$-\Delta P$ pressure drop. ($N\,m^{-2}$)
$-\Delta P_f$ pressure drop due to friction. ($N\,m^{-2}$)
$-\Delta P_m$ pressure drop in the air–slurry mixture. ($N\,m^{-2}$)
$-\Delta P_s$ pressure drop across water slugs. ($N\,m^{-2}$)
$-\Delta P_{sm}$ pressure drop across slurry slugs. ($N\,m^{-2}$)
R pipe radius. (m)
Re_{MR} Reynolds number (Metzner and Reed equation (11)). (−)
t time. (s)
V velocity. ($m\,s^{-1}$)
V_o rising velocity of single slug in stagnant liquid. ($m\,s^{-1}$)
V_f velocity of the liquid in the film. ($m\,s^{-1}$)
V_G linear gas velocity. ($m\,s^{-1}$)
V_L linear liquid velocity. ($m\,s^{-1}$)
V_m superficial mixture (No-slip) velocity $=V_{SG}+V_{SL}$. ($m\,s^{-1}$)
V_{SG} superficial velocity of gas phase. ($m\,s^{-1}$)
V_{SL} superficial velocity of liquid phase. ($m\,s^{-1}$)
V_{SP} slip velocity. ($m\,s^{-1}$)
V_s linear velocity of a gas slug. ($m\,s^{-1}$)
V_{sl} superficial slurry velocity. ($m\,s^{-1}$)
$(V_{sl})_c$ critical value of V_{sl}. ($m\,s^{-1}$)
Y mass rate of pickup of liquid from film to slug. ($kg\,s^{-1}$)

Greek letters

α void fraction, time-averaged proportion of pipe cross-sectional area occupied by gas phase. (−)
β average liquid holdup ($=1-\alpha$) (−)
β_f average film holdup during slug flow. (−)
β_s average slug holdup during slug flow. (−)
γ parameter in equations (5) and (11). ($N\,s^n\,m^{-2}$)
$\dot{\gamma}$ shear rate. (s^{-1})
Δ finite change in variables. (−)
δ film thickness. (m)
μ viscosity. ($kg\,m^{-1}\,s^{-1}$)
ν_s slug frequency. (s^{-1})
ρ density. ($kg\,m^{-3}$)
τ_i interfacial shear stress. ($N\,m^{-2}$)
τ_w shear stress at wall. ($N\,m^{-2}$)
ϕ_T^2 Lockhart–Martinelli parameter defined as ratio two-phase pressure drop to single phase liquid pressure drop. (−)
χ parameter used in Lockhart and Martinelli correlation. (−)
χ' parameter used in Farooqi and Richardson correlation defined in equation (17a). (−)

Subscripts

Acc accelerational term
c value at laminar–turbulent transition
Fr total frictional term
Fs wall frictional term in slug flow
f film
G gas
Gr gravitational or hydrostatic term
L liquid
m mixture
s slug
sl slurry
SP single-phase
TP two-phase
t total

Superscript

* modified value of pressure difference or friction factor along slug

REFERENCES

1. Boneva, L. I., Kendall, D. G. and Lambert, J. A. *Technical Report* CC-7401 (Computer Centre, University of Newcastle, New South Wales) 1971.
2. Brown, R. A. S. and Govier, G. W., 1965, *Can J Chem Eng* 43: 224.
3. Davies, R. M. and Taylor, G. I., 1950, *Proc R Soc London*, Ser.A 200: 375.
4. Dukler, A. E. and Hubbard, M. G., 1975, *Ind Eng Chem Fundl*, 14: 337.
5. Farooqi, S. I. and Richardson, J. F., 1982, *Trans I Chem E*, 60: 292, 323.
6. Griffith, H. and Wallis, G. B., 1961, *J Heat Transfer, Trans ASME, Ser C* 83: 307.
7. Heywood, N. I. and Charles M. E., 1978, *Fifth Int Conf Hydraulic Transport of Solids in Pipes*, May 8–11.
8. Heywood, N. I. and Richardson, J. F., 1979, *Chem Eng Sci*, 34: 17.
9. Heywood, N. I. and Richardson, J. F., 1978, *J Rheology*, 22 (6): 599.
10. Jones, O. C. and Zuber, N., 1975, *Int J Multiphase Flow*, 2: 273.
11. Kemblowski, Z. and Kolodziejski, J., 1973, *Int Chem Eng*, 13 (2): 265.
12. Lockhart, R. W. and Martinelli, R. C., 1949, *Chem Eng Prog*, 45: 39.
13. Mahalingam, R. and Valle, M. A., 1972, *Ind Eng Chem Fundl*, 11 (4): 470.
14. Nicklin, D. J., Wilkes, J. O. and Davidson, J. F., 1962, *Trans I Chem E*, 40: 61.
15. Oliver, D. R. and Young Hoon, A., 1968, *Trans I Chem E*, 46: T106.
16. Richardson, J. F. and Higson, D. J., 1962, *Trans I Chem E*, 40: 169.
17. Taitel, Y., Bornea, D. and Dukler, A. E., 1980, *AIChE J*, 26: 345.
18. Taylor, G. I., 1961, *J Fluid Mech*, 10: 161.

ADDRESSES

Correspondence in connection with this paper should be addressed to Professor J. F. Richardson, Department of Chemical Engineering, University College of Swansea, Singleton Park, Swansea SA2 8PP.

The manuscript was originally received 4 October 1982, and accepted for publication after revision on 26 August 1983.

VOL. 62 1984

BIOMASS HOLD-UPS AND OVERALL RATES OF SUBSTRATE (GLUCOSE) UPTAKE OF SUPPORT PARTICLES CONTAINING A MIXED MICROBIAL CULTURE

By B. ATKINSON (FELLOW), J. D. CUNNINGHAM and A. PINCHES (COMPANION)

The biomass hold-ups and overall rates of substrate (glucose) uptake have been determined for 6 mm diameter biomass support particles (porosity 80%) in a fluidised bed recycle reactor. The experimental data have been interpreted using the biological rate equation of Atkinson and Davies (1974) which allows both diffusional limitations and the presence of biomass other than that within the support particles to be taken into account. Both the particle biomass hold-ups and the overall rates of substrate uptake were found to depend upon the substrate concentration in the reactor. The former followed an hyperbolic relationship and the latter half-order kinetics. A reduced form of the biological rate equation has been used to devise a model for the overall rate of substrate uptake by a biomass support particle and this allowed the intrinsic kinetic parameters to be estimated.

INTRODUCTION

The contribution which immobilised biomass could make to biological process engineering and the intensification of biological processes, i.e. a reduction in size while maintaining performance, has been explored[1,2]. Biomass support particles[3] provide a practical form of immobilised biomass, whereby this potential can be realised. In principle this innovation[4] allows biological particles of any size, shape, and density to be produced for a wide variety of microorganisms.

One version of biomass support particle (Figure 1) consists of a sphere made of fine stainless steel wire arranged to give a uniform porosity of 80% throughout. Microorganisms grow within the particles by 'attaching' themselves to the surface of the wire and, subsequently, largely fill the interstices. When the particles are in motion, one relative to another as in a fluidised bed, any growth which takes place beyond the particle matrix is removed by attrition. The overall result is that biological particles of predetermined size containing a constant amount (hold-up) of biomass can be maintained within a reactor which operates at steady state in perpetuity. The fluidisation characteristics of stainless steel biomass support particles, both filled and empty have been the subject of a recent publication[5].

The biomass support particle structure facilitates the immobilisation of microorganisms to a large degree independent of their flocculative or adhesive properties[3]. Presently the most serious disadvantage is associated with the physical restrictions on size, say > 2–3 mm, due to the limited range of methods of preparation available. However it is anticipated that future work aimed at alternative materials and preparative methods, will allow particles of any required size, bulk density and shape to be used.

Among the advantages of the use of biomass support particles in reactors[6] are that:

(*a*) there are virtually no physical limitations on the throughput, e.g. by wash-out of biomass;

(*b*) high biomass concentrations (>20 g (d.w.) l^{-1}) can be achieved independent of throughput and without recourse to centrifugation or sedimentation devices;

(*c*) they provide possibilities for the development of new methods of biomass recovery and subsequent concentration[7];

(*d*) they provide possibilities for the exploitation of diffusion limitations as a way of enhancing yields, controlling reaction rates[8], and for open mixed cultures, of enhancing a desired reaction, e.g. nitrification; and

(*e*) they provide a basis for improvements in process design.

The performance efficiency of any reactor containing biomass support particles[9] depends upon:

(*a*) the number of support particles per unit reactor volume;

(*b*) the average biomass hold-up per particle;

(*c*) the average overall specific rates of reaction of the immobilised biomass; and

(*d*) the average overall yield coefficients of the immobilised biomass.

The present work is largely concerned with items (*b*) and (*c*) although some consideration was given to items (*a*) and (*d*).

The overall rate of substrate uptake by immobilised biomass with a characteristic size considerably greater than that of a single organism is determined by the intrinsic kinetics of the microbial species, i.e. the dependency of the specific rate of reaction on substrate concentration, and on any diffusion limitations on the passage of substrate.

The most commonly applicable relationship describing the intrinsic kinetics of microorganisms is the Monod Equation[7]. It has been shown[10] that this equation can be used to describe the kinetics of open mixed cultures in the form of very thin films adhering to planar support surfaces. Some other equations suggested for

© Institution of Chemical Engineers

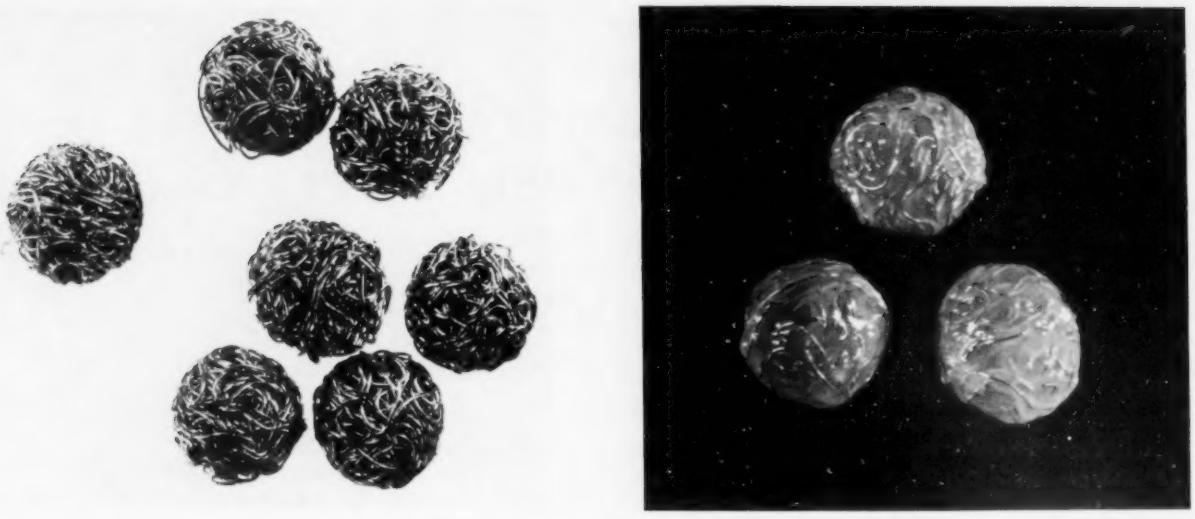


Figure 1. Biomass support particles (80% porosity; each prepared from a single strand of stainless steel wire).

use in describing intrinsic microbial kinetics have been listed[11].

The overall rates of substrate uptake by open mixed cultures immobilised within support particles such as those illustrated in Figure 1 are concerned therefore with diffusion and Monod kinetics. Atkinson and Davies[12] provided a generalised numerical solution for such problems, they expressed the results in algebraic form for convenience, and for brevity referred to the result as a biological rate equation. This equation relates the overall rate of substrate uptake to the intrinsic kinetic parameters of the reaction and to such physical parameters as the biomass size and the reactor substrate concentration. Experimental substantiation of the equation has been provided[13–15] using biological film reactors of the plain sheet and packed bed varieties in conjunction with open mixed microbial cultures. In view of this confirmation, Atkinson and Rahman[16] extended the biological rate equation for application to microbial flocs, thus providing a basis for application to spherical biomass support particles.

Given the complexity of microbial systems, their sensitivity to the presence of very low concentrations of a wide variety of chemical species and to such physicochemical factors as pH, osmotic pressure and ionic strength, it is doubtful that other than a 'bulked' parameter approach can be adopted. In these circumstances the basic assumption involves the equation used to describe the intrinsic kinetics, each separate equation leading to a separate biological rate equation.

Atkinson and Ali[15] were able to characterise the present microbe–substrate system within a reactor of known physical characteristics using the biological rate equation of Atkinson and Davies[12] and subsequently to use the same system to characterise a reactor of unknown physical characteristics, specifically interfacial area, microbial film thickness and liquid phase diffusional limitation.

Thus while the biological rate equation is unlikely to uniquely describe diffusion with microbial reaction it has proved to have application to open mixed cultures and has the particular benefit of separating the intrinsic microbial parameters from those of engineering importance, e.g. biomass size, substrate concentration and biomass density.

It follows that the biological rate equation provides a basis for:

(*a*) the development of a theory for the overall rates of reaction of biomass support particles such as those illustrated in Figure 1;

(*b*) the interpretation of experimental data obtained from reactors containing biomass support particles; and

(*c*) the development of design equations.

EXPERIMENTATION

Apparatus

Figure 2 contains a schematic representation of the apparatus used to investigate the 'reaction' properties of biomass support particles of the type shown in Figure 1. The feed entered prior to the pump and the exit stream was taken from the top of the column. The majority of the flow through the bed was recycled to ensure homogeneity of the conditions in the 'reaction' zone and to provide sufficient pressure drop to fluidise the particles irrespective of the throughput being used. The recycle flow was adjusted to provide conditions approximating to incipient fluidisation. This procedure led to constant particle/particle attrition, uniform conditions of heat and mass transfer, and resulted in a fixed area of column surface susceptible to film growth. Refrigerated fluid was used in the column jacket to maintain a constant temperature of 20°C and the system was pH-stated using sodium hydroxide solution.

The column (Figure 3) was made up from two 7.6 mm diameter QVF glass sections; the lower tube had a length of 107 mm and the upper (30 mm) tube was fitted with an exit side arm some 15 mm from the top. A stainless steel perforated plate at the bottom of the column acted as both particle support and as an aid to even distribution of liquid.

VOL. 62 1984

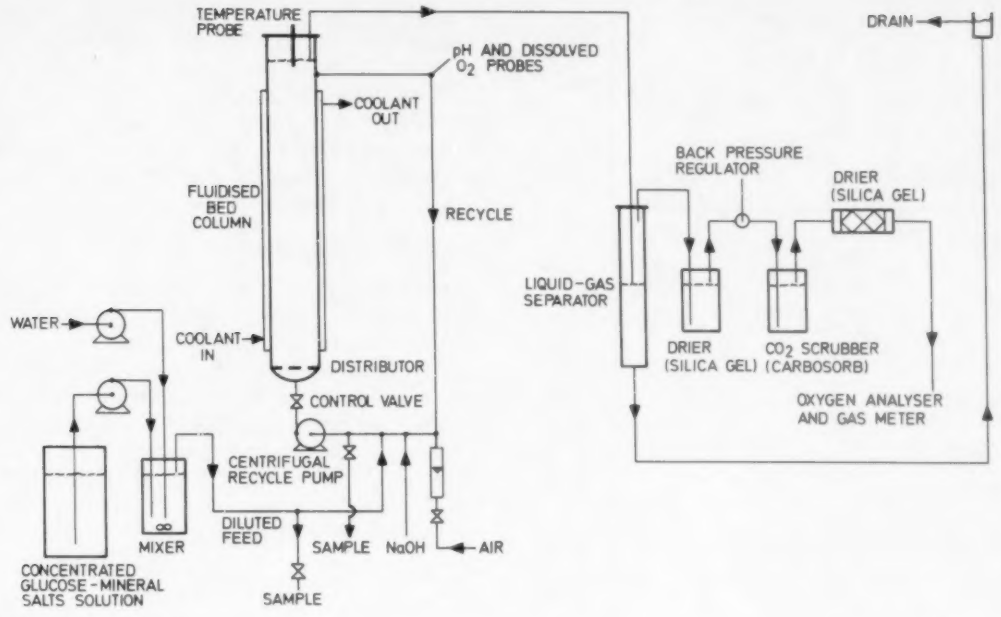


Figure 2. Experimental apparatus.

The bed contained some 16,000 × 6 mm diameter particles prepared by die-pressing fine stainless steel wire to a porosity of 80%[3]. The total biomass support volume of the particles was approximately 1500 cm^3 and their external surface area exceeded 18,000 cm^2 (equivalent sphere basis).

Procedure

The feed to the system consisted of glucose and the corresponding stoichiometric amount of nitrogen added as diammonium hydrogen orthophosphate. The trace elements etc. required for microbial growth were taken as being amply provided by the tap water and as impurities in the reagents.

The feed liquor was supplied as concentrate (100 $g\,l^{-1}$ glucose; 70 $g\,l^{-1}$ diammonium hydrogen orthophosphate) and diluted prior to entry into the reactor using a system of mix-pots and metering pumps (Figure 2). Air was introduced via a rotameter at a rate of approximately 60 $l\,h^{-1}$.

The reactor was operated on an 'open' basis resulting in the development of a mixed microbial culture and the inoculum was produced in shake-flasks using the operating medium in conjunction with washings from soil.

The effluent from the top of the column (Figure 3) consisted of a gas-liquid mixture which was fed to a further vessel (Figure 2) where separation was effected; the resultant gas was scrubbed of CO_2, dried, and fed to an oxygen analyser.

The glucose concentration in the reactor was changed by using various combinations of feed-rate and inlet concentration. Altogether three inlet concentrations were used, i.e. 0.68 $g\,l^{-1}$, 1.5 $g\,l^{-1}$, and 3–4 $g\,l^{-1}$, and each of these was taken in conjunction with a range of flow-rates. The result of this procedure was that the particles were exposed to a wide range of reactor glucose concentrations.

Steady state feed and effluent samples were analysed for glucose, TOC, COD, and suspended biomass; the exit gas was analysed for oxygen; and the support particles were assayed for biomass hold-up (Appendix).

Results

The data obtained during the experimental programme have been plotted in Figures 4, 5 and 6 for the

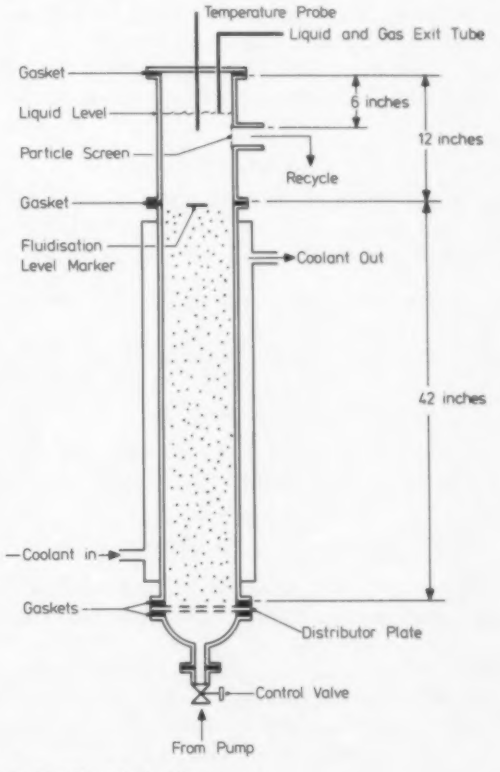


Figure 3. Fluidised bed column.

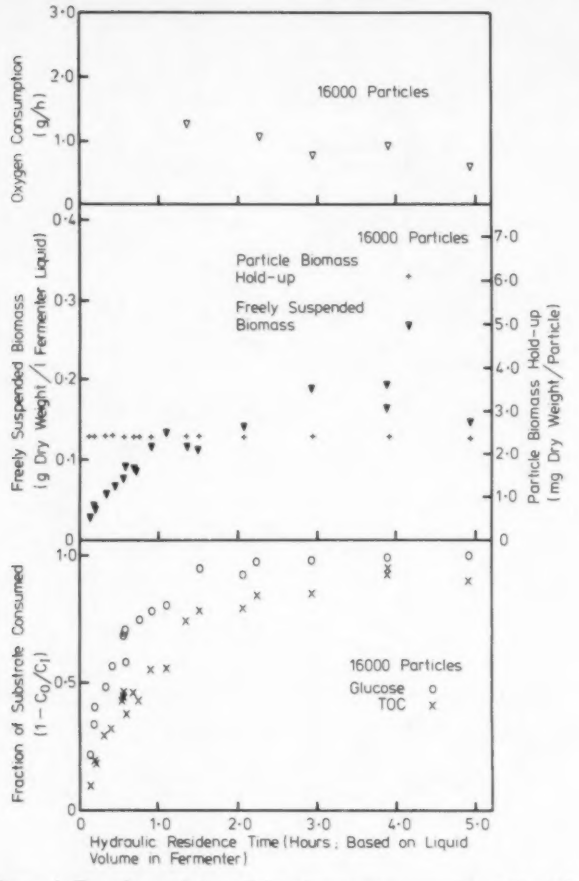


Figure 4. Experimental data (inlet glucose concentration 0.68 g l^{-1}).

three inlet concentrations used. The figures contain data on conversion efficiency (expressed as glucose, TOC and COD), freely suspended biomass, particle bound biomass and oxygen uptake rates as a function of throughput.

Carbon Mass Balance

The essential correctness of the experimental techniques and procedures was established by the determination of carbon mass balances as given by:

In glucose carbon, carbon dioxide, soluble inorganic carbon;

Out glucose carbon, carbon dioxide, soluble inorganic carbon, soluble organic carbon products, biomass carbon.

The balances achieved were in excess of 98% and typical examples are given in the Appendix.

THEORETICAL CONSIDERATIONS

The apparatus was designed and operated such that the biomass associated with the support particles made the most significant contribution to the conversion efficiency. However, Atkinson and Fowler[17] have pointed out the importance of film growth even in 'non-film' fermenters and it cannot be assumed arbitrarily that the effect of the films adhering to the pipe walls was negligible.

In general, the overall rate of substrate removal in the reactor (R_f), i.e. mass of substrate consumed per unit time, results from the combined effects of the support particles, films and suspended flocs. The latter were produced by the erosion of growing biomass from the particles and pipe-work, and by 'auto-catalytic' growth of the freely suspended flocs themselves.

It follows that:

$$R_f = R_p M_p + NA + R_s M_s \tag{1}$$

where R_p and R_s are the overall specific rates of substrate uptake by the biomass support particles and the suspended flocs respectively; N is the overall rate of substrate uptake per unit area of microbial film; M_p and M_s are respectively the total quantities of biomass present within the support particles and freely suspended; and A is the area of microbial film.

On the assumption that the intrinsic microbial kinetics are described by the Monod equation the rates of substrate uptake in equation (1) are given by:

$$\left.\begin{aligned} R_p &= \lambda_p R_{max} \frac{C_p^*}{K_m + C_p^*} \\ N &= \lambda_f N_{max} \frac{C_f^*}{K_m + C_f^*} \\ R_s &= \lambda_s R_{max} \frac{C_s^*}{K_m + C_s^*} \end{aligned}\right\} \tag{2}$$

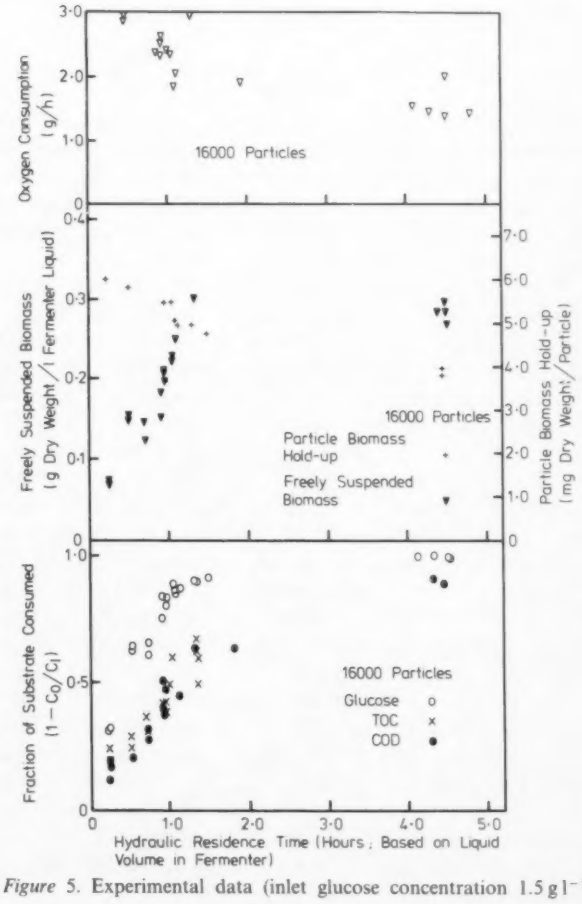


Figure 5. Experimental data (inlet glucose concentration 1.5 g l^{-1}).

VOL. 62 1984

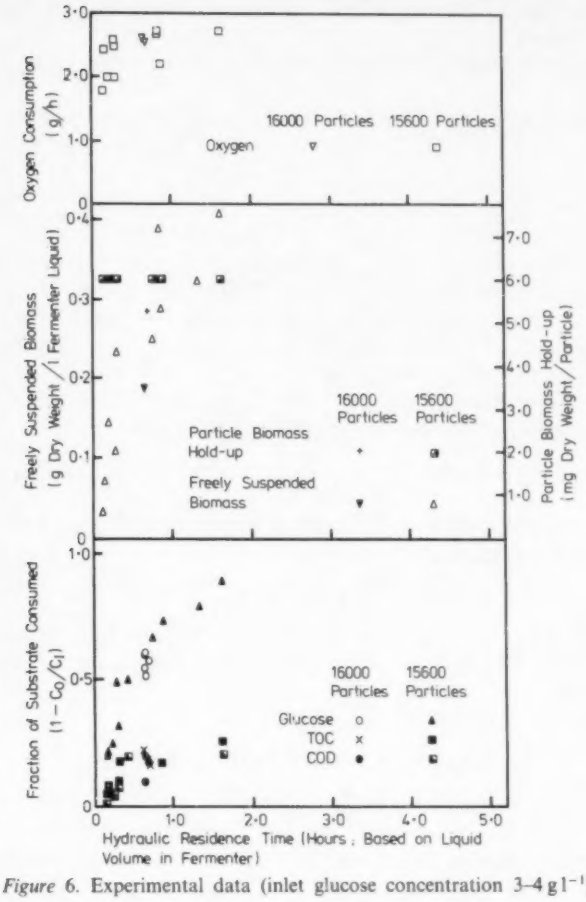


Figure 6. Experimental data (inlet glucose concentration 3–4 g l^{-1}).

where C_i^* are the substrate concentrations at the 'solid'-liquid interfaces; λ_i are a measure of the 'solid' phase diffusion limitations, i.e. the effectiveness factors; K_m is the Monod coefficient; R_{max} is the maximum specific rate of substrate uptake; and N_{max} is the maximum rate of substrate uptake per unit area of film of a given thickness.

The values of λ_i lie between zero and unity with magnitudes determined by the characteristic sizes of the biomass and by the kinetic parameters. When λ_i is equal to unity, no diffusional limitation exists, and the corresponding rate equation reduces to the Monod expression. Conversely the smaller λ_i the greater the diffusional limitation and the deviation from Monod kinetics.

The biological rate equation of Atkinson and Davies[12] has a number of asymptotic reductions applicable over various ranges both of the substrate concentration (C_i^*) and the characteristic size of the biomass. It is convenient to use these reductions in conjunction with equations (1) and (2).

Given the conditions in the reactor it is reasonable to assume that:

(*a*) There is a strong diffusional limitation within the 6 mm diameter particles i.e. $\lambda_p \ll 1$;

(*b*) Since the microbial films on the pipe-work are subject only to erosion by flowing fluid, their characteristic thickness is large, resulting in a strong diffusional limitation, i.e. $\lambda_f \ll 1$; and

(*c*) Since the freely suspended flocs pass repeatedly through the pump (a zone of high shear), their characteristic size is very small, resulting in a minimal diffusional limitation, i.e. $\lambda_s \simeq 1$.

Under the circumstances defined in (*a*) and (*b*) i.e. large biomass size and strong diffusional limitations, the biological rate equation of Atkinson and Davies[12] and equation (2) reduce[7] to:

$$R_p = \frac{R_{max}}{\alpha k_{2p} d_p/6} \frac{(1 + 2\,C_p^*/K_m)^{1/2}}{(1 + C_p^*/K_m)} \left[\frac{C_p^*}{K_m}\right] \tag{3a}$$

$$N = \frac{R_{max}\,\rho_{of}}{k_{2f}} \frac{(1 + 2\,C_f^*/K_m)^{1/2}}{(1 + C_f^*/K_m)} \left[\frac{C_f^*}{K_m}\right] \tag{3b}$$

$$R_s = R_{max} \frac{C_s^*}{K_m + C_s^*} \tag{3c}$$

where

$$k_{2i} = \left[\frac{\rho_{oi} R_{max}}{K_m D_e}\right]^{1/2}$$

In equations (3) the k_{2i} are biological rate equation coefficients; d_p is the overall diameter of the particles; α is a shape factor (given as 1.16 for spherical particles[16]); D_e is the diffusion coefficient of the substrate within the biomass; and ρ_{oi} is the microbial density (dry weight per unit wet volume) corresponding to the particular form of biomass.

When $C_i^*/K_m \gg 1$ equations (3*a*) and (3*b*) reduce to

$$R_p = \frac{R_{max}}{\alpha k_{2p} d_p/6} \left[\frac{2C_p^*}{K_m}\right]^{1/2} \tag{4a}$$

$$N = \frac{R_{max}\,\rho_{of}}{k_{2f}} \left[\frac{2C_f^*}{K_m}\right]^{1/2} \tag{4b}$$

Support for assumptions (*a*) and (*b*) above and the applicability of equations (4*a*) and (4*b*) is provided by the work of Atkinson and Ali[15] who found that open microbial films of 0.5–1 mm thickness over the glucose concentration range 0–400 mg l^{-1} could be adequately described by half-order kinetics.

It is well known[18] that diffusion with zero order kinetics leads to overall rates of reaction with half-order kinetics. Atkinson and Daoud[19] have explored the comparison between zero order and Monod kinetics when diffusion limited and the ranges of concentration over which the mathematical solutions lead to the same numerical results. At high values of C_i^*/K_m when Monod kinetics apply, the region in which local values of C/K_m fall below C_{crit}/K_m contributes little to the overall rate of reaction.

RATE EQUATION FOR BIOMASS SUPPORT PARTICLES

Observations on dissected biomass containing support particles using a stereo-microscope suggest that the biomass is distributed largely uniformly throughout the entire volume of an individual particle, even when less than full. This situation no doubt results from the continual re-distribution of biomass within the particles

under the combined effects of growth, erosion due to liquid flow, detachment due to particle movement, and adhesion.

It follows that the effective biomass concentration throughout the 'free' space within a support particle can be taken as:

$$\rho_{oe} = \frac{m_p}{\phi V_p} \tag{5}$$

where m_p is the biomass associated with a support particle of volume V_p, and ϕ is the particle porosity.

Equation (4*a*), though describing an homogeneous particle with a diffusion path r_p and a biomass density ρ_{oi}, can be used as a basis for the development of a rate equation for large biomass support particles exposed to relatively high substrate concentrations. The diffusion path of the latter is identified with the actual particle radius but a judgement has to be made as to the most appropriate biomass density, i.e. the local density (defined by equation (5)) or a bulk density (m_p/V_p) based upon the whole particle. The arguments in favour of equation (5) are that it represents the actual biomass concentration through which the substrate has to diffuse and since ϕ is relatively large (0.8), is more representative of the conditions for which the biological rate equation was established. Ideally, from a rate of reaction standpoint, ϕ should be as large as possible, i.e. tend to unity, and further developments of the biomass support particle concept have led in this direction[9]. Thus the use of equation (4*a*) has some justification from a theoretical standpoint and is compatible with current trends in biomass support particle development.

Consequently from equations (3)

$$k_{2p} = \left[\frac{\rho_{oe} R_{max}}{K_m D_e}\right]^{1/2} \tag{6}$$

and

$$k_{2f} = \left[\frac{\rho_{of} R_{max}}{K_m D_e}\right]^{1/2}$$

where ρ_{of} is constant and refers to the biomass density of the microbial films.

Given the flow-rate through the fluidised bed it is reasonable to neglect any liquid phase diffusion limitations, i.e.

$$C_o = C_p^* = C_f^* = C_s^*$$

where C_o is the reactor concentration, which is everywhere constant due to the high recycle ratios used (24–1000 to 1), i.e. completely mixed conditions exist throughout the reactor.

Further the relatively high throughput through the system resulted in low suspended biomass concentrations (Figures 4, 5, 6) allowing the assumption:

$$R_p M_p + NA \gg R_s M_s \tag{7}$$

Thus combination of equation (7) with equations (1), (4) and (6) leads to:

$$R_f = (2R_{max} D_e)^{1/2} \left[\frac{m_p n_p}{\alpha \rho_{oe}^{1/2} d_p/6} + A\rho_{of}^{1/2}\right] C_o^{1/2} \tag{8}$$

where n_p is the number of support particles in the reactor.

Combination of equations (5) and (8) leads to:

$$R_f = (2R_{max} D_e)^{1/2} \left[\left(0.8^{1/2} \frac{n_p V_p^{1/2}}{\alpha d_p/6}\right) m_p^{1/2} + A\rho_{of}^{1/2}\right] C_o^{1/2} \tag{9}$$

Estimates of the area of the microbial film (A) present in the reactor led to a value of 2783 cm^2 by measurement of individual components, while ρ_{of} can be taken as the density of the wet, drained biomass recovered from the particles, i.e. 0.0664 g cm^{-3}.

Insertion of the various numerical values for V_p, α, d_p, A and ρ_{of} into equation (9) leads to:

$$R_f = 3.667 (R_{max} D_e)^{1/2} [n_p m_p^{1/2} + 276.5] C_o^{1/2} \tag{10}$$

or, if the microbial films are neglected in addition to the freely suspended biomass

$$R_f = 3.667 (R_{max} D_e)^{1/2} [n_p m_p^{1/2}] C_o^{1/2} \tag{11}$$

where m_p is expressed in g(d.w.), R_{max} in h^{-1}, D_e in cm^{2}h^{-1}, C_o in g cm^{-3}, R_f in g h^{-1} and 3.667 has units of cm$^{1/2}$.

INTERPRETATION OF RESULTS

Particle Stability

The data given in Figures 4, 5 and 6 were obtained over a period of 24 months virtually continuous operation. In the case of individual experiments conditions were judged 'steady' when the biomass hold-ups and conversion efficiencies had remained unchanged for more than 3 days operation. During the whole period the steady state particle biomass hold-ups and conversion efficiencies remained self-consistent, uniquely determined by the reactor conditions, and independent of previous conditions. Furthermore, there was no evidence of physical deterioration of the particles or indication of unusual occurrences either from a microbiological or morphological stand-point.

Particle Biomass Hold-up

The accumulation of biomass results from the fact that while some of the growth within a particle is removed by attrition and is subsequently washed from the reactor, the remainder stays attached to the particle. Thus when the overall specific growth rate (G) exceeds the specific rate of attrition (T) the particle biomass hold-up (m_p) will increase according to:

$$\frac{dm_p}{dt} = (G - T) m_p \tag{12}$$

From the biological rate equation it can be deduced that as m_p increases G falls, due to the greater diffusional limitation on entering substrate, until a balance (steady state) is achieved such that at a given reactor substrate concentration (C_o)

$$G \rightarrow T \tag{13a}$$

VOL. 62 1984

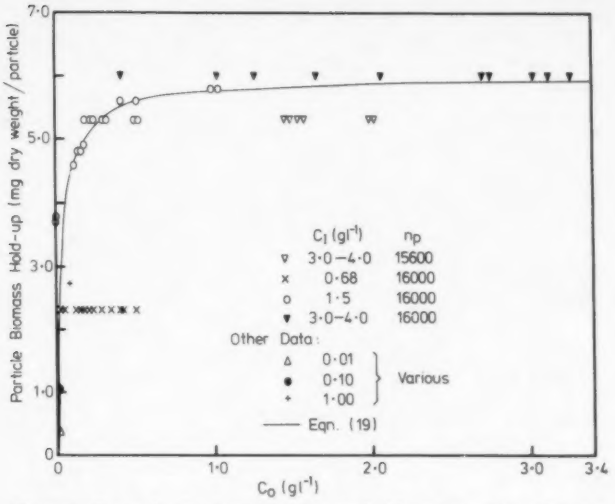


Figure 7. Dependence of particle biomass hold-up on reactor substrate concentration.

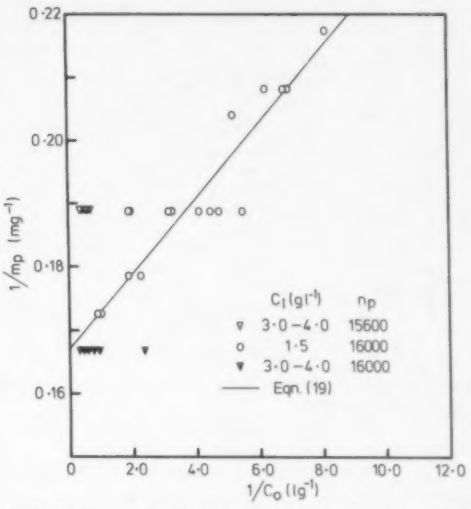


Figure 8. 'Lineweaver–Burke' plot of data given in Figure 7. (Excludes data for $C_i = 0.68\ g\,l^{-1}$ and outside range $0.1 < C_o < 3.0$).

and

$$m_p \rightarrow \text{constant} \qquad (13b)$$

It seems reasonable to postulate that for given particles and bed expansion (particle vibration), the specific rate of attrition is either constant or depends upon the quantity of biomass present, e.g.

$$T \propto m_p \qquad (14a)$$

or

$$T \text{ is constant} \qquad (14b)$$

Combination of equations (13) and (14) for steady conditions leads to:

$$m_p \propto G \qquad (15a)$$

or

$$m_p \text{ is constant} \qquad (15b)$$

For present purposes it is convenient to use the empirical relationship

$$G \propto \frac{C_o}{\beta + C_o} \qquad (16)$$

to describe the dependency of the specific growth rate on reactor substrate concentration rather than the more complex biological rate equation.

Combination of equations (15) and (16) leads to:

$$m_p \propto \frac{C_o}{\beta + C_o} \qquad (17a)$$

$$m_p \text{ is constant} \qquad (17b)$$

The particle biomass hold-up data have been plotted on Figure 7 in terms of $m_p = g(C_o)$ as suggested by equations (17). The prevailing impression of the total data is of a monotonic dependence of m_p on C_o and the existence of a maximum value ($m_{p(max)}$) as C_o is increased. Both these factors are compatible with equation (17*a*) supporting the contention

$$m_p = m_{p(max)} \frac{C_o}{\beta + C_o} \qquad (18a)$$

$$T \propto m_p \qquad (18b)$$

The data in Figure 7 has been replotted in Figure 8 using the Lineweaver–Burke re-arrangement $1/m_p = g(1/C_o)$ and provides some support for the functional form of equation (18*a*). Linear regression leads to:

$$m_p = 5.99 \frac{C_o}{0.0355 + C_o} \qquad (19)$$

where m_p is expressed in mg (d.w.) and C_o in g l^{-1}.

For an expression in the form of equation (18*a*), when C_o exceeds 19β, then $m_p > 0.95\ m_{p(max)}$. Thus it follows that

$$\text{when } C_o > 0.7\ g\,l^{-1};\ m_p \simeq m_{p(max)} \simeq 6\ \text{mg(d.w.)} \qquad (20)$$

i.e. the 'critical' substrate concentration leading to $m_{p(max)}$ is 0.7 g l^{-1}.

Thus equation (18) provides the basis for a very useful semi-theoretical expression relating the particle biomass hold-up to the reactor substrate concentration.

This relatively crude method of analysis was used to quantify equation (18*a*) because it was judged that the dependence of m_p on C_o was at an early stage of exploration and that further elaboration was unjustified given limited data.

The values of particle biomass hold-up obtained at an inlet concentration of 0.68 g l^{-1} have been omitted from Figure 8, since they appear to be inconsistent with the bulk of the data. On the basis of experience resulting from handling various types of support particles[9], their use in fluidised beds, and gravimetric assays on full, partially full, and empty particles, the most likely explanation for these particular results lies in the entrapment of air within the particle structure. The data obtained at 0.68 g l^{-1} was in fact the first ever obtained on biomass support particles containing a mixed culture in an aerated fluidised bed and inexperience in the use of the apparatus no doubt led to this situation. Some of the other data notably that at 3–4 g l^{-1} inlet concentration shows a remarkable constancy when evaluated to the nearest 0.1 mg dry biomass per particle, while the data at 1.5 g l^{-1} inlet concentration shows a more natural variation. The latter was the last of the data to be

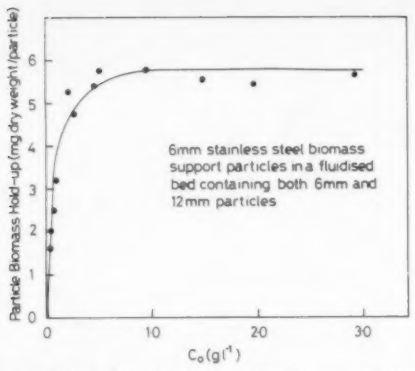


Figure 9. Dependence of particle biomass hold-up on reactor substrate concentration (6 mm particles).

obtained and, perhaps paradoxically could be judged the most acceptable as it coincides with increasing experience of particle recovery and biomass assay. The data obtained at 0.68 and 3–4 g l^{-1} can, of course, be judged to correspond to 'full' particles under the various conditions and therefore subject to less variation.

In order to confirm the dependency of the biomass hold-up on the fermenter substrate concentration suggested by equations (18*a*) and (19) an independent series of experiments was carried out using a fluidised bed containing a mixture of 6 and 12 mm particles. The steady state values of m_p obtained for a range of values of C_o are plotted on Figures 9 and 10 for both sizes of particle. These data support the basic form of the relationship between m_p and C_o, while the data for the 6 mm particles compares well with that given on Figure 7. The ratio of the values of $m_{p(max)}$ for the two sizes of particle is between 5 and 6 while the ratio of the respective volumes is 8. This difference suggests either that the particle porosities were different due to the fact that the 12 mm particles were hand-formed or that the critical substrate concentration for the large particles exceeded 3 g l^{-1}.

Overall Rate of Substrate (glucose) Uptake

All the experimental data given on Figures 4, 5 and 6 have been replotted on Figures 11 and 12 in terms of equations (10) and (11). Subsequent least squares anal-

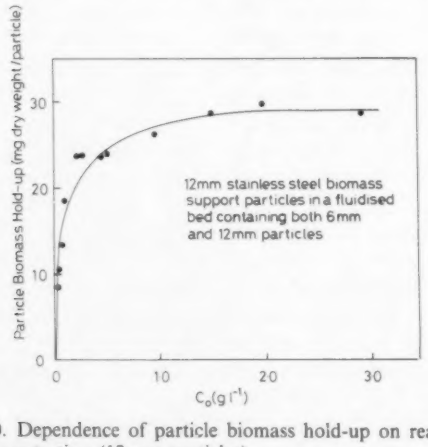


Figure 10. Dependence of particle biomass hold-up on reactor substrate concentration (12 mm particles).

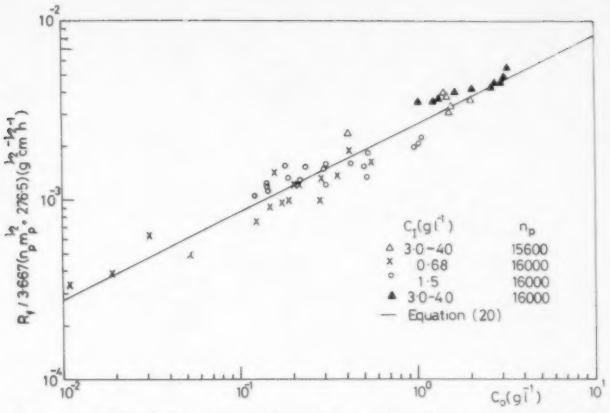


Figure 11. Correlation of experimental data based upon equation (10).

ysis led to:

$$\frac{R_f}{3.667\,(n_p m_p^{1/2} + 276.5)} = 0.00264\ C_o^{0.49} \qquad (20)$$

and

$$\frac{R_f}{3.667\,(n_p m_p^{1/2})} = 0.00333\ C_o^{0.48} \qquad (21)$$

where m_p is expressed in g(d.w.), C_o in g l^{-1} and R_f in g h^{-1}.

Since the exponents on C_o in equations (20) and (21) are approximately 0.5 they give support to the theoretical suppositions and it could be argued that equation (21) underestimates the contribution of the films while equation (20) over-compensates.

It follows from equations (10), (11), (20) and (21) that

$$0.084\ \text{cm h}^{-1} < (R_{max} D_e)^{1/2} < 0.105\ \text{cm h}^{-1} \qquad (22)$$

Equation (22) in essence quantifies a 'lumped' parameter with the aid of the biological rate equation but from which the intrinsic parameters can only be estimated, for example, by inserting a reasonable value for the diffusion coefficient (D_e) and obtaining an approximate value of R_{max}.

Estimation of Maximum Specific Rate of Reaction

The diffusion coefficient for glucose in water is 6.9×10^{-6} cm^2 s^{-1}. Following experimental work using

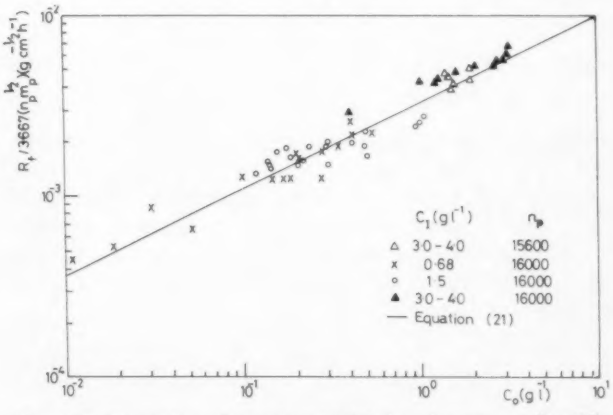


Figure 12. Correlation of experimental data based upon equation (11).

VOL. 62 1984

microbial films of various thicknesses, the effective diffusion coefficient of glucose within biomass was estimated[10,13] as approximately $7.67 \times 10^{-6}\,cm^2\,s^{-1}$. This latter value for D_e is sufficiently close to that for glucose in water to suggest that it is a very reasonable estimate. Thus insertion of $D_e = 7.67 \times 10^{-6}\,cm^2\,s^{-1}$ into equation (22) leads to a value of R_{max} in the range:

$$0.253\,h^{-1} < R_{max} < 0.402\,h^{-1} \quad (23)$$

TOC/COD and Oxygen Uptake

The experimental results contained in Figures 4, 5 and 6 demonstrate that the removal efficiency achieved in the reactor, when measured in terms either of TOC or COD, is lower than the removal efficiency of glucose. This situation arises because TOC is a measure of both the substrate and product carbon in solution, while COD is the sum of the oxidative states of all the oxidisable components.

Thus it is perhaps simplistic to anticipate that either TOC or COD removal would be described by a theory based on the removal of a single substrate. However, biological systems are concerned invariably with complex mixtures of non-specific carbonaceous components, both as substrates and products, and TOC and COD are employed as convenient measures of the oxidisable material present.

For the above reasons the TOC/COD data was plotted empirically using the form suggested by equation (21), namely:

$$\frac{R_{f(TOC/COD)}}{n_p m_p^{1/2}} = g\,(C_{o(TOC/COD)}) \quad (24)$$

Unfortunately neither the plot based upon TOC nor that based upon COD resulted in the quality of correlation achieved in Figures 11 and 12.

A further plot of oxygen uptake versus substrate (glucose) uptake resulted in a strongly non-linear curve suggesting a complex relationship between substrate uptake and product formation.

The above observations together with Figures 11 and 12 suggests that the reduced form of the biological rate equation adequately describes the rate of substrate uptake but that the types and yields of the products formed depends upon oxygen uptake and the extent of the aerobic/anaerobic zones within the particles.

CONCLUSIONS

Experimental data obtained on the biomass hold-ups and the overall rates of substrate (glucose) uptake of 6 mm diameter biomass support particles suggests that the former depends upon the substrate concentration up to a critical value, and the latter follows half-order kinetics over the range of substrate concentrations investigated, i.e. up to $4\,g\,l^{-1}$.

The biological rate equation provides a basis for the interpretation of experimental data, allows the presence of the microbial films within the reactor to be taken into account, and leads to an estimate of the maximum specific rate of substrate (glucose) uptake in the region of $0.253–0.402\,h^{-1}$.

Both microscopic observations on the location of the biomass within the support particles and the agreement between the experimental data and the theoretical postulations support the contention that the biomass occurs largely uniformly throughout the particles.

With increased substrate concentration the biomass fills the interstices until at approximately $0.7\,g\,l^{-1}$ the particles are largely full and contain about 6 mg(d.w.) of biomass. The dependency of particle biomass hold-up on substrate concentration is described reasonably by an hyperbolic relationship which has a semi-theoretical justification.

The theory for glucose uptake provides a basis for the development of understanding of product formation, the role of oxygen uptake and the existence of aerobic/anaerobic zones within diffusion limited particles.

SYMBOLS USED

A	area of microbial film in the reactor L^2
C_i^*	substrate concentration at a 'solid'-liquid interface ML^{-3}
C_1	inlet substrate concentration ML^{-3}
C_o	reactor substrate concentration ML^{-3}
d_p	particle diameter L
D_e	effective diffusion coefficient of substrate within biomass L^2T^{-1}
G	overall specific growth rate T^{-1}
k_{2i}	biological rate equation coefficient (defined by equations (3)) L^{-1}
K_m	Monod coefficient ML^{-3}
m_p	quantity of biomass within a support particle M
$m_{p(max)}$	maximum quantity of biomass within a support particle M
M_p	quantity of immobilised biomass in the reactor M
M_s	quantity of freely suspended organisms in the reactor M
n_p	number of support particles in the reactor —
N	rate of substrate uptake per unit area of microbial film $ML^{-2}T^{-1}$
N_{max}	maximum rate of substrate uptake per unit area of microbial film $ML^{-2}T^{-1}$
R_f	mass of substrate consumed in the reactor per unit time MT^{-1}
R_{max}	maximum specific rate of substrate uptake T^{-1}
R_p	overall specific rate of substrate uptake by biomass support particles T^{-1}
R_s	overall specific rate of substrate uptake by freely suspended organisms T^{-1}
T	specific rate of attrition T^{-1}
V_p	volume of particle L^3
α	geometric factor —
β	empirical coefficient ML^{-3}
ρ_{oe}	effective biomass concentration within a support particle (defined by equation (4)) ML^{-3}
ρ_{of}	density of a microbial film ML^{-3}
λ_1	effectiveness factor —
ϕ	particle porosity —

REFERENCES

1. Atkinson, B. and Kossen, N. W. F. 1978, *Proceeding First European Congress on Biotechnology*, (Dechema Monographien, 82) p 37.
2. Atkinson, B., 1980, in *Biological Fluidised Bed Treatment of Water and Waste Water*, Eds P. F. Cooper and B. Atkinson. (Ellis Horwood, Chichester) Chap. 1.
3. Atkinson, B., Black, G. M., Lewis, P. J. S. and Pinches, A., 1979, *Biotech and Bioeng*, 21: 193.
4. British Patent Application 1978, Number 38267/78 and similar foreign applications.

5. Webb, C., Black, G. M. and Atkinson, B., 1983 *Trans IChemE* 61: 125.
6. Atkinson, B., Black, G. M. and Pinches, A., 1980, *Process Biochemistry*, 15: 24, May.
7. Atkinson, B. and Mavituna, 1982, *Biochemical Engineering and Biotechnology Handbook*, (Macmillan, London). Chapters 4, 10 and 13.
8. Rahman, F. U., 1982, *PhD Thesis*, (University of Manchester).
9. Atkinson, B., Black, G. M. and Pinches, A., 1980, in *Biological Fluidised Bed Treatment of Water and Waste Water*, Eds. P. F. Cooper and B. Atkinson (Ellis Horwood, Chichester) Chap. 5.
10. Atkinson, B., Daoud, I. S. and Williams, D. A., 1968, *Trans IChemE* 46: 245.
11. Atkinson, B., 1974, *Biochemical Reactors* (Pion Press, London) p 77.
12. Atkinson, B. and Davies, I. J. 1974, *Trans IChemE* 52: 248.
13. Atkinson, B. and Daoud, I. S. 1970, *Trans IChemE* 48: 245.
14. Atkinson, B. and How, S. Y., 1974, *Trans IChem E* 52: 260.
15. Atkinson, B. and Abdel Rahman Ali, 1976, *Trans IChemE* 54: 239.
16. Atkinson, B. and Rahman, F. U. 1979, *Biotech. and Bioeng.*, 21: 221.
17. Atkinson, B. and Fowler, H. W., 1974, in *Advances in Biochemical Engineering* (Springer-Verlag, Berlin), Vol 3, Chap 6.
18. Peterson, E. E. 1965, *Chemical Reaction Analysis* (Prentice-Hall, New Jersey) p 55.
19. Atkinson, B. and Daoud, I. S., 1976, in *Advances in Biochemical Engineering*, (Springer-Verlag, Berlin), Vol. 4, Chap 2.

ACKNOWLEDGEMENTS

The authors would like to thank ICI Agricultural Division, the Science Research Council and the Department of Education, N.I., for the financial support which allowed this work to be carried out. Thanks are also due to Ian Winstanley for assistance in obtaining the data contained in Figures 9 and 10.

ADDRESSES

Correspondence on this paper should be addressed to Professor B. Atkinson, The Brewing Research Foundation, Lyttel Hall, Nutfield, Redhill, Surrey RH1 4HY.

The manuscript was received 16 May 1983 and accepted for publication 19 October 1983.

APPENDIX

Carbon Mass Balances

The carbon mass balance is given by:

IN
glucose-C + soluble inorganic-C + gaseous CO_2-C

OUT
glucose-C + soluble inorganic-C + gaseous CO_2-C + soluble organic-C products + biomass-C

Experimental Data

The complete experimental data obtained for one experiment consisted of:

(*a*) Direct measurements

	Parameter	Location	Experimental method	Experimental data ($g\,h^{-1}$)
(i)	Glucose	IN	Reagent kit	1.7500
(ii)	Total TOC	IN	Wet chemical	0.7130
(iii)	Soluble inorganic-C	IN	Wet chemical	ND
(iv)	Gaseous CO_2-C	IN	Absorption in sat. $Ba(OH)_2$	0.0064
(v)	Glucose	OUT	Reagent kit	0.3770
(vi)	Total TOC	OUT	Wet chemical	0.5110
(vii)	Soluble TOC	OUT	Wet chemical	0.4430
(viii)	Biomass dry wt	OUT	Dry weight	0.1290
(ix)	Gaseous CO_2-C	OUT	Absorption in sat. $Ba(OH)_2$	0.2030

(b) Derived Data

	Parameter	Location	Method	Values ($g\,h^{-1}$)
(i)	Glucose-C	IN	Glucose × 0.4	0.7000
(ii)	Glucose-C	OUT	Glucose × 0.4	0.1510
(iii)	Soluble organic Carbon products	OUT	Soluble TOC —glucose-C	0.2920
(iv)	Biomass carbon	OUT	Total TOC-Soluble TOC	0.0680

Experimental Carbon Balances (data for the 2 tests)

	Experiment 1 ($g\,h^{-1}$) (data given above)		Experiment 2 ($g\,h^{-1}$)	
	IN	OUT	IN	OUT
Glucose-C*	0.7130	0.1510	0.6530	0.2160
Soluble organic Product-C	0	0.2920		0.1340
Biomass-C	0	0.0680		0.1117
Soluble Inorganic-C	ND	ND	ND	ND
Gaseous CO_2-C	0.0064	0.2030	0.0064	0.187
	0.7194	0.7140	0.6594	0.6487
	99.2% C recovery		98.4% C recovery	

*For the glucose-C, IN, the total TOC IN value was used.

Other Experiment Information

liquid volume (V)	= 2650 ml
number of 6 mm particles (n_p)	= 2150
temperature	= 22°C
pH	= 6.8
liquid feed flow rate	= 2.48 l h^{-1} (experiment 1)
liquid feed flow rate	= 3.43 l h^{-1} (experiment 2)
air flow rate	= 12 l h^{-1}

VOL. 62 1984

BOOK REVIEWS

Heat Exchanger Design Handbook
(Five Volumes each in the form of a loose leaf binder)
Editor-in-Chief: Ernst U. Schlünder
Hemisphere Publishing Corporation, 1983
US $600 for the 5-Volume set (2080 pages).

Each volume is reviewed below by a separate reviewer. The complete set is available for consultation in the IChemE Library at Rugby.

Volume 1. Heat Exchanger Theory.

This introduction to the Heat Exchanger Design Handbook provides material for all people involved with heat exchangers whether they are university lecturers or students, researchers industrial designers or plant operators. It is gratifying to find that the nomenclature comes first, but unfortunately the listing is not alphabetical either in symbol or quantity specified. The list of most frequently used dimensionless numbers is alphabetical. However, the definition of Grashof number is somewhat strange. This includes the change in density divided by the density, whereas normally one would expect the quotient of the coefficient of thermal expansion and the temperature difference. The five sections of Volume 1 are well written and introduce the reader to the configurations, flow patterns and interfaces presently employed in heat exchangers. The definitions and quantitative relationships for heat exchangers are presented, including notes on important thermodynamic concepts, which often are not found in text books. Transfer coefficient dependences are discussed for both heat transfer and pressure drop, and analogous mass transfer relationships are included. Overall balance equations applied to complete equipment are presented and three methods of heat exchanger performance are discussed: the F-correction-factor method, the P-NTU method and the θ method. This is followed by the differential equations which can be used to present the fluid flow and transfer within equipment. A short discourse is then included as to the ways and means of solving these equations. The final section includes a comprehensive set of charts of both F and θ methods for shell-and-tube exchangers using the TEMA accepted shell configurations. Similar charts are presented for cross-flow arrangements. Several examples are included on how to utilise these charts for differing calculation procedures. This is a refreshing introduction to heat exchanger theory, which does not leave out the many pitfalls that present text books ignore, i.e. the assumptions inherent in the design methods presently employed.

P. J. Heggs

Volume 2. Fluid Mechanics and Heat Transfer.

The General Editor in his preface describes the Handbook as "a first step rather than a final result". We certainly have come a long way since the days of D. Q. Kern! The Editor of Volume 2 recognises the reliance of the practising heat transfer engineer on experimentally derived correlations. His principal objective, therefore, is to evaluate and present the best available correlations. The reader is certainly in a very good position (short of repeating the laboratory work!) to critically evaluate the chosen correlations, since the contributors have gone to considerable lengths to present—in readily assimilable form—much of the most recent experimental data. To ensure continuing access to the most up-to-date material, subscribers to the Handbook are promised regular up-dates. The entire science of heat transfer is certainly comprehensively covered. As one would expect, the bulk of the volume is concerned with single and two-phase fluid flow and convective heat transfer. There are, however, additional and welcome sections which provide valuable insight into the more difficult and less well documented areas of conduction, radiation and gas-solid systems.

Why, one might ask, is such a Handbook necessary in these days of powerful and readily available programs for the computer-aided design of heat transfer equipment? Well, firstly, although the computer programs will handle maybe 90% of routine heat transfer design problems it is—and always was—the oddball 10% which sends the engineer running to the library for a book just like this one. Secondly, design supervisors are, rightly, very reluctant to let trainees loose on proprietary computer programs until they have mastered the principles of thermal and mechanical design by traditional methods. The correlations presented in the Handbook will certainly provide a rigorous and comprehensive basis for such work and are especially useful for trainees since the contributors have very wisely refused to succumb to the temptation, so prevalent in these days of powerful pocket calculators, to present the correlations in exclusively algebraic form. On the contrary; the extensive use of clearly drawn curves will benefit both the trainee and the experienced designer who would like some "feel" as to the interdependence of variables within the correlations.

So, this volume is very much for the technical library and the specialist; however, any organisation that has either a technical library or a heat transfer specialist should, in my opinion, have one.

C. J. Norman

Volume 3. Thermal and Hydraulic Design of Heat Exchangers.

The expressed purpose of the handbook is to collect heat transfer information available in the open literature in order to create a heat transfer information base. Volume 3 is concerned with the detailed thermal and hydraulic design of heat exchangers and builds on heat transfer theory elaborated in Volumes 1 and 2. The coverage of equipment types is wide with an emphasis on process type exchangers. Topics treated include shell-and-tube, air-cooled, plate, double-pipe and compact exchangers together with chapters on heat pipes, furnaces, cooling towers, driers and agitated vessels. Each section is written by an international authority in the field. The question that immediately comes to mind with such a comprehensive publication is: for whom is it meant? It is certainly not for the engineer in a hurry and neither is it an updated version of Kern's *Process Heat Transfer*: such a book has yet to be written. Furthermore, about half the volume is devoted to shell-and tube and air-cooled exchangers. These are areas where most advances over the past twenty years or so have been made by cooperative research organisations, so at first sight the value of these particular sections might appear to be confined to those who do not have access to proprietary information. However it is salutary for all heat transfer practitioners independently of any access to sophisticated computer programs to be able to undertake hand calculations whether or not they have access to proprietary information. In this context the calculation procedures laid down either for approximate sizing or detailed design should prove invaluable. The volume goes some way towards dispelling the illusion that the only type of heat exchanger is the shell-and-tube variety, although the balance of emphasis does not always reflect the relative importance of the various types of equipment available. It does, however, contain within its covers comprehensive and up to date references from a diffuse literature with relevant design data extracted for a wide variety of equipment. Stylistically the volume suffers from the multiplicity of authors, some sections being much easier to read than others. However, this does not detract from the value of the book. It is a book that should be accessible to both the designer and user of heat exchange equipment over the whole spectrum of heat exchanger usage.

G. H. Walter

Volume 4. Mechanical Design of Heat Exchangers.

Volume 4 is divided into eight chapters, seven of which are mainly concerned with shell-and-tube heat exchangers. The remaining chapter covers air coolers, plate, platefin and other types of heat exchanger, such as double pipe, spiral plate, scraped surface, direct contact, Hampson and heat pipes. Volume 4 will form a useful reference work for students and should become a valuable handbook for designers whose main speciality lies outside the field of heat exchangers. Not since the publication of Kern's *Process Heat Transfer* in 1950 has there been such a comprehensive work specifically oriented towards Design. Presentation is clear and readable throughout. The units for pressure or stress could, however, have been more consistent—MN/m^2, kN/m^2 and kPa are all used. The elements of shell-and-tube construction are described in the second chapter, amplifying the standards of the Tubular Exchanger Manufacturers' Association (TEMA). Surprisingly, however, in dealing with the attachment of tubes to tubesheets, their relative yield stress values are not discussed, and no reference is made to the OCMA Standard for tube-end welding (TEW-1). The third chapter compares the principal Mechanical Design Codes: ASME Section VIII Division 1, TEMA, BS 5500, and A. D. Merkblatter. A notable omission is ASME Section VIII Division 2, which finds frequent application for heat exchangers designed for pressures above $10\,MN/m^2$. There is no discussion of the "thin tubesheet" design philosophy commonly used for fire-tube waste heat boilers. The optimisation of flange design for lowest cost or weight is not discussed. In the General chapter (4), the air cooler section dwells mostly on thermal design and does not cover the mechanical design of headers. A reference to ASME VIII Division 1, Appendix 13 should have been made. The scraped surface exchanger described cannot be regarded as typical for refinery applications. Submerged combustion LNG evaporators are omitted. The fifth chapter describing materials of construction and corrosion is lucid, concise and informative. The sixth chapter covers flow induced vibration. A thorough treatment is given, although the damage number method for predicting vibration damage to tube bundles is not mentioned. The shellside fluid property parameter, which reflects tube damping, has been found by the writer to give reasonable predictions when used together with damage numbers, although prediction methods for tube life due to fretting have still to be developed. The seventh chapter covering testing and inspection is rather superficial. The following topics have not been covered: alloy verification techniques, production control test plates, tube end weld procedure tests, minimum temperature and maximum chloride permissible for hydrotesting. The eighth chapter gives approximate methods for estimating the cost of shell-and-tubes, air coolers and plate exchangers.

D. J. Wilson

The review of Volume 5 follows on page 172.

VOL. 62 1984

MOLECULAR SIEVING EFFECTS OF ZEOLITES IN THE DEHYDRATION OF ALCOHOLS

By P. L. YUE and O. OLAOFE

School of Chemical Engineering, University of Bath

The dehydration of ethanol, isopropanol and *n*-butanol has been studied over Laporte 13X, 4A and Norton Zeolon ZNa. The patterns of activity and product selectivity of the zeolites have been examined in the light of cage size, molecular shape and the effect of reaction temperature. The relative reactivity of the alcohols is related to molecular structure and acidic strength of the catalyst. A dual-site mechanism requiring an acid-base paired site is proposed for the dehydration of alcohol to olefin. Results of the pre-exponential factor and activation energy show a compensation effect.

INTRODUCTION

The pore structure of zeolites is characterised by small uniform intracrystalline cavities. It is well established that[1-4] since the majority of the catalytic sites are confined within this pore structure, the geometry and configuration of the pores and of the reactant and product molecules will give rise to shape-selective catalysis. Only molecules less than a certain critical size can gain access to the internal catalytic sites and those molecules which can leave the pore will appear in the product. Bulkier molecules can only react on the external sites of the zeolite crystals. The relation between zeolite or molecular sieve structure and catalytic activity and the accessibility of catalytic sites has been masterfully reviewed by Venuto and Landis[5].

Shape selectivity has been observed[6] when straight chain primary alcohols dehydrated in the presence of branched ones. *n*-butanol dehydrates very much faster than isobutanol over Linde CaA. Furthermore, at higher temperatures, the rate constant of secondary butanol dehydration over Linde CaA is between two to three orders of magnitude smaller than over faujasite-type CaX which has much larger pores. This difference is consistent with the difference between internal and external surface areas. Bryant and Kranich[7] have reported strong influence of product selectivity in ethanol and *n*-butanol dehydration by the type of zeolite as well as by reaction temperature.

Catalytic activity too, varies the type of zeolite and the charge and location of exchanged cations[7,8]. The acid sites in the α-cages have frequently been invoked[8,9] as the active centres for alcohol dehydration. The number of acid sites increases with the silica content in the zeolite, thus the silicon to aluminium ratio in the skeleton of the zeolite will influence its activity. Topchieva and Tkhoang[10,11] have observed maximum activity of Y zeolites with a SiO_2/Al_2O_3 ratio between 6 to 8 in the dehydration of isopropanol. Both strong and weak acid sites were believed to be responsible for the catalytic activity. For the dehydration of ethanol, Krishnaprasad and Ravindram[12] have shown that the surface acidity of Linde 10X, 13X and 5A is related to the reaction rate constant.

Selectivity between the formation of olefin and ether has also been found to be dependent on the length of the alcohol chain[7,13-15]. Increasing alcohol chain length favours the rate of formation of olefin and reactivity rises with higher chain length[13,16]. Branching of the alcohol molecule promotes olefin formation and enhances reactivity[17,18], thus reactivity increases in the order of primary, secondary and tertiary alcohols.

EXPERIMENTAL

The dehydration of ethanol, isopropanol and *n*-butanol has been studied over Laporte 13X and 4A and Norton Zeolon ZNa zeolites. Ethanol and *n*-butanol are, of course, primary alcohols, while isopropanol is a branched one. This combination therefore gives a varied chain length, as well as molecular structure. The physical and chemical properties of the three different types of zeolite are shown in Table 2 of our previous paper[19]. The Norton Zeolon, which is a ZNa modernite, is in the form of cylindrical extrudates while the Laport zeolites are spherical beads. The size of the cages in the zeolites increases in the order 4A < ZNa < 13X. The pore structures of the 4A and 13X are roughly spherical, but that of ZNa is made up of tubes of elliptical sections. The most acidic of the three zeolites is the ZNa modernite, which has a SiO_2/Al_2O_3 ratio of 10. The value of this ratio drops to only 2 in the case of 4A.

The dehydration reactions were conducted in a continuous stirred gas–solid reactor where the catalyst was housed in a spinning basket. Details of the reactor with the associated equipment and product analysis have been reported in an earlier paper[19]. The reactor spinning speed was varied to establish the conditions when the reaction rates were not controlled by interphase diffusion. In the present experiments, intra-crystalline diffusion cannot be eliminated and is an interesting subject which has been studied in a different reactor and will be discussed independently[20].

RESULTS AND DISCUSSION

The principal products of the dehydration reaction are the olefins and ethers. The kinetics of the reactions have

© Institution of Chemical Engineers

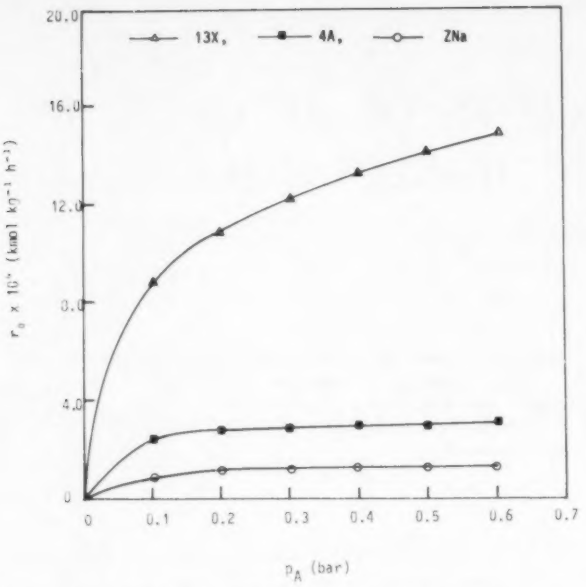


Figure 1. The dehydration of *n*-butanol to olefin at 280 °C.

been analysed and modelled previously[19]. The results and discussion presented here relate to the activity and selectivity of the zeolites and the reactivity of the alcohols.

Activity of Zeolites

Consider first the activity of the zeolites in promoting the formation of olefins. Figure 1 shows the performance of the zeolites on the dehydration of *n*-butanol to olefin at 280°C. The order of activity is found to be:

Laporte 13X > Laporte 4A > Norton Zeolon

Bryant and Kranich[7] obtained the same sequence of activity for the dehydration of ethanol over a similar family of zeolites (Linde 13X, 4A and Norton ZNa). Type 13X zeolite has a highly developed surface area of 359 $m^2 g^{-1}$ and the largest cage size among the three catalysts. Undoubtedly these factors contribute to the high activity of 13X in olefin formation. Although Norton Zeolon has the highest Si/Al ratio, it has the lowest activity. It is possible that there is an optimum Si/Al ratio similar to that reported by Topchieva and Tkhoang[10,11] who obtained maximum activity at a Si/Al ratio of 6 to 8. Furthermore, the low activity of ZNa suggests that the dehydration reaction takes place via an acid–base mechanism which will be discussed in greater detail later. The scarcity of basic sites in the modernite makes the abstraction of a hydrogen atom from the β-carbon atom difficult.

The activity of the same zeolites in the dehydration of isopropanol at the same temperature (280 °C) is shown in Figure 2. The sequence obtained is:

Laporte 13X > Norton Zeolon > Laporte 4A

While 13X zeolite remains the most active, 4A zeolite becomes the least active. The reason that the sequence of activity obtained is different from that for the primary alcohols, ethanol and *n*-butanol, must be due to the limitation of intra-crystalline diffusion. The cages of 4A are the smallest, thus the movement of isopropanol, a branched chain alcohol, is restricted. However, the cages of the modernite (5.7–7.0 Å) are sufficiently large not to stop the diffusion of isopropanol. Once again, even though ZNa has the highest Si/Al ratio, its activity is less than that of 13X.

The activity of the zeolites in the production of ether from n-butanol and isopropanol follows the sequence:

Laporte 13X > Norton Zeolon > Laporte 4A

which corresponds to the decreasing order of cage size. The ether molecules are, of course, much bulkier and the geometrical and molecular shape factors clearly become significant. The effects of these factors on ether formation are best discussed in terms of selectivity.

Geometrical Selectivity

Selectivity is defined as the ratio of the rate of formation of olefin to that of ether.

$$s = r_O/r_E \qquad (1)$$

The present results show that as the partial pressure of alcohol increases, selectivity decreases for all the zeolites, as shown in Figures 3 and 4 in the dehydration of *n*-butanol and isopropanol. At low partial pressures, the formation of olefin is favoured. This behaviour suggests that the dehydration reactions to olefin and ether proceed in parallel rather than according to a consecutive scheme. Had the latter been the case, the results at low alcohol concentrations would have favoured the intermediate product, ether. Possible reaction schemes have been discussed previously[19].

The influence of cage size on selectivity is evident. Type 13X zeolite has the largest cages, which allow both olefin and ether molecules to move in and out of the crystals, therefore this catalyst shows the lowest select-

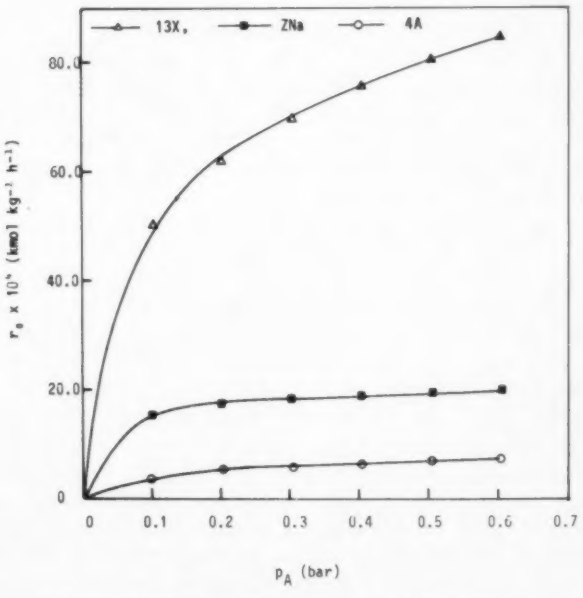


Figure 2. The dehydration of isopropanol to olefin at 280 °C.

VOL. 62 1984

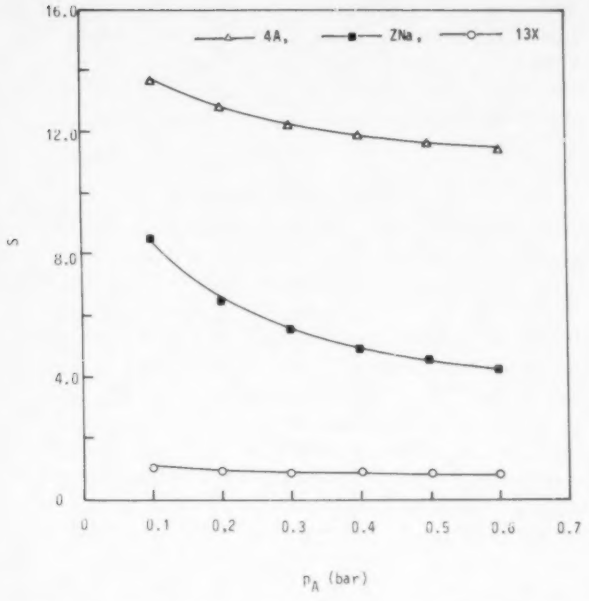


Figure 3. The effect of *n*-butanol partial pressure on olefin selectivity at 280 °C.

ivity. The cages of zeolite 4A are too small to give passage for the bulky di-isopropyl ether molecules to diffuse out of the crystals. The ether obtained in the products represents the reaction which occurs at external catalytic sites. The modernite has cylindrical cages of medium size and manifests a selectivity intermediate between that of 13X and 4A. The present results give further evidence to the significance of cage size in the dehydration of alcohols over zeolites seen in the limited data of Bryant and Kranich and Weisz et al[1].

Molecular Shape Selectivity

This type of selectivity arises from the shape of the molecules. Intra-crystalline movement of straight chain molecules is much easier than that of branched molecules. The latter is, in fact, often prohibited, as is the case in the dehydration of isobutanol. Weisz et al[1] have established molecular shape selectivity by dehydrating *n*-butanol and isobutanol over zeolite 5A. The latter was found to be hardly converted, while *n*-butanol dehydration proceeded rapidly.

In the present study molecular shape selectivity can be observed in the dehydration of *n*-butanol and isopropanol. A di-isopropyl ether molecule has four branched methyl groups and therefore has a very bulky structure. Not only is its movement within the cages of 4A forbidden, but also in the large cages of 13X the migration of this ether is restricted. Figure 4 shows that selectivity in the dehydration of isopropanol is higher than that of *n*-butanol over 13X. The alignment difficulties of the four methyl groups has considerably slowed down the process of diffusion out of the crystals. Further evidence of molecular shape selectivity is seen in comparing the rates of ethanol and *n*-butanol dehydration. Figure 5 shows the rates of formation of di-ethyl ether and di-*n*-butyl ether. Thermodynamically the latter is favoured, but the results show that the former is produced more readily. The resistance to diffusion within the zeolite cages must have been higher for the ether with longer chain length.

Effect of Reaction Temperature

Olefin selectivity increases with increasing temperature in the case of 4A and ZNa, as illustrated in Figure 6. Thermodynamically the production of olefin is favoured at higher reaction temperatures. The effect of tem-

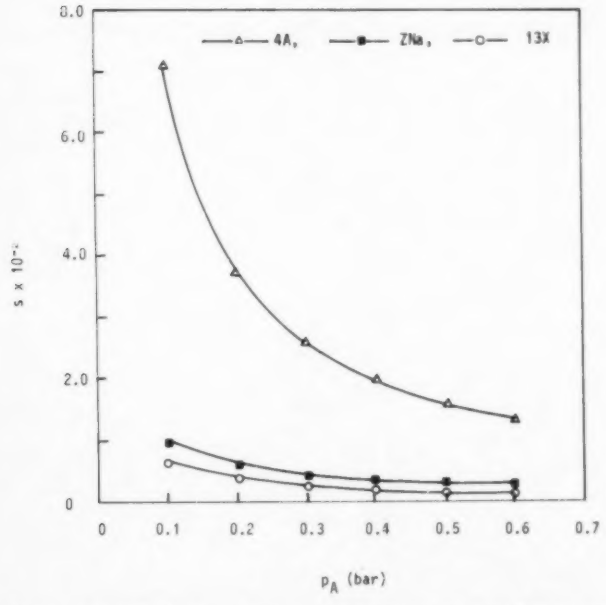


Figure 4. The effect of isopropanol partial pressure on olefin selectivity at 280 °C.

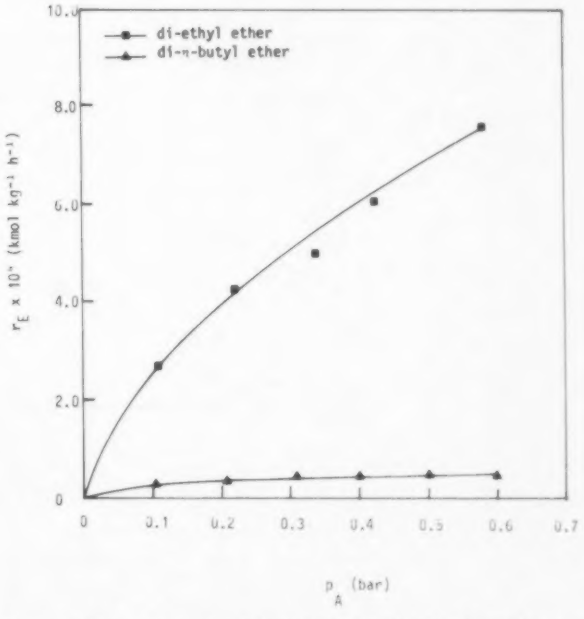


Figure 5. The rates of di-ethyl and di-*n*-butyl ether formation over zeolite 4A at 280 °C.

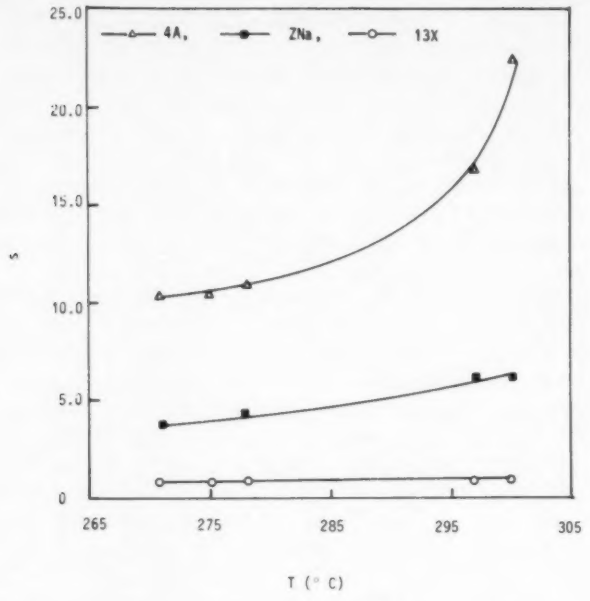


Figure 6. The effect of temperature on olefin selectivity in the dehydration of *n*-butanol.

perature is most prominent with zeolite 4A. The formation of ether over this zeolite is partly from internal catalytic sites and partly from external ones. The latter are not affected by molecular shape selectivity. Higher temperature therefore enhances the formation of ether despite the unfavourable thermodynamics. However, the formation of olefin is unhampered by intra-crystalline diffusional effects and the rate rises exponentially with increasing reaction temperature. The net effect is a sharp increase in olefin selectivity at higher temperatures. This behaviour is less pronounced with ZNa which has larger cages than 4A. Temperature does not have a noticeable effect on olefin selectivity over 13X. Probably the diffusion of di-*n*-butyl ether within the large cages of this zeolite is sufficiently enhanced at high temperature. Similar influence of reaction temperature on selectivity has been observed by Bryant and Kranich[7] for the dehydration of ethanol and *n*-butanol.

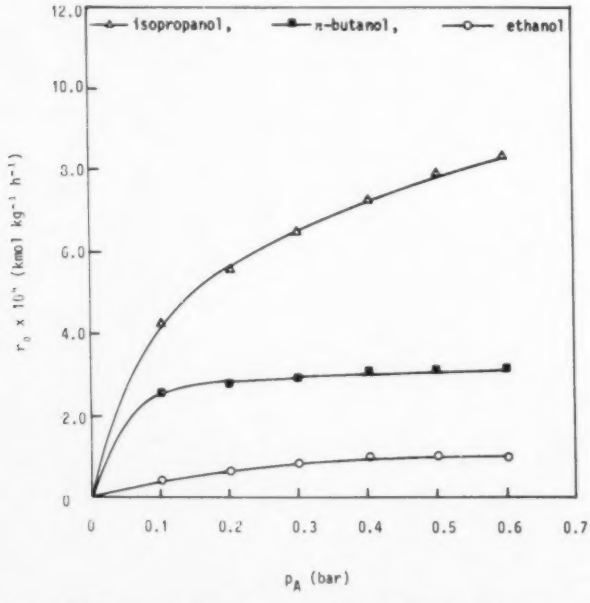


Figure 7. The reactivity of alcohols over zeolite 4A at 280 °C.

Reactivity of Alcohols

The reactivity of alcohols has been found to increase with chain length[7,13–16] and branching[17,18]. It would, however, be interesting to see whether a branched chain alcohol with n carbon atoms is more reactive than a straight chain alcohol with $n+1$ carbon atoms. Figure 7 shows the effect of dehydrating *n*-butanol, isopropanol and ethanol over zeolite 4A. The order of reactivity of the alcohols is shown in Figure 8(*a*). The trend is the same for zeolites 13X and ZNa. The sequence in Figure 8(*a*) shows that isopropanol is more reactive than *n*-butanol, even though the latter has one more carbon atom. The high reactivity of isopropanol is due to the effect of the substituted methyl groups on the hydroxyl group attached to the α-carbon atom. *n*-butanol is more reactive than ethanol because of the longer chain of the alkyl group. The trend of reactivity observed here is similar to that for the elimination of halo-alkanes over TiC oxide catalyst[16], Figure 8(*b*).

Activation energies for the dehydration reactions have been evaluated and reported previously[19]. It is instructive to note that the activation energies follow the sequence in Figure 8(*c*), for all the three zeolites. This order shows that activation energy increases with alkyl chain length in primary alcohols, but decreases with branched alcohol. The sequence of decreasing activation energy corresponds to decreasing acidic strength of the hydrogen atom on the β-carbon atom. The lower the acidicity, the higher the energy required for hydrogen atom abstraction. When the acidic sites on the catalyst are strong enough to give complete abstraction of hydroxyl groups, the abstraction of hydrogen from the β-atom becomes the rate limiting step of the activated complex state. The present results indicate that the dehydration of the most

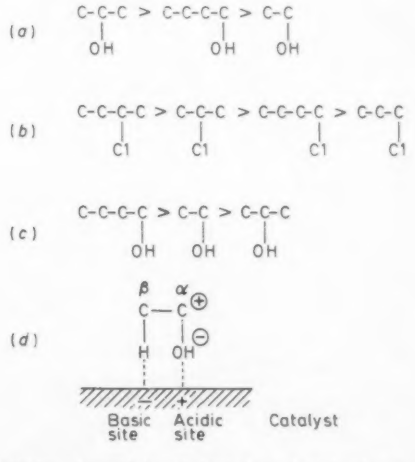


Figure 8. (a) Order of reactivity of alcohols in dehydration over zeolites 4A, 13X and ZNA. (b) Order of reactivity for elimination of halo-alkanes over TiC oxide catalyst. (c) Sequence of activation energies. (d) Proposed transition state for dehydration reactions.

VOL. 62 1984

reactive alcohol requires the least activation energy. In the catalytic dehydration of aliphatic alochols, the alkyl chain length therefore affects both the abstraction of the hydroxyl group from the α-carbon atom and the hydrogen atom from the β-carbon atom. The alkyl chain length exerts an inductive effect on the hydroxyl group, increasing the electron density of the latter. This increase in electron density favours strong interaction between the hydroxyl group and the acidic sites on the catalyst surface. Kinetic analysis[19] has already indicated that the dehydration of alcohol to form olefin proceeds according to ionic mechanism which may be of the so-called E1 or E2 type. The mechanisms for elimination reactions have been extensively discussed in the literature[5,16,21]. Alcohol dehydration via E1 mechanism produces an intermediate carbenium ion. The E2 mechanism involves the simultaneous abstraction of the hydrogen atom from the β-carbon by the basic site and the hydroxyl group from the α-carbon by the paired acidic site. The inductive effect of the alkyl chain on the hydroxyl group probably shifts the reaction mechanism from E2 to E1 type in the dehydration of the longer chain alcohol.

It is proposed that the dehydration reactions proceed through a transition state, as represented in Figure 8(d). The dehydration reaction therefore requires an intermediate adsorbed species in which an alcohol molecule is bonded to both acidic and basic sites. The above proposal is consistent with the Hougen–Watson rate model based on dual-site mechanism which has been shown[19] to correlate very well the kinetics of alcohol dehydration to olefin over zeolites. Experimental results and conclusions on ethanol and isopropanol dehydration over both zeolites and other oxide catalysts reported in the literature[10,22,23] support this dual acid–base site mechanism.

Finally, the so-called compensation effect is quite remarkably demonstrated in the present results. This effect is sometimes observed in reactions with a group of reactants having analogous molecular structures or with reactions with the same reactant, but over catalysts of the same family. The effect can be shown on a plot of logarithm of pre-exponential factors versus activation energies, as illustrated in Figure 9. The figure shows two straight lines in parallel. The first straight line passes through all the points for the primary alcohols which have analogous molecular structure over a family of three zeolites. The second straight line passes through all the points for isopropanol which has a different molecular structure but over the same family of zeolites.

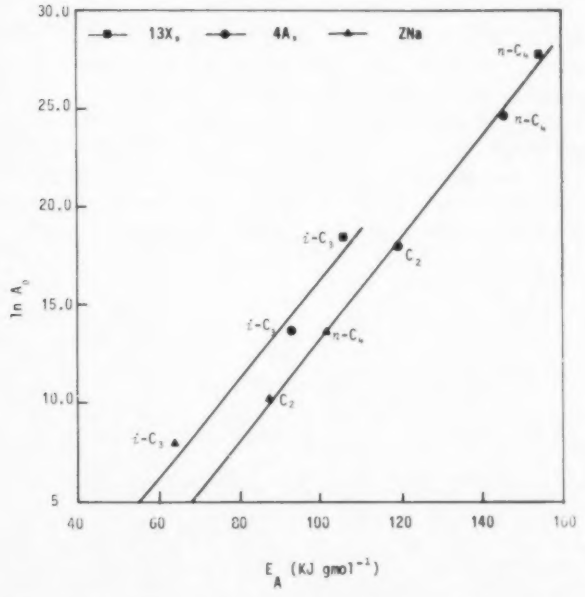


Figure 9. Compensation effect in the dehydration of primary and secondary alcohols over a family of zeolites.

A linear least square analysis of the data yielded the following expressions:

Primary alcohols

$$\ln A_O = -2.01 + 0.26E_O \quad (2)$$

Isopropanol

$$\ln A_O = 1.40 + 0.25E_O \quad (3)$$

The R-squared values for the two equations are 99.5 and 96.3% respectively. The straight line representation of the results is good and it is evident that the two lines are indeed parallel.

CONCLUSIONS

Laporte 13X is the most active for the dehydration of alcohol among the three zeolites because of its large surface area and cage size. Laporte 4A has the smallest cages, low surface area and is therefore the least active in the dehydration of isopropanol which has branched molecules. However, 4A is more active than the modernite Norton zeolon in the dehydration of straight chain alcohols because of the scarcity of basic sites in the latter catalyst.

Product selectivity is affected by cage size, shape of molecules and reaction temperature. Intra-crystalline diffusion of reactants and products are least restricted in 13X zeolite, which therefore shows the lowest selectivity for olefin. The bulky di-isopropyl ether molecules cannot find free passage in the small 4A cages. The migration of this ether with four branched methyl groups is limited even in 13X and the effect is reflected in the results on selectivity. Resistance to diffusion within the zeolite cages is higher for the ether with longer chain length. Higher temperature enhances the selectivity for olefin in the case of 4A and ZNa, but not 13X.

Of the three alcohols dehydrated, the branched alchol, isopropanol, is the most reactive and reactivity also increases with chain length. The patterns of reactivity and activation energies lead to a proposal in that the dehydration of alcohol to olefin is considered to proceed through a dual-site mechanism. An intermediate species is formed in which the hydroxyl group is bonded to an acidic site and the hydrogen to a basic site. However, the effect of the acidic site predominates, thus making the abstraction of the hydrogen atom from the β-carbon the rate limiting step.

A relation called the compensation effect exists between the pre-exponential factor and activation energy both for the dehydration of the primary alcohols and the secondary alcohol.

SYMBOLS USED

A_O	pre-exponential factor for the formation of olefin (kmol $kg^{-1} h^{-1}$)
E_O	activation energy for the formation of olefin (kJ $gmol^{-1}$)
p_A	partial pressure of alcohol (bar)
r_E	rate of formation of ether (kmol $kg^{-1} h^{-1}$)
r_O	rate of formation of olefin (kmol $kg^{-1} h^{-1}$)
s	selectivity for olefin
T	reaction temperature (°C)

REFERENCES

1. Weisz, P. B. and Frilette, V. J., 1960, *J Phys Chem*, 64: 382.
2. Miale, J. N., Chen, N. Y. and Weisz, P. B., 1966, *J Catalysis*, 6: 278.
3. Chen, N. Y. and Weisz, P. B., 1967, *Chem Eng Prog Symp Ser* 63(73): 86.
4. Csicsery, S. M., 1976, *Zeolite Chemistry and Catalysis*, Rabo, J. A. (ed.), (American Chemical Society, Washington D.C.), p. 680f.
5. Venuto, P. B. and Landis, P. S., 1968, *Adv Catalysis*, Eley, D. D., Pines, H. and Weisz, P. B., (eds), (Academic Press, New York and London), 18: 259.
6. Weisz, P. B., Frilette, V. J., Maatman, R. W. and Mower, E. B., 1962, *J. Catalysis*, 1: 307.
7. Bryant D. E. and Kranich, W. L., 1967, *J Catalysis*, 8: 8.
8. Stone, F. S. and Agudo, A. L., 1969, *Z Phys Chem*, Frankfurt, 64: 161.
9. Winfield, M. E., 1960, *Catalysis*, Emmett, P. H. (ed.), (Reinhold, New York), Vol. 7, p. 93.
10. Topchieva, K. V. and Tkhoang, H. S., 1973, *Kinetics and Catalysis, USSR*, 14: 398.
11. Topchieva, K. V. and Tkhoang, H. S., 1973, *Kinetics and Catalysis, USSR*, 14: 1320.
12. Krishnaprasad, T. N. and Ravindram, M., 1977, *Hungarian J Ind Chem* 5: 13.
13. Stauffer, J. E. and Kranich, W. L., 1962, *Ind Eng Chem Fund*, 7(2), 107.
14. Gryaznova, Z. V., Ermilova, M. M., Tsitsishvili, G. V., Andronikashvili, T. G. and Krupennikova, A. Yu., 1969, *Kinetics and Catalysis, USSR*, 10: 1099.
15. Miller, D. N. and Kirk, R. S., 1962, *AIChEJ* 8(2): 183.
16. Noller, H. and Kladnig, W., 1976, *Catalysis Review*, 13: 149.
17. Maurer, J. F. and Sliepcevich, C. M., 1952, *AIChE Prog Symp Ser* 48(4): 31.
18. Butler, J. D., Poles, T. C. and Wood, B. T., 1970, *J Catalysis*, 16: 239.
19. Yue, P. L. and Olaofe, O., 1984, *Chem Eng Res Des*, 62: 81.
20. Birk, R. H., Yue, P. L. and Thomas, W. J., paper to be published.
21. Pines, H. and Manassen, J., 1966, *Advances in Catalysis*, 18: 259.
22. De-Mourgues, L., Peyron, F., Trambouze, Y. and Pettre, M. J., 1967, *J Catalysis*, 7: 117.
23. Bakshi, K. R. and Gavalas, G. R., 1975, *AIChEJ*, 21(3): 494.

ACKNOWLEDGEMENTS

The generous gifts of zeolite from Laporte Industries Ltd. and Norton Chemicals Ltd are gratefully acknowledged. The work was also supported by a Commonwealth Scholarship to one of the authors, O. Olaofe.

ADDRESSES

Correspondence on this paper should be addressed to Dr P. L. Yue, School of Chemical Engineering, University of Bath, Claverton Down, Bath BA2 7AY. Dr Olaofe is now at the Department of Food Technology, The Federal Polytechnic Akure, Nigeria.

The manuscript was received 2 June 1983 and accepted for publication 6 September 1983.

VOL. 62 1984

Book Reviews continued from page 166

Heat Exchanger Design Handbook

Volume 5. Physical Properties.

This volume does not cover correlations for the design itself, but rather those for the physical property parameters relating to the fluids and surfaces involved in heat transfer. The first two sections concentrate on describing some of the predictive methods used to obtain data for pure and mixed fluids where none are available from literature or in-house sources. Not aiming to be exhaustive, the review concentrates on the simpler rules and methods, with the proviso that more elaborate methods, or the services of a data centre, be called upon if accuracy and reliability are required. The descriptions provided are clear and the second section improved by the inclusion of worked examples. The third part covers the interesting area of fluids such as emulsions, lubricants and polymers which exhibit non-Newtonian behaviour; while the following section deals with solid properties, mainly for materials of construction. In both cases prediction is difficult, varies from case to case and can require input harder to come by than the data itself. The authors, therefore, concentrate on obtaining qualitative rather than exact results. The final, and potentially the most useful section, contains numerical data including a range of properties for some 67 fluids. Its weakness is that these seem to have been based on other compilations rather than original references and no assessment is made on accuracy (and some data are known to be in error by as much as 100%). Overall, although each individual section has probably been more extensively covered elsewhere, it is a well presented compilation of physical property data and methods and a useful support tool for the design engineer.

B. Edmonds

BUBBLE SIZE MEASUREMENTS AND CORRELATION IN A FLUIDISED BED AT HIGH TEMPERATURES

By J. F. STUBINGTON (MEMBER), D. BARRETT and G. LOWRY

Department of Fuel Technology, University of New South Wales, Australia

Extensive measurements of bubble sizes have been made in a fluidised bed of electrode carbon at temperatures ranging from ambient to 1000 °C, using a three-dimensional resistivity probe. When compared at constant excess fluidising gas velocity and height above the distributor, the equivalent spherical bubble diameter was found to decrease by 5 to 15% as temperature increased from ambient to about 300 °C and thereafter remained constant up to 1000 °C (within the limits of experimental measurement). For high temperatures (i.e. above 300 °C), a correlation similar to that of Darton *et al.* correctly predicts the effects of excess fluidising gas velocity and height above the distributor on bubble size. Bubble growth in our equipment was slower than their correlation would predict. For the tuyere cap type of distributor plate the shorter penetration of horizontal jets into the fluidised bed at higher temperatures would cause an increase in the number of bubble streams at the distributor and may explain the decrease in bubble size.

INTRODUCTION

A project aimed at investigating the fundamental aspects of fluidised bed gasification of coal-derived chars has been pursued for a number of years in the University of New South Wales Department of Fuel Technology. As part of this project, a study was made of the behaviour of the fluidised bed in the same experimental equipment as used for the gasification experiments, to provide basic fluidisation parameters for use in the analysis of the gasification results. Extensive measurements of minimum fluidising velocity, minimum bubbling velocity, bubble size and bubble rise velocity were made[1,2] at temperatures ranging from 26 °C to 1006 °C. This paper is directed towards a presentation and analysis of the results of bubble size measurement only.

EXPERIMENTAL STUDY

A cylindrical reactor was constructed from 310 stainless steel, with fluidisation chamber dimensions of 102.3 mm diameter by 900 mm high. A stainless steel tuyere cap distributor plate (Figure 1) was used, since problems were encountered with perforated and porous plates. The reactor and preheater for the fluidising gas (nitrogen) were contained within a specially designed furnace, radiantly heated by Crusilite heating rods. Electrode carbon, with its high electrical conductance, was used as the bed material, and the particle size ranged from 250 to 300 μm, with a surface mean diameter of 265 μm. Experimentally measured values of the minimum fluidising velocity are shown in Figure 2 for the full range of temperatures used.

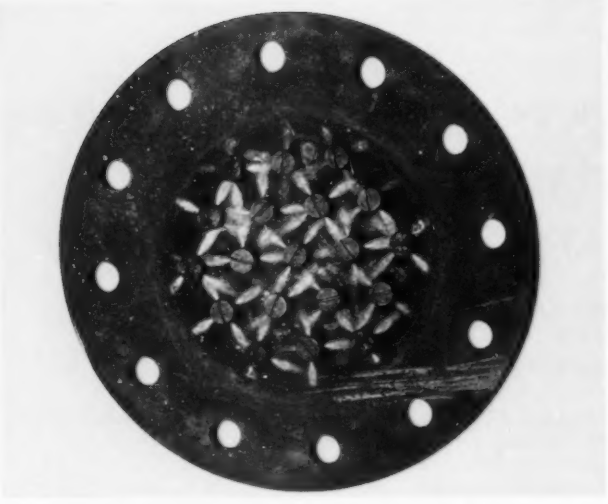
A high temperature resistivity probe was developed to measure bubble properties. This was similar to the three-dimensional probe of Burgess and Calderbank[3], but was constructed from high temperature platinum and ceramic components (Figure 3). A probe, and particularly its supporting stem, inserted into a fluidised bed causes some distortion of the bubbles[4]. Lateral bubble displacement was minimised by arranging the support and tip on the same vertical axis. To minimise distortion of the bubble shape, each of the four probe tips was supported by a small diameter (1.4 mm o.d.) mullite tube projecting 100 mm from the ceramic body supporting the probe. With such a long projection, the effect of the support should be negligible at the probe tips where the measurements were made. The probe tips were small relative to the bubble sizes measured, to minimise the effect of the tips on bubble shape.

Bubble data from the probe were collected and analysed online by a DEC P.D.P. 11/34 computer. With the four-tip probe, bubbles which were not aligned axially on the central (and lower) tip could be rejected. In addition, three other types of bubble encounter with the probe were rejected. First, bubbles smaller than the vertical spacing of the probe tips (5 mm) were rejected because the analysis sequence requires the central probe to be in the bubble when the other probes enter the bubble. Second, bubbles with vertical spacings less than the probe vertical separation were rejected. Third, malformed or erratic bubbles which cause an outer probe tip to re-enter the particulate phase before the central probe tip were rejected.

The two dimensionless discrimination ratios developed by Burgess and Calderbank[3] were used to select those bubbles which were axially aligned with the probe. A series of runs were undertaken with varying discrimination ratios, and the chord height was found to be constant for values down to 0.4. Discrimination ratios of $T^* = t^* = 0.5$ were therefore used in this study to take advantage of the reduced sample time while maintaining a margin for accuracy.

The probe was calibrated in a two-dimensional fluidised bed (205 mm × 440 mm × 15 mm) with a sintered brass distributor plate, which allowed visual obser-

© Institution of Chemical Engineers



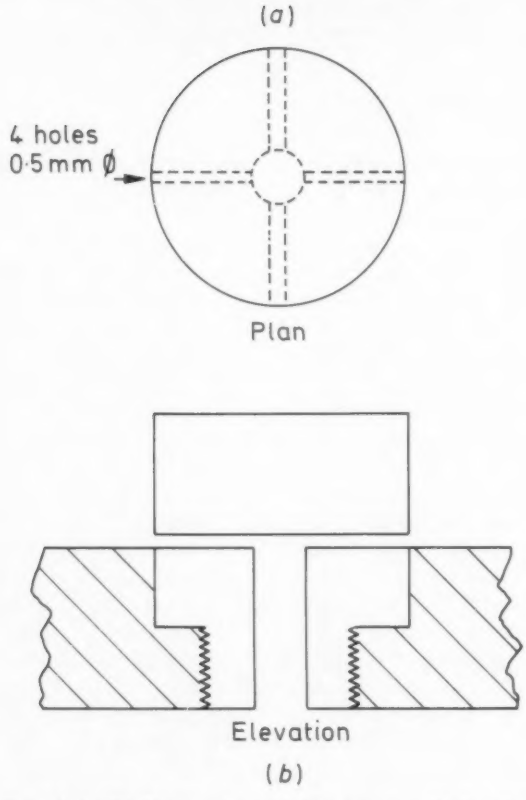


Figure 1. (*a*) Distributor plate with 19 tuyere caps (*b*) Detail of tuyere cap.

vation of the bubbles. The probe was located on the centre-line of the bed and the electrode carbon was fluidised at a little above U_{mf} while a known volume of air was injected into the bed below the probe by means of a syringe. The bubbles produced were of known size and the bubble velocity was measured visually using a stop-watch. Figure 4 compares the bubble height and rising velocity given by the probe with the observed values. From this Figure, it is apparent that the probe accurately measures both bubble size and velocity.

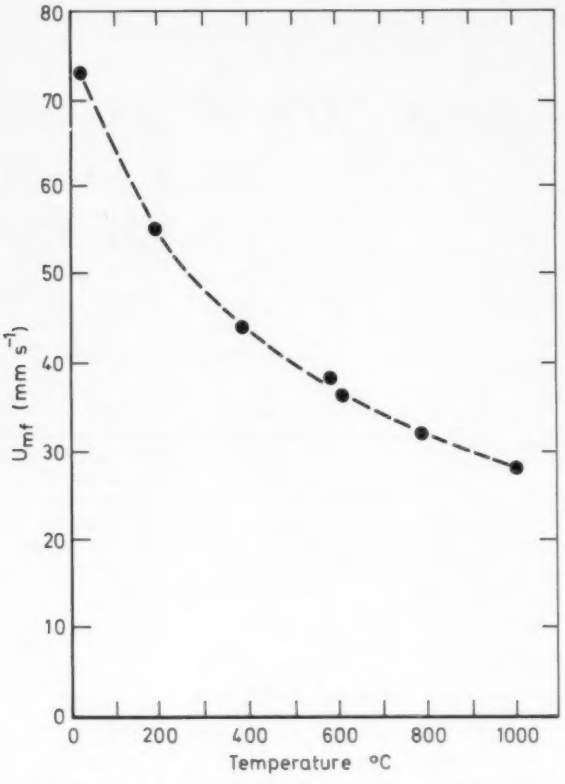


Figure 2. Measured minimum fluidising velocities for electrode carbon, $\bar{d}_p = 265\ \mu m$.

The probe was inserted vertically into the fluidised bed from above and was always positioned at the centre of the bed's circular cross-section. Measurements were made at a number of different heights above the distributor plate by moving the probe axially up and down. For each set of conditions, the central vertical chord lengths of 1000 bubbles were collected. The bubbles were sorted into 81 size ranges starting at 0 and increasing in increments of 2.5 mm up to 200 mm. The resulting histogram was a point distribution, i.e. it gave the

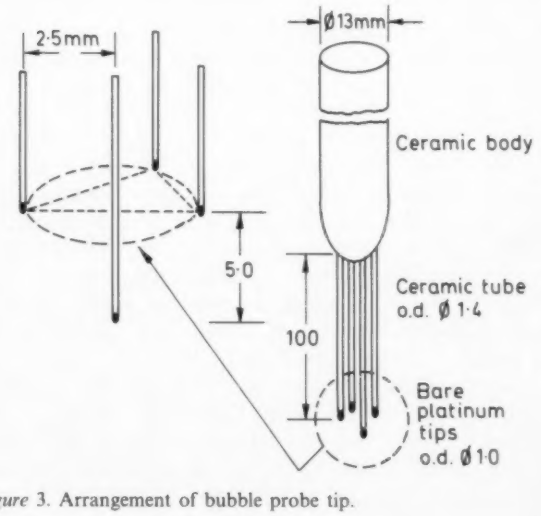


Figure 3. Arrangement of bubble probe tip.

VOL. 62 1984

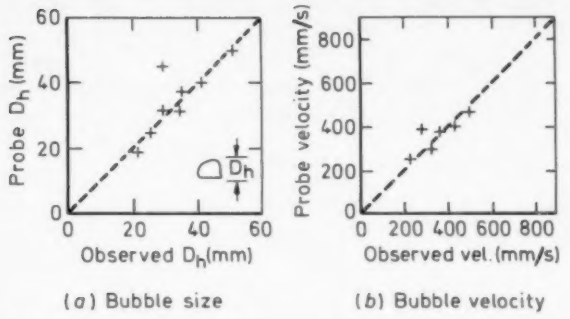


Figure 4. Comparison of probe measurements with observed values.

distribution of bubble sizes at a given point in the bed per unit time. To obtain the bubble distribution per unit bed volume, i.e. the spatial size distribution, the point distribution was corrected for:-

(i) The projected area of the bubble. The probability that a bubble will contact the probe is proportional to this area.

(ii) The bubble velocity. The actual number of bubbles in unit bed volume at any instant is proportional to the rise velocity of the bubble.

Thus, the spatial size distribution for interval i was calculated from the point size distribution by:

$$f_i = \frac{y_i/A_i u_i}{\sum_i y_i/A_i u_i} \tag{1}$$

The surface, volume mean chord height of the overall population was then determined from:

$$\bar{D}_h = \frac{\sum_i f_i D_{hi}^3}{\sum_i f_i D_{hi}^2} \tag{2}$$

A spherical cap shape was assumed for the bubbles, with a wake fraction of 0.17 (as reported by Rowe and Partridge[5]), and the diameter of a spherical bubble with the same volume was calculated to be:

$$D_e = 1.27\,\bar{D}_h \tag{3}$$

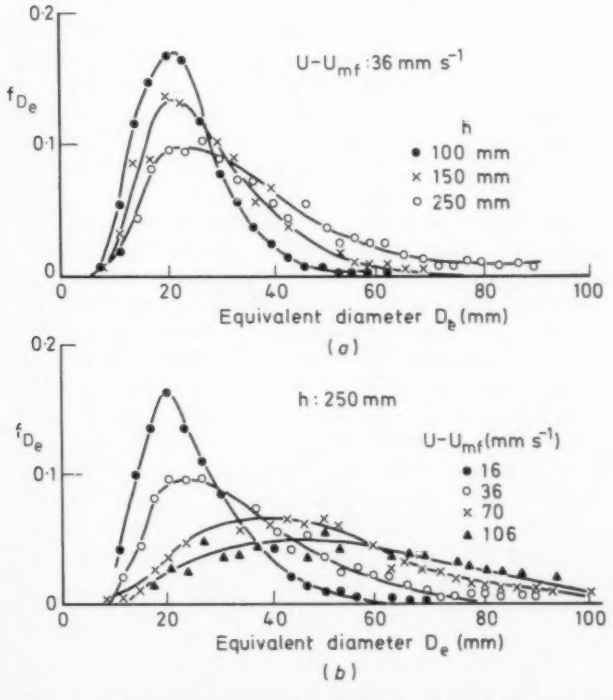


Figure 5. Typical bubble size distributions, $\bar{d}_p = 265\,\mu$m, $H = 310$ mm, Temperature = 793 °C. (*a*) Variation of bubble size distribution with height above distributor. (*b*) Variation of bubble size distribution with excess fluidising velocity.

RESULTS

Typical bubble size distributions are given in Figure 5, and are similar to the distributions found by Burgess and Calderbank[3] and Park et al[6] at ambient temperature. At the higher flow rates, many of the bubbles were in the transition region between free bubbles and slugs, according to the criterion of Hovmand and Davidson[7].

The experimental measurements of average bubble size have been tabulated (Table 1) to show the effect of bed temperature at constant excess gas velocity ($U - U_{mf}$) and constant probe height above the distributor. For high temperatures (i.e. greater than 300 °C), no effect of temperature on bubble size is observed. The fluctuations in bubble diameter measured at these temperatures are of the same order as the reproducibility of the results (see $h = 250$ mm, $U - U_{mf} = 36$ mm s^{-1}, at 793°C). Therefore, the high temperature data have been analysed as a single set.

As the bed temperature increases from ambient to 'high' temperature, the bubble size decreases

Table 1. Measured average bubble size

		Ambient Temperature		Intermediate Temperature		High Temperature	
h (mm)	$U - U_{mf}$ (mm s^{-1})	T (°C)	D_e (mm)	T (°C)	D_e (mm)	T (°C)	D_e (mm)
100	36	26	24.6	197	22.3	397	22.7
		30	24.1			590	21.7
						793	21.9
						1006	22.6
100	70	30	31.2	197	30.5	397	29.6
						590	27.7
						793	28.9
						1006	29.5
150	36	30	28.6	197	25.8	397	26.4
						590	24.6
						793	25.6
150	70	30	38.6	197	34.7	397	33.3
						590	32.2
						793	33.7
250	16	30	26.4	197	24.2	397	24.6
						590	23.7
						793	23.4
250	36	30	33.4	197	31.3	397	32.1
						590	32.2
						793	30.3
						793	32.2
250	70	30	49.4	197	44.9	397	44.9
						590	42.1
						793	43.0
250	106					397	57.6
						793	52.6
300	36	26	40.1				
300	70	26	53.7				

Table 2. Effect of excess gas velocity on bubble size

h (mm)	Values of exponent m in $D_e \propto (U - U_{mf})^m$		
	Ambient Temperature	Intermediate Temperature	High Temperature
100	0.37	0.47	0.40
150	0.45	0.45	0.39
250	0.42	0.41	0.43
300	0.44		

Table 3. Correlation parameters in equation (5), with $n = 0.8$

Temperature (°C)	No. of Points	a	b (mm)	λ	A_0 (mm^2)	No. of bubble streams at distributor
Ambient (26–30)	10	0.471	130.0	1.38	759	10.8
Intermediate (197)	7	0.408	153.2	1.66	735	11.2
High (>300)	26	0.430	127.2	1.55	578	14.2

significantly (for the same h and $U - U_{mf}$). Most of the decrease occurs between ambient temperature and 200 °C, with only a slight decrease from 200 °C to 400 °C. This decrease in bubble size of about 5 to 15% between ambient temperature and 300°C has also been observed by other workers. Geldart and Kapoor[8] concluded that bubbles at 200°C and 300°C were only 75 to 85% of the size of bubbles observed at room temperature. The data of Yoshida et al[9] when replotted using $U - U_{mf}$ as a basis also give similar trends although there are some anomalies. Otake et al[10] implied a similar trend by stating that bubble size was proportional to the inverse of bubble frequency and in turn bubble frequency increased significantly between ambient temperature and 300 °C but remained substantially unchanged thereafter up to 600 °C. However, it should be noted that all of these studies were performed with small particles ($d_p < 500\,\mu$m), and Sitthiphong et al[11] have reported an increase in bubble eruption diameter for large particles ($d_p = 3200\,\mu$m) as temperature increased from 427 °C to 757 °C.

The bubble size at the intermediate temperature (197 °C) is greater than the corresponding mean of the high temperature measurements, for all but one case in Table 1. Since our major interest is gasification (which occurs at high temperatures), the intermediate temperature data have not been included with the high temperature data, but have been analysed separately.

CORRELATION OF EXPERIMENTAL RESULTS

Most recent workers[12-17] have correlated the bubble size with excess gas velocity, as one would expect from the two-phase theory of fluidisation. Within the framework of their basic model, Darton et al[12] show that bubble diameter should be proportional to

$$g^{-x}(U - U_{mf})^{2x}(h + b)^{1-x}$$

as required by dimensional analysis. We have tested the dependence of bubble diameter on excess fluidising velocity by assuming an expression of the form

$$D_e \propto (U - U_{mf})^m \qquad (4)$$

for each height above the distributor and for each of the temperature ranges. The exponent m was determined by linear regression on a plot of $\ln D_e$ against $\ln(U - U_{mf})$, and the results are given in Table 2. (It should be noted that only two points were available for some of the ambient and intermediate temperatures, whereas the high temperature results were obtained from at least six points). Owing to the small number of points and the scatter in the results, the exponent is only significant to one decimal place, so a single value of $m = 0.4$ will be used to fit the experimental results for all temperatures.

Comparison with the correlations of previous workers shows that the correlations of Yacono[15], Darton et al[12] and Bar-Cohen et al for small particle systems[13] predict the same dependence on $U - U_{mf}$ as we have measured. Other correlations generally predict a greater dependence on excess fluidising velocity, with values for m from 0.5 to 0.77.

The correlation of Darton et al was derived by fitting experimental results to determine the value of λ, a constant such that each bubble size in a coalescing stream lives for a height λD_e. The correlation may therefore be viewed as having two constants (λ and A_0) which can be adjusted to fit the experimental results. Accordingly, we have derived correlations of the form

$$D_e = a(U - U_{mf})^{0.4}(h + b)^n g^{-0.2} \qquad (5)$$

for our results over the three temperature ranges. Rosenbrock's hill-climbing method was used to determine the best fit values of a, b and n to minimise the sum of the squared errors between predicted and measured values of D_e. Values of the exponent n from this curve fitting procedure were found to be 0.80, 0.80 and 0.81 for each of the temperature ranges—virtually identical to the value given by Darton et al. Consequently, we have taken the value $n = 0.8$ and the fitted values of a and b are given in Table 3 for each temperature range. (The special case of $b = 0$ was found to give a poorer fit at each temperature than the corresponding correlation in Table 3.).

Comparison of the experimental results with the correlations of Table 3 are given in Figures 6 (*a*)–(*c*) for ambient, intermediate and high temperatures respectively. Reasonable agreement is obtained, with the possibility of underprediction of bubble size at high fluidising velocities and large bed heights. The criteria for slug flow given by Darton et al[12] were used to calculate conditions in our bed when slugging may occur, although these criteria have not been tested at elevated temperatures. At excess gas velocities greater than 70 mm s^{-1} and bed heights greater than 263 mm, slugs may be expected to form in our bed. None of our results were obtained in this slug flow regime, although some conditions were certainly approaching it. It is expected that bubbles measured at excess gas velocities of 70 and 106 mm s^{-1} and at bed heights of 250 mm would be in the transition region from bubbles to slugs. Under these conditions, the spherical cap shape would not be correct and our analysis would generate a larger value of D_e than actually occurred, as may be observed in Figure 6 (*a*)–(*c*).

VOL. 62 1984

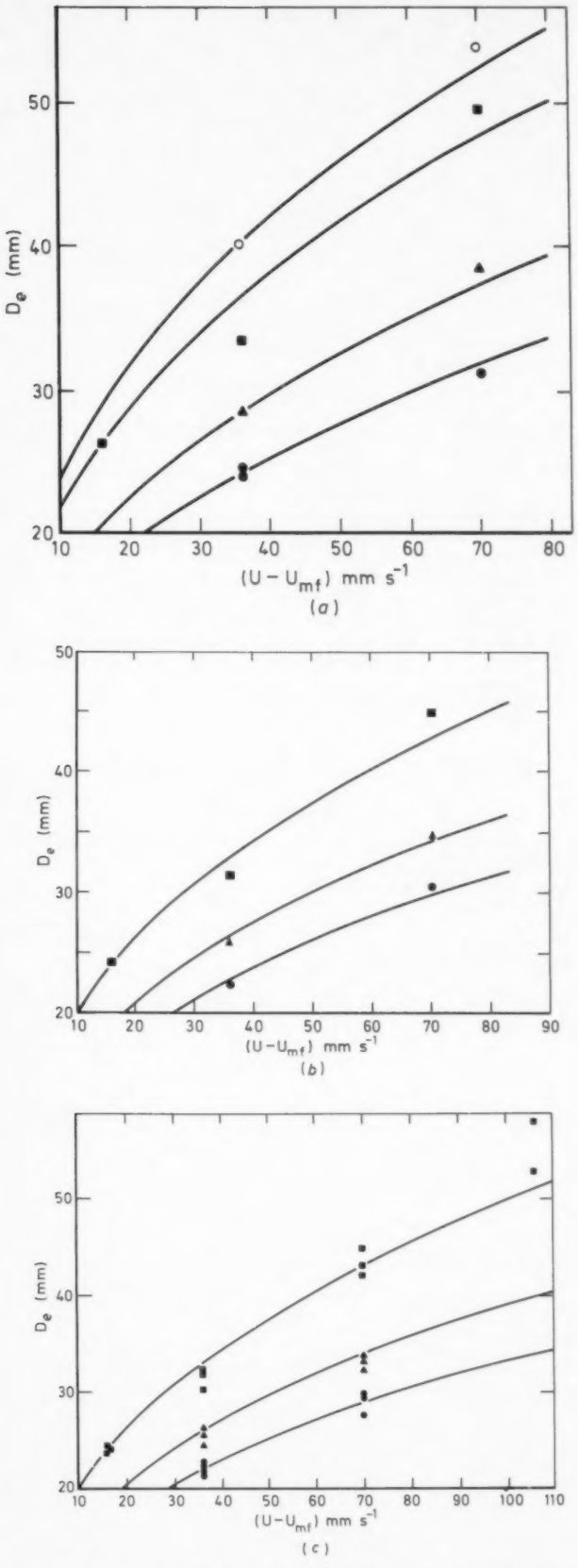


Figure 6. Comparison of bubble size measurements with correlation at (*a*) ambient temperature (*b*) 197 °C (*c*) 300–1000 °C. ● $h = 100$ mm, ▲ $h = 150$ mm, ■ $h = 250$ mm, ○ $h = 300$ mm.

PHYSICAL SIGNIFICANCE OF THE CORRELATION PARAMETERS

From the parameters a and b, the constants λ and A_0 were calculated for a correlation of the same form as Darton et al and are also given in Table 3. The variations in the value of λ are within the range expected from the scatter of our experimental results. The values (1.4 to 1.7) are significantly greater than the value (1.17) given by Darton et al, indicating that the bubbles in our experiments did not grow as quickly as predicted by their correlation. Bar-Cohen et al[13] report some results of Hughes[18], in which λ was found to vary from approximately 0.5 to 2.45 with an average of 1.7. Our results therefore lie within the range of reported values for λ.

Darton et al defined A_0 as the catchment area for a bubble stream at the distributor plate, and so we have used the A_0 values to calculate the number of bubble streams at the distributor for our experiments. (See Table 3.) The effective number of bubble streams at the distributor increases with temperature. However, this number of bubble streams bears no relation to the number of fluidising gas supply points in the distributor. The distributor plate contained 19 tuyere caps with four horizontal jet holes in each, for a total of 76 gas supply jets. Figure 1 clearly shows the interaction between jets from adjacent caps. Thus, it is not surprising that the effective number of bubble streams (10.8 to 14.2) is much less than the number of gas supply points (76).

The observed decrease in bubble size as temperature increases would be a result of the increase in the number of bubble streams at the distributor. This, in turn, may be explained by considering the penetration of horizontal jets into the fluidised bed. From the correlation of Merry[19], the penetration of the jets from the tuyere cap distributor will decrease when the temperature increases, as a result of the lower density and nozzle velocity. (At an excess fluidising velocity of 70 mm s^{-1}, the calculated jet penetration decreases from 11.8 mm at ambient temperature to 2.1 mm at 1000 °C.) Thus, a larger number of bubble streams is formed at the distributor, leading to smaller bubble sizes throughout the bed.

CONCLUSIONS

1. For the small diameter particles (250–300 μm) of electrode carbon used in these experiments, bubble size was found to decrease by 5 to 15% when the temperature was increased from ambient to about 300 °C. Above 300 °C and up to 1000 °C, no measurable change in bubble size occurred. (These comparisons were made at constant $U - U_{mf}$ and constant height above the distributor.)

2. A correlation of the same form as that of Darton et al correctly predicts the effects of excess fluidising velocity and height above the distributor on bubble size. However, the parameter values required to fit the results of this study differ significantly. In particular, values of $\lambda = 1.4$ to 1.7 fitted our results better than the value of 1.17 recommended by Darton et al.

3. For the tuyere cap distributor plate, the effective number of bubble streams at the distributor is much less than the number of gas supply jets, owing to significant interaction between jets. In fact, for the distributor used

in this work, the number of bubble streams at the distributor (10.8 to 14.2) was even less than the number of tuyere caps (19). This number of streams increased with increase in temperature from ambient to about 300°C and thereafter remained constant.

4. The correlation (5) with $a = 0.43$, $n = 0.8$ and with $b = 127.2$ mm may be used to predict the bubble sizes in our equipment for temperatures from 300 °C to 1000 °C. The parameters in such a correlation appear to vary significantly for different designs of experimental apparatus (particularly the distributor). Owing to the interaction between jets at the distributor, the value of the parameter b (or A_0 in the correlation of Darton et al) should be determined by experimental observation rather than estimation from the number of gas supply points in the distributor plate.

NOMENCLATURE

a, b	constants in the bubble size correlation
A_i	projected area of bubbles in size fraction i
A_0	catchment area for a bubble stream at the distributor
$\bar{d}_p$	mean particle diameter
D	bed diameter
D_e	equivalent spherical diameter of bubble
D_h	maximum vertical chord length of a bubble
f_i	spatial frequency distribution of bubbles of size fraction i
g	acceleration due to gravity
h	height above the distributor
H	static bed height
m, n	exponents in the bubble size correlation
T	bed temperature
t^*, T^*	discrimination ratios defined by Burgess and Calderbank[3]
u_i	rise velocity of bubbles in size fraction i
U	superficial fluidising gas velocity, measured at bed temperature
U_{mf}	superficial minimum fluidising gas velocity, measured at bed temperature
x	exponent in the bubble size correlation
y_i	point frequency distribution of bubbles of size fraction i
λ	constant in the bubble size correlation of Darton et al[12].

REFERENCES

1. Lowry, G., 1982, *MSc Thesis* (University of New South Wales).
2. Lowry, G. and Barrett, D., 1980, *CHEMECA 80, Eighth Australian Chemical Engineering Conference*, 109.
3. Burgess, J. M. and Calderbank, P. H., 1975, *Chem Eng Sci* 30: 743 and 1511.
4. Rowe, P. N. and Masson, H., 1981, *Trans IChemE*, 59: 177.
5. Rowe, P. N. and Partridge, B. A., 1965, *Trans IChemE*, 43: 157.
6. Park, W. H., Kang, W. K., Capes, C. E. and Osberg, G. L., 1969, *Chem Eng Sci*, 24: 851.
7. Hovmand, S. and Davidson, J. F., 1971, *Fluidization*, Davidson, J. F. and Harrison, D. eds. (Academic Press, New York and London) p. 195.
8. Geldart, D. and Kapoor, D. S., 1976, *Chem Eng Sci*, 31: 842.
9. Yoshida, K., Fugii, S. and Kunii, D., 1976, in *Fluidization Technology*, Vol. 1, Keairns, D. L. ed. (Hemisphere Books, Washington, D.C.) p. 43.
10. Otake, T., Tore, S., Kawashima, M. and Skibata, T., 1975, *J Chem Eng Japan*, 8(5): 388.
11. Sitthiphong, N., George, A. H. and Bushnell, D., 1981, *Chem Eng Sci*, 36: 1259.
12. Darton, R. C., LaNauze, R. D., Davidson, J. F. and Harrison, D., 1977, *Trans I Chem E*, 55: 274.
13. Bar-Cohen, A., Glicksman, L. R. and Hughes, R. W., 1981, *Int J Multiphase Flow*, 7: 101.
14. Geldart, D., 1972, *Powder Tech*, 6: 201.
15. Yacono, C. X. R., 1975, *PhD Thesis* (University of London).
16. Werther, J., 1976, in *Fluidization Technology*, Vol. 1, Keairns, D. L. ed., (Hemisphere Books, Washington D.C.), p. 215.
17. Rowe, P. N., 1976, *Chem Eng Sci*, 31: 285.
18. Hughes, R. W., 1978, *MS Thesis* (Massachuetts Institute of Technology).
19. Merry, J. M. D. (1971) *Trans IChem*, 49: 189.

VOL. 62 1984

ADDRESS

Correspondence on this paper should be addressed to Dr J. F. Stubington, Department of Fuel Technology, School of Chemical Engineering and Industrial Chemistry, University of New South Wales, Australia 2033.

The manuscript was received 19 May 1983 and accepted for publication after revision 4 October 1983.

EFFECT OF SCALE-UP ON SECONDARY NUCLEATION KINETICS FOR THE SODIUM CHLORIDE–WATER SYSTEM

By P. A. M. GROOTSCHOLTEN, L. D. M. v. d. BREKEL and E. J. de JONG

Laboratory for Process Equipment, Delft University of Technology, The Netherlands

Nucleation rates have been measured for the sodium–water system in crystallisers of different geometry and volume (volumes ranging from 55 litre to 280 m^3, scale-up ratio 1:5000). Nucleation kinetics could be conveniently correlated by a power law model, comprising the speed of the agitator, the solids residence time and the magma concentration within the crystalliser. The effect of scale-up on the nucleation rate constant could be successfully accounted for by the dimensionless impeller number and the diameter of the impeller used.

INTRODUCTION

One of the major headaches in the scale-up of industrial crystallisers is the prediction of nucleation on large scale. From the numerous studies, reported in literature over the past decade, it can generally be concluded that secondary nucleation is the major source of nuclei in industrial crystallisers. Nucleation kinetics have frequently been the object of theoretical and experimental studies. Many authors used their observations to model nucleation kinetics as a function of the operating conditions in attempts to derive scale-up rules for industrial applications. Scaling up of the nucleation process involves understanding of the main mechanisms of nucleation and the way they interfere with crystalliser geometry and scale.

Hydrodynamic interactions between suspended crystals, solution and crystalliser will clearly be important if contact nucleation[1,2] or fluid shear induced secondary nucleation[3,4] is an important mechanism. Theoretical models for secondary nucleation, resulting from contact mechanisms have been developed by a number of authors (Ottens et al.[5], Evans et al[6], Jancic[7]).

From consideration of the hydrodynamics in the impeller area Ottens et al.[5] developed a model describing the variation of nuclei production with the rate of energy transfer to crystals by collision with the impeller. Consideration of crystal–wall collisions led to an equation of a form identical to that proposed for a crystal–impeller collision mechanism. Crystal–crystal collisions were found to result in a second order dependence on magma concentration.

In addition to crystal–impeller collisions driven by steady bulk flow motion Evans et al[6] considered crystal–crystalliser collisions, which were assumed to be driven by turbulent fluid motion. The authors estimated that the relative importance of the bulk flow collisions increased with increasing crystalliser size. Crystal–crystal collisions were assumed to be driven by either gravitational forces or turbulent eddies, the former being more important for the smaller crystals. From experiments in an agitated ice crystalliser and theoretical considerations it was estimated that crystal–crystalliser collisions were more than twice as important as crystal–crystal collisions. Calculations by Evans suggested that the only mechanism dependent on crystalliser size was that of crystal–crystalliser collisions driven by steady agitator bulk flow. The total rate of collisions energy associated with a crystal–impeller impact was found to be proportional to the square root of the agitator diameter, so becoming increasingly important with increasing equipment size.

The concept of a target efficiency has been used by Bauer et al[8], Janic[7] and Nienow[9] to allow for the fact that not all crystals passing the impeller area will undergo collisions. Bauer et al[8] visually observed that larger crystals were more likely to undergo collisions than smaller ones. Similar trends have been reported by Grootscholten et al[10], Ramshaw[11] has demonstrated that the collision frequency between crystals and agitator strongly decreases with increasing agitator size and hence increasing scale of operation, which is in line with suggestions made by Nienow[9]. Ramshaw[11] even suggests that crystal–impeller collisions probably do not represent the main source of nuclei at the plant scale.

The work by Janic[7] suggests that nucleation rates of potash alum as obtained from differently sized draft tube agitated crystallisers are directly proportional to impeller pitch, to the ratio of impeller swept volume and the crystalliser volume, to the 5th power of impeller diameter and that they are inversely proportional to the square of the crystalliser draft tube diameter. The model presented by Janic[7] takes into account the impeller characteristics and hydrodynamic conditions in the impeller area rather than in the whole of the crystalliser (i.e. specific power input).

It has recently been shown by Garside and Davey[12] that the approaches proposed by Ottens[5], Evans[6] and Jancic[7] are actually rather similar. They all show that scale-up on the basis of constant specific power imput should at most produce a modest increase in nucleation rate. Alternatively scale-up on the basis of either constant tip-speed or the particle suspension criteria (Zwietering[13]) is in all cases predicted to result in a decrease in nucleation rate with increasing scale.

© Institution of Chemical Engineers

Bourne and Hungerbuehler[14] described the crystallisation of potash alum in two contoured base tanks of 1.67 and 42 litre capacity. Scale-up at constant tip-speed resulted in a reduction in nucleation rate on scale-up. The magnitude of the reduction was found to be in broad agreement with what is predicted on the basis of crystal–impeller collision mechanism.

A semi-empirical power law relation, describing the nucleation rate of sodium chloride in a pilot scale crystalliser, has been presented by Bennett et al[15]. Nucleation rates, derived from the slope and intercept of the best straight line through their experimental semi-log population density plots, were related to impeller tip-speed, turnover-time of the slurry, growth rate and the fourth moment of the product population density distribution. Interpretation of their results is, however, complicated by pronounced non-linearity in the experimental population density plots and the limited amount of experimental data used to verify the kinetic exponents in their postulated power law relation.

It is due to the complexity of the phenomenon of secondary nucleation that the nucleation models, presented in the literature, are by necessity based on often oversimplified assumptions. They are therefore of restricted practical use and they cannot yet be used for the *a priori* evaluation of the nucleation rate in a large scale crystalliser.

The parameters affecting laboratory size units (up to 100 litre volume) have been partially elucidated but extending this information to the industrial scale (10–500 m^3) requires knowledge of how the individual parameters will be affected by unit size and geometry and this is a complex matter. Experimental data from full scale industrial units to confirm laboratory results are not available in the literature, thus hampering the evaluation of reliable design and scale-up rules for industrial crystallisers.

OBJECTIVES

The experimental work, presented in this paper, was aimed at elucidating empirical scale-up factors for the nucleation rate in forced circulation crystallisers. The evaporative crystallisation of sodium chloride from brine has been used as the vehicle for the experimental study. This system was thought to be reasonably typical of most inorganic aqueous crystallisation systems.

Relying upon comparative studies involving laboratory MSMPR crystallisers (liquor volumes being 55 and 91 litre) as well as a 1.5 m^3 pilot scale model of an industrial external forced circulation crystalliser, it has been attempted to establish the relation between the hydraulic properties of the system and the salt nucleation rate and to derive data, which are relevant to industrial systems. In this latter context results obtained in laboratory and pilot scale configurations have been compared with performance figures obtained in two full scale industrial crystallisers.

EXPERIMENTAL STUDY USING LABORATORY MSMPR CRYSTALLIZERS

An experimental study has been undertaken to elicit the kinetics of sodium chloride crystallisation in attempt to derive scale-up rules for industrial application. The major problem in deriving basic scale-up trends is that observed crystallisation behaviour is often the result of the continuous interaction of mechanisms, which are all differently dependent on the geometry and size of the crystalliser. Contributions of different scale-up factors are then difficult to disentangle. For instance, scale-up according to geometric similarity results in differences in turnover-time of the slurry as well as differences in the dimensions of the agitator. The influence of these individual scale-up factors on nucleation kinetics should actually be investigated independently. Part of the work conducted in the MSMPR crystallisers was aimed at studying the influence of turnover time, impeller diameter and impeller design on the effective nucleation kinetics. These parameters have been independently varied, all other features characterising operation of the crystallisers remaining constant as far as possible. The crystallisers, being of the draft tube–impeller type, were designed so that conditions of mixed suspension and mixed product removal were as nearly as possible achieved.

DESIGN AND CONSTRUCTION OF THE MSMPR CRYSTALLISERS

The design of the crystallisers used for the work was that of a stirred vessel with a draft tube. The crystallisers were of the equal area configuration (i.e. cross sectional area of the draft tube is half that of the vessel). Baffles were used to eliminate vortexing and to straighten out the magma flow. The magma flow was down the draft tube.

The 55 litre vessel was initially used by Asselbergs[17] in a former study. Its outline design has been depicted in Figure 1. Representative and continuous product removal was achieved via a discharge pipe mounted parallel to the main flow path in the vessel draft tube annulus. A series of off-take tubes of different diameter was available to meet iso-kinetic velocity conditions around the off-take point under all relevant conditions. The operating temperature was restricted to 50–55°C by materials of construction and heat transfer characteristics. The hollow draft tube also served as a double pipe heat-exchanger.

The crystalliser shown in Figure 1 has been adapted to an effective liquor volume of 91 litre by extending the length of the draft tube from 800 mm up to 1800 mm, retaining all other features characterising the 55 litre vessel. A more detailed description of the 55/91 litre crystalliser is given by Grootscholten et al[10,16]

Hydraulic Properties of the MSMPR Crystallisers

The MSMPR crystallisers have been operated with impellers of different design and diameters. Considering the influence of hydrodynamics on crystallisation kinetics, a number of hydraulic properties of the various configurations have been established. These included

(i) Pump discharge coefficient

$$K_p = \phi_{vc}/Nd^3 \qquad (1)$$

VOL. 62 1984

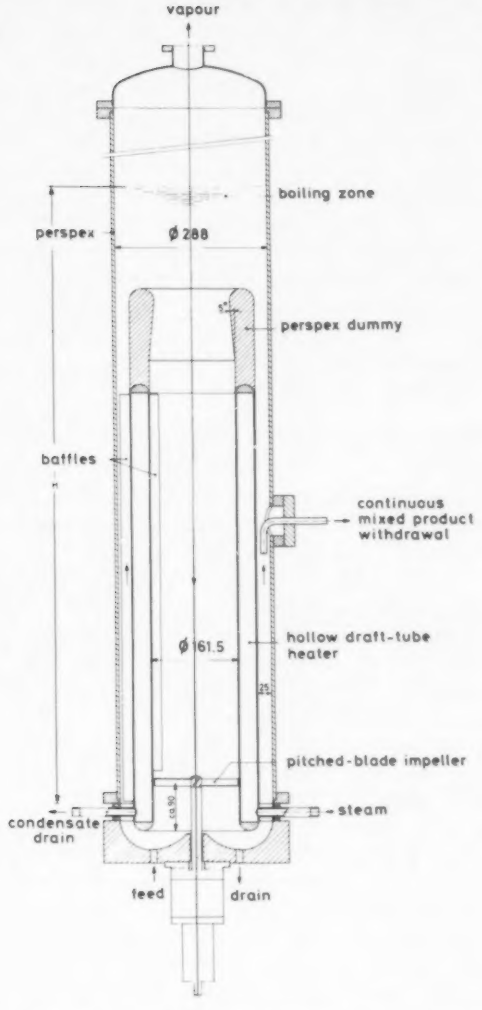


Figure 1. MSMPR crystalliser with internal circulation (55 litre).

where ϕ_{vc} is the circulating flow rate ($m^3 s^{-1}$), N is the impeller speed (rps) and d is the impeller diameter (m).
(ii) Impeller power number

$$P_0 = P/\rho N^3 d^5 \quad (2)$$

where P is the stirred-in power (W) and ρ is the slurry density ($kg\,m^{-3}$).
(iii) Dimensionless impeller number

$$K_{im} = \frac{2\pi N \phi_{vc}^{0.5}}{(g H_m)^{0.75}} \quad (3)$$

where H_m is the total head delivered by the impeller (m H_2O). The impeller number is an appropriate quantity to characterize the performance of the impeller and is related to the specific impeller speed[18].

Experimental techniques and procedures involved in the determination of these hydraulic quantities have been described previously[16,17]. For a 156.3 mm pitch (= one marine propeller used in the 55 litre vessel) the pump constant was found to be 0.52. For various impellers pump constants were determined in the 91 litre vessel. For the 159.0 and 156.3 mm pitched paddles and 156.3 mm marine propeller values of k_p were in the range 0.48 to 0.52. Apparently extension of the 55 litre vessel to 91 litre volume did not affect the flow characteristics, which implies comparable pumping rates at 55 and 91 litre volume. For the 150.5 mm propeller and pitched blade impeller the pump constants were slightly lower, being in the range 0.42–0.45. Boiling was not found to influence the pumping rate. A 120 and 140 mm pitch (= one marine propeller) gave k_p-values of 0.57 and 0.48 respectively.

Table 1. Power numbers as function of impeller design in the 91 litre draft tube crystalliser (internal draft tube diameter 161.5 mm)

Type of impeller	Diameter (mm)	Power number P_0
propeller pitch = one	120.0	0.16
propeller pitch = one	140.0	0.19
propeller pitch = one	150.5	0.24
propeller pitch = one	156.3	0.23
4 bladed pitched paddle	150.5	0.33
4 bladed pitched paddle	156.3	0.35

Power measurements in the 55 litre crystalliser gave a value for the power number P_0 of 0.22 for the 156.3 mm marine propeller (pitch = one). Power consumption measurements have been performed in the 91 litre vessel for various impellers. Results of these measurements are given in Table 1.

For the impellers used in the 55 and 91 litre crystallisers an attempt was made to determine the dimensionless impeller number. For all the impellers the impeller number K_{im} was found to be in the range 11–15, which values reflect that in the studied draft tube vessels the suspension is circulated at a high speed against a relatively low head.

Sampling, Sample Treatment and Sieve Analysis

The crystallisers were normally operated for at least ten residence times to achieve steady state. At the end of each experimental run two samples of approximately 80 g (dry salt) each were taken from the product stream. Before sampling, a small amount of inhibitor (0.5 g ferro-cyanide) was added to the sample flask to minimise changes in the crystal size distribution (CSD) resulting from crystal growth or dissolution during sampling and sample treatment. The carrier brine was removed from the samples by filtering. Then the samples were washed with an ethanol-water mixture and two times with pure di-ethyl ether. The salt crystals were dried under an infra-red lamp. The CSD was measured using sieves. Apertures of the sieves were based on a 74 μm screen and increased by a factor of 2.25 from 44 to 837 μm. Sieve analysis was carried out using a shaking machine. Population density distributions were calculated from the sieve analysis data. Values of the shape factor $k_v = 1$ and crystal density $\rho_s = 2155\,kg\,m^{-3}$ were consistently used in the evaluation of the population densities.

Nucleation and Growth Rates

Most of the experimental nucleation and growth rates, obtained in the MSMPR crystallisers, have been derived using the surface area technique proposed by Scrutton

and Grootscholten[19], rather than from the slope and intercept of the best straight line through the experimental semi-log population density plot[20]. Kinetics derived from the MSMPR equations for the second and third moment of the experimental population density distribution are subject to the assumption that the experimental semi-log population density plot follows a straigh line of which the theoretical second and third moment (representing surface area and respectively magma concentration) are in accordance with the experimentally determined values. In this work crystal surface area has been calculated from the second moment of the experimental population density distribution using a surface area shape factor $k_a = 6$. The magma concentration was determined directly from a sample taken from the product stream from the crystalliser.

Salt Nucleation Kinetics

Earlier work (Scrutton[21], Asselbergs[17]) with a 10 and 55 litre MSMPR crystalliser showed that the crystallisation kinetics of sodium chloride could be conveniently expressed by the relationship:

$$B^0 = k_N N^2 G^2 M \tag{4}$$

where B^0 is the nucleation rate ($\# \, m^{-3} \, s^{-1}$), N is the impeller speed (rps), G is the linear growth rate ($m \, s^{-1}$), M is the magma concentration ($kg \, m^{-3}$) and k_N is the nucleation rate constant ($\# \, s^3 \, m^{-2} \, kg^{-1}$). Similar results were obtained from concurrent work with a 5 and 91 litre MSMPR crystalliser.

For crystalliser design purposes equation (4) can be rewritten in terms of residence time rather than growth rate by eliminating the growth rate between equation (4) and the MSMPR-equation for the magma concentration[20]. This yields:

$$B^0 = 0.023 \, k_N^{0.6} \, N^{1.2} \, \tau^{-1.6} \, M \tag{5}$$

where τ is the crystal residence time (s).

From earlier work (Scrutton and Grootscholten[19]) it was found that the clearance between impeller tip and draft tube wall may have a dominant influence on the nucleation rate rather than process conditions, shape of the impeller or crystalliser scale. With decreasing clearances the crystallisation kinetics of sodium chloride were increasingly dominated by crystal fragmentation as the clearance approached the size of the largest crystals present in the crystalliser. Crystal breakage was found to occur due to crushing of crystals between impeller tip and draft tube wall. Breakage alters the shape of the crystal size distribution and it deteroriates particle size. Such behaviour may be interpreted as enhanced effective nucleation kinetics. The relative importance of the clearance was found to decrease with increasing crystalliser scale[19]. It should therefore be considered as being less relevant to large scale units.

The established influence of the clearance and ensuing change in nucleation mechanism introduces problems with the applicability of kinetic data, obtained from laboratory scale draft tube agitated crystallisers, for the scale-up and sizing of large scale units. If such kinetic data are to be used for scale-up purposes they should at least be determined with sufficiently large clearances between moving and non-moving parts of the crystalliser.

Recent work[10,19] has moreover indicated that the contribution of macro-attribution processes to the development of the crystal size distribution may be reduced by extending the volume of the crystalliser (i.e. slurry turnover time), all other features characterising operation of the crystalliser remaining constant. In this context it should be noted that in the 91 litre no noticeable influence of the clearance was observed for clearances larger than 2.6 mm. In the current course of this paper results obtained with small clearances (smaller than 2.6 mm) will be left out of consideration for reasons mentioned above.

Effect of Turnover Time on Crystal Size Distribution and Nucleation Kinetics

In order to study the effect of turnover time on the rate of nucleation the 55 litre crystalliser, previously used by Asselbergs[17], was adapted to a working volume of 91 litre by extending the length of the draft tube (i.e. length of the circulation pathway) from 800 mm to 1800 mm. To ensure identical impeller–draft tube configuration at 91 litre volume the same marine propeller (pitch = one, diameter = 156.3 mm) was used as in the 55 litre crystalliser. As mentioned previously extension of the liquor volume did not affect the flow characteristics, which implies similar volumetric circulation rates for similar impeller speeds.

Results obtained in both volumes have been previously presented[10,16]. The effect of turnover time on nucleation and growth kinetics is best illustrated by the semi-log population density plots in Figure 2.

Comparison of the crystal size distributions obtained in the 55 and 91 litre crystalliser indicates that for identical impeller speed, residence time and magma concentration the size distributions have similar slopes. This implies that growth rates and, to satisfy the mass balance, the effective nucleation rates are not affected by the scale of operation. The observed differences in population density in the middle range of the above distributions are due to differences in the experimental

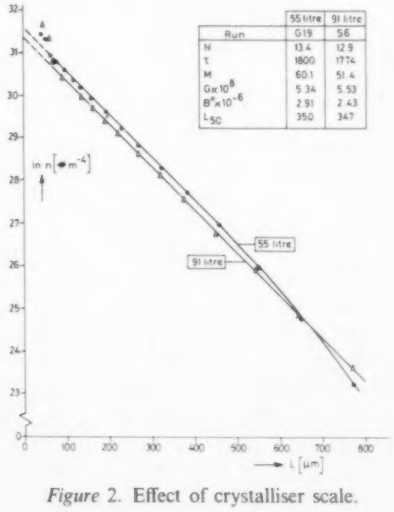


Figure 2. Effect of crystalliser scale.

VOL. 62 1984

magma concentrations. It can further be seen that for approximately the same operating conditions the size distribution from the 91 litre crystalliser exhibits less curvature downwards in the large size range. Also less rounding of the crystals was observed. It will be obvious that the state of rounding of a crystal is dominated by the number of impacts exerted on that particular crystal as well as the impact energy. A longer turnover time will then reduce the circulation frequency and hence the chance of a crystal to get involved in degradation processes in the impeller area. Results obtained in both volumes have been correlated by the power law relation $B^0 = k_N N^2 G^2 M$. The good quality of the fits suggests that the kinetic exponents are not affected by the scale of operation. For both scales kinetic data, obtained from the slope and intercept of the semi-log population density plot, could be described by the relation:

$$B^0 = 8 \times 10^{16} N^2 G^2 M \quad (6)$$

where the regression coefficients R^2 are 0.98 and 0.99 for the 55 and 91 litre results respectively.

The results indicate that turnover time is not an important factor in the scale up of the studied sodium chloride crystallisers. A slight difference in nucleation constant appears when the effective kinetic rates are derived by the surface area technique. It appears that the 55 litre volume generates a slightly higher crystal surface area for the same operating conditions compared to the 91 litre volume. According to the surface area technique this results in slightly lower growth rates and higher nucleation rates resulting in a slightly higher nucleation constant. Resulting k_N-factors are:

$k_N = 9 \times 10^{16}$ for 55 litre volume ($R^2 = 0.98$)
$k_N = 8 \times 10^{16}$ for 91 litre volume ($R^2 = 0.99$)

The generation of extra surface area is due to the fact that with increasing degradation rates the size distribution is increasingly hampered to develop in the larger size ranges where degradation processes are most intensive. The mass balance constraint then forces the system to distribute the crystallised mass over a greater number of smaller particles, regardless of the mechanism by which these extra particles are formed. It is not difficult to see that small particles represent a larger surface area per unit mass than large ones.

Effect of Impeller Design on Effective Kinetics

Part of the work conducted in the MSMPR crystallisers was aimed at studying the relation between impeller design and nucleation rate. Considering the findings with respect to the impeller–draft tube clearance it will be obvious that the influence of impeller design on the effective kinetics should at least be studied with sufficiently large clearances.

To elucidate the relation between impeller design and kinetics additional experiments have been performed in the 91 litre MSMPR crystalliser. Values of the nucleation rate, growth rate and operating conditions have been presented by Grootscholten et al[10,16]. To provide a quantitative basis of comparison the effect of impeller design has been quantified in terms of the nucleation rate constant k_N, which has been defined by the relation $B^0 = k_N N^2 G^2 M$. Results obtained with the various impellers are presented in Table 2. The results obtained with the marine propellers and pitched blade impellers show that the effect of impeller design on the crystallisation kinetics of sodium chloride is much less pronounced than initially suggested on basis of results obtained in the 55 litre crystalliser as described by Asselbergs[17] and Grootscholten et al[10].

Table 2. k_N-values as function of impeller type

Impeller type	Diameter (mm)	Radial clearance (mm)	$k_N \times 10^{-16}$ ($\#s^3\ kg^{-1}\ m_i^{-2}$)
marine propeller pitch = one	150.5	5.5	7
pitched blade impeller	150.5	5.5	11
marine propeller pitch = one	156.3	2.6	8
pitched blade impeller	156.3	2.6	11

Since the pumping capacities of the impellers mentioned in Table 2 were approximately the same, giving the same axial velocities and circulation times for the same impeller speed, it is clear that the difference in observed effective kinetic rates may be primarily attributed to the design of the used impellers. This could indicate that crystal–impeller collisions play a role in the formation of secondary nuclei. The linear relation between nucleation rate and magma concentration argues in the same direction.

Alternatively differences in nucleation characteristics of the two types of impellers could perhaps be explained by differences in abrasion and breakage intensity, induced by the shape of the impeller. This speculative suggestion is supported by the observed degree of rounding of the large crystals, which was higher for the pitched blade impellers. Moreover the size distributions obtained with the pitched blade impellers exhibited somewhat more curvature downwards in the large size range, resulting in slightly lower coefficients of variation compared to the marine propeller results. These findings are indicative of higher crystal degradation rates caused by the pitched blade impellers. Abrasion and breakage alter the shape of the size distribution and deteriorate particle size, which is interpreted as increasing nucleation rates. The influence of degradation processes on the produced crystal size distribution may then have been camouflaged in the derived nucleation rate constants, which are highest for the pitched blade impellers.

After all it may be concluded that the design of the impeller is not an important factor in the successful product crystal size control in the investigated crystalliser (differences less than 6% in product median size). In view of the above findings it needs no argument to state that the importance of crystal–impeller collisions as principal source of secondary nuclei has to be reconsidered.

Influence of Hydrodynamics on Nucleation Kinetics

From the kinetic data obtained from the various MSMPR crystallisers it has been found that the nucleation rate of sodium chloride is proportional to the square of the impeller speed. This conclusion, however, leaves us with no clear idea with what parameter the rate

of nucleation should be correlated in order to proceed properly with increase in scale.

The difference between the nucleation rate constants, obtained with the 156.3 mm impellers is appreciably reduced if nucleation rates are related to specific power input rather than impeller speed. Using the power numbers reported in Table 1 the nucleation rate equation (8) can be rewritten in terms of the specific power input ε ($\varepsilon = P_0 N^3 d^5/V$) as:

marine propeller:

$$B^0 = 2.0 \times 10^{19} \varepsilon^{2/3} G^2 M \tag{7}$$

pitched blade impeller:

$$B^0 = 2.1 \times 10^{19} \varepsilon^{2/3} G^2 M \tag{8}$$

The above results tentatively suggest that in the 91 litre crystalliser the influence of impeller design may be adequately represented by the specific power input, i.e. the impeller power number. Apart from slight differences in the exponents of ε this is in broad agreement with what is predicted by Ottens[5], Evans [6] and Jancic[7]. A nucleation rate equation very similar to equations (7) and (8) has been reported by Beer and Mersmann[22] for the KCl–water system, of which the kinetics were determined in a 6 litre MSMPR crystalliser.

Specific power input, however, does not seem appropriate to correlate the data obtained from the 55 litre crystalliser using the 156.3 mm marine propeller. As power number was not significantly affected by the volume of the crystalliser, the specific power input in the 55 litre vessel is approximately a factor 95/55 higher than in the 91 litre vessel provided the same impeller speed and slurry densities. As the nucleation rate constants k_N were not affected by the scale of operation (i.e. length of the draft tube) correlation of nucleation rates from the 55 litre vessel results in a lower value of the proportionality constant, being 1.6×10^{19}, than found for the 91 litre results.

Results from the 55 and 91 litre vessel can be conveniently described by the equation:

$$B^0 = 1.0 \times 10^{20} (P_0 N^3 d^5)^{2/3} G^2 M \tag{9}$$

in which nucleation rates have been related to power input rather than specific power input. These findings could suggest that power input should be related to a volume where power dissipation rates are highest (e.g. areas of flow inversion, boiling zone and area around the impeller) and not to the whole volume of the crystalliser. This suggestion is in line with the nucleation model of Jancic[7], which takes into account the impeller characteristics and hydrodynamic conditions in the impeller area rather than the whole of the crystalliser.

Whether power input is the appropriate quantity to account for the influence of hydrodynamics cannot yet be concluded, as power input has only been varied by the power number and speed of the impellers. Information about the parameter to be correlated can be obtained from experiments with impellers similar to those already studied, but with different diameter. Such experiments should on correlation with power input, provided that this is warranted, give the following proportionality between the rate of nucleation and the diameter of the impeller:

$$B^0 \alpha \propto d^{3.3} \tag{10}$$

By the choice of an impeller the attempt should be made to keep the power number P_0 and the pump discharge coefficient k_p as constant as possible, so that in the interpretation the results can always be related on the same basis of comparison.

Influence of Impeller Diameter on Nucleation Kinetics

To study the effect of impeller diameter, the 91 litre MSMPR crystalliser has been operated with pitch = one marine propellers of different diameters, namely 120.0, 140.0, 150.5 and 156.3 mm respectively. In order to improve the performance of the 120.0 mm propeller the 161.5 mm draft tube was narrowed by suspending a specially profiled perspex ring with an internal diameter of 125.2 mm at a height corresponding to the tip of the impeller (resulting radial clearance 2.6 mm). From flow measurements the pump discharge coefficients of the 120.0 and 140.0 mm propellers were found to be 0.57 and 0.48 respectively. The power numbers were 0.16 and 0.19 respectively. Unfortunately these values slightly differ from the values of the 156.3 mm equivalent, which *a priori* hampers the ultimate interpretation.

Operating conditions were varied over the ranges $\tau = 1430 - 2896$ s, $N = 7$–17 rps and $M = 35$–70 kg m^{-3}. A listing of resultant values of B^0, G and operating conditions have been presented by Grootscholten[16]. Curve fitting of the data obtained by the surface area technique showed that for all the propellers the nucleation rates could be conveniently correlated by the relation:

$$B^0 = k_N N^2 G^2 M \tag{10}$$

as found previously. Apparently the kinetic exponents have not been affected by the size of the impellers used. Resulting values of the nucleation rate constants are given in Table 3. Values of k_N have been presented as function of the impeller diameter in the double log plot in Figure 3. From the slope of the straight line in this figure it can be inferred that correlation of k_N with d comes to the tentative proportionality:

$$k_N \propto d^3 \tag{11}$$

which is not very different from what was expected to result from correlation of the nucleation rate with power input. It is, however, important to note that pump discharge coefficient and power number could not be kept constant. Their possible influence may have been camouflaged in the order of the nucleation constant–impeller diameter dependence.

Table 3. Nucleation rate constants as a function of the impeller diameter

Impeller diameter (mm)	$k_N \times 10^{-16}$ (#s^3 m^{-2} kg^{-1})
120.0	3.5
140.0	5.6
150.5	7
156.3	8

VOL. 62 1984

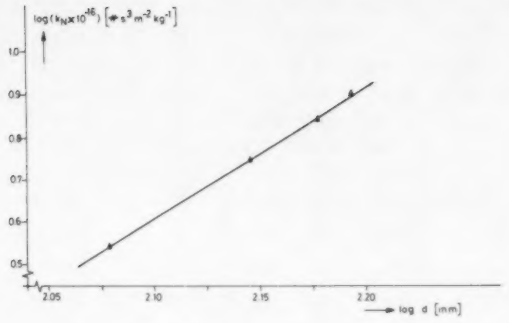


Figure 3. Effect of impeller diameter on nucleation rate constant.

If nucleation rates obtained with the 120.0 and 140.0 mm propellers are related to power input, the resulting proportionality constants (being 1.4×10^{20} and 1.2×10^{20} respectively) considerably differ from the value obtained for their 156.3 mm equivalent (being 1.0×10^{20}, see equation (9)). This indicates that power input is not the appropriate quantity to describe the influence of power number, impeller speed and impeller diameter. So far these results have to be considered as being inconclusive.

In addition to the diameter-variation an independent variation of P_0 and k_p is also possible. Variation of diameter, having regard to its practical feasibility and the accuracy with which P_0 for example can be determined, initially seemed to be the most attractive procedure. So as to arrive at a correct impression of the parameter with which the hydrodynamics in the vessel are to be related in the description of secondary nucleation, very systematic experiments should be performed, varying only one of the relevant parameters and keeping all others characterizing hydrodynamics of the system constant.

EXPERIMENTAL NUCLEATION STUDY ON PILOT PLANT CRYSTALLISER

Nucleation and crystal growth have frequently been the object of theoretical and experimental work under conditions which are highly oversimplified and very often remote from industrial relevance. This means that most experimental studies have been orientated to the derivation of crystallisation kinetics at conditions where the level of driving force was carefully controlled and where population events, other than nucleation and crystal growth, were suppressed. In an industrial configuration, however, solid/liquid contacting and transport of materials through the crystalliser cannot be established without simultaneous occurrence of additional population events. The main motivation in this research has been to gain understanding of mechanisms and kinetics of such population events in terms of solids residence time distribution, liquid maldistribution and by considering crystal–crystal and crystal–crystalliser interactions. There are no published data on these population events obtained under realistic conditions and expecially in large scale crystallisers. It has been the object of the pilot plant work to define the controlling population events and to put them in a form suitable for

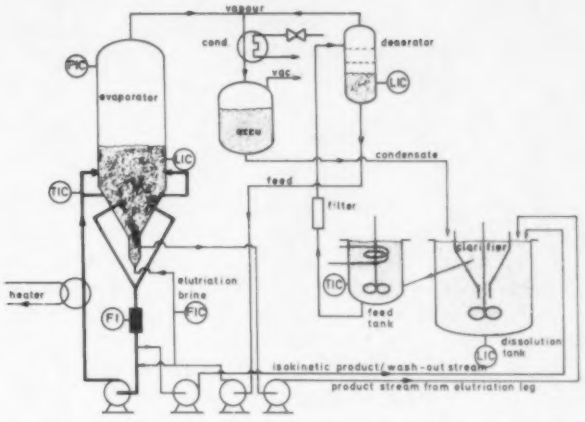


Figure 4. Pilot plant crystalliser and ancillary equipment.

combination with crystallisation kinetics in order to be able to formulate design and scale-up strategies. The experimental pilot plant work, described in this paper, was primarily aimed at elucidating factors affecting the nucleation rate in a large scale crystalliser. The experimental work was performed in a 1500 litre, 10 ton/day capacity model of an industrial external heater forced circulation evaporative crystalliser. The semi-technical unit was designed so that the crystallisation behavior of its industrial equivalent was appropriately reproduced.

Description of Pilot Scale Crystalliser

The crystalliser, used for the work, featured a double radial inlet according to the design of a full scale production crystalliser used by ICI at the Weston Point salt works. A schematic diagram of pilot scale crystalliser and ancillary equipment has been depicted in Figure 4. Two downwards directed outlets were mounted to recycle the circulating slurry to the calandria. Circulation of the slurry was achieved by a variable speed axial flow pump (Begemann Ltd). The impeller diameter was 159.1 mm, giving a radial clearance of 1.5 mm. From consideration of the relatively long turnover times in the pilot crystalliser (50–150 s against 2–5 s for the 91 litre MSMPR crystalliser) as well as the absence of large crystals (largest crystals being about 900 μm) this clearance of 1.5 mm is thought not to influence effective nucleation kinetics. The external loop was characterised by a power number of 0.80 and a pump discharge coefficient of 0.27. The dimensionless impeller number K_{im} as defined by equation (3) was found to be about 4.2. The circulating magma was heated up in a single shell-and-tube heat-exchanger by low pressure steam. The bottom cone of the evaporator body was fitted with an elutriation leg to withdraw the product from the system. Alternatively product could be withdrawn isokinetically from the circulation mains (vertical part between magnetic flowmeter and axial flow pump).

Crystallisation Experiments

Continuous crystallisation experiments were carried out over a wide range of operating conditions. Magma

Table 4. Operating conditions

magma concentration in circulation mains	100–200 kg m^{-3}
circulation flow rate	45–75 m^3 h^{-1}
liquor volume	1.00–1.80 m^3
vapour production rate	0.06–0.17 kg s^{-1}

concentration (measured in the circulation mains), liquor volume, circulation flow rate (i.e. impeller speed) and vapour production rate have been varied. The ranges of variation are given in Table 4. The operating temperature was approximately 55°C. For each experiment the crystalliser has been operated for not less than 10 solids residence times to ensure steady state. Population density data and cumulative numbers oversize distributions were derived from sieve analysis data. It was due to significant non-linearity of the semi-log population density distributions that nucleation rates were determined from the cumulative numbers oversize distributions using the equation:

$$B^0 = \frac{1}{\tau}\int_0^\infty n \, dL \tag{12}$$

where τ is the draw-down time which is defined as V/ϕ_{vp}. Extrapolation to zero size has been made by drawing a straight line from $\ln n$ at $L = 44\,\mu$m (smallest average sieve size) to $L = 0$ with a slope equal to $d \ln n/dL$ at $L = 44\,\mu$m. Integration of the resulting population density distribution according to equation (12) gives an effective nucleation rate, which is subjected to the assumption that nuclei are born at zero size and grow at a constant rate, being G (44), to size $L = 44\,\mu$m. A typical semi-log population density plot is shown in Figure 5.

Nucleation rates were in the range 0.3×10^6–2.0×10^6 # m^{-3} s^{-1}. These are of the same order of magnitude as those reported by Bennett et al[15] and they are not very different from values obtained in the laboratory MSMPR crystallisers.

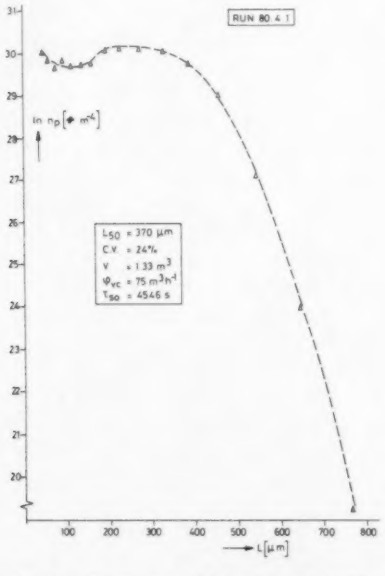


Figure 5. Crystal size distribution obtained in pilot plant crystalliser.

The crystallisation experiments have revealed that classification of solids occurs in the studied crystalliser. Classification may be attributed to segregation in the evaporator body as well as to a hydrodynamic selection process in the neighbourhood of the product removal point. Phenomena of classification lead to a difference in residence time of crystals and solution, the former being a function of size. Identification of classification mechanisms is discussed elsewhere[16,17]

Nucleation Rates Obtained in Pilot Plant Crystalliser

Correlation of Experimental Data

From consideration of kinetic results, obtained in the various MSMPR crystallisers it was thought that a power law relation of the same form as that of equation (5) could perhaps be used to correlate the experimental nucleation rates obtained in the pilot scale crystalliser. Considering occurring solids classification this relation should then contain the overall solids residence time τ_{so} and the cup-mixing magma concentration M_c, rather than liquid residence time and magma concentration in the product stream. Both quantities have been evaluated from so-called wash-out experiments. The technique relied upon wash-out transients and these involved experiments with the salt/brine system. Details have been given by Grootscholten[16]

Curve fitting showed that the experimental results obtained from the pilot scale crystalliser could indeed be correlated by the power law relation:

$$B^0 = 0.023\, k_N^{0.6}\, N^{1.2}\, \tau_{so}^{-1.6}\, M_c \tag{13}$$

whereby k_N was found to be 5×10^{15} (# s^3 m^{-2} kg^{-1}). A graphical representation of this relation has been depicted in Figure 6. The reasonable quality of this correlation (regressin coefficient $R^2 = 0.979$) tentatively suggests that the applicability of the power law relation used is not restricted to the relatively simple MSMPR-configuration. The derived nucleation relation apparently has general applicability for sodium chloride as long as the relation contains the appropriate quantities. The present findings moreover indicate that in a comparatively large pilot scale until the same kinetic laws are valid as have been established in the small-scale MSMPR-units.

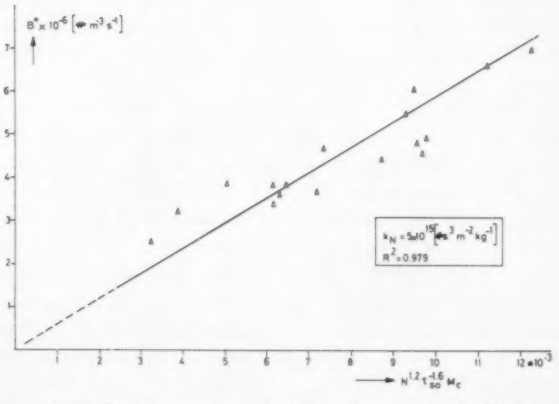


Figure 6. Nucleation rates as a function of process variables in pilot scale crystalliser.

VOL. 62 1984

Nucleation Rate Constant for Pilot Scale Unit Axial Flow Pump

The nucleation rate constant k_N, as defined by equation (13), was estimated at 5×10^{15}, which is considerably lower than values obtained with the 156.3 mm marine propeller and pitched blade impeller in the 91 litre MSMPR crystalliser (8×10^{16} and 11×10^{16} respectively). Initially this difference in nucleation rate constant was thought to be caused by differences in the design of the impellers. To verify this presupposition the 91 litre MSMPR-unit has been operated with the axial flow pump impeller from the pilot scale unit. For this purpose the impeller was trimmed off from 159.1 mm to 156.3 mm to give a radial clearance of 2.6 mm. Crystallisation experiments performed with this impeller gave a k_N-value of 13×10^{16}, which is, unexpectedly, a 26-fold increase compared with the value obtained with the same impeller in the pilot scale unit. Low values of coefficient of variation (ranging from 40–45%) as well as the presence of highly rounded crystals in the large size fractions indicated that abrasion affected the size distribution to a large extent. At conditions of mild agitation and low residence times ($N = 7$ rps and $\tau = 1800$ s) the larger crystals became more cubic and coefficient of variation values up to 48% were obtained.

From reconsideration of operation of both units it has been concluded that the substantial difference in nucleation rate constant is due to differences in the hydraulic characteristics of the internal circulation MSMPR crystalliser compared with the external circulation pilot scale unit. In the latter the magma is circulated against much higher heads compared to the draft tube units. This difference in hydraulic characteristics may be quantified in terms of the dimensionless impeller number K_{im}, being 4–6 for the circulator of the pilot unit and approximately 11–15 for the used impellers in the draft tube crystalliser. Implication is that impeller speeds, required to achieve comparable slurry velocities are higher in the pilot scale unit (approximately factor 2) than in the draft tube unit. As nucleation rates, which have been related to impeller speed were roughly of the same order of magnitude, the mathematics of equation (13) results in a lower proportionality constant for the external circulation unit.

To further elucidate the influence of hydraulics of the circulation loop, additional pilot scale experiments have been carried out in the final stage of the project. This involved experiments in which the internal resistance of the circulation loop was changeable by means of a 15 cm (6 inch) rubber-lined diaphragm valve at the pressure side of the circulation pump. This value enabled the dimension-less impeller number to be varied from 6.6 (fully open valve) down to 3.4 (75% closed valve). The pump constant k_p reduced from 0.32 to 0.12. Table 5 shows k_N-values obtained for different valve positions (fully open, 50 and 75% closed). Nucleation rate constants were calculated from experimental values of the nucleation rate, impeller speed, overall solids residence time and cup-mixing magma concentration, using equation (13). The k_N-values given in Table 5 are average values based on not less than three independent experiments. The data in this table clearly show a reduction in nucleation rate constant with decreasing impeller number K_{im}. Results obtained from the 91 litre draft tube vessel are in line with these results ($K_{im} = 11$–15, $k_N = 8$–13×10^{16}).

Table 5. Nucleation rate constant for different hydraulic properties of the circulation loop

Exp. no.	Valve position	p_0 (−)	K_p (−)	K_{im} (−)	k_N (#s^{3}m^{-2}kg^{-1})
1	fully open	0.85	0.32	6.6	1.5×10^{16}
2	50% closed	0.81	0.29	4.7	1.0×10^{16}
3	75% closed	0.75	0.12	3.4	0.4×10^{16}

The results in Table 5 can more conveniently be interpreted on the basis of a predefined similarity between the three systems. So it can be inferred from equation (13) that for the same circulating flow (i.e. $k_p N d^3$ is constant), overall solids residence time and cup-mixing magma concentration the 75% closed valve gives rise to a 1.4-fold increase in nucleation rate compared to the fully open valve. In formula:

$$\frac{(B^0)_3}{(B^0)_1} = \left(\frac{k_{N3}}{k_{N1}}\right)^{0.6} \left(\frac{k_{p1}}{k_{p3}}\right)^{1.2}_{\phi_{vc}} = 1.4 \qquad (14)$$

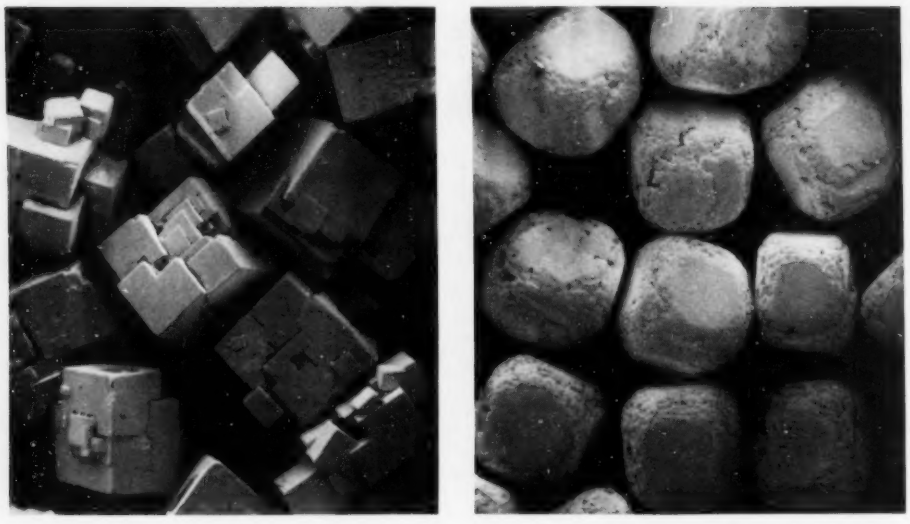
This increase in nucleation rate is to be attributed to the 2.6-fold increase in impeller speed (to achieve the same slurry-velocities) as well as enhanced friction in the valve. Microscopic examination of the product crystals showed that the large crystals obtained with the 75% closed valve were considerably more rounded than crystals obtained with the fully open valve. Moreover, over the whole size range the product crystals obtained at the high impeller speed exhibited a much lower degree of polycrystallinity than crystals obtained under open valve conditions (low impeller speed). The effect of impeller speed on crystal shape is shown by the photomicrographs in Figure 7.

It probably needs no argument to state that from a dewatering and drying point of view a low degree of polycrystallinity is desirable. This permits us to state that a slight degree of macro-attrition is not unfavourable if a good crystal habit product with a low degree of polycrystallinity is desired. Whether abrasion and simultaneous growth reduces crystal purity is not likely, but should be further examined.

From the data in Table 5 it can further be deduced that for the same impeller speed, overall solids residence time and cup-mixing magma concentration the open valve system produces 2.2 times more nuclei than the 75% closed valve system, which is the result of a 2.6 fold increase in circulating flow rate.
In formula:

$$\frac{(B^0)_1}{(B^0)_3} = \left(\frac{k_{N1}}{k_{N3}}\right)^{0.6}_N = 2.2 \qquad (15)$$

The results obtained on the basis of equations (14) and (15) tentatively suggest that volumetric through-put and hence slurry-velocity is more decisive for secondary nucleation rather than impeller speed itself. This suggestion is in line with findings of Van't Land and De Waal[24] and Van't Land and Wienk[23], who reported that mean crystal size (and hence effective nucleation kinet-



(*a*) (*b*)

Figure 7. Crystal shape for constant circulating flow rate but different impeller speeds. ($\phi_{vc} = 48\ m^3\ h^{-1}$, $V = 1.33\ m^3$, $\tau = 3860\ s$, $\phi_{mv} = 0.10\ kg\ s^{-1}$, $M = 50\ kg\ m^{-3}$). (*a*) 13.2 *rps*, 498 μm. (*b*) 30 rps, 498 μm. Magnification is 40×.

ics) obtained in an internal circulation crystalliser was greatly affected by velocity in the heater tubes rather than by the tip-speed of the impeller (both velocities were independently varied).

Empirical Correlation

In addition to the interpretation in the former section nucleation rate constants have been collected for different crystallisers, in volume ranging from 55 litre to 280 m^3 (scale-up ratio 1:5000). The various crystallisers have all been operated at temperatures ranging from 50 to 60°C. Values of k_N, hydraulic properties of the various systems and diameters of the impellers have been listed in Table 6. It should be noted that the k_N-values estimated for Western Point No. 3 Evaporator (ICI plc) and a large scale Swanson–Escher Wyss design evaporator (AKZO Ltd) are based on limited experimentation. Nevertheless these k_N-values have great statistical value due to the size of these units (280 and 121 m^3 respectively).

It has been attempted to correlate the results in Table 6 by mathematical relations using least-squares techniques. The nucleation rate constants were best correlated by the relation:

$$k_N = 0.9 \times 10^{16}\, K_{im}^{2.25}\, d^2 \qquad (16)$$

The regression coefficient R^2 was 0.972 and suggests a reasonable quality of the fit. This equation does not include the radial clearance between impeller tip and draft tube, since the results obtained with small clearances were not considered to have significance for scale-up purposes. A graphical representation of equation (16) is given in Figure 8. The form of equation (16) suggests that impeller diameter and dimensionless impeller number are decisive parameters in determining the nucleation rate constant. For a given impeller speed these quantities determine the pumping capacity of the impeller slurry circulation pump. The second order dependence on diameter deviates from what was suggested on basis of experiments in the 91 litre crystallizer ($k_N \propto d^3$). This is possibly due to apparent covariance among the variables in equation (16). Moreover, the influence of impeller number could have been camouflaged in the third order dependence previously suggested by equation (11). If equation (16) is to be used

Table 6. Nucleation rate constants for different crystalliser configurations

Crystalliser	Volume (m^3)	Impeller type	Diameter (m)	P_0 (−)	k_p (−)	K_{im} (−)	$k_N \times 10^{-16}$ (#$s^3\ m^{-2}\ kg^{-1}$)
MSMPR	0.055	marine propeller	0.1563	0.22	0.52	13.1	8
MSMPR	0.091	marine propeller	0.1200	0.16	0.57	11.5	3.5
MSMPR	0.091	marine propeller	0.1400	0.19	0.48	14.5	5.6
MSMPR	0.091	marine propeller	0.1505	0.24	0.45	15.2	7
MSMPR	0.091	marine propeller	0.1563	0.23	0.52	13.2	8
MSMPR	0.091	pitched paddle	0.1563	0.35	0.48	14.5	11
pilot unit	1.33	axial flow pump	0.1563	0.85	0.32	6.6	1.5
pilot unit	1.33	axial flow pump	0.1563	0.81	0.29	4.7	1.0
pilot unit	1.33	axial flow pump	0.1563	0.75	0.12	3.4	0.4
pilot unit	1.0–1.8	axial flow pump	0.1591	0.80	0.77	4.2	0.5
pilot unit†	1.0–1.8	axial flow pump	0.1591	0.75	0.37	4.0	1.5
Weston Point	280	axial flow pump	0.68	1.69	0.51	2.0	2.5
Swenson Evap.	121	axial flow pump	1.10	1.56	0.62	3.1	10–20

† Tangential inlet crystalliser used by Asselbergs[17].

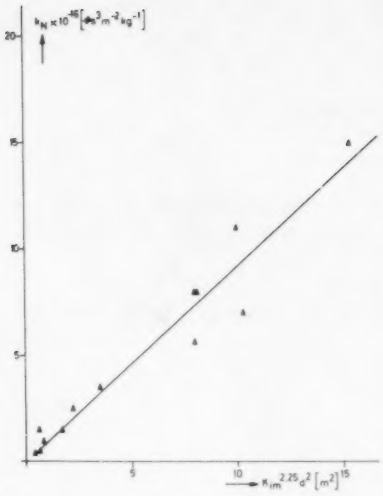


Figure 8. Nucleation rate constants as function of dimensionless impeller number and impeller diameter.

for scale-up purposes, it should be kept in mind that it is fully empirical in character and as such it does not supply further insight into the mechanisms of nucleation.

CONCLUSIONS

From the results presented in this paper, it may tentatively be concluded that the nucleation rate in a large scale crystalliser is controlled by the slurry velocity rather than by the impeller speed. This may indicate that nuclei mainly arise from forces induced by fluid motion rather than from crystal–impeller collisions. This conclusion is not in contradiction with results of theoretical work by Ramshaw[11], who suggested that crystal–impeller collisions probably do not represent the main source of nuclei at the plant scale.

Dimensionless impeller number and impeller diameter can be conveniently used to translate nucleation kinetic data, obtained in laboratory crystallisers, to the plant scale.

SYMBOLS USED

B^0	nucleation rate ($\# m^{-3} s^{-1}$)
d	impeller diameter (m, mm)
K_{im}	dimensionless impeller number (–)
g	linear crystal growth rate ($m s^{-1}$)
H_m	head (m H_2O)
k_N	nucleation rate constant ($\# s^3 m^{-2} kg^{-1}$)
k_p	pump discharge coefficient (–)
L	crystal size (μm)
M	magma concentration ($kg m^{-3}$)
M_c	cup-mixing magma concentration ($kg m^{-3}$)
n	population density ($\# m^{-4}$)
N	impeller speed (rps)
P	stirred-in power (W)
P_0	power number (–)
V	Volume (m^3)

Greek letters

ε	specific power input ($W kg^{-1}$)
ρ	slurry density ($kg m^{-3}$)
ϕ_{mv}	vapour production rate ($kg s^{-1}$)
ϕ_{vc}	circulating flow rate ($m^3 s^{-1}$, $m^3 h^{-1}$)
ϕ_{vp}	volumetric production rate ($m^3 s^{-1}$)
τ	residence time (s)
τ_{so}	overall solids residence time (s)

REFERENCES

1. Clontz, N. A. and McCabe, W. L., 1971, *CEP Symp Ser* 67 (110): 6.
2. Johnson, R. F. et al., 1972, *AIChE Symp Ser* 68 (121): 31.
3. Sung, C. Y. et al., 1973, *AIChE J.*, 19: 957.
4. Estrin, J. et al., 1975, *AIChE J.*, 21: 392.
5. Ottens, E. P. K. and de Jong, E. J., 1972, *5th Symp Ind Cryst* (Usti nad Labem, Yugoslavia).
6. Evans, T. W. et al., 1974b, *AIChE J.*, 20: 959.
7. Jancic, S. J., 1976, *PhD Thesis* (University of London).
8. Bauer, L. G., 1974, *AIChE J.*, 20: 4.
9. Nienow, A. W., 1976, *Trans I Chem E.* 54: 205.
10. Grootscholten, P. A. M. et al., 1982, *AIChE J.*, 28 (5): 728.
11. Ramshaw, C., 1974, *The Chemical Engineer*, 287/8: 446.
12. Garside, J. and Davey, R. J., 1980, *Chem Eng Comm*, 4: 393.
13. Zwietering, T. N., 1959, *Chem Eng Sci*, 11: 1.
14. Bourne, J. R. and Hungerbuehler, K., 1980, *Trans I Chem E*, 58: 51.
15. Bennett, R. C. et al., 1973, *Chem Eng Progr*, 69 (7): 86.
16. Grootscholten, P. A. M., 1982, *PhD Thesis* (Delft University of Technology).
17. Asselbergs, C. J., 1978, *PhD Thesis* (Delft University of Technology).
18. Stepanoff, A. J., 1957, *Centrifugal and Axial Flow Pumps*, (New York).
19. Scrutton, A. and Grootscholten, P. A. M., 1982, *Trans I Chem E*, November issue.
20. Randolph, A. D. and Larson, M. A., 1971, *Theory of Particulate Process* (Academic Press, New York).
21. Scrutton, A., 1980, *5th Int Symp Salt* (Hamburg, Germany).
22. Beer, W. F. and Mersmann, A. B., 1981, *2nd World Cong Chem Eng* 4:68 (Montreal, Canada).
23. Van't Land, C. M. and Wienk, B. G., 1978, *6th Symp Ind Cryst*, p. 51, (Plenum Press).
24. Van't Land, C. M. and de Waal, K. J. A., 1978, *6th Symp Ind. Cryst.*, p. 449, (Plenum Press).

ACKNOWLEDGEMENT

The authors would like to thank Imperial Chemical Industries plc for financially supporting this project.

ADDRESSES

Correspondence about this paper should be addressed to Professor E. J. de Jong, Laboratory for Process Equipment, Delft University of Technology, Leeghwaterstraat 44, 2628 CA Delft, The Netherlands. P. A. M. Grootscholten and L. D. M. v.d. Brekel are now at the Unilever Research Laboratory, Vlaardingen, The Netherlands.

This paper was received 9 *August* 1983 *and was communicated by Professor J. M. Smith, Associate Editor of the journal for Continental Europe.*

CORRESPONDENCE

From
Professor P. N. Rowe
Department of Chemical and Biochemical Engineering
University College London
Torrington Place
London WC1E 7JE

A slight change in definition coupled with a straightforward experimental fact simplifies the rather confusing hydrodynamic discussion in Joshi's recent review[1].

Using the same symbols but defining drag coefficient, C_D in terms of projected area (as is logical)

$$\frac{\pi}{6} d_p^3 (\rho_s - \rho_L) g\varepsilon = C_D \frac{\pi}{4} d_p^2 \tfrac{1}{2} \rho_L V^2 \quad (1)$$

applies[2] to a single spherical particle either isolated in extensive fluid and falling at its terminal velocity or one of many in a fluidised bed. For the isolated sphere (note: $\varepsilon_T = 1$)

$$C_D/\varepsilon_T = f(Re_T) \quad (2)$$

$$= 24/Re_T \text{ for}$$

$$Re_T \lesssim 0.2 \text{ (Stoke's regime)} \quad (3)$$

$$= 0.44 \text{ for}$$

$$Re_T \gtrsim 10^3 \text{ (Newton's regime)} \quad (4)$$

from which the well known expressions

$$V_T = g(\rho_s - \rho_L)\, d_p^2/18\mu \quad (Re_T \gtrsim 0.2) \quad (5)$$

and

$$V_T = \sqrt{[3g(\rho_s - \rho_L)\, d_p/\rho_L]} \quad (Re_T \gtrsim 10^3) \quad (6)$$

The relevant experimental fact[3] is that when a spherical particle is closely surrounded by other similar ones the drag coefficient is increased by a factor of about 70. Thus equation (2) becomes

$$C_{Dmf}/\varepsilon_{mf} \doteqdot 70 \times f(Re_{mf}) \quad (7)$$

where C_{Dmf} refers to closely packed spheres as under minimum fluidisation conditions. The form of the function of Re is the same in both cases. From equations (1), (2) and (7) it follows that

$$V_T^2/V_{mf}^2 = \varepsilon_T C_{Dmf}/C_{DT}\varepsilon_{mf} \quad (8)$$

$$= 70 \times f(Re_{mf})/f(Re_T) \quad (9)$$

This can be solved explicitly for the two regimes defined by equations (3) and (4) leading to

$$V_{mf} = 8 \times 10^{-4} g(\rho_s - \rho_L)\, d_p^2/\mu \quad (Re_{mf} \lesssim 0.2) \quad (10)$$

and

$$V_{mf} = 0.206\, g^{1/2} (\rho_s - \rho_L)^{1/2} d_p^{1/2} \rho_f^{-1/2} \quad (Re_{mf} \gtrsim 10^3) \quad (11)$$

which give roughly correct predictions for uniform spheres.

If the Richardson and Zaki equation is used[4] with $\varepsilon_{mf} = 0.4$, the observed value for uniform spheres,

$$V_{mf} = V_T \varepsilon_{mf}^m \quad (12)$$

and the following table can be constructed

Re_{mf}	m	V_T/V_{mf}
0.1	4.65	71
1	4.35	53
10	3.53	26
100	2.81	13
1000	2.39	8.9

This agrees quite well with the end conditions of equations (10) and (11) and gives some intermediate values.

This line of reasoning can also be applied to mass transfer from a single fluidised particle using the empirical equation[5]

$$Sh/Sc^{1/3} = A + (2/3\varepsilon)\, Re^n \quad (13)$$

where

$$A = 2/[1 - (1 - \varepsilon)^{1/3}]\, Sc^{1/3} \quad (14)$$

and n is found from

$$(2 - 3n)/(3n - 1) = 4.65\, Re^{-0.28} \quad (15)$$

Combining (13) with the Richardson Zaki equation gives

$$Sh/Sc^{1/3} = A + (2/3)\, Re_T^{1/m}\, Re^{n - 1/m} \quad (16)$$

The following table comes from ascribing values to the indices

Re	$n - 1/m$
1	0.16
10	0.15
100	0.11
1000	0.08

The mass transfer coefficient is thus seen to be a very slowly varying function of Re and is effectively constant within the range $Re_{mf} < Re < Re_T$, a fact that is easily verified experimentally.

REFERENCES

1. Joshi, J. B., 1983, *Chem Eng Res Des*, 61: 143.
2. Foscolo, P. U., Gibilaro, L. G. and Waldram, S. P., 1983, *Chem Eng Sci*, 38: 1251.
3. Rowe, P. N., 1961, *Trans I Chem E*, 39: 178.
4. Richardson, J. F. in Davidson, J. F. and Harrison, D. (eds.) 1971, *Fluidisation* (Academic Press, London).
5. Rowe, P. N., Claxton, K. T. and Lewis, J. B., 1965, *Trans I Chem E*, 43: T14.

VOL. 62 1984

SHORTER COMMUNICATION

SCALING-UP DISTILLATION TRAY EFFICIENCY UNDER CONDITIONS OF WEEPING OR ENTRAINMENT WHEN LIQUID CHANNELLING ALSO OCCURS

By T. PLAKA, I. S. AHMED and M. J. LOCKETT (MEMBER)

Department of Chemical Engineering, UMIST, Manchester

This note deals with the effects of entrainment and weeping on the efficiency of a tray having no provision for liquid residence time control and on which liquid channelling occurs. It is predicted that the effect of weeping on tray efficiency depends on tray diameter, and that large diameter trays may be relatively insensitive to weeping. In contrast, entrainment causes a reduction in efficiency at all diameters.

INTRODUCTION

Scale-up of distillation trays is complicated by the phenomenon of liquid channelling which causes a loss of efficiency for medium to large diameter trays but which has no effect at small diameters. The problem can largely be overcome by the use of liquid flow control devices on the tray to give uniform liquid residence time, and a well-known example is the use of Union Carbide slotted sieve trays for this purpose. Today an increasing number of designers are realising the benefits of liquid residence time control and the advantage it can bring of increased tray efficiency and reduced energy costs through the opportunity to use lower reflux ratios. At the same time it must be said that the majority of trays presently being installed still incorporate no provision for liquid residence time control. Apparently their designers are prepared to accept a larger number of lower efficiency trays in preference to the relative unfamiliarity of fewer, but more advanced, trays.

This note deals with the effects of entrainment and weeping on the efficiency of an ordinary tray having no provision for liquid residence time control and on which liquid channelling occurs. The only previous contribution on this subject is by workers at Atomic Energy of Canada[1,2]. It is shown that under conditions of liquid channelling, the effects of entrainment and weeping on tray efficiency exhibit quite different and unexpected scale-up effects.

FLOW REGIMES

The published flow regime diagrams of Hofhuis and Zuiderweg[3] and of Porter and Jenkins[4] clearly show that many columns working around atmospheric pressure operate in the spray regime. For these columns, the effect of entrainment on efficiency is obviously relevant. On the other hand, it is not difficult to show that large diameter vacuum columns operate in the froth regime because such columns operate at a relatively low percentage flood so as to achieve a low tray pressure drop. Evidence for this is given in Figure 1 which was constructed for the ethylbenzene–styrene separation using an interactive tray design computer program[5]. Columns working at medium to high pressures generally operate in the froth or emulsion regimes. However, as these columns are usually either of relatively small diameter or multipass, the effects of liquid channelling are probably less important.

It is likely that liquid channelling has its biggest effect on efficiency during froth regime operation. It is suspected that the considerably increased liquid mixing which obtains in the spray regime may help reduce the loss of efficiency caused by liquid channelling. However this is, as yet, speculative and needs confirmation by experiment.

MATHEMATICAL MODEL

The basic liquid flow pattern considered is that used by Porter, Lockett and Lim[6] and shown in Figure 2. Although this flow pattern is over-simplified, it does

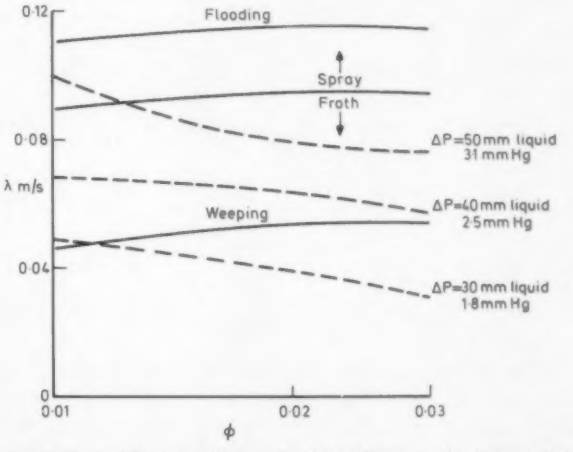


Figure 1. Typical loading diagram for 7.0 m diameter single pass sieve tray (vacuum distillation).

© Institution of Chemical Engineers

contain the essential features of what happens in practice and more detailed flow patterns, such as those proposed by Bell and Solari[7], for example, lead to very similar conclusions.

The procedure adopted was tray to tray calculation starting from the bottom of the column. For weeping calculations it was necessary to make an initial assumption about the liquid concentration on each tray and then repeat the calculations over the whole column a number of times until convergence was achieved. Special provision had to be made for the bottom and top trays which receive no entrainment and weeping respectively. The reported tray efficiencies are for the fourth tray from the bottom in an eight tray column and these values are independent of the terminal tray assumptions. The calculation procedure was basically that described by Lockett et al[8] modified for entrainment and weeping. No vapour mixing was assumed between trays. The differential equations for the liquid concentration on a general tray took the following form:

Entrainment

Active Region (Region I)

$$\frac{1}{Pe}\left[\frac{d^2x_n}{dz^2}+\frac{d^2x_n}{dw^2}\right]-\frac{dx_n}{dz}$$
$$-\left[\frac{\lambda_0}{1+A_0}\right]\left[\frac{WD}{A}\right]E_{0G}(x_n-x^*_{en-1})$$
$$+\left[\frac{A_0}{1+A_0}\right]\left[\frac{WD}{A}\right](x_{n-1}-x_n)=0$$

Weeping

Active Region (Region I)

$$\frac{1}{Pe}\left[\frac{d^2x_n}{dz^2}+\frac{d^2x_n}{dw^2}\right]-\frac{dx_n}{dz}$$
$$-\left[\frac{\lambda_0}{1-\beta_0}\right]\left[\frac{WD}{A}\right]E_{0G}(x_n-x^*_{en-1})$$
$$+\left[\frac{\beta_0}{1-\beta_0}\right]\left[\frac{WD}{A}\right](x_{n+1}-x_n)=0$$

In the stagnant regions (Region II) in each case the second term corresponding to liquid flow is omitted.

The nomenclature is identical to that given previously[6,8] and in addition

$$\lambda_0 = mG/L_0$$
$$A_0 = eG/L_0$$
$$\beta_0 = QA/L_0$$

Newly introduced symbols are defined in the nomenclature.

The equations above were solved numerically to obtain the concentration profile over each tray. These were then numerically integrated to give the apparent Murphree tray efficiency in the presence of either entrainment or weeping.

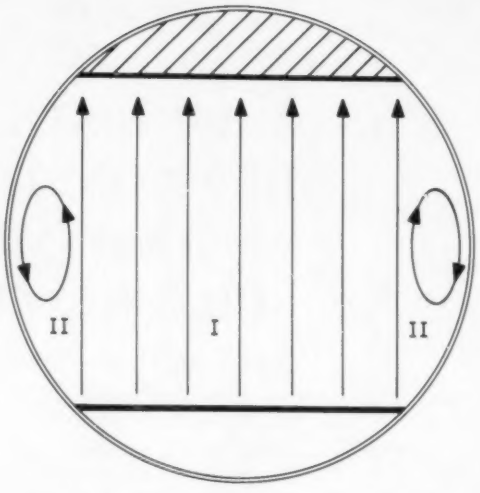


Figure 2. Liquid flow model with stagnant regions.

RESULTS

In Figures 3–6, the following conditions hold

$$\lambda_0 = 1.0, \quad E_{OG} = 0.8, \quad W/D = 0.65$$

The effect of entrainment on tray efficiency under liquid channelling conditions is shown in Figures 3 and 4. They show no unexpected features and both entrainment and liquid channelling contribute to a lowering of tray efficiency. The typical values of the hydraulic parameters on the tray, such as eddy diffusivity, froth height, etc., which were used by Porter et al[6], have also been used here to relate Peclet number to tray diameter. In this way, tray diameter is also included on the Figures.

The effect of weeping on tray efficiency under liquid channelling conditions shows interesting and at first sight unexpected behavior—Figures 5 and 6. For very small diameter trays (low Peclet number) the liquid is completely mixed and weeping has little effect on tray efficiency, as is well known. For small to medium diameter trays weeping causes a reduction in tray efficiency, as is generally accepted. However, for large diameter trays the calculations indicate that weeping has little effect on tray efficiency.

The reason for this behaviour is not difficult to explain. Under conditions of liquid channelling weeping

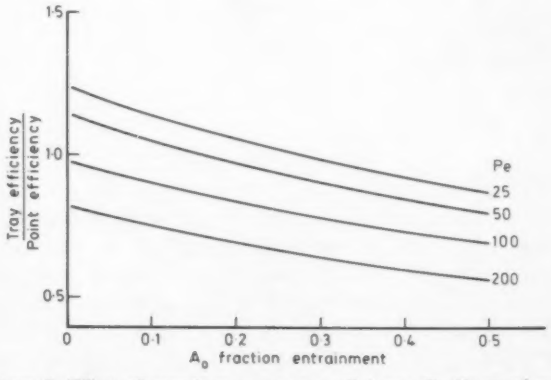


Figure 3. Effect of entrainment on tray efficiency (Peclèt number as parameter).

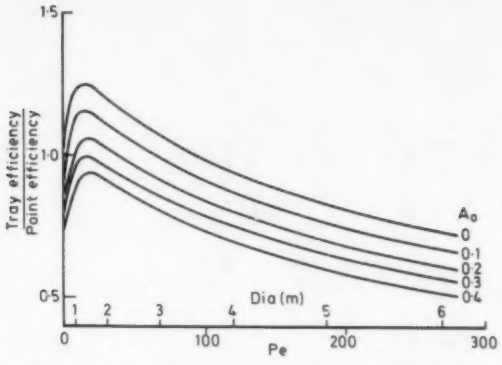


Figure 4. Effect of entrainment on tray efficiency, showing effect of tray diameter.

has two opposing effects on tray efficiency. That part of the weeping which takes place over the active zone reduces tray efficiency in the usual way. However that part of the weeping which takes place over the stagnant zones has a beneficial effect on tray efficiency. This arises because fresh liquid is introduced into the stagnant zones of a given tray by the liquid weeping onto it from the tray above. In the absence of weeping, the liquid in a stagnant zone approaches equilibrium with the vapour passing through it, so that subsequent vapour passing through the stagnant zones undergoes little or no composition change and contributes to a lowering of tray efficiency. Normally fresh liquid is introduced into the stagnant zones only by liquid mixing from the active zone of the same tray. However under weeping conditions, there is another source of supply of fresh liquid from the tray above which is of higher concentration of more volatile component. This tends to ameliorate the loss of efficiency caused by the stagnant zones. For large diameter trays ($Pe \simeq 200$) it appears that the beneficial and detrimental effects of weeping are about equal so that weeping has no net effect on efficiency. For small to medium trays the adverse effects of the stagnant zones are overcome by liquid mixing from the active zones, so that the only contribution of weeping is to lower the

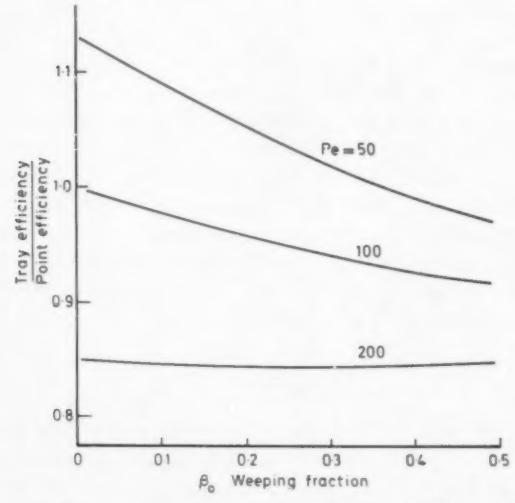


Figure 5. Effect of weeping on tray efficiency (Peclèt number as parameter).

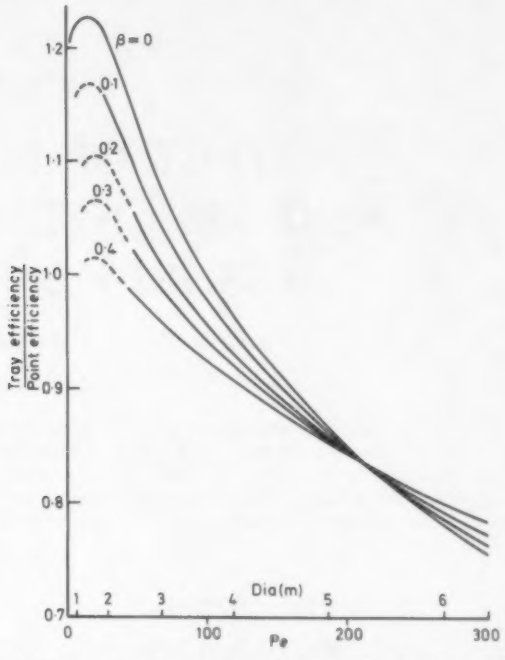


Figure 6. Effect of weeping on tray efficiency, showing effect of tray diameter.

efficiency of the active zones and thus to lower the efficiency of the tray.

Although fresh liquid is introduced into the stagnant zones when entrainment occurs this, of course, has no beneficial effect since it has also already been in contact with the same vapour which it must again contact on the tray above.

CONCLUSION

It is predicted that the effect of weeping on tray efficiency depends on tray diameter, and that large diameter trays may be relatively insensitive to weeping. In contrast, entrainment causes a reduction in efficiency at all diameters.

NOMENCLATURE

A	bubbling tray area (m^2)
A_0	fraction entrainment (kmol entrainment/kmol liquid)
D	column diameter (m)
E_{OG}	Murphree point efficiency
e	entrainment rate (kmol/kmol vapour)
G	vapor rate (kmol/s)
L_0	liquid rate in absence of entrainment or weeping (kmol/s)
m	slope of equilibrium line
Pe	Liquid Peclèt number
ΔP	Tray pressure drop (mm)
Q	weeping rate per unit bubbling area (kmol/m^2 s)
U_s	superficial vapour velocity (m/s)
W	weir length (m)
β_0	fraction weeping
λ	capacity factor $U_s[\rho_G/(\rho_L - \rho_G)]^{0.5}$ (m/s)
λ_0	stripping factor
ϕ	flow parameter $\frac{L_0}{G}\left(\frac{\rho_G}{\rho_L}\right)^{0.5}$
ρ_G, ρ_L	vapour and liquid densities (kmol/m^3)

This shorter communication is concluded on page 200.

SHORTER COMMUNICATION

EFFECT OF FLOW RATIO ON THE PERFORMANCE OF AN EXPERIMENTAL ABSORPTION COOLING SYSTEM

By P. KUMAR, S. DEVOTTA and F. A. HOLLAND (FELLOW)

Department of Chemical and Gas Engineering, University of Salford

Further experiments have been carried out on an existing absorption cooling system operating on water–lithium bromide. Heat losses were reduced and experiments were carried out at very high flow ratios. These experiments show that the generator temperature can be reduced by about 10°C for given condenser and evaporator temperatures. These results broaden the scope for using low grade heat sources to drive absorption cooling systems. The experiments were carried out without an economiser heat exchanger. The performance data have been correlated as a function of the Carnot coefficient of performance and flow ratio.

INTRODUCTION

There is a lack of published comprehensive experimental performance data for absorption cooling systems. An experimental absorption cooling system operating on water–lithium bromide was designed and installed in the Department of Chemical and Gas Engineering, University of Salford, UK. The details of this experimental system and some preliminary results have been presented previously[1,2]. The authors established the feasibility of air cooling the absorber and condenser in absorption cooler. The objective of this work is to study the possibility of lower generator temperatures for a given cooling requirement. This will facilitate the use of low temperature heat energy sources such as waste heat from industrial processes, geothermal energy and solar energy to produce cooling.

ANALYSIS OF REPORTED DATA

The coefficient of performance of a cooling system is defined as the ratio of the energy extracted in the evaporator Q_{EV} to produce the desired cooling to the energy supplied to the generator Q_{GE}:

$$(COP) = \frac{Q_{EV}}{Q_{GE}} \tag{1}$$

The flow ratio (FR) which is defined as the ratio of the mass flow rate of solution from the generator to the absorber to that of the mass flow rate of vapour from the evaporator to the absorber, is used in this anaylsis. The flow ratio can be defined in terms of concentration as follows

$$(FR) = \frac{X_{AB}}{X_{GE} - X_{AB}} \tag{2}$$

From the experimental results reported by Landauro Paredes et al[1,2] some data points were selected for which the concentration of lithium bromide in the generator was constant. Figure 1 illustrates the behaviour of the typical parameters as a function of the flow ratio for a fixed concentration in the generator $X_{GE} \simeq 0.65$. It can be seen that $(COP)_A$ remains nearly constant over the range of these experiments. It is also interesting to note that all the four temperatures T_{GE}, T_{CO}, T_{AB} and T_{EV} show similar trends with flow ratio and the temperature differences $(T_{CO} - T_{EV})$, $(T_{AB} - T_{EV})$ and $(T_{GE} - T_{CO})$ remain almost constant. These constant values of $(T_{CO} - T_{EV})$ and $(T_{AB} - T_{EV})$ imply that, if higher condenser and absorber temperatures are required the system can only operate with correspondingly higher evaporator temperatures. Figure 2 shows the variation of heat loads with flow ratio. The trends of these heat loads are more or less the same so that $(COP)_A$ is substantially independent of flow ratio. The performance of the economiser heat exchanger was found to vary with changes in flow ratio. The heat losses from the original experimental system were also seen to be high so that the lagging was improved.

EXPERIMENTAL

Theoretical considerations indicate that for a required evaporator temperature, the generator temperatures can be decreased by operating at relatively high flow ratios[3]. Therefore, further experiments were carried out with the flow ratio as the main variable. The heat flux in the economiser varies with changes in flow ratio and this can complicate the interpretation of the results. Therefore the experiments were carried out without it. For a particular condition the effect of the economiser heat exchanger on the performance is straightforward and the results obtained can be suitably modified. The flow ratio (FR) was varied from 7.5 to 128.0 but most of the runs were taken for flow ratios below 40.0

RESULTS

Figure 3 shows the variation of different parameters with varying flow ratio for an absorber solution concentration X_{AB} of about 59.5%. The $(COP)_A$ values and the T_{GE} values have been plotted for different condenser temperatures. It can be seen that with increasing flow

© Institution of Chemical Engineers

VOL. 62 1984

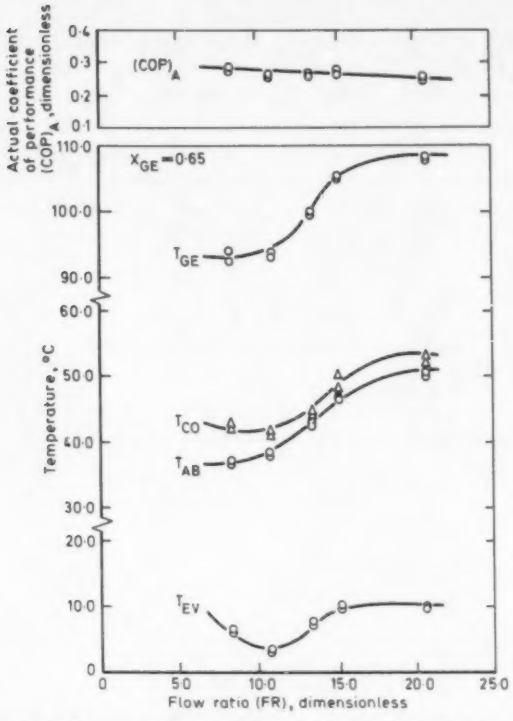


Figure 1. Performance characteristics of the experimental absorption cooling system as a function of flow ratio using water-lithium bromide, for $X_{GE} = 0.65$.

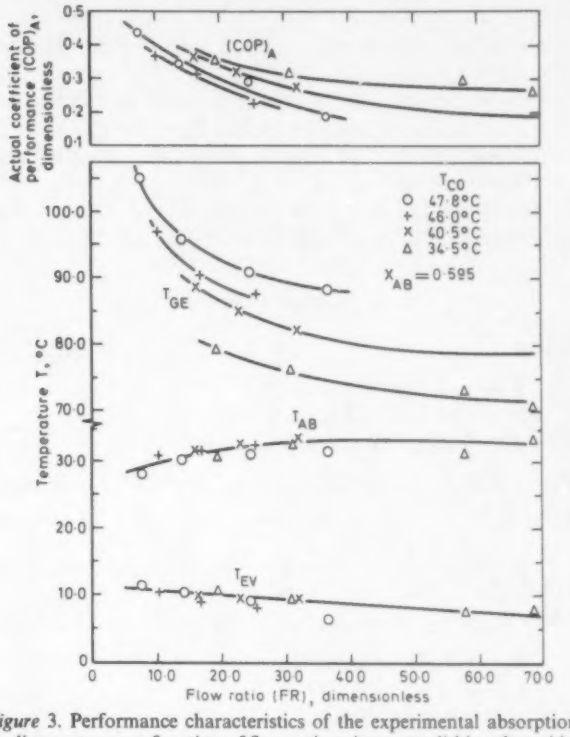


Figure 3. Performance characteristics of the experimental absorption cooling system as a function of flow ratio using water-lithium bromide, for $X_{AB} = 0.595$.

ratio, the T_{GE} values decrease by about 10°C for given condenser and evaporator temperatures and the curves tend to become flat for (FR) values beyond 30.0. It can also be seen that for a given flow ratio, T_{GE} decreases and $(COP)_A$ increases with decrease in T_{CO}, but this limit is fixed by the temperature of the cooling medium. As the flow ratio is increased, the absorber temperature T_{AB} increases because of the enhanced thermal carry over by the hot solution from the generator. If the temperature T_{AB} could be kept constant by increasing the flow rate of the cooling medium to the absorber, the system could be operated without affecting the evaporator. However, because of the limitations in a practical system T_{AB} could not be maintained constant although the variation of T_{EV} is not significant. This is due to the fact that the heat loads Q_{GE} and Q_{EV} had to be manipulated to obtain this condition. This can be seen from Figure 4 which shows the variation of the heat loads for the corresponding range of flow ratios. Figure 4 shows that as the flow ratio is increased, Q_{AB} increases and Q_{CO} decreases. Both these heat loads are complimentary to each other. Therefore the total cooling load of the absorber and the condenser can be met by nearly the same amount of the cooling medium. Therefore if the generator is to be operated at a higher flow ratio (FR), i.e., at a lower heat source

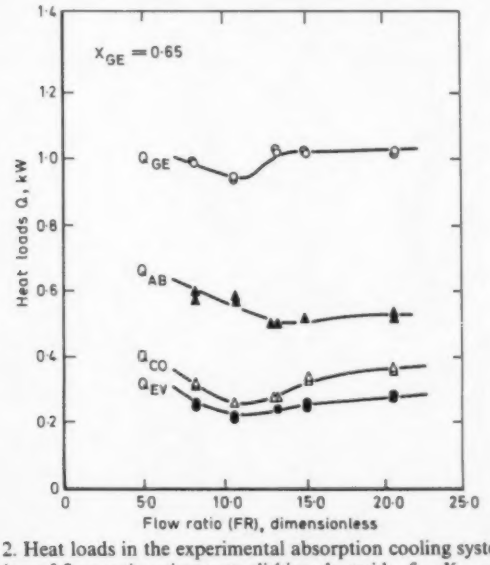


Figure 2. Heat loads in the experimental absorption cooling system as a function of flow ratio using water-lithium bromide, for $X_{GE} = 0.65$.

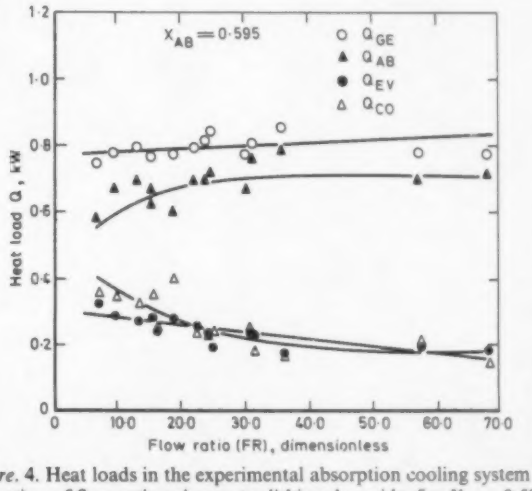


Figure. 4. Heat loads in the experimental absorption cooling system as a function of flow ratio using water-lithium bromide, for $X_{AB} = 0.595$.

temperature, the penalty is slight reduction in the cooling capacity.

Although the economiser was not used in these experiments, $(COP)_A$ values are higher than the previous set of values presented in Figure 2. This can be attributed to the improved lagging on the unit.

The actual coefficient of performance $(COP)_A$ values were correlated by an equation of the following form with a root mean square residual ($RMSR$) of 0.0328:

$$(COP)_A = B_1 + B_2(FR) + B_3(COP)_C \quad (3)$$

where

$$B_1 = -1.7039111\,E-01$$
$$B_2 = -9.9557484\,E-04$$
$$B_3 = 3.9336917\,E-01$$

where $(COP)_C$ is the Carnot coefficient of performance defined by

$$(COP)_C = \left(\frac{T_{EV}}{T_{CO} - T_{EV}}\right)\left(\frac{T_{GE} - T_{AB}}{T_{GE}}\right) \quad (4)$$

The ranges of experimental conditions were as follows

$X_{AB} = 0.575$ to 0.625
$T_{GE} = 72.0$ to $107.0°C$
$T_{CO} = 34.5$ to $49.0°C$
$T_{AB} = 24.0$ to $42.5°C$
$T_{EV} = 5.5$ to $15.0°C$

CONCLUSION

It has been demonstrated experimentally that by using high flow ratios in an absorption cooling system it is possible for a given evaporator temperature, to reduce the generator temperature. This broadens the scope for relatively low temperature heat source to be used in absorption cooling systems.

It has also been shown that coolant temperatures in excess of 45°C can be used to reject heat from a water–lithium bromide absorption cooling system producing temperatures as low as 10°C without incurring problems of crystallisation. Therefore it is feasible to operate such a system using air cooling of the condenser and absorber. This can be very beneficial for hot countries which have limited amounts of water.

SYMBOLS USED

(COP)	coefficient of performance (dimensionless)
(FR)	flow ratio (dimensionless)
Q	heat load (kW)
T	temperature (°C or K)
X	weight fraction of LiBr (dimensionless)

Subscripts

AB	absorber
CO	condenser
EV	evaporator
GE	generator
A	actual
C	Carnot

REFERENCES

1. Landauro-Paredes, J. M., 1982, *PhD Thesis* (University of Salford)
2. Landauro-Paredes, J. M., Watson, F. A. and Holland, F. A., 1983, *Chem Eng Res Des*, 61: 362.
3. Kumar, P. and Devotta, S., Paper communicated.

VOL. 62 1984

ADDRESS

Correspondence on this paper should be addressed to Professor F. A. Holland, Department of Chemical and Gas Engineering, University of Salford, Salford, M5 4WT.

The manuscript was received 3 *October* 1983 *and accepted for publication* 14 *November* 1983.

SHORTER COMMUNICATION

RÔLE OF CAVITY FORMATION IN STIRRED GAS–LIQUID–SOLID REACTORS

By M. M. C. G. WARMOESKERKEN, M. C. van HOUWELINGEN, J. J. FRIJLINK (COMPANION) and J. M. SMITH (FELLOW)

Laboratory for Physical Technology, Delft University, The Netherlands

The behaviour of sand particles suspended in a turbine stirred gas-liquid dispersion has been studied. If aeration is started in a system in which the sand is just suspended, sedimentation increases rapidly only beyond the point when large cavities are formed behind the blades of the impeller. The critical gas flow number, *Fl*, for this phenomenon is 0.03 in the present equipment. The presence of solids at mass concentrations between 0.1 and 5.0% has no measurable effect on the formation of gas filled cavities nor on the gassed power demand characteristics.

INTRODUCTION

Stirred reactors involving three phases, gas–liquid–solid, are very common in the chemical and food industries. Nevertheless little is known about the behaviour of such systems. Knowledge of gas–liquid and liquid–solid two phase systems may be helpful in designing and operating a three phase reactor. However, two central questions remain; does the dispersed gas influence the solid–liquid suspension, and the inverse, do suspended solids affect the behaviour of the gas–liquid dispersion?

The present investigation deals with the role of cavity formation behind the blades of a Rushton turbine in a three phase reactor. Attention is focussed on the conditions when the solids are initially just suspended.

There are several statements in the literature to the effect that solid particles will sediment when gas is introduced into a stirred suspension.[1-6] However it is not clear why and under what conditions this phenomenon occurs. The roles of the gas flow rate, power consumption and particle properties are largely unknown. The aim of this study has been to determine whether there is a connection between the impeller hydrodynamics, especially in the formation of large gas cavities, and possible sedimentation.

Zwietering[7] presented a correlation for the critical stirrer speed N_{js} at which solids in a suspension do not remain for longer than one or two seconds on the bottom of the tank. This correlation was later confirmed and extended by Nienow.[8] At this just-suspended condition a combination of the circulating liquid flow and turbulence at the scale of the particle size is just sufficient to re-entrain a particle which has settled out.[9,10] It is to be expected that if the influence of these mechanisms is reduced as a result of the presence of a gas phase, then the just-suspended condition will not be maintained and the particles will sediment.

The gas filled cavities which form behind the blades of a Rushton turbine operating in a gas–liquid system have a significant influence on the hydrodynamics of the stirrer. Van't Riet[11] distinguished and defined three characteristic cavity forms which develop successively with increasing gas rates at constant stirrer speeds: vortex, clinging and large cavities. It has recently been shown that at intermediate gas rates a six blade disc turbine preferentially develops a stable 3–3 configuration of alternating large and clinging cavities.[12] As this is established there is a major drop in the power demand. Since the latter is associated with the pumping of liquid, we might expect this to affect sedimentation, among other things.

EXPERIMENTAL ARRANGEMENT

The experiments have been carried out in a Perspex cylindrical vessel with a diameter T of 0.44 m, provided with a dished bottom with a radius of curvature equal to the vessel diameter, Figure 1. Four baffles of 0.1 T width were mounted with a clearance of 1 cm from the vessel wall. A six-blade Rushton turbine with a diameter D of 0.176 m, $[T/D = 2.5]$ was located with an off-bottom clearance equal to its diameter. The liquid height H was equal to the tank diameter T. The gas distributor was a perforated ring with a diameter of 10 cm mounted 5 cm below the stirrer. Tap water, compressed air and sand were used. The density of the sand particles was 2570 kg m^{-3}.

The size distribution of the sand was determined by a sedimentation balance and is given in Table 1. The power consumption was measured by a Vibro torque meter, mounted on the stirrer shaft.

The conditions under which the three stable large cavities develop have been established with a technique which is based on detecting the differences in radial outflow between blades with large and clinging cavities. A vane sensor, made of spring steel to which strain gauges were cemented, was mounted near the stirrer, Figure 2. The output of the strain gauge bridge was processed by a frequency analyser. The peak frequency of this signal changes from the blade passage frequency to half that when three stable large cavities are formed.

© Institution of Chemical Engineers

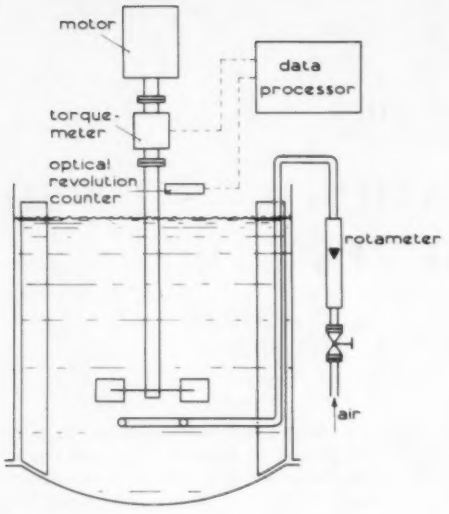


Figure 1. General tank arrangement.

RESULTS AND DISCUSSION

Stirrer Hydrodynamics

The results of the measurements of the formation of three large cavities are given in Figure 3. The points here represent the minimum gas supply rate at which the three large cavity configuration has just been achieved, as a function of the stirrer speed. To the left of the line, only vortex or clinging cavities exist while to the right there are at least three large cavities. In the present equipment this cavity formation line is well described in terms of the dimensionless gas flow number by:

$$Fl = 0.03$$

In the range of this investigation this value appears to be relatively insensitive to gas recirculation. Figure 3 also includes the measurements obtained in the presence of a solid phase. From this it is quite clear that there is no effect from low concentrations of solids on the formation of large cavities.

This independence may be explained by the density differences between the solids, liquid and gas. In the vortex flows behind the blades there are very strong centrifugal forces which will expel solids at the same time as drawing gas inwards to be captured by the under-pressure. The results shown in Figure 3 also imply that the solids will not affect the form of the gassed power curves because these are mainly determined by the stirrer hydrodynamics. The absolute power consumption is proportional to the density of the suspension pumped by the stirrer, although this is only a minor effect at low solid concentrations.

Table 1. Size distribution of sand used

Particle size	Mass fraction
$\leqslant 100\,\mu m$	10%
$\leqslant 127\,\mu m$	50%
$\leqslant 160\,\mu m$	90%

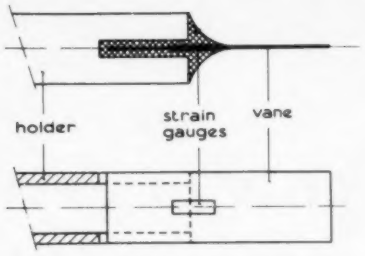


Figure 2. The vane sensor.

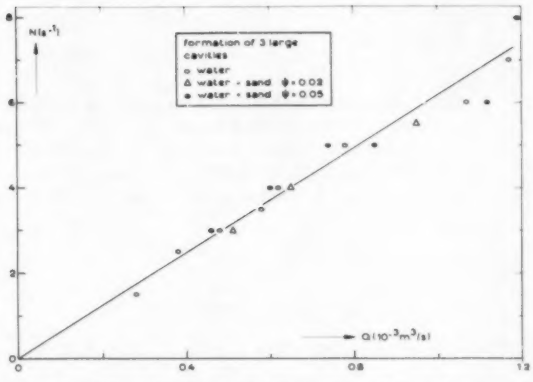


Figure 3. Conditions for the initial formation of three large cavities.

Measurements of the gassed power demand with and without a solid phase have confirmed that solids do not have a significant influence, Figure 4. This is in marked contrast to the results of Chapman et al[13] who report a large effect from the solids. Their divergent data were however obtained in a system in which the solids were initially settled out and formed a false bottom. This modifies the effective tank geometry from that when the solids are suspended.

Solid Suspension

In the present experiments the critical stirrer speed for complete solid suspension was determined visually using the Zwietering criterion. The results of these measurements for solid concentrations up to 5% by mass are shown in Figure 5. The dashed line in this figure was

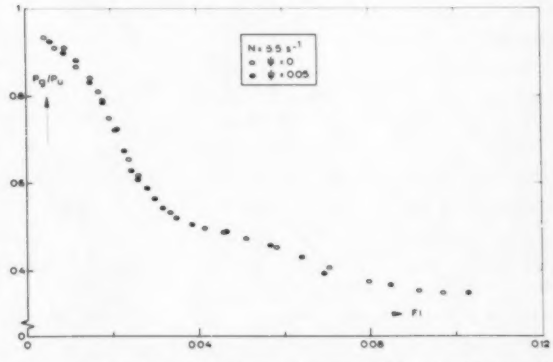


Figure 4. The relative gassed power demand with and without solids suspension.

VOL. 62 1984

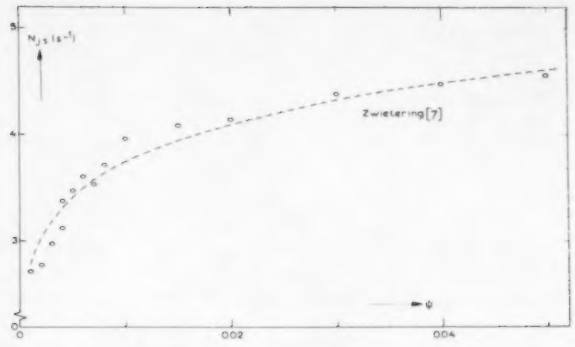


Figure 5. Critical stirrer speed needed to attain the just suspended condition in an unaerated suspension as a function of the solid massfraction.

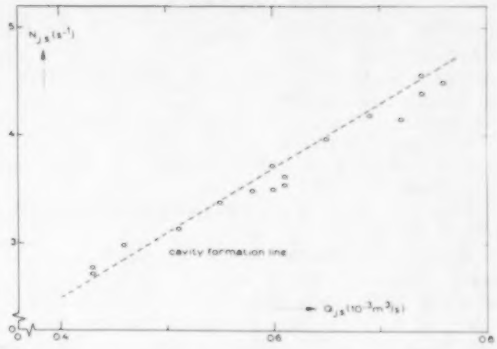


Figure 6. The relationship between the minimum stirrer speed needed to suspend solids in a given unaerated system and the gas flow rate which produces the same just suspended conditions at that stirrer speed. The dotted line is taken from Figure 3.

calculated from Zwietering's correlation, and it is clear that this is valid for this vessel geometry and system.

Gassed Suspensions

Experiments were carried out starting from a just-suspended liquid–solid system, and maintaining a constant stirrer speed of N_{js}. The effects of the introduction of a small amount of gas were directly observed. Conditions near the tank bottom appeared to become more disturbed and there was a clear improvement in the effectiveness of suspension.

With increasing gas rates however, more solids reached the bottom and eventually the suspension character passed through the just-suspended condition to a regime where massive sedimentation occured. The gas flow rate at which the conditions passed the just-suspended state, again determined visually in terms of the Zwietering criterion, was called the critical gas rate Q_{js}. The experiment was repeated with various solid concentrations up to 5% by mass. Figure 6 shows how the values found for Q_{js} depend on the suspension concentration, here characterised in terms of N_{js}.

The dashed line in Figure 6 corresponds to the cavity formation line of Figure 3. It is quite clear that the development of large cavities plays a dominant role with respect to the sedimentation of the solid particles. The cavities reduce the pumping capacity of the impeller to the point that the liquid flow is no longer sufficient to keep the particles suspended. The expression for the cavity formation line may serve to calculate the critical gas flow rate.

The improvement in suspension conditions over the range of gas flows up to $Fl = 0.03$ is the more remarkable since in this region the power demand falls to about half its ungassed value. Suspension as such is clearly not determined solely by the specific impeller power input. There is of course a local airlift pumping effect associated with the introduction of gas from the sparger, though the power input from this source is only a few percent of that from the agitator. It is also possible that flow irregularities resulting from the somewhat indeterminate conditions around vortex and clinging cavities contribute to the improved suspension performance at low gas rates. These effects are counterbalanced at higher gas rates by the steady development of large cavities with the associated loss of dissipated power and pumping capacity.

Chapman et al[13], did not find improved suspension in a flat bottomed tank even at small aeration rates. Some preliminary experiments in the present series confirm their result, emphasising the importance of the details of the equipment geometry.

Our results are a confirmation of remarks made by Arbiter et al[1]. They defined a critical gas flow number on the basis of the sharp fall of power demand with aeration rate in flotation equipment and reported that good suspension was maintained up to that point. From other work[12] it is known that this decrease in power level is associated with the formation of large cavities.

CONCLUSIONS

The suspension of solids in a three phase system maintained by a Rushton turbine agitator in a dished bottom vessel is greatly affected by the two phase hydrodynamics of the impeller. In a three phase system, suspension is at first more easily maintained than in a liquid–solid system. In the experiments reported here this continues to the point that gas loading leads to the formation of large cavities. It is only beyond this that higher stirrer speeds are required in order to keep the particles in suspension. The solids have no measurable influence on the turbine hydrodynamics for the gassed power consumption in the experimental range studied.

SYMBOLS USED

D	Stirrer diameter (m)
Fl	Dimensionless gas flow number. (Q/ND^3) (–)
H	Liquid depth in vessel (m)
N	Stirrer rotation rate (s^{-1})
N_{js}	Critical stirrer speed for suspension (s^{-1})
P_g	Gassed power demand (W)
P_u	Ungassed power demand (W)
Q	Gas flow rate ($m^3 s^{-1}$)
Q_{js}	critical gas rate to return to just suspended condition ($m^3 s^{-1}$)
T	Vessel diameter (m)
ψ	Solids concentration ($kg\,kg^{-1}$)

REFERENCES

1. Arbiter, N., Harris, C. C. and Yap, R. F., 1976, *Int J Mineral Processing*, 3: 257.
2. Queneau, P. B., Jan, R. J., Richard, R. S. and Lowe, D. F., 1975, *Metallurgical Trans, B* 6B: 149.
3. Subbarao, D. and Taneja, V. K., 1979, *Proc. 3rd Euro Conf Mixing* (BHRA, Cranfield), 1: 229.
4. Wiedman J. A., Steiff, A. and Weinspach, P. M., 1980, *Chem Ing Techn* 52: *MS* 773/80.
5. Wiedman, J. A., Steiff, A and Weinspach, P. M., 1980, *Chem Ing Techn* 52: MS 860/80.
6. Chapman, C. M., Nienow, A. W., and Middleton, J. C., 1981, *Trans I Chem E* 59: 134.
7. Zwietering, Th. N., 1958, *Chem Eng Sci*, 8: 244.
8. Nienow, A. W., 1968, *Chem Eng Sci* 23: 1453.
9. Conti, R. and Baldi, G. 1978, *Proc Int Symp Mixing* (Mons, Belgium), B2-1.
10. Bruxelmane, M., 1979, *Proc 3rd Euro Conf Mixing* (BHRA, Cranfield) II: 36.
11. Riet, K. van't, 1974, *Doctoral Thesis* (Delft University of Technology).
12. Warmoeskerken, M. M. C. G. and Smith, J. M., 1982, *Proc 4th Euro Conf Mixing*, (BHRA, Cranfield) 237.
13. Chapman, C. M., Nienow, A. W., Cooke, M. and Middleton, J. C.,1983, *Chem Eng Res Des*, 61: 167.

ADDRESS

Correspondence on this paper should be addressed to Professor J. M. Smith, Laboratory for Physical Technology, Delft University of Technology, Prins Bernhardlaan 6, 2628 BW Delft, The Netherlands.

The paper was communicated 21 *September* 1983 *by Professor J. R. Bourne, Associate Editor for the Journal in Continental Europe.*

Continuation from page 193

T. PLAKA *et al.*

REFERENCES

1. Neuburg H. J. and Chuang K. T., 1982 *Can J Chem Eng* 60: 504.
2. Neuburg H. J. and Chuang K. T., 1982 *Can J Chem Eng* 60: 510.
3. Hofhuis P. A. M. and Zuiderweg F. J., 1979 *IChemE Symp Series* 56: 2.2/1.
4. Porter K. E. and Jenkins J. D., 1979 *IChemE Symp Series* 56 (2): 5.1/1.
5. Ahmed I. S., 1982 *PhD Thesis* (UMIST).
6. Porter K. E., Lockett M. J. and Lim C. T., 1972 *Trans IChemE* 50: 91.
7. Bell R. L. and Solari R. B., 1974 *AIChE J* 20: 688.
8. Lockett M. J., Lim C. T. and Porter K. E., 1973 *Trans IChemE*, 51: 61.

ADDRESS

Correspondence on this paper should be addressed to Dr M. J. Lockett, Union Carbide Corporation, Linde Division, P.O. Box 44, Tonawanda, New York 14151-0044, U.S.A.

The manuscript was received 20 September 1983 and accepted for publication 14 November 1983.

VOL. 62 1984

CORRECTIONS

In *Chem Eng Res Des*, Vol 62, No 1, January 1984, there are printing errors in one line of the letter from Dr M. J. Slater. The last sentence of the second paragraph on page 62 should read:
"For viscosity 1 mPa s is better than 1×10^{-3} kg m^{-1} s^{-1} or 1 g m^{-1} s^{-1}."

In *Chem Eng Res Des*, Vol 62, No 2, March 1984, the work reported in the paper commencing on page 128 was carried out at Loughborough University of Technology by Mr D. Burfoot and Dr P. Rice. The correct authorship details are as printed below:

By D. BURFOOT (STUDENT) **and P. RICE**
Department of Chemical Engineering, University of Technology, Loughborough

CHEMICAL ENGINEERING RESEARCH & DESIGN

Transactions of The Institution of Chemical Engineers

EDITORIAL

The Review Paper in this issue is "Developments in anaerobic treatment of high strength industrial waste waters" by M. A. Bull, R. M. Sterrit and J. N. Lester. Waste waters of this type have traditionally been processed by aerobic treatment. However cost analyses suggest that at high concentrations anaerobic treatment could be more economic. The authors review the microbiology of anaerobic digestion, kinetic equations and a range of types of reactor suitable for this process. The review is completed by a discussion of factors which may affect adversely the choice of anaerobic treatment: slow start-up time, sensitivity to toxic substances, incomplete treatment and lack of operating experience. It is concluded that there is an urgent need for pilot and full-scale evaluation.

As remarked before in this column, the topic of particle behaviour continues to fascinate chemical engineers. A. P. van der Meer, C. M. R. J. P. Blanchard and J. A. Wesselingh report a study of 'Mixing of particles in liquid fluidised beds'. A photographic method was used to determine axial solids dispersion coefficients over a range of column diameters (0.02–0.06 m) with particles of 0.5–0.7 mm diameter. An empirical equation describing the results and a substantial amount of literature data is presented but the authors had less success in obtaining dimensionless relationships. An interesting and novel result of the work is the marked effect on mixing patterns of even a small misalignment from the vertical.

'The effect of pressure on combustion of char in fluidised beds' is reported by E. Turnbull, E. R. Kossakowski, J. F. Davidson, R. B. Hopes, H. W. Blackshaw and P. T. Y. Goodyer. The work described covers 0.25–1.7 mm carbon particles in an air fluidised 100 nm diameter bed of sand at pressures up to 17 bar and temperatures of 1023–1173 K. Seven different carbons were employed. Among many interesting results the authors note that as pressure increases combustion becomes diffusion controlled, that the effect of carbon reactivity can be approximately allowed for and that smaller particles burn faster at high pressure, their combustion rate being chemical rate-controlled.

G. McKay considers 'Mass transfer processes during the adsorption of solutes in aqueous solutions in batch and fixed bed adsorbers'. He presents a theoretical analysis of the performance of batch and fixed bed adsorbers allowing for external mass transfer and pore diffusion. The theory enables the prediction of breakthrough curves in fixed bed adsorbers. As the author points out, the work is relevant to the use of adsorption for water and waste water purification.

In 'Solid–liquid mass transfer coefficient in mechanically agitated contactors' V. K. Patil, J. B. Joshi and M. M. Sharma report experimental data for solid–liquid mass transfer at a variety of locations in mechanically agitated contactors. Various designs of agitator and the effect of gas sparging were studied. The authors report correlations for the solid–liquid mass transfer coefficient in the plane of the impeller and note that the variation of the mass transfer coefficient depends mainly upon the impeller characteristics including the critical impeller speed.

E. Capuder and T. Koloini report on 'Gas hold-up and interfacial area in aerated suspensions of small particles'. In an experimental study of the carbonisation of lime suspensions with air–CO_2 mixtures the gas hold-up and interfacial area were measured in both a bubble column and a stirred reactor. the results are analysed by treating the three-phase systems as a two phase system with the liquid phase exhibiting non-Newtonian flow properties. By this means the experimental results were successfully correlated. The authors note that introduction of larger solid particles significantly affects the behaviour of the system.

The contribution on 'Enhanced collection efficiency for cyclone dust separators' by M. Biffin, N. Syred and P. Sage describes performance data for a new design of cyclone dust separator. Improved collection efficiencies, lower pressure drops and less tendency to choking were found compared to a conventional cyclone. In particular the authors note the capacity of the device to meet stringent emission regulations for coal combustion systems and its potential for use in high temperature combined cycle power generation systems.

In a Shorter Communication P. Srinivasan, V. R. Patwardhan, S. Devotta and F. A. Watson report on the thermal decomposition of trichlorotrifluoroethane. Data for decomposition in the presence of copper and steel are presented for static and dynamic conditions. An Arrhenius plot of the rate constant is given and reference is made to the effect of the presence of lubricating oils.

Brian Gay
Honorary Editor

Notes for Authors

Editorial Policy and Standards

1. Papers published in the Journal will be original contributions to chemical engineering knowledge, not previously published. In particular, the Editorial Board encourages the submission of papers which show how the results of research may be used in chemical engineering design. Such implications for design should be brought out clearly in the paper and its summary.

Accounts of research work of an experimental or theoretical nature which throw new light on established principles, which identify problems not yet solved, or indicate practical areas to which research effort may usefully be applied are also invited. Reports from industry and from research establishments are particularly welcome.

Papers may also deal with new developments of plant or processes if these developments are related to underlying principles and can be given quantitative expression.

2. Authors need not be members of the Institution. Papers must be in English and should normally be of 2500 to 5000 words, including Appendices. Figures should also be included in this count, each being estimated as equivalent to 250 words.

3. The Editorial Board will, however, also welcome Shorter Communications (less than 2500 words) for consideration for publication; these would describe, for example, novel research techniques, new analyses of previous work, or interesting aspects of work still in progress. A faster refereeing procedure has been arranged for such short Papers.

4. The Journal also publishes a limited number of longer Review Papers, which are critical assessments of previously published work in a selected area of chemical engineering. In conformity with editorial policy, Reviews should show how the results of research can be used in the design of plant and equipment.

Most Reviews are specially commissioned by the Editorial Board, but authors are also invited to offer Reviews for consideration for publication. In view of the substantial effort required, authors are advised to communicate with the Editor before embarking on a Review.

5. It is the policy of The Institution to publish only papers of the highest quality. To help maintain these standards all papers submitted are sent to referees familiar with the branch of chemical engineering covered. They advise as to whether the paper is acceptable or not and, in addition, indicate to the author possible ways in which, in their opinion, the paper might be improved. The final decision on publication is taken by the Editor in light of this advice.

Manuscript Requirements

1. The text should be typewritten, using one side of the paper only, double-spaced and with adequate margins to allow for revision and copy preparation marks. A summary, preceding the text, should briefly describe the essential original contents of the paper.

2. Mathematical expressions can sometimes be more easily interpreted by the printer if carefully written by hand. Where many equations appear, a list of symbols used should be inserted at the end of the paper, before the references. SI units should *always* be used; the negative index notation is preferred to the oblique stroke.

3. References are listed in the order in which they are first cited in the text, where they are indicated by superscript numbers. They should give in order: Authors' surnames and initials, Year, Title of book or journal, Volume, Issue, Page numbers , followed by name and town of publisher in the case of a book.

4. Tables, drawings and photographs should be on separate sheets at the end of the manuscript and not interspersed in the text. Tabulated data should not duplicate values detailed in the text or on graphs. Drawings submitted should be clear and complete and preferably in a form suitable for direct reproduction. Photographs should be restricted to the minimum necessary.

5. Where limitations of space preclude publication of detailed results, mathematical derivations, etc, authors are invited to include in their paper a statement that this information is available from them on application. Authors may make an appropriate charge for supplying items requested in this way. Such material should be supplied with the paper when submitted to the Editor.

Submission of Papers

1. Three copies of the paper should be sent to:

The Editor, Chemical Engineering Research and Design,
Institution of Chemical Engineers,
George E. Davis Building,
165–171 Railway Terrace,
Rugby CV21 3HQ, England.

or to an Associate Editor as follows:

Australia:
Prof R. G. H. Prince,
Department of Chemical Engineering,
University of Sydney,
Sydney 2006, New South Wales, Australia.

Continental Europe:
Prof Dr J. R. Bourne,
Technisch-Chemisches Laboratorium,
ETH-Zentrum,
CH-8092 Zürich, Switzerland.

Continental Europe:
Prof J. M. Smith,
Laboratorium voor Fysische Technologie,
Technische Hogeschool Delft,
Prins Bernhardlaan 6,
2628 BW Delft, Holland.

India:
Prof M. M. Sharma,
Department of Chemical Technology,
University of Bombay,
Matunga Road,
Bombay 400 019, India.

New Zealand:
Prof R. B. Keey,
School of Engineering,
University of Canterbury,
Christchurch 1, New Zealand.

USA:
Prof J. O. Wilkes,
Department of Chemical Engineering,
University of Michigan,
Ann Arbor,
Michigan 48109, USA.

2. A full address to which readers may send correspondence should be specified, including the post code. The address at which the work was carried out, if different, should also be indicated. Where there are several authors, one should be nominated to check proofs and to receive all correspondence.

3. A proof will be sent to the nominated author, to be checked for possible typographical errors. Other alterations cannot be incorporated at this late stage without incurring higher printing costs, and extensive alterations would necessitate postponement of publication of the paper to a later issue.

4. Following publication the nominated author will receive 50 off-prints of the paper (or 25 where there is just one author). Any further off-prints required should be ordered at proof stage. Reprints, ordered after publication, are more expensive.

VOL.
62
1984

REVIEW PAPER

DEVELOPMENTS IN ANAEROBIC TREATMENT OF HIGH STRENGTH INDUSTRIAL WASTE WATERS

M. A. BULL, (GRADUATE), R. M. STERRITT and J. N. LESTER
Department of Civil Engineering, Imperial College, London

The suitability and advantages of anaerobic digestion for the treatment of various industrial waste waters is discussed. Recent developments in the understanding of the anaerobic degradation process are reviewed together with recent advances in reactor design. Typical operating parameters and performance data for each reactor type are given. Theoretical and semi-empirical predictions of reactor performance are presented and their applicability is discussed.

INTRODUCTION

Waste waters containing high concentrations of soluble organic matter are discharged from many industries including dairies[1], abattoirs[2], and fruit processing plants[3]. Due to an increased dependence on water re-use in the UK legislation has been introduced to protect surface waters[4], thus treatment before discharge is necessary. Disposal to a municipal sewer is an alternative, however the industry will generally be charged by the local water authority, the cost usually being related to the strength and volume of the waste water[5]. If economic processes are available for the treatment of such waste waters there may be considerable cost advantage if on-site treatment processes are used[6].

Traditionally, aerobic treatment has been the method used for the treatment of such waste waters. Anaerobic processes have not generally been considered suitable due to their low rates of organic removal and their extreme sensitivity to fluctuations in process parameters[7]. In aerobic systems oxygen transfer to the liquid phase is generally the rate limiting stage[8], high-rate aerobic systems require the use of pure oxygen which not only adds to the treatment costs but places a heavy reliance on an external source of supply for a key element of the process[8]. High strength waste waters require such long residence times or high rates of aeration that for increasing waste strength anaerobic processes become more economic than aerobic systems. Cillié et al[9] examined the operating and capital costs of waste water treatment systems and concluded that for waste waters with a chemical oxygen demand (COD) of 4000 mg l^{-1} or more anaerobic processes are the cheapest option whilst at a COD of 20000 mg l^{-1} anaerobic systems cost a quarter of equivalent aerobic processes. Cillié et al[9] only considered conventional low-rate reactors in this analysis, with the development of new high-rate anaerobic reactor types even dilute wastes may be treated economically[6,10]

Microbiology of the Anaerobic Digestion Process

Anaerobic digestion is a complex process involving various groups of organisms including bacteria[11], fungi[12] and protozoa[13] which have all been observed in the digestion process; however only bacteria are considered to be present in sufficient numbers to have a significant role in treatment[11].

The anaerobic process may be arbitrarily divided into two phases; the non-methanogenic phase where complex organic compounds are hydrolysed and fermented into simple compounds, usually short-chain fatty acids, and the methanogenic phase where methane is produced from simple organic compounds[11]. The biochemical transformations in each of these phases are performed by two distinct groups of bacteria generally termed the acid formers and methane formers. It has recently been shown that there is another important group of organisms, the obligatory hydrogen producing acetogenic (OHPA) bacteria, which produce acetate from higher molecular weight fatty acids[14].

The non-methanogenic bateria can utilise many complex organic substrates. Lipids[15], proteins[16] and carbohydrates[17] are all successfully degraded to short chain organic acids. These diverse reactions require many different types of bacteria, the presence of different bacterial groups have been demonstrated by many authors[11]. Non-methanogenic bacteria are mainly obligate anaerobes and although facultative bacteria are found they typically account for less than 10% of the population[18].

It is presently thought that methanogenic bacteria can utilise only formate, acetate, methanol, hydrogen and carbon dioxide as substrates[19] and thus the action of the OHPA bacteria is essential in breaking down longer chain organic acids to acetate[20]. It has been estimated that 54% of the acetate and hydrogen is formed through the action of the OHPA[20]. These two groups of bacteria must grow in close association with one another since the OHPA bacteria depend on the methanogens to remove the hydrogen they have produced to maintain ideal thermodynamic conditions (the pH_2 of an anaerobic system should ideally[14] be maintained below 10 Nm^{-2}). Although the methanogenic bacteria are generally considered to be the rate-limiting step of the soluble phase of anaerobic digestion the OHPA bacteria generally have far greater doubling times (typically 2–6 days[21,22]) than the methanogenic bacteria (0.2–2.0 days[23]) thus maintaining favourable conditions for growth of the OHPA bacteria is of the utmost importance. A summary of the anaerobic digestion process is shown in Figure 1.

© Institution of Chemical Engineers

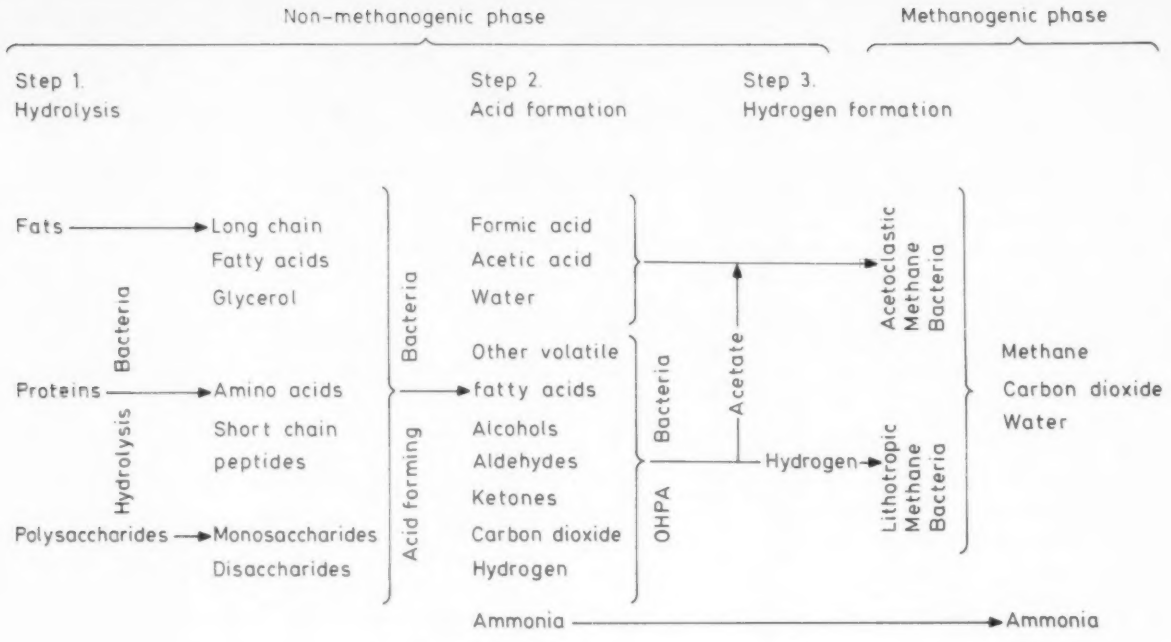


Figure 1. Anaerobic degradation of organic material.

Both the OHPA and the methanogenic bacteria are obligate anaerobes but their precise physiological characteristics have not been defined due to difficulties in obtaining pure cultures[19].

Methane is produced by two distinct mechanisms, approximately 70% originates from acetate;

$$CH_3COOH \rightarrow CH_4 + CO_2$$

Stadtman and Barker[24] concluded from tracer studies that the methane was formed entirely from the methyl group and carbon dioxide from the carboxyl carbon of the acetate molecule.

The remaining 30% of the methane is formed by the reduction of carbon dioxide;

$$CO_2 + 4H_2 \rightarrow CH_4 + 2H_2O$$

The hydrogen consumed in this reaction is produced by the OHPA bacteria during the degradation of the longer chain organic acids, a typical reaction in this phase is the degradation of propionate[25]

$$Prop^- + 3H_2O \rightarrow Acetate + HCO_3 + H^+ + 3H_2$$

Thus there is an equilibrium between these two reactions since hydrogen is only detected in very low concentrations in anaerobic digesters[26] indeed it has been shown that in a typically loaded digester the hydrogen removal rate is only 1% of the maximum possible[20].

Gas formation is inhibited by many substances, in particular certain heavy metals such as cadmium, copper, chromium, zinc and iron and certain organic compounds such as chloroform[27,28]. Low concentrations of iron (0.2–2 mM) have, however, been shown to stimulate methane production especially in conjunction with sulphate ions[29,30].

The somewhat delicate nature of the anaerobic digestion process has restricted its use for the treatment of industrial waste waters. The only established process is the anaerobic lagoon which is simply an open pond loaded to such an extent that anaerobic conditions prevail throughout the liquid volume. Excess undigested grease floats on the surface forming a natural cover for retention of heat and strict anaerobic conditions. Biochemical Oxygen Demand (BOD) loadings are low, typically in the range 0.16–0.4 kg m^{-3} d^{-1} with retention times of 4 days or more[31]. Anaerobic lagoons are generally used as a pretreatment stage before final treatment, although they operate at very low organic removal rates they are reported for treatment of a wide variety of waste waters including fruit processing[32,33] and meat packing wastes[34], where the system is often more economical than equivalent aerobic systems[35].

Biological Kinetics

Various basic equations occur frequently in theoretical models of biological unit operations. The growth rate of the biomass is assumed to be related to the biomass concentration, X

$$\frac{dX}{dt} = \mu X \tag{1}$$

The specific growth rate μ is not a constant but is related to the substrate concentration S. Monod[36] developed a semi-empirical equation which predicts that

$$\mu = \frac{\hat{\mu} S}{K_s + S} \tag{2}$$

where $\hat{\mu}$ is the maximum specific growth rate. K_s is the substrate concentration at which the specific growth rate is half the maximum rate, thus giving an indication of how easily the substrate is assimilated by the biomass.

VOL. 62 1984

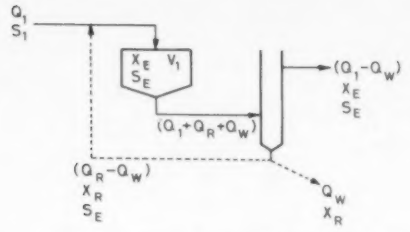


Figure 2. Mass balance over anaerobic contact reactor (ref 6).

A similar relationship is used to relate substrate utilisation rate U to initial substrate concentration

$$U = \frac{K_m S}{K_s + S} \tag{3}$$

where K_m is the maximum substrate utilization rate.

Monod[36] found that a constant relationship existed between the mass of bacteria produced and the mass of substrate utilised, this led to the definition of the growth yield Y.

$$Y = \frac{\text{mass of organisms formed}}{\text{mass of substrate utilised}} \tag{4}$$

This relationship may also be expressed as a differentiation[37],

$$\frac{dX}{dS} = -Y \tag{5}$$

The growth yield has important implications for the economics of a particular process as it is an indication of the quantity of excess sludge that will be produced and which will need subsequent treatment and disposal.

REVIEW OF REACTOR TYPES

Anaerobic Contact Reactor

The simplest reactor type reported for anaerobic degradation is the stirred-tank reactor. This has been widely employed for the stabilisation of sewage sludge and the treatment of industrial wastes containing high concentrations of solids such as palm oil wastes[38]. In this type of reactor the solids retention time (SRT) is equal to the hydraulic retention time (HRT) and hence the use of such reactors for high-rate treatment is not possible due to wash-out of the biomass[39]. The anaerobic contact (or anaerobic activated sludge) process employs a settling tank after a contact reactor, such that a portion of the settled sludge can be recycled[40].

The anaerobic contact reactor has been used for the treatment of a wide variety of waste waters. Schroepfer and Ziemke[41] evaluated the process for the treatment of packing house fatty acids, domestic sewage, a wood fibre, and synthetic milk waste waters. To aid settling in the second stage a vacuum degasification system was placed between the reactor and the settling tank. Typical BOD removals were between 69.9–97.9% for BOD loadings of between 0.44 and 2.5 $kg\,m^{-3}\,d^{-1}$. BOD removals when the reactors treated a domestic sewage were poorer, 74.5–69.9% for BOD loadings of 0.56–0.94 $kg\,m^{-3}\,d^{-1}$. The reactor configuration is widely reported for the treatment of higher strength waste waters[42,43,9], the treatment of dilute wastes generally being impracticable due to the long retention times required[44].

Anderson and Donnelly[7] derived a theoretical approach to predict the performance of an anaerobic contact system by taking mass balances across the reactor, their reactor system is shown in Figure 2.

At steady state these balances reduce to (see list of Symbols Used):

$$\mu = \frac{1}{\tau_s} + k_D \tag{6}$$

for the biomass and

$$\frac{1}{\tau_s}\cdot\frac{1}{Y} + \frac{k_D}{Y} = \frac{Q(S_e - S_i)}{XV} \tag{7}$$

for the substrate.

By operating laboratory scale digesters at steady state the kinetic coefficients $\hat{\mu}$, K_s, k_D and Y may be determined and used in the model to predict unsteady state operation.

Two digester systems were evaluated by this method, a semi-continuous system where sludge is wasted daily and a continuous system where a constant biomass volume was maintained in the settling tank. A simple substrate based on glucose was fed to the semi-continuous digester whilst a more complex substrate with 40% of the COD obtained from a meat extract and peptone was fed to the continuous system. The results obtained are summarised in Table 1 together with some comparative aerobic data.

Table 1. Typical biological kinetic coefficients of aerobic and anaerobic systems

Ref.	Reactor Type	Substrate Type	$\hat{\mu}$ (days)	K_s (mg l^{-1}) COD	K_D (days)	Y ($mg_{VSS}\,mg^{-1}_{COD}$)
6	Continuous Anaerobic Contact	Complex	0.274	2953	0.0215	0.192
6	Semi-Continuous Anaerobic Contact	Glucose	0.158	212	0.029	0.208
45	Activated Sludge	Sewage	5.0	40	0.06	0.4
94	Anaerobic Fluidised Bed	Whey Permeate	N.R.	N.R.	N.R.	0.24

The difference in k_D values for the two anaerobic systems is an indication of the relative biodegradability of the two substrates. It is also important to note the much lower yield coefficients for anaerobic systems as this indicates that smaller amounts of biomass will be produced and hence the sludge disposal problem will be diminished.

Above a sludge loading of 0.25 $kg_{COD}\,kg^{-1}_{MLVSS}\,d^{-1}$ the settling properties of sludge began to deteriorate and above a mixed liquor volatile suspended solids (MLVSS) concentration of 18000 $mg\,l^{-1}$ separation of the biomass was impaired. These two difficulties are the basic limitation on the ultimate rate of the process[46].

A novel anaerobic contact digestion system has been described which uses a gas-mixed reactor followed by an upflow sludge-blanket clarifier[47]. The system was used to treat a piggery waste and was loaded up to 38 $kg_{COD}\,m^{-3}\,d^{-1}$ whilst still maintaining methanogenic conditions. Satisfactory treatment was obtained at loadings of 4 $kg_{COD}\,m^{-3}\,d^{-1}$ and HRT of 3–5 days. It was found that the effluent quality deteriorated linearly with increasing organic loading and a close fit to the system's performance was obtained by the following equations

$$S_e = 1.5 + 0.151\,R \tag{8}$$

$$N = 89 - 1.01\,R \tag{9}$$

Kinetic coefficients were also derived in a similar manner to Anderson[7]; the growth yield was 0.213 and the endogenous decay coefficient −0.016. It should be noted that the system was operated without sludge recycle which tends to result in higher yield coefficients than systems with recycle[47,48].

The separation of the biomass from the treated liquor is one of the main problems with the anaerobic contact reactor. To improve separation various modifications have been suggested. One system employs a cold thermal shock, reducing the temperature of the effluent from 35°C to 15°C. This arrests gasification in the settling tank and also encourages flocculation of the solids[49].

Some authors have reported the use of coagulant chemicals[50,51]. A 90% reduction in effluent solids was possible by treating the effluent with sodium hydroxide to pH 8.3 and then ferrous chloride at concentrations between 60 and 230 $mg\,l^{-1}$. An increase in gas production was found, due to the increased recycle of active biomass[50].

Anaerobic Sludge-Blanket Reactor (ASBR)

The anaerobic sludge-blanket reactor consists of a single reactor vessel, the waste enters at the base of the reactor and passes upwards through the biomass which takes the form of a 'sludge blanket'. Mechanical mixing and sludge recirculation are kept to a minimum to aid settlement of the sludge flocs. Since retention of the sludge depends on an effective separation of the gas produced, a gas–solids separation unit is included in the reactor.

The reactor has been employed in laboratory, pilot plant and full-scale systems, generally treating high-strength wastes[53,54].

Using an 18 litre reactor the treatment of a skimmed-milk type waste water with a COD of 1500 $mg\,l^{-1}$ has been reported. COD reductions of 90% were obtained with COD loadings up to 7 $kg\,m^{-3}\,d^{-1}$ and sludge loadings between 0.4 and 0.6 $kg\,kg^{-1}_{MLVSS}\,d^{-1}$, the reactor was operated[55] at 30°C. A sugar-beet waste with a COD of between 5000 and 9000 $mg\,l^{-1}$ has also been treated by the ASBR, with COD loadings of between 4 and 14 $kg\,m^{-3}\,d^{-1}$, 65–95% COD reductions were achieved[53,56].

Upflow sludge-blanket reactors have been used typically for the treatment of high-strength wastes at elevated temperatures. Pretorius[57] reported the application of the process for the treatment of a raw sewage using a laboratory scale reactor followed by an anaerobic filter, both stages had a reactor volume of 8 litres. The digesters were maintained at a constant 20°C and the waste strength was adjusted to a constant COD of 500 $mg\,l^{-1}$. COD removals were typically 90–78% at total loadings of 0.25–0.47 $kg\,m^{-3}\,d^{-1}$, typical reactor MLVSS was 25000 $mg\,l^{-1}$. Following the laboratory experiments a small pilot plant was constructed with a reactor volume of 2000 litres, the unit gave almost identical results to the laboratory study. Apart from periodically breaking up the sludge layer in the conical section, best results were obtained without mixing.

Somewhat lower removals have been found in a system treating an acetate-rich waste water, COD removal was up to 70% without a primary settling tank, the optimum BOD loading for gas production was only 1.6 $kg\,m^{-3}\,d^{-1}$, however since the system was self-scrubbing the gas contained up to 99% methane[58].

Anaerobic Filter

To overcome the problem of settling and recycling of the biomass inherent in anaerobic free-floating systems the anaerobic filter has been developed. This consists of a reactor filled with a coarse packing media such as rock or gravel; as with its aerobic equivalent the reactor name is a misnomer since treatment occurs mainly due to biological action rather than any filtration effect. The waste water enters at the base of the reactor and flows upwards through the filter bed. Anaerobic organisms appear to accumulate in the void spaces between the media as well as becoming attached to the media surface, thus the waste comes into intimate contact with a large active biomass as it passes through the reactor[59].

The anaerobic filter was initially tested in laboratory-scale experiments where it was evaluated for the treatment of two synthetic substrates, a mixed volatile acids waste and a protein carbohydrate waste. The filter was packed with smooth quartzite stones 2.5–3.8 cm in diameter and dispersion rings were placed at 0.3 m intervals up the column to prevent channelling of the flow. The filter was tested by applying COD loadings between 0.425 and 3.40 $kg\,m^{-3}\,d^{-1}$ at an operating temperature of 25°C. The influent was diluted to give various waste strengths from 1500 to 6000 $mg\,l^{-1}$ COD. BOD removals increased with increasing waste strengths at the same organic loading, highest removals were up to 80% over the range tested[59]. The performance of the reactor (BOD removal efficiency, E) could be predicted by the empirical equation

VOL. 62 1984

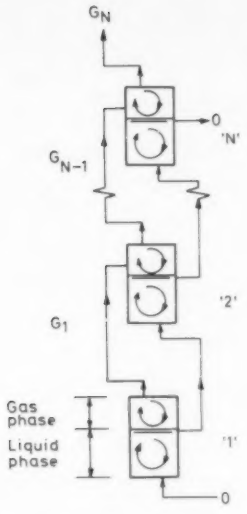


Figure 3. Completely mixed reactor series and mass balance for anaerobic filter modelling (ref 69).

$$E = 100\left(1 - \frac{1.8}{HRT}\right) \tag{10}$$

Plumer et al[60] extended this work by using a filter to treat a carbohydrate waste which contained significant concentrations of suspended solids. The filter operated at 35°C and treated a waste with influent characteristics of 1508 mg l^{-1} SS and 8475 mg l^{-1} COD. pH adjustment with sodium bicarbonate was necessary to maintain optimum pH conditions.

The anaerobic filter has also been reported for a wide variety of industrial waste waters including pharmaceutical wastes[61], abattoir wastes[62], dairy wastes[63] and vegetable processing wastes[64].

The kinetics of substrate removal in an anaerobic filter employing a large recycle rate have been studied[65]. Due to the recycle the system was interpreted as a completely-mixed reactor. By equating Fick's law of diffusion with the substrate utilisation rate equation the following equation was obtained

$$\frac{d^2S}{dz^2} = \frac{1}{D}\cdot\frac{UX}{K_s + S} \tag{11}$$

This equation does not have a simple general solution and was solved by assuming S to be either much smaller or larger than K_s. When S is larger and the expression for the thickness of the biofilm layer developed by other workers[66,67] is substituted the mass transfer rate dF/dt is given by

$$\frac{1}{V}\frac{dF}{dt} = k_1\frac{A}{V}\sqrt{S_b} \tag{12}$$

When S_b is much smaller than K_s the mass transfer rate is given by

$$\frac{1}{V}\frac{dF}{dt} = \frac{k_2 AS_b}{V} \tag{13}$$

By examining experimental data the authors found that equation (12) was more applicable, however insufficient data was available to make a final conclusion[65].

Using an anaerobic filter with a substantial amount of recycle enables the process to treat waste waters of a toxic nature which would be difficult to treat anaerobically in a single-pass reactor. Chian and DeWalle[68] used this reactor configuration to treat an acidic waste water with a pH of 5.4 and a COD of 54 000 mg l^{-1}. The filter was 55 l in volume and packed with a commercial plastic packing with a porosity of 0.94. Reactor start up was initially attempted without any biological seeding material, however no significant biodegradation was noted. Following this experiment the filter was seeded with active digester sludge and the reactor successfully treated the waste water, provided a sufficiently high recycle ratio was maintained. The reactor was evaluated over a range of retention times and it was found that COD removal rapidly decreased from over 95% to 52% when the retention time was less than 7.5 days[68].

The single pass anaerobic filter has been considered as a series of completely mixed reactors[69], the model is shown in Figure 3. By taking unsteady-state differential equations over each reactor the following are obtained for the liquid and gas phase

liquid phase

$$\frac{dS_{i_n}}{dt} = \frac{Q}{V_n^l}(S_{i_{n-1}} - S_{i_n}) + \Sigma_{i_n}^l \tag{14}$$

gas phase

$$\frac{dP_{i_n}}{dt} = \frac{G_{n-1}P_{i_{n-1}} - G_nP_{i_n}}{V_n^g} + \frac{V_n^l RT\Sigma_{i_n}^g}{V_n^g M_i} \tag{15}$$

see list of Symbols Used; l and g denote liquid and gas phases respectively.

By summing the sources and sinks for each substrate the differential equations were solved numerically by computer. The first-order approximation and Michaelis–Menton substrate kinetics (equation 3) were used in the calculation. The simulation based on Michaelis–Menton kinetics described the system adequately whilst it was considered that the model based on first-order kinetics was more readily usable for design.

Various packing materials have been evaluated for use in the anaerobic filter. These materials include gravel[70], crushed stone[71], rashig and various commercial packings[60,68,72]. Khan et al[73] compared two packing materials, a non-porous anthracite coal and surface-active granular carbon particles. The filters were used to treat a stripping bath waste water and a synthetic substrate, a typical influent COD was 1350 mg l^{-1}. It was found that the activated carbon packed filter gave removals superior to the anthracite packed filter (71–74% as against 58–69%), methane yields were up to 100% greater. The ability of the activated carbon surface to protect dense populations of bacteria was considered one of the main reasons for superior performance.

A similar reactor to the anaerobic filter has been described, known as 'the stationary fixed-film reactor'. In its simplest form the reactor is merely a vertical glass tube through which the waste water is pumped[74]. In a downflow-reactor biomass is retained almost entirely as a film on the reactor walls whilst in the upflow reactor biomass accumulates in the reactor as biological flocs.

Initial experiments consisted of testing reactors with varying surface-to-volume ratios. COD removal efficiency increased with decreasing reactor diameter at the same volumetric loading. The reactor configuration was refined to consist of several small tubes contained in a larger vessel. Several materials were tested for use in the reactor including clay, polyvinyl chloride and needle-punched polyester[75]. Red clay and needle-punched polyster were found to be the most effective supports due to the ability of the bacteria to become entrapped on the surface.

Using fired-clay support tubes (2.8 cm i.d., 3.8 cm o.d.) contained in a larger glass tube the reactor was able to effectively treat a waste water with a COD of 14 000 mg l^{-1} at loadings of up to 17.9 kg_{COD} m^{-3} d^{-1} at 35°C with COD reductions between 78–84%. The reactors were shown to be able to tolerate severe hydraulic overloading for 24 hours without serious problems[76]. Operation of the reactors was found to be more efficient when applying intermittent rather than continuous loading[77].

Anaerobic Rotating Biological Contactor (ARBC)

The ARBC consists of a series of disks mounted on a central rotating shaft in an enclosed cylindrical tank. This reactor configuration is widely reported for aerobic reactors[78] but in its anaerobic mode the disk submergence is greater (>70%) and the reactor is in a closed vessel. The reactor was evaluated in a laboratory-scale experiment treating a synthetic waste water, with glucose as the sole carbon source[79]. The reactor consisted of four stages, each with ten 12.7 cm diameter disks constructed from polymethylmethacrylate, the total reactor volume was 5.25 l. During the start-up procedure part of the glucose was replaced by methanol in order to encourage the growth of methanogenic bacteria. The reactor was operated over a range of TOC loadings from 1.44 to 12.06 kg m^{-3} d^{-1}. TOC removals varied from 96% to 46%, effluent suspended solids were relatively high, between 296 and 361 mg l^{-1}.

Two approaches were used to describe the performance of the reactor. The first was an empirical solution where

$$\ln S_e = \ln S_i - K_t(HRT) \tag{16}$$

From the experimental data K_t was found to be

$$K_t = 0.3744 - 7.96 \times 10^{-5} S_i.$$

Although this approach gave good agreement with the experimental results it was only considered applicable to this particular reactor.

A different approach was used to develop a more general solution. The removal in each stage is described by

$$M_n = \frac{kS_i^2}{K^i + S_i} \tag{17}$$

This was developed from previous work on aerobic RBCs[80],

In the first stage it can often be assumed that $S_i \gg K^i$ then the equation may be approximated by

$$M_n = kS_i \tag{18}$$

thus k may be calculated from experimental data and an approximation for K^i may be found. The model was found to agree closely with the experimental results however no independent data was available to verify the model.

It has been reported that rotation of the discs in an ARBC has virtually no effect on the efficiency of the process; thus an anaerobic baffled reactor has been developed through which the liquid flows horizontally and around several baffles which serve to retain the biomass. Little reported information is available for this reactor configuration, however COD reductions of 60–80% for loadings of 10–20 kg m^{-3} d^{-1} have been noted[81].

Anaerobic Expanded and Fluidised Bed Reactors (AEBR and AFBR)

Fluidised beds can be considered to be a hybrid between fixed film and free-floating reactor systems. A fluidised bed reactor consists of a bed of particles contained in a vertical column, through which waste water flows upwards (through the column) at a sufficient velocity to maintain the particles in constant motion, but with the flowrate adjusted to avoid particle carry-over in the effluent. This arrangement provides a large specific surface (m^2 m^{-3}) available for microbial growth as a thin film, typically 3000 m^2 m^{-3} for sand particles[82]. Thus high biomass concentrations may be developed which are not subject to diffusional limitations. An expanded bed reactor is a similar type of reactor except that the bed expansion is limited to approximately 5% and the particles remain in constant contact with one another.

Initial experience with the fluidised bed reactor for waste water treatment applications has been for the denitrification of treated sewage[84,85] and the use of aerobic reactors for COD removal[83]. The anaerobic expanded bed reactor has been reported for the treatment of a dilute waste water[86] and a domestic waste water[87]. These laboratory scale studies used 1 litre volume reactors and were filled with either aluminium oxide pellets or polyvinyl chloride and expanded ion exchange resins. In the domestic waste water treatment study[87] the reactors were operated at 20°C and treated a waste water with an average COD of 186 mg l^{-1} and a suspended solids (SS) of 86 mg l^{-1}. The performance of the AEBR was studied at COD loadings of between 0.65 and 35 kg m^{-3} d^{-1}, effective treatment was obtained up to COD loadings of 4 kg m^{-3} d^{-1}. Above this loading treatment efficiency rapidly declined to less than 50% at 19 kg m^{-3} d^{-1}. Effluent suspended solids were generally very low, below 5 mg l^{-1} but rose rapidly at retention times of less than 30 min.

The results from the synthetic substrate experiments were subjected to a kinetic analysis, the effluent concentration was given by

$$S_e = K_1 S_i B \tag{19}$$

$$S_e = K_2 S_i C \tag{20}$$

These equations are simplified forms of equations (2) and (3) and their pseudo-first-order nature relies on assuming K_s is high compared to the substrate concen-

VOL. 62 1984

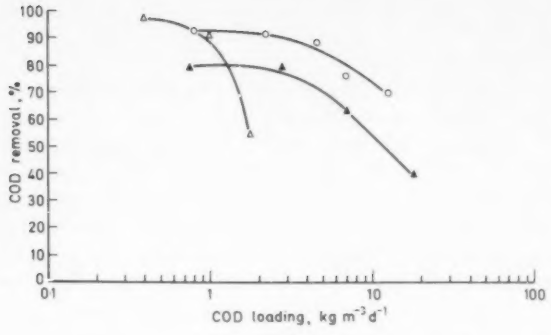


Figure 4. COD removal versus COD loading for (△) anaerobic filter (ref 59), (▲) anaerobic expanded bed (ref 7) and (○) anaerobic fluidized bed reactor (ref 90).

tration. Applying the experimental results to these equations gave a reasonably good fit with correlation coefficients between 0.76 and 0.96.

Matsui et al[88] reported on the treatment of a dilute waste water in a fluidised bed reactor. COD removals were generally very low (typically 23.8%) but a very high range of COD loadings were tested, between 18.6 and 131.6 kg m^{-3} d^{-1}. The use of particles with a diameter less than 0.42 mm was found to be less efficient due to the inability of biomass to adhere to the surface of the media.

The performance of the anaerobic expanded bed reactor whilst treating a domestic sewage has been studied. The TOC of the influent varied between 40 and 260 mg l^{-1}. It was found that operating under these conditions TOC removal was poor (17–25%) except when the TOC loading was low (<0.5 kg_{TOC} m^{-3} d^{-1}) and it was considered that under real operating conditions the reactor would be unsuitable for treatment of waste waters of this nature[89].

The use of anaerobic fluidised bed reactors for treatment of higher-strength waste waters appears to be more promising, with far higher removal rates being attained. Treatment of a synthetic milk based waste at 37°C and 25°C and a synthetic meat based waste has been reported on a laboratory scale. At 37°C the reactors were able to remove 70% of the COD at COD loadings[90,91] of up to 12.5 kg m^{-3} d^{-1} however the reactors were not stable at loadings of over 6 kg m^{-3} d^{-1} and additional buffering chemicals were required. This, however, is a common problem associated with milk-based waste waters[1]. These reactors have also been operated at unsteady-state and maintained high removal efficiencies[92,93]. Removals of up to 70% were reported at ambient temperatures when treating a meat-extract waste water. Figure 4 summarises these results and compares them with other similar processes.

Sutton and Li[94] used the approach developed by Anderson[7] to evaluate the kinetic parameters in a fluidised bed process, the observed values for the reported kinetic values are shown in Table 1. Two sand particle sizes (0.5 and 0.7 mm) were evaluated for use in the reactor. It was found that the smaller particles gave marginally superior COD reductions (68% compared to 63%).

The effect of particle size and biofilm thickness on substrate removal has been examined in a theoretical analysis[95]. The simultaneous transport and utilisation of substrate in an individual particle's biofilm was equated to give

$$D\frac{1}{r^2}\frac{\mathrm{d}}{\mathrm{d}r}\left(r^2\frac{\mathrm{d}S}{\mathrm{d}r}\right) = KS \tag{21}$$

The equation was arranged into a dimensionless form by substituting the following variables

$$\phi = r_m\sqrt{(K/D)} \tag{22}$$

$$\beta = (r_p - r_m)\sqrt{(K/D)} \tag{23}$$

$$= \phi(r_p/r_m - 1) \tag{24}$$

$$\bar{r} = r/r_m \tag{25}$$

$$\bar{S} = S/S_b \tag{26}$$

Substrate removal per unit volume of the reactor, J, was given by

$$J = -aD\left(\frac{\mathrm{d}S}{\mathrm{d}r}\right)_{r_p} = \eta kS \tag{27}$$

where η is effectiveness factor, and

$$a = \frac{3(1-\varepsilon)}{r_p}$$

where ε is porosity.

The dimensionless form of equation (21) may be solved to give an expression for S which when combined with equation (27) gives an expression for

$$\frac{\eta}{3(1-\varepsilon)} = \frac{1}{(\beta+\phi)^2}\left[\frac{\beta+\phi-1}{1+(\phi-1)/(\phi+1)}\cdot e^{-2\beta} - \frac{\beta+\phi+1}{1+(\phi+1)(\phi-1)}\cdot e^{2\beta}\right] \tag{28}$$

Removal of substrates is greatest when η is at a maximum thus $\eta/3(1-\varepsilon)$ was evaluated for several values of β and ϕ. It is apparent that there is an optimum biofilm volume per unit volume of reactor and hence based on this analysis there is no optimum particle diameter.

Rittman[96,97] has examined biofilm kinetics in detail and has used this analysis to compare four different reactor configurations[98]. The analysis equates mass transport and the film substrate utilisation

$$D_f\frac{\mathrm{d}^2S_f}{\mathrm{d}z^2} = \frac{KX_fS_f}{K_s+S_f} \tag{29}$$

and includes a term for mass transfer resistance from the bulk liquid into the biofilm surface.

$$J = (D/L)(S - S_s) = K_L(S - S_s) \tag{30}$$

These equations may be simultaneously solved for J when the other kinetic parameters are known[96,97]. Steady-state biofilm-thickness was found by assuming that total amount of biofilm mass is equal to that which can be supported by the substrate flux thus;

$$JY = k_D X_f L_f \quad (31)$$

or

$$L = JY/k_D X_f \quad (32)$$

General reactor performance is given by a mass balance over a control volume

$$\frac{dS}{dt} = -V\frac{dS}{dx} + D\frac{d^2S}{dx^2} - aJ - \frac{\varepsilon k_m XS}{K_s + S} \quad (33)$$

These equations were solved numerically by a finite difference method. Five reactor types were compared, a completely mixed reactor and packed and fluidised beds with and without recycle.

The model predicted that a once-through fluidised bed reactor would achieve superior performance as the biofilm is evenly distributed throughout the reactor whilst the liquid regime is 'plug-flow'. Adding recycle to fixed and fluidised bed reactors makes performance approach that of completely mixed units which had the lowest removal efficiency.

Separated-Phase Anaerobic Digestion

Separated-phase anaerobic digestion involves the use of two reactors to separate physically the non-methanogenic and methanogenic phases. The use of two separate reactors allows the two phases to operate at their ideal environmental conditions (e.g. pH, temperature and organic loading), and allows the delicate methanogenic and OHPA bacteria to be protected from process fluctuations. This reactor configuration also enables the components of the effluent from the first stage to be adapted to obtain the best possible substrates for the OHPA bacteria[13]. Since these bacteria have the longest doubling-times of the organisms found in anaerobic digestion use of suitable substrates can enhance the possible reaction rates. It has been shown that the OHPA bacteria operate more efficiently when treating a single acid substrate rather than a mixed acid substrate[99].

Phase-separation has been achieved by three methods; a dialysis technique[100,101], inhibition of the methanogenic phase by the addition of certain chemicals[102] or by kintic controls in each reactor[103].

Hammer and Borchardt[100] utilised two completely-mixed reactors separated by a vinyl dialysis membrane. This apparatus was used to determine the oxidation/reduction potential and pH for acidification and methane fermentation of digester sludge. Optimum pH conditions were 6.9–7.0 and 7.05–7.2 and oxidation/reduction potential −508 to −516 mV and −520 to −527 mV for the acidification and methane formation steps respectively. It was concluded that when an anaerobic digester operated under ideal conditions for the methanogenic phase the acidification step was rate limiting since it only operated at 75% of its optimum rate.

pH optima of 5.8 and 7.8 were found for a mixture of domestic refuse and sewage sludge. Near-complete liquefaction was obtained in the range 20–240 $kg_{MLVSS}\,m^{-3}\,d^{-1}$ at volatile solids concentrations of 11–13%. Some alkaline pretreatment had taken place previously[104].

By adjusting the residence times and environmental conditions in a reactor, optimum conditions for acid and gas formation may be achieved[105–107].

This concept has been applied to the treatment of a glucose-based waste and an effluent from a confectionery industry. With an influent COD of 3581 $mg\,l^{-1}$ between 54 and 73% acidification was achieved at hydraulic retention times of between 10 and 23 h in the first reactor. The methanogenic-phase reactor operated at longer retention times of between 47.6 and 116.8 h where conversion of the volatile acids varied between 61 and 19%. By connecting the gas phase of each reactor together improved COD removals were obtained. The biomass from the second stage reactor had poor settling properties and gravity sedimentation was not feasible[103].

Cohen et al[108,109] studied the anaerobic digestion of a 1% glucose substrate with separated acid and methane production. At a retention time of 10 h in the acidic reactor over 96% of the glucose was degraded to hydrogen, carbon dioxide, butyrate and acetate at 30°C and pH 6.0; 98% of the organic substrates were converted to carbon dioxide, methane and biomass in the methanogenic reactor at a retention time of 100 h. Approximately 11% of the glucose fed to the system was converted to biomass. It was possible to apply an organic loading to the two-phase system which was 2.7 times that applied to an equivalent single-phase system.

Stability of one- and two-phase systems treating glucose solutions has also been investigated under conditions of organic overloading[110]. In a single-phase system accumulation of the volatile acids occurred, especially propionic acid, and degradation of these acids took up to 120 h. Overloading the methanogenic-phase of a two-phase system with high concentrations of volatile acids led to an immediate breakdown of the acids within 60 h, indicating that the two-phase system was more stable.

Bull et al[111] conducted a comparison of an anaerobic fluidised bed reactor and a two-phase system consisting of a stirred-tank acidification reactor followed by a methanogenic fluidised bed. Both systems were supplied with a glucose-based waste-water. The two-phase system had a consistently superior effluent quality and was more stable than the single-phase reactor under conditions of shock loading. The specific degradation rates for acetate and propionate in the two-phase system were approximately twice those obtained in the single-phase reactor.

Two-phase digestion of activated sludge in completely mixed reactors has been described. Acidification of the activated sludge took place at a pH of 5.7 and an oxidation/reduction potential of −240 mV. Acid-phase digestion could be operated satisfactorily at sludge loadings between 0.055 and 0.139 $kg_{MLVSS}\,m^{-3}\,d^{-1}$ with retention times between 10 and 24 h. The acidified activated sludge could be gasified efficiently in the methane digester at a retention time of 6.46 d. The performance of the system was favourably compared with a single phase system which operated at a retention[112] time of 14 d.

DISCUSSION

Many new processes have been developed which have shown considerable potential for successful treatment of

VOL. 62 1984

organic waste waters. Several of these processes have been applied to the treatment of dilute wastes on a laboratory scale at steady-state. However results when treatment is under real process conditions have been less successful. Reliable and economic treatment of organic waste waters may therefore only be viable for higher-strength wastes. This is due to the relatively high half-rate coefficients encountered in anaerobic conditions; with typical values of $>2000\ mg\ l^{-1}$, only wastes with a strength above this value would be treated at a rate approaching the maximum possible. Although processes which can achieve treatment at these rates have been developed, and many industries discharge waste waters of a suitable organic strength, few industries have adopted anaerobic systems. This has been attributed to the following reasons.

1. Slow start-up times.
2. Sensitivity to toxic compounds and elements.
3. Rarely offers complete treatment.
4. Little practical operating experience.

Start-up periods of between one month to one year have been reported[7,86], the major limitation being the slow doubling-times of both the OHPA and the methanogenic bacteria. Growth of these bacteria can be encouraged by careful manipulation of the environmental conditions, inoculation with digester sludge and supplementing the feed with essential nutrients and a suitable substrate for the methanogenic bacteria such as methanol. Using these techniques it has been reported that reactor start-up may be achieved more rapidly[79]; within a month in some cases[91].

Anaerobic processes have long been associated with difficult and unstable operation under fluctuating process conditions[90]. This is perhaps the case with simple reactor types, however the new reactors have much higher biomass concentrations and solids retention times and are hence able to tolerate extreme organic overloading, of[70] up to $94\ kg_{COD}\ m^{-3}\ d^{-1}$ and variations in other process conditions[92] such as temperature and pH.

Suspended- and attached-growth systems have been compared as to their ability to withstand a variety of toxic materials such as chloroform, cyanide and formaldehyde[81]. In both cases it has been shown that prolonged periods of up to 4 d of zero gas production do not necessarily indicate complete process failure[81]. Fixed-film reactors, however, have been shown to be more tolerant of such conditions, especially if effluent recycle was not employed[81]

Evaluation of a system's performance at steady-state may not give a true indication of its performance at full-scale and treating waste waters of a variable nature. Many theoretical and semi-empirical models have been developed for prediction of the performance of various reactors. However, virtually all of these rely on steady-state operation and idealised operation and idealised conditions. Although many of these predict reactor performance successfully the simplifications used limit their usefulness more to comparative purposes.

Fixed-film reactors, as well as the ASBR appear to be the most promising development for anaerobic treatment of waste water due to their ability to retain large quantities of biomass, typically 10–40 $kg\ m^{-3}$ compared to 1–3 $kg\ m^{-3}$ of a typical aerobic activated sludge reactor. These high biomass concentrations allow anaerobic reactors to operate at organic loadings at least one order of magnitude higher than aerobic processes. One of the major problems associated with these anaerobic processes is the high effluent suspended solids concentrations encountered. This will probably necessitate aerobic treatment to produce an effluent acceptable for direct discharge to a natural watercourse, but data on aerobic degradation of anaerobic effluent is scarce and thus the amenability of anaerobic effluents to aerobic treatment will require further investigation. However the anaerobic reactor types will probably be ideal for pre-treatment of waste water before discharge to a municipal sewer and could result in cost savings to industry.

Only some of the new systems described have been evaluated on an industrial scale. There is therefore an urgent requirement for pilot- and full-scale evaluation of these developments before their widespread use can be expected.

Although most reactor evaluation has taken place on a laboratory scale many different waste waters have been treated successfully including some that are rarely considered suitable for anaerobic treatment such as dairy wastes[90]. Problems may arise where the influent contains high concentrations of suspended solids ($>1000\ mg\ l^{-1}$). In a single-stage reactor high solids concentrations may clog the reactor (e.g. in an anaerobic filter) or the solids may pass through the reactor largely untreated due to the low hydraulic retention times (e.g. in an anaerobic fluidised bed). However by careful design of pre-treatment stages these problems can be avoided.

Although many of the reactor designs are in an early stage of development, they offer the potential for energy savings and an ability to operate at organic loadings far in excess of equivalent aerobic reactor types, which will ultimately result in more economic industrial waste water treatment.

SYMBOLS USED

A	Area (L^2)
B	Net specific film growth rate (T^{-1})
C	Specific film utilization rate ($ML^{-3}T^{-1}$)
D	Diffusivity of substrate (L^2T^{-1})
D_f	Diffusivity of substrate through film (L^2T^{-1})
E	BOD removal efficiency (%)
dF/dt	Mass transfer rate (MT^{-1})
G	Gas flowrate (L^3T^{-1})
J	Substrate removal per unit volume ($ML^{-3}T^{-1}$)
k	Rate constant (T^{-1})
k_D	Endogenous respiration coefficient (T^{-1})
k_1	Rate constant based on zero order kinetics ($M^{\frac{1}{2}}L^{-\frac{1}{2}}$)
k_2	Rate constant based on first order kinetics (LT^{-1})
K_m	Maximum substrate utilization rate ($ML^{-3}T^{-1}$)
k'	Rate constant ($L^3M^{-1}T^{-1}$)
K'	constant in equation (17) (ML^{-3})
K_s	Half rate coefficient (ML^{-3})
K_s	pseudo-first-order rate constant
K_L	Mass Transfer Coefficient (LT^{-1})
K_1, K_2	Pseudo first order rate coefficients (T^{-1})
L	Length of reactor (L)
M	Molecular weight (M)
M_n	Mass of organic removal per stage per unit time in an RBC (MT^{-1})
N	COD removal efficiency (%)
P	Pressure (MT^{-1})

Q	Liquid flowrate (L^3T^{-1})
R	Volumetric organic loading, COD ($ML^{-3}T^{-1}$)
r	radial distance from the centre of support particle (L)
r_m	Support particle radius (L)
r_p	Total particle radius including biofilm (L)
S	Substrate concentration (ML^{-3})
S_b	Bulk substrate concentraton (ML^{-3})
S_e	Effluent substrate concentration, COD (ML^{-3})
S_f	substrate concentration in film
S_i	Influent substrate concentration (ML^{-3})
t	Time (T)
U	Substrate utilization rate ($ML^{-3}T^{-1}$)
V	Reactor volume (L^3)
X	Biomass Concentration (ML^{-3})
X_f	biomass concentration in film
Y	Growth Yield ($M\,M^{-1}$)
z	Length dimension normal to biofilm surface (L)
ε	Porosity (dimensionless)
η	Effectiveness factor (dimensionless)
μ	Specific growth rate (T^{-1})
$\hat{\mu}$	Maximum specific growth rate (T^{-1})
Σ_{in}	accumulation of component in reactor
τ	Solids retention time (sludge age) (T)

REFERENCES

1. Bull, M. A., Sterritt, R. M. and Lester, J. N., 1981, *J Chem Technol Biotechnol*, 31: 579.
2. Bull, M. A., Sterritt, R. M. and Lester, J. N., 1982, *Environ Technol Lett*, 3: 117.
3. Sterritt, R. M. and Lester, J. N., 1982, *Environ Technol Lett*, 3: 63.
4. UK Act of Parliament, *Control of Pollution Act*: 1974.
5. Dart, M. C., 1977, *Wat Pollut Control*, 76: 192.
6. Anderson, G. K. and Donnelly, T., 1978, in Mattock, G. (ed), *New Processes of Waste Water Treatment and Recovery*. (Ellis Horwood Ltd., Chichester).
7. Jewell, W. J., Switzenbaum, M. S. and Morris, J. W., 1981, *J Wat Pollut Control Fed*, 53: 482.
8. Forster, C. F., 1980, *Environ Technol Lett*, 1: 253.
9. Cillié, G. G., Henzen, M. R., Stander, G. J. and Baillie, R. D., 1969, *Water Res*, 3: 623.
10. Wheeldon, D. H. V. and Bayley, R. W., 1981, in Cooper, P. F. and Atkinson, B. (eds), *Biological Fluidized Bed Treatment of Water and Wastewater* (Ellis Horwood Ltd., Chichester).
11. Toerein, D. F. and Hattingh, W. H. J., 1969, *Water Res*, 3: 385.
12. Cooke, W. B., 1965, *Proc 20th Industrial Waste Conf*, Purdue Univ, 6.
13. Lackey, J. B., 1949, *Sewage Works J*, 21: 659.
14. Verstraete, W., Baere, L. De, and Rozzi, A., 1981, *Trib Cebedeau*, 34: 367.
15. McCarty, P. L., Jeris, J. S., McKinney, R. E., Reed, K. and Vath, C. A., 1962, *Sedgwich Laboratories of Sanitary Science. Report* No. R62-29, M.I.T. Cambridge, Mass.
16. Lackey, J. B. and Hendrickson, E. R., 1958, in *Biological Treatment of Sewage and Industry Wastes* Vol. II. (Reinhold, New York).
17. Kotzé, J. P., Thiel, P. G., Toerein, D. F., Hattingh, W. H. J. and Siebert, M. L., 1968, *Water Res*, 2: 195.
18. Toerein, D. F., Siebert, M. L. and Hattingh, W. H. J., 1967, *Water Res*, 1: 497.
19. Balch, W. E., 1979, *Microbiological Revs*, 43: 260.
20. Kaspar, H. F. and Wuhrmann, K., 1978, *Appl Environ Microbiol*, 36: 1.
21. McInerney, M. J., Bryant, M. P. and Pfennig, M., 1979, *Arch Microbiol*, 122: 129.
22. Boone, D. R. and Bryant, M. P., 1980, *Appl Environ Microbiol*, 40; 626.
23. Ghosh, S. and Klass, D. L., 1978, *J Process Biochem*, 13: 15.
24. Stadtman, T. C. and Barker, H. A., 1949, *Arch Biochem*, 21: 256.
25. Thaver, R. K., Jungermann, J. and Decher, K., 1977, *Bact Revs*, 41: 100.
26. Blanc, F. E. and Moioff, A. H., 1973, *J Wat Pollut Control Fed*, 45: 655.
27. Mosey, F. E. and Hughes, D. A., 1975, *J Inst Wat Pollut Control*, 1, 3.
28. Mosey, F. E., Swanwick, J. D. and Hughes, D. A., 1971, *Wat Pollut Control Fed*, 70: 668.
29. Hoban, D. J. and van den Berg, L., 1979, *J Appl Bact* 47: 153.
30. van den Berg, L., Lamb, K. A., Murray, W. D. and Armstrong, D. W., 1980, *J Appl Bact* 48: 437.
31. Clark, J. W. and Viessman, W., 1965, *Water Supply and Pollution Control*. (International Textbook Co., USA).
32. Balakrishnan, S. and Lisanti, A. F., 1974, *Proc 29th Industrial Waste Conf*, Purdue Univ, 262.
33. Parker, C. D., 1966, *Proc. 21st Industrial Waste Conf*, Purdue Univ, 275.
34. Saucier, J. W., 1969, *Proc 24th Industrial Waste Conf*, Purdue Univ, 534.
35. Camin, K. Q., 1970, *Proc. 25th Industrial Waste Conf*, Purdue Univ, 193.
36. Monod, J., 1949, *Ann Rev Microbiol*, 3: 371.
37. Moser, H., 1958, *The Dynamics of Bacterial Populations Maintained in the Chemostat*. (Carnegie Inst Washington Publ No. 614).
38. Morris, J. E., 1979, in *First Int Symp Anaerobic Digestion*, Cardiff (Appl Science Publishers, London).
39. Atkinson, B. and Davies, I. J., 1972, *Trans I Chem E*, 50: 208.
40. Winkler, M., 1981, *Biological Treatment of Waste Water* (Ellis Horwood Ltd., Chichester).
41. Schroepfer, G. J. and Ziemke, N. K., 1959, *Sewage Ind Wastes*, 31: 164.
42. Hemens, J. and Shurban, D. G., 1959, *Food Trade Rev*, 29.
43. van den Berg, L. and Lentz, C. P., 1977, *Proc 32nd Industrial Waste Conf*, Purdue Univ, 252.
44. Simpson, D. E., 1971, *Water Res*, 5: 523.
45. Metcalf and Eddy Inc., 1972, *Wastewater Engineering: Collection, Treatment, Disposal*. (McGraw-Hill, New York).
46. Anderson, G. K. and Donnelly, T., 1977, *Public Health Eng*, 5, 64.
47. Oleszkiewicz, J. A. and Koziarski, S., 1982, *J Environ Eng Div, ASCE*, 108: 367.
48. Chin, K. K., 1981, *Water Res*, 15: 199.
49. Anderson, G. K. and Duarte, A. C., 1980, *Environ Technol Lett*, 1: 484.
50. Dague, R. R., 1970, *J Wat Pollut Control Fed*, 42: R29
51. Shea, T. G., Ramas, E., Rodriguez, J. and Dorion, H. J., *Proc 5th Nat Symp Food Processing Wastes*.
52. Lettinga, G., van Velsen, A. F. M., de Zeeuw, W., Hobma, S. W. and Klapwijk, A., 1980, *Biotech Bioeng*, 22: 669.
53. Lettinga, G., de Zeeuw, W. and Ouborg, E., 1981, *Water Res*, 15: 171.
54. Lok, J. H. G., 1978, *De Ingeniur*, 90: 765.
55. Lettinga, G. and van Velsen, A. F. M., 1974, H_2O, 7: 281.
56. Lettinga, G., 1978, *4th Euro Sewage and Refuse Symp* 226, EAS, Munich.
57. Pretorius, W. A., 1971, *Water Res*, 5: 681.
58. Godwin, S. J., Wase, D. A. J. and Forster, C. F., 1982, *Process Biochem*, 17: 33.
59. Young, J. C. and McCarty, P. L., 1969, *J Wat Pollut Control Fed*, 41: 2160.
60. Plummer, A. H., Malina, J. F. and Eckenfelder, W. W. *Proc 23rd Industrial Waste Conf*, 467.
61. Sachs, E. F., Jennett, J. C. and Rand, M. C., 1982, *J Environ Eng Div, ASCE*, 108: 297.
62. Arora, H. C. and Routh, T., 1981, *Indian Association for Water Pollution Control Technical Annual* VI and VII: 67–78.
63. Peterson, D., 1975, *MSc Thesis* (Univ of Newcastle upon Tyne).
64. Perkins, C. W., Tsugita, R. A. and Tekippe, R. J., 1975, *Proc 30th Industrial Waste Conf*, Purdue Univ, 192.
65. DeWalle, F. B. and Chain, E. S. K., 1975, *Biotech and Bioeng*, 18: 1275.
66. Pirt, S. J., 1973, *J Appl Chem Biotechnol* 23: 389.
67. Saunders, P. T. and Bazin, M. J., 1973, *J Appl Chem Biotechnol*, 23: 847.
68. Chian, E. S. K. and DeWalle, F. B., 1977, *Water Res*, 2: 295.
69. Mueller, J. A. and Mancini, J. L., 1975, *30th Industrial Waste Conf*, Purdue Univ, 423.
70. Sachs, E. F., Jennett, J. C. and Randi, M. C., 1978, *Proc 33rd Industrial Waste Conf*, Purdue Univ, 507.
71. Lovan, C. R. and Foree, E. G., 1971, *Proc 26th Industrial Waste Conf*, Purdue Univ, 1074.

VOL. 62 1984

72. Anderson, G. K. and Ibrahim, A. B., 1978, *Progressive Waste Technol*, 10: 237.
73. Khan, K. A., Suidan, T. and Cross, W. H., 1982, *J Environ Eng Div, ASCE*, 108: 269.
74. van den Berg, L. and Lentz, C. P., 1979, *Proc 34th Industrial Waste Conf*, Purdue Univ, 319.
75. van den Berg, L. and Kennedy, K. J., 1981, *Biotechnol Lett*, 3: 165.
76. Kennedy, K. J. and van den Berg, L., 1982, *Water Res*, 16: 1391.
77. van den Berg, L. and Kennedy, K. J., 1982, *J Chem Tech Biotechnol*, 32: 427.
78. Birks, C. W. and Hynek, R. J., 1971, *Proc 26th Industrial Waste Conf*, Purdue Univ, 89.
79. Tait, S. J. and Friedman, A. A., 1980, *J Wat Pollut Control Fed*, 52: 2257.
80. Schroeder, E. D., 1977, *Water and Wastewater Treatment*, (McGraw Hill Book Co., New York).
81. Josephson, J., 1982, *Environ Sci Technol*, 16: 380.
82. Cooper, P. F., 1981, *Chem Eng*, No. 371/2, 373.
83. Cooper, P. F. and Wheeldon, D. H. V., 1980, *Wat Pollut Control*, 79: 286.
84. Jeris, J. S., Owens, R. W., Hickey, T. and Flood, F., 1977, *J Wat Pollut Control Fed*, 49: 816.
85. Jeris, J. S., Beer, C. and Muetter, J. A., 1974, *J Wat Pollut Control Fed*, 46: 2118.
86. Switzenbaum, M. S. and Jewell, W. J., 1980, *J Wat Pollut Control Fed*, 52: 1953.
87. Jewell, W. J., 1981, in Cooper, P. F. and Atkinson, B. (eds), *Biological Fluidized Bed Treatment of Water and Wastewater*, 251.
88. Matsui, S., Shibata, T. and Imai, A., 1979, *Water Purification and Liquid Wastes Treatment*, 20: 1117.
89. Rockey, J. S. and Forster, C. F., 1982, *Environ Technol Lett*, 3: 487.
90. Bull, M. A., Sterritt, R. M. and Lester, J. N., 1982, *Trans I Chem E*, 60: 373.
91. Bull, M. A., Sterritt, R. M. and Lester, J. N., *Biotechnol Lett*, 5: 333.
92. Bull, M. A., Sterritt, R. M. and Lester, J. N., 1983, *Water Res*, 17: 1563.
93. Bull, M. A., Sterritt, R. M. and Lester, J. N., 1983, *J Chem Tech Biotechnol*, 33B: 221.
94. Sutton, P. M. and Li, A., 1981, *Proc 36th Industrial Waste Conf*, Purdue Univ.
95. Kargi, F. and Park, J. K., 1982, *J Chem Tech Biotechnol*, 32: 744.
96. Rittman, B. E. and McCarty, P. L., 1980, *Biotech and Bioeng*, 22: 2343.
97. Rittman, B. E. and McCarty, P. L., 1980, *Biotech and Bioeng*, 22: 2359.
98. Rittman, B. E., 1982, *Biotech and Bioeng*, 24: 1341.
99. Lescure, J. P. and Bourlet, P., 1979, *Comptes Rendus de la XVI Assemblée Générale de la Commission Internationale Technique de Sucrerie*, Amsterdam, 71.
100. Hammer, M. J. and Borchardt, J. A., 1969, *J Sanitary Eng Div, ASCE*, 95: 907.
101. Schaumberg, F. D. and Kirsch, E. J., 1966, *Appl Microbiol*, 14: 761.
102. Pohland, R. G. and Mancy, J. H., 1969, *Biotech Bioeng*, 11: 683.
103. Massey, M. L. and Pohland, F. G., 1978, *J Wat Pollut Control Fed*, 50: 2204.
104. Ishida, M., Odawara, Y., Gejo, T. and Okumura, H., 1979, in Thomé, K. J. and Kozmiensky, E. (eds), *Recycling Berlin*, (Freitag Verlag für Umweltttechniek, Berlin.
105. Pohland, F. G. and Ghosh, S., 1971, *Env Lett*, 1: 255.
106. Pohland, F. G. and Ghost, S., 1971, in Canale, R. P. (ed), *Biological Waste Treatment*, (Wiley Interscience Pub., New York).
107. Pohland, F. G. and Massey, M. L., 1975, *Prog Water Technol*, 7: 173.
108. Cohen, A., Zoetemeyer, R. J., van Deursen, A. and van Andel, J. G., 1979, *Water Res*, 13: 571.
109. Cohen, A., Breure, A. M., van Andel, J. G. and van Deursen, A., 1980, *Water Res*, 14: 1439.
110. Cohen, A., Breure, A. M., van Andel, J. G. and van Deursen, A., 1980, *Water Res*, 14: 449.
111. Bull, M. A., Sterritt, R. M. and Lester, J. N., 1983, *Biotechnol Bioeng*, submitted.
112. Ghosh, S., Conrad, J. R. and Klass, D. L., 1975, *J Wat Pollut Control Fed*, 60: 30.

ADDRESSES

Correspondence on this paper should be addressed to Dr J. N. Lester, Public Health and Water Resource Engineering, Department of Civil Engineering, Imperial College, London SW7 2BU. M. A. Bull is now with the British Gas Corporation, London Research Station, Michael Road, London SW6 2AD.

The manuscript was received 29 March 1983 and accepted for publication after revision 17 November 1983.

MIXING OF PARTICLES IN LIQUID FLUIDISED BEDS

By A. P. VAN DER MEER, C. M. R. J. P. BLANCHARD and J. A. WESSELINGH

Delft University of Technology, Laboratory of Chemical Technology

Axial solids dispersion has been studied in a liquid fluidised bed using a two-bed technique. Ion-exchange particles (0.500–0.700 mm) were fluidised with water. In the range of column diameters studied (0.02–0.06 m) no effect of the column diameter was found. The dispersion coefficients were strongly dependent on the superficial liquid velocity. Our measurements and the greater part of data from the literature are well described by an empirical equation. Attempts to obtain a dimensionally homogeneous equation were not very successful. Column misalignment was found to have a very large effect. An angle of only 0.3° already noticeably changes the mixing pattern in the column.

INTRODUCTION

Many pieces of chemical engineering equipment contain two flowing phases. Some of these are:

Oslo or Krystal type crystallisers
Flotation separators
Liquid–liquid extraction columns
Fluidised ion-exchange or absorption columns
Granular filters during backwashing
Fluidised organic waste water treatment columns

Usually one of the phases is dispersed, the other continuous. The dispersed phase may have an overall motion which is not necessarily followed by each separate particle. These deviations from the average are caused by several effects which can be lumped together as 'dispersion'. If density or size gradients of the particles exist, they may be classified in different layers.

In an earlier paper an investigation was presented on the classification effect. The falling velocity of a sphere in a swarm of different spheres was studied[1]. This paper uses the results presented there to obtain axial particle dispersion data in liquid fluidised beds. The method applied is similar to that used previously[2–4]. The system studied consists of ion-exchanger particles in water.

PREVIOUS WORK

Practically all previous work on axial dispersion of the solid phase in liquid–solid fluidisation has been done at superficial liquid velocities larger than 0.02 m s^{-1}. Most of the data were obtained using glass beads, fluidised with water.[2–6] Since the particle sizes also were in the same range, there are many data in the range of superficial iiquid velocities between 0.01–0.3 m s^{-1}. Systems other than glass/water studied are: coppershot/water[7]; glass/methylbenzoate[8]; glass/glycol and lead/glycol[2]; glass/dimethylphthalate[9]; ion-exchange resin/water[10]; and firebrick, limestone and marble fluidised with water[6,11].

So far no work has been reported on the effect of the column diameter. Nor has work been reported on the effect of column misalignment. Data were obtained in many ways[6]. The scatter in the reported values will partly be due to these different methods. A summary of all available data is given in Table 1.

Gunn[12] makes the only attempt to correlate the data. Several authors[4,6,8], applying three different techniques, find a maximum in the dispersion coefficient at a void fraction $\epsilon = 0.7$. All other authors, sometimes applying the same techniques, do not find this. For example a study[13] of the length of the mixing zone when two layers of glass beads of different size are fluidised with water did not find aggregative behaviour of the particle layers at intermediate voidages ($0.65 < \epsilon < 0.80$), and segregation at high and low voidages[4], but a steady increase in the height of the mixing zone with increasing voidage[13]. It must be said that size ranges of the two layers in one study[4] were from adjacent sieve cuts and in the other[13] the sizes were more clearly differentiated.

Many authors report on the critical size ratio, d_R, above which particles of the same density tend to stratify. Defining a size ratio as the ratio of the largest to the smallest particle sizes present in the mixture of sizes, Wen and Yu[14], suggested a critical value of $d_R = 1.3$. Others have suggested values of 1.58[15], 2.0[16] and 2.2[4]. Martin[17] found that two fluidised layers of ion-exchange particles with $d_R = 1.07$ were not entirely mixed. The length of the mixing zone in which the lower layer gradually runs into the upper layer was strongly dependent on the liquid velocity[13]. So it seems there is no single critical d_R value for a given system. The d_R value will depend on the liquid velocity, the length of the bed and the criterion used for segregation.

THEORETICAL DESCRIPTION

When two layers of particles, of about the same diameter, but with sufficient density difference are fluidised by a liquid they will be well classified, Figure 1(*a*). The same applies for particles of the same density but with a sufficient diameter difference. In this work we consider the first case. If the density difference between the two layers becomes smaller a mixing zone will be formed between them. The length of this mixing zone will depend on the liquid velocity and the density difference, Figure 1(*b*) (and 12*a*). In this case we have partial classification. There are two phenomena which maintain the bed in its steady state,

(*a*) Classification: a heavy particle amongst lighter ones will fall and a lighter particle between heavier ones will rise, Figure 2(*a*)
(*b*) Dispersion: heavy particles will be transported out of their layer into the layer of lighter ones by irregular motions, Figure 2(*b*)

© Institution of Chemical Engineers

VOL. 62 1984

Table 1. A summary of experimental studies on particle mixing

Authors	ρ_p (kg m^{-3})	ρ (kg m^{-3})	η 10^3 (Ns m^{-2})	d (mm)	σ_d (mm)	D (mm)	Flow rates (m s^{-1})	Remarks
Al-Dibouni and Garside (1979)[4]	2300	998.1	1	1.83 2.20 2.60 3.07	0.10	52.0	0.056 to 0.25	Uses hypothesis of Kennedy and Bretton for the classification velocity, statistical method.
Brotz (1952)[5]	2351	1000	1	10	—	—	—	
Carlos and Richardson (1972)[9]	2490	1190	10.7	8.89	0.14	101.6	0.076 to 0.161	Non stationary method. Liquid: methyl phthalate
Gledhill and Slater (1971)[10]	1280	1000	1	0.775	0.21	76.0	0.0037 and 0.0074	Pulse response technique
Handley et al (1966)[8]	2500	1087	2.067	1.09 1.54	0.5	76.0	0.028 to 0.091	Correlation function method Liquid: methyl benzoate
Kennedy and Bretton (1966)[2]	2862	998	1 and 15	0.959	0.059	25.4 50.76	0.0019 to 0.09	Diameter difference between bead lots very small: water, glycol
Martin (1979)[17]	1197 and 1364	997	0.89	0.666 to 0.736	0.017	20.1	0.004 to 0.02	Same approach as applied in this work
Muchi et al (1961)[11]	2710 and 2360	997	1	0.555 0.681 0.841	—	—	0.01 to 0.05	Pulse response method used
Rowe (1965)[7]	8760	1000	1	0.39	—	101.6	0.001 to 0.063	Same method as Carlos and Richardson
Toyokura et al (1973)[3]	glass beads	1000	1	0.38 0.64	0.1	50	0.019 to 0.063	Uses hypothesis of Kennedy and Bretton
Yutani et al (1982)[8]	2500	1000	1	0.42 0.543 0.772	—	53.5	0.01 to 0.05	Uses a partical velocity distribution function

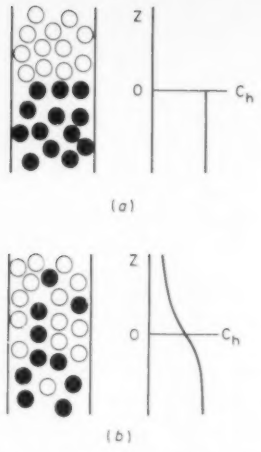


Figure 1. (*a*) Well classified bed, (*b*) Partly classified bed.

After a steady-state situation has been established one might consider the dispersion flux, J_d, and the classification flux J_c, for the heavy particles to balance:

$$J_d - J_c = 0 \tag{1}$$

We follow here the approach of Kennedy and Bretton[2], later used by others[3,4,17].

The dispersive flux, for the heavy particles, can be described by analogy to Fick's first law, using a dispersion coefficient E:

$$J_d = -E\frac{dc_h}{dz} \tag{2}$$

Representing the falling velocity of a heavy particle as a function of its vertical position in the bed $w(z)$, we obtain:

$$J_c = c_h w(z) \tag{3}$$

Since $w(z)$ depends on the environment of the heavy particles we may write:

$$w(z) = w(c_h) \tag{4}$$

The limiting values are:

$$w(c_h) = 0 \text{ if } c_h = c_h^{\infty}$$
$$w(c_h) = w_h \text{ if } c_h = 0$$

where c_h^{∞} is the concentration well below the mixing zone. A linear relation is assumed between these limiting values:

$$w(z) = w_h\left(1 - \frac{c_h}{c_h^{\infty}}\right) \tag{5}$$

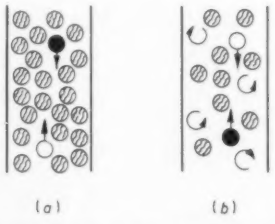


Figure 2. (*a*) A heavy particle falling in a fluidised swarm of lighter ones, (*b*) Axial dispersion, a heavy particle rising in a fluidised swarm of lighter ones.

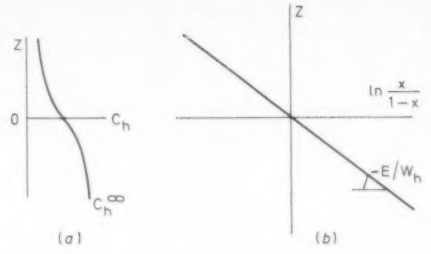


Figure 3. (*a*) Concentration profile of the heavy particles in the mixing zone, (*b*) Plot of $\ln[x/(1-x)]$ against z (equation 7).

As we shall see this yields results in agreement with experiment. Combining relations (1), (2), (3) and (5) and integrating leads to:

$$\frac{c_h}{c_h^{\infty}} = \frac{1}{1 + \exp(w_h z/E)} \tag{6}$$

See Figure 3(*a*). Writing c_h/c_h^{∞} as x we can transform equation (6) to:

$$\frac{w_h z}{E} = -\ln\frac{x}{1-x} \tag{7}$$

The dispersion coefficient can be found by multiplying the slope of a plot of $\ln[x/(1-x)]$ against z by the calculated values of w_h, Figure 3(*b*).

CORRELATIONS USED

The classification velocity w_h has been studied by Martin et al[1] in systems very similar to those used here:

$$w_h = \frac{v_h - v}{v}\,2.5\,(u - u_{mf}) \text{ for } u > u_{mf} \tag{8}$$

and $u/v < 0.4$, where v and v_h are the free-falling velocities of the two spheres in a tube filled with liquid and u_{mf} is the liquid flux at minimum fluidisation; v_h is the larger velocity.

The free-falling velocities can be quite accurately calculated from a relation, also found for the ion-exchange resin/water system, given by Martin et al[1].

$$Re = \left(\frac{23}{Ga} + \frac{0.6}{Ga^{0.5}}\right)^{-1}\frac{1}{1 + 2.35\,d/D} \tag{9}$$

with $700 < Ga < 2000$

in which D is the tube diameter and d the particle diameter. Re and Ga are dimensionless groups (see lists of symbols).

Wen and Yu's relation[14] was used to calculate the minimum fluidisation velocity:

$$\frac{u_{mf}\,d}{v} = \sqrt{[(33.7)^2 + 0.0408\,Ga]} - 33.7 \tag{10}$$

EXPERIMENTAL

Fluidisation Apparatus

Four different columns, diameters 20.4, 42.85, 51.1 and 61.0 mm diameter, each 1 m long made from plexiglass were used. A schematic presentation of our equipment is given in Figure 4. Glass frit and metal sinter plates were used as liquid distributors. The tem-

VOL. 62 1984

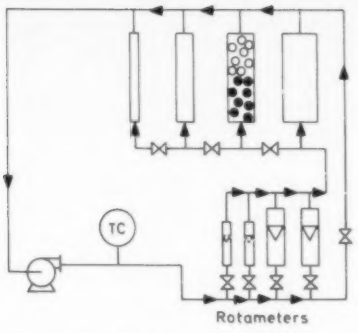


Figure 4. Sketch of the experimental set-up.

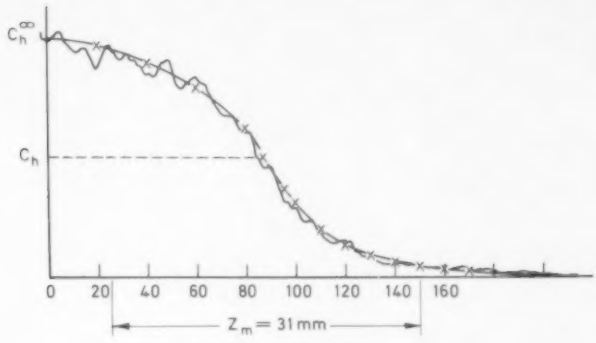


Figure 5. A typical transmission curve.

perature of the de-ionised water was kept at 25°C. A peristaltic pump with pulsation suppressors was used to transport the water in the closed circuit. Liquid flowrates were measured using a series of calibrated rotameters. Superficial liquid velocities were varied between 0.003 to 0.02 m s^{-1}. The particles used were cation exchange beads in the sodium form. The properties of the particles and liquid are summarised in Table 2.

Technique

We used narrow particle fractions obtained by wet sieving first and then classifying the batches in a separate fluidised bed. As ion-exchange particles may swell or shrink we characterised them in the same state as they have in the column. Diameters are measured with a microscope, with the beads submerged under 0.5 mm of the column liquid. The beads were very nearly spherical. The density of the particles was measured using a picnometer.

Equation (7) shows that to obtain E, the concentration c_h along the vertical axis of the mixing zone has to be known. Martin[17] labelled one of the layers with radioactive material. The amount of radiation along the column length was measured. He also carried out preliminary tests using light transmission through the bed. In the latter case one of the layers was a transparent one. Both techniques give information from inside the column. The light transmission technique has the disadvantage that only small diameter columns can be used.

We have looked for a somewhat faster and less troublesome technique to study various column diameters. Even with fairly dense beds, $\epsilon \approx 0.5$, one can look into the bed, through a plexiglass column, for several bead diameters. What one sees on the outside, appears to represent what is happening inside the column. That wall effects can be neglected was justified by

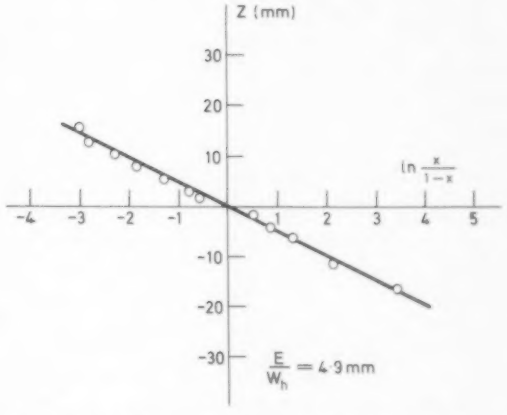


Figure 6. The $\ln [x/(1-x)]$ versus z curve from Figure 5.

fluidising a transparent and an opaque layer of particles at high void fraction. We used particles with a density difference large enough to obtain a classified bed. A flat boundary between the two layers over the whole column diameter could be seen. So by taking a picture of the mixing zone a representation of what occurs inside the bed is obtained. At every liquid velocity three pictures were taken of the mixing zone, which was well away from the liquid distributor.

The negatives were scanned with a laser beam. Since the mixing zone gradually changes in colour, the negative gradually changes from transparent (white) to almost black. A transmission curve is obtained; see Figure 5 for a typical example. From the smoothed transmission curve x is directly obtained. A plot of $\ln [x/(1-x)]$ against z is constructed. Its slope is multiplied with the calculated value of the classification velocity and the dispersion coefficient E is found; Figure 6. In some cases the optical contrast between the two

Table 2. Physical properties of the particles and the liquid

	d (mm)	σ_d (mm)	ρ_p (kgm^{-3})	$v^\infty 10^2$ (m s^{-1})	$v\ 10^2$ (m s^{-1}) in column of diameter 0.02 m	0.04 m	0.05 m	0.06 m	$U_{mf}\ 10^3$ (m s^{-1})
A C264	0.658	0.033	1375.1	3.88	3.607	3.745	3.766	3.78	0.108
B C26 CI	0.695	0.023	1262.6	3.17	2.94	3.06	3.08	3.09	0.085
C C26 CI	0.519	0.021	1262.6	2.20	2.07	2.14	2.15	2.16	0.048
D IR 122	0.663	0.023	1320.2	3.60	3.35	3.48	3.50	3.51	0.094
E IR 118	0.713	0.021	1196.8	2.73	2.44	2.53	2.65	2.66	0.067

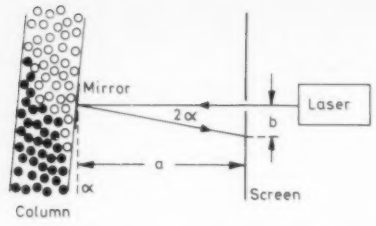


Figure 7. Sketch of the set-up for studying column obliquity.

particles was enlarged by colouring one of them with methylviolet.

The effect of column misalignment was investigated with the set-up given in Figure 7. A mirror was mounted on the column. On a vertical column, the beam is reflected in the same horizontal plane. On an oblique column the laser beam is also reflected in the vertical direction. From the distances a and b, in Figure 7 the angle is found.

Scanning Equipment for Negatives

Photographs were taken with a Leica (Leitz Wetzlar) camera with a 90 mm lens at the maximum aperture 2.8 using flash light. The film used was Pantomic X, 18 DIN, exposure time 1/60 s. The negatives were scanned with the equipment shown in Figure 8. It consisted of a Philips Spectra helium–neon laser, emitting 632.8 nm rays. The laser beam passes through a divergent 104 mm lens, falls on a 0.7 mm slit which is placed shortly before the negative. The negative is moved in a stepwise manner to scan the mixing zone. A micrometer coupled to the movement of the negative indicates the distance the negative has travelled. The transmitted light is reconverged with another 104 mm lens and falls on a photoelectric cell. The signal given by the cell is received by a counter (Picoammeter, type BP-X-42). The signal from the counter is recorded. The horizontal velocity of the recorder is fixed at 2 mm s^{-1}. The whole system is controlled by a microcomputer, type TRS-80. The microcomputer permits an automatic control of the movement of the negative and the recorder.

RESULTS

In all cases a linear plot of $\ln[x/(1-x)]$ against z (Figure 6) was obtained. This shows the validity of the proposed model. The reproducibility was tested by taking two pictures of the same situation. The difference in the E calculated amounts up to 15%.

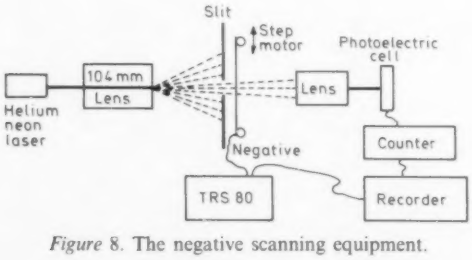


Figure 8. The negative scanning equipment.

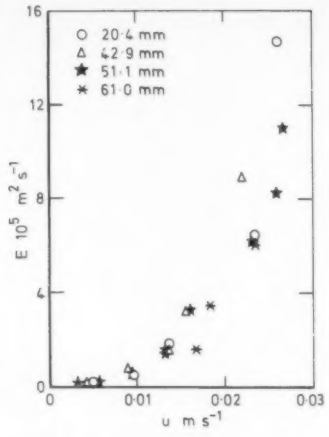


Figure 9. Axial dispersion against liquid velocity, for the column diameters studied.

A typical set of results from Table 2 is presented in Figure 9 for the combination: C264 lower, heavy layer, C26 CI, B, light, upper layer. The strong increase of E with the liquid velocity is notable. Two sets of results of log E against log μ are given in Figures 10 and 11. In all cases such logarithmic plots were straight. No distinct influence of the column diameter can be found. This is obviously in marked contrast to other types of dispersed systems such as gas/solid fluidised beds and bubble columns.

Figures 9, 10 and 11 give results for different combinations of particles. The lengths of the mixing zones are different, nevertheless the dispersion coefficients appear to be equal. So there is little influence of the density difference between the two batches of particles.

The best fit to our data, using a least squares method is:

$$E = 0.04\,u^{1.8}\ \mathrm{m^2\,s^{-1}} \qquad (11)$$

with $0.5 < \epsilon < 0.9$

and $0.002 < u < 0.02\ \mathrm{m\,s^{-1}}$

The correlation coefficient is 0.93.

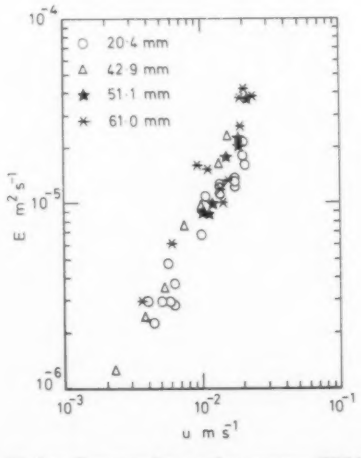


Figure 10. log E versus log u plot, system C264/IR118.

VOL. 62 1984

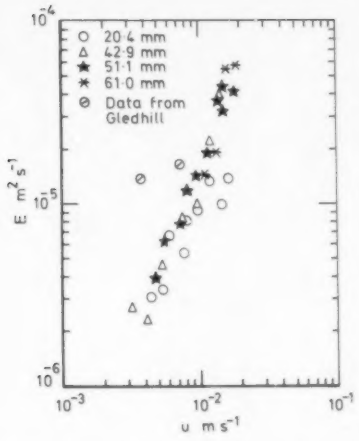


Figure 11. log E versus log u plot, system IR122/IR118.

Effect of vertical alignment of the column

In Figure 12 the effect of column alignment can be seen. Three photographs are shown, one with a vertical column and two with 0.6° and 2.1° column misalignment at the same superficial liquid velocity. With the equipment shown in Figure 7 misalignment between 0.3° and 3° was investigated. The effect was already apparent at 0.3°. In fact the behaviour of the fluidised layers is a more sensitive indication for column misalignment than a water well. The scanning technique as described above, could not be used, since the particle concentrations vary over the column diameter. Column misalignment strongly effects the mixing. This may be a problem in large scale equipment.

In a recent paper by Horvath et al[18] the effect of vertical alignment on continuous-phase axial mixing in liquid/liquid spray columns is reported. Also for this type of equipment it has been found that axial mixing is greatly reduced if the column is well aligned vertically. The same might be expected to apply to gas/solid fluidisation and bubble columns.

Comparison with previous work

Comparison of our data with the results obtained by Martin[17] show no significant difference. By looking at the transparent column we do not seem to have lost information from inside the column. Martin's work also did not show any significant change of the dispersion coefficient on changing the particle system at one given liquid velocity.

The only other available data on axial solids mixing, measured with ion-exchanger particles, from Gledhill and Slater[10], are also plotted in Figure 11. These data show significantly higher values of E. A possible explanation is that they did not measure in a steady state fluidised bed, but in a counter-current bed. Even the trend in our data is not observed. The maximum of E against ϵ found by others[4,6,8], at $\epsilon \approx 0.7$ (corresponding in our case with $u = 0.013\ \mathrm{m\ s^{-1}}$) is not found in our work.

A common presentation of axial dispersion data in liquid fluidised beds is Gunn's diagram[12]. In Figure 13 we plotted our data together with data from the literature. As already indicated by Al-Dibouni et al[4] this kind of presentation in terms of the Peclet number and the Reynolds number based on the superficial liquid velocity is not adequate.

The most important variable governing E appears to be the superficial liquid velocity. In Figure 14 all known data are presented in this way. All data fall roughly in a single band. It must be noted that many kinds of measurement techniques were used. This partly explains the large scatter. From Figure 14 we learn that there is little effect of the liquid viscosity and the liquid density which were very important in Gunn's diagram[12].

Some comment on data from others must be made. Mixing zone experiments only give proper results if the mixing zone is shorter than the column length. This is not so in some of the experiments of Kennedy and Bretton[2] and Martin[17]. Rowe et al[7] seem to have measured a different kind of diffusivity from that in this work. He probably measured unsteady-state situations after increasing the liquid flux, as is apparent from his pictures. In our bed vigorous mixing is seen just after starting. We get a homogeneous bed; only after some time, in some cases 5 min, the liquid bubbles and eddies diminish and the particles classify in two layers. Also an increase of the liquid flux causes extra mixing.

With a least squares method the best line to fit all data, leaving out the above mentioned, is:

$$E = 0.25\, u^{2.2}\ \mathrm{m^2\ s^{-1}} \qquad (12)$$

with $0.5 < \epsilon < 0.9$

and $0.002 < u < 0.3\ \mathrm{m\ s^{-1}}$

The correlation coefficient is 0.97, the constant 0.25 is not dimensionless.

DISCUSSION

The Table 3 some data are given where E was measured and the mixing zone height, z_m was determined visually. For all our data the value of $E/w_h z_m$ varies between 0.14 and 0.23.

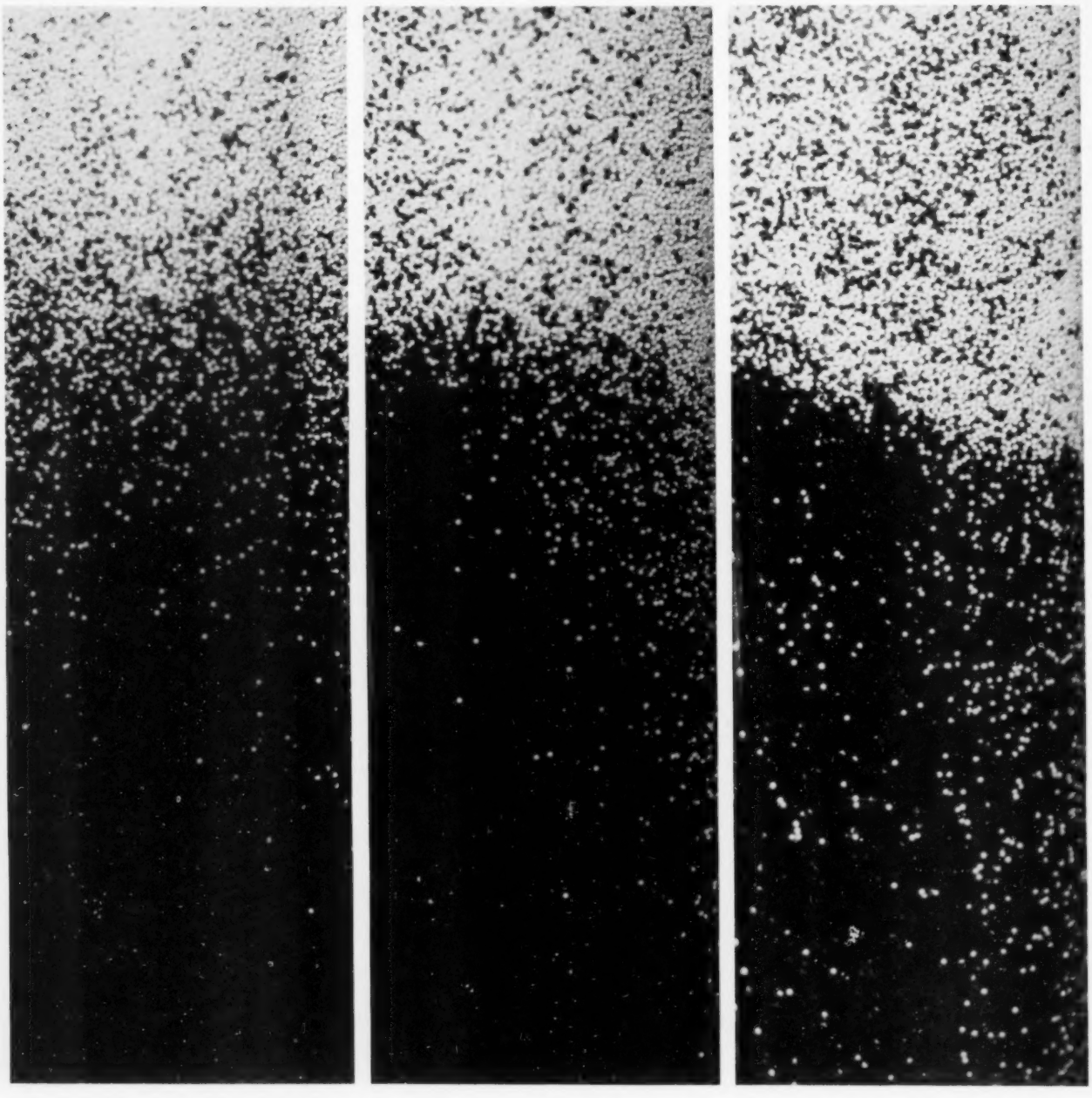
The same is found from the data of Martin[17]. It seems there is a faster though less precise method of measuring the dispersion coefficient, by simply observing the length of the mixing zone. This is to be expected from equation (7); it is easily derived that:

$$\frac{dx}{dz} = -\frac{(w_h/E)\exp(w_h z/E)}{[1+\exp(w_h z/E)]^2} \qquad (13)$$

The mixing zones presented by Juma and Richardson[13] have been analysed in this way. Where the classification velocities were calculated from equation (8), the free-falling velocities of the different particles were calculated from equation (9). The E values found are well within the range of others reported in the literature.

DIMENSIONAL ANALYSIS

A dimensional analysis was performed on the available dispersion data. The axial dispersion coefficient is



(a) (b) (c)

Figure 12. Effect of column obliquity, (*a*) vertical column, (*b*) 0.6° obliquity, (*c*) 2.1° obliquity. Superficial liquid velocity 3.06×10^{-3} m s^{-1}.

expected to be a function of the following parameters:

$$E = f(u, d, D, \alpha, g, \rho, \rho_p - \rho, \eta) \tag{14}$$

We restrict ourselves to vertical columns, $\alpha = 0$. Our experiments show no distinct influence of the column diameter. From the literature and our results it appears that E depends strongly on the superficial liquid velocity. There is only a residual effect of the other variables, with the possible exception of g, which was not varied:

$$E = f(u, g, \ldots) \tag{15}$$

The simplest non-dimensional equation in agreement with this function is:

$$\frac{Eg}{u^3} = \text{constant} \tag{16}$$

The data are roughly described by this equation, but the fit is poor. A much better fit is obtained if a small effect is allowed of either $\nu = \eta/\rho$ or d:

$$\frac{E}{\nu} = \text{const}\left(\frac{u}{g^{1/3}\nu^{1/3}}\right)^{2.3} \tag{17}$$

VOL. 62 1984

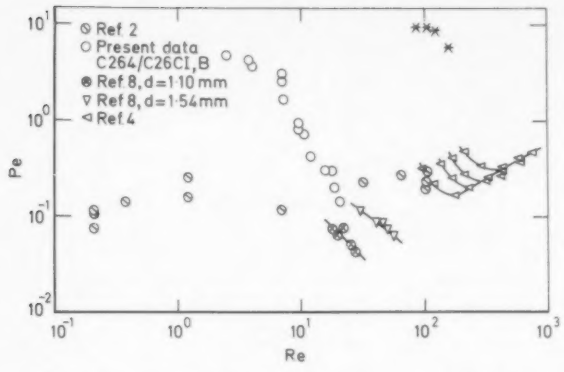


Figure 13. *Pe* versus *Re*, Gunn's presentation. (*Ref 9)

Table 3. Results for the system C264/C26 CI(B), 51.1 mm column

$u\,10^3$ (ms^{-1})	$(-E/w_h)\,10^3$ (m)	$w_h\,10^3$ (ms^{-1})	$z_m\,10^2$ (m)	$-E/w_h z_m$ (−)	$E\,10^5$ (m^2 s^{-1})
5.1	0.538	2.84	3.26	0.17	0.153
9.69	0.865	5.44	4.67	0.19	0.471
9.69	1.023	5.44	5.38	0.19	0.557
13.77	2.352	7.76	14.06	0.17	1.826
23.46	4.895	13.27	31.00	0.16	6.495
26.01	8.169	13.86	46.83	0.17	14.718

or

$$\frac{E}{u\,d} = \text{const}\left(\frac{u^2}{g\,d}\right)^{0.65} \tag{18}$$

Both expressions lead to $E \simeq u^{2.3}$ which roughly follows from Figure 14. Equation (17) is compared with literature data in Figure 15 with const. = 70.

Other sets of dimensionless groups such as the 'classic' $Pe = f(Re, Ga)$ have also been tried. They gave a poor fit however.

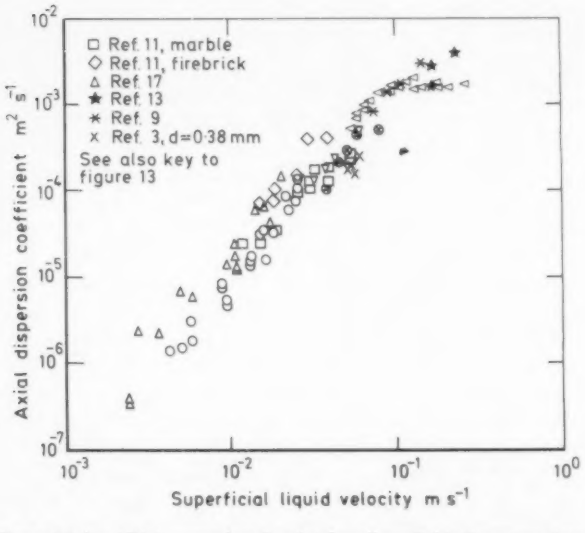


Figure 14. log (E/v) versus log Re plot for all available literature data. Some of the literature data in the crowded portion of the graph have been left out for clarity.

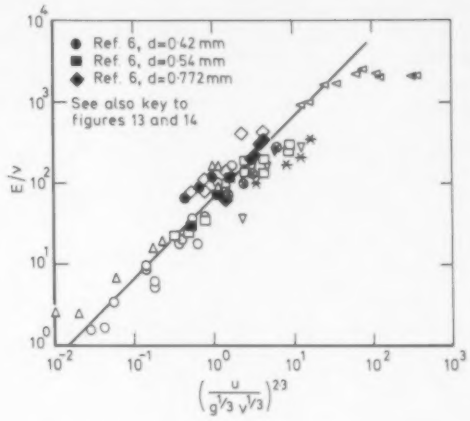


Figure 15. Equation (17) together with literature data.

SYMBOLS USED

c_h concentration of the heavy particles (m^{-3})
c_h^∞ concentration of the heavy particles well below the mixing zone (m^{-3})
D column diameter (m)
d particle diameter (m)
d_R critical size ratio, d_{max}/d_{min}, (−)
E axial dispersion coefficient of particle (m^2 s^{-1})
g gravitational acceleration (ms^{-2})
J_c classification flux (m^{-2} s^{-1})
J_d dispersion flux (m^{-2} s^{-1})
u superficial liquid velocity (ms^{-1})
u_{mf} superficial liquid velocity at minimum fluidization (ms^{-1})
v falling velocity of a single particle (ms^{-1})
v^∞ falling velocity of a single particle in a tube of infinite diameter (ms^{-1})
w_h classification velocity of a particle in a bed consisting of different particles (ms^{-1})
x c_h/c_h^∞, (−)
z vertical distance from the centre of the mixing zone (m)
z_m length of the mixing zone (m)

Greek letters

α column obliquity (degree of arc)
ϵ void fraction
η dynamic liquid viscosity (Nsm^{-2})
ν kinematic liquid viscosity (m^2 s^{-1})
ρ liquid density (kg m^{-3})
ρ_p particle density (kg m^{-3})
σ_p standard deviation of the particle size distribution (m)

Dimensionless groups

$Ga = \dfrac{g(\rho_p - \rho)d^3}{\rho\nu^2}$ Galileo number

$Pe = \dfrac{u\,d}{E\epsilon}$ Peclet number

$Re = \dfrac{u\,d}{\nu}$ Reynolds number; $\dfrac{v\,d}{\nu}$ in equation (9)

REFERENCES

1. Martin, B. L. A., Kolar, Z. and Wesselingh, J. A., 1981, *Trans IChemE*, 59: 100
2. Kennedy, S. C. and Bretton, R. H., 1966, *AIChEJ*, 12: 24
3. Toyokura, K., Tanaka, H., and Tanahashi, J., 1973, *J Chem Eng Japan*, 6: 325
4. Al-Dibouni, M. R. and Garside, J., 1979, *Trans IChemE*, 57: 94
5. Brotz, W., 1952, *Chem Ing Tech*, 24: 60
6. Yutani, N., Ototake, N., Too, J. R. and Fan., L. T., 1982, *Chem Eng Sci*, 37: 1079

7. Rowe, P. N., et al, 1965, *Trans IChemE*, 43: T271
8. Handley, D., Doraiswamy, A., Butcher, K. and Franklin, N., 1966, *Trans. IChemE*, 44: 260
9. Carlos, C. R. and Richardson, J. F., 1968, *Chem Eng Sci*, 23: 825
10. Gledhill, C. and Slater, M. J., *Proc. Symp. Theory and Practice of Ion-Exchange, Cambridge*, (Soc. Chem. Ind, London) 46.1
11. Muchi, I., Hakaie, S., Kamo, S. and Okamoto, M., 1961, *Kagaku Kogaku*, 25: 757
12. Gunn., D. J., 1968, *The Chemical Engineer*, (219): 153
13. Juma, A. K. A. and Richardson, J. F., 1979, *Chem Eng Sci*, 34: 137
14. Wen, Y. and Yu, Y. H., 1962, *Chem Eng Symp Ser*, 62: 100
15. Hoffmann, R., Lapidus, L. and Elgin, J. C., 1960, *AIChEJ*, 6: 321
16. Scarlett, R., and Blogg, M. J., 1967, *Proc Int Symp Fluidization* 81 (Netherlands University Press, Amsterdam)
17. Martin, B. L. A., 1979, *PhD Thesis* (Universite de Strasbourg)
18. Horvath, M., Pikios, C. and Cavers, S. D., 1982, *AIChEJ*, 28: 858

ACKNOWLEDGEMENTS

The authors of this paper would like to thank K. Kamps for the photographs and W. van Willigen and C. K. Oostdijk from the Laboratorium voor Technische Natuurkunde for help with the scanning technique.

ADDRESSES

Correspondence about this article should be addressed to Professor J. A. Wesselingh, Laboratory of Chemical Technology, Delft University of Technology, Julianalaan 136, 2628 BL Delft, The Netherlands.

This paper was communicated 9 August 1983 by Professor J. M. Smith, Associate Editor for the journal in Continental Europe.

BOOK REVIEWS

Handbook of Solvent Extraction
Editors: C. Lo Teh, M. H. Baird and C. Hanson
John Wiley & Sons, 1983
pp 980, £118.75

This handbook is a comprehensive reference work on solvent extraction ranging from general principles, industrial equipment and processes to cost engineering. More than 70 authors have contributed with the result that there is a wide range of expert experience brought together but there is variation of presentation in style and depth of treatment. Some chapters are superficial while others show great depth and understanding of the subject, undoubtedly based on wide and intense experience.

The book is organised in four sections. The first on "General Principles" starts with a presentation of phase equilibria and covers the thermodynamics of liquid systems and the standard methods of correlating equilibrium data. This includes a brief treatment of the N.R.T.L. and Uniquac equations with hints of methods of application to multicomponent systems. This is followed by chapters on Extraction and Reaction and a very useful, largely descriptive, chapter on the principles of the extraction of metals. Following this there are chapters presenting the general principles of mass transfer, stagewise analyses, coalescence, axial dispersion and unsteady-state extraction. These chapters adequately cover the particular topics and will be helpful to students and engineers working in the field of extraction. The chapters on the analysis of stagewise processes and unsteady state operations have been carefully presented and are noteworthy, but the final chapter on "Special Methods" is so brief that it is unhelpful.

Part II deals with Industrial Extraction Equipment and starts with reviews of the design and operation of Mixer-Settler Equipment. These are largely descriptive chapters of different types of equipment and will be a helpful introduction to engineers entering this field of operations. The analytical treatment of the design of this type of equipment should have been dealt with in greater detail for the benefit of practising engineers. These chapters are followed by chapters on extraction columns and most types of columns are considered. The sections on non-agitated columns have been well written, although some of the statements made must be treated with caution, e.g. raffinate dispersed in sieve plate columns is not generally beneficial—depends on the system! The chapters on agitated columns present comprehensive information on the practical operation of this type of equipment that will be beneficial to practising engineers; particularly that treatment of the different forms of the R.D.C. and Oldshue-Rushton columns.

The final chapter of Part II is a discussion of the Selection, Testing and Scale-up of extraction columns. The presentation is based on the selection procedure originally developed by Pratt in 1954 but up-dated by other workers and will prove to be a useful guide to process engineers contemplating an extraction operation.

Part III deals with industrial processes and covers both organic and inorganic separations based on liquid extraction. The chapters on the extraction of organics are mostly confined to the petroleum and petrochemical industries with short chapters devoted to food and pharmaceutical processes. These are of different style and emphasis; all present process flowsheets, but thereafter the emphasis varies from details of particular processes to the special properties of the solvents employed. In a few chapters the equilibrium data of solvents such as TETRA and those in the caprolactam extractions are given, but generally the chapters offered in this section of Part III are descriptive with only superficial data of design and operation. The result is that from a "handbook" point of view, this text will be of limited value.

The sections of Part III treating Inorganic processes is similar to Part IIIa and is largely devoted to metal extraction. The opening chapters are noteworthy and form a useful basis for the rest of this section. Thereafter the format varies in emphasis from chapter to chapter but generally the treatment is more quantitative than Part IIIa.

The final section is concerned with costs and engineering and embraces computational and modelling techniques, control procedures together with plant layouts in addition to the analysis of the costs of equipment and processes. The tabular data of various cost items will

Book Reviews continue on page 234

VOL. 62 1984

EFFECT OF PRESSURE ON COMBUSTION OF CHAR IN FLUIDISED BEDS

By E. TURNBULL (GRADUATE), E. R. KOSSAKOWSKI (GRADUATE), J. F. DAVIDSON (FELLOW)
Department of Chemical Engineering, University of Cambridge

and R. B. HOPES, H. W. BLACKSHAW, P. T. Y. GOODYER
Science and Engineering Research Council, Rutherford Appleton Laboratory, Chilton.

Measurements of burn-out time are reported, for 0.25–1.7 mm carbon particles in an air-fluidised 100 mm dia bed of sand at pressures up to 17 bar absolute and bed temperatures of 1023–1173 K. A variety of carbons was used including (i) coke (ii) chars formed from coals of different ranks: thus the carbons had various porosities and surface areas.

The effect of increased pressure is to increase the combustion rate, because of the higher oxygen concentration which accelerates the chemical reactions of combustion. On the other hand, pressure has virtually no influence on diffusion of oxygen towards a burning particle, because the higher oxygen concentration is offset by a proportionately lower diffusion coefficient. The overall effect is that as pressure increases, the chemical rate controlling steps become less important, so at very high pressure, combustion is diffusion controlled.

The effect of carbon reactivity can be allowed for, approximately, by using an effective pore area together with an intrinsic rate constant based on the work of Smith. For highly reactive carbons, such as are formed from low rank coals, combustion tends to be diffusion controlled. For solid carbons, e.g. coke, chemical rates have a significant influence on combustion rate.

A heat balance for the burning carbon particle was adjusted so that for carbon particles about 1 mm dia, the particle temperature T_p was about 140 K above bed temperature T_b. As the particle size is reduced, $T_p \rightarrow T_b$, because of the high heat transfer coefficient for small particles. This explains why small particles burn slowly, their combustion being chemical rate-controlled. The chemical rates increase with pressure. Hence small particles burn faster at high pressure, reducing elutriation and thereby increasing combustion efficiency.

INTRODUCTION

This paper is about the effect of pressure on the burning of carbon particles in hot air-fluidised sand. Data are presented from the new high pressure fluidised combustor at the Rutherford Appleton Laboratory (RAL) of the Science and Engineering Research Council. The measurements show the effect of pressures up to 17 bar absolute on the burn-out times of a variety of carbon particles.

In recent years there have been many design studies for power cycles incorporating a pressurised fluidised bed; a number of pilot scale combustors have been built. Such power cycles have the promise of appreciably higher thermal efficiency than the units with atmospheric coal burners now in use[1].

The combustion of carbon in an air-fluidised bed at atmospheric pressure has been studied exhaustively[2,3], but as far as we are aware, nothing has been published as to the effect of pressure on combustion mechanisms. Pressure P is an important parameter because the concentration of oxygen, c_O, in the fluidising air is proportional to P; but on the other hand, gas-phase diffusion coefficients D_G are inversely proportional to P. It has been shown[3] that the diffusion of oxygen towards a carbon particle is proportional to $D_G c_O$ and hence this effect should be independent of P. It follows that for large carbon particles, whose combustion is diffusion controlled, the burn-out time should be independent of pressure. More complex effects are to be expected in respect of (i) cross-flow from rising bubbles and (ii) chemical kinetics. Chemical rate processes must be faster at higher pressures on account of the higher oxygen concentrations: small carbon particles, which burn slowly at atmospheric pressure[3], must burn faster at high pressures; hence the small particles elutriate less readily, thus giving higher combustion efficiency. The object of this paper is to elucidate the effect of pressure on these diffusion and chemical rate processes.

The method used was similar to that described previously[2,3]: a batch of closely sized carbon particles was injected into a hot air-fluidised bed of sand and the off-gas concentration of CO_2 measured as a function of time. A variety of char particles was used from coals of differing ranks, and also coke. This showed the effect of carbon reactivity and of pore structure: thus study of the effect of the nature of the carbon was facilitated through being able to vary the pressure.

THEORY

Ross[2,3] studied the fluidised combustion of solid carbon with the following conclusions.

(i) The combustion process is limited by one or more of the following: (*a*) the transfer of oxygen from the bubble phase to the particulate phase, (*b*) the transfer of oxygen locally around each burning particle, (*c*) the rate of consumption of oxygen at the particle surface.

(ii) A single coke particle larger than 1 mm dia burning in an air-fluidised bed at 1173 K does so at a temperature approximately 140 K above that of the bed. At this low temperature, the reaction

$$C(s) + CO_2(g) \rightarrow 2CO(g)$$

© Institution of Chemical Engineers

may be ignored. Rather, carbon is consumed by

$$C(s) + \tfrac{1}{2}O_2(g) \rightarrow CO(g)$$

with the reaction

$$CO(g) + \tfrac{1}{2}O_2(g) \rightarrow CO_2(g)$$

occurring in the gas phase around the particle. Note that the combustion of CO contributes approximately two thirds of the heat released by the reaction

$$C(s) + O_2(g) \rightarrow CO_2(g).$$

(iii) Particles smaller than about 0.5 mm diameter burn at a temperature close to that of the fluidised bed. Ross[2,3] suggested that because the Sherwood number

$$Sh = k_g d_p / D_G$$

(d_p is particle diameter and D_G is gas phase diffusion coefficient of oxygen) is nearly constant, a small particle has a large mass transfer coefficient k_g; hence the combustion of CO produced at the particle surface occurs far enough from the particle to be considered independent of it. This allows the small particles to burn cooler, i.e. near bed temperature. It follows that small particles burn slowly.

Assuming (*a*) the two phase theory of fluidisation[4], (*b*) a shrinking sphere model, (*c*) first order kinetics for the intrinsic (heterogeneous) combustion reaction and (*d*) a constant *Sh*, Ross[2,3] derived the following expression for the burn-out time t_b of a mass m of carbon injected into a fluidised bed,

$$t_b = \frac{m}{12 c_O A [U - (U - U_{mf})e^{-X}]} + \frac{\rho_c d_i^2}{48 Sh D_G c_O} + \frac{\rho_c d_i}{24 k_F c_O} \quad (1)$$

A constant particle temperature was assumed. Here U is the superficial fluidising velocity at bed temperature and $U = U_{mf}$ at incipient fluidisation, c_O is the inlet oxygen concentration, A is the bed cross-sectional area, X is the cross-flow factor, ρ_c is the carbon density and d_i is the initial diameter of the particles. Ross[2,3] used the rate constant k_F proposed by Field *et al.*[5] (see Table 1) for the reaction between solid carbon and oxygen.

The terms in (1) represent respectively the three processes (*a*), (*b*), (*c*) given in (i) above. Note that the only effect of carbon properties is in the value of ρ_c.

Intrinsic Reactivity

For a porous carbon, Smith[6] defines the intrinsic reactivity as "the reaction rate per unit of pore surface (area) in the absence of any mass transfer limitations". Much time has been spent in predicting intrinsic reactivity, a task complicated by (i) the presence of impurities which promote or inhibit combustion reactions[7], (ii) the effect of heat treatment on char reactivity[6,8] and (iii) the difficulties associated with the interpretation of BET data[9]. Wicke[10] describes three reaction regimes as follows.

(i) Kinetic control is called regime I. For a non-porous carbon, it occurs at temperatures typical of fluidised combustion, say 1200 K; reaction is at the exterior surface of the particle, which shrinks with constant density. For porous carbons, regime I applies at temperatures below about 800 K: combustion occurs throughout the particle; consequently particle density but not particle size decreases during combustion. For both types of carbon, the observed activation energy and reaction order are equal to the actual chemical activation energy and reaction order and are referred to as 'true values'.

(ii) Regime II is an intermediate regime appropriate for porous carbons. There is limited penetration of oxygen into the solid. For this regime the observed activation energy is half the true value[10] and the apparent reaction order $n = (m + 1)/2$ where m is the true value[10].

(iii) Diffusion control, called regime III, implies reaction at the external surface of the particle which therefore shrinks with constant density. For this regime the observed activation energy is small and the observed reaction order with respect to oxygen is unity.

The following analysis is for regime II: oxygen diffuses into the burning particle; the depth of penetration is so small that the particle appears to shrink at constant density.

An oxygen balance within the pores of the burning particle gives:

$$D_E d^2c/dx^2 - k_i S_E c = 0 \quad (2)$$

where x is distance measured inwards normal to the external surface, k_i is the intrinsic rate constant, S_E is the effective pore area for combustion per unit volume and D_E is the diffusion coefficient of oxygen within the solid carbon. For a thin reaction zone, the boundary conditions are $c = c_s$ at $x = 0$ (outer surface of particle), $c = 0$ as $x \rightarrow \infty$. The latter implies that the particle is large compared with the thickness of the reaction zone and is valid if[11]:

$$\phi = (V_p/A_p)(k_i S_E/D_E)^{0.5} > 3 \quad (3)$$

Table 1. Rate expressions for combustion of carbon. The rate of oxygen consumption $= k_0 c_s$.

	Field et al[5]	Smith[6]
Overall chemical rate constant k_0(m s^{-1})	k_F (F1)	$(S_E D_E k_S)^{0.5}$ (S1)
Rate expression as given (m s^{-1})	$k_F = 595 T_p \exp(-149200/RT_p)$ (F2)	$k_S = 21 T_p \exp(-179400/RT_p)$ (S2)
	Regime II analysis	
Overall chemical rate constant k_0(m s^{-1})	$(S_E D_E k_{MF})^{0.5}$ (F3)	$(S_E D_E k_{MS})^{0.5}$ (S3)
Modified rate expression k_i(m s^{-1})	$k_{MF} = 19320 T_p^2 \exp(-298400/RT_p)$ (F4)	$k_{MS} = 470 T_p \exp(-179400/RT_p)$ (S4)

VOL. 62 1984

Here V_p is the particle volume and A_p is its external area.

Solving equation (2) with its boundary conditions gives the rate of combustion per unit of external surface, $R_s = (k_i S_E D_E)^{0.5} c_s$. The equivalent expression given by Ross[2,3] is $R_s = k_F c_s$. Hence k_F may be replaced by $(k_i S_E D_E)^{0.5}$ so that equation (1) becomes

$$t_b = \frac{m}{12 c_O A[U - (U - U_{mf})e^{-X}]} + \frac{\rho_c d_i^2}{48 Sh D_G c_O} + \frac{\rho_c d_i}{24(k_i S_E D_E)^{0.5} c_O} \quad (4)$$

The assumption that the reaction zone never reaches the centre of the burning particle can be justified as follows. Using the plausible values $S_E = 0.25 \times 10^6\ m^2\ m^{-3}$, $D_E = 5 \times 10^{-5}\ m^2\ s^{-1}$ and $k_i = 2.5\ m\ s^{-1}$ gives, from equation (3), $\phi = 3$ when $d_p = 0.04$ mm. This suggests from inequality (3) that equation (4) is applicable to fluidised combustion because the particle diameter is typically larger than 1 mm.

A further justification for equation (4) comes from a steady state particle energy balance similar to Ross *et al.*[12]:

$$(d_p^3 - d_r^3)\pi\rho_c S_E \Delta H k_i/72 = Nuk\pi d_p(T_p - T_b) + \sigma\epsilon_r \pi d_p^2 (T_p^4 - T_b^4) \quad (5)$$

Here d_r is the diameter of the unreacting core, ΔH is the effective heat of combustion for solid carbon, Nu is the Nusselt number, k is the effective thermal conductivity of the particulate phase, T_p is the particle temperature, T_b is the bed temperature and ϵ_r is the particle emissivity. Putting $d_r = 0$ gives a quadratic in d_p, the solution of which is the diameter d_p^* at which combustion occurs throughout the whole of the particle. Using conservative values[12], $T_p = T_b + 140 = 1313$ K, $Nu = 7$, $k = 0.24\ W\ m^{-1}\ K^{-1}$, $\epsilon_r = 0.8$, $\Delta H = 300 \times 10^3\ J\ mol^{-1}$, $\rho_c = 500\ kg\ m^{-3}$, $S_E = 0.25 \times 10^6\ m^2\ m^{-3}$, $k_i = 0.5\ m\ s^{-1}$, gives $d_p^* = 0.001$ mm. This very small value of d_p^* is further evidence that combustion does indeed occur in a thin porous layer near the particle surface for most of its life.

Rate Expressions

Table 1 summarises the rate expressions proposed by Field *et al.*[5] and Smith[6]. In each case the rate of carbon consumption is expressed as (overall rate constant k_0) × (surface concentration of oxygen c_s). For the regime II analysis, k_0 is given in terms of an intrinsic rate constant k_i (which may be k_S, k_{MS} or k_{MF}) for the reaction of gaseous oxygen with an impure carbon surface, S_E, D_E and T_p. Except where noted, S_E is approximated by S_V the total pore area determined by adsorption of N_2 at 77 K.

Table 2. Properties of carbons used in order of decreasing surface area

Carbon	ρ (kg m^{-3})	ρ_c (kg m^{-3})	ϵ_p	S_V (m^2 m^{-3} × 10^{-6})
Activated carbon	1478	1393	0.128	535
Lignite char	1883	1130	0.132	147
Illinois 5 char (1)	1800	1368	0.120	17.8
Merthyr Vale char	1765	1483	0.121	5.9
Illinois 5 char (2)	1689	1385	0.125	1.5
Bedwas char	1903	1351	0.117	1.2
Phurnacite Breeze	1741	1393	0.128	0.95
Tymawr char	1917	1476	0.137	0.50
Coke (Ross[2])	1608	1447	0.210	0.42
Coke	1627	1448	0.210	0.30

$\rho_c = \rho \times$ (%C as received)/100.
S_V determined by adsorption of N_2 at 77 K (NCB).

Ross[2,3] found that a single coke particle (the properties of which are given in Table 2 together with the properties of the carbons used in these experiments) in an air-fluidised bed of sand at 1173 K burnt at a temperature of 1313 K. The rate constant determined from equation (1) with $Sh = 3.5$ agreed with the value of $0.9\ m\ s^{-1}$ predicted by Field *et al.*'s[5] rate expression (equation F2, Table 1). This information will be used to develop a rate expression for use in equation (4).

Smith[6] used published data for the rate of combustion of various carbons over a wide range of conditions to show that the effect of carbon type could be eliminated by considering combustion to occur within regime II; the resulting intrinsic rate expression is given in Table 1 (equation S2). Inserting the properties of Ross's[2] coke and assuming that[13] $D_E = \epsilon_p D_G/\tau$, where the tortuosity factor $\tau = 1$, ϵ_p is the porosity of the particle and $D_G = 208 \times 10^{-6}\ m^2\ s^{-1}$, then the value of the overall rate constant for the conditions described above is $k_0 = 0.19\ m\ s^{-1}$ for $S_E = S_V = 0.42 \times 10^6\ m^2\ m^{-3}$; this is lower than the value of $0.9\ m\ s^{-1}$ determined by Ross[2]. Now the BET areas used by Smith[6] are approximately two orders of magnitude greater than those determined at the National Coal Board (NCB). It is not surprising therefore that when the areas determined by the NCB are used in Smith's[6] expression a low value for the reaction rate is obtained. One possible reason for the discrepancy in BET areas is that Smith's[6] areas were determined by the adsorption of CO_2 at 298 K which is known[9] to give larger values than by the adsorption of N_2 at 77 K, the method used by the NCB. Areas determined by both methods should be valid provided the areas used to determine the intrinsic rate expression are consistent with those to be used.

A rate expression for use with areas determined by the adsorption of nitrogen was obtained as follows. Smith's[6] activation energy was retained. A new pre-exponential term A_s was obtained for regime II from the equation

$$k_F = [A_s S_E D_E T_p \exp(-179400/RT_p)]^{0.5}$$

with $S_E = S_V$ and using the properties of Ross's[2] coke and his chemical rate constant. This procedure is justified because the pre-exponential term in an Arrhenius rate expression is normally considered to be related to the number of active sites on the solid surface and therefore should relate to the BET area. But there is no justification for changing the activation energy which is related to the net energy for adsorption and desorption of the reacting species: the premise of Smith's[6] work is that the activation energy for reaction between carbon and oxygen is constant for most impure carbons.

Field *et al.*'s[5] rate expression (F2, Table 1), often used in fluidised combustion models, was developed by using the external surface area of the particle and consequently

is not suitable for use in equation (4). A modified rate expression (F4, Table 1) was obtained for use in equation (4) by the method used to alter Smith's[6] expression. Note that the activation energy in equation (F4) is twice the value in equation (F2) because the latter is an observed value; this follows because, for regime II, the observed value is half the true value.

The modified rate expressions (S4) and (F4) in Table 1 have very different activation energies which will be discussed in considering experimental data.

Particle Temperatures

Particle temperature affects the rate of chemical reaction. An energy balance on a burning particle is complicated because the combustion of CO produced at the particle surface occurs in the gas phase around the particle; consequently it is difficult to predict how much of the energy from this reaction heats the particle.

Many simplifying assumptions have been made to perform a particle energy balance. Baron *et al.*[14] and Congaldis and Georgakis[15] assumed that the CO produced at the particle surface is consumed far from the particle. Ross *et al.*[12] and Mon and Amundson[16] lumped the two oxidation reactions on the particle surface. Mulcahy[7] studied the combustion of pulverised fuel and concluded that about 40% of the energy produced by the oxidation of CO heats the particle.

The rate of heat production by a burning particle is:

$$Q_p = \pi d_p^2 \eta \Delta H_T c_p / (1/k_0 + d_p/ShD_G) \quad (6)$$

where k_0 is an overall chemical rate constant which depends upon the model used (see Table 1) and $\eta\Delta H_T$ is the heat reaching the carbon from combustion of carbon to CO_2; ΔH_T is the heat of combustion of carbon to CO_2 at bed temperature.

Equating the rate of heat generation to the rate of heat loss from the right hand side of equation (5) gives

$$\eta \Delta H_T c_p / (1/d_p k_0 + 1/ShD_G) = Nuk(T_p - T_b) + \sigma \epsilon_r d_p (T_p^4 - T_b^4) \quad (7)$$

The thermal conductivity k is an effective value based on conduction through first a stagnant gas film of thickness δ around the particle and then the particulate phase. The particulate phase thermal conductivity is calculated using the relationship of Yagi and Kunii[17] or Yagi *et al*[18] for an incipiently fluidised bed with Kunii and Smith's[19] effective packed bed thermal conductivity. Ross *et al*[12] put $\epsilon_r = 0.85$, close to the value 0.8 used here and recommended by Lindsay[20], who recently studied radiative heat transfer in fluidised beds.

Substituting $Nu = 7$, k calculated for $d_a/10 < \delta < d_a/6$ (Ross *et al*[12]) and Field's rate expression (F2, Table 1) with $\eta = 1$ into equation (7) gives a particle temperature that is too high. Either (i) the heat loss equation is inapplicable or (ii) $\eta < 1$.

The heat loss equation was checked as follows. Stainless steel balls, 3.2 and 4.6 mm dia, were fixed on to very fine thermocouples (0.05 mm) and dropped into fluidised beds of 0.5 mm sand at temperatures around 1123 K and a velocity of 0.5 m s^{-1}. The temperature responses of the balls were obtained for 30 experiments. The balls were assumed to be isothermal: this was checked by heating the balls to around 470 K and dipping them in water to deduce boiling heat transfer coefficients. The resulting values based upon the assumption of uniform temperature throughout the ball compared well with published data[21]. It was concluded that temperature gradients within the ball were negligible.

With $Nu = 7$ the theoretical temperature response for the ball, obtained by solving the unsteady state energy balance

$$-c_B \rho_B V_p \frac{dT_p}{dt} = Nuk\pi d_p(T_p - T_b) + \sigma \epsilon_r \pi d_p^2 (T_p^4 - T_b^4) \quad (8)$$

agrees with the experimental response if k is calculated using $\delta = d_a/5$.

With this value of k, $T_b = 1173$ K, $T_p = 1313$ K, $k_0 = 0.9$ m s^{-1}, $c_p = 2.18$ mol m^{-3} and $d_p = 1$ mm equation (7) gives $\eta = 0.71$. Therefore approximately 55% of the energy released during the combustion of CO produced at the particle surface heats the particle.

This is valid if the diameter d_p of the particle to or from which heat is transferred is larger than the diameter d_a of the inerts in the bed. For $d_p < d_a$ another relationship for δ is required for the following reason. If δ is given as some fraction of d_a then for $d_p \ll d_a$, theory predicts that k approaches the thermal conductivity of the fluidising gas. However, Witkowski's[22] film of the surface and freeboard of a fluidised combustor suggests that even for small particles of carbon the thermal conductivity of the particulate phase exceeds that of the fluidising gas. In this film, small particles of carbon elutriated from the combustor cannot be seen leaving the bed. This must be because the thermal conductivity of the particulate phase is large enough to prevent an appreciable temperature difference between the particles of carbon and the inert bed particles. However, the thermal conductivity of the gas in the freeboard is not large enough to prevent a rise in the temperature of the carbon particles so they glow brightly and can be seen passing through the freeboard.

The relationship, $\delta = d_p/5$, used in this work to calculate k for $d_p < d_a$ is suggested by the geometry of the system and allows k to be continuous in d_p. The effect of d_p on k is then, from equation (6) from Ross *et al*[12]: for $d_p > d_a$, $\delta = d_a/5$ so k decreases as d_p approaches d_a; for $d_p \leqslant d_a$, $\delta = d_p/5$ so k remains constant as d_p decreases further. Hence for $d_p \ll d_a$, theory does not predict that k approaches the thermal conductivity of the fluidising gas.

Thus equation (7) predicts plausible particle temperatures when $\eta\Delta H_T = 279 \times 10^3$ J mol^{-1}, $Sh = 3.5$, $Nu = 7$ and $\delta = d_a/5$ for $d_p > d_a$, or $\delta = d_p/5$ for $d_p < d_a$. The particle temperatures given in this paper are for Sh and Nu assumed constant. Turnbull[23] presents an analysis in which Sh and Nu are given by equations of the form suggested by Frössling; the results are similar to those with constant Sh and Nu.

For combustion of coke at atmospheric pressure in a bed at 1173 K with $c_p = 2.18$ mol m^{-3} (air) equation (7) predicts that particle temperature increases slowly as the particle shrinks to approximately 1.5 mm dia ($T_p = 1298$ K, 1329 K for $d_p = 3$ mm, 1.5 mm respectively) and then decreases rapidly to T_b as the particle shrinks further ($T_p = 1314$ K, 1306 K, 1268 K

VOL. 62 1984

for $d_p = 1.0$ mm, 0.8 mm, 0.4 mm respectively). This provides an alternative explanation to that proposed by Ross[2,3] for his observation that small particles burn at a temperature close to that of the bed (see item (iii) of the section on 'Theory' above). The outcome of these calculations is that small particles burn cooler because of large heat transfer coefficients which are a consequence of the Nusselt number being nearly constant.

EXPERIMENTAL

Data were obtained from two fluidised combustors with conditions given in Table 3.

The burn-out time of a single particle or of small charges can only be visually determined because of the small amounts of CO_2 produced. Accordingly, a 50 mm dia, 300 mm high electrically heated fluidised combustor was constructed. The burn-out time for small charges was measured by viewing from the top. The distributor was a perforated stainless steel plate with 19 × 0.2 mm dia holes; the pressure drop was greater than 1.5 times the weight per unit area of the bed for all conditions. Air and nitrogen could be supplied to the bed.

The pressurised combustor at RAL is 100 mm dia × 1.2 m high with bed heights up to 0.6 m. The combustor is contained in a pressure vessel approximately 1 m dia × 2.4 m high: this pressure vessel operates at about room temperature and contains air at about the same pressure as the combustor; this pressure can be up to 20 bar gauge. Thus the container for the combustor, which operates at temperatures up to 1273 K, does not have to withstand substantial internal pressure. The maximum fluidising velocity at 20 bar gauge and 1173 K is 0.5 m s^{-1}. The flow-sheet is shown in Figure 1.

The rig is fully instrumented. Coal or carbon can be added in batches or continuously and the concentrations of O_2, CO_2 and CO in the off-gas can be measured.

The primary experiment at RAL was to measure the burn-out time for a batch of closely-sized carbon particles suddenly introduced into an air-fluidised bed of sand at 1073–1173 K and at a pressure between 1.1 bar and 17 bar absolute. For the small carbon charges used, there was negligible CO in the off-gas. Hence the off-gas concentration of CO_2 showed the progress of combustion: when 95% of the injected carbon was consumed, burn-out was assumed. The injected carbon agreed, within 5%, with the total exit carbon deduced from the CO_2 in the flue gas. A wide variety of carbons was used (see Table 2) to show the effect of reactivity on combustion rate.

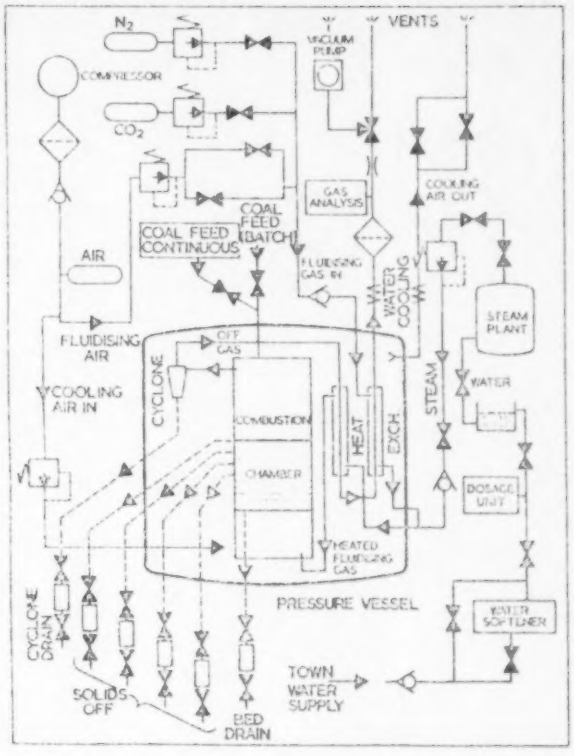


Figure 1. Flow sheet for the pressurised combustor at the Rutherford Appleton Laboratory.

RESULTS

Effect of Pressure

Figures 2–9 show burn-out time t_b plotted against (mass of carbon charged m)/(combustor pressure P). The use of m/P as abscissa is suggested by equations (1) and (4): the first term in both equations is dependent

Table 3. Range of Experimental Conditions

	Rutherford Combustor		
	Large Particles	Small Particles	Cambridge Combustor
Bed conditions			
Bed diameter (mm)	100	100	50
Sand size (mm)	0.3–0.7	0.15–0.30	0.3–0.7
U_{mf} at 1173 K (m s^{-1})	0.08	0.03	0.08
U at T_b (m s^{-1})	0.3	0.15	0.5
Static bed height (m)	0.3	0.3	0.05
Maximum T_b (K)	1173	1173	1200
Minimum T_b (K)	1073	1173	973
Pressure (bar abs)	1.1–17	1.1–12	1
Carbon conditions			
No of carbons	6	1	5
Size ranges (mm)	0.71–1.0	0.15–0.25	1.0–1.4
	1.0–1.4	—	1.0–1.7
Maximum BET area (m^2 m^{-3})	535×10^6	0.95×10^6	17.8×10^6
Minimum BET area (m^2 m^{-3})	0.3×10^6	—	0.3×10^6
Maximum charge (g)	50	50	—

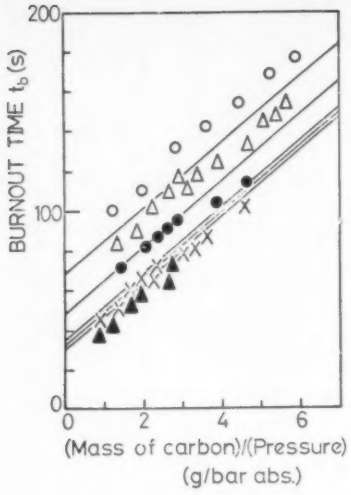


Figure 2. Burn-out times for 1.0–1.4 mm coke (RAL bed). $T_b = 1173$ K, $U = 0.3$ m s^{-1}. The lines are from theory: equation (4) with k_i from equation (F4) Table 1 and $S_E = S_V = 0.3 \times 10^6$ m^{-1}

Data point	○	△	●	×	▲
Absolute pressure (bar)	1.1	2	7	12	17
Estimated T_p(K), equation (7)	1295	1335	1373	1381	1385

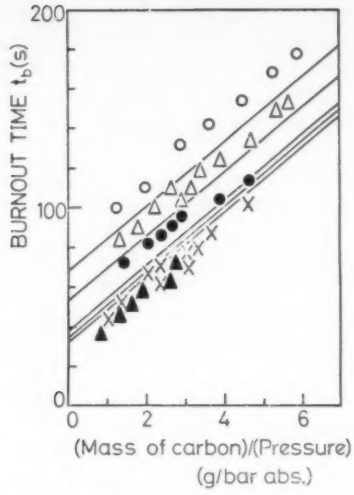


Figure 4. Burn-out times for 1.0–1.4 mm coke (RAL bed). $T_b = 1173$ K, $U = 0.3$ m s^{-1}. The lines are from theory: equation (4) with k_i from equation (S4) Table 1 and $S_E = S_V = 0.3 \times 10^6$ m^{-1}.

Data point	○	△	●	×	▲
Absolute pressure (bar)	1.1	2	7	12	17
Estimated T_p(K), equation (7)	1302	1328	1363	1373	1378

upon m and determines the slope of the plots. Since the inlet oxygen concentration is a function of pressure, $c_O \propto P$; hence the slope of a plot of t_b against m/P should be independent of pressure provided the cross-flow factor X is also independent of pressure.

The intercept of such a plot is, to a good approximation, the burn-out time t_{bs} for a single particle and is the sum of a diffusion term and a kinetic term. The diffusion term is independent of pressure because $D_G \propto P^{-1}$ whilst $c_O \propto P$ and therefore $D_G c_O$ is constant (see equations (1) and (4)). The effect of increasing pressure is to increase the rate of chemical reaction and hence to reduce the kinetic term. Thus as pressure is increased, t_b diminishes, reaching a minimum when the kinetic term is negligible; so at high pressures, combustion is entirely controlled by diffusion. This behaviour is evident in Figures 2–9: the data confirm the theoretical prediction that there is diffusion control at high pressure.

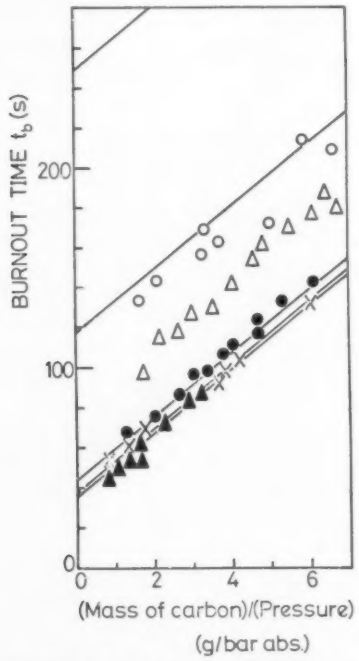


Fig. 3. Burn-out times for 1.0–1.4 mm coke (RAL bed). $T_b = 1123$ K, $U = 0.3$ m s^{-1}. The lines are from theory: equation (4) with k_i from equation (F4) Table 1 and $S_E = S_V = 0.3 \times 10^6$ m^{-1}.

Data point	○	△	●	×	▲
Absolute pressure (bar)	1.1	2	7	12	17
Estimated T_p(K), equation (7)	1168	1202	1305	1322	1330

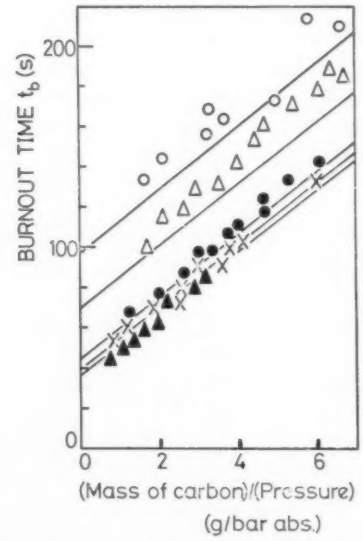


Figure 5. Burn-out times for 1.0–1.4 mm coke (RAL bed). $T_b = 1123$ K, $U = 0.3$ m s^{-1}. The lines are from theory: equation (4) and k_i from equation (S4) Table 1 and $S_E = S_V = 0.3 \times 10^6$ m^{-1}.

Data point	○	△	●	×	▲
Absolute pressure (bar)	1.1	2	7	12	17
Estimated T_p(K), equation (7)	1226	1257	1307	1320	1327

VOL. 62 1984

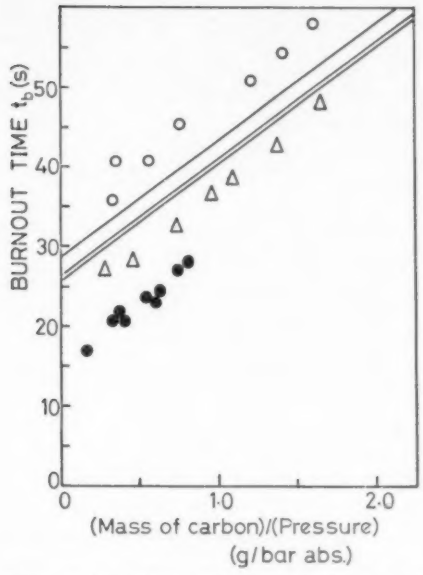


Figure 6. Burn-out times for 1.0–1.7 mm lignite char (RAL bed). $T_b = 1073$ K, $U = 0.3$ m s^{-1}. The lines are from theory: equation (4) with k_i from equation (S4) Table 1 and $S_E = S_V = 147 \times 10^6$ m^{-1}.

Data point	○	△	●
Absolute pressure (bar)	1.1	2	7
Estimated T_p(K), equation (7)	1301	1303	1306

The particle temperatures, T_p, shown on Figures 2–9 were calculated from equation (7) with the appropriate k_0 (either equation (F3) or (S3) from Table 1) for the initial particle diameter d_i and inlet oxygen concentration c_O and were used to calculate the kinetic term for each case. Particle temperature was assumed constant during combustion.

Equation (1) is rejected because, whilst it is adequate for moderately reactive carbons at atmospheric pressure and temperatures close to 1173 K, it does not predict quantitatively the effect of pressure on burn-out time nor does it make allowance for differences in char reactivity.

To decide between the two chemical rate equations (F4) and (S4) in Table 1 consider the combustion of 1.0–1.4 mm coke at pressures up to 17 bar absolute.

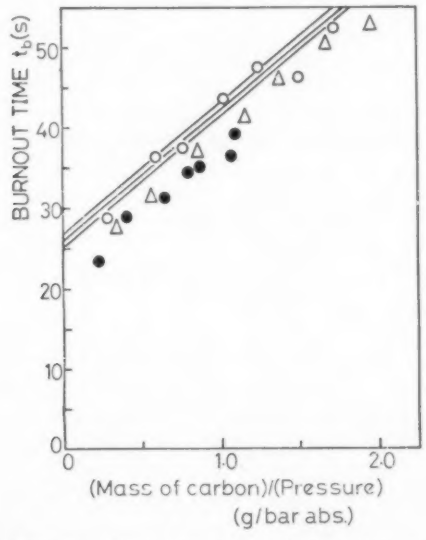


Figure 7. Burn-out times for 1.0–1.7 lignite char (RAL bed). $T_b = 1173$ K, $U = 0.3$ m s^{-1}. The lines are from theory: equation (4) with k_i from equation (S4) Table 1 and $S_E = S_V = 147 \times 10^6$ m^{-1}.

Data point	○	△	●
Absolute pressure (bar)	1.1	2	7
Estimated T_p(K), equation (7)	1390	1391	1393

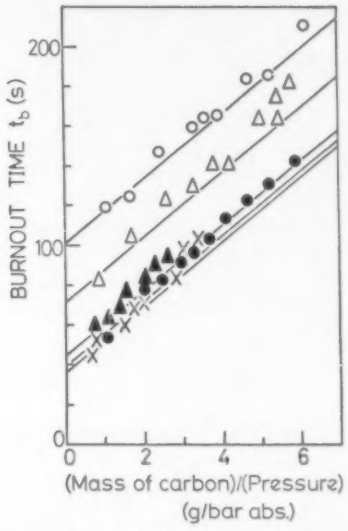


Figure 8. Burn-out times for 1.0–1.4 mm Illinois 5 char (2) (RAL bed). $T_b = 1173$ K, $U = 0.3$ m s^{-1}. The lines are from theory: equation (4) with k_i from equation (S4) Table 1 and an effective pore area for combustion, $S_E = 0.25 \times 10^6$ m^{-1}.

Data point	○	△	●	×	▲
Absolute pressure (bar)	1.1	2	7	12	17
Estimated T_p(K), equation (7)	1269	1298	1346	1360	1367

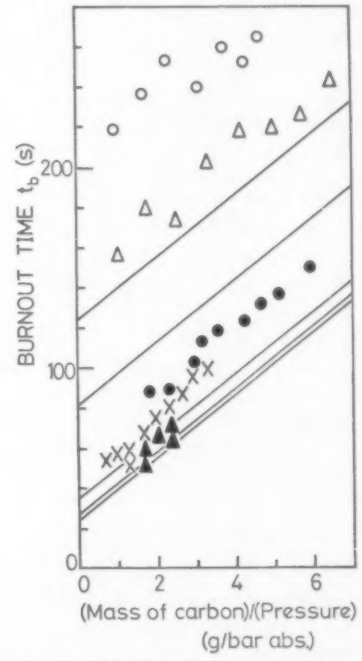


Figure 9. Burn-out times for 0.7–1.0 mm Illinois 5 char (2) (RAL bed). $T_b = 1123$ K, $U = 0.3$ m s^{-1}. The lines are from theory: equation (4) with k_i from equation (S4) Table 1 and an effective pore area for combustion, $S_E = 0.25 \times 10^6$ m^{-1}.

Data point	○	△	●	×	▲
Absolute pressure (bar)	1.1	2	7	12	17
Estimated T_p(K), equation (7)	1180	1205	1283	1311	1325

Figures 2 and 4 show that burn-out times predicted by equation (4) with k_i equal to either expression fit the data at 1173 K. However, at 1123 K (Figure 3) equation (4) over-predicts burn-out times for pressures less than 7 bar absolute if k_i is given by equation (F4); Figure 5 shows that predictions with k_i given by equation (S4) agree closely with the data. The activation energy suggested by Field *et al*[5] (F4) is too large because it was from experiments with non-porous carbons (regime I) whereas the data of Figures 3 and 5 are for porous carbons (regime II). Accordingly, subsequent theoretical burn-out times are calculated using equation (4) with k_i given by equation (S4) and particle temperatures predicted by equation (7) with k_0 given by equation (S3). Important points to note from Figures 4 and 5 are:

(i) The data do show linear relations between t_b and m/P for a given pressure, proof that the form of equation (4) is correct and that the combustion process, whether diffusion or chemical rate controlled, depends upon the first order of the oxygen concentration.

(ii) Comparing Figures 4 and 5 shows that the effect of pressure on burn-out time at 1123 K is significantly greater than at 1173 K, consistent with increased importance of chemical kinetics at lower temperatures.

(iii) As pressure is increased, the theoretical and experimental lines approach a common asymptote which represents the limit imposed by diffusion of oxygen locally around each particle (hereafter this limit will be referred to as diffusion control).

The burn-out times of a more reactive carbon, lignite char, are given in Figures 6 and 7 for bed temperatures of 1073 K and 1173 K. This char was prepared *in-situ* by charging the lignite into a hot nitrogen-fluidised bed. After two minutes, by which time devolatilisation should have been complete, the fluidising gas was changed to air and combustion began.

The rate of combustion of a reactive char should be diffusion limited; increasing pressure should therefore not greatly affect the intercepts of plots of t_b against m/P. Figures 6 and 7 show that this is true for lignite char. Even at the lower temperature of 1073 K (Figure 6) where kinetics should be more important, the combustion is primarily diffusion controlled. Note that (i) the burn-out times at 1073 K and 7 bar absolute (Figure 6) are considerably shorter than the theory predicts, which suggests that fragmentation of the char particles had occurred and (ii) the dependence of burn-out time on pressure is greater than predicted; possibly because the use of BET area gives an over-prediction of the reactivity of the char.

Effect of Pore Area

The reactivity of a char may be a function of its treatment at high temperature. Two chars were produced as follows from the same parent coal and burnt to examine this effect.

(1) A reactive char was produced from Illinois 5 coal (termed Illinois 5 char (1)) by the method just described.

(2) NCB produced an unreactive char at 1173 K in coke ovens. The residence time, typically three hours, was enough to anneal active sites.

The two chars have very different BET areas, see Table 2.

Burn-out times for the Illinois 5 char (1) were determined at bed temperatures of 1073 K, 1123 K and 1173 K and pressures of 1.1, 2 and 7 bar absolute: theoretical predictions were within ± 5 s of the experimental values for 80% of the 70 data points collected. It was evident that combustion was diffusion controlled for this reactive char.

Although Illinois 5 char (2) has a BET area greater than that of coke, it is less reactive; hence the theory underestimates single particle burn-out times t_{bs} obtained from plots like Figures 2–9 with $m = 0$. For example for 1.0–1.4 mm Illinois 5 char (2) burnt at 1173 K and 0.3 m s^{-1} and pressures up to 17 bar absolute, using equation (4) with S_E = the BET area from Table 2 gives values of t_{bs} less than 70% of the experimental values. Consequently the BET area is too large for use in equation (4). The effective pore area S_E for combustion can be deduced from t_{bs} as follows. For 1.0–1.4 mm particles at 1173 K and 1.1 bar absolute $t_{bs} = 99$ s of which 25.5 s is the diffusion term. Setting the kinetic term in equation (4) equal to 73.5 s and solving for T_p and S_E simultaneously with equation (7) gives $T_p = 1269$ K and $S_E = 0.25 \times 10^6$ m^2 m^{-3}. Figure 8 shows that the theoretical predictions using this surface area agree well with the data.

However, Figure 9 shows that for 0.7–1.0 mm Illinois 5 char (2) particles burnt at 1123 K the agreement between experiment and theory using $S_E = 0.25 \times 10^6$ m^2 m^{-3} is poor; it appears that the assumed activation energy is too low. Possibly this unreactive char burns under conditions approaching regime I rather than regime II; if this were true, the observed activation energy would be up to twice the value for regime II. Burn-out times for 0.71–1.0 mm coke ($S_E = S_V = 0.3 \times 10^6$ m^2 m^{-3}) at 1123 K also suggest transition to regime I[23]. However, for Tymawr char ($S_E = S_V = 0.5 \times 10^6$ m^2 m^{-3}) results presented in Figure 10 agree well with the theoretical predictions. These data suggest that the theory presented here is only applicable for chars with S_E greater than 0.3×10^6 m^2 m^{-3}. As the area decreases below this value, regime I is approached and the observed activation energy increases.

Experimental data reported by Ashu *et al*[24] suggest that pores smaller than 130Å do not take part in combustion reactions. The mean free path of molecules λ can be estimated from[25]

$$\lambda = 10^3 TP_0/T_0P \simeq 4000 \text{ Å}$$

at atmospheric pressure and 1200 K, suggesting that small pores do not take part in combustion reactions. This is significant because Essenhigh[8] points out that up to 95% of internal surface area can be composed of pores smaller than 20Å.

For lignite char and Illinois 5 char (2) the total BET areas S_V were larger than the effective pore areas S_E for combustion. Similarly, an activated carbon (anthracite-based, supplied by the NCB) with a BET area of 535×10^6 m^2 m^{-3} was only slightly more reactive than coke[23]. From values of t_{bs} for this carbon $S_E = 0.5 \times 10^6$ m^2 m^{-3} was deduced, close to a modified

VOL. 62 1984

BET area, $S_M = 1.5 \times 10^6\ m^2\ m^{-3}$, including only pores with diameter bigger than 150Å.

The suggestion that the modified BET area S_M characterises char reactivity better than the total BET area S_V cannot be tested rigorously here because the pore structures of the remaining chars are not well characterised. However a preliminary analysis[23], using pore size distributions determined by mercury porosimetry, showed promise.

Small Particles

The rate of combustion of small particles (<0.2–0.5 mm) is controlled by the rate of chemical reaction (see (iii) in Theory, above) and so burn-out should be more rapid at high pressure. Burn-out times for Phurnacite Breeze of diameter 0.15–0.25 mm show that this is true[23]; at 1173 K the value of t_{bs} falls from 23 s at 1.1 bar absolute to 8 s at 7 bar absolute. Hence carbon elutriation from combustors should be reduced by increased pressure and this may be an important advantage of high pressure fluidisation.

Effect of Bed Temperature

Bed temperature is an important parameter and Figure 10 shows how t_{bs} varies with bed temperature for five different carbons. The reactivity of the carbons varies considerably yet the theoretical predictions, equation (4) with k_i given by equation (S4) from Table 1 and $S_E = S_V$, are generally in agreement with the experimental results. Coke is the least reactive of the carbons and its rate of combustion should therefore be controlled by the rate of chemical reaction. As Figure 10 shows, the burn-out time for a single coke particle is sensitive to changes in bed temperature which suggests a strong kinetic influence. Illinois 5 char (1) is the most reactive carbon and Figure 10 shows that bed temperature has little effect on the burn-out time for a single particle, suggesting control by diffusion. The temperature dependence of burn-out time for the remaining carbons lies between these two extremes, reflecting different extents of chemical rate control; the theory is able to predict these variations in behaviour.

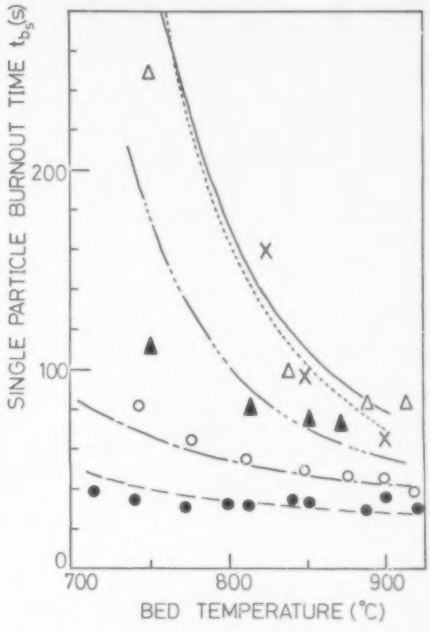


Figure 10. Burn-out times for single carbon particles at various bed temperatures. The lines are from theory: equation (4) with k_i from equation (S4) Table 1 and $S_E = S_V$ for all carbons (Table 2). The results were visually determined from the Cambridge bed.

Carbon	Coke	Merthyr Vale	Illinois 5 Char (1)	Bedwas	Tymawr
Data point	×	○	●	▲	△
Theory	-----	—·—	— —	—··—	——

DISCUSSION

Two key assumptions require comment.

(i) *Definition of burn-out time*

Small particles burn slowly and so at low pressures the CO_2 trace, particularly for an unreactive carbon, can have a long tail; combustion during this period is not representative of the initial size of particle. The accuracy of the CO_2 analyser used in this study was $\pm 0.5\%$; therefore the 95% burn-out criterion was chosen so that for Illinois 5 char (2) (the least reactive carbon) CO_2 concentrations below about 1.5% were not included.

(ii) *Assumption of constant particle temperature*

Particle temperature T_p is assumed to be constant to give an analytical expression for t_b. However the oxygen concentration in the particulate phase, and consequently the oxygen concentration at the particle surface, varies during burn-off. Therefore T_p must also vary. The assumption of constant T_p can be justified because in most cases diffusional effects are significant, and are independent of T_p. It is useful to compare experimental and theoretical CO_2 traces assuming (*a*) T_p is constant and (*b*) T_p varies during burn-off; the theoretical derivation is given in the Appendix.

Figure 11 compares experimental and theoretical CO_2 traces for 1.0–1.4 mm coke burnt at 1.1 bar absolute. When T_p is assumed constant, the theoretical trace has no tail and higher CO_2 concentrations must therefore be

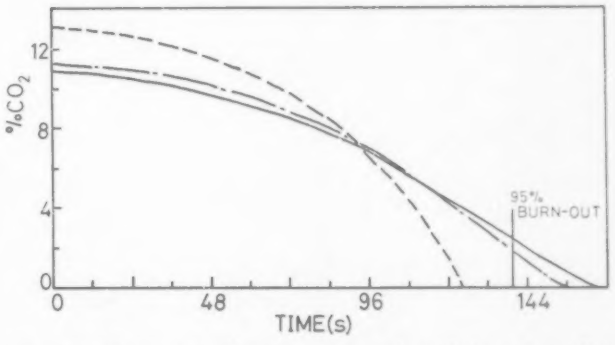


Figure 11. Comparison of experimental and theoretical (see Appendix) CO_2 traces after injection of 3.7 g of 1.0–1.4 mm coke into a bed at 1173 K at atmospheric pressure, $U = 0.3\ m\ s^{-1}$. $S_E = S_V = 0.3 \times 10^6\ m^{-1}$.

Experimental trace ——
Theoretical trace, T_p constant -----
Theoretical trace, T_p varies —·—

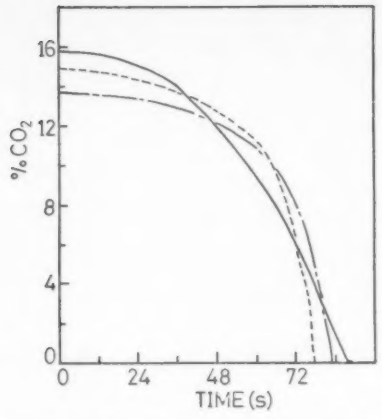


Figure 12. Comparison of experimental and theoretical (see Appendix) CO_2 traces after injection of 46.7 g of 1.0–1.4 mm coke into a bed at 1173 K at absolute pressure 17 bar, $U = 0.3\ m\ s^{-1}$, $S_E = S_V = 0.3 \times 10^6\ m^{-1}$.
Experimental trace ——
Theoretical trace, T_p constant -----
Theoretical trace, T_p varies —·—

predicted during the initial stages of combustion. The theoretical trace obtained when T_p varies during combustion has a tail because T_p falls rapidly as the particle size decreases below about 1.5 mm as predicted by equation (7); agreement with experiment is good.

At high pressures, small particles burn quickly (see Small Particles, above). Accordingly, Figure 12 shows that for 1.0–1.4 mm coke burnt at 17 bar absolute the experimental CO_2 trace has no tail. At this pressure, combustion is diffusion controlled, the influence of T_p is small, and the two theoretical traces are closer together.

For pure chemical rate control it would be inappropriate to assume constant T_p. But for fluidised combustion, this limit is seldom encountered and so this assumption normally gives satisfactory estimates for t_b.

The data for unreactive chars suggest that the model presented is inappropriate for chars with pore areas smaller than $0.3 \times 10^6\ m^2\ m^{-3}$ because of transition to regime I conditions. This conclusion may not be justified, because the assumption of constant T_p removes the tail of the CO_2 trace, explaining why the theory under-predicts burn-out times for these chars. Predicted times for 95% burn-out of 3.5 g of 0.71–1.0 mm Illinois 5 char (2) at atmospheric pressure, $T_b = 1123$ K and $U = 0.3\ m\ s^{-1}$ are 178 s for constant T_p and 159 s when T_p varies. The model with constant T_p unexpectedly predicts a longer burn-out time than the model with variable T_p. This is because the theory for variable T_p also allows the bed temperature to vary and the bed temperature is, with this theory, initially higher than when T_p is constant through the combustion. The conclusions reached earlier are therefore valid.

CONCLUSIONS

1. The burn-out time of seven different carbons in a fluidised bed, for bed temperatures between 1023 and 1173 K and bed pressure up to 17 bar absolute, is predicted by equation (4) with k_i replaced by k_{MS} from equation (S4) Table 1.

2. The theory allows for limited penetration of the porous burning carbon by oxygen, represented by the last term in equation (4). The choice of effective pore area S_E depends on a number of considerations. BET areas comprising all pores were measured but it appears that only pores bigger than 150Å are effective. If the pore area of the char S_E is above $0.3 \times 10^6\ m^{-1}$, as it is for most chars formed in a fluidised bed from medium or low rank coals, equation (4) is applicable. For $S_E \gg 0.3 \times 10^6\ m^{-1}$, combustion tends to be diffusion controlled. For $S_E < 0.3 \times 10^6\ m^{-1}$, combustion is restricted to the external carbon surface and is controlled by reaction rate.

3. Increased pressure gives higher oxygen concentration and therefore faster reaction rates. With regard to diffusion, the higher oxygen concentration is offset by the decrease of diffusion coefficient due to higher pressure, therefore diffusion of oxygen to the particle is unaffected by pressure. Consequently at higher pressure, combustion is more likely to be diffusion controlled than at low pressure.

4. A heat balance on a burning carbon particle, allowing for the particle receiving a proportion of heat from combustion of CO around it, predicts the particle temperature T_p: T_p tends to bed temperature as the particle diameter becomes small. This explains why small particles burn slowly. But as pressure increases, such particles burn faster, because their combustion is controlled by chemical kinetics and the higher oxygen concentration gives faster reaction rates. It follows that there should be less elutriation of unburnt carbon from high pressure fluidised beds, and hence higher combustion efficiency.

APPENDIX

Prediction of CO_2 trace after injection of a batch of carbon into a fluidised bed

(*a*) T_p *Constant*

A simple analytical result is not possible but the following steps can be performed on a calculator.

(i) Calculate T_p using equation (7) for d_i and c_O.
(ii) Calculate t_b from equation (4).
(iii) Obtain the relation between d_p and t from[2]:

$$\frac{m}{12c_O A[U-(U-U_{mf})e^{-X}]}\left(\frac{d_p}{d_i}\right)^3 + \frac{\rho_c d_i^2}{48ShD_G c_O}\left(\frac{d_p}{d_i}\right)^2 + \frac{\rho_c d_i}{24(S_E D_E k_i)^{0.5} c_O}\left(\frac{d_p}{d_i}\right) = t_b - t \qquad \text{(A1)}$$

(iv) The two phase theory of fluidisation[4] and an overall CO_2 balance on the combustor give the concentration of CO_2 in the off-gas as

$$KN\pi d_p^2 c_O\left[AU + \frac{KN\pi d_p^2 U}{\{U-(U-U_{mf})e^{-X}\}}\right]^{-1} \qquad \text{(A2)}$$

where K is an overall rate constant for combustion and

$$1/K = 1/(S_E D_E k_i)^{0.5} + d_p/ShD_G \qquad \text{(A3)}$$

and N is the number of particles in the batch of carbon. Substitute for d_p from (iii) to give the outlet CO_2 concentration in terms of t.

VOL. 62 1984

(*b*) T_p *Varies During Combustion*

This procedure requires the use of a computer and the steps required in the program are as follows.

(i) Set $d_{pOLD} = d_i$, $c_p = c_O$, $T_p = T_{AMB}$, T_b = desired value.

(ii) Increment time.

(iii) Solve unsteady state particle energy balance for T_p; equation (8) with rate of heat production, equation (6), included and with the properties of the carbon inserted.

(iv) Solve equation (A1) for d_{pNEW} with

(*a*) ratio of diameters equal to d_{pNEW}/d_{pOLD},
(*b*) k_i evaluated for T_p from (iii),
(*c*) t equal to the time increment,
(*d*) t_b from equation (4) calculated for d_{pOLD} using the current value for k_i.

(v) Calculate the CO_2 concentration in the off-gas using equations (A2) and (A3) with d_{pNEW} and k_i.

(vi) If d_{pNEW} is less than some critical value, stop.

(vii) Perform bed energy balance to obtain new T_b.

(viii) Set d_{pOLD} equal to d_{pNEW} and calculate c_p from an overall oxygen balance[4],

$$c_p = \frac{Uc_H - (U - U_{mf})c_O e^{-X}}{[U - (U - U_{mf})e^{-X}]}$$

where c_H is the outlet oxygen concentration.

(ix) Return to step (ii).

SYMBOLS USED

A	cross-sectional area of combustor	m^2
A_p	external surface area of particle	m^2
A_s	pre-exponential term in Arrhenius-type rate expressions	$m\,s^{-1}\,K^{-1}$
c	oxygen concentration	$mol\,m^{-3}$
c_B	specific heat of stainless steel ball	$J\,g^{-1}\,K^{-1}$
c_H	oxygen concentration in off-gas from the combustor	$mol\,m^{-3}$
c_O	oxygen concentration of the inlet gas	$mol\,m^{-3}$
c_p	oxygen concentration in the particulate phase	$mol\,m^{-3}$
c_s	oxygen concentration at the particle surface	$mol\,m^{-3}$
D_E	diffusion coefficient of oxygen in solid carbon	$m^2\,s^{-1}$
D_G	gas phase diffusion coefficient of oxygen	$m^2\,s^{-1}$
d_a	diameter of bed material	m
d_i	initial particle diameter	m
d_p	particle diameter	m
d_p^*	particle diameter at which $d_r = 0$	m
d_{pNEW}	current particle diameter in program—see Appendix	m
d_{pOLD}	previous particle diameter in program—see Appendix	m
d_r	diameter of unreacting core of burning particle	m
ΔH	heat that reaches particle from combustion of solid carbon to carbon dioxide $= \eta \Delta H_T$	$J\,mol^{-1}$
ΔH_T	heat of combustion for carbon burnt to carbon dioxide at bed temperature	$J\,mol^{-1}$
K	overall rate constant	$m\,s^{-1}$
k	effective thermal conductivity of particulate phase	$W\,m^{-1}\,K^{-1}$
k_F	rate constant proposed by Field et al[5]	$m\,s^{-1}$
k_g	mass transfer coefficient	$m\,s^{-1}$
k_i	intrinsic rate constant	$m\,s^{-1}$
k_{MF}	modified Field et al[5] rate constant	$m\,s^{-1}$
k_{MS}	modified Smith[6] rate constant	$m\,s^{-1}$
k_0	overall chemical rate constant	$m\,s^{-1}$
k_S	rate constant proposed by Smith[6]	$m\,s^{-1}$
m	true reaction order, i.e. when chemical rate controlled	—
m	mass of carbon injected into bed	g
N	number of particles injected into bed	—
Nu	Nusselt number for heat transfer	—
n	apparent reaction order	—
P	bed pressure	bar abs.
P_0	reference pressure (= atmospheric pressure)	bar abs.
Q_p	effective rate of heat production by a particle	$J\,s^{-1}$
R	universal gas constant = 8.314	$J\,mol^{-1}\,K^{-1}$
R_s	overall reaction rate of one particle per unit of external surface area	$mol\,m^{-2}\,s$
S_E	effective pore surface area for combustion	$m^2\,m^{-3}$
Sh	Sherwood number for mass transfer	—
S_M	modified pore surface area including only pores bigger than 150Å dia.	$m^2\,m^{-3}$
S_V	total pore surface area of a particle per unit volume	$m^2\,m^{-3}$
T	temperature	K
T_{AMB}	ambient temperature	K
T_b	bed temperature	K
T_0	reference temperature = 273 K	K
T_p	particle temperature	K
t	time	s
t_b	burn-out time for a batch of carbon	s
t_{bs}	burn-out time for a single carbon particle	s
U	fluidising velocity	$m\,s^{-1}$
U_{mf}	minimum fluidising velocity	$m\,s^{-1}$
V_p	volume of a particle	m^3
X	bubble/particulate phase cross-flow factor	—
x	distance measured inwards normal to the external surface of the particle	m

Greek symbols

δ	thickness of gas film around a burning particle	m
ϵ_p	porosity of a particle	—
ϵ_r	emissivity of particle	—
η	ratio $\Delta H/\Delta H_T$	—
λ	mean free path of gaseous molecules	Å
ρ_B	density of stainless steel ball	$g\,m^{-3}$
ρ_c	carbon density	$g\,m^{-3}$
σ	Stefan–Boltzmann constant	$W\,m^{-2}\,K^{-4}$
τ	tortuosity	—
ϕ	Thiele modulus, see equation (3)	—

REFERENCES

1. National Coal Board, 1980, *Fluidised Bed Combustion of Coal* (Adprint, Cheltenham).
2. Ross, I. B., 1979, *Ph.D. dissertation* (University of Cambridge).
3. Ross, I. B. and Davidson, J. F., 1982, *Trans I Chem E*, 60: 108.
4. Davidson, J. F. and Harrison, D., 1963, *Fluidised Particles* (Cambridge University Press).
5. Field, M. A., Gill, D. W., Morgan, B. B. and Hawksley, P. G. W., 1967. *Combustion of Pulverised Fuel* (BCURA).
6. Smith, I. W., 1978, *Fuel*, 57: 409.
7. Mulcahy, M. F. R., 1978. Paper presented to First BOC Priestley Conference, The Chemical Society, London.
8. Essenhigh, R. H., 1981, In *Chemistry of Coal Utilization*, Ch. 19. Second Supplem Vol, Elliott, M.A. (ed.) (McGraw-Hill, New York).
9. Gan, H., Nandi, S. P. and Walker, P. L., 1972, *Fuel*, 51: 272.
10. Wicke, E., 1955, *Proc Fifth Symp (Int) Combustion* (Reinhold, New York) p. 245.
11. Petersen, E. E., 1965, *Chemical Reaction Analysis* (Prentice-Hall, New Jersey) Ch. 4.

12. Ross, I. B., Patel, M. S. and Davidson, J. F., 1981, *Trans I Chem E*, 59: 83.
13. Sherwood, T. K., Pigford, R. L. and Wilke, C. R., 1975 *Mass Transfer* (McGraw-Hill, New York).
14. Baron, R. E., Beer, J. M., Borghi, G., Hodges, J. L. and Sarofim, A. F., 1977, Paper presented to Fifth International Conference on Fluidized Combustion (DOE, Washington).
15. Congaldis, J. P. and Georgakis, C., 1981, *J Inst Energy*, 54: 48.
16. Mon, E. and Amundson, N. R., 1978, *Ind Eng Chem Fundam*, 17, 4: 313.
17. Yagi, S. and Kunii, D., 1957, *AIChEJ*, 3: 373.
18. Yagi, S., Kunii, D. and Wakow, N., 1961, *Int Develop Heat Transfer*, 4: 742.
19. Kunii, D. and Smith, J. M., 1960, *AIChEJ*, 6: 71.
20. Lindsay, J., 1982, *Ph D dissertation* (University of Cambridge).
21. Holman, J. P., 1976, *Heat Transfer*, 4th Ed. (McGraw-Hill Kogakusha).
22. Witkowski, S., 1979, *Final year report* (Department of Chemical Engineering, University of Cambridge).
23. Turnbull, E., 1983, *PhD dissertation* (University of Cambridge).
24. Ashu, J. T., Nsakala, N., Mahajan, O. P. and Walker, P. L., 1978. *Fuel*, 57: 250.
25. de Boer, J. H., 1953. *The Dynamical Character of Adsorption* (Oxford University Press).

ACKNOWLEDGEMENTS

This work was supported by grants from the Science and Engineering Research Council and the National Coal Board. We are grateful to the staff of the Rutherford Appleton Laboratory for assistance with the complex high pressure rig. We are also grateful to the National Coal Board which (i) supplied all of the coals used in this work and (ii) provided the analyses and BET areas given. E. Turnbull was supported by a scholarship from the Commonwealth Scholarship Commission.

ADDRESS

Correspondence on this paper should be addressed to Professor J. F. Davidson, Department of Chemical Engineering, University of Cambridge, Pembroke Street, Cambridge, CB2 3RA.

The manuscript was received 1 June 1983 and accepted for publication 6 September 1983.

Book Reviews continued from page 222

be most welcome to practising engineers and with appropriate indexing will be valuable for some years to come.

In conclusion the editors have taken on an enormous task and have endeavoured to cover all aspects of solvent extraction engineering and technology. The result is more a text book than a handbook. The analytical content is modern and sound but the depth of treatment is variable and some of the chapters are so short that they are not able to make significant contributions, and do not appear to link different aspects of the subject. Quantitative data is sparse in the text but techniques of design of operations are competently treated by some very eminent contributors, with the result that this book will become a respected reference of solvent extraction.

G. V. Jeffreys.

Fundamentals of Fluidized-bed Chemical Processes
J. G. Yates
Butterworth, 1983
pp 222, £25.00

This is a good book. The first chapter, and nearly one-third of the book provides a clear and up-to-date account of the physical principles fundamental to fluidised bed technology. Fluidised bed reactor models are then introduced with the general approach well depicted both by diagram and by tabular review; Chapter 2 succinctly compares and contrasts seven reactor models available in the literature. Accounts are given in Chapter 3 of catalytic cracking and in Chapter 4 of the combustion and gasification of coal and heavy oils. The author begins his final chapter with the apologia that, in some contrast to the processes described in detail in earlier chapters, the open literature does not at present permit well-documented descriptions of many other processes to be prepared. Nevertheless Chapter 5 does contain useful accounts of a number, including the roasting of sulphide ore and the production of phthalic anhydride, vinyl chloride, and compounds of uranium.

Dr Yates's book provides an excellent addition to the literature of fluidisation and it has final-year undergraduate and postgraduate students of chemical engineering particularly in mind. His work is valuable in two specific respects which deserve mention in this short review. Firstly, the book's emphasis on the chemically-orientated aspects of gas-solids systems: the full chapter on catalytic cracking—which includes sections on catalysts, process chemistry and modelling, energy considerations, and chemical kinetics—is especially welcome. And, secondly, although Dr Yates has suggested that his work might give a 'biased model' I did not find it so. Certainly, and not least with regard to the book's primary market, reactor models need to be presented with clarity and precision, but Dr Yates has throughout kept a sense of balance in the arrangement of his material. This book should therefore not only serve as an admirable text for students but should also—because so many matters in fluidisation remain unresolved (e.g. the nature of bubble stability)—be a spur to future research.

David Harrison

VOL. 62 1984

MASS TRANSFER PROCESSES DURING THE ADSORPTION OF SOLUTES IN AQUEOUS SOLUTIONS IN BATCH AND FIXED BED ADSORBERS

By G. McKAY (MEMBER)

Department of Chemical Engineering, The Queen's University of Belfast

A theoretical mass transfer model has been developed to describe the adsorption of solutes from aqueous solutions onto adsorbent particles in batch and fixed bed adsorbers. The theoretical model is based on the unreacted core theory and yields an analytical solution for batch adsorbers, providing the assumption of a pseudo-irreversible isotherm is applicable, and all operating and tie lines terminate on the monolayer. The effects of adsorbent mass and pollutant concentration are considered. The diffusion coefficient from the batch adsorption system may be used in an analytical model for predicting theoretical breakthrough curves in fixed bed adsorbers. The main data required in this model are geometric factors, physical properties of pollutant and adsorbent, an external mass transfer coefficient and an effective diffusion coefficient. The external mass transfer coefficient is predicted from available fixed bed correlations. The variables, which can be studied in fixed beds, include bed height, solution flowrate and pollutant concentration. The models have been applied to two theoretical systems which differ considerably in their adsorption capacities.

INTRODUCTION

In recent years the use of adsorption techniques to purify water and waste water has increased considerably. The mass transport within the particles is assumed to be either a pore diffusion or a surface diffusion process.

The pore diffusion model outlined in this paper is based on the unreacted shrinking core model and involves a pseudo-steady-state approximation. In the pore diffusion model there is an adsorption of the adsorbate into the pores with a concurrent distributed adsorption all along the pore walls.

The theoretical system considered in this study is applicable to the design of batch and fixed bed adsorbers. The system reported is the adsorption of solute in aqueous solution onto a porous adsorbent. In a batch adsorption system the variables studied were adsorbent mass and initial pollutant concentration. In the fixed bed experiments the variables include: the effect of bed height, the effect of solution flow rate and initial pollutant concentration.

LITERATURE REVIEW

A survey of batch and fixed bed adsorption studies shows that the adsorption rate is determined on the basis of adsorption equilibrium (unfavourable, linear, favourable or completely irreversible) and the controlling mechanism (external diffusion, internal pore diffusion, internal solid-phase diffusion, or longitudinal diffusion).

The simplest model is that in which there is no mass transfer. DeVault[1] and Gleuckauf[2], developed this case for gas chromatography. For the special case of single mechanism rate-controlled adsorption processes, a number of mathematical models have been proposed for fixed-bed column operations. Hougen and Marshall[3] present a solution for the case of external diffusion-controlled resistance to mass transfer. Rosen[4] and Thomas[5], solved the case in which internal pore diffusion controlled the rate of mass transfer. Furnas[6] and Goldstein[7], have treated the case for systems in which either external diffusion or surface adsorption controls the rate of mass transfer, and Bohart and Adams[8] and Masamune and Smith[9a,b] have solved the case for surface adsorption controlling. The three possible two-resistance cases have also been solved[9a,4,10]. Tien and Thodos[11] have provided solutions for the problem of combined external and pore diffusion.

A general solution for the case of three-resistance controlled mass transfer is given in integral form by Masamune and Smith[12]. Other integral equations have been drawn up to calculate the concentration distribution in the column for linear adsorption-isotherms and pore diffusion[13,14] and also for diffusion in homogeneous adsorbents[15,16].

The fixed bed models presented by these authors are based on a linear isotherm for mathematical expediency. However, compounds typical of dissolved wastewater components have been found to exhibit adsorption isotherms of the favourable type and in some cases approach irreversibility[17,18,19].

When linear adsorption is not used to describe the adsorbate distribution, the solution of the mass balance equation for column adsorber performance leads to increased mathematical complexity. For Langmuir or Freundlich adsorption isotherms, assuming both pore diffusion and diffusion in homogeneous granules, the breakthrough curves can be determined purely numerically[20,21]. By means of such methods breakthrough curves have been calculated for various adsorption equilibria, assuming either diffusion in homogeneous particles[18,22,23a,24,25] or pore diffusion[23b,25,26].

© Institution of Chemical Engineers

Table 1. Review of adsorption model

Ref.	Diffusion model	Equilibrium	Adsorbate phase	Contacting system	Film resistance	Mathematical treatment
3	H	LI	G	Bed	Yes	A
5	H	LI	G	Bed	No	A
4, 15	H	LI	L	Bed	Yes	A
38	H	LI	L	Batch	No	A
11	H	LI	L	Bed	Yes	A
16	H	LI	L	Bed	Yes	A
18, 22	H	NL	L	Bed	Yes	N
44	H	NL	L	Batch	No	A
37	H	NL	L	Batch	No	N
16	H	NL	L	Bed	Yes	N
30	H	IR	L	Bed	No	A
30	H	IR	L	Bed	Yes	A†
27	H	IR	L	Bed	No	A
14	P	LI	G	Batch	No	A
45	P	LI	L	Batch	No	A
39	P	LI	L	Batch	Yes	A
46	P	LI	—	Bed	Yes	A
47	P	LI	—	Bed	No	A
9, 12	P	LI	G	Bed	Yes	A
48	P	LI	L	Multi-bed	Yes	N
40	P	NL	L	Batch	No	N
42	P	NL	L	Batch	No	A
26	P	NL	G	Bed	Yes	N
41	P	NL	L	Batch	Yes	N & A
49	P	NL	L	Bed	Yes	N
32	P	NL	L	Bed	No	A
25	P & H	NL	L	Batch & Bed	Yes	N
31	P	NL & IR	L	Bed	Yes	N & A
35	P	IR	L	Batch	Yes	A
36	P	IR	L	Bed	Yes	A
50, 51	P	IR	L	Batch	Yes	A
52	P	IR	L	Bed	Yes	A
53, 54	P	IR	L	Batch & Bed	Yes	A

†Approx. solution.
Key: H = homogeneous solid, P = pore; LI = linear, NL = nonlinear, IR = irreversible; G = gas, L = liquid; A = analytical, N = numerical.

Cooper[27], assuming the homogeneous model and no film resistance, presents a general solution for the case of an irreversible isotherm. In addition to the solution for the true diffusion in spheres, solutions are also presented for: (*a*) 'early time' approximations; (*b*) linear driving force[28]; and (*c*) quadratic driving force[29]. Vermeulen[30], presents a solution for the homogeneous model assuming constant pattern conditions and no film resistance. The pore model has also received considerable study for the case of an irreversible isotherm. Hall et al.[31] consider the case of constant pattern conditions, with film resistance. A special case of the general solution by Cooper and Liberman[32] deals with the case of constant pattern, without film resistance. Weber and Chakravorti[33] present a general solution of the pore model accounting for film resistance. The solution is a special case of the treatment of catalytic de-activation in fixed-bed ractors presented by Bischoff[34]. Assuming film and pore diffusion and irreversible adsorption, an analytical function has been obtained[35] for the determination of adsorption rates of single organic solutes in batch tests. Using this analytical function, Brauch and Schlunder[36], have derived a differential equation, without the constant pattern assumption, for the prediction of concentration distribution in adsorption columns. In some cases, the mechanism for the internal mass transfer has been determined from batch studies, but the results have not been extended to deal with column adsorption; assuming either diffusion in homogeneous particles[37,38] or pore diffusion[39b,40–42]. In most cases film diffusion is also taken into account.

Other useful methods employed in adsorber design include the LUB (equivalent length of unused bed)/equilibrium section concept[43], and the NTU (number of transfer units) method[30], which can be used when the mass transfer in the adsorbent particle is described by a constant mass transfer coefficient.

A fairly comprehensive review[44–54] of these and other adsorption models and their important features is presented in Table 1.

MATHEMATICAL DEVELOPMENT

Batch Studies

Many adsorption models have been based on restrictive assumptions, such as: (*a*) no film resistance between the solution and adsorbent, and (*b*) linear equilibrium between the solute and adsorbent. After careful consideration of the assumptions made in each of the models presented in Table 1, the work proposed by Spahn and Schlunder[35] and Brauch and Schlunder[36], has been selected as a basis for developing the model reported in this paper. The model is based on the unreacted core theory by Levenspiel[55] and Yagi and Kunii[56].

Due to external mass transfer resistance the concentration of pollutant in the water drops from a value C_0, in the bulk solution, to the equilibrium value $C_e(t)$ on the particle surface. A number of assumptions have been made in order to predict the adsorption rate.

(*a*) The solute in the pore water is transferred only by molecular diffusion from the particle surface to the interior. The concentration of solute in the pore water, therefore, decreases from $C_e(t)$ to zero at some point r_F in the particle.

(*b*) Adsorption equilibrium occurs between the pore-solute solution and adsorbent throughout the adsorption process, and thus the transfer of solute to the adsorbent surface is higher than the rate of diffusion.

(*c*) The adsorption process is irreversible.

Based on these assumptions the rate of adsorption for a series of batch tests can be expressed in terms of an analytical function of the concentration of solute in water and in the adsorbent and the Biot number *Bi*, where

$$Bi = \frac{\beta_L R}{D_{eff}} \tag{1}$$

The essential steps of the model are summarised.

The mass transfer in the external layer is given by

$$N = A\beta_L(C_t - C_e) \tag{2}$$

and the internal mass transfer in the adsorbent particle is obtained from

$$N = A\rho_s\beta_s(q_e - \bar{q}) \tag{3}$$

The concentrations at the adsorbent surface (C_e, q_e) remain in equilibrium during the adsorption period as described by the isotherm equation (20). The instantaneous adsorption rate at time t, $N(t)$, is obtained by differentiation yielding the differential mass balance

$$N(t) = -V\frac{dC_t}{dt} = S\frac{d\bar{q}}{dt} \tag{4}$$

At time $t = 0$, the mass transfer is completely restricted to the external layer on the particle, and hence β_L can be determined from

$$\beta_L = -\frac{V}{AC_0}\left(\frac{dC_t}{dt}\right)_{t\to 0} \tag{5}$$

The β_L values for the appropriate conditions may be determined[57–59] and then the equilibium concentrations (C_e, q_e) may be obtained as functions of C_t, q, using

$$C_e(t) = C_t + \frac{V}{A\beta_L}\left(\frac{dC_t}{dt}\right) \tag{6}$$

Equations (4) and (6) imply graphical differentiations of the concentration versus time curve, a process susceptible to considerable error. However, for the assumption of a pseudo-irreversible isotherm all operating and tie lines terminate on the monolayer, resulting in a constant q_e value for all C_e values. Providing this limiting condition applies, the sequence of equations (4), (6) and (7) can be solved analytically. Figure 1 shows that for an initial solute concentration of 450 mg dm^{-3} the assumption of pseudo-irreversibility is reasonable since all tie lines between 5 min and 1440 min terminate on the monolayer.

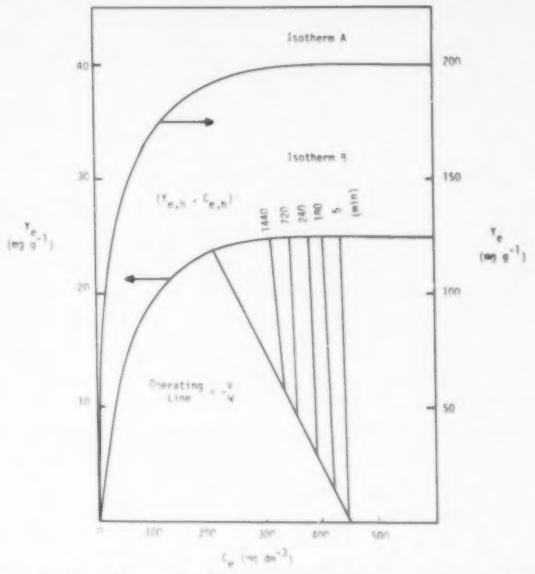


Figure 1. Two Langmuir isotherms showing the effect of different uptakes.

Hence $C_e(t)$ and the corresponding equilibrium value of $q_e(t)$ may be determined. Knowing C_t, $\bar{q}(t)$, C_e and q_e at any time, the time-dependent internal mass transfer coefficients, β_s, can be calculated in the form,

$$\beta_s = \frac{\beta_L}{\rho_s}\frac{C_t - C_e}{[q_e - q(t)]} \tag{7}$$

Equations (1) to (7) have been solved by a time consuming procedure of graphical differentiation[35] enabling a constant effective diffusivity to be predicted, D_{eff}, which describes the concentration versus time decay curves over the whole range of the isotherm for which it applies. However, the method is complex and tedious, and an analytical solution using the basic equations (but applying the constraint of a saturated isotherm) has been developed[60–62]. This analytical solution enables D_{eff} to be determined easily and quickly and is shown in equation (8).

$$\tau = \frac{1}{6C_h}\left[\ln\left(\left|\frac{x^3 + a^3}{1 + a^3}\right|^{2B - 1/a}\right)\right] + \ln\left(\left|\frac{x + a}{1 + a}\right|^{3/a}\right) + \left[\frac{1}{(a\sqrt{3})C_h}\left(\tan^{-1}\frac{2 - a}{a\sqrt{3}} - \tan^{-1}\frac{2x - a}{a\sqrt{3}}\right)\right] \tag{8}$$

The mathematical equations leading to the solution of equation (8) are presented in Appendix A.

Therefore by converting dimensionless time, τ, into real time it is possible to compare experimental and theoretical concentration decay curves.

The integration limits for equation (8) are:

$\tau = 0, \eta = 0$ and $x = 1$

$\tau = \tau, \eta = \eta$ and $x = x$

and the terms in the equation are:

$$B = 1 - \frac{1}{Bi} \tag{9}$$

$$x = (1 - n)^{1/3} \tag{10}$$

$$a = \left(\frac{1 - C_h}{C_h}\right)^{1/3} \tag{11}$$

The isotherm data and batch contact time results can be incorporated into a model to predict the concentration distribution within the fluid and solid phase in fixed beds of adsorbent.

Column Studies

A differential equation was obtained to predict the concentration distribution of solute in the columns based on the adsorption rate data developed from the batch studies. The analytical solution of the differential equation is obtained without the constant pattern assumption and includes the transitional adsorption period as well as the range of constant pattern.

The following steps are considered: (*a*) the rates of diffusion from the external bulk solution; (*b*) diffusion in pore liquid according to Fick's law, and (*c*) introducing dimensionless parameters.

The adsorption rate for a single particle can be expressed as a function of solute concentrations in the aqueous phase, ξ, in the adsorbent phase η and of the Biot number. The general form of the equation is shown.

$$\frac{\partial \eta}{\partial \tau} = \xi f(\eta)_{\mathrm{Bi}} \tag{12}$$

The differential mass balance in the column is given by

$$\frac{\partial \xi}{\partial \zeta} + \frac{\partial \eta}{\partial \tau} = 0 \tag{13}$$

This equation yields a differential equation for the prediction of the time-dependent concentration history in the solid phase.

$$\frac{\partial^2 \eta}{\partial \tau \partial \zeta} \frac{f'(\eta)}{f(\eta)} \frac{\partial \eta}{\partial \tau} \frac{\partial \eta}{\partial \zeta} \frac{\partial \eta}{\partial \zeta} f(\eta) = 0 \tag{14}$$

The dimensionless parameters are given as,

$$\tau = \frac{C_0}{\rho_s q_e^h} \frac{D_{\mathrm{eff}} t}{R^2} \tag{15}$$

$$\eta = \frac{\bar{q}}{q_e^h} \tag{16}$$

$$\xi = \frac{C_t}{C_0} \tag{17}$$

The theoretical adsorption rate $\mathrm{d}\eta/\mathrm{d}\tau$, is determined using the following equation and experimental values were obtained using data from the batch tests.

$$\frac{\mathrm{d}\eta}{\mathrm{d}\tau} = \frac{3(1 - C_h \eta)(1 - \eta)^{1/3}}{[1 - (1 - 1/Bi)](1 - \eta)^{1/3}} \tag{18}$$

where C_h is the capacity factor defined by

$$C_h = \frac{S q_e^h}{V C_0} \tag{19}$$

The solution of equation (14) has been presented by Brauch and Schlunder[36] and a similar procedure was adopted for the adsorption of solute in this model. Equations (1–19) were incorporated into a program relating solute on adsorbent, η, to dimensionless time, τ, and solute in the effluent, ξ, to dimensionless time, τ. Since monitoring the solute in the effluent was the particular aim of this study; the Fortran program, developed for this system, was adapted to print out the dimensionless solute concentration in effluent, $C_t/C_0 = \xi$, against the volume of effluent treated, V. A graphical output of this information was obtained by incorporating pseudo-plotting facilities into the program.

The mathematical equations leading to the solution are presented in the Appendices.

DISCUSSION AND RESULTS

Adsorption Isotherm

Two general theoretical equilibrium isotherms for the adsorption of solutes on adsorbent are shown in Figure 1. The isotherms follow Langmuir type plots forming a monolayer at $C_e = 200\ \mathrm{mg\ dm^{-3}}$. The analysis of the equilibrium data are given by the following equations, although for any system (using the model presented in this paper) only the monolayer capacity value is required.

$$\left.\begin{aligned} q_e &= \frac{20\, C_e}{1 + 0.10\, C_e} \quad \text{(A)} \\ q_e &= \frac{0.5\, C_e}{1 + 0.016\, C_e} \quad \text{(B)} \end{aligned}\right\} \tag{20}$$

It was assumed in the model that the solute concentration in the adsorbent is independent of that in water, that is, the adsorption is completely irreversible. Consequently, the equilibrium concentration $q_{e,\infty}$ is constant for an irreversible system and can be replaced by a hypothetical equilibrium concentration $q_e^h = \mathrm{const}$, corresponding to the equilibrium monolayer adsorption capacity. In the two isotherms in Figure 1, the assumption of irreversibility is valid for systems in which $C_e > 200\ \mathrm{mg\ dm^{-3}}$, that is, the operating line for the system terminates on the monolayer.

Spahn and Schlunder[35] found that this hypothetical equilibrium capacity did not give the best fit between experimental and theoretical data and a modification was made to the program. In fact they[35] were unable to use q_e^h to fit experimental and theoretical data for $C_h > 1$ and selected a value of $0.5\, q_e^h$. The condition $C_h > 1$ corresponds to a system in which the final equilibrium solid phase concentration, $q_{e,\infty}$ is significantly lower than the equilibrium concentration $q_{e,\infty}$, corresponding to the initial liquid phase concentration, C_0. Furthermore, analysis of the experimental data, for operating lines not terminating on the isotherm monolayer, imposes a numerical procedure. Such an approach involves deriving gradients for curves tending towards a plateau which must inevitably result in some inaccuracy. Nevertheless the work of Spahn and Schlunder enables a constant effective diffusivity to be predited which describes the concentration–time profile in batch adsorbers over a wide range of adsorbate and adsorbent concentrations. However, in the present work the range of application was restricted, to enable the two previous problems, namely, limiting q_e^h to $q_{e,\infty}$ and the inaccuracy and time-dependence of graphical differentiation, to be eliminated. Under these conditions

$$C_{e,\infty} = f(q_{e,\infty}) \tag{21}$$

VOL. 62 1984

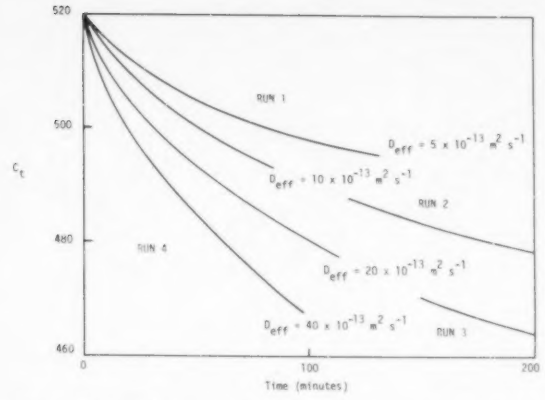


Figure 2. Effect of varying D_{eff} on concentration decay curves. ($k_f = 80 \times 10^{-8}$ m s^{-1}).

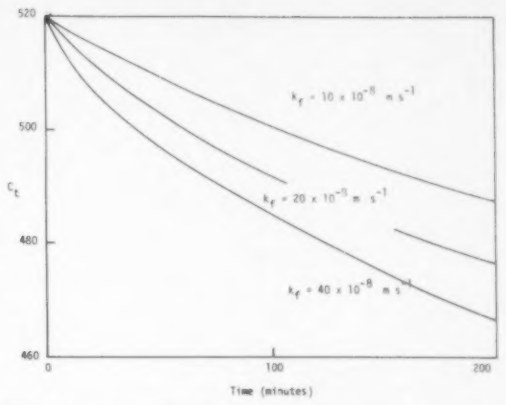


Figure 3. Effect of varying k_f on concentration decay curves. ($D_{eff} = 20 \times 10^{-13}$ m^2 s^{-1}).

Consequently, by assuming pseudo-irreversibility, such problems were overcome and a rapid analytical technique for predicting the behavior of batch adsorbers was established. The assumption of a pseudo-irreversible isotherm may be tested numerically using theoretical data. The results of run 9 have been determined numerically using equations (2)–(6) and the operating line has been plotted on Figure 1. Graphical differentiation of C_t gives dC_t/dt enabling $N(t)$ to be obtained, hence $q_{e,\infty}$ and $C_{e,\infty}$ values can be calculated at various constant time values, as plotted on Figure 1. A range of results from run 9 are shown on Figure 1 from $t = 5$ min to $t = 1440$ min, all confirming the assumption of a pseudo-irreversible isotherm is reasonable to within 2.5% and covers over 95% of the adsorption process, i.e. $C_{e,\infty} = C_{e,h}$.

Batch Adsorption Studies

The effect of initial solute concentration and adsorbent mass were considered and theoretical correlations were obtained analytically using a Fortran progam. The input to the program was the following eight parameters; initial solute concentration, adsorbent mass, adsorbent particle diameter, adsorbent voidage, adsorbent density, external mass transfer coefficient, effective diffusivity and a capacity factor based on the monolayer saturation capacity, $q_{e,h}$.

The effect of varying certain design parameters for the batch adsorber systems is now made.

Concentration–Time Curves

The analytical solution to the problem of solute adsorption onto an adsorbent can be investigated by generating theoretical results. Equation (18) has been used to generate concentration decay curves for different D_{eff} and different β_L values. Figure 2 shows the influence of varying the effective diffusivity while maintaining β_L constant and the initial solute concentration constant at 520 mg dm^{-3}. Figure 3 shows the influence of varying the film mass transfer coefficient while the effective diffusivity is maintained constant. Further details of the parameters used in the Figures are given in Table 2.

The technique of iterating between D_{eff} and β_L values may be adopted using a Fortran program to generate concentration–time curves for a wide range of experimental conditions. It should thus be possible to fix a single effective diffusion coefficient, and a single film mass transfer coefficient, which fit all experimental results with reasonable accuracy for adsorption processes based on pore diffusion and external mass transfer. Figures 4 and 5 show the effects of varying: the initial solute concentration and the mass of adsorbent. Figure 4 is based on isotherm B and Figure 5 using a monolayer capacity of 200 mg g^{-1} on isotherm A and the other relevant parameters are presented in Table 2.

Table 2. Design variables for batch adsorber studies

Run	C_0 (mg dm^{-3})	d_p (10^{-3} m)	$q_{e,h}$ (mg g^{-1})	C_h	S (g)	V (dm^3)	k_f (10^{-8} m s^{-1})	D_{eff} (10^{-13} m^2 s^{-1})
1	520	0.605	25	0.481	17	1.7	80	5.0
2	520	0.605	25	0.481	17	1.7	80	10
3	520	0.605	25	0.481	17	1.7	80	20
4	520	0.605	25	0.481	17	1.7	80	40
5	520	0.605	25	0.481	17	1.7	10	20
6	520	0.605	25	0.481	17	1.7	20	20
7	520	0.605	25	0.481	17	1.7	40	20
8	450	0.605	25	0.553	17	1.7	80	20
9	410	0.605	25	0.610	17	1.7	80	20
10	500	0.605	200	0.400	17	1.7	100	2.0×10^3
11	500	0.605	200	0.300	12.7	1.7	100	2.0×10^3
12	500	0.605	200	0.200	8.5	1.7	100	2.0×10^3
13	500	0.605	200	0.100	4.25	1.7	100	2.0×10^3

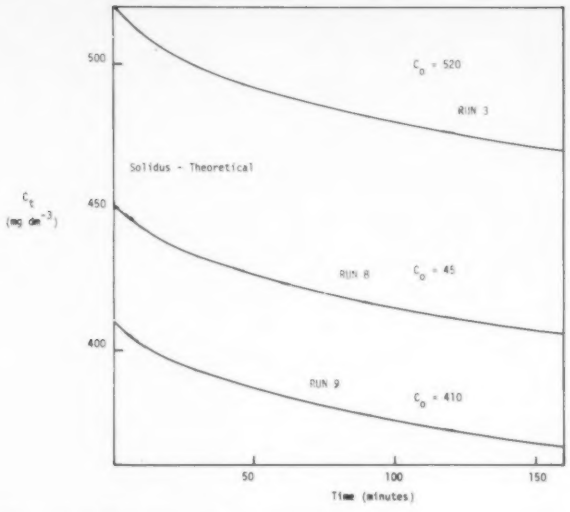


Figure 4. Effect of initial dye concentration.

Internal Mass Transfer

Using the results and the pseudo-irreversibility assumption C_t, q_t, $C_{e,h}$ and $q_{e,h}$ are all known at any time, t, and thus using equations (2) and (3) the internal mass transfer coefficients can be computed. The effect of C_0 and adsorbent mass on the time-dependent β_s values are readily obtained.

In the case of homogeneous solid phase diffusion β_s is proportional to the square root of the adsorption time. However, in the present system, for the adsorption of the solute on adsorbent at long contact times, the β_s values do not follow the ordinary diffusion laws for homogeneous particles.

An attempt was made previously[57-59] to define an intraparticle diffusion parameter which was dependent on the square root of time for the adsorption of Astrazone Blue on silica. The model met with only limited success for although a 'square root of time' dependence was observed it was only over a short time period. Furthermore, the internal mass transfer coefficient appears to be a time-dependent function of initial solute concentration and solid/liquid ratio. Consequently, if this effect is observed in the experimental

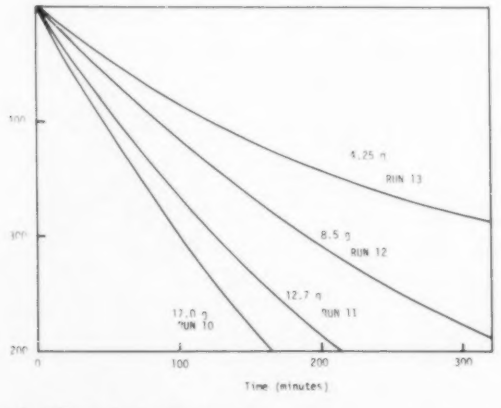


Figure 5. Effect of adsorbent mass.

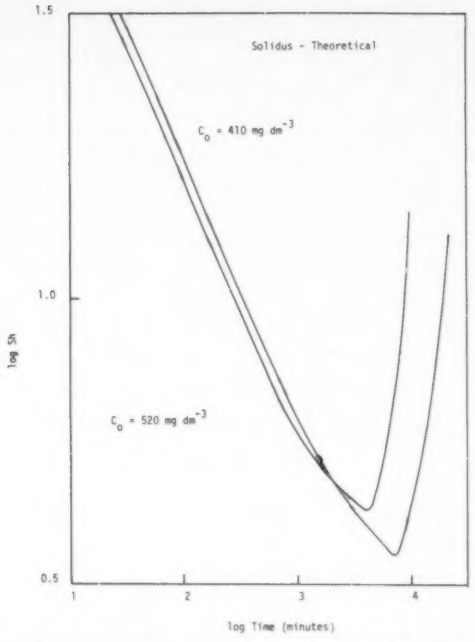


Figure 6. Log Sherwood number against log time for different initial dye concentrations.

results, a homogeneous solid phase diffusion model is not applicable to this system, and it would appear therefore that for much of the adsorption process, the solute is transferred within the liquid filled pores of the particle by molecular diffusion.

The internal mass transfer coefficients, $\beta_s(t)$, for Runs 3 and 9 are presented in Figure 6 in the form of Sherwood numbers. Towards the ends of the adsorption runs $\beta_s(t)$ tends to infinity for the conditions selected in this study due to the high initial solute concentrations.

The theoretical and experimental internal mass transfer coefficients may be compared in the form of a modified Sherwood number, Sh^*, which may be obtained from equations (3) and (4).

$$Sh^* = \frac{1}{3(1-\eta)} \frac{d\eta}{d\tau} \tag{22}$$

Equation (22) enables experimental Sherwood numbers to be obtained while equation (18) enables theoretical values to be predicted. By applying experimental constraints to equation (18) it is possible to predict theoretical limiting values for the model.

Consider the following

$$C_h < 1, \quad \text{then as} \quad \eta \to 1, Sh^* \to \infty$$

and

$$C_h > 1, \quad \text{then as} \quad \eta \to 1, Sh^* \to 0$$

The results apply to the case where $C_h < 1$ and at long times $\eta \to 1$. The $\beta_s(t)$ and Sh^* values in Figure 6 are tending to infinity as predicted by the model. None of the data are related to the second group of limiting values since all conditions were selected so that the operating lines terminated on the monolayer, resulting in $C_h < 1$, and thus the assumptions in the model were not invalidated.

VOL. 62 1984

Table 3. Fixed bed column operating conditions

Run	C_0 (mg dm^{-3})	d_p (10^{-3} m)	q_e^* (10^{-3} g g^{-1})	F (cm^3 s^{-1})	Z (m)	D_{eff} (m^2 s^{-1})	D_{mol} (m^2 s^{-1})
14	500	0.605	200	2.0	0.25	10×10^{-10}	5×10^{-10}
15	500	0.605	200	2.0	0.25	20×10^{-11}	5×10^{-10}
16	500	0.605	200	2.0	0.25	20×10^{-12}	5×10^{-10}
17	500	0.605	200	2.0	0.25	20×10^{-13}	5×10^{-10}
18	500	0.605	200	2.0	0.30	20×10^{-11}	5×10^{-10}
19	500	0.605	200	2.0	0.20	20×10^{-11}	5×10^{-10}
20	500	0.605	200	2.0	0.20	20×10^{-11}	5×10^{-10}
21	500	0.605	200	2.0	0.20	20×10^{-11}	5×10^{-10}
22	500	0.605	200	1.0	0.20	20×10^{-11}	5×10^{-10}
23	500	0.605	200	2.0	0.20	20×10^{-11}	5×10^{-10}
24	500	0.605	200	3.0	0.20	20×10^{-11}	5×10^{-10}

Column Studies

Since a pore diffusivity of 20×10^{-13} m^2 s^{-1} was adopted in the batch studies, this value will also be used throughout the majority of the column work. The data used in the program are given in Table 3 and the molecular diffusion coefficient of the solute in solution, D_{mol}, may be determined using the Wilke–Chang[63] correlation. In this work a value of 20×10^{-13} m^2 s^{-1} has been assumed. A review of molecular diffusion coefficients has been undertaken by Skelland[64] and this indicates an average error in the Wilke–Chang correlation, shown by equation (23), of 10%.

$$D_{mol} = 7.4 \times 10^{-8} \frac{TM^{0.5}}{\mu V_m^{0.6}} \tag{23}$$

Effective diffusivities may be either smaller or larger than molecular diffusivities; the latter case has been demonstrated experimentally.[40,41] The value of the mass transfer coefficient, β_c, in the liquid phase in the column is essential in the analysis of the measured values and this coefficient was computed using a correlation, for mass transfer in packed beds at low particle Reynolds numbers, 0.5 to 900, proposed by Carberry[65] and Kataoka et al.[66]

$$\beta_c = 1.15 \frac{D_{mol}}{d_p} \left(\frac{d_p \rho u_0}{\nu} \right)^{1/2} \left(\frac{\nu}{D_{mol}} \right)^{1/3} \tag{24}$$

The mathematical model based on the equations presented in this paper enabled a program to be developed. The parameters relevant to the model were abstracted from isotherm A and used to determine the capacity factor in equation (15). For an initial dye concentration of 0.5 kg m^{-3} the equilibrium capacity should be constant at 200×10^{-3} kg kg^{-1}.

However, the solution to the fixed bed model is analytical over the whole isotherm range and therefore may be applied to lower initial solute concentrations which correspond to a solid phase solute concentration, q_e. Consequently providing that the diffusion coefficient is constant over the whole isotherm range, the capacity factor may be re-defined as

$$C_h = \frac{Sq_e}{VC_0} \tag{25}$$

where q_e has replaced q_e^h.

The effect of varying effective diffusivity on the system is shown in Figure 7. The data used are given in Table 3 and four values of D_{eff} were used. The influence of D_{eff} on the shape and capacity of the breakthrough curve can be observed.

The influence of bed height is shown in Figure 8, the data are related to Table 3, Run 14. Breakthrough curves at six bed heights are shown.

Two other variables which affect the design of fixed bed absorbers are solution flowrate and initial solute concentration. The effect of flowrate is shown in Figure 9 and the influence of initial solute concentration is shown in Figure 10.

Careful consideration of Figure 8 indicates that even at low adsorbent bed heights theoretical breakthrough curves can be predicted. Certain of the curves illustrated show that the stable breakthrough curves have not yet been established and the data are in the transitional region. This effect highlights a major advantage of this particular model which is developed mathematically from two components (i) the transition region and (ii) the constant pattern region.

In order to evaluate equation (14), a partial solution, (developed by van Meel[67] for the drying of porous solids), is employed with the appropriate initial boundary conditions

$$\frac{\partial \eta(\zeta, 0)}{\partial \zeta} = 0 \tag{26}$$

and as demonstrated in Appendix B this yields the general solution:

$$I_1 = \int_\eta \frac{\partial \eta}{\eta f(\eta)} = -\int_\zeta \partial \zeta \tag{27}$$

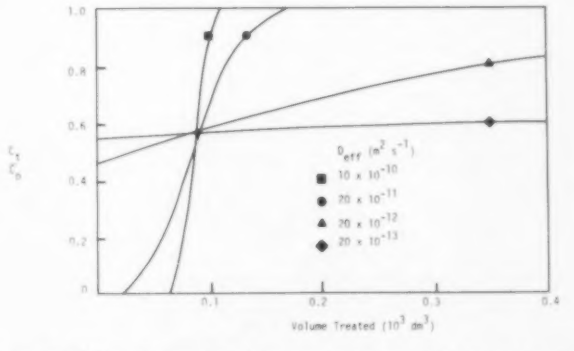


Figure 7. Effect of pore diffusivity on the shape of the breakthrough curves (Runs 14–17).

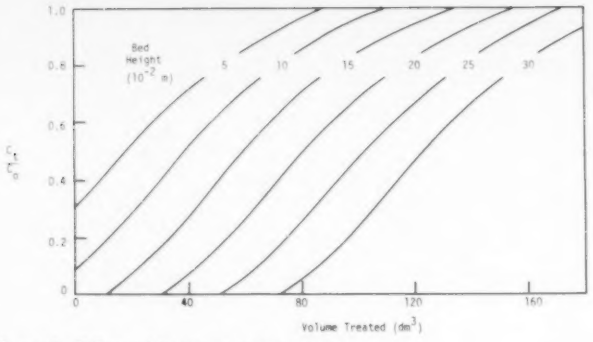


Figure 8. Effect of bed height (Run 518).

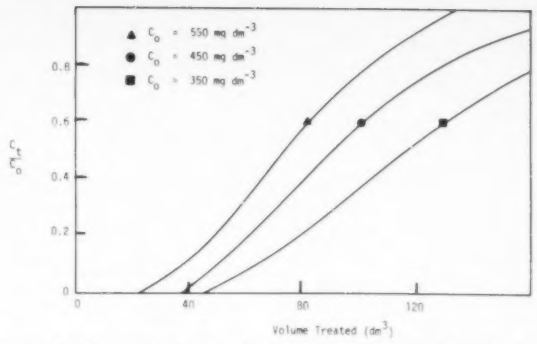


Figure 10. Effect of initial solute concentration using a fixed bed height of 0.20 m (Runs 19–21).

To compute these integrals, it is necessary to divide the whole integration up into the two regions, namely, transition and constant pattern. The first section, represents that part of the adsorption bed it is necessary to saturate until a stable breakthrough curve is established. The two regions are separated by a time τ_1 which is reached when the first adsorbent layer $\zeta = 0$, at the adsorber extrance is saturated, thus

$$\eta(\zeta = 0, \tau > \tau_1) = 1. \tag{28}$$

The solution to this equation presented in Appendix B is based on the column model developed by Spahn and Schlunder[35] but using the kinetic data obtained from the batch model developed earlier in this paper. In the constant pattern region the following equation holds:

$$\int_1^{\xi} \frac{\partial \xi}{\xi} = \int_1^{\eta} \frac{\partial \eta}{\eta} \tag{29}$$

yielding:

$$\xi(\zeta, \tau) = \eta(\zeta, \tau) \tag{30}$$

Equation (30) is the continuity equation for the constant pattern region[68] which is developed after time τ_1. The solution to this equation is presented in Appendix B.

The solutions to equations (28) and (30) enable theoretical liquid and solid phase dye concentrations to be predicted at various times. The success of both equations is demonstrated in Figures 7–10.

CONCLUSION

A model based on the unreacted core theory has been developed to predict the performance of batch and fixed bed adsorbers. The model is based on external mass transfer and pore diffusion and, providing the assumption of a pseudo-irreversible isotherm is assumed, a rapid analytical solution, to predict the concentration decay curve in batch adsorbers, is available. This procedure enables an effective pore diffusion coefficient for the particular system to be obtained which may be utilised in the fixed bed model. The column model offers an analytical solution for predicting breakthrough curves for a range of solute concentrations over the whole isotherm range.

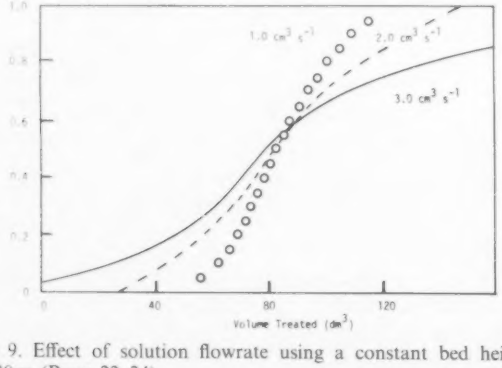


Figure 9. Effect of solution flowrate using a constant bed height. $z = 0.20$ m (Runs 22–24).

APPENDIX A

Application of the Fundamental Kinetic Equation to Calculate the Extent of Adsorption with Respect to Time for Batch Adsorbers

The adsorption rate equation developed for a single particle is obtained using equation (18) in the paper. By defining $x = (1 - \eta)^{1/3}$ and $B = 1 - 1/Bi$ as in equations (10) and (9) so that

$$\eta = 1 - x^3 \tag{A1}$$

then equation (18) becomes

$$-3x^2 \frac{dx}{d\tau} = \frac{3[1 - C_h(1 - x^3)]x}{1 - Bx}. \tag{A2}$$

Rearranging;

$$d\tau = -\frac{x(1 - Bx)}{1 - C_h(1 - x^3)}\,dx$$

$$= \frac{Bx^2 - x}{C_h[(1 - C_h)/C_h + x^3]}\,dx \tag{A3}$$

Defining $a^3 = (1 - C_h)/C_h$ as in equation (11), then

$$d\tau = \frac{1}{C_h}\frac{Bx^2 - x}{x^3 + a^3}\,dx \tag{A4}$$

To obtain the integral J_1 of (A4),

$$J_1 = \int d\tau = \frac{1}{C_h}\int \frac{Bx^2 - x}{x^3 + a^3}\,dx$$

$$= \frac{B}{C_h}\int \frac{x^2\,dx}{x^3 + a^3} - \frac{1}{C_h}\int \frac{x\,dx}{x^3 + a^3}$$

$$= \frac{B}{3C_h}\ln|x^3 + a^3| - \frac{1}{C_h}\int \frac{x\,dx}{x^3 + a^3}. \tag{A5}$$

Which can be written:

$$J_1 = \frac{B}{3C_h}\ln|x^3 + a^3| + J_2 \tag{A6}$$

VOL. 62 1984

To evaluate the integral J_2 it is first necessary to express the term $x^3 + a^3$ in partial fractions.

$$\frac{1}{x^3+a^3} = \frac{1}{(x+a)(x^2-ax+a^2)}$$

$$= \frac{A}{x+a} + \frac{Fx-G}{x^2-ax+a^2} \quad \text{(A7)}$$

$$1 = A(x^2-ax+a^2) + (Fx+G)(x+a) \quad \text{(A8)}$$

Hence,

$$A + F = 0$$

$$-Aa + aF + G = 0$$

$$a^2A + aG = 1$$

and

$$A = \frac{1}{3a^2}, F = -\frac{1}{3a^2}, G = \frac{2}{3a}$$

Substitution of these relationships into (A7) gives

$$\frac{1}{x^3+a^3} = \frac{1}{3a^2(x+a)} + \frac{2a-x}{3a^2(x^2-ax+a^2)} \quad \text{(A9)}$$

Thus

$$J_2 = -\frac{1}{C_h}\int \frac{x\,dx}{3a^2(x+a)} - \frac{1}{C_h}\int \frac{(2a-x)x\,dx}{3a^2(x^2-ax+a^2)}$$

$$= \frac{1}{3a^2C_h}\int \frac{x\,dx}{x+a} + \frac{1}{3a^2C_h}\int \frac{x^2-2ax}{x^2-ax+a^2}\,dx$$

$$= -\frac{1}{3a^2C_h}\left(\int dx - \int \frac{a\,dx}{x+a}\right)$$

$$+ \frac{1}{3a^2C_h}\left(\int \frac{x^2-ax+a^2}{x^2-ax+a^2}\,dx\right.$$

$$\left. - \int \frac{ax+a^2}{x^2-ax+a^2}\,dx\right) \quad \text{(A10)}$$

$$= -\frac{1}{3a^2C_h}\left(\int dx - a\ln|x+a| - \int dx\right.$$

$$\left. + \int \frac{ax+a^2}{x^2-ax+a^2}\,dx\right)$$

$$= \frac{1}{3aC_h}\ln|x+a| - \frac{1}{3aC_h}\int \frac{(x+a)\,dx}{x^2-ax+a^2}. \quad \text{(A11)}$$

Then (A6) can be written:

$$J_1 = \frac{B}{3C_h}\ln|x^3+a^3| + \frac{1}{3aC_h}\ln|x+a| + J_3 \quad \text{(A12)}$$

where

$$J_3 = -\frac{1}{6aC_h}\left(\int \frac{(2x-a)\,dx}{x^2-ax+a^2} + \int \frac{3a\,dx}{x^2-ax+a^2}\right)$$

$$= -\frac{1}{6aC_h}\ln|x^2-ax+a^2|$$

$$-\frac{1}{2C_h}\left(\int \frac{dx}{(x-a/2)^2+(\sqrt{3}a/2)^2}\right)$$

$$= -\frac{1}{6aC_h}\ln|x^2-ax+a^2|$$

$$-\frac{1}{2C_h}\left(\frac{1}{\sqrt{3}a/2}\right)\tan^{-1}\left(\frac{x-a/2}{\sqrt{3}a/2}\right)$$

$$= -\frac{1}{6aC_h}\ln|x^2-ax+a^2|$$

$$-\frac{1}{aC_h\sqrt{3}}\tan^{-1}\left(\frac{2x-a}{a\sqrt{3}}\right) \quad \text{(A13)}$$

Now substitution of (A13) into (A12) gives

$$J_1 = \frac{B}{3C_h}\ln|x^3+a^3| + \frac{1}{3aC_h}\ln|x+a|$$

$$-\frac{1}{6aC_h}\ln|x^2-ax+a^2| - \frac{1}{aC_h\sqrt{3}}\tan^{-1}\left(\frac{2x-a}{a\sqrt{3}}\right)$$

$$= \frac{1}{6C_h}[\ln(|x^3+a^3|^{2B}) + \ln(|x+a|^{2/a})$$

$$- \ln(|x^2-ax+a^2|^{1/a})]$$

$$= \frac{1}{6C_h}[\ln(|x^3+a^3|^{2B-1/a} + \ln(|x+a|^{3/a})]$$

$$-\frac{1}{aC_h\sqrt{3}}\tan^{-1}\left(\frac{2x-a}{a\sqrt{3}}\right) \quad \text{(A14)}$$

The limits over which the integral in (A14) is to be are: when

$$\tau = 0, \eta = 0 \text{ and } x - 1$$

$$\tau = \tau, \eta = \eta \text{ and } x = x.$$

Thus (A14) becomes

$$[\tau]_0^\tau = \left[\frac{1}{6C_h}\{\ln(|x^3+a^3|^{2B-1/a}) + \ln(|x+a|^{3/a})\}\right.$$

$$\left. -\frac{1}{aC_h\sqrt{3}}\tan^{-1}\left(\frac{2x-a}{a\sqrt{3}}\right)\right]_1^x. \quad \text{(A15)}$$

Hence,

$$\tau = \frac{1}{6C_h}\left[\ln(|x^3+a^3|^{2B-1/a}) + \ln(|x+a|^{3/a})\right.$$

$$\left. -\frac{1}{aC_h\sqrt{3}}\tan^{-1}\left(\frac{2x-a}{a\sqrt{3}}\right)\right]$$

$$-\left[\frac{1}{6C_h}\{\ln(|1+a^3|^{2B-1/a}) + \ln(|1+a|^{3/a})\}\right.$$

$$\left. -\frac{1}{aC_h\sqrt{3}}\tan^{-1}\left(\frac{2-a}{a\sqrt{3}}\right)\right] \quad \text{(A16)}$$

which reduces to equation (8) in the text.

APPENDIX B

Application of Pore Diffusion Model to the Fixed Bed Column Results

It is the object of this investigation, based on the fundamental kinetic law developed from equation (12), to predict the concentration distribution in both fluid and solid phase in fixed beds and to compare predicted with experimental results.

A combination of the fundamental kinetic equation (12), with the differential mass balance in the column, equation (13), yields a differential equation for the prediction of the local and time-dependent concentration history in the solid phase, equation (14).

A partial solution of this equation is known from the non-stationary drying of porous solids[67] in the form

$$\frac{1}{f(\eta)}\frac{\partial(\eta)}{\partial\zeta}+\eta=P(\zeta) \tag{B1}$$

with the initial condition

$$\eta(\zeta,0)=0 \tag{B2}$$

equation (26), $\partial\eta(\zeta,0)/\partial\zeta=0$, follows and equation (B1) becomes

$$\frac{1}{f(\eta)}\frac{\partial\eta}{\partial\zeta}+\eta=0. \tag{B3}$$

Integration of equation (B3) yields the general solution, equation (27). For computation of these integrals it is convenient to divide the whole integration region into two sections, separated by a time τ_1. The solution of the integral, I_1, on the LHS of equation (27) is shown in Appendix C and the general result is

$$I_1=\int_\eta\frac{\partial\eta}{\eta f(\eta)}=-\frac{1}{6}\ln\frac{\eta^{2B}[(1-\eta)^{2/3}+(1-\eta)^{1/3}+1]}{[1-(1-\eta)^{1/3}]^2}+\frac{1}{\sqrt{3}}\tan^{-1}\frac{2(1-\eta)^{1/3}+1}{\sqrt{3}} \tag{B4}$$

where $B=1-1/Bi$.

The lower limits of the integral in (B4) will be: in section 1 ($0\leqslant\tau\leqslant\tau_1$):

$$\eta=\eta(0,\tau)\quad\text{and}\quad\zeta=0 \tag{B5a}$$

in section 2 ($\tau\geqslant\tau_1$):

$$\eta=1\quad\text{and}\quad\zeta=\zeta_1 \tag{B5b}$$

The concentration at the adsorber entrance $\eta(0,\tau)$ follows from equation (18), considering that $\xi(\zeta=0,\tau)$ is always unity:

$$\int_0^{\eta(0,\tau)}\frac{\partial\eta(0,\tau)}{3[1-\eta(0,\tau)]^{1/3}}-\int_0^{\eta(0,\tau)}\frac{B}{3}\partial\eta(0,\tau)=\tau \tag{B6}$$

or

$$\tfrac{1}{2}[1-\{1-\eta(0,\tau)\}^{1/3}]^2-\tfrac{1}{3}B\eta(0,\tau)=\tau \tag{B7}$$

τ_1 follows immediately from (B7) because $\eta(0,\tau)=1$ for $\tau\geqslant\tau_1$:

$$\tau_1=\tfrac{1}{2}-\tfrac{1}{3}B \tag{B8}$$

For the explicit solution for (B7) with respect to $\eta(0,\tau)$, a cubic equation has to be solved to obtain

$$\eta(0,\tau)=1-B^{-3}[\tfrac{1}{2}+\cos\{\tfrac{1}{3}\pi+\tfrac{1}{3}\cos^{-1}\{12B^2(\tau_1-\tau)-1\}\}]^3 \tag{B9}$$

In section 2, ζ_1 is required, which is computable by integration of equation (27) with equation (18)

$$\zeta_1=\tau-\tau_1. \tag{B10}$$

With the known integration limits of equation (27) the concentration distribution in the solid phase is obtained

$$\zeta=g_1(\eta)-g_{2,i}(\tau),\quad i=1,2 \tag{B11}$$

with

$$g_1(\eta)=\frac{1}{6}\ln\frac{(1-C_1^3)^{2B}(C_1^2+C_1+1)}{(1-C_1)^2}-\frac{1}{\sqrt{3}}\tan^{-1}\frac{2C_1+1}{\sqrt{3}} \tag{B12}$$

where

$$C_1=(1-\eta)^{1/3}$$

In section 1 ($0\leqslant\tau\leqslant\tau_1$):

$$g_{2,1}(\tau)=\frac{1}{6}\ln\frac{(1-C_0^3)^{2B}(C_0^2+C_0+1)}{(1-C_0)^2}-\frac{1}{\sqrt{3}}\tan^{-1}\frac{2C_0+1}{\sqrt{3}} \tag{B13}$$

where $C_0=[1-\eta(0,\tau)]^{1/3}$, and in section 2($\tau\geqslant\tau_1$):

$$g_{22}(\tau)=\tau_1-\tau-(\pi/18)\sqrt{3} \tag{B14}$$

The concentration distribution in the liquid phase follows from equations (18) and (B3)

$$\frac{1}{\xi}\frac{\partial\eta}{\partial\tau}+\frac{1}{\eta}\frac{\partial\tau}{\partial\tau}=0 \tag{B15}$$

In section 1 the limits are

$$\int_1^\xi\frac{\partial\xi}{\xi}=\int_{\eta(0,\tau)}^\eta\frac{\partial\eta}{\eta} \tag{B16}$$

whence

$$\xi(\xi,\tau)=\frac{\eta(\zeta,\tau)}{\eta(0,\tau)} \tag{B17}$$

In section 2 equation (29), yielding equation (30).

The detailed equations for the prediction of the concentration distribution in the liquid phase are then:

For section 1:

$$\tau=h_{11}(\xi,\tau)-h_{21}(\tau) \tag{B18}$$

with

$$h_{11}(\xi,\tau)=\frac{1}{6}\ln\frac{(1-C_2)^{2B}(C_2+C_1+1)}{(1-C_2)^2}-\frac{1}{\sqrt{3}}\tan^{-1}\frac{2x_2+1}{\sqrt{3}} \tag{B19}$$

where

$$x_2=[1-\eta(0,\tau)]^{1/3}$$

and

$$h_{21}(\tau)=\frac{1}{6}\ln\frac{(1-C_0^3)^{2B}(C_0^2+C_0+1)}{(1-C_0)^2}-\frac{1}{\sqrt{3}}\tan^{-1}\frac{2C_0+1}{\sqrt{3}} \tag{B20}$$

where $C_0=[1-\eta(0,\tau)]^{1/3}$.

VOL. 62 1984

For section 2:

$$\zeta = h_{12}(\xi) - h_{22}(\tau) \tag{B21}$$

with

$$h_{12}(\xi) = \frac{1}{6}\ln\frac{(1-C_2^3)^{2B}(C_2^2+C_2+1)}{(1-C_2)^2} - \frac{1}{\sqrt{3}}\tan^{-1}\frac{2C_2+1}{\sqrt{3}} \tag{B22}$$

where

$$h_{22}(\tau) = \tau_1 - \tau - (\pi/18)\sqrt{3} \tag{B23}$$

and $C_2 = (1-\xi)^{1/3}$.

For $\tau \to 0$ there exists a limiting value computable from the expansion as a power series of

$$C_2 = (1-\eta_0\xi)^{1/3} = 1 - \tfrac{1}{3}\eta_0\xi - \tfrac{1}{9}\eta_0^2\xi^2 - \ldots \tag{B24}$$

where $\eta_0 = \eta(0, \tau)$

$$\lim_{\tau\to 0}\xi = \exp(-3Bi\tau) \tag{B25}$$

The value of the mass transfer coefficient B_L in the liquid is essential in the analysis of the measured values. This coefficient is computed using correlations for the mass transfer in packed beds at low Reynolds numbers[69]. The characteristic parameter, the mass transfer Biot number is then obtained from $Bi = B_L R/D_{eff}$, where the value for the effective diffusion coefficient was adapted to give the theoretical fit.

APPENDIX C

Application of the Fundamental Kinetic Equation to Calculate the Concentration Distribution in Adsorbent Columns

Equation (27) with

$$f(\eta) = \frac{3(1-\eta)^{1/3}}{1-(1-1/Bi)(1-\eta)^{1/3}} \tag{C1}$$

gives

$$I_1 = \int_\eta \frac{1-(1-1/Bi)(1-\eta)^{1/3}}{3\eta(1-\eta)^{1/3}}\,d\eta \tag{C2}$$

let $B = (1-1/Bi)$, therefore substituting B in equation (C2) and rearranging

$$I_1 = -\int_\eta \frac{B}{3}\frac{d\eta}{\eta} + \int_\eta \frac{d\eta}{3\eta(1-\eta)^{1/3}} \tag{C3}$$

hence

$$I_1 = -\frac{1}{3}\ln\eta^B + \frac{1}{3}\int_\eta \frac{d\eta}{\eta(1-\eta)^{1/3}}. \tag{C4}$$

Calling the integral on the RHS of (C4) I_2, and with $x = (1-\eta)^{1/3}$, so that $\eta = 1-x^3$ and $d\eta = -3x^2\,dx$, gives

$$\begin{aligned} I_2 &= -\int_{1-x^3}\frac{x\,dx}{1-x^3} \\ &= -\int_{1-x^3}\frac{x\,dx}{(1-x)(x^2+x+1)} \\ &= -\frac{1}{3}\int_{1-x^3}\frac{x\,dx}{1-x} - \frac{1}{3}\int_{1-x^3}\frac{x(x+2)\,dx}{x^2+x+1} \end{aligned} \tag{C5}$$

$$I_2 = I_3 + I_4. \tag{C6}$$

Rearranging I_3 and integrating

$$\begin{aligned} I_3 &= \frac{x}{3} - \frac{1}{3}\int\frac{dx}{1-x} \\ &= \frac{x}{3} + \frac{1}{3}\ln(1-x). \end{aligned} \tag{C7}$$

Rearranging I_4 and integrating

$$\begin{aligned} I_4 &= -\frac{x}{3} - \frac{1}{3}\int\frac{x-1}{x^2+x+1}\,dx \\ &= -\frac{x}{3} - \frac{1}{6}\int\frac{2x+1}{x^2+x+1}\,dx \\ &\quad -\frac{1}{6}\int\frac{-3\,dx}{(x+1/2)^2+(\sqrt{3}/2)^2} \\ &= -\frac{x}{3} - \frac{1}{6}\ln(x^2+x+1) + \frac{1}{\sqrt{3}}\tan^{-1}\left(\frac{2x+1}{\sqrt{3}}\right). \end{aligned} \tag{C8}$$

Adding (C7) and (C8) as in (C6):

$$\begin{aligned} I_2 &= \frac{1}{3}\ln(1-x) - \frac{1}{6}\ln(x^2+x+1) \\ &\quad + \frac{1}{\sqrt{3}}\tan^{-1}\left(\frac{2x+1}{\sqrt{3}}\right) \\ &= -\frac{1}{6}\ln\left(\frac{x^2+x+1}{(1-x)^2}\right) + \frac{1}{\sqrt{3}}\tan^{-1}\left(\frac{2x+1}{\sqrt{3}}\right). \end{aligned} \tag{C9}$$

Substituting this in (C4):

$$\begin{aligned} I_1 &= -\frac{1}{3}\ln\eta^B + \frac{1}{\sqrt{3}}\tan^{-1}\left(\frac{2x+1}{\sqrt{3}}\right) \\ &\quad -\frac{1}{6}\ln\left(\frac{x^2+x+1}{(1-x)^2}\right) \\ &= -\frac{1}{6}\ln\left(\eta^{2B}\frac{x^2+x+1}{(1-x)^2}\right) + \frac{1}{\sqrt{3}}\tan^{-1}\left(\frac{2x+1}{\sqrt{3}}\right). \end{aligned} \tag{C10}$$

Finally substituting for $x = (1-\eta)^{1/3}$ gives equation (B4), as required.

SYMBOLS USED

A	surface area of adsorbent particle (m^2)
a	simplifying term used in equation (8) $= [(1-C_h)/C_h]^{1/3}$
B	simplifying term used in equation (8) $= (1-1/Bi)$
Bi	Biot number $= \beta_L R/D_{eff}$
C	concentration of solute in solution ($kg\,m^{-3}$, $mg\,dm^{-3}$)
C_e	concentration of solute in solution at equilibrium ($kg\,m^{-3}$, $mg\,dm^{-3}$)
C_h	capacity factor $= Sq_e^h/VC_0$
C_0	initial concentration of solute solution ($kg\,m^{-3}$, $mg\,dm^{-3}$)
C_t	concentration of solute in solution at time, t ($kg\,m^{-3}$, $mg\,dm^{-3}$)
D_{eff}	effective diffusivity ($m^2\,s^{-1}$)
D_{mol}	molecular diffusivity ($m^3\,s^{-1}$)
d_p	diameter of adsorbent particle (m)
F	flow rate ($m^3\,s^{-1}$)
K	Freundlich constant
M	molecular weight of solute
N	mass transfer rate ($kg\,s^{-1}$)
n	Freundlich exponent
q	concentration of solute on adsorbent ($kg\,kg^{-1}$)
$\bar{q}$	mean concentration of solute on adsorbent ($kg\,kg^{-1}$)

q_e concentration of solute on adsorbent at equilibrium (kg kg^{-1})
q_e^h hypothetical concentration of solute on adsorbent at equilibrium (kg kg^{-1})
R radius of adsorbent particle
S mass of adsorbent (kg)
Sh^* modified Sherwood number $= \dfrac{\beta_s R}{D_{eff}} \dfrac{\rho q_e^h}{C_0}$
T temperature (°C, K)
t time (s)
u_0 solute solution velocity (m s^{-1})
V solute volume (m^3)
V_m molecular volume
x simplifying term used in equation (8) $= (1-\eta)^{1/3}$
Z bed height (m)

Greek symbols

β mass transfer coefficient
β_c external mass transfer coefficient for fixed beds defined by equation (23) (m s^{-1})
β_L external mass transfer coefficient in agitated batch adsorber studies (m s^{-1})
β_s internal mass transfer coefficient (m s^1)
ζ dimensionless bedlength $= \dfrac{SD_{eff}}{F\rho_s R^21}$
μ dynamic viscosity
μ_K kinetic factor
ν kinematic viscosity
ξ dimenionless liquid phase concentration $= C_t/C_0$
ρ density
η dimensionless solid phase concentration $= q/q_e$
τ dimensionless time $= \dfrac{D_{eff}t}{R^2} \dfrac{C_0}{\rho_s q_e^*}$

Subscripts

e equilibrium
eff effective
L liquid
mol molecular
S solid
0 initial
h hypothetical
– mean condition
* graphical

REFERENCES

1. De Vault, D. J., 1943, *J Am Chem Soc*, 65: 532.
2. Gleuckauf, E., 1947, *J Chem Soc*, 1312.
3. Hougen, O. A. and Marshall, W. R., Jr, 1947, *Chem Eng Prog*, 43: 197.
4. Rosen, J. B., 1954, *Ind Eng Chem*, 46: 1590.
5. Thomas, H. C., 1951, *J Chem Phys*, 19: 1213.
6. Furnas, C. C., 1930, *Trans AIChE*, 24: 142.
7. Goldstein, S., 1953, *Pr R Soc (London)*, A219: 151.
8. Bohart, G. S. and Adams, E. Q., 1920, *J Chem Soc*, 42: 523.
9. Masamune, S. and Smith, J. M., 1965, *AIChEJ*, 11: (*a*) 34 and (*b*) 41.
10. Amundson, N. R., 1956, *Ind Eng Chem*, 48: 35.
11. Tien, C. and Thodos, G., 1961, *Chem. Eng Sci*, 13: 120.
12. Masamune, S. and Smith J. M., 1964, *Ind Eng Chem Fundl*, 3: 179.
13. Kasten, P. R., Lapidus, L. and Amundsen, N. R., 1952, *J Phys Chem*, 56: 683.
14. Wicke, E., 1939, *Z Kolloid*, 86: 169, 295.
15. Rosen, J. B., 1952, *J Chem Phys*, 20: 387.
16. Colwell, C. J. and Dranoff, J. S., 1966, *AIChEJ*, 6: 460.
17. Di Giano, F. A. and Weber, W. J., Jr, 1972, *Pr Am Soc Civ E, J San Eng Div*, 98: 1021.
18. Tien, C. and Thodos, G., 1959, *AIChEJ*, 5: 373.
19. Weber, W. J., Jr and Morris, J. C., 1964, *Pr Am Soc Civ E, J San Eng Div*, 90: SA3, 79.
20. Crank, J. and Nicolson, P., 1947, *Pr Camb Phil Soc*, 43: 50.
21. Crank, J., *Mathematics of Diffusion*, 2nd edn, (Clarendon Press, Oxford).
22. Tien, C. and Thodos, G., 1965, *AIChEJ*, 11: 845.
23. Garg, D. R. and Ruthven, D. M., 1973, (*a*) *Chem Eng Sci*, 28: 799, (*b*) *AIChEJ*, 19: 852.
24. Wheeler, J. M. and Middleman, S., 1970, *Ind Eng Chem Fundl*, 9: 624.
25. Neretnieks, I., 1976, *Chem Eng Sci*, 31: 107.
26. Lee, R. G. and Weber, T. W., 1969, *Can J Chem Eng*, 47: 54.
27. Cooper, R. S., 1965, *Ind Eng Chem Fund*, 4; 308.
28. Gleuckauf, E., 1955, *Trans Faraday Soc*, 51:1540.
29. Vermeulen, T., 1958, *Separation by Adsorption Methods*, (Academic Press, New York), 2: 147.
30. Vermeulen, T., 1953, *Ind Eng Chem*, 45: 1664.
31. Hall, K. R., Eagleton, L. C., Acrivos, A. and Vermeulen, T., 1966, *Ind Eng Chem Fundl*, 5: 212.
32. Cooper, R. S. and Liberman, D. A., 1970, *Ind Eng Chem Fundl*, 9: 620.
33. Weber, T. W. and Chakravorti, R. K., 1974, *AIChEJ*, 20: 228.
34. Bischoff, K. B., 1969, *Ind Eng Chem Fundl*, 8: 665.
35. Spahn, H. and Schlunder, E. U., 1975, *Chem Eng Sci*, 30: 529.
36. Brauch, V. and Schlunder, E. U., 1975, *Chem Eng Sci*, 30: 539.
37. Millar, C. O. M. and Clump, C. W., 1970, *AIChEJ*, 16: 169.
38. Dryden, C. E. and Kay, W. B., 1954, *Ind Eng Chem*, 46: 2294.
39. Edeskuty, F. J. and Amundson, N. R., 1952, (*a*) *Ind Eng Chem*, 44: 1698, (*b*) *J Phys Colloid Chem*, 56: 148.
40. Weber, W. J., Jr and Rumer, R. R., 1965, *Water Resources Res*, 1: 361.
41. Furusawa, T. and Smith, J. M., 1973, *Ind Eng Chem Fundl*,12: 197.
42. Dedrick R. L. and Beckmann, R. B., 1967, *Chem Eng Prog Symp Ser*, 74(63): 68.
43. Collins, J. J., 1967, *Chem Eng Prog Symp Ser*, 63: 31.
44. Tien, C., 1960, *Can J. Chem Eng*, 38: 25.
45. Wilson, A. H., 1948, *Phil Mag*, 39: 48.
46. Kasten, P. R. and Amundson, N. R., 1952, *Ind Eng Chem*, 44: 1704.
47. Lapidus, L. and Amundson, N. R., 1952, *J Phys Chem*, 56: 984.
48. Svedberg, U. G., 1976, *Chem Eng Sci*, 31: 345.
49. Fleck, R. D., Kirwan, D. J. and Hall, K. R., 1973, *Ind Eng Chem Fundl*, 12: 95.
50. Liapis, A. I. and Rippin, D. W. T., 1977, *Chem Eng Sci*, 32: 619.
51. Liapis, A. I. and Rippin, D. W. T., 1978, *Chem Eng Sci*, 33: 593.
52. Balzli, M. W., Liapis, A. I. and Rippin, D. W. T., 1978, *Trans I Chem E*, 56: 145.
53. Fritz, W. and Schlunder, E. U., 1981, *Chem Eng Sci*, 36: 721.
54. Fritz, W., Merk, W. and Schlunder, E. U., 1981, *Chem Eng Sci*, 36: (*a*) 731, (*b*) 741.
55. Levenspiel, O., 1972, *Chemical Reaction Engineering*, (Wiley, New York).
56. Yagi, S. and Kunii, D., 1961, *Chem Eng Sci*, 16: 372.
57. McKay, G. and Poots, V. J. P., 1980, *J Chem Tech Biotech*, 30: 279.
58. McKay, G. and Allen, S. J., 1980, *Can J Chem Eng*, 58: 521.
59. MKay, G., Otterburn, M. S. O. and Sweeney, A. G., 1980, *Water Res*, 14: 15.
60. Neretnieks, I., 1974, *Swedish Paper J*, 77: 407.
61. Weber, T. W., 1978, *Can. J Chem Eng*, 56: 187.
62. McKay, G., Unpublished work.
63. Wilke, C. R., 1955, *AIChEJ*, 1: 264.
64. Skelland, A. H. P., 1974, *Diffusional Mass Transfer*, (Wiley, Chichester).
65. Carberry, J. J., 1960, *AIChEJ*, 6: 460.
66. Kataoka, T., Yoshida, H. and Ueyama, K., 1972, *J Chem Eng (Japan)*, 5(2): 132.
67. Van Meel, D. A., 1958, *Chem Eng Sci*, 9: 63.
68. Vermeulen, Th., Klein, G. and Heister, N. K., 1973 in Perry, R. H. and Chilton, C. H., eds, *Chemical Engineer's Handbook* 5th edn. (McGraw-Hill, New York) ch 16.
69. Wilson, E. J. and Geankoplis, C. J., 1966, *Ind Eng Chem, Fundl*, 5: 9.

ADDRESS

Correspondence on this paper should be addressed to Dr G. McKay, Department of Chemical Engineering, The Queen's University, 21 Chlorine Gardens, Belfast, BT9 5DL.

The manuscript was originally submitted 6 July 1982 and was accepted, following revisions, 4 October 1983.

VOL. 62 1984

SOLID–LIQUID MASS TRANSFER COEFFICIENT IN MECHANICALLY AGITATED CONTACTORS

By V. K. PATIL, J. B. JOSHI and M. M. SHARMA (FELLOW)

Department of Chemical Technology, University of Bombay, India

A study of the variation of local solid–liquid mass transfer coefficient, $(k_{SL})_L$ with position in mechanically agitated contactors (MAC) was made at different impeller speeds by studying the dissolution of a stationary copper test piece in acidic dichromate solutions. Mechanically agitated contactors of 0.305 and 1.0 m i.d., with different types of impellers (disk turbine, curved blade turbine, pitched blade turbine and propeller), were used. The effect of gas sparging on the variation of $(k_{SL})_L$ was studied at superficial gas velocities of 0.0075 and 0.015 m s^{-1} and the differences have been explained. Values of $(k_{SL})_L$ in the plane of the impeller have been correlated in terms of operating parameters for radial flow impellers. Mechanically agitated contactors have been compared with bubble columns on the basis of wall side solid–liquid mass transfer coefficient.

INTRODUCTION

Mechanically agitated contactors (MAC) are very widely used in the chemical industry with different objectives, such as blending, heat transfer, mass transfer with or without chemical reaction in the presence or absence of solid particles, and for various processes like carbonation, chlorination, hydrogenation, oxidation, ozonation, etc. Further, there are several industrially important electrolytic reactions which are carried out in MAC.

One of the important design parameters for MAC is the wall side heat transfer coefficient. These can be conveniently measured by estimating wall side solid–liquid mass transfer coefficient and subsequently applying the analogy between mass and heat transfer. Further, for the design of mass transfer controlled electrolytic operations, the knowledge of mass transfer coefficient, k_{SL}, at the electrode surface is desirable. The value of k_{SL} strongly depends upon the location of the electrode in a mechanically agitated contactor.

Keey and Glen[1] have measured $(k_{SL})_L$ values in a 0.15 m i.d. MAC using a six-straight-bladed turbine. Mass transfer controlled electrochemical reaction was used for the measurement of k_{SL}. Spherical particles of 1.5 mm diameter were held stationary at different radial and axial positions. They have shown that $(k_{SL})_L$ varies as the square root of the particle Reynolds number $(\pi N D d_p \rho/\mu)$. However, the variation of $(k_{SL})_L$ with respect to position has not been reported and the experiments were performed in the absence of gas.

Askew and Beckmann[2] have investigated wall side solid–liquid mass transfer coefficient using dissolution of benzoic acid in water. In this study a 0.25 m i.d. MAC with straight and pitched blade turbines and propeller was used. Mass transfer coefficients, $(k_{SL})_L$, at several axial and tangential positions were measured. They have shown that, at any impeller Reynolds number, $(k_{SL})_w$ is highest for a straight blade turbine, medium for a pitched bladed turbine and lowest for a propeller. In this investigation also, the gas phase was not present.

There is practically no information available in the published literature on $(k_{SL})_L$ and $(k_{SL})_w$ values in *gas–liquid* mechanically agitated contactors. The flow patterns in the presence of gas are drastically different from those in its absence. Therefore, a systematic investigation was undertaken to investigate the effect of the presence of gas on the local and wall side solid–liquid mass transfer coefficients using relatively large size (0.305 and 1.0 m i.d.) MAC. For the purpose of comparison, experiments were also carried out in the absence of gas. Measurements of k_{SL} were made by a study of the dissolution of copper samples in acidic dichromate solutions[3].

The comparative performance of mechanically agitated versus sparged contactors is of inherent interest to designers. An attempt will be made to present this comparison on the basis of experimental results on $(k_{SL})_w$ from both types of equipment. Theoretical explanations will be provided by analysis of the flow patterns in sparged and mechanically agitated contactors.

EXPERIMENTAL

Two mechanically agitated contactors with flat bottom, fully baffled, made of perspex, having an i.d. of 0.305 m and 1.0 m, were used. The 0.305 and 1.0 m i.d. contactors will be referred to as MAC-1 and MAC-2, respectively. Impellers and shafts were coated with an epoxy resin to prevent corrosive action of acidic dichromate solution. Figure 1 shows the arrangement made to hold test pieces (copper Raschig rings) at different axial and radial positions in MAC-2. Clean, weighed test pieces were tied with the help of teflon tapes at the desired axial location on a mild steel pipe (12 mm o.d.). The mild steel pipes were coated with an acid resistant paint and provided with PVC sleeves (18 mm o.d.) for fitting test pieces snugly so that only the outside surface of the test piece could take part in the reaction. Four such pipes were used for four different radial positions at right angles. In the case of MAC-1, three stainless steel rods having 3 mm diameter were used to study three different radial positions at angles of 120°. Pipes or rods with copper test pieces were inserted at the desired radial positions in the contactor at zero time and held station-

© Institution of Chemical Engineers

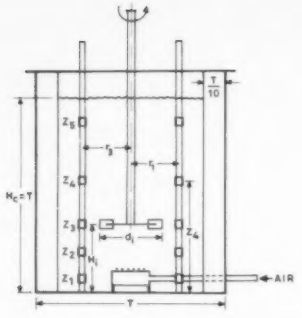


Figure 1. Arrangement made to study k_{SL} at different locations in the 1.0 m i.d. mechanically agitated contactor.

ary with a suitable clamping arrangement. The agitator was started and gas was sparged (whenever necessary) simultaneously. Batch times, t_f, were 300 s for MAC-1 and 600–900 s for MAC-2. After time t_f, both the agitator and gas were stopped. The pipes or rods were removed from the liquid phase and washed immediately with water. Test pieces were untied, washed again, dried and weighed. A liquid sample from the bulk of the liquid phase was analysed for dichromate concentration.

The wall side solid–liquid mass transfer coefficients in MAC-2 were obtained using rectangular copper test pieces. The arrangement used was similar to that used by Patil and Sharma[3]. Table 1 gives the pertinent details about the geometry and dimensions of the various impellers and gas spargers used in the present study, and other relevant factors which describe the system. Impellers were situated at a height one-third of the diameter of the contactor. The clear liquid height was always equal to the diameter of the contactor. The experiments were carried out at a temperature of 303 ± 2°K. It may be emphasised that the reproducibility of any experiment was within 5% error.

The method of measuring k_{SL} essentially consists of measuring the rate of dissolution of copper in acidic solutions of dichromate. Patil and Sharma[3] have discussed the relevant details pertaining to this method. The following equation was used to calculate values of k_{SL}:

$$k_{SL} = \frac{W_i - W_f}{Z_s \cdot A_s M_s t_f [B]} \quad (1)$$

where W_i and W_f are initial and final weights of the sample. A_s is the active surface area of the copper test piece, M_s is the atomic weight of copper, Z_s is the stoichiometric factor for the reaction between dichromate and copper which is equal to 3, t_f is the batch time in seconds and $[B]$ is the dichromate ion concentration.

The impeller power consumption in the absence and presence of gas was measured in MAC-1 by using a strain gauge torque sensor. The results were reproducible within 2% error.

RESULTS AND DISCUSSION

The impellers used in the present work were of two types, namely, (1) radial flow impellers and (2) axial flow impellers. The disk turbine and the curved blade turbine produce radial flow of the liquid. The pitched blade turbine and the propeller produce axial flow parallel to the shaft of the impellers though a pitched blade turbine also produces some radial flow. The power consumption in the case of disk turbines and curved blade turbines is higher than that in the case of pitched blade turbines and propellers, operated under similar conditions (the diameter of impellers is the same). The power numbers ($P/\rho N^3 D^5$) for the disk turbine, the pitched blade turbine and the propeller used in MAC-1 are approximately 5.7, 1.5 and 1.0, respectively[4,5] and those for the disk turbine, the curved blade turbine and the pitched blade turbine used in MAC-2 are 5.08, 4.04 and 1.54, respectively[6].

Table 1. Details of impellers used and operating parameters

Contactor details	Impeller details: Type	Impeller details: Dia D (m)	Sparger details	Specimen dimensions	Operating parameters: N (rps)	Operating parameters: $V_G \times 10^3$ (ms^{-1})	Operating parameters: Positions studied: Axial Z (m)	Operating parameters: Positions studied: Radial r (m)
MAC-1 Dia = 0.305 m Height = 0.5 m 3 baffles of 0.03 m width	Six bladed disk turbine $l/D = 0.25$, $b/D = 0.20$	0.103	5 nozzles of 2.5 mm dia, centrally located 25 mm above the bottom	Hollow copper cylinder i.d. = 4 mm o.d. = 6 mm Active length = 15 mm	6.67 13.33 and 20.00	0, 7.5 and 15.0	0.025, 0.105 and 0.21	0.08 0.11 and 0.15
	Four bladed 45° pitched blade turbine $b/D = 0.3$	0.101						
	Propeller (Marine) three blades	0.101						
MAC-2 Dia = 1.0 m Height = 1.2 m	Six bladed disk turbine, $l/D = 0.25$, $b/D = 0.20$	0.34	Sieve plate sparger, 98 nozzles of 2.5 mm dia., centrally located 0.1 m above the bottom	Copper Raschig rings i.d. = 18 mm o.d. = 21 mm Active length = 18 mm	0.67 1.33 and 2.00	0, 7.5 and 15.0	0.075, 0.21, 0.35, 0.56 and 0.85	0.185, 0.285 0.36, 0.45 and 0.497
4 baffles of 0.10 m width	Six bladed, 45° pitched blade turbine	0.34						
	Six bladed curved blade turbine $b/D = 0.21$	0.34		Rectangular copper plates of 25 mm × 19 mm				

VOL. 62 1984

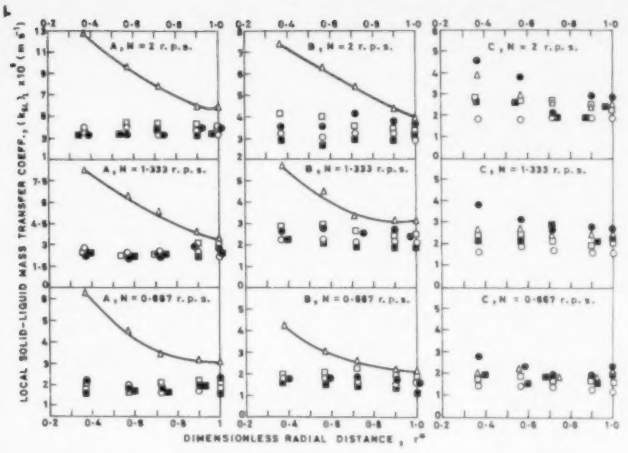


Figure 2. Variation of $(k_{SL})_L$ in the absence of gas with dimensionless radial and axial distances in MAC-2.
A. Six bladed disk turbine, B. Curved bladed turbine, C. Pitched bladed turbine. (For the details of impellers refer to Table 1). Symbols: ○ = $Z_1^* = 0.075$, □ = $Z_2^* = 0.21$, △ = $Z_3^* = 0.35$, ■ = $Z_4^* = 0.58$, ● = $Z_5^* = 0.85$.

LOCAL SOLID–LIQUID MASS TRANSFER COEFFICIENT

In the Absence of Gas Sparging

(i) *Six Bladed Disk Turbine*. In the absence of gas sparging Figure 2 shows the variation of local solid–liquid mass transfer coefficient with dimensionless radial distance, r^*, at various axial distances in MAC-2. Values of $(k_{SL})_L$ at all the locations increased with an increase in the impeller speed. It can be seen from Figure 2 that the extent of radial variation of $(k_{SL})_L$ was dependent on the axial position and was maximum in the plane of the impeller and it was practically insignificant near the top and the bottom of the contactor.

The value of $(k_{SL})_L$ depends upon the local velocity and turbulence fields. In the case of disk turbines, the flow of the liquid in the plane of the impeller is radial and relatively high as compared with other locations in the rest of the contactor. The radial velocity is maximum near the tip of the impeller and is minimum near the wall. The radial velocity at a distance r from the centre is proportional to $ND(D/2r)$ and the values of local solid–liquid mass transfer coefficient in the plane of the impeller can be conveniently correlated with $ND^2/2r$ by the following equation (with a standard deviation of 15%, Figure 3):

$$(k_{SL})_L = 15 \times 10^{-5} (ND^2/2r)^{2/3} \qquad (2)$$

The axial variation of $(k_{SL})_L$ was considerable near the impeller tip (Figure 2, Table 2). Values of $(k_{SL})_L$ increased from the bottom to the impeller plane and decrease again in the top section of the contactor. Values of $(k_{SL})_L$ in the plane of the impeller were two to four times higher than those at the same radial position but near the top or the bottom of the contactor. However, the axial variation reduced as the radial distance increased and was minimum at the wall (50–80%).

(ii) *Curved Bladed Turbine*. Figure 2 shows $(k_{SL})_L$ values in MAC-2 using a curved bladed turbine and without gas sparging. The flow pattern generated by a curved bladed turbine is similar to that of a disk turbine and the variation of $(k_{SL})_L$ is also similar. In the plane of the impeller, $(k_{SL})_L$ can be correlated by equation (2) with a constant of 11.3×10^{-5}. It is known that the power number for the curved bladed turbine (4.04) is lower than that for the disk bladed turbine (5.08). However, the coefficient of pumping capacity is higher for the curved bladed turbine. This indicates that, in the case of the disk turbine, more power is dissipated in generating turbulence. Since the values of $(k_{SL})_L$ are higher for the disk turbine (Figure 2), it appears that the turbulence parameters dominate in influencing k_{SL} as compared with the bulk liquid flow.

(iii) *Pitched Bladed Turbine and Propeller*. In the absence of gas, the values of $(k_{SL})_L$ provided by the pitched bladed turbine are shown in Figure 2 and Table 2 and by the propeller in Table 2. When the liquid flow is downward, $(k_{SL})_L$ at any radial position increases from top to bottom. Similarly, when the liquid flow is upward, $(k_{SL})_L$ at any radial position increases from bottom to top. The values of $(k_{SL})_L$ provided by the pitched bladed turbine are lower as compared with the disk turbine. Further, the axial and radial variation in the case of the pitched bladed turbine is much lower as compared to that in the disk turbine. Similar observations have been reported by Askew and Beckmann[2].

(iv) *Correlation for* $(k_{SL})_w$ *in Absence of Gas*. Values of $(k_{SL})_L$ at r^* equal to 0.984 and 0.994 in MAC-1 and MAC-2 respectively, represent the values of wall side solid–liquid mass transfer coefficient $(k_{SL})_w$ at various locations on the wall. Values of $(k_{SL})_w$ vary considerably with height (axial distance on the wall) in the MAC-1 and MAC-2 with different types of impeller. However, values of $(k_{SL})_w$ were graphically averaged and were

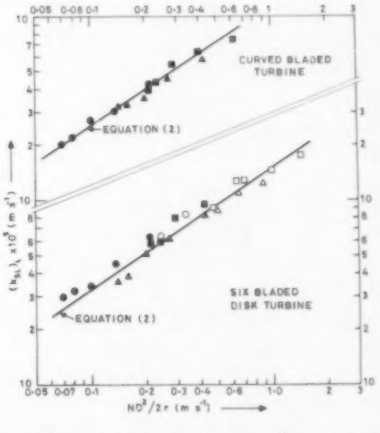


Figure 3. Correlation of solid–liquid mass transfer coefficient in the plane of the impeller.

Symbol	Contactor	Impeller speed (rps)
○	MAC-1	6.67
△	MAC-1	13.33
□	MAC-1	20.00
●	MAC-2	0.67
▲	MAC-2	1.33
■	MAC-2	2.00

Table 2 Local values of solid–liquid mass transfer coefficient in 0.305 m i.d. mechanically agitated contactor

Dimensionless axial distance Z^*	Dimensionless radial distance r^*	Local values of solid–liquid mass transfer coefficient $(k_{SL})_L \times 10^5$ (m s^{-1}) for diferent impellers and at different speeds of agitation, N (rps). Six bladed disk turbine speed 6.67	13.33	20	Pitched bladed turbine speed 6.67	13.33	20	Propeller speed 6.67	13.33	20
					(A) $V_G = 0$ mm s^{-1}					
	0.52	6.08	7.45	9.08	7.24	10.19	12.42	6.67	9.01	11.12
0.082	0.72	5.99	7.08	9.12	6.19	8.16	10.82	5.08	7.47	9.41
	0.98	4.00	5.95	8.48	4.90	7.07	9.43	4.89	6.98	8.71
	0.52	9.27	12.23	17.73	5.28	7.45	9.65	5.42	7.36	9.30
0.344	0.72	8.29	10.82	14.62	4.37	6.89	7.95	4.19	6.20	7.84
	0.98	6.16	8.87	12.91	3.91	5.62	7.69	3.87	5.70	6.55
	0.52	5.16	7.00	9.08	4.72	6.98	8.00	3.72	6.48	6.80
0.690	0.72	4.90	6.60	8.15	3.71	6.03	7.74	3.46	4.85	6.09
	0.98	4.58	5.98	8.16	3.39	4.87	6.65	2.76	3.87	5.30
					(B) $V_G = 7.5$ mm s^{-1}					
	0.52	6.00	6.84	8.62	3.00	6.79	9.50	3.43	4.57	9.19
0.082	0.72	4.19	6.82	8.42	2.78	6.22	7.69	2.60	3.35	8.01
	0.98	3.92	5.99	8.00	2.76	4.89	7.00	2.62	3.67	6.72
	0.52	8.40	11.17	15.98	5.32	6.62	6.81	5.60	6.14	8.54
0.344	0.72	6.56	10.04	13.87	5.34	4.86	6.30	3.78	4.40	6.94
	0.98	5.57	8.42	11.89	3.90	4.01	5.74	3.19	3.76	5.51
	0.52	6.13	6.30	8.04	4.21	5.62	6.00	3.38	4.10	5.70
0.690	0.72	4.55	6.51	7.83	3.62	3.63	5.81	3.63	4.63	5.64
	0.98	3.96	5.63	7.94	3.61	3.66	4.80	2.83	3.23	4.16
					(C) $V_G = 15$ mm s^{-1}					
	0.52	3.63	6.85	7.84	3.18	6.56	8.08	3.01	5.65	6.25
0.082	0.72	2.98	6.70	7.92	2.86	4.49	7.26	4.90	4.75	4.75
	0.98	3.60	5.61	7.62	2.44	4.74	7.36	3.61	3.99	4.33
	0.52	7.10	10.36	14.03	4.43	5.79	7.57	4.72	6.92	7.51
0.344	0.72	6.39	8.68	13.06	4.23	4.62	6.63	4.30	3.58	5.60
	0.98	5.52	7.68	10.96	3.74	4.13	5.81	4.06	3.38	4.20
	0.52	5.12	6.47	7.02	4.03	5.11	6.77	3.49	5.16	4.17
0.690	0.72	4.71	6.43	7.02	5.14	3.85	6.06	3.81	3.41	5.03
	0.98	4.08	5.89	7.57	3.47	3.54	4.74	2.94	3.41	4.16

correlated with ND^2/T (the limiting case of $ND^2/2r$ at $2r = T$) by the following equation:

$$(k_{SL})_w = \alpha(ND^2/T)^{\beta} \tag{3}$$

Values of α and β were obtained by using a regression analysis technique and are given in Table 3. Joshi[7] has shown that the average circulation velocity, V_c, in the mechanically agitated contactor is proportional to ND^2/T. The constant of proportionality depends on the position of the impeller and power number. Thus, in equation (3), $(k_{SL})_w$ is proportional to V_c^{β} and the value α depends on the power number and position of the impeller. From Table 3, it can be seen that the values of β are very close to 0.66 for all the impellers except the pitched blade turbine (upflow).

(v) *Comparison between MAC and Bubble Columns.* In the previous sections, a discussion was presented on $(k_{SL})_L$ and $(k_{SL})_w$ in MAC operated in the absence of gas. At this stage, a comparison between MAC and bubble columns will be given. The relative performance of MAC in the presence of gas is somewhat complex and will be discussed later.

Pandit and Joshi[8] have compared MAC with bubble columns as regards mixing. For the same power consumption per unit volume and for the same contactor volume, they have shown that a bubble column ($L/D = 1$) provides 30–50% lower mixing time as compared to that by MAC. This is because, in bubble columns the liquid flow pattern is directional and the power dissipated produces a practically uniform turbulence field. In the case of MAC a substantial amount of power is dissipated in the impeller region and only part of the input power is available for generating the bulk flow. This point can be further illustrated on the basis of average liquid circulation velocities (V_c).

In the case of bubble columns, Joshi[7] has given the following equation for V_c. It holds in the column diameter range of 0.15 to even 5.5 m and V_G range of 20–900 mm s^{-1}:

$$V_c = 1.31\{g\,T\,(V_G - \varepsilon_G V_{b\infty})\}^{1/3} \tag{4}$$

In the case of mechanically agitated contactors, V_c can

Table 3. Values of constants a and β in equation (3)

No.	Type of impeller	Contactor	$\alpha \times 10^5$	β
1.	Six bladed disk turbine	MAC-1, MAC-2	10.9	0.65
2.	Curved blade turbine	MAC-2	8.53	0.66
3.	Propeller (downflow)	MAC-1	8.13	0.63
4.	Pitched blade turbine (downflow)	MAC-1	9.14	0.64
5.	Pitched blade turbine (upflow)	MAC-2	3.4	0.23

VOL. 62 1984

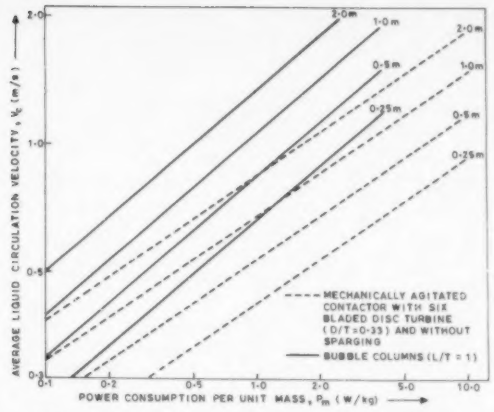


Figure 4. Variation of average liquid circulation velocity with power consumption per unit mass in mechanically agitated contactors (without sparging) and bubble columns of different diameters.

be calculated on the basis of mixing time. Joshi et al[9,10] have shown that the mixing time (t_M) is about five times the circulation time (t_c). In the case of a disk turbine two doughnut shaped circulation cells are developed above and below the impeller. For the central location of the impeller the longest length of the circulation path is given by:

$$L_c = T + H \tag{5}$$

Circulation time is the ratio of circulation path to circulation velocity:

$$t_c = L_c/V_c \tag{6}$$

and

$$t_M = 5\,t_c \tag{7}$$

The value of V_c can be calculated on the basis of experimental values of mixing time equations (5)–(7). Joshi et al[9] have shown that the values of V_c calculated from mixing time agree favourably with those measured experimentally by Van der Molen and Van Mannen[11]. Figure 4 shows the values of V_c in bubble columns and mechanically agitated contactors (with six bladed disk turbine of power number five) of 0.25, 0.5, 1.0 and 2.0 m i.d. Power consumptions per unit mass in bubble column and MAC are given by the following equations, respectively:

$$P_m = g\,V_G \tag{8}$$

$$P_m = P_0\,\rho\,N^3D^5/\tfrac{1}{4}\pi T^2\,H\rho \tag{9}$$

In equation (9), P_0 is the power number and for a standard six blade disk turbine P_0 equals five. From Figure 4 it can be seen that bubble columns provide 30–50% higher circulation velocities. Joshi et al[10] have shown that bubble columns and mechanically agitated contactors provide practically the same value of heat transfer coefficient (h_w) at the same liquid circulation velocity. In other words, at the same power consumption per unit mass, wall side heat transfer coefficient is higher by 20–30% ($h_w \propto V_c^{2/3}$) in bubble columns.

Figure 5 shows $(k_{SL})_w$ in bubble columns (Patil and Sharma[3]) and in MAC (in the absence of gas), each of 1.0 m i.d. and 1.0 m height. It may be emphasised that, in both the cases, the same system (dissolving of copper in aqueous dichromate solutions) was used. It can be seen from Figure 5 that $(k_{SL})_w$ from bubble columns is higher by 10–20%.

In the Presence of Gas Sparging

In the presence of gas, the combined effect of sparging and impeller action is complex. In the absence of impeller action the average liquid circulation velocity (V_c) in bubble columns is given by equation (4) and in the absence of gas V_c in MAC is given by equations (5)–(7). At any given value of superficial gas velocity, V_G (it may be noted that the range of V_G used in MAC is relatively low: 1–30 mm s^{-1}) when impeller speed is low, the liquid circulation generated by sparging is stronger than that generated by the impeller. However, with an increase in impeller speed (N), the flow generated by the impeller increases, and at sufficiently high N sparging makes little contribution to the overall liquid flow. Therefore, at low impeller speeds, sparging dominates the flow behaviour whereas at high impeller speeds the impeller action dominates. At a given V_G, the transition from sparging dominated region to impeller dominated region occurs over a range of impeller speed. We can perhaps characterise an impeller speed at which the circulation velocities generated by sparging and impeller are same. For the six bladed disk turbine, Pandit and Joshi[8] have shown that the above condition occurs at the critical impeller speed.

Chapman et al[12] have explained the above transition on the basis of visual observations. At low impeller speeds the contactor can be considered to be a bubble column. However, below the impeller a chain of large bubbles appear. These bubbles are broken and distributed by the impeller and in the region above the impeller better distribution of gas occurs. The intensity of liquid circulation is perhaps stronger above the impeller. At a certain critical speed, bubbles from the top (above impeller) region are carried downward because of the liquid flow generated by the impeller. Above the critical impeller speed, the average bubble diameter and fractional gas hold-up are practically the same in both the regions.

It may be remembered that, in the presence of the impeller the fractional gas hold-up (ε_G) is higher than that in its absence and it can be seen from equation (4) that V_c because of sparging (at a given V_G) decreases with an increase in the impeller speed. Similarly, in the

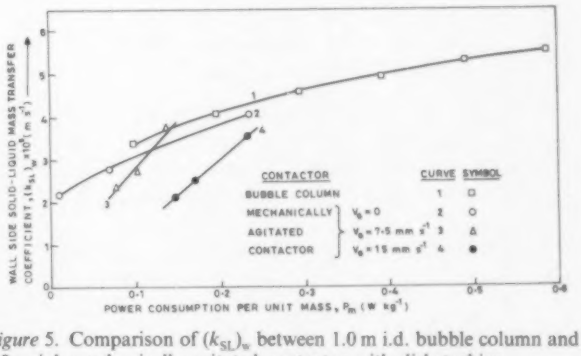


Figure 5. Comparison of $(k_{SL})_w$ between 1.0 m i.d. bubble column and 1.0 m i.d. mechanically agitated contactor with disk turbine.

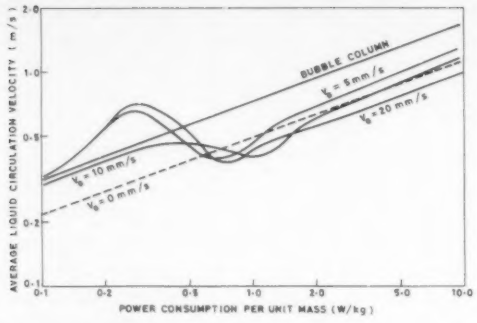


Figure 6. Variation of average liquid circulation velocity with power consumption per unit mass in mechanically agitated contactor (with sparging) and bubble column. Vessel/column diameter = 0.305 m.

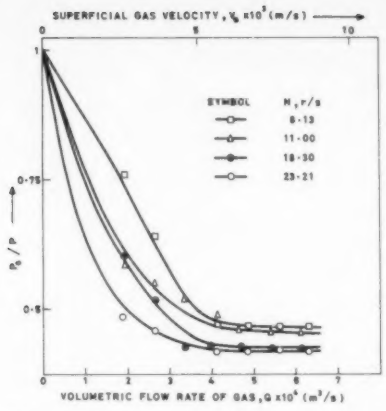


Figure 7. Reduction in the impeller power consumption in the presence of gas.

presence of gas the impeller pumping capacity decreases and the extent of decrease depends upon the impeller speed. The combined value of V_c can be estimated from the mixing time data when both the sparging and the impeller action are in operation. Pandit and Joshi[8] have collected such mixing time data. Using the procedure discussed in the previous section, the values of V_c were calculated and they are shown in Figure 6. The impeller power consumption was calculated by the following equation:

$$P_{mT} = P_m G + V_g g \tag{10}$$

where P_{mG} is the specific impeller power consumption in the presence of gas. It is well-known that impeller power consumption decreases in the presence of gas. The impeller power consumption in the presence and absence of gas was measured in MAC-1. The results on P_G/P at various impeller speeds and superficial gas velocities are shown in Figure 7. Power consumption measurements were also made in a 0.57 m i.d. MAC with 0.19 m diameter six bladed disk turbine ($l^* = 0.25$, $b^* = 0.2$). Chapman et al[12] have reported power consumption data for a 0.56 m i.d. MAC provided with a 0.187 m diameter six bladed disk turbine ($l^* = 0.25, b^* = 0.2$). The values of P_G/P obtained in these two investigations (under otherwise similar conditions) were found to be within 10%. In view of the above, it would be reasonable, for the calculation of P_G in MAC-2 (1.0 m i.d.) to accept the scale-up criterion of Chapman et al[12] which recommends that the reduction in power consumption is the same at the same value of VVM (volume of gas per minute per unit liquid volume) if geometrical similarity of the impeller (D/T, l/D, b/D) is maintained.

From the foregoing discussion and Figure 6 the following points may be emphasised:

(1) Below the critical impeller speed (N_{CD}), the average liquid circulation velocity in MAC can be higher than that in bubble columns. However, above the critical impeller speed, MAC provides low liquid circulation velocities.

(2) All the experiments in MAC-1 were carried out above the critical impeller speed (N_{CD}) and the results are listed in Table 2. In the case of MAC-2 all the experiments were carried out below N_{CD} and are reported in Figures 8 and 9. Below the critical impeller speed, the gas bubbles are practically absent in a region below the impeller. The bubbles are well dispersed by the impeller and the region above the impeller behaves similar to a bubble column. As a result, the liquid circulation is more intense above the impeller as compared to that below the impeller. Above the critical impeller speed, bubbles are present in the lower region as well and the difference between the two regions diminishes with an increase in the impeller speed.

(3) At a given impeller speed above N_{CD}, an increase in superficial gas velocity (V_G) reduces the liquid velocity at any point. It may be remembered that the impeller power consumption also decreases with an increase in V_G.

Local and Wall-side Mass Transfer Coefficient in the Presence of Gas

The values of $(k_{SL})_L$ and $(k_{SL})_w$ from MAC-1 and MAC-2 obtained in the presence of gas are shown in Table 2 and in Figures 8 and 9. In the case of MAC-1

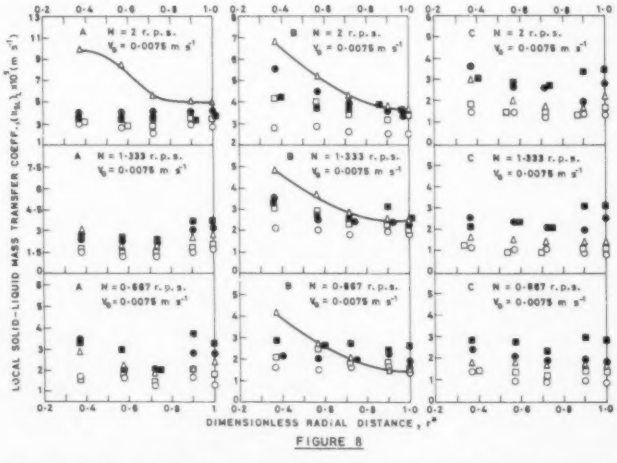


FIGURE 8

Figure 8. Variation of $(k_{SL})_L$ with dimensionless radial and axial distances in MAC-2. Superficial gas velocity = 7.5 mm s^{-1} (For symbols, refer to Figure 2).

VOL. 62 1984

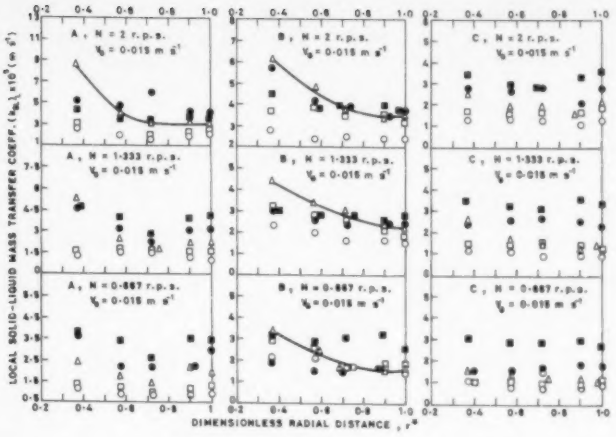


Figure 9. Variation of $(k_{SL})_L$ with dimensionless radial and axial distances in MAC-2. Superficial gas velocity = 15.0 mm s^{-1} (For symbols, refer to Figure 2).

the critical impeller speed (N_{CD}) was found to be 7.65 rps whereas it was 2.2 rps in the case of MAC-2 (Joshi et al[9]). It can be seen from Figures 8 and 9 that, in the case of MAC-2 the impeller speed was always below N_{CD}.

The effect of the presence of gas was studied for six bladed disk turbine, curved bladed turbine, pitched bladed turbine and propeller.

In all the cases, below N_{CD} the introduction of gas decreases $(k_{SL})_L$ in the region below the impeller and increases it in the region above the impeller. Above N_{CD}, the values of $(k_{SL})_L$ decrease at all locations with an increase in the superficial gas velocity. Both these observations are consistent with the liquid flow pattern discussed in the previous section.

Table 4 shows the values of K^* [ratio of $(k_{SL})_w$ with gas sparging to that without gas sparging at the same impeller speed]. This indicates that below the critical impeller speed introduction of gas improves the mixing by improving the circulation velocity which increases the value of K^* above unity, indicating improvement in k_{SL}. Above the critical impeller speed introduction of gas does not interfere with the flow pattern created by the intense impeller action. The decrease in power consumption above the critical impeller speed, because of the introduction of gas, reduces the liquid circulation velocities created by the impeller and hence the k_{SL} value decreases, which is apparent from the values of K^* being less than unity. In the vicinity of the critical impeller speed liquid circulation velocities generated by gas sparging and impeller action are comparable and hence the value k_{SL} is not affected. Joshi et al[9] have analysed the published information on wall-side heat transfer coefficient (h_w). They have shown that, because of introduction of gas, h_w increases below N_{CD} where it decreases above N_{CD}. However, it may be emphasised that the maximum deviation in $(k_{SL})_w$ and h_w because of the introduction of gas is only 30%.

Comparison Between MAC with Sparging and Bubble Columns

It was discussed in the previous section that, at the same power consumption, MAC provides better values of wall-side mass and heat transfer coefficients below the critical impeller speed whereas bubble columns are superior when impeller speeds are greater than N_{CD}. Here we note the following important points:

(i) For impeller speeds less than N_{CD}, the sparger design is very important. The gas distribution should be uniform throughout the cross-section. Gopal and Sharma[13] have discussed the pertinent details.

(ii) When the impeller speed is less then N_{CD}, the values of gas–liquid effective interfacial area (a) and mass transfer coefficients are very low (Mehta and Sharma[14], Joshi et al[9]). To obtain reasonable values of a and k_La it may be desirable to operate at higher values of power consumption per unit mass ($N > N_{CD}$). Under these conditions bubble columns may prove to be advantageous.

(iii) Bubble columns have the additional advantages of (a) lower gas phase backmixing, and (b) no problems associated with the shaft sealing.

Table 4. Effect of V_G on K^*

Contactor and type of impeller	N (rps)	$(k_{SL})_w \times 10^5$ (m s^{-1} at $V_G = 0$)	K^* (at $V_G = 7.5$ mm s^{-1})	K^* (at $V_G = 15$ mm s^{-1})
MAC-1; Six bladed	6.67	4.85	0.874	0.886
disc turbine	13.33	6.20	0.992	0.992
	20.00	8.86	0.975	0.927
MAC-2; Six bladed	0.667	2.17	1.088	0.968
disk turbine	1.33	2.76	0.978	0.906
	2.00	4.06	0.931	0.803
MAC-2 Curved	0.667	1.60	1.231	1.288
blade turbine	1.33	2.37	0.987	1.013
	2.00	3.20	1.056	1.069
MAC-1; Pitched	6.67	3.70	0.862	0.803
blade turbine	13.33	5.35	0.748	0.708
(downflow)	20.00	7.35	0.741	0.721
MAC-1; Propeller	6.67	3.20	0.897	1.038
(downflow)	13.33	5.00	0.688	0.700
	20.00	6.15	0.866	0.699
MAC-2; Pitched	0.667	1.89	1.048	1.011
blade turbine	1.33	2.18	1.009	1.032
(upflow)	2.00	2.44	1.066	1.086

CONCLUSIONS

The local values of solid–liquid mass transfer coefficient in a mechanically agitated contactor vary with position and the variation mainly depends on the impeller characteristics. The nature of the variation of solid–liquid mass transfer coefficient changes substantially with gas sparging when the impeller is operated below its critical impeller speed. Above the critical impeller speed, values of solid–liquid mass transfer coefficient at all locations in the contactor decrease with gas sparging but the nature of axial and radial variation of solid–liquid mass transfer remains practically unaffected.

Values of solid–liquid mass transfer coefficient in the plane of the impeller vary as $15 \times 10^{-5}\ (ND^2/2r)^{2/3}$ and as $11 \times 10^{-5}\ (ND^2/2r)^{2/3}$ for six bladed disk turbines and curved bladed turbines, respectively. Average wall side solid–liquid mass transfer coefficient is dependent on the circulation velocity and impeller characteristics.

Bubble columns offer higher values of wall side solid–liquid mass transfer coefficient and heat transfer coefficient than those in the mechanically agitated contactor with same vessel diameter and equal power consumption per unit mass.

ACKNOWLEDGEMENTS

The financial support given to V. K. Patil by the University Grants Commission, New Delhi, India is gratefully acknowledged. We are thankful to Mr A. D. Raidoo and Mr A. B. Pandit for making the power consumption measurements.

SYMBOLS USED

A_s	active surface area of the copper test piece (m^2)
a	effective gas–liquid interfacial area, (m^2/m^3)
$[B]$	concentration of dichromate in liquid ($kmol\ m^{-3}$)
b	width of the impeller blade (m), $b^* = b/D$
D	impeller diameter (m)
d_p	particle diameter (m)
g	acceleration due to gravity ($m\ s^{-2}$)
h_w	wall-side heat transfer coefficient ($W\ m^{-2}\ K^{-1}$)
k_La	liquid-side volumetric mass transfer coefficient at the gas–liquid interface (s^{-1})
k_{SL}	solid–liquid mass transfer coefficient ($m\ s^{-1}$)
$(k_{SL})_L$	local value of k_{SL} ($m\ s^{-1}$)
$(k_{SL})_w$	wall-side solid–liquid mass transfer coefficient ($m\ s^{-1}$)
K^*	ratio of $(k_{SL})_w$ with gas sparging to that without gas sparging (−)
l	length of the impeller blade (m), $l^* = l/D$
L,H	height of liquid in the contactor (m)
L_c	length of the circulation path (m)
M_s	atomic weight of copper = 63.54 ($kg\ katom^{-1}$)
N	impeller speed (rps)
N_{CD}	critical impeller speed (rps)
P_0	power number = $P/\rho N^3 D^5$ (−)
P	power consumption of an impeller (W)
P_G	power consumption of an impeller in presence of gas (W)
P_m	power consumption per unit mass of liquid or specific power consumption ($W\ kg^{-1}$)
P_{mG}	specific power consumption in the presence of gas in mechanically agitated contactors ($W\ kg^{-1}$)
P_{mT}	total power consumption per unit mass ($W\ kg^{-1}$)
Q	volumetric gas flow rate ($m^3\ s^{-1}$)
r	radial distance (m)
r^*	dimensionless radial distance = $2r/T$ (−)
T	contactor diameter (m)
t_c	circulation time (s)
t_f	batch time (s)
t_M	mixing time (s)
V	volume of the liquid phase (m^3)
V_c	average liquid circulation velocity ($m\ s^{-1}$)
V_{cT}	total average liquid circulation velocity ($m\ s^{-1}$)
V_G	superficial gas velocity ($m\ s^{-1}$)
$V_{b\infty}$	terminal rise velocity of bubbles ($m\ s^{-1}$)
W_i	initial weight of the copper test piece (kg)
W_f	final weight of the copper test piece (kg)
Z	axial distance (m)
Z_s	stoichiometric factor for the reaction between copper and dichromate = 3 (−)
Z^*	dimensionless axial distance = Z/T (−)
α, β	constants defined in equation (2)
ρ	density of the liquid phase ($kg\ m^{-3}$)
ε_G	fractional gas hold-up (−)
μ	liquid viscosity (Pa s)

REFERENCES

1. Keey, R. B. and Glen, J. B., 1966, *AIChEJ*, 12: 401.
2. Askew, W. S. and Beckmann, R. B, 1965, *Ind Eng Chem Proc Des Dev*, 4: 311.
3. Patil, V. K. and Sharma, M. M., 1983, *Chem Eng Res Des* 61; 21.
4. Nienow, A. W. and Miles, D., 1971, *Ind Eng Chem Proc Des Dev*, 10; 41.
5. Ruston, J. H., Costich, E. W. and Everett, H. J., 1950, *Chem Eng Prog*, 46: 396.
6. Juvekar, V. A., 1976, *PhD (Tech) Thesis* (Department of Chem Technology, University of Bombay).
7. Joshi, J. B., 1980, *Trans I Chem E*, 58: 155.
8. Pandit, A. B. and Joshi, J. B. 1983, *Chem Eng Sci*, 38: 1189.
9. Joshi, J. B., Pandit, A. B. and Sharma, M. M., 1982, *Chem Eng Sci*, 37: 813.
10. Joshi, J. B., Sharma, M. M., Shah, Y. T., Singh, C. P. P., Ally, M. and Klinzing, G. E., 1980, *Chem Eng Comm*, 6: 257.
11. Van der Molen, K. and Van Mannen, H. R. E., 1978, *Chem Eng Sci*, 33: 1161.
12. Chapman, C. M., Nienow, A. W., Cooke, M. and Middleton, J. C., 1983, *Chem Eng Res Des*, 61: 82; 61: 167.
13. Gopal, J. S. and Sharma, M. M., 1982, *Can J Chem Eng*, 60: 353.
14. Mehta, V. D. and Sharma, M. M., 1971, *Chem Eng Sci*, 26: 461

ADDRESS

Correspondence on their paper should be addressed to Professor M. M. Sharma Department of Chemical Technology, University of Bombay, Matunga Road, Bombay 400 019, India.

The manuscript was originally received 29 November 1982 and was accepted for publication, after revision, 12 March 1984.

VOL. 62 1984

GAS HOLD-UP AND INTERFACIAL AREA IN AERATED SUSPENSIONS OF SMALL PARTICLES

By E. CAPUDER and T. KOLOINI

Department of Chemistry and Chemical Technology, E. Kardelj University, Yugoslavia

The gas hold-up and the interfacial area were measured in a bubble column and in a mixing tank reactor during the carbonisation of lime suspensions with CO_2–air mixture. The influence of solids concentration on the gas hold-up and interfacial area was studied over a wide range of superficial gas velocities and power inputs. Both the interfacial area and the gas hold-up decrease at all operating conditions with increasing solids concentration. We found it useful to treat the three-phase systems $CaCO_3$–water–air and $Ca(OH)_2$–water–air as two-phase systems with liquid phase exhibiting non-Newtonian flow properties. A successful correlation of the experimental data was achieved by modification of the existing correlations valid for gas dispersions in Newtonian liquids. However, both gas hold-up and interfacial area were found to increase by introduction of large solid particles in the bubble column. No correlation of the experimental data could be obtained in this case.

INTRODUCTION

Gas hold-up and interfacial area are two important parameters necessary for practical design of three-phase systems. Most authors have found decrease of interfacial area and gas hold-up with increasing solids concentration[1–3]. Contrary to this, Juvekar and Sharma[4] did not observe any decrease of interfacial area with increasing concentration of solids in the carbonisation of $Ca(OH)_2$ except at very high concentration of solids. The data of their work in the bubble column was measured at very high superficial gas velocity ($v_G = 0.22\ m\ s^{-1}$) and at very high power input per unit volume in the mixing vessel. Lee et al.[5] presented experimental data which show that high-momentum solid particles can increase interfacial area by the mechanism of bubble break-up if Weber number $We > 3$, while if $We < 3$ the interfacial area, a, is expected to decrease.

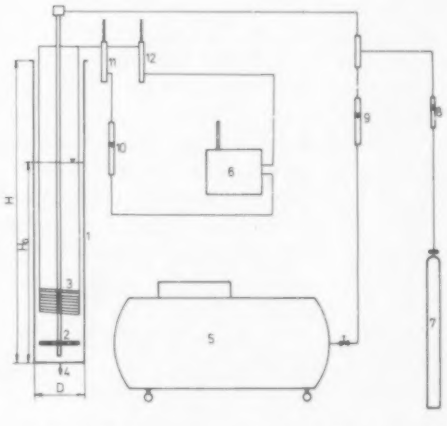
In our study of carbonisation of lime suspensions we observed considerable decrease of interfacial area as well as decrease of gas hold-up with increasing concentration of solids. This led us to a systematic study of this phenomenon.

EXPERIMENTAL

Experiments were carried out in a 0.19 m inside diameter bubble column (Figure 1) to which gas was introduced through a pipe distributor having 60 holes, 1 mm diameter evenly spread over the column cross-section. A constant temperature was kept during carbonisation with the aid of a cooling coil connected to a thermostat. Gas hold-up and interfacial area were measured in the experiments at various concentrations of $Ca(OH)_2$ and $CaCO_3$ particles. In a series of experiments, carbonisation of the 5% $Ca(OH)_2$ solution was carried on also in the presence of large 0.4 mm sand particles of irregular shape. The mean particle size of the $CaCO_3$ particles after carbonisation varied between 10 and 15 μm. Concentration of CO_2 in the inlet gas mixture was 5–10% by volume, and the outlet concentration varied between 1.5 and 6% by volume depending on interfacial area and gas flow rate.

Gas hold-up was measured also in a 0.3 m inside diameter fully baffled mixing tank reactor of standard configuration. The gas was introduced through the opening of a 7 mm i.d. pipe under the six-blade Rushton turbine with $d = 0.1$ m. The impeller speed was varied in the range $315 \leqslant N \leqslant 775$ rpm with a resulting power input of $200 \leqslant P_G \leqslant 2500\ W\ m^{-3}$ (Table 1).

A $Ca(OH)_2$ suspension of known concentration was prepared, filtered and left for 12 h to hydrate. After that the solution was brought to the choosen temperature (30°C) and then an air–CO_2 mixture of the desired composition was introduced to the column. During carbonisation samples of the slurry were withdrawn with a sampling tube and concentration of $Ca(OH)_2$ was determined acidimetrically.



1 plexiglass column
2 pipe distributor
3 cooling coil
4 suspension drein
5 compressor
6 thermostat
7 storage tank for CO_2
8-10 flowmeters
11,12 thermometers
D = 0.19 m, column diameter
H_0 = 4D, height of suspension
H = 6D

Figure 1. Sketch of the equipment.

© Institution of Chemical Engineers

Table 1. Range of the operating variables

Variable	Bubble column	Mixing tank
v_G(m s^{-1})	0.04–0.14	0.01–0.05
solids concentrations (wt%)	0–18.8	0–15
P_G(W m^{-3})	400–1500	200–2500

Interfacial area was calculated on the basis of reaction rate according to the method described in detail in the work of Juvekar and Sharma[4]. Only a brief outline therefore is given here. The experimental conditions during the measurement of interfacial area were such that CO_2 absorption was the rate controlling factor. Under these conditions reaction rate is related to interfacial area[4] by:

$$R = \frac{aHp_A\sqrt{(D_A k_2[B_S] + k_L^2)}}{1 + \{aH\sqrt{(D_A k_2[B_S] + k_L^2)}\}/k_G a} \quad (1)$$

The following values of D_A, H and k_2 were obtained by the methods described by Danckwerts and Sharma[6]:

$$D_A = 2.2 \times 10^{-9}\ m^2\ s^{-1}$$

$$H = 28.9\ mol\ bar^{-1}\ m^{-3}$$

$$k_2 = 12.4\ m^3\ s^{-1}\ mol^{-1}$$

Only an approximate value of k_L is needed. By carrying out the absorption of CO_2 in a buffer solution, Na_2CO_3–$NaHCO_3$, in which calcium carbonate particles were suspended we found $k_L = (3–4) \times 10^{-4}$ m s^{-1} following the procedure of Juvekar and Sharma[4]. In the absence of a reliable correlation for $k_G a$ we used an approximate value, $k_G a = 50$ mol m^{-3} s^{-1} bar^{-1}, quoted[4] at $v_G = 10$ cm s^{-1}. The results were only slightly affected by this approximation since

$$1 \gg \frac{aH\sqrt{(D_A k_2[B_s] + k_L^2)}}{k_G a}$$

Although there must obviously be some axial mixing in the gas phase, plug flow of gas was assumed in evaluation of interfacial area. This assumption is supported by the work of Morris and Woodburn[7] who have shown that in the presence of solid particles a gas moves essentially in plug flow even when intensive agitation is applied. The plug flow assumption is also considered to be appropriate by others[4,8]. The problem of taking account of axial dispersion of gas is further complicated by absence of appropriate gas dispersion data applicable to conditions of the present work. Using data of Carleton et al[9] we found that the correction for axial dispersion could be estimated to be between 10% and 30% of the value measured. However, the data of the present work were not corrected, for the reasons just explained. All values of interfacial area are given per unit volume of solid–liquid suspension.

Gas hold-up was determined by measuring the height of the dispersion.

EXPERIMENTAL RESULTS AND DISCUSSION

Experimental observations

Gas hold-up data are presented in Figures 2, 3, and 4. In Figure 2 gas hold-up is shown as a function of superficial gas velocity and of concentration of solids in the bubble column. The gas hold-up changed only slightly during carbonisation of the lime suspensions although the concentration of solids measured by weight increased due to the reaction. A 1% by weight $Ca(OH)_2$ suspension was taken as the basis of comparison instead of water, since the surface tension change and the presence of dissolved $Ca(OH)_2$ increases hold-up and interfacial area. It can be seen that the gas hold-up decreases with increasing concentration of solids at all gas velocities. The data presented in Figure 3 show the opposite effect if large 400 μm particles are introduced. Here the gas hold-up increases with increasing particle concentration. The gas hold-up data measured in the mixing tank show similar decrease of gas hold-up with increase of carbonate concentration to the bubble column data in the whole range of gas velocities.

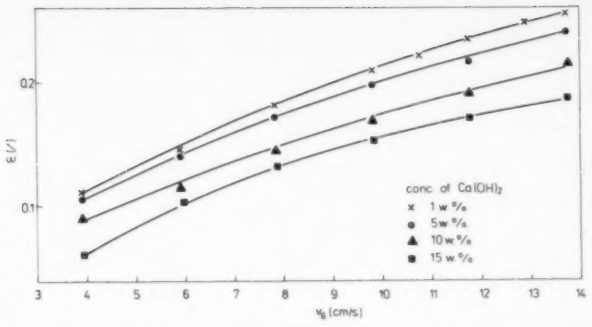


Figure 2. Gas hold-up in the bubble column in the presence of small $Ca(OH)_2$ and $CaCO_3$ particles; $d_p \simeq 10\ \mu$m.

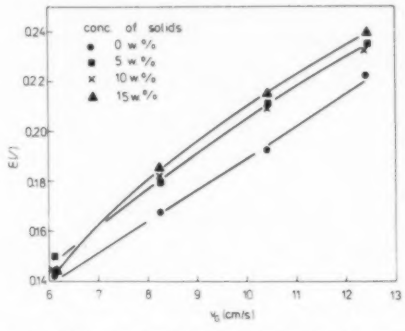


Figure 3. Gas hold-up in the bubble column in the presence of the large sand particles; $d_p \simeq 400\ \mu$m.

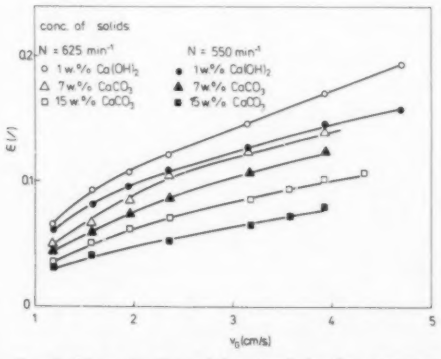


Figure 4. Gas hold-up in the mixing tank in the presence of small $CaCO_3$ particles.

VOL. 62 1984

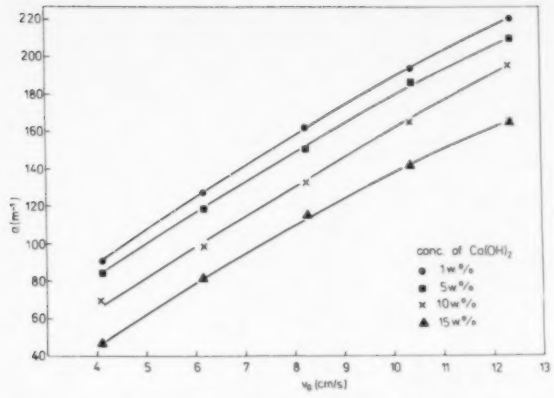


Figure 5. Interfacial area in the bubble column in the presence of small $Ca(OH)_2$ and $CaCO_3$ particles; $d_p \simeq 10\,\mu m$.

In Figures 5 and 6 interfacial area in the bubble column is presented as a funciton of gas velocity and of solids concentration. Similar behaviour to the case of gas hold-up is observed here. The interfacial area decreases with increasing concentration of solids in the case of the small $Ca(OH)_2$ and $CaCO_3$ particles and increases with increasing concentration of solids if large particles are present.

Correlation of Experimental Data in the Bubble Column

An explanation of the experimental data will be attempted. In the case of small solid particles we can treat the three-phase system as a two-phase system, regarding the suspension of carbonate and hydroxide particles as a homogeneous liquid phase. Examination of flow properties showed us the non-Newtonian behaviour of these liquids. The suspensions can be regarded as power law fluids, as can be seen from the experimental flow curves presented in Figures 7 and 8, where the apparent viscosity η_a is plotted as a function of the shear rate $\dot{\gamma}$. The flow curves were measured with a Brookfield viscometer in coaxial cylinder configuration.

Thus it appears that the influence of small solid particle concentration on gas hold-up and interfacial area could be related to the viscosity of suspensions, since all other relevant physical properties, with the exception of suspension density, do not change with increasing concentration of solids. One of the approaches in correlation of the various experimental data in non-Newtonian systems is to modify the existing correlations developed for the Newtonian systems by introducing an effective viscosity which is a function of the operating conditions. The same method of correlation was used in this work and whenever possible the original form of the dimensionless equations was retained, even in cases when a variation of a particular dimensionless group was not large.

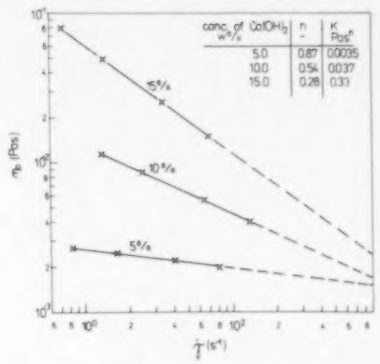


Figure 7. Rheological properties of $Ca(OH)_2$ suspensions.

The effective viscosity is related to the average shear rate by:

$$\eta_{ef} = K\dot{\gamma}_a^{n-1} \tag{2}$$

In the study of heat transfer from non-Newtonian liquids (solutions of CMC) Nishikawa et al[10] found for the bubble column the following relationship between average shear rate $\dot{\gamma}_a$ and gas superfacial velocity v_G

$$\dot{\gamma}_a = 50 v_G \tag{3}$$

were v_G was given in cm s^{-1}.

Several authors[11-14] have attempted to correlate gas hold-up with gas superfacial velocity v_G and physical properties of liquid and gas. We took as the basis of our

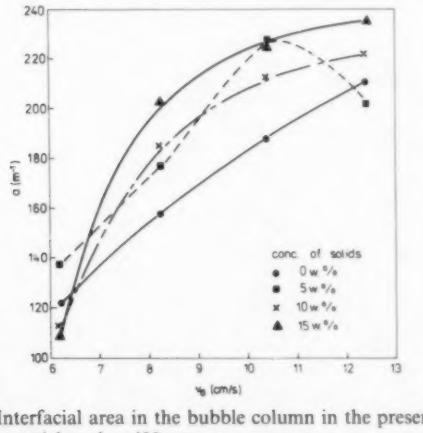


Figure 6. Interfacial area in the bubble column in the presence of the large sand particles; $d_p \simeq 400\,\mu m$.

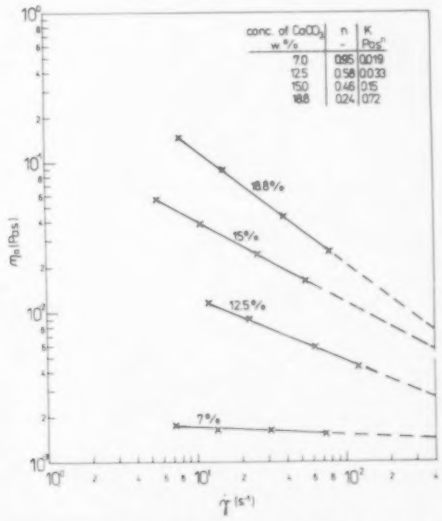


Figure 8. Rheological properties of $CaCO_3$ suspensions.

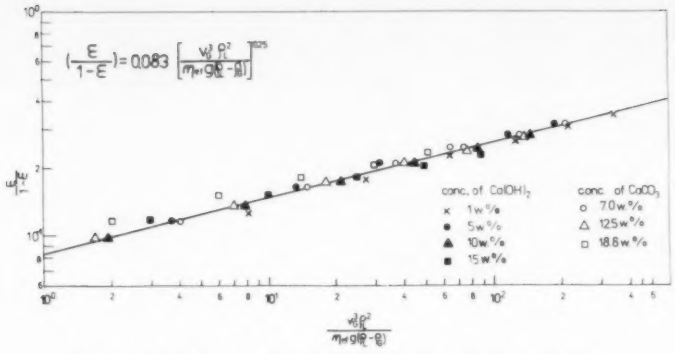


Figure 9. Correlation of the bubble column gas hold-up data.

consideration the functionality given by Bach and Pilhofer[11]:

$$\frac{\epsilon}{1-\epsilon} = a\left(\frac{v_G\rho_L^2}{\eta_L(\rho_L-\rho_G)g}\right)^b \tag{4}$$

who found for Newtonian liquids and their distributor, $a = 0.115$ and $b = 0.23$. By replacement of η_L with the effective viscosity, η_{ef}, where the shear rate was taken as $\dot{\gamma}_a = 40v_G$ so that

$$\eta_{ef} = K(40v_G)^{n-1} \tag{5}$$

we obtained an acceptable correlation of the gas hold-up data which is plotted in Figure 9:

$$\frac{\epsilon}{1-\epsilon} = 0.083\left(\frac{v_G^3\rho_L^2}{\eta_{ef}(\rho_L-\rho_G)g}\right)^{0.25} \tag{6}$$

The exponent over the effective viscosity, -0.25, is almost the same as found by Bach and Pilhofer for Newtonian liquids. The difference in the constant a is attributed to the differences in the distribution system. The validity of correlation (6) can be used also to explain apparent contradiction between the results obtained by Juvekar and Sharma and our data in the bubble column for the interfacial area. Since the gas velocity in their 5 cm diameter bubble column was very high, 22 cm s^{-1}, the average shear rate must have been very large also. At these conditions the viscosity of suspensions approaches the same value at all particle concentrations as can be seen by extrapolation of the flow curves to high shear rates.

Correlation of interfacial area was also tried. As the basis we used the dimensionless form introduced by Akita and Yoshida[15]

$$aD = k_1\left(\frac{gD^2\rho_L}{\sigma}\right)^{k_2}\left(\frac{gD^3\rho_L^2}{\eta_L^2}\right)^{k_3}\epsilon^{k_4} \tag{7}$$

By adopting k_2 and k_4 from the work of Akita and Yoshida[15] we obtained, by least-squares analysis, the correlation:

$$aD = 1.67\left(\frac{gD^2\rho_L}{\sigma}\right)^{0.5}\left(\frac{gD^3\rho_L^2}{\eta_{ef}^2}\right)^{0.021}\epsilon^{1.13} \tag{8}$$

(The group to the power 0.021 varied in the range 6.6×10^8 to 1.1×10^{11} and their variation could not be neglected). The experimental results are quite successfully correlated since most of the data differ for less than 10% of the value measured. The values of the gas hold-up in Figure 10 are the experimental ones, the values of ϵ in Figure 11 were calculated by correlation (6).

Correlation of Experimental Data Measured in the Mixing Tank

Gas hold-up data measured in the mixing tank cannot be correlated with any existing equation, since no vis-

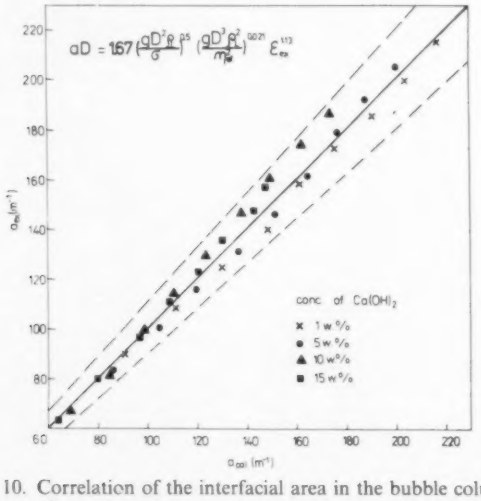


Figure 10. Correlation of the interfacial area in the bubble column. ϵ values experimental.

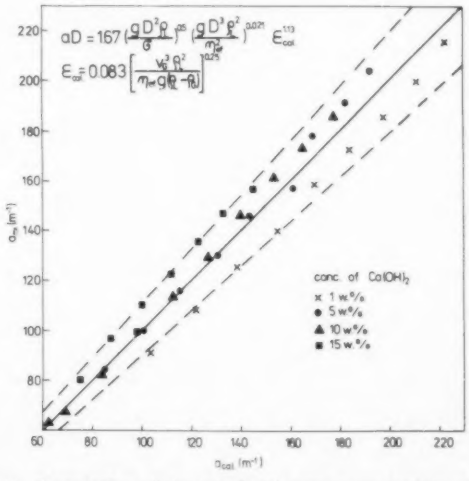


Figure 11. Correlation of the interfacial area in the bubble column. ϵ calculated by equation (5).

VOL. 62 1984

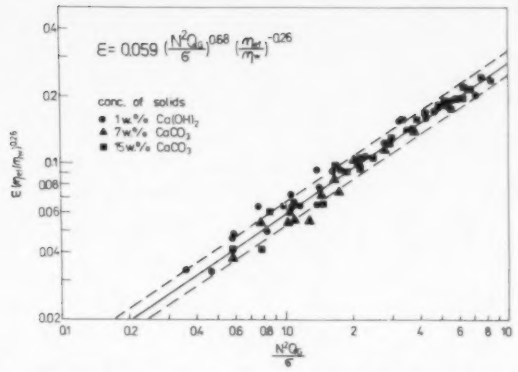


Figure 12. Correlation of the mixing tank gas hold-up data. Dimensionless form.

cosity effect is included in these equations. Hassan and Robinson[16] presented the following type of correlation for ϵ

$$\epsilon = C\left(\frac{Q_G N^2}{\sigma}\right)^z \tag{9}$$

where z and C depend on the geometry and on the concentration of electrolytes. By introduction of effective viscosity into equation (9) we obtain the relationship:

$$\epsilon = C_1\left(\frac{Q_G N^2}{\sigma}\right)^{z_1}\left(\frac{\eta_{ef}}{\eta_w}\right)^{z_2} \tag{10}$$

The effective viscosity in the geometry used in our work was calculated via the equation:

$$\eta_{ef} = K(11.83N)^{n-1} \tag{11}$$

which was introduced by Metzner and Otto[17] and has been confirmed by others[18]. Least-squares analysis of the experimental data plotted in Figure 12 gives the correlating equation:

$$\epsilon = 0.059\left(\frac{N^2 Q_G}{\sigma}\right)^{0.68}\left(\frac{\eta_{ef}}{\eta_w}\right)^{-0.26} \tag{12}$$

which covers the experimental data satisfactorily. A dimensional type of correlation of the same experimental data is:

$$\epsilon = 0.0132 P_G^{0.47} v_G^{0.78} \eta_{ef}^{-0.26} \tag{13}$$

plotted in Figure 13.

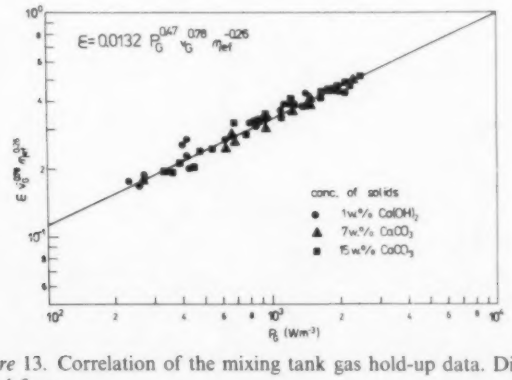


Figure 13. Correlation of the mixing tank gas hold-up data. Dimensional form.

The correlating equations (12) and (13) can be compared with the correlation of Hassan[16] valid for the six-blade flat disc turbine and for standard configuration;

$$\epsilon = 0.114(N^2 Q_G/\sigma)^{0.57}$$

and with the correlation of Rushton[19]:

$$\epsilon = k P_G^{0.47} v_G^{0.53}$$

where k varies between 0.013 and 0.016 depending on vessel geometry. The correlation of Rushton and equation (13) give the same dependence of ϵ on P_G, also the constant is within the same range. The stronger dependence of hold-up on v_G or Q_G in suspensions is understandable.

The higher gas throughput increases the average shear rate in the vessel and in this way contributes to a further decrease in effective viscosity which is not accounted for by equation (11). Since it is expected that η_{ef} approaches the viscosity of a clear solution at very high power inputs, at all solid concentrations, it is understandable that there will be no decrease of ϵ or interfacial area with increasing concentration of solids except if it becomes very large. This might be an explanation of Juvekar and Sharma's data[4] measured in the mixing tank, where they did not detect any decrease in hold-up for particle concentration less than 0.200 kg l^{-1}.

It is worth comparing the correlations for gas hold-up in bubble column and mixing tank. In the bubble column correlation of Bach and Pilhofer, equation (4), no effect of surface tension is included, whereas the correlation of Hassan and Robinson, equation (9), disregards the viscosity effect. In the analysis of experimental data we retained the form introduced by Bach and Pilhofer, since the surface tension was not changed in the experiments of the present work, although it was slightly lower than the surface tension of water due to the presence of dissolved $Ca(OH)_2$. On the other hand the effect of apparent viscosity on the gas hold-up could not be included in the correlation of Hassan and Robinson without introduction of an additional term, which we have done, since the viscosity effect was studied in our work.

Influence of Large Particles on Gas Hold-up and Interfacial Area in Bubble Column

Increase of gas hold-up and of interfacial area in the presence of large solid particles is due to bubble break-up, as observed by Lee et al[5]. The Weber number in the experiments of the present work with 0.4 mm particles

$$We = \frac{\rho_p v_B^2 d_p}{\sigma} \tag{14}$$

was in the range $2.75 \leqslant We \leqslant 5.02$, thus exceeding the critical value $We \simeq 3$ below which no bubble break-up was observed by Lee et al[5]. The measured values of particle density and of surface tension of water saturated with $Ca(OH)_2$ were $\rho_p = 2580$ kg m^{-3} and $\sigma = 60 \times 10^{-3}$ N m^{-1}. The bubble rise velocity calculated

with the aid of the experimental gas hold-up and superficial velocity data

$$v_B = \frac{v_G}{\epsilon} \tag{15}$$

was in the range $0.40 \leqslant v_B \leqslant 0.55\ m\ s^{-1}$.

Under the conditions of our experiments the visual observations showed considerable non-uniformities in concentration of particles in the bubble column, especially at low superficial gas velocities, with higher concentration of particles in the region of the distributor. In this region it appears most of the bubble break-up occurs. By increasing the particle concentration at a certain superficial gas velocity, increase of interfacial area is observed. On the other hand increase of gas velocity at a fixed particle concentration leads to bed expansion and eventually to decrease of interfacial area (Figure 6). No correlation was obtained between gas hold-up, interfacial area and concentration of large solid particles.

CONCLUSIONS

Gas hold-up and interfacial area were measured in a bubble column and gas hold-up was measured in a mixing tank in the presence of small $CaCO_3$ and $Ca(OH)_2$ particles. A substantial decrease in hold-up and interfacial area was observed with increasing concentration of solids in a broad range of gas velocities and power inputs per unit volume. The suspensions of particles were found to behave as non-Newtonian pseudo-plastic fluids with increasing non-Newtonian properties as the concentration of solids increased.

Correlations applicable to Newtonian fluids were modified and used successfully in the correlation of these experimental data. By replacement of the viscosity with effective apparent viscosity the correlating equations for gas hold-up and interfacial area in a bubble column were obtained, equations (6) and (8), in which the effective viscosity was related to the gas superficial velocity by equation (5).

The same approach to correlation of the mixing tank data led to a correlation for gas hold-up expressed in equation (13), or in dimensionless form in equation (12). The effective viscosity being calculated by equation (11).

It appears that a stronger dependence on v_G compared to Newtonian liquids is due to a further decrease in effective viscosity due to velocity gradients caused by rising bubbles.

It is worth noticing that almost the same exponent over η_{ef} was obtained in the correlation of the bubble column and mixing tank data.

Gas hold-up and interfacial area were found to be increased by the presence of large solid particles for which the criterion $We > 3$ applied. No correlation was obtained in this case.

SYMBOLS USED

a	interfacial area	(m^{-1})
$[B_s]$	saturation concentration of OH^- ions in system water/$Ca(OH)_2$	$(mol\ m^{-3})$
D	vessel diameter	(m)
D_A	diffusivity of CO_2 in water	$(m^2\ s^{-1})$
d	impeller diameter	(m)
d_p	particle diameter	(m)
g	gravitational acceleration	$(m\ s^{-2})$
H	Henry's coefficient of solubility	$(mol\ m^{-3}\ bar^{-1})$
K	fluid consistency index	$(Pa\ s^n)$
$k_G a$	gas side mass transfer coefficient	$(mol\ m^{-3}\ s^{-1}\ bar^{-1})$
k_L	liquid side mass transfer coefficient	$(m\ s^{-1})$
k_2	reaction rate constant	$(m^3\ s^{-1}\ mol^{-1})$
N	stirrer speed	(s^{-1})
n	flow behaviour index	$(-)$
P_G	power input per unit volume	$(W\ m^{-3})$
p_A	Partial pressure of CO_2	(bar)
Q_G	gas throughout	$(m^3\ s^{-1})$
R	reaction rate per unit volume of suspension	$(mol\ m^{-3}\ s^{-1})$
v_B	average bubble velocity	$(m\ s^{-1})$
v_G	superficial gas velocity	$(m\ s^{-1})$
We	Weber number $= \rho_p v_B^2 d_p/\sigma$	$(-)$
Greek symbols		
$\dot{\gamma}$	shear rate	$(m\ s^{-1})$
$\dot{\gamma}_a$	average shear rate in the vessel	$(m\ s^{-1})$
ϵ	gas hold-up	$(-)$
η_a	apparent viscosity	$(kg\ m^{-1}\ s^{-1})$
η_{ef}	effective viscosity	$(kg\ m^{-1}\ s^{-1})$
η_L	liquid viscosity	$(kg\ m^{-1}\ s^{-1})$
η_w	water viscosity	$(kg\ m^{-1}\ s^{-1})$
ρ_G	gas density	$(kg\ m^{-3})$
ρ_L	density of liquid suspension	$(kg\ m^{-3})$
σ	surface tension	$(kg\ s^{-2})$

REFERENCES

1. Kürten H. and Zehner P., 1979, *Ger Chem Eng* 2: 220.
2. Hammer H., 1979, *Chem Ing Tech* 51: 295.
3. Wiedmann J. A., Steiff A. and Weinpach P. M., 1980, *Ger Chem Eng* 3: 303.
4. Juvekar V. A. and Sharma M. M., 1973, *Chem Eng Sci* 28: 825.
5. Lee J. C., Sherrard A. J. and Buckley P. S., 1973, in H. Angelino et al. eds. *La fluidisation et ses applications* (Toulouse).
6. Danckwerts P. V. and Sharma M. M., 1966, *The Chemical Engineer* (202): CE244.
7. Morris R. M. and Woodburn E. T., 1967, *S. Afr Chem Proc*, Cp 88.
8. Mashelkar R. A., 1970, *Br Chem Eng* 15: 1297.
9. Carleton A. J., Flain R. J., Rennie J. and Valentin F. H. H., 1967, *Chem Eng Sci* 22: 1839.
10. *Nishikawa M., Kato H. and Hashimoto K.*, 1977, *Ind Eng Chem. Proc Des Dev* 16: 133.
11. Bach H. F. and Pilhofer Th., 1977, *Chem Ing Tech* 49: 435.
12. Akita K. and Yoshida F., 1973, *Ind Eng Chem, Proc Des Dev* 12: 76.
13. Meresmann A., 1977, *Chem Ing Tech* 49: 679.
14. Hikita H., Asai S., Tanigawa K., Segawa K. and Kitao M., 1980, *Chem Eng J* 20: 59.
15. Akita K. and Yoshida F., 1974, *Ind Eng Chem, Proc Des Dev* 13: 84.
16. Hassan I. T. M. and Robinson C. W., 1977, *AIChE J*, 23: 48.
17. Metzner A. B. and Otto R. E., 1957, *AIChEJ*, 3: 3.
18. Calderbank P. H. and Moo-Young M. B., 1959, *Chem Eng Sci* 37: 26.
19. Nagata S., 1975, *Mixing*, p. 350 (Kodansha Ltd, Tokyo).

ADDRESS

Correspondence on this paper should be addressed to Prof. Dr. T. Koloini, Department of Chemistry and Chemical Technology, Edvard Kardelj University, Murnikova 6, P.O.B. 537, 61001 Ljubljana, Jugoslavia.

The manuscript was received 26 May 1983, and accepted for publication after revision 26 September 1983.

VOL. 62 1984

ENHANCED COLLECTION EFFICIENCY FOR CYCLONE DUST SEPARATORS

By M. BIFFIN, N. SYRED and P. SAGE

Department of Mechanical Engineering and Energy Studies, University College, Cardiff

In recent years cyclone dust separators have received renewed interest. Their low constructional costs, and ability to operate at high temperatures and pressures make them prime candidates for use in the proposed new generation of combined cycle power generating systems. For lower temperature applications such as industrial coal fired boilers, enhanced cyclone performance will enable the gas cleaning requirements of a wider range of plant to be met relatively cheaply. This paper describes a novel dust separator which offers higher collection efficiencies, lower pressure drop and an increased resistance to choking—without affecting the advantages of conventional cyclones.

INTRODUCTION

Whilst cyclones have been successfully used for many years throughout the process industries, their grade collection efficiency falls off dramatically for particles smaller than about 5 μm and this limits their application. To achieve high collection efficiencies for these small particles, alternative clean-up systems (such as bag filters, scrubbers and electrostatic precipitators) are used in preference for, or in addition to, cyclone separators.

At high temperatures (in excess of 700°C) these alternative systems either fail or require prohibitively expensive technology and techniques to extend their operating range. Cyclones can readily be used at high temperatures and pressures provided that they are manufactured from appropriate materials. Indeed, ceramic units[1] have already been employed at temperatures in excess of 1000°C.

The successful development of combined cycle power generating systems[2] depends on producing gas clean-up equipment capable of removing all particles larger than 5 μm diameter and operating continuously at pressure of up to 20 bar and temperatures up to 1000°C. Cyclones would be ideal for this application if they could be adapted to meet the stringent requirements set by the manufacturers for the allowable level of particulates at entry to their gas turbines. A recent estimate[3] is 4.6×10^{-3} g m^{-1} with General Electric further stipulating that all particles greater than 5 μm are removed[4]. This specification may possibly be relaxed when developments in gas turbine design and materials allow. The limited experience with ceramic materials for turbine blades suggests that these have much better erosion resistance than any metallic elements[5], and would allow higher inlet temperatures producing even higher operating efficiency[6].

The present specification is generally held to be beyond conventional cyclone technology. Nevertheless, cyclones offer simple design, relatively cheap construction, low maintenance and, more importantly, use proven technology—having already been used at high temperatures and pressures in the fluidised catalytic cracking units of the petroleum industry[7].

Experiences with cyclones at high temperatures and pressures have produced many conflicting results. Parker et al[8] show that the collection efficiency is reduced at high temperatures and although it is restored to a certain degree at higher pressures (probably due to density and viscosity changes), they doubt the applicability of cyclones for use at high temperatures. Conversely, following the results of their 1000 h evaluation trials, Roberts et al[9] suggest that cyclones are already capable of adequately protecting gas turbines.

Any improvements in cyclone efficiency however, would be beneficial. In the high temperature and pressure environment of the Combined Cycle Power Generating System, turbine life would be extended and the tail-end stack gas clean-up required to meet emission regulations would be reduced.

At lower temperatures, of boiler applications there are also advantages to be gained from increased performance. Systems could be designed to meet statutory limits without the need to use electrostatic precipitators, bagfilters or venturi scrubbers, which are respectively 9, 4.5 and 4 times more expensive in capital, and also have higher running costs than cyclone separators[10]. Where present cyclone separators already meet emission requirements, the number of cyclones can be reduced, with a corresponding reduction in cost and complexity.

The principle of the conventional cyclone has been largely retained, therefore any methods already proposed to reduce pressure drop or increase collection efficiency could be incorporated (e.g. the use of scroll inlets), although the effects will be less marked because of the increased baseline efficiency of the new design.

IMPROVING COLLECTION EFFICIENCY

For a particle to be collected, it must not only be displaced from the flow, but also removed from the displacement region. Thus the problem of improving collection efficiency not only involves improving the particle displacement mechanism but also of removing the displaced particle from the separator before it can be re-entrained.

In a conventional cyclone, swirl imparted to the gas flow, centrifuges particles to the wall of the separator where they are swept down to a hopper and collected.

© Institution of Chemical Engineers

The main particle-dispalcement mechanism in this case is a balance between the centrifugal force field and the radially inwards Stokes drag force on a particle.

The resulting radial drift velocity, V_r, towards the wall is given by the equation.

$$V_r = \frac{2}{9}\frac{d_p^3 \rho w^2}{\mu r} \quad (1)$$

where

d_p = particle diameter
ρ = particle density
w = tangential velocity
μ = gas viscosity
r = radius

The effects of turbulence on collection efficiency are complex but generally lead to a reduction in separation performance since the turbulence provides an effective mixing and transport mechanism between inlet and outlet of the separator. For a conventional cyclone this flow can be satisfactorily described using the constant 'back-mixing model' derived by Leith and Licht[11], to give an expression for dust removal efficiency, η, of:

$$\eta = 1\text{-}\exp\left\{-2\left[\frac{\rho}{9\mu}\left(\frac{d_p w_{in}}{R}\right)^2 (n+1)t_s\right]^{1/(2n+2)}\right\} \quad (2)$$

where

ρ = particle density
d_p = particle diameter
w_{in} = inlet gas velocity
n = vortex exponent (in wr^n = constant)
t_s = residence time
μ = gas viscosity
R = radius of cyclone

For a given particle density, gas temperature and pressure, this reduces to

$$\eta = 1\text{-}\exp\{-2[K(d_p w_{in}/R)^2]^{1/(2n+2)}\} \quad (3)$$

The expression is relatively insensitive to the vortex exponent n and thus increased efficiency can only be achieved by reducing the radius (i.e. diameter of cyclone) or increasing the tangential inlet velocity. The latter is only effective up to a certain point with conventional cyclone separators. Particulate re-entrainment, attrition or de-agglomeration, rebound effects, and vortex core precession all combine to reduce any corresponding improvement in separation efficiency for higher inlet velocities[12]. Erosion of the cyclone wall may also be increased, especially near the inlet and in the lower part of the cone. Penalties would also be paid in terms of pressure drop (since for a given geometry ΔP is proportional to w_{in}^2).

The alternative to increasing velocity is to reduce the diameter. It is well-known[13] that the collection efficiency of cyclones rapidly declines once the main barrel diameter exceeds 300 mm keeping the diameter as small as possible is therefore recommended. Small cyclones, however, are susceptible to plugging in the cone. Indeed, this has been cited[14] as the primary cause of operating problems in a Pressurised Fluidised Bed Combustion Pilot Plant in the USA. A compromise must therefore be made between efficiency and the necessity to avoid plugging.

In industrial applications, where large volumes of gases are to be cleaned, many smaller cyclones are manifolded together in parallel—introducing flow distribution and maintenance problems. This is further complicated by the fact that the pressure drop across a cyclone is affected by the dust loading due to apparent viscosity changes[15]. The randomly occurring pressure differential thus generated produces a non-uniform flow distribution. The resulting cross-flow through cyclones sharing a common hopper seriously affects the efficiency of the unit. Similarly, any ingress of air into the dust hopper or cyclone will disrupt the separation process. This is often difficult to detect and control, for even if a positive pressure is maintained at inlet and outlet, a subatmospheric pressure may exist in the dust hopper due to the low pressure region in the vortex core. Removal of a blowdown stream of gas with the dust from the collecting hopper is beneficial and is advocated in some designs to aid collection efficiency.

A new type of cyclone separator has been produced at Cardiff which combines two stages in one compact unit. The primary stage removes the larger particles from the flow before the gas stream enters a conventional small cyclone, where the smaller particles are captured.

The reduced dust burden in the centre reduces erosion in the lower part of the cone and allows a smaller diameter central cone to be used without fear of choking. The Cardiff separators are described in the next section.

NOVEL CYCLONE DESIGN

A simplified diagram of one of the advanced cyclone separators is shown in Figure 1. It consists of a central standard cyclone cone, surrounded by an annular chamber. The gas is admitted to this annulus by means of a tangential inlet. Attached to the outer wall is a cylindrical chamber (a vortex collector) whose circumference just intersects that of the annulus[16]. A weak forced vortex is generated in the chamber by viscous

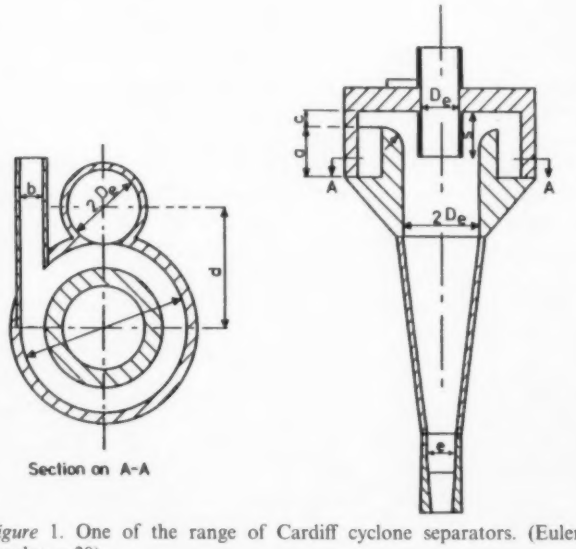


Figure 1. One of the range of Cardiff cyclone separators. (Euler number = 20).

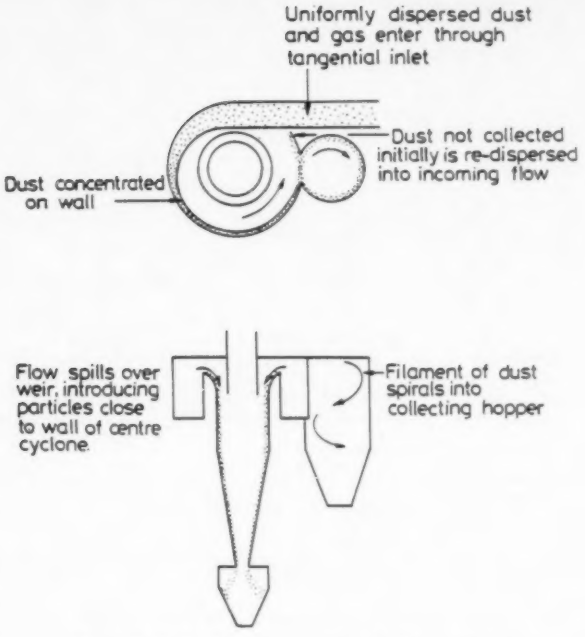


Figure 2. Collection processes within the separator.

adhesion—with no nett gas flow into or out of the chamber.

A significant amount of particulates are removed from the annulus by the vortex collector before the gases and remaining particles enter the main body of the cyclone to be separated in the normal manner. The collection principle is shown diagrammatically in Figure 2. Larger particles become concentrated in a thin boundary layer region close the outer wall and, on encountering the vortex collector, continue tangentially into the low velocity region, which allows the particles to spiral downwards into the collecting hopper. The large opening makes it suitable for removing a wide size-range of particles—from less than 10 μm to wood chips and shavings—without fear of blocking. This reduction of dust concentration (by as much as 80%), and the absence

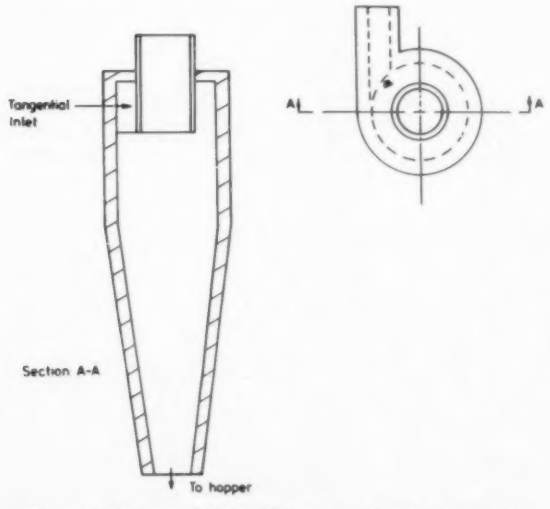


Figure 3. Stairmand high efficiency cyclone dust separator.

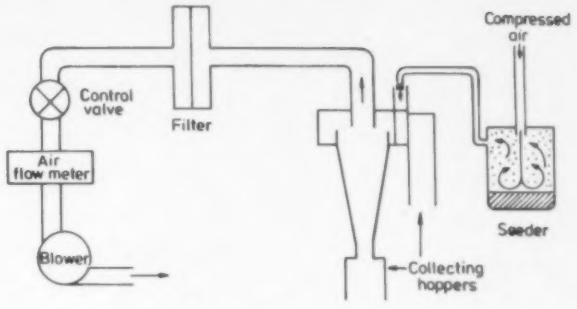


Figure 4. Cyclone testing apparatus.

of any large particles in the central cone ensures that plugging in the lower part of the cone does not occur and also reduces abrasion in this region.

Dividing the outer annulus from the central cone is a 'weir'. This serves several purposes. The residence time of the gas within the separator is increased, allowing more time for particles to be separated. It also provides a region where the dirty incoming gases can be partially cleaned without contaminating the clean exhaust gases. Further, it allows swirling flow to spill over into the central cyclone region around the whole periphery, producing a much more symmetrical, low-turbulence vortex structure. Thus turbulence levels (a major by-pass transport mechanism) are reduced, and particles are introduced close to the cone wall which aids separation[17].

Initial tests, carried out at ambient temperatures and pressures have shown that the new Cardiff separator achieves consistently higher collection efficiencies than a comparable Stairmand design (Figure 3). The experimental apparatus is shown schematically in Figure 4. The test media (in this case Fullers' Earth) was evenly dispersed in the inlet air. This was drawn through the cyclone where the majority of particles were removed. A filter in the exit collected any fine particles which were not captured by the cyclone.

The dust entering, collected by or escaping the cyclone was weighed and particle size distributions obtained using a Malvern ST 2200 laser diffraction particle sizer.

EXPERIMENTAL RESULTS

It can be seen from Figure 5 that the collection efficiency of the new design of cyclone dust separator is generally insensitive to variations in dust or gas loading. Figure 6 shows that the vortex collector, by reducing the dust loading on the central cyclone also decreases the total changes in pressure drop with dust loading compared to a conventional cyclone.

These features are particularly important where several cyclones are grouped together, since they ensure an even flow distribution between the individual units. Moreover, the outer vortex collector operates at a positive pressure—typically 80–90% of the inlet pressure. Since the vortex collector operates at a static pressure which is close to inlet pressure, it is less affected by changes in system pressure drop or dust loading, thus enabling large numbers or banks of these devices to be assembled into multi-cell units with no cross-flows be-

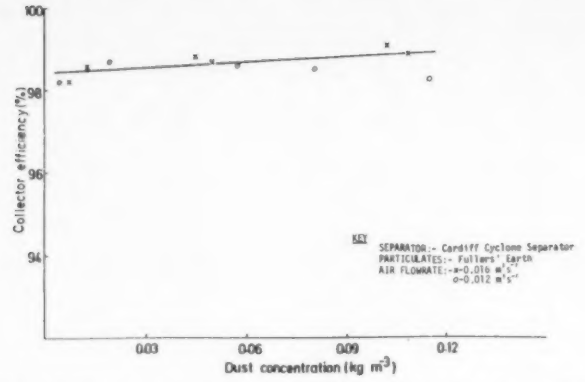


Figure 5. Comparison of collecting efficiency with dust loading for Cardiff separator.

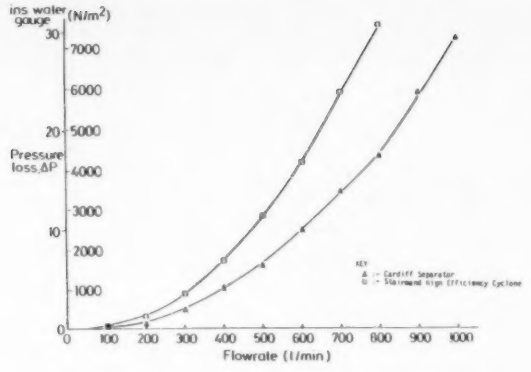


Figure 7. Variation of pressure drop with flowrate.

tween the individual cells. Any leaks in the system are also quickly observed and can be rectified, restoring the collection performance.

Removing dust in the vortex collector also allows the separator to be used where there is a danger of sudden surges of high dust concentration. The dust is removed effortlessly by the vortex collector without choking, change in pressure drop or collection efficiency.

An important consideration in any clean-up system is the pressure drop. The pressure/flowrate characteristic is shown in Figure 7 for the Cardiff cyclone separator, along with that for a similar High Efficiency Stairmand cyclone (based on exit diameter and throughput). It can be seen that for any given flowrate the pressure drop across the Cardiff cyclone is consistently lower. This represents a significant saving in power consumption especially since the Cardiff separator combines two stages in one unit in order to achieve improved collection efficiencies.

Lower pressure drops are often associated with a lower collection efficiency, since the pressure drop reflects the strength of the vortex, in addition to inlet and outlet losses. It can be seen from Figure 8 however that the collection efficiency of the Cardiff cyclone is greater than that of a similar High Efficiency Stairmand cyclone both when operated at the same volume throughout and for the same inlet velocities. The test media used in the characterisation of both these separators was Fullers' Earth, having a median diameter of around 10 μm, with a significant amount less that 5 μm as illustrated in Figure 9. The exit diameter of each separator was 30 mm and at this scale, the overall collection efficiencies of Cardiff and Stairmand cyclones were 96.6% and 96.0% respectively.

Following these encouraging results, the National Coal Board installed a pair of Cardiff cyclones (ten times the size of the laboratory units) on a 2.8 MW fluidised bed. Preliminary measurements show that the overall collection efficiency of the separators is 96%—easily meeting statutory emission levels, with an emission rate of only 2.4 kg h.$^{-1}$

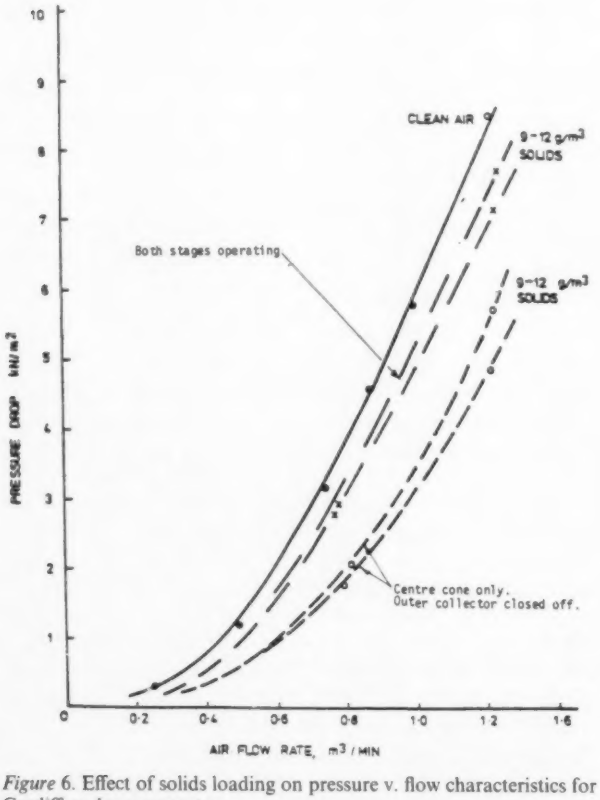


Figure 6. Effect of solids loading on pressure v. flow characteristics for Cardiff cyclone separator.

CONCLUSIONS

The new Cardiff cyclone separator offers many advantages over conventional cyclones—higher collection efficiencies, lower pressure drops and less tendency to

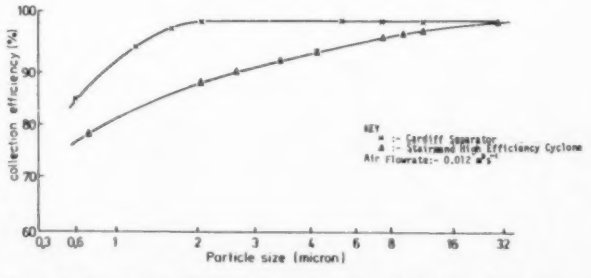


Figure 8. Fractional efficiencies for Cardiff and Stairmand separators.

VOL. 62 1984

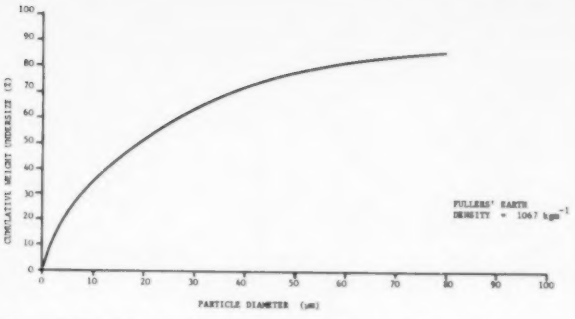


Figure 9. Particle size distribution of fuller's earth.

choking. The combination of two cleaning stages into one compact unit is also a useful feature, reducing pipework joints, and manifolding as well as power consumption.

Since larger particles are removed in the outer annulus, higher velocities can be tolerated in the central cone to remove the smaller particles, without the associated problems of increased erosion and particle bouncing inherent in other designs. Small cyclones can thus be used to increase separation efficiency without fear of plugging or particle bouncing effects due to high dust loadings and high velocities. In addition, fluctuations in gas flow rates and particle concentration can be tolerated with little effect.

The principle of the conventional cyclone has been largely retained, therefore traditional dust handling equipment can be retained. Moreover, any methods already proposed to reduce pressure drop or increase collection efficiency can be incorporated to produce similar results.

The enhanced efficiency of these dust separators allows conventional coal combustion systems to meet existing and even more stringent emission regulations without recourse to expensive technology.

The enhanced efficiency of these dust separators will allow inertial collectors to meet the gas cleaning requirements of a wider range of industrial coal-fired plant relatively cheaply. There is also potential for their use in higher temperature applications such as combined cycle power generation systems, where protection of turbines from particulates is also a consideration.

ACKNOWLEDGEMENTS

The authors gratefully acknowledge the support of the Science and Engineering Research Council in this work as well as the National Coal Board. The view expressed are those of the authors and not necessarily those of the National Coal Board.

REFERENCES

1. Stairmand, C. J., 1980, *Filt Sep*, 17(3):220–261.
2. Robson, B., and Thurlow, G. G., 1979, *J Inst Energy*, June, 94.
3. Meyer, J. P., and Edwards, M. S., 1978, *Oak Ridge National Laboratory Report*, ORNL/TM-6072:207.
4. Brooks, R. D., Peterson, J. R. and Weth, G. 1977, *Pr Intersoc Energy Conv Eng Conf, Washington* (Am Nuc Soc) 704–711.
5. Stringer, J., Ehrlich, S. and Slaughter, W. S. 1980, *J Eng Power, Trans ASME*, 102: 468–475.
6. Stasa, F. L., and Osterle, F., 1981, *J Eng Power, Trans ASME*, 103: 572–581.
7. Batel, W., 1976, *Dust Extraction Technology* (Technicopy, Stonehouse, Gloucester).
8. Parker, R., Jain, R., and Calvert, S., 1981, *Env Sci Tech*, 15(4): 451–458.
9. Roberts, A. G., Raven, P., Phillips, R. N., Barker, S. N., Pillai, K. K. and Wood, P. 1980 *Pr Conf Fluidised Combustion* (Inst Energy, London) paper III-1.
10. Gibson, J., 1983, *Pr Conf Coal New Ind Opport*, (Inst Energy, London).
11. Leith, D., and Licht, W., 1972, *Air Pollution and its Control, AIChE Symp Ser*, 68 (126): 196–206.
12. Jackson, R., 1963, *Mechanical Equipment for Removing Grit and Dust from Gases* (Br Coal Utilisation Res Assoc, Cheltenham) 263.
13. Walton, W. H., 1974, in Dorman, R. G., ed, *Dust Control and Air Cleaning*, (Pergamon Press, Oxford) ch 7.
14. Morrison, G. F., 1979, *Report* ICTIS/TR03 (IEA Coal Research, London).
15. Sproull, W. T., 1966, *J Air Pollut Control Assoc*, 16(8): 439–441.
16. Biffin. M., and Syred, N., 1982, *Filt Sep*, 20(3): 189–191.
17. Boysan, F., Ayers W. H., and Swithenbank, J., 1982, *Trans I Chem E*, 60(4): 222–230.

ADDRESSES

Correspondence on this paper should be addressed to Mr M. Biffin, Department of Mechanical Engineering and Energy Studies, University College Cardiff, Newport Road, Cardiff CF2 1TA. P. Sage is with the National Coal Board Coal Research Establishment, Stoke Orchard, Cheltenham.

The manuscript was received 11 *May* 1983 *and accepted for publication* 5 *September* 1983.

SHORTER COMMUNICATION

THERMAL DECOMPOSITION OF TRICHLOROTRIFLUOROETHANE (R113) UNDER STATIC AND FLOW CONDITIONS

By P. SRINIVASAN, V. R. PATWARDHAN, S. DEVOTTA and F. A. WATSON (FELLOW)

Department of Chemical and Gas Engineering, University of Salford

Experimental results are presented for the decomposition of R113 as a function of time in the presence of metallic copper and steel when tested statically at constant temperature or under flow conditions with cyclically varying temperatures. It is shown that the rate constants for the irreversible decomposition of R113 to R1113 under either method of operation may be estimated from $\ln k = 3.1615 - 4098/T$, between 220°C and 400°C, with a correlation coefficient of 0.97. Results are also presented for static, constant temperature tests with the additional presence of either a conventional naphthenic lubricating oil, a synthetic alkylbenzene oil or a synthetic hydrocarbon oil. These show that the rate of decomposition of R113 is increased with the naphthenic oil having the greatest effect and the synthetic hydrocarbon oil the least.

INTRODUCTION

R113 ($FCl_2C.CClF_2$, trichlorotrifluoroethane) is potentially useful as a working fluid for both heat pump systems and Rankine power cycle systems. The critical temperature of R113 is 214.1°C and its critical pressure is 31.4 bar so that it is potentially suitable for use in condensing systems in which heat is transferred at temperatures up to about 200°C at relatively low pressures.

Holland and co-workers[1,2] have evaluated various theoretically achievable thermodynamic paramters for heat pump and Rankine cycle systems using R113 as the working fluid. Whether R113 is suitable for use in a given system additionally depends on its thermal stability under the chosen operating conditions.

The rate of decomposition of R113 has been the subject of several experimental investigations[3-8]. It is difficult to draw general conclusions from the published results as they are not always in agreement. This is due, in part, to the adoption of different criteria for determining the extent of decomposition. The present paper presents the results of an investigation of the thermal stability of R113 in contact with various combinations of materials likely to be found in working systems under both static and cyclically varying temperature conditions. These materials include steel, copper and three types of lubricating oil.

EXPERIMENTAL

The equipment, experimental procedure and analytical techniques used were similar to those used in previous investigations[9,10]. Steel was always present, being the material of construction of the reaction vessel used in the static experiments and of the piping and heat exchanger of the circulating flow equipment. To these were added copper and/or one of three lubricating oils. The oils chosen as being typical of their class were a normal naphthenic mineral oil, a synthetic alkylbenzene based oil (referred to as SAB oil) and a synthetic hydrocarbon oil (referred to as SHC oil). Experiments were carried out at constant temperatures of 220°C, 240°C, 260°C and 280°C under static conditions for reaction times up to 720 h.

When operating under flow conditions the temperature of the circulating R113 was raised to 140°C in a heat exchanger and was then allowed to impinge on a copper target plate maintained within ± 2°C of a preset temperature in the range 360°–440°C. The R113 was then cooled in a second heat exchanger to 100°C before returning via a compressor to the original heat exchanger. In this way, the characteristics of a vapour compression heat pump cycle were simulated with the target representing the high temperatures reached at the valves or the piston crown of the compressor. Since the compressor used required lubrication and had brass and copper parts, combinations of materials were necessarily involved. However, every effort was made to avoid lubricating oil being carried onto the target and the result of any experiments where carry over of oil was suspected was discarded. Because of the effect of the relatively high temperatures of the target, sufficient data were obtained within a period of 25 h to establish the percentage decomposition of R113 with time at a given temperature. The advantage of the flow method over the static method for the rapid elimination of unsuitable combinations of working fluid, lubricant and materials of construction is clear. The progress of decomposition was monitored by the analysis of samples taken at regular time intervals. A Pye Unicam 204 Gas Chromatograph was used for the analysis.

RESULTS

The percentage decomposition of R113 with time under static conditions in the presence of steel and

© Institution of Chemical Engineers

VOL. 62 1984

copper is presented in Figure 1 with temperature as paramter. For each temperature the results are well represented statistically by a straight line passing through zero decomposition at zero time. Such a relationship implies a constant rate of decomposition. It can be seen that this rate, as indicated by the slope of the line, increases progressively with temperature.

The effect of adding lubricating oil to the combination of steel and copper is shown by the typical results presented in Figure 2. As previously reported for other working fluids, the presence of lubricating oil increases the rate of decomposition significantly in all cases[9,10]. For R113 it appears that SHC oil has the least and mineral oil the most influence on the rate of decomposition. It appears that SAB, although not as good as SHC, is as good at 260°C as a standard mineral oil is at 220°C. Stabilities of working fluids in the presence of lubricating oils are the subject of further work.

Results obtained under circulating conditions are presented in Figure 3. It can be seen that for each of five target temperatures between 360°C and 440°C the data can be represented by a straight line. The temperature of the lubricating oil used in the system should not significantly exceed 140°C, except briefly during the compression stroke, and the oil was prevented from reaching the high temperature target. It is to be expected, therefore, that this set of results could closely represent the results which would be obtained in the absence of lubricating oil but in the presence of the steel of the equipment and the copper of the target.

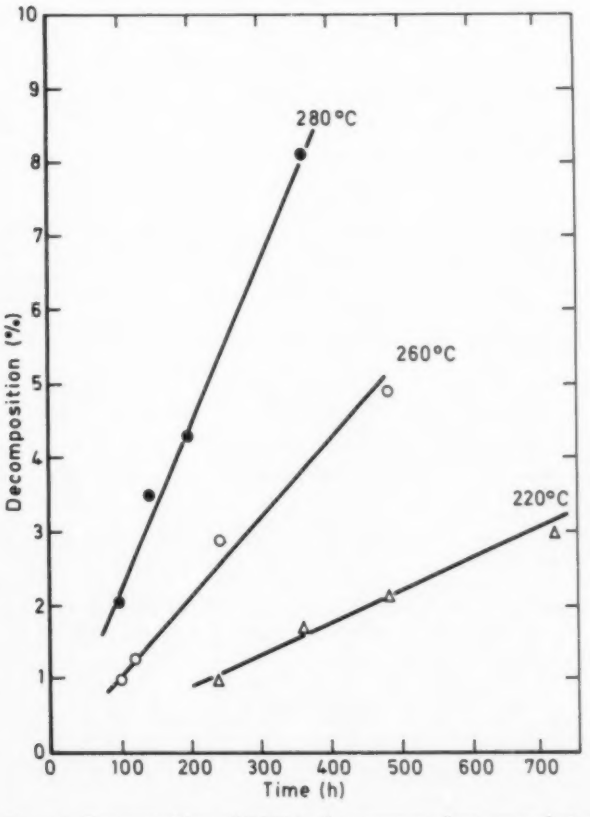


Figure 1. Decomposition of R113 in the presence of copper and steel under static conditions.

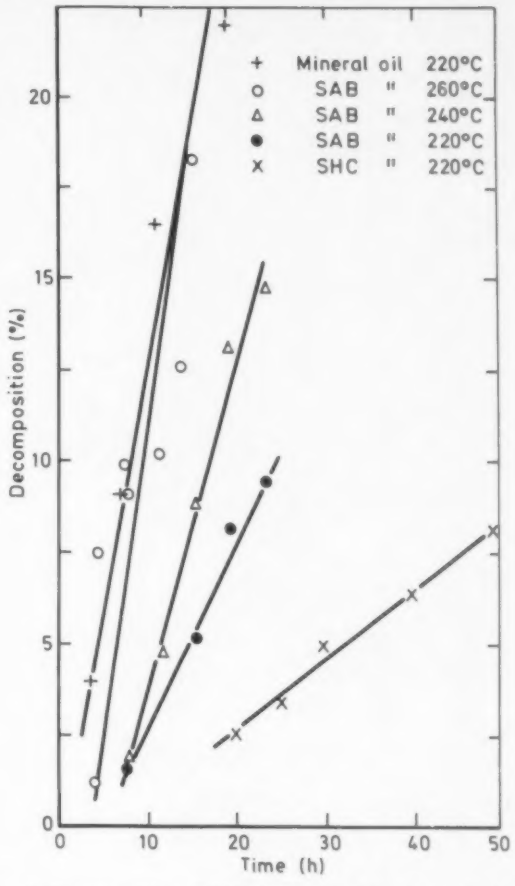


Figure 2. Decomposition of R113 in the presence of copper, steel and lubricating oils under static conditions.

Analysis of samples obtained under static conditions by means of gas chromatographic and mass spectrographic analysis showed that the major decomposition product of R113 was R1113 (F_2C: CClF, chlorotrifluoroethylene) in all the cases. The presence of R123 (FClHC.$CClF_2$, dichlorotrifluoroethane) was also confirmed but as R123 was also present as an impurity in the R113 supplied no particular conclusion can be drawn from this observation. When lubricating oil was present further decomposition products were identified. These included R1123(F_2C:CHF), R1243(CH_3.FC:CF_2), R133($FH_2C.CClF_2$ and $F_2HC.CHClF$). It is to be expected that kinetic analysis of the decomposition of R113 in the presence of lubricating oils will be difficult. However, in the absence of lubricating oil both static and flow tests suggest a simple mechanism for the breakdown, namely

$$\underset{\text{(R113)}}{F\,Cl_2C.CCl\,F_2} \rightarrow \underset{\text{(R1113)}}{F\,ClC:C\,F_2} + Cl_2 \qquad (1)$$

The linear relationships of Figures 1 and 3 imply that the decomposition reaction is zero order with respect to R113. The slopes of the lines of Figures 1 and 3 were used to obtain reaction rate constants and these values are presented in Figure 4 in the form of an Arrhenius plot. A statistically fitted straight line based on all the data is also presented in Figure 4 which suggests that the results from the static and flow tests may be accounted

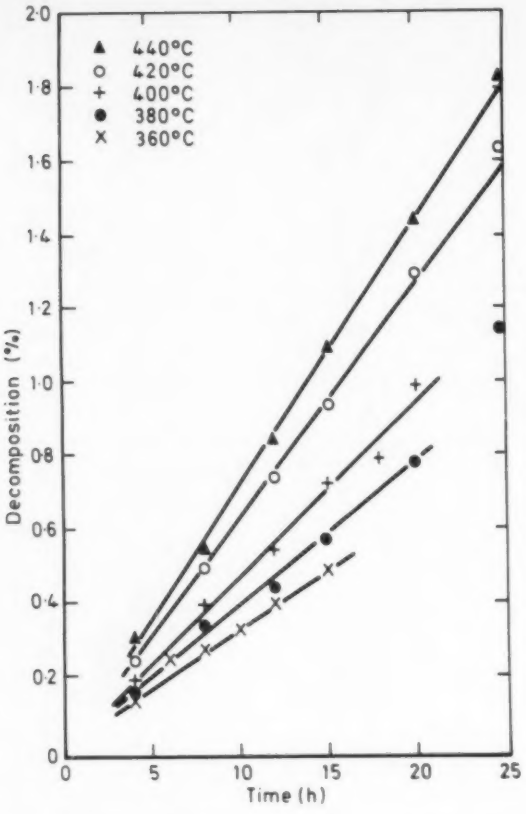


Figure 3. Decomposition of R113 circulating between 100°C and 140°C with a copper target at various temperatures.

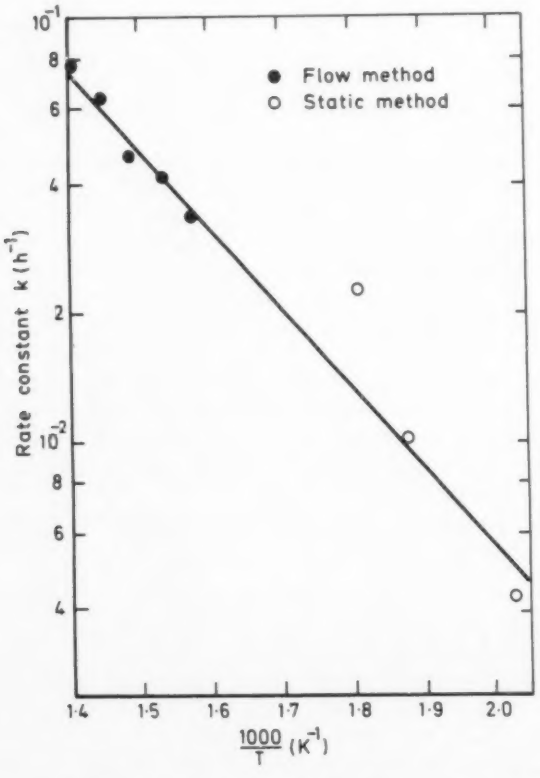


Figure 4. Combined Arrhenius plot for the decomposition of R113.

Table 1. Extrapolated time (days) required for the decomposition of R113 in the presence of copper and steel but in the absence of lubricating oil

Temp. (°C)	Decomposition (mole per cent) 1%	2%	5%	10%
100	104	208	520	1040
125	52	104	208	520
150	28	56	140	280

for by the same breakdown mechanism. The combined data cover the temperature range $T = 220°C$ to 440°C and the rate constants, k, in this range are represented by equation (2) with a correlation coefficient of 0.97.

$$\ln k = 3.1615 - 4098/T \quad (2)$$

where k is in h^- and T in K. It is to be expected that equation (2) should be applicable at temperatures below 220°C.

The use of equations similar to (2) for the estimation of the life of a working fluid in a vapour compression heat pump using an unlubricated compressor was illustrated in an earlier communication[11]. Typical working time values for R113 so calculated are presented in the Table. Since the presence of any lubricating oil currently available will shorten this working life, any system for which these times are unacceptable can be eliminated form further experimental evaluation. It follows that the use of the flow equipment in conjunction with suitable analytical techniques should greatly reduce the time and cost required for the development of heat pump and Rankine cycle fluids which appear to be thermodynamically suitable for a given purpose.

VOL. 62 1984

ACKNOWLEDGEMENTS

The authors wish to thank the Science and Engineering Research Council, UK for financial support. Thanks are also due to Professor F. A. Holland, Chairman of the Department of Chemical and Gas Engineering, University of Salford, UK for his active involvement and continued interest in and support of this work.

REFERENCES

1. Holland, F. A., Watson, F. A. and Devotta, S., 1982, *Thermodynamic Design Data for Heat Pump Systems* (Pergamon Press, Oxford, U.K.)
2. Adefila, S. S., Devotta, S. and Holland, F. A., 1983, *J. Heat Recovery Systems*, 3(2): 103–107.
3. Callighan, J. A., 1971, *Heating, Piping, Air Conditioning*, 43(9): 119–126.
4. Eiseman, B. J. Jr., 1964, *ASHRAE Trans*, 69: 371–379.
5. Giolito, F. and Mide Moncult, 1982, *Proc Int Conf Ind Appl Heat Pumps* (BHRA, Cranfield, UK).
6. Parmelee, H. M., 1965, *ASHRAE Trans*, 71(1): 154–161.
7. Snider, K. L., 1967, *ASHRAE J* 9(11): 54–58.
8. Walker, W. O., Rosen, S. and Levy, S. L., 1962, *ASHRAE Trans*, 4(8): 59–72.
9. Abbas, S. P., Srinivasan, P., Devotta, S. and Watson, F. A., 1981 *Heat Pumps, Energy Savers for the Process Industries*, (IChemE North West Branch) 7.1–7.13.
10. Watson, F. A., Abbas, S. P., Srinivasan, P. and Devotta, S., 1982, *Proc. Int Conf Ind Appl Heat Pumps* (BHRA, Cranfield, UK).
11. Srinivasan, P., Devotta, S. and Watson, F. A., 1984, *Chem Eng Res Des.*, 62: 57–59.

ADDRESSES

Correspondence on this paper should be addressed to Dr S. Devotta, Department of Chemical and Gas Engineering, University of Salford, Salford M5 4WT.

The manuscript was received 29 *November* 1983 *and accepted for publication* 21 *December* 1983.

CORRESPONDENCE

From
Dr J. J. J. Chen
Department of Mechanical Engineering
University of Hong Kong
Hong Kong

Hills[1] showed that his data for the radial voidage distribution in a two-phase bubbly gas–liquid upward flow system scatter about a single curve represented by the following empirical polynomial equation.

$$\frac{\varepsilon}{\bar{\varepsilon}} = 1.74\left(1-\frac{r}{R}\right)^{0.42} - 0.22\left(1-\frac{r}{R}\right)^{4.07} \tag{1}$$

where ε is the voidage, $\bar{\varepsilon}$ the mean voidage, r the radial distance and R the tube radius.

Chen et al.[2] have shown that the radial voidage distribution may be represented by the Prandtl type of power-law equation

$$\frac{\varepsilon}{\varepsilon_c} = \left(1-\frac{r}{R}\right)^{1/n} \tag{2}$$

where ε_c is the voidage at the tube axis, and n the power-law exponential index.

Equation (2) had been used with success by a number of writers including Bankoff[3] and Zuber[4] who showed that the Armand equation[5], which is a limiting case of the Nicklin equation[6], may be derived from equation (2). See also Chen and Spedding[7], Zuber and Findlay[8]. It is possible to determine the mean voidage $\bar{\varepsilon}$ from equation (2) by the following integral

$$\bar{\varepsilon} = \frac{1}{\pi R^2}\int_0^R 2\pi r\varepsilon \, dr \tag{3}$$

Substitution of equation (2) into equation (3) gives, after rearranging,

$$\frac{\bar{\varepsilon}}{\varepsilon_c} = \frac{2}{R^2}\int_0^R r\left(1-\frac{r}{R}\right)^{1/n} dr \tag{4}$$

The solution of equation (4) is[9]

$$\frac{\bar{\varepsilon}}{\varepsilon_c} = \frac{2n^2}{(1+n)(1+2n)} \tag{5}$$

Eliminating ε_c between equations (2) and (5) gives

$$\frac{\varepsilon}{\bar{\varepsilon}} = \frac{(1+n)(1+2n)}{2n^2}\left(1-\frac{r}{R}\right)^{1/n} \tag{6}$$

Figure 1 shows equation (6) with $n = 3$ and $n = 5$ as well as equation (1). Equation (6) with $n = 3$ is nearly identical with equation (1) and represents well the voidage distribution data of Hills[1]. Because of the success and wide acceptance of the Armand[5], Bankoff[3] and Nicklin[6] equations in two-phase flow studies, all of which may be derived from the power-law distribution, equation (6) is therefore preferred over the empirical equation given by Hills[1].

Furthermore, Hills[1] observed that the voidage distribution when slugging occurs does not greatly alter the voidage distribution and the data is equally well represented by equation (1), and hence equation (6). This provides further justification for the use of the Armand equation[5] for both bubbly and slug flows as shown by Chen and Spedding[7].

Hills[1] also showed that the velocity profile obeys the one-seventh power law when measured using a Pitot-static tube although this was not borne out by the results shown which are obtained using the Pavlov tube. The reasons for the discrepancy have already been discussed[1]. The one-seventh power velocity profile is consistent with the derivation of the Nicklin equation[6] which require that $U_c/\bar{U} = 1.2$, i.e., that ratio of the centre-line velocity to the mean velocity ($U_c/\bar{U}$) is equal to 1.2. By considering the one-seventh power law

$$\frac{U}{U_c} = \left(1-\frac{r}{R}\right)^{1/7} \tag{7}$$

where U is the point velocity, the ratio ($\bar{U}/U_c$) may be obtained by writing, from continuity, the average velocity $\bar{U}$ as

$$\bar{U} = \frac{1}{\pi R^2}\int_0^R 2\pi r U \, dr \tag{8}$$

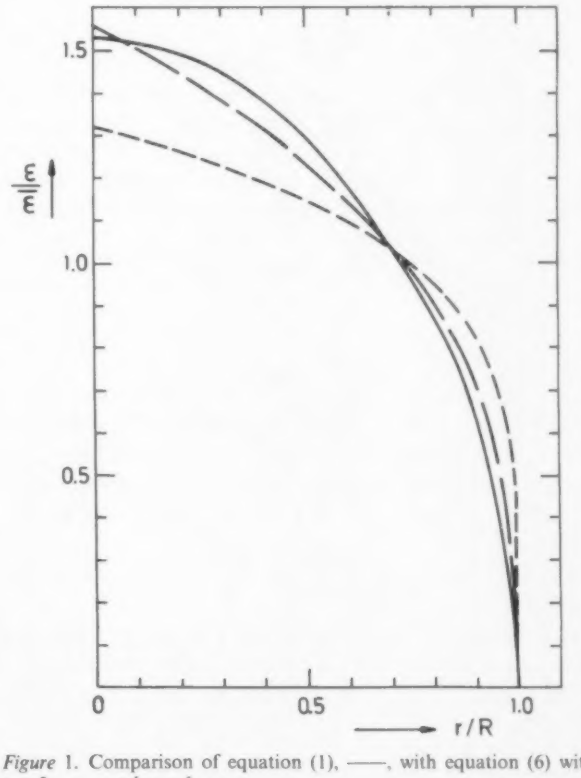


Figure 1. Comparison of equation (1), ——, with equation (6) with $n = 3$, – – –, and $n = 5$, – – – –.

Substituting equation (7) into (8) and rearranging gives

$$\tfrac{1}{2}R^2\frac{\bar{U}}{U_c}=\int_0^R r\left(1-\frac{r}{R}\right)^{1/7}\mathrm{d}r \tag{9}$$

By following equations (3), (4) and (5) but substituting U for ε, then $(U_c/\bar{U})$ is simply given by the reciprocal of the right hand side of equation (5) when $n = 7$, i.e. 1.22.

Comparison of equation (9) with equations (2) and (3) of Hills[1], implies that

$$\frac{\bar{U}}{U_c}=\sqrt{k} \tag{10}$$

where k is a parameter employed by Hills[1].

Now, Nicklin derived the following equation for slug flow

$$U_s=\Gamma(U_{GS}+U_{LS})+0.35(gD)^{1/2} \tag{11}$$

where U_s is the velocity of the slug and consists of two components. U_{GS} and U_{LS} are the superficial gas and liquid velocities respectively, D is the tube diameter and g the acceleration due to gravity. The first term on the RHS is due to the motion of the liquid while the second term is the characteristic rising velocity of an infinitely long bubble in a close tube attributed to Davies and Taylor[10] and Dumitriscu[11]. For upward flow, Γ was the ratio of the centre line velocity to the average velocity, i.e. $(U_c/\bar{U})$ and for Reynolds number greater than 8000, Γ was determined to be 1.2 experimentally.

Because of the relationship given by equation (10), one gets

$$\sqrt{k}=1/\Gamma \tag{12}$$

The mean voidage for slug flow may be obtained from equation (11) as

$$\bar{\varepsilon}=\frac{U_{GS}}{\Gamma(U_{GS}+U_{LS})+0.35(gD)^{0.5}} \tag{13}$$

Nicklin also pointed out that for bubbly flow, U_B, the rising velocity of bubbles in still water should be used instead of $0.35\ (gD)^{0.5}$. See also Martin[12]. Lorenzi and Sotgia[13] and Arosia et al[14] in downward bubbly flow in a 100 mm diameter test section used the value for U_B as given by equation (14) which was also recommended by Zuber and Findlay[8] for vertical upward flow

$$U_B=B\left[\frac{\sigma g(\rho_L-\rho_G)}{\rho_L^2}\right]^{1/4} \tag{14}$$

where σ is the surface tension, and ρ_L and ρ_G the densities of liquid and gas respectively. The value for B was 1.41 and 1.53 according to Levich[15] and Harmathy[16] respectively. For the air–water system, U_B as calculated by equation (14) may be taken as $0.24\ \mathrm{m\,s^{-1}}$. Thus, Nicklin's equation for upward air–water bubbly flow becomes

$$\bar{\varepsilon}=\frac{U_{GS}}{\Gamma(U_{GS}+U_{LS})+0.24} \tag{15}$$

In either equation (13) or (15), if the first term in the denominator is dominant, the equation reduces to a form similar to the Armand equation given as equation (16)

$$\bar{\varepsilon}=\frac{0.83\,U_{GS}}{U_{GS}+U_{LS}}. \tag{16}$$

It would be interesting to compare the predictions of equations (13) and (15) with the data listed in Fig. 7 of Hills[1] which contains also the values for k which may be used in equations (13) and (15) through equation (12). The comparisons are given in Table 1. Additional data are listed by Hills in Figures 5 and 6, however these did not contain values for k. For these, the predictions of equations (13) and (15) with a constant value of $k = 0.75$ are given in Table 2. The predictions by equation (16) are also shown in either case.

Table 1. Comparison of the predictions of equations (13), (15), and (16) with the data listed in Figure 7 of Hills[1].

U_{GS} ($\mathrm{m\,s^{-1}}$)	U_{LS} ($\mathrm{m\,s^{-1}}$)	k	$\bar{\varepsilon}$	Predictions of equation (13)	(15)	(16)
0.02	0.77	0.71	0.02	0.01	0.02	0.02
0.04	0.77	0.72	0.04	0.03	0.03	0.04
0.18	0.87	0.77	0.13	0.11	0.13	0.14
0.35	0.85	0.76	0.21	0.19	0.22	0.24
0.50	0.83	0.86	0.27	0.27	0.30	0.31
1.11	0.84	0.86	0.41	0.44	0.47	0.47

From an inspection of Tables 1 and 2, it is apparent that equations (13), (15) and (16) all give reasonable predictions of the voidage. However, in general, equations (13) and (15) which require the value of k are more reliable with equation (13) giving more accurate prediction at the high gas rate range where slugging is expected to occur, while equation (15) is preferred at the low gas range where the flow is expected to consist predominantly of bubbles.

In conclusion, it has been shown that the voidage and velocity distribution data reported by Hills[1] may be represented by the power-law distribution. The factor k introduced by Hills[1] is none other than the square of the ratio of the mean flow velocity to the centre-line velocity which may be incorporated into the Nicklin equation of voidage. The resultant equations agree well with experimental data.

Table 2. Comparison of the prediction of equations (13), (15) and (16) with the data listed in Figure (5) and Figure (6) of Hills[1]. A constant value of $k = 0.75$ was used in the calculation using equations (13) and (15).

U_{GS} ($\mathrm{m\,s^{-1}}$)	U_{LS} ($\mathrm{m\,s^{-1}}$)	$\bar{\varepsilon}$	Predictions of equation (13)	(15)	(16)
0.19	0.27	0.21	0.20	0.25	0.34
0.04	0.81	0.02	0.03	0.03	0.04
0.52	0.84	0.27	0.26	0.29	0.32
0.19	1.58	0.09	0.08	0.08	0.09
~0.04	0.81	0.03	~0.03	~0.03	~0.04
0.13	1.38	0.07	0.06	0.07	0.07
0.56	2.13	0.19	0.16	0.17	0.17
1.10	1.42	0.34	0.33	0.35	0.36
2.03	2.66	0.37	0.35	0.36	0.36

REFERENCES

1. Hills, J. H., 1983, *Chem Eng Res Des*, 61: 371–376.
2. Chen, J. J. J., Leung, Y. C. and Spedding, P. L., 1983, *Chem Eng Res Des*, 61: 325–328.
3. Bankoff, S. G., 1960, *Trans ASME, J Heat Transfer*, 265–272.
4. Zuber, N., 1960, *Trans ASME, J Heat Transfer*, 255–258.

VOL. 62 1984

5. Armand, A. A., 1946, *IZV VTI*, 1: 16–23, also *AERE Trans.* 828.
6. Nicklin, D. J., Wilkes, J. O. and Davidson, J. F., 1962, *Trans I Chem E*, 40: 61–68.
7. Chen, J. J. J. and Spedding, P. L., 1983, *Int J Multiphase Flow*, 9: 147–159.
8. Zuber, N. and Findlay, J. A., 1965, *Trans ASME, J Heat Transfer*, 453–468.
9. Burington, R. S., 1973, *Handbook of Mathematical Tables and Formulas*, 5th Edition, p. 74, McGraw-Hill.
10. Davies, R. M. and Taylor, G. I., 1950, *Pr R Soc. A* 200, 375–391.
11. Dumitriscu, V. D. T., 1943, *Z Angew Math Mech*, Bd 23: Na 3, 139.
12. Martin, C. S., 1976, *Trans ASME, J Fluids Engng.*, 715–722.
13. Lorenzi, A. and Sotgia, G., 1976, *Energia Nucleare*, 23: 396–401.
14. Arosio, S., Bartoloni, R., Lorenzi, A. and Sotgia, G., 1976, *Engeria Nucleare*, 23: 224–232.
15. Levich, V. G., 1962, *Physicochemical Hydrodynamics*, Prentice-Hall.
16. Harmathy, T. Z., 1960, *AIChE J*, 6: 281–288.

Reply from

Dr J. H. Hills
Department of Chemical Engineering
University of Nottingham
Nottingham NG7 2RD

Dr Chen makes two points about my article[1].

The first concerns the radial variation of voidage, for which I suggested the equation

$$\frac{\varepsilon}{\bar{\varepsilon}} = 1.74\left(1-\frac{r}{R}\right)^{0.42} - 0.22\left(1-\frac{r}{R}\right)^{4.07} \quad (1)$$

Figure 6 of my article suggests that

$$\frac{\varepsilon}{\bar{\varepsilon}} = f\left(\frac{r}{R}\right) \quad (2)$$

and the only *theoretical* constraint on the form of the function in equation (2) is that

$$\int_0^R 2\pi R f\left(\frac{r}{R}\right) \mathrm{d}r = 1. \quad (3)$$

My equation (1) obeys this relationship, as can be proved by substitution.

Dr Chen proposes a power law equation

$$\frac{\varepsilon}{\varepsilon_c} = \left(1-\frac{r}{R}\right)^{1/n} \quad (4)$$

which by substitution in (3) and integrating yields:

$$\frac{\varepsilon}{\bar{\varepsilon}} = \frac{(1+n)(1+2n)}{2n^2}\left(1-\frac{r}{R}\right)^{1/n} \quad (5)$$

The power law form has been used by previous authors, as noted by Dr Chen, but equation (1) gives a better fit to the data of Figure 6, especially near the wall, and I cannot see that (1) is any more, or less, *empirical* than (4) or (5).

His second point concerns the calibration factor k, defined by

$$\frac{g\Delta h}{U^2} = k \quad (6)$$

Equation (6) merely expresses the expectation that the mean pressure deviation Δh will be proportional to U^2, and the constant k will depend on fluid flow patterns round the transverse Pavlov tube and the definition of Δh.

Since, on the evidence of Figure 4, there is a discrepancy between the Pavlov tube and the Pitot-static tube, I deduce that k is also dependent on radial position and possibly the flow patterns in the main, single-phase pipe flow. However, Dr Chen's suggested relationship

$$\frac{U_{Ave}}{U_c} = \sqrt{k} \quad (7)$$

would make k dependent *only* on the flow patterns in the pipe, and independent of flow round the transverse Pavlov tube and of the definition of Δh. This cannot be correct, on physical grounds.

The confusion has perhaps arisen because *numerically* the mean value of $\sqrt{k}$ from Figure 4 (0.868) is close to the value predicted by the 1/7 power law for U_{Ave}/U_c (0.820). This must, however, be a coincidence.

In view of this, Dr Chen's Tables 1 and 2, calculated with a near constant value of $\sqrt{k}$, merely confirm that my mean voidage data are well represented by Nicklin's model: a point I have already made in a previous paper (2), and discussed in some detail there. They do not, unless you believe the Nicklin argument as applied to bubbly flow, say anything about the velocity profile; they most certainly do not say anything about the calibration constant, k, of the Pavlov tube.

REFERENCES

1. Hills, J. H., 1983, *Chem Eng Res Des* 61: 371.
2. Hills, J. H., 1976, *Chem Eng J*, 12: 89.

From

Dr J. B. Joshi
Department of Chemical Technology
University of Bombay
Bombay - 400 019, India

A reply to the letter from Professor P. N. Rowe that was published in the May issue.

My recent review paper addressed the following points regarding solid–liquid fluidised beds (SLFB). (Symbols used are as in the paper[1].)

(i) During the past three decades, substantial experimental data have been accumulated. Several empirical models and correlations have been developed for the estimation of velocity–voidage relationship, mass and heat transfer coefficients, and extent of liquid phase mixing. It is now high time to reduce the empiricism and to understand particle–liquid interactions.

(ii) In the past, separate correlations have been developed for each design parameter and there have been very few attempts to show the relationships among design parameters of SLFB. The development of such relationships is possible if the flow patterns are understood. On the basis of energy balance, the particle–liquid interactions in SLFB were analysed[1] and equations were derived for the liquid phase turbulence intensity. Very good agreement was shown between the predicted and experimental values of turbulence intensity (u'). It was shown that, in the turbulent regime, u' is the unique parameter which forms the basis for velocity–voidage

relationship (for spherical and nonspherical particles), classification of heavy and light particles, particle–liquid mass transfer coefficient and bed–wall heat and mass transfer coefficients.

In addition, the following unique characteristics of SLFB and discrepancies in the behaviour of SLFB were explained:

(*a*) The ratio of hindered settling velocity to terminal settling velocity is independent of the particle Reynolds number in laminar and turbulent regimes.

(*b*) In a fluidised bed of uniform particles, a criterion was developed for the prediction of the suspension of light and heavy particles. There is excellent agreement between the predicted and experimental values.

(*c*) The peculiar behaviour of bed–wall mass (k_{WB}) and heat transfer (h_W) coefficients was explained. With an increase in solid phase hold-up it is known that the values of k_{WB} and h_W increase in the turbulent regime, show maxima in the transition regime and decrease in the laminar regime.

(*d*) On the basis of liquid phase turbulence characteristics it was shown that the bed–wall mass transfer coefficient varies with the superficial liquid velocity whereas the particle–liquid mass transfer coefficient is independent of the superficial liquid velocity. These predictions are in excellent agreement with all the experimental data reported so far.

(*e*) A criterion was presented for the prediction of transition from particulate to aggregative fluidisation.

(*f*) In the case of aggregative type fluidisation a procedure was developed to calculate continuous phase velocity profiles. Very good agreement was shown between the predicted and experimental velocity profiles.

(*g*) The behaviour of a solid–liquid fluidised bed after the introduction of gas was explained.

From the foregoing, it can be seen that, all the design parameters of the solid–liquid fluidised bed have been related to the hydrodynamic characteristics, which are obtained from first principles.

The letter from Professor Rowe[2] considers a very small aspect of the velocity–voidage relationship only. It still uses an empirical approach and provides little understanding regarding particle–liquid interactions. As a result, this approach cannot explain other characteristics of SLFB as listed above. In addition, it suffers from the following limitations:

(i) The force balance given by equation (1) needs re-examination for the following reasons: (*a*) the buoyancy force has been taken proportional to the suspension density; (*b*) on the right hand side, V represents the superficial liquid velocity, and not the relative velocity between particle and liquid.

(ii) The table constructed for V_T/V_{mf} is incorrect. The value of index (m) in the Richardson–Zaki equation[3] is calculated on the basis of Re_T and not Re_{mf}.

(iii) It was found earlier[4] that the drag coefficient under the condition of minimum fluidisation increases by a factor of 70 as compared to that when the particle is settling under infinite conditions. However, the factor of 70 was not obtained directly. It was selected on the basis of rise velocities of closely packed assemblies of spheres.

(iv) The section on mass transfer [equations (13)–(16)] again states the experimental fact that the value of particle–liquid mass transfer coefficient is practically independent of the superficial liquid velocity (V_L). No attempt has been made to give any explanation. The relevant fact is that the liquid phase turbulence intensity is independent of V_L which can be proved on the basis of energy balance[1].

It may be emphasized that the model developed[1] can successfully explain the data on particle–liquid mass transfer coefficient in SLFB consisting of multisize particles[5]. The approach suggested[2] predicts values which deviate from those obtained experimentally.

REFERENCES

1. Joshi, J. B. 1983, *Chem Eng Res Des* 61: 143.
2. Rowe, P. N. 1984, *Chem Eng Res Des* 62: 190.
3. Richardson, J. F. and Zaki, W. N. 1954, *Trans IChemE*, 32: 35.
4. Rowe, P. N. 1961, *Trans IChemE*, 39: 178.
5. Rowe, P. N. and Claxton, K. T., 1965, *Trans IChemE*, 43: T.320.

VOL.
62
1984

CHEMICAL ENGINEERING RESEARCH & DESIGN

Transactions of The Institution of Chemical Engineers

VOL.
62
1984

EDITORIAL

The Review Paper in this issue is "Particle deposition behaviour from turbulent flows" by P. G. Papavergos and A. B. Hedley. The authors review a number of theories of particle deposition and classify them into those based on classical concepts of turbulence and those based on a stochastic approach. It is concluded that the choice of a theory depends on the application concerned and the degree of accuracy of the results required. The authors note that more experimental results involving fine particles ($<10\,\mu$m) are needed to validate certain aspects of the reviewed theories.

J. W. Mullin and J. R. Williams describe apparatus and techniques for crystallisation studies in "Comparison between indirect and direct contact cooling methods for the crystallisation of potassium sulphate". Specifically they are concerned with direct contact cooling using a inert coolant. Using iso-octane as the coolant the authors report results for batch and continuous crystallisation and direct and indirect cooling. The authors conclude that direct cooling has little if any effect on nucleation and growth rates and on product quality.

In "Absorption during gas injection through a submerged nozzle. Part I: gas side and liquid side transfer coefficients" F. A. N. Rocha and J. R. F. Guedes de Carvalho report experiments on the rate of transfer of solute between a gas being injected through a submerged nozzle and the surrounding liquid. In analysing the results the processes of mass transfer during bubble formation and bubble rise were considered separately. Theoretical predictions of mass transfer coefficients fall below experimental values but the authors conclude that the concept of a two-stage transfer process seems sound. Correlations for the various transfer coefficients are given.

A theoretical analysis is described in "Fixed bed sorption with recycle. Part I: mathematical model and single reversible reactions" by J. T. Casey and A. I. Liapis. The system considered is a well-stirred reactor whose product stream is cycled to a sorbent bed to remove the product and then returned to the reactor. Zeroth, first the second-order, reversible reactions and linear and non-linear equilibrium adsorption isotherms are considered. From their simulations of these systems the authors note the increased production possible under certain circumstances and the usefulness of the simulation in determining operating conditions etc.

H. Dhulesia reports work on "Clear liquid height on sieve and valve trays". Experimental results show that a single correlation of clear liquid height cannot be used for both the froth and spray regimes. Correlations for clear liquid height for sieve and valve trays in the froth regime are presented.

"Electrostatic hazards associated with marine chemical tanker operations. Criteria of incendivity in tank cleaning operations" are considered by M. R. O. Jones and J. Bond". The paper is concerned with the hazard of ignition of a flammable atmosphere within a chemical cargo tank by an electrical discharge from a water slug originating from a washing machine. A mathematical model for the threshold electrostatic condition of the tank atmosphere which would give rise to a hazardous situation is developed. Measured values from marine chemical tankers were found to be below the predicted thresholds. This result is supported by the good record experienced by marine chemical tankers using water washing. Conversely, the authors consider that steam cleaning of chemical tankers should be avoided.

In a Shorter Communication D. A. Lewis, R. S. Nicol and J. W. Thompson describe a detection and analysis method for measuring bubble sizes and velocities in bubbly gas—liquid flows using a two-electrode conductivity system.

Brian Gay
Honorary Editor

Notes for Authors

Editorial Policy and Standards

1. Papers published in the Journal will be original contributions to chemical engineering knowledge, not previously published. In particular, the Editorial Board encourages the submission of papers which show how the results of research may be used in chemical engineering design. Such implications for design should be brought out clearly in the paper and its summary.

Accounts of research work of an experimental or theoretical nature which throw new light on established principles, which identify problems not yet solved, or indicate practical areas to which research effort may usefully be applied are also invited. Reports from industry and from research establishments are particularly welcome.

Papers may also deal with new developments of plant or processes if these developments are related to underlying principles and can be given quantitative expression.

2. Authors need not be members of the Institution. Papers must be in English and should normally be of 2500 to 5000 words, including Appendices. Figures should also be included in this count, each being estimated as equivalent to 250 words.

3. The Editorial Board will, however, also welcome Shorter Communications (less than 2500 words) for consideration for publication; these would describe, for example, novel research techniques, new analyses of previous work, or interesting aspects of work still in progress. A faster refereeing procedure has been arranged for such short Papers.

4. The Journal also publishes a limited number of longer Review Papers, which are critical assessments of previously published work in a selected area of chemical engineering. In conformity with editorial policy, Reviews should show how the results of research can be used in the design of plant and equipment.

Most Reviews are specially commissioned by the Editorial Board, but authors are also invited to offer Reviews for consideration for publication. In view of the substantial effort required, authors are advised to communicate with the Editor before embarking on a Review.

5. It is the policy of The Institution to publish only papers of the highest quality. To help maintain these standards all papers submitted are sent to referees familiar with the branch of chemical engineering covered. They advise as to whether the paper is acceptable or not and, in addition, indicate to the author possible ways in which, in their opinion, the paper might be improved. The final decision on publication is taken by the Editor in light of this advice.

Manuscript Requirements

1. The text should be typewritten, using one side of the paper only, double-spaced and with adequate margins to allow for revision and copy preparation marks. A summary, preceding the text, should briefly describe the essential original contents of the paper.

2. Mathematical expressions can sometimes be more easily interpreted by the printer if carefully written by hand. Where many equations appear, a list of symbols used should be inserted at the end of the paper, before the references. SI units should *always* be used; the negative index notation is preferred to the oblique stroke.

3. References are listed in the order in which they are first cited in the text, where they are indicated by superscript numbers. They should give in order: Authors' surnames and initials, Year, Title of book or journal, Volume, Issue, Page numbers , followed by name and town of publisher in the case of a book.

4. Tables, drawings and photographs should be on separate sheets at the end of the manuscript and not interspersed in the text. Tabulated data should not duplicate values detailed in the text or on graphs. Drawings submitted should be clear and complete and preferably in a form suitable for direct reproduction. Photographs should be restricted to the minimum necessary.

5. Where limitations of space preclude publication of detailed results, mathematical derivations, etc, authors are invited to include in their paper a statement that this information is available from them on application. Authors may make an appropriate charge for supplying items requested in this way. Such material should be supplied with the paper when submitted to the Editor.

Submission of Papers

1. Three copies of the paper should be sent to:

The Editor, Chemical Engineering Research and Design,
Institution of Chemical Engineers,
George E. Davis Building,
165–171 Railway Terrace,
Rugby CV21 3HQ, England.

or to an Associate Editor as follows:

Australia:
Prof R. G. H. Prince,
Department of Chemical Engineering,
University of Sydney,
Sydney 2006, New South Wales, Australia.

Continental Europe:
Prof Dr J. R. Bourne,
Technisch-Chemisches Laboratorium,
ETH-Zentrum,
CH-8092 Zürich, Switzerland.

Continental Europe:
Prof J. M. Smith,
Laboratorium voor Fysische Technologie,
Technische Hogeschool Delft,
Prins Bernhardlaan 6,
2628 BW Delft, Holland.

India:
Prof M. M. Sharma,
Department of Chemical Technology,
University of Bombay,
Matunga Road,
Bombay 400 019, India.

New Zealand:
Prof R. B. Keey,
School of Engineering,
University of Canterbury,
Christchurch 1, New Zealand.

USA:
Prof J. O. Wilkes,
Department of Chemical Engineering,
University of Michigan,
Ann Arbor,
Michigan 48109, USA.

2. A full address to which readers may send correspondence should be specified, including the post code. The address at which the work was carried out, if different, should also be indicated. Where there are several authors, one should be nominated to check proofs and to receive all correspondence.

3. A proof will be sent to the nominated author, to be checked for possible typographical errors. Other alterations cannot be incorporated at this late stage without incurring higher printing costs, and extensive alterations would necessitate postponement of publication of the paper to a later issue.

4. Following publication the nominated author will receive 50 off-prints of the paper (or 25 where there is just one author). Any further off-prints required should be ordered at proof stage. Reprints, ordered after publication, are more expensive.

VOL.
62
1984

REVIEW PAPER

PARTICLE DEPOSITION BEHAVIOUR FROM TURBULENT FLOWS

P. G. PAPAVERGOS (GRADUATE) and A. B. HEDLEY

BP Research Centre Sunbury-on-Thames and
Department of Chemical Engineering and Fuel Technology, University of Sheffield

Most theories of particle deposition from turbulent flows are reviewed with regard to their assumptions, accuracy and range of application to research and design. The theories are classified into those based on the classical concepts of turbulence and those based on stochastic approaches. It is concluded that the choice of a theory depends on the application concerned and the degree of accuracy of the results required. More experimental measurements involving fine particles ($d_p \leqslant 10\,\mu m$) are needed to validate certain aspects of the reviewed theories.

INTRODUCTION

The transport of particles (or droplets) from a turbulent flow stream to an adjacent surface is of paramount importance in numerous engineering and life science applications. This subject is applicable to the following areas: atmospheric pollution; health physics; the design of air (or gas) cleaning and sampling devices; fouling of heat transfer surfaces; pneumatic transport; reactor design; two phase flow; and many others.

The aim of this review is to assess the limitations and assumptions involved in the application of past and contemporary theories to engineering design, and to discuss their accuracy in the light of experimental evidence. Although this review is not directly concerned with the deposition behaviour of molecular size particles, some of the outlined theories have attempted to include such particles. Very fine particles ($d_p \ll 1\,\mu m$) deposit on to surfaces due to Brownian (or molecular) diffusion.

Larger particles whose deposition behaviour is influenced by inertial effects, and which are insignificantly affected by the turbulent nature of the flow field they are entrained in, due to their large size, mass, or both, are not covered in this review.

Most theories are formally concerned with spherical particles or droplets depositing on smooth surfaces, to simplify the mathematical equations involved. However, appropriate modifications may accommodate particles of shapes other than spheres, and rough depositing surfaces. Most investigators make reference to aerosol droplets entrained in duct air streams, rather than solid particles in liquid streams; because experimentally the choice of the former system offered operational convenience and low cost. Hence, the term particle and (aerosol) droplet are interchangeable throughout the text, except where otherwise indicated.

Although parameters other than those associated with the particle–turbulence interactions were considered to be beyond the scope of this work, a very brief account is given in the Discussion section of this paper about the effect of certain factors on particle deposition, which could be important in a number of practical situations. These factors are: wall roughness, thermophoresis and electrical charge. The effect of particle re-entrainment on the deposition rate was not considered in the majority of the theories discussed in the text. The experimental results chosen for direct comparison with the theoretical predictions were taken under conditions in which the particle re-entrainment was insignificant.

EARLY THEORIES

The concept of the transport and deposition of particles from a fluid stream was first studied by Albrecht[1] some 50 years ago. Albrecht's work was concerned with the collection of water drops and ice crystals, suspended in an air stream, by the surface of a hygrometer. Equations were derived to describe the relative motion and trajectory of a particle in a two-dimensional flow field. His assumptions included non-turbulent initial flow, Newtonian aerosol flow, no interparticle collisions or mutual interactions through gravitational or electrostatic forces and Stokesian particle resistance.

Albrecht was one of the first to recognise the parameter $\pi g_p d_p^2/6c$ (a function of the now known Stokes' number) as a fundamental constant in his results analysis, and to introduce what is now called the collection efficiency as the ratio of the projected area of the obstacle to the area of the stream from which particles impinge on the obstacle. The conclusions of his theory, although not complete, as other workers on this subject later suggested, were original and yielded useful information for further research.

Much later, Langmuir[2] and Davies et al[3,4] modified Albrecht's theoretical approach to accommodate changes in the Reynolds number of the flow and the particle size. Their modified theories were verified with reasonable accuracy by the experimental results of Gregory[5], who used lycopodium particles of mean diameter $2\,\mu m$, for potential and viscous fluid flow in a limited range of conditions.

© Institution of Chemical Engineers

PARTICLE DEPOSITION MODELS BASED ON CLASSICAL THEORIES OF TURBULENCE

The transport rate of particles carried in a fluid stream to a surface over which the stream is flowing, is usually expressed by:

$$W = (D_B + \varepsilon_{m,r})\frac{dN_r}{dy}$$

or in dimensionless form:

$$\frac{W}{u^* N_{r,max}} = V_d^+ = \left(\frac{D_B}{\nu} + \frac{\varepsilon_{m,r}}{\nu}\right)\frac{dN_r^+}{dy^+} \quad (1)$$

where

$$N_r^+ = \frac{N_r}{N_{r,max}}$$

The fluid eddy viscosity of momentum, $\varepsilon_{m,r}$ (or $\varepsilon_{m,r}/\nu$ when expressed in dimensionless form) was assumed to be equal to or directly proportional to the particle eddy diffusivity, $\varepsilon_{p,r}$ (or $\varepsilon_{p,r}/\nu$ when expressed in dimensionless form) in most of the ensuing theories. By this assumption the influence of the fluid turbulence on the transport rate of particles was taken into account in equation (1). Most of the theories of particle deposition were developed based on knowledge of $\varepsilon_{p,r}$, mainly from empirical correlations and following the classical view of turbulent flow.

Particle Deposition due to Inertial Impaction, using the Concept of 'Stopping Distance'

Friedlander and Johnstone[7] were among the first to develop a major theory on this subject. They proposed a projective mechanism for particle deposition, which was based on the idea that the turbulent eddies carried particles in the radial direction during pipe flow. The particles reached the region near the wall through turbulent diffusion, and were subsequently projected through the relatively stagnant fluid next to the wall boundary independently of the fluid motion, having gained some specified initial velocity. The turbulent diffusivity for the particles was assumed to be equal to the eddy viscosity of the gas, except in the region near the wall, where the difference was pronounced. The existence of turbulent fluctuations close to the boundary was realised, and the expression for the eddy viscosity in the region immediately adjacent to the wall, suggested by Lin et al[8] was adopted. Central to this idea was the concept of stopping distance; the distance a particle with a certain momentum will travel into the essentially laminar region without the need of the turbulent fluctuations, $S = U_{pr}\tau_p$. The free flight particle velocity (U_{pr}) was assumed to be equal to the root mean square (r.m.s.) radial fluid velocity, and independent of the position at which a particle was considered to begin its free flight, i.e.:

$$U_{pr} = u_r' = 0.9\bar{U}_{x,mean}\sqrt{(f/2)} = 0.9u^* \quad (2)$$

The r.m.s. radial fluid velocity was taken from the data of Laufer[9], while the particle relaxation time (τ_p) was calculated according to Stokes' Law. Friedlander and Johnstone's theory implied that the sink (at which the particle concentration is zero) was located one stopping distance from the wall, rather than at the wall itself. Displacing the point of zero concentration this short distance from the wall, resulted in the predicted mass transfer coefficient changing considerably, due to the highly damped eddy viscosity and the high resistance to turbulent transfer. The derivation of the transport rate of momentum and mass to the depositing surface was analogous to von Karman's approach. The final equations of their theory, expressed in dimensionless form are:

$$\frac{1}{V_d^+} = \frac{1}{\sqrt{(f/2)}} + \frac{1525}{S^{+2}} - 50.6 \quad \text{for} \quad S^+ < 5 \quad (3)$$

$$\frac{1}{V_d^+} = \frac{1}{\sqrt{(f/2)}} - 13.75 + 5\ln\frac{5.04}{\frac{1}{2}S^+ - 0.959}$$

$$\text{for} \quad 5 \leqslant S^+ \leqslant 30 \quad (4)$$

$$\frac{1}{V_d^+} = \frac{1}{\sqrt{(f/2)}} \quad \text{for} \quad S^+ > 30 \quad (5)$$

Friedlander and Johnstone supported their theory with an extensive series of experimental results from vertical pipe flows (Figure 2), but from the results as originally presented, it was difficult to visualise the dependence of the deposition velocity on the stopping distance. Later investigators[10] recalculated Friedlander and Johnstone's results to find that theory and experimental results agreed to within factors of between 2 and 10. In this theory many original ideas were projected and it is widely used in design calculation even today. However, the drawbacks of adopting the theory are:

(*a*) Basing the model theory on equation (2) and accepting Laufer's results, it was implied that the free flight velocity starts at a distance $S^+ = 80$ from the wall and the flow was assumed to be fully developed turbulent. At that distance, the particles were still in the turbulent core and hence the accepted value of U_{pr} was unrealistic.

(*b*) The derived transport equations above did not account for molecular particle diffusion.

(*c*) All equations (3) to (5) being functions of the Fanning friction factor f, suggested that V_d^+ increased with f, where $f = 0.039Re_D^{-0.17}$. Hence V_d^+ increased as Re_D decreased, which was contrary to reality. To improve the application of the derived equations, u^* should be related to the pressure drop along the duct, i.e.:

$$u^* = \sqrt{\left(\frac{D}{4\rho_f}\frac{\Delta P}{\Delta L}\right)} \quad (6)$$

The theoretical predictions of Friedlander and Johnstone's theory are presented as V_d^+ versus τ_p^+ in Figure 1, along with predictions of other proposed theories.

VOL. 62 1984

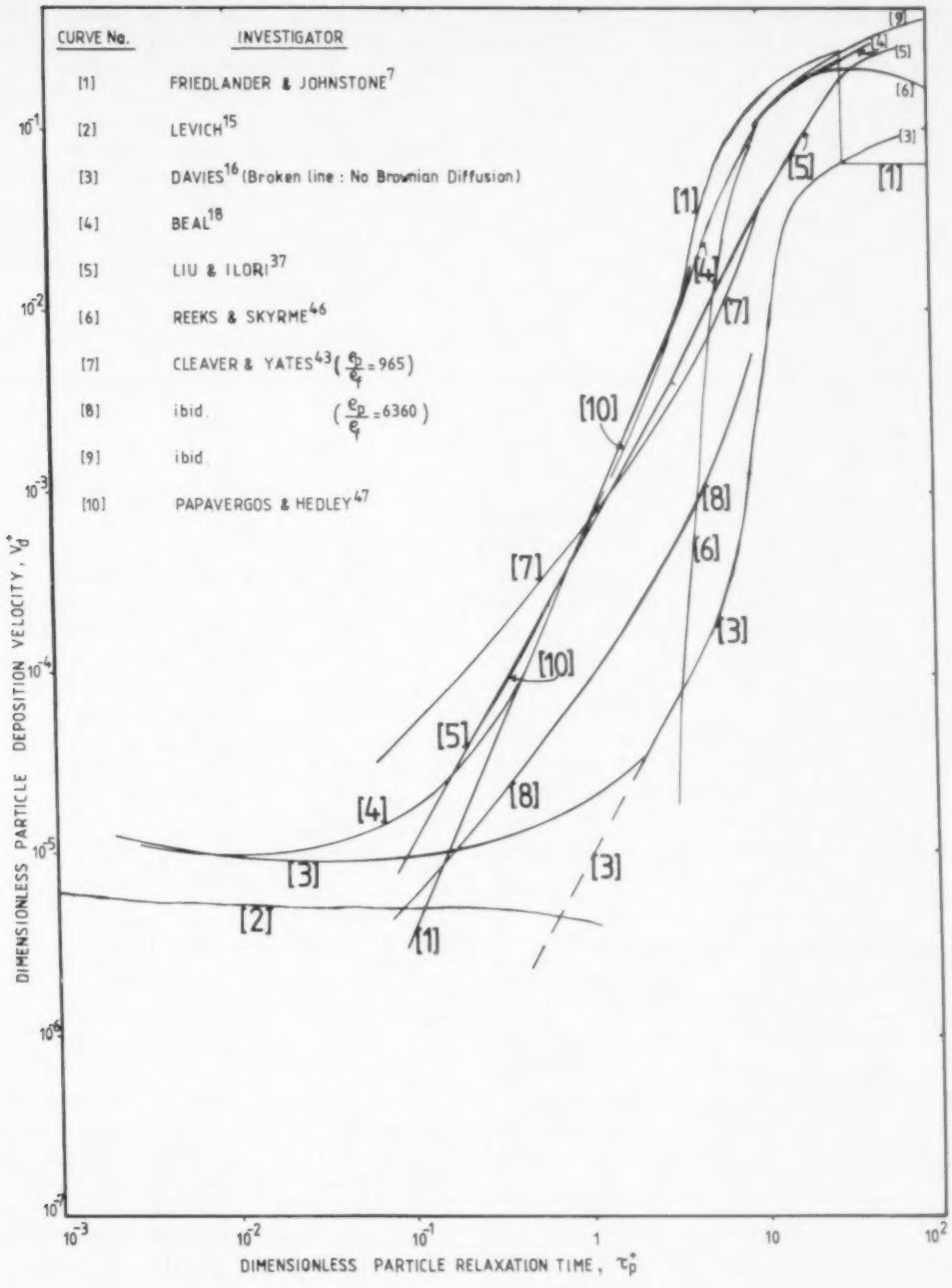


Figure 1. Predictions of particle deposition models expressed as V_d^+ versus τ_p^+.

Sehmel and Schwendiman[11], in an attempt to improve equation (5) and to fit in their own experimental data, suggested the following empirical equation:

$$\frac{1}{V_d^+} = \frac{30}{S^+\sqrt{(f/2)}} \text{ for } S^+ > 30 \text{ at } Re_D = 5 \times 10^5 \quad (7)$$

Although this equation takes particle size into consideration, it has the same drawbacks as above and is restricted in its general application, i.e. it is only applicable to particles of $d_p > 2\,\mu$m dispersed in flows of $Re_D = 5 \times 10^5$.

Particle Diffusion-Projection Mechanism of Deposition, including the Effect of Gravity

Owen[12] independently proposed a theoretical model similar in many ways to Friedlander and Johnstone's. His theoretical analysis considered the effect of gravity on particle deposition, in an attempt to explain the mechanism of roof, floor and side walls deposition in a horizontal turbulent pipe flow. In his model of diffusion-projection of particles to the wall, Owen regarded particle diffusivity and eddy viscosity to be proportional rather than being equal to one another as

in Friedlander and Johnstone's theory. Basing his derivations on Laufer's results, Owen obtained the following eddy viscosity distributions:

$$\frac{\varepsilon_{m,r}}{\nu} = 0.001y^{+3} \quad \text{for} \quad 0 < y^+ < 5 \tag{8}$$

$$\frac{\varepsilon_{m,r}}{\nu} = 0.012(y^+ - 1.6)^2 \quad \text{for} \quad 5 < y^+ < 20 \tag{9}$$

$$\frac{\varepsilon_{m,r}}{\nu} = 0.4(y^+ - 10) \quad \text{for} \quad y^+ > 20 \tag{10}$$

According to Owen, particle diffusion occurred up to a distance $y^+ = l^+$; the distance over which free flight took place. The distance l^+ was regarded as an experimental constant obtained from the results of Dawes and Slack[13], which were based on coal dust dispersions in a wind tunnel. Upon these assumptions Owen deduced rather lengthy expressions for the particle deposition rates on the floor, the roof and the side walls, taking $l^+ = 1.6$. The idea of accepting a constant free flight distance for all particle sizes and velocities was not realistic, despite the fact that the model theory satisfactorily fitted Dawes and Slack's data. In fact, Owen's theory advanced an earlier work by Pereles[14], who also attempted to explain Dawes and Slack's results. Pereles too, considered the effect of gravity, but the flaw in his argument was that he did not take the effect of particle inertia into account, and as a result of this, the agreement of his plots with Dawes and Slack's results was poor.

Deposition of Molecular Size Particles

Levich's[15] theory on this subject considered only molecular size particles of $Sc \gg 1$. In deriving the equation governing the deposition flux of particles, he assumed that the turbulent eddies penetrated the viscous sublayer and died out only at the wall surface. The final equation for the dimensionless deposition velocity was:

$$V_d^+ = 0.13337(Sc)^{-3/4} \tag{11}$$

and for the derivation of equation (11), $\varepsilon_{m,r} \propto y^{+4}$.

In this simple theoretical model, the diffusional displacement appeared to be the only particle deposition mechanism, without any provision for including the effect of Re_D on V_d^+. Levich's theory was only applicable to submicron particles, due to its inherent assumptions. The results predicted by this theory were completely different from those predicted by Friedlander and Johnstone's as shown in Figure 1, since in the latter, inertial diffusion was the predominant deposition mechanism.

Diffusive and Inertial Mechanisms of Particle Deposition

Davies[16] modified and refined Friedlander and Johnstone's theory, while retaining the basic idea of the stopping distance. His theory took into account both inertial and diffusive mechanisms of particle transport. The assumption that the initial projection particle velocity was constant was questioned, and it was proposed that the initial free flight velocity started at $y^+ = S^+ + \frac{1}{2}d_p^+$, equal to the local turbulent fluctuation velocity; this yielded an implicit solution for the inertial velocity. The theory assumed that the particle eddy diffusivity was equal to the eddy viscosity of the fluid, and Lin et al's[8] empirical relationships were adopted, i.e. the region near the boundary wall was divided into three layers, in each one of which the eddy viscosity was given by:

$$\frac{\varepsilon_{m,r}}{\nu} = \left(\frac{y^+}{14.5}\right)^3 \text{ for the viscous sublayer } (y^+ < 5) \tag{12}$$

$$\frac{\varepsilon_{m,r}}{\nu} = \frac{y^+}{5} - 0.96 \quad \text{for the buffer layer } (5 < y^+ < 30) \tag{13}$$

$$\frac{\varepsilon_{m,r}}{\nu} \gg 1 \text{ for the turbulent core region } (y^+ > 30) \tag{14}$$

In addition, the theory considered three regimes; diffusive, inertial and transitional, where both diffusive and inertial mechanisms were present. According to Davies, in the viscous sublayer (defined by equation (12)), submicron particles ($0.001 < d_p < 1\ \mu m$) of density about $1000\ kg\ m^{-3}$ and $Sc \leqslant 283$, were subject to diffusion and the expression for V_d^+ was given by integrating equation (1) within $N_r^+ = 0$ (at $y^+ = 0$) and $N_r^+ = 1$ (at $y^+ = 5$) as follows:

$$V_d^+ = Sc^{-2/3} \Big/ 14.5\left[\tfrac{1}{6}\ln\frac{(1+\phi_D)^2}{1-\phi_D+\phi_D^2} + \frac{1}{\sqrt{3}}\tan^{-1}\frac{2\phi_D - 1}{\sqrt{3}} + \frac{\pi}{6\sqrt{3}}\right] \tag{15}$$

where

$$\phi_D = 0.345(Sc)^{2/3}$$

In the case of particles of $d_p \geqslant 1\ \mu m$, of density about $1000\ kg\ m^{-3}$ and $Sc \geqslant 540{,}000$ the particle inertia was considered to be the prevailing cause of deposition. Based on the experimental data of Laufer, Schlinger and Sage[17] for the fluid eddy viscosity, as well as Owen's previously mentioned relationships, Davies derived the following empirical equation for the eddy viscosity across the entire boundary layer:

$$\frac{\varepsilon_{m,r}}{\nu} = \frac{(y^+)^{4-(y^+)^{0.08}}}{1000(2.5 \times 10^7/Re_D)^{y^+/(400+y^+)}} \quad \text{for } 0.01 < y^+ \leqslant 10{,}000 \tag{16}$$

The molecular diffusivity D_B was not taken into consideration, since $D_B \ll \varepsilon_{m,r}$ for particles of $d_p > 1\ \mu m$. The final equations for V_d^+ were:

$$V_d^+ = (u_r'^+)_{S^+ + r_p^+}(N_r^+)_{S^+ + r_p^+} = \frac{1}{[I]_{S^+ + r_p^+}^{R^+} + \dfrac{1}{(u_r'^+)_{S^+ + r_p^+}}} \tag{17}$$

VOL. 62 1984

where

$$[I]_{S^+ + r_p^+}^{R^+} = [1 - (N_r^+)_{S^+ + r_p^+}](V_d^+)^{-1}$$

$$= \int_{S^+ + r_p^+}^{R^+} \left(\frac{\varepsilon_{m,r}}{\nu}\right)^{-1} dy^+ \quad (18)$$

and $(u_r'^+)_{S^+ + r_p^+}$ was determined from Laufer's results, which in the viscous sublayer are expressed by:

$$\frac{y^+}{u_r'^+} = y^+ + 10 \quad (19)$$

and

$$r_p^+ = \frac{d_p^+}{2}, \quad y^+ = S^+ + r_p^+$$

For small values of r_p^+ equation (19) reduces to:

$$(u_r'^+)_{S^+ + r_p^+} = \frac{r_p^+}{10} \quad (20)$$

In the regime where both eddy and molecular diffusion were present, Davies assumed that D_B was an important parameter to deposition until $\varepsilon_{m,r}/D_B > 8$. He also assumed that for small values of y^+ and small particles, the eddy viscosity given by equation (16) approximated closely to equation (8). When $\varepsilon_{m,r} < 8D_B$, the diffusion layer thickness was given by:

$$y_D^+ \simeq 10(8D_B/\nu)^{1/3} = 20Sc^{-1/3} \quad (21)$$

Hence, inside this layer the coefficient of diffusion was given by $D_B/\nu + (y^+/10)^3$ and outside by equation (16). The deposition velocity of particles having $(S^+ + r_p^+) < 20Sc^{-1/3}$ from $S^+ + r_p^+$ to R^+ was given by:

$$\frac{1}{V_d^+} - \frac{1}{(u_r'^+)_{S^+ + r_p^+}} = 10Sc^{2/3} f(\phi_0) + [I]_{20Sc^{-1/3}}^{R^+} \quad (22)$$

where

$$f(\phi_0) = 0.7877 - \tfrac{1}{6} \ln \frac{(1+\phi_0)^2}{1 - \phi_0 + \phi_0^2} - \frac{1}{\sqrt{3}} \tan^{-1} \frac{2\phi_0 - 1}{\sqrt{3}}$$

$$\phi_0 = \tfrac{1}{10}(S^+ + r_p^+)Sc^{1/3}$$

Therefore, equation (22) assumed that the particles were transported by eddy diffusion up to y_D^+ and they travelled further to $S^+ + r_p^+$ by molecular or eddy diffusion, before they made their final trip to the wall on their own inertia. For large particles, $\varepsilon_{m,r} \gg D_B$ and $S^+ + r_p^+ > y_D^+$, while $f(\phi_0) \to 0$. Hence, equation (22) takes the form of equation (17). Similarly, for small particles where the value of D_B is significant, equation (22) approaches equation (15). The results of this theory are shown in Figure 1 together with the predictions of other theories.

Davies provided tables which evaluated the complex integrals in his theory, but no attempt was made to compare the available experimental data with his theory. Despite the apparent logical extension of this theory, the resulting analysis disagreed with the experimental data by at least two orders of magnitude in some cases, as discussed by Beal[18], Wells and Chamberlain[19], Hutchinson et al[20] and Rouhiainen and Stachiewicz[21].

Inertial-Diffusive Deposition Mechanism for Particles of $0.1 \leqslant d_p \leqslant 100$. Concept of Sticking Probability

In an attempt to develop a comprehensive theory, Beal[18] combined Friedlander and Johnstone's approach with that of Lin et al in a similar way to Davies. His approach intended to cover particles varying from molecular size to about 100 μm in diameter, by a general theory rather than classifying particles into inertial, inertial and eddy, and molecular diffusion regimes. The basic difference between Beal's and Davies' theory was the calculation of the stopping distance. According to Beal the free flight velocity within the viscous and buffer layer used for the calculation of the stopping distance was taken to be one-half of the axial velocity, irrespective of the position of the particles relative to the walls. This unrealistic assumption was made to fit Friedlander and Johnstone's, Schwendiman and Postma's[22], Wells and Chamberlain's[19] and Sehmel's[23] experimental data. Beal postulated that the concentration at $y^+ = S^+ + r_p^+$ was not zero, contrary to Friedlander and Johnstone's assumption, but that a steady rate of accumulation of particles at this region was taking place. This non-zero concentration then acted as a resistance to particle deposition flux on the walls. The [deposition velocity]$^{-1}$ was expressed as the sum of two resistances, one representing the resistance to transport from the turbulent core to $y^+ \leqslant S^+ + r_p^+$, and the other representing the resistance to transport through the region $y^+ \leqslant S^+$, which was analogous to thermal resistances in series. The particle velocity towards the wall was also assumed to have two components, one from Brownian diffusion and the other from the fluid motion which was determined from Laufer's data. Beal's final equation for particle deposition with no re-entrainment was:

$$K_D = \frac{1}{1/K + 1/PU_{p,r}} \quad (23)$$

The equations for K and $U_{p,r}$ are given in Appendix A. Beal's results are shown in Figure 1.

In a much later study, Beal[24] raised doubts about the sticking probability P being equal to 1.0 in his theory, and he attempted to correlate P with the dimensionless stopping distance S^+. He proceeded by defining a parameter x as:

$$x = \frac{K_{D(P=P)}}{K_{D(P=1)}} = \frac{KPU_{p,r}/(K + PU_{p,r})}{KU_{p,r}/(K + U_{p,r})} \quad (24)$$

The values of x were mainly determined from Sehmel's[23,25] deposition data. The computed values of P (equation (24)) were correlated to S^+ by a least squares method and the following relationships were derived:

$$P = 1 \quad \text{at} \quad S^+ \leqslant 4.5$$

$$P = (4.5/S^+)^4 \quad \text{at} \quad S^+ \geqslant 4.5 \quad (25)$$

The following relationships were derived, based on Watkinson's[26] experimental data, using 15 μm diameter

sand grains suspended in water through a pipe:

$$P = 1 \quad \text{at} \quad S^+ \leqslant 2.4$$

$$P = (2.4/S^+)^4 \quad \text{at} \quad S^+ \geqslant 2.4 \tag{26}$$

The similarity of expressions (25) and (26) was the main criterion for choosing S^+ as the correlating parameter. Beal reported values of $P > 1.0$, which were due to $x > 1.0$. The explanation offered for this inconsistency was that either the predicted value of $K_{D(P=1)}$ was too low in comparison to $K_{D(P=P)}$, or $K_{D(P=P)}$ was relatively too high.

Although Beal's idea of the sticking probability was original and analogous in some respects to the idea of the probability of a particle reaching the wall in the downsweep-ejection mechanism, discussed later in greater detail, no attempt was made to rectify the violation of the definition of the probability P.

Deposition of Particles with an 'Effective Particle Diffusivity'

Sehmel[27,28] proposed a theoretical model similar in many respects to Davies' analysis. Adopting equation (1) and Lin et al's equations (12) and (13) for the radial turbulent diffusion coefficient, he derived the following integral equation:

$$\frac{1}{V_d^+}\int_{(N_r^+)_{S^++r_p^+}}^{1} dN_r^+ = \int_{S^++r_p^+}^{5} \frac{dy^+}{\left(\frac{D_B}{\nu}\right)+\left(\frac{y^+}{14.5}\right)^3} + \int_5^{30} \frac{dy^+}{\frac{D_B}{\nu}+\frac{y^+}{5}-0.959} \tag{27}$$

Integrating equation (27) and following the same procedure as from equation (17) to equation (18), V_d^+ was expressed by:

$$V_d^+ = \frac{1}{\text{Int} + [1/(U_{pr}^+)_{S^++r_p^+}]} \tag{28}$$

where

$$\text{Int} = 14.5(Sc)^{2/3}\left\{\tfrac{1}{6}\ln\frac{(1+\phi_S)^2}{1-\phi_S+\phi_S^2} - \frac{1}{\sqrt{3}}\tan^{-1}\frac{2\phi_S^{-1}}{\sqrt{3}}\right\}\Bigg|_{y^+=S^++r_p^+}^{y^+=5} + 5\ln\left(\frac{D_B}{\nu}+\frac{y^+}{5}-0.959\right)\Bigg|_{y^+=5}^{y^+=30}$$

and

$$\phi_S = \frac{y^+}{14.5}(Sc)^{1/3}$$

Equation (27) is essentially the same as equation (22) except for the analytical expression of the eddy diffusivity, equation (16). Equation (28) has the following inherent assumptions:

(*a*) The eddy and the molecular diffusion are the only deposition forces.
(*b*) The wall surface is a particle sink.
(*c*) The particle eddy diffusivity is equal to the fluid eddy diffusivity.
(*d*) The particle concentration is constant for $y^+ \geqslant 30$.
(*e*) A free flight mechanism is the final cause of deposition.
(*f*) The particle velocity, $U_{p,r}$, is known at the start of the free flight.

Sehmel's theoretical predictions were compared with experimental measurements from a vertical flow system

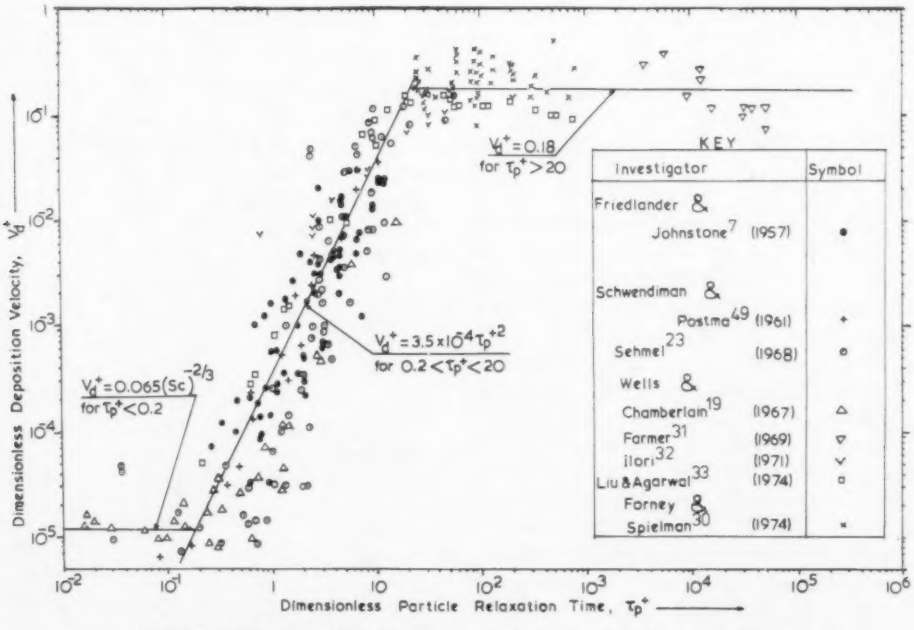


Figure 2. Summary of experimental deposition data in vertical flow systems.

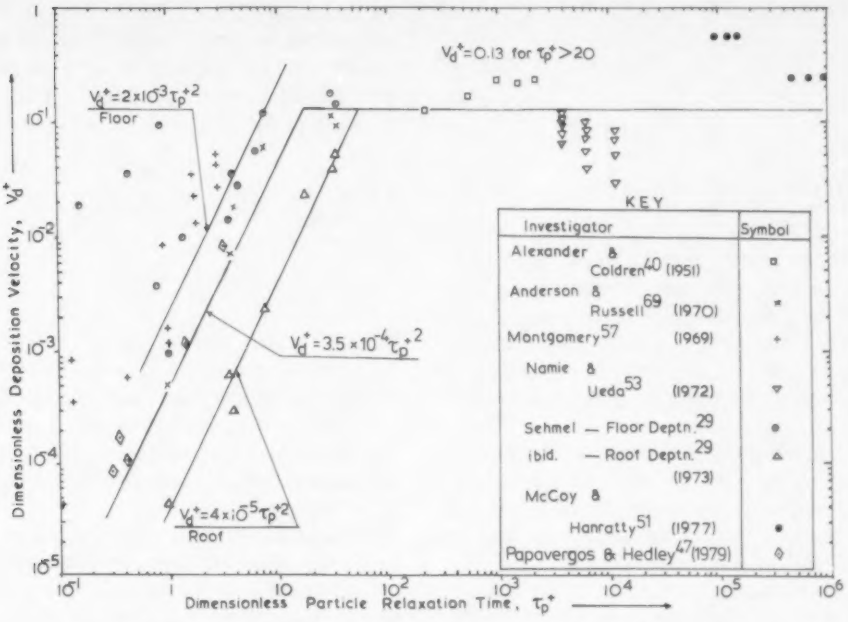


Figure 3. Summary of experimental deposition data in horizontal flow systems.

(Figure 2). The deposition velocity was determined from concentration profile measurements followed by the mass balance over a duct length L as follows:

$$V_d^+ = \frac{\Delta N_{r,mean}}{u^*(N_{r,mean})_{L=0}}\left(\frac{\bar{U}_{x,mean}}{4}\right)\left(\frac{D}{L}\right) \tag{29}$$

Sehmel found poor agreement between the predicted values of V_d^+ from equation (28) and the experimental ones from equation (29). In view of this discrepancy, he discarded the concept that the particle velocity at the start of the free flight was related to the r.m.s. radial component of the fluctuating fluid velocity. He also abandoned the assumption that $\varepsilon_{p,r} = \varepsilon_{m,r}$ and he viewed the particles as depositing to the wall with an effective particle diffusivity, $\varepsilon'_{p,r}$, which was the sum of inertial effects, turbulent diffusion effects and residual lift forces, due to the shear near the wall. From the available experimental data from vertical ducts, Sehmel back-calculated the free flight velocity, which he correlated with the relaxation time, using a least squares method, which gave:

$$U_{pr}^+ = 1.49(\tau_p^+)^{-0.49} \tag{30}$$

He also empirically determined with a least squares analysis, the correlation of $\varepsilon'^+_{p,r}$ with y^+ and τ_p^+ as follows:

$$\varepsilon'^+_{p,r} = \varepsilon'_{p,r}/\nu = 0.011(y^+)^{1.1}(\tau_p^+)^{1.1} \quad \text{for } y^+ < 20 \tag{31}$$

and

$$\varepsilon'^+_{p,r} = 0.04y^+ \quad \text{for} \quad y^+ > 20 \tag{32}$$

V_d^+ was calculated from equation (1), which was integrated within the following limits:

$$N_r^+ = 0 \text{ at } y^+ = r_p^+ \text{ and } N_r^+ = 1 \text{ at } y^+ = 30$$

The experimental values of deposition were found to be 24% lower than the predicted values using equation (30), which was a considerable improvement on his previous theory. The effective eddy diffusivity given by equations (31) and (32) was found to correspond to the experimental data on an average basis, but no significant improvement was offered to the existing scatter of data. This empirical approach did not advance the concept of particle deposition mechanism, but it predicted deposition velocities over a wide particle size range, without having to assume the concept of a multilayered wall region.

Sehmel[29] extended his theory to predict deposition velocities in horizontal duct flows (Figure 3), taking into account the effect of gravity on particles for which such forces contribute significantly to deposition. Although the derived equations were intended to cover a wide range of particle sizes, they were only obeyed by a limited set of data and their use in predicting new data led to inaccuracies. In certain cases higher wall deposition velocities than those on the floor were found, and the need for modifying Sehmel's empirical equations was evident. Equation (30) opposed the intuitive idea of how U_{pr}^+ should vary with τ_p^+, for as τ_p^+ decreases it should be expected that the particle would detach itself from the eddy closer to the wall and subsequently possess a smaller U_{pr}^+.

Effect of Shear-Flow-Induced Transverse Lift Force on Particle Deposition

Rouhiainen and Stachiewicz[21] questioned the assumptions of (*a*) $\varepsilon_{p,r} = \varepsilon_{m,r}$ and (*b*) the inertial coasting of particles being the only means of transportation in the viscous sublayer. Their approach to evaluate $\varepsilon_{p,r}/\varepsilon_{m,r}$ was the same as that of Besset, Boussinesq and Ossen for the

particle motion in a turbulent fluid. The expression derived was:

$$\frac{\varepsilon_{p,r}}{\varepsilon_{m,r}} = \frac{\int_0^\infty \eta^2 E_f(n)\mathrm{d}n}{\int_0^\infty E_f(n)\mathrm{d}n} \tag{33}$$

To obtain values of the energy spectra in equation (33), the Lagrangian energy spectra was related to the Eulerian, by extrapolating Mickelsen's[34] results and adopting Comte-Bellot's[35] results for the Eulerian energy spectra. Their results for $\eta^2 E_f(n)$ were expressed as a function of n and subsequently equation (33) was integrated numerically.

As regards the inertial coasting of particles through the viscous sublayer to the wall in vertical tubes, it was claimed that there was an extra transverse particle motion due to the relative motion between particles and fluid in the axial direction. The effect of a lift force on the spherical particle concerned, moving in the viscous fluid in shear flow, was considered in a way comparative with the Stokes drag force. The expression used for the lift force was derived by Saffman[36], and was included in the force balance equations governing the motion of a dense particle moving in the viscous sublayer, when the main flow was directed vertically upwards. Rouhiainen and Stachiewicz's results analysis produced the following conclusions:

(*a*) the lift force enhanced deposition for downflow and inhibited it for upflow;

(*b*) at low Re_D (<4000) and for small particles, the effect of the lift force was negligible, but as the particle size increased the lift force also increased to a comparative value with Stokes drag force;

(*c*) at high Re_D (>4000) and for small particles, the effect of the lift force favourably influenced particle deposition, but for large particles the lift force was negligible;

(*d*) the effect of the lift force increased with particle-to-fluid density ratio.

In this approach only the particle motion in the viscous sublayer was considered, where the motion of the fluid was assumed to be quasi-laminar. Rouhiainen and Stachiewicz's contribution would have been of more practical value if the theory was extended to predict particle deposition fluxes and was compared with experimental evidence to verify their conclusions, the validity of which remains uncertain.

Turbulent Inertia Diffusivity

Liu and Ilori[37] presented a model where the particles were viewed diffusing to a stopping distance from the wall with an 'effective particle diffusivity', and subsequently depositing onto the wall with the local r.m.s. fluctuating velocity component normal to the wall. The effective particle diffusivity was expressed as:

$$\varepsilon_{P,T} = D_B + \varepsilon_{m,r} + \varepsilon' \tag{34}$$

Liu and Ilori adopted Sehmel's derivation for the deposition velocity. The one-dimensional diffusion equation was expressed in cylindrical coordinates, and the 'turbulent inertia' diffusivity was included in the development of their theoretical model. The dimensionless deposition velocity V_d^+ was expressed by:

$$\frac{1}{V_d^+} = \int_{S^+ + r_p^+}^{R^+} \frac{\mathrm{d}y^+}{[1 - y^+/R^+](\varepsilon_{m,r}^+ + \varepsilon'^+)} + \frac{1}{(u_\tau'^+)_{S^+ + r_p^+}[1 - (S^+ + r_p^+)/R^+]} \tag{35}$$

The fluid near the boundary wall regions was divided into two layers, $S^+ + r_p^+ < 30$ and $30 \leqslant S^+ + r_p^+ \leqslant R^+$, in each of which the dimensionless deposition velocity, V_d^+, was expressed based on equations (34) and (35). The derived expressions for V_d^+ were related to a dimensionless deposition velocity, U_d^+, of a vapour with $Sc = 1$.

To take into account the Re_D, Liu and Ilori assumed that the concentration profile was the same as the velocity profile in the turbulent flow field. Empirical and semi-empirical mass and heat transfer relationships were used for the derivation of the velocity profile. Their theoretical results are shown in Figure 1.

Their theoretical model was supported by experimental results obtained in vertical tubes using two particle sizes of 6 and 9 μm in diameter, shown in Figure 2. The experimental data were found to give a better fit to their theoretical model than the theoretical predictions of the previous models of Friedlander and Johnstone and of Davies. The mass rate of particle deposition was found to be increasing with particle size, and independent of the tube material. The results showed that the deposition velocity profile was similar to the developing fluid velocity profile, remaining constant after a certain inlet length of the tube, and this length was decreasing with increasing Re_D. Therefore, higher deposition rates would be expected where the flow was not fully developed. Ilori's work[32] was extended experimentally to include particle deposition at the tube end and tube joints, and tubes with rough depositing surfaces.

When compared with available experimental data, the theory of Liu and Ilori gave reasonable agreement for values of $2 < \tau_p^+ < 20$. Liu and Agarwal[33] found good agreement between Liu and Ilori's theory and their own experimental results. This theoretical model was not widely used by others, perhaps due to the questionable assumptions upon which it was based, and the lack of comparison with a wider range of available results.

Particle Deposition Model Incorporating a Continuous Function for the Eddy Diffusivity over the Fluid Wall Region

Wasan et al's[38] investigation of this subject for particles of $d_p \ll 100\,\mu$m was based on Beal's, and Friedlander and Johnstone's analyses. In their theory, the deposition velocity was determined by correlating the shear stress equation with the mass transfer equation and expressing the eddy diffusivity as a continuous function over the wall region. In the course of deriving

VOL. 62 1984

the deposition velocity equations the following assumptions were made:

(*a*) the shear stress and mass transfer were constant in the wall region;
(*b*) in the fully developed turbulent region, the ratio of the shear stress to the mass transfer flux was constant and the molecular diffusivity, D_B, was negligible compared to the eddy diffusivity, $\varepsilon_{m,r}$;
(*c*) the interfacial velocity, in the case of mass transfer, was negligible;
(*d*) the eddy diffusivities of momentum, $\varepsilon_{m,r}$, and mass, $\varepsilon_{d,r}$, were equal.

Two regions near the wall were considered: $0 \leqslant y^+ \leqslant 19.75$ and $y^+ \geqslant 19.75$. In the former region the eddy diffusivity was taken to be a function of the local Fanning friction factor, f, and in the latter[39] a function of y^+, Sc and f. Their final equations for the deposition velocity in the absence of gravitational and electrostatic forces were:

$$V_d^+ = (f/2) \Big/ \left\{ 1 + (f/2)^{1/2} \times \left[\int_{S^+}^{19.75} \frac{dy^+}{(1/Sc) + \varepsilon_{m,r}/\nu} - 13 \right] \right\}$$

$$\text{for } 0 \leqslant S^+ \leqslant 19.75 \tag{36}$$

and

$$V_d^+ = \frac{f/2}{1 - 13(f/2)^{1/2}} \quad \text{for} \quad S^+ \geqslant 19.75 \tag{37}$$

where

$$S^+ = \frac{f}{40}\left(\frac{d_p}{D}\right)^2 \left(\frac{\rho_p}{\rho_f}\right) Re_D^2 + r_p^+$$

and

$$r_p^+ = d_p \bar{U}_{x,mean} (f/2)^{1/2}/2\nu$$

The expressions for S^+ and r_p^+ above were the same as those used by Beal[18].

Wasan et al's theory was supported with experimental data obtained using aerosol powder particles ranging from 0.6 to 6.0 μm in diameter. Particle size number concentrations and size distributions were measured upstream and downstream of the main flow. Their results were expressed in a graphical form as percentage deposition (or deposition efficiency) versus particle size for Re_D values ranging from 5000 to 18,200. The conclusions of their work were: (*a*) The deposition of particles from an aerosol dispersion was dependent on particle size and Re_D. The deposition velocity increased with increasing Re_D and decreased with decreasing Re_D. At very low mean fluid velocities, gravitational settling was enhanced. (*b*) At low Re_D values, particle re-entrainment was minimised, while higher Re_D values gave rise to particle re-entrainment.

Wasan et al found that their theory was in better agreement with their experimantal results than the theoretical predictions of Friedlander and Johnstone. Their results were compared with limited data available on the subject and no apparent distinction between particle and eddy diffusivity was made throughout their work. Earlier evidence[40], however, contradicted assumption (*d*) of Wasan et al and questioned the validity of the other assumptions, in spite of the apparent agreement found between theory and experiments.

RANDOM WALK AND PROBABILISTIC THEORIES

Many early investigators recognised that a stochastic approach could relate fluid and particle interactions in the turbulent flow field and in the region adjacent to the wall region, but no such theory was put forward.

Hutchinson et al[20] were the first to propose a stochastic theory for particle deposition. In the course of developing their theory, Hutchinson et al viewed the particles moving at the mean fluid velocity and executing a two-dimensional random walk, on a hypothetical disc plane normal to the direction of the main flow. The particles approaching the wall at a given distance downstream were determined statistically, and provision was made for the possibility that the eddy and the particle motion were not identical. Those particles with high enough momentum were able to penetrate the region of the damped turbulence near the wall and subsequently to deposit on to the wall surface. The rest, having insufficient momentum and hence unable to reach the wall, were entrained in the wall region fluid until they eventually passed out of the duct. The transport of particles in the turbulent core was described as a diffusion process in which the particle–eddy interactions were the primary factors to particle deposition. The particle momentum appeared to be the deciding parameter determining whether or not a particle was deposited onto the boundary wall of a duct.

Hutchinson et al adopted a very simplified description of turbulence, in which the turbulent structure in the cross-section concerned was assumed to comprise numerous eddies, all of a constant characteristic length, lifetime and speed but with random direction. A brief outline of Hutchinson et al's theory is given in Appendix B. The predictions of this stochastic approach were compared with the experimental data of Friedlander and Johnstone[7], Alexander and Coldren[40], and Cousins and Hewitt[42], and good agreement was found.

Cleaver and Yates[43], following an earlier suggestion by Owen[44] and aware of the developments of the eruptive three-dimensional instabilities of the flow near the wall[45,46,47], developed a sublayer particle deposition model. In their theory the particles appeared to be subjected to the occurring fluid 'downsweeps' and 'upsweeps or ejections' in a turbulent 'burst' near the wall. Once a particle was entrained in a downsweep it was expected to continue within the downsweep with little interruption. Whether the particle was deposited on the wall surface or not depended on the position at which it entered the downsweep and whether its inertia allowed it to follow the fluid motion. Only the particles between turbulent bursts were considered to have the possibility of approaching the surface, while the rest were swept away from the region near the wall into the turbulent

core. The 'bursting' process of events near the wall of a turbulent flow is reviewed by Hinze[45]. Cleaver and Yates considered a two-dimensional stagnation point flow across an axial section of the flow near the wall to approximate the flow pattern within the viscous sublayer, in which the only acting force on the particle was the Stokes viscous drag, to deduce the particle trajectory equations. In their analysis, the importance of the particle relaxation time and the particle-to-fluid density ratio was assessed and incorporated into their results. The agreement between predictions and available experimental data for large ($\tau_p^+ \geqslant 10$) and small ($10^{-1} \leqslant \tau_p^+ < 10$) particles was good. The predictions of Cleaver and Yates' theory were compared with the predictions of other theories in Figure 1, as V_d^+ versus τ_p^+ (for $\rho_p/\rho_f = 965$ and 6360).

Reeks and Skyrme[46] proposed a stochastic model similar in many ways to that of Hutchinson et al. Particles outside the molecular range were considered, which were dispersed in the turbulent duct flow according to Fick's law of diffusion. The particle behaviour in the turbulent core was described by the law of diffusion up to an arbitrary 'diffusion edge' where diffusion stops and inertial convection dominates in the region near the wall. The ratio of r.m.s. particle to fluid velocity was determined from the equation of motion of the particle as a function of the fluid and particle densities, fluid kinematic viscosity, duct dimensions and particle diameter.

The theoretical results of Reeks and Skyrme were plotted alongside Liu and Agarwal's[33] experimental data as $\log V_d^+$ versus $\log \tau_p^+$, in which the dimensionless particle deposition velocity appeared to be a continuous function of the dimensionless particle relaxation time in the region of $1 < \tau_p^+ \leqslant 10^3$ as shown in Figure 4. The theoretical curve gave a very steep slope (about 11) in the region of $\tau_p^+ = 1$ to 3 and a decrease in V_d^+ when $\tau_p^+ > 30$. This high slope was contrary to the experimental evidence shown in Figure 2, which may be attributed to the parameters selected for the derivation of their final expression for the deposition velocity, in order to obtain a good fit with Liu and Agarwal's results. Apparently in Reeks and Skyrme's theory, the dimensionless deposition velocity was related to the concentration of particles in the viscous sublayer rather than the bulk particle concentration as most other investigators, including Liu and Agarwal, had chosen. Experimental results involving concentration measurements in the viscous sublayer region are very scarce because of the difficulties involved in obtaining them.

The slight decrease in V_d^+ when $\tau_p^+ > 30$ could be explained by the fact that some of the larger particles

VOL. 62 1984

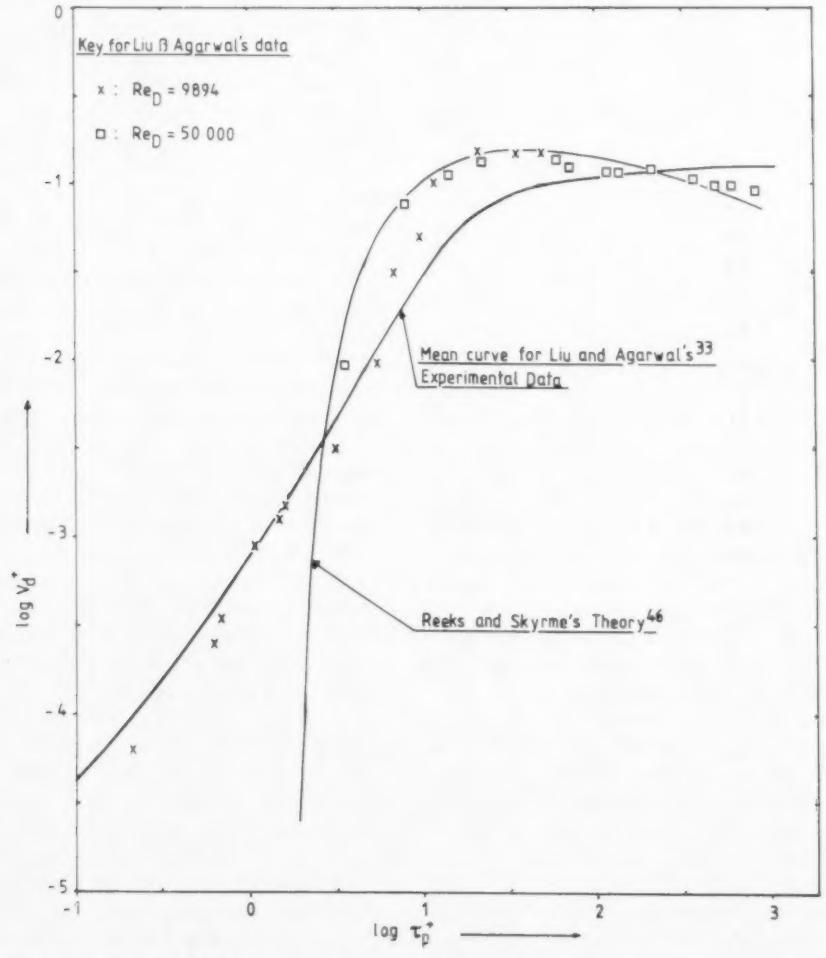


Figure 4. Comparison of Reeks and Skyrme's predictions with Liu and Agarwal's experimental data.

were re-entrained in the high velocity fluid in a similar way to a boundary surface that was not a perfect sink[76].

Papavergos and Hedley[47] combined Hutchinson et al's theory with the sublayer model of Cleaver and Yates in an attempt to describe the particle behaviour relative to the fluid, throughout all the stages from the turbulent core to the boundary wall. Hutchinson et al's approach was considered to be the first stage to particle deposition, in which the particle momentum appeared to be the predominant parameter and was referred to as the 'macro-mechanism' for particle deposition. Cleaver and Yates' model was considered to be the second stage to particle deposition, in which those particles that failed to reach the boundary wall in the first stage, were subject to the turbulent bursts occurring near the wall, and was referred to as the 'micro-mechanism' for particle deposition. From the analysis of results of the macro-mechanism, and in the light of reliable experimental data, it was found that the rate of deposition was underpredicted for particles of $d_p \leqslant 10\ \mu$m. The tendency to underpredict mass loss by the macro-mechanism was compensated for by the incorporation of the micro-mechanism. Allowance was also made in this theory for the deposition of particles in the submicron range. The predictions of this two-stage theory of particle deposition were found to be in good agreement with the experimental results (which involved particles of $0.5 \leqslant d_p < 5.0\ \mu$m) and the experimental results of other workers[58,69]. The theoretical predictions of Papavergos and Hedley's model are compared with previous theories in Figure 1, while some of the experimental results are shown in Figure 3.

EXPERIMENTAL STUDIES OF THE DEPOSITION OF PARTICLES FROM TURBULENT FLOWS

Most of the theoretical models above were intended to apply to either vertical or horizontal flow systems, since evidence has shown that such a distinction is not critical when dealing with fine particles in highly turbulent flows. When Owen[44], and later Sehmel[29], introduced the effect of gravity on deposition in their theories for horizontal flows, the choice of flow system became more deliberate.

The experimental results in this section, which lacked sufficient detail to be expressed in the same units as those in Figures 2 and 3, were excluded from these graphs.

Vertical Flow Systems

The deposition data obtained in vertical flow systems are summarised in Figure 2, where V_d^+ is a function of τ_p^+.

Stavropoulos[48] investigated experimentally the deposition of 24.5 μm diameter lycopodium spores ($\rho_p = 650\ \text{kg m}^{-3}$) inside a vertical glass tube of 0.0254 m i.d., the inside walls of which were coated with petroleum jelly to prevent re-entrainment. The fluid Reynolds number, Re_D, was varied from 3.52×10^3 to 4.35×10^4. The deposition rates on the coated surface were determined microscopically, and the results were correlated with von Karman's analysis for turbulent transfer assuming that the particles diffused with the fluid eddies to within one stopping distance of the wall. Stavropoulos found that the deposition velocity, V_d, rapidly increased with increasing Re_D, but at high Re_D values a decrease in V_d was reported. This was contrary to the theoretical predictions, and to later experimental results, which led to speculation about the reliability of his results.

At a much later date Forney and Spielman[30] attempted to reproduce Stavropoulos' results in a similar experimental facility, and found that their deposition velocities were an order of magnitude higher than those of Stavropoulos, under reportedly similar conditions. A close examination of their data covering four values of particle-to-fluid density ratios and of particle-to-tube diameter ratios, indicated no effect of either of these dimensionless groups on the deposition velocity.

Schwendiman and Postma[22,49] measured the particle deposition velocity of fluorescent grade ZnS particles ($\rho_p = 420\ \text{kg m}^{-3}$) of 2 and 4 μm diameter, and glass spheres ($\rho_p = 2500\ \text{kg m}^{-3}$) of 30 μm diameter, in 0.0254, 0.0180 and 0.0138 m i.d. aluminium, steel and brass tubes respectively, coated inside with silicone oil to avoid re-entrainment of the glass beads. The Re_D was varied from 3×10^3 to 2×10^4. The deposition rates were determined microscopically and their results were expressed as a relationship of the ratio of deposition velocity to the mean fluid velocity, with the ratio of the particle stopping distance to the thickness of the viscous sublayer. Parallel measurements were made on rough surfaces too, the results of which suggested that there was no significant difference in the particle deposition velocity values between polished and rough surfaces. In certain cases the deposition velocity values appeared to be higher for the polished surfaces than for the rough ones, under the same experimental conditions. Beal[18], correlating Schwendiman and Postma's results for smooth surfaces with his theoretical model, found closer agreement than the experimental results of Friedlander and Johnstone[7].

Wells and Chamberlain's[19] experimental work involved the measurement of radioactively tagged particles of 0.17 to 5 μm in diameter and of varying density from 1000 to 1180 kg m^{-3}. The deposition rate was measured on smooth and rough surfaces of a 0.0381 m i.d. tube, in which the Re_D could be raised to 5×10^4. No measures were taken to prevent the re-entrainment of the larger size particles. Colburn's analogy was used to correlate the theoretical with the experimental results for the molecular size particles, and reasonable agreement was found. Wells and Chamberlain[19] and Chamberlain[50] found that very small surface roughness substantially increased the particle deposition rate. They were the first to verify the minimum particle deposition rate predicted in Davies'[16] theory over the range of $1.3 \times 10^4 \leqslant Re_D \leqslant 3.0 \times 10^4$.

Farmer's[31] particle deposition velocity results were determined from measurements of large water drops (100 to 260 μm volume mean diameter) injected in a 0.0127 m i.d. vertical tube of a downward flow system. His results appeared to obey the following trend:

$$V_d = f(d_p^{-1}, \bar{U}_{x,\text{mean}}^{-1/2}) \qquad (38)$$

More recently Liu and Agarwal[33] investigated experimentally the deposition of particles in vertical turbulent pipe flows over a broad range of experimental conditions. Monodisperse olive oil aerosol droplets (containing $<10\%$ by weight of uranine, used as a tracer) were produced ranging from 1.4 to 21 μm in diameter. After the aerosol droplets had been electrically neutralised and diluted with air they were allowed to travel along various sections of a pipe flow, to be subsequently deposited on a 0.0127 m i.d. glass tube of 1.02 m length. The concentration of the deposited particles was determined fluorometrically at two nominal Re_D values of 10^4 and 5×10^4 respectively. The deposition velocity was calculated from equation (29) and their results were expressed graphically as V_d^+ versus τ_p^+ for each Re_D value (Figures 2 and 4).

From their results it was concluded that: $V_d^+ = 6 \times 10^{-4}(\tau_p^+)^2$ for $\tau_p^+ < 10$ and in the region of $10 \leqslant \tau_p^+ \leqslant 30$ a peak of $V_d^+ = 0.14$ was found. In the region of $\tau_p^+ > 30$ a moderate dependence of V_d^+ on τ_p^+ was reported which appeared to be decreasing slightly at higher τ_p^+ values. In effect their results suggested that the mass transfer coefficient changes fairly abruptly to a slowly falling value with respect to particle size. As the particle size rises still further, the particle inertia becomes so large that the particles cannot attain the eddy velocity during the time they are caught up by an eddy and, in consequence, the deposition rate falls more rapidly. The variation of V_d^+ approximately as $(\tau_p^+)^2$ was also suggested by Kneen and Strauss[10], and in a later review by McCoy and Hanratty[51]. The results of Liu and Agarwal were found to be in reasonable agreement with the predictions of Friedlander and Johnstone's[7] and Beal's[18] theories for $\tau_p^+ < 20$. Equally good agreement was found with Liu and Ilori's[37] theory for $2 < \tau_p^+ < 20$, but the deposition velocities predicted by Davies'[16] theory were considerably lower at $\tau_p^+ < 30$ than those measured.

Horizontal Flow Systems

The deposition data obtained in horizontal flow systems are shown in Figure 3, where V_d^+ is a function of τ_p^+.

Experimental results associated with the particle deposition in turbulent horizontal flow systems are comparatively limited.

One of the early publications was that of Alexander and Coldren[40]. In their experiments water droplets, generated by an atomising nozzle, were injected into an air stream of a horizontal 0.0472 m i.d. duct, the droplet size distribution of which was calculated by Nukiyama and Tanasawa's[52] correlation for this type of nozzle spraying, rather than measured. The average calculated droplet diameter was about 25 μm. Concentration profiles were measured by pitot tubes downstream from the duct, from which the total flow rate at any given cross section was determined by integration. The rate of deposition on the wall over any given length was subsequently calculated from the change in droplet concentration throughput, over the range of $7.7 \times 10^4 \leqslant Re_D \leqslant 2.9 \times 10^5$. The deposition rates paradoxically appeared to be higher in the developing region than those in the developed region of the turbulent flow. This was possibly due to the high radial component of the droplet velocity relative to the axial component that was impaired from the atomisation process, which resulted in an elutriation effect that decelerated the particles in the free stream[31]. The droplet concentration profiles were axisymmetric throughout, indicating that the effect of gravity on deposition was negligible. From their work it was concluded that the main resistance to mass transfer towards the wall was in the thin viscous sublayer adjacent to the wall.

Namie and Ueda[53], working on a 0.06×0.01 m horizontal channel, also measured deposition rates of water drops, of estimated[52] Sauter mean diameter 131 to 187 μm, by following the drop concentration decrease with axial distance. Their results showed that the concentration profiles were asymmetric, exhibiting a maximum close to the wall.

McCoy[54] also measured deposition rates of water drops in a horizontal 0.305×0.0254 m channel. The drop size distribution was measured by an electric probe developed by Tatterson[55]. Even more asymmetric concentration profiles than those obtained by Namie and Ueda above were reported, since the size range of drops measured was 413 to 617 μm Sauter mean diameter. Both the studies of Namie and Ueda, and McCoy were associated with large size particles for which the most predominant deposition mechanism was inertial diffusion or gravitational settling rather than turbulent diffusion.

Yoder and Silverman[56] investigated the deposition and agglomeration of monodisperse polystyrene latex spheres ($\rho_p = 1060\ \mathrm{kg\ m^{-3}}$) of $d_p = 0.26$ and 0.80 μm inside a 0.026 m i.d. horizontal copper tube over the range of $3 \times 10^4 < Re_D \leqslant 10^5$. In their experiments deposition and agglomeration were taking place simultaneously, and their objective was to distinguish the two effects quantitatively. Their deposition results were higher by a factor of 10 to 100 than those predicted by the theories of Davies and Beal. These results are doubtful and of little value, since a narrow range of experimental conditions was covered and about 20% of the experimentally determined deposition coefficients were negative, which was ignored in their results analysis.

Montgomery[57,58] measured mass and number droplet concentrations in the fully developed turbulent flow section of a 0.152 m i.d. horizontal wind tunnel. Homogeneous droplets of 0.44 to 2.16 μm diameter were dispersed in flows of $5.0 \times 10^3 \leqslant Re_D \leqslant 3.65 \times 10^5$. From the design details of the wind tunnel and the measurements of the axial mean velocity and wall friction velocity, it was suggested that the flow field turbulence characteristics were analogous to Laufer's[9]. Montgomery actually measured droplets already deposited onto the walls of the test section by light microscopy, in addition to the concentration profiles measured by isokinetic sampling. In his work all the relevant experimental conditions under which measurements took place were reported in detail. His results were compared with the predictions of the various current theories, rather than other investigators' results which were either incomplete (in terms of experimental details) or not di-

rectly comparable. The main conclusions of his work were:

(*a*) The deposition velocities predicted by previous theories[7,15,16,18,25] were several orders of magnitude lower in some cases, than those determined experimentally;
(*b*) V_d^+ was found to be very strongly dependent on Re_D but was a weak function of τ_p^+;
(*c*) Beal's theory appeared to give better predictions than Friedlander and Johnstone, or Levich's theories in relation to his experimental results. Davies' predictions were found to be of narrow range and in certain cases the deposition velocities, when compared with his experimental data, were up to 1000 times lower.

THE DEPOSITION OF DROPS FROM ANNUALAR TWO-PHASE FLOWS

Most studies in this area of research are concerned with the behaviour of drops produced from a liquid (usually water) introduced as an annulus into a turbulent gas stream (usually air). The entrained drops in the gas phase redeposit onto the walls of the duct, forming a new film of liquid downstream of the main flow. The original annulus of liquid film is prevented from coming into contact with the new one formed by the redeposited drops, so that accurate measurements of the deposition rates may be obtained. The origin of drop formation depends on the large disturbance waves (or roll waves) formed during annular flow. The gas 'undercuts' the wave, forming an open-ended bubble, which when burst releases its pressure to give a rapid acceleration to the gas phase, that is then transferred to the entrained drops.

The size of the drops produced in an annular flow was found to be dependent on the turbulent characteristics of the gas phase; the flow rate and physical properties of the liquid phase[59]; to a lesser extent the type of flow system (vertical or horizontal)[60], and the dimensions of the channel[55]. In most experimental studies on the subject, the size of the drops produced covered a wide range and a large number of them were of $d_p > 100\ \mu$m[54,61,70]. The influence of the initial drop release process was found to be significant during the lifetime of a drop (i.e. from its formation to its redeposition), as its size increased and/or the ejection velocity it acquired during the bubble-burst, increased[60,62]. To avoid possible re-entrainment of the drops already deposited in the gas phase, the liquid film formed by the drops should be kept thin[63,64].

Experimental evidence[62] suggests that the fine droplets ($d_p \leqslant 10\ \mu$m) entrained in the gas phase are rapidly deposited onto the boundary walls due to their interaction with the turbulent eddies. Larger drops ($50 < d_p \leqslant 100\ \mu$m) tend to deposit more slowly because they are partly influenced by the turbulent gas phase, not having acquired a large initial momentum during their release from the liquid film. Drops of $d_p > 150\ \mu$m are unaffected by the turbulent gas phase eddies due to their high momentum, and their destination is determined by the initial release process. The trajectories of large drops tend to be parabolic under the influence of gravity and, like the fine ones, spend very little time in the gas phase, unlike those in the 50 to 100 μm range.

The mechanism of deposition for those drops that are subjected to a succession of interactions with the gas phase eddies, may be described by a diffusional type process[64,65,66], similar to that of Hutchinson et al[20]. The deposition of drops with high enough momentum acquired during their release process, and upon which the gas phase turbulence has no significant effect, may be explained by an impaction type mechanism[62,65,66]. The mathematical models[60,62] on the subject interpret the deposition process as a combination of the diffusion and the impaction mechanisms, in the absence of adequate evidence concerning their generality. Although improvements on the two individual contributing mechanisms were made in the light of reliable experimental evidence[60,67], much speculation still exists over combining the two.

In view of the nature of events and the number of physical parameters affecting the production and redeposition of drops in an annular flow, most experimentalists designed their flow systems (vertical and horizontal) depending on where their interests lay. One of the early experimental studies by Cousins and Hewitt[42,68] used a vertical upflow system of air and water in 0.00953 and 0.0318 m i.d. tubes. The remaining liquid film, originally used for the production of drops, was removed by suction through a porous wall. The drops produced were entrained in the turbulent gas phase and were subsequently allowed to deposit on the wall surface downstream of the test section of the tube. The deposition rates were also determined by sucking off the wall layer at the end of the deposition test section. Cousins and Hewitt made drop size measurements in the 0.00953 m i.d. tube, which were found to be within the range of 40 to 100 μm Sauter mean diameter. The results of their studies indicated that the deposition velocity was independent of the mean gas phase velocity and drop concentration. The deposition rate results agreed with the later results by Farmer[31], but unlike more recent studies in annular flows[53,54,55], the size of the drops reported was rather small. This was perhaps due to the small tube diameter used, since theoretical predictions[55] showed that larger tube diameters produced larger drops in annular two-phase flow systems. Also in small diameter tubes, the film thickness formed by the deposited drops is required to be comparatively small to avoid drop re-entrainment[71]. Some of the results of Cousins and Hewitt could have been affected by drop re-entrainment, which gave rise to small size drops being produced.

Anderson and Russell[69] made deposition rate measurements in a horizontal flow system of air and water of 0.0254 m i.d. tube of $4.7 \times 10^4 \leqslant Re_D \leqslant 7.0 \times 10^4$. From their results it was concluded that drop deposition was partly influenced by gravity.

Jagota et al[70] used dye tracers to determine the deposition rates in a vertical upflow system of air and water, using a 0.0254 m i.d. tube. Their results showed a tendency for the deposition velocity to increase with increasing gas phase velocity, contrary to the results of Farmer[31], and Cousins and Hewitt[42].

More recent experimental studies on this subject have been contributed by Namie and Ueda[53], and McCoy[54] mentioned earlier. Many more peripheral studies on the

subject have been published over the years, and a considerable amount of work is still in progress because of its direct application to evaporating and condensing flows. Of all the past and current studies on annular two-phase flows, little has been offered to advance the mechanisms involved in the droplet deposition behaviour from turbulent flows. This is due to the completely different nature of phenomena occurring in an annular flow from a turbulent gas flow, in which uniformly sized particles are injected under carefully controlled conditions.

DISCUSSION

The development over the years of the theories reviewed, follows the progress made in understanding the structure of turbulence.

Models Based on Classical Theories of Turbulence

The deposition theories based on the classical concepts of turbulence, made use of simplified assumptions involving empirical or semi-empirical correlations for the derivation of the governing equations. The common features of these theories may be summarised as follows:

(*a*) Use of the concept of 'stopping distance';
(*b*) Acceptance of a multilayered picture of the fluid layer adjacent to the wall (the viscous sublayer, the buffer layer and the turbulent core);
(*c*) Assumption that the particle diffusivity is equal (or proportional) to the eddy diffusivity of momentum;
(*d*) Assumption that the free flight particle velocity is equal to the r.m.s. radial fluid velocity (or directly proportional to the axial fluid velocity);
(*e*) When compared with experimental results, the theoretical predictions are usually presented graphically as relations of V_d^+ against τ_p^+ and less frequently as V_d^+ against Re_D.

The assumption that the fluid properties were the same in many respects as the properties of the particles entrained in it, led to many questions being raised about the validity of the mathematical models concerned. In the absence of experimental evidence, due to the physical difficulties involved in making measurements to examine the credence of these assumptions, the above features were cautiously accepted with slight variations in application among authors. As a result of this, many theories in the light of experimental evidence, were found not to be as widely applicable and accurate as they had intended to be. As a general rule, most past theories having the above common features underpredicted the rate of particle deposition. For certain applications these theories were adequate and are still preferred today because of their simplicity. Some empirical relationships, based on the experimental data of various investigators[7,22,30,31,33], were also found to be very useful in design and are as follows:

$$V_d^+ = k_1(Sc)^{-2/3} \quad \text{at} \quad \tau_p^+ < 0.2 \tag{39}$$

$$V_d^+ = k_2(\tau_p^+)^2 \quad \text{at} \quad 0.2 < \tau_p^+ < 20 \tag{40}$$

$$V_d^+ = k_3 \quad \text{at} \quad \tau_p^+ > 20 \tag{41}$$

Typically $k_1 = 0.07$, $k_2 = 3.5 \times 10^{-4}$ and $k_3 = 0.18$.

In the above correlations of the experimental results, there is no indication of the influence of ρ_p/ρ_f and Re_D on deposition, and this may be responsible for the scatter in the results of previous studies.

The increasing demands imposed by new and improved industrial processes necessitate a deeper understanding of the mechanisms involved in the deposition of particles from turbulent flows, to produce more accurate mathematical models. The particle–eddy interactions in the turbulent core of a pipe flow are partly responsible for the deposition of particles, while simultaneously determining the conditions under which the particles approach the region near the wall. However, the hydrodynamics of the fluid layer adjacent to the wall also contribute to particle deposition.

Random Walk and Probabilistic Theories

The random motion of particles in the turbulent core of a duct flow is best simulated by a stochastic approach, in which each particle is considered to execute a random walk and interact with the fluid eddies. Because of the close analogy between random walk processes and diffusion processes, the theory of Hutchinson et al[20] is also referred to as a diffusion type model. Such an approach marked a significant change in the way this topic was previously examined, and was recognised as phenomenologically realistic. In both Hutchinson et al and Reeks and Skyrme's[46] theories the particle momentum, gained from the particle–eddy interactions in the turbulent core, was the deciding factor as to whether a particle was deposited or not. Those particles which approached the fluid layer near the wall but were short of sufficient momentum to reach the wall surface, were basically considered to pass out with the rest of the fluid irrespective of the hydrodynamics in that region. Hence, the deposition rate predicted by their theory was lower than the true value for small (or low momentum) particles.

Cleaver and Yates[43], who examined the effect of bursting of the viscous sublayer on particle deposition, predicted deposition rates of small particles accurately. The deposition behaviour of large (or high momentum) particles, which penetrate the fluid layer near the wall regardless of the occurrence of bursts, was not included in their analysis. Calculating the deposition rate of particles of a wide size distribution (e.g. $1 \leqslant d_p < 100\,\mu$m), by either theory leads to underprediction. It is therefore apparent that both theories above should be considered for either developing a general mathematical model or calculating deposition rates of dispersions of wide particle size distributions, while an understanding of the particle deposition behaviour mechanism is simultaneously provided[47].

The oversimplified picture of turbulence of Hutchinson et al, and the somewhat incomplete explanation of the sequence of events in the fluid layer near the wall of Cleaver and Yates, could be more accurately described in the light of recent evidence[72,73,74], using sophisticated measuring techniques and powerful computers.

Other Factors Affecting Particle Deposition

Common to all theories was the assumption that the viscous sublayer thickness was much smaller than the

duct radius and much larger than the size of the moving spherical particles in it. The duct wall surface was assumed to be smooth, i.e. any surface roughness was considered to be much smaller than the size of the particles concerned. The particles considered in the theories were assumed to be small and therefore subject to Stokes' Law, as well as electrically neutral.

Factors other than those attributed to turbulence–particle interactions were not considered in most fundamental theories, in view of the experimental and theoretical difficulties involved in accurately incorporating these factors into an already complex area of research. To apply any of the above theories to a practical situation, perhaps additional factors to those discussed should be considered. Although the scope of this review is not to examine such factors in detail, the importance of some is briefly highlighted in this section.

Wall Surface Roughness. Once particles commence depositing on surfaces, smooth surfaces become rough and the size of the roughness elements on surfaces increases as particle deposition progresses. Early work on the deposition of particles on rough surfaces[19,50] has shown that the surface roughness has an increasing effect on the rate of depositing particles, in comparison with smooth surfaces. Recent theories[76,77,78] revealed that even micro-rough surfaces have a marked effect on particle deposition, while the effect on u^* is very small. Further experimentation is needed to fully validate these theories, the predictions of which are in many cases compared with deposition data obtained from systems with smooth surfaces.

Thermophoresis. The interactions between particles and fluid in a non-uniform temperature environment result in a thermophoretic particle force[79,80,81]. The deposition of particles due to thermophoresis is significant to small particles (molecular size) provided that there is a temperature gradient. The thermophoretic force increases with temperature gradient but decreases with increasing particle size. Thermophoresis is shown to be an effective mechanism for particle deposition when the size of particles is $d_p < 2\,\mu$m[82].

Electrically Charged Particles. Entrained particles in flow streams tend to acquire electrical charge as do surfaces upon which they are deposited, unless appropriate measures are taken to minimise the occurrence of this effect. The rate of particle deposition can be significantly affected by the presence of electrical charge[58,83], when compared with electrically neutral systems. There is a need for experimental results to accurately explain the mechanism of turbulent particle deposition involving electrically charged particles.

It is pointed out that when any of the reviewed theories is to be applied to hydrosol systems, their assumptions need to be re-examined and appropriate modifications should be implemented. Particles in liquid systems have larger particle Reynolds numbers than in gas systems, and the Stokesian particle behaviour may not apply due to the larger particles present. Under these circumstances, factors such as the Saffman lift force[36], the Besset force[76] as well as other forces smaller in magnitude than these (van der Waals and magnetic forces) may also influence hydrosol particle deposition behaviour. The extent of each force affecting turbulent deposition behaviour of particles needs detailed evaluation, before applying the existing data of Figures 1, 2 and 3 (which were mainly obtained in gas flow systems).

Deposition of Drops from Two-Phase Annular Flows

Studies of the deposition of drops from two-phase annular flows are normally concerned with drops over a whole range of sizes, some of which interact with the turbulent eddies and others which are completely unaffected. The effect of the ejection velocity and gravity on the entrained drops are parameters influencing their deposition. The wavy nature of the liquid surface is analogous to a rough surface, and therefore increased deposition rates would be expected over those encountered for smooth surfaces. It is therefore clear that the results from such studies are not directly comparable with those studies involving uniform monodisperse particles (or droplets) injected in the fully developed turbulent flow of a gas duct with smooth walls. The application of the results from annular two-phase flows is limited to fundamental work on this subject, and it is normally preferable to treat annular flows as a separate concept.

Summary

By gaining physical insight and adopting a phenomenological approach to explain the concept of particle deposition, more accurate and realistic models are developed. At the same time, by increasing the level of sophistication, mathematical models become more demanding in experimental data and tend to be too complex to apply to routine design. The equations of such phenomenological approaches can be simplified to an amenable form, without impairing the fundamental principles of the theory, by resorting to valid experimental data[75]. Also, if accurate designs are to be achieved, more familiarisation with sophisticated models would be necessary.

CONCLUSIONS

1. The choice of a theory depends on the application concerned and the degree of accuracy of the results required. The Table summarises the main features and conclusions of each major contribution in this field, and was produced to assist the reader in that selection.

2. Those theories that are based on the classical concepts of turbulence are of limited application and accuracy, but easy to use in design calculations. The largest discrepancies among these theories in predicting the dimensionless particle deposition velocity, V_d^+, lie within $10^{-1} < \tau_p^+ \leqslant 2 \times 10$ (Figure 1). These discrepancies are due to the different assumptions made, which, as shown in Figure 1, can have a significant effect on the predictions of V_d^+. Similar wide variations of V_d^+ are also found within the same τ_p^+ range as above among different experimental studies (Figures 2 and 3). The large scatter of the experimental results is possibly due

to the influence of ρ_p/ρ_f and Re_D on V_d^+, which was not taken into account in the results analysis of most authors. In Figure 5 the predictions of the major theories are compared alongside the available experimental data as V_d^+ versus τ_p^+, and the magnitude of the aforementioned discrepancies is clearly shown.

3. Those theories that have adopted a stochastic approach to explain the deposition behaviour of particles from turbulent flows, tend to be more reliable than the previous theories because they are free of their questionable assumptions (associated with the concept of the stopping distance). Stochastic approach theories

Table 1. Summary of Major Theories on the Deposition of Particles from Turbulent Flows

Investigator	Type of theoretical model	Range of application	Additional features	Remarks and conclusions
Friedlander and Johnstone[7]	Particle diffusion-projection to the wall, adopting the concept of stopping distance	Where particle inertia is the main deposition mechanism	$U_{pr} = 0.9u^* = u_r'$. $\varepsilon_{p,r} = \varepsilon_{m,r}$. Multilayered wall concept	Theory makes questionable assumptions, which tend to limit its application in cases other than those were particle inertia is the dominant mechanism
Owen[12]	Particle diffusion-projection to the wall, incorporating the effect of gravity	Where gravity effects influence particle deposition	$\varepsilon_{p,r} \propto \varepsilon_{m,r}$. Multilayered wall concept	Lengthy expressions for the particle deposition rate on the floor, roof and side walls are derived, without the support of reliable experimental evidence
Davies[16]	Inertial and diffusive (eddy and molecular) mechanisms considered, while retaining the concept of stopping distance	Intended to cover all cases, ie $0.001 \leqslant d_p \leqslant 100\,\mu$m in the absence of extraneous forces	$\varepsilon_{p,r} = \varepsilon_{m,r}$. Multilayered wall concept. Empirical equation for $\varepsilon_{m,r}$ to apply across the entire boundary layer	Theory underpredicts deposition rates and is complex to use in routine design, but provides more physical insight into the occurring phenomena than the previous theories
Beal[18]	Similar to Davies', with the addition of a steady state particle accumulation near the wall	Cases involving particles ranging from molecular size to 100 μm in d_p	Free flight velocity is taken to be one half of the axial fluid velocity	In spite of the unrealistic free flight velocities assumed, the predictions tend to fit the experimental data more satisfactorily than the previous theories
Sehmel[23–29]	Similar to Davies', adopting empirical expressions for $\varepsilon_{p,r}$ to fit experimental results	Empirical relationships limit application of theory to within the specified range	The empirical relationships adopted are physically incorrect	The theory was tested over a narrow range of experimental conditions, and therefore lacks generality. The empirical relationships undermine the theory
Liu and Ilori[37]	Similar to Davies'. New relationship for $\varepsilon_{p,r}$ introduced	Intended for a wide range of conditions, but reliable only within $2 < \tau_p^+ < 20$	$\varepsilon_{p,T} = D_B + \varepsilon_{m,r} + \varepsilon'$. $\varepsilon' = (u_r')^2 \tau_p$	Despite the questionable assumptions of the theory, better fit with the available experimental data was obtained than the previous theories of Friedlander and Johnstone, and Davies
Wasan et al[38,39]	Similar to Beal's. $\varepsilon_{m,r}$ expressed as a continuous function	Cases involving particles of $d_p \ll 100\,\mu$m	$\varepsilon_{m,r} = \varepsilon_{p,r}$; two layered wall region: $0 \leqslant y^+ \leqslant 19.75$ $y^+ \geqslant 19.75$	The expressions of particle deposition rates are based on mass and momentum analogies, and $\varepsilon_{m,r} = \varepsilon_{d,r}$. Later work revealed that these analogies are not valid
Hutchinson et al[20]	Probabilistic theory-random walk concept	Intended to cover all cases, with no extraneous forces present	$\varepsilon_{p,r} \neq \varepsilon_{m,r}$. Simple definition of the relevant turbulence parameters	The theory is more realistic than all the previous theories and satisfactorily predicts deposition rates of particles of $d_p \geqslant 10\,\mu$m
Cleaver and Yates[43]	Probabilistic theory, including the occurrence of 'bursts' near the boundary wall	All cases not involving extraneous forces	Quasi-steady two-dimensional flow picture near the boundary wall	Provides physical insight into the mechanics of deposition, without taking into account particle behaviour in the turbulent core. Satisfactory agreement between predictions and available experimental data
Reeks and Skyrme[46]	Similar to Hutchinson et al's in principle	All cases involving particles outside the molecular range	Diffusion appears to stop at an arbitrary 'diffusion edge' near the wall	The theory is very difficult to verify experimentally and therefore its validity remains uncertain
Papavergos and Hedley[47]	Combined Hutchinson et al's with Cleaver and Yates' theories	Cases involving all particle sizes, and free from extraneous effects	Two stages for particle deposition: (a) macro-mechanism (b) micro-mechanism	Theory examines particle behaviour from the turbulent core to the wall until its final deposition. satisfactory agreement with experimental data

VOL. 62 1984

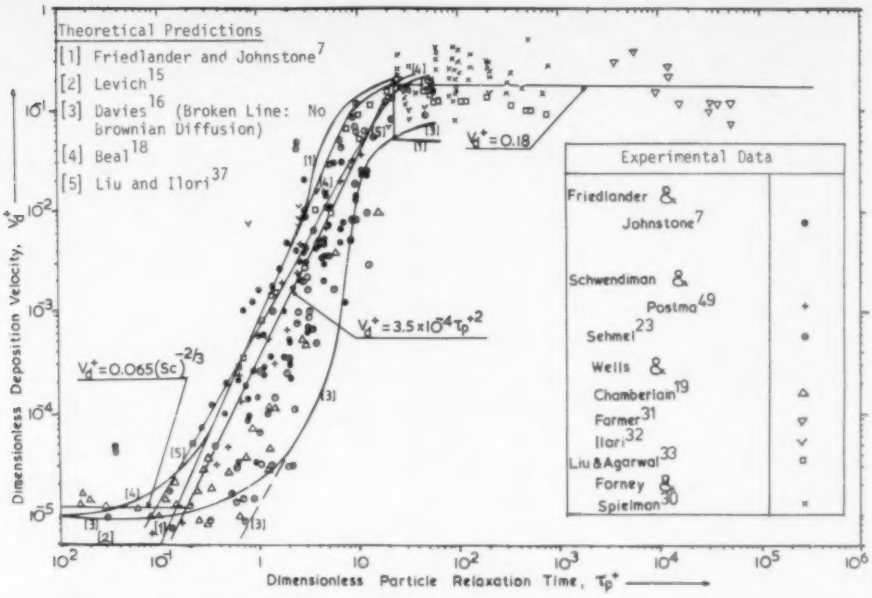


Figure 5. Comparison of major theories based on the classical concepts of turbulence with experimental data.

provide a physical insight into the phenomena that occur, but because these are complex and therefore need more parameters to define them, the theories tend to demand more input data. In Figure 6 the theoretical predictions are compared with experimental results. The agreement between theoretical and experimental results is satisfactory (except Reeks and Skyrme's theory–see text), considering that existing experimental results lack sufficient information to be directly compared with the theory, and in a number of cases authors make assumptions to produce such a comparison. Future experimental results need to be complete with adequate details to provide all the information required for direct comparison with the theories.

4. The experimental evidence suggests that the particle deposition rate is influenced by the particle relaxation time, τ_p, and the fluid Reynolds number Re_D. The effect of τ_p^+ on V_d^+ is pronounced for particles of $0.2 < \tau_p^+ < 20$ (Figures 1–6), while the influence of Re_D on V_d^+ becomes important for $Re_D \gtrsim 10^5$. Figure 7 shows the dependence of V_d^+ on Re_D based on experimental data. Factors other than τ_p^+ and Re_D may also have a direct or indirect effect on the particle deposition behaviour of particles which would come to light as more phenomenological familiarisation is gained. This will be a new departure from the traditional relationships expressed mostly as V_d^+ versus τ_p^+ and less frequently as V_d^+ versus Re_D, which may explain the wide variation of the present results.

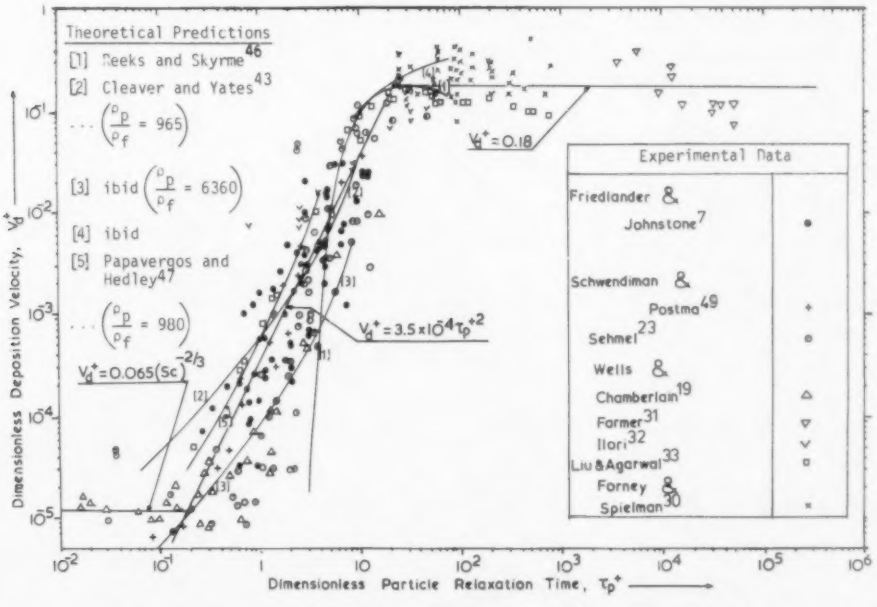


Figure 6. Comparison of major stochastic theories with experimental data.

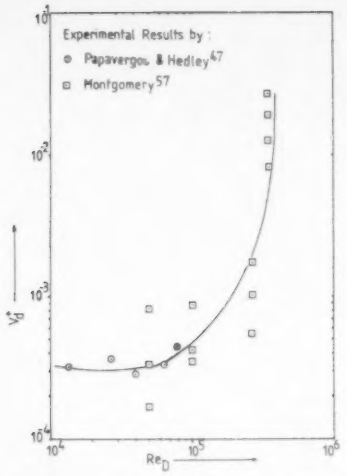


Figure 7. The Variation of the dimensionless particle deposition velocity, V_d^+, with the fluid Reynolds number, Re_D.

This could form the basis of further research on the subject, especially in those areas where discrepancies are pronounced.

5. The concepts outlined in the random walk and probabilistic theories can be applied to explain the deposition behaviour of particles or droplets in two-phase annular flows. Data from two-phase annular flows have limited application in fundamental research on this subject, due to the different nature of events that are taking place, as explained in the text. The basic difference being that during a two-phase annular flow there is a tendency towards a hydrodynamic equilibrium in which the rate of droplet entrainment from the liquid film becomes equal to the rate of droplet deposition on the film. From all the studies reviewed here, it becomes clear that the phenomena involved do not favour such a hydrodynamic equilibrium.

6. A general phenomenological approach to particle deposition would be better explained, if the particle–eddy interactions were taken into account in both the turbulent core and the fluid layer near the boundary wall. Attempts should be made to simplify these theories so that they are readily accessible for routine design, and can accommodate factors other than those attributed to particle–eddy interactions.

APPENDIX A

Additional Equations Associated with the Formulation of Beal's Model[18]

The transport coefficient, K, and the particle radial velocity, $U_{p,r}$, of equation (23) are given as follows:

For $0 \leqslant S^+ < 5$

$$K = \bar{U}_{x,mean}\sqrt{(f/2)}\left\{\frac{14.5}{3}Sc^{2/3}F(Sc,S^+) - \frac{(14.5)^2}{1.5D^+}Sc^{1/3}G(Sc,S^+) + \left[5+\frac{50}{\nu D^+}(D_B-0.959\nu)\right]\ln\left(\frac{D_B+5.04\nu}{D_B+0.04\nu}\right) - \frac{250}{D^+} + \frac{1-13.73\sqrt{(f/2)}}{\sqrt{(f/2)}}\right\}^{-1} \quad (A1)$$

where

$$F(Sc,S^+) = \tfrac{1}{2}\ln\left\{\frac{[1+(5/14.5)Sc^{1/3}]^2}{1-(5/14.5)Sc^{1/3}+(5/14.5)^2Sc^{2/3}}\right\} - \tfrac{1}{2}\ln\left\{\frac{[1+(S^+/14.5)Sc^{1/3}]^2}{1-(S^+/14.5)Sc^{1/3}+(S^+/14.5)Sc^{2/3}}\right\} + \sqrt{3}\tan^{-1}\left[\frac{(10/14.5)Sc^{1/3}-1}{\sqrt{3}}\right] - \sqrt{3}\tan^{-1}\left[\frac{(2S^+/14.5)Sc^{1/3}-1}{\sqrt{3}}\right] \quad (A2)$$

$$G(Sc,S^+) = \tfrac{1}{2}\ln\left\{\frac{1-(5/14.5)Sc^{1/3}+(5/14.5)^2Sc^{2/3}}{[1+(5/14.5)Sc^{1/3}]^2}\right\} - \tfrac{1}{2}\ln\left\{\frac{1-(S^+/14.5)Sc^{1/3}+(S^+/14.5)^2Sc^{2/3}}{[1+(S^+/14.5)Sc^{1/3}]^2}\right\} + \sqrt{3}\tan^{-1}\left[\frac{(10/14.5)Sc^{1/3}-1}{\sqrt{3}}\right] - \sqrt{3}\tan^{-1}\left[\frac{(2S^+/14.5)Sc^{1/3}-1}{\sqrt{3}}\right] \quad (A3)$$

For $5 \leqslant S^+ < 30$

$$K = \left[\left\{\left(1+\frac{10}{\nu D^+}(D_B-0.959\nu)\right)\ln\frac{D_B+5.04\nu}{D_B+\nu[(S^+/5)-0.959]} - \frac{10}{D^+}\left(6-\frac{S^+}{5}\right)\right\} + \frac{1-13.73\sqrt{(f/2)}}{\sqrt{(f/2)}}\right]^{-1} \frac{\bar{U}_{x,mean}\sqrt{(f/2)}}{5} \quad (A4)$$

For $S^+ \geqslant 30$

$$K = \frac{\bar{U}_{x,mean}(f/2)}{1-13.73\sqrt{(f/2)}} \quad (A5)$$

Also, for $0 < r_p^+ \leqslant 5$

$$U_{p,r} = u_r' = \sqrt{\left(\frac{k_B T}{2\pi m_p}\right)} + 0.5 r_p^+ \bar{U}_{x,mean}\sqrt{(f/2)} \quad (A6)$$

For $5 < r_p^+ \leqslant 30$

$$U_{p,r} = u_r' = \sqrt{\left(\frac{k_B T}{2\pi m_p}\right)} + 0.5(-3+5\ln r_p^+)\,\bar{U}_{x,mean}\sqrt{(f/2)} \quad (A7)$$

VOL. 62 198

APPENDIX B

Brief Outline of Hutchinson et al's Theory[20]

The fraction of particles which were deposited at a distance L downstream in the duct from a source was given by:

$$J = KF(L/D) \tag{B1}$$

The fraction $F(L/D)$ over a time period τ (or distance L) was defined by:

$$F(L/D) = \frac{\int_0^\tau M(t)\mathrm{d}t}{\int_0^R 2\pi r' f(r')\mathrm{d}r'} \tag{B2}$$

where

$$M(t) = -2\pi R \frac{\dot{n}\langle l_p^2\rangle}{4}\left[\frac{\partial N(r,t)}{\partial r}\right]_{r=R} \tag{B3}$$

$$N(r,t) = \frac{2}{R^2}\sum_{N=1}^{\infty}\frac{J_0(r\alpha_N/R)}{J_1^2(\alpha_N)}\exp(-\beta_N) \times \int_0^R r' f(r') J_0\left(\frac{r'}{R}\alpha_N\right)\mathrm{d}r' \tag{B4}$$

$$\beta_N = \frac{\dot{n}\langle l_p^2\rangle}{4R^2}\alpha_N^2 t \quad \text{and} \quad t = L/\bar{U}_{x,\mathrm{mean}}$$

Incorporating equations (B3) and (B4) into (B2), the final expression for $F(L/D)$ was given by:

$$F(L/D) = 1 - 2\sum_{N=1}^{\infty}\frac{\exp(-\beta_N)}{\alpha_N J_1(\alpha_N)} \times \int_0^R r' f(r') J_0\left(\frac{r'}{R}\alpha_N\right)\mathrm{d}r' \Big/ \int_0^R r' f(r')\mathrm{d}r' \tag{B5}$$

Equation (B5), when applied to a point or ring source of constant density, was simplified from its present form by expanding $J_0(r'\alpha_N/R)$ in series up to the first term, i.e.:

$$F(L/D) \simeq 1 - 2\sum_{N=1}^{\infty}\frac{\exp(-\beta_N)}{\alpha_N J_1(\alpha_N)}$$

for a point source (B6)

and

$$F(L/D) \simeq 1 - 4\sum_{N=1}^{\infty}\frac{\exp(-\beta_N)}{\alpha_N^2}$$

for a ring source (B7)

The fraction K was defined by:

$$K = \int_{-\pi/2}^{\pi/2}\int_{U_{pth}}^{\infty} P(U_p, \Theta)\mathrm{d}U_p\mathrm{d}\Theta \tag{B8}$$

$$\Theta = \tan^{-1}\frac{U_{pr}}{U_{p\phi}}$$

Following the mathematical derivation for $P(U_p, \Theta)$ according to Papoulis[41]:

$$P(U_p, \Theta) = \frac{U_p}{\pi\sigma^2}\exp\left(-\frac{U_p^2}{2\sigma^2}\right) \tag{B9}$$

Integrating equation (B8) with respect to U_p:

$$K = \int_{-\pi/2}^{\pi/2}\exp\left(-\frac{U_{pth}^2}{2\sigma}\right)\mathrm{d}\Theta \tag{B10}$$

$$U_{pth} = L_p\tau_p^{-1}$$

SYMBOLS USED

The dimensions are in terms of: Mass (M), Length (L), Time (T) and Temperature (Θ).

c	Stokes constant ($=3\pi\mu$)	$ML^{-1}T^{-1}$
D	Duct diameter	L
D^+	Dimensionless duct diameter ($=Du^*/\nu$)	
D_B	Brownian (or molecular) diffusivity	L^2T^{-1}
d_p	Particle (or droplet) diameter	L
$E_f(n)$	Lagrangian energy spectrum of the velocity fluctuations	
f	Fanning friction factor	
$f(r')$	Radial density distribution for a unit strength source at $r = r'$—equation (B2)	
$F(L/D)$	Fraction of the entrained particles that approach the wall	
g_p	Specific gravity of the particle (or droplet) relative to the fluid	
$J_0(\alpha_N)$	Bessel function of the first kind of order zero—equation (B4)	
$J_1(\alpha_N)$	Bessel function of the first order—equation (B4)	
K	Transport coefficient defined in Appendix A—equations (23), (24)	LT^{-1}
K	Fraction of particles that have penetrated the wall fluid layer and subsequently deposited onto the wall surface of the duct—equation (B1)	
k_1, k_2, k_3	Proportionality constants in equations (39), (40), (41) respectively of slightly variable magnitude among experimentalists	
k_B	Boltzmann constant	
K_D	Deposition coefficient (equivalent to particle deposition velocity)—equations (23), (24)	LT^{-1}
L	Distance measured in the longitudinal (x) – direction	L
L_p	Particle penetration distance—equation (B10)	L
l^+	Dimensionless distance measured from the duct's wall ($=lu^*/\nu$)	
$\langle l_p^2\rangle$	Mean square displacement distance for the particles	L^2
m_p	Mass of particle (or droplet)	M
$M(t)$	Rate of particles approaching the wall region—equation (B2)	$ML^{-2}T^{-1}$
n	Wave number or frequency—equation (33)	T^{-1}
N_r	Mean local aerosol concentration	ML^{-3}
N_r^+	Dimensionless mean local aerosol concentration ($=N_r/N_{r,\max}$ in Davies' theory and $=N_r/N_{r,\mathrm{mean}}$ in Sehmel's)	
$\dot{n}$	Number of displacements of a particle per unit time	T^{-1}
$N_{r,\max}$	Centre line aerosol concentration	ML^{-3}
$N_{r,\mathrm{mean}}$	Average aerosol concentration over the cross-section of the duct	ML^{-3}
$\Delta N_{r,\mathrm{mean}}$	The average concentration difference over a length of duct L—equation (29)	ML^{-3}
$N(r,t)$	The general solution of the diffusion equation adopted for the transport of particles in Hutchinson et al's theory	ML^{-3}

P	Fraction of particles sticking on impact—equation (23)	
$P(U_p, \Theta)$	Joint density function for $U_p = (U_{p\phi}^2 + U_{pr}^2)^{1/2}$—equation (B8)	
$\Delta P/\Delta L$	Pressure drop along duct	$ML^{-2}T^{-2}$
R	Duct radius	L
r_p^+	Dimensionless particle radius $(=r_p u^*/\nu)$	
Re_D	Fluid Reynolds number $(=D\bar{U}_{x,mean}/\nu)$	
S	Particle stopping distance $(=\rho_p d_p^2 U_{pr}/18\mu)$	L
S^+	Dimensionless particle stopping distance $(=Su^*/\nu)$	
Sc	Schmidt number $(=\nu/D_B)$	
T	Absolute temperature	Θ
t	Time	T
u^*	Wall friction velocity of fluid $[=(\tau_w/\rho_f)^{1/2}]$	LT^{-1}
U_d^+	Dimensionless deposition velocity of vapour $(=U_d/u^*)$	
U_{pr} (or $U_{p,r}$)	Mean particle velocity component in the radial direction	LT^{-1}
U_{pr}^+ (or $U_{p,r}^+$)	Dimensionless mean particle velocity component is the radial direction $(=U_{pr}/u^*$ or $U_{p,r}/u^*)$	
$U_{p\phi}$	Mean particle velocity component in the peripheral (tangential) direction	LT^{-1}
U_{pth}	Threshold velocity a particle required to penetrate the viscous sublayer and subsequently be deposited onto the boundary wall	LT^{-1}
u_r'	Root mean square (r.m.s.) fluctuating fluid velocity in the radial direction	LT^{-1}
$u_r'^+$	Dimensionless r.m.s. fluctuating fluid velocity in the radial direction	
$\bar{U}_{x,max}$	Centre line mean local fluid velocity component in the x-direction	LT^{-1}
$\bar{U}_{x,mean}$	Average fluid velocity over the cross-section of the duct	LT^{-1}
V_d	Particle deposition velocity $[=W/N(r,t)]$	LT^{-1}
V_d^+	Dimensionless particle deposition velocity $(=V_d/u^*)$	
W	Aerosol deposition flux to the wall of the duct	$ML^{-2}T^{-1}$
y	Distance measured from the duct wall $(=R-r)$	L
y^+	Dimensionless distance measured from the duct wall $(=yu^*/\nu)$	
y_D	Diffusion layer thickness	L
y_D^+	Dimensionless diffusion layer thickness $(=y_D u^*/\nu)$	

Greek Letters

α_N	Roots of the Bessel function $J_0(\alpha_N)=0$—equation (B4)	
ε'	Particle diffusivity due to particle inertia, after Ilori[32] $[=(u_r')^2\tau_p]$	L^2T^{-1}
ε'^+	Dimensionless particle diffusivity due to particle inertia, after Ilori[32]	
$\varepsilon_{d,r}$	Fluid eddy viscosity of mass in the radial direction	L^2T^{-1}
$\varepsilon_{m,r}$	Fluid eddy viscosity of momentum in the radial direction	L^2T^{-1}
$\varepsilon_{m,r}^+$	Dimensionless fluid eddy viscosity of momentum in the radial direction $(=\varepsilon_{m,r}/\nu)$	
$\varepsilon_{p,r}$	Particle eddy diffusivity in the radial direction	L^2T^{-1}
$\varepsilon_{p,r}^+$	Dimensionless particle eddy diffusivity in the radial direction $(=\varepsilon_{p,r}/\nu)$	
$\varepsilon_{P,T}$	Total diffusivity of aerosol particle, after Ilori[32]—equation (34)	L^2T^{-1}
η	Ratio between amplitudes of oscillation of the particle and fluid—equation (33)	
μ	Absolute viscosity of fluid	$ML^{-1}T^{-1}$
ν	Kinematic viscosity of fluid	L^2T^{-1}
ρ_f	Density of fluid	ML^{-3}
ρ_p	Particle density	ML^{-3}
σ	Variance of the r.m.s. particle velocity in the radial or tangential direction—equation (B10)	LT^{-1}
τ_p	Particle relaxation time $(=\rho_p \cdot d_p^2/18\nu\rho_f)$	T
τ_p^+	Dimensionless particle relaxation time $(=\tau_p u^{*2}/\nu)$	

REFERENCES

1. Albrecht, F., 1931, *Phys Z*, 32: 48.
2. Langmuir, I., 1948, *J Met*, 5: 175.
3. Davies, C. N. and Aylward, M., 1951, *Proc Phys Soc*, B64: 889.
4. Davies, C. N. and Peetz, C. V., 1956, *Proc Phys Soc*, A234: 269.
5. Gregory, P. H., 1951, *Ann Appl Biol*, 38: 357.
6. Ranz, W. E. and Wong, J. B., 1952, *Ind Eng Chem*, 44: 1371.
7. Friedlander, S. K. and Johnstone, H. F., 1957, *Ind Eng Chem*, 49: 1151.
8. Lin, C. S., Moulton, R. W. and Putman, G. L., 1952, *Ind Eng Chem*, 45: 636.
9. Laufer, J., 1953, *Natl Advs Commt Aeronaut, Tech Note* 2954.
10. Kneen, T. and Strauss, W., 1969, *Atm Environmt*, 3: 55.
11. Sehmel, G. A. and Schwendiman, L. C., 1963, *Hanford Atomic Products Operations, Rep* HW-SA-3183, Richland, Washington, USA
12. Owen, P. R., 1960, *Aerodynamic Capture of Particles* (Pergamon Press, Oxford), 8.
13. Dawes, J. G. and Slack, A., 1954, *Safety in Mines Res Estblt, Res Rep* 105.
14. Pereles, E. G., 1958, ibid, *Res Rep* 144.
15. Levich, V. G., 1962, *Physiochemical Hydrodynamics* (Prentice-Hall, Englewood Cliffs, NJ), 155.
16. Davies, C. N., 1966, *Aerosol Science* (Academic Press, London and New York), 393.
17. Schlinger, W. G. and Sage, B. H., 1953, *Ind Eng Chem*, 45: 657.
18. Beal, S. K., 1970, *Nucl Sci Eng*, 40: 1.
19. Wells, A. C. and Chamberlain, A. C., 1969, *Atm Environmt*, 3: 494.
20. Hutchinson, P. C., Hewitt, G. F. and Dukler, A. E., 1971, *Chem Eng Sci*, 26: 419.
21. Rouhiainen, P. O. and Stachiewicz, J. W., 1970, *J Heat Transfer*, 92: 169.
22. Schwendiman, L. C. and Postma, A. K., 1961, *Hanford Lab Rep* HW-SA-2236, Richland, Washington, USA; also 1962, *Tech Inf Div Rep* TID-7628, Book 1 (USAEC) 1.
23. Sehmel, G. A., 1968, *Batelle Northwest Lab Rep* BNWL-578, Richland, Washington, USA.
24. Beal, S. K., 1978, *J Aerosol Sci*, 9: 455.
25. Sehmel, G. A., 1966, *Pacific Northwest Lab Rep* BNWL-235-3:61, Richland, Washington, USA.
26. Watkinson, A. P., 1968, *PhD Dissertation*, (Univ British Columbia).
27. Sehmel, G. A., 1970, *J Geophys Res*, 75: 1766.
28. Sehmel, G. A., 1971, *J Coll Int Sci*, 37 (4): 891.
29. Sehmel, G. A., 1973, *J Aerosol Sci*, 4: 125.
30. Forney, L. J. and Spielman, L. A., 1974, *J Aerosol Sci*, 5: 257.
31. Farmer, R. A., 1969, *ScD Thesis*, (MIT, USA).
32. Ilori, T. A., 1971, *PhD Thesis*, (Univ Minnesota, USA).
33. Liu, B. Y. H. and Agarwal, J. K., 1974, *J Aerosol Sci*, 5: 145.
34. Mickelsen, W. R., 1955, *NACA Rep* TN-3570.
35. Comte-Bellot, G., 1965, *Publications Scientifiques et Techniques du Ministriere de l'Air*, No 418, France.
36. Saffman, P. Q., 1965, *J Fluid Mech*, 22: 385.
37. Liu, B. Y. H. and Ilori, T. A., 1973, *ASME Symp Flow Studies in Air and Water Pollution*, Atlanta, Georgia, USA, 103.
38. Wasan, D. T., Sood, S. K., Davies, R. and Lieberman, A., 1973, *J Coll Interf Sci*, 43 (1): 144.
39. Wasan, D. T., Subramaniam, T. K. and Randhava, S. S., 1966, *Chem Eng*, 165 (14).
40. Alexander, L. G. and Coldren, C. L., 1951, *Ind Eng Chem*, 43: 1325.
41. Papoulis, A., 1965, *Probability of Random Variables and Stochastic Processes*, McGraw-Hill, Chap 7.
42. Cousins, L. B. and Hewitt, G. F., 1968, *Atom Energy Res Estblt, Rep* R5657, Harwell, UK.
43. Cleaver, J. W. and Yates, B., 1975, *Chem Eng Sci*, 30: 983.
44. Owen, P. R., 1969, *J Fluid Mech*, 39 (2): 407.
45. Hinze, J. O., 1975, *Turbulence*, McGraw-Hill, 2nd Ed, Chap 7.

VOL. 62 1984

46. Reeks, M. W. and Skyrme, G., 1976, *J Aerosol Sci*, 7: 485.
47. Papavergos, P. G. and Hedley, A. B., 1979, *Pr 2nd Multi-Phase Flow and Heat Transfer Symp. Workshop*, Miami, Florida, USA.
48. Stavropoulos, N., 1957, *MSc Thesis*, (Columbia Univ, New York, USA).
49. Postma, A. K. and Schwendiman, L. C., 1960, *Hanford Lab Rep* HW 65308, Richland, Washington, USA.
50. Chamberlain, A. C., 1967, *Pr R Soc*, A296 (1444): 45.
51. McCoy, D. D. and Hanratty, T. J., 1977, *Int J Multiphase Flow*, 3: 319.
52. Nukiyama, S. and Tanasawa, Y., 1938, *Trans JSME* 4, Report 2, 524.
53. Namie, S. and Ueda, T., 1972, *Bull JSME*, 15: 1568.
54. McCoy, D. D., 1975, *MSc Thesis*, (Univ Illinois at Urbana, Champaign, USA).
55. Tatterson, D. F., 1975, *PhD Thesis*, (Univ Illinois at Urbana, Champaign, USA).
56. Yoder, J. D. and Silverman, L., 1967, *60 Ann Air Pollut Control Assoc Mtg*, Paper 67, Cleveland, Ohio, USA.
57. Montgomery, T. L., 1969, *DSc Dissertation*, (Univ Pittsburgh, USA).
58. Montgomery, T. L. and Corn, M., 1970, *J Aerosol Sci*, 1: 185.
59. Azzopardi, B. J., Freeman, C. and King, D. J., 1980, *AERE*, R9634, Harwell, UK.
60. Wilkes, N. S., Conkie, W. and James, P. W., 1980, *AERE*, R9691, Harwell, UK.
61. Whalley, P. B., Hewitt, G. F. and Terry, J. W., 1979, *AERE*, R9383, Harwell, UK.
62. James, P. W., Hewitt, G. F. and Whalley, P. B., 1980, *AERE*, R9711, Harwell, UK.
63. Fisher, S. A. and Pearce, D. L., 1978, *Int Seminar Momentum, Heat and Mass Transfer in Two-Phase Energy and Chemical Systems*, Dubrovnik, Yugoslavia.
64. Hutchinson, P. and Whalley, P. B., 1972, *AERE*, R1726, Harwell, UK.
65. Wilkes, N. S., Azzopardi, B. J. and Willetts, I., 1982, *HTFS* RS 425, *AERE*, R10571, Harwell, UK.
66. James, P. W., Hewitt, G. F. and Whalley, P. B., 1980, *Int Topical Mtg Nucl Reactor Therm Hydrant*, Saratoga Springs, NY, USA.
67. Hutchinson, P. and Brown, D. J., 1974, *AERE*, R7813, Harwell, UK.
68. Cousins, L. B. and Hewitt, G. F., 1968, *AERE*, R5693, Harwell, UK.
69. Anderson, R. J. and Russell, T. W. F., 1970, *AIChE J*, 16: 626.
70. Jagota, A. K., Rhodes, E. and Scott, D. S., 1973, *Can J Chem Engng*, 51: 139.
71. Henstock, W. H., 1976, *AIChE J*, 22: 990.
72. Cantwell, B. J., 1981, *Ann Rev Fluid Mech*, 13: 457.
73. Kreplin, H. P. and Eckelmann, H., 1979, *Phys Fluids*, 22 (7): 1233.
74. Wood, P. E. and Petty, C. A., 1983, *AIChE J*, 29 (1): 164.
75. Gardner, G. C., 1975, *Int J Multiphase Flow*, 2: 213.
76. Ponting, A. C., 1982, *CEGB* Rep (Berkeley Nuclear Laboratories RD/B/5232N82, Job XB 149), UK.
77. Davies, J. T., 1983, *Ann NY Acad Sci*, 404: 313.
78. Davies, J. T., 1983, *Chem Eng Sci*, 38 (1): 135.
79. Byers, R. L., 1967, *PhD Thesis*, (Pennsylvania State Univ, USA).
80. Brock, J. R., 1967, *J Coll Interf Sci*, 23: 448.
81. Tong, N. T. and Bird, G. A., 1971, *J Coll Interf Sci*, 35: 403.
82. Im, K. H. and Chung, P. M., 1983, *AIChE J*, 29 (3): 498.
83. Zebel, G., 1965, *J Coll Sci*, 20: 522.

ACKNOWLEDGEMENTS

The authors would like to acknowledge the assistance and cooperation of the BP Research Centre. This paper is published with the permission of the British Petroleum Company p.l.c.

ADDRESS

All correspondence should be addressed to Dr P. G. Papavergos, BP Research Centre, Fuels Branch, Chertsey Road, Sunbury-on-Thames, Middlesex, TW16 7LN.

The manuscript was submitted 4 August 1983 and accepted for publication after revision 11 May 1984.

COMPARISON BETWEEN INDIRECT AND DIRECT CONTACT COOLING METHODS FOR THE CRYSTALLISATION OF POTASSIUM SULPHATE

By J. W. MULLIN (FELLOW) and J. R. WILLIAMS

Department of Chemical and Biochemical Engineering, University College London

Techniques and procedures have been developed for studying the effect of cooling mode on crystal nucleation and growth kinetics. The multi-purpose cooling crystalliser, which provided for both direct and indirect heat transfer, was capable of being operated either batch-wise or continuously under seeded or unseeded conditions. Potassium sulphate crystallising from aqueous solution was used as the working system and iso-octane (2,2,4 trimethylpentane) was selected as the coolant. Direct contact cooling virtually eliminated encrustation in the crystalliser, had no detectable influence on either the nucleation or growth kinetics and no deleterious effect on the crystal product quality as expressed by the crystal size distribution.

INTRODUCTION

The conventional method of heat removal in industrial cooling crystallisation is by indirect heat exchange, e.g. jacketed vessel, internal cooling coil or external heat exchanger, but the disadvantage of indirect cooling is that the cold surfaces in contact with supersaturated solution are prone to crystal encrustation which severely reduces the heat transfer efficiency. One method of circumventing this problem is to use adiabatic evaporative cooling (vacuum operation). Another is to employ direct contact heat transfer by intimately contacting the crystallising solution with an inert coolant.

In principle, direct contact coolants can be solids, liquids or gases, but in practice only liquids are important and they fall into four basic categories, all of which have been proposed for commercial exploitation:

(i) immiscible coolants which do not change phase[1]
(ii) miscible coolants which do not change phase[2]
(iii) immiscible coolants which change phase[3]
(iv) miscible coolants which change phase[4]

Despite the increasing use of direct contact cooling (DCC) in crystallisation processes, there is virtually no information available on its effects, if any, on crystalliser performance. The objective of the present study was to develop simple laboratory procedures to assess the suitability of the DCC technique as an alternative to conventional cooling methods.

SYSTEM SELECTION

Potassium sulphate was chosen as the solute in the present investigation because it is a well characterised substance and has been employed in numerous previous crystallisation studies in different types of crystalliser.[5–11] It has a positive solubility–temperature coefficient in aqueous solution and, as it crystallises as an anhydrous salt, its concentration may be determined by simple gravimetric methods. Pure-grade potassium sulphate recrystallised from de-ionised water was used in all the experimental work.

For immiscible non-boiling DCC crystallisation where water is the solvent, the choice of coolant is restricted to organic compounds. In the present case, for operation at around ambient temperatures, a coolant with a freezing point lower than say 0°C, a boiling point higher than say 100°C and a density less than say 900 kg m^{-3} was considered desirable.

Over 30 coolants met these criteria,[12] but judged against the best combination of low solubility, low density and high interfacial tension, three compounds were identified: n-octane, iso-octane (2,2,4 trimethylpentane) and 2,2,5 trimethylhexane. Since all seemed equally acceptable, iso-octane (Table 1) was arbitrarily selected. Analar–grade iso-octane was employed in the present investigations without further purification.

Three major factors that influence crystalliser performance are solute solubility (which affects supersaturation) and the kinetics of both nucleation and crystal growth. These were assessed in turn.

The solubility of potassium sulphate in water was determined both in the presence and absence of dissolved iso-octane, since any change in solubility would affect the supersaturation achieved and hence the crystallisation kinetics. Solution in contact with excess solute was stirred for 100 h at a given temperature ± 0.1°C after which a sample of the supernatant liquor was transferred to pre-weighed bottles and evaporated to dryness. The solubilities, determined with an estimated precision of ±0.005% over the temperature range 20–45°C, were in good agreement with those reported by Gaska.[14] The presence of iso-octane had no measurable effect.

Table 1. Some physical properties of 2,2,4 trimethylpentane (iso-octane)

Melting point	−107°C
Boiling point	99.2°C
Density (20°C)	691.9 kg m^{-3}
Refractive index (20°C)	1.3915
Interfacial tension with water (20°C)	50 mJ m^{-2}
Specific heat capacity (25°C)	236 J mol^{-1} K^{-1}
Solubility of iso-octane in water (25°C)	2.44 ppm
Solubility of water in iso-octane (25°C)	115 ppm

© Institution of Chemical Engineers

VOL. 62 1984

It was planned to measure the nucleation kinetics of the chosen system (K_2SO_4–water–iso-octane) by the Nývlt technique,[13] which involves cooling a saturated solution at a constant rate and noting the temperature at which nuclei first appear, so it was necessary to ensure that the solution remained clear throughout the operating procedure. Indirect cooling poses no problems in this respect, but DCC might, because any precipitation of coolant droplets in the solution as a result of temperature changes would make the detection of nucleation difficult. To check this possibility, mixtures of potassium sulphate solution and iso-octane in volume ratios 2:1 and 1:2 respectively were allowed to cool from 40° to 20°C in vigorously agitated flasks. In both cases the solutions remained clear, so no problems were envisaged in applying the Nývlt technique.

As the growth of potassium sulphate crystals is to some extent influenced by the diffusion step,[5] any effect of dissolved iso-octane on the diffusion coefficient would be important. Differential diffusivities for the K_2SO_4–H_2O system were therefore measured, with a Zeiss diffusion interferometer,[12] for

(i) K_2SO_4–H_2O at 25°C over the concentration range 0.005 to 0.0105 kg/kg H_2O
(ii) K_2SO_4–H_2O saturated with iso-octane at 25°C over the same concentration range as (i)
(iii) K_2SO_4–H_2O saturated with iso-octane at 25°C over the temperature range 25–50°C and concentration range 0.009 to 0.11 kg/kg H_2O.

Good agreement was obtained with data previously reported[15] for pure aqueous solutions of K_2SO_4. Again the presence of iso-octane had no measurable effect.

BATCH CRYSTALLISATION

Nucleation kinetics were characterised by metastable zone width measurements made by the Nývlt technique[13,16] in which the mass nucleation rate is expressed by the empirical relationship

$$M^0 = k_m \Delta c_{max}^m \tag{1}$$

and by the mass balance

$$M^0 = \rho_w (d\Delta c/dt) \tag{2}$$

and as the initial solution concentration is independent of time, then

$$d\Delta c/dt = -dc^*/dt \tag{3}$$

and

$$M^0 = \rho_w \dot{\theta} (dc^*/dt) \tag{4}$$

The maximum supersaturation allowed before nucleation occurs (the metastable zone width) may be expressed in terms of the maximum allowable undercooling as

$$\Delta c_{max} = (dc^*/d\theta)\Delta\theta_{max} \tag{5}$$

Thus, from equations (1), (4) and (5):

$$\log \dot{\theta} = m \log \Delta\theta_{max} + (m-1)\log(dc^*/d\theta) + \log(k_m/\rho_w) \tag{6}$$

and a plot of log $\dot{\theta}$ against log $\Delta\theta_{max}$ should yield a straight line of gradient m, the so-called 'order' of the mass nucleation process. For the case of a solute crystallising as a hydrate from aqueous solution, the third term on the right-hand side of equation (6) becomes[12] $\log(k_m/\varepsilon\rho_w)$ (see list of Symbol Used).

Crystal growth rates were measured by the seeded-batch technique[17] in which a solution is desupersaturated at constant temperature, by adding a known mass of closely sized crystal seeds, and the decrease in solution concentration followed over a period of time. The increase in crystal mass is proportional to the decrease in solution concentration:

$$dW = -W_w dc \tag{7}$$

and the overall mass growth rate on the added seed crystals, assuming no secondary nucleation, is

$$R_G = dW/A\,dt = -(W_w/A)(dc/dt) \tag{8}$$

The crystal surface area at any time t, assuming no habit changes, may be expressed by

$$A_t = A_0(W_t/W_0)^{2/3} \tag{9}$$

where

$$A_0 = FW_0/\rho_c L \tag{10}$$

and

$$W_t = W_0 + W_w(c_0 - c_t) \tag{11}$$

The crystal surface growth area at any given time during the desupersaturation period may therefore be estimated from the corresponding solution concentration measurement by

$$A_t = \frac{FW_0}{\rho_c L}\left(\frac{W_0 + W_w(c_0 - c_t)}{W_0}\right)^{2/3} \tag{12}$$

and the crystal growth rate at any chosen level of supersaturation can then be calculated from equation (8).

CONTINUOUS CRYSTALLISATION

The product crystal size distribution (CSD) for an MSMPR crystalliser, when the crystal growth rate is independent of the crystal size, is quantified by population balance theory,[18] as

$$n = n^0 \exp(-L/G\tau) \tag{13}$$

where τ represents both the liquor and crystal residence times. The population density of nuclei, n^0, is related to the number nucleation rate, B^0, and crystal growth rate, G, by

$$B^0 = n^0 G \tag{14}$$

The graphical procedures for evaluating n^0, G and B^0 from experimental CSD data are simple and well-documented.[18]

For the case of size-dependent crystal growth, equation (13) is modified to

$$n = \frac{K}{G}\exp\left(-\frac{1}{\tau}\int_0^L \frac{dL}{G}\right) \tag{15}$$

but evaluation of the constant of integration, K, which

is constrained by the mass balance, necessitates the use of complex procedures.[12,19] For practical assessment, however, a more simple approach may be adopted. Crystal growth rates frequently exhibit a strong size-dependence in the small-size region (below about 40 μm for potassium sulphate) and in such cases evaluation of n^0 by the standard procedure of extrapolating a population density plot to $L = 0$ (equation 13) becomes unreliable due to the severe upward curvature of the data points in the small-size region (see Figure 6 later). However, even though large numbers of very small crystals may be present in a given crystal product, their contribution on a mass basis is generally quite negligible and the product CSD can, for most practical purposes, be considered to be governed by some 'effective' population density of nuclei, n_e^0, which may be estimated by ignoring the data points in the small-size region and extrapolating only the major 'linear grouping' of data points to $L = 0$. In this way it is possible to relate 'effective' growth and nucleation rates by a modified equation (14):

$$B_e^0 = n_e^0 G_e \tag{16}$$

EXPERIMENTAL

The major components of the experimental rig were a dual-purpose draft-tube agitated crystalliser and storage vessels for the direct (iso-octane) and indirect (water) coolants (Figures 1 and 2 respectively), all thermostatically controlled. The crystalliser, modelled on one used in earlier studies,[6,8] was an 8 L cylindrical glass vessel, 150 mm diameter, with a bottom shaped to allow smooth circulation through the draft tube. Two valves (of which only one is shown in Figure 1) facilitated removal of either solution or coolant when the contents exceeded about 6 L. The 90 mm internal diameter hollow draft tube could be used as an indirect heat exchanger, by circulating water through it, and its internal cross-sectional area was approximately equal to that of the external annulus. The agitator was a close-clearance 3-bladed marine-type propeller rotating at about 500 rpm in the batch (seeded) runs and about 1500 rpm in the continuous (MSMPR).

When the crystalliser was used as a direct contact cooler, iso-octane passed down the hollow bore of the agitator shaft and entered the vessel through six 1 mm holes located 10 mm above the propeller (see Figure 2). To minimise indirect heat transfer between the cold shaft and the surrounding solution, the shaft was encased by a stainless steel tube to within 2 cm of the coolant outlet holes. Iso-octane entered the vessel as small droplets, which were pumped out of the draft tube into the annular zone. The coolant layer collecting at the top of the vessel was removed through one of the valves.

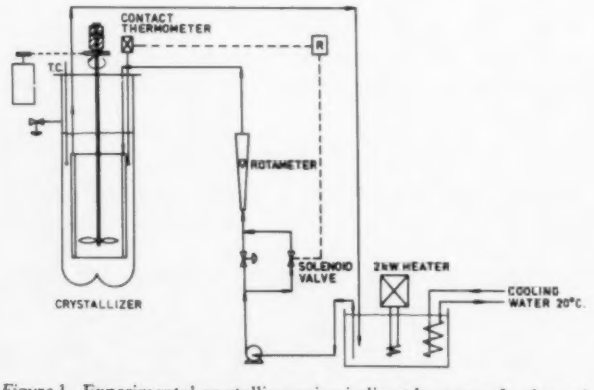


Figure 1. Experimental crystalliser using indirect heat transfer through a jacketed draft tube

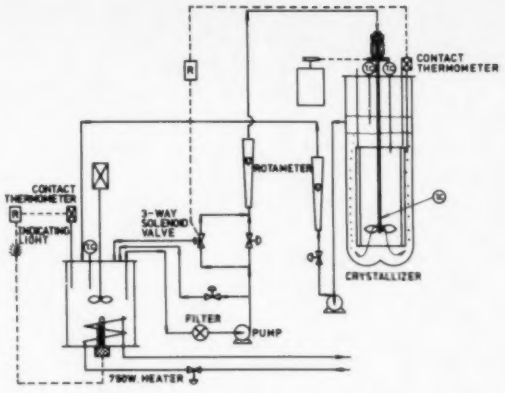


Figure 2. Experimental crystalliser using direct contact heat transfer with iso-octane

For continuous operation, the equipment was modified to allow for the storage and introduction of feed solution, and for the removal of a mixed slurry. Slurry was withdrawn intermittently and isokinetically through a 10 mm diameter tube. The sampling arrangement to ensure that the population density was representative of the slurry was found by trial and error.[12]

Batch Runs

Approximately 5 L of hot solution (saturation temperature = 40°C) was filtered through a sintered glass filter (effective pore size 15 μm) into the crystalliser. Its concentration was determined gravimetrically and its saturation temperature deduced from the solubility diagram.

The nucleation temperature of the solution was determined at different cooling rates, by indirect cooling, both in the absence and in the presence of seed crystals. The solution was heated to 50°C, i.e. 10°C above saturation for 10 min and then cooled by 5°C. The set point of the contact thermometer was adjusted to this value and programmed cooling started. A linear cooling rate was maintained by controlling both the cooling water temperature about 7°C below that of the solution and its flowrate through the draft tube.

The nucleation temperature was taken as that at which large numbers of crystal nuclei suddenly appeared in the solution. The difference between the saturation and nucleation temperatures represents the maximum allowable undercooling, $\Delta\theta_{max}$. For the seeded runs, 50 potassium sulphate crystals (mean sieve size ~925 μm) were added to the solution when it reached its saturation temperature and $\Delta\theta_{max}$ was then determined in the same manner as before. In all the runs it was necessary either to refilter or renew the solution at regular intervals due

to fungal (aspergillus) growth, commonly observed in potassium sulphate aqueous solutions.[14]

The use of a direct contact coolant could possibly affect the nucleation characteristics of a solution first by its mere presence and second because of the temperature difference ($\Delta\theta_{diff} = \theta_s - \theta_c$) between the two immiscible phases.

The first possibility was tested by bubbling iso-octane through the potassium sulphate solution for one hour, maintaining the temperature at 10°C above the saturation value. The nucleation temperature was then determined as described above.

The second possibility, the effect of $\Delta\theta_{diff}$, was studied as follows. To avoid spurious cooling effects, the coolant (iso-octane) was initially supplied at 5°C above the solution saturation temperature. The solution temperature was then adjusted to a value $(\Delta\theta_{diff} + 7)$°C above its saturation value by supplying heat through the draft tube and kept at this elevated temperature for 30 min. The solution temperature was then reduced at a predetermined linear rate by direct contact cooling. The coolant temperature was also reduced at the same predetermined rate, thus maintaining a constant $\Delta\theta_{diff}$. The nucleation temperature was determined by the same general technique as described above. The difficulty of visually detecting the onset of nucleation at high iso-octane flowrates was overcome by the use of a polarised light source.

For the determination of crystal growth rates by the seeded batch technique,[17] the crystalliser was charged with 5 L of hot filtered (sintered glass, effective pore size 15 μm) solution of known concentration and rapidly cooled to the experimental temperature. A known mass (~30 g) of closely sieved seed crystals (mean sieve size ~925 μm) was then added. 10 mL samples of solution were removed at 2 min intervals for concentration measurement during the ~20 min run. The final crystal mass was rapidly filtered, dried and weighed.

A similar procedure was followed during the runs made in the presence of iso-octane: after charging the crystalliser with 5 L of hot solution, 100 mL of iso-octane was added and the mixture was agitated for 20 min. Growth rates were then measured as before, with the exception that the seed crystals were added down a glass tube which penetrated the iso-octane layer to prevent initial contamination.

Continuous Runs

For the indirect cooling runs the cooling water temperature in the draft tube was maintained at about 7°C below that of the crystalising solution. For direct contact cooling, the coolant (iso-octane) flow was controlled to provide the required $\Delta\theta_{diff}$.

To ensure that no crystalline particles were introduced with the feed, the temperature of the stock solution was maintained at about 5°C above its equilibrium saturation temperature. The crystalliser contents were cooled to the required temperature and, once nucleation had occurred, feed solution was pumped in at the desired rate. Crystal slurry was removed intermittently from the vessel in 500 mL aliquots when the total volume present reached 5 L. After 14 residence times the run was terminated and the crystals and mother liquor were separated. The volume of mother liquor was measured and the crystals were dried for sieve analysis and shape factor measurement.

RESULTS AND DISCUSSION

Nucleation Kinetics from Batch Runs

The experimental results were analysed by the method of least squares in accordance with equation (6). For potassium sulphate solution over the temperature range 20–60°C, the simple relationship $dc^*/d\theta = 0.00181$ kg solute/kg water °C may be used.[5]

Results for the indirect cooling of seeded and unseeded solutions, summarised in Figure 3, confirm that seeding reduces the maximum allowable undercooling. Also included in Figure 3 are some results obtained from a nucleation cell of a type used in previous studies.[16,20] The virtual identity of the small-scale (250 mL) and large-scale (5 L) data provides a good illustration of the utility of small-scale experimentation. The fact that the 'orders of nucleation', m, for the seeded systems are lower than those for the unseeded at a given temperature (Table 2) is consistent with the hypothesis that different nucleation mechanisms operate in the two cases.[16] The value of k_m is extremely sensitive to the slope of the log–log plot in Figure 3 and its calculation is not reliable. Nevertheless, the observation that for potassium sulphate both k_m and m are strong functions of the solution temperature was confirmed (Table 2) and the values are consistent with those calculated from the results of Gaska.[14] The full significance of the 'order of nucleation', m, is still not entirely clear, however, as is discussed in several recent papers.[21–25]

The results for the seeded DCC runs are given in Figure 4 together with the correlation line for the corresponding indirect cooling runs from Figure 3. The presence of iso-octane does not appear to affect the nucleation characteristics. Further, although the data points are more scattered than those for indirect cooling, they broadly lead to the conclusion that the temperature

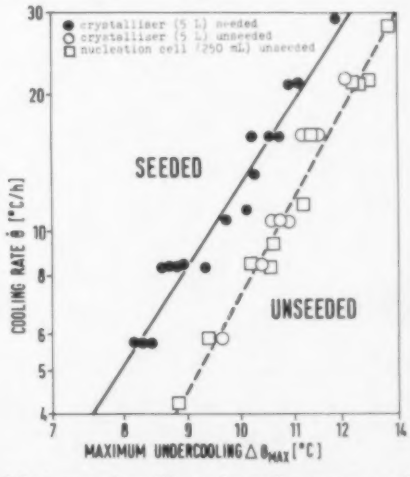


Figure 3. Maximum allowable undercooling versus cooling rate for unseeded and seeded potassium sulphate solutions under conditions of indirect heat transfer (no contact with coolant)

Table 2. The nucleation parameters as a function of temperature

Temperature (°C)	Seeded	k_n (kg m^{-3} × 10^{-6})	m
40.0	yes	0.178	3.95
36.2	yes	15.9	5.46
31.3	yes	5740	6.96
46.2	no	0.0007	3.18*
41.2	no	0.103	4.45*
40.0	no	4.2	5.19
35.6	no	351	6.54*

*Values calculated from the data of Gaska.[14]

difference between the solution and the inlet coolant, over the 3–15°C range studied, has no effect either. A similar conclusion was drawn[12] from the unseeded indirect and direct contact cooling runs (not reported here).

Growth Kinetics from Batch Runs

Figure 5 shows a plot of crystal growth rate as a function of supersaturation for three runs, one in pure solution and the other two in solutions saturated with iso-octane. The seeds for Runs 1 and 3 were taken from the same batch. The seeds for Run 2 were taken from the crystals grown in Run 1. The resulting second-order dependence

$$R_G = k_G(c - c^*)^2 \qquad (17)$$

in all three cases, is in agreement with previous reports on the pure-solution growth of potassium sulphate.[5–11] The values of overall growth rate coefficient, k_G, (5–7 kg m^{-2} s^{-1}) are also similar to those obtained in a previous study,[5] although exact comparability in respect of crystal size, degree of agitation, temperature, etc. is not possible, and values of k_G are notoriously sensitive to precise experimental conditions.

It has to be noted, however, that the data in Figure 5 unexpectedly indicate that the value of k_G for the solution containing iso-octane is higher than that for the uncontaminated solution. No logical explanation can be advanced at the moment other than to suspect that some unrecorded change in experimental condition might have occurred in either Runs 1 and 2 or in Run 3. It would seem highly unlikely that the presence of iso-octane would enhance the mass transfer step since the diffusivity and solubility of K_2SO_4 in water are both apparently unaffected by the presence of dissolved iso-octane in the solution (see under "System Selection"), as is the 'order' of the crystal growth process. The nucleation kinetics are also unaffected, and there is an element of 'growth' already associated with the determination of nucleation kinetics by the Nývlt method since the 'nuclei' have already grown into crystals of about 50 μm in size before they are detected in the nucleation cell. The only other possibility is an enhancement of the surface contribution to the growth process caused by the presence of iso-octane, but further work would be necessary to establish any such effect.

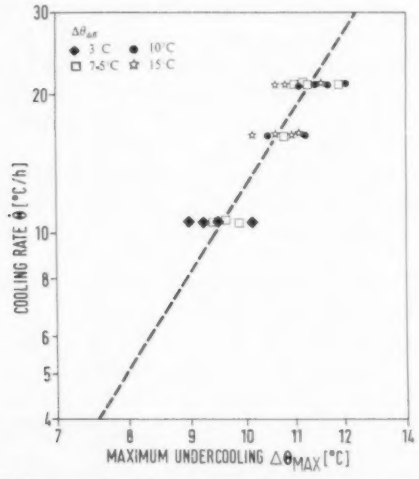


Figure 4. Maximum allowable undercooling versus cooling rate for seeded potassium sulphate solutions under conditions of direct contact heat transfer (solution saturated with coolant). The broken line indicates the correlation between $\Delta\theta_{max}$ and cooling rate for the seeded indirect contact runs in Figure 3

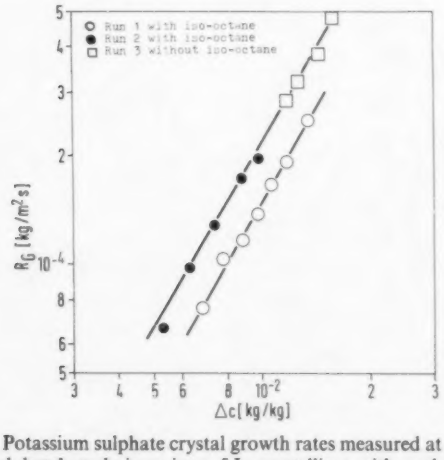


Figure 5. Potassium sulphate crystal growth rates measured at 25°C by the seeded batch technique in a 5 L crystalliser with and without dissolved iso-octane present in the solution

Nucleation and Growth Kinetics from Continuous Runs

Figure 6 shows the MSMPR crystal size distributions obtained under indirect and direct contact cooling at two different values of $\Delta\theta_{diff}$. The severe upward curvature of data points in the small-size region (referred to under "Continuous Crystallisation") makes it difficult to estimate a meaningful value of n^0 (Equation 13). Extrapolation of the small-size data points, for example, yields a value of $n^0 > 10^7\ \mu m^{-1}\ m^{-3}$ compared with $< 10^6\ \mu m^{-1}\ m^{-3}$ for those of the bulk data. Estimates of the crystal growth rate, G, in these two regions are around 2×10^{-8} and 2×10^{-7} m s^{-1} respectively.

In the small-size range ($< 100\ \mu$m) the data points fall reasonably well on a common line, suggesting that the nucleation and growth rates for these small crystals are virtually independent of the crystallisation technique, the presence of iso-octane and the temperature difference between the immiscible phases. The picture is not so clear for crystals $> 100\ \mu$m, since the data are more scattered, but there is no evidence of any significant difference in behaviour between the different modes of operation. This conclusion matches that for the batch-operated runs reported above.

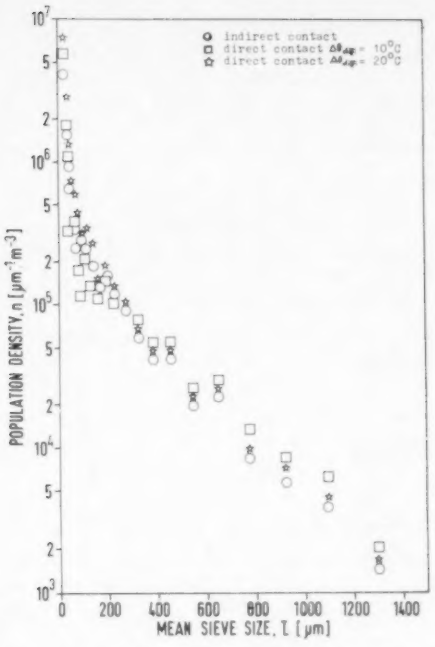


Figure 6. Potassium sulphate crystal size distributions from the continuous MSMPR crystalliser operated at 40°C and $\tau = 20.6$ min with either indirect or direct contact heat transfer ($\Delta\theta_{diff} = 10$°C or 20°C)

Several investigators[5,10,11,26] have observed that the shape factors of potassium sulphate crystals are functions of crystal size. Photographic evidence[12] has established, however, that although the change in crystal habit over the range 180–1400 μm is quite pronounced, the habit for a specific size is usually the same irrespective of how the crystals had been prepared. The shape factor for a given crystal size appears to be unaffected by the presence of dissolved coolant in the solution or by the mode of cooling.

Finally, one of the advantages of DCC crystallisation, the absence of heat exchanger fouling, was clearly demonstrated in the continuous runs. At the end of an indirect heat transfer run, crystalline deposits covered some 5% of the draft tube surface, even though the temperature differences used (~7°C) were generally less than the metastable zone width (8–12°C). No crystalline deposits built up in the system when operating in the DCC mode.

CONCLUSIONS

The apparatus and techniques described in this paper should provide useful guidelines for the development of procedures for assessing the feasibility of DCC crystallisation as an alternative method to conventional cooling crystallisation.

The results of the present investigation with potassium sulphate and iso-octane are encouraging since they give a clear indication that, provided the direct contact coolant is virtually insoluble in the mother liquor, similar nucleation and growth rates, and hence crystalliser performance, should be expected for both indirect and direct contact cooling.

SYMBOLS USED

a	surface area of an individual crystal	(m^2)
A	total crystal surface area	(m^2)
B^0	number nucleation rate	($s^{-1}m^{-3}$)
c	solute concentration	(kg/kg of solvent)
c^*	equilibrium solute concentration	(kg/kg of solvent)
Δc	supersaturation (concentration driving force) ($= c - c^*$)	(kg/kg of solvent)
Δc_{max}	maximum allowable supersaturation	(kg/kg of solvent)
f_s	surface shape factor ($= a/L^2$)	(−)
f_v	volume shape factor ($= m_c/\rho_c L^3$)	(−)
F	overall shape factor ($= f_s/f_v$)	(−)
g	order of the crystal growth process	(−)
G	linear growth rate of crystal ($= dL/dt$)	($m\,s^{-1}$)
i	relative kinetic order ($= m/g$)	(−)
k_G	overall rate constant for growth	($kg\,m^{-2}s^{-1}$ (kg/kg)^g)
k_m	nucleation rate constant (mass basis)	($kg\,m^{-3}s^{-1}$)
K	constant of integration in equation (15)	(−)
L	characteristic size of crystal (sieve size)	(m)
$\bar{L}$	characteristic mean sieve size of crystals	(m)
m	order of nucleation	(−)
m_c	mass of an individual crystal	(kg)
M^0	mass nucleation rate	($kg\,m^{-3}s^{-1}$)
M_T	mass of crystals per unit volume of magma	($kg\,m^{-3}$)
n	crystal population density	($\mu m^{-1}m^{-3}$)
n^0	population density of nuclei ($L \to 0$)	($\mu m^{-1}m^{-3}$)
R	molar mass ratio, hydrated:anhydrous salt	(−)
R_G	crystal growth (mass deposition) rate	($kg\,m^{-2}s^{-1}$)
t	time	(s)
T	temperature	(K)
W	mass of crystals	(kg)
W_s	mass of solution	(kg)
W_w	mass of solvent (water)	(kg)

Greek letters

ε	variable $= R/[1 - c^*(R-1)]^2$	(−)
θ_c	temperature of inlet coolant	(°C)
θ_s	temperature of bulk solution	(°C)
$\Delta\theta_{max}$	maximum allowable undercooling	(°C)
$\Delta\theta_{diff}$	temperature difference ($\theta_s - \theta_c$)	(°C)
$\dot{\theta}$	cooling rate ($d\theta/dt$)	($°C\,s^{-1}$)
ρ_c	crystal density	($kg\,m^{-3}$)
ρ_s	solution density	($kg\,m^{-3}$)
ρ_w	solvent (water) density	($kg\,m^{-3}$)
τ	residence time	(s)

Subscripts

e	effective value
o	value at time zero
t	value at time t

REFERENCES

1. Torobin, L. B., 1967 *US Patent* 3,350,296.
2. Gudelis, D. A., Eagen, J. F. and Bushnell, J. B., 1973 *Hydroc Proc* (September): 141.
3. Denton, W. H., Hall Taylor, N. S., Klaschka, J. T., Smith, M. J. S., Diffey, H. R. and Rumary, C. H., 1970 *3rd Int Symp Fresh Water from the Sea*, 3: 51.
4. Bozeman, P. P., 1971 *US Patent* 3,554,896.
5. Mullin, J. W. and Gaska, C., 1969 *Can J Chem Eng*, 47: 483.
6. Mullin, J. W. and Nývlt, J., 1971 *Chem Eng Sci*, 26: 369.
7. Jones, A. G. and Mullin, J. W., 1973 *Trans I Chem E*, 51: 302.
8. Jones, A. G. and Mullin, J. W., 1974 *Chem Eng Sci*, 28: 105.
9. Garside, J., Mullin, J. W. and Das, S. N., 1974 *Ind Eng Chem Funda*, 13(4): 299.
10. Rosen, H. N. and Hulbert, H., 1971 *Chem Eng Prog Symp Ser* 67(110): 18.
11. Randolph, A. D. and Cise, M. D., 1972 *AIChE J*, 18: 798.
12. Williams, J. R., 1976 *PhD Thesis* (University of London).
13. Nývlt, J., 1968 *J Crystal Growth*, 314: 377.
14. Gaska, C., 1966 *PhD Thesis* (University of London).
15. Mullin, J. W. and Nienow, A. W., 1964 *J Chem Eng Data*, 9(4): 526.

16. Mullin, J. W., 1972 *Crystallisation*, 2nd edn (Butterworths, London).
17. Bujac, P. D. B. and Mullin, J. W., 1969 *Industrial Crystallisation, I Chem E Symp Ser*, 36: 121.
18. Randolph, A. D. and Larson, M. A., 1970 *Theory of Particulate Processes*, (Academic Press, New York).
19. Lieb, E. B. and Osmers, H. R., 1973 *Chem Eng Comm*, 1: 13.
20. Mullin, J. W., Chakraborty, M. and Mehta, K., 1970 *J Appl Chem*, 20: 367.
21. Söhnel, O. and Nývlt, J., 1975 *Coll Czech Chem Comm*, 40: 511.
22. Hulburt, H., 1975 *Chem Ing Tech* 47: 375.
23. Janse, A. H. and de Jong, E. J., 1978 *Trans I Chem E*, 56: 187.
24. Mullin, J. W. and Jančić, S. J., 1979 *Trans I Chem E*, 57: 188.
25. Nývlt, J., 1983 *Coll Czech Chem Comm*, 48: 1977.
26. Garside, J., Mullin, J. W. and Das, S. N., 1973 *Ind Eng Chem Proc Des Dev*, 12: 369.

ACKNOWLEDGEMENT

The authors are indebted to the Science and Engineering Research Council for financial assistance and to the United Kingdom Atomic Energy Authority for providing experimental facilities. The supervision of the work at UKAEA Harwell by Dr A. G. Duncan and Dr P. Hawtin is gratefully acknowledged.

ADDRESS

Correspondence on this paper should be addressed to Professor J. W. Mullin, Department of Chemical and Biochemical Engineering, University College London, Torrington Place, London, WC1E 7JE.

The manuscript was received 24 June 1983 and accepted for publication 6 September 1983.

BOOK REVIEWS

Industrial Enzymology
T. Godfrey and J. Reichelt, (eds)
Macmillan, The Nature Press, (1983)
x + 582 pp, £4

This inexpensive book has brought together much of the available literature on the practical application of enzymes but, despite its subtitle of "Application of Enzymes in Industry", the inclusion of chapters on kinetics and legislation makes *Industrial Enzymology* a broad based text and not merely a source book of enzymes and processes. The editors and authors, all of whom are involved in a number of European companies which either produce or use enzymes, have produced an authoritatively written text which brings together much of the information which is frequently difficult to obtain on the types of enzyme available, their characteristics, major uses, conditions for optimum action and details of suppliers, trade names, activities, etc.

The first three chapters of the book serve as an introduction to the application of the enzymes to a variety of industries, such as starch and milk processing, paper and textile manufacture, and potable alcohol production, as well as the less obvious applications such as detergent production and edible oil processing, whereas Chapter 4 which occupies 50% of the book, provides the essential information on the applications in the varied industries involved. The last chapter seeks to compare the key characteristics of the major enzymes according to their type and source. The book is concluded with a number of indices which tabulate the vast amount of information on enzymes available, suppliers, assay conditions and essential biochemical data.

If any criticism can be made of the book it is the sparse coverage of current research in immobilization technology and the use of immobilized enzymes, cells and organelles, and the need for the inclusion of more original literature references, but the restrictions of space dictate that some aspects had to be abbreviated. *Industrial Enzymology* has no direct competitors and provides a very useful reference text to complement the more usual texts on enzymology and, because of its ease of understanding by non-enzymologists, is essential reading for all those involved in industrial applications of enzymes, be they managers, technologists, students or teachers.

J. F. Kennedy and C. A. White

Industrial Crystallisation—The State of the Art (2nd revised edition)
J. Nyvlt
Verlag-Chemie, 1983
180 pp, US$38.75

This second revised edition of Nyvlt's 'State of the Art' is virtually identical to the first (1978), there being only minor corrections, additions and deletions. It is a poor relation to the author's 1971 book (Butterworths) on essentially the same subject. A comment in the preface to the English edition of the latter work, that "it nevertheless remains true that a concise handbook on chemical engineering design related to industrial crystallisation is still required" remains true today.

The main usefulness of this handbook is that it brings together under one cover, key references to the work of the two Czechoslovak 'schools' of crystallisation at Prague and Usti-nad-Labem. Approximately half the references cited are East European. It appears to be primarily intended for the chemical engineer, however, it is strongly biased to the physical chemical aspects of crystallisation and small-scale laboratory techniques, and would be of most use to the university researcher.

The book contains three main chapters and one short one on types of crystallisers. The first one on selecting a suitable design of crystalliser describes requirements concerning product crystal size and size distribution,

Book Reviews continued on page 314

VOL. 62 1984

ABSORPTION DURING GAS INJECTION THROUGH A SUBMERGED NOZZLE

Part I: Gas Side and Liquid Side Transfer Coefficients

By F. A. N. ROCHA and J. R. F. GUEDES DE CARVALHO

Centro de Engenharia Química, Universidade do Porto, Portugal

A study is described of the rate of transfer of solute between a gas being injected through a submerged nozzle, and the surrounding liquid. Nozzles of 5 mm and 10 mm i.d. were used with gas issuing downwards at velocities up to 6.5 m s^{-1} in a shallow liquid pool. Cine-photography was used to follow gas movement inside the liquid, and the individual gas-side and liquid-side transfer coefficients were measured (with the systems NH_3(gas)–HCl(soln) and O_2(gas)–water, respectively). The processes of mass transfer during bubble formation and bubble rise were considered separately and the corresponding coefficients determined. A comparison between experimental results and some simple theories is presented; theoretical predictions fall below (sometimes far below) the observed rates of transfer, but the idea of describing quantitatively the process of transfer in two stages (namely bubble formation and bubble rise) seems sound. Correlations for the various transfer coefficients are given.

INTRODUCTION

Liquid reservoirs with fixed roof need to allow for air admission and exhaust during their operation. In many instances, the air may have to be cleaned upon admission to the reservoir to avoid contamination of the liquid. This is often done by means of an absorber that will have to be designed for intermittent operation and low pressure drop (to avoid collapse of the roof). In Figure 1 a multi-tube absorber is shown in sketch, with pressure drop adjustable by means of depth of immersion of the tubes, h; with such an absorber there is no problem of 'weeping' even at zero gas flowrate. Furthermore the operation of this absorber is self-regulated when coupled to the liquid reservoir, if a 'hydraulic valve' is connected to the latter for gas exhaust. This again is shown in Figure 1 where the situation of liquid let out (a) and liquid fed in (b) are illustrated. An important feature is the relation between the cross-sectional area inside the tubes to that outside both in the absorber and in the 'hydraulic valve'. As far as the liquid in the absorber is concerned, the operation is batchwise, with occasional liquid removal for regeneration or replacement. This means that the absorber is only suitable for washing impurities present in low concentration in the gas.

The need to predict the performance of this type of absorber prompted the study described in the present paper. It is hoped that this study will also lead to a better understanding of mass transfer during bubble formation.

If the depth of tube immersion, h, is small (less than 0.1 to 0.2 m say) and if the distance between neighbouring tubes is large enough (greater than three to five tube diameters, say), the gas issued from each tube rises through the liquid without mixing with that issued from its nearest neighbours. Under these conditions the performance of the whole absorber may be scaled up from the performance of a single tube absorber. Hereafter a study is described of the mass transfer characteristics of a single submerged tube absorber, Figure 2, as influenced by tube diameter, depth of immersion and gas flowrate.

A meaningful retention of gas contaminants in the absorber may be achieved only if those contaminants are made to react very fast with the absorbing liquid. However, a fuller understanding of the mass transfer

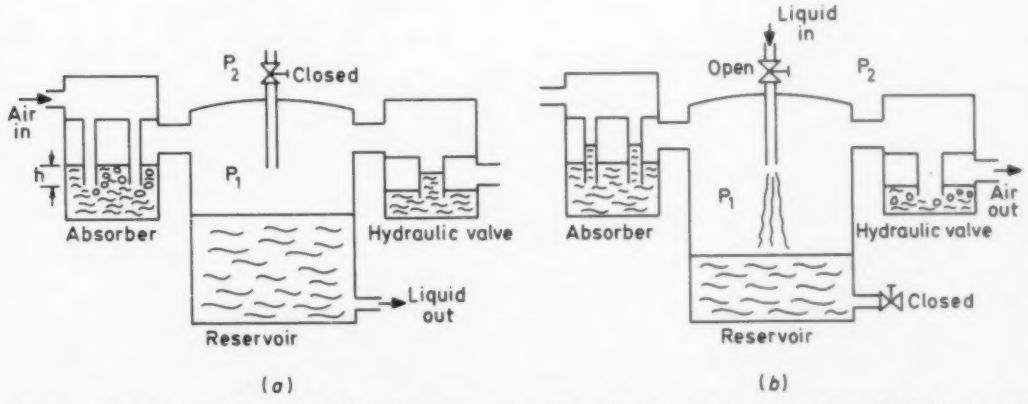


Figure 1. Multi-tube absorber connected to liquid reservoir (a) Liquid is let out ($P_1 < P_2$); (b) liquid is fed in ($P_1 > P_2$).

© Institution of Chemical Engineers

mechanisms involved may be achieved if both very fast chemical reaction in the liquid, and simple physical absorption are considered. This was the approach adopted and the results obtained are useful in assessing the applicability of some simple theories of interphase mass transfer during bubble formation and bubble rise.

EXPERIMENTAL METHOD

The systems used to characterise the absorber were absorption of NH_3 in solutions of hydrochloric acid (instantaneous reaction, gas-phase control) and absorption of O_2 from air in water (liquid phase control).

Two sizes of absorber were used. Absorber A was a glass cylinder, 66 mm internal diameter and 250 mm high with the bubbling tube (made of glass) placed axially with the tip at 65 mm from the bottom. The inner diameter of the tube, ϕ, was 5 mm. Absorber B was a cubic box, with 240 mm sides, made of perspex. The bubbling tube was again held centred from above with the tip at 70 mm from the bottom; tubes with $\phi = 10$ mm (made of perspex) and $\phi = 5$ mm (made of glass) were used. In both absorbers the gas outlet was at the top and no entrainment of liquid occurred. The depth of immersion of the tube was changed, varying the amount of liquid in the absorber. In each run, the liquid in the absorber was not renewed (batch operation). The gas fed to the absorber was previously saturated with water and the absorbers were in a constant temperature bath at 18.5°C. In the system NH_3–HCl (sol) the fraction of NH_3 in the inlet gas was very low (typically 5% or less) and the concentration of reactant in the liquid sufficiently high to allow operation for extended periods without significant change of conditions. In the absorption of O_2 in water, on the other hand, the rate of absorption varied with time and this variation was followed. Details of the experimental methods for each system are given below.

Absorption of NH_3 in solutions of HCl

Air at a given flowrate (measured by means of an orifice meter) was bubbled through water to saturate it, after which it was mixed with a metered stream of NH_3 supplied from a gas cylinder. The mixture was fed to the absorber, A or B, under study where most of the NH_3 was retained. The gas leaving the absorber was bubbled through three washing bottles in series, in order to remove virtually all the NH_3, and then vented to the atmosphere. The experiment was conducted for some time (usually 10–45 min) after which the NH_3 supply was shut off. The amount of NH_3 absorbed was determined directly as concentration of NH_4^+ in each solution by means of a specific electrode (ORION). The fraction of NH_3 retained in the absorber, X, was easily determined as the ratio

$$X = n_A/(n_A + n_1 + n_2 + n_3)$$

where n_A is the number of moles of NH_4^+ in the absorber after the run and n_1, n_2 and n_3 are the corresponding values for each of the washing bottles. In all cases n_2 and n_3 were virtually zero. The total number of moles absorbed was also calculated from the product of NH_3 flowrate and duration of the run and this was used as a check.

Absorption of O_2 in Water

Unsteady State Experiments

In these experiments the rate of oxygen intake by the water decreased during each run on account of increasing concentrations. It was therefore necessary to determine the variation of concentration of dissolved oxygen with time. Distilled water was initially stripped of most of the dissolved oxygen by bubbling pure nitrogen through it under vacuum (absolute pressure approx. 0.065 bar). After this, the water was placed in the absorber and bubbling with humidified air started at a given flowrate. At suitable intervals of time, samples of liquid were removed from the absorber, their oxygen content determined by means of an electrode (ORION 97.08), and the samples returned to the absorber. A curve of dissolved oxygen concentration against time was thence obtained, from which the overall transfer coefficient could be calculated. Only absorber B was used in these experiments, given its larger capacity; in absorber A the water would have been saturated far too quickly. Only the tube with $\phi = 5$ mm was used with this system.

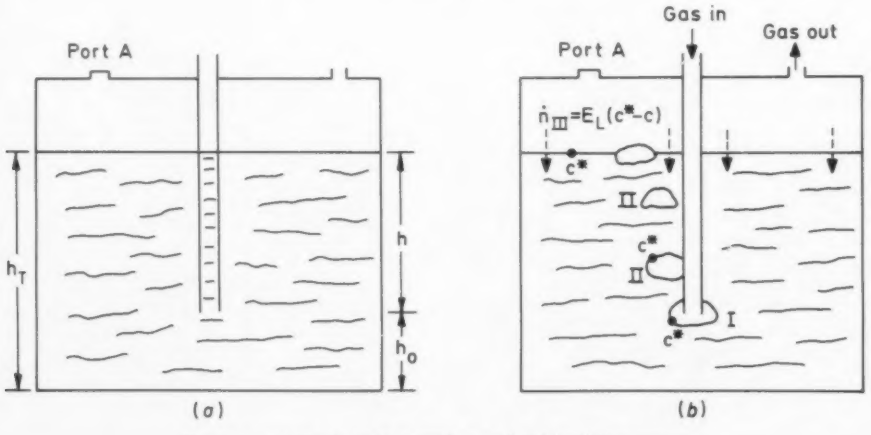


Figure 2. (*a*) Single tube absorber and (*b*) bubbling process.

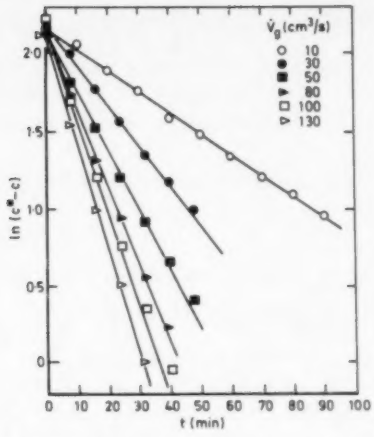


Figure 3. Experimental data on oxygen transfer to water, with $h = 30$ mm.

Steady State Experiments

For each gas flowrate and depth of immersion, a steady state experiment was performed to determine the extent of mass transfer across the free surface of the liquid. In these experiments a continuous stream of nitrogen was fed to the absorber in the space above the free surface, through port A (Figure 2), while air bubbled continuously in the liquid. A stirrer ensured 'perfect mixing' in this gas space and the oxygen content in the outlet gas was continously measured by means of an analyser. A steady state was reached when the rate of oxygen transfer from the bubbles to the liquid equalled the rate of oxygen desorption through the free surface. The corresponding partial pressure of oxygen in the gas, p (steady), and its concentration in the liquid C (steady) were recorded.

The range of gas flowrates used in the O_2-absorption experiments was 10–130 $cm^3\,s^{-1}$. The corresponding values of gas velocity inside the injection nozzle were in the range 0.51–6.6 $m\,s^{-1}$.

THEORY

The different systems studied call for different theoretical descriptions and consideration is given separately to the cases of purely physical absorption, and absorption with fast and irreversible reaction in the liquid.

There was no liquid fed or withdrawn during the experiment and perfect mixing of the liquid was assumed. This is a good approximation if the ratio of height to width of the liquid pool is not large compared to unity. The gas was assumed to be in plug flow as is expected in bubbling without mechanical agitation. Films of the bubbling process support this view.

It is common practice to account for the mass transfer process by means of one (overall) transfer coefficient. A more fundamental approach is adopted here and the process of mass transfer is considered to occur in two steps; mass transfer during bubble formation and mass transfer during bubble rise. Finally the existence of mass transfer at the free surface due to its continuous renewal was also considered. Figure 2 helps characterise the different steps and a more detailed description of these is given later. In that figure, bubble I is being formed while bubbles II are in the process of rising. Mass transfer across the surface is indicated by dashed arrows.

Purely Physical Absorption

In this case two possibilities exist depending on the solubility of the absorbed species (say A). For slightly soluble gases (like O_2 in water) the concentration of A in the gas may be considered constant all the way up the absorber whereas for more highly soluble species (like NH_3 in water) variation of concentration of A during bubble rise has to be taken into account. The latter case is considered in the Appendix.

For a sparingly soluble gas, if $\dot{n}$ is the total molar rate of transfer of A to the liquid at any instant, we may write

$$\dot{n} = \dot{n}_{\mathrm{I}} + \dot{n}_{\mathrm{II}} + \dot{n}_{\mathrm{III}}$$

where the subscripts refer to each of the steps illustrated in Figure 3; p is the partial pressure of A in the gas, C its concentration in the liquid, and Henry's law with $p = HC^*$ is supposed to hold. In the unsteady state experiments p is the same in the gas bubbles and above the free surface of the liquid and therefore

$$\dot{n}_{\mathrm{I}} = F_{\mathrm{L}}\,(C^* - C) \tag{1}$$

$$\dot{n}_{\mathrm{II}} = K_{\mathrm{L}}S\,(C^* - C) \tag{2}$$

$$\dot{n}_{\mathrm{III}} = E_{\mathrm{L}}\,(C^* - C) \tag{3}$$

where F_{L} is equivalent to the product of a mass transfer coefficient and an average area for bubbles in the formation period, S is the total surface area of bubbles rising in the liquid after detachment from the nozzle and K_{L} the overall transfer coefficient for these bubbles; E_{L} is equivalent to the product of the transfer coefficient and surface area at the free surface of the liquid. All these coefficients depend on the relevant gas and liquid properties and on the operating conditions. For a given gas–liquid system it is expected that F_{L} depends on gas flowrate and nozzle configuration, $K_{\mathrm{L}}S$ on the size of bubbles and their velocities and E_{L} on rate of renewal of the free surface.

A material balance on solute A gives

$$V_{\mathrm{T}}\frac{\mathrm{d}C}{\mathrm{d}t} = \dot{n}_{\mathrm{I}} + \dot{n}_{\mathrm{II}} + \dot{n}_{\mathrm{III}} \tag{4}$$

where V_{T} is the total volume of liquid in the absorber. With C^* constant this may be written as

$$-V_{\mathrm{T}}\frac{\mathrm{d}\ln(C^* - C)}{\mathrm{d}t} = F_{\mathrm{L}} + K_{\mathrm{L}}S + E_{\mathrm{L}} \tag{5}$$

At a given depth of immersion and for each gas flowrate the r.h.s. of (5) should be constant during a run and plots of $\ln(C^* - C)$ against t give straight lines as shown in Figure 3.

Now in the steady state experiments with nitrogen being fed to the gas space above the liquid, the concentration of oxygen in the liquid at the free surface C^{**} is given by $C^{**} = p_{\mathrm{steady}}/H$ and therefore

$$E_{\mathrm{L}}\,(C_{\mathrm{steady}} - C^{**}) = (F_{\mathrm{L}} + K_{\mathrm{L}}S)\,(C^* - C_{\mathrm{steady}}) \tag{6}$$

From (5) and (6) and the experimental data, the values of E_{L} and $(F_{\mathrm{L}} + K_{\mathrm{L}}S)$ may be determined separately.

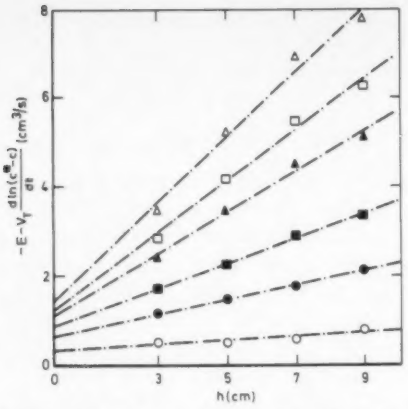


Figure 4. Experimental data for oxygen absorption plotted as suggested by equation (5); symbols as in Figure 3.

Experimental values of E_L and $(F_L + K_L S)$ are given in Figure 6. Lower case letters e, f and k are used for film coefficients and they coincide with overall coefficients represented by upper case letters E, F and K when the whole resistance is on one side of the interface only. The value of F_L should be independent of h and for each gas flowrate it is reasonable to write $K_L S = K_L a^* h$ where a^* is the interfacial area of rising bubbles per unit depth of immersion for the 'string' of bubbles issuing from the tube, and is assumed constant up the absorber, for each gas flowrate.

Under these assumptions, values of $K_L a^*$ and F_L may be obtained as slope and intercept, respectively in a plot of $[-E_L - V_T \mathrm{d} \ln (C^* - C)/\mathrm{d}t]$ against h as suggested by (5) and this is shown in Figure 4.

Chemical Absorption

If the absorbed species, A, reacts in the liquid, and if the reaction is irreversible and fast enough, C is zero away from the bubbles. The partial pressure of A in the gas phase is going to vary significantly between inlet and outlet and a material balance over an elementary height ($\mathrm{d}z$) is necessary to account for mass transfer during bubble rise. Starting with the period of bubble formation it is expected that

$$\dot{n}_I = F^r_G (C^g_{in} - 0) \tag{7}$$

where C^g_{in} is the molar concentration of A in the gas inlet to the absorber, and F^r_G is equivalent to F_L in (1) (the superscript r indicates that there is reaction in the liquid). The proportionality of $\dot{n}_I$ to C^g_{in} is reasonable since the interface encloses the nozzle tip during the whole period of bubble formation and C^g_{in} is the concentration of A at the tip.

In the process of rising however, a material balance over a differential height, $\mathrm{d}z$, is required to describe mass transfer:

$$-\dot{V}_g \mathrm{d}C^g = (K^r_G a^*)\, \mathrm{d}z\, (C^g - 0) \tag{8}$$

where $\dot{V}_g$ is the volumetric gas flowrate assumed constant, K^r_G is the overall mass transfer coefficient for the rising bubbles with reaction in the liquid. Integration from $z = 0$ to $z = h$ yields

$$\frac{C^g_2}{C^g_I} = \exp[-(K^r_G a^*/\dot{V}_g)h] \tag{9}$$

where C^g_I is the concentration of A immediately upon detachment from the nozzle tip and C^g_2 the corresponding value as the bubble reaches the free surface of the liquid.

The total rate of transfer from rising bubbles is given by

$$\dot{n}_{II} = \dot{V}_g (C^g_I - C^g_2) \tag{10}$$

and if C^g_2 from (9) is substituted in (10) there results

$$\dot{n}_{II} = \{1 - \exp[-(K^r_G a^*/\dot{V}_g)h]\} C^g_I \dot{V}_g \tag{11}$$

The extent of mass transfer at the liquid free surface was expected to be very small for the system studied on account of the low concentration of A observed at the outlet and this was confirmed by estimates. Now, from (7) and

$$\dot{n}_I = \dot{V}_g (C^g_{in} - C^g_I) \tag{12}$$

it is possible to obtain

$$\frac{C^g_I}{C^g_{in}} = 1 - \frac{F^r_G}{\dot{V}_g} \tag{13}$$

The product of (13) and (9) gives

$$1 - X = \frac{C^g_{out}}{C^g_{in}} = \left(1 - \frac{F^r_G}{\dot{V}_g}\right) \exp\left[-\left(\frac{K^r_G a^*}{\dot{V}_g}\right) h\right] \tag{14}$$

where C^g_{out} is used instead of C^g_2. Taking logarithms leads to

$$\ln (1 - X) = \ln\left(1 - \frac{F^r_G}{\dot{V}_g}\right) - \left(\frac{K^r_G a^*}{\dot{V}_g}\right) h \tag{15}$$

and this shows how a plot of $\ln (1 - X)$ against h may be used to yield the mass transfer parameters. Data plotted in the fashion suggested by (15) are shown later (in Figure 8).

EXPERIMENTAL DATA AND THEIR INTERPRETATION

The method developed in the previous sections is now used to obtain the various mass transfer coefficients; a more fundamental interpretation of these coefficients is given in another section.

Absorption of O_2 in Water

Figure 3 shows experimental data plotted as $\ln (C^* - C)$ against t and these are well approximated by straight lines, for each flow rate and submersion, as suggested by (5). Figure 4 shows data for different flowrates plotted as $[-E_L - V_T \mathrm{d} \ln (C^* - C)/\mathrm{d}t]$ against h and reasonably straight lines are obtained, in agreement with theory. The straight lines drawn in these figures were obtained by least squares fit and the slope and intercept for each set of data in Figure 4 used to calculate F_L and $K_L a^*$. These coefficients were expressed as overall coefficients, but in the case of absorption of O_2 in water, they correspond to liquid side coefficients, since the resistance to transfer on the gas side is negligible; lower case letters f_L, e_L and k_L are used to stress this fact.

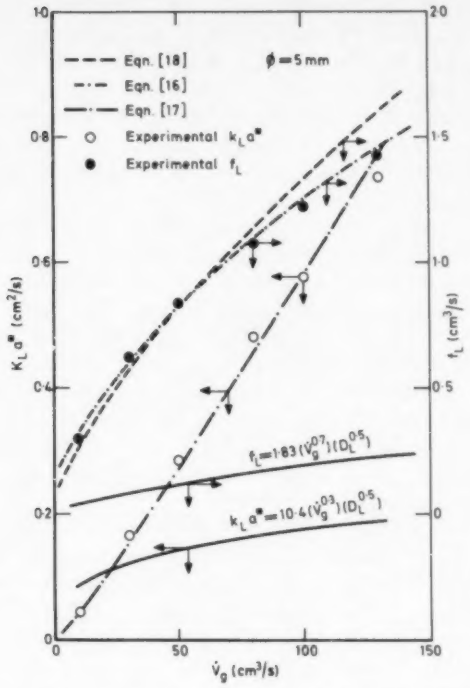


Figure 5. Variation of liquid side transfer coefficients with gas flowrate ($D_L = 1.79 \times 10^{-5}$ cm^2 s^{-1}).

Figures 5 and 6 show the variation of f_L, (k_La^*) and E_L (same as e_L in this case), with gas flowrate. The best straight line through the data in log-log plots of coefficient versus $\dot{V}_g$ yields the following empirical formulae, which may be used for design purposes:

$$f_L = 0.079\,(\dot{V}_g)^{0.60}\ \text{cm}^3\ \text{s}^{-1} \tag{16}$$

$$k_La^* = 0.0039\,(\dot{V}_g)^{1.09}\ \text{cm}^2\ \text{s}^{-1} \tag{17}$$

where $\dot{V}_g$ is in cm^3 s^{-1} measured in the experimental conditions (1 bar and 18.5°C).

A simple theory for mass transfer presented in another section predicts $f_L = \alpha(\dot{V}_g)^{0.70}\ (D_L)^{0.50}$ where α is a constant independent of nozzle diameter and D_L is diffusivity of the solute in the liquid. This suggests the fit of a straight line of slope 0.70 to the data plotted as (ln f_L) versus $\dot{V}_g$.

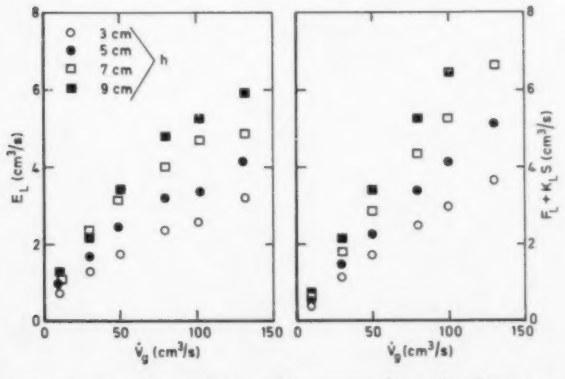


Figure 6. Transfer coefficients for oxygen absorption in water.

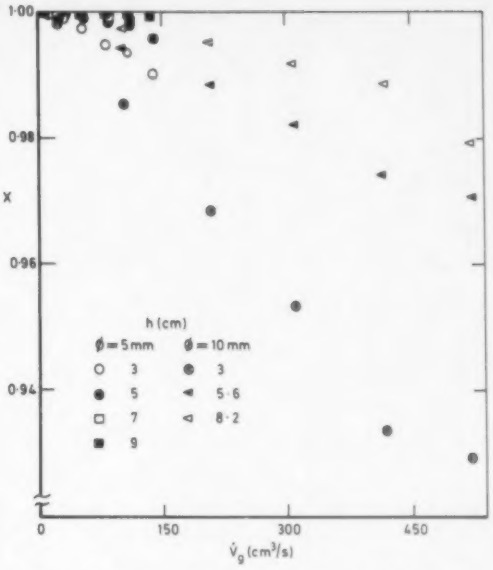


Figure 7. Fractional retention of NH_3 in absorber.

The best line corresponds to

$$f_L = 12.5\,(D_L)^{0.50}\ (\dot{V}_g)^{0.70}\ \text{cm}^3\ \text{s}^{-1} \tag{18}$$

and this expression is shown alongside the data in Figure 5 ($\dot{V}_g$ in cm^3 s^{-1} and $D_L = 1.79 \times 10^{-5}$ cm^2 s^{-1}).

Experimental values of E_L are shown in Figure 6, alongside values of ($F_L + K_LS$), and it may be seen that for each flowrate and depth of immersion the values of E_L and ($F_L + K_LS$) are of similar magnitude; this result together with equations. (1)–(3) shows that about half of the oxygen transfer to the solution took place at the free surface. This is a weakness of the present experimental method and an alternative approach to the problem is being developed at present. The increase in E_L with h and $\dot{V}_g$ shown in Figure 6 is in line with behaviour of 'circulation cells'.

Absorption of NH_3 in Solutions of HCl

Raw data for this system are given in Figure 7 as fraction of NH_3 retained in the absorber, X, against gas flowrate. It may be seen that X is always very high (above 0.92) even for the lowest values of submersion, and this is no doubt because of the high transfer rates at the nozzle tip. The experimental values were interpreted in terms of equation (15) and for that purpose plots of ln$(1 - X)$ against h were made as in Figure 8 and least squares straight lines determined. The coefficients obtained in this case refer to the gas side, since the resistance to transfer in the liquid is negligible. Lower case letters, f_G and (k_Ga^*) are again used to stress this fact and Figure 9 shows plots of the transfer coefficients versus gas flowrate. It is remarkable that the values of f_g fall so close to the line of slope unity through the origin, showing that virtually all the NH_3 is absorbed at the nozzle tip.

Empirical formulae for design purposes were again obtained by straight line fit as in the previous section and these are

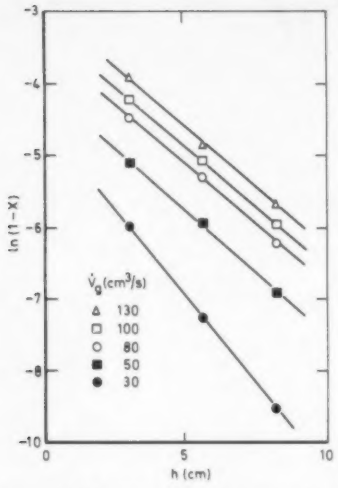


Figure 8. Variation of NH_3 retention with depth of immersion plotted as suggested by equation (15).

$$f_G = (\dot{V}_g) - 0.000404\,(\dot{V}_g)^{1.99}\ \text{cm}^3\,\text{s}^{-1} \tag{19}$$

and

$$k_G a^* = 0.566\,(\dot{V}_g)^{0.90}\ \text{cm}^2\,\text{s}^{-1} \tag{20}$$

Experimental values for the 5 mm nozzle in both absorbers, A and B, are represented in Figure 9 and they are seen to be very close; this fact suggests that scale up of a shallow multi-tube absorber should be a feasible proposition. It is convenient to mention here the importance of mass transfer across the free surface for the system NH_3–HCl. In Figure 6, E_L may be seen to increase with h, and if this also happens for the gas side coefficient at the free surface in the absorption of NH_3, the values of $k_L a^*$ determined are likely to be in error. A resonable estimate of this transfer at the free surface may be obtained in terms of a coefficient $e_G = e_L\,(D_G/D_L)^{1/2}$ and this was done; the resulting correction would be to bring the points for absorber B closer to those for absorber A, in Figure 9.

FUNDAMENTAL INTERPRETATION OF THE RESULTS

It is interesting to see how the results described relate to the more detailed aspects of mass transfer during bubble formation and bubble rise. Indeed in the past twenty years a lot of research effort has been directed towards the understanding of the fluid mechanics and transfer processes around single bubbles, and yet the connection between these detailed studies and the practical situations where bubbles are present is not often made clear. This connection is attempted here for the case of the absorber described. The information required to do this relates to the size, frequency and rise velocity of bubbles formed as well as to the rates of mass transfer from the individual bubbles.

Size, Frequency and Rise Velocity of Bubbles

A fast cine-camera was used (at the University of Cambridge) to follow closely the processes of bubble formation and bubble rise from both the 5 mm and 10 mm i.d. submerged nozzles. At each gas flowrate sequences at 100 frame/s with individual frame exposures of 1/2400 s were taken. The field of view was sufficiently large to allow individual bubbles to be followed as they rose for a few cm above the nozzle tip. The width of the bubbling tubes was used as length scale; for the filming sequences the liquid (water) was contained in a cubic perspex box (side = 0.3 m) to avoid distortion, with the bubbling tube placed centrally.

The films obtained were analysed frame by frame and some sequences are shown in Figure 10; (*a*) and (*c*) are typical of undisturbed bubble formation whereas (*b*) and (*d*) are typical of bubble formation with tearing off. Sequences of alternating (*a*) and (*b*) or (*c*) and (*d*) type patterns were typical. It is clear that formation as in (*b*) and (*d*) is likely to yield much higher mass transfer coefficients on account of increased surface-area-to-volume ratio and turbulence.

A bubble was considered to be in the formation period while there was contact between it and the tube mouth. The number of frames for bubbles to form was recorded and so were the velocities of rise after formation. The gas flowrate through the nozzle mouth was assumed constant, and from it individual bubble volumes could be calculated.

Plots as in Figure 11 were used to summarise the data as percentage of bubbles formed versus time of formation. From these, the volume average time of formation, $\bar{t}_f$, of bubbles, as well as the average volume of bubble formed, $\bar{V}_0$, were calculated for each gas flowrate, $\dot{V}_g$. Figure 12 provides a comparison between experiment and the theory of Davidson and Schüler[1] for bubble formation in inviscid liquids. The fact that the gas was issuing downwards from the nozzle is of no importance as long as gas momentum is negligible. In this figure two sets of points are given, one for average volumes over all the bubbles and the other for average over bubbles formed 'undisturbed'; the fact that the global average volumes are often larger than those for undisturbed bubbles is the result of bubble coalescence before detachment from the nozzle. It may be seen that the agreement between theory and experiment is excellent for the 10 mm nozzle and reasonable for the 5 mm one.

Bubble rise velocities were also determined in the frame-by-frame analysis of the films; it was observed

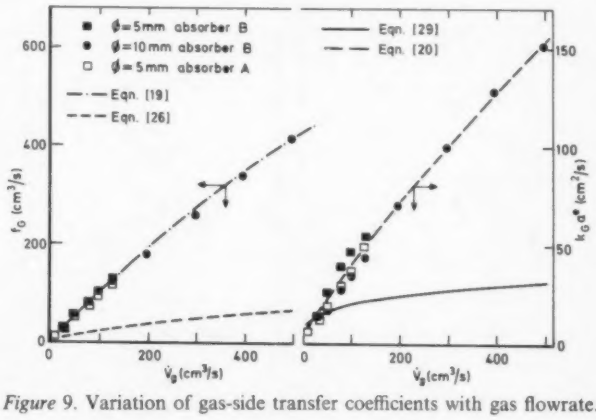


Figure 9. Variation of gas-side transfer coefficients with gas flowrate.

VOL. 62 1984

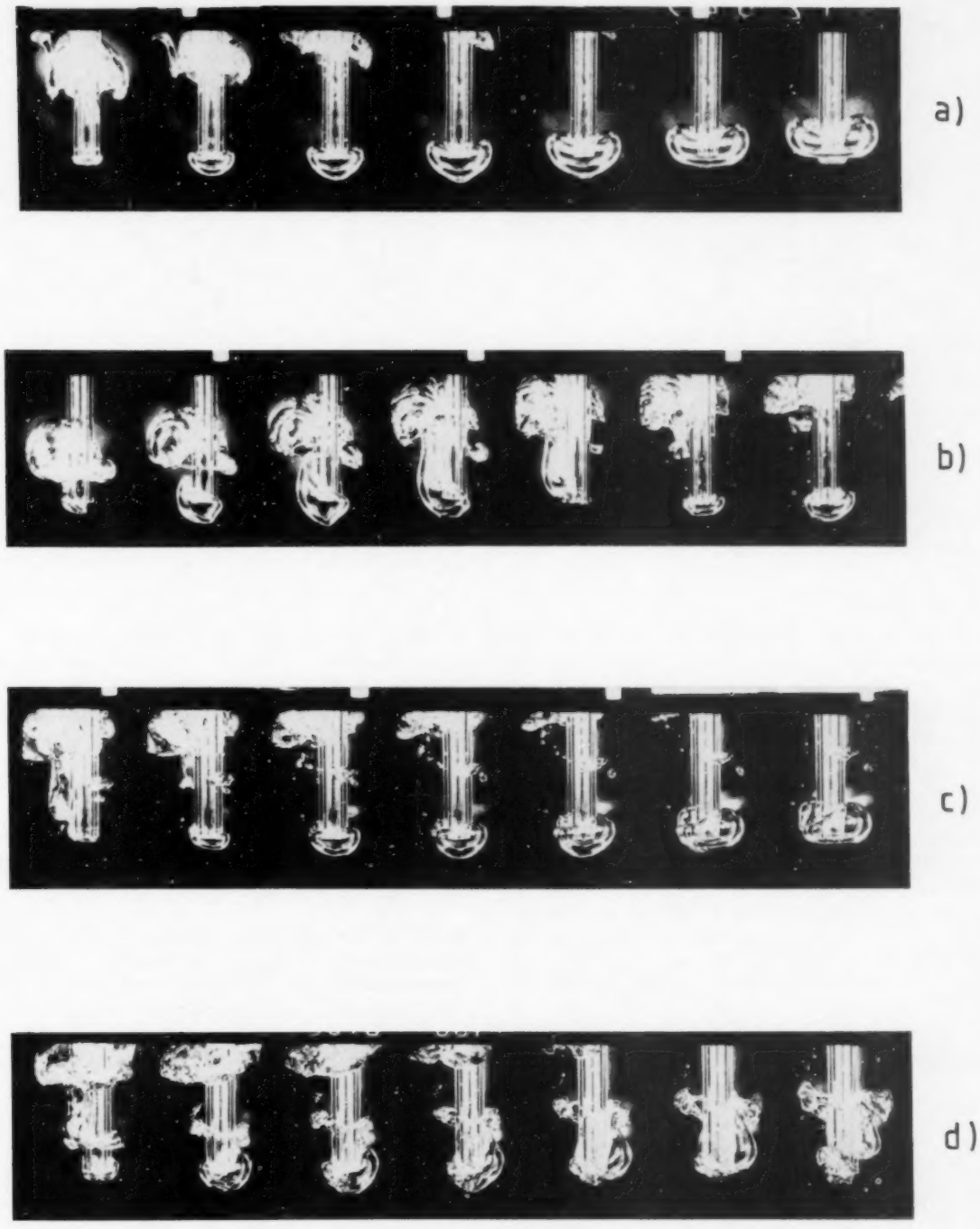


Figure 10. Cine-film sequences of bubble formation; sequences (*a*) and (*b*) are for nozzle i.d. = 5 mm, o.d. = 7 mm, $\dot{V}_g = 69\ cm^3\ s^{-1}$; sequences (*c*) and (*d*) are for nozzle i.d. = 10 mm, o.d. = 15 mm, $\dot{V}_g = 239\ cm^3\ s^{-1}$. In all sequences the film speed was 100 frame s^{-1}.

that except for a very small percentage of bubbles which were sucked into other bubbles' wakes, the rise velocities fell within a narrow band for each gas flowrate. An average (by number) velocity of rise was determined for each gas flowrate and the results are plotted in Figure 13. Also shown are the curves corresponding to the velocity of rise of spherical cap bubbles $v_b = 0.71\sqrt{(gd_e)}$ where $d_e = [(6/\pi)\bar{V}_0]^{1/3}$ is the equivalent average bubble diameter and the dependence $\bar{V}_0 = 1.138\ \dot{V}_g^{6/5}/g^{3/5}$ predicted by theory[1], where g is the acceleration of gravity, is accepted. The agreement is good particularly as no account is taken of the interference of the tube with the rising bubbles and of any liquid circulation induced by the bubbling process.

Mass Transfer During Bubble Formation

The importance of mass transfer near gas spargers is well known and there is some controversy as to its importance. Most authors mention an enhanced mass

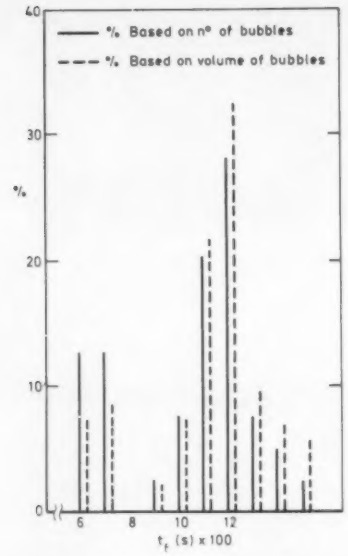


Figure 11. Histogram of time of formation of bubbles in continuous bubbling for the 5 mm i.d. nozzle at $\dot{V}_g = 35\ \text{cm}^3\ \text{s}^{-1}$.

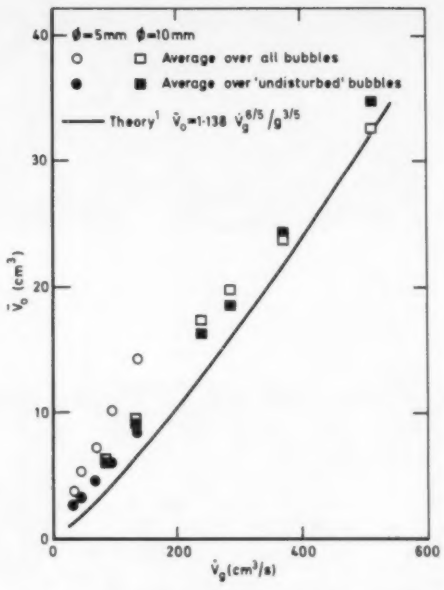


Figure 12. Average volume of bubbles formed as a function of flowrate.

transfer near the distributor; however Calderbank and Patra[2] measured transfer rates during bubble formation and concluded that "the formation of bubbles is not accompanied by an enhanced rate of mass transfer, when the resistance to mass transfer is in the liquid phase".

These authors provide a simple theory for mass transfer based on the idea of Beek and Kramers[3] that conceives the bubble surface in expansion to be made up of elements with different ages. An alternative theory, leading to very similar results, is presented by Sherwood *et al.*[4] based on an analysis by Levich[5]. These authors consider the growth of a spherical bubble, at constant gas flowrate, with resistance to diffusion confined to a thin film of liquid surrounding the growing bubble. The thickness of this layer is assumed to be small compared with the bubble radius.

The resulting expression for instantaneous molar flux of solute to the liquid is

$$\dot{N} = (7/3)^{1/2}\,(D_L/\pi t)^{1/2}\,(C^* - C) \qquad (21)$$

where D_L is the solute diffusivity in the liquid, t is time since the bubble started to form $C^* - C$ is the difference in solute concentration between the interface and the bulk of the liquid. The surface area of the bubble, assumed to be spherical, A_b, grows as $A_b = (6\pi^{5/2}\,\dot{V}_g t)^{2/3}$ and the amount of solute transferred during the formation time, t_f, of a bubble is given as

$$n_f = \int_0^{t_f} \dot{N}\,A_b\,dt = 3.57\,\dot{V}_g^{2/3}\,t_f^{7/6}\,D_L^{1/2}\,(C^* - C) \qquad (22)$$

If it is assumed that for a given flowrate all bubbles take the same time t_f to form it follows that

$$\dot{n}_l = n_f/t_f = 3.57\,\dot{V}_g^{2/3}\,t_f^{1/6}\,D_L^{1/2}\,(C^* - C) \qquad (23)$$

and

$$f_L = 3.57\,\dot{V}_g^{2/3}\,D_L^{1/2}\,t_f^{1/6} \qquad (24)$$

This is a theoretical expression for f_L derived from first principles and all that is required now is a relation between t_f and $\dot{V}_g$. This relation could be provided by our experimental data, but instead the equation of Davidson and Schüler[1]

$$t_f = 1.138\,\dot{V}_g^{1/5}/g^{3/5}$$

(where g is the acceleration of gravity) was used because it approximates our data closely enough and it has a physical basis. The resulting theoretical expression is

$$f_L = 1.83\,\dot{V}_g^{\,0.70}\,D_L^{\,0.50}\ (\text{cm}^3\ \text{s}^{-1}) \qquad (25)$$

and plots are shown in Figure 6 together with experimental results. These are seen to be much above the theoretical predictions and this confirms the view that mass transfer during bubble formation is much enhanced. The piercing and tearing of bubbles by the nozzle may be responsible for this. A comparison

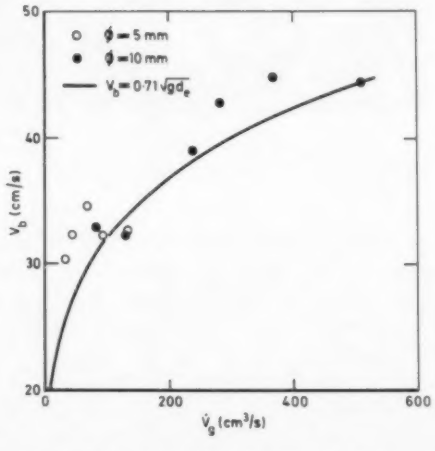


Figure 13. Velocity of rise of bubbles formed. The line corresponds to $v_b = 0.71\sqrt{(gd_e)}$ with d_e predicted from theory[1].

VOL. 62 1984

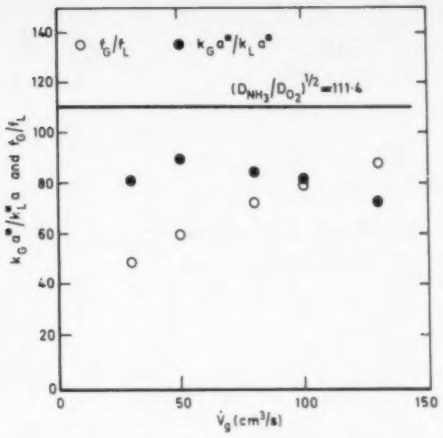


Figure 14. Ratio of gas to liquid side transfer coefficients.

between equations (25) and (16) or (18) suggests that the variation of f_L with $\dot{V}_g$ is well predicted by theory, but the constant derived from theory is far too low.

Equation (18) was developed maintaining the functional dependence of f_L on $\dot{V}_g$ predicted by theory, but with an adjusted constant and it may be seen to represent well the data, in Figure 5.

An expression for the transfer coefficient on the gas side, f_G, may be derived in a similar fashion to (24) but with gas diffusivity, D_G, instead of D_L; however it should be noted that the diffusion layer near the bubble surface is much thicker on the gas side and for the experimental conditions observed its thickness should be a significant proportion of the bubble radius. Also, significant gas circulation may be present inside the bubble while it is attached to the nozzle, and this again may lead to significant deviations from the theory. Indeed, it may be seen in Figure 9 that not only the expression

$$f_G = 1.83\, \dot{V}_g^{0.70}\, D_G^{0.50} \tag{26}$$

gives values far below experiment, but also the dependence of f_G on $\dot{V}_g^{0.70}$ is far from being followed. Equation (19) is proposed, to correlate the data for f_G but its validity is restricted to the conditions in the experiments.

The dependence of f_G on D_G is certainly not the one indicated by equation (26); to show this it is enough to see that for values of D_G say twice those of NH_3 in air ($D_{G(NH_3-air)} = 0.222\ cm^2\ s^{-1}$ at 1 bar; 18.5°C) a prediction of $f_G \propto D_G^{1/2}$ would lead to amounts of solute absorbed higher than those fed to the absorber.

Mass Transfer from Rising Bubbles

The convenience of referring the coefficients to a^*, the interfacial area per unit depth of liquid, was stressed before. The interfacial area per unit volume of liquid above the nozzle is $a' = a^*/A_0$ and if gas issues from m independent nozzles $a' = ma^*/A_0$ where A_0 is the cross-sectional area of the absorber. Values of $k_L a^*$ and $k_G a^*$ were obtained from experimental data by means of plots as in Figures 4 and 8 and the corresponding values are plotted as a function of flowrate in Figures 5 and 9; again it is interesting to compare these values with the predictions from a simple theory.

If mono-sized bubbles of volume $\bar{V}_0$ are assumed to form at the nozzle mouth at a frequency $1/\bar{t}_f$, and these are assumed to rise individually through the liquid at constant velocity $v_b = 0.71\sqrt{(gd_e)}$, it takes a time $t_r = h/v_b$ for each bubble to rise through a height h to the free surface and in this time $N_b = t_r/\bar{t}_f$ bubbles are released from the nozzle tip and are in the process of rising. The total equivalent surface area ($=\pi d_e^2$ for one bubble) or bubbles in the liquid at any instant is then $A_e = N_b\, \pi\, d_e^2$ and $a_e^* = N_b\, \pi\, d_e^2/h$. Now the coefficient, k_{Le}, for individual bubbles based on the equivalent area is given by the theory of Baird and Davidson[6] as

$$k_{Le} = 0.975\, d_e^{-1/4}\, D_L^{1/2}\, g^{1/4} \tag{27}$$

and this is in good agreement with reported experimental values which scatter widely between 0.01 and 0.035 cm s^{-1} for one system studied; all these data refer to single bubbles rising undisturbed in water. A theoretical value of $k_L a^*$ ($=k_{Le} a_e^*$) may now be obtained if the expression of Davidson and Schüler is again used to give t_f and d_e in terms of $\dot{V}_g$ and this is

$$k_L a^* = 10.4\, \dot{V}_g^{0.30}\, D_L^{0.50} \tag{28}$$

For the gas side the transfer coefficient is predicted[7] by an expression similar to (28) but with D_G instead of D_L

$$k_G a^* = 10.4\, \dot{V}_g^{0.30}\, D_G^{0.50} \tag{29}$$

Plots of (28) and (29) are shown in Figures 5 and 9 and comparison with experimental data shows that the theory underpredicts the coefficients significantly, except for the lowest values of $\dot{V}_g$. This is not surprising considering that the transfer coefficients used hold for bubbles rising singly in undisturbed liquid; in the absorber studied the bubbles are pierced as they rise (see Figure 10) and they often break and re-coalesce. All these phenomena will increase the interfacial transfer, and therefore the fact

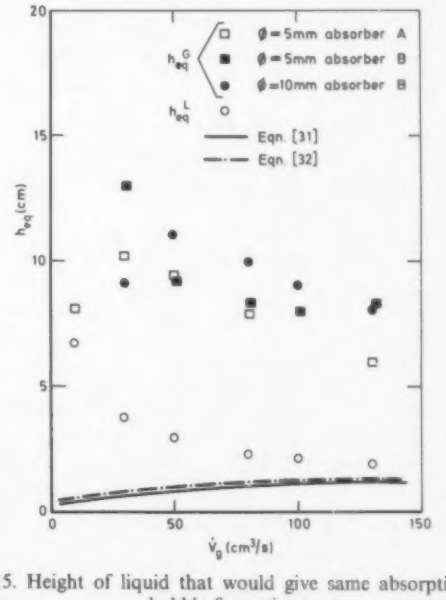


Figure 15. Height of liquid that would give same absorption as in bubble formation.

that the ratio between experiment and theory is between 1 and 4 for k_La^* and between 1 and 5 for k_Ga^* is good support for the two-zone absorption model presented in this paper; it should be stressed in particular that equations (28) and (29) are fully based on theory with no adjustable parameters. Further, Figure 9 shows that k_Ga^* is virtually independent of nozzle diameter, in agreement with theory, and also that the values of k_Ga^* do not depend on the size of the absorber when plotted as function of flowrate through the bubbling tube (instead of superficial gas velocity as is common practice). One last way of checking the data is by comparison of $(k_Ga^*)/(k_La^*)$ with $(D_G/D_L)^{1/2}$; according to theory the two ratios should have the same value (=111 in this case). Figure 14 shows that the ratio of the coefficients is fairly constant at around 80. A simple calculation shows that for the bubbles studied, the boundary layer on the gas side has a thickness of several mm, and this could explain why k_Ga^* is less than would have been predicted from k_La^* corrected for the diffusivity. In principle, the ratio f_G/f_L might be expected to be greater than $(D_G/D_L)^{1/2}$ on account of gas circulation inside the forming bubble; this circulation (not present in the liquid) would increase the mass transfer coefficient by reducing the boundary layer thickness. However, the large coefficients observed result in considerable depletion of solute inside the forming bubbles and this in turn reduces significantly the effective driving force (Figure 7 shows that over 90% of solute is absorbed in the formation stage, when control is on the gas side). This effect is not present in the absorption of oxygen in water and as a result the driving force is virtually unchanged during bubble formation in that case, thus leading to lower values of f_G/f_L.

THE HEIGHT EQUIVALENT TO THE INLET PORT

The experiments described show that mass transfer is enhanced near the nozzle outlet; it is important to know the height of liquid that would give a fractional amount of solute absorbed equal to that observed at the nozzle outlet, in order to assess the relative extent of this 'entrance effect'.

Purely Physical Absorption

In this situation and for cases where the concentration of solute in the gas does not vary much between inlet and outlet

$$f_L(C^* - C) = k_La^* h_{eq}^L (C^* - C)$$

and therefore

$$h_{eq}^L = f_L/k_La^* \tag{30}$$

If the real depth of immersion in an absorber h, is much above this value, the entrance effect may be neglected and only mass transfer from rising bubbles needs to be considered. Figure 15 shows the values of h_{eq}^L deduced from our experiments and a plot of the theoretical value for the system oxygen–water:

$$h_{eq}^L = 0.175\ \dot{V}_g^{0.40} \tag{31}$$

obtained from (30) with (25) and (28).

Absorption with Gas Phase Resistance Only

In the absorption of NH_3 by solutions of HCl it was shown that

$$f_G C_{in}^g = \dot{V}_g (C_{in}^g - C_1^g)$$

and therefore

$$C_1^g/C_{in}^g = (\dot{V}_g - f_g)/\dot{V}_g$$

an equivalent fractional absorption would be observed over a height h_{eq}^G such that

$$C_1^g/C_{in}^g = \exp[-(k_Ga^*/V_g)h_{eq}^G]$$

and therefore

$$h_{eq}^G = \frac{\dot{V}_g}{k_Ga^*} \ln\left(\frac{\dot{V}_g}{\dot{V}_g - f_G}\right) \tag{32a}$$

Figure 15 shows the values of h_{eq}^G calculated from our experiments together with a plot of

$$h_{eq}^G = 0.204\ \dot{V}_g^{0.70} \ln[\dot{V}_g/(\dot{V}_g - 0.862\ \dot{V}_g^{0.70})] \tag{32}$$

which is the theoretical curve obtained from (32a) with (26) and (29).

Once again it may be seen that the importance of the entrance effect is more pronounced than could be expected from theory alone.

CONCLUSIONS

For the absorber studied it may be concluded that:

(i) Mass transfer parameters correlate well with gas flowrate through the nozzle rather than with superficial gas velocity in the absorber; therefore, scale-up of a shallow multi-tube absorber based on the study of a corresponding single tube appears as a reasonable proposition.

(ii) The separate consideration of mass transfer for bubble formation and for bubble rise is physically sound and a lot better than description through one overall transfer coefficient. This is particularly so for shallow absorbers and Figure 5 provides a good guide as to when the entrance effect may be neglected.

(iii) Simple theory for mass transfer from bubbles forming and rising undisturbed, underpredicts markedly the observed rates of transfer. This is not surprising and may be accounted for by the disruptive presence of the nozzle and turbulence due to continuous bubbling.

(iv) With gas phase control, mass transfer during bubble formation is particularly effective and no doubt this explains why stage efficiences near unity are obtained in such systems.

APPENDIX

Purely Physical Absorption of a Solute of Moderate to High Solubility

In this case the solute concentration in the gas bubbles decreases up the absorber while in the well-mixed pool of liquid its concentration is uniform, but increases with time. If p_{in} is the partial pressure of solute in the gas inlet to the absorber

$$\dot{n}_1 = F_G(p_{in} - p^*) \tag{A1}$$

where $p^* = HC$ is the partial pressure of solute that

VOL. 62 1984

would be in equilibrium with the bulk of the liquid; p^* varies only with t. Now

$$\dot{n}_1 = \frac{\dot{V}_g}{RT}(p_{in} - p_1) \tag{A2}$$

where p_1 is the average partial pressure of solute in the gas bubble as it detaches from the nozzle tip. A material balance for a differential height dz, followed by integration between $z = 0$, $p = p_1$ and $z = h$, $p = p_{out}$ gives

$$\frac{p_{out} - p^*}{p_1 - p^*} = \exp\left[-RT(K_G a^*/\dot{V}_g)h\right] \tag{A3}$$

$\dot{n}_1$ may be eliminated between (A1) and (A2) to give

$$\frac{p_1 - p^*}{p_{in} - p^*} = 1 - \frac{RT}{\dot{V}_g}F_G \tag{A4}$$

and multiplication by (A3) followed by rearrangement gives

$$p_{in} - p_{out} = (p_{in} - p^*)\left\{1 - \left(1 - F_G\frac{RT}{\dot{V}_g}\right) \times \exp\left[-RT\left(\frac{K_G a^*}{\dot{V}_g}\right)h\right]\right\} \tag{A5}$$

A material balance to the liquid at any instant gives

$$V_T\frac{dC}{dt} = \frac{\dot{V}_g}{RT}(p_{in} - p_{out}) \tag{A6}$$

and if Henry's law holds, $p_{in} = HC^*_{in}$ and $p^* = HC$ and combination of (A5) and (A6) may be written as

$$-V_T\frac{d(C^*_{in} - C)}{dt} = \frac{\dot{V}_g H}{RT}(C^*_{in} - C)\left\{1 - \left(1 - F_G\frac{RT}{\dot{V}_g}\right) \times \exp\left[-RT\left(\frac{K_G a^*}{\dot{V}_g}\right)h\right]\right\} \tag{A7}$$

since p_{in} and therefore C^*_{in} is constant. Now, it may be seen that a representation of $\ln(C^*_{in} - C)$ versus t should yield a straight line for an absorption experiment at constant gas flowrate for a given depth of immersion h. If $\alpha = d\ln(C^*_{in} - C)/dt$ for a given h and if experiments are performed for different values of h at the same flowrate $\dot{V}_g$, a plot of $\ln(1 + \alpha V_T RT/\dot{V}_g H)$ against h should again yield a straight line with slope $[-RT(K_G a^*/\dot{V}_g)]$ and intercept

$$\ln\left(\frac{1 - F_G RT}{\dot{V}_g}\right)$$

from which F_G and $K_G a^*$ may be obtained.

SYMBOLS USED

a^* interfacial area of rising bubbles issued from one nozzle, per unit depth of immersion
a^*_e total equivalent surface area of bubbles in the liquid at any instant, per unit depth of immersion
A_b surface area of a bubble
A_e total equivalent surface area of bubbles in the liquid at any instant
C concentration of solute in the bulk of the liquid
C^* concentration of solute at the interface on the liquid side
C^*_{in} solute concentration in liquid that would equilibrate gas at the inlet to absorber
C^{**} concentration of solute at the free surface on the liquid side during the steady state experiments
C^g molar concentration of solute in the gas
C^g_{in} molar concentration of solute in the gas at the inlet to the absorber
C^g_{out} molar concentration of solute in the gas leaving the absorber
C^g_1 molar concentration of solute in the gas upon detachment of bubble from nozzle
C^g_2 molar concentration of solute in the gas bubbles as they reach the free surface
C_{steady} concentration of dissolved oxygen in the bulk of the liquid during steady state experiments
d_e equivalent bubble diameter $[=(6.\bar{V}_0/\pi)^{1/3}]$
D_G diffusivity of solute in the gas
D_L diffusivity of solute in the liquid
e_L liquid side transfer coefficient at the free surface of absorber
E_L mass transfer coefficient for free surface, defined by (3)
f_G gas side transfer coefficient for forming bubbles
f_L liquid side transfer coefficient for forming bubbles
F_G mass transfer coefficient for forming bubbles, based on overall gas driving force; defined by (A1)
F^r_G mass transfer coefficient for forming bubbles, with chemical reaction in the liquid; defined by (7)
F_L mass transfer coefficent for forming bubbles, defined by (1)
g acceleration of gravity
h depth of immersion of bubbling tubes
h^G_{eq} absorption height equivalent to nozzle outlet, with gas phase control
h^L_{eq} absorption height equivalent to nozzle outlet, with liquid phase control
H Henry's law constant in $p = HC^*$
k_G gas side transfer coefficient for rising bubbles
k_L liquid side transfer coefficient for rising bubbles
k_{Le} liquid side transfer coefficient for bubbles based on equivalent area
K_G mass transfer coefficient for rising bubbles based on overall gas driving force
K^r_G mass transfer coefficient for the rising bubbles, with chemical reaction in the liquid; defined by (8)
K_L mass transfer coefficient for rising bubbles defined by (2)
n_f number of moles of solute transferred from a bubble in its formation period
n_A number of moles of NH_4^+ in the absorber after a run
n_1 number of moles of NH_4^+ in first washing bottle after a run
n_2 number of moles of NH_4^+ in second washing bottle after a run
n_3 number of moles of NH_4^+ in third washing bottle after a run
$\dot{n}$ rate (molar) of transfer of solute to the liquid at any time
$\dot{n}_I$ rate (molar) of transfer of solute from forming bubbles to the liquid
$\dot{n}_{II}$ rate (molar) of transfer of solute from rising bubbles to the liquid
$\dot{n}_{III}$ rate (molar) of transfer of solute to the liquid across free surface
p partial pressure of solute in the gas
p^* partial pressure of solute in equilibrium with liquid concentration C
p_1 average partial pressure of solute in gas bubble as it detaches from nozzle
p_{in} partial pressure of solute in gas at inlet to absorber
p_{out} partial pressure of solute in gas at outlet from absorber
p_{steady} partial pressure of oxygen above the liquid in the absorber, during steady state experiments
R gas constant
S total surface area of bubbles rising in the absorber
t time
t_f time of formation of a bubble
$\bar{t}_f$ average (by volume) time of formation of bubbles
T temperature, absolute
v_b velocity of rise of bubbles
V_T total volume of liquid in absorber
$\dot{V}_g$ volumetric gas flowrate
$\bar{V}_0$ average volume of bubbles formed
X fraction of solute retained in absorber
z vertical co-ordinate
α constant or slope
ϕ internal diameter of nozzle

REFERENCES

1. Davidson, J. F. and Schüler, B. O. G., 1960, *Trans I Chem E* 38: 335
2. Calderbank, P. H. Patra, R. P., 1966, *Chem Eng Sci* 21: 719
3. Beek, W. J. and Kramers, H., 1962, *Chem Eng Sci* 16: 909
4. Sherwood, T. K., Pigford, R. L. and Wilke, C. R., 1975, *Mass Transfer*. (McGraw Hill, New York) p. 73
5. Levich, V. G., 1962, *Physicochemical Hydrodynamics* (Prentice Hall, Englewood Cliffs, N.J.)
6. Baird, M. H. I. and Davidson, J. F., 1962, *Chem Eng Sci* 17: 87
7. Davidson, J. F. and Harrison, D., 1963, *Fluidised Particles* (Cambridge University Press) p. 134

ACKNOWLEDGEMENTS

The authors are grateful to Prof J. F. Davidson, F.R.S., for permission to use the filming facilities at the University of Cambridge and to Calouste Gulbenkian Foundation, Lisbon, for financial assistance.

ADDRESSES

Correspondence on this paper should be addressed to Dr J. R. F. Guedes de Carvalho, Centro de Engenharia Quimica, Faculdade de Engenharia, Rua dos Bragas, 4099 Porto Codex, Portugal.

Book Reviews continued from page 302

crystal habit and purity, together with a detailed table on the additives affecting the shape of crystals. The second chapter deals with which mode of crystallisation to adopt for production and the relative advantages/disadvantages of batch or continuous operation. There are short sections on sizing heat exchangers, and incrustation, together with a detailed table on heats of crystallisation. The chapter on types of crystalliser consists mainly of a table listing the different designs, with some comments. The chapter on crystalliser size and performance covers nucleation and growth mechanisms, the influence of seeding and intensity of agitation, mathematical modelling, measurement of supersaturation and scaling up.

The printing and layout is of poor quality, some of the diagrams being unintelligible, and the text needs revising to improve its readability. This book tries to cover similar ground to J. W. Mullin's classical work, regretably it rarely approaches A. W. Bamforth's correctly entitled book on 'Industrial Crystallisation'.

A. Scrutton

Mixing in Continuous Flow Systems
E. B. Nauman and B. A. Buffham
John Wiley and Sons, 1983
xxvi + 271 pp, Price not stated

The aim of this book is to provide an introduction to the continuous flow mixing phenomena important in the design of chemical reactors. This is not to imply however that the book is narrowly directed solely to the subject of chemical reactors, since it deals with broad underlying principles and refers to a number of other applications such as chromatography and laminar flow in extruders.

The book is divided into two parts. The first, which occupies 80% of the whole, is described as "Mixing in Time", i.e. mixing between molecules or particles that have remained in a flow system for different lengths of time. The first chapter is concerned with Residence Time Distributions, covering their mathematical properties, measurements techniques and data analysis. The second chapter deals with various models for Residence Time Distributions including tank flow and laminar flow models while the third is devoted to dispersion models, with proper attention to the boundary conditions as might be expected. Together these three chapters occupy half the book. The remainder of Part One deals with chemical reactions and micromixing and extensions of residence time theory to systems other than the basic isothermal homogeneous steady state case.

Part Two of the book is described as "Mixing in Space" and examines more closely the detailed mixing processes that actually occur inside a reactor. Firstly various measures of mixedness are discussed, essentially in the context of batch processes. Subsequently these are applied to continuous flow processes and the book ends with a short chapter on the problem of scaling-up processes in such a way that the desired mixing characteristics are attained.

Altogether this is a very interesting and intellectually stimulating book. Mixing is a subject which requires great clarity of thought and precision of argument, as anyone who has attempted to teach it will recognise. The authors have not only achieved the degree of clarity demanded by their subject but have produced a book which is a pleasure to read as well. The pleasure is enhanced by the high quality of printing and presentation of the publishers. As they say in the Preface, the authors themselves enjoyed writing the book and possibly it is that enjoyment which comes across in the text.

Another possible reason for the book being easy to read is that the mathematics used is pitched at the level of a first degree in chemical engineering. This and the sets of problems included at the end of each chapter will encourage its use as a postgraduate course text in an area where good books are scarce. No doubt time and its use as a student text will show up a few shortcomings. One is that the concept of a "mixing cup" concentration average appears to have fallen somewhere between the responsibilities of the two authors; it is mentioned only briefly on page 31, again on page 114 and not at all in the index. Also the problems tend to stress amplification of the theory rather than practical handling of numerical data. Nevertheless this book is very welcome as an authoritative account of a branch of chemical engineering science which is important not only in its practical applications, but in a deeper philosophical sense as well.

J. C. Lee

Book Reviews continued on page 320

VOL. 62 1984

FIXED BED SORPTION WITH RECYCLE
Part I: Mathematical Model and Single Reversible Reactions

By J. T. CASEY and A. I. LIAPIS

University of Missouri-Rolla, Department of Chemical Engineering, Rolla, Missouri, USA

A mathematical model that describes single and multicomponent recycle sorption systems is presented. The model accounts for the generation of the adsorbed species by chemical reactions occurring in a single perfectly mixed tank, in the bulk fluid of the sorbent bed, and in the fluid in the pores of the adsorbent particles. Results are presented for zeroth, first, and second order reversible reactions which occur only in the perfectly mixed reactor of the recycle sorption system, and show some of the unique and interesting features of the fixed bed sorption with recycle processes. The recycle systems are found to be more efficient in producing much larger quantities of the reaction product than those obtained in a batch reactor for first and second-order reversible reactions with low equilibrium constants. Both single component linear and non-linear equilibrium adsorption isotherms are considered.

INTRODUCTION

The modeiling of the operation of packed-bed adsorption columns is of importance in the understanding and design of separation and purification systems[1-3], catalytic fixed-bed reactors[4,5], ion exchange columns[6,7], artificial kidney systems[8,9], and more recently haemoperfusion cartridges[10-12]. Essentially, the process involves the removal of one or more species from a fluid containing various species passing through the particle bed at a certain volumetric flow rate.

There are several types of processing operations in which a stream is taken from a source, fed to a sorption bed, and then recycled back to the source[9,13,14]. A schematic representation of the system is shown in Figure 1, where a sorbent bed is being used to remove a desired product B from a reacting mixture. Unreacted component A is recycled back to the reactor. Besides recovering product, the sorbent bed ensures that the reaction mixture remains low in B and thus, if the reaction is reversible, the reverse reaction is suppressed and nearly complete conversion of A is obtained. It should be noted that more than one species may be adsorbed, if so desired, by using appropriate adsorbents in systems involving multiple reactions.

In recycle sorption processes, the economic point for bed replacement is often not the point at which breakthrough of the adsorbed species is observed[15]. It may well be the time when more solute is leaving the bed than is entering. In any case, in order to establish the time that the sorber should be taken off stream, it is important to know the dynamic behaviour of the various variables in the recycle system. Also, the dynamic behaviour of a recycle system is required if its performance is to be compared with that of other alternative systems involving reaction and separation units. The most general approach to solving such problems, especially those involving non-linear isotherms, is via numerical integration of the pertinent differential equations.

The behavior of sorption systems with recycle has not been studied extensively, and because there are features about such systems[9-15] which are unique and interesting, the present work develops a mathematical model for recycle sorption processes and results are presented for the case of single reaction product recovering systems involving zeroth, first, and second-order reversible reactions and linear and non-linear equilibrium adsorption isotherms.

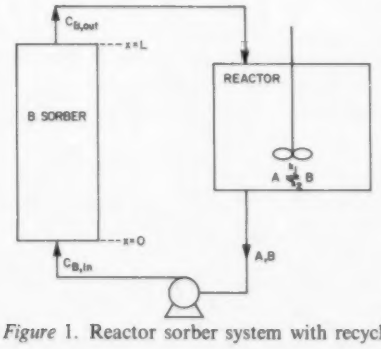


Figure 1. Reactor sorber system with recycle.

MATHEMATICAL MODEL

The model describes the adsorption of solutes from a flowing liquid stream onto a fixed bed of particles, and the generation of solutes in the source (chemical reactor), in the bulk fluid of the bed, and in the fluid in the pores under isothermal operation. The mass transfer effects included in the model are intraparticle diffusion, surface film diffusion and axial dispersion. The essential assumptions are constant coefficients of dispersion and diffusion, constant porosities, no radial gradients in the bed, dilute solutions[16] and that the spherical adsorbent particles have uniform size and homogeneous structure. The intraparticle diffusion is assumed to take place in the liquid within the pores of the particle. The pore diffusional resistance for concentrated solutions as well as the solid diffusional resistance for both types of solutions is discussed in the work of Liapis and Rippin[17]. It is also assumed that local equilibrium exists between solid and fluid phases at each point in the pore, since the

© Institution of Chemical Engineers

process of adsorption onto the surface is rarely rate limiting[18,19].

It is considered that there are n components in the reactor and $m < n$ solutes are adsorbed in the bed[9,13].

A differential material balance for each component in the flowing fluid stream and within the porous adsorbent of the sorption bed provides the following expressions:

$$\frac{\partial C_{di}}{\partial t} - D_{Li}\frac{\partial^2 C_{di}}{\partial x^2} + \frac{V_f}{\varepsilon}\frac{\partial C_{di}}{\partial x} = \frac{1-\varepsilon}{\varepsilon}\frac{3}{r_0}K_{fi}(C_{pi}\mid_{r=r_0} - C_{di}) + R_{di}, \quad i = 1, 2, \ldots, n \tag{1}$$

$$\varepsilon_p\frac{\partial C_{pi}}{\partial t} + \delta\frac{\partial C_{si}}{\partial t} = \varepsilon_p\frac{1}{r^2}\frac{\partial}{\partial r}\left(r^2 D_{pi}\frac{\partial C_{pi}}{\partial r}\right) + R_{pi}, \quad i = 1, 2, \ldots, n \tag{2}$$

where R_{di} and R_{pi} denote the rate of generation of species i (sometimes zero) in the flowing fluid phase and in the fluid in the pores, respectively; also $\delta = 1$ for the case that species i is adsorbed, and $\delta = 0$ when species i is not adsorbed on the surfaces of the adsorbent particles.

The residence time of the fluid in the circuit external to the reactor is usually short enough[9,11,13] to permit one to assume that no reaction takes place in the bulk stream of the bed, thus, implying $R_{di} = 0$. Also, in most systems[5,9,11,13] only the adsorbed species enter into the pores of the adsorbent particles, and in many cases their residence times before adsorption are fairly short so that $R_{pi} \cong 0$.

The condition of local equilibrium between solid and fluid phases at each point in the pore gives

$$\frac{\partial C_{si}}{\partial t} = \sum_{j=1}^{m}\left(\frac{\partial f_i}{\partial C_{pj}}\frac{\partial C_{pj}}{\partial t}\right), \quad i = 1, 2, \ldots, m \tag{3}$$

since

$$C_{si} = f_i(C_{p1}, C_{p2}, \ldots, C_{pm}), \quad i = 1, 2, \ldots, m \tag{4}$$

The functions f_i represent the equilibrium adsorption isotherms for which the functional forms given by Liapis and Rippin[17] will be used.

For the source (chemical reactor) one would have, assuming it were a single perfectly mixed tank

$$\frac{dC_{i,in}}{dt} = \frac{Q}{V}(C_{i,out} - C_{i,in}) + R_i, \quad i = 1, 2, \ldots, n \tag{5}$$

where R_i is the rate of generation of species i (sometimes zero). Note that the subscripts in and out refer (Figure 1) to the bed inlet and outlet concentrations, not to the chemical reactor inlet and outlet concentrations.

The initial and boundary conditions of equations (1), (2) and (5) are as follows, when the sorbent bed is clean at $t = 0$,

$$C_{di} = C_{pi} = C_{si} = 0 \text{ for } 0 \le x \le L \text{ and } 0 \le r \le r_0 \text{ at } t = 0, i = 1, 2, \ldots, n \tag{6}$$

$$C_{i,in} = C_i^0 \text{ at } t = 0, i = 1, 2, \ldots, n \tag{7}$$

$$\frac{V_f}{\varepsilon}C_{di} - D_{Li}\frac{\partial C_{di}}{\partial x} = \frac{V_f}{\varepsilon}C_{i,in} \text{ at } x = 0, t > 0, i = 1, 2, \ldots, n \tag{8}$$

$$\frac{\partial C_{di}}{\partial x} = 0 \text{ at } x = L, t > 0, i = 1, 2, \ldots, n \tag{9}$$

$$\varepsilon_p D_{pi}\frac{\partial C_{pi}}{\partial r} = K_{fi}(C_{di} - C_{pi}\mid_{r=r_0}) \text{ at } r = r_0, t > 0, i = 1, 2, \ldots, n \tag{10}$$

$$\frac{\partial C_{pi}}{\partial r} = 0 \text{ at } r = 0, t > 0, i = 1, 2, \ldots, n \tag{11}$$

The above model equations can be solved using orthogonal collocation[1,20]. Casey[21] has found that the orthogonal polynomials $P_8^{(1,1)}(x')$, $x' = x/L$, and $P_6^{(1,1)}(r')$, $r' = (r/r_0)^2$, proved to be sufficient to obtain accurate predictions of solute concentrations as compared to the higher approximation. The method of orthogonal collocation was applied to equations (1) and (2) to obtain a set of non-linear coupled ordinary differential equations[21] which were integrated together with equation (5) using Michelsen's[22] implicit third order Runge–Kutta method.

In the next section, results for the recycle sorption process shown in Figure 1 are presented for the case of a single reaction product recovery system involving zeroth, first, and second-order reversible reactions which occur only in the reactor of the system; this implies that R_{di} and R_{pi} are taken to be equal to zero in equations (1) and (2).

The equilibrium isotherm for species B is given by the following expression

$$C_{sB} = \alpha C_{pB}^{\beta} \tag{12}$$

which is known as the Freundlich isotherm[17].

RESULTS AND DISCUSSION

The values of the parameters used in order to obtain the results presented in the following paragraphs are given in Table 1 and in the following figures. It should also be noted that in the results presented for first and second-order reversible reactions, the volumes of the batch reactor and of the reactor in the recycle system are taken to be equal. In Figures 2–4, total bed solute content means the amount of B in the adsorbent particles of the sorption bed plus the amount of B which is in the flowing fluid stream of the sorber.

For single component adsorption with a linear isotherm and a zeroth-order reaction in the reactor of the system shown in Figure 1, previous investigators[10,12,14,15] have provided qualitative and quantitative results on the characteristics and practical implications of the fixed bed sorption with recycle system involving rather low production rates of species B. In Figure 2, the variations of bed inlet and outlet concentrations and total bed solute content with time are shown for a system involving a non-linear isotherm and a zeroth-order reaction. The results show that the concentration $C_{B,in}$ reaches its minimum value at a time before breakthrough occurs

Table 1. Parameter values for the recycle sorption system of Figure 1

$D_{LA} = D_{LB} = 4.0 \times 10^{-6}$, $r_0 = 5.0 \times 10^{-4}$,
$D_{pB} = 7.40 \times 10^{-10}$,
$K_{fB} = 2.12 \times 10^{-5}$, $\varepsilon = 0.45$, $\varepsilon_p = 0.94$,
$V = 5.0 \times 10^{-3}$, $Q = 1.0 \times 10^{-6}$, $r_b = 0.03$,
$L = 0.5$, $V_f = 0.35 \times 10^{-3}$.

VOL. 62 1984

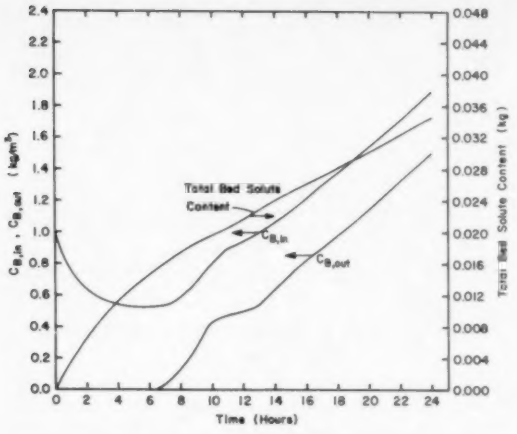


Figure 2. Variation of bed inlet and outlet concentrations and total bed solute content with time in a zeroth-order reaction product recovery system; $\alpha = 33.52$, $\beta = 0.5$, $R_B = 1.04 \times 10^{-4}\,kg\,m^{-3}\,s^{-1}$, $C_B^0 = 1.0\,kg\,m^{-3}$.

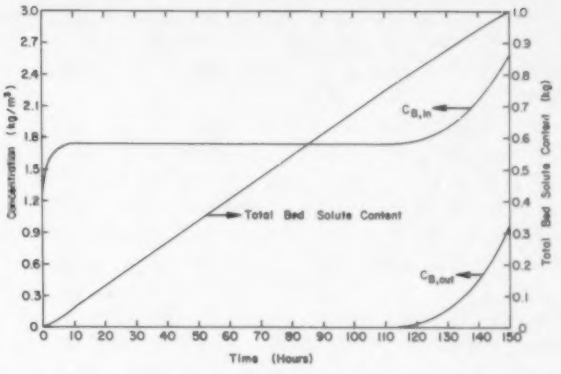


Figure 4. Variation of bed inlet and outlet concentrations and total bed solute content with time in zeroth-order reaction product recovery system; $\alpha = 948.68$, $\beta = 0.5$, $R_B = 3.47 \times 10^{-4}\,kg\,m^{-3}\,s^{-1}$, $C_B^0 = 1.0\,kg\,m^{-3}$.

while in the systems involving linear isotherms with zeroth-order reactions, it has been found[10,15,21] that the minimum value of $C_{B,in}$ occurs after the breakthrough time. For fairly large values of R_B, the results in Figures 3 and 4 show that for linear and non-linear isotherms the concentration $C_{B,in}$ increases with time in a continuous manner and changes slope at a time before breakthrough occurs. In systems with a small production rate R_B, the recycle of fluid free of species B from the bed outlet to the reactor is such that it causes the concentration of component B in the reactor to decrease. This occurs because the rate of dilution of species B in the reactor by the effluent from the sorber, is greater than the rate of production R_B. For relatively large values of R_B, the rate of production of B in the reactor is large enough to overcome the dilution occurring by recycle of the component-B-free effluent of the sorber. In Figures 3 and 4, it is clearly shown that the sorbent with the non-linear isotherm not only removes considerably larger amounts of product B, but also increases substantially the time for which the slope of $C_{B,in}$ is zero, and the value of $C_{B,in}$ for that time interval is considerably lower than that of the system with a linear isotherm.

In a recycle sorption system involving a zeroth-order reaction, the dynamic behaviour of the variables as shown in Figures 2–4 has to be known in detail before proper economic considerations could be established that would allow the selection of a criterion for bed removal. A set of possible criteria for bed removal is given by Cooney and Shieh[15].

In Figures 5–9 results are shown for recycle sorption systems involving first and second-order reversible reactions, and sorbents with linear and non-linear isotherms. The equilibrium constants of these reactions are taken to be less than or equal to unity, implying that low concentrations of product B may significantly inhibit the forward reaction. A recycle sorption system that would remove only product B in a continuous manner can ensure that the reaction mixture remains low in B and thus the reverse reaction is suppressed and nearly complete conversion of A may be obtained. In Figure 5, one can see that the recycle systems can produce about 60–84% more product B than the maximum amount of B that could be obtained if the first-order reversible reaction occurred in a batch reactor. It is also clear that

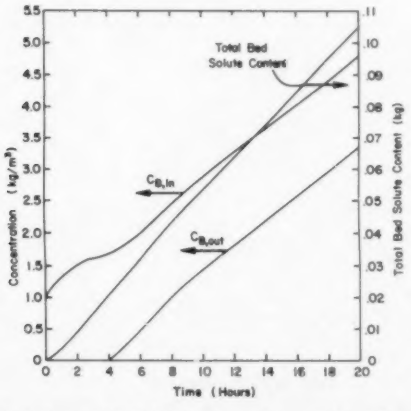


Figure 3. Variations of bed inlet and outlet concentrations and total bed solute content with time in a zeroth-order reaction product recovery system; $\alpha = 30.00$, $\beta = 1.0$, $R_B = 3.47 \times 10^{-4}\,kg\,m^{-3}\,s^{-1}$, $C_B^0 = 1.0\,kg\,m^{-3}$.

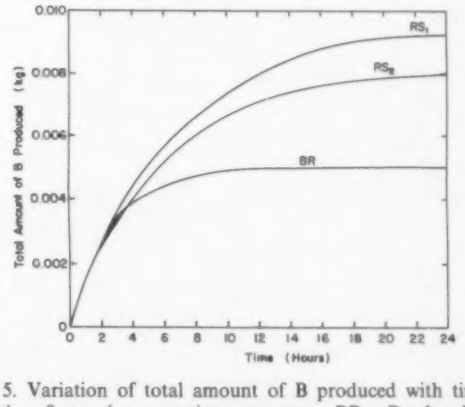


Figure 5. Variation of total amount of B produced with time in a reversible first-order reaction system. BR ≡ Batch Reactor. RS_1 ≡ Recycle System with $\alpha = 33.52$, $\beta = 0.5$. RS_2 ≡ Recycle System with $\alpha = 30.00$, $\beta = 1.0$. $k_1 = k_2 = 5.0 \times 10^{-5}\,s^{-1}$. $C_A^0 = 2.0\,kg\,m^{-3}$. $C_B^0 = 1.0 \times 10^{-4}\,kg\,m^{-3}$.

the non-linear isotherm allows the sorbent bed to remove B with a higher rate than the bed with the linear isotherm, and thus resulting in a higher production rate of B.

For operational times of less than 3 h, the recycle and the batch systems do not show significant differences in the amounts of B produced. In fact, within that time interval, the batch system has produced an amount of B slightly higher than the recycle system with the linear isotherm. These initial differences in the production of B between the recycle systems and the batch reactor, Figures 5, 7 and 8, occur because the volumes of the reactor in the recycle system and of the batch reactor are taken to be equal and also $R_{di} = R_{pi} = 0$. This implies that a volume of an inert fluid equal to the volume of fluid held in the sorber is added to the recycle system. Thus, for an initial, short time period, $C_{A,in}$ and the total amount of A in the reactor of the recycle system are smaller than those in the batch reactor. But this short time interval is not of practical importance in reversible reactions with low equilibrium constants.

Another aspect that one should consider is the separation that has already occurred in the product B at any given time through the use of the recycle system, while in the batch reactor when the concentration of B is close to its equilibrium value then one connects the reaction mixture to a separation unit in order to remove B. This additional time required for separation of B should be added to the batch reactor cycle time.

In the recycle system a certain part of the total amount of product B is in the sorber, Figure 6, and the rest is in the perfectly mixed tank. In all cases studied by Casey[21], it has been found that, with the exception of a short initial time of operation, the amount of B in the sorber is many times larger than that in the reactor. Thus, depending on the type of sorber that is used, one would have to remove very little, if any, of the product B from the reaction mixture at the end of operation of a recycle system. The dynamic behavior of the concentrations $C_{B,in}$ and $C_{B,out}$ shown in Figure 6, has been found[21] to be typical of recycle systems involving first and second-order reversible reactions with low equilibrium constants.

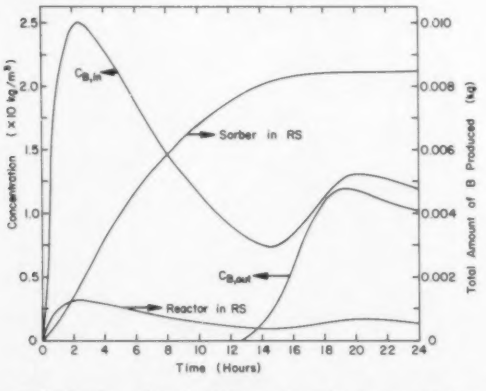


Figure 6. Variation of bed inlet and outlet concentrations, and amounts of B in the sorber and reactor of the recycle system with time for a reversible first-order reaction; $\alpha = 33.52$, $\beta = 0.5$, $k_1 = k_2 = 5.0 \times 10^{-5}\,s^{-1}$, $C_A^0 = 2.0\,kg\,m^{-3}$, $C_B^0 = 1.0 \times 10^{-4}\,kg\,m^{-3}$.

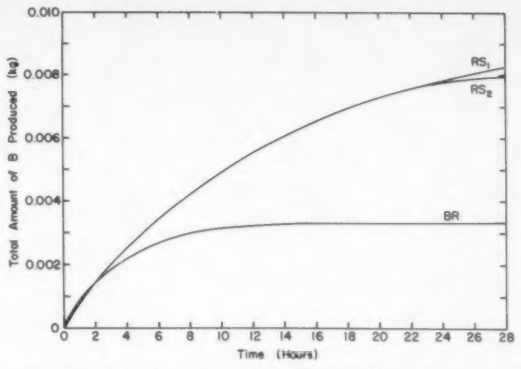


Figure 7. Variation of total amount of B produced with time in a reversible first-order reaction system. BR ≡ Batch Reactor. RS_1 ≡ Recycle System with $\alpha = 948.68$, $\beta = 0.5$. RS_2 ≡ Recycle System with $\alpha = 33.52$, $\beta = 0.5$. $k_1 = 2.5 \times 10^{-5}\,s^{-1}$. $k_2 = 5.0 \times 10^{-5}\,s^{-1}$. $C_A^0 = 2.0\,kg\,m^{-3}$. $C_B^0 = 1.0 \times 10^{-4}\,kg\,m^{-3}$.

In Figure 7, the results show the effect of the parameter α of the isotherm on the total amount of product B produced by a first-order reversible reaction with an equilibrium constant of 0.5. It is seen that for this particular system the value of α has some effect during the final stages of operation. Also, the recycle systems produce more than *two times* the amount of B that would be produced in a batch reactor.

The results shown in Figure 8 are for a second-order reversible reaction with $k_1/k_2 = 1.0$, and for three different sets of values of α and β. It is observed that the recycle systems produce about 40–60% more product B than the maximum amount of B that could be obtained if this second-order reversible reaction occurred in a batch reactor. It is also evident that the recycle system with the non-linear isotherms is more effective than that with the linear isotherm. The effect of the value of α can be seen by comparing the curves of RS_1 and RS_2 in Figure 8. The higher value of α in RS_1 causes that recycle system to produce about 2.0% more of product B than the recycle system RS_2 for a time of operation of 30 h. If the operation was extended to infinite time, then system RS_1 would produce 9.5% more of product B than the RS_2 system whose production of B at infinite time would amount to 9.12×10^{-3} kg.

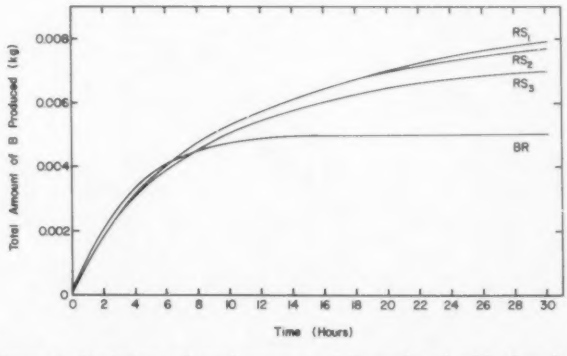


Figure 8. Variation of total amount of B produced with time in a reversible second-order reaction system. BR ≡ Batch Reactor. RS_1 ≡ Recycle System with $\alpha = 948.68$, $\beta = 0.5$. RS_2 ≡ Recycle System with $\alpha = 33.52$, $\beta = 0.5$. RS_3 ≡ Recycle System with $\alpha = 30.00$, $\beta = 1.0$. $k_1 = k_2 = 2.0 \times 10^{-5}\,m^3\,kg^{-1}\,s^{-1}$. $C_A^0 = 2.0\,kg\,m^{-3}$. $C_B^0 = 1.0 \times 10^{-4}\,kg\,m^{-3}$.

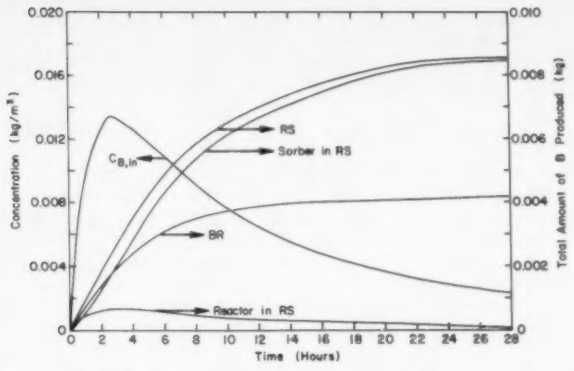


Figure 9. Variation of bed inlet and amounts of B with time for a reversible second-order reaction. BR ≡ Batch Reactor. RS ≡ Recycle System with $\alpha = 948.68$, $\beta = 0.5$. $k_1 = 1.25 \times 10^{-5}\,m^3\,kg^{-1}\,s^{-1}$. $k_2 = 2.50 \times 10^{-5}\,m^3\,kg^{-1}\,s^{-1}$. $C_A^0 = 2.0\,kg\,m^{-3}$. $C_B^0 = 1.0 \times 10^{-4}\,kg\,m^{-3}$.

In Figure 9, the dynamic behaviour of a recycle system is shown in which a second-order reaction occurs with an equilibrium constant of 0.5. The recycle system produces more than *two times* the amount of B produced by a batch reactor for an operational time of 28 h. If an infinite time of operation is considered, then the recycle system would produce 2.41 times more B than the batch reactor whose production of B would be 4.14×10^{-3} kg. At the end of 28 h of operation, the amount of B in the sorber is about 103 times larger than that in the reactor of the recycle system. For infinite time of operation, the amount of B in the sorber is about 9600 times larger than that in the reactor of the recycle system which contains 1.04×10^{-6} kg of species B. Finally, in Figure 9, it is apparent that $C_{B,out}$ is zero since the sorber has a substantial capacity to remove B from its inlet stream.

Numerous simulations involving small changes in the values of K_{fB} and D_{pB}, have shown[21] that the dynamic behaviour of recycle systems is much more sensitive to variations of the effective pore diffusivity than to variations of the film mass transfer coefficient.

CONCLUSIONS AND REMARKS

A mathematical model for single and multicomponent recycle sorption systems has been presented, accounting for the generation of the adsorbates by chemical reactions in a perfectly mixed flow reactor as well as in the bulk fluid of the sorbent bed and in the fluid of the porous structure of the adsorbent particles.

Results were presented for the case of a single reaction product recovery system, involving zeroth, first, and second-order reversible reactions which occur only in the reactor of the recycle system. The dynamic behaviour of the recycle system with a zeroth-order reaction has provided us with some interesting features for the case of a non-linear isotherm as well as for the cases involving linear and non-linear isotherms with large production rates. These types of dynamic behaviour had not been reported in the literature before, and their knowledge is necessary in order to establish proper economic considerations that would allow the selection of a criterion for bed removal.

Recycle systems involving first-order reversible reactions with low equilibrium constants can produce 60% to more than 200% more product B than the maximum amount of B that could be obtained if the reactions occurred in a batch reactor. When second-order reactions with low equilibrium constants are involved, the recycle systems were found to produce 40% to more than 200% more product B than the maximum amount of B that could be obtained if the reactions occurred in a batch reactor. The effectiveness of a recycle system is higher for reactions with equilibrium constants less than unity, and sorbents with non-linear isotherms. The dynamic behavior of the recycle systems involving first and second-order reactions must be known in order to determine the optimum design and operation of such systems.

It was also shown that with the exception of a short initial time of operation, the amount of B in the sorber is many times higher than that in the reactor of the recycle system.

In Part II of this work, results are to be presented involving multicomponent competitive adsorption in recycle systems involving multiple reactions.

SYMBOLS USED

C_{di}	concentration of solute i in fluid phase of the bed ($kg\,m^{-3}$)
C_i^0	concentration of solute i in the reactor at $t = 0$ ($kg\,m^{-3}$)
$C_{i,in}$	concentration of solute i in the reactor ($kg\,m^{-3}$)
$C_{i,out}$	inlet concentration of solute i in the reactor ($kg\,m^{-3}$)
C_{pi}	concentration of solute i in pore fluid phase ($kg\,m^{-3}$)
C_{si}	concentration of solute i in solid phase (per unit volume of particles) ($kg\,m^{-3}$)
D_{Li}	axial diffusivity of solute i ($m^2\,s^{-1}$)
D_{pi}	effective diffusivity of solute i in pore fluid ($m^2\,s^{-1}$)
f_i	equilibrium function of solute i
K_{fi}	film mass transfer coefficient of solute i ($m\,s^{-1}$)
k_1	rate constant of the forward reaction
k_2	rate constant of the reverse reaction
L	length of sorber (m)
m	number of sorbed species
n	number of solutes
Q	recycle flow rate ($m^3\,s^{-1}$)
R_{di}	generation rate of solute i in fluid phase of the bed ($kg\,m^{-3}\,s^{-1}$)
R_i	generation rate of solute i in the reactor ($kg\,m^{-3}\,s^{-1}$)
R_{pi}	generation rate of solute i in pore fluid phase ($kg\,m^{-3}\,s^{-1}$)
r	radial distance in particle (m)
r_b	radius of sorber (m)
r_0	radius of particle (m)
r'	dimensionless radius
t	time (s)
t_{bB}	breakthrough time of species B (s)
V	volume of reactor (m^3)
V_f	superficial fluid velocity ($m\,s^{-1}$)
x	bed length coordinate (m)
x'	dimensionless bed length coordinate
Greek letters	
α	constant in equation (12)
β	constant in equation (12)
δ	0 for non-adsorbed species i 1 for adsorbed species i
ε	void fraction in the bed
ε_p	void fraction in particles
Subscripts	
B	species B
i	integer
j	integer
p	pore
s	solid

REFERENCES

1. Liapis, A. I. and Rippin, D. W. T., 1979, *AIChE J*, 25: 455-460.
2. Balzli, M. W., Liapis, A. I. and Rippin, D. W. T., 1978, *Trans I Chem E*, 56: 145–156.
3. Liapis, A. I. and Crosser, O. K., 1982, *Chem Eng Sci* 37: 958–961.
4. Hlavacek, V., 1970, *Ind Eng Chem* 62: 8–26.
5. Froment, G. F. and Bischoff, K. B., 1979, *Chemical Reactor Analysis and Design* (John Wiley & Sons, New York, USA).
6. Brauch, V. and Schlünder, E. U., 1975, *Chem Eng Sci*, 30: 539–548.
7. Holl, W. and Sontheimer, H., 1977, *Chem Eng Sci*, 32: 755–762.
8. Cooney, D. O., 1971, *J Biomed Materials Res*, 5: 407–410.
9. Dorson, W. J., Jr., Pizziconi, V. B., Voorhees, M. E., Calkins, J. M., Christianson, H. B., Cotter, D. J., Fargotstein, R., Markovitz, M., Monty, D. E. Jr. and Tomisaka, D. M., 1973, *Trans Am Soc Artificial Internal Organs*, 19: 109–146.
10. Skalsky, M., 1978, *PhD Thesis* (Department of Chemical Engineering, University of New South Wales, Australia).
11. Shettigar, U. R. and Deepak, D., 1977, *Med Biol Eng Computing*, 15: 589–597.
12. Mor, L., Mor, L. A., Sideman, S. and Brandes, J. M., 1980, *Chem Eng Sci*, 35: 725–736.
13. Lapidus, L. and Amundson, N. R., 1977, *Chemical Reactor Theory* (Prentice–Hall, New Jersey, USA).
14. Chang, F. H. I., Tan, K. S. and Spinner, I. H., 1973, *AIChE J*, 19: 188–191.
15. Cooney, D. O. and Shieh, D. F., 1972, *AIChE J*, 18: 245–247.
16. Liapis, A. I. and Litchfield, R. J., 1981, *Trans I Chem E*, 59: 122–124.
17. Liapis, A. I. and Rippin, D. W. T., 1977, *Chem Eng Sci*, 32: 619–627.
18. Santacesaria, E., Morbidelli, M., Danise, P., Mercenari, M. and Carra, S., 1982, *Ind Eng Chem, Proc Des Dev*, 21: 440–445.
19. Johansson, R. and Neretnieks, I., 1980, *Chem Eng Sci* 35: 979–986.
20. Villadsen, J. and Michelsen, M. L., 1978, *Solution of Differential Equation Models by Polynomial Approximation* (Prentice–Hall, New Jersey, USA).
21. Casey, J. T., 1984, *PhD Thesis* (Department of Chemical Engineering, University of Missouri, Rolla, USA).
22. Michelsen, M. L., 1976, *AIChE J*, 22: 594–597.

ADDRESS

Correspondence on this paper should be addressed to Professor A. I. Liapis, Department of Chemical Engineering, University of Missouri-Rolla, 143 Schrenk Hall, Rolla, Missouri 65401, U.S.A.

The manuscript was received 25 *August* 1982 *and accepted for publication after revision* 11 *May* 1984.

VOL. 62 1984

Book Reviews continued from page 314

Foundations of Boundary Layer Theory for Momentum Heat and Mass Transfer
J. E. Schetz
Prentice Hall, 1984
219 pp, £36.05

This book on boundary layers is written "for the benefit of advanced undergraduaters or beginning graduate students" who are presumably taking courses in aerodynamics. The treatment assumes no previous knowledge of boundary layer theory and the presentation is straight-forward and clear. The author, however, makes no attempt to cover the more complicated aspect of boundary layer theory such as the statistical theories of turbulence, turbulent length scales and correlation functions and the mathematics is kept simple by, for example, avoiding tensorial notation. This makes the book suitable for the average Chemical Engineer who wishes to learn the basic fluid mechanics of boundary layer theory and thereby equip himself to read more advanced texts.

In the first four chapters, the author considers flow in laminar boundary layers by starting with the derivation of the viscous flow equations and progressing via the momentum balance solution of the boundary layer equations. All this is of considerable general interest and his comments on numerical methods are well worth reading even by those not concerned with boundary layers. Chapter 5, on compressible and high speed boundary layers, is more specialised and will be of little interest to the average Chemical Engineer. The phenomenon of laminar/turbulent transition is well explained in Chapter 6 and the early parts of Chapter 7 give a valuable account of turbulent flow in both boundary layers and pipe flow. The latter parts of Chaper 7 are rather specialised but Chapter 8 gives a good account of jets and wakes.

I found Chapter 9, on heat and mass tranfer, rather disappointing and indeed throughout the book the treatment of velocity and shear stress distributions is far better than the treatment of heat and especially mass transfer. Both these topics are dealt with briefly at the end of each section and are often expressed in terms which appear strange to the Chemical Engineer. Thus the Sherwood number is referred to as the Nusselt number for diffusion and Fick's law is expressed in terms of mass fractions. This would make it difficult to extend the results of this book to cases of rich mixtures or reacting systems. Whilst the heat transfer sections give some results of use to Chemical Engineers, the author seems to think that the only mass transfer process of interest is the injection of a foreign fluid through a porous wall. There is no mention of volatile surfaces, gas absorption at an interface or of mass transfer to a catalyst surface.

Thus while the average Chemical Engineer will find this book to be a clear and interesting account of the basic fluid mechanics of boundary layers theory, he will find that it does not address itself sufficiently to his main interest, the prediction of the heat and mass transfer rates.

R. M. Nedderman

CLEAR LIQUID HEIGHT ON SIEVE AND VALVE TRAYS

By H. DHULESIA

Department of Chemical Engineering, University of Manchester Institute of Science and Technology

The clear liquid height on sieve and valve trays of a large hydraulic simulation column operating at commercial gas and liquid loadings has been measured. Experimental work shows that a single correlation of clear liquid height cannot be used to span both froth and spray regimes. Hothuis and Zuiderweg's correlation of clear liquid height on a sieve tray has been modified for the froth regime using the present experimental results. A correlation for clear liquid height on a Glitsch V1 valve tray has also been developed.

INTRODUCTION

The determination of clear liquid height on a distillation tray is useful to predict its performance. Clear liquid height is defined as liquid hold-up per unit of vapour bubbling area of tray. Clear liquid height is an essential input in predicting the operating flow regime, the rate of entrainment, the rate of local mass transfer etc. In the literature, considerable experimental data of clear liquid height on sieve trays, covering a wide range of operating conditions and tray geometries, are available, but most of the data have been taken from small scale simulation columns. Data for valve trays[1-3] are scarce in the literature.

The clear liquid height data of Todd and Van Winkle[1] and Picqueur and Verhoeye[2] are under question because they did not mention how the clear liquid height was measured. Moreover, the data of Todd and Van Winkle were for rectangular valves which are generally not used in practice.

Weiss and Langer[3] calculated the clear liquid height on a valve tray by integrating the vertical dispersion density profile measured by the Gamma ray absorption technique. But they reported clear liquid height only for low liquid flow rates i.e. 0.6 to 6.1 $m^3 h^{-1} m^{-1}$.

It seems obvious that clear liquid height on sieve and valve trays of a large simulation column needs to be measured for commercial liquid and gas loadings in order to develop generalised correlations. This is the subject of the present work.

HYDRAULIC SIMULATION COLUMN

Many academic institutes and private organisations have distillation and absorption simulators, but most of them are either of small scale or equipped with a single tray. A large hydraulic simulation column, occupying four floors in the pilot plant of UMIST, was commissioned in order to study the hydrodynamics of sieve and valve trays at high liquid and gas loadings. The simplified diagram of the simulation column is shown in Figure 1. The principal characteristics of this hydraulic simulation column are as follows:

(*a*) The column has a nominal cross section of 1.2 m × 0.63 m and is equipped with multi-trays. The tray spacing can be changed at intervals of 100 mm.

(*b*) Liquid and gas are circulated in closed loops, hence it is possible to use various systems in the column.

(*c*) As the column is made of stainless steel, corrosive systems can be used.

(*d*) The column is equipped with four windows of laminated glass of size 1.2 m × 1.2 m, two on each side of the column, which enable good visual observation of the two phase mixtures on the trays.

During the present experimental work, the simulation column contained three sieve trays and a valve tray. The top three trays were sieve trays and the bottom tray was a valve tray. The characteristics of the sieve and valve trays are given in Table 1. The inlet weir of 12 mm was

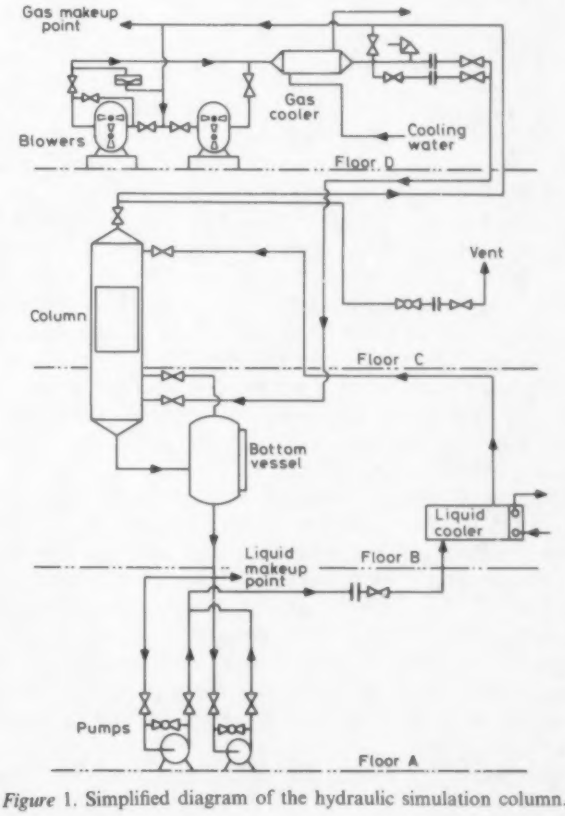


Figure 1. Simplified diagram of the hydraulic simulation column.

© Institution of Chemical Engineers

Table 1. Characteristics of sieve and valve trays

Sieve Tray	A	B	C
Hole diameter	3.17 mm	6.35 mm	12.7 mm
Triangular pitch	10 mm	20 mm	40 mm
No. of holes	5280	1292	328
Hole area	0.0418 m^2	0.0409 m^2	0.0415 m^2
% free area	10.2	10.2	10.2
Material	St. Steel	St. Steel	St. Steel
Thickness	3 mm	3 mm	3 mm
Weir length	0.63 m	0.63 m	0.63 m
Distance between two downcomers	0.887 m	0.887 m	0.887 m

Valve Tray

Tray:	Material—Stainless Steel
	Thickness—3 mm
	Valve hole diameter—48 mm
	Weir length—0.63 m
	Distance between two downcomers—0.887 m
	Triangular pitch—76.2 mm
Valve:	Type—Glitsch Ballast valve V1
	Gauge—12
	Leg length—15.87 mm
	Material—Stainless Steel
	Valve diameter—38 mm
	Weight of valve—27.0 g

used for the valve tray to prevent the excessive weeping at the inlet of the tray especially at a high liquid loading. Three exit weirs of 25, 50 and 75 mm were used for the valve tray. For the sieve trays, no inlet weir was used in keeping with commercial practice and an exit weir of 50 mm was used. The tray spacing was 700 mm. At the gas inlet of the column, the turning vanes were fixed and adjusted to obtain a uniform air distribution below the valve tray. Moreover, two gas distributor grids were installed between the valve tray and the turning vanes to ensure a uniform air distribution. More details of the simulation column are given elsewhere[4].

EXPERIMENTAL

As mentioned earlier, the basic objective of commissioning the hydraulic simulation column was to study the hydrodynamics of sieve and valve trays operating at high liquid and gas loadings. The initial intention was to measure hydraulic gradient, but while doing experiments a significant hydraulic jump at the liquid inlet to the tray was observed. Consequently, it was not possible to detect the hydraulic gradient due to the inlet and exit effects of the tray (i.e. a hydraulic jump at the liquid inlet and froth and spray throwing over the exit weir).

The second objective of the experimental work was to identify the different operating flow regimes on the valve tray and to measure their mutual transitions. These results have been published[5].

For the air–water system, the clear liquid height was deducted from the measurement of dynamic head. The dynamic head at seven different positions was measured along the length of tray using manometers set on the centre line. One limb of each manometer was mounted flush with the tray floor and the other was connected to the manifold which was connected to the air space above the liquid on the tray. A needle valve (Rotaflow type) was also incorporated in the manometer line to damp out fluctuations

(*a*) *Sieve trays*: The dynamic head along the sieve tray was corrected as usual for the vertical momentum of air passing through the holes of tray to give the clear liquid height.

(*b*) *Valve tray*: The measurement of clear liquid height on a valve tray either by manometer or by the Gamma ray absorption technique gives rise to the following problems:

(1) When air passes through the valves, it is deflected from the inner surface of the valves which gives an additional thrust on the manometric head. This problem was also reported by Brambilla et al[6] and they mentioned that this effect is marked when the F factor is greater than 1.3 $m\,s^{-1}(kg\,m^{-3})^{1/2}$. The air thrust on the manometer tapping for dry tray operation (i.e. without liquid flow) was measured. It was found that the magnitude of the air thrust not only depends on superficial air velocity, but also on the position of the valve-legs. The maximum air thrust measured versus superficial air velocity is shown in Figure 2.

(2) By using the Gamma ray absorption technique, it is not possible to measure the dispersion density between the tray floor and the lift of valves. As this region has a high value of dispersion density, its assumption or omission may lead to a considerable degree of discrepancy from the actual value of clear liquid height.

The problem of using a manometer was overcome by modifying the manometer tappings mounted on the tray floor. The manometer tappings were mounted in the centres of three adjacent valves in such a way that the incoming liquid stream enters that region from one side rather than two sides (Figure 3). Three rectangular pieces of aluminium plate were fixed between the manometer tapping and three adjacent valves as shown in Figure 3. This modification around the manometer tappings prevented the deflected air from influencing the manometric head. The gap of about 5 mm between two adjoining aluminium pieces allows liquid to flow without any major obstruction.

The reliability of the above modification can be seen from Figure 4 where the dynamic heads measured with and without modification of manometer tappings are

VOL. 62 1984

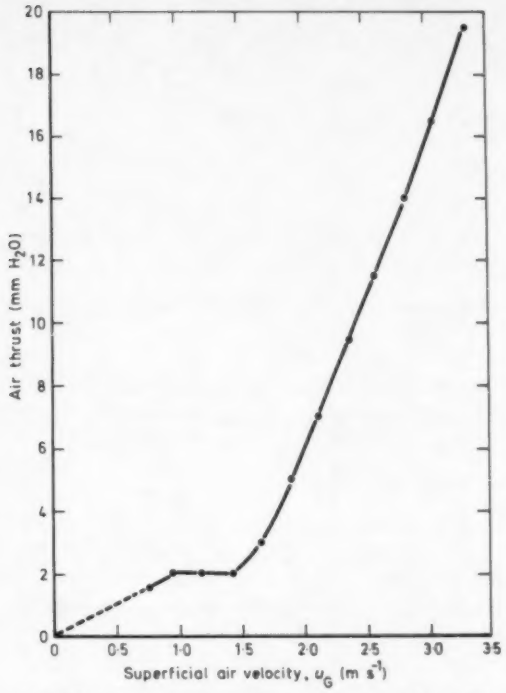


Figure 2. Maximum air thrust on the manometer tappings of the valve tray.

compared. Using Figure 2, the upper limit of correction can be applied to the dynamic head measured without modification of manometer tappings. This is also plotted in Figure 4. The actual correction should be less than the upper limit of air thrust shown in Figure 2. As expected, the dynamic head measured with the modified manometer tappings lies between two extreme limits of correction for the air thrust.

The dynamic head along the valve tray was also corrected for the vertical air momentum to obtain clear liquid height in a similar way as for a sieve tray. This almost definitely overestimates the momentum correction as it neglects the horizontal component of the air velocity as it leaves the valve.

It is not possible to compare the data of clear liquid

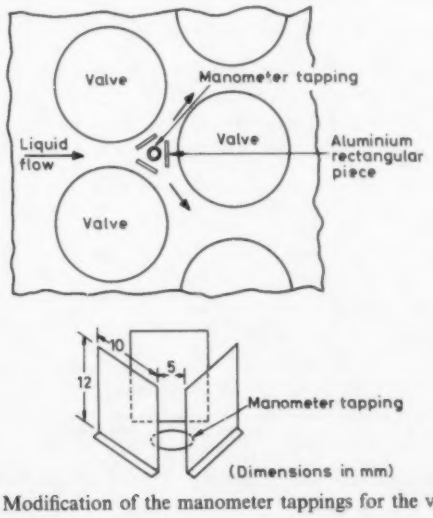


Figure 3. Modification of the manometer tappings for the valve tray.

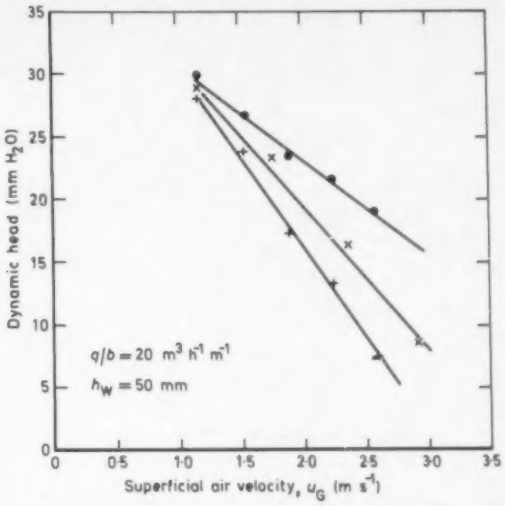


Figure 4. Reliability of the modification of manometer tappings (valve tray).

height on the valve tray with those from the literature because the latter are either for low liquid flow rates (less than 6 m^3 h^{-1} m^{-1}) or for valve trays other than a Glitch valve tray.

RESULTS AND DISCUSSION

Clear Liquid Height on Sieve Trays

Hofhuis and Zuiderweg's[7] correlation for clear liquid height on a sieve tray is

$$h_L = 0.6\,\Psi^{0.25}\,h_W^{0.5}\,p^{0.25} \tag{1}$$

where

$$\Psi = \frac{q/b}{u_G}\sqrt{\left(\frac{\rho_L}{\rho_G}\right)} \tag{2}$$

The data of average clear liquid height on the centre part of the trays, which were not affected by the hydraulic jump, are compared with equation (1) in Figure 5. Data are considerably scattered from equation (1). Each symbol in Figures 5, 6 and 8 represents a run at a particular superficial air velocity and sieve tray (see the key to Figure 8).

In Figure 6, the clear liquid height is plotted versus the flow ratio group, Ψ, for froth and spray regimes. Using

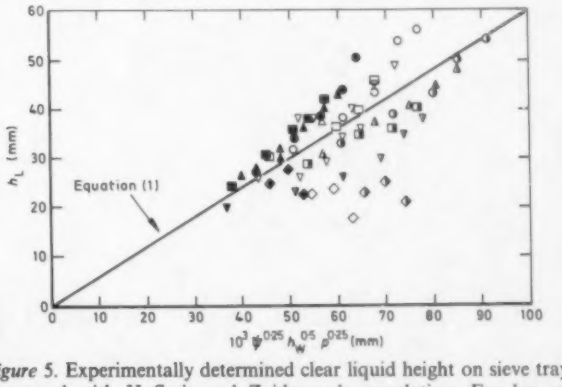


Figure 5. Experimentally determined clear liquid height on sieve trays compared with Hofhuis and Zuiderweg's correlation. For key see Figure 8.

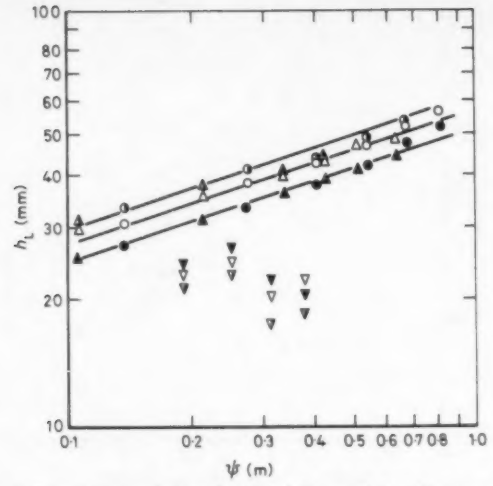


Figure 6. Dependence of clear liquid height on Ψ for sieve trays. For key see Figure 8.

the equation of Pinczenski and Fell[8] for froth-to-spray transition, it was found that $u_G = 2.21$ m s^{-1} corresponds to the spray regime. As expected, the data of three trays for the froth regime fall on three different lines because each tray had a different pitch. For each line it is found approximately that $h_L \propto \Psi^{0.33}$. This is not in accordance with Hofhuis and Zuiderweg's correlation. For the spray regime the data are scattered, so the dependence of h_L on Ψ for this regime cannot be established.

The effect of hole pitch on the clear liquid height is shown in Figure 7. For most of the data in the froth regime, $h_L \propto p^{0.17}$ and for the spray regime h_L is nearly independent of hole pitch. This conclusion again is not in agreement with Hofhuis and Zuiderweg's correlation.

This work indicates that different correlations are required in each regime for clear liquid height. This is not surprising as it has also been found that different correlations are required in each regime for most of the other parameters which characterise tray operation, i.e. entrainment, eddy diffusivity, point efficiency etc. Consequently, Hofhuis and Zuiderweg's single correlation cannot be used to span both froth and spray regimes.

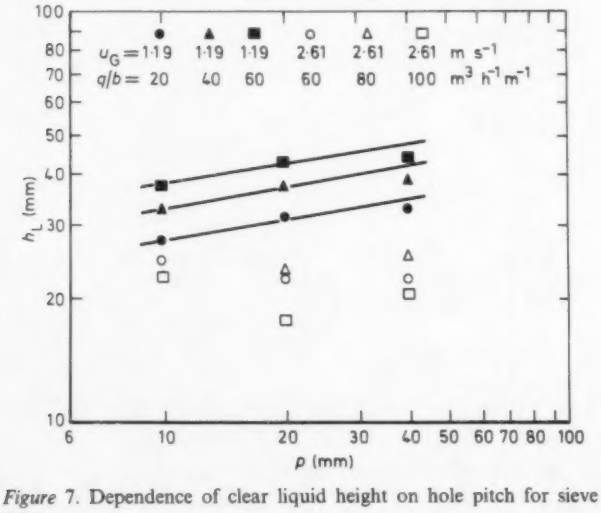


Figure 7. Dependence of clear liquid height on hole pitch for sieve trays.

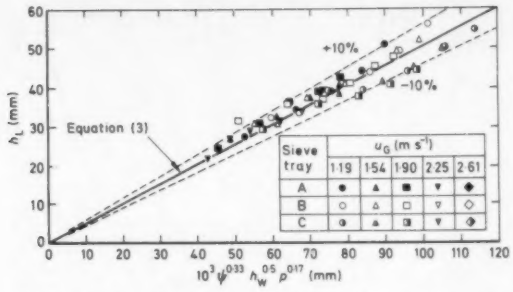


Figure 8. Correlation of clear liquid height on sieve trays operating in the froth regime.

From the conclusion of Figures 6 and 7, Hofhuis and Zuiderweg's correlation may be modified to describe the clear liquid height for the froth regime as:

$$h_L = 0.5\, \Psi^{0.33}\, h_W^{0.5}\, p^{0.17} \qquad (3)$$

Figure 8 represents the comparison of equation (3) with the experimental data for the froth regime. The agreement between them is within $\pm 10\%$. Figure 9 compares predicted values by equation (3) with the data of Brambilla et al[6] and Lockett[9].

It is interesting to notice that most of the data of the sieve tray having hole diameter of 12 mm fall below the present correlation in Figure 8. This indicates that hole diameter might have an effect on clear liquid height. Inclusion of a term for hole diameter in equation (3) could result in a further improvement in the present correlation of clear liquid height.

Clear Liquid Height on Valve Tray

The data of average clear liquid height on a centre part of valve tray are reported for liquid rates up to 40 m^3 h^{-1} m^{-1}. For a liquid rate above 40 m^3 h^{-1} m^{-1}, the hydraulic jump at the inlet of the tray becomes significant and affects considerably the clear liquid profile along the tray. A typical profile of clear liquid height along the tray in the presence of hydraulic jump is shown in Figure 10. Because of the above reason, the experimental results, which were not affected by the hydraulic jump, are studied here to develop a correlation for clear liquid height.

Effect of Weir Height

Three different weir heights were used in the experiments. The effect of weir height on the clear liquid height can be seen from Figures 11, 12 and 13. In general, a higher weir height gives the higher liquid height. But this

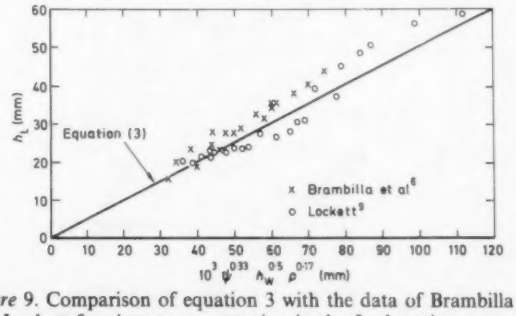


Figure 9. Comparison of equation 3 with the data of Brambilla et al and Lockett for sieve trays operating in the froth regime.

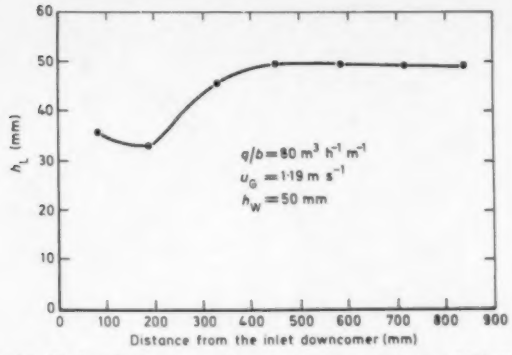


Figure 10. Hydraulic jump on the valve tray operating at high liquid load.

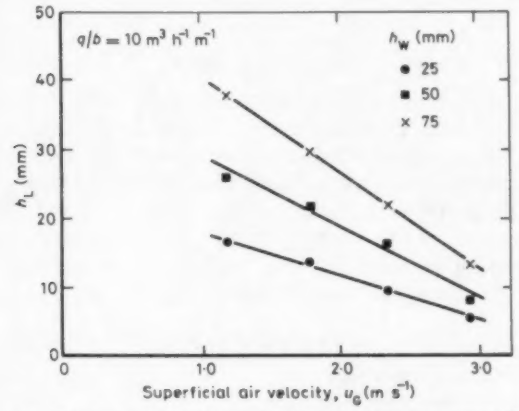


Figure 11. Effect of weir height on clear liquid height at constant liquid rate (valve tray).

effect of the weir height on the clear liquid height decreases on increasing either the gas rate (Figure 11) or the liquid rate (Figure 12). So, the clear liquid height at high liquid and gas rates is nearly independent of the weir height. This explains why the mutual transitions of different operating flow regimes on this valve tray[5] are independent of weir height above the liquid flow rate of $30\ m^3\ h^{-1}\ m^{-1}$. The three different flow regimes, i.e. froth, mixed and spray, on the valve tray were identified. The froth regime corresponds to negligible entrainment, the spray regime to excessive entrainment and the mixed regime to intermediate entrainment between these two limits. More details on this subject have been published[5].

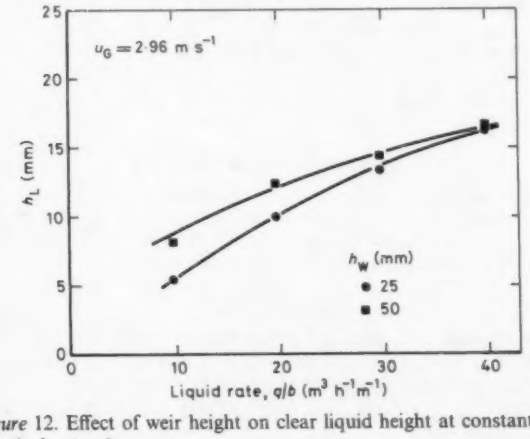


Figure 12. Effect of weir height on clear liquid height at constant gas rate (valve tray).

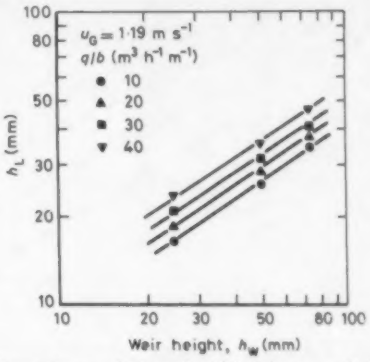


Figure 13. Dependence of clear liquid height on weir height for the valve tray operating in the froth and froth-spray mixed flow regimes.

In Figure 13, the clear liquid height and weir height are plotted on log–log axes for the superficial air velocity of $1.19\ m\ s^{-1}$ which corresponds to the froth or mixed flow regime depending on the liquid rate and the weir height[5]. Figure 13 shows that in the froth and mixed regimes $h_L \propto h_W^{2/3}$.

Effect of Liquid and Gas Rates

Clear liquid height versus liquid rate is plotted for the 25 mm weir in Figure 14 which shows that the clear liquid height increases with the liquid rate.

The effect of the gas rate is shown in Figure 15. The clear liquid height reduces on increasing the superficial air velocity. It is believed that when the spray regime is fully developed on the tray, the clear height starts increasing with the superficial gas velocity due to the dominating vertical component of gas velocity. It was not possible to run the hydraulic simulation column at very high gas loading because flooding occured on the three top sieve trays.

Correlation for Clear Liquid Height

From the approach of Hofhuis and Zuiderweg[7] for the clear liquid height on sieve trays, it seems possible that a similar correlation may describe the clear liquid height on the valve tray.

In order to develop a correlation for the valve tray, h_L versus Ψ is plotted in Figure 16 on log–log axes which shows that $h_L \propto \Psi^{1/3}$ for the froth and mixed regimes. The effect of weir height on the clear liquid height, as

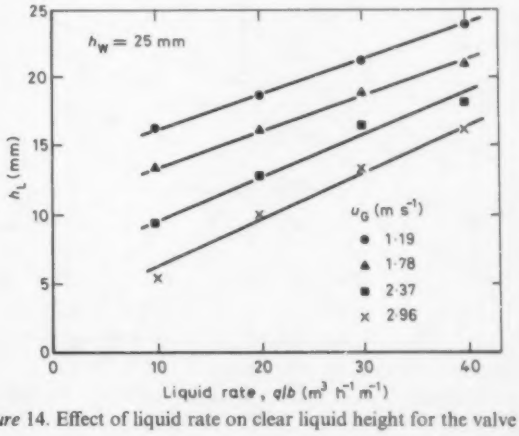


Figure 14. Effect of liquid rate on clear liquid height for the valve tray.

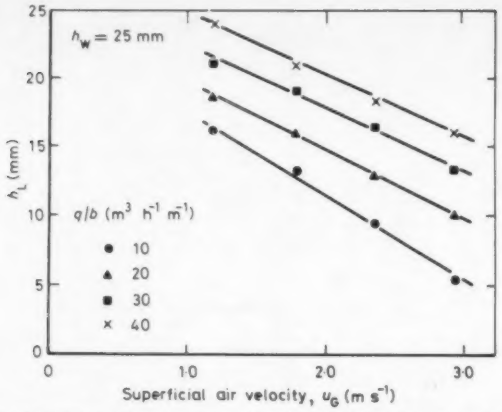


Figure 15. Effect of gas rate on clear liquid height for the valve tray.

discussed earlier, is $h_L \propto h_W^{2/3}$ for the froth and mixed regimes. Therefore, a generalised form of the correlation for clear liquid height on the valve tray can be expressed as:

$$h_L = k\,\Psi^{1/3}\,h_W^{2/3} \tag{4}$$

where k is a dimensionless constant.

In Figure 17, the group $\Psi^{1/3}\,h_W^{2/3}$ is plotted against the measured clear liquid height for the froth and mixed regimes. The constant k of value 0.42 gives a good agreement within $\pm$ 10% error. Thus, for a valve tray having valves similar to Glitch V1, the clear liquid height on the tray for the froth and mixed flow regimes can be determined from the equation:

$$h_L = 0.42\,\Psi^{1/3}\,h_W^{2/3} \tag{5}$$

In the absence of sufficient data of liquid height for the spray regime, a similar correlation cannot be proposed.

It merits a mention here that equation (5) does not include the effect of valve pitch on the liquid height. The valve pitch is generally standard as used in these experiments. The experiments were carried out for the air–water system and the effect of liquid and gas density has been incorporated in the flow ratio group Ψ, however, it needs to be verified by experiments.

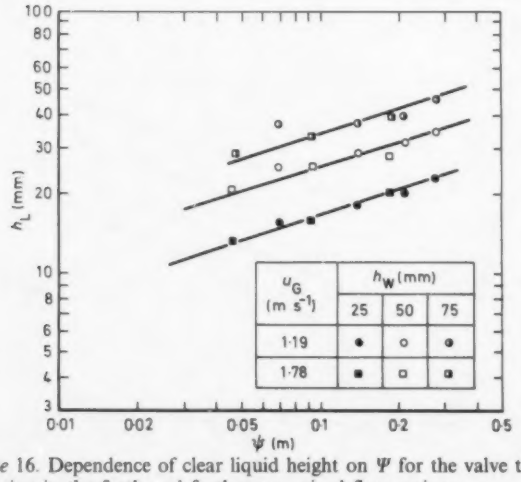


Figure 16. Dependence of clear liquid height on Ψ for the valve tray operating in the froth and froth-spray mixed flow regimes.

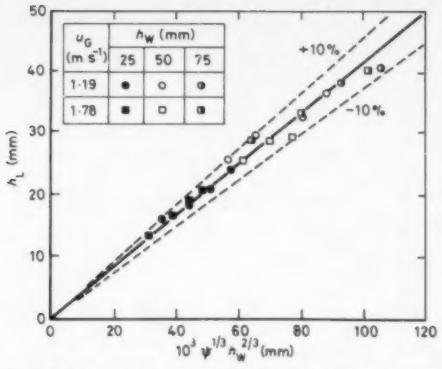


Figure 17. Correlation of clear liquid height on the valve tray operating in the froth and froth-spray mixed flow regimes.

CONCLUSION

It is evident from this work that different correlations are required to describe clear liquid height on a tray operating in the froth and spray regimes. For a sieve tray operating in the froth regime, the clear liquid height can be predicted accurately by equation (3). Clear liquid height on a valve tray, similar to a Glitsch V1 tray, operating in the froth and froth–spray mixed regimes can be predicted using equation (5).

SYMBOLS USED

b	exit weir length (m)
h_L	clear liquid height (m)
h_W	weir height (m)
p	hole pitch (m)
q	liquid flow rate (m^3 s^{-1})
u_G	superficial gas or vapour velocity (m s^{-1})
ρ_L	liquid density (kg m^{-3})
ρ_G	gas or vapour density (kg m^{-3})
Ψ	flow ratio group, defined by equation 2 (m)

REFERENCES

1. Todd, W. G. and Van Winkle, M., 1972, *Ind Eng Chem Proc Des Dev*, 11 (4): 589.
2. Piqueur, H. and Verhoeye L., 1976, *Can J Chem Eng*, 54: 177.
3. Weiss, S. and Langer, J., 1979, *Distillation*, 2.3,1 (IChemE Symp Series No 54).
4. Dhulesia H., 1980, *PhD Thesis* (Department of Chemical Engineering, UMIST).
5. Dhulesia H., 1983, *Chem Eng Res Des*, 61: 329.
6. Brambilla, A., Nardini, G., Nercetti, C. F., and Zanelli, S., 1969, *Distillation*, 2.63 (IChemE Symp Series No 32).
7. Hofhuis, P. A. M. and Zuiderweg, F. J., 1979, *Distillation*, 2.2,1 (IChemE Symp Series No 56).
8. Pinczewski, W. V. and Fell C. J. D., 1982, *Ind Eng Chem Proc Des Dev*, 21: 774.
9. Lockett, M. J., 1981, *Trans IChemE*, 59: 26.

ACKNOWLEDGEMENTS

The author wishes to express his gratitude to: Dr M. J. Lockett, for his helpful supervision, criticism and guidance in carrying out this work, and to Messers F. Taylor and D. Andrew, for their assistance in commissioning the hydraulic simulation column.

ADDRESSES

Correspondence on this paper should be addressed to Dr H. Dhulesia, Direction Recherche Opérationnelle, Compagnie Française des Pétroles (TOTAL), 24 rue Erlanger, 75016 Paris, France.

The manuscript was received 7 February 1983 and accepted for publication after revision 14 November 1983.

VOL. 62 198

ELECTROSTATIC HAZARDS ASSOCIATED WITH MARINE CHEMICAL TANKER OPERATIONS

Criteria of Incendivity in Tank Cleaning Operations

By M. R. O. JONES and J. BOND (FELLOW)
B.P. Research Centre, Sunbury-on Thames, and B.P. Chemicals Ltd, London

The paper considers the hazard of ignition of a flammable atmosphere within a chemical cargo tank by an electrical discharge from a water slug originating from a washing machine. A mathematical model is developed to establish a threshold electrostatic condition of the tank atmosphere which would give rise to a hazardous situation. The model involves worst case assumptions regarding minimum ignition energy, slug size, spark cooling by water mist, vapour concentration, charge transfer and geometrical factors. The calculated hazardous threshold potentials obtained from the model for various chemicals are compared, for the same tank volume and position, with actual measured values obtained on marine chemical tankers. All measured values are below the threshold, although some are very close. The historical fire and explosion data for marine chemical tankers has been examined and confirms that no incident of ignition within a cargo tank has occurred as a result of static generated by water washing machines. The paper shows that the good record experienced by marine chemical tankers when washing tanks, sometimes in the presence of a flammable vapour air mixture, is due to design conditions of tank size and the lack of large water slugs from the washing machines.

DL.
62
984

INTRODUCTION

Flammable liquids have been carried in bulk in marine tankers for about 100 years and the first recorded cargo tank explosion appears to have occurred in 1886 in Liverpool[1]. Oil tankers have occasionally suffered fires and explosions in cargo tanks, some of which have been attributed to ignition by electrostatic discharges during water washing operations. Significant work has been carried out by van der Meer, van de Weerd and others[2-6] on the problems presented by oil tankers. Chemical tankers, on the other hand, have an even better overall record of safety with only a few incidents of cargo tank explosions. Recently work was reported by Edwards[7] on levels of electrostatic charging during various operations on board marine chemical tankers. This work showed that loading of large tanks did not produce levels of static electricity above the liquid surface hazard criteria of -20 to -45 kV established for this operation in the most critical tank size[9,10] of 8 m^3. Cleaning with portable water washing equipment was shown by Edwards to give levels of static electricity which were dependent upon the residue left in the tank and the tank size. Charge levels when steaming were relatively insensitive to residue type. It is, however, recognised that the conditions necessary to produce incendive sparks in a flammable atmosphere had to be established, i.e. the hazard criterion, and these conditions compared with those occurring in practice to establish whether a hazard in fact exists.

The hazard criterion must take account of:—

(*a*) the existence of flammable gas concentrations,
(*b*) the energy required for ignition of the particular gas or vapour,
(*c*) the occurrence of insulated conductors such as water slugs, their size and location,
(*d*) the level of static electrification in the tank. In effect this includes size of tank, whether steaming or washing, types and number of washing machines, duration of wash, the temperature of the wash water, the types and quantity of the residues.

This report is concerned with establishing criteria for incendive discharges during water washing or steaming operations on board chemical tankers.

IGNITION MECHANISM

Cargo tanks on marine chemical tankers are often cleaned with hot or cold water jets or steam. These methods form a persisting water mist which may be electrically charged. As the mist accumulates, so the space potential (see Appendix A) of any region increasingly differs from that of the wall. On a tanker, the wall potential is effectively the zero or earth value. Earthed conductors such as water washing machines which protrude into the tank gain charge to oppose the space potentials acting at their locations. Clearly the magnitude of the space potential determines the magnitude of the charge. This is also true of a water jet in electrical contact with the washing machine.

Consider a slug which has detached from the main jet at the centre of a tank containing a uniform charge distribution. As this slug nears a wall, so the magnitude of the space potential falls—this is intuitively obvious as the potential must fall to zero at the wall. If the charge on the slug is conserved, a potential of different polarity to the space potential develops upon the slug. This is because the charge was determined by the higher space potential at the tank centre. The greater the difference between the acting space potential and that where the

© Institution of Chemical Engineers

slug was formed, the greater the potential difference between the slug and the wall. If the electric field between the slug and wall becomes sufficient to ionise the gas in that space, a discharge might result which could ignite a flammable atmosphere.

A discharge could also occur given a reverse situation to the above i.e. a slug detaching from a wall, and discharging to a washing machine or water jet located in a higher space potential region.

CRITERIA FOR INCENDIVITY

Previous Work

For the case of oil tankers the criteria sometimes used to specify hazardous conditions are[11]:—

(*a*) A space potential exceeding 10 kV in the region around the cleaning gun (i.e. where the slug detaches from the main jet) and
(*b*) Water slugs of length exceeding 0.5 m.

It has been suggested that the above criteria follow from the experimental work of van de Weerd[8], who found that a mixture of 5% propane in air was ignitable by an electrical discharge between an earthed metal ball and a water slug. In fact the publication concerned does not propose the criteria, and does not give sufficient experimental data to properly support their validity. Essentially the results confirm the existence of this ignition mechanism. However, the reported results do provide the criteria with credibility where slug diameters exceed a few centimetres, and atmospheres are made flammable by saturated hydrocarbons. Whilst these may apply generally for very large crude carriers (VLCCs), they need not for chemical tankers. The portable washing machines often used on chemical tankers may be expected to give narrower slugs than the fixed types on VLCCs and the cargoes carried on chemical tankers are not typically hydrocarbons. Because the minimum ignition energies of different chemicals may differ considerably, as shown in Table 1, this point is of great importance.

Table 1. Tank Centre Space Potentials TCSP for 3000 m^3 tank

	Min. Ignition Energy mJ	Measured values scaled to 3000 m^3 kV	Calculated Hazard Threshold TCSP for worst case. slug: length 0.5 m width 1.0 cm kV
Acrylonitrile	0.16*	6.4	8.1
Alkane	0.20*	2.8	12.7
Alkyl benzene	0.26	2.8	14.5
Benzene	0.23	8.0	13.6
Butyl acrylate	0.40*	8.7	18.0
Diethylene glycol	0.13*	1.1	10.3
Ethyl acetate	0.43	18.1	18.6
2 Ethyl hexyl acrylate	0.90*	11.4	26.9
Methyl acrylate	0.30*	14.9	15.6
Naphtha	0.20*	7.4	12.7
Polymethylene polyphenyl isocyanate	0.90*	8.3	26.9
Styrene	0.30	10.1	15.6
Vinyl acetate	0.23*	10.7	13.6
o-Xylene	0.30*	7.0	15.6

*Estimate

Model

Cargo tanks on marine chemical tankers are generally free of ledges, as these may impede thorough cleaning. Thus only slugs originating from washing machines, giving discharges to walls, are considered here. The model is based upon the physical picture given above, and is fully described in Appendix B. Outlined briefly, water slugs of length to diameter ratios greater than or equal to 10 are considered, in cuboid tanks with sides greater than or equal to four times the slug-length. The slugs approach the tank wall with their long axes either parallel or perpendicular. In each case the tank centre space potential (TCSP) and size of slug giving rise to a discharge of a given energy, typically the relevant minimum ignition value, are evaluated. These are then related to some measurable quantity to assess the hazard. As tank centre space potential (TCSP) has often been used in the past[7], this is specified here.

The required input conditions are tank size, slug length, slug width and the relevant ignition energy of the cargo residue. These are discussed in the next section.

It is assumed that charge relaxation processes are very rapid on timescale of other factors affecting the slug, and so the slug is always at a uniform potential.

Generally, the assumptions made within the model relate to the worst conceivable case.

The system of equations may also be used to obtain other outputs, given relevant inputs. For example, given TCSP rather than slug length, the latter may be found. This would require that simple modifications be made to the existing model.

It is worth noting that the model is in no way able to quantify the charging rates due to different conditions, and so cannot predict the TCSP value in any instance. This has to be measured. The model only indicates whether a TCSP may be hazardous.

Model Inputs

Tank Size. The volumes of tanks on marine chemical tankers generally lie between a few hundred cubic metres and a few thousand cubic metres. In this work, three thousand cubic metres is taken to be a realistic upper limit.

Slug Size. The water washing machines generally used on chemical tankers are portable, with two nozzles per machine. An analysis of the slug sizes originating from such machines has been performed by Bustin[12]. His findings of a machine with an 11 mm nozzle tip (Butterworth K) were:—

(*a*) Indications of jet break-up at about 1.5 m from nozzle.
(*b*) Slug lengths of 10 to 50 cm at about 4.5 m.
(*c*) All slug lengths less than 25 cm after about 6 m.
(*d*) All slug lengths less than 10 cm after about 7.5 m.

The above relate to a supply pressure of about 10 bar giving a flow rate of 28 $m^3 h^{-1}$ per machine; lower pressures caused jet break-up closer to the nozzle, and gave smaller slugs.

Larger machines were also observed (48–175 $m^3 h^{-1}$ per machine). These gave jets which broke up at greater

VOL. 62 1984

distances, into larger slugs. However, these machines are not typical of chemical tankers at this time.

Ignition Energy. Difficulties were experienced in selecting minimum ignition energy values as the number of vapours and gases for which measurements have been published is relatively small. Also, there is some confusion regarding the definition of minimum ignition energy within the literature in that some values relate to stoichiometric conditions, and others to the fuel/air compositions giving the lowest values, which need not be stoichiometric. The latter values are generally smaller, and were used in this work whenever available for ambient temperatures and atmospheric pressure[13].

When relevant measured values were unavailable, estimates were made using the findings of Calcote *et al.*[14] These estimates related to stoichiometric mixtures, and so were not necessarily the lowest possible values. In recognition of this, and in the absence of a more rigorous approach, these values were divided by three—a factor considered realistic on the basis of available data.

The values of minimum ignition energy used in this work are given in Table 1. Estimated values are indicated by an asterisk.

Van de Weerd[8] has noted that the minimum ignition energy of a near-stoichiometric mixture of propane in air, for a water slug to metal conductor discharge, is about twice that of a metal to metal discharge. To account for this finding, the ignition energy used for calculation purposes here was also taken to be twice the minimum ignition energy. In practice, energies even greater than this value may be required for ignition. Possible reasons are:—

(*a*) Water mist may increase the effective heat capacity of the discharge zone, so increasing the discharge energy required to achieve ignition. For example, taking a mist content of x kg m^{-3} in a stoichiometric propane/air mixture, the discharge energy required to achieve the autoignition temperature, assuming the water and gases to be in thermodynamic equilibrium at all times, would be $0.25 + 1.34\,x$ mJ—e.g. 0.1 kg m^{-3} of mist could increase the minimum ignition energy of propane from 0.25 mJ to 0.38 mJ. As the magnitude of space potential occurring within a tank will depend upon the concentration of water mist present, this is an important consideration.

(*b*) The discharge energy required to ignite any fuel/air mixture is strongly dependent upon the composition of that mixture[15]. Generally, the minimum ignition energy coincides roughly with stoichiometric proportions. In many circumstances the equilibrium residue-vapour/air mixtures at liquid residue temperatures will be well away from stoichiometric.

RESULTS AND DISCUSSION

Water Washing

Some model predictions are presented in Figures 1 and 2. The former shows the effect on TCSP of varying slug length and width for a given tank size (3000 m^3) and

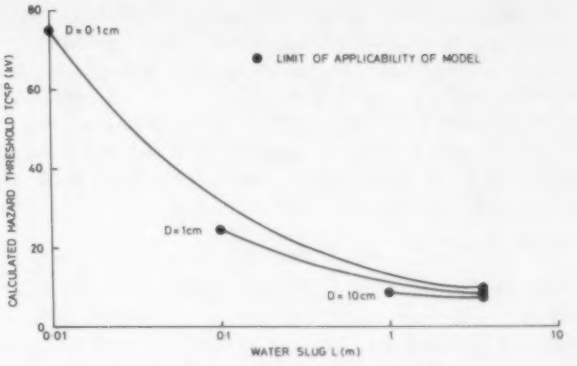


Figure 1. Calculated hazard threshold TCSP against slug length for different slug widths, with 0.5 mJ ignition energy and 3000 m^3 tank.

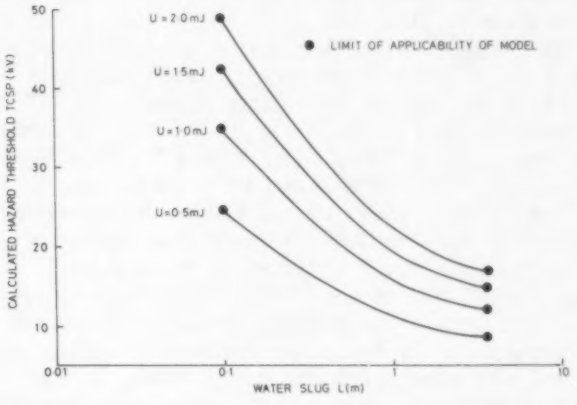


Figure 2. Calculated hazard threshold TCSP against slug length for different ignition energies, with 1 cm slug width and 3000 m^3 tank.

ignition energy (0.5 mJ). The latter shows the effect of varying slug length and ignition energy for a given tank size (3000 m^3) and slug width (1 cm).

Although not shown, the effect on the calculated hazardous level of TCSP of varying tank size, all other things being equal, is small for tank volumes above 100 m^3. Overall the main factors affecting hazardous levels of TCSP are slug size and ignition energy: the larger the slug size, or the smaller the ignition energy, then the smaller the calculated TCSP.

It is interesting to compare the results of the model with measurements already made on chemical tankers[7]. The actual measurements have been scaled to give TCSPs corresponding to 3000 m^3 tanks. This was done by firstly obtaining the TCSP within the tank where the measurements were made using a parabolic potential distribution (see Appendix B), and then further scaling to a 3000 m^3 tank by assuming a linear dependence upon the square root of tank width[7]. The resultant TCSP corresponds to the largest risk value likely to be encountered. The results for the various chemicals considered are presented in Table 1.

Also shown are the hazard threshold values calculated using the minimum ignition energies for slugs of length 0.5 m and width 1 cm. On the basis of Bustin's work[12], such a slug size is representative of the largest, and consequently most hazardous, likely to occur.

In all cases, the calculated hazard thresholds TCSP values exceed the scaled measured values, although in two, the margin of excess is small. Noting that the ignition energies used for calculation purposes are probably well below the relevant appropriate values, as discussed earlier, it does appear that the static levels encountered in the washing operations monitored are not hazardous, even in 3000 m^3 tanks.

Steaming

The space potential which develops at any location within a tank when water washing is dependent upon the charge level on mist droplets within the tank. This is determined largely by the nature of the interactions occurring at the walls between the water jet, residue and wall surface. Residue type is clearly a major factor—e.g. compare the measured TCSP for ethyl acetate and diethylene glycol in Table 1.

The same, however, is not true of steam cleaning. Steam is inherently highly charged, and residue type is unlikely to influence the charge density and TCSP occurring within the tank. On the basis of published measurements[7] TCSP values of around 30 kV are likely to occur within 3000 m^3 tanks when steam cleaning. This exceeds many of the calculated TCSP values presented in Table 1, and substantially exceeds all of the measured water washing values. However, for a hazard to exist there must also co-exist isolated conductors and because chemical tankers are generally devoid of ledges, the existence of water slugs (due to condensate) likely to create a problem is considered improbable. The ejection of condensate from a steam line is more likely to occur during the initial steaming operation when the TCSP is low rather than later, so again the hazard is considered small. However, this aspect needs further study, so in the meantime, steaming of flammable atmospheres should be avoided.

HISTORICAL INCIDENT DATA FOR CHEMICAL TANKERS

The records on fires and explosions in all chemical tankers have been examined to establish the nature of the problem. However, the definition of a chemical tanker is not clear, particularly in the earlier years, and also the records of those earlier years are suspect. Nevertheless Table 2 is based on the Bulletin of Tanker Casualties published in recent years by the Lloyd's Register of Shipping, and on the recollections of many mariners.

Table 2. Fire/explosion in chemical tankers 1973–1983

Year	Position of fire/explosion: Cargo tank	Pump room	Engine room	Other
1973	2	0	0	0
1974	0	1	0	1
1975	1	1	5	2
1976	2	3	2	2
1977	1	1	6	2
1978	1	0	4	1
1979	1	0	3	1
1980	1	0	3	0
1981	1	2	5	1
1982	1	0	3	1
1983	3	1	3	0
	14	9	34	11

Each case of an in-tank fire or explosion was examined further to ascertain the nature of the operation and the cause of the ignition. These were found to be as follows:

1973 (*a*) Ship 34430 dwt
In this incident the residues from the washing of a tank were being pumped overboard. As these slops contained light hydrocarbons and water the ship was directed to put them into a tank. This was done by putting the flexible hose into an opening in the tank. A fire preceded the explosion in the tank receiving the slops. The most probable source of the ignition was considered to be a frictional spark when the flange of the hose hit the inside of the tank. Static electricity was considered to be less likely as the source of ignition.

(*b*) Ship 27000 dwt
This tanker had two explosions. Slops from the washing of one tank were being pumped into a second tank where an explosion of low magnitude occurred. Nearly three days later a further explosion occurred in a tank containing slops and where water was falling into the tank. No conclusion on the source of ignition was made but static electricity was mentioned as a possibility.

1975 Ship 19101 dwt
This incident, although reported as an explosion was not. Acrylic acid in a tank started polymerising causing a high temperature and rupture of the tank. No fire or explosion occurred.

1976 (*a*) Ship 610 dwt
The explosion occurred during the inspection of the tank by a crewman. A naked portable light was considered to be the source of the ignition.

(*b*) Barge 1383 dwt
This incident occurred when residues were being sucked out of the tank through a 2 inch flexible hose and into a vacuum truck. Ignition was attributed "... to a static charge occurring when the steel bands on the end of the cargo stripping hose made contact with a part of the cargo tank."

1977 Ship 800 dwt
The explosion on this small ship occurred during inspection of the tank by two crewmen using a portable light. Water spray caused the glass of the electric bulb to break and the filament to ignite a flammable mixture in the tank.

VOL. 62 1984

1978 Ship 837 dwt
The tank involved in this incident was overpressured when blowing the pipeline with nitrogen. No fire or explosion occurred.

1979 Ship 650 dwt
On this small ship a tank was being washed using fresh water from a rubber hose with a wooden nozzle when the explosion occurred. The source of ignition was attributed to 'electrical charge of the water mist'.

1980 Barge. Assumed less than 1000 dwt
This tank barge suffered an explosion while full of methanol and "while being pushed by a tug". No source of ignition was given.

1981 Ship 20890 dwt
In this incident a tank of 814 m^3, which previously contained benzene, was being cleaned using live steam through an ullage port. Water washing with a portable machine may also have been taking place. No final conclusion on the source of ignition was made but static electricity was considered a possibility.

1982 Ship 7603 dwt
The explosion in this incident occurred when 3 crewmen were in the tank. The source of ignition was not given.

1983 (*a*) Ship 16682 dwt
This explosion occurred after steaming a tank for half an hour. The previous cargo had been methanol.

(*b*, *c*) Two barges. Assumed less than 1000 tons dwt each.
An explosion occurred while filling with acrylonitrile. The vapour space was connected to a vapour return line and to a flare stack. One barge was 10% full when the explosion occurred. It is believed that the ignition occurred from the flare stack as the molecular seal was out of commission for maintenance and there was a path through the flame arrestor.

An analysis of these incidents is given in Tables 3, 4 and 5.

From this analysis it is clear that static electricity is considered the most probable source of ignition in the few explosions that have occurred on chemical tankers. One aspect, however, of the incident investigations seen is that there is a poor understanding of the mechanism of static formation and the mechanism of spark formation. Static is usually attributed as the source of ignition when no other source is obvious. There were two explosions involving steaming, one of which may have been washing also.

Table 3. Operation involved in cargo tank incidents

Inspection/cleaning by persons inside tank	3
Handling of slops	3
Polymerisation of product	1
Overpressurisation of tank with nitrogen	1
Steaming out tank	2
"While being pushed by a tug"	1
Water washing with rubber hose and wooden nozzle	1
Loading	2

Table 4. Size of chemical tanker involved in cargo tank incidents

Less than 1,000 tonnes DW	7
1,000–9,999 tonnes DW	2
10,000–19,999 tonnes DW	2
20,000 and above tonnes DW	3

Table 5. Source of ignition

Static electricity, attributed or probable	5
Frictional spark	1
Light bulb	2
Flare stack	2
Unknown	2
No ignition	2

CONCLUSIONS

From this work and that reported by Edwards we can conclude that levels of static electricity measured during water washing operations and scaled to tank sizes of 3000 m^3 were below that which could be considered incendive. This view is confirmed by the history of chemical tanker operations.

Steaming operations have already been shown to produce high levels of space potential and the extent is dependent on many external factors to the tank; the rate of boiler operation, etc. The presence of a slug of water is also uncertain. Consequently due to these uncertain factors, steaming operations in a flammable atmosphere must be considered a hazardous operation and therefore avoided.

APPENDIX A

Space Potential

Within this paper it is the potential imposed upon a water slug due to the surrounding space charge within a tank and its mirror charge on the tank wall which is referred to as "space potential". This is taken to be invariant at any location for a fixed tank shape, and central value.

The influence of other charged objects such as water slugs and washing guns are neglected. These generally act to reduce the space potential at any location.

In applying this definition here a visualisation of the system is used where charge migration to, and capture by, a water slug from the charge-cloud is ignored. These processes will continually modify the charge distribution within and around any slug, and hence the values of space and slug potential, until some equilibrium state is reached. The consequence of neglecting these processes is not known for all circumstances. This is because their complex transient nature prevents modelling by anything other than highly sophisticated means, and this has

not yet been done. Nevertheless, it seems plausible here that this is a cautious simplification when related to hazard levels. This follows for an isolated earthed slug released at the point of highest space potential in tank; charge capture will reduce the net charge on the slug, and hence its potential difference from earth as the slug moves to regions of lower space potential.

APPENDIX B

The Model

The physical picture corresponding to the model is described briefly within the main text. Here some of the equations comprising the model are specified, together with the assumptions made. Only perpendicular approach is described, although the model also assesses parallel approach.

The first assumption concerns the distribution of space potential within a tank. This is assumed to be parabolic along any line drawn through the tank centre, with the peak magnitude at the tank centre and the walls at earth[16,17]. So, along a line between walls which passes through the tank centre, the space potential is assumed to vary as:

$$S(Z) = S(B)\left[1 - \left(\frac{B-Z}{B}\right)^2\right] \quad (1)$$

where B is the wall to tank centre distance, and so:

$$S(B) = S_{MAX} \quad (2)$$

where S_{MAX} is, of course, the TCSP.

Next, the slug itself is considered. It is assumed that this is formed at the centre of the tank, as this is the region of highest space potential. Such a slug experiences the largest change in space potential in travelling to the wall, and so represents the most hazardous case.

By assuming that the response time of the slug to changes in space potential is fast on the timescale of such changes, the potential of the slug may be taken as uniform. However, the calculated space potential will not be constant throughout the slug. Account of this is taken within the model for two locations. Where the slug is formed, at the tank centre, the use of the TCSP is unrealistic. Overall the slug is exposed to a lower value. This is taken to be that acting one quarter of a slug length away from the tank centre, i.e.:

$$S_{FORM} = S_{MAX}\left[1 - \left(\frac{L}{4B}\right)^2\right] \quad (3)$$

Where the slug approaches a wall the mid-point value is used. When the long axis is perpendicular to the wall this is:

$$S = S_{MAX}\left[1 - \left(\frac{B-H-L/2}{B}\right)^2\right] \quad (4)$$

Parallel approach is also similarly considered within the model, substituting D for L.

In order to establish the response of the slug potential, V, to changes in location, and hence space potential, a knowledge of changes in charge and capacitance are necessary. It is assumed that the former is conserved once the slug is formed until electrical breakdown or contact with the walls occurs. This is cautious assumption as the polarity of the charge on the slug is the opposite of that in the tank, and so charge capture will reduce the net charge on the slug and hence the hazard.

Capacitance expressions are available for ellipsoids in voids, and for roughly ellipsoidal shapes with long axes normal to, and parallel to, earthed planes[18]. These apply generally to length to diameter ratios much greater than 1. These are the expressions used in the model, taking the overall dimensions of the shape considered as those of the slug, i.e. length and width. Their use is limited to slug length to diameter ratios greater than or equal to 10.

The case of an ellipse in a void is used to describe the slug capacitance (with respect to the water jet, washing gun and tank wall) at the tank centre, giving:

$$C_{FORM} = 2\pi\varepsilon L/\ln\left(\frac{2L}{D}\right) \quad (5)$$

Because of the close proximity of the water jet, which is responding to a similar space potential, this is probably excessive, so causing a cautious overestimation of slug charge. For a slug approaching a wall with long axis perpendicular to the surface, the slug/wall capacitance is taken to be that of the combination in isolation:

$$C = 4\pi\varepsilon L/\ln\left[\left(\frac{2L}{D}\right)^2 \frac{2H + L/2}{2H + 3L/2}\right] \quad (6)$$

This is a cautious assumption with regard to the influence of the other walls and earthed objects; their effect is to increase this term, and so reduce the potential on the slug due to any charge carried. In practice the model uses Equation (6) (and the equivalent parallel approach expression), but limits its use to where the tank width exceeds four times the slug length. The influence of other earthed objects upon the slug is then assumed negligible when discharge occurs.

A discharge may occur when the average electric field between the slug-end and wall, given by:

$$E = \frac{V}{H} \quad (7)$$

exceeds[19] 500 kV m^{-1}. It is assumed that the corresponding electric field at the closest point on the slug to the wall then exceeds the breakdown value for the gas there (i.e. greater than 3000 kV m^{-1} for air). Should this not be so, and so the relevant value of E exceeds 500 kV m^{-1}, the effect upon TCSP is small (up to 3000 kV m^{-1}). For parallel approach, the hazardous TCSP threshold increases, indicating this to be a cautious assumption.

The possibility of the water slug deforming and bridging the slug-to-wall gap[20] in such a way as to prevent discharge, or other quenching mechanisms, is neglected. Again, this is a cautious assumption.

The energy released in the discharge is taken to be:

$$U = \tfrac{1}{2}QV \quad (8)$$

This is a cautious over-estimate as the charge transferred will normally be less than Q.

The manner of combination of these equations is now described. Firstly, the space potential where the slug is formed is related to the charge on the slug. When formed the slug is assumed to be at earth potential. Thus:

$$V_{FORM} = 0 \quad (9)$$

VOL. 62 1984

This is the sum of the potential on the slug due to its own charge level, and the acting space potential. Using the capacitance expression (Equation 5) and the space potential expression (Equation 3), Equation (9) becomes:

$$S_{MAX} = -Q \ln \frac{2L}{D} \Big/ 2\pi\varepsilon L\left[1 - \left(\frac{L}{4B}\right)^2\right] \qquad (10)$$

When the slug approaches the wall, the potential difference between the wall and the slug is taken as the sum of the space potential at the location of the slug, and the potential difference between the slug and wall due to the charge on the former. Assuming the charge to be conserved, and using the relevant capacitance expression (Equation 6), this gives:

$$V = \frac{Q}{4\pi\varepsilon L} \ln\left[\left(\frac{2L}{D}\right)^2 \frac{2H + L/2}{2H + 3L/2}\right] + S \qquad (11)$$

There are now sufficient equations, for the number of unknowns, to obtain a solution. Namely, using Equations (4), (7), (8), (10) and (11), and given B, L, E, U and D then S, H, Q, S_{MAX} and V may be calculated.

A modified version of the model described above was used to assess the effect upon the important output parameters such as Q and S_{MAX} of slug orientation. This was only done for slugs approaching walls with their long axes parallel to the walls, as capacitance expressions for other orientations were not readily available. Nevertheless this represents an opposite extreme to the case of perpendicular incidence. Thus the Q and S_{MAX} values corresponding to other orientations may reasonably be expected to lie between the calculated values, for fixed input conditions.

As it was considered sensible that the model should give the lowest values of slug charge or TCSP corresponding to the onset of incendive conditions, the case of parallel approach was incorporated into the final model.

SYMBOLS USED

B	Tank centre to wall distance (m)
C	Capacitance of a water slug approaching a wall (F)
C_{FORM}	Capacitance of a water slug when formed (F)
D	Width, or small dimension, of a water slug (m)
E	Breakdown electric field (taken as 5×10^5 V m^{-1})
H	Smallest wall to slug surface distance (m)
L	Length, or long dimension, of a water slug (m)
Q	Charge on a water slug (C)
S	Space potential acting on a slug (V)
S_{FORM}	Space potential acting on a slug when formed (V)
S_{MAX}	Space potential acting at the tank centre, which is the maximum value (V)
U	Minimum ignition energy of the cargo residue (J)
V	Potential of the slug relative to the tank walls (V)
V_{FORM}	Potential of the slug relative to the tank walls when formed (V)
x	Mist concentration in tank (kg m^{-3})
Z	Distance variable from a wall along an axis passing through the tank centre (m)
ε	Permittivity of gas/vapour/liquid mixture in the tank (taken to be 8.85418 F m^{-1}, vacuum value, in this work)

Abbreviations

TCSP	Tank centre space potential, equal to the magnitude of S_{MAX}(V)
VLCC	Very large crude carrier

REFERENCES

1. Watson, P., 1981, *Hazardous Cargo Bulletin* June: 24.
2. van der Meer, D., 1971, *Pr 3rd Conf Static Electrification* (Inst Phys, Bristol), pp 153–157.
3. van der Weerd, J. M., 1971, ibid, pp 158–173.
4. Smit, W., 1971, ibid, pp 178–183.
5. Vos, B., 1971, ibid, pp 184–192.
6. van der Meer, D., *et al.*, 1973, *2nd Int Conf Static Electricity Special Colloquium: Problems on Tank Washing in Very Large Crude Tankers* (Dechema, Frankfurt).
7. Edwards, H. R., 1983, *4th Int Symp Loss Prevention in the Process Industries* (Institution of Chemical Engineers, Rugby) Vol 2, C1–C14.
8. van de Weerd, J. M., 1975, *J Electrostatics*, 1(3): 295–309.
9. Rees, W. D., 1981, *J Electrostatics*, 11(1): 13–25.
10. Strawson, H. and Lyle, A. R., 1975, *4th Conf Static Electrification*, pp 276–289.
11. Mills, J. S. and Oldham, R. C., 1983, *Marine Engr Rev* (June): 10.
12. Bustin, W. M., 1973–1974, *API Statics Research Program*, (Part 2) (American Petroleum Institute).
13. Kravchenko, V. S. and Bondar, V. A., 1976, *Explosion Safety of Electrical Discharges and Frictional Sparks*, Part 1, Ch 1, Moscow.
14. Calcote, H. F., Gregory, C. A., Barnett, C. M. and Gilmer, R. B., 0000, *Ind Eng Chem* 44(11): 2656–2662.
15. Lewis, B. and von Elbe, G., 1961, *Combustion Flames and Explosions of Gases* (Academic Press).
16. van der Meer, D. and van de Weerd, J. M., 1975, *Int Tanker Safety Conf* (INTASAFCON III), Bergen, Norway, Session 2, Paper 6.
17. Chubb, J. N., Brown, K. P. and Butterworth, G. J., 1980, *J Electrostatics*, 9(1): 71–88.
18. Weber, E., 1965, *Electromagnetic Theory: Static Fields and their Mapping* (Dover Publications Inc.).
19. Butterworth, G. J., Brown, K. P. and Chubb, J. N., 1982, *J Electrostatics*, 13(1): 9–27.
20. Johnson, J. K., 1977, *J Electrostatics*, 4(1): 53–65.

ACKNOWLEDGEMENTS

The authors would like to thank Dr W. D. Rees and Mr R. P. M. Dawson for their helpful comments during this work.

The permission of the British Petroleum Company to publish this paper is gratefully acknowledged.

ADDRESS

Correspondence on this paper should be addressed to Dr John Bond, BP Chemicals Ltd, Belgrave House, 76 Buckingham Palace Road, London SW1W 0SU.

The manuscript was received 12 April 1984 and accepted for publication 30 April 1984.

SHORTER COMMUNICATION

MEASUREMENT OF BUBBLE SIZES AND VELOCITIES IN GAS–LIQUID DISPERSIONS

By D.A. LEWIS (GRADUATE), R.S. NICOL (GRADUATE) and J.W. THOMPSON

Department of Chemical Engineering, Cambridge University

A detection and analysis method for measuring bubble sizes and velocities in bubbly gas–liquid flows using a two electrode conductivity system is described. The velocity and intercepted chord length of each bubble is determined and bubbles with significant lateral or varying velocity can be rejected. A method to obtain the bubble diameter distribution that accounts for the effect of the rejected bubbles is presented.

SYMBOLS USED

A	$4/\pi d^2$, equation (6)
c	intercepted bubble chord
$C(c)$	number fraction bubble chord distribution
d	bubble diameter
$D(d)$	actual number fraction bubble diameter distribution
n	number of bubbles intercepted per unit time
n_c	number of bubbles with chord c intercepted per unit time
n'	number of bubbles accepted per unit time
n'_c	number of bubbles with chord c accepted per unit time
Pr	probability of a bubble chord in the range c to $c + dc$
t_1, t_2, t_3	see Figure (2)
v	absolute bubble velocity
V_G	superficial gas velocity
x	horizontal distance between bubble centre and intercepted chord
δ	electrode spacing
ε	volume fraction gas holdup

INTRODUCTION

The velocities and sizes of gas bubbles in a conducting liquid can be determined using a conductivity detector. Two electrode systems with conducting tips aligned parallel to the direction of flow of the gas bubbles have been widely used[1,2]. Cross-correlating the changes in conductivity as bubbles pass over the electrodes enables the mean bubble velocity to be determined. Severe limitations of this technique are that lateral bubble motion is ignored and, to derive information about the bubble size, assumptions have to be made about the bubble velocity, e.g. that all bubbles are travelling at the same velocity[2].

Multiple electrode systems have also been developed[3–5]. These are designed to determine the shape, size and velocity of bubbles striking them. The large size of some of these probes[3,4] means that only bubbles larger than ~ 3 mm can be detected, causing serious errors in the data analysis due to the preferential detection of larger bubbles. Making this type of probe smaller[5] means that the additional information gained is of doubtful accuracy.

This paper describes a two electrode conductivity detector and analysis system which eliminates some of the difficulties and errors identified above.

DETECTOR OPERATION AND ANALYSIS

Details of the two electrode systems are shown in Figure 1.

Each electrode is driven from a 15 kHz oscillator, and the detector output, as a bubble intercepts the electrodes, is converted to a series of pulses denoting the arrival of the front and rear of a bubble on the two electrodes. These pulses are on separate outputs and a microprocessor stores times t_1, t_2, t_3 for each bubble. Several thousand bubble intercepts can be recorded in a few minutes. If a bubble strikes the detector obliquely t_2 and

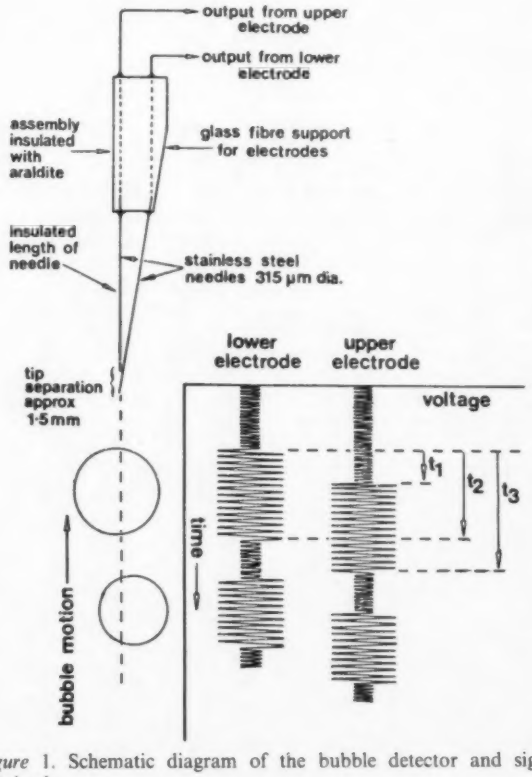


Figure 1. Schematic diagram of the bubble detector and signals obtained.

© Institution of Chemical Engineers

$t_3 - t_1$ will be different and this bubble is rejected from the analysis. If the velocity of the bubble varied while it was passing over the detector t_1 and $t_3 - t_2$ will be different and this bubble is rejected from the analysis. A tolerance of $\pm 15\%$ on the above times decided whether or not a bubble was rejected. Typically, about 20–40% of bubbles intercepted were rejected. For each bubble not rejected, its absolute velocity [the mean of δ/t_1 and $\delta/(t_3 - t_2)$] and the intercepted chord [the mean of $\delta t_2/t_1$, $\delta t_2/(t_3 - t_2)$, $\delta(t_3 - t_1)/t_1$ and $\delta(t_3 - t_1)/(t_3 - t_2)$] are calculated. Hence the velocity and chord of each bubble are independently determined.

The performance of the detector was checked by two methods in a bubble column with co-current air–water upflow and downflow.

(i) *Gas Holdup Measurement*

The mean volume fraction gas holdup, ε, was determined from the electrode output at several radial positions across the bubble column. An independent value of ε was obtained from pressure tappings. The two values agreed to $\pm 4\%$ for $\varepsilon < 0.2$. Thus the electrodes were detecting the correct amount of gas in the system.

(ii) *Gas Phase Volume Balance*

Because a proportion of the bubbles intercepting the detector are rejected in the data analysis, a gas volume balance cannot be derived directly from the bubble sizes measured. For a bubble with absolute velocity v and intercepted chord c an electrode will be in the gas phase for a time c/v. If n' bubbles are accepted from the total number n which intercept the electrodes in unit time,

$$n'/n = (1/\varepsilon)\sum_0^{n'} c/v \tag{1}$$

It is assumed that

$$\frac{n_c'}{n'} = \frac{n_c}{n} \tag{2}$$

where n_c', n_c are the accepted and intercepted numbers of bubbles/unit time with chord c. The velocity of the gas past the detector (which is the superficial velocity of the gas, V_G, in the column) is

$$V_G = \sum_{c=0}^{\infty} n_c \cdot c \tag{3}$$

i.e. the sum of all the chords to pass the detector in unit time. From equations (1), (2) and (3)

$$V_G = \varepsilon \sum_{c=0}^{\infty} n_c' c \left(\sum_0^{n'} c/v\right)^{-1} \tag{4}$$

Table 1. Comparison of the superficial gas velocity measured by the bubble detector with that given by rotameters

Direction of flow	Superficial gas velocity ($m\,s^{-1}$)	
	Rotameters	Conductivity probe
Up	0.125	0.113
Up	0.209	0.205
Up	0.301	0.297
Down	0.055	0.050
Down	0.087	0.085
Down	0.145	0.138

No assumption is made about the bubble shape. The terms on the right of equation (4) were calculated from the detector output, integrated across the column cross-section, and agreed well with V_G measured by calibrated rotameters as shown in Table 1.

CALCULATION OF BUBBLE DIAMETER DISTRIBUTION

Existing methods for the calculation[2] of the number fraction bubble diameter distribution, $D(d)$, do not allow for the rejection of bubbles due to their lateral motion. $D(d)$ is calculated as follows.

Step (i)

For a spherical bubble intercepted a distance x from its centre, perpendicular to the direction of motion, the chord length c detected is given by

$$c^2 = d^2 - (2x)^2 \tag{5}$$

where d is the bubble diameter. The probability of a detected chord in the range c to $c + dc$ is proportional to[2] $c\,dc$.

Step (ii)

A bubble is rejected if it moves laterally during measurement. For a given lateral deflection dx the probability of the bubble being recorded is $\propto (dc/dx)^{-1}$, i.e. the less c changes with dx the more likely the bubble is to be accepted. The longer the intercepted chord of a bubble the more time and hence greater possibility of the bubble being deflected by turbulence, giving a probability of rejection $\propto c$. This is cancelled out by making the rejection criterion for differences in the bubble chord as measured by the two electrodes also $\propto c$.

Hence the overall probability, Pr, of a chord in the range c to $c + dc$ being detected and accepted is, from (i) above and equation (5),

$$Pr \propto \left(\frac{dc}{dx}\right)^{-1} c\,dc = \frac{Ac^2 dc}{(d^2 - c^2)^{1/2}} \tag{6}$$

where $A = 4/\pi d^2$.

If a known number of bubbles with diameter d are intercepted along their diameters, equation (6) gives the

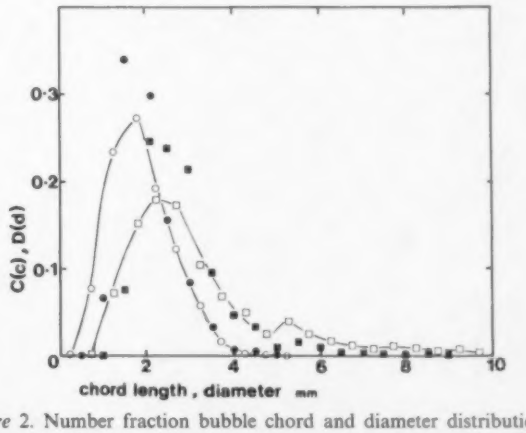


Figure 2. Number fraction bubble chord and diameter distribution, $C(c)$ and $D(d)$ obtained for air-water co-current upflow and downflow on the centre line of a 0.24 m dia. bubble column. Data are: □, ■; $C(c)$ and $D(d)$ for upflow: ○, ●; $C(c)$ and $D(d)$ for downflow. The results are shown in histogram form, with lines drawn connecting related points to clarify the diagram.

number of bubble intercepts of a particular chord length, c, that will be recorded from bubbles of this diameter. The detected number fraction chord distribution at a particular value of c, $C(c)$, is made up of: (a) chords detected from bubbles with diameters $> c$ and (b) bubbles of diameter c intercepted along their diameters. (b) is obtained by subtracting from $C(c)$ the proportions of chords of length c detected from bubbles of diameter $> c$. The largest value of c, $c = c'$, for which $C(c) > 0$ is the diameter of the largest bubbles present, as no larger chords are detected. Hence $C(c')$ corresponds to the proportion (b) of bubbles of diameter c' intercepted along their diameters. From this value, and equation (6), (b) for the next smaller value of c is calculated, and so on, through the $C(c)$ distribution from $c = c'$ to smaller values of c.

Step (iii)

The probability of the detector intercepting a bubble of diameter d is proportional to the projected frontal area of the bubble. $D(d)$ is obtained by weighting the calculated diameter distribution by d^{-2} to correct for this[2].

Figure 2 shows $C(c)$ measured and the corresponding values of $D(d)$ calculated as described in (ii) and (iii) above. The superficial velocity of the water was $1.5\ \mathrm{m\ s^{-1}}$.

REFERENCES

1. Hewitt, G. F., 1978, *Measurement of Two Phase Flow Parameters*, (Academic Press, London).
2. Thang, N. T. and Davis, M. R., 1979, *Int J Multiphase Flow*, 5: 17.
3. Burgess, J. M. and Calderbank, P. H., *Chem Eng Sci* 30: 743.
4. Buchholz, R., Tsepetonides, J., Steinemann, J. and Onken, U., 1983, *Ger Chem Eng* 6: 105.
5. Raper, J. A., Kearney, M. S., Burgess, J. M. and Fell, C. J. D., 1982, *Chem Eng Sci*, 37(4): 501.
6. Needle Industries Ltd., Medical Division, P.O. Box 3, Redditch, Worcestershire.
7. Xylan 8340/904A, supplied by Whitford Plastics Limited, Brindley 86, Astmoor, Runcorn, Cheshire.

ACKNOWLEDGEMENTS

This work was supported by the ICI Joint Research Scheme. One of us (R.S.N.) wishes to acknowledge the financial support of a Postgraduate Fellowship from the New Zealand National Research Advisory Council. The authors would also like to thank Needle Industries Ltd[6], for supplying suitable stainless steel needles, and Whitford Plastics Ltd[7], for supplying the Xylan coating.

ADDRESSES

Correspondence on this paper should be addressed to Dr J. W. Thompson, Department of Chemical Engineering, University of Cambridge, Pembroke Street, Cambridge CB2 3RA.

Dr D. A. Lewis is now at: Sudy Cia, Racine 3000, Montevideo, Uruguay.

The manuscript was received 10 *February* 1983 *and accepted for publication after revision* 4 *October* 1983

VOL.
62
1984

CHEMICAL ENGINEERING RESEARCH & DESIGN

Transactions of The Institution of Chemical Engineers

EDITORIAL

In "Metal deposition in residuum hydrodesulphurisation catalysts", L. O. Oyekunle and R. Hughes propose a simple pore-plugging model to describe catalyst deactivation due to metal deposition for a second order reaction. The influence of the deposits in reducing the pore size, which accounts for increasing diffusional resistance of the large reactant molecules, is considered. Computational results indicate that the rate of deactivation decays linearly with time. The model has been used to predict catalyst life and good agreement obtained with commercial data.

Part II of "Fixed bed sorption with recycle" by J. T. Casey and A. I. Liapis applies the mathematical model described in Part I (see the September issue) to study the performance of recycle sorption systems when two parallel first or second order reactions occur in the perfectly mixed reactor of the recycle system, and both reaction products may be adsorbed. The results show that, if the proper adsorbent is used in the fixed bed, the recycle sorption system can be very effective in enhancing significantly the formation of a desired product, and in reducing the formation of undesired product. This leads to dramatic increases in the overall selectivity of the desired product.

Jasbir Singh in "Gas explosions in compartmented vessels: pressure piling" presents results of experimental work on gas explosions in pairs of cylindrical chambers connected to each other by small tubes. The relative importance of parameters such as the volume and shape of the chambers, the point of ignition, the size of the connecting tube and the type of gas mixture are discussed and equations for the calculation of maximum pressures in such systems derived.

In "Forced convection heat transfer of power law fluid at low Peclet number flow", Vi-Duong Dang analyses heat transfer of Newtonian and non-Newtonian fluids in a tube with axial conduction and heat generation. An inlet boundary condition which accounts for the axial conduction effect is applied. Comparisons of the present results with those of previous researchers show good agreement. The effect of Peclet number, power law model index and heat generation on the temperature field and Nusselt number is discussed.

Minh S. Le and J. A. Howell describe an "Alternative model for ultrafiltration". A limiting flux model is developed to account for a variety of phenomena occurring during ultrafiltration. It is first shown that a new model is required to replace the old gel polarisation model. The new limiting flux model is based on concentration polarisation but postulates that the limiting concentration, occurring at the membrane surface as transmembrane pressure is raised, is a result of the interactions between the solute and the surface. Limiting flux occurs when the pores are blocked most of the time. They remain in a dynamic blocked–unblocked state responding to convective blockage and reverse mass transfer to clear the blockage. Existing and new data is fitted by the model using a small number of adjustable parameters.

D. O. Hagon considers the "Use of frequency-consequence curves to examine the conclusions of published risk analyses and to define broad criteria for major hazard installations. While the mathematics of such curves appear to be well understood, the practical application of their meaning when used to develop criteria has not been widely pursued in the literature.

In the transport-line (or raining solids) reactor (TLR) or its dense-phase equivalent, the moving bed reactor (MBR), fresh solids (catalyst) are continuously introduced whilst spent solid agents are withdrawn in the presence of a continuous reactant-bearing fluid flow. In their paper A. A. Shaikh and J. J. Carberry present analyses of isothermal conversion (with mole change) for arbitrary order and selectivity in the important instance of linear simultaneous-consecutive reactions—each step suffering deactivation of differing severity.

In "Application of modelling and computer simulation to pharmaceutical processes: the Williamson synthesis" by A. R. Wright a mathematical model is developed for the reaction of a substituted phenol with sodium chloroacetate. The model is based on an actual industrial pharmaceutical process and includes semi-batch operation and closed loop pH control. Agreement between simulation and process results is demonstrated for the limited data available. The model is used to predict operating conditions whereby chemical yields and batch times can be improved.

This issue concludes with some correspondence and a report of the 11th Annual Research Meeting. The 1984 volume is completed by the Annual Indexes and List of Referees.

Brian Gay
Honorary Editor

Notes for Authors

Editorial Policy and Standards

1. Papers published in the Journal will be original contributions to chemical engineering knowledge, not previously published. In particular, the Editorial Board encourages the submission of papers which show how the results of research may be used in chemical engineering design. Such implications for design should be brought out clearly in the paper and its summary.

Accounts of research work of an experimental or theoretical nature which throw new light on established principles, which identify problems not yet solved, or indicate practical areas to which research effort may usefully be applied are also invited. Reports from industry and from research establishments are particularly welcome.

Papers may also deal with new developments of plant or processes if these developments are related to underlying principles and can be given quantitative expression.

2. Authors need not be members of the Institution. Papers must be in English and should normally be of 2500 to 5000 words, including Appendices. Figures should also be included in this count, each being estimated as equivalent to 250 words.

3. The Editorial Board will, however, also welcome Shorter Communications (less than 2500 words) for consideration for publication; these would describe, for example, novel research techniques, new analyses of previous work, or interesting aspects of work still in progress. A faster refereeing procedure has been arranged for such short Papers.

4. The Journal also publishes a limited number of longer Review Papers, which are critical assessments of previously published work in a selected area of chemical engineering. In conformity with editorial policy, Reviews should show how the results of research can be used in the design of plant and equipment.

Most Reviews are specially commissioned by the Editorial Board, but authors are also invited to offer Reviews for consideration for publication. In view of the substantial effort required, authors are advised to communicate with the Editor before embarking on a Review.

5. It is the policy of The Institution to publish only papers of the highest quality. To help maintain these standards all papers submitted are sent to referees familiar with the branch of chemical engineering covered. They advise as to whether the paper is acceptable or not and, in addition, indicate to the author possible ways in which, in their opinion, the paper might be improved. The final decision on publication is taken by the Editor in light of this advice.

Manuscript Requirements

1. The text should be typewritten, using one side of the paper only, double-spaced and with adequate margins to allow for revision and copy preparation marks. A summary, preceding the text, should briefly describe the essential original contents of the paper.

2. Mathematical expressions can sometimes be more easily interpreted by the printer if carefully written by hand. Where many equations appear, a list of symbols used should be inserted at the end of the paper, before the references. SI units should *always* be used; the negative index notation is preferred to the oblique stroke.

3. References are listed in the order in which they are first cited in the text, where they are indicated by superscript numbers. They should give in order: Authors' surnames and initials, Year, Title of book or journal, Volume, Issue, Page numbers , followed by name and town of publisher in the case of a book.

4. Tables, drawings and photographs should be on separate sheets at the end of the manuscript and not interspersed in the text. Tabulated data should not duplicate values detailed in the text or on graphs. Drawings submitted should be clear and complete and preferably in a form suitable for direct reproduction. Photographs should be restricted to the minimum necessary.

5. Where limitations of space preclude publication of detailed results, mathematical derivations, etc, authors are invited to include in their paper a statement that this information is available from them on application. Authors may make an appropriate charge for supplying items requested in this way. Such material should be supplied with the paper when submitted to the Editor.

Submission of Papers

1. Three copies of the paper should be sent to:

The Editor, Chemical Engineering Research and Design,
Institution of Chemical Engineers,
George E. Davis Building,
165–171 Railway Terrace,
Rugby CV21 3HQ, England.

or to an Associate Editor as follows:

Australia:
Prof R. G. H. Prince,
Department of Chemical Engineering,
University of Sydney,
Sydney 2006, New South Wales, Australia.

Continental Europe:
Prof Dr J. R. Bourne,
Technisch-Chemisches Laboratorium,
ETH-Zentrum,
CH-8092 Zürich, Switzerland.

Continental Europe:
Prof J. M. Smith,
Laboratorium voor Fysische Technologie,
Technische Hogeschool Delft,
Prins Bernhardlaan 6,
2628 BW Delft, Holland.

India:
Prof M. M. Sharma,
Department of Chemical Technology,
University of Bombay,
Matunga Road,
Bombay 400 019, India.

New Zealand:
Prof R. B. Keey,
School of Engineering,
University of Canterbury,
Christchurch 1, New Zealand.

USA:
Prof J. O. Wilkes,
Department of Chemical Engineering,
University of Michigan,
Ann Arbor,
Michigan 48109, USA.

2. A full address to which readers may send correspondence should be specified, including the post code. The address at which the work was carried out, if different, should also be indicated. Where there are several authors, one should be nominated to check proofs and to receive all correspondence.

3. A proof will be sent to the nominated author, to be checked for possible typographical errors. Other alterations cannot be incorporated at this late stage without incurring higher printing costs, and extensive alterations would necessitate postponement of publication of the paper to a later issue.

4. Following publication the nominated author will receive 50 off-prints of the paper (or 25 where there is just one author). Any further off-prints required should be ordered at proof stage. Reprints, ordered after publication, are more expensive.

VOL.
62
1984

METAL DEPOSITION IN RESIDUUM HYDRODESULPHURISATION CATALYSTS

By L. O. OYEKUNLE and R. HUGHES (FELLOW)
Department of Chemical Engineering, University of Salford.

A simple pore-plugging model to describe catalyst deactivation due to metal deposition for a second order reaction has been proposed. The influence of the deposits in reducing the pore size and which accounts for increasing diffusional resistance of the large reactant molecules was considered. Computational results indicate that the rate of deactivation decays linearly with time. The model has been used to predict catalyst life and good agreement was obtained with commercial data. The total life of a catalyst increases with increasing initial pore size.

INTRODUCTION

Current world consumption of petroleum is relatively high and fossil fuels still account for more than 50% of the world energy supply.

Crude oil with an extremely low sulphur content, such as that produced in Nigeria, North Africa, North America and the North Sea, is available, but oil with a high sulphur content is generally more abundant. In a number of European countries, the United States and Japan, strict controls have been placed on environmental pollution by sulphur product emissions from combustion fuels. There is, therefore, an increasing demand for the removal of sulphur from residuum oils as well as from coal and shale derived liquids. Commercially, this is achieved by hydrodesulphurisation of residua and numerous commercial plants are now in operation.

Hydrodesulphurisation of residua takes place over a fixed bed of porous catalyst under severe temperature and pressure conditions. The reactions that occur during this process result in the loss of catalyst activity with time on stream. This is due to two factors:

(*a*) the deposition of carbonaceous materials, and
(*b*) the adsorption of organometallic compounds onto the catalyst surface.

The residua of some petroleum feedstocks contain significant concentrations of metal complexes, mainly of vanadium and nickel which react to give inorganic products in a residuum demetallation process that occurs in parallel with hydrodesulphurisation. The metal sulphide products so formed can accumulate in the reactor and ultimately plug the pores of a catalyst or the interstices of a fixed bed of catalyst particles[1,2]. The deactivation resulting from adsorption of metallics onto the catalyst surface occurs slowly over a long span of time in an irreversible manner[3,4]. During catalyst regeneration (to remove the coke deposits) the metallic compounds are converted to the oxides which are then permanently bound to the catalyst surface. Thus, deposition from metal complexes causes permanent effects which cannot be removed by oxidation as is the case for coking.

Both vanadium and nickel are present in high molecular resin and asphaltene species with sulphur, oxygen and nitrogen hetero-atoms included in the ring structures. These compounds have high molecular weights ranging from about 300 to 100000. The diameters of the molecules have a size distribution[2] from 2 nm to 100 nm with peaks at 7 nm to 10 nm. These dimensions approach or exceed catalyst pore size and diffusion into the small pores of the catalyst is greatly retarded. Catalysts having the appropriate pore structure are necessary to remove both sulphur and metals and demetallation increases with increase in average pore size. Metals have a greater tendency than coke to form deposits when the relative pore size is large[2]. This results in heavy metal deposition at the entrance to the upper portion of the catalyst bed where the feed reactants enter the reactor; deposition becomes less further along the bed. Deposition of metals on the catalyst is the principal cause of reduced activity.

Scott and Bridge[5] reported that the kinetics of hydrodesulphurisation are generally not first order and the overall desulphurisation reaction can be represented by a second order process. Residuum demetallation shows that the rate of reaction of metal-containing molecules in the feed (V and Ni) is high compared to their rate of diffusion. Newson[6] and Ohtsuka[2] state that demetallation and desulphurisation rates can be represented by second order kinetics.

A model for predicting the life of demetallation catalysts assuming uniform pore-plugging was developed by Newson[6]. Rajagopolan and Luss[7] have presented a model for predicting the influence of pore size on the rate of demetallation of a residuum. However, first order kinetics were employed instead of second order kinetics which are now generally accepted as being obeyed. In addition, a relatively complex model was used by Rajagopolan and Luss to predict the effect of various parameters on the life of the catalyst.

The aim of the present paper is to predict the effect of metal deposition in residuum hydrodesulphurisation catalysts on catalyst life. A simple model based on a pore plugging mechanism with a uniform pore size is developed, similar in concept to that of Rajagopolan & Luss, but with transient analysis and incorporating second order kinetics. Comparisons are made with data from commercial reactors and good agreement is obtained for catalyst life using the present simplified model.

© Institution of Chemical Engineers

DEVELOPMENT OF MODEL

Reaction in a Single Cylindrical Pore

In treatments of diffusion and reaction within porous catalysts, one idealised pore structure frequently assumed is that of an assemblage of open cylinders of uniform radius.

A model of metal deposition in a single cylindrical pore of length L_p is developed. The catalyst pellets are assumed to be isothermal in the reactor and the reaction is second order with respect to the feed and metal concentrations.

Diffusion and reaction in a pore can be described by the equation:

$$D\frac{d^2C}{dx^2} = \frac{2}{r_0}K_s C^n + \frac{dC}{dt} \tag{1}$$

Introducing dimensionless parameters:

$$\alpha = \frac{C}{C_0}, \tag{1a}$$

$$\beta = \frac{x}{L} \tag{1b}$$

$$h_0 = L\sqrt{\left(\frac{2K_s C_0^{n-1}}{r_0 D}\right)} \tag{1c}$$

$$\tau = \frac{tD}{L^2} \tag{1d}$$

Equation (1) becomes:

$$\frac{d^2\alpha}{d\beta^2} = h_0^2\alpha^n + \frac{d\alpha}{d\tau} \tag{2}$$

with boundary conditions

$$\alpha = 1 \quad \text{at} \quad \beta = 0 \tag{3}$$

$$\frac{d\alpha}{d\tau} = 0 \quad \text{at} \quad \beta = 1 \tag{4}$$

$$\alpha = 1 \quad \text{at} \quad \tau = 0. \tag{5}$$

Reaction with Poisoned Pore Mouths

After the initial metal sulphide deposit, the original pore diameter is reduced resulting in a restricted diffusivity in the pore. It is assumed that the deposit does not affect the intrinsic demetallation activity per unit surface area, but will reduce the surface area and may affect the restricted diffusion in the pores.

Metal sulphide deposition is assumed to be uniform within the cylindrical pore. The restricted diffusivity is given by:

$$D_r = Df(\lambda) \tag{6}$$

where D is the bulk diffusivity and

$$\lambda = \frac{r_m}{r_p} \tag{7}$$

r_m is the radius of the reactant molecule.

Spry and Sawyer[8] have shown that $f(\lambda)$ may be approximated by:

$$f(\lambda) = (1-\lambda)^4 \tag{8}$$

It follows that:

$$D_r = D(1-\lambda)^4. \tag{9}$$

Introducing new dimensionless parameters:

$$h_r = L\sqrt{\left(\frac{2K_s C_0^{n-1}}{r_p D_r}\right)} \tag{9a}$$

$$\tau_r = \frac{tD_r}{L^2} \tag{9b}$$

$$\frac{d^2\alpha}{d\beta^2} = h_r^2\alpha^n + \frac{d\alpha}{d\tau_r}. \tag{10}$$

The concentration profiles (α) along the pores at different time intervals were evaluated by the use of both the orthogonal collocation method[9,10] with four internal collocation points and the Runge–Kutta polynomial approximation to solve equation (10). This same method was closely followed in the solution of all other subsequent equations derived in this paper.

Metal Sulphide Deposit

The rate of metal deposition per unit length of pore is:

$$\frac{dm}{dt} = \varepsilon 2\pi r_p K_s C^n M_{ms}. \tag{11}$$

With metal deposit thickness $\delta = r_0 - r_p$

$$m = \rho_{ms}\pi\{r_0^2 - r_p^2\} = \rho_{ms}\pi\{r_0^2 - (r_0-\delta)^2\}$$

$$m = \rho_{ms}\pi r_0^2(1-\gamma^2) \tag{12}$$

where

$$\gamma = \frac{r_p}{r_0}.$$

Therefore:

$$\frac{dm}{dt} = \frac{d}{dt}\{\rho_{ms}\pi r_0^2(1-\gamma^2)\} = \varepsilon 2\pi r_p K_s C^n M_{ms} \tag{13}$$

which on differentiation yields

$$\frac{d\gamma}{dt} = -\frac{\varepsilon K_s C_0^n M_{ms}\alpha^n}{\rho_{ms} r_0} = -K_m\frac{\alpha^n}{r_0}. \tag{14}$$

Where

$$K_m = \frac{\varepsilon K_s C_0^n M_{ms}}{\rho_{ms}}. \tag{15}$$

When $n = 2$

$$\frac{d\gamma}{dt} = -K_m\frac{\alpha^2}{r_0}. \tag{16}$$

With the boundary condition:

$$\gamma = 1 \quad \text{at} \quad t = 0.$$

The metal deposition thickness, δ, is related to γ by the equation:

$$\delta = r_0(1-\gamma). \tag{17}$$

VOL. 62 1984

DEMETALLATION IN CATALYST PELLET

The instantaneous reaction in a single pore is given by:

$$R_r = \int_{x=0}^{x=L} 2\pi r_p K_s C^n \, dx = 2\pi r_0 L K_s C_0^n \eta \qquad (18)$$

where the instantaneous effectiveness factor

$$\eta = \int_0^1 \alpha^n \gamma \, d\beta \qquad (19)$$

α, γ are functions of β and $n = 2$.

Therefore:

$$R_r = 2\pi r_0 L K_s C_0^2 \int_0^1 \alpha^2 \gamma \, d\beta. \qquad (20)$$

In the pore structure model due to Wheeler[11], the pellet is assumed to consist of many non-intersecting pores of different lengths, which originate at the exterior surface and terminate at various positions inside the sphere. The randomly oriented cylindrical pores are of one fixed diameter and intersect any plane at an average angle of 45°. Hence, a tortuosity factor (ψ) of 2 is applicable. The maximum length of the pore is twice the thickness of the pellet which is of flat slab geometry.

The number of pores per unit external surface area is given by:

$$N = \frac{\theta}{\pi r_0^2 \psi^{1/2}} = \frac{\theta}{\pi r_0^2 \sqrt{2}} \qquad (21)$$

where the average pore radius

$$r_0 = 2\frac{V_g}{S_g}. \qquad (22)$$

The reaction rate per unit volume of catalyst is:

$$R_v = \frac{\theta}{\pi r_0^2 L \sqrt{2}} R_r. \qquad (23)$$

Substituting equation (20) for R_r:

$$R_v = \frac{\theta}{\pi r_0^2 L \sqrt{2}} 2\pi r_0 L \sqrt{2} K_s C_0^2 \int_0^1 \alpha^2 \gamma \, d\beta$$

which gives:

$$R_v = \frac{2}{r_0} \theta K_s C_0^2 \int_0^1 \alpha^2 \gamma \, d\beta \qquad (24)$$

where R_v is the reaction rate in the pellet.

RATE AND DISCUSSION

Rate and other data employed in the predictions are listed in the nomenclature with the appropriate parameters. These values are typical of those found in commercial practice.

Solution of equation (16) yields values of γ for varying concentration profiles (α) obtained through equation (11) for different pore sizes. The metal deposition thickness (δ) is then evaluated using equation (17). Figure 1 shows that the metal deposition decreases with increasing pore size and increases with the number of days the catalyst is on stream. It can also be seen that virtually complete pore blocking can occur for pores of radius 4 nm or less at times in excess of 40–50 days.

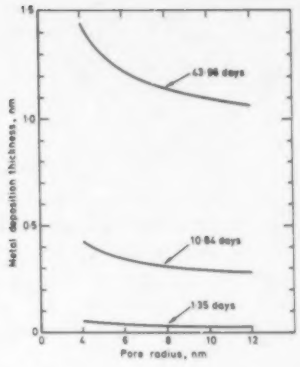


Figure 1. Variation of metal deposition thickenss with different pore sizes.

Equation (19) was solved by the interior collocation method to yield values for the instantaneous effectiveness factor which were then substituted into equation (24) to compute the corresponding values of reaction rate for pellets of different average pore sizes.

Figure 2 shows the variation of effectiveness factor (η) of different pore sizes as a function of the catalyst age. The value of η decreases uniformly with time and changes more rapidly with catalysts having smaller pore sizes. The plots also clearly indicate that the larger the pore size the greater the value of the effectiveness factor, showing the advantage of catalyst with larger pores to provide easy access for organic metal-containing compounds.

The values of the effectiveness factor obtained are comparable but slightly smaller than those found in the literature. Adlington and Thompson[12] estimated that effectiveness factors for hydrodesulphurisation at 415° C and 35 bar were about 0.6 for 3.2 mm diameter pellet catalyst. Cecil et al[13] investigated hydrodesulphurisation of Middle East residua and found an effectiveness factor of 0.4 for cylindrical particles 1.6 mm in diameter; when the average pore diameter was increased from 7.8 to 10.3 nm, the estimated effectiveness factor increased to 0.8.

Most of the catalyst pores have diameters small enough to exclude the metal-containing asphaltenes, while most of the sulphur-containing molecules could enter the catalyst pores and penetrate toward the particle interior. Consequently, the effectiveness factor for demetallation could be less than that of desulphurisation.

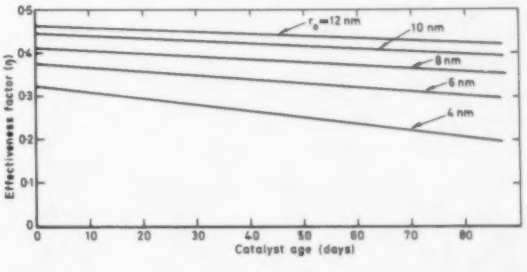


Figure 2. Variation of effectiveness factor (η) with catalyst age.

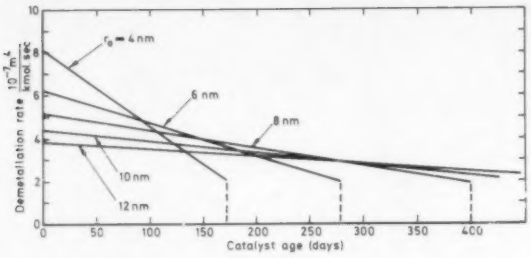


Figure 3. Dependence of demetallation rate on catalyst age for different pore sizes.

Prediction of Catalyst Life

Catalyst activity comparisons were made for pores varying from 4 nm to 12 nm radius. Figure 3 describes the dependence of demetallation rate on catalyst age for several pore sizes. The plots indicate that catalyst activity decays in a linear fashion. The initial activity is high with pores of smaller radius but decreases more rapidly than that of pores of larger size. The total life of a catalyst thus increases with increasing initial pore size due to the increase in the number of available pores for the reactant molecules. However, increasing pore size must be balanced against loss in strength and loss in catalytic surface area.

In practice, catalysts are usually replaced when their activity reaches a certain limiting value and before they become completely inactive. This limiting value may be expressed as a fraction of the initial demetallation rate. A limiting rate of 2×10^{-7} m^4 kmol^{-1} s^{-1} was used in Figure 3 to obtain 170, 280 and 400 days for catalysts of 4 nm, 6 nm and 8 nm pore radius respectively. A 50–65 wt% metals deposit on new catalyst has been reported as an appropriate tolerance level and can also be used to forecast life[2]. Since the demetallation rate will be reduced proportionately by the deposit, a 50% rate reduction gives a catalyst life of 110, 220 and 330 days for pore sizes of 4 nm, 6 nm and 8 nm respectively.

These values compare favourably with the catalyst life-times reported in the literature, as shown in Table 1. Gulf commercial plants provided values ranging from 187.5 to 208.3 days while kinetic studies of commercial plant by Ozaki et al[14] gave 145 and 155 days at 80% and 85% efficiency respectively. Newson[6] obtained a value of 145.8 days by his model prediction and Ohtsuka[2] reported values ranging from 41.7 to 291.7 days found through model prediction.

Table 1. Some catalyst life-times reported in the literature.

Catalyst life in days	Method	Source	Feed
145.8	Model prediction	Newson, E. J.	—
187.5–208.3	Commercial plant (Gulf)	Newson, E. J.	—
155	Commercial plant kinetic studies (85% efficiency)	Ozaki et al	Kuwait 340°C +
145	Commercial plant kinetic studies (80% efficiency)	Ozaki et al	Kuwait 340°C +
291.7	Model prediction	Ohtsuka, T.	Arabian Light
41.7	Model prediction	Ohtsuka, T.	Khafji
125	Model prediction	Ohtsuka, T.	Kuwait
41.7	Model prediction	Ohtsuka, T.	Gach Saran Iranian (Heavy)

CONCLUSIONS

A pore-plugging model has been proposed to describe catalyst deactivation in residuum hydrodesulphurisation. The pores of the catalyst are plugged due to metal sulphide deposits, a reaction occurring in parallel to desulphurisation. A simplified approach was taken in describing a catalyst pellet as containing a set of non-interconnecting cylindrical pores of an average fixed diameter. The reactant molecules of organometallic compounds were also treated as having a uniform size.

Predictions were made for catalyst life based on the present analysis and comparison with commercial data showed good agreement.

A more rigorous approach needs to be considered which will involve pores of different diameters, pore structures and pore size distribution. In practice, the molecular size of the metal containing compounds in the reactant is not uniform and this should be examined to evaluate the impact of the size distribution.

SYMBOLS USED

C	instantaneous concentration of reactant (kmol m^{-3})
C_0	initial concentration of reactant (2×10^{-2} kmol m^{-3})
D	bulk diffusivity (7×10^{-2} m^2 s^{-1})
D_r	restricted diffusivity (m^2 s^{-1})
h_0	Thiele Modulus (equation 1c)
h_r	Thiele Modulus with restricted diffusivity (equation 9a)
K_m	deposition velocity defined by equation (15)
K_s	reaction rate constant per unit surface area (5×10^{-13} m^4 kmol^{-1} s^{-1})
L	half pore length (m)
L_p	maximum pore length equivalent to pellet diameter (m)
m	mass of metal deposit per unit length of pore
M_{ms}	molecular weight of metal sulphide deposit
N	number of pores in the pellet per unit surface area
n	order of reaction (=2)
R_r	instantaneous reaction rate in a pore
R_s	reaction rate of a single pellet
r_p	instantaneous pore radius (m)
r_m	radius of reactant molecule (m)
r_0	initial pore radius (m)
S_g	surface area per unit weight of catalyst (m^2 kg^{-1})
t	time element (s)
V_g	catalyst pore volume per unit weight of catalyst (m^3 kg^{-1})
x	distance coordinate along the length of a pore
Greek Letters	
α	dimensionless concentration (C/C_0)
β	dimensionless distance (x/L)
γ	ratio of instantaneous pore radius to the initial pore radius (r_p/r_0)
δ	metal deposition thickness (nm)
ε	number of metal sulphide molecules per molecule of reactant (=2)
η	instantaneous effectiveness factor
θ	porosity (=0.5)
λ	ratio of molar to pore radius (r_m/r_p)
ρ_{ms}	density of metal sulphide (3000 kg m^{-3})
τ	dimensionless time (equation 1d)
τ_r	dimensionless time for restricted diffusivity (equation 9b)
ψ	tortuosity factor (=2)

REFERENCES

1. Schuit, G. C. A. and Gates, B. C., 1973, *AIChE J*, 19: 417.
2. Ohtsuka, T., 1977, *Catal Rev Sci Eng*, 16: 291.
3. Kovach, S. M., Castle, L. J., Bennett, J. V. and Schrodt, J. T., 1978, *Ind Eng Chem, Prod Res Dev*, 17: 62.
4. Ocampo, A., Schrodt, J. T. and Kovach. S. M., 1978, *Ind Eng Chem, Prod Res Dev*, 17: 56.
5. Scott, J. W. and Bridge, A. G., 1971, *Adv Chem. Ser*, 103.
6. Newson, E., 1975, *Ind Eng Chem, Proc Des Dev*, 14: 27.
7. Rajagopalan, K. and Luss, D., 1979, *Ind Eng Chem, Proc Des Dev*, 18: 459.
8. Spry, J. C. and Sawyer, W. H., 1975, Paper 16-20 AIChE 68th Annual Meeting, Los Angeles, Calif.
9. Villadsen, J. V. and Stewart, W. E., 1967, *Chem Eng Sci*, 22: 1483.
10. Finlayson, B. A. 1974, *Catal Rev*, 10: 69.
11. Wheeler, A., 1951, *Ad Catal*, 3: 249.
12. Adlington, D. and Thompson, E., 1965, *3rd Euro Symp Chem React Eng*, p. 203, (Pergamon Press, Oxford).
13. Cecil, R. R., Mayer, F. Z. and Cart, E. N., 1968, paper presented at AIChE Meeting, Los Angeles.
14. Ozaki, H., Satomi, Yo. and Hisamitsu, T., 1975, 9th World Petroleum Conference, Tokyo, PD18 (4).

ACKNOWLEDGEMENTS

L. O. Oyekunle is very grateful to the Department of Chemical Engineering, University of Salford, Salford M5 4WT, England, who paid for the computation work. The authors are indebted to Dr E. K. T. Kam for the valuable discussions during the running of the computer programs.

ADDRESS

Correspondence on this paper should be addressed to Dr R. Hughes, Department of Chemical and Gas Engineering, University of Salford, Salford M5 4WT.

Mr Oyekunle was on leave of absence from the Chemical Engineering Department, University of Lagos, Nigeria.

The manuscript was received 19 September 1983 and accepted for publication 22 November 1983.

BOOK REVIEWS

Unified Analysis and Solutions of Heat and Mass Diffusion
M. D. Mikhailov and M. N. Ozisik
John Wiley & Sons Inc, 1984
pp 517, £55.00

Professors Mikhailov and Ozisik have presented a very advanced text on the analysis and solution of heat and mass diffusion problems. The emphasis throughout the book is on 'analytical solutions', although most of the worked examples given in the different chapters could be solved numerically. However, the authors claim, with considerable justification, that there are vast classes of problems of practical importance that can be studied analytically and furthermore, when these solutions are available they provide a significant insight into the system parameters affecting the transport processes. Analytical solutions have hitherto been developed to provide specific solutions to particular problems and the authors of this text have successfully attempted a unification of the solution of linear heat and mass diffusion problems. In this respect they have chosen to concentrate their study on seven different classes of time dependent linear heat and mass transfer problems, and the classes cover a vast number of problems of practical interest.

The mathematical treatment throughout is advanced and would generally be unsuitable for undergraduate chemical engineering courses. Parts of the text would be of interest to final year students but generally the treatment is postgraduate. Equations are generally presented in vectorial notation for conciseness and the authors frequently transform the coordinate system in the analysis of the different problems presented. The solution procedures presented draw heavily on integral transforms which will not be appreciated by readers who have not previously undertaken a course in mathematics extending beyond the Laplace transformation into Fourier transforms and other integral transformation procedures. For readers with this background this text will be greatly appreaciated.

The classes of problem treated cover, in Class 1: Problems of steady and unsteady heat and mass diffusion (of a single species) in solids subject to generalised boundary and initial conditions. Class II problems consider a generalisation of Class I problems in a finite composite medium consisting of n subregions. Class III problems are characterised by consideration of two non-homogeneous time dependent diffusion equations coupled through their boundary conditions. These problems treat heat and mass transfer in co-current flow conditions. Class IV problems deal with sets of diffusion equations in which the temperature or concentration are coupled through source-sink terms in the equations. For example, problems in mass transfer and chemical reaction. Class V considers similar types of problems but with no symmetry, e.g. flow and heat/mass transfer in packed bed reactors. These types of problems are treated in greater depth in Class VI and VII problems but are modelled through sets of equations.

In conclusion this is an advanced text presenting a unified analysis and solution of heat and mass diffusion problems. It is a specialised treatment of the subject, written in a scholarly manner and supported by excellent examples. The general solutions developed in the seven problem classes will cover most diffusion problems of interest to graduate students, research workers and practising engineers.

G. V. Jeffreys

Book Reviews continue on page 350

FIXED BED SORPTION WITH RECYCLE
Part II: Parallel Reversible Reactions

By J. T. CASEY and A. I. LIAPIS

University of Missouri-Rolla, Department of Chemical Engineering, Rolla, Missouri, USA

This work studies the performance of recycle sorption systems when two parallel first or second order reactions occur in the perfectly mixed reactor of the recycle system, and both reaction products may be adsorbed. The results show that, if the proper adsorbent is used in the fixed bed, the recycle sorption system can be very effective in enhancing significantly the formation of a desired product, and in reducing the formation of undesired product. This leads to dramatic increases in the overall selectivity of the desired product. If the goal is to produce relatively large quantities of both products, this can be achieved by terminating the recycle sorption operation at an appropriate time when relatively significant amounts of both products have been produced. In this case as well as for the overall selectivity, the recycle system may provide a better performance than that obtained by a batch reactor.

INTRODUCTION

In Part I[1] of this work, a mathematical model that describes single and multi-component reaction adsorption systems with recycle was constructed, and results were presented for single, reversible reactions of zero, first, and second order. In the systems examined[1], only the reaction product was adsorbed onto the surface of the porous adsorbent particles.

Reaction adsorption units with recycle can be used in chemical and biomedical systems[1-7], and potential applications in biochemical engineering have been demonstrated recently[8,9]. In the biochemical systems, one or more reaction products are removed continuously from one or multiple biochemical reactors; this leads to a substantial increase in the production rates, and also the concentration of a certain product or products may be kept below a critical level, so that inhibitory effects on the reaction rates can be minimised, and in some cases the mechanisms of inhibition could become totally inactive.

The present work studies a recycle–sorption system involving two parallel, reversible reactions, and the removal of two products by the adsorbent particles. The performance of the recycle sorption system is also compared with the performance of a batch reactor.

THE RECYCLE SORPTION SYSTEM

In this work the system shown in Figure 1 is studied, and the parallel, reversible reactions

$$A \underset{k_2}{\overset{k_1}{\rightleftharpoons}} C \tag{1}$$

$$A \underset{k_4}{\overset{k_3}{\rightleftharpoons}} B \tag{2}$$

are assumed to take place only in the chemical reactor of the reaction adsorption unit with recycle. This implies that R_{di} and R_{pi} (i = A, B, C) are taken to be zero in equations (1) and (2) of the mathematical model presented in Part I[1]. In the fixed bed of the system, only components B and C are adsorbed, and the equilibrium constants of the above reactions are taken to be less than or equal to unity. This condition on the equilibrium constants implies that low concentrations of products B and C may significantly inhibit the forward reactions[1,2,7], and it can be encountered in chemical, biomedical, and biochemical systems of practical interest.

In Part I[1] single component adsorption with linear and nonlinear isotherms was considered, but in the present work the isotherms will always be nonlinear since multi-component adsorption takes place. Two sets of isotherms are used, both of which are of the so-called Fritz and Schlünder type[10], and their functional properties are discussed in the works of Liapis and Rippin[11], and Liapis[12]. The two sets of isotherms are given by the following expressions[11,16]:

$$C_{sC} = \frac{64.61\, C_{pC}^{1.217}}{C_{pC}^{0.812} + 27.58\, C_{pB}^{0.264}} \tag{3}$$

$$C_{sB} = \frac{96.70\, C_{pB}^{1.254}}{C_{pB}^{0.906} + 0.295\, C_{pC}^{0.634}} \tag{4}$$

$$C_{sC} = \frac{64.61\, C_{pC}^{1.217}}{C_{pC}^{0.812} + 0.873\, C_{pB}^{0.764}} \tag{5}$$

$$C_{sB} = \frac{96.70\, C_{pB}^{1.254}}{C_{pB}^{0.906} + 0.295\, C_{pC}^{0.634}} \tag{6}$$

Species B is always more preferentially adsorbed than component C, and this is clearly shown if one compares equations (3) and (4) as well as equations (5) and (6). The adsorptivity of B from equation (4) is greater than

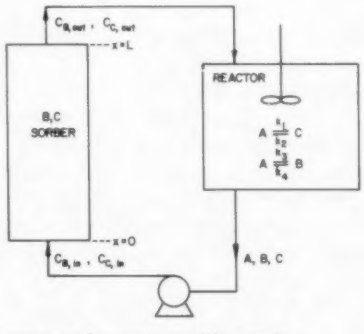


Figure 1. Reactor sorber system with recycle.

© Institution of Chemical Engineers

VOL. 62 1984

Table 1. Parameter values for the recycle sorption system of Figure 1

$C_A^0 = 3.0$, $C_B^0 = C_C^0 = 1.0 \times 10^{-4}$, $D_{LA} = D_{LB} = D_{LC} = 4.0 \times 10^{-6}$, $D_{pB} = 13.03 \times 10^{-10}$, $D_{pC} = 7.40 \times 10^{-10}$, $K_{fB} = 1.95 \times 10^{-5}$, $K_{fC} = 2.12 \times 10^{-5}$, $L = 0.5$, $Q = 1.0 \times 10^{-6}$, $r_b = 0.03$, $r_0 = 5.0 \times 10^{-4}$, $V = 5.0 \times 10^{-3}$, $V_f = 0.35 \times 10^{-3}$, $\varepsilon = 0.45$, $\varepsilon_p = 0.94$.

the adsorptivity of C from equation (3), and also the adsorptivity of B from equation (4) is greater than the adsorptivity of B from equation (6) and of C from equation (5). It is clear that the only difference between the two sets of isotherms is in the term of C_{pB} in equations (3) and (5), and this is sufficient to introduce large differences in the relative adsorptivities of B and C. While B is more preferentially adsorbed than component C, in the reactions considered in the present work the equilibrium constant of the reaction given in expression (2), is always taken to be less than or equal to the equilibrium constant of the reaction producing species C.

In Table 1, typical values of the parameters of the model are given, and these are used in the simulations of the recycle sorption system and of the batch reactor studied in this work.

The model equations presented in Part I[1] are solved by using the orthogonal collocation method[13–15] and a Gear's algorithm[14,15] appropriate for integrating stiff ordinary differential equations.

RESULTS AND DISCUSSION

The values of the parameters used in the simulations are given in Table 1 and in the following Figures. It is of interest to note that for all systems studied, the volumes of the batch reactor and of the reactor in the recycle system are taken to be equal, as was the case in Part I[1] of this work. This implies that a volume of an inert fluid equal to the volume of fluid held in the sorber should be added in the recycle sorption system.

In Figures 2–4 the time variation of the inlet and outlet sorber concentrations of species B and C is shown, as well as the concentration of component A in the reactor of recycle sorption systems in which two parallel, first-order, reversible reactions occur. The breakthrough of component C occurs earlier than that of species B,

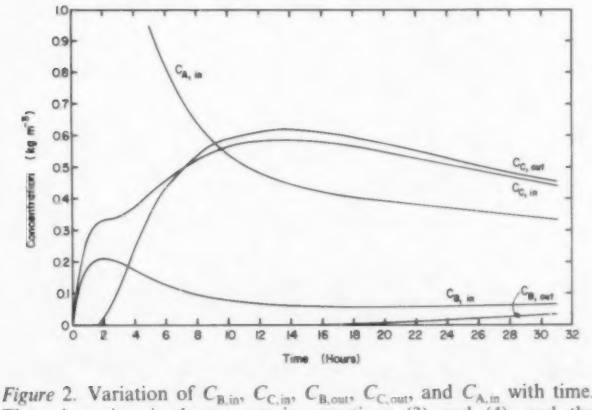


Figure 2. Variation of $C_{B,in}$, $C_{C,in}$, $C_{B,out}$, $C_{C,out}$, and $C_{A,in}$ with time. The adsorption isotherms are in equations (3) and (4), and the reactions are of first order with $k_1 = k_2 = 5.0 \times 10^{-5}\,s^{-1}$, $k_3 = 3.4 \times 10^{-5}\,s^{-1}$, and $k_4 = 6.8 \times 10^{-5}\,s^{-1}$.

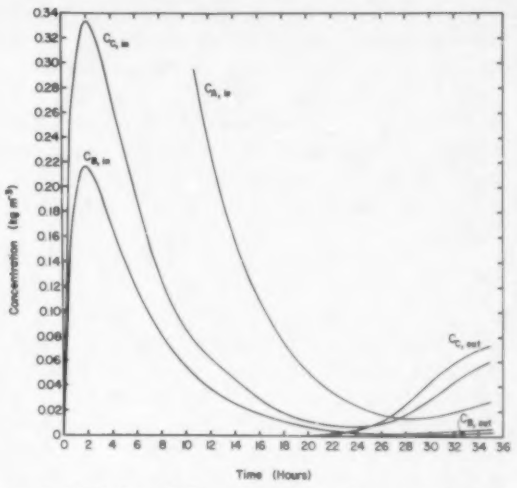


Figure 3. Variation of $C_{B,in}$, $C_{C,in}$, $C_{B,out}$, $C_{C,out}$, and $C_{A,in}$ with time. The adsorption isotherms are in equations (5) and (6), and the reactions are of first order with $k_1 = k_2 = 5.0 \times 10^{-5}\,s^{-1}$, $k_3 = 3.4 \times 10^{-5}\,s^{-1}$, and $k_4 = 6.8 \times 10^{-5}\,s^{-1}$.

since B is preferentially adsorbed over C. The difference in breakthrough times is significantly larger for the system with isotherms given by equations (3) and (4). The phenomenon of competitive adsorption is clearly demonstrated by the fact that $C_{C,out}$ is higher than $C_{C,in}$ after a certain period of operation. This implies that species B displaces component C from the adsorbent particles, as the sorption bed is loaded and there are not enough active sites on the internal surfaces of the particles to accommodate both components. By comparing the curves of $C_{C,in}$ in Figures 2 and 3, it is observed that the maximum value of $C_{C,in}$ in Figure 3 occurs at a time substantially smaller than that of $C_{C,in}$ in Figure 2, but the magnitude of the maximum value of $C_{C,in}$ in Figure 2 is more than 1.5 times larger than that of the system shown in Figure 3. This latter difference results from the fact that the variation in the adsorptivities of species B and C is much larger for the system in Figure 2 than that of Figure 3 as it is clearly demonstrated by the larger breakthrough time of C in Figure 3.

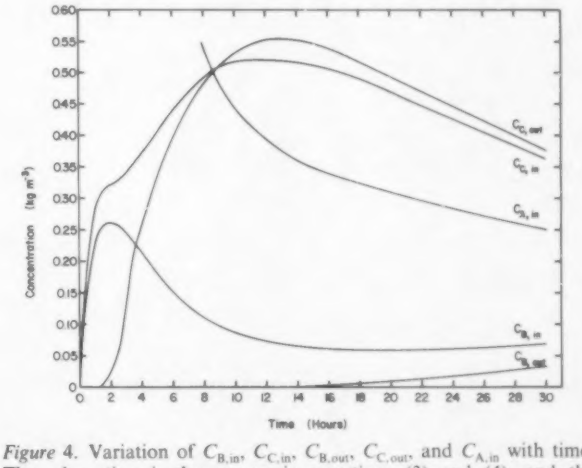


Figure 4. Variation of $C_{B,in}$, $C_{C,in}$, $C_{B,out}$, $C_{C,out}$, and $C_{A,in}$ with time. The adsorption isotherms are in equations (3) and (4), and the reactions are of first order with $k_1 = k_2 = 5.0 \times 10^{-5}\,s^{-1}$, and $k_3 = k_4 = 4.0 \times 10^{-5}\,s^{-1}$.

The curves for A are plotted after certain initial times, because the concentration values shown in the ordinates of Figures 2–5 are lower than the concentrations of component A for earlier times than those indicated. For those earlier times, $C_{A,in}$ decreases in a monotonic fashion. The concentration of species A is shown to decrease with time in a monotonic manner in Figures 2 and 4, while in Figure 3 species A attains a minimum value in the reactor near the breakthrough time of component B, and then $C_{A,in}$ increases with time. This clearly demonstrates that the concentrations of species A, B, and C in the reactor are such that after breakthrough of B occurs, there is net production of reactant A from its product C. Of course, the concentration of C in the reactor is sometimes such that species A is produced by the reaction given in equation (1), but the concentration of A still decreases with time since the forward reaction in equation (2) is dominant because the concentration of B in the reactor is extremely low. This phenomenon is clearly illustrated in Figures 2 and 4 where after a certain time, $C_{C,in}$ is greater than $C_{A,in}$. This indicates that since $k_1/k_2 = 1$, species C produces A in the reactor which in turn produces component B that is continuously removed in the sorber by displacing adsorbed C. Thus, there is no net production of A for the systems in Figures 2 and 4 while this is not the case for the recycle sorption unit in Figure 3. Also, in Figures 2 and 4 the change in the slope of $C_{C,in}$ occurs shortly after the breakthrough time of C, and $C_{C,in}$ increases for a certain time interval because $C_{C,out}$ increases and also C is produced in the reactor.

In Figure 5 the time variation of the same variables as in Figures 2–4 is shown for a recycle sorption system in which two parallel, second-order, reversible reactions occur. The dynamic behavior of the variables shown in Figures 2–5 has to be known in detail before proper economic considerations could be established that would allow the selection of a criterion for bed removal.

In Figures 6 and 7 the concentration profiles of C and B in the solid phase of the adsorbent particles are shown for various times, and halfway down the length of the fixed bed. It is shown that the concentrations of B are significantly higher than those of C, for times larger than 10 h. For times less than 10 h most of component B loads the bed close to the entrance of the sorber[15], and thus the less preferentially adsorbed species C is displaced and is being readsorbed at bed lengths in which the concentration of B is very low. As time progresses, the displacement wave propagates down the length of the bed so that the concentration of B increases while that of C decreases. In Figure 7 and for the time of 30 h, it is shown that the concentration of B is lower than that at 20 h, and also the concentration gradient indicates that elution of species B occurs. This happens because the concentration of B in the flowing fluid stream of the bed, is lower than that of the fluid in the pores of the adsorbent particles, and therefore component B is transferred from the center of the particle towards its outer surface. The concentration profiles in Figures 6 and 7 are representative[15] profiles, in qualitative terms, and are

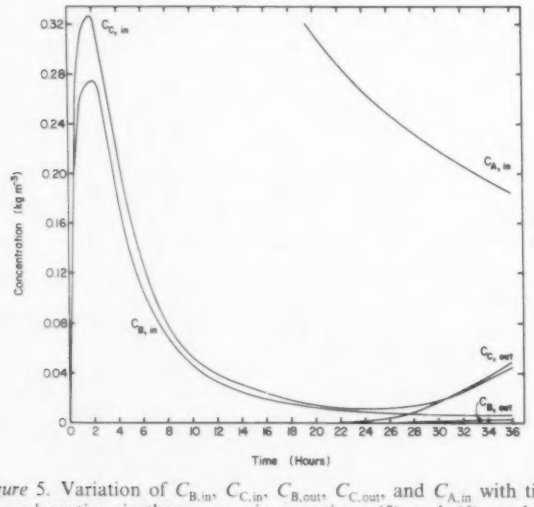


Figure 5. Variation of $C_{B,in}$, $C_{C,in}$, $C_{B,out}$, $C_{C,out}$, and $C_{A,in}$ with time. The adsorption isotherms are in equations (5) and (6), and the reactions are of second order with $k_1 = k_2 = 2.4 \times 10^{-5}\,m^3\,kg^{-1}\,s^{-1}$, and $k_3 = k_4 = 2.0 \times 10^{-5}\,m^3\,kg^{-1}\,s^{-1}$.

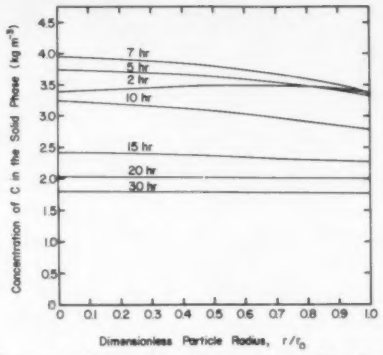


Figure 6. Concentration profiles of component C in the solid phase of the adsorbent particles for different times, at $x = 0.5\,L$. The adsorption isotherms are in equations (3) and (4), and the reactions are of first order with $k_1 = k_2 = 5.0 \times 10^{-5}\,s^{-1}$, $k_3 = 3.4 \times 10^{-5}\,s^{-1}$, and $k_4 = 6.8 \times 10^{-5}\,s^{-1}$.

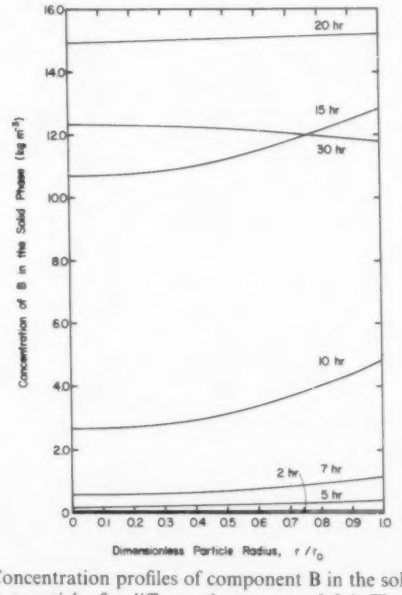


Figure 7. Concentration profiles of component B in the solid phase of the adsorbent particles for different times, at $x = 0.5\,L$. The adsorption isotherms are in equations (3) and (4), and the reactions are of first order with $k_1 = k_2 = 5.0 \times 10^{-5}\,s^{-1}$, $k_3 = 3.4 \times 10^{-5}\,s^{-1}$, and $k_4 = 6.8 \times 10^{-5}\,s^{-1}$.

VOL. 62 1984

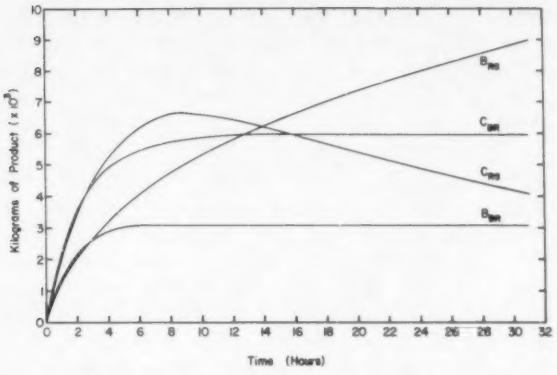


Figure 8. Variation of the total amounts of B and C produced with time. The adsorption isotherms are in equations (3) and (4), and the reactions are of first order with $k_1 = k_2 = 5.0 \times 10^{-5}\,s^{-1}$, $k_3 = 3.4 \times 10^{-5}\,s^{-1}$, and $k_4 = 6.8 \times 10^{-5}\,s^{-1}$.

encountered in various recycle sorption systems involving two parallel, first or second-order reversible reactions.

In Figures 8–11, the production of species B and C in various recycle-sorption systems is compared with the amounts of the same components produced in a batch reactor. It is observed that for a short initial time period the batch reactor may produce slightly larger amounts of B and C than the recycle sorption system. This time is fairly short when compared to the time scale of practical operation of recycle sorption systems[2,7], and this difference in production occurs because during the initial stage of operation, $C_{A,in}$ in the reactor of the recycle system is lower than the concentration of A in the batch reactor since the volume of fluid held in the sorber contains reactant A, and R_{di} and R_{pi} (i = A, B, C) are taken to be zero. This phenomenon was also observed in the systems studied in Part I[1] of this work.

In the systems of Figures 8 and 10, it is shown that the production of C in the recycle system reaches a maximum and then decreases with time and attains substantially lower values than those obtained in a batch reactor at fairly large times of operation. The reason for this is that species B is much more preferentially adsorbed over C with this set of isotherms than with the isotherms used in the systems of Figures 9 and 11, and thus, the decrease in the production of C occurs because after a certain

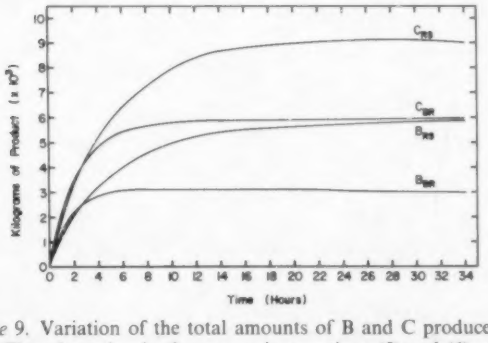


Figure 9. Variation of the total amounts of B and C produced with time. The adsorption isotherms are in equations (5) and (6), and the reactions are of first order with $k_1 = k_2 = 5.0 \times 10^{-5}\,s^{-1}$, $k_3 = 3.4 \times 10^{-5}\,s^{-1}$, and $k_4 = 6.8 \times 10^{-5}\,s^{-1}$.

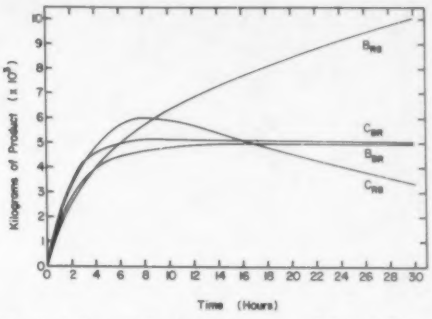


Figure 10. Variation of the total amounts of B and C produced with time. The adsorption isotherms are in equations (3) and (4), and the reactions are first order with $k_1 = k_2 = 5.0 \times 10^{-5}\,s^{-1}$, and $k_3 = k_4 = 4.0 \times 10^{-5}\,s^{-1}$.

time species C is converted to A which then produces more B that is continuously removed by the sorber.

If the goal, in the systems of Figures 8 and 10 is to produce large quantities of C, then the recycle sorption system operation may be terminated at the time when C has reached its maximum value. Otherwise, if the desired product is B then, at long times, the recycle system has a very favorable overall selectivity for B when it is compared with the selectivity obtained in the batch reactor, as is clearly shown in Figures 12 and 13.

The overall selectivity, S_0, is defined as the ratio of the total amount of B produced in a given system to the total amount of C produced in the same system. The selectivity S_0 at $t = 0$, is taken to be $S_0 = k_3/k_1$ which is equivalent to the point selectivity of the forward reactions in expressions (1) and (2), and this is done because at $t = 0$, the concentrations of B and C are so small that the reverse reactions in equations (1) and (2) do not occur to any extent. For infinite time of operation, the recycle system of Figure 12 would have a selectivity $S_0 = 12.0$, while the selectivity of the batch reactor is $S_0 = 0.5$. The recycle system of Figure 13 has an overall selectivity $S_0 = 34.5$ if infinite time of operation is considered, while the selectivity of the batch reactor would be $S_0 = 1.0$.

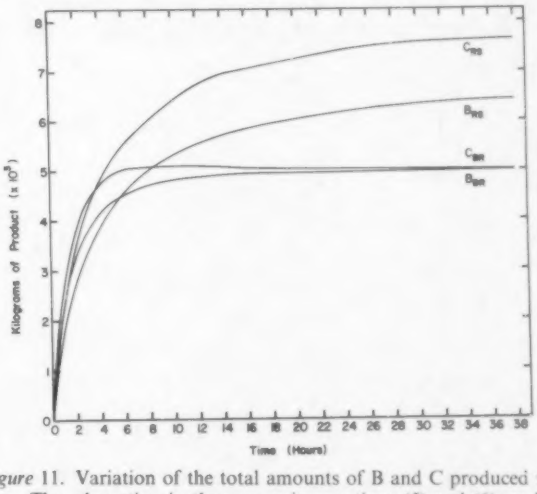


Figure 11. Variation of the total amounts of B and C produced with time. The adsorption isotherms are in equations (5) and (6), and the reactions are of second order with $k_1 = k_2 = 2.4 \times 10^{-5}\,m^3\,kg^{-1}\,s^{-1}$, and $k_3 = k_4 = 2.0 \times 10^{-5}\,m^3\,kg^{-1}\,s^{-1}$.

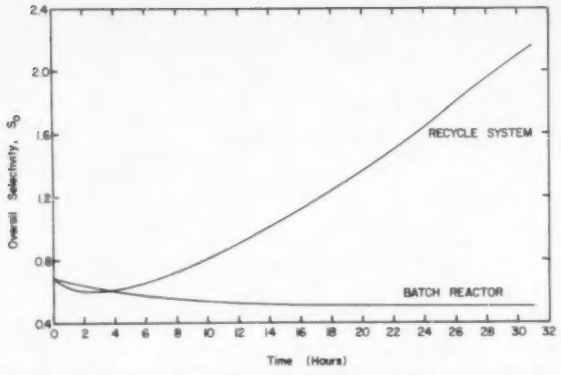


Figure 12. Variation of the overall selectivity, S_0, with time, in a recycle sorption system and in a batch reactor. The adsorption isotherms are in equations (3) and (4), and the reactions are of first order with $k_1 = k_2 = 5.0 \times 10^{-5}\,s^{-1}$, $k_3 = 3.4 \times 10^{-5}\,s^{-1}$, and $k_4 = 6.8 \times 10^{-5}\,s^{-1}$.

These results show that the recycle system, for the reaction networks considered in Figures 12 and 13, can dramatically increase the overall selectivity over that obtained from a batch reactor, especially when long times of operation are considered. The effect of the reaction rate constants can be observed by comparing the results in Figures 8 and 10, and 12 and 13.

The recycle system in Figure 8 may produce 2.92 times more B than the batch reactor, while the recycle system in Figure 10 can provide about 100% more of component B than the batch system. If an infinite time of operation is considered, then the recycle system in Figure 8 would produce 13.11×10^{-3} kg of B and 1.09×10^{-3} kg of C; the recycle system in Figure 10 would produce 13.68×10^{-3} kg of B and 0.396×10^{-3} kg of C. The batch reactor in Figure 8 would produce 3.0×10^{-3} kg of B and 6.0×10^{-3} kg of C as $t \to \infty$, while the batch reactor in Figure 10 would provide 5.0×10^{-3} kg of B and 5.0×10^{-3} kg of C.

In Figures 9 and 11, it is clearly shown that the recycle sorption system produces substantially more B and C than the batch reactor for all practical times of operation. In fact, the recycle system may produce 50% more of C and about 100% more of B than the batch reactor, for the first-order reaction system of Figure 9. In the second-order reaction system of Figure 11, the recycle system can provide about 30% more of B and 53% more of C than the batch reactor. For infinite time of operation, the reaction system in Figure 9 would have $B_{RS} = 7.24 \times 10^{-3}$ kg, $C_{RS} = 7.52 \times 10^{-3}$ kg, $B_{BR} = 3.0 \times 10^{-3}$ kg and $C_{BR} = 6.0 \times 10^{-3}$ kg. At equilibrium ($t = \infty$), the recycle system and the batch reactor in Figure 11 would give $B_{RS} = 9.79 \times 10^{-3}$ kg, $C_{RS} = 4.76 \times 10^{-3}$ kg, and $B_{BR} = C_{BR} = 5.0 \times 10^{-3}$ kg. These results show that the recycle system has a higher overall selectivity than the batch reactor, and produces significantly larger amounts of B than the batch system.

In Figures 14 and 15, the time variations of the amounts of C and B in the sorber and in the reactor of the recycle system are shown. It is observed that for the system with the isotherms given by equations (3) and (4), Figure 14, the amount of B in the sorber can be about 22.25 times larger than that of B in the reactor, while the amount of C in the reactor may be higher than that of C in the sorber. For certain times of operation it is shown that the amount of C in the sorber can be larger than that of C in the reactor but, as time increases and component C is being displaced by species B in the sorber, and also component C is converted to A which then becomes B in the reactor, the amount of C in the sorber and the reactor decreases with the rate of decrease being higher in the sorber. At the end of the recycle system operation, the ratios of the amount of B to that of C in the reactor and in the sorber, are 0.18 and 4.81 respectively, so that efficient separations of the products B and C may be realized[14,17]. If an infinite time of operation is considered, the ratios of the amount of B to that of C in the reactor and in the sorber of the recycle system, are 0.50 and 33.38 respectively. The results in Figure 8 show that for the batch reactor the ratio of the amount of B to that of C is 0.5 and therefore, the separation of species B and C may not be as efficient at the end of the batch system operation when compared with that for the recycle system.

The data in Figure 15 are for a system whose reaction rate constants are the same as in the system of Figure 14, but its isotherms are given by equations (5) and (6). For these isotherms, the difference in the relative adsorptivities of B and C is smaller than that provided by equations (3) and (4). Thus, at the end of the recycle operation the ratios of the amount of B to that of C in

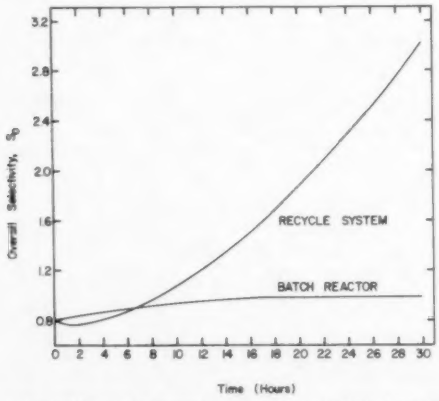


Figure 13. Variation of the overall selectivity, S_0, with time, in a recycle sorption system and in a batch reactor. The adsorption isotherms are in equations (3) and (4), and the reactions are of first order with $k_1 = k_2 = 5.0 \times 10^{-5}\,s^{-1}$, and $k_3 = k_4 = 4.0 \times 10^{-5}\,s^{-1}$.

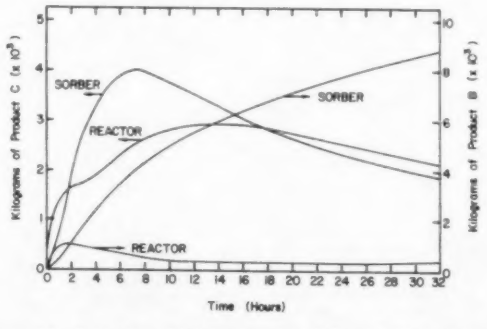


Figure 14. Variation of the amounts of B and C in the sorber and reactor of the recycle-sorption system with time. The adsorption isotherms are in equations (3) and (4), and the reactions are first order with $k_1 = k_2 = 5.0 \times 10^{-5}\,s^{-1}$, $k_3 = 3.4 \times 10^{-5}\,s^{-1}$, and $k_4 = 6.8 \times 10^{-5}\,s^{-1}$.

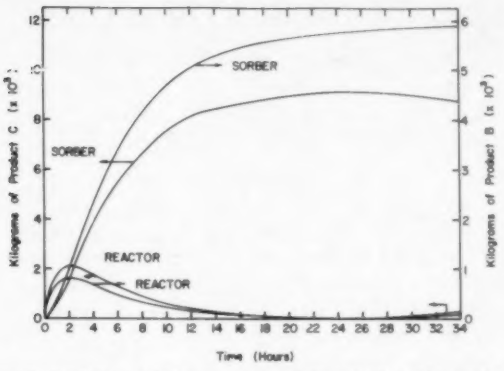


Figure 15. Variation of the amounts of B and C in the sorber and reactor of the recycle sorption system with time. The adsorption isotherms are in equations (5) and (6), and the reactions are first order with $k_1 = k_2 = 5.0 \times 10^{-5}\,s^{-1}$, $k_3 = 3.4 \times 10^{-5}\,s^{-1}$, and $k_4 = 6.8 \times 10^{-5}\,s^{-1}$.

the reactor and in the sorber, are 0.16 and 0.68 respectively. The ratio of 0.68 in the sorber indicates that the separation of species B and C will not be as efficient[17] as for the system of Figure 14, but the separation of the contents of the reactor may be as efficient as that for the system in Figure 14. In fact, the amount of B and C in the reactor in Figure 14, is about 7.29 times larger than that in the reactor in Figure 15. At equilibrium ($t = \infty$), the ratios of the amount of B to that of C in the reactor and in the sorber of the recycle system, are 0.50 and 0.98 respectively. Finally, the results in Figure 9 show that the ratio of the amount of B to that of C in the batch reactor is 0.5, and therefore the separation of species B and C may not be as efficient at the end of the batch system operation, when compared with that for the recycle system.

For the parallel second-order reaction system, Figures 5 and 11, the distributions of species B and C in the recycle sorption unit are qualitatively similar to those shown in Figure 15.

More details and results of the effects of the reaction rates of parallel, reversible reactions and of the multicomponent isotherms on the performance of recycle sorption systems, are found in the work of Casey[15].

CONCLUSIONS AND REMARKS

The results of this work have demonstrated that, if the proper adsorbent is employed in the sorber, the recycle sorption system can be very effective in reducing the formation of an undesired product, and in enhancing significantly the formation of a desired product when our reaction network consists of two parallel, reversible reactions and both products may be adsorbed in the sorber. The desired product is more preferentially adsorbed than the undesired product, and this leads to the displacement of the undesired product from the adsorbent particles and its conversion to the reactant, which is then converted to the desired product. This can lead to dramatic increases in the overall selectivity of the desired product, especially when the overall selectivity is compared with that obtained in a batch reactor. If it is desired to produce relatively large quantities of both products, then the recycle sorption operation may be terminated at a certain time in which relatively significant amounts of C and B have been produced (i.e. system in Figure 8.), and in this case the recycle system also provides a better performance than that obtained by a batch reactor.

It should be noted that if the adsorbent bed removes only one product, then the analysis presented in Part I[1] of this work is appropriate for treating such a system.

Finally, it was also shown that elution of the more preferentially adsorbed species B can occur, because the concentration of B in the flowing fluid stream of the sorber is lower than that of B in the fluid in the pores of the adsorbent particles.

In Part III of this work results are to be presented involving consecutive reactions in a recycle sorption system.

SYMBOLS USED

B_{BR}	total amount of B in the batch reactor (kg)
B_{RS}	total amount of B in the recycle-sorption system (kg)
B_S	total amount of B in a given system (kg)
C_{BR}	total amount of C in the batch reactor (kg)
C_i^0	concentration of solute i in the reactor at $t = 0$ (kg m^{-3})
$C_{i,in}$	concentration of solute i in the reactor (kg m^{-3})
$C_{i,out}$	inlet concentration of solute i in the reactor (kg m^{-3})
C_{RS}	total amount of C in the recycle sorption system (kg)
C_S	total amount of C in a given system (kg)
C_{pi}	concentration of solute i in pore fluid phase (kg m^{-3})
C_{si}	concentration of solute i in solid phase (per unit volume of particles) (kg m^{-3})
D_{Li}	axial diffusivity of solute i (m^2 s^{-1})
D_{pi}	effective diffusivity of solute i in pore fluid (m^2 s^{-1})
K_{fi}	film mass transfer coefficient of solute i (m s^{-1})
k_1, k_3	rate constants of the forward reactions
k_2, k_4	rate constants of the reverse reactions
L	length of sorber (m)
Q	recycle flow rate (m^3 s^{-1})
R_{di}	generation rate of solute in the fluid phase of the bed (kg m^{-3} s^{-1})
R_{pi}	generation rate of solute i in pore fluid phase (kg m^{-3} s^{-1})
r	radial distance in particle (m)
r_b	radius of sorber (m)
r_0	radius of particle (m)
S_0	overall selectivity, $\dfrac{B_S(t) - B_S(t=0)}{C_S(t) - C_S(t=0)}$
t	times (s)
V	volume of reactor (m^3)
V_f	superficial fluid velocity (m s^{-1})
x	bed length coordinate (m)
Greek letters	
ε	void fraction in the bed
ε_p	void fraction in particles

REFERENCES

1. Casey, J. T. and Liapis, A. I., 1984, *Chem Eng Res Des*, 62(5): 315–320.
2. Cooney, D. O. and Shieh, D. F., 1972, *AIChE J*, 18: 245–247.
3. Mor, L., Mor, L. A., Sideman, S. and Branders, J. M., 1980, *Chem Eng Sci*, 35: 725–736.
4. Holl, W. and Sontheimer, H., 1977, *Chem Eng Sci*, 32: 755–762.
5. Brauch, V. and Schlünder, E. U., 1975, *Chem Eng Sci*, 30: 539–548.
6. Shettigar, U. R. and Deepak, D., 1977, *Med Biol Eng Computing*, 15: 589–597.
7. Skalsky, M., 1978, *PhD Thesis* (Department of Chemical Engineering, University of New South Wales, Australia).
8. Walsh, P. K., Liu, C. P., Findley, M. E., Liapis, A. I. and Siehr, D. J., 1983, *Pr Fifth Symp Biotechnol Fuels Chemicals*, Gatlinburg, Tennessee, May. pp 629–647 (Wiley, New York).

9. Walsh, P. K., Liu, C. P., Findley, M. E. and Liapis, A. I., 1983, *Pr Fund Adsorption*, Schloss Elmau, Bavaria, West Germany, May. pp 667–678 (Engineering Foundation, New York).
10. Fritz, W. and Schlünder, E. U., 1974, *Chem Eng Sci*, 29: 1279–1282.
11. Liapis, A. I. and Rippin, D. W. T., 1977, *Chem Eng Sci*, 32: 619–627.
12. Liapis, A. I., *PhD Thesis*, 1977 (Eidgenössische Technische Hochschule, Zürich, Switzerland).
13. Villadsen, J. and Michelsen, M. L., 1978, *Solution of Differential Equation Models by Polynomial Approximation* (Prentice-Hall, New Jersey, USA).
14. Holland, C. D. and Liapis, A. I., 1983, *Computer Methods for Solving Dynamic Separation Problems* (McGraw-Hill Book Co, New York, USA).
15. Casey, J. T., 1984, *PhD Thesis* (University of Missouri, Rolla, USA).
16. Liapis, A. I. and Rippin, D. W. T., 1978, *Chem Eng Sci*, 33: 593–600.
17. Sherwood, T. K., Pigford, R. L. and Wilke, C. R., 1975, *Mass Transfer* (McGraw-Hill Book Co, New York, USA).

ADDRESS

Correspondence on this paper should be addressed to Professor A. I. Liapis, Department of Chemical Engineering, and Biochemical Processing Institute, University of Missouri-Rolla, 143 Schrenk Hall, Rolla, Missouri, 65401, USA.

The manuscript was received 4 January 1984 and accepted for publication 11 May 1984.

Book Reviews continued from page 343

Chemical Reactor Design and Operation
K. R. Westerterp, W. P. M. van Swaaij and A. A. C. M. Beenackers
John Wiley & Sons Inc., 1984
pp 746, £49.50

This book is a second edition of a text by Kramers and Westerterp first published by Chapman and Hall in 1963. Comparison of these two editions indicates how the subject of Chemical Reaction Engineering has expanded and developed over the last two decades. The new volume with almost 750 pages is three times the size of the first with major revisions and extensions particularly in chapters on non-ideal flow and heterogeneous systems. The approach of the book, however, remains very much the same with the authors attempting to specify from general principles what reactor type, size and mode of operation are most appropriate for a specific set of circumstances.

The text starts with an introductory chapter which closely resembles that in the first edition. Mass, energy and economic balances are covered briefly as are the subjects of thermodynamics and chemical kinetics. My feeling is that the pace of this and subsequent chapters is probably far too brisk for an undergraduate student of only average ability and that the style is more appropriate for those with an established interest and background in Chemical Reaction Engineering. Chapter 2 concerns ideal reactions including well-stirred vessels in series and the recycle reactor and the following three chapters introduce multiple reactions, residence time distributions and micromixing respectively. There then follow two long chapters on heat effects (95 pages) and multiphase reactors involving single reactions (133 pages). Chapters 8 and 9 then introduce the complexities of multiple reactions and the heat effects in multiphase situations and the final chapter concerns optimisation. There are no problems at the end of chapters but well over one hundred good illustrative examples appear throughout the book.

The text is written precisely with equations presented in a generalised nomenclature which, however, is not always easy to remember: for instance the choice of Φ to denote flowrates does seem unnecessarily at variance with widespread European and North American practice. References are quoted extensively and listed at the end of each chapter. There is a heavyness about the prose which perhaps arises because the authors are not writing in their mother tongue and this, together with the exorbitant price of the text, will certainly mean that it will not appeal to undergraduates. However, its detailed encyclopaedic coverage will earn it an important place amongst research groups and on the shelves of reference libraries.

A significant number of errors have escaped the attention of the proof readers and were these of a purely typographical nature they would not need mentioning. However, in several places sentences or parts of sentences are missing rendering the text incomprehensible (e.g. the bottom of page 228) or, in the case of section 1.3.2 on page 11, where the error of omission has led to the implication that thermodynamic equilibrium constants are a function of pressure and composition, wrong. I was so surprised to read this latter section that I went bact to the first edition and it was only then apparent that words had been inadvertently omitted from the text.

S. P. Waldram

VOL. 62 1984

GAS EXPLOSIONS IN COMPARTMENTED VESSELS: PRESSURE PILING

By J. SINGH (GRADUATE)

Dept. of Chemical Engineering, Imperial College, London

Maximum pressures and rates of pressure rise resulting from gas explosions in isolated vessels can be calculated fairly accurately and so appropriate steps can be taken to design process equipment adequately. Evidence from explosions in vessels divided into two compartments which are connected by a small opening, show that ignition in one can propagate into the other producing peak pressures and rates of pressure rise several times greater than in single vessel explosions. Calculation of these pressures and rates of pressure rise has up to now not been possible. Results of recent experimental work on gas explosions in pairs of cylindrical chambers connected to each other by small tubes are presented. The relative importance of parameters such as the volume and shape of the chambers, the point of ignition, the size of the connecting tube and the type of gas mixture are discussed and equations for the calculation of maximum pressures in such systems derived.

INTRODUCTION

Consider a vessel which is in the form of two chambers connected to each other by a small diameter tube and both containing a flammable gas. If the gas is ignited in one chamber, then the peak pressure that will be realised in the other can be many times greater than would be experienced if the explosion had occured in either one of the chambers in isolation. For example, whilst stoichiometric mixtures of most hydrocarbons in air (initially at atmospheric temperature and pressure) produce explosion pressures of about 8 bar in single vessels, these same mixtures have been shown to produce peak pressures in excess of 35 bar in compartmented vessels. The explosion of gases in multicompartmented vessels is usually referred to as "pressure piling".

Pressure piling was recognised as a special explosion hazard by Beyling[1] in 1906. He was working on the strength needed for commercial enclosures for electrical apparatus to be used in flammable atmospheres, when he noticed that enclosures that were divided into separate compartments and connected by small tubes, tended to suffer very violent and destructive explosions. Beyling identified the two most important parameters, namely that the enclosures were always compartmented and that they were connected by small diameter openings.

In the chemical industry interconnecting vessels and pipes handling flammable materials are commonplace and the hazard posed by pressure piling is therefore of considerable relevance.

The first piece of work undertaken specifically to investigate pressure piling was by Grice and Wheeler[2], who were initially working with spheres of up to 8 litres capacity, connected by short lengths of steel tubing 3.2 cm diameter, and a mixture of 9.5% methane in air. Their first set of experiments were done with spheres whose volume ratio was less than 10.0; it was found that although the pressure gradient in the sphere into which the explosion progressed was steeper than one would expect for a single spherical vessel, there was no evidence of pressure piling in terms of a high pressure. When the ignition source was moved from the centre to the wall furthest away from the connecting tube, the rate of pressure rise was further accelerated. The volume ratio of the spheres was then raised to 12.0 (by using larger spheres), and it was found that when the gas was ignited in the larger sphere, a gradual rise in pressure was followed by a peak of about 11.4 bar, maintained for a few milliseconds duration in the smaller vessel. (This pressure should be compared with a value of about 6.5 bar observed by these investigators in explosions of this mixture in single vessels). When, however, the explosion was initiated in the smaller vessel, neither the high rates of pressure rise nor the large pressure peaks were observed.

The rates of pressure rise recorded were explained in terms of the flame movement. It was observed in a different set of experiments using a carbon-monoxide/air mixture that as the flame proceeds towards the passage connecting the two compartments, the turbulence in the system causes the flame to vibrate. It was suggested that the rapid development of pressure when the ignition was started in the larger vessel was caused by the inflammation of a small volume of gas (corresponding to a small vessel) by a large source. Clearly when the flame travels from the smaller vessel into the larger one, the volume of gas to be burnt is larger and also the flame will not be as violent. The combined effect of these would reduce the rate at which the pressure can rise in the larger vessel.

The effect of the size of the passage connecting the compartments upon the extent of pressure piling was studied by Brown[3] using a pair of cylinders whose volume ratio was 13.5. A 3% pentane–air mixture was ignited at the extreme end of the larger cylinder whose length was about 45.7 cm and diameter 15.2 cm. The diameter of the connecting tube was varied from 0.64 cm to 2.54 cm, and its length from 6.35 cm to 38.10 cm. Pressure development in both chambers was recorded. The value of the pressure in the smaller chamber, when the rate of pressure rise in that chamber began to accelerate (after rising steadily for some time), was assumed by Brown to represent the total amount of gas compressed just before ignition. This "primary" pressure

© Institution of Chemical Engineers

(as Brown called it) and the time taken to reach it, were both recorded. Although the entry of the flame into the smaller chamber was not recorded, the criterion by which he estimated this time has been shown to correctly correspond with entry of the flame into the smaller chamber[4].

The results of this study showed that the effect of change in the length of the connecting tube is much less marked than the effect of change in diameter—both on the primary pressures and the peak pressures. Indeed, over the range of lengths used the primary pressure and peak pressure remained virtually constant at about 3.5 bar and 34.5 bar respectively. The primary pressure went up with increase in the diameter of the connecting tube, but the peak pressures went down, showing a maximum at 0.95 cm diameter.

A thorough study of the subject was also undertaken by Gleim and Marcy[5]. They worked with a box constructed from steel plate which could be sub-divided into different sections of different volume ratios by partition plates having openings of various sizes. The box could be divided into volumes of ratio 7.0, 3.0, 5.0 and 1.0; the partition plates had centrally located holes of diameters 25.4 cm, 20.3 cm, 10.2 cm, 5.1 cm and 10.2 cm square hole. A 9.5% natural gas–air mixture was used. Apart from changing the volume ratios and the size of the hole in the partition plates, they investigated the effect of varying the position of the spark.

Some of the results obtained by Gleim and Marcy appear to be inconsistent with those obtained by earlier workers; furthermore no attempt was made to measure the amount of compression in the compartment remote from the ignition. They did show that as the point of ignition was moved away from the separating plate, the explosion pressures recorded in the chamber remote from the ignition point, increased. However, contrary to the results obtained by previous workers, they found that as the volume ratio of the compartments was reduced the explosion pressures *increased*. They also observed that peak pressures in both compartments (i.e. the one in which the ignition was started, and the one remote from the ignition point) were very similar, irrespective of the condition of the experiment. The criticisms of this work relate to the few sets of experiments where pressure piling occurred. For example when the chamber was divided into two equal compartments, the maximum explosion pressure differed considerably depending on which compartment the ignition source was in, even though the relative position of the ignition source was virtually unaltered. Another anomaly was that the explosion pressure in the compartment remote from the ignition point was often much *lower* than that in the compartment containing the ignition source. In some cases the pressure in the compartment *containing* the ignition source was nearly three times the value expected in single chambers—an observation which not only contradicts all other findings but seems impossible to explain.

The experimental work described up to now has been quite extensive and in some cases fairly detailed. However it is difficult to use it all collectively due to the lack of a firm basis for comparison. The difficulty is that different workers used different shapes and sizes of vessels, measured different parameters—often with varying degrees of reliability—and used a variety of gas mixtures. Also, only Brown[3] measured the compression pressure in the vessel remote from the point of ignition.

The aim of the experimental work to be described[4,6] was to investigate all the parameters important to pressure piling on the same system in order to assess their relative importance and their interrelationship. This data will then be used to develop a model for the prediction of explosion pressures in compartmented vessels.

EXPERIMENTAL DETAILS

Explosion Vessels

All the experiments were carried out in a pair of cylindrical chambers connected to each other by a small tube. The larger chamber, referred to as the primary chamber, could be made up by joining any combination of three cylinders whose internal diameter was 30.48 cm and whose lengths were 22.86 cm, 29.85 cm and 45.09 cm. Seven different lengths could be achieved in this way.

The small, secondary chamber was a cylinder made of mild steel whose internal diameter was 15.24 cm, and effective length 38.1 cm. The volume of this chamber could be varied by adjusting the position of a gas-tight piston fitted inside it. The piston was made from a solid piece of dural, 7.65 cm thick and 15.20 cm in diameter; it had two "Dowty" 'u' seal rings fitted round it, one to enable the chamber to be evacuated, and the other, fitted in the reverse direction, to prevent any leakage when the cylinder was pressurised internally.

The arrangement had the flexibility to allow the volume ratio between the chambers to be altered whilst keeping the size of the primary chamber constant. Also the volume of the primary chamber could be varied without altering the volume ratio, simply by adjusting the position of the piston to compensate for the change in the volume of the primary chamber.

The two chambers were connected to each other by a cylindrical tube whose internal diameter was 7.62 cm and into which pipes (made of dural) of various wall thickness could be inserted, and in this way the internal diameter of the connection was altered. The length of the connection was fixed at 26.0 cm.

Gas Mixtures

The gas mixtures used in the course of the experiments were 9.5% methane in air, and 4.05% propane in air, both corresponding to approximately stoichiometric concentrations.

Ignition Source

The ignition source was a spark on the end of a specially made rod and powered by an induction coil. The ignition source was kept in the large chamber, the ignition rod being passed into the large chamber through the centre of the end plate and fixed at the required position along the axis. In the set of results to be described, the point of ignition was at the centre of the primary (large) chamber. Results of a later set of experi-

VOL. 62 1984

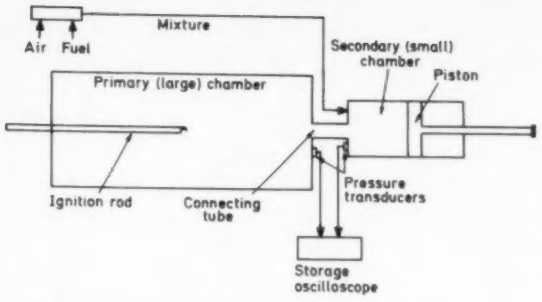


Figure 1. Arrangement of apparatus.

ments in which the point of ignition was moved are presented in a later section.

Pressure Sensors

Two different pressure transducers were used, a piezo-electric type in the small chamber and one consisting of a strain-gauge mounted on a specially designed aluminium diaphram in the large chamber.

Recording System

The outputs from the amplifiers of the strain gauge and piezo-electric transducers were displayed on a dual channel storage oscilloscope. The relevant parameters were obtained from the oscillograms after every run. From time to time, photographs of the oscillograms were taken using a conventional camera with an extension fitted to it. The photographs were developed and studied more carefully on an analyser which enlarged the negatives to 'A4' size and enabled the coordinates of the pressure-time curves to be determined. A diagram of the complete experimental set-up is shown in Figure 1.

RESULTS

The pressures generated in both chambers were displayed simultaneously on the storage oscilloscope and the important parameters recorded. In all these experiments the point of ignition was at the centre of the primary chamber. Only a sample of results can be reproduced here due to space limitations.

In the primary chamber, three parameters were considered to be of importance:

(i) P_m, the maximum pressure;
(ii) t_m, the time at which maximum pressure is attained;
(iii) P_z, the pressure in the primary chamber when the flame transfers into the secondary one.

In the secondary chamber, four parameters were measured:

(iv) t_1, the time at which the flame transfers from the primary chamber into the secondary one;
(v) P_1, the pressure in the secondary chamber at time t_1;
(vi) P_k, the peak pressure;
(vii) t_k, the time at which the peak pressure P_k is attained.

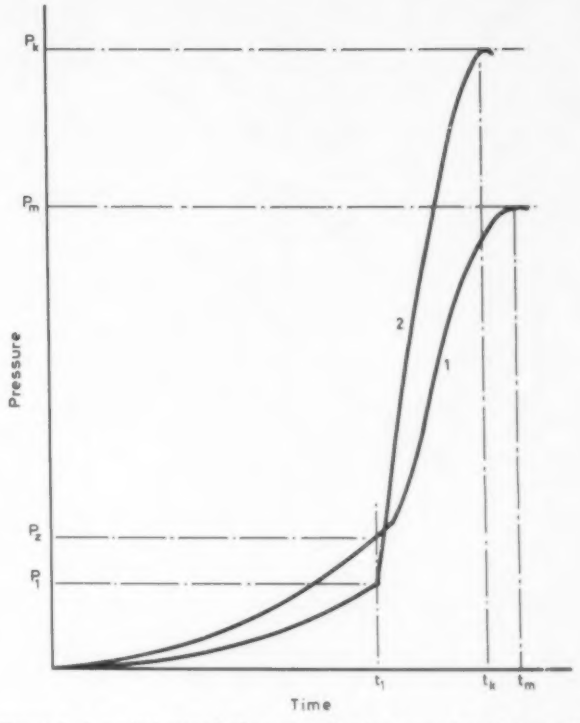


Figure 2. A typical record of an explosion in compartmented vessels, showing the variables measured. Pressure-time history in: 1, primary chamber; 2, secondary chamber.

These parameters are illustrated in Figure 2 which is a sketch of a typical oscillogram of an explosion in a compartmented vessel.

The only parameter which is ultimately of interest is P_k, the peak pressure (which occurs in the secondary chamber). The other six parameters are useful in building up a model of such explosions since they record the progress of the explosions before P_k is attained. Looking at all the parameters in turn, the following trends are observed from the experimental results:

P_m: this is similar to the maximum pressure observed in explosions in single vessels for the gas mixture used. The values of P_m for propane–air mixtures are higher (by about 0.5 bar) than for methane–air mixtures, in line with the results from single vessel explosion;

t_m: the time required to reach P_m is less than the time it would take to reach the maximum pressure in a single vessel equal in volume to the primary chamber.

P_z: this is found to be less than the maximum pressure in the primary chamber, P_m, varying between about 0.07 bar and 3.5 bar (gauge pressures), depending upon the experimental arrangements. As the diameter of the connecting tube increases (for given sizes of vessels), it decreases initially but then increases after reaching a minimum. For a fixed diameter connecting tube, P_z increases with the size of primary chamber.

P_1: generally follows the same trend as P_z, except that P_z is always greater than P_1, although the two

CERD 62/6–B

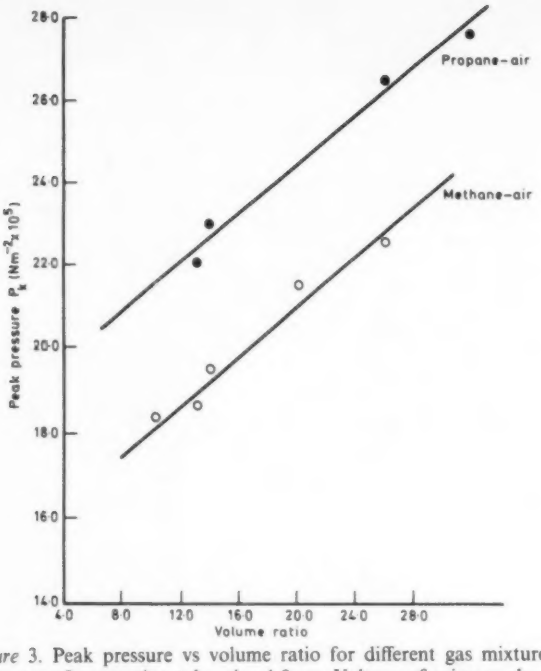


Figure 3. Peak pressure vs volume ratio for different gas mixtures. Diameter of connecting tube, $d_c = 1.9$ cm. Volume of primary chamber, $V_0 = 7.14 \times 10^{-2}$ m^3.

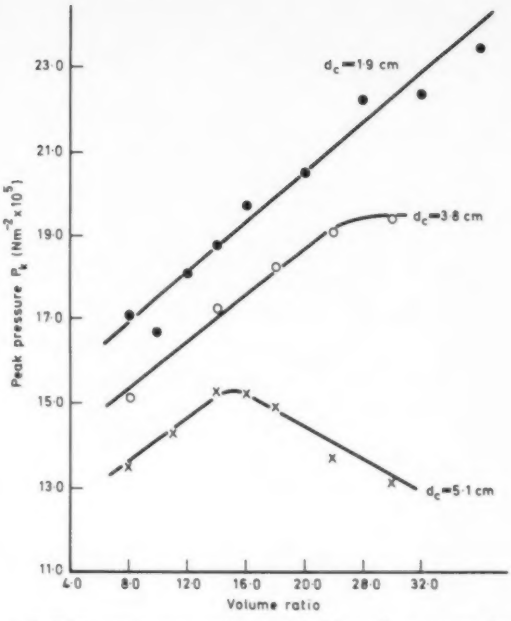


Figure 5. Peak pressure vs volume ratio for various connecting tube diameters. Gas: propane–air. Volume of primary chamber, $V_0 = 5.46 \times 10^{-2}$ m^3.

become closer as the connecting tube diameter increases.

t_1: this is always less than t_m (for the same experimental set-up); in general it increases with the size of the primary chamber.

t_k: this is about 3 to 10 ms greater than t_1, depending on the size of the primary chamber and the diameter of the connecting tube. The interval $(t_k - t_1)$ shows no real dependence upon the size of the secondary chamber.

P_k: (*a*) *Variation of P_k with volume ratio between the chambers*

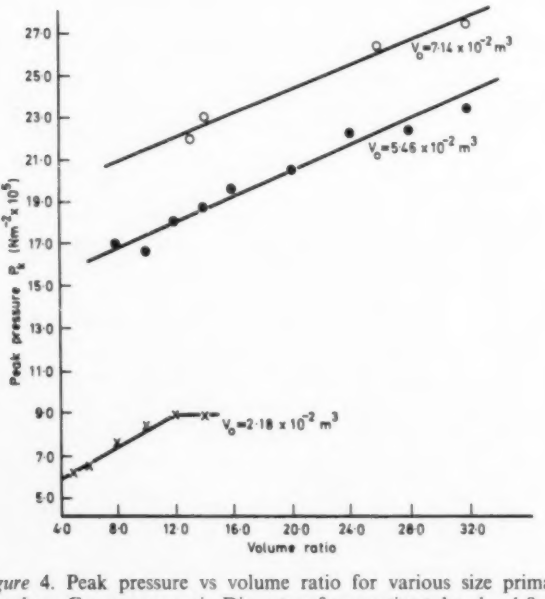


Figure 4. Peak pressure vs volume ratio for various size primary chambers. Gas: propane–air. Diameter of connecting tube, $d_c = 1.9$ cm.

The results, plotted in Figures 3 to 5, show that the peak pressure increases with volume ratio. (Volume ratio is defined as the volume of the primary chamber V_0 divided by that of the secondary chamber V_s.) This applies both for methane–air and propane–air mixtures at all sizes of large chamber and connecting tube diameter, up to a certain 'limiting' value of the volume ratio. Above this, the peak pressure levels off and eventually decreases with increasing volume ratio.

The 'limiting' value of the volume ratio increases with increasing volume of the large (primary) chamber, and decreases with increasing diameter of connecting tube. Also, the 'limiting' value is higher for propane–air than for methane–air. Under any given set of conditions, peak pressures for the propane–air mixtures were higher than for methane–air, see (Figure 3 for example).

(*b*) *Variation of P_k with diameter of connecting tube*
The results of these experiments (see Figure 6) show that the peak pressure decreases with the connecting tube diameter for propane–air. Similar conclusions apply for methane–air.

These generalizations do not apply when the diameter of the connecting tube is so small that the flame is unable to pass from the large chamber to the small one (due to quenching), nor when the volume ratio at which the diameters are varied is above the 'limiting' value mentioned earlier.

(*c*) *Variation of P_k with the size of the apparatus.*
The effect of scale of operation was studied by changing the volume of the large chamber, but keeping the diameter of the connecting tube fixed, and altering the size of the small chamber to compensate for changes in the volume of the large chamber so as to keep the volume ratio constant.

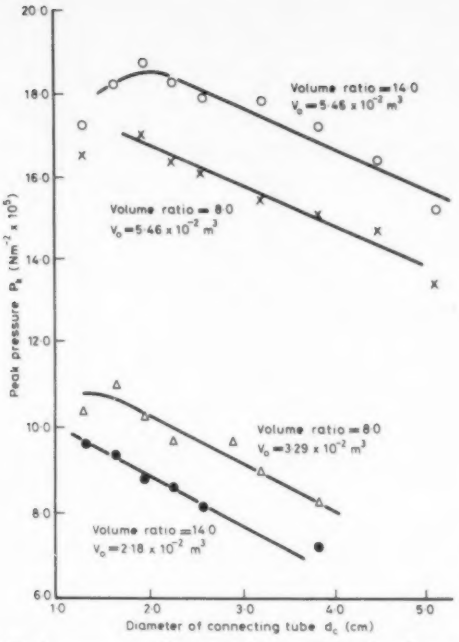


Figure 6. Peak pressure vs diameter of connecting tube. Gas: propane–air.

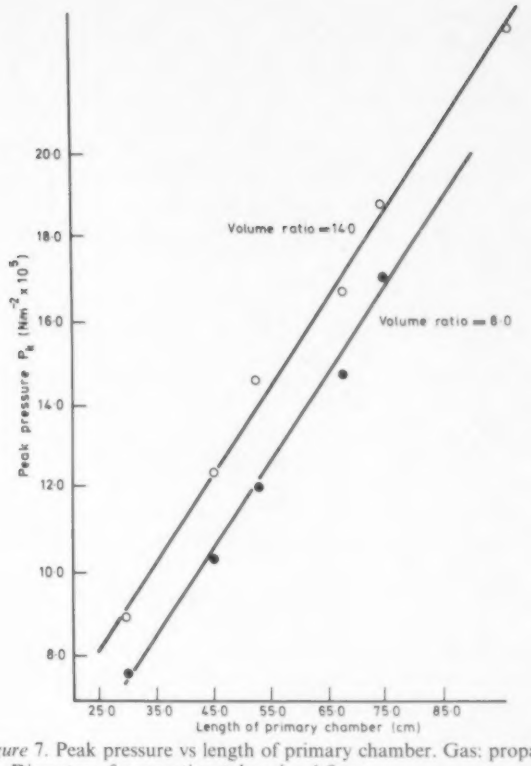


Figure 7. Peak pressure vs length of primary chamber. Gas: propane–air. Diameter of connecting tube, $d_c = 1.9$ cm.

A sample of the results are plotted in Figure 7. Clearly, P_k varies approximately linearly with size of large chamber over a variety of volume ratios (and connecting tube diameters). Both gas mixtures show a similar trend.

A MODEL FOR PRESSURE PILING

Basic Principles

The pressure–time relationship for explosions in single vessels follow the well documented 'S' shape and methods for accurate analytical description are available[7]. The maximum explosion pressures P_f in such explosions, which vary with the type and concentration of the flammable mixture and the initial conditions of temperature and pressure, can be calculated from:

$$P_f = P_0 \frac{\bar{T}_b}{T_0} \frac{M_f}{M_0} \tag{1}$$

where P_0 is the initial pressure, T_0 the initial temperature, $\bar{T}_b$ the mean burnt gas temperature and M_0 and M_f are the moles of reactants and products respectively. Approximate values for fuel–air mixtures can be obtained from:

$$P_f \cong P_0 T_f / T_0 \tag{2}$$

where T_f is the flame temperature of the fuel–air mixture.

Let us now consider a pair of vessels connected to each other by a pipe as shown in Figure 1, with both vessels containing the same flammable mixture at a pressure of P_0. If the mixture is ignited in the primary chamber at some point near the centre, the ensuing flame will expand outward from the ignition point causing a simultaneous rise in pressure. This will immediately produce a pressure difference between the primary and secondary chamber causing unburnt gas to be pushed out into the latter chamber. This process will continue until the flame propagates into the secondary chamber itself and ignites the gas within it. However, whereas the system was originally at a pressure P_0, the pressure in the secondary chamber at the point of ignition will be $P_1 > P_0$. Hence from equation (2), the maximum possible pressure in the secondary chamber will be

$$P'_k \cong \eta P_1$$

where η is a constant for the particular gas mixture and approximately equal to (T_f/T_0). (Strictly, the value of η for the initial mixture (at P_0) will be different to that for the compressed gas at P_1, but the difference is relatively minor.) The actual peak pressure experienced by the secondary chamber will be P_k, less than P'_k due to the fact that some gas will be vented back into the primary chamber. Hence in general,

$$P_k = P'_k - \Delta P = \eta P_1 - \Delta P \tag{3}$$

where ΔP is the reduction in pressure caused by the back-venting.

Even from this simple description of the explosion process, a number of the features observed in the experiments can be explained. Consider for example an increase in the length of the primary chamber, the position of the ignition source being altered such that it is still in the centre of the chamber. The initial influence of this will be to delay the time at which ignition in the secondary chamber will occur (since the flame will now travel a greater distance). Thus the quantity of gas that will be pushed out from the primary chamber and as a consequence the pre-ignition pressure P_1 in the secondary chamber will be higher than before, causing in turn

an increase in the peak pressure P_k. The effect of other parameters can be similarly discussed but this will not be pursued now as they will be discussed in detail in the forthcoming sections.

If equation (3) is taken as the starting equation, then P_1 and ΔP need to be determined in order to calculate P_k. In order to arrive at P_1, the rate of pressure rise in the primary chamber needs to be known since this is the driving force which leads to the compression in the secondary chamber.

Explosion Development in the Primary Chamber

General Pressure–Time Equations. Consider the ignition of a flammable mixture, of mass W_0 which has a fundamental burning velocity S_u, inside a primary chamber of volume V_0. As the pressure in this chamber rises due to the combustion, unburnt gas escapes. If W_u is the mass of unburnt gas in the primary chamber at time t then, prior to ignition in the secondary chamber,

$$-\left(\frac{dW_u}{dt}\right) = A_f S_u \rho_u + \frac{d}{dt}(\theta W_0) \tag{4}$$

where A_f is the area of the flame, ρ_u the density of the unburnt gas and θ = (mass of unburnt gas expelled from the primary chamber)/W_0.

Assuming adiabatic compression of the unburnt gas, it can be shown[6] that

$$\frac{dP}{dt} = \left(\frac{S_u A_f}{V_0}\right)^{(P/P_0)^x} \left(\frac{dn}{dP}\right)^{-1} \tag{5}$$

which is independent of θ and in fact identical to the equation describing explosions in single (non-compartmented) vessels[7] (where x is the inverse of γ_u, the ratio of specific heats). The value of n in equation (5) is equal to the fraction of the original gas in the primary chamber which is burnt at any pressure P and by definition is given by:

$$n = \frac{\rho_b}{\rho_u}\frac{V_0 - V_u}{V_0}$$

$$= \frac{V_0 - V_u}{V_0}\alpha$$

where V_u is the volume of unburnt gas, ρ_u the density of the gas originally in the primary chamber and ρ_b the mean density of the burnt gas and $\alpha = \rho_b/\rho_u$. If the flame is assumed to propagate spherically and the primary chamber is equivalent to a vessel of radius r, then for adiabatic compression of the unburnt gas[6]:

$$n = \alpha\frac{(P/P_0)^x - 1 + \theta}{(P/P_0)^x - \alpha} \tag{6}$$

and

$$r_b = r\left(\frac{(P/P_0)^x - 1 + \theta}{(P/P_0)^x - \alpha}\right) \tag{7}$$

where r_b is the radius of the sphere formed by the flame front. Putting $\theta = 0$ in equations (6) and (7) reduces them to equations for single vessels[7].

Solutions to General Equations. The pressure rise in the primary chamber as a function of time follows from equation (5) together with equation (6). This in turn will allow the pressure in the secondary chamber to be calculated. However, equation (5) cannot be solved as θ in equation (6) is unknown.

Further investigation of the variables involved allows some simplification. If V_s is the volume of the secondary chamber then the quantity of gas expelled into it when the pressure inside it is P_s is given by

$$W_{ex} = (P_s - P_0)V_s/(R\,T_u)$$

where R is the universal gas constant and T_u is the unburnt gas temperature. Hence,

$$\theta = (P_s - P_0)V_s/(P_0 V_0)$$
$$= (P_s - P_0)/(P_0 V_R) \tag{8}$$

where V_R is the volume ratio.

Analysis of the pressure profiles in the two chambers during the initial phase (see for example Figure 2) suggests that

$$\frac{P_s - P_0}{P - P_0} = \text{constant} = \sigma$$

If a pressure profile in the primary chamber is assumed and the resulting profile in the secondary chamber calculated, the same result is obtained.

Substituting for θ into equations (6) and (7) respectively,

$$n = \frac{(P/P_0)^x - 1 + \chi(P - P_0)/P_0}{(P/P_0)^x - \alpha}\alpha \tag{9}$$

$$r_b = \left(\frac{(P/P_0)^x - 1 + \chi(P - P_0)/P_0}{(P/P_0)^x - \alpha}\right)^{1/3} r \tag{10}$$

where $\chi = (\sigma/V_R)$. It is now possible to solve the P–t equations for the primary chamber as a function of χ. The value of χ must be established by trial-and-error for any given configuration (see the next section). Physically, χ is a measure of the influence of compartmentation on the pressure profile in the primary chamber. With $\chi = 0$, the equations reduce to those for a single chamber.

Using an experimentally determined value of χ and assuming $\alpha = P/\eta P_u$ (which is known to be a reasonable assumption[6]), equation (5) was solved for a stoichiometric methane–air explosion ($\eta \cong 7.5$) and the results are shown in Figure 8 together with the experimental results. The calculated values show reasonable agreement with experiment.

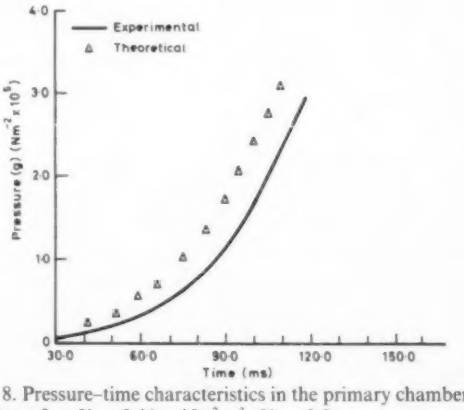


Figure 8. Pressure–time characteristics in the primary chamber prior to flame transfer. $V_0 = 5.46 \times 10^{-2}$ m^3. $V_R = 8.0$.

VOL. 62 1984

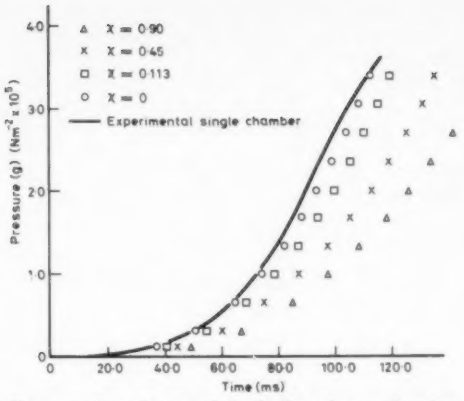


Figure 9. Pressure–time characteristics in the primary chamber prior to flame transfer. $V_0 = 5.46 \times 10^{-2}$ m^3.

This establishes the basic validity of the above equations and they can now be used to establish various parameters. It should be remembered that the analytical equations discussed so far are applicable only up to a time t_1 (see Figure 2), after which ignition in the secondary chamber occurs. The means for establishing this point has still to be evolved.

The values of χ for a range of experimental conditions[6] indicates that $\chi \ll 1.0$, the maximum observed value being approximately 0.11. The sensitivity of the results to χ is shown in Figure 9 and the results are compared with the experimental results of a single vessel explosion. Clearly, the effect of χ is minor in the practically observed range.

This leads to two important conclusions regarding explosion development in the primary chamber, viz.:

1. The pressure profile and the overall flame geometry, in compartmented and single vessel explosions are similar.

2. During the initial stages, the effect of compartmentation can be neglected without serious error, for most practical purposes.

Explosion Development in the Secondary Chamber

Calculation from First Principles. Having established the ability to trace the pressure–time characteristics in the primary chamber, the corresponding behaviour in the secondary chamber can now be predicted. The basic procedure from first principles is:

(*a*) assume a value of σ (and hence χ) and solve the equations for P–t in the primary chamber,

(*b*) using the P–t characteristics, calculate the quantity of gas lost into the secondary chamber at small increments of pressure,

(*c*) from the last two steps, evaluate the value of σ (and hence χ) and compare this with the value assumed in the first step and repeat the procedure until agreement is obtained.

Calculations of this type for a number of systems shows[6] that the pressure profile obtained is in reasonable agreement with experiment. However, this procedure is not amenable to hand calculation or even simplification to nomograms and so an empirical route is now proposed.

Calculation by Empirical Method. The relative pressures in the two compartments, as expressed by σ for example, will be governed by a number of parameters acting in different directions. The most significant of these are:

(*a*) the cross-sectional area of the connecting tube (proportional to d_c^2), which directly governs the rate of gas flow into the secondary chamber

(*b*) the volume of the secondary chamber (V_s) which determines the pressure rise in this chamber for a given quantity of gas transferred

(*c*) the period of time over which gas transfer occurs, which is related to the rate of pressure rise in the primary chamber. This may be expressed in terms of (S_u/r) provided spherical flame propagation in the primary chamber can be assumed. (This requires that the primary chamber should be of a fairly compact shape and that ignition is in the centre. The modifications required in the case of ignition at other points in the vessel are discussed in later sections.)

It should therefore be possible to correlate experimentally determined values of σ in terms of the parameter λ where

$$\lambda = \frac{d_c^2}{V_s}\frac{r}{S_u}$$

The plot of σ versus λ is shown in Figure 10; also shown are values of σ_z which is defined thus:

$$\sigma_z = \frac{P_1 - P_0}{P_z - P_0} \qquad (11)$$

The difference between σ and c_z is that whereas the former is a mean value for pressure ratio between the two chambers (prior to ignition in the secondary chamber), the latter represents the ratio at the moment when the flame enters the secondary chamber. It can be seen from Figure 10 that σ and σ_z level off at values of about 0.90 and 0.96 respectively, the corresponding value of λ being about 0.20 s m^{-1}. (For λ equal to 0.46 s m^{-1} and 0.56 s m^{-1}, beyond the range plotted, the values of σ and σ_z are still respectively 0.90 and 0.96).

Mechanism of Flame Transfer Between Chambers

General Description of Flame Behaviour. The use of Figure 10 or the equivalent analytical procedure allows simultaneous pressures in the connected chambers to be calculated up to a pressure P_z in the primary chamber. At this point flame transfer to the secondary chamber occurs and the entire process alters. A criterion for

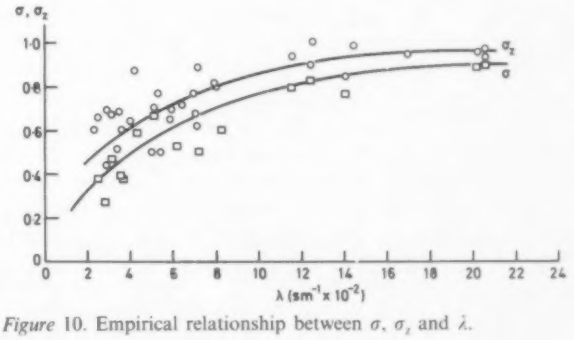


Figure 10. Empirical relationship between σ, σ_z and λ.

establishing this critical point will now be discussed, starting with available experimental observations.

In the experiments by Grice and Wheeler[2] on pressure piling in spherical chambers, some photographs showing flame movement were taken. For central ignition in the larger sphere, the flame travelling towards the smaller, the photographs showed that in the early stages the flame propagated symmetrically in all directions just as it would in the absence of compartmentation. After a few centimetres travel, it displayed a tendency to move more quickly towards the opening into the smaller chamber than in other directions; eventually it very quickly acclerated into the smaller chamber (half the size of the larger one), in which the gas was in a state of turbulence, before the flame in the larger chamber had reached the walls.

These observations are largely to be expected. Certainly at the start of the explosion, when the pressure in the primary chamber has risen only slightly above the pre-ignition pressure, the flame front would not show much distortion since the rate of flow into the secondary chamber would be small. As the pressure in the primary chamber increases, the flow rate through the connecting tube would increase and therefore the flame speed (i.e. the rate at which the flame moves relative to the walls of the chamber) will be greater towards the connecting tube than in other directions. This would explain the tendency to move more quickly in the direction of the connecting tube.

The tendency for the flame to dart across into the connecting tube and then into the secondary chamber in a very short period of time after it reached a point close to the connection is more difficult to explain. It seems that the unburnt gas between the flame front and the connecting tube assumes a velocity similar to that in the connecting tube (which is much higher than in the primary chamber generally) at some point ahead of the entry to the tube and when the flame reaches this point it is seen to accelerate into the tube and across to the secondary chamber. In fact it could be said that the *effective* entrance to the connecting tube is some distance ahead of the real entrance. This distance, Z say, determines the point at which flame transfer to (and subsequently ignition in) the secondary chamber will result.

The most direct method of obtaining further information to substantiate this theory is to photograph the development of the explosion in the same way as Grice and Wheeler did, for a range of variables such as the diameter of the connecting tube, the volume ratio, the type of gas mixture etc. As far as the experimental facilities in the present study were concerned, this was considered to be impractical. However, the pressure in the primary chamber at the moment of flame transfer, P_z, was measured, and this reveals the following trends:

(a) when the diameter of the connecting tube was less than about 3.2 cm, P_z remained constant with volume ratio (see Table 1a). Coincidentally P_z was greater than P_1 and λ much less than $0.20\ \mathrm{s\,m^{-1}}$ (and so $\sigma < 0.9$).

(b) at connecting tube diameters greater than about 3.2 cm (and generally implying that $\lambda > 0.20\ \mathrm{s\,m^{-1}}$, $P_z \cong P_1$ and so $\sigma \cong 0.9$), P_z increased with the volume ratio (see Table 1b).

Table 1. Some experimentally observed trends regarding P_z. (All results for system with $V_0 = 5.46 \times 10^{-2}\ \mathrm{m^3}$)

(a) $d_c = 1.9$ cm; 9.5% CH_4–air						
P_z ($\mathrm{Nm^{-2}} \times 10^5$, abs.):	3.89	3.41	3.69	3.51	3.55	
Volume ratio:	8.0	14.0	18.0	20.0	28.0	
(b): $d_c = 5.1$ cm, 9.5% CH_4–air						
P_z ($\mathrm{Nm^{-2}} \times 10^5$, abs):	2.43	3.00	3.21	3.66	4.06	4.45
P_1 ($\mathrm{Nm^{-2}} \times 10^5$, abs):	2.77	3.08	3.05	3.72	4.09	4.47
Volume Ratio:	11.0	14.0	16.0	18.0	22.0	26.0
(c): Volume ratio = 14.0						
P_z‡ ($\mathrm{Nm^{-2}} \times 10^5$, abs):	3.93	3.55	3.09	2.93	2.69	2.69	3.00
P_z† ($\mathrm{Nm^{-2}} \times 10^5$, abs):	4.10	3.41	3.30	2.90	2.70	2.70	3.00
d_c (cm)	1.6	1.9	2.2	3.2	3.8	4.4	5.1

(†9.5% CH_4–air, ‡4.05% C_3H_8–air)

(c) P_z showed no dependence upon the type of flammable mixture (see Table 1c).

From results such as these, it was postulated that the moment at which the flame transfers from the primary to the secondary chamber is determined entirely by the unburnt gas flow rate through the connecting tube; and at this point the distance between the entry to the connecting tube and the edge of the flame nearest to it is Z. Furthermore, Z increases with increase in the flow rate, and for a given flow rate, Z is fixed.

The implications of this proposal, with verification by further experimental data, are discussed later.

Quantification of Flame Transfer: Relationships for Z and P_z. It is possible to express Z as a function of the corresponding pressure P_z using established equations[7] between flame position and pressure (in the primary chamber) prior to flame transfer. Then, using known (experimental) values of P_z, the distance Z can be calculated.

It was shown above that compartmentation has little effect upon the position of the flame front in the primary chamber (apart from some distortion near the point of flame transfer). If the primary chamber is spherical and ignition occurs at the centre, then

$$Z = r - r_b(P_z)$$

From equation (7) for r_b, with $\theta = 0$,

$$Z = r\left[1 - \left(\frac{(P_z/P_0)^x - 1}{(P_z/P_0)^x - (P_z/\eta P_0)}\right)^{1/3}\right] \tag{12}$$

For a cylindrical chamber with $L \leqq 2r_c$, the flame will also propagate spherically and so for central ignition,

$$Z = L/2 - r_b(P_z) = L/2 - r_s\left(\frac{(P_z/P_0)^x - 1}{(P_z/P_0)^x - (P_z/\eta P_0)}\right)^{1/3} \tag{13}$$

where L is the length of the cylinder, r_c its radius and r_s is the radius of a sphere equal in volume to the cylinder. For longer cylinders (ideally $L \gtrsim 4\,r_c$), it has been found[7] that for central ignition, the position of the flame front measured from the point of ignition can be described by:

$$d(P) = r_c + d_1(P) - d_1(P_x)$$

where

$$d_1(P) = (L/2)\frac{(P/P_0)^x - 1}{(P/P_0)^x - (P/\eta P_0)} \tag{14}$$

VOL. 62 1984

and P_x is the pressure at which $r_c = r_b$ in equation (10). Hence for such a system,

$$Z = L/2 - d(P_z) = L/2 - r_c - d_1(P_z) + d_1(P_x) \quad (15)$$

Use of equations (12) to (15) (with $\theta = 0$) is justified by the simulations of explosion development in the primary chamber, given above, which show that in the initial stages the effect of compartmentation on the development of the flame is negligible.

Using experimentally measured values of P_z for a number of different connecting tubes (some experiments were undertaken specifically to measure P_z), values of z were calculated using the above equations. Configurations with $\sigma \cong 0.9$ were not used and this meant that values of d_c were less than 3.2 cm. The results of these calculations indicate that the relationship between the two parameters is

$$Z = d_c^{1.8} \quad (16)$$

both Z and d_c being in centimetres.

Thus a very simple relationship is obtained and it further verifies that Z is related to the flow rate (which is itself proportional to d_c^2). Using equation (16), together with the appropriate equation for a spherical chamber or for a cylindrical chamber, it is now possible to predict the pressure P_z, at which transfer of the flame into the secondary chamber will take place, given the size of d_c. However, equation (16) is strictly only valid in the 'small' diameter region i.e. when the pressure drop across the connecting tube is large enough to maintain a value for σ of less than about 0.9. When σ reaches this value, Z can take any value below the value given by equation (16), depending upon the volume of the secondary chamber (and the volume ratio).

Explicit Equations for P_z

In principle the primary chamber pressure at the point of flame transfer can be calculated from equations (12), (13) or (15), by substituting for Z from equation (16). In practice the equations are rather awkward, particularly equation (15) for long cylinders. Simplifications are therefore required for practical purposes. Consider first the nonlinear pressure term:

$$(P/P_0)^x = \left(\frac{P_0 + P - P_0}{P_0}\right)^x = \left(1 + \frac{P - P_0}{P_0}\right)^x \quad (17)$$

Provided, $(P - P_0)/P_0 < 1$, i.e. $P < 2P_0$, then

$$(P/P_0)^x \cong 1 + x\,(P - P_0)/P_0 = 1 + x\,(\bar{P} - 1) \quad (18)$$

where $\bar{P} = P/P_0$.
Substituting for $(P/P_0)^x$ into equation (7) (with $\theta = 0$)

$$r_b = r\left(\frac{\bar{P}x - x}{1 + x\bar{P} - x - (\bar{P}/\eta)}\right)^{1/3} \quad (19)$$

Therefore,

$$\bar{P} = \frac{x\,(r_b/r)^3 - (r_b/r)^3 - x}{x\,(r_b/r)^3 - (1/\eta)(r_b/r)^3 - x} \quad (20)$$

Hence, for a spherical chamber, the pressure P_z is given by,

$$\bar{P}_z = \frac{x\,(1 - Z/r)^3 - (1 - Z/r)^3 - x}{x\,(1 - Z/r)^3 - (1/\eta)(1 - Z/r)^3 - x} \quad (21)$$

where $\bar{P}_z = P_z/P_0$.
For a cylindrical vessel with $r_c \geqq L/2$, for which $r^3 = \frac{3}{4} r_c^2 L$:

$$\bar{P}_z = \frac{(4x/3r_c^2 L)(L/2 - z)^3 - (4/3r_c^2 L)(L/2 - z)^3 - x}{(4x/3r_c^2 L)(L/2 - z)^3 - (4/3r_c^2 L\eta)(L/2 - z)^3 - x} \quad (22)$$

For long cylinders, equation (14) becomes,

$$d_1(\bar{P}) = \frac{L}{2}\,\frac{(\bar{P}x - x)}{1 + x\bar{P} - x - (\bar{P}/\eta)} \quad (23)$$

Calculation of Z using equation (15) is now straightforward with P_x obtained from equation (20) with $r_b = r_c$ and $r = (3V_0/4\pi)^{1/3}$, and then $d_1(P_x)$ and $d_1(P_z)$ calculated from equation (23).

These equations can be simplified considerably if typical values for γ_u and η are substituted. For most mixtures of hydrocarbon–air or hydrogen–air, $\eta \cong 7.5$ and $\gamma_u \cong 1.4$. Therefore equation (21) for spherical chamber becomes

$$\bar{P}_z = \frac{-0.265\,(1 - Z/r)^3 - 0.735}{0.602\,(1 - Z/r)^3 - 0.735} \quad (24)$$

and equation (22) for a short length cylinder reduces to

$$\bar{P}_z = \frac{(0.353/r_c^2 L)(L/2 - z)^3 - 0.735}{(0.802/r_c^2 L)(L/2 - z)^3 - 0.735} \quad (25)$$

For long cylinders substituting $(3/4r_c^2 L)$ for r^3 and inserting numerical values for γ_u and η into equation (20) with $r_b = r_c$:

$$\bar{P}_x = \frac{-0.353\,(r_c/L) - 0.735}{0.847\,(r_c/L) - 0.735}$$

where $\bar{P}_x = P_x/P_0$. Equation (23) reduces to

$$d_1(P) = (L/2)\,\frac{0.735\,(\bar{P} - 1)}{0.602\,\bar{P} + 0.265} \quad (26)$$

Therefore, the value of $d_1(P_x)$ is given by

$$d_1(P_x) = \frac{0.735\left(\dfrac{-0.353\,(r_c/L) - 0.735}{0.847\,(r_c/L) - 0.735} - 1\right)}{0.602\left(\dfrac{-0.353\,(r_c/L) - 0.735}{0.847\,(r_c/L) - 0.735}\right) + 0.265}(L/2)$$

i.e.

$$d_1(P_x) = \frac{L}{2}\,\frac{-0.882\,(r_c/L)}{2 - 0.0825\,(r_c/L) - 0.637}$$

but $(r_c/L) \lesssim 0.2$ for large cylinders, hence

$$d_1(P_x) = 0.675\,r_c \quad (27)$$

Substituting for $d_1(P_x)$ and $d_1(P_z)$ from equations (27) and (26) into equation (15) gives the following expression for large cylinders:

$$\bar{P}_z = \frac{0.5\,(L/Z) - 0.0861\,(r_c/Z) - 0.265}{0.0665\,(L/Z) + 0.196\,(r_c/Z) + 0.602} \quad (28)$$

Using the simplified equations above, the position of the flame at a given pressure, or more important the pressure at a given flame position, can be easily calculated.

Maximum Pressure in the Secondary Chamber

General Approach. When the flame transfers from the primary to the secondary chamber, the gas mixture that it encounters in the secondary chamber is at a pressure, P_1, higher than when ignition occurred in the primary chamber. Also as a result of the compression, the gas in the secondary chamber is likely to be at a temperature, T_u, higher than the initial temperature, T_0. It is important to know the value of T_u because it can affect the value of η as indicated by equation (2). Some simple analysis[6] of various experimental systems showed that isothermal compression in the secondary chamber is a better assumption than adiabatic, so that $T_u \cong T_0$.

Ignition in the secondary chamber causes the pressure within that chamber to rise very rapidly (due to the fact that the gas is in a state of turbulence.) As a result, this pressure soon exceeds the level in the primary chamber, causing burnt gas to be vented back into the primary chamber. There is, however, lack of detailed information regarding the combustion process in the secondary chamber and the fluid flow. There is uncertainty regarding the nature of the turbulent combustion and hence the rate of pressure rise, the transport properties of the gas vented out of the secondary chamber, the gas flow mechanism through the connecting tube and the degree of choking that takes place inside it.

In view of these limitations, it is not possible to calculate accurately the amount of gas vented into the primary chamber. It is however possible to set up the basic equations required quite easily. If the mean molar gas flow rate during the venting period is $\bar{G}$ then the total amount of gas lost from the secondary chamber is $(t_k - t_1)\,\bar{G}$.

Therefore, the effect of the back-venting, in terms of a loss in pressure in the secondary chamber, is given by

$$\Delta P = \frac{\bar{G}\,(t_k - t_1)\,R\,\bar{T}_b}{V_s} \tag{29}$$

where $\bar{T}_b$ is the temperature of the burnt gas.

This equation assumes ideal gas behaviour. Hence recalling equation (3), the true peak explosion pressure, P_k, can now be calculated from the expression

$$P_k = P'_k - \frac{\bar{G}\,(t_k - t_1)\,R\,T_b}{V_s} \tag{30}$$

The difficulty in using this equation is that the interval $(t_k - t_1)$ is unknown.

The results of various studies confirm that turbulence plays a major role in the explosion mechanism in the secondary chamber. Rather surprisingly, a change in the volume of the secondary chamber has no detectable effect upon $(t_k - t_1)$. However, this may simply be due to the fact that the range of volumes with which experiments were done in this study was not large enough to influence the time duration significantly.

Empirical Equation. In the absence of further information regarding combustion in the secondary chamber, no progress can be made towards calculating $(t_k - t_1)$ directly. However, using the experimental results of the present study, an indirect method has been evolved. If g is the molar flow rate per unit area then ΔP may be rewritten as

$$\Delta P = Kg\,d_c^2\,(t_k - t_1)\,R\,\bar{T}_b/V_s$$
$$= J\,(d_c^2\,P_1/V_s)$$

where K is a constant and

$$J = \bar{T}_b\,K_g\,R\,(t_k - t_1)/P_1$$

There is a good reason to believe that J should be fairly constant for a wide range of systems. If this is so, then a plot of $(d_c^2\,P_1/V_s)$ against P_k should produce a straight line of slope J, for any number of different systems. Figure 11 shows such a plot for four different systems and lines of the same slope have deliberately been drawn through the data points; it is clear that to a good approximation J is constant. The value of J from Figure 11 is 4.62 m. A variable that this figure does not adequately take into account is the burning velocity of the mixture. This will effect $(t_k - t_1)$, an increase in the burning velocity for example will reduce this interval. Hence, assuming the time interval is proportional to the burning velocity, the value of J becomes 4.62 $(0.5/S_u)$, where 0.5 m s^{-1} is the average burning velocity for the two gases used in the present study and S_u that of the actual mixture. This gives a value for J of $(2.31/S_u)$.

Therefore the peak explosion pressure in the secondary chamber of a compartmented system can be obtained from

$$P_k = P_1\left(\eta - \frac{2.31}{S_u}\frac{d_c^2}{V_s}\right) \tag{31}$$

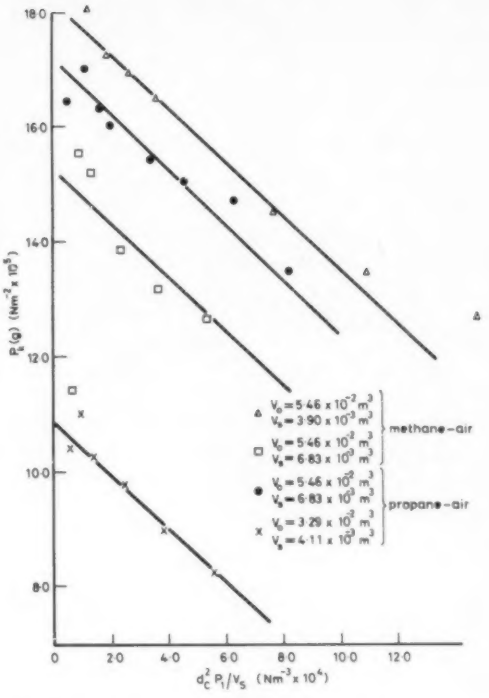


Figure 11. Peak explosion pressure against $d_c^2 P_1/V_s$.

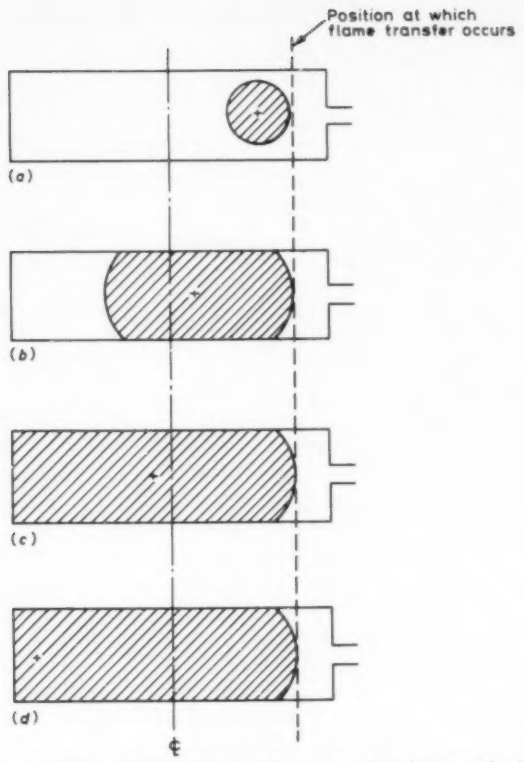


Figure 12. Effect of the position of the source of ignition on the degree of combustion prior to flame transfer.

Effect of Variations in the Point of Ignition: Qualitative Aspects

Consider a pair of connected cylinders, the primary one being of length L and radius r_c, where $r_c \ll L$. Suppose the distance from the point of ignition to the primary chamber end furthest from the connecting tube is y, which can be varied from L to 0, and that the diameter of the connecting tube is such that $Z \ll L$. The last condition ensures that the explosion will be reasonably developed before flame transfer occurs.

When the position of the point of ignition is such that y is nearly equal to L, the pressure in the primary chamber (and in the secondary) will rise by only a small amount when flame transfer occurs (i.e. P_z will be small). Essentially, under these conditions, the flame will expand spherically and when it gets to a distance Z from the connecting tube, it will flash across.

As y is decreased, the distance that the flame has to travel, and hence also the degree of burning that takes placed prior to flame transfer, will increase and consequently so will P_z. This is illustrated in Figures 12a and 12b where the shaded areas represent the volume of gas burnt.

Eventually, as y is decreased to below $L/2$, a critical point of ignition, y_c, will be reached when all the gas between the point z and the extreme end of the primary chamber will be burnt at the precise moment of flame transfer. This is shown in Figure 12c. If y is decreased still further, the amount of gas burnt prior to flame transfer will be unchanged (see Figure 12d) and hence P_z will also be unchanged. Clearly then, if the point of ignition is anywhere between $y = 0$ and $y = y_c$, the value of P_z should remain constant.

The pre-ignition pressure in the secondary chamber, P_1, corresponding with values of P_z is related by the parameter σ_z which is itself a function of λ. In general λ (and σ_z) are functions of the gas mixture and the experimental system only, except that when the flame propagation rate changes (as a result of ignition at one end of a vessel as opposed to the centre, for example) the *effective* burning velocity is altered. This will alter both λ and σ_z. Thus P_1 will increase as the point of ignition is moved away from the connecting tube (during the initial stages as a result of increase in P_z, with σ_z constant, and later for values of $y \leqq y_c$, when P_z is constant, due to increase in the value of σ_z.)

Hence, unlike P_z, P_1 would not be expected to become constant for y less than y_c. Furthermore, as P_k is proportional to P_1 (assuming equation (31) to be valid) the former should also increase continuously as the ignition point is moved away from the connecting tube.

Peak Explosion Pressure Due to Ignition at the Extreme End of the Primary Chamber

From a practical view point, it is of interest to know the maximum possible hazard, irrespective of where ignition takes place. In practice this necessitates determining the maximum explosion pressure when the source of ignition is at the primary chamber end furthest from the connecting tube. The analysis for doing such a calculation changes in two ways compared with central ignition: firstly it changes because the explosion develops more slowly, and secondly because the amount of gas burnt in the primary chamber prior to flame transfer increases.

The decrease in the rate of pressure rise in the primary chamber (prior to flame transfer) is reflected in σ_z, which increases slightly. For cylinders of the shape discussed in the last section, (and used in this study) σ_z can be determined in the same manner as for explosions due to central ignition (i.e. from Figure 10) provided S_u in λ is replaced by the 'effective' burning velocity $S_{u,eff}$, where

$$S_{u,eff} = S_u 2^{-1/3}$$

to reflect the fact that ignition is at one end.[7]

The increase in the amount of gas burnt in the primary chamber (prior to flame transfer), which is the second main effect of moving the point of ignition from the centre to the extreme end of the primary chamber, results in an increase in P_z. The pressure P_z is dependent upon the development of the flame front and its position prior to flame transfer and therefore in order to calculate P_z, the movement of the flame front must be quantified. Initially, the flame will develop as a hemispherical shell, its distance r_b from the point of ignition being given by[7]: $r_b = 2^{1/3} r_b$ (central ignition).

For short cylinders flame transfer into the secondary chamber will take place whilst the flame-front is still hemispherical.
Hence,

$$Z = L - r_b(P_z)$$

$$= L - 2^{1/3} r_s \left(\frac{\bar{P}_z x - x}{1 + \bar{P}_z x - x - \bar{P}_z/\eta} \right)^{1/3}$$

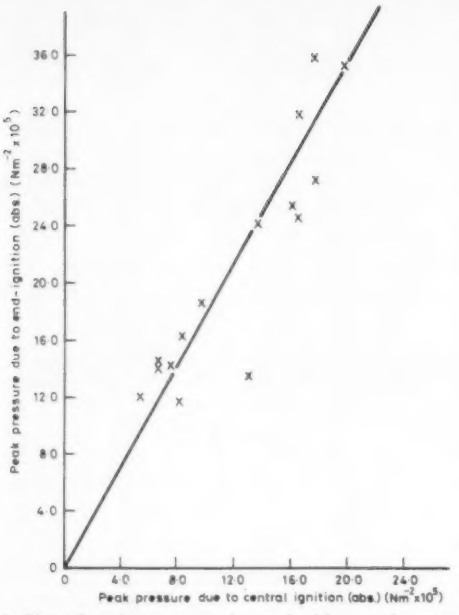


Figure 13. Plot of peak pressures due to ignition at the extreme end of the primary chamber against those due to ignition at the centre.

Rearranging,

$$\bar{P}_z = \frac{x[(L-Z)/r_s]^3 - [(L-Z)/r_s]^3 - 2x}{x[(L-Z)/r_s]^3 - (1/\eta)[(L-Z)/r_s]^3 - 2x} \quad (32)$$

For longer cylinders, the hemispherical shell will eventually change into a single, constant area flame front travelling towards the connecting tube. The relationship for Z changes[6] from equation (15) to

$$Z = L - r_c - d_2(P_z) + d_2(P_x) \quad (33)$$

where $d_2(P) = 2d_1(P)$.

Hence, it is possible to use the equations for central ignition but with L replaced by $2L$. The only objection to this replacement is that P_x is different in the two cases since the equations for r_b differ by a factor of $2^{1/3}$. However this difference is very small, and in any case P_x is normally very small compared with P_z. Therefore, putting $L = 2L$ in equation for P_z due to central ignition, the equivalent equation for explosions caused by ignition at the extreme end of the primary chamber becomes

$$\bar{P}_z = \frac{(L/Z) - 0.0861\,(r_c/Z) - 0.265}{0.1330(L/Z) + 0.196(r_c/Z) - 0.602} \quad (34)$$

As a final guide, a set of experiments with ignition at the extreme end of the primary chamber were carried out for a variety of systems. The results of these experiments are plotted in Figure 13 together with the corresponding peak pressures due to central ignition. This indicates that

$$\frac{P_k\,(\text{end-ignition})}{P_k\,(\text{central-ignition})} \cong 1.80$$

Therefore it is possible, for any system, to calculate P_k initially for central-ignition and then modify this value according to the above ratio.

REASSESSMENT OF MODEL ASSUMPTIONS

Flame Transfer Mechanism

One of the corner-stones of the model is the method for quantification of the point of flame transfer from the primary to the secondary chamber. It is suggested in the model that the flame approaches the connecting tube and at a distance Z from it, flashes across in the secondary chamber. It is further assumed that this critical distance is proportional to the (unburnt) gas flow rate ahead of the flame.

It was not possible (with the experimental facilities available) to substantiate the above mechanism directly, for example by recording the flame position and the corresponding gas flow rate through the connecting tube. However, by recalling that the flame position at point of flame transfer is related to pressure P_z (by definition), some progress is possible. For example, if under a certain range of conditions P_z is observed to remain constant (as in Table 1a) then Z would also have been constant; verification of the model then only requires that the gas flow rate into the secondary chamber was also constant.

Fortunately, it is fairly simple to estimate the flow rate from pressure records. If the pressure in the secondary chamber at time t after ignition in the primary chamber is P_s and the mean molar gas flow rate into the secondary chamber over this time is G then the amount of gas transferred must be Gt. If the volume of the secondary chamber is V_s, then it follows from the perfect gas law that,

$$P_s - P_o = (G\,t\,R\,T_u)/V_s \quad (35)$$

Clearly then,

$$G \propto (P_s - P_o)\,V_s/t \quad (36)$$

If the pressure–time history in the secondary chamber prior to flame transfer is availabe, then the mean flow rate, G, through the connecting tube can be calculated at any pressure in the primary chamber.

The flame transfer mechanism can therefore be tested against the experimental trends highlighted in Table 1. First of all, it was observed that for the 'small' diameter connecting tubes (where $\sigma < 0.9$) P_z remained constant with increase in volume ratio (Table 1a).

Consider now the primary chamber of volume 7.14×10^{-2} m^3, connected to the secondary chamber via a tube of diameter 1.9 cm. In a series of experiments with these chambers it was found[6] that with volume ratios between the chambers of 10.3, and 14.0 and methane as the flammable, σ had values of 0.47 and 0.59 respectively. When the volume ratio was 14.0, but the gas mixture changed to propane air, σ was 0.39. Clearly then, these cases fall into the category above where $\sigma < 0.9$. Also, in line with previous results the value of P_z in these three instances was constant at about 2.69×10^5 N m^{-2} (gauge). Now if P_z remains constant in the three cases then so must z; since flame transfer is dependent only upon z and the flow rate through the connecting tube, the latter must also be constant if the original postulate is true. The problem then, is to show that the flow rate in all three instances was the same.

For the purpose of comparison, the parameter $(P_s - P_o)V_s/t$, as in equation (36) can be used to repre-

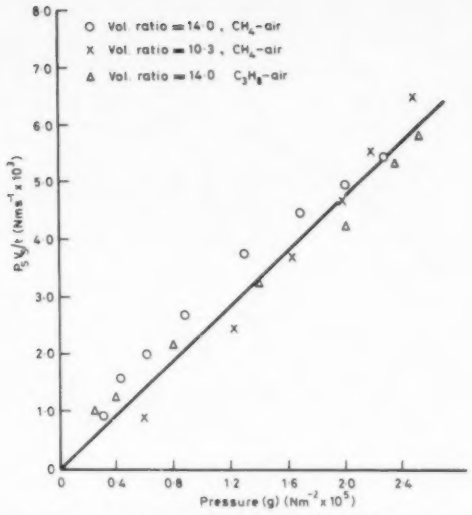


Figure 14. Flow rate (represented by P_sV_s/t) into the secondary chamber against pressure in the primary chamber ($d_c = 1.9$ cm).

sent the flow rate. Such a comparison is shown in Figure 14, which is a plot of the pressure in the primary chamber against $(P_s - P_o)V_s/t$ during the process of the three explosions; clearly, to very good approximation, the mean flow rate was the same during all three explosions.

The process that takes place when 'large' diameter connecting tubes are used (where $\sigma \cong 0.9$) must also be explained by the postulate. It was mentioned earlier that in this region when the volume ratio is increased, σ remains constant at about 0.9 and P_z increases (see Table 1b). If P_z increases then clearly Z must decrease, and if the proposal regarding flame transfer is correct, then the flow rate through the connecting tube must also decrease.

In order to test this, consider the primary chamber of volume 5.46×10^{-2} m^3 connected to the secondary chamber by a tube of diameter 5.1 cm and three different volume ratios, 22.0, 18.0 and 8.0 between the chambers. A plot of the pressure in the primary chamber against the pressure in the secondary chamber, prior to flame transfer during explosions in these systems shows[6] that σ is the same for all three volume ratios, and that its value is about 0.9. These three cases therefore fall into the 'large' diameter category and the problem is to show that the flow rate through the connecting tube decreased as the volume ratio was increased (i.e. as the volume of the secondary chamber was decreased).

Figure 15 is a plot of pressure in the primary chamber against $(P_s - P_o)V_s/t$ for these systems. It can be seen that the flow rate decreases as the volume ratio is increased, confirming the model prediction. Hence, it is reasonable to claim that the proposed mechanism for flame transfer is supported by available data.

Effect of Point of Ignition

The majority of experiments carried out were concerned with central ignition in the primary chamber and the basic model parameters were derived from this data. Based on this model, the effect of the ignition point on

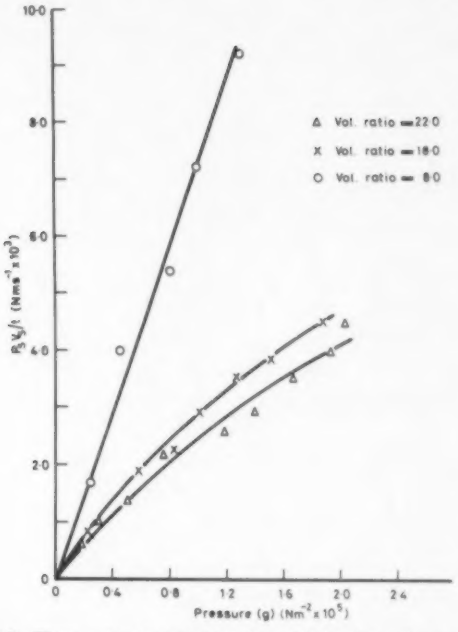


Figure 15. Flow rate (represented by P_sV_s/t) into the secondary chamber against pressure in the primary chamber ($d_c = 5.1$ cm).

P_1, P_z, and P_k was predicted and produced some interesting results as discussed earlier. It was predicted that the parameters P_1 and P_k should increase continuously as the ignition point is moved away from the connecting tube. However, P_z should increase initially but then at some position between the centre and the extreme end of the primary chamber, it should level off. The flame transfer mechanism discussed above is an essential element in these predictions.

Experimental verification of the above trends is clearly essential to establishing the credibility of the model. Therefore, an experiment with a stoichiometric methane–air mixture using a primary chamber of volume 3.29×10^{-2} m^3 was carried out. The volume ratio between the chambers was 14.0, the diameter of the connecting tube 1.6 cm and the point of ignition was moved along the axis of the primary chamber. The results of this experiment are summarised in Figures 16 and 17. Clearly the results relating to P_1, P_z and P_k are all in agreement with the predictions.

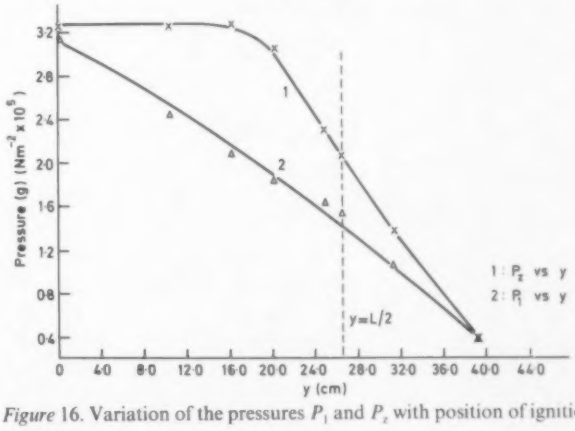


Figure 16. Variation of the pressures P_1 and P_z with position of ignition source, y.

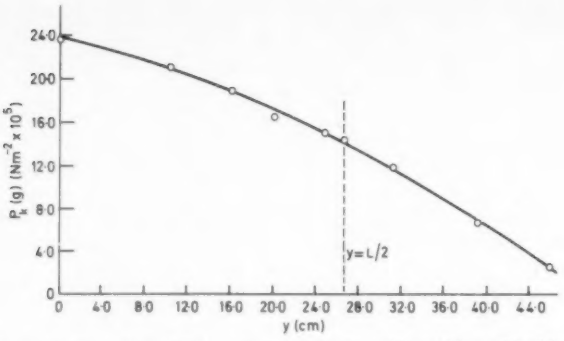


Figure 17. Variation of the peak pressure, P_k, with position of ignition source, y.

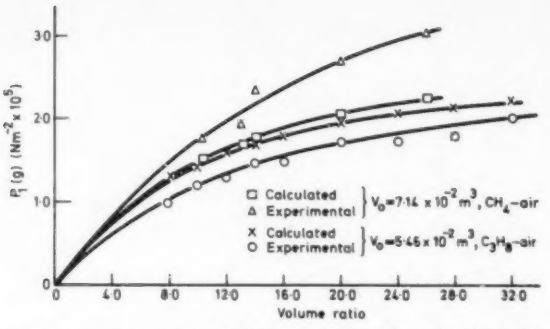


Figure 18. Comparison of calculated and experimental values of the pressure P_1 ($d_c = 1.9$ cm).

APPLICATION OF THE MODEL

Basic Procedure

The information required in order to use the model is the following:

(a) dimensions of the primary chamber
(b) diameter of the connecting tube
(c) volume of the secondary chamber
(d) S_u, η, and γ_u for the unburnt gas at the pre-explosion conditions.

Before proceeding with the calculation it is necessary to decide the likely point of ignition, the centre or the extreme end of the primary chamber being the two points considered in detail in the model. If the ignition point is unknown, then ignition at the extreme end should be taken, this being the most pessimistic.

For central ignition the calculation procedure is the following;

1. Calculate $\lambda = d_c^2 r / S_u V_s$.

For a cylindrical vessel, replace r by r_s, the radius of a sphere equivalent in volume to the primary chamber.

2. Using Figure 10, evaluate σ_z
3. From equation (16) calculate Z.
4. Using the equation appropriate for the primary chamber geometry, evaluate P_z. The simplified equations (which incorporate physical properties of stoichiometric hydrocarbon–air mixtures) for P_z are the following:

—spherical chambers, equation (24).
—short length cylinders, equation (25).
—long cylinders, equation (28).

5. Evaluate P_1 from the expression

$$\sigma_z = \frac{P_1 - P_o}{P_z - P_o}$$

6. Substitute P_1 into equation (31) to give P_k.

If ignition is assumed to be at the end of the primary chamber furthest from the connecting tube, two alternatives are available. The first is to use the above procedures for central ignition and then multiply the value of P_k by 1.80. The second is to apply suitable modifications to the above steps and thus calculate P_k 'rigorously'.

The modifications required are the following:

(a) In calculating λ, (step 1), use ($S_u 2^{-1/3}$) in place of S_u. This may lead to an over-estimate as discussed later, and so is not critical.

(b) The expressions relating to P_z are entirely different. For spheres or short cylinders equation (32) is relevant while for long cylinders, equation (33) (or the simplified equation (34)) should be used.

Comparison with Experimental Results

The first parameter compared is P_1, the pressure in the secondary chamber at the moment of ignition in it. Two systems are presented: a 7.14×10^{-2} m^3 chamber with methane–air explosion and a 5.46×10^{-2} m^3 chamber with propane–air explosion. The results, both calculated and experimental for the two systems at various volume ratios are shown in Figure 18. Agreement between them is quite reasonable.

The values of P_k from equation (31) for methane–air explosions in primary chambers of volumes 7.14×10^{-2} m^3 and 5.46×10^{-2} m^3 with a 1.9 cm connection are shown in Figures 19 and 20 at various volume ratios together with the experimental results. Good agreement is again obtained.

Finally, values for P_k due to ignition at the end of the primary chamber were calculated for three different

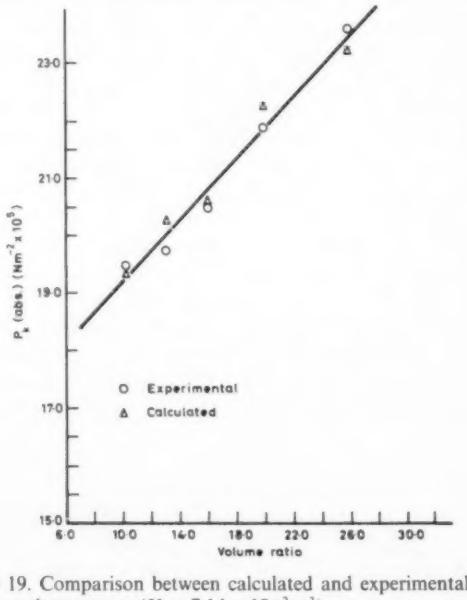


Figure 19. Comparison between calculated and experimentally determined peak pressures ($V_0 = 7.14 \times 10^{-2}$ m^3).

VOL. 62 1984

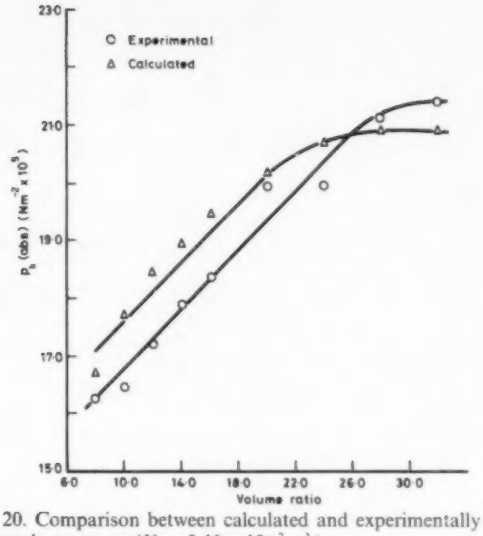


Figure 20. Comparison between calculated and experimentally determined peak pressures ($V_0 = 5.46 \times 10^{-2}$ m^3.)

systems. Also calculated were values of P_k using the true value of burning velocity (instead of $2^{-1/3} S_u$ as suggested by the analysis). The results are given in Table 2 together with the experimental values. It seems from this that the overall agreement is quite good and in fact use of the true burning velocity gives better agreement.

CONCLUSIONS

The equations presented should enable the explosion hazard presented by a pair of interconnected vessels to be assessed from a knowledge of the system geometry and the nature of the flammable gas. Although experimental verification will be necessary, it is expected that the results can be extrapolated to larger systems than studied at present.

Possible areas of application include electrical equipment casings in flammable atmospheres, and vessels and reactors for flammable gas handling systems such as in hydrocarbon oxidation plants. If the magnitude of the hazard is identified during the design stage, then either the process equipment can be designed to contain the explosion or the phenomenon can be 'designed out' by selecting suitable equipment geometries.

It has been suggested[8] that if the connecting tube as used in this study is replaced by a short orifice type connection, the system behaviour could be substantially altered due to the difference in turbulence that this would cause compared with a tube. The fact that varying the length of the connecting tube[3] from about 6 cm to 38 cm had no effect upon the explosion behaviour and that the degree of turbulence in the secondary chamber is so large even with a tube connection that it behaves almost like a stirred reactor, suggests that changing to an orifice type connection should have little or no effect. However, this also needs to be confirmed experimentally.

Another feature that would particularly benefit from further analysis is the mechanism of flame transfer from the primary to the secondary chamber. The complexity of this process is probably not adequately reflected by the model.

Table 2. Calculation of explosion pressures due to ignition at the extreme end of the primary chamber.
($V_0 = 5.46 \times 10^{-2}$ m^3, $d_c = 1.9$ cm)

System	Ratio of P_k (end-ignition) to P_k (central-ignition) Experimental	Calculated 1†	Calculated 2‡
9.5% CH_4–air $V_R = 14.0$	1.51	1.77	1.91
9.5% CH_4–air $V_R = 8.0$	1.58	1.71	1.97
4.05% C_3H_8–air $V_R = 14.0$	1.79	1.83	1.83

† Using true value of S_u.
‡ Using an 'effective' value of ($2^{-1/3} S_u$) for burning velocity.

SYMBOLS USED

A_f	area of flame front
d	position of non-spherical flame front from the point of ignition
d_1	see equation (14)
d_2	$2 d_1$
d_c	diameter of connecting tube
G	molar gas flow rate of unburnt gas from primary to secondary chamber
$\bar{G}$	mean molar burnt gas flow rate from secondary to primary chamber
g	$\bar{G}/Kd_c^2$
J	$\bar{T}_b KgR\,(t_k - t_1)/P_1$
K	(discharge coefficient) $\pi/4$
L	length of cylinder (primary chamber)
M_f	moles of burnt gas (products)
M_0	moles of unburnt gas (reactants)
n	fraction of original gas in the primary chamber burnt at any moment
P	absolute pressure in the primary chamber
P_1	pressure (absolute) in secondary chamber just prior to ignition in it i.e. at time t_1
P_f	peak pressure (absolute) in a single vessel explosion
P_k	peak pressure (absolute) in the secondary chamber
P_o	initial pressure (absolute)
P_s	pressure in secondary chamber ($P_o \leqq P_s \leqq P_1$)
P_x	the pressure at which flame ceases to expand after reaching the walls of the chamber
P'_k	$P_1 \eta$
P_m	maximum pressure in primary chamber
P_z	pressure in primary chamber at time t_1
$\bar{P}_f$	P_f/P_o
$\bar{P}$	P/P_o
$\bar{P}_x$	P_x/P_o
ΔP	$P'_k - P_k$
R	universal gas constant
r	radius of a sphere
r_b	distance of flame from point of ignition during a spherical explosion
r_c	radius of cylinder
r_s	$[(3/4)\, r_c^2 L]^{1/3}$ i.e. radius of sphere equal in volume to a cylinder
S_u	fundamental burning velocity
$S_{u,\text{eff}}$	'equivalent' value of S_u which can be used in spherical explosion equations to represent 'non-spherical' explosions.
T_0	initial (unburnt gas) temperature
T_b	burnt gas temperature
T_f	flame temperature
$\bar{T}_b$	mean temperature of burnt gas vented back into secondary chamber
T_u	unburnt gas temperature after compression
t	time
t_1	time at which flame transfers from primary to secondary chamber
t_m	time at pressure P_m
t_k	time at pressure P_k
V_0	volume of primary chamber
V_s	volume of secondary chamber
V_R	volume ratio $= V_0/V_s$

V_u	volume of unburnt gas
W_0	mass of gas in the primary chamber prior to ignition
W_u	mass of unburnt gas in the primary chamber after ignition
W_{ex}	amount of unburnt gas expelled from the primary to the secondary chamber
x	$1/\gamma_u$
y	distance from point of ignition to the primary chamber end furthest from the connecting tube
y_c	value of y below which P_z remains constant
Z	distance effective entrance to connecting tube is ahead of real entrance
α	ρ_b/ρ_u
γ_u	ratio of specific heats for unburnt gas
η	(peak explosion pressure in a single vessel)/(initial pressure) $= (P_f/P_0)$
θ	W_{ex}/W_0
λ	$d_c^2 r/V_s S_u$
ρ_u	density of unburnt gas
ρ_b	mean density of burnt gas
σ	$(P_s - P_0)/(P - P_0)$
σ_z	$(P_1 - P_0)/(P_z - P_0)$
χ	σ/V_R

REFERENCES

1. Beyling, E., 1906, *Glückauf*, 42: 97–99 and 129–138.
2. Grice, C. S. W. and Wheeler, R. V., 1929, *Papers, Safety-in-Mines Res. Bd*, No. 49, (HMSO, London).
3. Brown, T. J. A., 1959, *Tech Rep, Br Elec Allied Ind Res Assoc*, D/T 109.
4. Singh, J., 1975, *MSc Thesis* (University of London, Imperial College).
5. Gleim, E. J., and Marcy, J. F., 1952, *Rep Investig, U.S. Bur Mines*, No. 4904.
6. Singh, J., 1977, *PhD Thesis* (University of London, British Library Ref. No. D24652/78).
7. Singh, J., 1983, "The Calculation of Explosion Parameters in Non-spherical Vessels", paper summarising relevant single explosion equations.
8. Fitt, J. S., 1981, *The Chemical Engineer*, No. 368, p. 237.

ACKNOWLEDGEMENTS

The author would like to express his thanks to Prof D. H. Napier (now of Toronto University) for his advice during the research of this material and the Science Research Council for financial support.

ADDRESS

Correspondence on this paper should be addressed to Dr Jasbir Singh, Badger Personnel, c/o Celanese Chemicals Co Inc, P.O. Box 937, Pampa, Texas, 79066, U.S.A.

The manuscript was originally submitted 2 *July* 1982. *The revised manuscript submitted* 16 *January* 1984 *was accepted for publication* 17 *May* 1984.

VOL.
62
1984

FORCED CONVECTION HEAT TRANSFER OF POWER LAW FLUID AT LOW PECLET NUMBER FLOW

By Vi-Duong DANG

Department of Chemical Engineering, The Catholic University of America, Washington DC, USA

Heat transfer of Newtonian and non-Newtonian fluids in a tube with axial conduction and heat generation is analysed. An inlet boundary condition which accounts for the axial conduction effect is applied. Comparison of the present results with those of the previous researchers shows good agreement. The effect of Peclet number, power law model index and heat generation on the temperature field and Nusselt number is discussed.

INTRODUCTION

Following the early work of Graetz[1] and Nusselt[2], numerous papers have been published on heat transfer of Newtonian and non-Newtonian fluids in laminar pipe flow because of its practical importance in nuclear heat transfer and polymer processing.

For Newtonian fluids, Leveque[3], Sellars et al[4], Kays[5], Brown[6], Newman[7] among others investigated heat transfer without axial conduction of laminar pipe flow for the entrance or downstream region. When axial conduction becomes significant or Peclet number is low, Hennecke[8] and Hsu[9] extended the fluid entrance plane to $x = -\infty$ for the case of constant heat flux at the tube wall. Tan and Hsu[10], Michelsen and Villadsen[11] considered a similar problem with constant wall temperature. Sorensen and Stewart[12] presented an exact and simplified analysis for heat transfer with constant wall temperature by the collocation method.

For non-Newtonian fluids, numerous works may also be mentioned. Lyche and Bird[13] extended the Graetz–Nusselt problem to power law fluids. Toor[14] analysed the similar problem considering viscous dissipation and compression work. Yet Toor lumped these two effects together in his analysis and therefore the individual effects of these mechanisms are not easily distinguished. Metzner et al[15,16] presented theoretical analysis and experimental correlation for heat transfer to non-Newtonian fluid. Christiansen and Craig[17] considered temperature dependent viscosity in their analysis so that they could get good agreement between experimental data and theoretical predictions. Oliver and Jensen[18] presented a new correlation expression which could be applied to cases where natural convection was significant. McKillop[19] applied the method of finite differences to investigate heat transfer of power law fluid in the entrance region of a pipe. A recent analysis of pseudoplastic fluids with arbitrary wall heat flux has been performed by Faghri and Welty[20]. Hieber[21] also investigated the viscous heating effect at the entrance and downstream region. All of this work was performed for high Peclet number flow. Little has been reported for non-Newtonian fluid heat transfer at low Peclet number flow.

Axial conduction in heat transfer can become significant in liquid metal heat transfer or high density polyethylene flow[22]. The former can be considered as Newtonian flow while the latter can be treated as non-Newtonian. For non-Newtonian fluid with significant axial conduction, the inlet temperature distribution may not be uniform and hence relatively little work has been reported in this subject. The objective of the present paper is to examine heat transfer of power law model fluid at low Peclet number flow in a pipe taking account of viscous dissipation and internal heat source.

ANALYSIS

When a non-Newtonian power law model fluid flows inside a tube with constant physical properties in the laminar flow region, one can obtain a microscopic energy balance for the system. When viscous dissipation and heat generation are also considered, as in polymer flow or nuclear thorium oxide slurry, the energy balance equation and the boundary conditions are

$$\rho C_p u_{max}\left[1-\left(\frac{r}{a}\right)^{s+1/s}\right]\frac{\partial T}{\partial x}=k\left[\frac{1}{r}\frac{\partial}{\partial r}\left(r\frac{\partial T}{\partial r}\right)+\frac{\partial^2 T}{\partial x^2}\right]+m\left|\frac{\partial U_x}{\partial r}\right|^{s-1}\left(\frac{dU_x}{dr}\right)^2+q \tag{1}$$

$$uT-\frac{k}{\rho C_p}\frac{\partial T}{\partial x}=uT_0 \quad \text{at} \quad x=0 \tag{2}$$

$$\frac{\partial T(x,0)}{\partial r}=0 \tag{3}$$

$$T(x,a)=T_w. \tag{4}$$

In equation (1), s is the power law model index and the last two terms are the viscous dissipation and heat generation term respectively. Equation (2) is a simplified inlet condition rather than uniform inlet temperature[23] when axial conduction is important. This kind of boundary condition has been applied to Newtonian fluid

© Institution of Chemical Engineers

systems previously[12,24,25]. A more exact method for the inlet boundary condition equation (2) is reported elsewhere[9,26]. Equation (3) is symmetric condition at the centre of the tube while equation (4) is constant wall temperature.

Introducing the following dimensionless parameters

$$\eta = \frac{r}{a},$$

$$\theta = \frac{T - T_w}{T_0 - T_w},$$

$$\xi = \frac{kx}{\rho C_p a^2 u_{max}} = \frac{x}{aPe},$$

$$\delta = \frac{qa^2}{k(T_0 - T_w)}$$

$$Br = \frac{mu_{max}^{s+1} a^{-1-s}}{k(T_0 - T_w)}$$

one can transform equations (1)–(4) to the following dimensionless form

$$(1-\eta^{s+1/s})\frac{\partial\theta}{\partial\xi} = \frac{1}{\eta}\frac{\partial}{\partial\eta}\left(\eta\frac{\partial\theta}{\partial\eta}\right) + \frac{1}{Pe^2}\frac{\partial^2\theta}{\partial\xi^2} + Br\left(\frac{s+1}{s}\right)^{s+1}\eta^{s+1/s} + \delta \quad (5)$$

$$(1-\eta^{s+1/s})(\theta - 1) - \frac{1}{Pe^2}\frac{\partial\theta}{\partial\xi} = 0 \quad \text{at} \quad \xi = 0 \quad (6)$$

$$\theta(\xi, 1) = 0 \quad (7)$$

$$\frac{\partial\theta(\xi, 0)}{\partial\eta} = 0. \quad (8)$$

Solution of equations (5)–(8) can be obtained by superposition as

$$\theta(\xi, \eta) = \theta_1(\eta) + \theta_2(\xi, \eta) \quad (9)$$

where $\theta_1(\eta)$ can be readily obtained as

$$\theta_1(\eta) = Br\left(\frac{s+1}{s}\right)^{s+1}\left(\frac{s}{3s+1}\right)^2(1-\eta^{3s+1/s}) + \frac{\delta}{4}(1-\eta^2) \quad (10)$$

$\theta_2(\xi, \eta)$ can be considered as series expansions as

$$\theta_2(\xi, \eta) = \sum_{n=1}^{\infty} A_n R_n(\eta)\exp(-\alpha_n^2\xi). \quad (11)$$

Substitute equation (11) into equations (5)–(8), one can obtain the governing equations for $R_n(\eta)$ as

$$\frac{1}{\eta}\frac{d}{d\eta}\left(\eta\frac{dR_n}{d\eta}\right) + \alpha_n^2\left[1 - \eta^{s+1/s} + \frac{\alpha_n^2}{Pe^2}\right]R_n = 0 \quad (12)$$

$$R_n(1) = 0 \quad (13)$$

$$\frac{dR_n(0)}{d\eta} = 0 \quad (14)$$

$$\sum_{n=1}^{\infty}\left[1 - \eta^{s+1/s} + \frac{\alpha_n^2}{Pe^2}\right]A_n R_n = (1-\eta^{s+1/s})[1 - \theta_1(\eta)]. \quad (15)$$

Eigenfunctions $R_n(\eta)$ can be obtained from equations (12)–(14). To determine the coefficients A_n, first multiply equation (15) by ηR_n and then integrate the whole equation with respect to η from 0 to 1. One then gets

$$A_n\int_0^1\left(1 - \eta^{s+1/s} + \frac{\alpha_n^2}{Pe^2}\right)\eta R_n^2\,d\eta + \sum_{\substack{m=1\\ m\neq n}}^{\infty}\int_0^1\left(1 - \eta^{s+1/s} + \frac{\alpha_m^2}{Pe^2}\right) \times A_m\eta R_n R_m\,d\eta = \int_0^1(1-\eta^{s+1/s})[1-\theta_1(\eta)]\eta R_n\,d\eta. \quad (16)$$

The second term of equation (16) can be further simplified by the following procedure. Multiply equation (12) in terms of R_n by R_m and equation (12) in terms of R_m by R_n and then take the difference of these two equations. Integrate the resulting difference equation with the application of equations (13) and (14). After rearrangement and simplification, one finally obtains the following set of algebraic equations.

$$A_n J_n + \sum_{\substack{m=1\\ m\neq n}}^{\infty}\Gamma_{n,m}A_m = I_n \quad (17)$$

where

$$J_n = \int_0^1\left[1 - \eta^{s+1/s} + \frac{\alpha_n^2}{Pe^2}\right]\eta R_n^2\,d\eta \quad (18)$$

$$\Gamma_{n,m} = -\frac{\alpha_n^2}{Pe^2}\int_0^1\eta R_n R_m\,d\eta \quad (19)$$

$$I_n = \int_0^1(1-\eta^{s+1/s})\left[1 - Br\left(\frac{s+1}{s}\right)^{s+1}\left(\frac{s}{3s+1}\right)^2(1-\eta^{3s+1/s}) - \frac{\delta}{4}(1-\eta^2)\right]\eta R_n\,d\eta. \quad (20)$$

The dimensionless average temperature is defined as

$$\theta_b = \frac{\int_0^a u_x\theta r\,dr}{\int_0^a u_x r\,dr}. \quad (21)$$

By substituting equations (9)–(11) in the dimensionless

VOL. 62 198

average temperature above, one can then get

$$\theta_b(\xi) = \frac{Br\left(\frac{s+1}{s}\right)^{s+1} s^2(24s^3+38s^2+16s+2)}{2(3s+1)^3(5s+1)(s+1)} + \frac{\delta(7s+1)}{8(5s+1)} + \frac{2(3s+1)}{s+1}\sum_{n=1}^{\infty} A_n \exp(-\alpha_n^2\xi) \times \int_0^1 (1-\eta^{s+1/s})\, R_n(\eta)\eta\, d\eta. \quad (21a)$$

The local Nusselt number is defined as

$$Nu = \frac{hD}{k} = \frac{-2a\left.\frac{\partial T}{\partial r}\right|_{r=a}}{T_{av}-T_w} = \frac{-2\left.\frac{\partial \theta}{\partial \eta}\right|_{\eta=1}}{\theta_b(\xi)} \quad (22)$$

$$Nu = \frac{2}{\theta_b(\xi)}\left[Br\left(\frac{s+1}{s}\right)^{s+1}\left(\frac{s}{3s+1}\right) + \frac{\delta}{2} - \sum_{n=1}^{\infty} A_n \frac{dR_n(1)}{d\eta}\exp(-\alpha_n^2\xi)\right]. \quad (23)$$

RESULTS AND DISCUSSIONS

Numerical results have been obtained for both Newtonian and non-Newtonian fluid from the solutions of equations (12)–(14) and (17)–(23). Twenty eigenvalues and eigenfunctions are obtained for one set of parameters, Pe, s, Br and δ. When viscous dissipation and heat of generation are not important, i.e. $Br = \delta = 0$, $s = 1$ and $Pe \to \infty$, the present problem reduces to the classical Graetz problem which has been investigated extensively. The Nusselt number versus ξ for this case is shown in Figure 1 and the present results agree well with those of Sellars et al[4]. Also shown in Figure 1 are the results with power law model index $s \neq 1$. When $s > 1$, the fluid is considered to be dilatant, when $s < 1$, the fluid is considered to be pseudoplastic. It is seen that Nusselt number is different for different values of s at downstream of the tube even when axial conduction is not important and $Br = \delta = 0$. At the region very close to the entrance, Leveque[3] obtained the following expression for the Nusselt number

$$Nu = 1.357\xi^{-1/3}. \quad (24)$$

The Nusselt number from Figure 1 deviates from that of equation (24) by about 5.5% at $\xi = 0.001$.

Axial conduction becomes more important as Peclet number decreases. Henneck[8] and Hsu[9] considered heat transfer in a tube with axial conduction but $Br = \delta = 0$ by matching heat transfer in region of $x \leq 0$ to region of $x \geq 0$. For the heat transfer case with uniform wall temperature as boundary condition, Hennecke[8] used two different values of wall temperature as the boundary conditions at region $x \leq 0$ and region $x \geq 0$. This leads to infinite heat fluxes at the discontinuities and therefore cannot be used for comparison with the present results. Sorensen and Stewart[12] extended the Graetz problem including axial conduction by two methods: (*a*) an exact method by matching the heat transfer results of region $x \leq 0$ and region $x \geq 0$, (*b*) a method with simplified inlet boundary condition as used by Wehner and Wilhelm[25]. They obtained their solutions by the collocation method. Comparison of the inlet temperature for different values of Peclet number by the present method and those of Sorensen and Stewart[12] is given in Figure 2. It is seen that the present results agree very well with those of the simplified inlet boundary condition method by Sorensen and Stewart[12]. Hence the present method is then extended to investigate heat transfer of non-Newtonian fluid with significant effect of axial conduction. Table 1 presents some results of the first eigenvalues and downstream Nusselt number of Newtonian fluid from the present and previous work for different values of Peclet number. Generally good agreement is obtained. It is noted that downstream Nusselt number varies slightly with Peclet number. Further results of eigenvalues and their related constants for $s = 1$ and $Pe = 0.025, 0.1, 0.25, 0.5, 0.75, 1, 1.5, 2.5, 3, 5, 10, 15, 20, 30, 50, 100, 10^8$ were reported elsewhere[30]. For the non-Newtonian fluid case, there do not seem to be

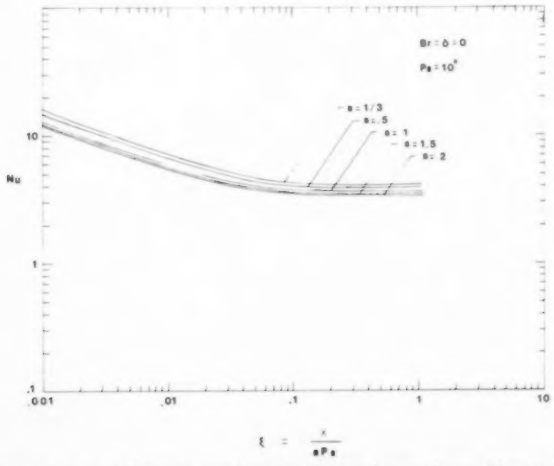


Figure 1. Local Nusselt number for Newtonian and non-Newtonian fluids along axial coordinate for $Pe = 10^8$, $Br = \delta = 0$.

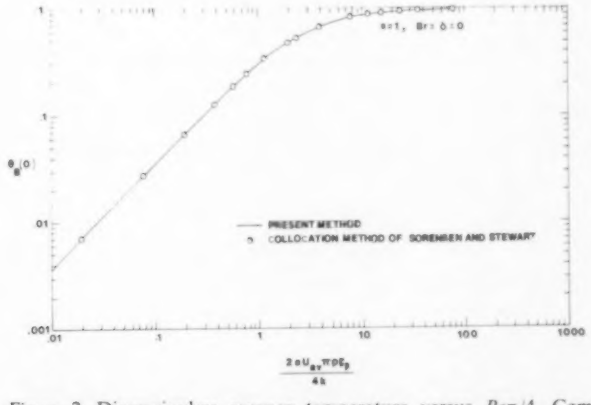


Figure 2. Dimensionless average temperature versus $Pe\pi/4$. Comparison of present results with those of Sorensen and Stewart[12].

Table 1. Comparison of the first eigenvalue (λ_1) and downstream Nusselt number (Nu) of Newtonian fluid ($s = 1$) for various values of Peclet number from present and previous work.

Pe	λ_1	Nu	Ref
0.025	0.0598768	4.17609	
0.1	0.2366032	4.16263	
0.25	0.5772455	4.13681	
0.5	1.1084779	4.09685	
	1.10848	4.09685	11(*a*)
	1.10468	4.08890	11(*b*)
0.75	1.5965671	4.06046	
1	2.0443678	4.02735	
	2.04437	4.02735	11(*a*)
	2.014	3.997	11(*b*)
		4.0273	22
		3.93	23
		4.40	24
1.5	2.8302765	3.96985	
	2.8304	3.96985	11(*a*)
	2.43	3.905	11(*b*)
	2.83025	3.9698	10
2.5	4.0364991	3.88314	
3	4.4942619	3.85072	
	4.49424	3.8507	10
5	5.6896746	3.76729	
	5.68967	3.7672	11(*a*)
	4.63	3.8363	11(*b*)
	5.68964	3.7672	10
		3.7672	22
10	6.7440489	3.69518	
	6.744049	3.69518	11(*a*)
	6.6436	3.70166	11(*b*)
	6.74400	3.6951	10
		3.6951	22
		3.67	23
		3.74	24
15	7.0380236	3.67532	
20	7.1534810	3.66754	
	7.15343	3.6675	10
		3.6675	22
30	7.2406920	3.66168	
	7.2406920	3.66168	11(*a*)
	7.23922	3.66178	11(*b*)
	7.24069	3.6616	10
		3.6616	22
45	7.2808308	3.65899	
	7.28078	3.6589	10
50	7.2870097	3.65858	
	2.83025	3.6585	10
100	7.3069065	3.65724	
	7.3069064	3.6572414	11(*a*)
	7.306894	3.6572421	11(*b*)
		3.6572	22
10^8	7.3135869	3.6568	
	7.31355	3.6567	10
		3.6567	22

(*a*) 17 point collocation.
(*b*) Equations 8A for λ_1 and 9A or 12A for Nu.

Table 2. Comparison of local Nusselt number between the present analysis and those of McKillop[19] for $s = 0.5$, $Br = \delta = 0$, $Pe \to \infty$.

ξ	Nu Present analysis	Nu McKillop[19]
0.006	7.99	7.97
0.012	6.40	6.40
0.024	5.25	5.25
0.048	4.47	4.47
0.06	4.29	4.30
0.12	3.99	4.00
0.18	3.95	3.95

results reported on this problem. Some of the eigenvalues and related constants for $Pe = 1, 5, 10$; $s = 0.25$, 0.5, 0.75, 1.5, 2; $Br = -1$, 1 and $\delta = -1$ were also reported previously[30]. It should be noted that $q \neq 0$ in the results and discussions of Figures 4–10.

When the fluid behaves like non-Newtonian fluid ($s \neq 1$) and $Br = \delta = 0$, $Pe \to \infty$, the present analysis reduces to one of the simplified case considered by Dang[23] where the effect of axial conduction on the inlet boundary condition is not significant. It has been shown that the eigenvalues, eigenfunctions and dimensionless average temperature obtained by Dang[23] give good agreement with those of Lyche and Bird[13]. For local Nusselt number, good agreement can also be obtained from the present analysis and those of McKillop[19] who solved the problem by the method of finite difference. Table 2 shows some of the comparison of the local Nusselt number for $s = 0.5$, $Br = \delta = 0$ and $Pe \to \infty$ between the present results and those of McKillop[19]. Comparison of the present analysis with previous experimental data is shown in Figure 3 for 3% carboxymethyl cellulose solution ($s = 0.67$) for $Pe \to \infty$, $Br = \delta = 0$. Correction has been made for the temperature dependent viscosity in the treatment of the Nusselt number in Figure 3. The data were reported by Christiansen and Craig[17]. It is seen that good agreement is obtained between the present analysis and the experimental data. It is also found that the data of Metzner and Gluck[16] for other values of the power law model index s also presented good agreement with the present analysis.

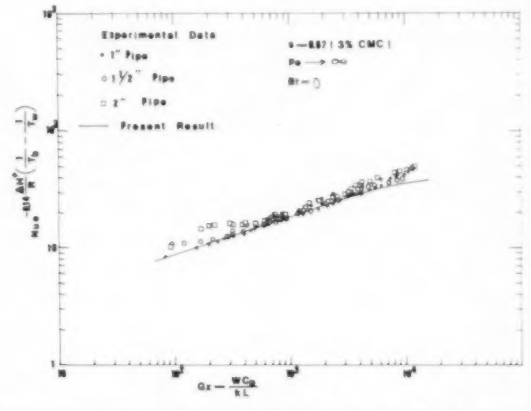


Figure 3. Comparison of present results with previous data of Christiansan and Craig[17].

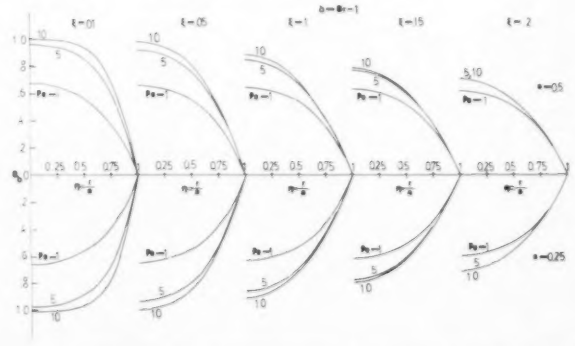


Figure 4. Dimensionless average temperature versus axial distance for $s = 0.25$ and 0.05.

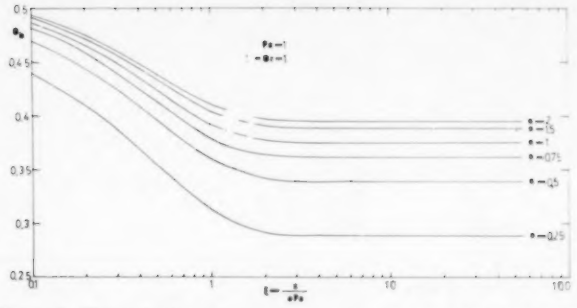


Figure 5. Dimensionless average temperature versus axial distance for different values of power law model index for $Pe = 1$, $Br = \delta = 1$.

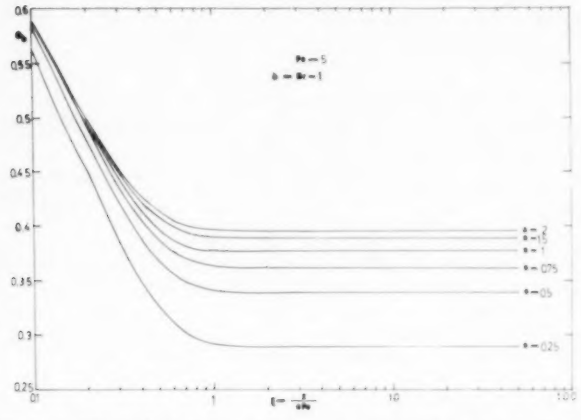


Figure 6. Dimensionless average temperature versus axial distance for different values of power law model index for $Pe = 5$, $Br = \delta = 1$.

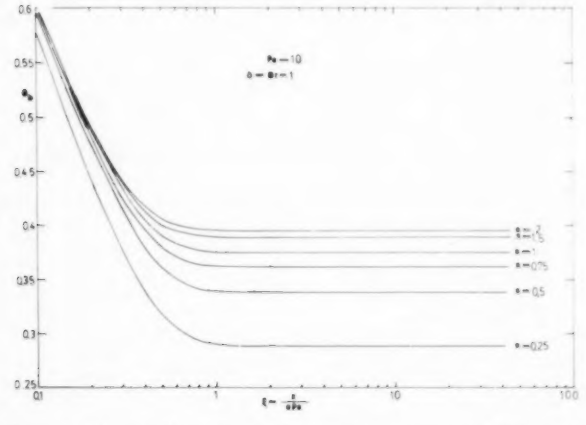


Figure 7. Dimensionless average temperature versus axial distance for different values of power law model index for $Pe = 10$, $Br = \delta = 1$.

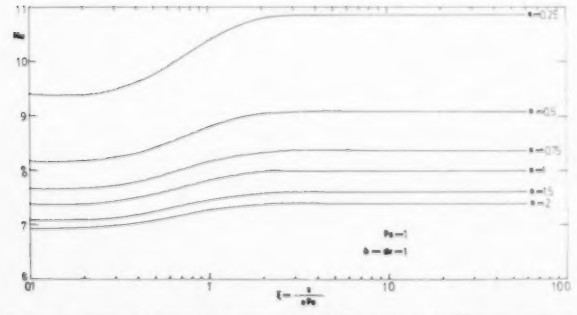


Figure 8. Nusselt number versus axial distance for different values of power law model index for $Pe = 1$, $Br = \delta = 1$.

Figure 4 shows the dimensionless radial temperature distribution at different axial position for $s = 0.25$ and 0.5 and $Br = \delta = 1$. It is seen that dimensionless average temperature decreases when Peclet number decreases or at distance further away from the entrance of the tube. Dimensionless average temperature decreases as ξ increases because of the heat transfer to the wall.

Figures 5–7 are the dimensionless average temperature along the axial distance of the tube for different values of Peclet number and power law model index when $Br = \delta = 1$. Dimensionless average temperature is larger closer to the entrance of the tube when Peclet number is larger. At far downstream of the tube, dimensionless average temperature does not seem to be affected by the values of Peclet number. However the dimensionless average temperature in the downstream increases as the value of power law model index increases. Dimensionless average temperature decreases rapidly and then slowly in some intermediate region, i.e. $0.01 \leq \xi \leq 1$ of the tube.

Local Nusselt number along the length of the tube is shown in Figures 8–10. Nusselt number decreases rapidly at the inlet but then increases to steady state values at downstream. Downstream Nusselt number increases as the power law model index s decreases. This agrees with the phenomena observed by Dang[23] previously. Downstream Nusselt number can be achieved at $\xi \simeq 60$. Table 3 tabulates some downstream Nusselt number for different values of Br, δ and s for $Pe = 1$. When the value of δ is negative, heat is removed from the fluid. This can be considered as endothermic reaction. There is opposite effect on the temperature field due to endothermic

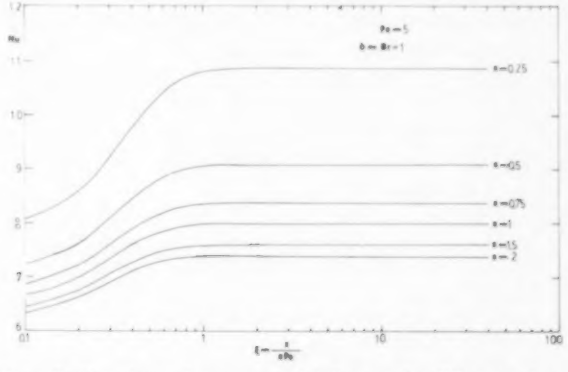


Figure 9. Nusselt number versus axial distance for different values of power law model index for $Pe = 5$, $Br = \delta = 1$.

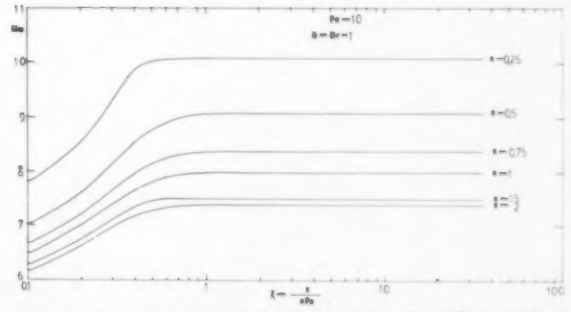


Figure 10. Nusselt number versus axial distance for different values of power law model index for $Pe = 10$, $Br = \delta = 1$.

Table 3. Downstream Nusselt number for different values of Br, s and δ for $Pe = 1$

δ	Br	s	Nu	δ	Br	s	Nu
−1	0	0.25	6.54546	1	0	0.25	6.54546
		0.5	6.22222			0.5	6.22222
		0.75	6.08000			0.75	6.08000
		1.5	5.91304			1.5	5.91304
		2.0	5.86667			2.0	5.86667
	0.5	0.25	−0.80161		0.5	0.25	9.37517
		0.5	−0.54763			0.5	8.16374
		0.75	−0.25222			0.75	7.66029
		1.5	0.37064			1.5	7.09098
		2.0	0.61847			2.0	6.93694
	1	0.25	−66.26987		1	0.25	10.87413
		0.5	61.84009			0.5	9.08454
		0.75	31.23309			0.75	8.37824
		1.5	18.91451			1.5	7.60338
		2.0	16.89452			2.0	7.39777

reaction (negative value of δ) and viscous dissipation (positive value of Br). When more heat is removed from the fluid, the temperature of the fluid can be lower than the temperature of the tube wall. Under these conditions, Nusselt number can be negative. For $Pe = 5$ and 10, Nusselt number is the same as those of $Pe = 1$ at Table 3.

SUMMARY AND CONCLUSION

An exact solution has been obtained for a non-Newtonian power law model fluid with axial conduction and heat generation in a pipe. An extreme case of the present analysis for $s = 1$ and without heat generation is the Graetz problem for high and low Peclet number. Comparison of the present results with those of previous researchers generally shows good agreement. For the case of non-Newtonian fluid, Nusselt number decreases when the fluid changes from pseudoplastic ($s < 1$) to dilatant ($s > 1$). When viscous dissipation and heat of generation are present, the downstream Nusselt number does not vary with Peclet number for the range $Pe = 1$, 5, 10 investigated.

SYMBOLS USED

a radius of tube
A_n coefficient of series expansion in equation (11)
Br Brinkman number $= \dfrac{mu_{\max}^{s+1} a^{-1-s}}{k(T_0 - T_w)}$
C_p heat capacity
h heat transfer coefficient
I_n integral defined by equation (20)
J_n integral defined by equation (18)
k thermal conductivity
m constant in power law model
Nu Nusselt number, defined in equation (23)
Pe Peclet number $= \rho C_p a u_{\max}/k$
q heat generation term
r radial coordinate of tube
R_n eigenfunctions
s power law model index
T temperature of fluid
T_0 inlet temperature
T_w wall temperature
$u_{\max}$ maximum velocity of fluid in tube
x axial coordinate of tube

Greek Symbols

α_n eigenvalues
$\Gamma_{n,m}$ integral defined by equation (19)
δ dimensionless parameter $= \dfrac{qa^2}{k(T_0 - T_w)}$
η dimensionless parameter $= \dfrac{r}{a}$
θ dimensionless temperature $= \dfrac{T - T_w}{T_0 - T_w}$
θ_b dimensionless average temperature, equation (21)
ξ dimensionless parameter $= \dfrac{x}{aPe}$

REFERENCES

1. Graetz, L., 1883, *Ann Phys*, 18: 79–95; *Ann Phys*, 25: 337–357.
2. Nusselt, W., 1910, *Z Ver Deutsch Ing*, 54: 1154–1158.
3. Leveque, J., 1928, *Ann Mines*, 13 (4, 5, 6): 201–299, 305–362, 381–415.
4. Seller, J. R., Tribers, M. and Klein, J. S., 1956, *Trans ASME*, 78: 441–448.
5. Kays, W. M., 1955, *Trans ASME*, 77: 1265–1274.
6. Brown, G. M., 1960, *AIChEJ*, 6: 179–183.
7. Newman, J., 1982, in A. J. Bard (ed) *Electroanalytical Chemistry* (Marcel Dekker Inc, New York) 6: 187–352.
8. Hennecke, D. K., 1968, *Warme und Stoffubertragung Bd*, 1: 177–184.
9. Hsu, C. J., 1971, *AIChEJ*, 17: 732–740.
10. Tan, C. W. and Hsu, C. J., 1972, *Int J. Heat & Mass Transfer*, 15: 2187–2201.
11. Michelsen, M. L. and Villadsen, J., 1974, *Int. J. Heat & Mass Transfer*, 17: 1391–1402.
12. Sorensen, J. P. and Stewart, W. E., 1974, *Chem. Eng Sci*, 29: 811–817.
13. Lyche, B. C. and Bird, R. B., 1956, *Chem Eng Sci*, 6: 35–41.
14. Toor, H. L., 1958, *AIChEJ*, 4: 319–323.
15. Metzner, A. B., Vaughn, R. D. and Houghton, G. L., 1957, *AIChEJ*, 3: 92.
16. Metzner, A. B. and Gluck, D. F., 1960, *Chem Eng Sci*, 12: 185.
17. Christiansen, E. B. and Craig, S. E. Jr, 1962, *AIChEJ*, 8: 154.
18. Oliver, D. R. and Jenson, V. G., 1964, *Chem Eng Sci*, 19: 115.
19. McKillop, A. A., 1964, *Int J Heat & Mass Transfer*, 7: 853.
20. Faghri, M. and Welty, J. R., 1977, *AIChEJ*, 23: 288–294.
21. Hieber, C. A., 1977, *Rheol Acta*, 16: 553–567.
22. Choi, S. Y. and Nakajima, N., 1968, *Pr 5th Int Cong Rheol*, 287–293.
23. Dang, V. D., 1979, *J Appl Polmer Sci*, 23: 3077–3103.
24. Danckwerts, P. V., 1953, *Chem Eng Sci*, 2: 1–18.
25. Wehner, J. F. and Wilhelm, R. H., 1956, *Chem Eng Sci*, 6: 89–93.
26. Dang, V. D., 1978, *Chem Eng Sci*, 33: 1179–1190.
27. Tan, C. W., 1970, *US AEC Health & Safety Lab Report*, HASL-238.
28. Schmidt, R. W. and Zeldin, B., 1970, *Appl Sci Res*, 23: 73–94.
29. Labuntsov, D. A., 1958, *Sov Phys Dockl*, 3: 33–35.
30. Dang, V. D., 1980, *Brookhaven Nat Lab Report*, BNL 27997.

ADDRESS

Correspondence on this paper should be addressed to Associate Professor Vi-Duong Dang, Department of Chemical Engineering, The Catholic University of America, Washington DC 20064, U.S.A.

The manuscript was submitted 18 July 1983 and accepted for publication 14 October 1983.

VOL. 62 1984

ALTERNATIVE MODEL FOR ULTRAFILTRATION

By M. S. LE (GRADUATE) and J. A. HOWELL (FELLOW)
Department of Chemical Engineering, University College of Swansea

A limiting flux model is developed to account for a variety of phenomena occurring during ultrafiltration. It is first shown that a new model is required to replace the old gel polarisation model. The new limiting flux model is based on concentration polarisation but postulates that the limiting concentration, occurring at the membrane surface as transmembrane pressure is raised, is a result of the interactions between the solute and the surface. Limiting flux occurs when the pores are blocked most of the time. They remain in a dynamic blocked–unblocked state responding to convective blockage and reverse mass transfer to clear the blockage.

The new model can predict correctly the effect of increased solute molecular weight, the effect of colloidal particles and the effect of a leaky membrane. New experimental evidence is obtained showing that a leaky membrane used in an unstirred cell soon becomes partially blocked in the smaller pores and passes solute freely through the larger pores. The rejection coefficient falls to near zero. This is correctly described by the new model.

In all cases, existing and new data is fitted by the model using a small number of adjustable parameters. For a normal membrane and solute the parameters are the pure solvent flux at all pressures, the limiting concentration (which is a function of solute–membrane interaction) and the mass transfer coefficient between membrane and bulk solution.

INTRODUCTION

Generally, it is accepted that ultrafiltration membranes are those which retain particles larger than 1.0 nm in diameter and they operate a sieving mechanism which distinguishes them from the tighter, diffusive membranes used for reverse osmosis. The independence of rejection efficiency on the applied pressure for the former was considered as the most important functional difference between these two types of membranes, and yet Nakao[1] demonstrated experimentally that the rejection coefficient of ultrafiltration membranes was not independent of pressure. It has often been assumed that separation in ultrafiltration is effected solely by the sieving mechanism and the rejection efficiency is determined by the solute molecular dimensions and the pore size distribution only. Such assumptions lead to apparent inconsistencies in the experimental observations of the solute rejection coefficient of ultrafiltration membranes. A theoretical model for solute rejection by the membrane seems to be required.

It is generally accepted that concentration polarisation occurs and that the solute concentration at the membrane surface (C_s) achieves a limiting value (C^*). Velicangil and Howell[2] have solved the transient equations governing the build-up of C_s to C^* and have shown that the process will be essentially complete within a few seconds, probably less than 1 second with most UF membranes. If the solute is totally rejected by the membrane it can be shown that the limiting flux (J^*) is related to C^* by

$$J^* = k_m \ln \frac{C^*}{C_b} \qquad (1)$$

where k_m is the mass transfer coefficient between the membrane and the bulk liquid at zero flux and C_b is the bulk liquid solute concentration. Early experiments suggested that for the same membrane solute system the value of C^* would not change as the bulk concentration was changed and k_m was kept constant, or even as k_m was changed by changing the hydrodynamic regime above the membrane. This observation led to the gel polarisation theory[3] which postulates that as the pressure across a UF membrane increases, concentration polarisation increases to a point where a gelation or solute precipitation occurs at the membrane surface. Further pressure increase deposits more gel, increasing membrane resistance. Subsequent flux reduction occurring with time is ascribed to hardening of the gel, increasing its specific resistance to filtration. There are a number of difficulties with this theory, although it correctly predicts the effect of changing the bulk concentration. The gel concentration (C_g) should presumably be a function only of the solute, yet changes in the membrane used alter the predicted gel concentration by up to 50%. The process can be modelled but the time scale calculated from the model is far faster than that observed in practice.

Nakao[1] showed that C_g is apparently a function of the bulk concentration and the feed velocity as well as the membrane type. He was of the opinion that C_g has no physical significance. The original advocates of the theory assumed that gelation or solute precipitation was a consequence of the membrane surface concentration (C_s) exceeding the solubility limit. However, Goldsmith[4] found that the limiting flux for polyethylene glycol (PEG MWt. 15,500) occurred at concentration as low as 5.3 to 9.8%. Now these concentrations are well below the solubility limit for PEG, which is hydrophilic and very soluble in water. Goldsmith[4] obtained C^* for different molecular weight fractions of dextran (Table 1).

De Gennes[5] (1979) has pointed out that while dilute polymer chains in a good solvent are swollen and the size increases as $n^{3/5}$ in a concentrated solution or melt the chain becomes ideal and has a size $R\ N^{1/2}$ and many chains overlap to build up the total concentration. This total concentration in mass terms is then likely to become gelling at a constant value irrespective of the molecular weight. Thus it would seem unlikely that C^* could be equated with a gelling concentration.

Shen and Probstein[6] attempted to predict the limiting flux in a parallel plate laminar ultrafiltration system

© Institution of Chemical Engineers

Table 1. Dependence of the limiting concentration on Mwt for dextran.

Mwt $\times 10^{-3}$	$C^*\%$
21.8	14.2
39.5	20.3
67.5	25.5
100.5	33.0

using concentration-dependent viscosity and diffusivity. These authors claimed that discrepancies from the use of the gel polarisation theory were due to the dependence of the diffusivity on the concentration, in direct contradiction with Kozinski and Lightfoot's report[7]. Trettin and Doshi[8] disputed Shen and Probstein's claim by showing that a constant property integral method (assuming a constant diffusivity) yielded less than 3% error betwen the theoretical prediction and experimental data for BSA. Leung and Probstein[9] explained the flux-pressure behaviour in terms of the osmotic pressure created by the concentration boundary layer. Most believe that in the ultrafiltration of macromolecules the osmotic pressure resulting from polarisation is quite small and that for all intents and purposes it can be ignored. The Leung and Probstein model does not take into account the effect of membrane blinding.

The major argument against the gel polarisation model is that firstly, the gel concentration should presumably be a function only of the solute, yet changes in the membrane used altered by up to 50% the predicted value[1,10]. The second failure of this theory is the inability to account for the anomalous high flux in the colloidal suspensions. Blatt et al[11] proposed that the permeation rate is not limited by the hydraulic resistance of the gel layer. Porter[10] argued that if the polarised layer is not the limiting factor then flux should be proportional to the applied pressure. In practice he found the opposite to be true. Henry[12] reported that in the ultrafiltration of 1.3% bacterial cells, flux was proportional to the applied pressure at pressure above 10 psi. Porter[10] showed that flux by styrene butadiene polymer latex (0.05–0.2 m) at a bulk concentration greater than 10% apparently reaches a pressure independent region at a pressure of 60 psi, and for concentrations lower than 5%, a strong dependence of flux on pressure at pressure beyond 90 psi. Porter employed the tubular pinch effect to explain his data, but Madsen[13] pointed out that this can only account for a small part of the high flux and that Porter's model would under-predict flux of colloidal suspensions by a factor of 50 in some cases. Another difficulty which confronts the gel polarisation theory is the fact that flux dependence on the feed velocity varies with the type of solute and the membrane system used[10,13]; this means that the mass transfer rate at the membrane surface deviates from any accepted theory of diffusive convective transport.

There has been in the past few years a move from the gel polarisation theory. Fane et al[14] adopted an empirical approach to relate concentration and flux for an activated sludge system. They ascribed the long term flux decline to an ageing process in the 'cake' and proceeded to fit flux data to a hyperbolic function. Velicangil[15] on the other hand, offered to a three-stage model for protein ultrafiltration. According to this model the concentration polarisation process is completed within the first few seconds, followed by an adsorption process in which the protein adsorbs to the membrane and causes flux depression. The adsorption stage takes no more than about 15 min to complete. Further flux loss is attributable to a polymerisation mechanism in which more protein from the bulk solution reacts with the adsorbed protein. The weakness of Velicangil's model is that it cannot account for the change in the apparent overall rate of polymerisation during a particular run, especially where a multi-protein solution such as cheese whey is involved. Furthermore, it makes no reference to the pressure-independent flux which is still the key issue in macrosolute ultrafiltration.

It seems that for over a decade the phenomenon of fouling, which leaves a layer of deposit on the membrane, has confused people and led them into believing that such a layer is the product of solute gelation which causes the flux to become independent of the applied pressure. Clearly fouling, gelation, and the pressure independent flux are three distinct and separate processes and are controlled by different mechanisms, and as such the distinction must be made.

THEORY

Retentive Membrane

Flux through an ideal membrane with complete rejection can be shown to be[3]

$$J = k_m \ln \frac{C_s}{C_b} \tag{2}$$

Figure 1 shows the concentration profile of solute near to the membrane surface. At steady state the rate of solute arriving at the membrane is balanced by the sum of the leakage and rate of back diffusion, i.e.

$$JC = D\frac{dC}{dx} + (1-E)C_s J$$

Since E is the true rejection of the membrane we have

$$Cp = (1-E)C_s$$
$$= \text{constant, at steady state}$$

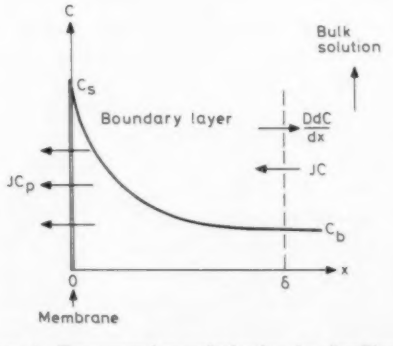


Figure 1. Concentration polarisation in ultrafiltration.

Table 2. $C_s N^{-1/2}$ at the limiting flux for different dextran fractions.

Mwt (N)	$C_s = C^*$ %	$C^* N^{-1/2}$
21,800	14.2	0.0962
39,500	20.3	0.1021
67,500	25.5	0.0981
100,500	33.0	0.1041

Hence

$$J(C - C_p) = D\frac{dC}{dx}$$

or

$$J\int_0^{\delta} dx = D\int_{C_b}^{C_s}\frac{dC}{C - C_p}$$

$$J = k_m \ln\frac{C_s - C_p}{C_b - C_p} \qquad (3)$$

where $k_m = D/\delta$, the mass transfer coefficient.

Experiments on a leaky membrane in an unstirred cell have shown that flux can be steadily increased by an increase in the transmembrane pressure, the value of C_p increases until $C_p = C_b$, and there is little apparent rejection by the membrane. Initial intuition suggests that as C_s increases the effective radius of the solute decreases and thus rejection decreases. Put another way, the molecules take up less room as the concentration increases and can squeeze through the pores. These considerations lead directly to the limiting flux model which requires that only pores which actually reject solute reach a pressure-independent flux.

Molecules close to a surface will be in a concentrated solution and thus, according to de Gennes, will be intimately entangled[5]. They behave as ideal molecules and the linear polymer occupies a space whose radius of gyration R scales as $\sqrt{N}$ where N is the number of polar groups in the proteins proportional to the molecular weight. The volume occupied by the molecule will scale as R^3, and the chance of a particular protein being in a particular region of space such as the surface will thus scale as N/R^3. The area of the surface where a segment of the molecule could adsorb will scale as R^2. The average number of attachments per molecule will then scale as $NR^2/R^3 = N^{1/2}$. As the concentration close to the surface C_s is a mass concentration the total number of molecules in the region will scale as C_s/N and thus the total number of adsorbed sites will scale as $C_s N^{-1/2}$.

Table 2 shows the result of calculations of $C_s N^{-1/2}$ for the dextran filtration experiment of Goldsmith[4], where the surface limiting concentration C^* was that obtained at the limiting flux, J^*

It appears that the flux becomes limiting at some fixed level of adsorption of segments of the polymer chain on the surface. This would relate directly to the chance of blocking a pore. This will also depend on the flow through the pore—a high flow convects molecules to the surface faster than reverse mass transfer effects can remove them. A single blocked pore will be subject to unblocking as there is a finite probability of desorption and no local convective forces forcing the molecule back to the pore until unblocking occurs and the pore is free to pass solvent again. Within the limiting flux region increasing the pressure would temporarily increase the flux, and the local concentration blocking enough pores, to drop the flux back to its original level, where the chance of blocking any given pore has become constant. Reducing the pressure, temporarily reducing flux, would allow some of the absorbed sites to become free and raise the flux back to the same level as before although this relaxation time might be quite long especially at the higher molecular weights where the Sherwood number[18] decreases sharply. De Gennes[5] has shown that the diffusion coefficient would scale as $N^{-2}\ C^{-1.75}$ and viscosity as $N^3\ C^{3.75}$; thus the Schmidt number would scale as $N^5\ C^{5.5}$. When a molecule with a fixed ternary structure such as protein is involved, intermingling of the chains is no longer likely even at high concentrations. The local density of chain adsorption sites is thus not going to exceed N/R^3 but the number of sites per molecule will still be N/R and total density of sites C/R as before. Just as for a totally entangled chain, the totally separate chain will also scale as $N^{1/2}$ although its overall size R will be less.

The limiting flux model then postulates that flux can be increased, by increasing the transmembrane pressure, only up to some limiting value which will depend on the bulk concentration of solute, its molecular weight and the hydrodynamic situation above the membrane. In all cases the probability of pore blockage is at the same constant value. Increasing the pressure results in a transitory increase in flux, an immediate increase in the solute concentration at the membrane surface and a consequent increase in the probability of pore blockage. A number of pores become blocked reducing the flux and the blocking probability to its original value. Reducing the pressure results in a temporary decrease in flux, an immediate decrease in the surface concentration and a consequent reduction in the probability of pore blockage. A number of pores become unblocked, increasing the flux, and the blocking probability returns back to its original value.

In actual practice some pores may become blocked and others unblocked in a dynamic fashion. This dynamic process is equivalent to cyclic blocking and unblocking of all the pores simultaneously. While a pore is blocked it is non-permeating and thus adsorbed protein is not held on the membrane by hydrodynamic forces, and while unblocked it always tends to pass a flux close to that for a pure solvent. The fraction of pores which may be blocked is C_s/C^*. Thus in the pre-limiting flux region a fraction of the pores $(1 - C_s/C^*)$ is not blocked at all, and the flow through this fraction will be proportional to the applied pressure. The flux contribution from the fraction which is not blocked at all is

$$J_1 = \left(1 - \frac{C_s}{C^*}\right) J_p$$

where J_p is the pure solvent flux at the applied pressure P.

$$J_p = \frac{P}{\mu R_m}$$

where μ = viscosity; R_m = constant.

If the net prevailing flux is J, then the flux contribution by the remaining partially blocked pores will be

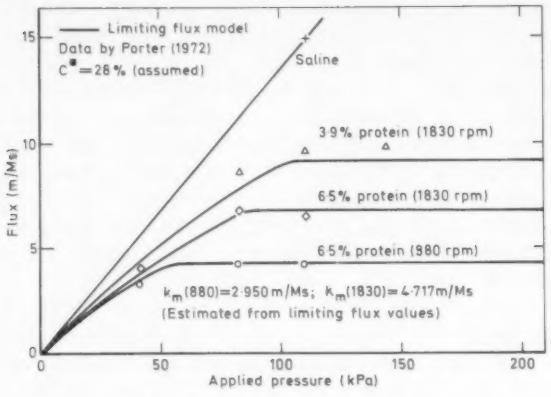


Figure 2. Dependence of flux on the applied pressure.

$$J_2 = J - J_1$$

The flow through a partially blocked pore, which for the present we call a pore in an occupied state, is smaller than the flow through an unoccupied pore, so

$$J_2 < J\frac{C_s}{C^*} \quad \text{or} \quad J_2 = X J \frac{C_s}{C^*}$$

where $O \le J \le J^*$

if $J = J^*$ then $C_s = C^*$, $J_1 = O$ and $J_2 = J^*$

Thus X is such that $X = O$ when $J = O$

$X = 1$ when $J = J^*$

and $O \le X \le 1$

X will be a function of C_s (related to J) and membrane solute interaction characterised by C^* (related to J^*). Of a number of functional forms tried

$$X = J/J^*$$

was both simple and gave satisfactory results. Hence

$$J = \frac{C_s}{C^*}\frac{J^2}{J^*} + \left(1 - \frac{C_s}{C^*}\right) J_p$$

This equation assumes that a limiting flux exists corresponding to a limiting concentration at the membrane surface. Noting that as C_b tends to zero, J tends to J_p and as C_s tends to C^*, J tends to J^*; thus the pressure flux profile must be as in Figure 2.

In Figure 2 the lines are those predicted by this model using best values of C^* and K_m for the data points by Porter[10]. The value of the mass transfer coefficient used in the prediction was calcualted at the limiting condition, i.e. for $C_s = C^*$, and it was assumed constant as shown n numerous linear/log-plots of flux versus concentration in the literature. Clearly at low bulk concentration the mass transfer coefficient is greatest and the discrepancy arising from the assumption of a constant coefficient is also greatest, as reflected very well by the plots. The assumption of a constant mass transfer coefficient for a constant feed velocity results in deviation from linearity in flux versus log concentration plots in many systems[19]. Belfort et al[20] have analysed the problem of ultrafiltration of colloidal materials and shown that apparent anomalies in mass transfer coefficient can arise from lateral migration of larger particles.

Multilayer adsorption can create a fouling film which decreases flux still further. Although the limiting flux model applies at all times it is most clearly interpreted in the early stages of flux through a clean membrane when a monolayer only is present.

Leaky Membrane

Consider a membrane with a pore size distribution such that a fraction of the pores is non-rejecting and the remainder is totally rejecting with a limiting flux. The flux contribution by the rejecting fraction will be

$$J_r = (1 - \alpha)J$$

where J is given by equation (4) and the contribution by the remaining fraction will be

$$J_\alpha = \alpha J_p$$

where J_p is the flow of the viscous solution through the pore and is dependent on the transmembrane pressure and the flowing solution viscosity only.

Total flux

$$J = J_r + J_\alpha \tag{5}$$

Total leakage $= C_s J_\alpha$

Permeate concentration

$$C_p = \frac{C_s + J_\alpha}{J_r + J_\alpha}$$

or at any instance

$$C_p = \frac{\alpha J_p}{(1-\alpha)J + \alpha J_p} C_s \tag{6}$$

Equation (6) clearly shows that the apparent rejection is a strong function of the pressure and this is illustrated by Nakao's data[1]. Note that as α tends to zero, i.e. in a totally rejecting membrane, C_p disappears. Clearly this expression shows that $C_p = C_s = C_b$ only when $\alpha = 1$ and for any other value of α the wall concentration $C_s > C_p$ always. Exceptionally, the rejecting pores may become virtually blocked and almost non-permeating, that is, if the probability of pore blockage is very high, which is likely to occur in non-stirred systems where the mass transfer coefficient is minimal. When this situation arises, j will be negligible and in equation (6)

$$C_p = C_s \tag{6a}$$

Thus, in systems of low mass transfer, initially there is concentration polarisation by action of the rejecting pores, but when they are blocked permeation is mainly through the non-rejecting pores and polarisation diminishes until the concentration everywhere is close to the bulk concentration. Figure 3 illustrates this process.

The ultrafiltration system employed for the leaky membrane experiments consisted of a single membrane tube 380 mm long by 13 mm diameter which was supported by porous stainless steel. The lower end of the tube was blanked off and the upper end was connected to a 300 cm^3 glass reservoir which was pressurised by compressed air. Before any measurement was taken the

VOL. 62 1984

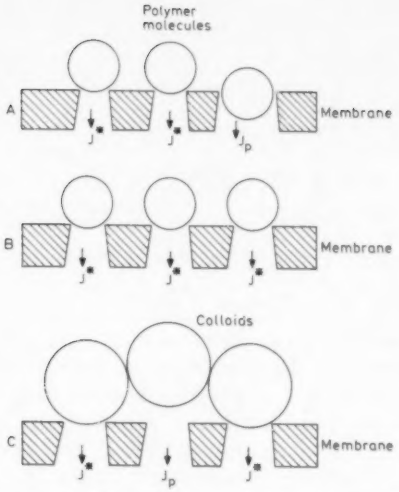


Figure 3. The flux limiting mechanism. A—leaky membrane. B—Normal system. C—Colloidal system. J*—limiting flux (pressure independent). J_p—solvent flux (pressure dependent).

cell was pressurised while exposed to a PEG solution to allow any adsorption of the solute to reach equilibrium. The pressure was released for a short time then re-applied.

The membrane (T6/B) was obtained from Paterson Candy International (Hampshire) and the PEG (polyethylene glycol, M.Wt. 20,000) was supplied by Fluka (Gloucester). The solute was dissolved in 0.1 M phosphate, pH 7 and its concentration was determined by a viscosity method for which a sample of 10 ml was required.

Figure 4 shows the dependence of the initial permeate concentration and rejection on the applied pressure. The solute concentration in the first 10 ml of permeate was measured so that the calculated rejection is an average value. It is quite clear that the initial rejection value of a leaky membrane is strongly influenced by the applied pressure. However, why this is so can be more readily explained by Figure 5 in which the permeate volume is plotted against time for various pressures. At low pressure the permeation rate declines noticeably at first then becomes constant for all time. At the higher pressure

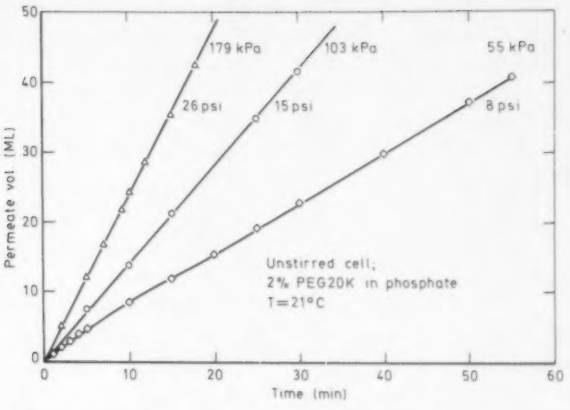


Figure 5. Permeation rate isobars for a leaky membrane.

range, there seems to be no variation of permeation rate with time. There is no doubt that flux takes a finite time to reach a steady state value and the higher the pressure the shorter the time required.

The limiting flux model compares well with published data for both normal membrane–solute systems and for colloidal solutions. It suggests that for a leaky membrane rejection would decrease with increasing pressure; and in a low mass transfer system a situation of diminishing concentration polarisation may take place. Furthermore, once all the rejecting pores have become blocked, remaining pores reject no solute and the permeation rate should be proportional to the applied pressure. In order to verify the model's implications the following experiments were performed with an unstirred ultrafiltration cell.

In a low mass transfer system the rejecting pores would become blocked and by inference one would expect the pores to be blocked much faster at high flux. Once the rejecting pores have become non-permeating through blockage, the total flux occurs solely through the non-rejecting pores and will attain a constant value as depicted by the plots in Figure 5. Figure 6 shows the rejection profile of a leaky membrane against time at a constant pressure of 138 kPa. The rejection coefficient first declines rapidly then more slowly to a steady state

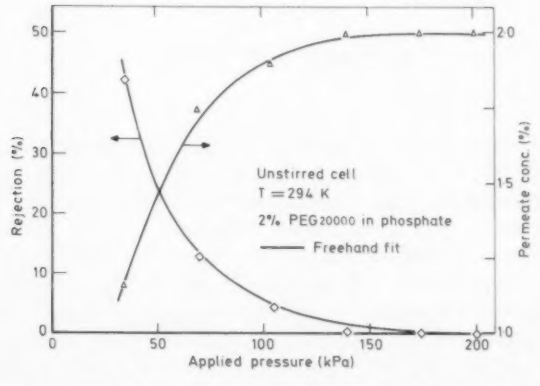


Figure 4. Dependence of initial permeate concentration and rejection on the applied pressure.

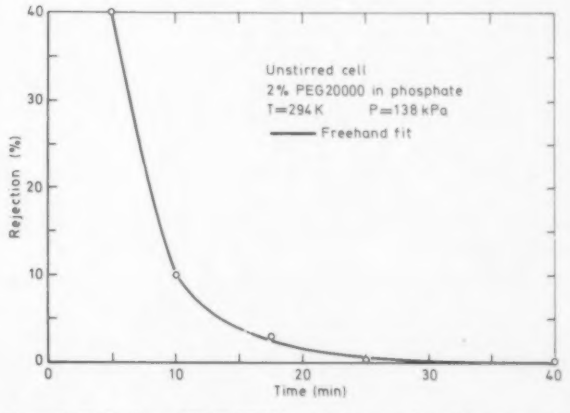


Figure 6. Rejection of PEG 2OK by a leaky membrane in an unstirred cell.

value of zero. This clearly shows a situation of diminishing concentration polarisation as expected from the model prediction. It is interesting to note that in Figure 6 the rejection takes about 30 min to reach a steady state value, but as Figure 5 shows, at the same pressure it would probably take less than 2 min to reach a steady state flux.

Ultrafiltration of Colloidal Suspension

Suppose there are n pores and only M particles in the surface region where $n > M$. At steady state the rate of particles landing on pores balances that of those leaving. Particle exchange can be considered as taking place only in a fraction M/n of pores at any time. It takes a finite time for two particles to swap places and it is only during this time that liquid can permeate through the occupied pore. According to the limiting flux model then only the occupied pores are flux limiting. This is quite clear, because the $(n - M)$ pores which are always open will permeate, according to the applied pressure, all the time. Hence in practice for limiting flux to be observed all pores must be in the occupied state.

Colloidal solutions behave effectively as ordinary solutions except that a true threshold pressure or true limiting flux is never reached. For instance, with a 1% colloidal polymer latex (average diameter 0.1 m) flux was still increasing strongly with pressure above 620 kPa, but for similar membranes and human plasma or BSA at 1% to 6.5% concentration limiting flux was found[4] at a pressure between 35 and 100 kPa. Considering a unit area of ideal membrane with hexagonally close pore arrangement the pore density n will be

$$n \propto \frac{1}{d}$$

where d = pore diameter.

Assume that only particles in direct contact with the pores can cause the flux to be limited and any one particle can cause only one pore to be fully flux limited, but by virtue of its larger size may decrease flux in adjacent pores to some extent by its projection over them. The maximum number of particles of radius D_p that may adsorb to the surface at any time will be

$$M^* \propto \frac{1}{D_p} \quad \text{where } D_p > d$$

Hence the maximum pore fraction that could be put into an occupied state is M^*/n. Then for $J \geq J^*$

$$J_2 = \gamma J^* \quad \text{where } \gamma = \frac{M^*}{n}$$

flow through these occupied pores is fully limited and J_2 is the flux contribution by this pore fraction.

Flow through the remaining pore fraction will be

$$J_1 = J - J_2$$

Since the remaining pore fraction $(1 - \gamma)$ is never fully blocked at any time, flow through it is nevertheless reduced to some extent by the particles' projection from the occupied pores.

Clearly

$$J_1 < J_p(1 - \gamma)$$

where J_p is the pure solvent flux or

$$J_1 = XJ_p(1 - \gamma).$$

Total prevailing flux is then

$$J = \gamma J^* + XJ_p(1 - \gamma) \text{ for } J \geq J^*$$

Note that for $\gamma = 1$ or for normal solution UF

$$J = J^* \quad \text{for pressure} > \text{threshold p}$$

For convenience the area γ which is fully blocked will be referred to as the blocking zone. In this zone the flux is fully limited and is completely independent of pressure. The term exclusion zone will apply to the remainder area $(1 - \gamma)$. This zone is affected by the colloid but is never completely blocked and the flux is pressure dependent. Within the exclusion zone at any instant a fraction of the area may be covered and therefore does not permeate and the remainder area would permeate freely. Thus one can write

$$\underset{C_s}{\text{Solute}} + \underset{1-\theta}{\text{free area}} \rightleftharpoons \underset{\theta}{\text{covered area}}$$

If one assumes Langmuir type adsorption then

$$\theta = \frac{C_s}{K + C_s}$$

where K = adsorption constant.

The flux contribution by the exclusion zone will be

$$J_1 = (1 - \gamma)(1 - \theta) J_p$$

the total prevailing flux is given by

$$J = J_1 + J_2$$

$$= (1 - \gamma) \frac{KJ_p}{K + C_s} + \gamma J^*$$

Note that when $J = J^*$, $C_s = C^*$ and $J_p = J_p{}^*$. C^* can be interpreted as the colloid concentration which can cause the adsorption of a complete monolayer on the membrane. $J_p{}^*$ is the pure solvent flux at the pressure when $J = J^*$. Solve for K and on substitution the above equation becomes

$$J = \gamma J^* + (1 - \gamma) J_p \frac{C^*}{(\sigma - 1)\, C_s + C^*} \tag{7}$$

where $\sigma = J_p{}^*/J^*$

for $J \geq J^*$

Figures 7 and 8 show the plots of equation (4) and equation (7). The model predictions for bacterial cells and colloidal latex polymer were good in both cases. The values of γ and C^* were obtained by a parameter estimation method and J^* values were estimated from the break points in the curves. The slight deviation of the data from the model in Figure 8 can be accounted for by the non-uniformity in the particle size of the polymer suspension and by the fact that the same mass transfer coefficient was employed for three different colloid concentrations.

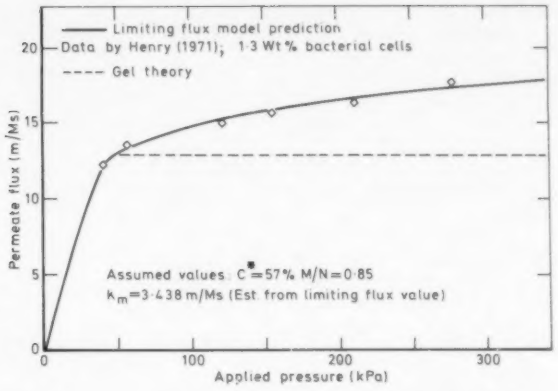


Figure 7. Dependence of flux on the applied pressure for bacterial cell suspension.

DISCUSSION

It is quite clear from the data used by the proponents of the gel polarisation theory that for a given membrane–solute system there exists a limiting concentration at the membrane surface under normal ultrafiltration conditions. The limiting flux varies with bulk solute concentration and mass transfer coefficient in exactly the way that would be expected were such a limiting concentration to exist. Where the older theory breaks down is that it would assume that the limiting concentration was invariant with the type of membrane, and only a function of the type of solute. Moreover it does not predict the correct variation of the limiting flux with molecular weight of the solute.

The alternative model expounded here assumes that the limiting concentration is a function of the interaction between solute and membrane. It is related to the relative size of membrane pore and solute particle or molecule and depends on some part of the solute coming into contact with the membrane surface. If this contact occurs very close to a pore the flow through the pore can be restricted through convective forces transporting the remainder of the molecule to the pore mouth and blocking flow completely. On this occurring the convective flow ceases and the molecular motion is now reversed as a result of diffusive tendency away from the membrane surface. The distance of this diffusion is limited by the rate of diffusion so when the pore mouth is once more freed and flow can resume, the solute molecule once more returns to block the flow. The resultant flux is invariant with transmembrane pressure as higher pressures merely serve to block the membrane faster owing to the higher flux prevailing during the shorter time that the pore remains unblocked.

When the development of the limiting flux is modelled it is apparent that there must be a relationship between the solute concentration at the membrane surface and the probability of a pore being in the partially blocked condition. A theoretical model for this relationship has not yet been developed from first principles. The alternative approach of trying some simple empirical relationships was adopted and, although simple functions of the ratio between the prevailing concentration and the limiting concentration were not successful, one which was a simple function of the ratio between existing and limiting fluxes was successful. As the flux is related directly to the surface concentration it remains a function of the concentrations, although not a simple one.

For a leaky membrane in an unstirred cell it is clear that since there is no stirring the mass transfer coefficient will be low and there will be very little tendency for molecules to be removed from the blocking position around the pores even when there is no flow through the pores. Accordingly blockage occurs at a very low limiting flux in all pores that have a tendency to block. There are pores whose size prevents blockage and they eventually become the only pores permitting flow. As they freely pass the solute the rejection coefficient drops to near zero and the permeate has the same composition as the retentate. Between the start of the ultrafiltration and the state of near zero rejection there is a time during which the blockage of the pores is occurring. In this period the membrane surface concentration is higher than the bulk concentration, rejection will occur, and then after blockage of the smaller pores is complete the larger pores pass this higher concentration unimpeded. The instantaneous rejection coefficient is then negative, although the cumulative average rejection coefficient is always positive. In analysing this case the flux is always related to the total membrane area.

In the case of colloidal solutions interaction occurs in such a way that the pore is not completely blocked, and the pore is so screened by the nearby large particle that there is no space for a blocking particle to attach. Here one must distinguish the ratio between the areas where a particle blocks a pore, and those areas where it protects the pore from blockage and merely hinders the flow.

Again developing the area concept, the limiting flux occurs through blocked pores, with a restricted flow, defined as some fraction of the pure solvent flux occurring through the hindered pore area. The ratio between the two areas will depend on particle diameter and pore pitch.

CONCLUSION

A new model has been developed to account for the limiting ultrafiltration flux that occurs as transmembrane pressure is raised. The model assumes that

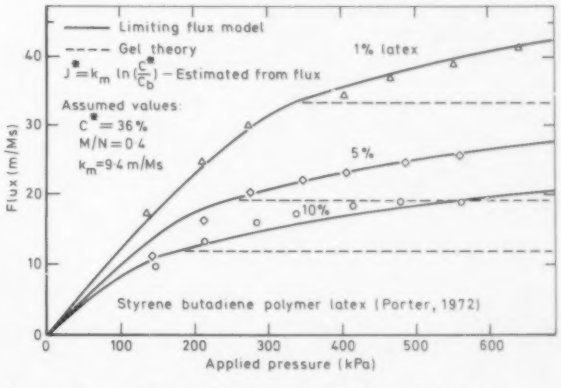


Figure 8. Dependence of flux on pressure for colloidal latex.

membrane pores are obstructed in a dynamic manner by solute molecules adsorbed to the membrane in the region of the pores. The limiting flux which is observed can be related to a limiting concentration of solute in the vicinity of the membrane surface by a concentration polarization equation. The flux is found to depend on the limiting concentration, bulk concentration and the mass transfer rate in the same way as with the older gel polarization model. The limiting concentration, however, is not simply a function of the solute but of the solute/membrane interaction. It is found to scale properly with solute molecular weight, and to change with membrane material.

Two asymptotic situations are also treated correctly by the new model. These are the case of solute particles (i.e. colloids) much larger than the pores, and those much smaller than some of the pores (leaky membranes). The older gel polarization model could not handle either case. Specifically it was predicted and then observed that a leaky membrane in an unstirred cell would pass a solution identical to the bulk solution after a short time during which non-leaky pores became blocked. The blocking was essentially irreversible because of the very low mass transfer coefficient in the unstirred cell. Existing data on ultrafiltration of colloids was fitted well by the new model.

The model requires three parameters, the mass transfer coefficient, the limiting concentration for the particular solute/membrane system and a parameter relating pore size distribution to solute particle size.

SYMBOLS USED

a	particle diameter (L)
C	concentration (M/L^3)
d	pore diameter (L)
D	diffusivity (L^2/T) or distance between pores/pore radius ratio (dimensionless)
D_p	particle diameter (L)
E	rejection coefficient (dimensionless)
J	flux (L/T)
J_1	flux contribution by unoccupied pores
J_2	flux contribution by occupied pores
K	Langmuir constant (M/L^3)
k_m	mass transfer coefficient
M	number of particles in surface region per unit area
N	molecular weight (M)
n	density of pores, No per unit area
P	pressure (M/LT^2)
Q	molal concentration (L^{-3})
R	radius (L)
R_m	membrane hydraulic resistance (L^{-1})
X	a function of flux of surface concentration (dimensionless)
x	longitudinal co-ordinate (L)
Y	transverse co-ordinate (L)

Greek letters

α	fraction of pore larger than the particle
γ	where $J_\alpha = \alpha J_p$
δ	boundary layer thickness
ξ	correlation distance (L)
θ	fraction of surface covered
μ	viscosity (M/LT)
σ	ratio of pure water flux to actual flux limiting pressure (equation 7)

Subscripts

b	at bulk condition
g	at gelling or limiting condition
m	fraction of blocked pores of the membrane
p	of permeate or pressure
r	radial or of rejecting pores
s	at membrane surface

Superscripts

*	at the limiting condition

REFERENCES

1. Nakao, S. I., Norumura, T. and Kimura, S., 1979, *AIChEJ* 25: 615–622.
2. Howell, J. A. and Velicangil, O., 1980, *Polymer Science & Technology*, Vol. 13, A. R. Cooper (ed) pp. 217 (Plenum Press, N.Y.).
3. Michaels, A. S., 1968, *Chem Eng Prog.* 64: 31 – 43.
4. Goldsmith, R. L., 1971, *Ind Eng Chem F*, 10: 113.
5. de Gennes, 1979, *Scaling Concept in Polymer Physics* (Cornell University Press, Ithaca, N.Y.).
6. Shen, J. J. S. and Probstein, R. F., 1977, *Ind Eng Chem F*, 16: 459–465.
7. Kozinsky, A. A. and Lightfoot, E. N., 1972, *AIChEJ*, 18: 1030.
8. Trettin, D. R. and Doshi, M. R., 1980, *Ind Eng Chem F*, 19: 189–194.
9. Leung, W. F. and Probstein, R. F., 1979, *Ind Eng Chem F*, 18: 274–278.
10. Porter, M. C., 1972, *Ind Eng Chem Prod Res Dev* 11: 234–248.
11. Blatt, W. F., Dravid, A., Michaels, A. S. and Nelson, L., 1970, *Membrane Science and Technology*, J. E. Flinn (ed) pp. 47, (Plenum Press, N.Y.).
12. Henry, J. D., 1972, in N. N. Li (ed) *Recent Developments in Separation Science* (CRC Press, Cleveland) pp 205–225.
13. Madsen, R. E., 1977, *Hyperfiltration and Ultrafiltration in Plate and Frame Systems* (Elsevier, N.Y.).
14. Fane, A. G., Fell, C. J. P. and Nor, M. T., 1980, *Polymer Science and Technology*, Vol. 13, A. R. Cooper (ed) pp. 631 (Plenum Press, N.Y.).
15. Velicangil, O., 1979, *Ph.D. Thesis* (University of Wales)
16. Fane, A. G., 1982, Notes for "Membrane Technology for Industry, an IChemE short course held at Imperial College, London.
17. Belfort, G., Chin, P. and Dziewulski, D. M., 1982, *World Filtration Congress III, Doningtown, PA. U.S.A. Sept* 14–16 (Uplands Press Ltd, Croydon)

ADDRESS

Correspondence on this paper should be addressed to Dr J. A. Howell, Department of Chemical Engineering, University College of Swansea, Singleton Park, Swansea SA2 8PP.

The manuscript was received 4 *February* 1983 *and accepted after revision* 27 *June* 1984.

VOL 62 198

USE OF FREQUENCY–CONSEQUENCE CURVES TO EXAMINE THE CONCLUSIONS OF PUBLISHED RISK ANALYSES AND TO DEFINE BROAD CRITERIA FOR MAJOR HAZARD INSTALLATIONS

By D. O. HAGON

Imperial Chemical Industries, Mond Division Safety Department, Winnington, Cheshire

It has become customary to express criteria for the frequency of occurrence of events involving differing numbers of fatalities in the form of plots of frequency f, or cumulative frequency F, versus consequence N. Also, consequence has been raised to the power α to express 'aversion' to events of greater consequence (e.g. multiple fatalities). While the mathematics of such curves appear to be well understood, the practical application of their meaning when used to develop criteria has not been widely pursued in the literature. Simple mathematical properties relating cumulative frequency F, aversion index α and total expectation of fatalities/year D, are used to examine some published F–N curves and to predict criteria for major hazard installations on a consistent basis for further discussion and comparison.

OL.
62
984

INTRODUCTION

Recent papers[1,2] have described the mathematical basis for using expressions of the form $fN^{\alpha} = r$ (r is a constant) to relate frequency f, consequence N and risk aversion index α.

This mathematical reasoning can be further developed, assuming N is a continuous function, to enable frequency f, cumulative frequency F, consequence N and α, the index of aversion, to be handled logically in relation to practical experience. A further integration can be used to calculate expected average total fatalities/year implied by the f–N curve. Computer calculations enable accurate numerical summations to be obtained from the exact equations and these are presented graphically in Figure 1.

The purpose of this paper is to demonstrate how practical use can be made of the relationships to test existing risk analyses and to set broad criteria for the design of major hazard installations with the potential to cause multiple fatalities.

RELATIONSHIPS BASED ON $fN^{\alpha} = r$

The following notation will be used:

f = frequency (years^{-1}).
f_1 = frequency of an event with unit consequence (e.g. 1 fatality). In general f_n represents an event with n fatalities.
F = cumulative frequency (years^{-1}).
$(F)_1^N$ = cumulative frequency of all events with consequence 1 to N.

$$S(K,\alpha) = \sum_{N=1}^{N=K} \frac{1}{N^{\alpha}}$$

M = maximum expected value of N
$F_N = (F)_N^M$, the cumulative frequency of N or more deaths. This quantity is of use where the upper bound of consequence is uncertain and a worst case assumption must be made. If necessary, M may have to be taken as infinite.
$(D)_1^N$ = total expected fatalities per year for events with consequence 1 to N.
r = a constant.
α = an index used to express aversion to risk.

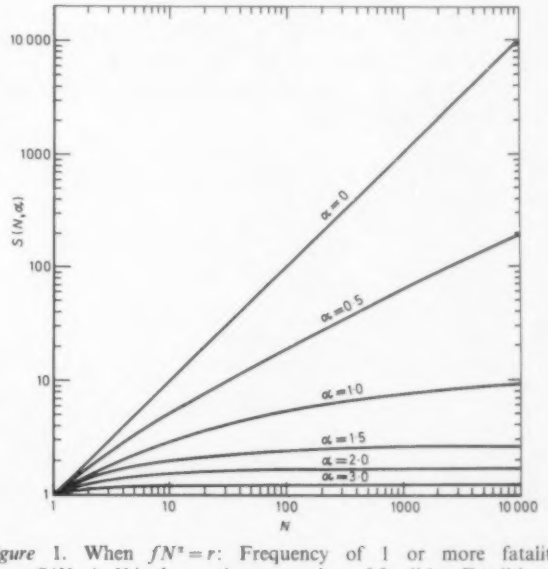


Figure 1. When $fN^{\alpha} = r$: Frequency of 1 or more fatalities $F_1 = rS(N,\alpha)$. N is the maximum number of fatalities. Fatalities per year = $D = rS(N,\alpha - 1)$.

© Institution of Chemical Engineers

Table 1. Integrals Based on $fN^{\alpha} = r$

Aversion Index	Cumulative Frequency $(F)_{N_1}^{N_2}$	$F_N = (F)_N^{\infty}$	Total Deaths/Year $(D)_{N_1}^{N_2}$
$\alpha = 1$	$r \ln \frac{N_2}{N_1}$	∞	$r(N_2 - N_1)$
$1 < \alpha < 2$	$\frac{r}{\alpha - 1}\left(\frac{1}{N_1^{\alpha-1}} - \frac{1}{N_2^{\alpha-1}}\right)$	$\frac{r}{\alpha - 1}\left(\frac{1}{N^{\alpha-1}}\right)$	$\frac{r}{2 - \alpha}(N_2^{2-\alpha} - N_1^{2-\alpha})$
$\alpha = 2$	$r\left(\frac{1}{N_1} - \frac{1}{N_2}\right)$	$\frac{r}{N}$	$r \ln \frac{N_2}{N_1}$
$\alpha > 2$	$\frac{r}{\alpha - 1}\left(\frac{1}{N_1^{\alpha-1}} - \frac{1}{N_2^{\alpha-1}}\right)$	$\frac{r}{\alpha - 1}\left(\frac{1}{N^{\alpha-1}}\right)$	$\frac{r}{\alpha - 2}\left(\frac{1}{N_1^{\alpha-2}} - \frac{1}{N_2^{\alpha-2}}\right)$ $= \frac{r}{\alpha - 2}$ for $N_2 = \infty$, $N_1 = 1$

Note: The above relations approximate to the exact equations (3), (4), (5) and (6) if $N > 30$ and limits are taken to be $N_2 + 0.5$, $N_1 - 0.5$.

Using the above notation, we assume as a basic relationship that

$$fN^{\alpha} = r \tag{1}$$

and it follows that

$$(F)_1^K = \sum_{N=1}^{N=K} f = r \sum_{N=1}^{N=K} \frac{1}{N^{\alpha}} \tag{2}$$

and since

$$S(K, \alpha) = \sum_{N=1}^{N=K} \frac{1}{N^{\alpha}}$$

then

$$(F)_1^N = rS(N, \alpha) \tag{3}$$

Computed values of $S(N, \alpha)$ for $N = 1$ to 10000 and a range of values of α are plotted in Figure 1.

Values of cumulative frequency between limits of consequence N_1 and N_2 can be obtained by difference. Thus:

$$(F)_{N_1}^{N_2} = r[S(N_2, \alpha) - S(N_1 - 1, \alpha)] \tag{4}$$

(Note if $N_1 - 1 < 1$ the relationship breaks down as does the frequency distribution $fN^{\alpha} = r$ when $N = 0$.)

Total fatalities per year can be obtained from a similar type of summation. Thus:

$$(D)_1^K = \sum_{N=1}^{N=K} fN = r \sum_{N=1}^{N=K} \frac{1}{N^{\alpha-1}} \tag{5}$$

or,

$$(D)_1^N = rS(N, \alpha - 1) \tag{6}$$

and

$$(D)_{N_1}^{N_2} = r[S(N_2, \alpha - 1) - S(N_1 - 1, \alpha - 1)].$$

Values of D can be obtained approximately by using Figure 1.

An appreciation of the functional relationships may be gained by treating f as a continuous function of N. Then,

$$(F)_1^K = \int_1^K f \, \mathrm{d}N \tag{7}$$

and,

$$(D)_1^K = \int_1^K fN \, \mathrm{d}N \tag{8}$$

The integrations of equations (7) and (8) are simple, but the functional relationships change at $\alpha = 2$ and consequently the integrals are shown in Table 1. It should further be noted that the approximation based on the assumption that N is continuous is not accurate for $N <$ approx 30.

EXAMPLES

Storage of Ammonia

Referring to Figure 2 which has been published[3] as an example of F–N curves for an ammonia storage sphere in the Rotterdam Europort area, we may make an approximation and choose $\alpha = 2$ and $(F)_1^N = 10^{-3}$ per year. The curves presented in Figure 2 all fall below the F–N curve that these choices represent (shown dashed in

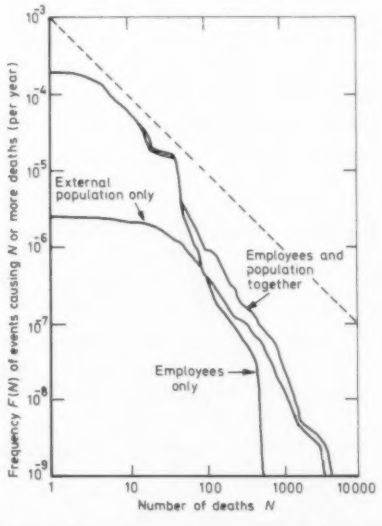


Figure 2. Example of $F - N$ curves for an ammonia storage sphere in Rotterdam/Europoort area[3,5].

VOL. 62 1984

Figure 2). We can now calculate the properties of our assumed F–N curve, knowing that the curves representing predicted events are below it and therefore the F–N curve could represent criteria which are not exceeded.

We have chosen $\alpha = 2$ and we note from the Table that:

$$F_N = \frac{r}{N}$$

Also $fN^2 = r$, so that the frequency of single fatalities $f_1 = F_1 = r$. This is untrue since F_1 is obviously greater than f_1 and it illustrates that the approximation based on the assumption that N is continuous is not accurate for $N <$ approx 30.

Using exact equation (3), r can easily be found from:

$$r = \frac{(F)_1^N}{S(N,\alpha)} = \frac{F_1}{S(N,\alpha)}, \text{ provided } N \text{ is large}$$

Choose $N = 5000$ (say) and read from Figure 1:

$S(5000, 2) = 1.65$ approx.

Now, from $fN^2 = r$ and $N = 1$, we have:

$$r = \frac{10^{-3}}{1.65} = 0.61 \times 10^{-3} = f_1$$

which now differs appreciably from F_1 which we have previously set at 10^{-3}/year.

Further figures can now be derived as follows: Cumulative frequency of accidents with 3–30 fatalities [exact solution shown in square brackets]:

$$(F)_3^{30} = 0.61 \times 10^{-3} \left[\frac{1}{3} - \frac{1}{30}\right]$$

$$= 1.8 \times 10^{-4}/\text{year} \quad [2.2 \times 10^{-3}]$$

and

$$(F)_{30}^{300} = 0.61 \times 10^{-3} \left[\frac{1}{30} - \frac{1}{300}\right]$$

$$= 1.8 \times 10^{-5}/\text{year} \quad [2.2 \times 10^{-5}]$$

And total expected deaths/year

$$(D)_{N_1}^{N_2} = r \ln \frac{N_2}{N_1}$$

So

$$(D)_1^{30} = \frac{10^{-3}}{1.65} \ln \frac{300}{1} = 3.5 \times 10^{-3}/\text{yr} \quad [2.4 \times 10^{-3}]$$

or if 3000 are exposed

$$(D)_1^{3000} = \frac{10^{-3}}{1.65} \ln \frac{3000}{1} = 4.8 \times 10^{-3}/\text{yr} \quad [5.2 \times 10^{-3}]$$

The increased expectation of fatalities when all events are considered is an informative consideration to the assessor. There are some who regard it as meaningless to talk of the deaths/year implied by an event that may happen only once in 10000 years, but the calculation reveals that by neglecting such events, a major portion of the average risk may be missed in the assessment.

In the above example, the problem of relating low frequency high consequence events to everyday experience which is mostly of high frequency low consequence events, is exposed. The idea of consistency with a known degree of risk aversion expressed by $\alpha = 2$ is also apparent.

The assumption that the F–N function is continuous gives rise to a number of relationships that give approximate results quite simply and are, therefore, retained where possible. Exact solutions for the discontinuous case will continue to be shown in brackets where appropriate. Regard is shown for the order of accuracy appropriate to this sort of work by quoting only the minimum number of significant figures.

Societal Risk Criteria—Provincial Waterstaat Groningen

The criteria represented by Figure 3 have been described as sophisticated and stringent[3]. We can use our relationships to examine whether they are reasonable. Thus if we examine the upper line we obtain the following data:

F_1 (one or more deaths) $= 10^{-2}$/year

F_{1000} (1000 or more deaths) $= 10^{-8}$/year

thus

$FN^2 =$ constant by inspection.

But we know that: $F_N N^{\alpha-1} = r/(\alpha - 1)$ (Table 1, as $N_2 \to \infty$) therefore $\alpha - 1 = 2$ or $\alpha = 3$ for 1 to 1000 deaths ($\alpha = \infty$ for >1000 deaths).

Here, N is large and we find, as expected, that the exact equations confirm the indications of the continuous functions that $\alpha = 3$. Also $r = 8.3 \times 10^{-3}$ and deaths/year $D = 1.4 \times 10^{-2}$/year.

The Provincial Waterstaat Groningen (PWG) have chosen a higher degree of aversion to risk than that proposed by Okrent[4] of $\alpha = 1.2$. In fact, Okrent comments that values as high as 2 or 3 would prohibit many technological endeavours and this is certainly likely to be so if the predictions of risk analysts continue to be so pessimistic. Nevertheless, this study aims to show that values of $\alpha < 2$ indicate an unduly high accumulation of risk if large numbers of people are involved. The boundary for the acceptable region (the lower line) can now be examined from the graph:

F_1 (one or more deaths) $= 10^{-6}$

F_{10} (ten or more deaths) $= 10^{-8}$

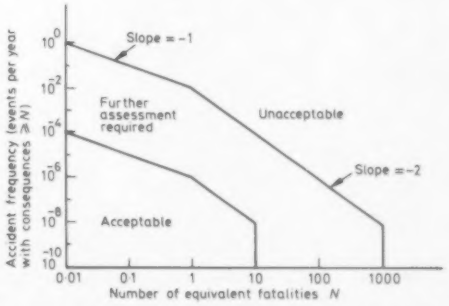


Figure 3. Societal risk criteria published by the Provincial Waterstaat Groningen[3].

Again FN^2 is constant by inspection and thus $\alpha = 3$, showing a degree of aversion consistent with the upper line and similarly from the exact equation we get:

$$\alpha = 2.8, \quad r = 8 \times 10^{-7} \quad \text{and} \quad D = 1.5 \times 10^{-6}$$

Note here, that this answer has been obtained by computer using an iterative trial and error technique with a slight reduction in α, although the F–N line appears to have the same slope. This is because the maximum credible event has been taken to be represented by $N = 100$ and the criteria can be met in the exact equations with a slightly lower value of α. Values of α are further discussed below under choice of aversion index.

We now see that an implied total of 1.5 fatalities in 10^6 years is the PWG acceptable criterion for societal risk. The unacceptable figure is 1.4×10^{-2} deaths/year and the region where further assessment is required lies between the two figures. It may be that current doubts about the value of risk assessment because of its inaccuracies are illustrated here and that because of such inaccuracies it is necessary to be extremely pessimistic in attempting to specify what is acceptable.

Canvey and Societal Risk

It is now possible to use the analysis to compare the predictions of the Canvey reports with one another.

Referring to Figure 4, the predictions of the First Canvey Report are represented by the upper line and its slope is approximately -0.1, implying $\alpha = 1.1$ and an aversion to risk lower even than the low figure of 1.2 that has been recommended by Okrent[4]. A similar aversion but at a lower frequency is exhibited in the middle line which represents the First Canvey Report improvements. The evidence of risk aversion of a higher level is only apparent for values of $N > 1000$ where the slope is equivalent to a value of $\alpha > 2$.

In view of the low value of α shown for $10 < N < 1000$, one would try to correct for this by choosing a value of F_1 and hence r which would allow the slope of the arbitrary boundary line to be increased.

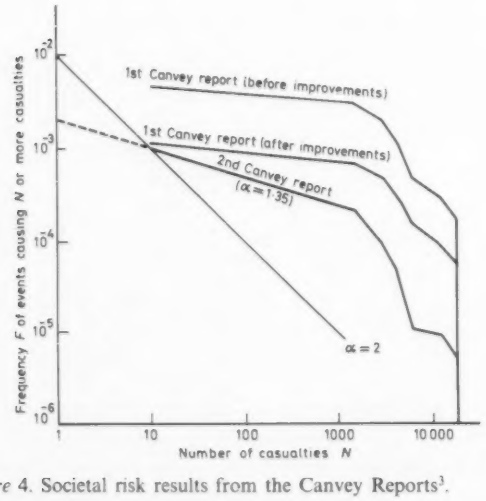


Figure 4. Societal risk results from the Canvey Reports[3].

Thus if

$$F_1 \text{ (one or more casualties)} = 10^{-1}/\text{year}$$

and

$$F_{1000} \text{ (1000 or more casualties)} = 3 \times 10^{-3}/\text{year}$$

we can use

$$F_N N^{\alpha - 1} = \frac{r}{\alpha - 1} \quad \text{(Table 1)}$$

to obtain

$$\alpha = 1.5 \text{ and } r = \frac{F_1}{S(1000, 1.5)}$$

$$= 0.04 \text{ (by equation 3).}$$

Such a value of α falls reasonably in the range suggested by Okrent[4] but obviously the average number of casualties/year implied by an increased value of r may be unacceptable.

Thus the implied average number of casualties from incidents with 30–300 fatalities, if this criterion is met, is given by:

$$(D)_{30}^{300} = \frac{r}{2 - \alpha}(N_2^{2-\alpha} - N_1^{2-\alpha})$$

$$= \frac{0.4 \times 10^{-1}}{2 - 1.5}(300^{0.5} - 30^{0.5})$$

$$= 0.95 \text{ casualties/year [0.9 casualties/year]}$$

In trying to fit a curve to the Canvey data, it must be emphasised that the purpose is to devise criteria for the risk of any event that we wish to consider. It does not mean that because there are not enough known events to 'fill up' the area under the curve, that the criteria should be changed or are invalid.

We can now consider the lower line which represents the figures in the Second Canvey Report in more detail.

Here again, the slope of the F–N curves gives an indication of the aversion index. (The actual value of index that fits any two given values of F_1 and F_N can be calculated by trial and error using the computer and is generally less than that indicated by the slope of the F–N line depending on the maximum number of people assumed to be affected. See below on choice of aversion index.)

Thus reading from figure 4:

$$F_{10} \text{ (10 or more casualties)} = 10^{-3}$$

$$F_{1000} \text{ (1000 or more casualties)} = 2 \times 10^{-4}$$

and the slope is -0.35, whence aversion index $\alpha = 1.35$ approx, equivalent to a low degree of aversion to risk until $N > 1000$ when the slope changes and the aversion index increases substantially.

Using the computer and the above information, we can derive:

F_1 (1 or more casualties)
$= 2 \times 10^{-3}$ (by producing the F–N line to $N = 1$)
$\alpha = 1.12$ (assumes maximum number affected $= 2000$)
$r = 4.2 \times 10^{-4}$

VOL. 62 1984

Table 2. For $F_1 = 10^{-2}$/year and $(F)_N^M = 10^{-3}$/year

Max Number Affected	$N = 10$			$N = 30$		
M	α	$r \times 10^{-3}$	$D \times 10^{-2}$	α	$r \times 10^{-3}$	$D \times 10^{-2}$
10	<1	—	—	—	—	—
30	1.63	4.9	3.7	<1	—	—
50	1.72	5.2	4.0	1.08	2.5	9.9
100	1.78	5.3	4.6	1.38	3.6	10.0
300	1.81	5.4	5.8	1.5	4.0	13.1
1000	1.83	5.4	7.6	1.56	4.2	19.9
5000	1.83	5.45	10.6	1.58	4.3	36.5

NB: $(F)_N^M$ is a particular case of equation (4) where $N_2 = M$ and $N_1 = N$, and $M > N$.

$D = 0.36$ casualties/year
$f_1 = 4.2 \times 10^{-4}$/year

This is a good example of using criteria that exhibit a low degree of risk aversion, for while the criterion for single casualty incidents f_1 might be 4.2×10^{-4}/year or once in about 2400 years, the accumulation of casualties from other events implied by the criteria mounts up to an average rate of 0.36 casualties/year, or one in about 3 years, which may be thought to be excessive.

In comparing Canvey 1 and 2, however, the key point remains that in Canvey 1, $F_{1000} = 3 \times 10^{-3}$/year was considered to be unacceptable and that in Canvey 2, a considerable improvement on the previous figure has been achieved to make $F_{1000} = 2 \times 10^{-4}$/year.

It is explained by Cox and Baybutt[2] that the choice of α is not entirely unrestricted. In particular, values of $\alpha < 2$ result in unduly high expectation of total consequences/year as the exposed population increases.

CRITERIA—CHOICE OF AVERSION INDEX

Referring again to Figure 4, an additional line has been drawn in, of slope corresponding to $\alpha = 2$ and passing through the point $(N = 1, F_1 = 10^{-2})$. This line contains sufficient information for computer calculations to be done, which illustrate what would be the implications if it were used as a risk criterion. The results of the calculations are given in Table 2 for two cases: Frequency of N or more deaths $= 10^{-3}$/year for $N = 10$ and for $N = 30$ as the maximum number thought to be affected (M) is allowed to increase.

It will be seen that not only can consistent frequency criteria be obtained from such calculations, but total average risk in terms of deaths per year can be obtained.

A further important property is that as the maximum number of people thought to be affected increases, a greater degree of aversion to risk is required to meet the given frequencies. This may, with hindsight, appear to be quite obvious but if so, it is surprising how many papers are published each year in which it seems there is difficulty in relating risk criteria for single fatality events to those for multiple fatalities and in development of criteria which warn of higher standards required where there is some dread risk which may affect a large number of people.

In choosing a value for the aversion index, one should consult Figure 1 and note that for $\alpha > 1.5$ there is considerably less increase in the value of $S(N, \alpha)$ as N increases. However, the further important factor to note is that deaths per year, D, is a function of $S(N, \alpha - 1)$ and to avoid high values of D as N increases, it is important to choose $\alpha - 1 > 1$, or $\alpha > 2$, if possible. It is obviously possible to live with lower values of α by limiting the maximum size of event or the number of people affected and this is currently under active consideration by risk analysts in terms of planning limitations in the vicinity of major hazard sites.

MAJOR HAZARD INSTALLATIONS

It is possible to use the analysis to stipulate criteria for the design of major hazard installations from surprisingly simple and apparently inadequate data. For example, a comprehensive description of the problems in the use of risk criteria is given by Griffiths[5] who uses finite difference methods. The continuous frequency distribution assumption here presented is an approximation, but it is simpler to use and accurate enough for the purpose.

If, for example, we consider that there are 500 installations capable of giving rise to such an event as happened at Flixborough, then if such an event occurs as often as once in 100 years, this immediately imposes a cumulative frequency $(F)_N^M$ per installation of, at most, 2×10^{-5}/year.

The foregoing analysis can now be used to derive criteria which could be imposed on the design of plants.

If we assume that between 30 and 300 fatalities are possible in the realisation of a major hazard, for $\alpha = 2$, we have from Table 1:

$$F_{30}^{300} = r\left(\frac{1}{30} - \frac{1}{300}\right) = 2 \times 10^{-5}$$

whence

$$r = 6.7 \times 10^{-4}$$

and the corresponding rate for single fatality accidents involving the major hazard risk is 6.7×10^{-4} per year or 1 in 1500 years per installation [exact equations 6.5×10^{-4}].

The total deaths per year $= r \ln(300/1) = 6.7 \times 10^{-4} \ln 300 = 3.8 \times 10^{-3}$/year [exact equations 4.1×10^{-3} or 1 in 263 years].

Having made some simple overall assumptions, we now have standards which are implied by the chosen

minimum allowable frequency and which dictate clearly the standards of design which must be bettered if the standard is to be achieved.

If Fatal Accident Rate (FAR) is to be related to the criteria, one must first note that this quantity is usually related to the hours of exposure of the man at most risk, giving the risk of death in 10^8 hours of such exposure. Nevertheless, it is wise to check that if a site has 500 employees whose average FAR is 2, then the average number of deaths to be expected is 1.7×10^{-2} per year (assuming 1700 worked hours/man/year) and to note that the expectation we have taken for major hazard risk is less than this at 4.1×10^{-3} per year. It may be here that we encounter the need to estimate the costs and the benefits of achieving even lower levels of risk. Moreover, as lower levels of FAR are achieved, the major hazard risk becomes a more significant part of the total risk.

CONCLUSIONS

There are many caveats to be applied to the over-enthusiastic use of F–N curves. These are carefully enumerated by Wu-Chien and Apostolakis[1]. Some of the assumptions that have to be made may appear daunting and arbitrary, but the contention is made here that practical use of simple relationships gives a greater consistency and insight into criteria and the meaning of some of the predictions of the risk analysts.

The equations presented in this paper enable exact numerical calculations relating to F–N curves to be carried out and, in particular, make clear distinction between frequency and cumulative frequency summed between defined limits of numbers of people thought to be exposed to risk. It has been thought useful also to present approximate equations based on the assumption of a continuous frequency consequence relationship which, if used within the appropriate constraints, give rapid solutions and a clear appreciation of the functional relationships implied by the apparently simple basic proposition that $fN^{\alpha} = \text{constant}$.

Further, it is important to be able to relate standards for single fatality incidents to those for multiple fatality incidents while incorporating a known degree of risk aversion. Operators and designers of plant may in their lifetimes unfortunately experience the smaller events but the larger ones are, thankfully, so few and far between that it is difficult to specify (and defend) design criteria and standards of operation that cannot exist without some residual risk. It is the object of this paper to provide a practical method of generating consistent criteria which the designer, operator and public official can use and defend with greater confidence in their integrity.

It should be emphasised that the figures given in this paper should be subject to further debate. They are not presented as standards which should henceforward be imposed, but rather as examples of consistent treatment of one area of a difficult multi-component or many factored system.

ACKNOWLEDGEMENTS

Support and encouragement for colleagues is gratefully acknowledged. In particular to J. T. Illidge and E. B. Ranby for their comments, L. W. Fielding for help with the computer calculations, and Maureen Young for typing many drafts. Permission from ICI to publish is gratefully acknowledged.

REFERENCES

1. Wu-Chien, J. S. and Apostolakis, G., 1981, *Reliability Engineering*, 2.
2. Cox, D. C. and Baybutt, P., 1982, *Nuclear Technology*, 57 (June).
3. Slater, D. H., 1982, *A Consultant's Approach to the Regulations*, (Technica, Oyez, London).
4. Okrent, D., 1981, *The Assessment and Perception of Risk* (The Royal Society of London).
5. Griffiths, R. F., 1981, *Dealing with Risk* (Manchester University Press).

ADDRESSES

Correspondence on this paper should be addressed to Mr D. O. Hagon, Ravelstone Lodge, Alvanley Road, Manley, Warrington, WA6 9ED.

The paper was submitted 6 February 1984 and accepted for publication 11 April 1984.

VOL. 62 1984

MODEL OF ISOTHERMAL TRANSPORT-LINE (RISER) AND MOVING-BED CATALYTIC REACTOR

By A. A. SHAIKH and J. J. CARBERRY

Laboratory of Catalysis, University of Notre Dame, Indiana, USA

When one is confronted with catalyst or non-catalytic solid decay as a function of real time, the transport-line (or raining solids) reactor (TLR) or its dense-phase equivalent, the moving bed reactor (MBR), deserves utilisation insofar as fresh solids (catalyst) are continuously introduced whilst spent solid agents are withdrawn in the presence of a continuous reactant-bearing fluid flow. There are presented herein analyses of isothermal conversion (with mole change) for arbitrary order and selectivity in the important instance of linear simultaneous-consecutive reactions—each step suffering deactivation of differing severity. Implications regarding the merits of selective poisoning are made evident.

INTRODUCTION

When one is confronted with a solid catalysed reaction marked by rather rapid deactivation (e.g. catalytic cracking with coke deposition) the need for continuous supply of fresh (or regenerated) catalyst coupled with removal of that spent (decayed) species demands a system which, in essence, requires continuous, steady-state contacting of reactant-bearing fluid with a continuous input and withdrawal of solids. Thus was born the moving-bed catalytic cracker (Mobil-MBCC) and, later, the transport-line cat-cracker (TLCC). The difference between the MBCC and TLCC is simply one of density of the moving dense phase. In the moving bed cat-cracker (MBCC), deactivating solids are passed countercurrently, as a packed bed, to the fluid stream. In the TLCC, co-current flow of fluid carries the solids upward into and from the reaction zone.

The MBCC and TLCC represent, respectively, dense and dilute phase fluid–solid contactors. In the instance of the moving bed, solids residence time is fixed by solids feed-withdrawal rate, whilst in the TLCC solids residence time is established by net solids velocity dictated by fluid velocity and solids terminal velocity. So the moving bed reactor (MBR) is nought but a countercurrent dense solids-phase version of the co-current dilute phase transport-line reactor (TLR). In either case one encounters a continuous addition and withdrawal of solid co-reactant or catalyst *only* when solids consumption or catalyst decay forbids fixed bed or batch fluid bed operation.

A number of workers have devoted attention to the TLR (or Riser Reactor). Theses rooted in a non-decaying catalyst system must be dismissed. Why use a TLR or, its equivalent, the moving-bed reactor (MBR), if the catalyst does *not* deactivate? In a non-catalytic gas–solid reaction system (e.g. coal gasification or volitilisation), decay is nought but co-reactant consumption.

However, studies which embrace such an unrealistic premise do prove of merit insofar as they clearly demonstrate that inter-intra-particle gradients are of total insignificance in the TLR[1,2]. This is hardly surprising, given the fact that TLRs host particles of about 50 to 100 μm in diameter.

So without recourse to subtle mathematics one can ascertain the magnitude of first-order rate coefficient which is required if the Thiele modulus is to achieve a value of unit, (i.e. a zero intraphase gradient):

$$\phi = \frac{d_p}{6}\sqrt{\left(\frac{k}{D}\right)} \qquad (1)$$

For $\phi = 1$, $D = 10^{-2}\,\mathrm{cm^2\,s^{-1}}$, and $d_p \simeq 100\,\mu\mathrm{m}$ or 10^{-4} cm, we find that $k = 3600\,\mathrm{s^{-1}}$—an extraordinary chemical velocity coefficient; one surely encountered solely in such systems as NH_3 oxidation over Pt/Rh gauzes[3]. Thus while we are indebted to analyses rooted in inter-intraphase diffusion-reaction in the TLR, they merely support the elementary conclusion that local gradients in the TLR are negligible.

One study[4] anticipates this simple conclusion *and* rightfully incorporates decay of the catalyst. Limited to first-order kinetics it nevertheless ignores volume change due to reaction; as is found in catalytic cracking. In the wake of the work of Weekman and Nace[5], Shah et al[6] compare model and data in a riser craker (TLR). However the Weekman–Nace analysis implicitly ignores volume change due to reaction—a signal effect in catalytic cracking.

There are presented herein conversion relationships for nth-order reactions in a TLR (and its dense phase equivalent—the MBR) with arbitrary volume change due to isothermal reaction, and catalyst decay. There follows a treatment of the general linear triangular network wherein each of the three steps suffers unique decay.

Our treatment thus extends prior analyses insofar as non-linear, decay-laden kinetics with volume change is embraced as well as unique decay of each of three steps in the important selectivity (yield) triangular network.

Further, the issue of assumed decay functionality is addressed.

© Institution of Chemical Engineers

TRANSPORT LINE REACTOR (TLR) CONVERSION

The reactor is schematically depicted in Figure 1. We initially address ourselves to an nth-order reaction with mole change

$$A \xrightarrow{k} mB \tag{2}$$

Plug flow is assumed, as taught by Venuto and Habib[7], and intraphase gradients, i.e., within the porous particles, have been shown to be absolutely negligible[2] as indeed one would expect.

Catalyst decay is assumed to be of the exponential form[5]

$$k = k_0 \exp(-\alpha\theta) \tag{3}$$

where $\theta = z/u_0$ is catalyst residence time, and $u_0 = u - u_t$. Here, z is reactor height, u is fluid velocity, u_t is particle terminal velocity, and α is a decay constant. Decay can also be described in the hyperbolic form

$$k = \frac{k_0}{1 + \alpha\theta} \tag{4}$$

In terms of conversion x of reactant A forming product B by reaction (2), for an nth-order reaction with mole change we have, for feed A_0

$$A_0 u \varepsilon \frac{dx}{dz} = (1 - \varepsilon) A_0^n \left(\frac{1 - x}{1 + ex}\right)^n k$$

where $e = m - 1$ and ε is the void fraction in the reactor ($\varepsilon \rightarrow 1$ in a TLR, $\varepsilon \rightarrow 0.3$–$0.4$ in a MBR). Or

$$\frac{dx}{dz} = \frac{1 - \varepsilon}{\varepsilon} \frac{1}{u} A_0^{n-1} \left(\frac{1 - x}{1 + ex}\right)^n k$$

Multiplying by u_0 and noting that $dz/u_0 = d\theta$, we obtain

$$\frac{dx}{d\theta} = \frac{1 - \varepsilon}{\varepsilon} \frac{u_0}{u} A_o^{n-1} \left(\frac{1 - x}{1 + ex}\right)^n k \tag{5}$$

where k is given by either equation (3) or (4).

For a reactor cross-sectional area a, we note that

$$\frac{1 - \varepsilon}{\varepsilon a} a \frac{u_0}{u} = \frac{Q_s}{Q_f} = P \tag{6}$$

where Q_s = volume of solids/time, and Q_f = volume of fluid/time. So P is the solids to fluid feed ratio. Equation (5) is readily expressed in the integral form

$$\int_0^x \left(\frac{1 + ex}{1 - x}\right)^n dx = P A_0^{n-1} \int_0^{\theta_0} k \, d\theta \tag{7}$$

where k is a function of θ. Note that $\theta_0 = z_0/u_0$ where z_0 is the reactor length.

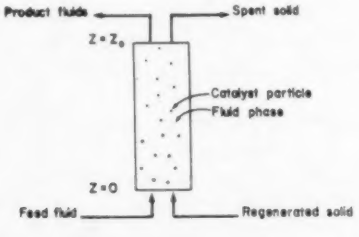


Figure 1. The transport-line reactor.

EXPONENTIAL DECAY

Should one assume[5] that k is described by equation (3), equation (7) then becomes

$$\int_0^x \left(\frac{1 + ex}{1 - x}\right)^n dx = \frac{P k_0 A_0^{n-1}}{\alpha} [1 - \exp(-\alpha\theta_0)] \tag{8}$$

The LHS of equation (8) is readily integrated for diverse values of reaction order, n, and extent of mole change due to reaction, e.

We illustrate the influence of order and mole change for first and second order, $n = 1$ and 2; and no mole change, $e = 0$, and a signal change, $e = 3$ (e.g., in catalytic cracking). In Figure 2, transport line isothermal conversion is plotted vs the design parameter function:

$$P\left(\frac{k_0 A_o^{n-1}}{\alpha}\right)[1 - \exp(-\alpha\theta_0)]$$

which mode of display demonstrates that earlier formulations[2] need not be parametric in P nor θ_0.

As far as isothermal conversion in a TLR is concerned, a signal influence of order and more importantly, molar expansion ($e > 1$) is surely manifested. Note that Figure 2 is of a semi-log display. In catalytic cracking, of apparent lumped order of[5] 2, neglect of mole change ($e \rightarrow 3$) results in a near order-of-magnitude error in P at a conversion of 90% for a given catalyst (k_0, α), residence time, θ_0, and feed, A_0; or a signal error in θ_0 results for a given P, catalyst character (k_0, α).

INFLUENCE OF DECAY FUNCTION

Should one assume hyperbolic decay (i.e., equation (4)), equation (7) becomes

$$\int_0^x \left(\frac{1 + ex}{1 - x}\right)^n dx = P \frac{A_0^{n-1} k_0}{\alpha} \ln(1 + \alpha\theta) \tag{9}$$

Clearly $\ln(1 + \alpha_1\theta) = 1 - \exp(-\alpha_2\theta)$ in Figure 2. So that $\alpha_1 \neq \alpha_2$ and the assumed form of the decay function affects an assessment of P for a desired conversion.

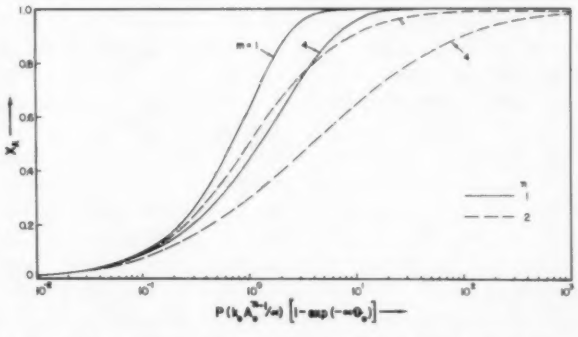
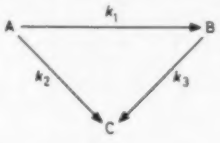


Figure 2. Gas conversion for diverse reaction orders and volume changes.

VOL. 62 1984

SELECTIVITY/YIELD

Consider the not uncommon triangular network



(10)

a lumped example being catalytic cracking where B is desired gasoline, C undesired coke and gas. This simultaneous and consecutive network lends itself to simple analysis, assuming linear kinetics and exponential decay: α_1, α_2 and α_3 for paths 1, 2 and 3, respectively. Thus

$$\frac{-\mathrm{d}A}{\mathrm{d}\theta} = PA\left[k_{1_0}\exp(-\alpha_1\theta) + k_{2_0}\exp(-\alpha_2\theta)\right] \quad (11)$$

$$\frac{\mathrm{d}B}{\mathrm{d}\theta} = PAk_{1_0}\exp(-\alpha_1\theta) - PBk_{3_0}\exp(-\alpha_3\theta) \quad (12)$$

or

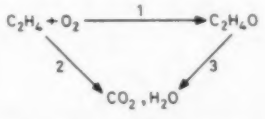
$$-\frac{\mathrm{d}B}{\mathrm{d}A} = \frac{1}{1+K_2\exp(\Delta_2\theta)} - \frac{K_3\exp(\Delta_3\theta)}{1+K_2\exp(\Delta_2\theta)}\frac{B}{A} \quad (13)$$

where $K_2 = (k_2/k_1)_0$, $K_3 = (k_3/k_1)_0$, $\Delta_2 = \alpha_1 - \alpha_2$, and $\Delta_3 = \alpha_1 - \alpha_3$. In general, point yield of B is

$$-\frac{\mathrm{d}B}{\mathrm{d}A} = \frac{1}{1+\bar{K}_2} - \frac{\bar{K}_3}{1+\bar{K}_2}\frac{B}{A} \quad (14)$$

where $\bar{K} = K\exp(\Delta\theta)$.

If B is the desired product as, say, in epoxidation of ethylene:



(15)

we desire $\Delta_2 < 0$ and $\Delta_3 < 0$. In practice, the condition $\Delta_2 < 0$ is achieved by organic halide poisoning of step 2 to the benefit of yield of ethylene oxide. Modest conversion levels minimize the import of step 3.

Equation (14) can be integrated to yield

$$\frac{B}{A_0} = \frac{1}{1+\bar{K}_2-\bar{K}_3}\left[(1-x)^{\bar{K}_3/(1+\bar{K}_2)} - (1-x)\right] + \frac{B_0}{A_0}(1-x)^{\bar{K}_3/(1+\bar{K}_2)} \quad (16)$$

Overall yield, B/A_0, vs conversion of A for diverse values of Δ_2 and Δ_3, is set forth graphically in Figures 3 and 4. In Figure 3, at fixed Δ_2, the influence of Δ_3 is made evident. In Figure 4, Δ_3 is fixed and Δ_2 varied. The base case in each instance is that of uniform decay, i.e., $\Delta_2 = \Delta_3 = 0$.

For hyperbolic decay, the point yield of B becomes

$$-\frac{\mathrm{d}B}{\mathrm{d}A} = \left[1 - \frac{B}{A}K_3\left(\frac{1+\alpha_1\theta}{1+\alpha_3\theta}\right)\right] \Big/ \left[1+K_2\left(\frac{1+\alpha_1\theta}{1+\alpha_2\theta}\right)\right] \quad (17)$$

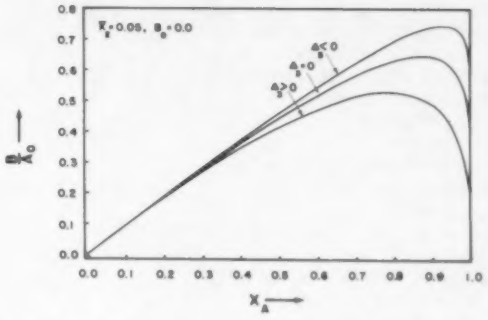


Figure 3. Effect of relative magnitude of decay constants, α_1 and α_3, on yield of species B. $\Delta_3 = \alpha_1 - \alpha_3$.

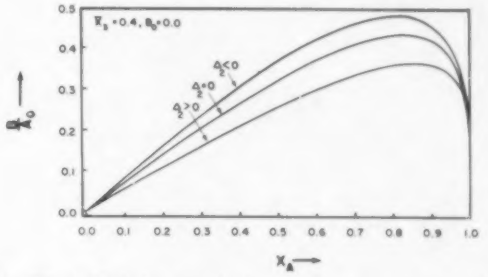


Figure 4. Effect of relative magnitude of decay constants, α_1 and α_2, on yield of species B. $\Delta_2 = \alpha_1 - \alpha_2$.

DISCUSSION

Both the isothermal transport line reactor (TLR) and moving bed reactor (MBR) admit to simple analyses with respect to conversion for any reaction order and extent of mole change due to reaction—for both exponential and hyperbolic decay functionalities.

Yield predictions in a linear triangular reaction network are shown to be dependent upon the relative differences between simultaneous and consecutive decay coefficients. This finding suggests that some merit may well exist in the tactic of relative poisoning, i.e. curtailing product destruction steps relative to its creation step.

Prior work and intuition decrees that any realistic model of the TLR and MBR must include catalyst (or non-catalytic solid) decay. The unimportance of inter-intraphase gradients is manifest, given the particle sizes capable of continuous transport in the TLR. In the MBR, hosting as it does much larger particles, the inter-intraphase issue may well be of importance, as well as non-isothermality.

While we have addressed ourselves to catalysts suffering decay, the issue of gas–solid non-catalytic reaction in the MBR, and therefore TLR, is one worthy of attention. Preliminary analyses of such systems have been set forth in Chapter 7 of Carberry (1976)[3].

SYMBOLS USED

- A reactant concentration (gmol cm^{-3})
- a cross-sectional area of TLR or MBR (cm^{-2})
- B product concentration (gmol cm^{-3})

C by-product concentration (gmol cm^{-3})
d_p particle, pellet diameter (cm)
D intraparticle diffusivity (cm^2 s^{-1})
e expansion due to reaction $= m - 1$.
k reaction rate coefficient (s^{-1})
K rate coefficients ratio
$\bar{K}$ $K \exp(\Delta\theta)$
m product stoichiometric coefficient
n reaction order
P solid/fluid flow ratio $= Q_s/Q_f$
u_0 net solids velocity (cm s^{-1})
u fluid velocity (cm s^{-1})
u_t solids terminal velocity (cm s^{-1})
x conversion of reactant A
z reactor length (cm)

Greek letters

α decay coefficient
ε void fraction
Δ_1 difference; $\alpha_1 - \alpha_i$
θ residence time (s)

REFERENCES

1. Pratt, K. C. 1974 *Chem Eng Sci* 29: 747; Robertson, A. D. and Pratt, K. C. 1975 *Chem Eng Sci* 30: 1185.
2. Varghese, P. and Varma, A., 1979 *Chem Eng Sci* 34: 337.
3. Carberry, J. J. 1976 *Chemical and Catalytic Reaction Engineering* 10 (McGraw-Hill, New York)
4. Fan, L. S. 1981 *Chem Eng J* 21: 179; 1981 *Chem Eng Sci* 36: 1736.
5. Weekman, V. W. and Nace, D. M. 1970 *Am I Chem EJ* 16: 397; see also Weekman, V. W. 1968 *Ind Eng Chem, Proc Des Dev* 7: 90.
6. Shah, Y. T. et al. 1976 *Ind Eng Chem, Proc Des Dev* 15: 165.
7. Venuto, P. and Habib, E. T. 1978 *Cat Rev Sci Eng* 18 (4).

ACKNOWLEDGEMENT

The authors are indebted to Mobil Oil Corporation for their support of this and allied work.

ADDRESS

Correspondence on this paper should be addressed to Professor J. J. Carberry, Laboratory of Catalysis, Department of Chemical Engineering, University of Notre Dame, Notre Dame, Indiana, 46556, USA. Dr Shaikh is now at the Chemical Engineering Department, Petroleum and Minerals University, Dhahran, Saudi Arabia.

The manuscript was received 5 *September* 1983 *and accepted for publication* 15 *November* 1983.

VOL.
62
198

APPLICATION OF MODELLING AND COMPUTER SIMULATION TO PHARMACEUTICAL PROCESSES: THE WILLIAMSON SYNTHESIS

By A. R. WRIGHT

Department of Chemical Engineering, University of Newcastle upon Tyne

A mathematical model is developed for the reaction of a substituted phenol with sodium chloroacetate. The model is based on an actual industrial pharmaceutical process and includes semi-batch operation and closed loop pH control. Agreement between simulation and process results is demonstrated for the limited data available. The model is used to predict operating conditions whereby chemical yields and batch times can be improved.

INTRODUCTION

Chemical reaction engineering is one of the cornerstone subjects of any chemical engineering course and there are several excellent teaching texts available to undergraduates and practising chemical engineers[1]. With the availability of powerful micro-computers there is now an opportunity to consider the application of modelling and simulation techniques to the complex reaction engineering problems of the pharmaceutical industry. The industry has generally relied on experience and empirical techniques for process development.

The majority of pharmaceutical and fine chemical processes are carried out batchwise or semi-batchwise in large steam-heated, water-cooled, stirred pots. A multipurpose plant usually has a number of such reactors producing a variety of established and development products at any one time. Many companies face the problem of scaling up a process from bench to full-scale production often with limited time available for pilot-scale process development and optimisation. The application of reaction engineering to solving these problems is obvious.

There are many reasons why pharmaceutical companies (and others) have not introduced modelling and simulation in the course of process development. Although it is not the intention of this paper to discuss these reasons in detail, some limited comments are appropriate.

Traditionally, much of the process development in the pharmaceutical industry has been made by chemists, with emphasis on mechanistic pathways and product yields rather than kinetics and physical data. Relatively few chemical engineers have been employed, and then mainly in the demanding discipline of production engineering. Thus, even if they had time to do some process simulation, the necessary data are rarely available.

Another possible reason for the relative lack of application of process modelling and simulation in the pharmaceutical industry is that the potential benefits of the techniques are not fully realised and therefore the effort involved cannot be justified. Below are listed some of the benefits which may be gained from the application of these techniques to chemical processes. The list is the result of the author's experiences in simulating actual industrial processes and is therefore subjective and incomplete. The benefits themselves, however, are real and generally applicable.

Why Model a Process?

To Understand the Process. The act of describing a process mathematically often provides a better understanding of the process. Mass and heat balances on a chemical reaction require both a scientific understanding (thermodynamics and reaction mechanisms) and an identification and quantitative appreciation of the process design and operating parameters (e.g. heat transfer coefficient and operating temperature). Through simulation the interaction between chemical reactions and chemical plant may become clearer. This is particularly true in the pharmaceutical industry where the concentrations of the various chemical species, often difficult or expensive to measure on line, may be followed throughout the batch.

To Design the Process. The effect of varying design parameters, and operating parameters, may be simulated and the effect of 'novel' operating conditions may be examined. Pharmaceutical and fine chemical processing tends to be less flexible in terms of varying reactor design, however reaction design is very important in terms of product yields, byproduct formation and batch time. Semi-batch operation involving time varying additions of a number of reactants together with, say, operating temperature sequencing would present a very difficult problem of optimisation if not done by simulation. It must be remembered that the cost of a 'failure' in simulation is the same as that of a 'success'. The same cannot be said for pilot and full-scale studies.

To Study Instrumentation and Control. The (dynamic) process simulation may also be used for controller design by incorporating control loops and control algorithms into the model. Alternatively, by connecting the

© Institution of Chemical Engineers

ADC/DAC channels of the simulation computer to an actual process control system, the proposed plant control may be tested. Also with the high cost of instrumentation the model can be used to identify which parameters have to be measured and those which do not.

To Aid Trouble Shooting. The interaction of chemistry and process variables is often very complex and problems discovered in plant operation or upon scale up may be difficult to explain and so correct. Modelling and simulation techniques may offer a means of examining the effect of varying plant and operating parameters on the process chemistry throught the batch and so improve the operation of an existing plant.

To Study Safety Problems. Simulation provides a good way of answering the question 'what if'. Again it costs no more to predict a dangerous operating condition than a safe one.

Method of Product Development

Perhaps the most important reason for the relative lack of application of process modelling in the pharmaceutical industry lies in the method of product development. During the long period of clinical trials it is common to examine a number of chemical routes simultaneously. As soon as a decision is made to manufacture the product, pressure is on to get it into full production as soon as possible and so maximise patent life. It is at this point that a model would be most useful; yet, unless the model is produced at the pilot stage, which may involve the evaluation of several possible routes, it is not likely to be developed before the process is scaled up. Even if developed after scale-up, however, the model may prove very useful for optimisation or trouble shooting.

This paper presents an application of process modelling and simulation during development of an actual pharmaceutical process, namely, the reaction of a sodium phenol salt with sodium chloroacetate, operating at pilot scale. This type of reaction is known as a Williamson Synthesis[2] and although not uncommon in pharmaceutical processing, it has received little attention in reaction engineering texts. The actual process was operated by Bridge Chemicals and at the time of the work was a pilot scale development. The original purpose of this collaborative venture between Bridge Chemicals and the Department of Chemical Engineering, Newcastle University, was to examine the application of modelling generally and, in particular, to simulate the process with a view to automating the regulation of pH upon scale-up.

The work is partly presented in terms of a case study and a description is given not only of the method and accuracy of the modelling but also of the importance, effort, successes and failures of the exercise.

THE PROCESS

A substituted phenol (ArOH) is reacted with sodium chloroacetate (ClAc) in the presence of sodium hydroxide and sodium iodide (all in aqueous solution). The reaction proceeds via a nucleophilic attack from a phenoxide ion (ArO^-) on the chloroacetate. The process is operated semi-batchwise in what will be regarded as an 'ideal' stirred tank reactor. The pH of the system is controlled throughout the batch at such a level that whilst the primary reaction is maintained, a second process, namely the hydrolysis of sodium chloroacetate, is minimised.

The Reaction Scheme

The model assumes the following chemical reactions:

$$ArOH = ArO^- + H^+ \quad (1)$$

$$H^+ + OH^- = H_2O \quad (2)$$

$$ArONa + ClCH_2CO_2Na \rightarrow \underset{(ClAc)}{} \quad \underset{(ArOAc)}{ArOCH_2CO_2Na} + NaCl \quad (3)$$

$$NaOH + ClCH_2CO_2Na \rightarrow \underset{(HOAc)}{HOCH_2CO_2Na} + NaCl \quad (4)$$

Reactions (1) and (2) are fast equilibrium reactions with equilibrium constants given by:

$$K_1 = \frac{[ArO^-][H^+]}{[ArOH]} \quad \text{where} \quad pK_a = -\log K_1$$

and

$$K_w = [H^+][OH^-] = 10^{-14}$$

In this model pH is defined as $-\log [H^+]$ and not in terms of hydrogen ion activity.

Reactions (1) and (2) may be combined to give the following reaction:

$$ArOH + OH^- = ArO^- + H_2O \quad (1a)$$

Hence we may define an equilibrium constant, K, as:

$$K = \frac{K_1}{K_w} = \frac{[ArO^-]}{[ArOH][OH^-]}$$

From titration data supplied by Bridge Chemicals a pK_a value of 7.5 was obtained, hence:

$$K = \frac{10^{-7.5}}{10^{-14}} = 3.16 \times 10^6 \text{ m}^3 \text{ kmol}^{-1}$$

Reactions (3) and (4) are assumed to be slow and irreversible. Kinetic expressions for their respective reaction rates are discussed below in the section on experimental data.

The Batch Process Scheme

The model is based upon the batch process scheme shown in Figure 1. Initially the stirred tank reactor contains ArOH and NaOH in aqueous solution. At time $t > 0$, chloroacetate is run into the tank via valve 1 in a prescribed manner. In response to pH changes from a set point of 8.5, the controller operates valve 2, thus allowing sodium hydroxide solution to regulate the pH to the set point. The flow rate of alkali is of course variable and may be determined from the control action as discussed later.

VOL. 62 198

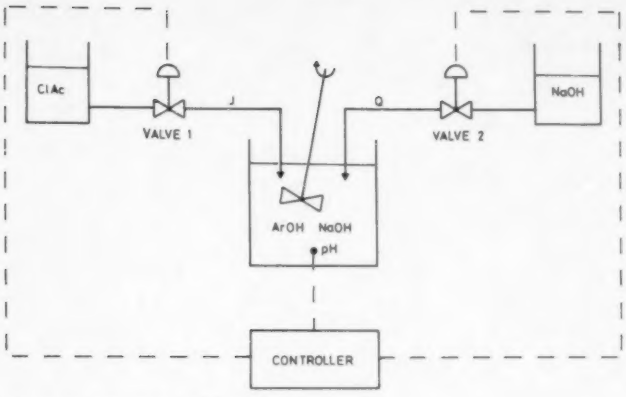


Figure 1. Schematic of the batch process

MODEL DEVELOPMENT AND SIMULATION

Mass Balances

The appropriate differential equations describing the system may be obtained by performing dynamic mass balances on all the chemical species. We may define for the three chemical reactions, (1a), (3) and (4), corresponding reaction rates as R_{1a}, R_3 and R_4. These reaction rates correspond to the rate of disappearance or appearance of particular species and have the units of kmol s^{-1}. Some confusion may arise from the assumption that the fast equilibrium reaction, (1a), has a rate R_{1a}. Because reactions (3) and (4) change the concentrations of the various species involved, reaction (1a) proceeds continuously throughout the batch. Rate R_{1a} is therefore a net rate of reaction due to the continuous imposition of the equilibrium relationship, in circumstances of decreasing ArOH concentration and time varying ArO^-. Details of the mass balances on the process are given in the Appendix. The resultant set of differential equations describing the process are (Alla), (A13), (A4), (A5), (A6), (A7), (A14) and (A15) derived in the Appendix.

Provided the initial conditions in the tank are known and that kinetic data are available for the terms R_3 and R_4 these equations may be solved numerically to predict the concentrations of the various species involved in the reaction throughout the batch together with yields, controller performance, alkali flow rate and consumption. All data used in the model are shown in Table 1.

Kinetic Data

Kinetic data for reactions (3) and (4) were very limited. According to the literature[3], reaction (4) should exhibit a decrease in reaction order with respect to [OH] upon decreasing pH. The reason for this is that the mechanism changes from a simple nucleophilic attack by OH^- at high pH to an internal attack upon the halo group. Indeed laboratory experiments showing alkali consumption during chloroacetate hydrolysis at a fixed pH, and at the process temperature, tended to support this mechanism. A rate expression was assumed to be of the form:

$$R_4 = V k_4[\mathrm{ClAc}][\mathrm{OH}]^N$$

By measuring the rate of alkali addition, whilst regulating pH to a fixed value, an estimate for N may be made. This was done at pH values of 8, 9 and 10. Thus an empirical relationship for the variation of N with OH^- concentration was derived:

$$N = -4.88/\log[\mathrm{OH}]$$

There was some uncertainty in the value for k_4 because of the presence of sodium iodide in the process mixture. It is used to catalyse reaction (3) but also catalyses reaction (4). Again simple laboratory experiments provided an estimate of k_4 which was then further tuned to fit the model.

Reaction (3) is a simple nucleophilic attack of phenoxide ion upon the chloroacetate, a 'Williamson Reaction'. A second order rate expression may be used:

$$R_3 = V k_3[\mathrm{ArO}^-][\mathrm{ClAc}]$$

Although no data were available as to a value for the rate constant a laboratory experiment had been carried out in which the ratio of unreacted phenol to product was determined. These conditions were set up in the model and the value of k_3 adjusted to fit the results. Thus the experimental results indicated a phenol-to-product ratio of 0.8:1 after 1 h and the model gave 0.78:1. Final conversions of phenol to product in production runs

Table 1. Data used in the model.

Kinetic data

$K_3 = 3.16 \times 10^6\ \mathrm{m^3\,kmol^{-1}}$
$k_3 = 1000\ \mathrm{m^3\,kmol^{-1}\,s^{-1}}$
$k_4 = 0.022\ \mathrm{m^3\,kmol^{-1}\,s^{-1}}$

Batch data

Run	P1 and S1	P2 and S2	P3 and S3	S4
Phenol charge (kmol)	0.872	0.704	0.590	0.872
NaOH charge (kmol)	0.792	0.64	0.538	0.792
ClAc conc. (kmol m^{-3})	4.28	4.28	4.28	2.05 kmol charge
ClAc addn time (h)	1.5	2.0	2.0	0
ClAc flow rate (l min^{-1})	6.4	4.31	3.3	0
[NaOH] pH control (kmol m^{-3})	10.98	10.98	10.98	10.98

Controller settings for all runs

$k_c = 30.0$
$T_i = 100$ min
$T_s = 0.1$ min

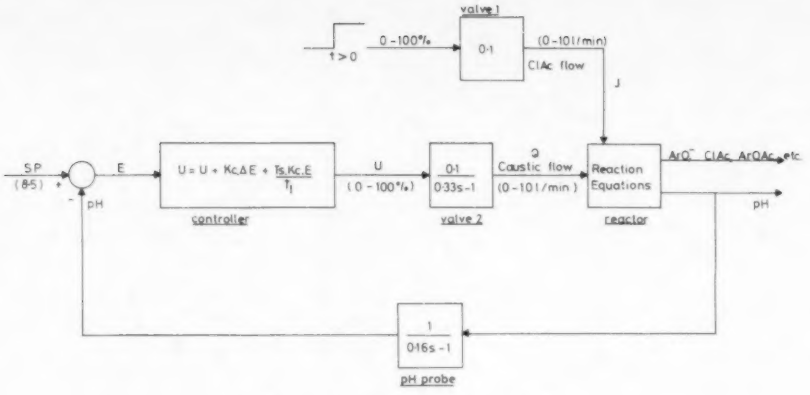


Figure 2. Block diagram of control system

were about 90–95%. The predictions of the model as shown below were very close to this.

Control Action

Reaction rates and product distribution were controlled by pH regulation as no other readily measurable parameter was available. A block diagram of the control scheme is shown in Figure 2. At time $t > 0$ valve 1 is opened to a allow a constant flow rate, (J), of ClAc into the reactor for a pre-specified time. In response to the deviation from a desired pH (set point), detected within the reaction vessel, the controller operates valve 2 to change the flow rate of alkali, Q, thus compensating for alkali consumed in the reaction. Both the pH electrode and valve 2 are assumed to exhibit first order dynamic responses with time constants of 0.16 min and 0.33 min respectively. Such responses are typical of these devices. The control algorithm action used in the simulation was incremental[4] proportional plus integral. The steady state valve flow characteristics were assumed to be linear with gains (0.1 for each) based on the maximum flow rates of the actual process streams and controller outputs normalised within a range of 0–100%.

Numerical Solution

A program was written in Fortran IV and mounted on a Cromenco System 3 mini-computer. A simple Euler technique using an integration step of 0.1 min was used to solve the differential equations.

RESULTS OF THE SIMULATION

The batch scheme, as operated by the company, consisted of initially charging the reactor with a measured amount of the phenol and NaOH solution and then running in sodium chloroacetate solution at a constant rate over a period of about 2 h. During this addition and for a further 3 h the pH of the mixture was controlled to a set point of 8.5 by the manual addition of caustic solution. Only the caustic addition and the final yields were measured and it is these data that are compared with the model.

Figure 3 shows the prediction of the model (with suitable adjustment of k_3) in terms of caustic addition throughout the batch compared to the actual process results. Details of the particular process (run P1) in terms of starting conditions, concentrations and flow rates are given in Table 1. The conditions set up in the simulated batch (run S1) were identical to those of the process.

When different starting amounts of phenol, NaOH and flow rate of chloroacetate were used, the results of the model, Figure 4, still show a good fit. Deviations from the pH set point of 8.5 during the manually controlled real process probably accounts for much of the difference in caustic consumption to that predicted by the simulation. Details of the two batch operations (runs P2 and P3) are given in Table 1. The predicted yields of the three simulated batches (S1, S2 and S3) were 95.3%, 94.1% and 95.7% respectively whilst those of the real processes, (P1, P2 and P3), based on recovered product, were 92.2% 86.5% and 88.3%. It must however be remembered that using the simulation, details of reacting species could be followed throughout the batch operation whilst this was not possible for the real process.

Control Requirement

The controller settings were primarily adjusted to ensure stable operation. Acceptable regulatory behaviour of the system was then achieved by using the

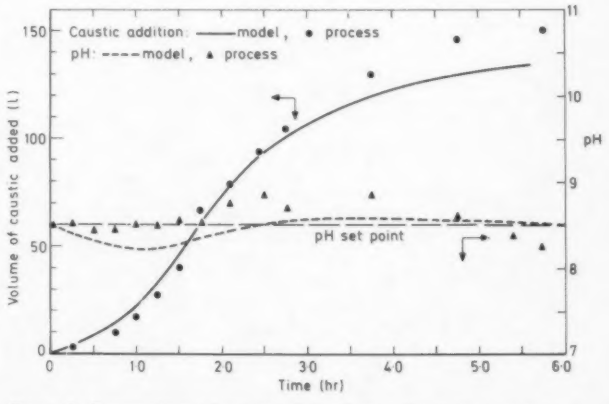


Figure 3. Comparison of results of simulation, S1, with actual process results P1.

VOL. 62 1984

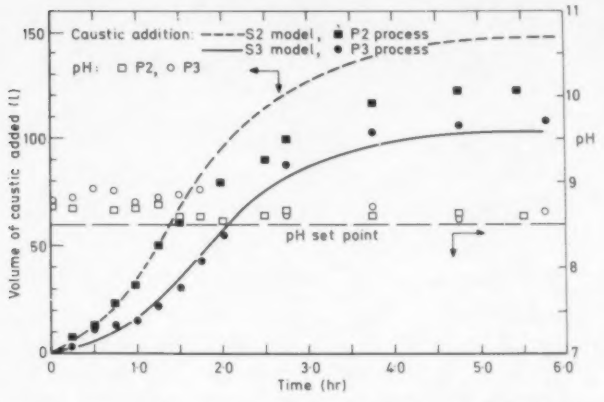


Figure 4. Comparison of results of simulations S2 and S3 with process results P2 and P3.

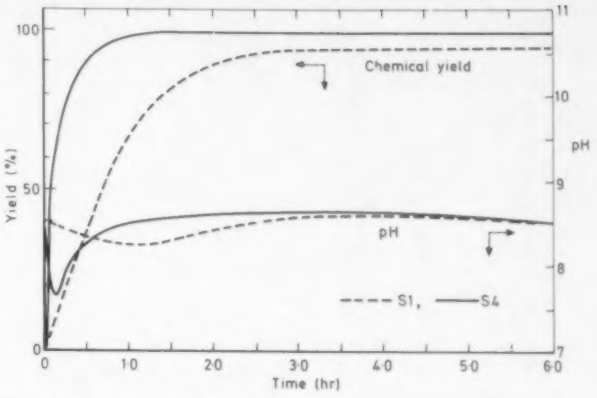


Fig. 5. Comparison of simulated performance of present process, S1, with improved batch operation, S4.

simulation to systematically examine proportional and proportional-plus-integral settings. The performance of the automatic control action may be judged from the predicted pH response shown in Figure 3. It would appear, that because of the considerable buffer capacity of the system, dynamic instability and oscillatory behaviour normally associated with pH control would not be a serious problem with the present batch scheme. The controller settings used in the simulation are given in Table 1. Although the regulatory performance appears sluggish it did ensure that overshoot to high pH conditions (thus favouring HOAc formation) was avoided. No attempt to further tune the control action was made at this stage because the batch process operation was not optimised.

DISCUSSION

The method of batch processing as operated by the company whereby the reactor is first charged with phenol and then chloroacetate is continuously added, is sensible. From equations (A5) and (A6) the ratio of product formation to byproduct formation depends on the ratio of the rate expressions, R_3/R_4:

$$d[ArOAc]/d[HOAc] \propto [ArO^-]/[OH]^N$$

$$\times \text{ or } K[ArOH][OH]^{1-N}$$

Thus product formation is selectively favoured by maximising the concentration of un-ionised phenol, to a much lesser degree by increasing [OH] ($N \approx 0.8$) and is independent of chloroacetate concentration. Initially charging the reactor with phenol partially fulfils these conditions. In this particular process the phenol was very expensive thus high chemical yields were important to the process economics. Using this method of batch processing it was necessary to use almost three times the stoichiometric amount of chloroacetate to obtain yields of about 90–95%.

A possible improvement in chemical yields could be made by reducing the pH set point (thus increasing [ArOH]) though this would reduce the overall reaction rate and increase batch times. However, by starting with a mixture of phenol and chloroacetate and simply adding caustic solution the reaction rate may be increased and so compensate for the effect of the lower pH set point on batch times. For the purpose of producing a lower operating pH in a simulation it was only necessary to maintain the existing set point of 8.5 and use the same controller settings. The control action was far too sluggish for the greatly increased reaction rates and so the pH fell to 7.6 as shown in Figure 5.

The concentrations of the various reactants and products throughout the batch, as predicted by the simulation (run S4), are shown in Figure 6. The corresponding species concentrations for the present batch scheme (run S1) are shown in Figure 7. The two different modes of semi-batch operation are reflected in the considerable differences in concentration profiles. In run S1 an aqueous solution of ClAc is run into the phenolic solution for a period of 90 min, whereas in the case of run S4 the chloroacetate and phenol are made up to the starting volume of run S1 before alkali is added. Improvements in process operation are clearly demonstrated: yield is up from 95% to over 99% (Figure 5) and batch times may be greatly reduced. In addition it may be possible to make savings on ClAc and alkali. Obviously the final choice of starting concentrations and pH profile would depend upon an optimisation study using simulation and experimental trials.

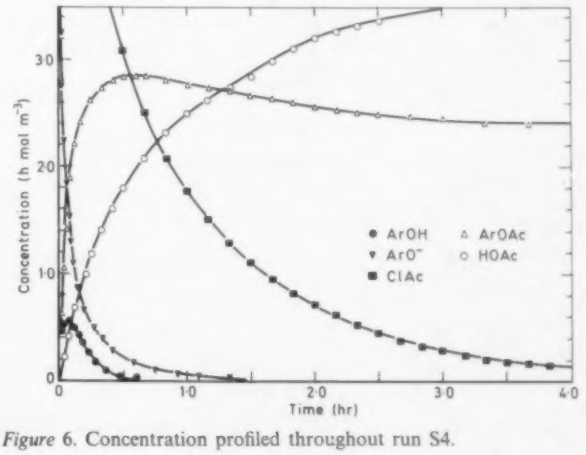


Figure 6. Concentration profiled throughout run S4.

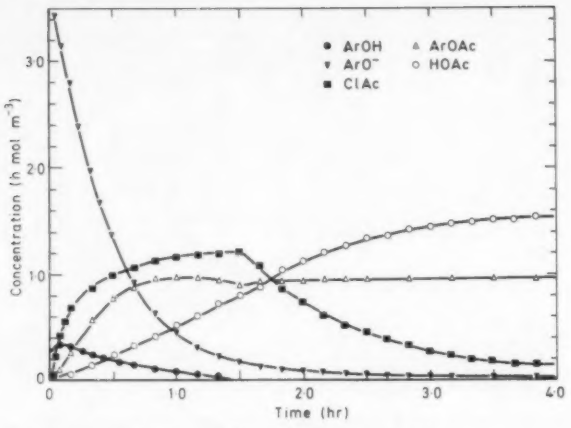


Figure 7. Concentration profiles throughout run S1.

Unfortunately at this point in the work the process was abandoned by the company, which meant that no more experimental results were available to test the model or to explore the predicted improved batch schemes. This exemplifies one of the problems of modelling and simulation of pharmaceutical processes as described in the introduction, i.e. is it worth the effort of producing a model at the development stage when a particular route or even the entire process may be abandoned?

Equilibrium controlled reaction models of the type described in this paper, if done rigorously, involve rather a lot of tedious algebra; this work took something like three man months to complete, excluding laboratory experiments. Many systems involving more conventional kinetics may take considerably less time and effort. This would seem to be not an unreasonable expenditure in manpower compared to the total effort involved at the development stage of a pharmaceutical process. A model could well produce considerable savings in development scale-up and optimisation.

CONCLUSIONS

The application of modelling and computer simulation to an actual pharmaceutical process has been demonstrated. The model gave reasonable agreement with the rather limited experimental data and allowed the method of batch processing to be examined and improved. The work partly served to illustrate some of the benefits to be gained using these techniques together with the difficulties involved.

APPENDIX

Mass Balance

Assuming the reactor to be well stirred the following mass balance may be made.

$$\frac{d\{[ArOH]V\}}{dt} = -R_{1a} \tag{A1}$$

$$\frac{d[OH]}{dt} = -\frac{R_{1a}}{V} - \frac{R_4}{V} + \frac{Q[OH]_{in}}{V} - \frac{[OH]}{V}\frac{dV}{dt} \tag{A2}$$

$$\frac{d[ArO^-]}{dt} = \frac{R_{1a}}{V} - \frac{R_3}{V} - \frac{[ArO^-]}{V}\frac{dV}{dt} \tag{A3}$$

$$\frac{d[ClAc]}{dt} = -\frac{R_3}{V} - \frac{R_4}{V} + \frac{J[ClAc]_{in}}{V} - \frac{[ClAc]}{V}\frac{dV}{dt} \tag{A4}$$

$$\frac{d[ArOAc]}{dt} = \frac{R_3}{V} - \frac{[ArOAc]}{V}\frac{dV}{dt} \tag{A5}$$

$$\frac{d[HOAc]}{dt} = \frac{R_4}{V} - \frac{[HOAC]}{V}\frac{dV}{dt} \tag{A6}$$

These equations form the basic mass balance, however it is necessary to eliminate the term R_{1a}, the net reaction rate of the equilibrium process, from equations (A1), (A2) and (A3). This may be achieved by the introduction of the equilibrium relationship:

$$[ArOH] = \frac{[ArO^-]}{K[OH]} \tag{A7}$$

Differentiating (A7) gives:

$$\frac{d[ArOH]}{dt} = \frac{1}{K[OH]}\frac{d[ArO^-]}{dt} - \frac{[ArO^-]}{K[OH]^2}\frac{d[OH]}{dt} \tag{A8}$$

From equations (A1), (A2), and (A8) we obtain:

$$\left(1 + \frac{[ArO^-]}{K[OH]^2}\right)\frac{d[OH]}{dt} - \frac{R_4}{V} - \frac{Q[OH]_{in}}{V} - \frac{[ArOH] - [OH]}{V}\frac{dV}{dt} = \frac{1}{K[OH]}\frac{d[ArO^-]}{dt} \tag{A9}$$

From (A2) + (A3) we obtain:

$$\frac{d[OH]}{dt} + \frac{d[ArO^-]}{dt} = -\frac{R_3}{V} - \frac{R_4}{V} + \frac{Q[OH]_{in}}{V} - \frac{[ArO^-] + [OH]}{V}\frac{dV}{dt} \tag{A10}$$

From equations (A9) and (A10) the term $d[ArO^-]/dt$ may be eliminated to give:

$$\frac{d[OH]}{dt} = \left(-\frac{R_3}{V} - \frac{(1 + K[OH])R_4}{V} + \frac{(1 + K[OH])Q[OH]_{in}}{V} + Z\right) \Big/ \left\{1 + K[OH]\left(1 + \frac{[ArO^-}{K[OH]^2}\right)\right\} \tag{A11}$$

where Z is given by:—

$$Z = -\frac{K[OH]}{V}\left([OH] + \frac{1}{K}\right)\frac{dV}{dt} \tag{A12}$$

If the right hand side of equation (A11) is called X then

$$\frac{d[OH]}{dt} = X \tag{A11a}$$

and from (A10)

$$\frac{d[ArO^-]}{dt} = -\frac{R_3}{V} - \frac{R_4}{V} + \frac{Q[OH]_{in}}{V} - X - \frac{[ArO^-] + [OH]}{V}\frac{dV}{dt} \tag{A13}$$

VOL. 62 1984

The un-ionised phenol concentration may be then obtained from equation (A7).

Changes in reaction volume are assumed only to be due to reactant inflow and not chemical reaction, hence:—

$$\frac{dV}{dt} = Q + J \tag{A14}$$

(where J = ClAc flow rate and Q = NaOH inlet flow rate) and finally

$$pH = -\log (10^{-14}/[OH]) \tag{A15}$$

REFERENCES

1. Dudukovic M. P., 1982, *Chem Eng Prog* (February).
2. Sykes P., 1970, *A Guide to Mechanisms in Organic Chemistry*, (Longmans, Harlow) 3rd edn.
3. Heindrickson J. M., Hammond G. S. and Cram D. J., 1970, *Organic Chemistry*, (McGraw-Hill, New York) 3rd edn.
4. Bibbero R. J., 1977, *Microprocessors in Instruments and Control*, (Wiley, New York).

ACKNOWLEDGEMENTS

The author would like to thank Bridge Chemicals for their support of this work and for permission to publish the paper, and also Dr Y. Nazer and Dr K. Chisolm formerly of the Department of Chemical Engineering, Newcastle University, for their help in programming the model.

ADDRESSES

Correspondence should be addressed to Dr A. R. Wright, Department of Chemical Engineering, University of Newcastle upon Tyne, Merz Court, Claremont Road, Newcastle upon Tyne, NE1 7RU.

The manuscript was received 25 *April* 1983 *and accepted for publication after revision* 22 *December* 1983

DL.
52
984

CORRESPONDENCE

From
Professor P. N. Rowe (FELLOW)
Department of Chemical and Biochemical Engineering
University College London
Torrington Place
London WC1E 7JE

I do not wish to prolong unnecessarily the correspondence over Dr Joshi's review[1,2,3] but I must insist that my equation (1) is correct and that, in particular, buoyancy force is proportional to suspension density and not to the density of fluid alone. This point is argued thoroughly in reference 2 of my original letter.

He is correct in pointing out that the Richardson-Zaki exponent is calculated on the basis of Re_T and this should stand at the head of the first column in my first table, not Re_{mf}.

REFERENCES

1. Joshi, J. B., 1983, *Chem Eng Res Des*, 61: 143.
2. Rowe, P. N., 1984, *Chem Eng Res Des*, 62: 190.
3. Joshi, J. B., *ibid*, 271.

From
Dr J. J. J. Chen (MEMBER)
Department of Chemical and Materials Engineering
University of Auckland
New Zealand

The following notes, arising from recent papers published in the journal, concern the correlation of hold-up and pressure drop in gas-liquid pipe flow.

Chhabra, Farooqi and Richardson[1,2] found that the average liquid holdup $\bar{R}_L$ was close to the Lockhart–Martinelli curve[3] for high values of X, the Lockhart–Martinelli parameter, but showed vast disagreements particularly in the range $2 < X < 30$. Subsequently, they gave the following for the correlation of holdup for the two-phase flow of air and china clay suspensions in horizontal and vertical pipelines, as well as when the liquid was inelastic and viscoelastic

$$\left.\begin{aligned} \bar{R}_L &= 0.186 + 0.0191X \quad \text{for} \quad X = 1 \text{ to } 5 \\ \bar{R}_L &= 0.1432X^{0.42} \quad \text{for} \quad X = 5 \text{ to } 50 \\ \bar{R}_L &= \frac{1}{0.97 + (19/X)} \quad \text{for} \quad X = 50 \text{ to } 500 \end{aligned}\right\} \quad (1)$$

Apart from having no theoretical basis and being purely empirical, these equations are rather cumbersome and inconsistent in form, and bear no relationship to existing holdup correlations.

Recently, a semi-empirical equation was derived[4,5] of the following form

$$\bar{R}_L = \frac{X^{2/3}}{k + X^{2/3}} \quad (2)$$

and since the voidage $\bar{R}_G = (1 - \bar{R}_L)$,

$$\bar{R}_G = \frac{k}{k + X^{2/3}} \quad (3)$$

The factor k was postulated to be dependent on a number of parameters, including the pipe size, and factors which influence the liquid film, such as the interfacial characteristics and the skewed velocity profile.

Equation (2) was shown to fit the extensive air–water data from a 4.55 cm diameter pipe[6] by taking $k = 6.0$, and the geothermal steam–water data of Harrison[7] obtained from a 20 cm diameter steel pipe when $k = 2.5$. Moreover, when $k = 3.5$, equation (2) becomes identical with the holdup correlation line given by Lockhart and Martinelli[3]. Equation (2) is also superior to the semi-empirical equation recommended by Turner and Wallis[8] for use in preliminary design purposes which is based on a so-called separate-cylinder model. The Turner–Wallis equation matches the Lockhart–Martinelli curve up to about $X = 10$ and is of a slightly more complicated form[4].

To simplify the comparison of the results of Chhabra et al[1,2] and equation (2), suppose that equation (1) is completely representative of the data. Attempts can then be made to fit equation (2) to equation (1). However, it is not possible to achieve good matching if some fixed value of k is assumed. In fact, it was found that the data would obey equation (2) if k was allowed to vary, with the value of k increasing from about 4 to 7.5 when X varied from 1 to 5; between $X = 5$ to 20, k remained reasonably constant; when X exceeded 20, the value of k began to decrease. The variation of k may be represented by the following expressions

$$k = 4.0X^{0.38} \qquad 1 < X < 5 \quad (4a)$$

$$k = 7.5 \qquad 5 < X < 20 \quad (4b)$$

$$k = 33.5X^{-0.5} \qquad 20 < X < 200 \quad (4c)$$

Farooqi and Richardson[1] also pointed out that there were insufficient data in the range of $X = 1$ to 5 to really substantiate the correlation in this range. Their correlation given by equation (1) appears to be levelling off when X approaches unity. However, inspection of the $\bar{R}_L$ data given in Chhabra, Farooqi and Richardson[1,2] indicates that the data in the $X < 20$ range may be reasonably well represented by equation (2) with a constant value of $k = 7.5$.

In Table 1 is shown a comparison of equation (1) with equation (2) where the values of k are given by equation

VOL.
62
198

Table 1. Comparison of the values of $\bar{R}_L$ as predicted by equation (1) and equation (2)

X	$\bar{R}_L$ [equation (1)]	$\bar{R}_L$ [equations (2) and (4)]
1	0.2051	0.2000
2	0.2241	0.2337
3	0.2433	0.2552
4	0.2624	0.2712
5	0.2815	0.2841
10	0.3766	0.3825
20	0.5039	0.4958
30	0.5975	0.6125
40	0.6742	0.6886
50	0.7405	0.7415
70	0.8055	0.8095
100	0.8624	0.8656
200	0.9390	0.9353
300	0.9677	0.9587
400	0.9828	0.9701
500	0.9921	0.9768

(4). The comparison in graphical form is not presented as the two lines are virtually indistinguishable when plotted in log–log form.

Besides being a more convenient form of expression to use, equation (2) which has some theoretical basis, brings in line the data of Farooqi et al. with the data of Chen and Spedding[4,5,6], the steam–water data of Harrison[7], and the generally accepted correlation of Lockhart and Martinelli[3]. All these data may be represented by the same equation and their deviations are accounted for by one single variable k which is postulated as being dependent on a number of factors including pipe size, interfacial characteristics and the skewing of the velocity profile.

Another convenient form of correlation for holdup which has not only been shown to be applicable to horizontal[9,10,11] and vertical flows[12,13], but also inclined flows[13,14], involves treating the parameter $(\bar{R}_G/\bar{R}_L)$ as a function of (Q_G/Q_L) where Q_G and Q_L are the volumetric flow rates for gas and liquid respectively. This form of data presentation has been shown by Butterworth[9] to represent the widely used models such as the homogeneous model, the Zivi model[15], the Turner–Wallis model[8], the Lockhart–Martinelli model[3], the Thom model[16] as well as the Baroczy model[17]. In addition, Chen and Spedding[10,11] showed that this form of expression also represents the Armand model[18], the Zuber–Findlay[19] model, the Nguyen–Spedding model[20] as well as the Smith model[21]. Furthermore, it has been shown that such correlations are also suitable for flow in rough pipes[22] and conveniently used for the determination of flow pattern transitions[23]. However, in the absence of detailed experimental data, consider the data in the form of $(\bar{R}_G/\bar{R}_L)$ in the light of equations (2), (3) and (4). Dividing equation (2) by equation (3)

$$\frac{\bar{R}_G}{\bar{R}_L} = \frac{k}{X^{2/3}} \tag{5}$$

substitution of the value of k from equation (4) gives

$$\frac{\bar{R}_G}{\bar{R}_L} = 4X^{-0.29} \quad 1 < X < 5 \tag{6a}$$

$$\frac{\bar{R}_G}{\bar{R}_L} = 7.5X^{-0.67} \quad 1 < X < 20 \tag{6b}$$

$$\frac{\bar{R}_G}{\bar{R}_L} = 33.5X^{-1.17} \quad 20 < X < 200 \tag{7b}$$

which have the simple basic form

$$\frac{\bar{R}_G}{\bar{R}_L} = AX^{-n} \tag{8}$$

These equations are even more convenient to use than equation (2) since $\bar{R}_L$ may be simply obtained from equation (8) by

$$\bar{R}_L = \frac{1}{1 + (\bar{R}_G/\bar{R}_L)} \tag{9}$$

which is simply the reciprocal of the sum of the values given by equation (8) and unity.

Equation (8) implies that when $(\bar{R}_G\bar{R}_L)$ is plotted against X on a log–log basis, a non-straight line curve will result with slope changing from -0.29 to -1.17. This is shown in Figure 1 on which are plotted the values of $(\bar{R}_G/\bar{R}_L)$ and X as calculated from equation (1).

On the correlation of pressure drop, a very simple correlation may be written as[24,25]

$$\Phi_L^2 = \frac{1}{\bar{R}_L^2} \tag{10}$$

Making use of equation (2) with $k = 3.5$ to conform to the Lockhart–Martinelli line, equation (10) becomes

$$\Phi_L^2 = \left(1 + \frac{3.5}{X^{2/3}}\right)^2 \tag{11}$$

It may be readily shown that the Φ_L^2 values of Chhabra, Farooqi and Richardson[2,26] in the turbulent conditions are well represented by equation (11). Equation (11) is somewhat simpler than the Chisholm equation[27] and has advantages over the Lockhart–Martinelli method which is presented only in graphical forms.

REFERENCES

1. Farooqi S. I., and Richardson J. F., 1982, *Trans I Chem E*, 60: 292–305.
2. Chhabra R. P., Farooqi S. I., and Richardson J. F., 1984, *Chem Eng Res Des*, 62: 22–32.
3. Lockhart R. W. and Martinelli R. C., 1949, *Chem Eng Prog*, 45: 39–48.
4. Chen J. J. J. and Spedding P. L., 1981, *Int. J. Multiphase Flow*, 7: 659–675.
5. Chen J. J. J., 1984, *Int. Comm. Heat Mass Transfer*, 10: 441–444.
6. Chen J. J. J. and Spedding P. L., 1979, *Univ. Aukland Engineering Report* 214.
7. Harrison R. F., 1975, *M. E. Thesis*, Univ. Aukland.
8. Turner J. M. and Wallis G. B., 1965, *Thayer School of Engineering Report* NYO-3114-6, Dartmouth College.
9. Butterworth D., 1975, *Int. J. Multiphase Flow*, 1: 845–850.
10. Chen J. J. J. and Spedding P. L., 1983, *Int. J. Multiphase Flow*, 9: 147–159.
11. Chen J. J. J. and Spedding P. L., 1983, *Proc. 3rd Multiphase Flow and Heat Transfer Symposium-Workshop*, 18–20 April, Miami Beach, Florida, U.S.A.

12. Isbin H. S. and Biddle D., 1979, *Int. J. Multiphase Flow*, 5: 293-299.
13. Spedding P. L. and Chen J. J. J., 1982, *Pacific Geothermal Conference*, Auckland.
14. Spedding P. L. and Chen J. J. J., 1984, *Int. J. Multiphase Flow* (To be published)
15. Zivi S. M., 1964, *Trans ASME, J. Heat Transfer*, 86C: 247–252.
16. Thom J. R. S., 1962, *Int. J. Heat Mass Transfer*, 7: 709–724.
17. Baroczy C. J., 1965, *AIChE CEP Symp. Series*, 61: 179–191.
18. Armand A. A., 1946, *IZV VTI*, 1: 16–23 and *AERE Trans*, 828.
19. Zuber N. and Findlay J. A., 1965, *Trans ASME, J. Heat Transfer*, 87C: 453–468.
20. Nguyen V. T. and Spedding P. L., 1977, *Chem Engng Sci*, 32: 1003–1014.
21. Smith S. L., 1971, *Heat Fluid Flow*, 1: 22–39.
22. Chen J. J. J., 1984 (Submitted for review).
23. Spedding P. L. and Chen J. J. J., 1981, *Int. J. Multiphase Flow*, 7: 729–731.
24. Wallis G. B., 1969, *One-Dimensional Two-Phase Flow* (McGraw-Hill, New York).
25. Owen R. G., and Lee W. C., 1983, *Chem Eng Res Des*, 61: 335–361.
26. Farooqi S. I. and Richardson J. F., 1982, *Trans I Chem E*, 60: 323–333.
27. Chisholm D., 1967, *Int. J. Heat Mass Transfer*, 10: 1767–1778.

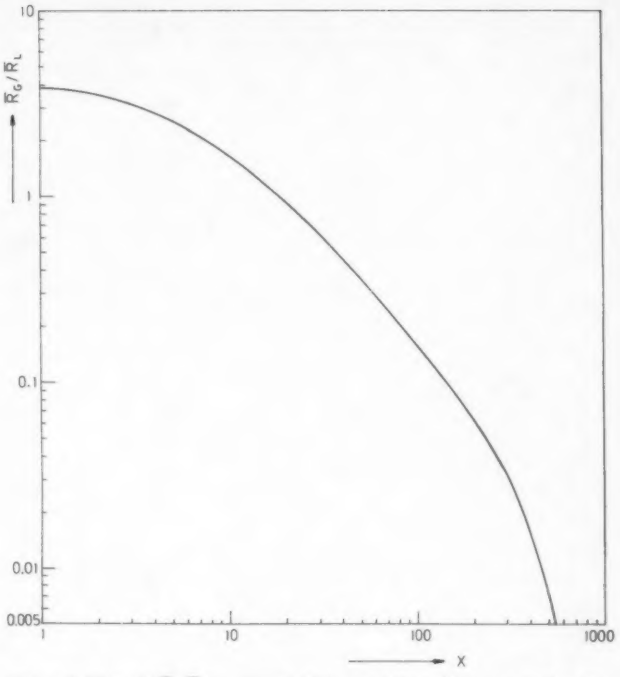


Figure 1. Plot of $(\bar{R}_G/\bar{R}_L)$ versus X. Values calculated from equation (1) due to Farooqi and Richardson[1].

VOL.
62
1984

LIST OF REFEREES 1984

The Editorial Board of *Chemical Engineering Research & Design* gratefully acknowledge the assistance of the following persons who refereed papers submitted for consideration for publication during the period 1 September 1983 to 31 August 1984.

Ashcroft, S. J.
Atkinson, B.

Bailes, P. J.
Bailey, A. G.
Blackburn, D. G.
Boothroyd, A.
Borland, J. N.
Bourne, J. R.
Bowen, J. H.
Bryant, J.
Burgoyne, J. H.

Chhabra, R. P.
Clift, R.

de Reuck, K. M.
Drakesmith, F. G.
Dunnill, P.

Edwards, M. F.

Field, R. W.
Fripiat, J. J.

Geldart, D.
Godfrey, J. C.
Greaves, M.
Green, A. A.

Haselden, G. G.
Holland, F. A.
Hughes, R.

Jeffreys, G. V.
Jenkins, J. D.

Kenney, C. N.
Kenning, D. B. R.
Korchinsky, W. J.

Lee, J. C.
Lees, F. P.
Liapis, A. I.
Lihou, D. A.
Litchfield, R. J.
Lockett, M. J.
Luckham, P.

Mann, R.
Marshall, V. C.
Mason, G.
Masson, H.
McClure, I.
Middleton, J. C.
Mitchell, P. C. H.
Mumford, C. J.

Nienow, A. W.
Nutt, C. W.

Owen, R. G.

Paterson, W. R.
Pickett, D. J.
Porter, K. E.
Poulter, R.
Purchas, D. B.

Quilter, J. A.

Ramshaw, C.
Raza, A.
Reay, D. A.
Richardson, J. F.
Richardson, S. M.
Rippin, D. W. T.
Robinson, E. R.
Rowe, P. N.

Sargent, R. W. H.
Schnurmann, R.
Shearn, R. B.
Stenhouse, J. I. T.

Thomas, W. J.
Thornton, J. D.
Tiu, C.

Walls, J. R.
Wilson, M. P.
Wragg, A. A.

Yates, J. G.

Zuiderweg, F. J.

11TH ANNUAL RESEARCH MEETING
Heat Transfer, Catalysis and Catalytic Reactors

P. J. HEGGS (FELLOW)
Dept of Chemical Engineering, University of Leeds

A. GILMORE (GRADUATE)
School of Chemical Engineering, University of Bath

The 11th Annual Research Meeting of the Institution of Chemical Engineers was held at Bath University on 9 and 10 April 1984. The sessions on Heat Transfer comprised 24 papers while the sessions on Catalysis and Catalytic Reactors included two keynote lectures and 15 papers.

HEAT TRANSFER

The first session, on *Convective Heat Transfer*, was chaired by P. J. Heggs (Leeds University) and the opening paper by D. A. Gardner (Leeds University) described 'Natural convection laminar flow with heat transfer through a vertical plane wall'. This theoretical study relaxed the classical assumption of an isothermal wall temperature, or a prescribed wall temperature profile, and considered the driving force to be condensing steam on one side of the wall which heated either a gas or a liquid on the other side. The results predicted that the total heat transferred was always less than that calculated by the usual sum of resistances approach using the classical correlations. This was more pronounced for heating liquids.

M. J. Tierney (AERE Harwell) presented 'Steady state experiments at very high Rayleigh numbers for turbulent free convection between the horizontal surfaces inside a cubiform cell'. The work is part of generic heat transfer studies into thermal stressing inside engineering structures. Temperature measurements revealed the occurrence of adverse temperature gradients and dye injection studies gave qualitative support for the thermal evidence that a circulation exists within the cell. Most of the temperature drop across the cell occurs within thin boundary layers near the heated floor and cooled roof, with the sides being well insulated.

The final paper in this session considered 'Natural convective heat transfer in large vessels'. M. Dillon (University of Strathclyde) described measurements taken during industrial tests on the cooling of water inside a large vessel by three different methods: free convective to the ambient air, a film of cold water flowing over the outside surface and cooling water through an internal tube coil. Each method altered the circulation patterns within the vessel and the second method resulted in the shortest time to cool the contents to the vessel. The cooling by the ambient air was the longest.

G. S. G. Beveridge (University of Strathclyde) chaired the second session, on *Heat Transfer Involving Phase Change*, and A. R. Akhanda (UMIST) presented the first two papers on 'Forced convection boiling from roughened surfaces' and 'Enhanced heat transfer from artificially prepared ribbed surfaces'. The aim of the first investigation was to determine the effect of mass flow rate, inlet subcooling and surface roughness on the heat transfer coefficient in forced convection boiling of water in a rectangular channel heated from one side only. The experimental data showed an augmentation in the heat transfer rate only to a surface roughness of 0.78 μm, and a simple correlation is presented which fitted the data to $\pm 25\%$. In the second investigation, ribbed surfaces were used in the same apparatus, and the effects of spacing of transverse rectangular ribs were explored. Spacings of less than 1.0 mm showed little improvement in heat transfer performance.

'Heat transfer in vertical condenser-subcoolers' in the production of malt whiskey was described by M. R. Bamforth (University of Strathclyde). Previous calculations had shown that 17% of the total fuel requirements of the distillery might be saved, if the outlet temperature of the condenser cooling water could be raised from 50°C to around 80°C. The experimental work revealed that it was possible to operate with high cooling water outlet temperatures and the height of the loop seal appeared to have little effect. Reasonable agreement between measured and predicted values of the overall heat transfer coefficient were obtained, with an average difference of +9.5%.

The final paper in this session considered 'The direct condensation of steam from steam-air mixtures on a low pressure solid cone water spray' and was delivered by E. V. Kaimakamis (Loughborough University). A countercurrent spray condenser was operated over a range of conditions: spray nozzle height, steam, air and water flow rates. The experimental data were presented in terms of a condenser volumetric heat transfer coefficient, which increased with higher water and steam flow rates, but decreased with greater nozzle height and larger water flow rates.

The next two sessions were chaired by B. Linnhoff (UMIST) and the scenario of *Heat Exchanger Networks* (HEN) came first. D. W. Townsend (UMIST) discussed 'Surface area targets for HEN' and considered the 3-fold

© Institution of Chemical Engineers

targeting concept: energy recovery targets, number of units targets and area targets. The first target needs to be maximised, whilst the other two need to be minimised. A new total network area target technique is proposed linked to individual stream loads in a section of the composite curves, and their own heat transfer coefficients. This allows the calculation of the target area to be independent of any network design.

S. Ahmad (UMIST) continued the theme of cost targets in 'Overall cost targets for HEN'. The total annualised cost: annual operating and capital charges are dependent on the minimum approach temperature ΔT_{min} used in HEN design. The optimum ΔT_{min} with respect to an assumed rate of return on capital can be found from stream and cost data, and thus the cost optimisation is achieved before design which makes network evolution also unnecessary.

T. N. Tjoe (UMIST) next considered 'HEN retrofits' and presented the basic philosophy of an extensive new development in the field of retrofit design of HEN. To ensure maximum reuse of existing equipment, the procedure evolves retrofit schemes starting from the existing network rather than a new minimum energy recovery design. Energy targeting coupled with payback expectations is used with ΔT_{min} to redesign the network within the bounds of process modifications and payback time.

'HEN with process modifications' dealt with a different aspect of the HEN design and S. Parker (UMIST) departed from the normal procedure of accepting the composite curves at face value, and considered changing them in order to improve the HEN. Here streams are arranged to move across the pinch by manipulating process conditions, e.g. pressure levels in distillation columns. A case study involving part of the flowsheet of an acetic anhydride process was used to illustrate the approach for retrofitting a process.

Finally, R. J. Morton (UMIST) provided insight into a better understanding of the fundamental physical principles governing energy interactions in overall sites in the paper entitled, 'Individual process improvements in the context of site-wide interactions'. He concluded that a general heat and power policy aimed at making the best use of the thermodynamic potential of the fuels supplied to the site should be devised. Also process improvements should always be assessed with reference to the economy of the total site, due to internal charging procedures and the demand pattern.

In the final session of the first day, dealing with *Heat Transfer at High Temperatures*, G. E. Andrews (Leeds University) reported experimental investigations into 'Impingement cooling using large arrays of holes' with particular reference to wall cooling of future gas turbine combustion systems operating at higher turbine entry temperatures. The experiments were designed to check the exponent of the Reynolds number in a correlation for predicting the impingement heat transfer coefficient. The results were interpreted in several ways and the methods of defining the values of various temperatures have a significant effect on the exponent.

'Transpiration and full coverage discrete hole film cooling' was discussed next by A. Asere (Leeds University). Again an experimental investigation was described whereby the air firstly cools the wall by passing through the holes, and secondly, protects the wall by forming a cool layer of gases adjacent to it. Three discrete hole arrangements and a rigid mesh were investigated, and the results compared with a previous investigation.

On the second day, the two sessions were chaired by M. A. Patrick (Exeter University) and the first paper on *Heat Transfer Simulation*, by O. Ta'eed (Leeds University) expounded 'A general systems approach to heat transfer and fluidised bed reactors: an application of catastrophe theory'. The ideas of catastrophe theory were reviewed and then applied to heat transfer for fluid flow through circular tubes over the laminar, transition and turbulent regimes, and finally, to fluidisation, considering the static bed, incipient, bubbling, slugging and turbulent fluidisation.

R. A. Colledge (Cambridge University) discussed the use of the swollen polymer technique to determine mass transfer coefficients at the wall of a packed bed experimentally and to relate these to heat transfer coefficients in the paper entitled 'Heat transfer at the wall of a packed bed: a j-factor analogy established'. Heat transfer experiments themselves create many difficulties in determining the wall coefficient, and the swollen polymer method was demonstrated to be an attractive means of obtaining data on mass transfer from a solid surface.

D. Burns (Leeds University) described the 'Simulation of the Leeds experimental regenerator apparatus' in an attempt to highlight the observed anomaly between experimental and theoretical values of thermal effectiveness at cyclic equilibrium. The simulation accounted for heat transfer to and from the peripheral pipework, and heat loss from the pipe work and the regenerator itself. Comparison with experimental findings indicated that the heat loss and the thermal storage in the pipewall were the major contributors to the anomaly.

In the final paper of this session, R. J. B. Hilton (University of York) discussed 'Improved mathematical modelling of thermal regenerators'. A lumped heat transfer coefficient for use in the simple regenerator theory was developed, which varies both with position and time, and is easily calculable. This provides accurate predictions of exit temperatures at all times, and may be used in calculations when the operating conditions vary.

The last session of the meeting dealt with *Mass Transfer Modelling* and was initiated by A. Ziai (Queen Mary College, London) who described 'Problems of electro-chemical modelling of heat transfer processes'. The argument centred on the theory of similitude and that the conditions of singularity are identical and the similarity criteria are invariants. Correlation rearrangements were presented for flow with fully developed layers and developing boundary layers.

J. G. A. Pembery (Exeter University) reported on 'The modelling of heat transfer in nuclear reactor core geometrics using the electrochemical technique'. Four types of physical model finned rod, bulged rod, necked tube and ballooned cluster, were used to approach the real situation progressively. The experimental results provided detailed information on mass transfer distribu-

VOL. 62 1984

tions, and hence, by use of appropriate analogies, on heat transfer.

'Mass-transfer modelling of two-phase heat transfer in sudden expansions' was presented by S. M. Chouikhi (Exeter University). The data presented highlighted the enhancing effect of the gas phase on the liquid-wall mass transfer rates in two-phase flows downstream of sudden changes in pipe cross-section. The magnitude and location of the peak transfer rate are dependent upon the overall volumetric quality of the two-phase flow at a given liquid flow rate.

N. G. Hyne (Edinburgh University) reported on 'The use of electronic speckle pattern interferometry for convective mass-transfer measurement: studies of transfer to a turbulent air jet impinging on a plane surface'. The technique uses a non-photographic interferometric method employing a helium-neon laser and a television camera. The experimental investigation used the electron speckle pattern interferometry to obtain the rate of recession of a swollen polymer subjected to an impinging turbulent air jet. The preliminary results indicate that the procedure is capable of providing local convective transfer coefficient data of high precision and spatial resolution.

Finally, M. R. Butcher (Coventry Polytechnic) described 'A comparison of preliminary measurements of mass and heat transfer made in a tube' for predicting forced heat transfer in recuperative burners. Two methods were compared: the swollen polymer technique with an electronic speckle pattern interferometer and a composite of a liquid-crystal sheet and a thin-heater element. Preliminary experimental results have revealed that the uncertainty estimates for the liquid-crystal method are much smaller than those for the swollen-polymer technique.

M. Bamforth (Strathclyde University) was awarded the Annual Research Meeting Prize for the best presentation by a registered student in the Heat Transfer Section.

CATALYSIS AND CATALYTIC REACTORS

The first session, on *Applied Catalysis* (*General*), was opened with a keynote lecture by N. D. Parkyns (British Gas Corporation) entitled 'New lamps for old? Recent developments in synthetic fuel production'. The lecture outlined the reasons why research is being undertaken in the field of synthetic fuel production. This was followed by a discussion of the processes used, paying particular attention to the Fischer-Tropsch process and giving examples of industrial applications.

G. R. Assar (Heriot-Watt University) presented the opening paper 'Reactivity and selectivity of alumina supported MoO_3 and Bi-Mo catalysts for the oxidation of methane' prepared jointly with C. W. Nutt. The paper examined the effects of different conditions during the preparation of the alumina support. The optimum content of MoO_3 catalyst was determined for the oxidation of methane to methanol and formaldehyde using the alumina support which was mechanically sound. Basic reaction studies were discussed, showing increased catalyst selectivity with the addition of bismuth.

A. J. Rennison (University of Bath) presented a paper by F. S. Stone and himself on 'Hydrogenation of carbon monoxide over reduced cobalt containing spinel catalysts'. This paper linked up with the keynote lecture by N. D. Parkyns discussing a way in which syngas, carbon monoxide and hydrogen derived from coal by gasification could be used as a feedstock for synthetic fuel production. Two catalysts were examined, $Co_{0.05}Mg_{0.95}Al_2O_4$, 5 Co/spinel, and $Co_{0.02}Mg_{0.80}Al_2O_4$, 20 Co/spinel. The catalysts were almost identical in terms of selectivity which was thought to be due to negligible particle size effects under the conditions investigated. In the $CO:H_2$ ratio range of 1:4 to 1:1 the selectivity, in terms of producing hydrocarbons other than methane, was shown to increase with increasing carbon monoxide content. The catalysts were said to display good stability and a greater resistance to coking than corresponding Co/MgO catalysts.

'Coking in catalyst pores from fundamentals of diffusion and reaction' by R. Mann and D. J. Bosworth (UMIST) was presented by D. J. Bosworth. As the title suggests, this was fundamental investigation of the processes of carbon deposition in cylindrical catalyst pores. Despite the basic approach, the results were said to display some physically observed phenomena. The greatest problem with the initial approach, it was admitted, was that the pores in a catalyst support are not simple single cylindrical holes of constant radii, but a series of interconnecting pores of varying radii. Random pore models had not yet been applied to the analysis, which might gain a better model for coke laydown. The problems of incomplete catalyst regeneration and its effect on coking had not yet been studied.

D. Sirl (University of Bath) presented his paper 'The application of bifurcation theory to the modelling of a catalytic monolith reactor' and discussed the application of recent mathematical techniques to complex reactor models. The mathematical techniques were applied to catalytic monolith reactors which are being developed to be used in car exhaust systems for the removal of carbon monoxide and oxides of nitrogen. Bifurcation theory was used to predict the oscillatory behaviour which is observed with the platinum catalysts used. The large number of complex equations were solved numerically by computer program.

A. E. Okoro (UMIST) presented a study on 'optimal operation of industrial multistage gas/solid catalytic acetaldehyde reactors: multiple water/steam injection control'. Examples of industrial multistage reactors were used to illustrate the problems of determining the optimal conditions for plant operation. Once the reactor conditions have been defined, it was argued, traditional maximum and minimum finding techniques do not always work because of conditions outside the range of feasible solutions. The paper showed a way in which this particular problem was overcome and applied to a working reactor system.

J. Watson (Teesside Polytechnic) opened the session on *Biochemical Reactors* by describing the 'Autolysis of *Bacillus amyloliquifaciens*' prepared with G. Street and R. H. Cumming. A method was described which uses the autolytic enzymes normally present within the cell to

disrupt the cell envelope allowing the isolation of intracellular enzymes. Physical and chemical methods were said often to be costly in terms of equipment, chemicals, energy and the loss of sensitive enzymes through denaturation. The proposed method was claimed to have the advantage of being a gentle, cheap and selective method. A reactor model was proposed with a growth vessel continually feeding a lysis vessel. An ultrafiltration unit would remove the cellular debris to leave a protein extract. The autolysis of *Bacillus amyloliquifaciens* was initiated by halting the supply of oxygen.

Long chain esters are currently manufactured by reacting a fatty acid and an alcohol at temperatures up to 250°C for up to 20 h. High temperature processes like this have high energy costs, and long reaction times make it possible to degrade the ester. T. Knox (Paisley College of Technology) who presented 'Synthesis of long chain esters in a loop reactor system using a fungal cell-bound enzyme' by K. R. Cliffe and himself offered an alternative route. This paper was the first stage of the evaluation of a low temperature route for the manufacture of long chain esters using lipolytic enzymes as a catalyst. The fungal mycelium used in this investigation was *Rhyzopus arrhizus*. A loop reactor was preferred to a fixed bed reactor for a number of reasons, including better pressure drop characteristics, easier study of reaction kinetics and the need to remove water from the system. Water was removed by passing the reactor exit stream through a column containing a molecular sieve.

The session was concluded by R. England (University of Bath) who presented a paper by J. Hubble and himself on 'Continuous regeneration of adenosine nucleotides in enzyme catalysed reactors'. Approximately 40% of the two thousand known enzymes require cofactors. If industrial use is to be made of enzymes as catalysts, the problems associated with the provision of the necessary cofactors must be investigated. This paper covered the derivatisation and regeneration of adenosine 5′-diphosphate and adenosine 5′-triphosphate.

Fluidised Bed Reactors were the subject of the next session. A widely held belief is that all gas in excess of that required just to fluidise the bed passes through as bubbles which originate from the orifices of the distributor. This is the basis for two-phase theory. Yang Xiao-tian (University College London) presented 'An experimental study of reaction in the distributor region of a fluidised bed reactor' prepared with D. G. Horne and J. G. Yates, which examined a deviation from this theory. Evidence was presented suggesting that in the region of the distributor some two-thirds of the excess gas flow penetrates the dense phase close to the point of entry causing its voidage to increase above the stable value at minimum fluidisation. At higher positions the bubble flow was said to approximate to the two-phase model. The importance of this mechanism is in the enhanced rates of reaction due to the increased gas-solid contact in the expanded dense phase of the bed.

The session was brought to an interesting conclusion by O. Ta'eed (University of Leeds) who presented a paper by N. Mann. B. M. Gibbs and himself on 'Determining the hydrodynamic characteristics of fluidised bed reactors'. It was argued that despite extensive research into the subject there are very few examples of fluidised bed reactors in industry in this country. The suggestion was made that a far more pragmatic approach was required to serve both academic research and industrial application. A cheap, simple-to-use two dimensional bed filled with sand was used to obtain particle tracks. A small amount of sand was coated with a fluorescent dye and was tracked using UV light and a camera. It was conceded that there were limitations to the bed, in particular the boundary effects due to its two dimensional structure. The results did seem to be more qualitative than quantitative but they did allow the solution of simple reactor problems such as in the effects of introducing tubes into the bed.

The final session on *Novel Applications and Packed Bed Reactors* was opened with a keynote lecture by D. L. Cresswell (New Science Group, ICI) discussing 'Developments in reactor modelling'. The lecture outlined the points to be considered when designing a chemical reactor. A number of items were stressed, including the problems of obtaining accurate catalyst data and the need for a flexible design to cope with any decreases in catalyst selectivity and activity with age. The lack of theoretical understanding in heat and mass transfer was discussed. A large number of correlations are empirical because of changes in the rate limiting step.

K. Halliday (University of Cambridge) presented 'New studies of flow in packed beds' prepared with W. R. Paterson and N. B. Griffiths. These studies concentrated on packed bed catalytic reactors with a low tube-to-particle diameter ratio. The lower the value of the ratio the greater the zone of high voidage near the wall. This zone gives rise to two important consequences, (i) the channelling of flow through the high voidage zone reducing gas-solid contact, and (ii) reducing radial heat transfer. As part of the studies stratified packed beds were investigated. The interpretation of packed bed behaviour is dependent on understanding the voidage distribution and the resulting velocity distribution. Established methods of determining the voidage distribution were used but because existing velocity distribution methods give conflicting and inaccurate results a new method was developed. The 'occluded bed method' compares the pressure drop across the whole bed with the pressure drop across specific areas of the bed. Firstly, pressure drop readings were taken for the bed at a series of flowrates, then, first the wall zone and finally the core of the reactor were occluded by wax, and pressure drop readings taken.

A. Guidom (University of Leeds) presented a paper by C. McGreavy, E. K. T. Kam, E. A. Foumeny and himself of the 'Measurement of concentration, temperature and velocity profiles in flows through packed beds'. New non-intrusive methods were explained for determining velocity, temperature and concentration profiles using laser techniques. Local gas velocities were measured using laser doppler velocimetry while temperature and concentration were measured by a recently developed technique based on coherent anti-Stokes Raman scattering. To allow measurements to be made optical pathways were required. The effects of introducing these pathways had not yet been studied.

VOL. 62 198

The reason for research interest in the catalytic conversion of synthesis gas into hydrocarbons had been given in the keynote lecture by N. D. Parkyns. The traditional method, the Fisher-Tropsch synthesis, has the problem of low selectivity. However, using methanol as an intermediate catalytic conversion produces hydrocarbons predominantly in the gasoline boiling range. The reasons for the paper presented by J. G. Pickering (University of Cambridge) on the 'Computer automated study of the kinetics of methanol synthesis' prepared with C. N. Kenney were twofold. The development of a compact computer-controlled system for the study of catalyst behaviour and the use of the system to study methanol synthesis. A summary of the results already obtained with the system was given with the paper.

J. Santamaria-Ramiro (University of Salford) presented a paper on the 'Characterisation of catalysts during coking in fixed bed reactors' prepared with colleagues A. Byrne, R. Hughes and V. Dakessian and by W. A. J. Seymour and C. J. Wright (A.E.R.E. Harwell). The distribution of coke within a reactor was measured by a number of methods. The coke was measured by oxidation and analysis of the resulting gases and by neutron radiography and counting. Profiles produced by each of these methods were similar but the neutron methods have the advantage of being non-invasive.

The final paper was a description of a method for 'Heavy oil cracking' presented by S. Acey (Teesside Polytechnic) and prepared with J. C. K. Lee and J. R. Walls. The problems with heavy oil as a feedstock were acknowleged as sulphur and metal content, and viscous residues causing transport difficulties. The steam reforming method studied was heated by electrical induction but the effect of metal deposited on the catalyst had not yet been studied.

K. Halliday (Department of Chemical Engineering, University of Cambridge) was awarded the Annual Research Meeting Prize for the best presentation by a registered research student in the Catalysis Section.

OL.
62
984